SEISMIC DEMANDS ON GRAVITY-LOAD COLUMNS OF REINFORCED CONCRETE SHEAR WALL BUILDINGS

by

POUREYA BAZARGANI

B.Sc. Shiraz University, 2006

A THESIS SUBMITTED IN PARTIAL FULFILLMENT OF
THE REQUIREMENTS FOR THE DEGREE OF

DOCTOR OF PHILOSOPHY

in

THE FACULTY OF GRADUATE AND POSTDOCTORAL STUDIES
(Civil Engineering)

THE UNIVERSITY OF BRITISH COLUMBIA
(Vancouver)

April 2014

Abstract

In shear wall buildings, walls serve as the seismic force resisting system while the gravity-load system consists of columns that are primarily designed to carry the weight of the building through frame action and are not detailed for seismic ductility. Design codes require the gravity-load system to be checked for deformation compatibility as the building deforms laterally. The process of checking the columns for adequate deformability still requires more work.

In addition to flexural deformations, components such as shear strain and rotation of the foundation contribute significantly to lateral deformations in the wall plastic hinge zone. Shear strains in flexural shear walls are analytically shown to be a result of large vertical tensile strains in areas with inclined cracks. Based on this theory, a simple design-oriented method for estimating shear strain profile of flexural shear walls is formulated, the accuracy of which is verified against experimental results from works of other researchers.

Rotation of shear wall foundations is studied through performing about 2000 Nonlinear Time-History Analysis (NTHA) considering the nonlinear interaction between the foundation and the underlying soil. Behaviour of shear walls accounting for foundation rotation is explained with emphasis on relative wall to foundation strengths. A simple method for obtaining the monotonic foundation moment-rotation response is formulated which is then used in a simple step-by-step method for estimating foundation rotation in a given shear wall building.

Curvature demand on columns pushed to a given wall deformation profile is studied using a structural analysis algorithm specifically designed for the task. In the absence of wall shear strain or significant foundation rotation, column curvature demand is found to remain close to the wall maximum curvature. Wall shear strain and foundation rotation are found to cause severe increase to column curvature demand. In a parametric study on column curvature demand, parameters including wall length, column length, height of column plastic hinge zone, first storey height, fixity of the column at grade level, and the effect of members framing into the column are studied. Several simple expressions for estimating column curvature demand are derived that can be implemented in design.

Preface

Unless otherwise noted below or in the body of the thesis, the research presented in this document is an original contribution by the author, Poureya Bazargani under the supervision of Professor Perry Adebar at the University of British Columbia, Vancouver. Research needs were identified and the research program was designed and developed under the guidance of Professor Adebar.

A condensed version of CHAPTER 2 is published in Adebar et al. (2012) of which I am a coauthor. A journal paper summarizing the content of CHAPTER 2 was submitted to the ASCE Journal of Structural Engineering in February 2014 of which I am the author. Computer simulation results of CHAPTER 3 had a direct impact on the foundation design clauses of the 2015 edition of the National Building Code of Canada (NBCC). Parts of CHAPTER 3 and CHAPTER 4 were published in Adebar et al. (2014) of which I am a coauthor. Figure 3.3 is reprinted from Anderson (2003) with written permission from D. L. Anderson. Data in Table 3.8, Table 3.9, and Table 3.10 was taken from Das (2001). Figure 3.15, Figure 3.16, and Figure 3.17 are reprinted from Negro et al. (1998) with written permission from P. Negro. Figure 4.1 is taken from Allotey and El Naggar (2003) and reprinted here with El Naggar’s permission. A more detailed version of the figure appears in FEMA 274. Parts of CHAPTER 6 and CHAPTER 7 were published in Bazargani and Adebar (2010) of which I am the author. Versions of Figure 5.13, Figure 7.2, and Figure 7.10 were published in Adebar et al. (2010) of which I am a coauthor.

Table of Contents

List of Tables

List of Figures

List of Symbols

a	:	Depth of uniform stress block underneath the foundation at factored soil bearing capacity in Chapter 3, depth of uniform stress block underneath the foundation in Chapter 4
A_g	:	Gross concrete cross-sectional area
Avg. Max.	:	Average of the maximum response quantity from each EQ
B	:	Foundation width
b	:	Column width
b_w	:	Wall width
c	:	Wall ultimate concrete compression depth in Chapter 2, soil compression depth underneath the foundation in Chapter 3, concrete compression depth in Chapter 5
C	:	QzSimple1 material type factor
C_r	:	QzSimple1 material type factor
C_t	:	Creep coefficient
E	:	Soil modulus of elasticity
e	:	Eccentricity of compressive load on foundation
E_{ct}	:	Concrete secant stiffness
EI	:	Column effective flexural stiffness
EI_g	:	Flexural stiffness of gross cross section
E_s	:	Elastic modulus of reinforcing steel
E_{sh}	:	Reinforcing steel strain hardening stiffness in VecTor2
e_{sh}	:	Reinforcing steel strain at the onset of strain hardening
$e_{\theta y}$	:	Foundation rotational stiffness embedment factor
f_c	:	Concrete stress
f'_c	:	28-day concrete compressive strength
f_{cr}	:	Concrete cracking strength in tension
F_u	:	Reinforcing steel ultimate tensile strength
F_y	:	Reinforcing steel yield strength
G	:	Soil shear modulus of elasticity
G_0	:	Small-strain soil shear modulus of elasticity
G_{eff}	:	Effective soil shear modulus of elasticity
H	:	Storey height
h_1	:	First storey height
h_f	:	Floor height
H_{st}	:	Wall uniform storey height
H_w	:	Total wall height
h_w	:	Wall height
I_e	:	Wall gross second moment of inertial
I_g	:	Wall effective second moment of inertial
I_y	:	Foundation second moment of inertia

k : Factor relating wall shear strain to curvature
k_e : Initial elastic stiffness of QzSimple1 soil springs
K_e : Effective foundation rotational stiffness
K_{oc} : Secant foundation rotational stiffness to the point with M_{oc} and θ_{oc}
k_θ : Soil reaction modulus
$K_{\theta y}$: Initial elastic foundation rotational stiffness accounting for foundation embedment
$K'_{\theta y}$: Initial elastic foundation rotational stiffness resting on the soil surface
L : Foundation length
l : Column length
L_0 : Clear span of members framing into the column
l_e : Length of heavily reinforced regions at the ends of rectangular walls
l_{pc} : Plastic hinge length of damaged column with uniform inelastic curvatures over the height
l_{pc}^* : Plastic hinge length of undamaged column with linearly varying inelastic curvatures over the height
l_{pw}^* : Wall plastic hinge length with linearly varying inelastic curvatures over the height
l_w : Wall length
L_w : Shear wall length
l_w : Wall length
m : Wall lumped mass at floor slab levels
M : Bending moment
M_{85} : Foundation overturning strength assuming a uniform stress block with bearing pressure of $0.85q_{ult}$ at the "toe" of the foundation
M_b : Bending moment at column base
$M_{elastic}$: Bending moment at the onset of inelastic behaviour
M_n : Nominal bending strength
M_{oc} : Overturning capacity of the foundation assuming uniform stress block at factored soil bearing capacity
M_{RSA} : Maximum bending moment demand of the wall with a fixed base calculated from response spectrum analysis using 70% of the uncracked flexural stiffness
M_y : Wall probable flexural strength accounting for steel strain hardening
N : Number of storeys
n : QzSimple1 material type factor
P : Compressive axial force carried by the shear wall uniformly distributed over the height of the wall in Chapter 3, compressive load on foundation in Chapter 4, compressive axial load on cross-section
P_f : Factored compressive axial load demand
P_i : Column storey force
P_{ns} : Net steel force
$P_{r\,max}$: Maximum factored compressive axial resistance
P_s : Axial load associated with seismic forces
q : Uniform bearing pressure underneath the foundation under gravity load (service) condition in Chapter 3, soil bearing pressure in Chapter 4
q_a : Allowable uniform bearing pressure underneath the foundation under gravity load (service) condition
q_f : Factored toe bearing pressure used to size the foundation for overturning
q_{max} : Maximum soil bearing pressure at the "toe" of the foundation

q_{ult}	:	Ultimate soil bearing capacity used in nonlinear dynamic analysis
$q_{unif.}$	:	Uniform bearing pressure of soil equivalent rectangular stress block
R_f	:	Ratio of maximum wall bending moment at base from RSA to foundation overturning capacity
R_w	:	Ratio of maximum wall bending moment at base from RSA to wall bending moment strength at base
s	:	Uniform foundation settlement due to compressive axial load on shear wall
$T_{estimate}$	:	Estimated first period of vibration of the wall-foundation system using square root of sum of squares of fundamental periods of the fixed base wall and the flexible foundation supporting a rigid wall
t_f	:	Wall flange thickness
T_f	:	First mode period of the wall-foundation system with the wall assumed to be rigid
T_{model}	:	First mode vibration period of the wall-foundation system from model
T_s	:	First mode period of wall-foundation structure
t_w	:	Wall web thickness
T_w	:	First mode period of the fixed-base wall
V	:	Shear force in members framing into the column induced due to framing action
V_i	:	Column storey shear force
V_s		Soil shear wave velocity
w_f	:	Wall flange width
Z	:	Compressive displacement of QzSimple1 soil springs
Z_{50}	:	Displacement at which 50% of the ultimate soil bearing capacity is mobilized
Z_e	:	Elastic compressive displacement of QzSimple1 soil springs
Z_{max}	:	Maximum soil compressive displacement at the "toe" of the foundation
Z_p	:	Plastic compressive displacement of QzSimple1 soil springs
α	:	Soil equivalent rectangular stress block pressure factor in Chapter 4, ratio of column flexural stiffness to that of the members framing into it in Chapter 7
α_1	:	Equivalent rectangular concrete stress block factor
α_w	:	Wall effective second moment of inertia factor
β	:	Soil equivalent rectangular stress block compression depth factor
β_1	:	Equivalent rectangular concrete stress block factor
γ	:	Soil equivalent rectangular stress block maximum compressive displacement factor
γ_{avg}	:	Wall average first storey shear strain
γ_{max}	:	Wall maximum shear strain at the base
γ_{xy}	:	Shear strain of a single reinforced concrete element under biaxial stresses
Δ_1	:	Envelope of 1st storey displacement
Δ_{10}	:	Envelope of 10th storey displacement
Δ_{20}		Envelope of 20th storey displacement
Δ_5		Envelope of 5th storey displacement
Δ_i	:	Wall displacement at the top of ith storey
Δ_{s1}	:	Shear deformation at the top of the first storey
$\varepsilon^*_{cen.}$	:	Tensile strain at wall centroid
ε_c	:	Concrete strain
ε'_c	:	Concrete strain at f'_c
ε_c^{max}	:	Maximum allowable concrete strain

ε_{cr}	:	Concrete cracking strain in tension
ε_t^{max}	:	Wall maximum tensile strain
ε_v	:	Average storey vertical tensile strain
ε_x	:	Vertical tensile strain
θ	:	Principle strain angle measured from wall vertical axis in Chapter 2, column rotation at grade level in Chapter 7
θ_1	:	Column rotation occurring in first basement storey
θ_2	:	Column rotation occurring in second basement storey
θ_b	:	Base rotation
$\theta_{elastic}$	:	Foundation rotation at the onset of inelastic behaviour
θ_{oc}	:	Base rotation at which the foundation overturning capacity is mobilized
θ_p	:	Total inelastic rotation in the wall plastic hinge
θ_y	:	Base rotation at which wall yield bending strength is reached
ν	:	Soil Poisson's ratio
ρ	:	Mass density of soil in Chapter 3, reinforcing steel area as a ratio of gross concrete area in Chapters 2 & 5
φ	:	Curvature
φ_{avg}	:	Wall average storey curvature
Φ_c	:	Concrete material strength reduction factor
φ_d	:	Total column curvature demand
φ_{max}	:	Wall maximum curvature
φ_{plc}	:	Curvature at onset of column plastic behaviour
φ_s	:	Seismic column curvature demand
φ_y	:	Wall yield curvature

Acknowledgements

I would like to extend my sincerest gratitude to my research supervisor, Professor Perry Adebar, for his ongoing guidance during the entire course of my graduate studies at UBC. His expert knowledge of reinforced concrete structures, extensive experience in engineering research and invaluable mentorship where key to development and completion of this work.

I am sincerely grateful to Drs. Donald Anderson and Ron DeVall for their time and insightful feedback as members of the supervisory committee. I would also like to thank Drs. Anderson and DeVall along with James Mutrie for their expert guidance in the research on rotation of shear wall foundations. Their informed input was detrimental to pointing the research on foundation rotation of shear walls in the right direction and helping problem-solve my way around obstacles along the way.

Decisions on modeling assumptions for the soil-structure interaction component used to study the rotation of shear wall foundations was made with the expert advice of Drs. Dharma Wijewickreme, Mahdi Taiebat, and John Howie to whom I am truly grateful. I would also like to extend my acknowledgements to Ernest Naesgaard for his crucial input into the decision making on soil properties used for studying foundation rotation in shear wall buildings and sharing his knowledge and experience in professional geotechnical engineering practice with me.

I like to thank my colleagues at the Civil Engineering Department at UBC especially Jeff Yathon for providing me with his RSA code written in MATHLAB.

I am humbly grateful to my aunt Dr. Nooshin Bazargani and her husband Rahim Faghihi for their ongoing encouragements and unconditional support.

Last but certainly not the least, I would like to thank my family, my mother Zohreh Seifaei, my father Naser Bazargani, and my sisters Parisa and Bahar for their selfless emotional support and encouragement, for believing in my potentials, and for being there for me whenever I needed them.

To my family to whose support I owe this work

CHAPTER 1 Introduction

1.1 Overview of Problem

Reinforced concrete shear wall buildings are a common form of construction for mid-rise and high-rise buildings in Canada and many other countries around the world. Figure 1.1 shows a simple sketch of the major structural components of a typical shear wall building. The shear walls are the designated seismic-force-resisting-system (SFRS) of the building and are typically designed to resist the entire lateral seismic force demands on the building. The shear walls are also detailed to be sufficiently ductile for the expected displacement demands on the building.

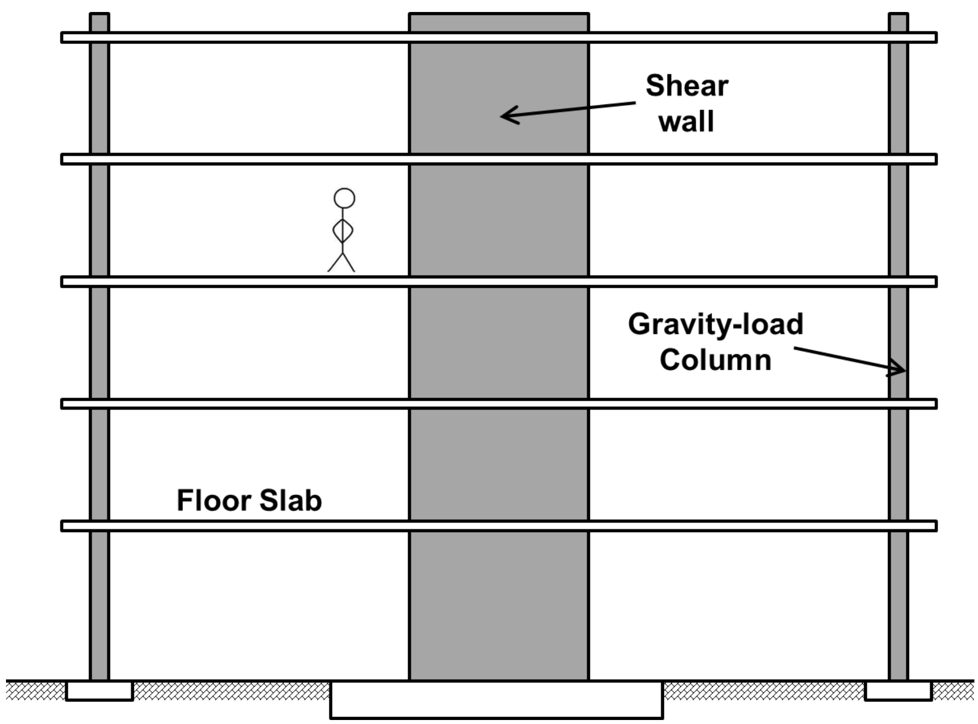

Figure 1.1 Gravity-load columns connected to the shear walls with closely spaced floor slabs.

The structure surrounding the shear walls, which includes floor slabs, beams and columns is referred to as the gravity-load-resisting system (GLRS). The GLRS is typically not designed to resist any seismic forces because it is usually much more flexible than the SFRS; but must be able to tolerate the deformations of the building due to the design earthquake. When the GLRS consists of long-span flat plate slabs and slender columns as shown in Figure 1.1, the seismic displacements of the building with stiff shear walls will usually not put any significant demands on the very flexible GLRS.

In Canada, gravity-load columns on the perimeter of shear wall buildings are often elongated in cross-section as shown in Figure 1.2 because such columns offer several architectural and structural benefits. Elongated columns can be more easily hidden inside partitions and therefore block less of the view from the windows. Elongated columns also reduce the slab span which in turn reduces the minimum slab thickness required for deflection control. Elongated columns however are much less flexible about the strong axis of bending making the GLRS much less flexible.

The lateral flexibility of a column reduces as the level of axial compression applied to the column increases. Thus the gravity-load columns are the least flexible near the base of the building. This is exactly where the shear walls are expected to experience the largest inelastic deformation demands and where the special ductile detailing is provided in the shear walls. In Canada, gravity-load columns typically do not contain any ductile detailing – no confinement reinforcement and no anti-buckling ties. From a very simple perspective, it seems very inappropriate to provide extensive ductile detailing in shear walls that are subjected to relative low levels of axial compression stress, while providing no ductile detailing in the wall-like columns that are subjected to much higher levels of axial compression stress and are directly tied to the shear walls by the numerous closely-spaced floor slabs. Accurately determining the seismic deformation demands on the gravity-load columns over the critical plastic hinge region of shear wall buildings and ensuring that the demands are less than the capacity of the columns is the main subject of this thesis.

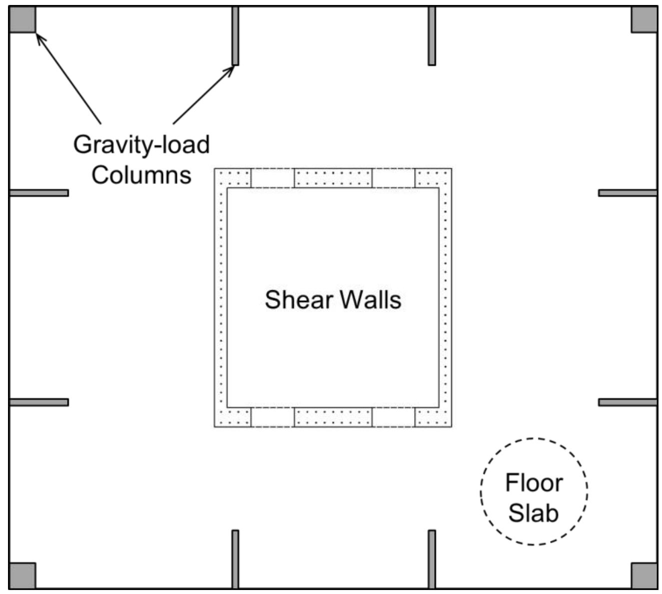

Figure 1.2 Schematic plan view of a shear wall building with elongated perimeter columns.

1.2 Important Elements of the Problem

Significant previous work has been done to relate the global seismic demand on shear wall buildings to the deformation demands at the base of shear walls. Dezhdar (2012) conducted numerous nonlinear response history analyses of shear wall buildings to establish the effective flexural rigidity EI_e to be used in a linear dynamic (response spectrum) analysis to determine the maximum horizontal displacement at the top of a shear wall. He also reaffirmed that the method developed by Adebar et al. (2005) can be used to accurately determine the maximum curvature at the base of a shear wall from the maximum horizontal displacement at the top of the wall. Bohl and Adebar (2011) conducted numerous nonlinear finite element analyses to determine the exact profile of inelastic curvatures at the base of shear walls. Thus the flexural deformation demands on shear walls over the plastic hinge region at the base of the building are well known.

The gravity-load columns are connected to the shear walls by closely spaced floor systems. The floor systems may be thin flat plate slabs as shown in Figure 1.1, or may include beams. When the floor system includes beams, the demands on the gravity-load columns may be increased to due frame action (transfer of bending moments from the floor to the columns); however, as the slabs and beams crack, they will become more flexible in bending. A simple lower-bound model of the floor system is to ignore the out-of-plane bending stiffness and assume the floor acts a rigid in-plane link that imposes the lateral deformation of the shear walls on the gravity-load columns at the floor levels. Such a simple model would be very accurate for flat plat floor slabs that are connected to elongated columns bending about the strong axis.

Figure 1.3 shows a cartoon view of a gravity-load column connected to a shear wall which is hinging at its base. Note that the slabs have to bend in order to achieve deformation compatibility. However, because the out-of-plane flexural stiffness of the slabs is relatively low, the slabs function mainly as a rigid links imposing the wall deformation profile onto the column. Bending of the slabs is idealized as concentrated hinges. The span of the slab is shown exaggeratedly short.

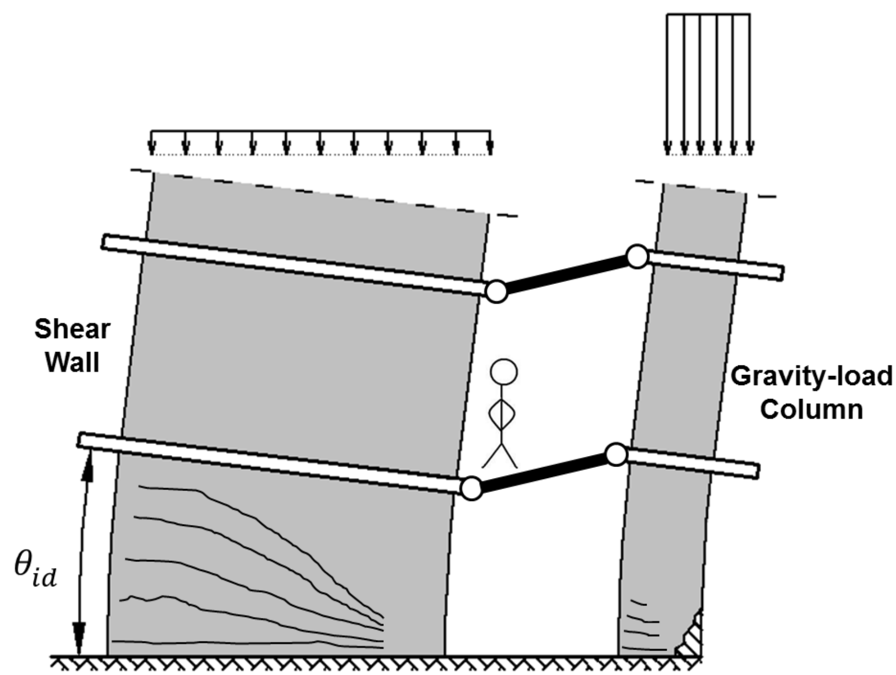

Figure 1.3 Deformation demands on gravity-load column due to plastic hinging of shear wall – column pushed to same lateral deformation as wall at flood slab levels. Floor slabs idealized as short-span rigid links due to their high in-plane stiffness.

Large inelastic rotation due to inelastic curvatures in the plastic hinge region at the base of the wall causes lateral displacement at the top of the first storey that the second floor slab will impose on the gravity-load column. If the column is not flexible enough to tolerate the displacement demand (e.g. because it is a large elongated column subjected to a large axial compression force), the imposed displacement may result in damage of the column in the form of concrete cover spalling, buckling of the outer layer of reinforcement, and fracturing of reinforcement subjected to tensile strains. Such damage to a gravity-load column may significantly reduce the axial load carrying capacity of the column. If the seismic performance and life-safety of the building are to be ensured, the level of damage to the gravity-load columns will have to be controlled. For this purpose, the seismic demand on the column has to be calculated and compared against the column deformation capacity.

Factors that are expected to influence the deformation demands on the gravity-load columns include the level of deformation of the shear walls and length of the shear wall, which will influence the inelastic wall curvature profile, the spacing of the floor slabs, and the support conditions at the base of the column. Factors that are expected to influence the deformation capacity of the gravity load columns include the level of applied axial compression, geometry of the cross section, arrangement of reinforcement and the concentration of damage in the column.

1.2.1 Wall shear strain

Top displacement of typical cantilever shear walls is caused primarily by flexural deformations of the walls. Shear deformations of the wall usually contribute a negligible portion to the top wall displacement. On the other hand, the shear deformation in flexural walls tends to be concentrated in the plastic hinge region near the base. Such shear deformation may contribute a very significant amount to the horizontal displacement of the shear walls at a short distance up from the base of the walls.

Figure 1.4 shows a cartoon view of a gravity-load column connected to a flexural shear wall with significant shear strain in the plastic hinge region. Wall shear strain produces significant lateral deformation at the second floor slab level that the floor imposes on the gravity load columns. If the column does not experience any shear deformation, the increased lateral displacement of the wall will increase the flexural damage to the columns. The effect of wall shear strain on column deformation demands needs to be considered.

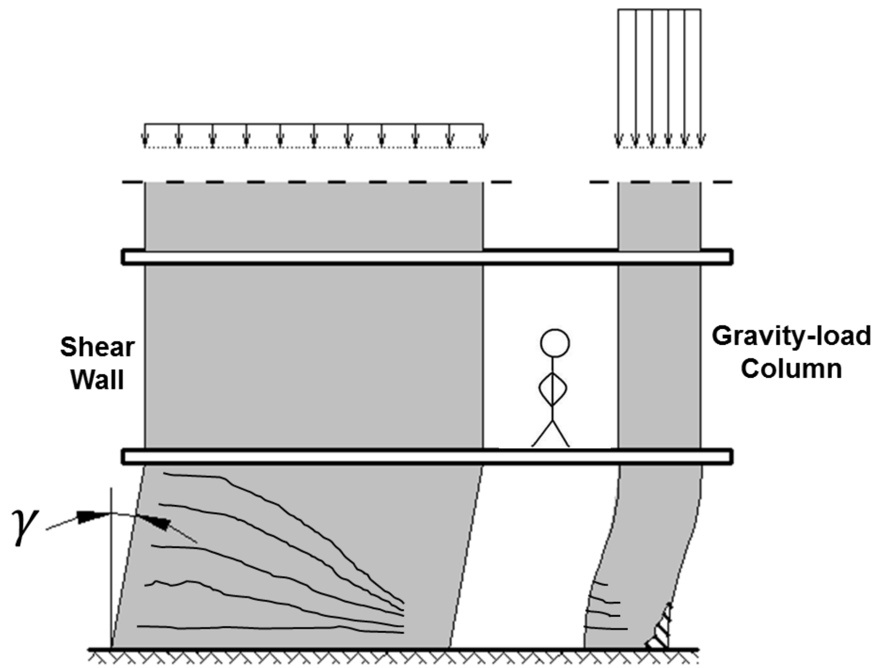

Figure 1.4 Deformation demands on the gravity-load column due to wall shear strain - column pushed to the same lateral deformation of the wall at flood slab levels.

1.2.2 Rotation of shear wall foundations

Another possible source of significant deformation in cantilever shear wall buildings is the rigid body movement of the shear wall due to foundation rotation. While the foundation is usually assumed to be fixed at the soil level in the analysis of a building, shear wall foundations will rotate due to the applied overturning moment. The rotation is due to foundation uplift (separation of foundation from underlying soil on the tension side) and compressive displacement of soil at the "toe" of the foundation.

Shown in Figure 1.5 is a cartoon view of a gravity-load column connected to a shear wall that experiences rigid body rotation due to rotation of the foundation. Although the shear wall is undeformed, it displaces horizontally and the floor slabs again impose that lateral displacement on the gravity-load columns at floor slab levels which may cause damage to the column.

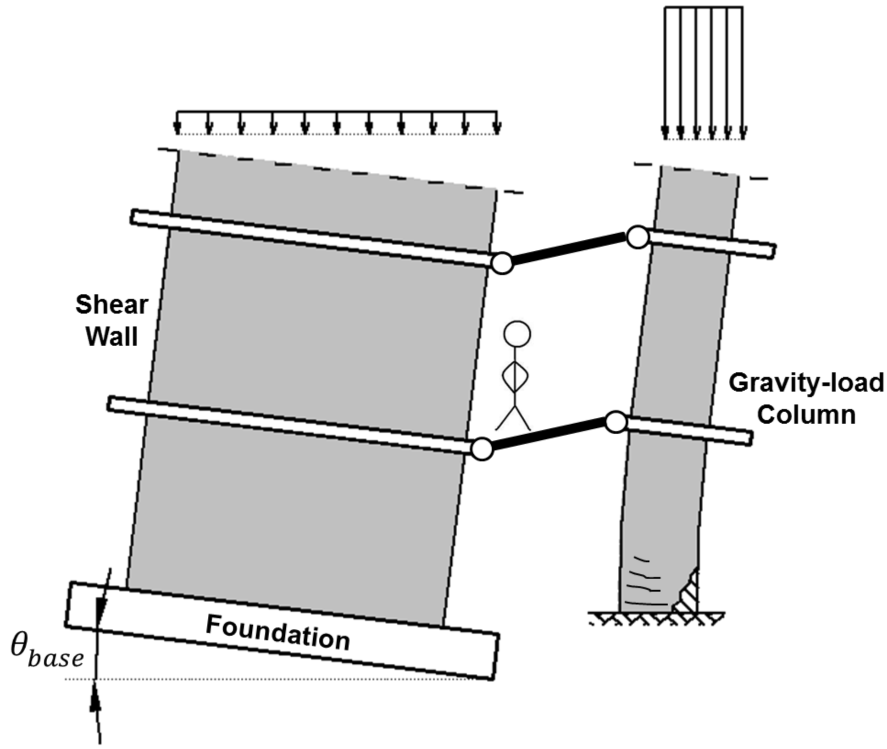

Figure 1.5 Deformation demands on gravity-load column due to rotation of shear wall foundation – column pushed to the same lateral deformation as wall at flood slab levels. Floor slabs idealized as short-span rigid links due to their high in-plane stiffness.

1.3 Moment-Curvature Response of Gravity-load Columns

The flexural behaviour of gravity-load columns is best represented by its moment-curvature response in combination with a model to account for the distribution of inelastic curvatures over the height of the column. An example moment-curvature response of a gravity-load column is shown in Figure 1.6. The onset of column nonlinear behaviour due to concrete cracking, the point of peak bending strength, and the column curvature capacity as governed by maximum compression strain of unconfined concrete are among the information that can be obtained from the moment-curvature response. Throughout this thesis, column curvature will be used to quantify the flexural deformation demands and flexural deformation capacity of the gravity-load columns.

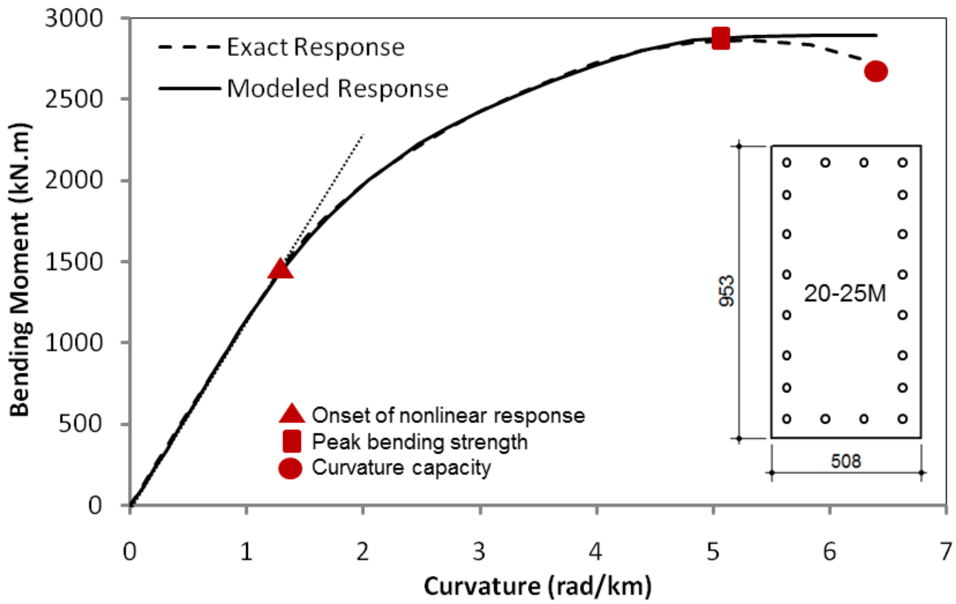

Figure 1.6 Example column moment-curvature response.

1.4 Main Parts of the Current Study

Figure 1.7 presents a "road map" to determining the seismic deformation demands on gravity-load columns. The first step is to define the lateral displacement profile of the shear walls. The flexural deformations of the shear walls are known from previous research. However very little is known about the shear deformation of shear walls and thus this is studied in detail in CHAPTER 2. Also, limited information is available on estimating the rotation of shear wall foundations so this is studied in CHAPTER 3 and CHAPTER 4.

Once the displacement profile of the shear walls is known, the curvature demands on the gravity-load columns must be determined accounting for the nonlinear bending moment-curvature response of the columns. A study on the bending moment- curvature response of typical gravity-load columns is presented in CHAPTER 5, while the simplified analysis method that was developed for shear wall – rigid link – gravity-load column systems is presented in CHAPTER 6.

In the third and final step, the effect of various wall and column parameters on column curvature demand is studied.

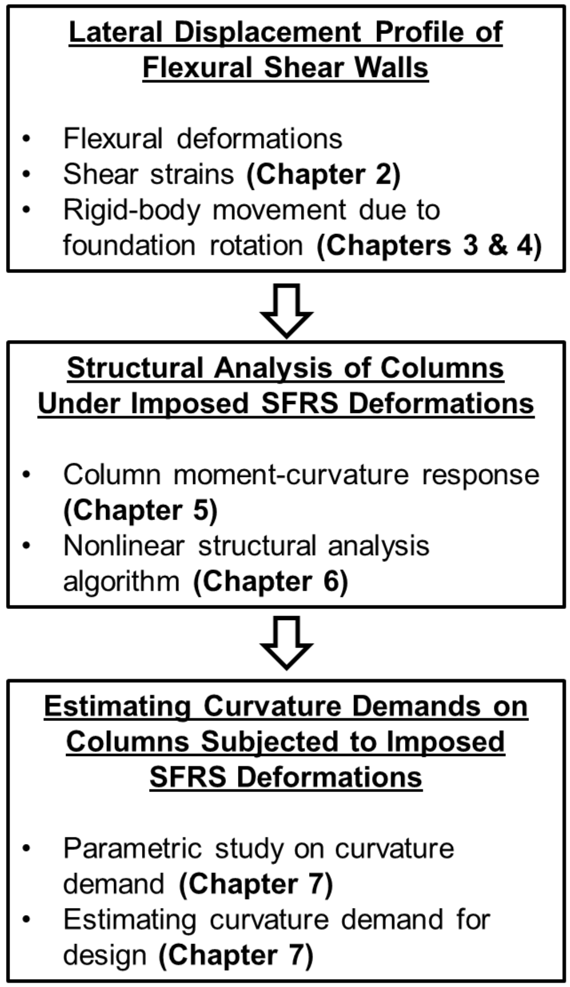

Figure 1.7 Main parts of the current study.

1.5 Summary of Research Objectives

The following are the main objectives of this dissertation sorted by research topic.

1.5.1 Shear strains in flexural shear walls (CHAPTER 2)

- To better understand the mechanisms of shear strains in flexural shear walls through surveying the existing experimental literature on flexural shear walls.
- To study the effect of the various parameters influencing shear strains in flexural walls using state-of-the-art experimentally-verified nonlinear finite element analysis.

- To develop a simple method that can be used to estimate shear strains in flexural shear walls.

1.5.2 Foundation rotation of cantilever shear walls

- To study the rotation of shear wall foundations through a series of Nonlinear Time-History Analysis (NTHA) considering various soil types, wall and foundation parameters and building configurations, where both the shear walls and the underlying soil are modelled as nonlinear elements (see CHAPTER 3).
- To develop a simple method for estimating foundation rotation in a given flexural shear wall building using the basic structural parameters and analytical tools available to the designer (see CHAPTER 4)

1.5.3 Curvature demands on gravity-load columns in the plastic hinge region of shear wall buildings with flat plate floor slabs

- To study the moment-curvature response of a broad range of gravity-load columns in order to better understand their nonlinear flexural behaviour (see CHAPTER 5).
- To develop a simple structural analysis algorithm to analyze curvature demands in gravity-load columns in buildings with flat plate floor slabs under imposed lateral shear wall deformation profiles (see CHAPTER 6).
- To investigate the seismic demands on gravity-load columns through a parametric study considering various column and wall parameters as well as building configurations (see CHAPTER 7).
- To develop simple methods for estimating maximum curvature demand on gravity-load columns pushed to the lateral deformation profile of the shear wall given the basic information available to the designer (see CHAPTER 7).

1.6 Thesis Overview

This thesis consists of eight chapters and four appendices. In terms of research topic, the thesis can be divided into three distinctive parts. The subject of shear strains in flexural shear walls is studied in CHAPTER 2. CHAPTER 3 and CHAPTER 4 deal with rigid body movement of shear walls due to rotation of their foundation. The main objective of this thesis which is estimating seismic demands on gravity-load columns connected to flexural shear walls with flat plate floor slabs is the topic of CHAPTER 5, CHAPTER 6, and CHAPTER 7. Results of CHAPTER 2, CHAPTER 3, and CHAPTER 4 could then be used as an input to the methods developed in CHAPTER 7 for estimating seismic curvature demands on gravity-load columns.

In CHAPTER 2, shear deformation of flexural shear walls is studied. The chapter begins with a literature review on experimental evidence of shear strains in flexural shear walls and the existing models for estimating shear strains in flexural shear walls. VecTor2 which uses the Modified Compression field Theory (MCFT) is chosen as the structural analysis platform and is proven to be a reliable tool for estimating shear strains in flexural shear walls by verifying it against selected experiments. A parametric study is conducted to identify critical factors that affect shear strains in the plastic hinge region of flexural shear walls. The results of the numerical study are then used towards the end of the chapter to develop a simple model for estimating shear strains in flexural shear walls the accuracy of which is then compared against experimental results.

CHAPTER 3 presents results of Nonlinear Time-History Analysis (NTHA) on shear walls accounting for foundation rotation. The chapter begins with a selective literature review of existing numerical techniques for modeling soil-structure interaction. Nonlinear Winkler springs are chosen as the modelling approach implemented in OpenSees in order to carry out the NTHA. Nonlinear behaviour of the wall is modelled by constructing the wall cross-section out of nonlinear concrete and reinforcing steel fibres. 10 carefully picked ground motion records are chosen and altered to provide spectra which closely match the Uniform Hazard Spectrum (UHS) for Vancouver. A pilot study is conducted on the effect of geotechnical parameters such as soil type, stiffness, and strength on the response of shear walls accounting for foundation rotation. Other parameters studied include level of radiation damping in the soil, wall height, and mass ratio (the ratio of the weight of the building supported directly by the shear wall to the total building weight). The Core NTHA was then designed based on the results of the parametric study. It included 5 types of soil and 5 shear walls of various bending strengths each supported on at least 5 foundations of various overturning strengths. Results of the NTHA of CHAPTER 3 are then used to better understand the interaction between shear wall and foundation strengths.

CHAPTER 4 utilizes the vast data obtained in CHAPTER 3 to formulate a simple step-by-step procedure for estimating foundation rotation in a shear wall building. A simple method for obtaining the monotonic foundation moment-rotation response is formulated first. An effective elastic rotational spring stiffness is then proposed that can be used at the base of the wall in a Response Spectrum Analysis (RSA) to estimate the total top wall displacement accounting for foundation rotation. Towards the end, a step-by-step method for estimating rotation of a shear wall foundation simple enough to be incorporated into design procedures is formulated. The chapter concludes with verifying the accuracy of the proposed method against NTHA results of CHAPTER 3.

Since deformation profile of gravity-load columns is dominated by flexure, CHAPTER 5 is entirely dedicated to studying the moment-curvature response of reinforced concrete gravity-load columns. To obtain a reasonable range for the probable axial load on the columns, a series of column cross-sections are designed based on provisions of NBCC 2005 and ASCE 7-05. In addition to the amount of axial load, the effect of concrete strength and steel ratio is also examined by varying those parameters over their expected range. The effect of column damage in the form of concrete cover spalling, bar buckling and fracture and creep of concrete on the moment-curvature response are studied. The chapter concludes with a discussion on methods of finding the neutral axis depth in a column cross section.

The main objective of CHAPTER 6 is to develop a structural analysis algorithm for analyzing curvature demands in gravity-load columns subjected to the imposed deformation profile of a wall assuming flexural stiffness of members framing into the column to be negligible compared to that of the column. At the beginning of the chapter, a selected number of publications by other researchers on the subject of plastic hinging of gravity-load columns are summarized. The concept behind development of the structural analysis procedure is then presented. Deformation profile of the wall is divided into flexural and shear components with bilinear curvature and shear strain profiles assumed. Accuracy of the proposed structural analysis method is then compared against results from a sophisticated Finite Element (FE) program such as VecTor2. The structural analysis algorithm is further refined for computational efficiency towards the end of the chapter.

CHAPTER 7 is primarily focused on estimating curvature demand on gravity-load columns connected to a flexural shear wall with flat plate floor slabs. A set of standard parameters are defined for the wall and the column and in each section, one of the parameters is varied keeping the rest at their standard value to investigate how that particular parameter influences column curvature demand. Parameters studied include wall shear strain, column length, wall length, height of column’s first storey, damage of the column cross-section, column plastic hinge height and flexibility of the column’s boundary condition at grade level. Several simple expressions are developed to estimate column curvature demand from wall maximum curvature using basic design parameters. At the end of the chapter, some guidance is provided on determining additional curvature demands induced in gravity-load columns due to flexural stiffness of members framing into the column to assist with decision-making on whether or not flexural stiffness of the framing members is negligible compared to that of the column.

The thesis includes four appendices. Appendix A provides a detailed summary of the results of all of the NTHA carried out in CHAPTER 3. Appendix B and Appendix C show calculations for estimating the probable range of axial load on gravity load columns designed to provisions of NBCC 2005 and ASCE 7-05 respectively. Mathematical representation of the structural analysis algorithm developed in CHAPTER 6 to analyze column demands when pushed to the given displacement profile of a shear wall is presented in Appendix D.

CHAPTER 2 Shear Deformation of Flexural Shear Walls

2.1 Overview of the Chapter

Although shear deformations do not contribute significantly to the total displacement at the top of a flexural shear wall, they constitute a substantial portion of the wall's displacement profile in the plastic hinge region where flexural deformations are relatively small. Wall shear strains are shown to be at their maximum in the first storey of the wall and that they may constitute up to one-half of the total wall displacement at the first floor slab level. Displacement demands on gravity-load columns are highly affected by wall displacement at the first few floor slab levels. Hence, shear deformation of flexural shear walls needs to be determined carefully if an accurate estimate of the deformation demands on the gravity-load system is to be made.

The chapter begins with a brief introduction of VecTor2, the finite element analysis software used to model the flexural and shear behaviour of reinforced concrete walls. Accuracy of shear strains predicted by VecTor2 is verified against test results by Thomsen and Wallace (1995) and Brueggen (2009). General concepts of wall shear deformation are then examined by modeling a 10-storey shear wall in VecTor2. The mechanism of formation of shear strains in the plastic hinge region of flexural shear walls is explained. Distribution of shear strain along the height of the wall is found to be similar to the curvature profile with the majority of the shear strain concentrated in the wall plastic hinge region.

Towards the end of the chapter, a simple model is introduced that can accurately estimate average shear strain in each storey of a shear wall. The method is formulated such that it can be incorporated into a standard design procedure that can be used by designers. The average storey shear strains multiplied by the storey heights give the amount of shear deformation occurring in each storey which when added to the flexural deformations, gives the total wall deformation profile accounting for the correct flexural and shear deformations.

2.2 Experimental Evidence of Wall Shear Strain from Previous Researchers

Evidence of wall shear deformation has been observed in tests on shear walls since the beginning of the last quarter of the 20th century. Among the earliest observations on wall shear strain is the report by Wang et al. (1975) on testing of four three-storey squat walls with aspect ratio of 1.27. The ultimate objective of the experimental program was to develop practical methods for the seismic design of combined wall-frame structural systems. Wang et al. reported that shear deformation was not only significant for the walls tested but dominant at the levels of the first and second storeys. Shear stiffness reduced significantly as the wall yielded in flexure causing pinching of the shear force-shear strain response similar to the bending moment-curvature response.

In 1976 (Phase I) and 1979 (Phase II), Oesterle et al. (1976 & 1979) conducted two series of tests on structural walls for the Portland Cement Association (PCA). The objective of the testing program was to evaluate earthquake resistance of semi-slender structural walls. Two rectangular, nine barbell shaped, and two flanged walls were tested all with height to length ratio of 2.4. All specimens in Phase I carried minimal axial compressive load while those tested in Phase II had to sustain a significant axial compression between 7.3% and 13.4% of $f'_c A_g$. Even though the focus of the tests was on developing design procedures to ensure adequate flexural and shear strength and ductility and energy dissipation capacity, the report offered thought-provoking observations on wall shear deformation. Oesterle et al. observed that shear yielding (i.e. the point beyond which shear deformations started to grow rapidly) occurred simultaneously with flexural yielding and was not necessarily accompanied by yielding of shear reinforcement; in fact, significant shear deformations were observed even in walls “over-reinforced for shear”.

In tests on squat structural walls with aspect ratios of 1.42 and 1.27 subjected to cyclic loading, Vallenas et al. (1979) also observed simultaneous yielding of the flexural and shear mechanisms. Despite the shear stress being constant over the height of the wall, shear yielding was only observed in areas were the flexural mechanism yielded. Vallenas et al. recognized the effect of diagonal cracks on reducing shear stiffness and increasing shear deformations of the wall. They also observed that shear deformation was almost a constant factor of flexural deformation for monotonic loading while the ratio of shear to flexural deformations increased with number of load reversals and increased deformation intensity.

Shear deformation has been observed not only in squat or semi-slender walls, but also in slenderer walls whose behaviour is dominated by flexure. Shiu et al. (1981) conducted a test to verify the effect of openings in walls on their seismic behaviour. Two 6-storey walls with aspect ratios of 2.9 were tested. Shiu et al. reported that despite the response of the walls being dominated by flexure, “shear deformation was dominant in the first storey region” where the flexural rotations were quite small. Shear distortions started to decrease and flexural rotations stated to increase in higher storeys such that at the second storey level, the contributions of flexural and shear deformations to the total deformation were almost equal.

Thomsen and Wallace (1995) conducted cyclic tests on two rectangular walls and two T-shaped walls with aspect ratios of 3.1 with primary objective of evaluating the effectiveness of using a displacement-based procedure for designing reinforced concrete structural walls. The walls were subjected to a sustained compressive axial load of 7% to 10% of $f'_c A_g$. Thomsen and Wallace measured shear strains in each of their specimens’ four storeys and affiliated the large shear distortion observed in the first storey of all specimens with flexural and shear cracking resulting from development of large inelastic tensile strains in the web area. However, because shear deformations constituted a relatively small portion of the wall top displacement and the focus of the test was on wall behaviour and design, Thomsen and Wallace concluded that “The exclusion of shear deformations from analytical models is not critical for slender walls”.

Dazio et al. (1999) conducted tests on 6 rectangular walls with aspect ratio of 2.3 and axial compressive loads between 5.7% and 10.8% of $f'_c A_g$. It was observed that while flexural deformations dominated the response of the walls, shear deformations were significant over the plastic hinge region of the walls. In addition, the ratio of shear to flexural deformations remained nearly constant over the entire inelastic drift range.

In tests on walls with highly-confined boundary elements where the walls had an aspect ratio of 4.0 and sustained an axial load of $0.10 f'_c A_g$, Hines (2002) also observed that ”the flexural and shear components of displacement are related to one another linearly at least at the displacement peaks" and that large shear deformations were a result of the flexure-shear mechanism in the plastic hinge region.

These general observations on wall shear deformation were not restricted to walls loaded in their plane of symmetry. For their two U-shaped specimens with aspect ratio of 2.8 or 2.6 subjected to multidirectional loading, Beyer et al. (2008) confirmed that "the ratio of shear to flexural displacements Δ_s/Δ_f at peak displacements remains approximately constant over the entire ductility range"; "however, the magnitude of the Δ_s/Δ_f ratio varied strongly with the direction of loading." They also confirmed that "the shear deformations were concentrated in the plastic hinge region at the base of the wall undergoing inelastic deformations" and that "the contribution of the shear displacements was largest when a wall section was under net tension".

Brueggen (2009) tested a T-shaped wall with aspect ratio of 3.2 under multidirectional cyclic loading with $0.03f'_cA_g$ sustained axial compressive force and confirmed that "the larger shear deformations toward the base provide an indication of the effect that plastic hinging and flexural damage have on shear deformations and reducing shear stiffness." Brueggen also mentioned that the ratio of shear to flexural deformations remained approximately constant over the inelastic drift range. What distinguishes Brueggen's work from the work of other researchers is illustrating the similarity between the shapes of the curvature and shear strains profiles of the wall and recognizing the direct link between curvature and shear strain. Brueggen also emphasized on the importance of capturing the shear deformation profile of the wall and not only the total shear deformation at the top.

A general trend that can be observed more or less in all of the existing experimental literature of wall shear strain is the link between formation of a flexural plastic hinge and development of large shear strains. This evidence has been stated in various forms such as flexural yielding resulting in simultaneous shear yielding, nearly constant shear deformation to flexural deformation ratio over the entire deformation range, or shear strain and curvature profiles of the flexural shear walls having the same shape. Shear strains are proven to constitute a substantial amount of the lateral deformation of flexural shear walls especially in the plastic hinge region. If the correct deformation profile of the shear wall is to be determined, the amount of shear deformation must be quantified.

2.3 Existing Models for Estimating Wall Shear Deformation

Oesterle et al. (1984) correlated web crushing strength to the deformations within the hinging region of structural reinforced concrete walls. Oesterle et al. based their analytical model on a truss analogy with 45 degree concrete compression struts, vertical tensile reinforcement carrying flexural tension, horizontal reinforcement acting as tension ties, and flexural compression carried by both concrete and longitudinal reinforcement. Due to the complexity of the relationship between shear distortion, flexural rotation, and total drift within the plastic hinge region, an experimental approach was used to produce a formula for estimating shear distortion. An empirical equation obtained from linear regression analysis on test results reported by Oesterle et al. (1976 & 1979) was proposed for estimating the ratio of shear distortion to total drift in the plastic hinge region. Axial compressive load (N) on the wall was considered the main parameter controlling the contribution of shear distortion to total drift in the plastic hinge region as shown in the following expressions by Oesterle et al.

$$\gamma = (0.76 - 2.6\frac{N}{f'_c A_g})\delta$$

$$for\ 0 < \frac{N}{f'_c A_g} < 0.09 \qquad \textbf{Eq 2.1}$$

And

$$\gamma = 0.52\delta$$

$$for\ \frac{N}{f'_c A_g} > 0.09 \qquad \textbf{Eq 2.2}$$

where γ is the average shear distortion occurring within the hinge region and δ is the total drift ratio within the hinge region. Oesterle et al. also pointed out the strong link between shear distortion and average vertical strains resulting from curvature to conclude that "shear distortions and flexural rotations are coupled" but did not base their analytical model on this observation. Although Oesterle et al. realized the importance of focusing on inter-storey drifts within the plastic hinge zone rather than just the top wall displacement and provided a simple model for predicting the interaction of flexural, shear, and axial loads, the proposed model lacks generality in that it is based on test results of fairly squat walls with aspect ratio of 2.4. Shear distortions are assumed to account for 52% of the total drift in the plastic hinge region for all walls under axial load exceeding $0.09f'_c A_g$ regardless of other properties such as wall length and concrete compression depth in the plastic hinge zone. This may result in inaccurate prediction of drifts due to shear distortion in slender walls.

Although the linear relationship between the total (top) flexural and shear deformations of flexural walls had been confirmed prior to 2002, Hines (2002) was among the first to utilize this approximation to propose a simple model for estimating shear deformation of a wall from its flexural deformation. In Hines's model, the concrete cracking pattern in the plastic hinge zone is used to derive a geometric relationship between total flexural and shear deformation of the wall. In this model, the ratio of total shear to flexural deformation is given as a constant factor of the aspect ratio of the wall whose shear transfer mechanism does not undergo severe damage. To account for the reduced shear stiffness of walls designed with inadequate shear reinforcement or walls experiencing shear failure, Hines added an empirical multiplier calculated from the ratio of the wall's shear capacity to resist diagonal tension and compression to the applied shear force respectively. For the walls tested by Hines himself, the model in its final form is given below

$$0.05 \ \leq \ \frac{\Delta_s}{\Delta_f} = 0.25\frac{D}{L}\left[1 + 2\left(\frac{V}{V_n} + \frac{V}{V_{wc}}\right)\right] \leq 0.35 \qquad \textbf{Eq 2.3}$$

where Δ_s and Δ_f are the total shear and flexural deformations respectively, D is the total length of the wall, L is the shear span, and the term in the bracket is the multiplier accounting for additional shear displacement from loss of strength of the shear-carrying mechanism.

Despite the simplicity of the final model, cumbersome derivations are required to formulate the proportionality constant (i.e. the 0.25 in the expression above) for the relationship between the ratio of shear to flexural displacements and aspect ratio of various walls. Furthermore, the cracking pattern of the plastic hinge region must also be known which makes Hines's model less attractive to a designer. Even though Hines's model captures the fundamentals of the interaction between the flexural and shear deformations of walls and provides a valuable insight into the mechanisms of shear deformation, it is formulated to evaluate total top wall displacement and hence cannot be used to predict inter-storey drifts resulting from shear deformation in the plastic hinge region.

Brueggen (2009) appears to be the first to recognize the similarity between curvature and shear strain profiles due to concentration of shear strains in the plastic hinge region where large curvatures are encountered. In Brueggen's method, shear strain is proportional to curvature with a proportionality factor called C constant over the entire inelastic drift range. The ratio of the flexural to shear stiffness of the wall at yielding is then used to calculate C. Equations below summarize Brueggen's model.

$$\gamma = C\varphi$$

$$C = \frac{M_y/\varphi_y}{K_v \times z} \qquad \textbf{Eq 2.4}$$

Flexural stiffness at yielding is the yield bending moment divided by the yield curvature. The shear stiffness is calculated from the expression for shear stiffness of cracked reinforced concrete beams by Park and Paulay (1975). For 45 degree cracks, this equation is given below in terms of the area ratio of shear reinforcement (ρ_v), steel elastic modulus, steel to concrete modular ratio (n), and width (b_w) and depth (d) of the wall.

$$K_{v,45} = \frac{\rho_v}{1 + 4n\rho_v} E_s b_w d \qquad \textbf{Eq 2.5}$$

This shear stiffness is multiplied by the shear span of the wall to give the desired units for C.

Brueggen's method is capable of predicting shear strain profile of the wall and not just the total shear displacement at the top. However, calculating the shear stiffness which is needed to estimate C requires having an estimate of the crack angle best representative of the plastic hinge zone which is generally not available to the designer. Brueggen suggests assuming 45 degree cracks for simplicity. Based on her report, the model does an acceptable job of estimating shear strains assuming 45 degree cracks; but, if the actual crack angles observed during tests are used in estimating wall shear stiffness from the general expression by Park and Paulay (1975), the accuracy of the prediction of shear strains is improved.

Despite its elegance in relating shear strain to curvature and being "intended for use by structural engineers", Brueggen's method is not simple enough to be used by the designer. Its shortcoming is in estimating the wall shear stiffness using an elastic truss model, for two reasons. First is that the elastic truss model does not account for the interaction between flexural and shear deformations in reinforced concrete members. In formulating their expression for shear stiffness of cracked reinforced concrete beams, Park and Paulay assumed infinitely rigid tension and compression truss cords. This means that shear deformation is assumed to be decoupled from flexural rotation which is not a realistic assumption. In addition, the derivation of the expression assumes significant elongation of shear reinforcements and shortening of compression struts whereas in flexural walls with adequate shear (horizontal) reinforcement, horizontal strains in the web are negligible and relatively small compressive strains are observed in the compression struts. Park and Paulay's expression for shear stiffness is not intended to account for shear strain resulting from large vertical tensile strains and because Brueggen's model is based on the same equation, neither does Brueggen's model capture shear strain coming from large vertical tensile strains. Secondly, estimating shear stiffness of flexural walls from Park and Paulay's expression requires knowledge of the probable crack angles in the plastic hinge region which is not available to the designer. Assuming a 45 degree crack angle reduces the accuracy in estimating wall shear strain and is not a viable solution to the problem.

Even though the link between the magnitudes of shear strain and vertical tensile strain had been observed in tests conducted by Vallenas et al. (1979), Oesterle et al. (1984), and Thomsen and Wallace (1995), Beyer et al. (2011) were the first to utilize this experimental observation directly to formulate a model for predicting shear deformation of walls. Beyer et al.'s method uses the geometry of the Mohr strain circle for a reinforced concrete membrane element under biaxial stress in conjunction with a plastic hinge model to estimate the ratio of shear to flexural displacements at the top of the wall. Similar to Hines's, Beyer et al.'s model assumes that the ratio of flexural to shear displacement at the top of the wall remains approximately constant for walls in which the shear transfer mechanism is not degrading in strength; an observation made in tests by Vallenas et al. (1979), Dazio (1999), and others. To incorporate this observation into the model, the contribution of horizontal strains and diagonal compression strains to shear strain of flexural walls is neglected which results in shear strain and vertical strain being proportional for a given crack angle. Furthermore, the assumption of linear variation of strain across the length of the wall along with constant concrete compression depth in the plastic hinge region makes vertical strains proportional to curvature. Both flexural and shear displacement at the top of the wall are then calculated from a plastic hinge model with constant curvature equal to maximum curvature of the wall assumed over a certain height. Beyer et al.'s model for the ratio of total shear to flexural displacement is given below

$$\frac{\Delta_s}{\Delta_f} = 1.5\frac{\varepsilon_m}{\varphi tan\beta}\frac{1}{H_n} \qquad \textbf{Eq 2.6}$$

where ε_m is the vertical tensile strain at the centroid of the wall section, φ is the maximum curvature of the wall, H_n is the total height of the wall, and β is the crack angle outside the fan area in the plastic hinge zone.

Despite its attractive concept, Beyer et al.'s method can only be used to estimate the total shear displacement of the wall at the top and is not formulated to give the shear strain profile or the shear deformation profile of the wall. Although the method is valuable to evaluation of shear wall behaviour, it cannot be used to estimate additional storey drift demands due to presence of shear strains in the plastic hinge region. Apart from that, the model still requires an estimate of the crack angle best representative of the fanned crack pattern within the plastic hinge zone. Beyer et al. suggest either assuming a 45 degree crack angle or estimating the crack angle from a complex equation presented by Collins and Mitchell (1997). The 45 degree crack angle assumption is too simplistic and gives inaccurate prediction of shear deformation; Beyer et al. compared predicted shear deformation of several walls against those observed during tests using the plastic hinge crack angles observed during the tests and yet, the accuracy of the prediction was not convincing. The equation given by Collins and Mitchell for predicting the crack angle requires knowledge of wall parameters that are not generally available to the designer and does not solve the problem.

In summary, Hines's and Beyer et al.'s models are not formulated to provide the shear strain profile or the distribution of shear deformation along the height of the wall. Because Oesterle et al.'s model is an empirical model based on a narrow range of wall tests all with aspect ratio of 2.4, the model lacks accuracy when used to estimate shear deformations in taller walls. The proportionality constant relating curvatures to shear strains provided Brueggen's model is derived from an expression for estimating shear stiffness of beams which does not capture shear softening resulting from presence of large tensile strains in a diagonally cracked web of flexural walls and hence, falls short of providing an accurate estimate of shear deformation. The need for a simple but accurate model for estimating shear deformation profile of flexural walls is therefore obvious.

2.4 Finite Element Analysis of Reinforced Concrete Structures Using VecTor2

VecTor2 was selected as the nonlinear finite element software for this research as it uses the state-of-the-art material models for cracked reinforced concrete subjected to axial, shear, and bending. VecTor2 uses the Disturbed Stress Field Model (DSFM) formulated by Vecchio (2000) which is a refinement of the Modified Compression Field Theory (MCFT) introduced by Vecchio and Collins (1986).

The MCFT determines the average and local strains and stresses of the concrete and reinforcement, and the widths and orientation of cracks throughout the load-deformation response of an element. Based on this information, the failure mode of the element can also be determined. The concrete model accounts for the reduction of compressive strength and stiffness due to transverse cracking and tensile straining. The reduction in concrete cracking strength due to transverse compressive stresses is also accounted for.

The theory utilizes a set of simplifying assumptions most important of which are uniformly distributed and rotating cracks, using average strains over a gage length including several cracks, compatibility of average concrete and reinforcement strains and negligible shear stress in reinforcement. The theory also assumes the orientation of principal average strain, θ_ε, and that of principal average stress, θ_σ, to be the same. Principle tensile and compressive concrete strains can then be determined using Mohr's circle for strains. To satisfy force equilibrium, summation of concrete and steel stresses is set equal to the applied stress resultants on the element. Local stress conditions at cracks are also considered to make sure steel reinforcement can bear the extra tensile stress carried through concrete tension stiffening elsewhere.

Adding constitutive relations for both concrete and steel makes the MCFT ready for FE implementation. However, VecTor2 uses a modified version of the theory called the Disturbed Stress Field Model (DSFM) introduced by Vecchio (2000). The DSFM addresses systematic deficiencies of the MCFT in predicting the response of certain structures and loading scenarios by accounting for the effect of shear slip on the state of stress and strains of 2D reinforced concrete membrane elements. Further information on the DSFM can be found in the VecTor2 manual (see Wong and Vecchio (2002)) and is therefore excluded from this discussion.

In VecTor2, the constitutive relationship used for reinforcing steel in tension has an initial linear-elastic response, a yield plateau, and a linear strain-hardening phase until rupture which can be easily fitted to the measured bare bar stress-strain relationships of the reinforcement.

VecTor2 uses three-node constant strain triangular elements with six degrees of freedom (DOF) and four-node plane stress rectangular elements with eight DOF to model concrete with distributed reinforcement and uses two-node truss bar elements with four DOF to model discrete steel reinforcement.

2.4.1 Previous works on verification of VecTor2

Vecchio first introduced the DSFM in 2000. The analytical method has been used by many researchers studying the behaviour of reinforced concrete structures since and has gained appreciable popularity. Among the early attempts to validate DSFM as a reliable analysis platform for reinforced concrete structures was the work published by Vecchio et al. (2001). Vecchio et al modeled tests on RC panels, beams, and shear walls using the DSFM. The DSFM was found to provide accurate estimates of strength, load-deformation response, and failure mode of the tests modeled with superior accuracy to the predictions made previously using the MCFT.

Palermo and Vecchio (2004) used VecTor2 to model two flexural walls with aspect ratio of 2.4, two semi-slender walls with aspect ratio of 2.0, and two squat walls with aspect ratios less than 1.0 in order to further validate VecTor2 and the DSFM as a reliable finite element (FE) analysis tool for RC structures subjected to reverse cyclic loading. To simplify their analytical model, Palermo and Vecchio used only rectangular elements with distributed steel reinforcement to construct their FE model. Despite their simple modeling procedure, the FE model accurately predicted the load-deformation response and the failure mechanism observed during the test. Palermo and Vecchio also mentioned that “The analyses indicated that slender walls, controlled by flexural mechanisms, are generally a test for reinforcement models, whereas squat walls, demonstrating shear-dominant behaviour, are a better test for concrete models.”

Following the publication in 2004, Palermo and Vecchio (2007) published a summary of their work in validating VecTor2 and the DSFM. After modeling a combination of slender, slender/squat, and squat walls totalling to more than 20 wall tests, they reported that the FE element analysis provided simulations that were in substantial agreement with the test results in terms of peak strength, post-peak response, ductility, energy dissipation, and failure mechanism despite using only low-powered rectangular elements with distributed steel reinforcement to construct their models.

Despite the numerous works on validating the DSFM and VecTor2 as reliable analysis tools for predicting strength, stiffness, and failure mechanism of RC structures subjected to cyclic loading, to the author’s knowledge, VecTor2 has not been verified for its accuracy in predicting various deformation components of a shear wall, specifically wall shear strain. In Section 2.5, shear strains obtained from VecTor2 are compared with those recorded in experiments to validate Vector2 as an appropriate analysis tool for predicting shear strains in flexural shear walls.

2.5 Verification of VecTor2 for Predicting Shear Strains in Walls

A summary of the available experimental literature with measurement of shear deformation is summarized by Beyer et al (2011). It is therefore beneficial to use this reference in choosing tests to validate Vector2 for predicting shear deformation in slender shear walls. The majority of the walls tested fall in the boundary range between slender and squat walls based on their aspect ratio. For this reason, only walls with aspect ratios of 3.0 or higher are chosen which narrows the choice down to tests carried out by Thomsen and Wallace (1995), Hines (2002), and Brueggen (2009). Hines only reported the total shear deformation of the wall specimens at the top and did not measure the distribution of shear strains or shear deformations over the height of the wall specimens; hence, his work cannot be used for the purpose of validating the analytical model used in this study.

2.5.1 Specimens RW2 and TW2 tested by Thomsen and Wallace (1995)

Thomsen and Wallace (1995) tested two rectangular specimens and two T-shaped specimens all with an aspect ratio of 3.0 subjected to reverse cyclic loading. Only one rectangular specimen (RW2) and one T-shaped specimen (TW2) are chosen here. In this section, Specimens RW2 and TW2 are simulated in VecTor2 to validate the shear strains predicted by the FE program against those observed in the tests.

The wall specimens were quarter scaled models of a 4-storey wall. The length of the wall specimens was 1220 mm and their total height was 4880 mm. Specimen TW2 had thin reinforced concrete plates constructed at floor slab levels to account for the effect of the floor slabs on crack pattern and other wall parameters. The average axial compressive stress applied to the walls during the test was 7% and 7.5% of $f'_c A_g$ for specimens RW2 and TW2 respectively. See Thomsen and Wallace (1995) for further details on cyclic loading routine, instrumentation, specimen construction, and test set-up.

FE models of the two specimens were constructed in VecTor2 using only rectangular elements with distributed reinforcing steel. The FE models were loaded using support displacements at the top to simulate the effect of hydraulic jacks pushing and pulling the test specimens. Stress-strain relationship for reinforcing steel was adjusted to match the bare bar characteristics reported by Thomsen and Wallace (1995).

Figure 2.1 shows a schematic view of the finite element model for specimen RW2 with each colour representing a different reinforcement arrangement embedded in the same concrete material with f'_c of 31.2 MPa. Although in Thomsen and Wallace's test report different concrete strengths were reported for different concrete pours, concrete strength of 31.2 MPa reported for the first storey of the specimen was used throughout the entire finite element model for simplicity. All of the steel reinforcement was modeled as distributed steel in reinforced concrete membrane elements.

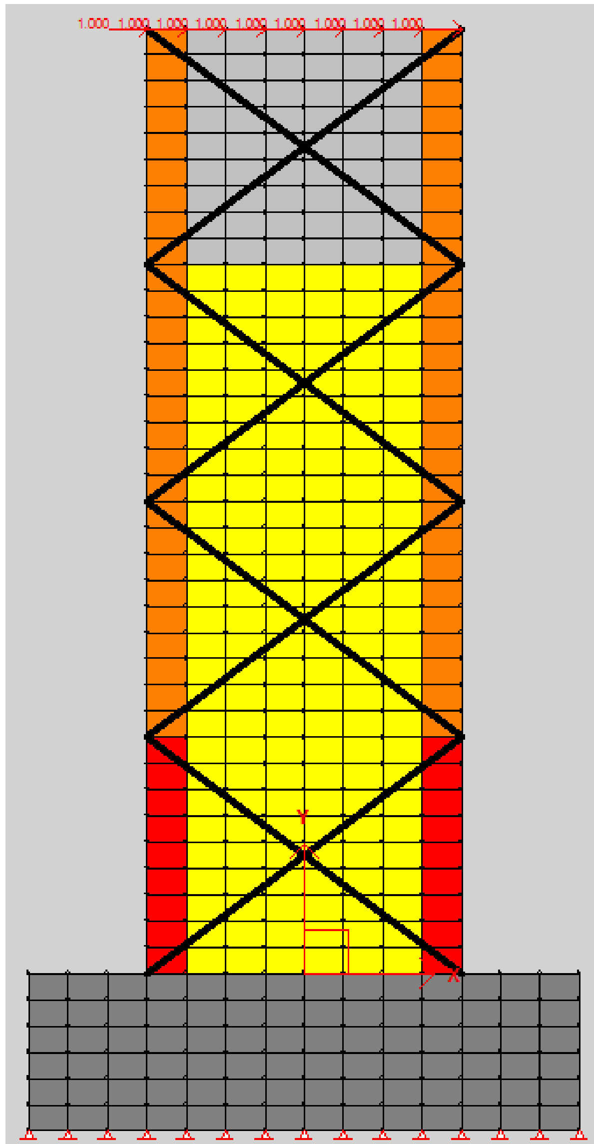

Figure 2.1 FE model for specimen RW2 in FormWorks (diagonal truss elements were modeled solely to simulate the procedure used by Thomsen and Wallace to measure average storey shear strain and have negligible stiffness).

Because the test was conducted in displacement-control mode, the push load at the top of the FE model was simulated using uniform support displacements along the top row of nodes of the model. The bottom row of the pedestal was fixed against movement using pin supports. The black diagonal elements are extremely thin truss bars modeled to simulate the shear strain computation mechanism used in the Thomsen and Wallace's test (explained later in the section).

Figure 2.2 shows a schematic view of the FE model for specimen TW2 in both 2D and 3D views. Thickness of the rectangular elements in the slab region was increased to simulate the effect of slabs on wall behaviour. Vertical steel ratio of the slab region was reduced accordingly such that the total amount of vertical steel in the slab region was equal to that of the adjacent regions of the wall. This ensured that the slabs did not add to flexural strength of the model. Extremely thin truss bars shown in black were again modeled to simulate the shear strain measurement mechanism used in the test report by Thomsen and Wallace.

A simple displacement-control pushover analysis was performed on the FE models despite the loading routine of the actual test being reverse cyclic. This meant that the results from the pushover analysis of the FE model had to be compared with the envelope of the hysteretic response observed during the tests.

Figure 2.3a shows a schematic of the deformed FE model at 2% lateral drift (deformation magnifier=5.0). Orientations of the red lines indicate the orientation of the cracks and their width is a coarse representation of the crack width.

To distinguish between flexural and shear components of the wall deformation, flexural deformations were computed by integrating curvatures over the height of the wall and then subtracted from the total deformation profile to obtain shear deformations. Because VecTor2 does not output curvatures, curvature profile of the wall also had to be calculated. If the slope of the straight line connecting the two nodes on the ends of a single row of nodes is considered to be the average rotation of the wall at that elevation, then the average curvature along a row of elements would be the change of rotation (slope) between the two rows of nodes which bound a row of elements. Average element curvatures calculated in this manner are plotted in Figure 2.3c and the flexural deformations obtained from integrating those curvatures over the height of the wall are shown in Figure 2.3b as the dotted line. The displacement profile of the specimen measured during the test is also plotted in Figure 2.3b which is in very good agreement with total displacement profile obtained from FE analysis. Subtracting flexural deformations from the total deformation profile resulted in shear deformations which were converted into average shear strains over the height of each row of elements (see Figure 2.3d).

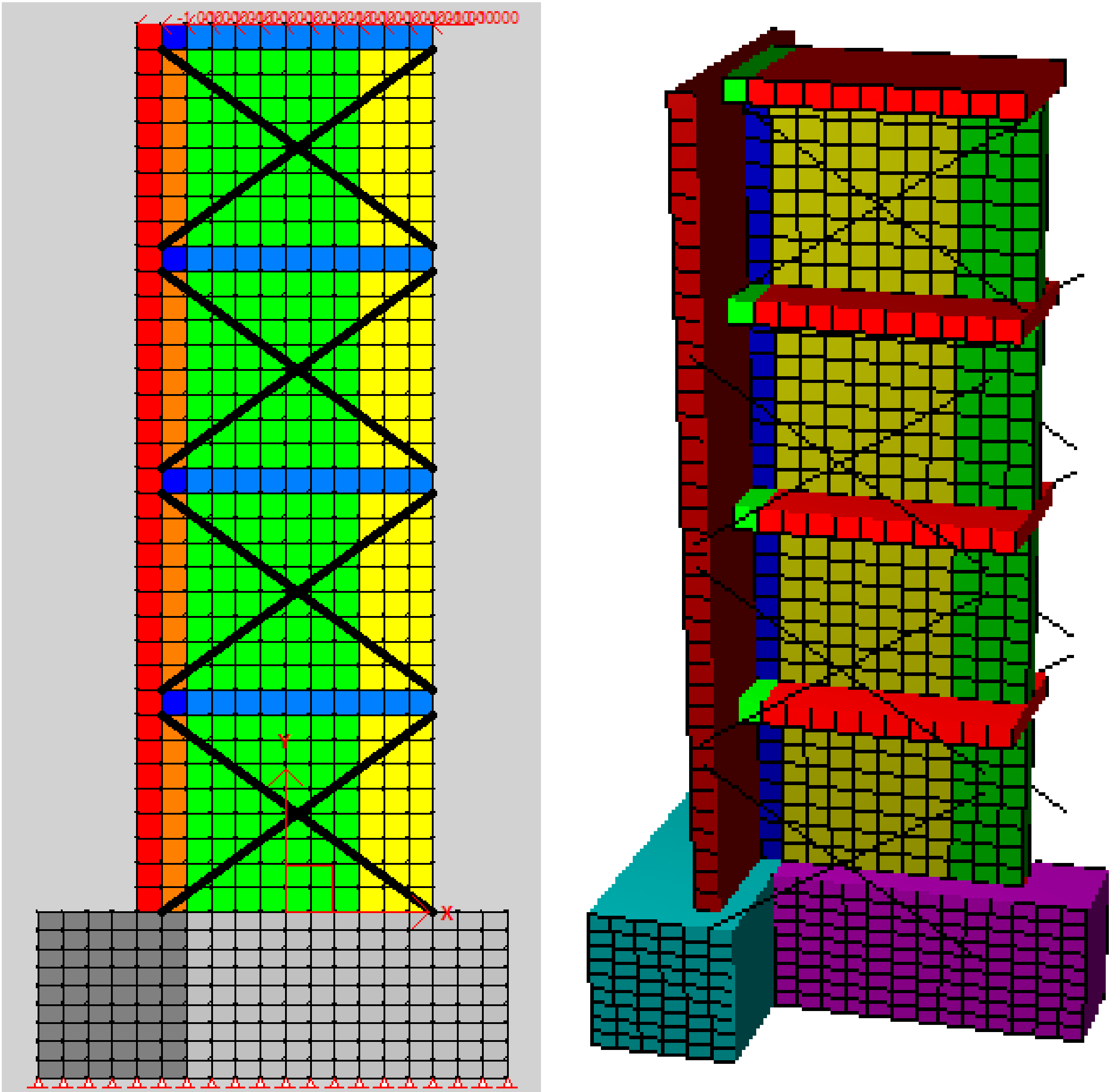

Figure 2.2 2D and 3D views of the 2D FE model for specimen TW2 in FormWorks.

It is important to note the similarity in the shape of the curvature and the shear strain diagrams for specimen RW2. VecTor2 analysis showed that shear strains were concentrated in the plastic hinge region of the wall where large vertical tensile strains were encountered. This agrees with the observation reported by Thomsen and Wallace in the test report.

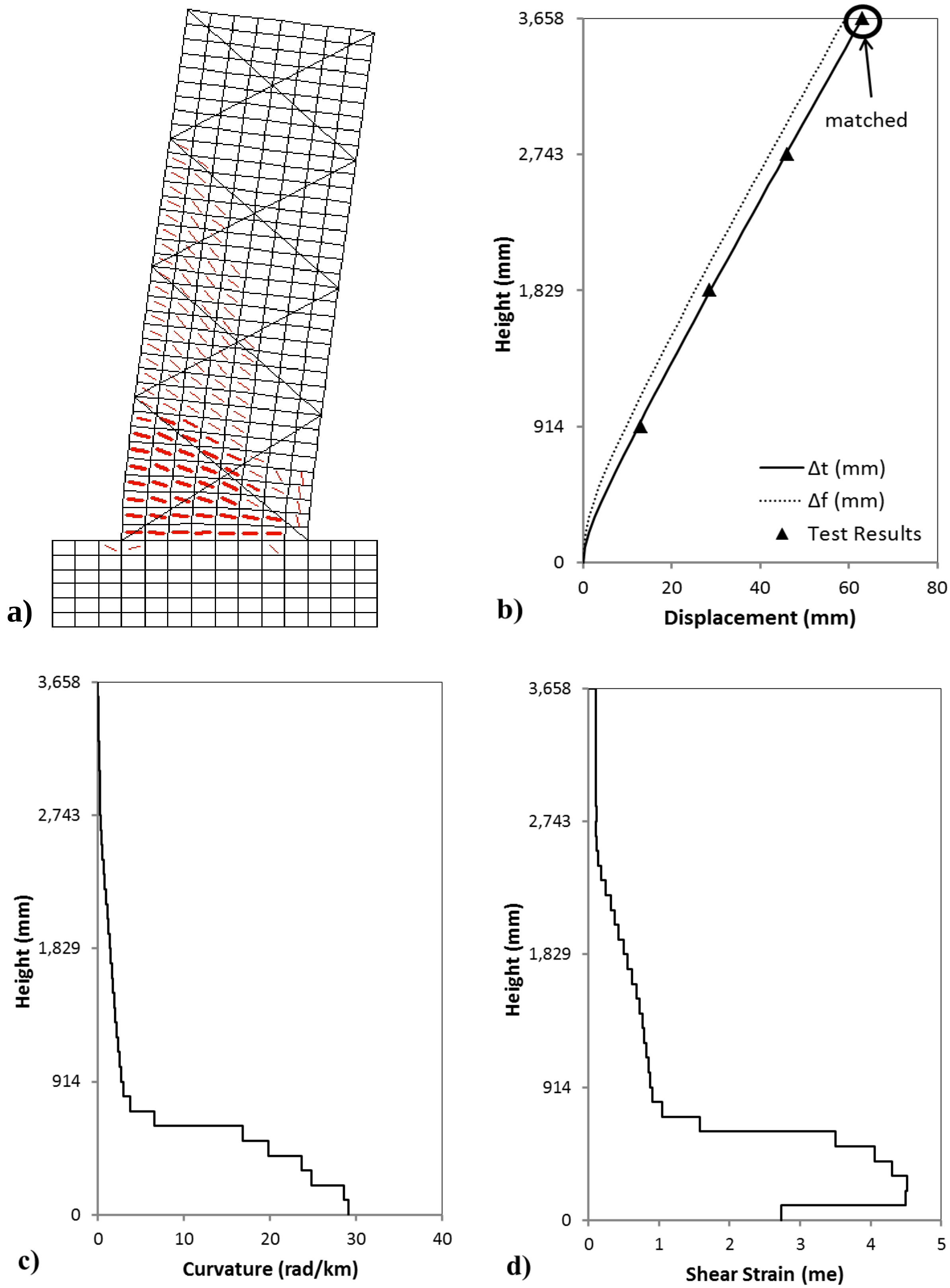

Figure 2.3 FE analysis results on specimen RW2 at 2% drift: a) cracking pattern, b) FE vs. observed displacement profile during testing, c) curvature profile, and d) shear strain profile.

Similar observations were made in the case of specimen TW2 and hence, corresponding figures for specimen TW2 are excluded for brevity.

As the objective of this section is to verify the accuracy of shear strains predicted using Vector2, shear strains from FE analyses are compared to those measured during the tests. Average panel shear distortion (strain) was measured using strain measurements of an X-type configuration.

Figure 2.4 shows the expressions that Thomsen and Wallace used to calculate shear distortion. Although this method of calculating average shear strain does not give the actual average shear strain of a panel due to the assumption of uniform curvature over the panel height, the same method is used to calculate average shear strain of the FE model to make comparison possible. This is done by modeling extremely thin truss-bar elements in X-type configuration shown in black in Figure 2.1 and substituting the deformed and un-deformed lengths of the truss-bars in the equation for average panel shear strain shown in Figure 2.4.

Figure 2.5 compares average panel shear strains obtained from FE results against those observed in the test at five different global drift (top displacement) levels. Top displacements of the FE model were matched to those observed during the test to make the comparison easier. As shown in Figure 2.5, VecTor2 was able to predict the average panel shear strain of the first storey quite accurately. The accuracy of the prediction was not as impressive in the case of average panel shear strain of the second storey. However, because the magnitude of the shear strain in the second storey was much smaller and hence less significant, it was concluded that VecTor2 is able to predict flexural and shear deformation profiles of a rectangular shear wall with good accuracy.

Figure 2.6 compares average panel shear strains obtained from FE analysis with test results for specimen TW2. VecTor2 was able to predict the average first storey shear strain with great accuracy when the flange was in compression. The accuracy of the prediction of the first storey shear strain was less accurate but still acceptable when the flange was in tension. VecTor2 predictions of the second storey average shear strains was not very accurate; however, because the magnitude of the second storey shear strain is relatively small compared to that of the first storey, the less accurate predictions of second storey shear strains can be neglected.

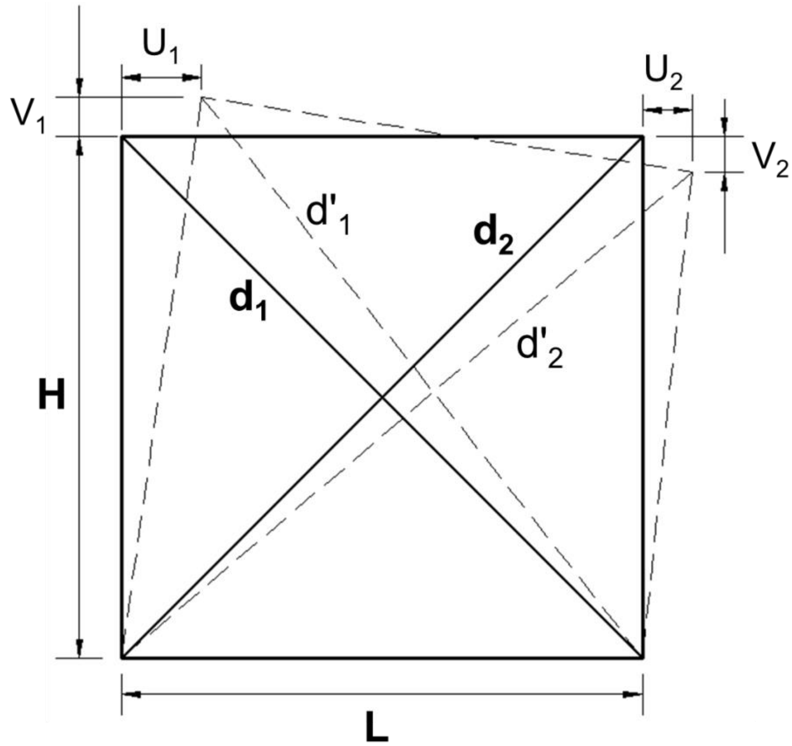

$$d'_1 = \sqrt{(H + V_1)^2 + (L - U_1)^2}$$

$$d'_2 = \sqrt{(H - V_2)^2 + (L + U_2)^2}$$

$$\gamma_{avg} = \frac{(d'_1 - d_1)d_1 - (d'_2 - d_2)d_2}{2HL}$$

Figure 2.4 Measurement of average panel shear distortion by Thomsen and Wallace (1995).

Figure 2.7 compares the relationship between average first storey shear strain and curvature obtained from test results and FE analysis. During the test, total shear deformation of the wall panels in each storey was measured using strain gages mounted on the diagonals of the wall panel in an X-type configuration. The differential change in the length of the diagonals was assumed to be solely due to shear deformation of the panel. In other words, curvature distribution over each storey height was assumed to be constant which leads to over-estimating shear deformations and strains. First storey average curvature was calculated assuming all the inelastic rotation takes place in the first storey. Total first storey deformation was divided by the storey height to give the total inelastic rotation from which average storey curvature was calculated. This procedure for calculating average first storey curvature overestimates curvature because some part of the first storey total deformation is inevitably due to shear. However, for the purpose of comparison, average first storey shear strain and curvature from FE analysis were calculated using the approach taken by Thomsen and Wallace to be consistent.

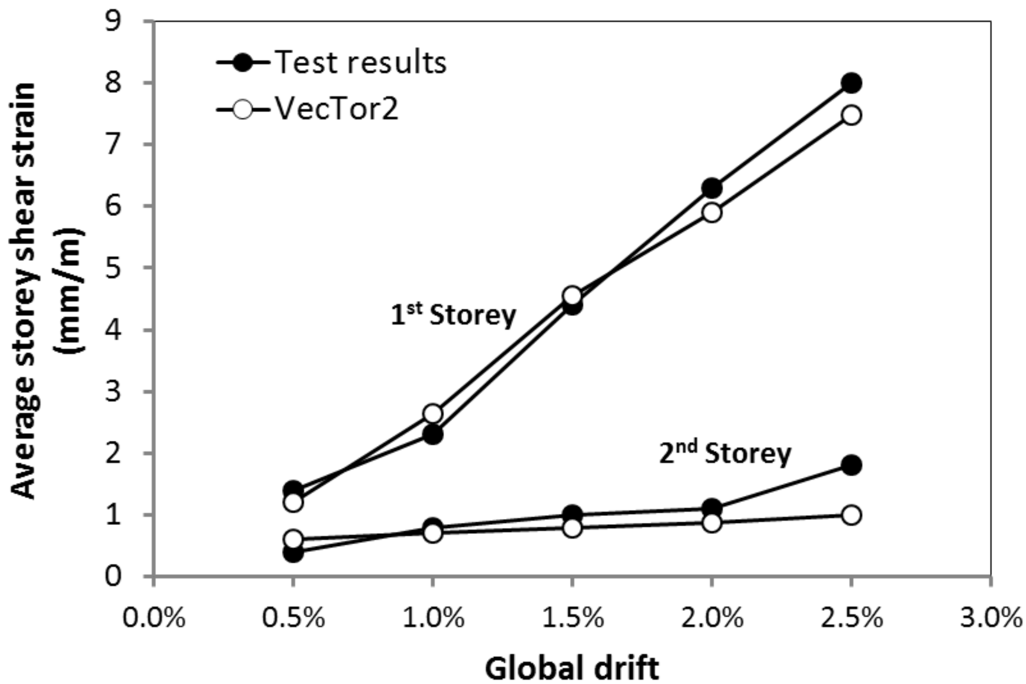

Figure 2.5 Comparison of average panel shear strain from FE model and test results for specimen RW2.

Based on Figure 2.7, VecTor2 was able to predict average first storey shear strains of the two specimens with good accuracy. There is an evident correlation between curvature and shear strains plotted in Figure 2.7. Shear strains seem to increase with curvature nearly proportionally. Thomsen and Wallace attributed this to shear strains being a result of large vertical tensile strains combined with diagonal cracking and damage of concrete. The larger the curvatures get, the larger the tensile strains become and hence, more shear strain is generated. This strong link between shear strains and curvature is used as the basis for formulating a simple model for estimating shear strain later on in this chapter.

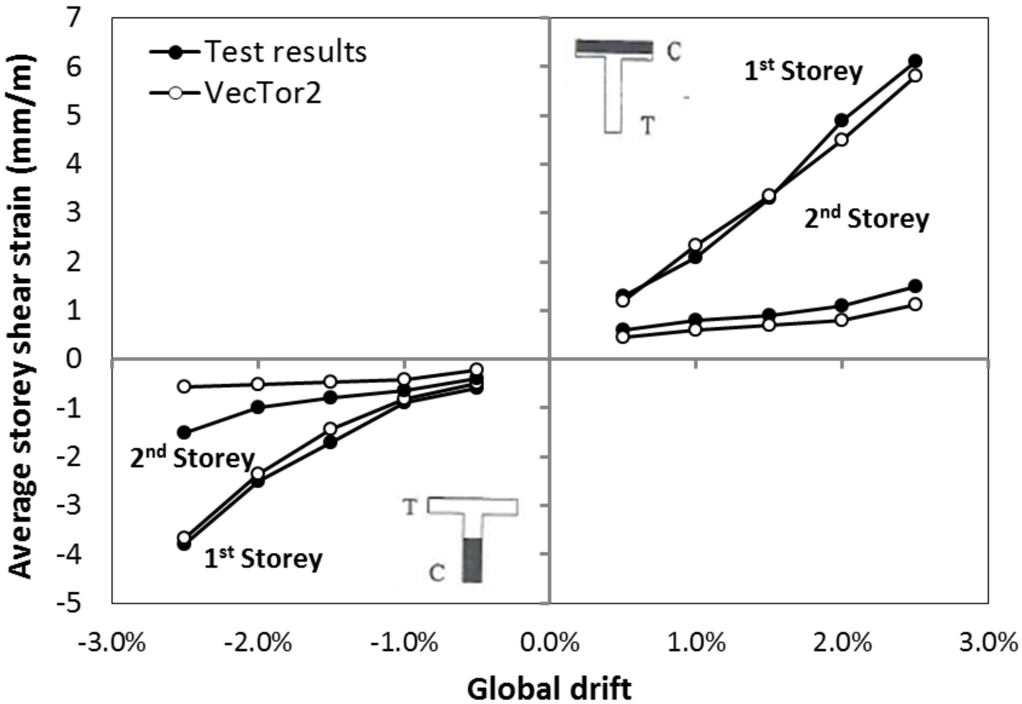

Figure 2.6 Comparison of average panel shear strain from FE model and test results for specimen TW2.

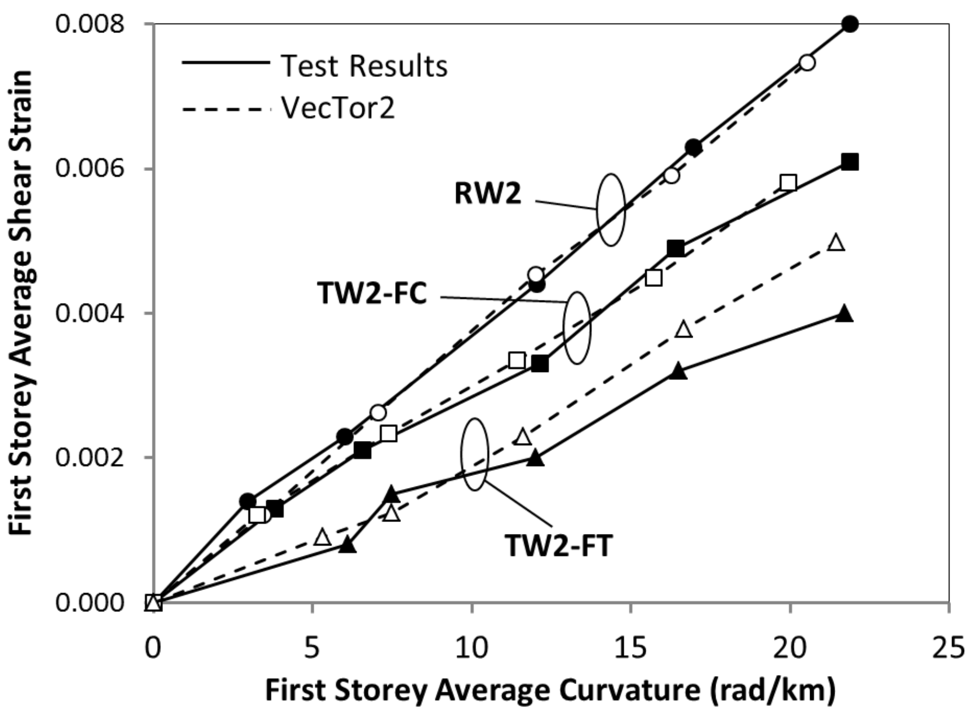

Figure 2.7 Proportionality of average first storey shear strain and curvature for specimens RW2 and TW2.

2.5.2 Specimen NTW1 tested by Brueggen (2009)

Another experimental work that was used to verify the accuracy of shear strains predicted by VecTor2 is the work of Brueggen (2009). Brueggen presented results of multi-directional loading of two T-shaped walls as a part of her PhD dissertation. The two specimens named NTW1 and NTW2 had aspect ratios of 3.2 and 1.6 respectively which makes specimen NTW2 a squat wall. Hence, only specimen NTW1 is considered here. Despite the test specimen being subjected to multi-directional loading, test data obtained for loading parallel to the web is used here because VecTor2 is a 2D FE analysis software.

Specimen NTW1 was a T-shaped wall with overall length of 2286 mm (90”), flange width of 1829 mm (72”) and equal web and flange thicknesses of 152.4 mm (6”). The overall height of the specimen was 7315 mm (288”) comprising 4 storeys. The specimen was subjected to a sustained axial compressive load of 2.7% of $f'_c A_g$ in addition to its self-weight. Floor slabs were constructed at storey levels to account for the effect of presence of floor slabs on the specimen’s cracking pattern and behaviour.

FE model of the specimen was constructed in VecTor2 using only rectangular elements with distributed reinforcing steel. Width of the rectangular elements located in the floor slab region was increased to model the effect of the floor slab on stiffness and cracking pattern of the model. The FE model was loaded using support displacements at the top to simulate the effect of hydraulic jacks pushing and pulling the test specimen at the top. Stress-strain relationship for reinforcing steel was adjusted to match the bare-bar characteristics reported in the test. Perfect bond between reinforcement and concrete material was assumed. Figure 2.8 shows 2D and 3D schematic views of the FE element model for specimen NTW1.

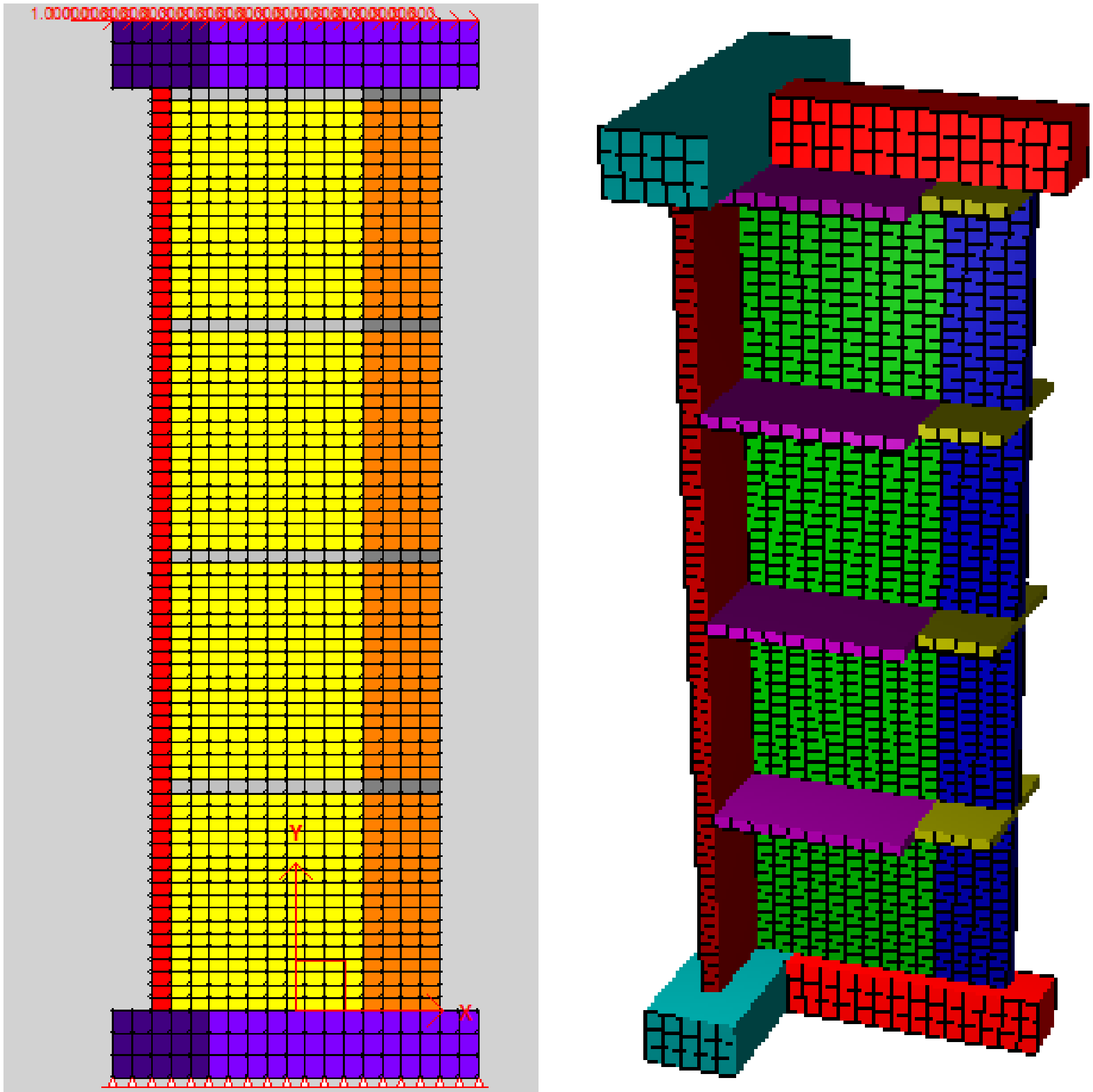

Figure 2.8 2D and 3D schematic views of FE model for specimen NTW1 in FormWorks.

Brueggen measured curvature and shear strain over 4 panels along the height of the first storey, 2 panels in the second storey, and 1 panel in the third and fourth storeys each with panel height being almost equal to the storey height. Curvature and shear strain profiles calculated from measurements during testing of specimen NTW1 with flange in tension are shown in Figure 2.9. The detailed instrumentation layout made observation of the direct link between curvature and shear strain possible. Curvature and shear strain profiles have similar shapes. High values of shear strain are concentrated in the plastic hinge region where large inelastic curvatures are encountered. This test evidence supports the theory of proportionality of curvature and shear strain in flexural walls; a theory which is used to formulate a simple model for estimating shear strains in flexural walls later in this chapter.

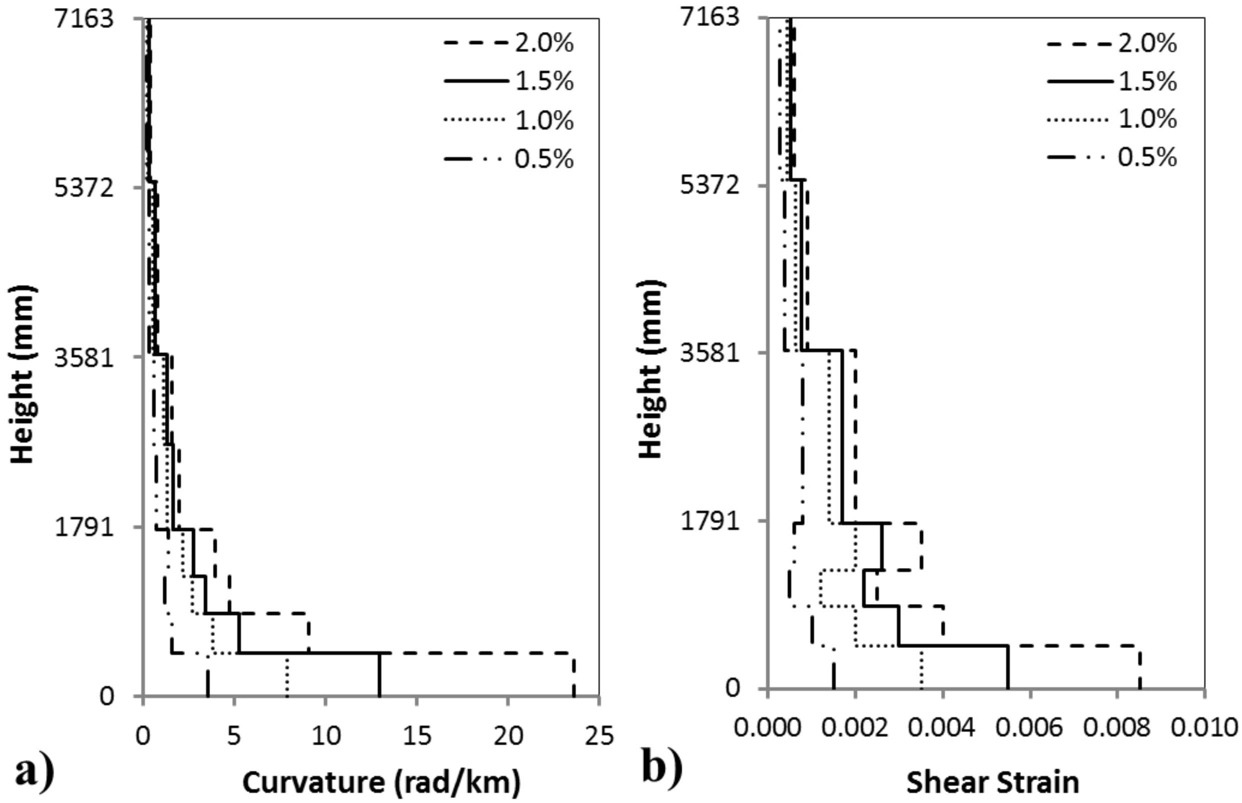

Figure 2.9 Strong link between curvature and shear strain profiles at various global drift levels observed during testing of specimen NTW1 with flange in tension.

Curvature and shear strain profiles of specimen NTW1 with flange in tension at 1.5% global drift obtained from VecTor2 are plotted in Figure 2.10. Although VecTor2 did not predict wall maximum curvature and shear strain with great accuracy, it was able to capture the general trend of the curvature and shear strain profiles rather well. Similar observation in terms accuracy of VecTor2 predictions is made at other drift levels, hence the reason for excluding similar plots at other global drift levels.

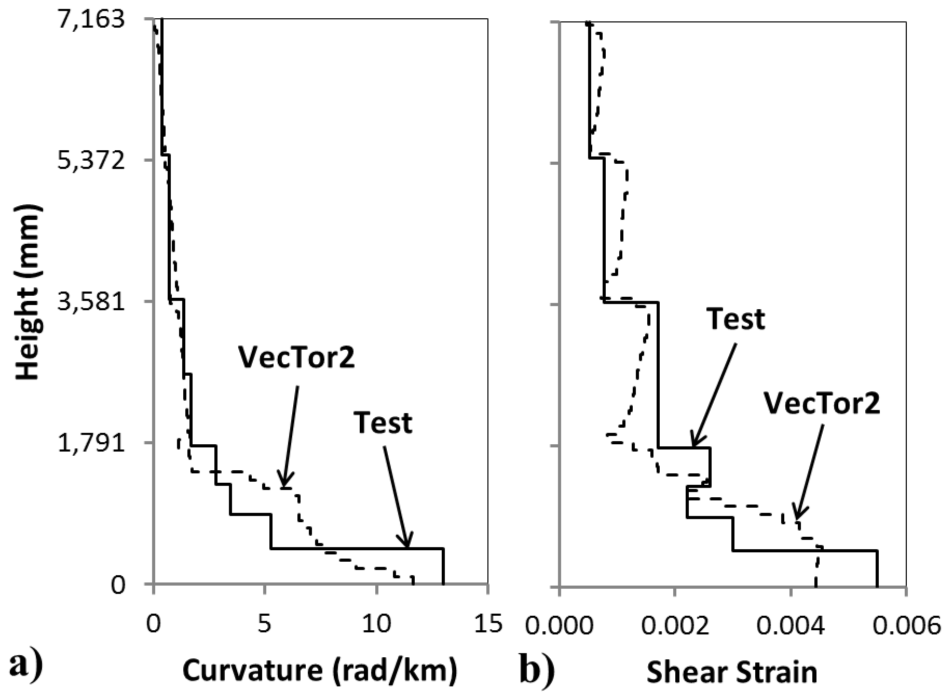

Figure 2.10 VecTor2 prediction of curvature and shear strain profiles of specimen NTW1 with flange in tension at 1.5% global drift.

Deformation components of specimen NTW1 with its flange in tension predicted by VecTor2 are compared to those reported by Brueggen in Figure 2.11. As for the test results, the values reported by Brueggen as flexural, shear, and total deformation at the four storey levels are plotted. VecTor2 predictions of shear and total deformation are the output data from the FE analysis directly. In order to obtain flexural deformations fromVecTor2 analysis, the slope of the straight line connecting the two points on the faces of the wall was assumed to represent total rotation at that particular level. Curvature was assumed to be constant over the height of each row of elements and was calculated by dividing the change in rotation from the bottom to the top of the row of elements by elements' height. Curvatures were then integrated to obtain flexural deformations. Deformation profiles obtained from VecTor2 and those reported by Brueggen were compared at matching total top displacement. Based on Figure 2.11, VecTor2 was able to predict both the flexural and shear deformation profiles with excellent accuracy when the FE model was pushed to the same total top displacement observed during the test.

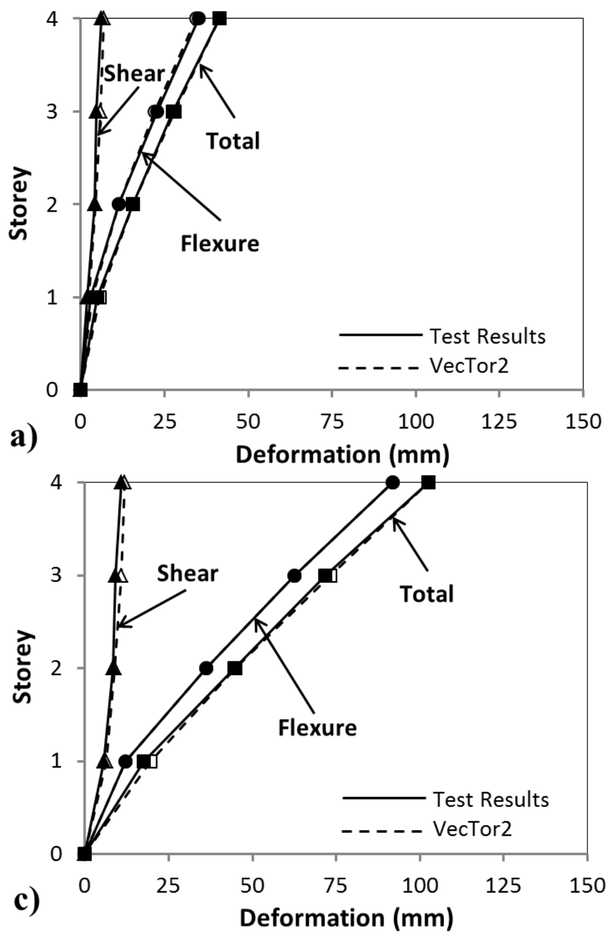

Figure 2.11 VecTor2 predictions of deformation components of specimen NTW1 with flange in tension at a) 0.5%, b) 1.0%, c) 1.5%, and d) 2.0% global drift.

2.5.3 Summary of verification study

Based on the evidence provided in the previous two sections, it is therefore concluded that Vector2 is a reliable tool for predicting shear deformation of flexural walls even without going through the complexity of modeling truss-bars, bond or link elements, or other advanced modeling techniques. Furthermore, both test results revealed a direct link between shear strains and curvatures. Shear strains grew as more curvature was induced in the wall. The shape of the curvature and shear strain profiles also looked similar. This observation was further confirmed in analytical modeling using VecTor2. The close relation between shear strains and curvature will be used later in this chapter to develop a simple method for estimating shear strains in flexural walls.

2.6 Example 10-storey Rectangular Wall

To further explore and better understand the behaviour of combined flexure and shear deformation of shear walls, a 10-storey rectangular wall was modeled in VecTor2.

Figure 2.12 shows the VecTor2 FE model. Storey height was 2743 mm. The wall cross-section was 5500 mm by 300 mm. Concrete strength was chosen to be 40 MPa. The regions at the ends of the wall (shown in red) were more heavily reinforced for additional strength and curvature capacity. Vertical reinforcement in the end regions of the wall was modeled using three sets of truss-bars (shown in green) totalling to a vertical steel ratio of 2%. In the same region, 1% distributed horizontal reinforcement and 0.5% distributed out-of-plane reinforcement was provided. 0.5% distributed steel was modeled in all the three directions over the web region of the wall (shown in yellow).

When a shear wall cracks under extreme deformation, the cracks usually do not propagate through floor slabs. Flexural (horizontal) cracks tend to form right above a floor slab and turn into flexural-shear (inclined) cracks as they move away from the slab. To account for the effect of the floor slabs on deformation profile of the shear wall, thickness of the elements located in the slab region was increased from 300 mm to 1500 mm with the element heights being equal to 203 mm (8”). Distributed vertical steel in the slab region was reduced to 0.1% so that it did not add to the total vertical steel and hence the flexural strength of the wall; however, distributed horizontal steel was kept at 0.5% to account for contribution of slab horizontal reinforcement to restraining horizontal expansion of the wall. Slab elements are shown in grey in Figure 2.12.

The bottom row of nodes was fixed against movement. Lateral load was applied at the top row of nodes using support displacements in order to carry out a displacement-controlled pushover analysis. Vertical point-loads totalling to a force of $0.10f'_cA_g$ were applied at the top of the wall and maintained throughout the analysis. Material models described in Section 2.2 were used to carry-out a monotonic pushover analysis with displacement steps of 5 mm. Sections below present analysis results and describe the observed behaviour of the FE model.

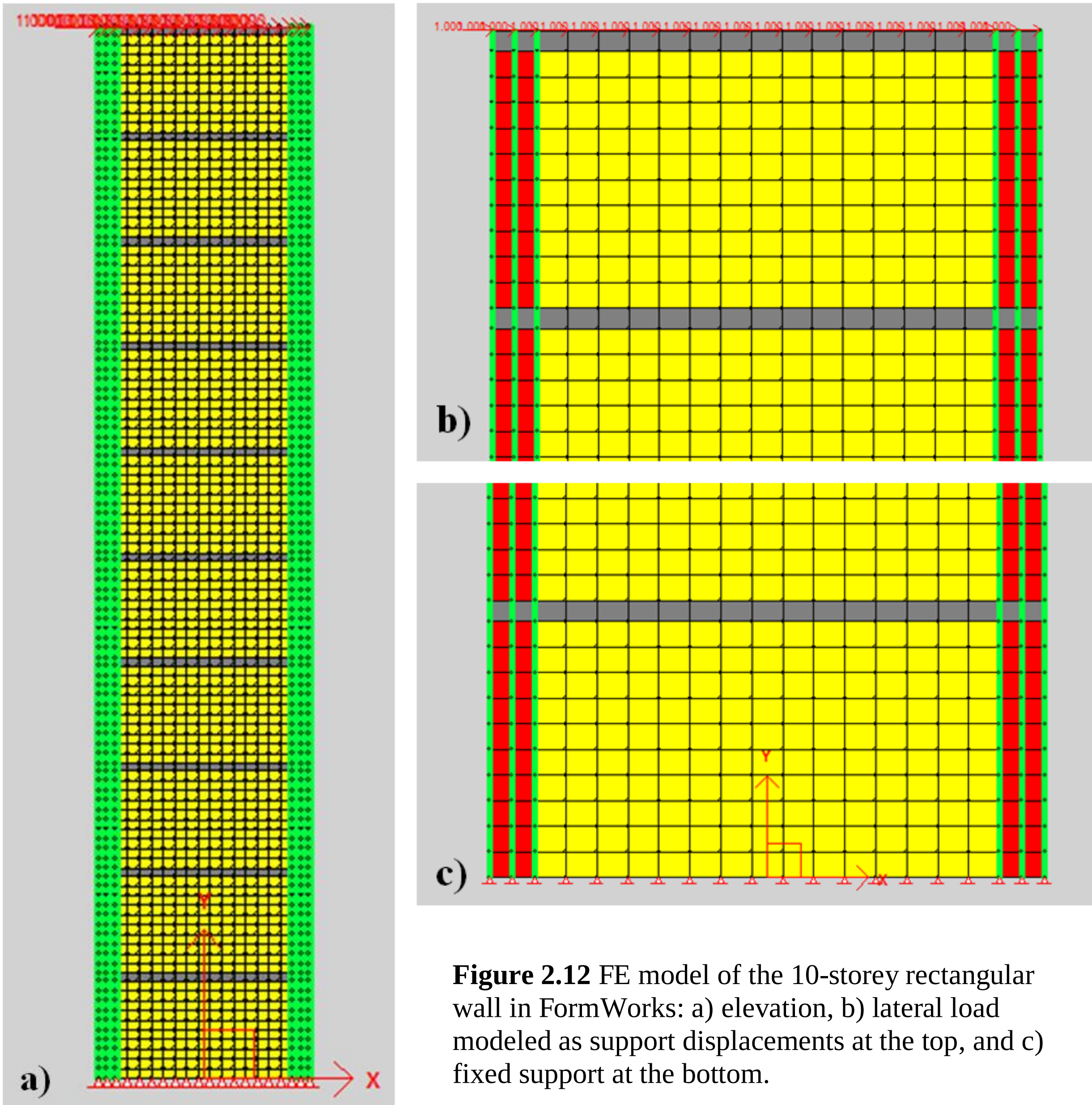

Figure 2.12 FE model of the 10-storey rectangular wall in FormWorks: a) elevation, b) lateral load modeled as support displacements at the top, and c) fixed support at the bottom.

2.6.1 Calculating flexural and shear deformations

Figure 2.13a shows the cracking pattern of the wall at 2% global drift. Thickness of the red lines within each element is an indicator of crack width while their orientation represents the crack angle. It is seen that floor slab regions have not cracked and hence serve their purpose of restraining crack propagation and force formation of flexural (horizontal) cracks right above each floor slab.

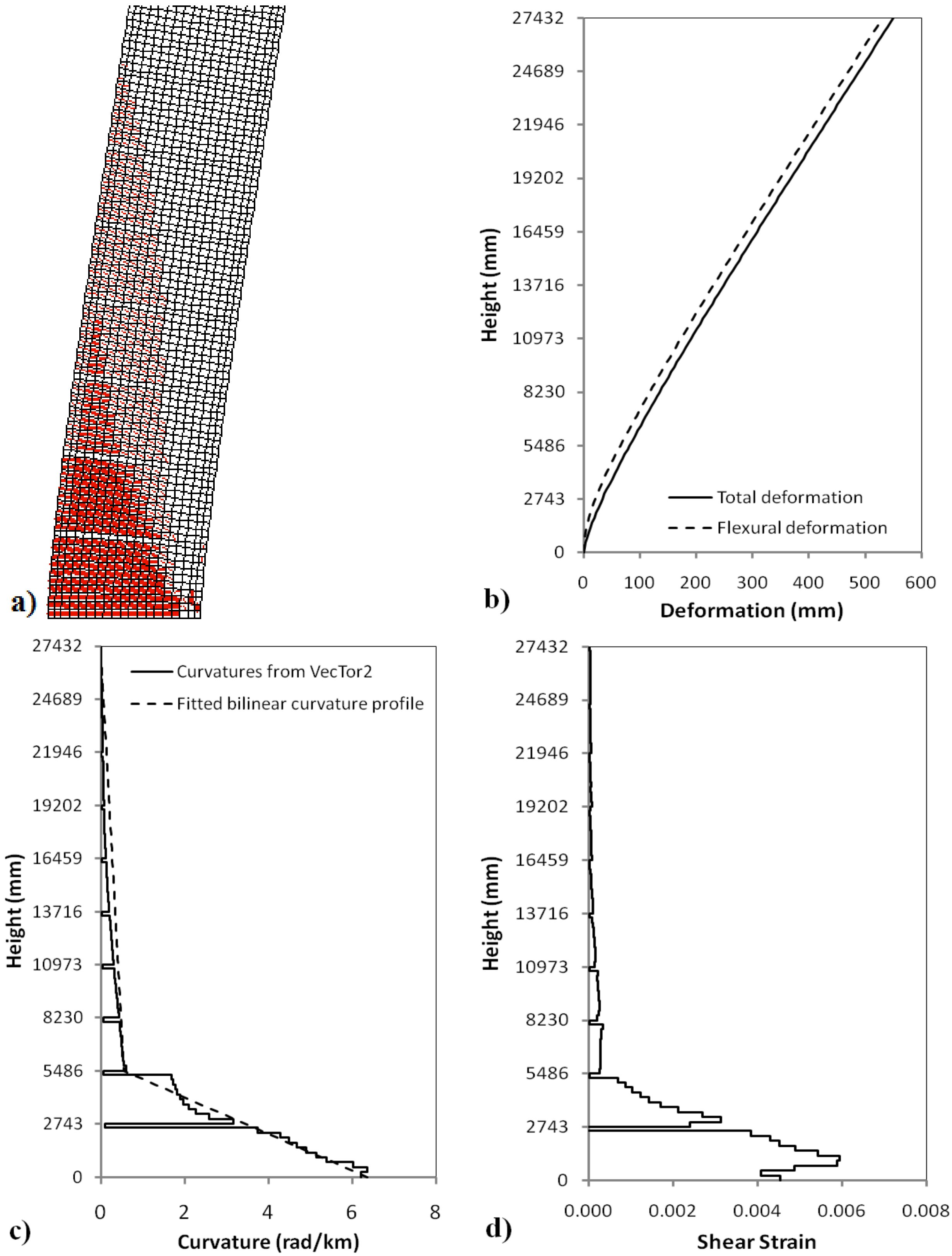

Figure 2.13 10-storey rectangular wall a) cracking pattern, b) deformation profile, c) curvature profile, and d) shear strain profile at 2% global drift.

Wall crack pattern is also a good visual tool for measuring wall plastic hinge length. The area with thicker red lines which indicate wider cracks is the plastic hinge region of the wall which in this case extends about two storeys high.

Wall total deformation profile at 2% global drift is shown in Figure 2.13b. The dashed line in the same figure indicates flexural deformations which were computed as follows. The slope of the line connecting the two end-points of each row of nodes was used as the average rotation (slope) of the wall at that level. Curvature was assumed to be constant over the height of each row of elements and was calculated as the change in average wall rotation between the two rows of nodes bounding the row of elements under consideration divided by the element height. Figure 2.13c shows the curvature profile of the wall. It can be seen that inelastic curvatures are concentrated in the first two storeys of the wall which means that wall plastic hinge length is two storeys high. Curvatures were then integrated twice to obtain wall flexural deformations (i.e. shown as the dashed line in Figure 2.13b.

Flexural deformations were then subtracted from total displacement profile to obtain shear deformations. Assuming constant shear strains over the height of elements, shear deformations were converted to the shear strain profile of the wall shown in Figure 2.13d. Note that due to the fixed-base condition of the wall and the assumed perfect bond between concrete and steel reinforcement, no additional deformation due to shear slip or bar slip occurred.

Inelastic curvatures in the plastic hinge region of the wall vary approximately linearly as demonstrated by the dashed line in Figure 2.13c. Variation of shear strain in the wall plastic hinge region is also approximately linear. Note that smaller shear strains observed in the first three rows of elements is due to boundary effects caused by the fixed-base condition of the wall. The similarity in the shapes of Figure 2.13c and Figure 2.13d indicates that shear strain and curvature are closely related and approximately proportional. This observation is in agreement with test results reported in the literature presented at the beginning of this chapter. In fact, this direct link between curvature and shear strain is the basis for the simple methods for estimating wall shear strain presented in the remainder of this chapter.

2.6.2 General observations on shear wall behaviour

Figure 2.14 shows strain profiles across the length of the wall at mid-height of the first storey at 2% global drift. Figure 2.14b reveals that vertical strain profile across the length is close to a straight line which suggests plane sections remain plane after bending of the wall. This observation holds true throughout the wall plastic hinge region other than in the first few rows of elements near the base. It is also another indication of the behaviour of the wall being dominated by flexure.

Element shear strains at first storey mid-height are plotted in Figure 2.14a. It is seen that shear strains are concentrated on the tension side of the wall with minimal shear strain observed on the compression side. The first two elements on the tension side fell into the wall's end-regions where higher vertical steel was provided to model an end-column. Presence of large amount of steel forced cracks to be flatter (i.e. closer to horizontal) which resulted in smaller shear strains in the end-regions. Flexural-shear (inclined) cracks were observed throughout the web area with lower percentage of distributed vertical steel where high levels of shear strain were observed. Shear strains become smaller moving towards the compression zone due to decreasing vertical strains. See Section 2.7.1 for the combined effect of the crack angle and vertical strain on shear strain development.

The dashed line in Figure 2.14a is the average shear strain of the corresponding row of elements. Average shear strain of each row of elements at 2% global drift is plotted in Figure 2.15 alongside the shear strain profile obtained from subtracting flexural deformations from total deformations. It is obvious that the two approaches yield very similar results for the wall shear strain profile which proves that the assumptions made for calculating wall curvature profile and flexural deformations are valid.

Plotted in Figure 2.14c are the horizontal strains. It is striking that horizontal strains are more than an order of magnitude smaller than vertical strains. Nearly zero horizontal strains exist on the tension side and those observed on the compression side do not compare with vertical or shear strains. This observation holds true throughout the wall plastic hinge length and is used later as a simplifying assumption in developing a simple model for estimating wall shear strain.

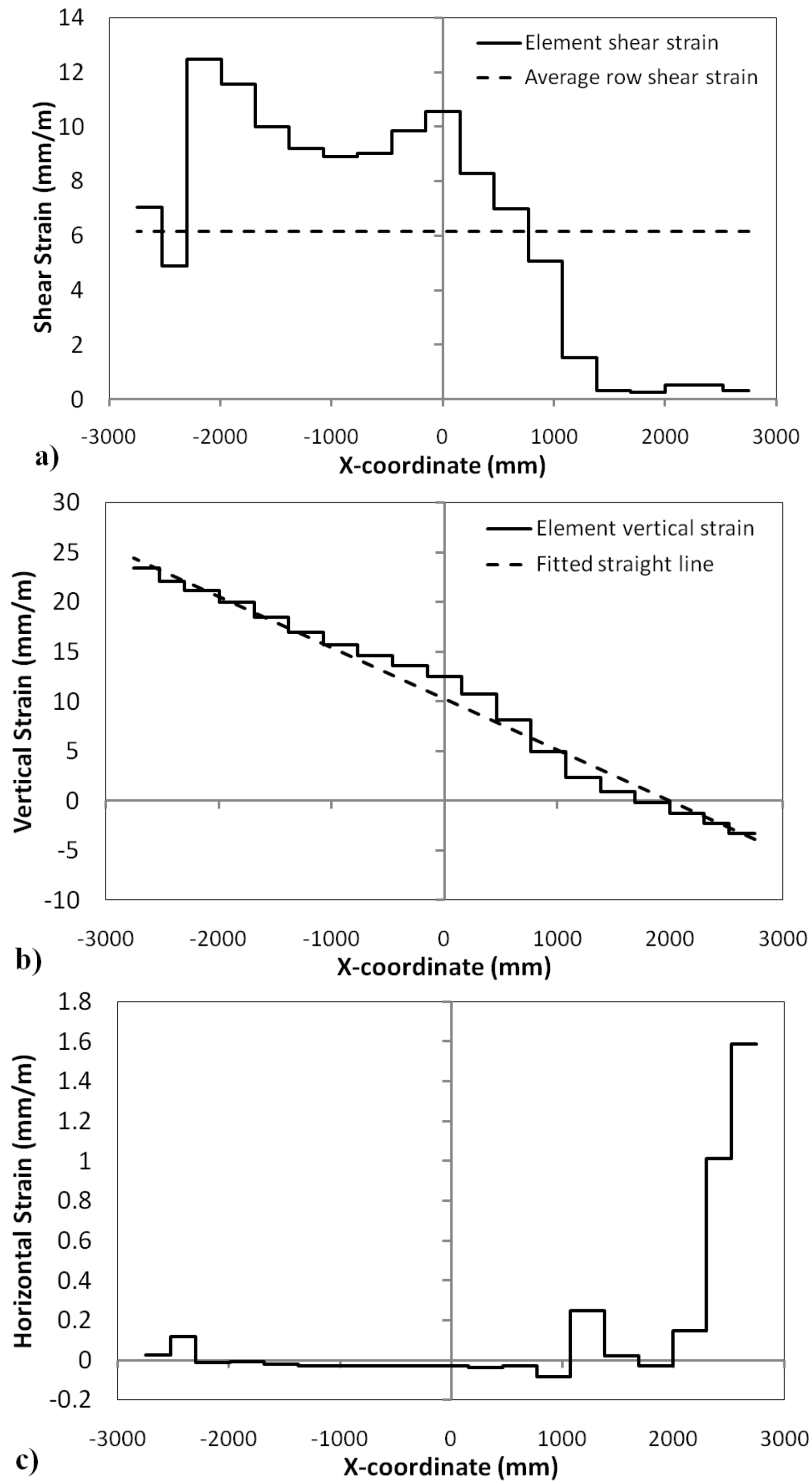

Figure 2.14 10-storey rectangular wall strains across the length at 2% global drift: a) shear strain, b) vertical strain, and c) horizontal strain at first storey mid-height.

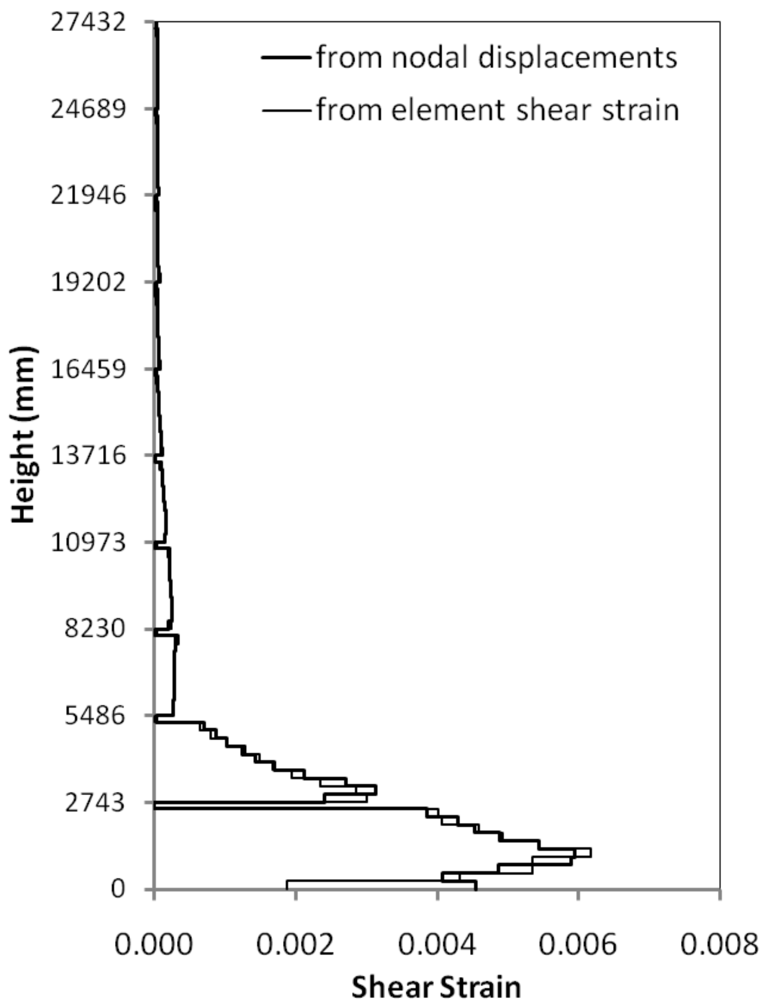

Figure 2.15 Comparison of shear strain profiles obtained from nodal displacements and average element shear strain.

Concrete stresses across the mid-height of the first storey are plotted in Figure 2.16 at 2% global drift. Figure 2.16a shows that very small shear stresses exist on the tension side of the wall despite the large shear strains encountered in that region. Due to large tensile strains and extensive opening of cracks on the tension face, very little shear can be transferred through the cracks compared to the shear carried on the compression side. This suggests that shear strains observed were not driven by shear stress.

A similar observation holds true for horizontal stresses plotted in Figure 2.16c. Horizontal stresses on the tension face of the wall are about two orders of magnitude smaller than the ones on the compression side.

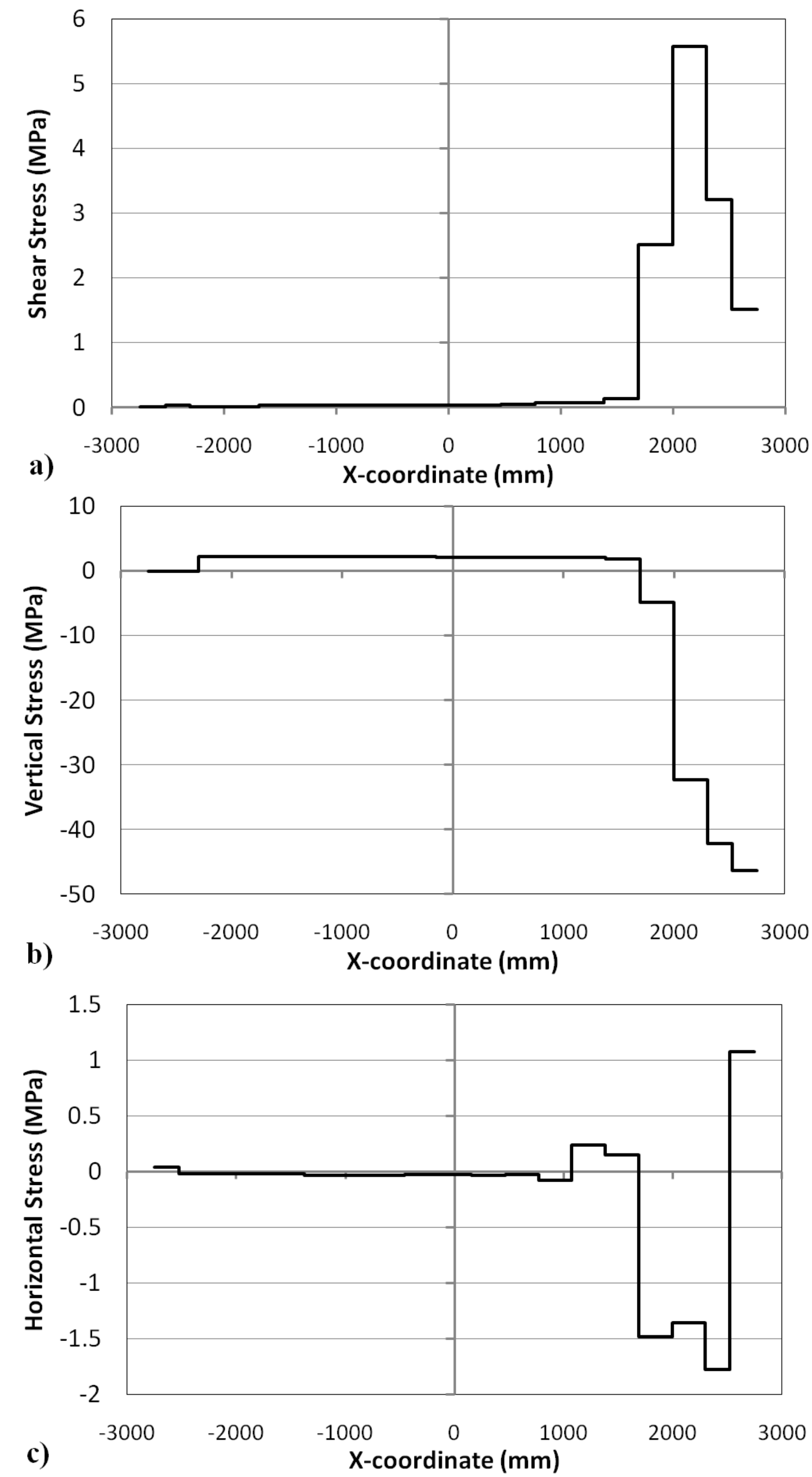

Figure 2.16 10-storey rectangular wall concrete stresses across the length at 2% global drift: a) shear stress, b) vertical stress, and c) horizontal stress at first storey mid-height.

From Figure 2.16b it can be seen that vertical tensile stresses over the majority of the tension side of the wall were small compared to vertical compressive stresses on the compression end. This was because at 2% global drift, due to very high tensile strains, concrete's contribution from tension stiffening was very small and hence, the only tensile stresses were those carried by the steel. Having nearly constant element tensile stresses in the web confirms that the vertical web steel had fully yielded. No element vertical stress is shown in the tension end because the vertical reinforcement of the end regions was modeled as truss-bars.

When the gravity system is to be checked for sufficient flexibility against imposed lateral deformations, it is only the deformation profile at floor slabs that are of importance since the gravity system is connected to the shear wall system by floor slabs. Average storey shear strain is a particularly useful measure of the shear deformation occurring in each storey. Expressing shear deformation as average storey shear strain which is equivalent to the storey shear drift is a good way to determine the proportion of flexural and shear deformation in each storey.

Figure 2.17 shows the growth in average storey shear strain with global drift for the first three storeys of the wall. Clearly, shear strains in the first and second storeys increased dramatically as the wall was pushed while average shear strain of the third storey did not undergo noticeable change. This can be explained by looking at the curvature and shear strain profiles of the wall.

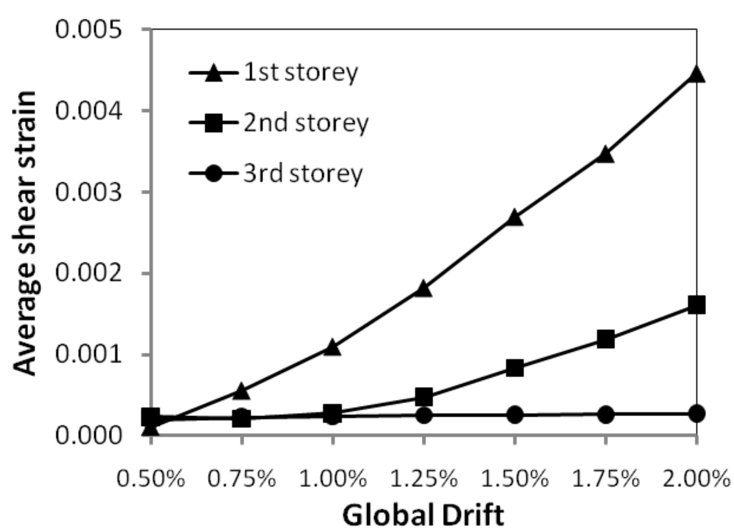

Figure 2.17 10-storey wall average shear strains at various global drift levels.

The plastic hinge length of the wall was two storeys high. After the wall yield curvature had been reached at the base, any further drift was a result of concentration of inelastic curvature in the plastic hinge zone while the elastic curvatures remain nearly constant. Increase in curvature forced an increase in vertical strains in the plastic hinge region which caused growth of shear strains as the wall was pushed beyond yielding. In this example, because the first two storeys were within the plastic hinge zone, their average shear strains kept increasing while in the third storey where curvatures remained nearly elastic, average shear strain did not change with global drift.

Since shear strains are a result of large vertical strains accompanied by inclined cracks, it is useful to plot average storey shear strains against maximum tensile strain (Figure 2.18). A trend similar to Figure 2.17 is observed which was mainly due to global drift being approximately linear in wall maximum tensile strain after the wall had yielded at its base.

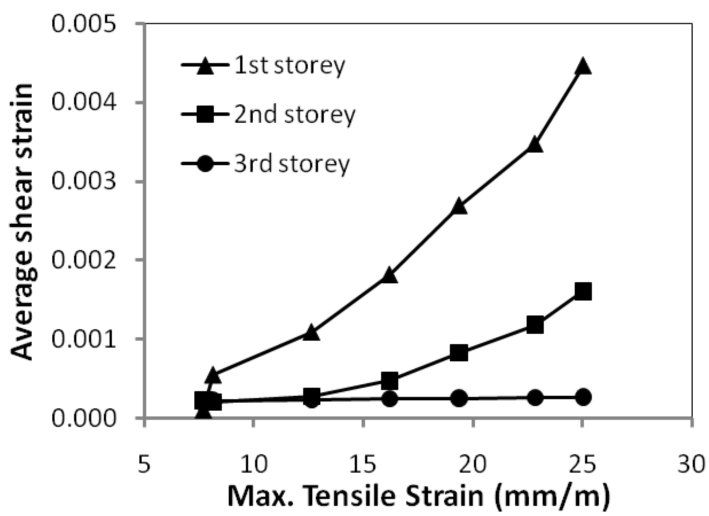

Figure 2.18 10-storey rectangular wall average shear strain at various maximum tensile strains.

The purpose of this section was to explain the general behaviour of shear deformation of flexural walls. The fundamental observations discussed in this section are utilized in formulating a simple method for estimating shear strain in flexural shear walls in the following section.

2.7 A Simple Method for Estimating Average Storey Shear Strain

A simple method for estimating average shear strain in each storey of a flexural shear wall is presented and its accuracy is examined using the 10-storey rectangular wall example described in the previous section. For this purpose, each storey of the rectangular wall is treated as a single biaxial stress Reinforced Concrete (RC) element having a shear strain close to the average storey shear strain. The following sections describe the method.

2.7.1 Shear strain of a biaxial stress RC element

Figure 2.19 shows the definition of axes used to measure total strains in a biaxial stress RC element. The X axis is parallel to the longitudinal axis of the wall and vertical reinforcements. Horizontal reinforcements are parallel to the Y axis. It is assumed that several cracks form over a single element so that all formulation could be made for average strains over a gage length equal to the element dimensions. Cracks form an angle ϴ with the X axis.

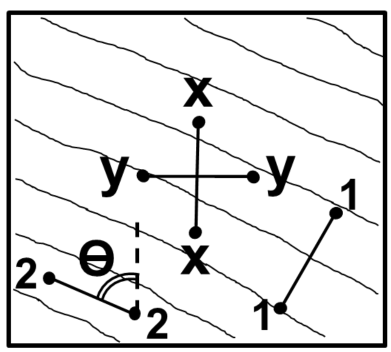

Figure 2.19 Definition of strain axes for a bi-axial stress reinforced concrete element.

According to Figure 2.14, for a RC element located on the tension side of a shear wall's plastic hinge region, horizontal strains are a couple of orders of magnitude smaller than vertical strains. Note that according to the same figure, this is the location where large shear strain is concentrated. If horizontal strains are neglected in comparison with vertical strains, the Mohr circle of strains for such an element can be approximated as the one shown in Figure 2.20.

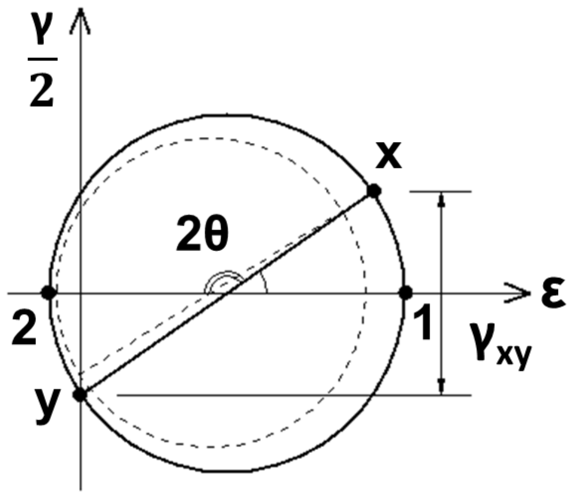

Figure 2.20 Mohr's circle for strains of a biaxial stress element with near zero horizontal strain.

Having made this simplifying assumption, shear strain of such an element is given by

$$\gamma_{xy} = \varepsilon_x \, . |\tan(2\theta)| \qquad \textbf{Eq 2.7}$$

Where ε_X is the vertical tensile strain and Θ is the principle strain angle measured from the vertical axis. Eq 2.7 shows that shear strain of a typical biaxial stress RC element located on the tension side in a shear wall's plastic hinge region is comprised of the combination of two parts. First is the vertical strain ε_X. The larger the vertical strain, the greater the element shear strain will be. Secondly, the steeper (smaller than 90°) the principle strain angle is, more shear strain will be produced for the same vertical strain. This is consistent with both the theory and the literature review of experimental evidence presented earlier in this chapter.

If an entire storey of the shear wall is to be modeled as a single biaxial stress element, estimates of the average storey vertical strain and the average storey principle strain angle need to be made for Eq 2.7 to give a good estimate of the average storey shear stress. The procedure for estimating average storey vertical strain and principle strain angle is present in the next two sections.

2.7.2 Estimating average storey vertical strain

Figure 2.14 showed that vertical strains vary approximately linearly across the wall length (i.e. plane sections remain plane after bending). This observation holds true throughout the plastic hinge region where the majority of the shear strain occurs. With the assumption of linearly varying vertical strain across the wall length, vertical strain profile across the wall section can be found knowing the curvature and the concrete compression depth (see Figure 2.21). In this case, the average vertical strain across the section would be the vertical strain of the centroidal axis given by

$$\varepsilon_v = \varphi(\frac{l_w}{2} - c) \qquad \textbf{Eq 2.8}$$

In this equation, φ is the curvature at the desired location, l_w is the wall length, and c is the concrete compression depth. According to Figure 2.13, inelastic curvatures concentrated in the wall plastic hinge region vary approximately linearly which means the value of the average storey curvature would be equal to the curvature at storey mid-height. Furthermore, if concrete compression depth does not change significantly over the height of the storey, linear variation of curvature would result in linear variation of vertical strain of the centroidal axis. Hence, if concrete compression depth is relatively constant over the storey height, the value of the curvature at storey mid-height and an appropriate value for the concrete compression depth can be used to obtain the average storey vertical strain.

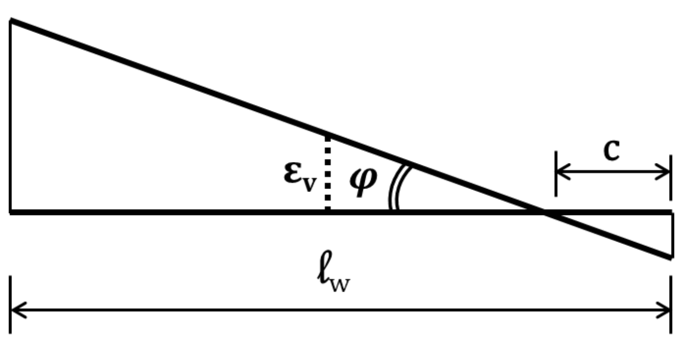

Figure 2.21 Linearly varying vertical strain assumption (i.e. plane sections remain plane).

Figure 2.22 shows concrete compression depth of the 10-storey rectangular wall cross-section obtained using three different methods. The triangular marks are data points obtained from linear interpolation between tensile and compressive vertical strains at the ends of the wall from the VecTor2 model. The solid line is obtained from section analysis using Response-2000. The dashed line is the ultimate concrete compression depth calculated using the equivalent rectangular stress block for concrete for the axial load of $0.1f'_cA_g$ applied to the section. As expected, the ultimate concrete compression depth envelopes results obtained from section analysis. Also, the variation of concrete compression depth from the ultimate value is not great for curvatures between 1.5 and 4.0 rad/km which is the range of curvatures observed throughout the wall plastic hinge range (see Figure 2.13). This suggests that the ultimate concrete compression depth is a good estimate for 'c' to be used in Eq 2.7. Note that using a smaller value for 'c' will result in a larger vertical strain which will give a larger (safer) estimate of average storey shear strain for the same average principle strain angle Θ.

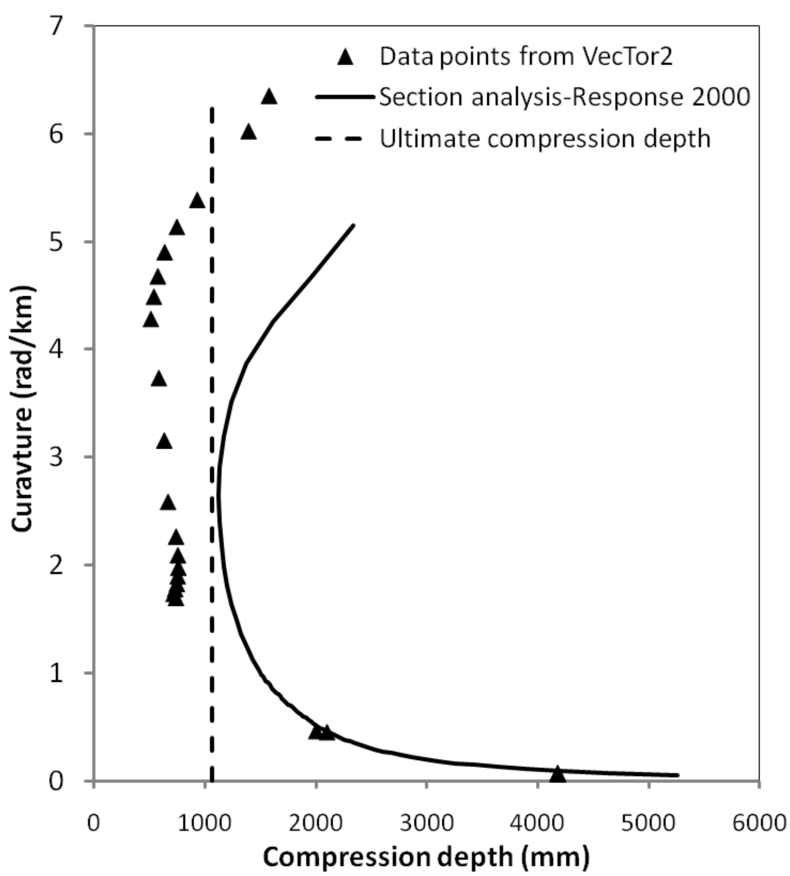

Figure 2.22 Concrete compression depth of the 10-storey rectangular wall section.

Data points obtained from VecTor2 however suggest noticeably smaller concrete compression depth than the ultimate value. The reason lies in the fundamental differences of analysis assumptions made by VecTor2 and the simple section analysis such as Response-2000. VecTor2 is a FE analysis program which accounts for concrete strength enhancement resulting from confinement or a biaxial state of stress. This means that at large maximum concrete compressive strains, concrete compressive stresses can exceed f'_c by more than 25%. Being able to sustain higher compressive stresses meant that less concrete area was needed to carry the axial load imposed on the wall which resulted in smaller concrete compression depth.

This explanation can be further enhanced by looking at Figure 2.23. Up to a curvature of 3.5 rad/km, the moment-curvature plots obtained from VecTor2 and Response-2000 are quite similar. As maximum curvature exceeds 4.0 rad/km, bending moment strength given by Response-2000 starts to decrease as concrete goes into the compression-softening region of its stress-strain relation while the strength obtained from VecTor2 keeps increasing due confinement in the horizontal and out-of-plane directions and their strength enhancement effects on concrete. This effect also results in curvature capacities obtained from the two methods to be different. If a large number of elements across the length are used in VecTor2 and strength enhancement is neglected, the two moment-curvature responses will converge.

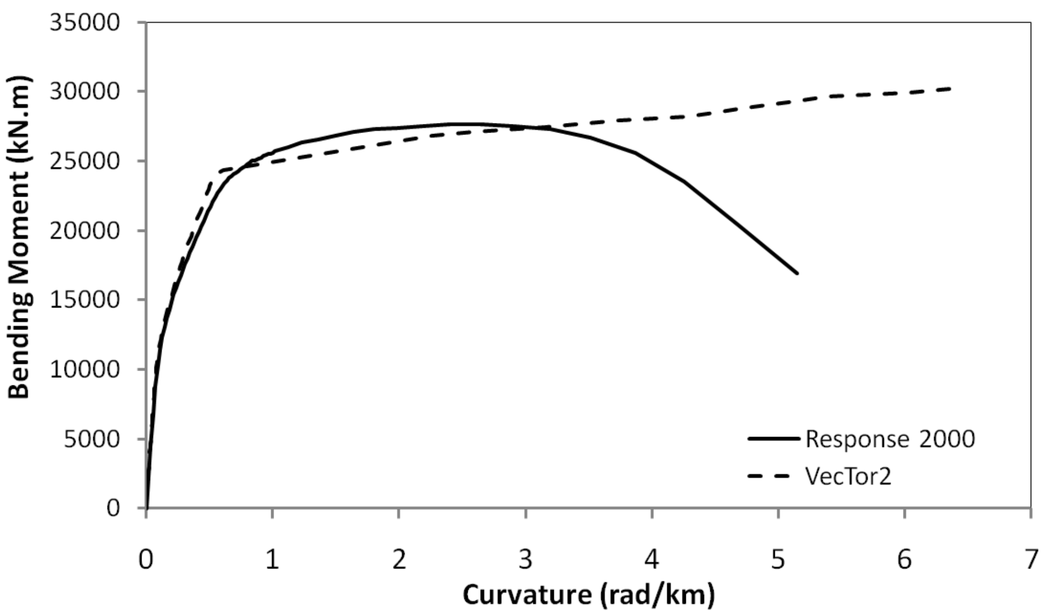

Figure 2.23 Moment-curvature response of the 10-storey rectangular wall section.

2.7.3 Estimating average storey strain angle

Element principle strain angles for the first three storeys of the 10-storey rectangular wall described in Section 2.6 are plotted in Figure 2.24 at 2% global drift. The rows of elements in the slab region have been excluded from the plots due to their distinct properties.

A similar pattern can be observed for variation of principle strain angle across the length of the wall. Neglecting the first three rows of elements in the first storey due to effects of fixity at the base, element principle strain angle tends to be relatively constant over the majority of the tension (left) side of the wall and abruptly deceases to near-zero values in the compression zone. The same pattern is seen throughout the second and third storeys with even less scatter in element principle strain angles. Note that elements with high shear strains are all on the tension side where variation of principle strain angle across the length is minimal. This suggests that taking the average of element principle strain angles over the tension zone of each storey can give a good estimate of the average storey principle strain angle to be used in Eq 2.7.

Figure 2.25 shows the average principle strain angles calculated for the first three storeys of the 10-storey rectangular wall at various global drift levels with the first three rows of elements of the first storey neglected to exclude effects of the fixed base. The angles range from 73° to 84°. Average principle strain angle of the first storey keeps dropping as global drift increases. The same behaviour is observed in the second storey beyond 1% global drift when the plastic hinge length has developed well above the first and into the second storey. Average principle strain angle of the third storey does not undergo noticeable change with global drift which is mainly due to strains remaining elastic in that region (i.e. wall plastic hinge does not extend into the third storey).

With the average storey principle strain angles in hand and the average storey vertical strain calculated using average storey curvature and ultimate concrete compression depth, average storey shear strain can be estimated using Eq 2.7. Average shear strains for the first three storeys of the 10-storey rectangular wall were estimated at various global drifts and compared against the values obtained from VecTor2. The results are summarized in Figure 2.26 in terms of global drift and in Figure 2.27 in terms of maximum tensile strain at the base of the wall.

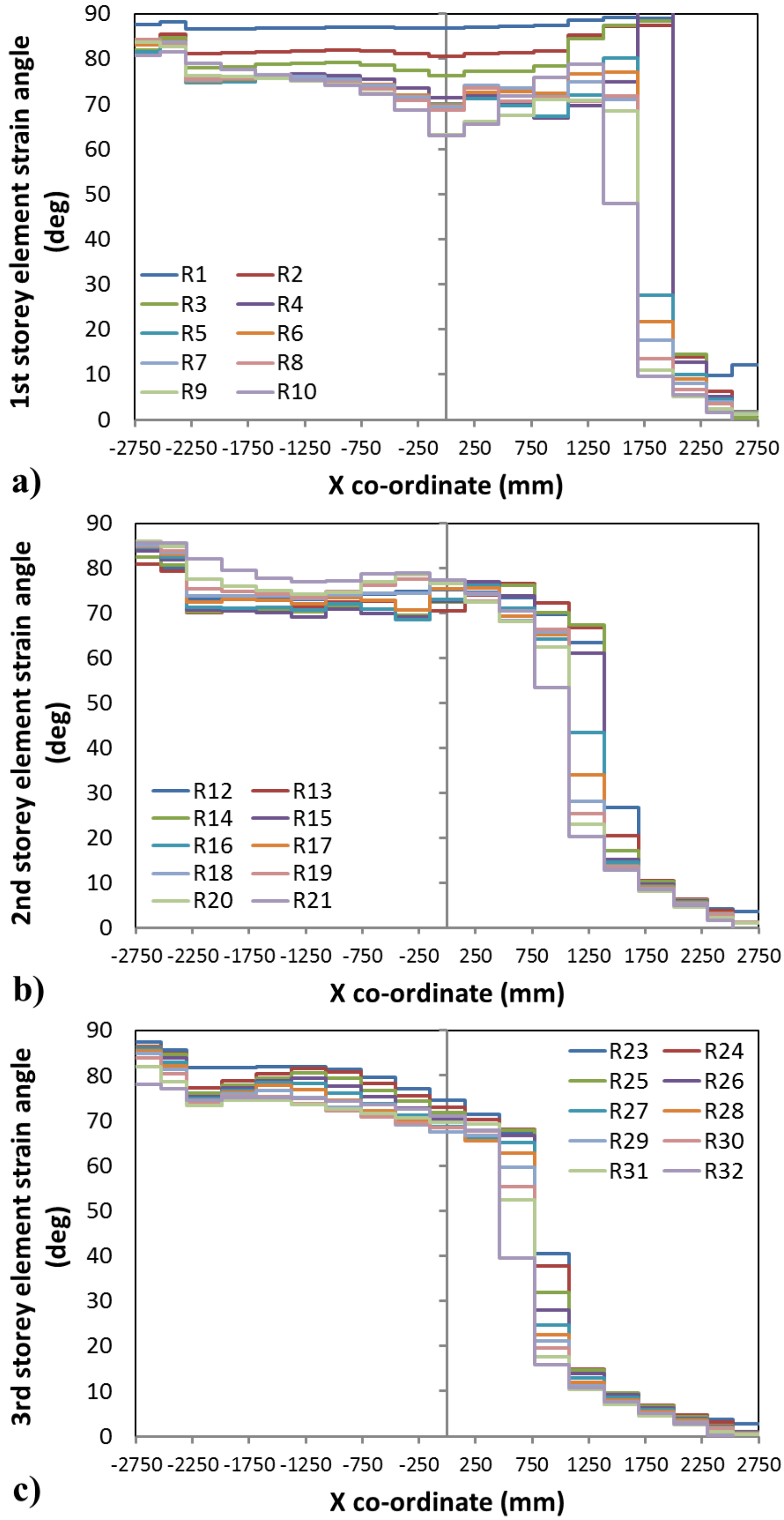

Figure 2.24 10-storey rectangular wall element strain angles at 2% global drift for: a) 1st, b) 2nd, and c) 3rd storeys.

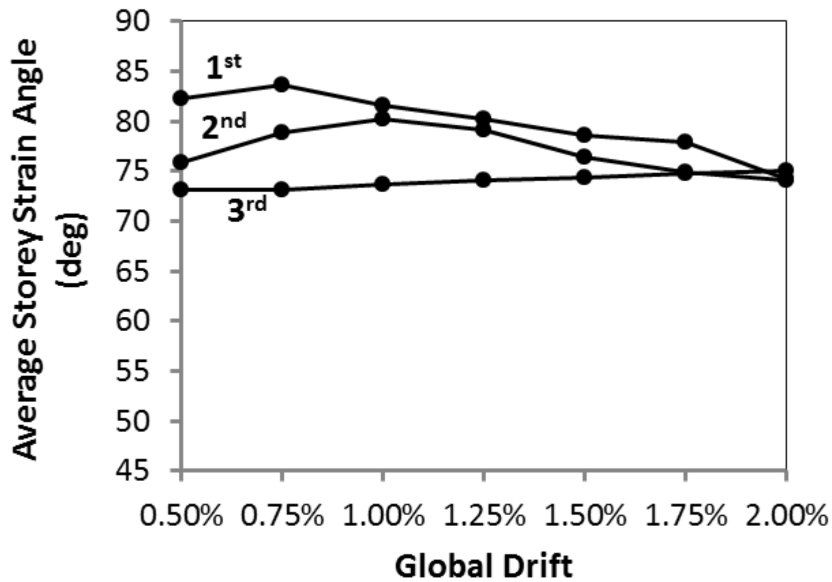

Figure 2.25 10-storey rectangular wall average storey strain angles from VecTor2.

As shown in Figure 2.26 and Figure 2.27, the simple method was capable of estimating average shear strain of the first storey with impeccable accuracy. An almost exact match was achieved between global drifts of 0.75% and 1.50%. The accuracy of the prediction decreased in the case of the second storey; however, the simple method still picked-up the pattern in variation in average storey shear strain with global drift (and maximum tensile strain) quite well. Also, the relatively smaller magnitude of average shear strains of the second storey compared to those encountered in the first storey makes the error in the estimation less significant. In addition, the simple method always gave a larger estimate of average storey shear strain which was reasonably conservative. As for the third storey, the simple method estimated almost double the amount of observed shear strain mainly due to using too small of a compression depth. However, the magnitude of the shear strains where so small that they can be entirely discarded.

The simple method for estimating average storey shear strain using average principle strain angle and average centroidal strain described earlier proved to be very accurate in this example and hence, a promising start to developing a simple model for estimating average shear strain of flexural shear walls. In the following sections, basic concepts introduced in this section are applied to a series of analysis on flexural shear walls with diverse properties. The analysis results are then combined to shape the shear strain model in its final form.

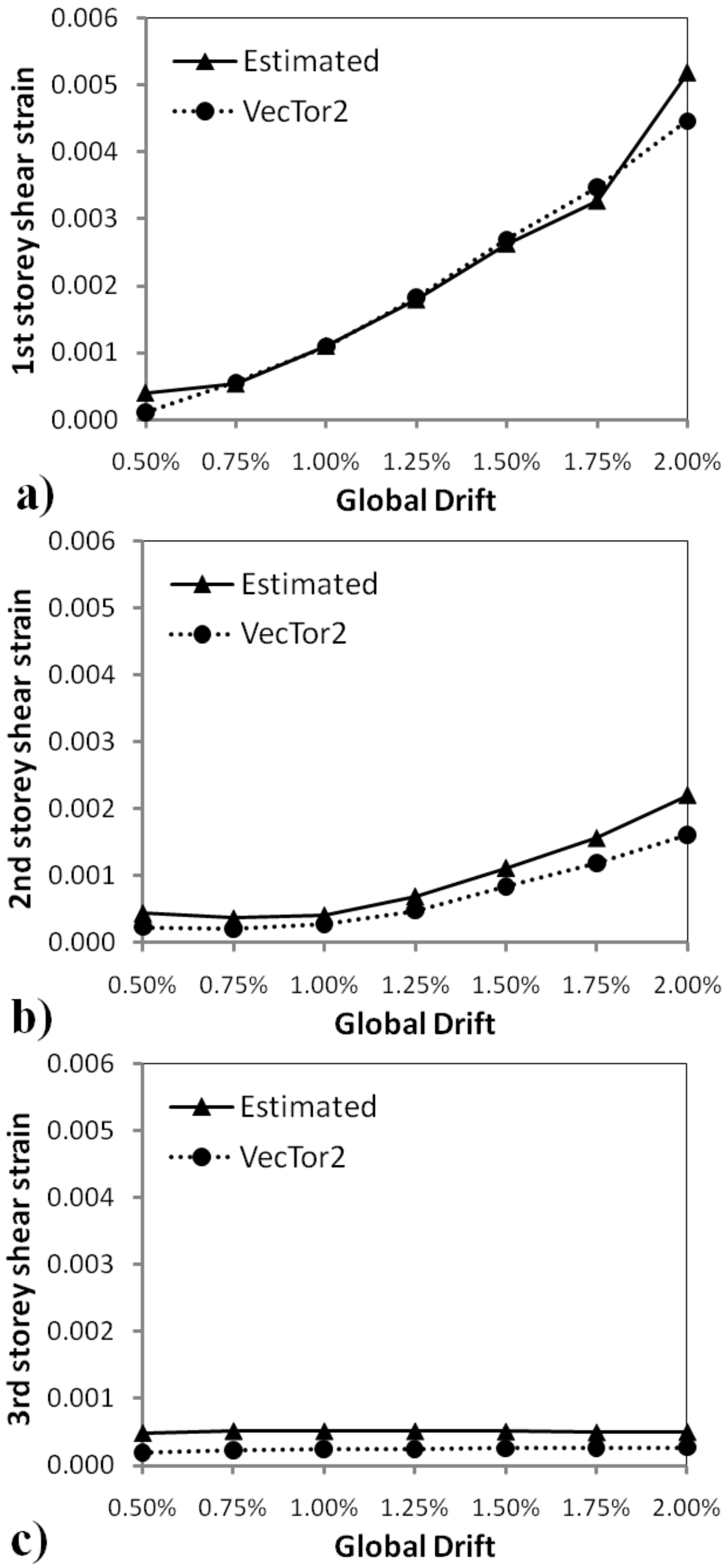

Figure 2.26 Estimating shear strain of the 10-storey rectangular wall at various global drift levels using average storey strain angles obtained from VecTor2.

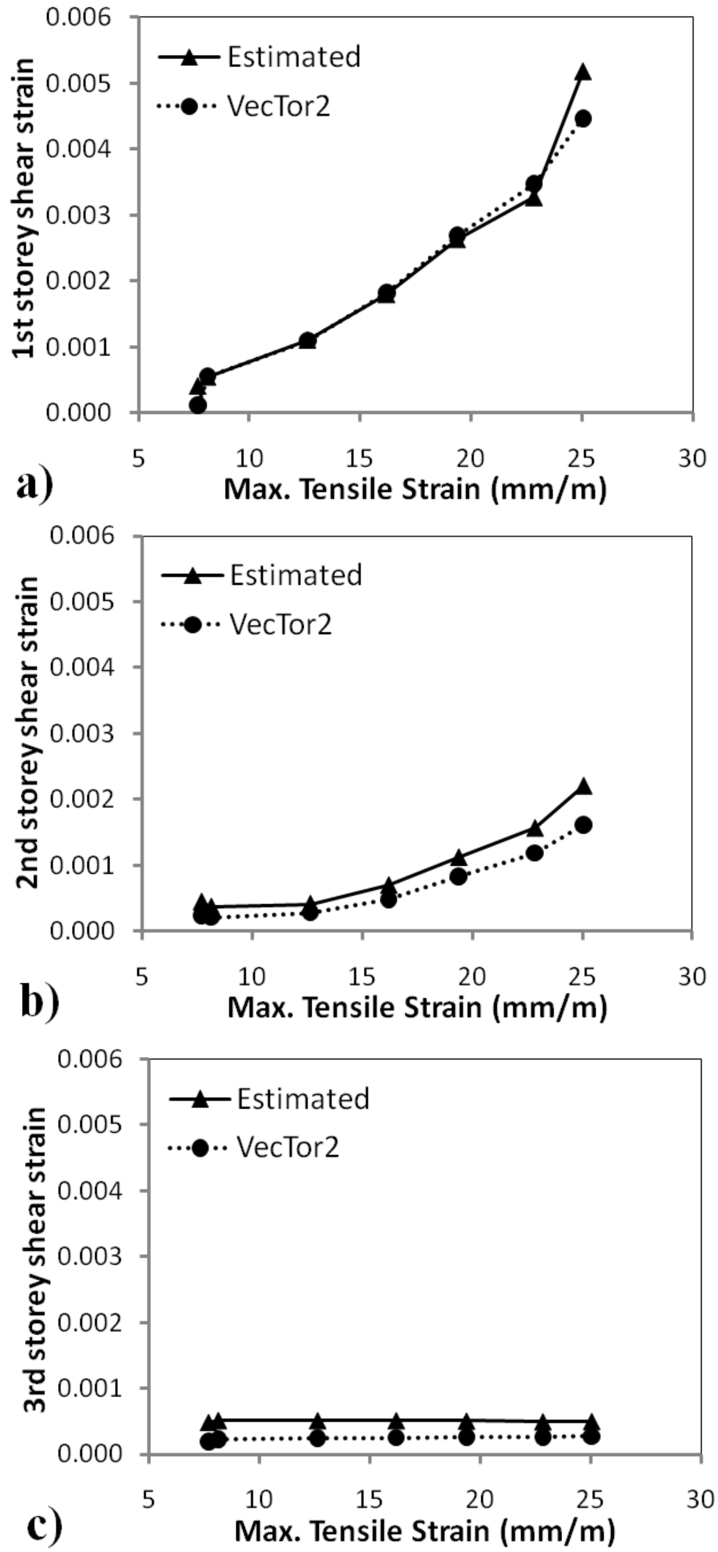

Figure 2.27 Estimating shear strain of the 10-storey rectangular wall at various maximum tensile strains at the base using average storey strain angles obtained from VecTor2.

2.8 Parametric Study on Average Storey Principle Strain Angle

Section 2.7 showed that accurate estimates of average storey shear strain can be made by using the average vertical strain of the centroidal axis and the average storey principle strain angle in Eq 2.7. Average storey centroidal vertical strain was in turn calculated using the ultimate concrete compression depth and the average storey curvature assuming plane sections remain plane. The average of element principle strain angles in each storey was used as the strain angle in Eq 2.7 to make the estimate.

There has been extensive research on estimating wall plastic hinge length resulting in several empirical relations readily available to the design engineer. Top displacement of a shear wall can be calculated using Response Spectrum Analysis (RSA) or other equivalent static methods. Contribution of shear deformation to the top displacement of a flexural wall is negligible in comparison to the total flexural deformation. With the wall plastic hinge length (height of linearly varying inelastic curvatures) and yield curvature available, one can obtain wall maximum curvature and hence the curvature profile of the wall in the plastic hinge region to meet the desired inelastic rotation demand. Ultimate concrete compression strain depth can also be computed easily by a simple section analysis using equivalent stress block for concrete. This means that average storey centroidal vertical strain can be calculated from information already available to the designer.

As for the principle strain angles however, if FE analysis is not conducted, average storey principle strain angles need to be estimated using other methods to make estimating average storey shear strain using Eq 2.7 possible. In this section, parameters that could potentially influence the average storey strain angle are identified and the effect of each parameter on the average storey strain angle is examined. This will facilitate formulating the simple method for estimating average storey shear strain of flexural shear walls presented in Section 2.9. To simplify the estimation process, a single value for the average strain angle is used throughout the wall plastic hinge region. The average strain angle is back-calculated such that an exact estimate of the value of average first storey shear strain is achieved. The same angle is then used to estimate average storey shear strain in storeys above the first storey and the accuracy of the estimation is compared against values obtained from VecTor2.

2.8.1 Effect of vertical compressive stress

The first parameter to be investigated is the amount of compressive vertical stress on the wall. The amount of axial load carried by the wall can significantly disturb the magnitude and distribution of vertical strains over the entire wall and hence, it can possibly affect average storey shear strains. Axial stress is expressed as a percentage of concrete compressive strength, f'_c, with 5% being a low value, 10% being an average value, and 20% as a high value.

Analysis was conducted on both rectangular and flanged walls. Table 2.5 and Table 2.6 summarize properties of rectangular and flanged walls considered respectively. All walls were 10 storeys tall with a uniform storey height of 2743 mm. Wall length was kept constant at 5500 mm which resulted in a wall aspect ratio of 5.0. Compressive axial load was applied at the top of the wall resulting in constant average axial stress throughout the walls' height. Point loads in the form of support displacements were applied at the top of the walls and the walls were pushed to large displacement ductility.

Additional vertical and horizontal reinforcing steel was provided in the end 450 mm of the rectangular walls to increase both strength and ductility. Flange width of the flanged walls was 2000 mm with uniform stress distribution over the flange area due to the 2D limitation of VecTor2. Vertical reinforcement in the end-regions of rectangular walls and flange region of flanged walls was modeled as truss-bars to ensure continuity of vertical steel strain in those regions. 0.5% distributed reinforcing steel was modeled in all three orthogonal directions of the web region of both rectangular and flanged walls.

To restrict cracks from propagating through the floor slabs, the width of elements in the slab region was chosen to be five times the width of the wall web region such that the high axial in-plane stiffness of the slab prevented it from cracking. However, to make sure that vertical steel in the slab did not add to flexural stiffness and strength of the wall because of the 2D analysis space in VecTor2, vertical reinforcement in the slab region was chosen to be one-fifth of that modeled in the web region of the wall to compensate for the slab width being five times the web thickness. All other parameters were kept constant as axial compressive stress varied from 5% to 20% of concrete compressive strength.

Table 2.1 Properties of 10-storey rectangular walls used to study the effect of compressive axial stress on average storey principle strain angle

Wall ID	Cross-section (mm)	Elevation Layout	P/f'_cA_g (%)	Concrete Properties	Reinforcing Steel Properties	Distributed Steel Reinforcement Layout: End Regions ρ_x	End Regions ρ_y	End Regions ρ_z	Web Region ρ_x	Web Region ρ_y	Web Region ρ_z	Slab Region ρ_x	Slab Region ρ_y	Slab Region ρ_z
10STRW-P5	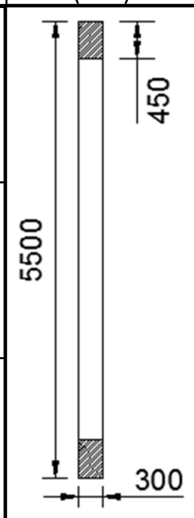	H_w=27432 mm H_{st}=2743 mm 10 storey wall	**5**	f'_c=40 MPa VecTor2 default values used for other parameters	F_y=400 MPa F_u=640 MPa E_s=200 GPa E_{sh}=3 GPa e_{sh}=0.007	1.0%	2.0%	0.5%	0.5%	0.5%	0.5%	0.5%	0.1%	0.5%
10STRW-P10			**10**			1.0%	2.0%	0.5%	0.5%	0.5%	0.5%	0.5%	0.1%	0.5%
10STRW-P20			**20**			1.0%	2.0%	0.5%	0.5%	0.5%	0.5%	0.5%	0.1%	0.5%

Table 2.2 Properties of 10-storey flanged walls used to study the effect of compressive axial stress on average storey principle strain angle

Wall ID	Cross-section (mm)	Elevation Layout	P/f'_cA_g (%)	Concrete Properties	Reinforcing Steel Properties	Distributed Steel Reinforcement Layout								
						Flange Region			Web Region			Slab Region		
						ρ_x	ρ_y	ρ_z	ρ_x	ρ_y	ρ_z	ρ_x	ρ_y	ρ_z
10STFW-P5	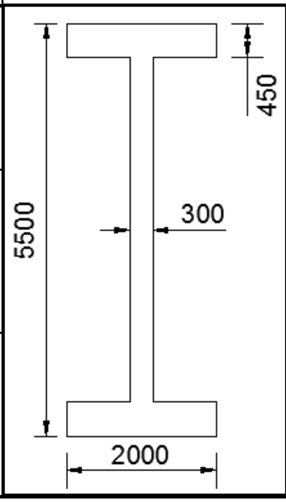	H_w=27432 mm H_{st}=2743 mm 10 storey wall	**5**	f'_c=40 MPa VecTor2 default values used for other parameters	F_y=400 MPa F_u=640 MPa E_s=200 GPa E_{sh}=3 GPa e_{sh}=0.007	0.5%	0.5%	0.5%	0.5%	0.5%	0.5%	0.5%	0.1%	0.5%
10STFW-P10			**10**			0.5%	0.5%	0.5%	0.5%	0.5%	0.5%	0.5%	0.1%	0.5%
10STFW-P20			**20**			0.5%	0.5%	0.5%	0.5%	0.5%	0.5%	0.5%	0.1%	0.5%

Table 2.3 and Table 2.4 summarize analysis results for rectangular and flanged walls respectively. All the parameters needed to make an estimate of average storey shear strain using Eq 2.7 are given in the tables. As expected, ultimate concrete compression depth 'c' increased dramatically as the average compressive axial stress on the wall was increased from 5% to 20% of f'_c in rectangular walls. This was because larger concrete area was needed to carry the additional axial load imposed on the wall. However, the change in concrete compression depth was not as great in the case of flanged walls due to the large flange width except for the case with an axial load of $0.20f'_cA_g$ where the compression depth exceeded the flange depth and caused a large increase in concrete compression depth due to relatively small web width.

Average storey curvatures were computed by fitting a straight line to the inelastic curvatures in the wall plastic hinge region. Average centroidal vertical strain, ε^*_{cen}, was then computed from average storey curvature and the ultimate concrete compression depth. As described earlier, the average strain angle was back-calculated such that an exact estimate of the value of average first storey shear strain was achieved. The same angle was then used to estimate average storey shear strain in storeys above the first storey. Because the plastic hinge region did not extend into the third storey in any case, only results for the first 2 storeys are presented. The back-calculated average strain angles are close to the average of element principle strain angles in the first storey of the wall in all cases. Furthermore, the two parameters demonstrate a similar trend. Estimations of second storey average shear strain using the average strain angle back-calculated to give a perfect match for average first storey shear strain are also reasonably close to those obtained from VecTor2. These statements hold true both rectangular and flanged walls.

To further examine the effect of average compressive stress one average strain angle, the back-calculated average strain angles are plotted against wall maximum tensile strain. Figure 2.28 and Figure 2.29 show these results for rectangular and flanged walls respectively. In both cases, the average strain angle decreased as the wall maximum tensile strain increased. This means that more shear strain per unit vertical strain was achieved at higher maximum tensile strains. According to Figure 2.28, higher levels of average compressive axial stresses on the wall resulted in smaller average strain angles. However, the effect was not seen to be substantial. A similar observation was made for the case of flanged walls with the average strain angle being affected by the average axial compressive stress even less than the case of rectangular walls.

Table 2.3 Analysis results: 10-storey rectangular walls with various compressive axial stresses (Note: values of 'c' reported were used to back-calculate the average storey strain angle and do not represent the actual concrete compression depth of the wall at the given global drift).

				1st storey				2nd storey				Average first storey strain angle (deg)	
Wall Type	**Drift**	ε_t^{max}	**c (mm)**	$\gamma_{VecTor2}$	Φ_{avg} (rad/km)	$\varepsilon^*_{cen.}$	$\gamma_{Estimate}$	$\gamma_{VecTor2}$	Φ_{avg} (rad/km)	$\varepsilon^*_{cen.}$	$\gamma_{Estimate}$	**Back-calculated**	**VecTor2**
10STRW-P5	0.50%	0.0076	724	0.0001	0.90	0.0018	0.0001	0.0002	0.49	0.0010	0.0001	88.5	83.1
	0.75%	0.0090	724	0.0007	1.46	0.0030	0.0007	0.0002	0.53	0.0011	0.0003	83.1	82.7
	1.00%	0.0131	724	0.0013	2.26	0.0046	0.0013	0.0003	0.75	0.0015	0.0004	81.9	80.5
	1.25%	0.0165	724	0.0021	2.95	0.0060	0.0021	0.0006	1.02	0.0021	0.0007	80.5	79.4
	1.50%	0.0203	724	0.0031	3.73	0.0075	0.0031	0.0010	1.42	0.0029	0.0012	78.8	77.3
	1.75%	0.0233	724	0.0040	4.37	0.0089	0.0040	0.0015	1.88	0.0038	0.0017	77.8	75.9
	2.00%	0.0250	724	0.0053	4.86	0.0098	0.0053	0.0020	2.21	0.0045	0.0024	75.9	74.3
10STRW-P10	0.50%	0.0077	1062	0.0001	0.92	0.0016	0.0001	0.0002	0.49	0.0008	0.0001	87.9	82.3
	0.75%	0.0081	1062	0.0006	1.46	0.0025	0.0006	0.0002	0.56	0.0009	0.0002	83.7	83.6
	1.00%	0.0120	1062	0.0011	2.15	0.0036	0.0011	0.0003	0.68	0.0012	0.0003	81.6	81.5
	1.25%	0.0159	1062	0.0018	2.98	0.0050	0.0018	0.0005	1.03	0.0017	0.0006	80.0	80.2
	1.50%	0.0196	1062	0.0027	3.69	0.0062	0.0027	0.0008	1.29	0.0022	0.0009	78.3	78.6
	1.75%	0.0228	1062	0.0035	4.34	0.0073	0.0035	0.0012	1.59	0.0027	0.0013	77.3	78.0
	2.00%	0.0250	1062	0.0045	5.01	0.0085	0.0045	0.0016	2.10	0.0036	0.0019	76.1	74.2
10STRW-P20	0.50%	0.0049	1754	0.0002	0.75	0.0007	0.0002	0.0002	0.49	0.0005	0.0001	82.8	80.9
	0.75%	0.0079	1754	0.0003	1.52	0.0015	0.0003	0.0002	0.56	0.0006	0.0001	83.9	84.6
	1.00%	0.0114	1754	0.0009	2.28	0.0023	0.0009	0.0002	0.76	0.0008	0.0003	79.3	79.9
	1.25%	0.0143	1754	0.0014	2.92	0.0029	0.0014	0.0003	1.01	0.0010	0.0005	77.3	79.1
	1.50%	0.0184	1754	0.0021	3.78	0.0038	0.0021	0.0005	1.31	0.0013	0.0007	75.3	77.2
	1.75%	0.0217	1754	0.0028	4.49	0.0045	0.0028	0.0007	1.48	0.0015	0.0009	73.9	76.0
	2.00%	0.0231	1754	0.0041	5.00	0.0050	0.0041	0.0018	1.78	0.0018	0.0021	75.6	73.6

Table 2.4 Analysis results: 10-storey flanged walls with various compressive axial stresses (Note: values of 'c' reported were used to back-calculate the average storey strain angle and do not represent the actual concrete compression depth of the wall at the given global drift).

				1st storey				2nd storey				Average first storey strain angle (deg)	
Wall Type	**Drift**	ε_t^{max}	**c (mm)**	$\gamma_{VecTor2}$	Φ_{avg} (rad/km)	$\varepsilon^*_{cen.}$	$\gamma_{Estimate}$	$\gamma_{VecTor2}$	Φ_{avg} (rad/km)	$\varepsilon^*_{cen.}$	$\gamma_{Estimate}$	**Back-calculated**	**VecTor2**
10STFW-P5	0.29%	0.0084	199	0.0001	0.72	0.0018	0.0001	0.0001	0.33	0.0008	0.0001	87.7	83.6
	0.44%	0.0092	199	0.0004	1.13	0.0029	0.0004	0.0001	0.34	0.0009	0.0001	85.9	84.2
	0.55%	0.0107	199	0.0009	1.44	0.0037	0.0009	0.0002	0.36	0.0009	0.0002	83.2	82.7
	0.69%	0.0127	199	0.0013	1.49	0.0038	0.0013	0.0002	0.34	0.0009	0.0003	80.4	81.4
	0.83%	0.0150	199	0.0018	2.03	0.0052	0.0018	0.0002	0.41	0.0010	0.0004	80.5	80.7
	0.96%	0.0170	199	0.0022	2.56	0.0065	0.0022	0.0004	0.71	0.0018	0.0006	80.7	80.3
	1.10%	0.0189	199	0.0028	2.77	0.0071	0.0028	0.0006	0.66	0.0017	0.0007	79.2	79.6
10STFW-P10	0.29%	0.0083	309	0.0001	0.73	0.0018	0.0001	0.0001	0.33	0.0008	0.0001	87.6	83.5
	0.44%	0.0090	309	0.0004	0.99	0.0024	0.0004	0.0002	0.34	0.0008	0.0001	85.6	83.7
	0.55%	0.0100	309	0.0008	1.26	0.0031	0.0008	0.0002	0.34	0.0008	0.0002	82.6	81.9
	0.69%	0.0121	309	0.0013	1.64	0.0040	0.0013	0.0002	0.37	0.0009	0.0003	81.1	80.9
	0.83%	0.0146	309	0.0017	2.18	0.0053	0.0017	0.0003	0.52	0.0013	0.0004	81.2	80.5
	0.96%	0.0166	309	0.0022	2.48	0.0060	0.0022	0.0004	0.55	0.0013	0.0005	80.0	79.2
	1.10%	0.0208	309	0.0030	3.18	0.0078	0.0030	0.0006	0.82	0.0020	0.0008	79.5	77.9
10STFW-P20	0.29%	0.0049	843	0.0002	0.57	0.0011	0.0002	0.0002	0.33	0.0006	0.0001	84.7	80.5
	0.44%	0.0086	843	0.0002	1.14	0.0022	0.0002	0.0002	0.34	0.0007	0.0001	86.7	84.3
	0.55%	0.0092	843	0.0006	1.37	0.0026	0.0006	0.0002	0.36	0.0007	0.0002	83.7	83.4
	0.69%	0.0114	843	0.0010	1.48	0.0028	0.0010	0.0002	0.34	0.0007	0.0002	79.8	80.9
	0.83%	0.0138	843	0.0015	2.04	0.0039	0.0015	0.0002	0.41	0.0008	0.0003	79.4	79.5
	0.96%	0.0159	843	0.0019	2.40	0.0046	0.0019	0.0003	0.48	0.0009	0.0004	78.8	79.4
	1.10%	0.0183	843	0.0024	2.82	0.0054	0.0024	0.0004	0.58	0.0011	0.0005	78.0	78.8

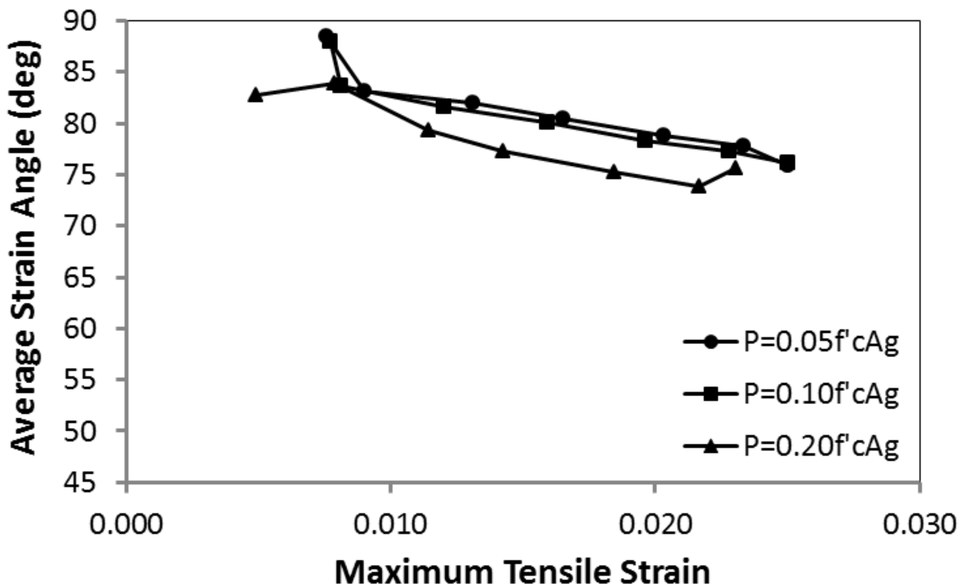

Figure 2.28 Effect of compressive axial stress level on average first storey strain angle of 10-storey rectangular walls.

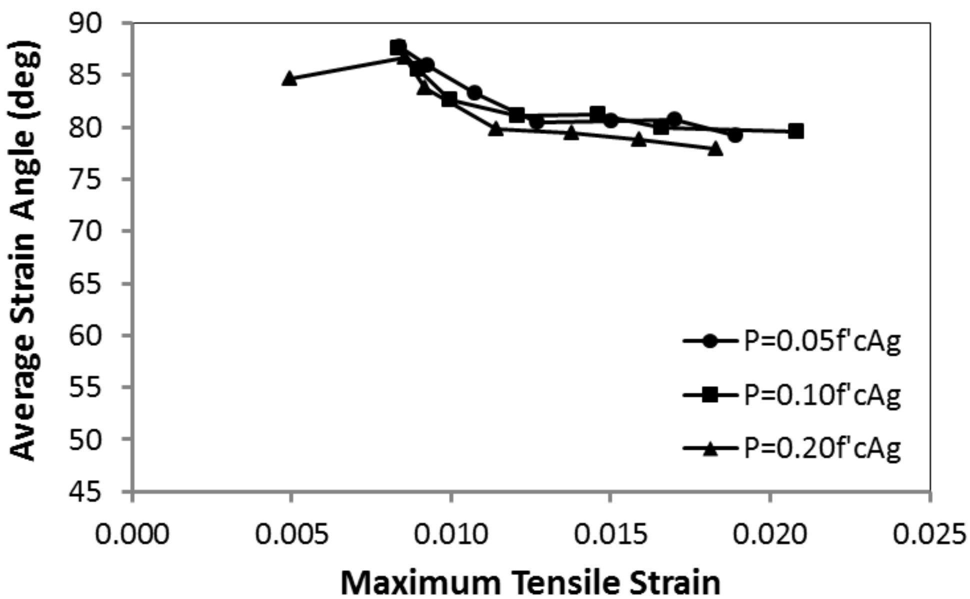

Figure 2.29 Effect of compressive axial stress level on average first storey strain angle of 10-storey flanged walls.

It is therefore concluded that the effect of average axial compressive stress on the wall on the average strain angle is not substantial and does not require further attention.

2.8.2 Effect of vertical steel ratio

Figure 2.14 demonstrated that horizontal strains in the web region were a couple of orders of magnitude smaller than vertical strains in the region. With the horizontal reinforcement of the web region not highly stressed, investigating their influence on the average strain angle is unnecessary.

Because vertical strains come into play directly in Eq 2.7 and on the tension side of the wall, vertical reinforcements play a key role in magnitude and distribution of vertical strains, the amount vertical steel is the next parameter to be studied. Looking back at Figure 2.14 one can see that the majority of the shear strain is concentrated in elements in the web-region of the wall. Therefore, there is no point in investigating the influence of vertical steel amount in the end regions of rectangular walls or in the flange region of flanged walls on the average principle strain angle. Vertical steel in the web region on the other hand are severely stressed which demands a study on their effect on the average principle strain angle.

Analysis was conducted on both rectangular and flanged walls with their properties summarized in Table 2.5 and Table 2.6 respectively. The walls were essentially the same as those presented in Section 2.8.1 with an average compressive axial stress of $0.10f'_cA_g$. The amount of distributed vertical steel in the web region was varied from 0.25% to 1.00% as the extremes with 0.50% chosen as an intermediate value.

Table 2.7 and Table 2.8 present analysis results for rectangular and flanged walls respectively. As expected, walls with larger amount of distributed vertical steel in the web had a larger concrete compression depth. This was because a larger concrete compression resultant force was required to balance the extra tensile stresses caused by the addition of distributed steel in the web. All the parameters needed for estimating average storey shear strains are given in the tables.

Again, with the average principle strain angles adjusted to give the exact first storey average shear strain, estimates of the second storey average shear strain is within a reasonable tolerance and the back-calculated average strain angles are close to the average of element principle strain angles over the first storey obtained from VecTor2.

Table 2.5 Properties of 10-storey rectangular walls used to study the effect of amount of distributed vertical reinforcement in the web region on average first storey principle strain angle.

Wall ID	Cross-section (mm)	Elevation Layout	P/f'_cA_g (%)	Concrete Properties	Reinforcing Steel Properties	Distributed Steel Reinforcement Layout: End Regions ρ_x	End Regions ρ_y	End Regions ρ_z	Web Region ρ_x	Web Region ρ_y	Web Region ρ_z	Slab Region ρ_x	Slab Region ρ_y	Slab Region ρ_z
10STRW-WS25	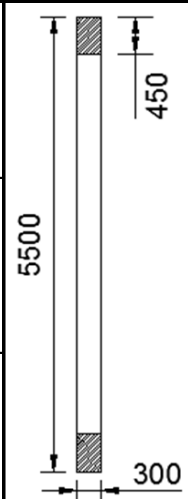	H_w=27432 mm H_{st}=2743 mm 10 storey wall	10	f'_c=40 MPa VecTor2 default values used for other parameters	F_y=400 MPa F_u=640 MPa E_s=200 GPa E_{sh}=3 GPa e_{sh}=0.007	1.0%	2.0%	0.5%	**0.25%**	0.5%	0.5%	0.5%	0.1%	0.5%
10STRW-WS50			10			1.0%	2.0%	0.5%	**0.50%**	0.5%	0.5%	0.5%	0.1%	0.5%
10STRW-WS100			10			1.0%	2.0%	0.5%	**1.00%**	0.5%	0.5%	0.5%	0.1%	0.5%

Table 2.6 Properties of 10-storey flanged walls used to study the effect of amount of distributed vertical reinforcement in the web region on average first storey principle strain angle.

						Distributed Steel Reinforcement Layout								
						Flange Region			Web Region			Slab Region		
Wall ID	Cross-section (mm)	Elevation Layout	P/f'_cA_g (%)	Concrete Properties	Reinforcing Steel Properties	ρ_x	ρ_y	ρ_z	ρ_x	ρ_y	ρ_z	ρ_x	ρ_y	ρ_z
10STFW-WS25	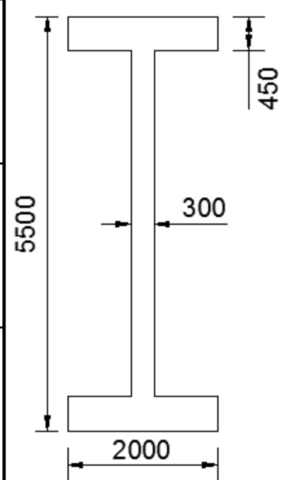	H_w=27432 mm	10	f'_c=40 MPa	F_y=400 MPa F_u=640 MPa	0.5%	0.5%	0.5%	**0.25%**	0.5%	0.5%	0.5%	0.1%	0.5%
10STFW-WS50		H_{st}=2743 mm	10	VecTor2 default values used for other parameters	E_s=200 GPa	0.5%	0.5%	0.5%	**0.50%**	0.5%	0.5%	0.5%	0.1%	0.5%
10STFW-WS100		10 storey wall	10		E_{sh}=3 GPa e_{sh}=0.007	0.5%	0.5%	0.5%	**1.00%**	0.5%	0.5%	0.5%	0.1%	0.5%

Table 2.7 Analysis results: 10-storey rectangular walls with various amounts of distributed vertical reinforcement in the web region (Note: values of 'c' reported were used to back-calculate the average storey strain angle and do not represent the actual concrete compression depth of the wall at the given global drift).

				1st storey				2nd storey				Average 1st storey strain angle (deg)	
Wall Type	**Drift**	ε_t^{max}	**c (mm)**	$\gamma_{VecTor2}$	Φ_{avg} (rad/km)	$\varepsilon^*_{cen.}$	$\gamma_{Estimate}$	$\gamma_{VecTor2}$	Φ_{avg} (rad/km)	$\varepsilon^*_{cen.}$	$\gamma_{Estimate}$	**Back-calculated**	**VecTor2**
10STRW-WS25	0.50%	0.0082	941	0.0001	0.90	0.0016	0.0001	0.0002	0.49	0.0009	0.0001	87.8	85.7
	0.75%	0.0092	941	0.0007	1.65	0.0030	0.0007	0.0002	0.60	0.0011	0.0003	83.3	84.1
	1.00%	0.0140	941	0.0014	2.52	0.0046	0.0014	0.0003	0.86	0.0016	0.0005	81.7	80.7
	1.25%	0.0173	941	0.0020	3.24	0.0059	0.0020	0.0004	1.29	0.0023	0.0008	80.7	79.6
	1.50%	0.0211	941	0.0028	3.79	0.0069	0.0028	0.0007	1.19	0.0021	0.0009	78.7	78.3
	1.75%	0.0241	941	0.0036	4.56	0.0083	0.0036	0.0009	1.66	0.0030	0.0013	78.1	77.4
	2.00%	0.0254	941	0.0049	5.09	0.0092	0.0049	0.0014	1.98	0.0036	0.0019	76.0	75.9
10STRW-WS50	0.50%	0.0077	1062	0.0001	0.92	0.0016	0.0001	0.0002	0.49	0.0008	0.0001	87.9	82.3
	0.75%	0.0081	1062	0.0006	1.46	0.0025	0.0006	0.0002	0.56	0.0009	0.0002	83.7	83.6
	1.00%	0.0120	1062	0.0011	2.15	0.0036	0.0011	0.0003	0.68	0.0012	0.0003	81.6	81.5
	1.25%	0.0159	1062	0.0018	2.98	0.0050	0.0018	0.0005	1.03	0.0017	0.0006	80.0	80.2
	1.50%	0.0196	1062	0.0027	3.69	0.0062	0.0027	0.0008	1.29	0.0022	0.0009	78.3	78.6
	1.75%	0.0228	1062	0.0035	4.34	0.0073	0.0035	0.0012	1.59	0.0027	0.0013	77.3	78.0
	2.00%	0.0250	1062	0.0045	5.01	0.0085	0.0045	0.0016	2.10	0.0036	0.0019	76.1	74.2
10STRW-WS100	0.50%	0.0043	1260	0.0002	0.72	0.0011	0.0002	0.0003	0.49	0.0007	0.0001	84.8	78.8
	0.75%	0.0073	1260	0.0003	1.41	0.0021	0.0003	0.0002	0.61	0.0009	0.0001	85.6	82.0
	1.00%	0.0101	1260	0.0009	2.05	0.0030	0.0009	0.0003	0.90	0.0013	0.0004	81.9	79.6
	1.25%	0.0132	1260	0.0014	2.66	0.0040	0.0014	0.0006	1.13	0.0017	0.0006	80.1	79.0
	1.50%	0.0170	1260	0.0022	3.47	0.0052	0.0022	0.0009	1.57	0.0023	0.0010	78.3	77.0
	1.75%	0.0201	1260	0.0031	4.20	0.0063	0.0031	0.0013	2.08	0.0031	0.0015	76.9	75.5
	2.00%	0.0231	1260	0.0041	5.01	0.0075	0.0041	0.0018	2.55	0.0038	0.0021	75.6	73.6

Table 2.8 Analysis results: 10-storey flanged walls with various amounts of distributed vertical reinforcement in the web region (Note: values of 'c' reported were used to back-calculate the average storey strain angle and do not represent the actual concrete compression depth of the wall at the given global drift).

				1st storey				2nd storey				Average 1st storey strain angle (deg)	
Wall Type	Drift	ε_t^{max}	c (mm)	$\gamma_{VecTor2}$	Φ_{avg} (rad/km)	$\varepsilon^*_{cen.}$	$\gamma_{Estimate}$	$\gamma_{VecTor2}$	Φ_{avg} (rad/km)	$\varepsilon^*_{cen.}$	$\gamma_{Estimate}$	Back-calculated	VecTor2
10STFW-WS25	0.29%	0.0113	286	0.0002	0.87	0.0022	0.0002	0.0001	0.33	0.0008	0.0001	87.4	78.8
	0.44%	0.0117	286	0.0004	1.19	0.0029	0.0004	0.0002	0.34	0.0008	0.0001	85.9	77.7
	0.55%	0.0137	286	0.0006	1.48	0.0036	0.0006	0.0002	0.34	0.0008	0.0001	85.5	76.8
	0.69%	0.0142	286	0.0009	1.66	0.0041	0.0009	0.0002	0.34	0.0008	0.0002	83.6	80.0
	0.83%	0.0169	286	0.0014	2.19	0.0054	0.0014	0.0002	0.37	0.0009	0.0002	82.8	79.8
	0.96%	0.0182	286	0.0019	2.47	0.0061	0.0019	0.0003	0.42	0.0010	0.0003	81.5	79.8
	1.10%	0.0202	286	0.0025	2.82	0.0070	0.0025	0.0003	0.51	0.0012	0.0005	80.0	79.6
10STFW-WS50	0.29%	0.0083	309	0.0001	0.73	0.0018	0.0001	0.0001	0.33	0.0008	0.0001	87.6	83.5
	0.44%	0.0090	309	0.0004	0.99	0.0024	0.0004	0.0002	0.34	0.0008	0.0001	85.6	83.7
	0.55%	0.0100	309	0.0008	1.26	0.0031	0.0008	0.0002	0.34	0.0008	0.0002	82.6	81.9
	0.69%	0.0121	309	0.0013	1.64	0.0040	0.0013	0.0002	0.37	0.0009	0.0003	81.1	80.9
	0.83%	0.0146	309	0.0017	2.18	0.0053	0.0017	0.0003	0.52	0.0013	0.0004	81.2	80.5
	0.96%	0.0166	309	0.0022	2.48	0.0060	0.0022	0.0004	0.55	0.0013	0.0005	80.0	79.2
	1.10%	0.0208	309	0.0030	3.18	0.0078	0.0030	0.0006	0.82	0.0020	0.0008	79.5	77.9
10STFW-WS100	0.29%	0.0064	356	0.0002	0.63	0.0015	0.0002	0.0002	0.33	0.0008	0.0001	87.0	80.3
	0.44%	0.0079	356	0.0003	1.03	0.0025	0.0003	0.0002	0.34	0.0008	0.0001	87.1	82.8
	0.55%	0.0088	356	0.0006	1.27	0.0030	0.0006	0.0002	0.36	0.0009	0.0002	84.0	81.3
	0.69%	0.0107	356	0.0010	1.35	0.0032	0.0010	0.0002	0.34	0.0008	0.0003	81.1	80.2
	0.83%	0.0128	356	0.0015	1.97	0.0047	0.0015	0.0003	0.51	0.0012	0.0004	81.3	79.6
	0.96%	0.0148	356	0.0019	2.36	0.0057	0.0019	0.0004	0.68	0.0016	0.0005	80.9	79.5
	1.10%	0.0171	356	0.0024	2.75	0.0066	0.0024	0.0006	0.84	0.0020	0.0007	80.0	79.0

Average strain angles are plotted against wall maximum tensile strain in Figure 2.30 and Figure 2.31 for rectangular and flanged walls respectively. Average strain angles reduced as the wall maximum tensile strain increased meaning that more shear strain per unit average centroidal vertical strain was observed. Although the average strain angle decreased slightly as the amount of distributed vertical steel was varied, the influence of vertical steel amount is considered not to be critical.

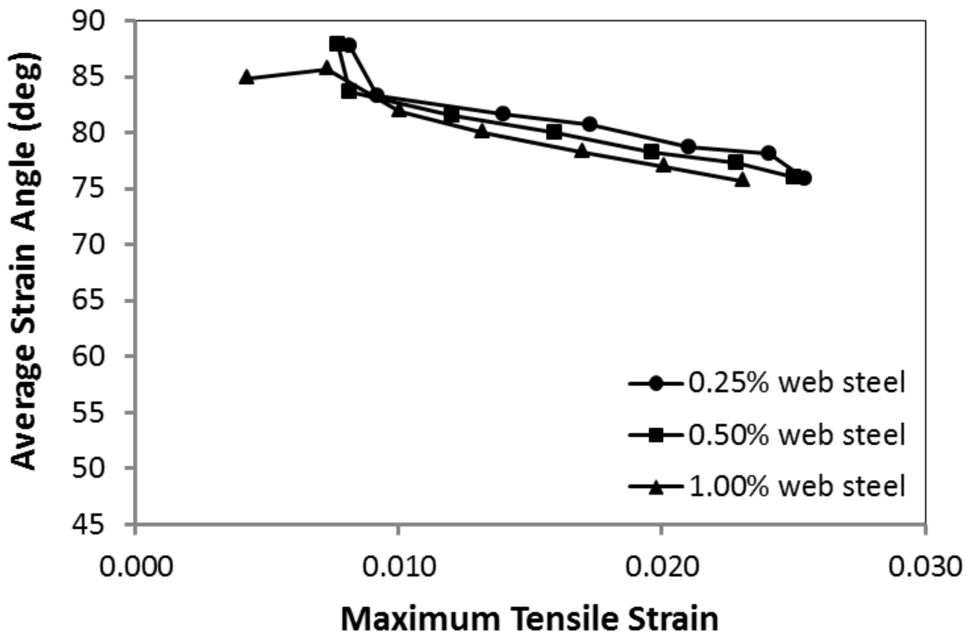

Figure 2.30 Effect of amount of distributed reinforcement in the web region of average first storey strain angle of 10-storey rectangular walls.

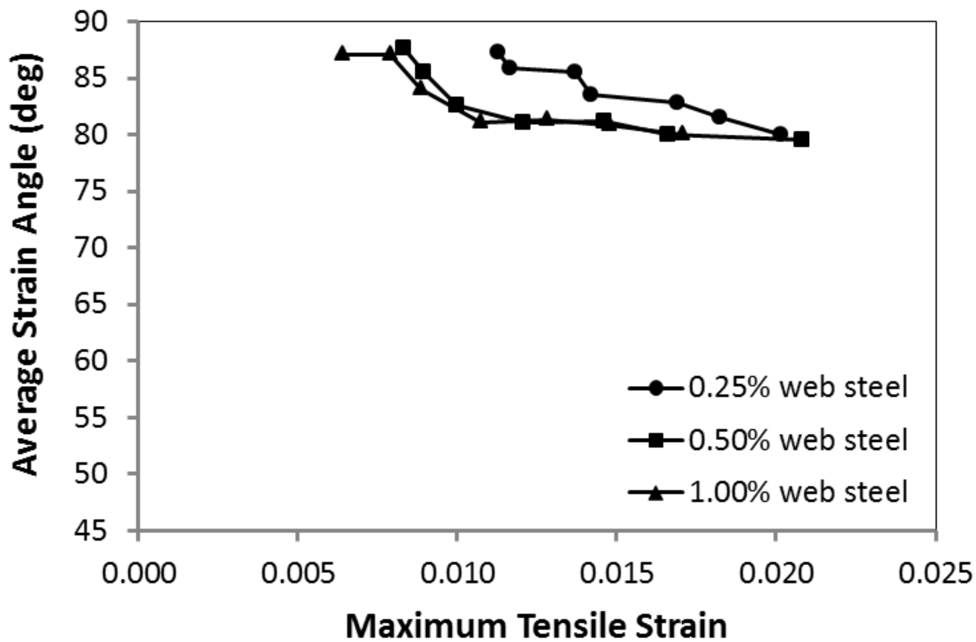

Figure 2.31 Effect of amount of distributed reinforcement in the web region of average first storey strain angle of 10-storey flanged walls.

2.8.3 Effect of wall length

Shear walls are designed and built in a broad range of lengths. It is therefore important to study the effect of wall length on the average principle strain angle. Wall lengths of 4, 6, 8, 10, and 12 m were chosen to carry out the parametric study. Both rectangular and flanged walls were considered in the analysis. Table 2.9 and Table 2.10 show properties of rectangular and flanged walls analyzed respectively. All the walls were loaded with axial compression at the top producing a uniform compressive stress of $0.10f'_cA_g$. Wall thickness was held constant at 300 mm while the length was varied from 4 m to 12 m. Zones at the end of the rectangular walls had more vertical, horizontal, and confinement reinforcement for the walls to be able to be pushed to large maximum curvatures. Flange width of the flange walls increased from 1 m to 3 m as the length increased from 4 m to 12 m.

To keep the wall aspect ratio the same, height of the wall was increased in proportion to wall length to achieve an aspect ratio of 4.13. Effect of wall aspect ratio on the average strain angle is studied in Section 2.8.4. Similar to the approach taken in previous sections, the average principle strain angle was back-calculated to give the exact average first storey shear strain. The same angle was then used to compute average second storey shear strain which was then compared to the value obtained from VecTor2.

Table 2.11 shows analysis results for rectangular walls. Effect of wall length on flexibility of the wall was the most obvious, as expected. At the same maximum tensile strain, shorter walls had larger curvatures due to the combined effect of smaller concrete compression depth. Wall plastic hinge length increased with wall length. At maximum tensile strain of 0.02, plastic hinge length of the 6STRW-L4 was 1750 mm while the 18STRW-L12 demonstrated a plastic hinge length of 3750 mm. Similar trends were seen in analysis results for the flanged walls shown in Table 2.12. Plastic hinge length of the 6STFW-L4 was 3500 mm at maximum tensile strain of 0.027 while the 18-STFW-L12 had a plastic hinge length of 7500 mm at the same maximum tensile strain. Because the flange width was increased with wall length, concrete compression depth did not undergo a dramatic change and never exceeded the flange thickness of 500 mm as the wall length was increased.

Table 2.9 Properties of rectangular walls used to study the effect of wall length on the average storey principle strain angle.

Wall ID	Cross-section	ℓ_w (mm)	ℓ_e (mm)	t_w (mm)	H_w (m)	Storey Height (m)	Number of Storeys	P/f'_cA_g (%)	Concrete Properties	Reinforcing Steel Properties	Distributed Steel Reinforcement Layout: End Regions ρ_x	End Regions ρ_y	End Regions ρ_z	Web Region ρ_x	Web Region ρ_y	Web Region ρ_z	Slab Region ρ_x	Slab Region ρ_y	Slab Region ρ_z
6STRW-L4	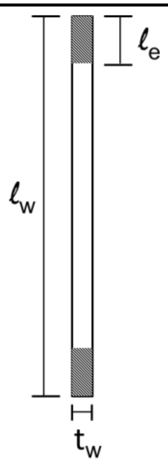	**4000**	500	300	**16.50**	2.75	**6**	10	f'_c=40 MPa	F_y=400 MPa	1.0%	3.0%	1.0%	0.5%	0.5%	0.5%	0.5%	0.1%	0.5%
9STRW-L6		**6000**	500	300	**24.75**	2.75	**9**	10	VecTor2	F_u=640 MPa	1.0%	3.0%	1.0%	0.5%	0.5%	0.5%	0.5%	0.1%	0.5%
12STRW-L8		**8000**	1000	300	**33.00**	2.75	**12**	10	default	E_s=200 GPa	1.0%	3.0%	1.0%	0.5%	0.5%	0.5%	0.5%	0.1%	0.5%
15STRW-L10		**10000**	1000	300	**41.25**	2.75	**15**	10	values used	E_{sh}=3 GPa	1.0%	3.0%	1.0%	0.5%	0.5%	0.5%	0.5%	0.1%	0.5%
18STRW-L12		**12000**	1000	300	**49.50**	2.75	**18**	10	for other parameters	e_{sh}=0.007	1.0%	3.0%	1.0%	0.5%	0.5%	0.5%	0.5%	0.1%	0.5%

Wall ID	Cross-section	ℓ_w (mm)	t_w (mm)	t_f (mm)	w_f (mm)	H_w (m)	Storey Height (m)	Number of Storeys	P/f'_cA_g (%)	Concrete Properties	Reinforcing Steel Properties	Distributed Steel Reinforcement Layout								
												Flange Region			Web Region			Slab Region		
												ρ_x	ρ_y	ρ_z	ρ_x	ρ_y	ρ_z	ρ_x	ρ_y	ρ_z
6STFW-L4	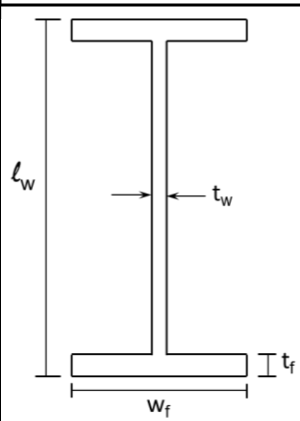	**4000**	300	500	1000	**16.50**	2.75	**6**	10	f'_c=40 MPa	F_y=400 MPa	0.5%	1.0%	0.5%	0.5%	0.5%	0.5%	0.5%	0.1%	0.5%
9STFW-L6		**6000**	300	500	1500	**24.75**	2.75	**9**	10	VecTor2 default values used for other parameters	F_u=640 MPa	0.5%	1.0%	0.5%	0.5%	0.5%	0.5%	0.5%	0.1%	0.5%
12STFW-L8		**8000**	300	500	2000	**33.00**	2.75	**12**	10		E_s=200 GPa	0.5%	1.0%	0.5%	0.5%	0.5%	0.5%	0.5%	0.1%	0.5%
15STFW-L10		**10000**	300	500	2500	**41.25**	2.75	**15**	10		E_{sh}=3 GPa	0.5%	1.0%	0.5%	0.5%	0.5%	0.5%	0.5%	0.1%	0.5%
18STFW-L12		**12000**	300	500	3000	**49.50**	2.75	**18**	10		e_{sh}=0.007	0.5%	1.0%	0.5%	0.5%	0.5%	0.5%	0.5%	0.1%	0.5%

Table 2.10 Properties of flanged walls used to study the effect of wall length on the average storey principle strain angle.

Table 2.11 Rectangular walls: analysis results on the effect of wall length on average storey principle strain angle (Note: values of ‘c’ reported were used to back-calculate the average storey strain angle and do not represent the actual concrete compression depth of the wall at the given global drift).

						1st storey				2nd storey			
Wall ID	Drift	ε_t^{max}	l_{pw}^* (mm)	c (mm)	θ°	$\gamma_{VecTor2}$	Φ_{avg} (rad/km)	$\varepsilon^*_{cen.}$	$\gamma_{Estimate}$	$\gamma_{VecTor2}$	Φ_{avg} (rad/km)	$\varepsilon^*_{cen.}$	$\gamma_{Estimate}$
	0.73%	0.0153	1000	800	86.5	0.0003	1.83	0.0022	0.0003	0.0003	0.81	0.0010	0.0001
	1.09%	0.0189	1750	800	81.6	0.0010	2.77	0.0033	0.0010	0.0004	0.85	0.0010	0.0003
	1.48%	0.0238	2500	800	79.8	0.0019	4.21	0.0051	0.0019	0.0004	0.89	0.0011	0.0004
6STRW-L4	1.88%	0.0276	2750	800	77.0	0.0030	5.16	0.0062	0.0030	0.0004	0.91	0.0011	0.0005
	2.24%	0.0309	3000	800	76.2	0.0038	6.06	0.0073	0.0038	0.0004	0.99	0.0012	0.0006
	2.61%	0.0347	3000	800	75.2	0.0046	6.75	0.0081	0.0046	0.0004	1.00	0.0012	0.0007
	2.91%	0.0376	3250	800	74.8	0.0053	7.61	0.0091	0.0053	0.0005	1.16	0.0014	0.0008
	0.48%	0.0118	1000	1334	87.0	0.0002	1.08	0.0018	0.0002	0.0003	0.58	0.0010	0.0001
	0.73%	0.0150	2000	1334	86.0	0.0004	1.71	0.0028	0.0004	0.0003	0.61	0.0010	0.0001
	0.99%	0.0171	2750	1334	82.5	0.0010	2.30	0.0038	0.0010	0.0003	0.63	0.0010	0.0003
9STRW-L6	1.37%	0.0219	3250	1334	79.3	0.0021	3.15	0.0053	0.0021	0.0003	0.73	0.0012	0.0005
	1.49%	0.0236	3500	1334	79.0	0.0023	3.49	0.0058	0.0023	0.0004	0.82	0.0014	0.0005
	1.74%	0.0275	3750	1334	78.6	0.0029	4.15	0.0069	0.0029	0.0005	0.97	0.0016	0.0007
	1.98%	0.0306	3750	1334	76.6	0.0039	4.60	0.0101	0.0051	0.0006	1.01	0.0022	0.0011
	0.36%	0.0027	0	1839	81.1	0.0003	0.48	0.0010	0.0003	0.0003	0.44	0.0009	0.0003
	0.55%	0.0133	500	1839	77.7	0.0007	0.71	0.0015	0.0007	0.0003	0.45	0.0010	0.0004
	0.74%	0.0165	1500	1839	81.6	0.0008	1.19	0.0026	0.0008	0.0003	0.46	0.0010	0.0003
12STRW-L8	0.94%	0.0184	2000	1839	80.1	0.0012	1.51	0.0033	0.0012	0.0007	0.47	0.0010	0.0004
	1.12%	0.0201	3000	1839	78.9	0.0019	2.11	0.0046	0.0019	0.0007	0.50	0.0011	0.0004
	1.30%	0.0218	3250	1839	76.8	0.0026	2.37	0.0051	0.0026	0.0008	0.55	0.0012	0.0006
	1.52%	0.0252	3500	1839	76.0	0.0032	2.81	0.0090	0.0048	0.0009	0.63	0.0020	0.0011
	0.29%	0.0024	0	2124	82.5	0.0002	0.27	0.0008	0.0002	0.0002	0.36	0.0010	0.0003
	0.44%	0.0032	0	2124	74.3	0.0006	0.35	0.0010	0.0006	0.0003	0.36	0.0010	0.0006
	0.59%	0.0159	1250	2124	83.1	0.0006	0.84	0.0024	0.0006	0.0003	0.37	0.0011	0.0003
15STRW-L10	0.75%	0.0174	2000	2124	83.0	0.0008	1.14	0.0033	0.0008	0.0006	0.38	0.0011	0.0003
	0.90%	0.0188	3000	2124	82.6	0.0012	1.56	0.0045	0.0012	0.0006	0.40	0.0012	0.0003
	1.04%	0.0204	3000	2124	80.3	0.0017	1.68	0.0048	0.0017	0.0006	0.41	0.0012	0.0004
	1.21%	0.0228	3500	2124	79.3	0.0023	2.00	0.0084	0.0033	0.0008	0.49	0.0021	0.0008
	0.24%	0.0024	0	2412	83.5	0.0002	0.20	0.0007	0.0002	0.0002	0.31	0.0011	0.0003
	0.36%	0.0029	0	2412	79.1	0.0004	0.27	0.0010	0.0004	0.0003	0.31	0.0011	0.0004
	0.49%	0.0148	750	2412	82.1	0.0006	0.55	0.0020	0.0006	0.0002	0.31	0.0011	0.0003
18STRW-L12	0.63%	0.0163	1500	2412	83.6	0.0006	0.77	0.0027	0.0006	0.0006	0.32	0.0011	0.0003
	0.75%	0.0176	3000	2412	83.5	0.0008	0.95	0.0034	0.0008	0.0006	0.34	0.0012	0.0003
	0.87%	0.0186	3500	2412	83.2	0.0012	1.37	0.0049	0.0012	0.0005	0.39	0.0014	0.0003
	1.01%	0.0203	3750	2412	81.2	0.0017	1.52	0.0079	0.0025	0.0006	0.44	0.0023	0.0007

Figure 2.32 shows the effect of length of rectangular walls on the average storey principle strain angle. Other than the clear reduction of the average strain angle with increasing maximum tensile strain, no other explicit trend can be seen.

Table 2.12 Flanged walls: analysis results on the effect of wall length on average storey principle strain angle (Note: values of 'c' reported were used to back-calculate the average storey strain angle and do not represent the actual concrete compression depth of the wall at the given global drift).

						1st storey				2nd storey			
Wall ID	Drift	ε_t^{max}	l_{pw}^* (mm)	c (mm)	$\theta°$	$\gamma_{VecTor2}$	Φ_{avg} (rad/km)	$\varepsilon^*_{cen.}$	$\gamma_{Estimate}$	$\gamma_{VecTor2}$	Φ_{avg} (rad/km)	$\varepsilon^*_{cen.}$	$\gamma_{Estimate}$
6STFW-L4	0.73%	0.0159	1500	437	85.8	0.0005	2.08	0.0033	0.0005	0.0005	0.83	0.0013	0.0002
	1.09%	0.0179	2000	437	83.2	0.0010	2.65	0.0041	0.0010	0.0006	0.86	0.0013	0.0003
	1.48%	0.0209	3250	437	80.8	0.0021	4.00	0.0063	0.0021	0.0006	1.04	0.0016	0.0005
	1.88%	0.0248	3500	437	80.3	0.0027	4.84	0.0076	0.0027	0.0007	1.18	0.0019	0.0007
	2.24%	0.0283	3750	437	80.0	0.0032	5.62	0.0088	0.0032	0.0009	1.38	0.0022	0.0008
	2.61%	0.0316	3750	437	79.7	0.0037	6.24	0.0098	0.0037	0.0012	1.44	0.0022	0.0008
	3.03%	0.0340	4500	437	78.8	0.0046	7.18	0.0112	0.0046	0.0021	2.20	0.0034	0.0014
9STFW-L6	0.61%	0.0168	1000	485	84.7	0.0006	1.19	0.0030	0.0006	0.0006	0.58	0.0015	0.0003
	1.01%	0.0205	3000	485	83.1	0.0015	2.44	0.0061	0.0015	0.0007	0.66	0.0017	0.0004
	1.41%	0.0243	3500	485	80.0	0.0028	3.07	0.0077	0.0028	0.0009	0.79	0.0020	0.0007
	1.82%	0.0284	4250	485	78.9	0.0039	3.83	0.0096	0.0039	0.0017	1.16	0.0029	0.0012
	2.22%	0.0304	5000	485	76.4	0.0056	4.31	0.0108	0.0056	0.0032	1.66	0.0042	0.0022
	2.63%	0.0336	5500	485	75.6	0.0067	4.86	0.0122	0.0067	0.0049	2.15	0.0054	0.0030
	3.03%	0.0360	6000	485	74.3	0.0081	5.31	0.0133	0.0081	0.0060	2.62	0.0066	0.0040
12STFW-L8	0.45%	0.0163	1000	485	85.2	0.0005	0.87	0.0031	0.0005	0.0006	0.45	0.0016	0.0003
	0.76%	0.0191	2250	485	83.7	0.0011	1.43	0.0050	0.0011	0.0007	0.47	0.0017	0.0004
	1.06%	0.0222	3750	485	81.4	0.0023	2.14	0.0075	0.0023	0.0009	0.64	0.0023	0.0007
	1.36%	0.0253	4750	485	79.4	0.0036	2.61	0.0092	0.0036	0.0016	0.99	0.0035	0.0014
	1.67%	0.0262	5000	485	75.8	0.0052	2.74	0.0096	0.0052	0.0029	1.11	0.0039	0.0021
	1.97%	0.0298	5750	485	75.7	0.0062	3.22	0.0113	0.0062	0.0040	1.56	0.0055	0.0030
	2.27%	0.0326	6250	485	75.0	0.0072	3.57	0.0125	0.0072	0.0053	1.88	0.0066	0.0038
15STFW-L10	0.46%	0.0170	1250	481	85.1	0.0006	0.72	0.0033	0.0006	0.0006	0.37	0.0017	0.0003
	0.70%	0.0191	2750	481	85.0	0.0012	1.52	0.0069	0.0012	0.0007	0.39	0.0017	0.0003
	0.95%	0.0216	4000	481	81.4	0.0024	1.69	0.0076	0.0024	0.0010	0.56	0.0025	0.0008
	1.19%	0.0238	5000	481	79.4	0.0035	1.97	0.0089	0.0035	0.0019	0.83	0.0037	0.0015
	1.43%	0.0250	5500	481	76.5	0.0049	2.12	0.0096	0.0049	0.0031	1.01	0.0045	0.0023
	1.67%	0.0284	6250	481	76.4	0.0057	2.47	0.0112	0.0057	0.0039	1.33	0.0060	0.0031
	1.92%	0.0300	7000	481	75.3	0.0068	2.66	0.0120	0.0068	0.0058	1.58	0.0071	0.0040
18STFW-L12	0.38%	0.0108	1500	478	84.4	0.0006	0.52	0.0029	0.0006	0.0006	0.32	0.0017	0.0003
	0.59%	0.0184	1750	478	83.9	0.0009	0.79	0.0044	0.0009	0.0007	0.32	0.0018	0.0004
	0.79%	0.0202	4500	478	82.8	0.0019	1.36	0.0075	0.0019	0.0008	0.53	0.0029	0.0008
	0.99%	0.0221	5000	478	80.3	0.0030	1.52	0.0084	0.0030	0.0017	0.66	0.0036	0.0013
	1.19%	0.0241	6000	478	78.7	0.0040	1.73	0.0095	0.0040	0.0027	0.92	0.0051	0.0021
	1.39%	0.0261	6250	478	77.1	0.0050	1.88	0.0104	0.0050	0.0035	1.03	0.0057	0.0027
	1.60%	0.0267	7500	478	75.4	0.0061	1.98	0.0110	0.0061	0.0054	1.26	0.0069	0.0039

A very similar story is observed by looking at variation of the average storey principle strain angle of flanged walls and how they are influenced by wall length (see Figure 2.33). It is concluded that wall length does not considerably affect the average storey angle.

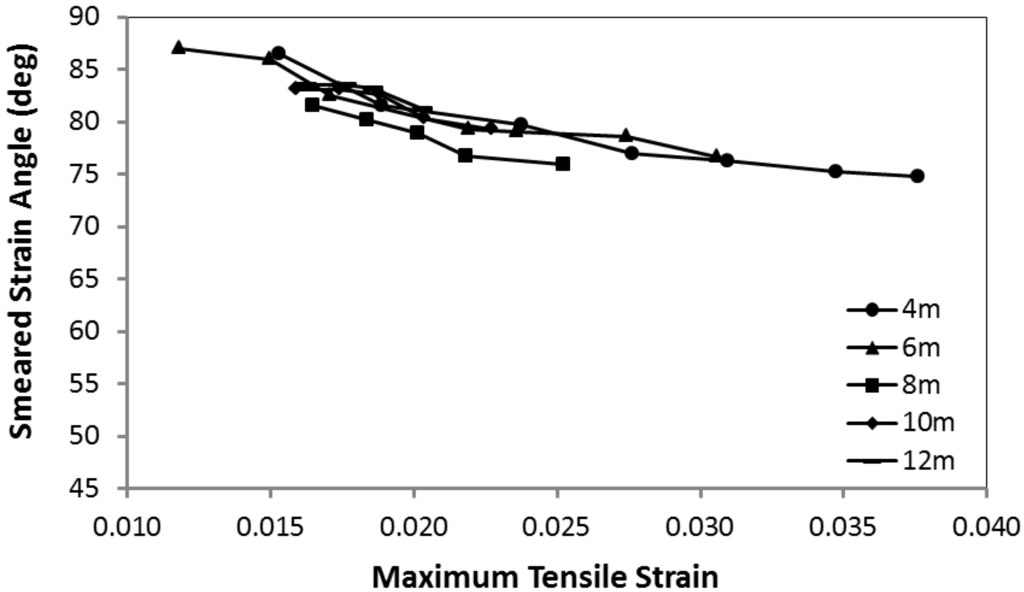

Figure 2.32 Effect of length of rectangular walls on the average storey principle strain angle.

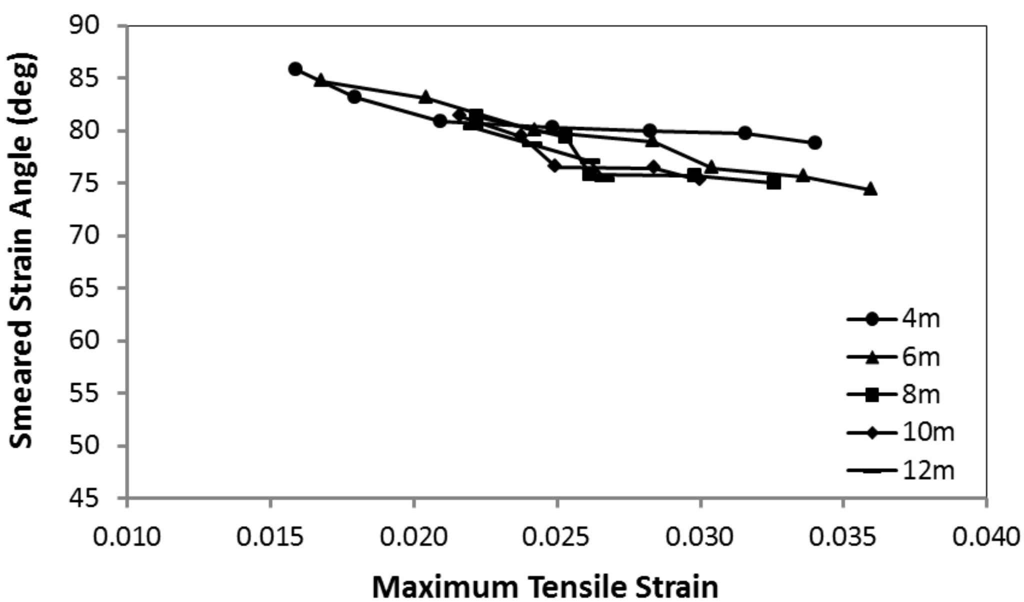

Figure 2.33 Effect of length of flanged walls on the average storey principle strain angle.

2.8.4 Effect of wall aspect ratio

Wall aspect ratio (height to length ratio) is the most detrimental parameter to a wall's failure mechanism. Walls with aspect ratios of 2.0 or smaller are more likely to fail in shear mechanism while taller walls fail in flexural mechanisms such as bar buckling, concrete crushing, and steel fracture. The amount of shear action in a wall also appears in the cracking pattern; hence, it seems likely that wall aspect ratio would affect the average principle strain angle.

To study the influence of wall aspect ratio on the average principle strain angle, rectangular and flanged walls having aspect ratios of 2.06, 4.13, 6.19, and 8.25 were chosen. Table 2.13 and Table 2.14 list properties of rectangular and flanged walls used in this analysis respectively. The cross-section of the walls is the same as the 8 m long walls in Section 2.8.3, namely, 12STRW-L8 and 12STFW-L8, while various aspect ratios were achieved by changing the number of storeys of the walls.

Table 2.15 presents analysis results for the rectangular walls of different aspect ratios. Wall flexibility increased dramatically with wall aspect ratio. This was because walls with larger aspect ratios had a larger plastic hinge length. At maximum tensile strain of 0.02, the wall with an aspect ratio of 2.06 had a plastic hinge length of 1750 mm while at the same maximum tensile strain, the wall that had an aspect ratio of 8.25 demonstrated a plastic hinge length of 5750 mm. Concrete compression depth however stayed the same for all walls because the sectional properties where the same. Similar observations hold true for the flanged walls (see Table 2.16).

Average storey principle strain angle was adjusted to give the exact first storey average shear strain. The second storey average shear strain was then calculated using the same principle strain angle and compared to that obtained from VecTor2. Figure 2.34 shows the effect of wall aspect ratio on the average principle strain angle. Compared to the parameters studied in the previous sections, wall aspect ratio has the most profound effect on the average strain angle. Walls with smaller aspect ratios had a smaller average strain angle producing more shear strain per unit mean vertical strain. This can be associated with the larger average shear stress in the walls with smaller aspect ratios which resulted in a smaller concrete stress angle in individual elements. Because in VecTor2 concrete stress angle and the total strain angle are the same, the decrease in the concrete stress angle of individual elements resulted in a smaller average strain angle.

Table 2.13 Properties of rectangular walls used to study the effect of wall aspect ratio on the average principle strain angle.

Wall ID	Cross-section	H_w (m)	Storey Height (m)	Number of Storeys	P/f'_cA_g (%)	Concrete Properties	Reinforcing Steel Properties	Distributed Steel Reinforcement Layout								
								End Regions			Web Region			Slab Region		
								ρ_x	ρ_y	ρ_z	ρ_x	ρ_y	ρ_z	ρ_x	ρ_y	ρ_z
6STRW-L8	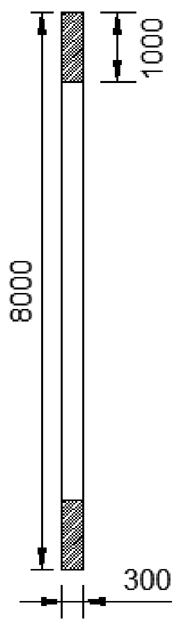	**16.5**	2.75	**6**	10	f'_c=40 MPa	F_y=400 MPa F_u=640 MPa E_s=200 GPa E_{sh}=3 GPa e_{sh}=0.007	1.0%	3.0%	1.0%	0.5%	0.5%	0.5%	0.5%	0.1%	0.5%
12STRW-L8		**33.0**	2.75	**12**	10	VecTor2 default values used for other parameters		1.0%	3.0%	1.0%	0.5%	0.5%	0.5%	0.5%	0.1%	0.5%
18STRW-L8		**49.5**	2.75	**18**	10			1.0%	3.0%	1.0%	0.5%	0.5%	0.5%	0.5%	0.1%	0.5%
24STRW-L8		**66.0**	2.75	**24**	10			1.0%	3.0%	1.0%	0.5%	0.5%	0.5%	0.5%	0.1%	0.5%

Table 2.14 Properties of flanged walls used to study the effect of wall aspect ratio on the average principle strain angle.

Wall ID	Cross-section	H_w (m)	Storey Height (m)	Number of Storeys	P/f'_cA_g (%)	Concrete Properties	Reinforcing Steel Properties	Distributed Steel Reinforcement Layout								
								End Regions			Web Region			Slab Region		
								ρ_x	ρ_y	ρ_z	ρ_x	ρ_y	ρ_z	ρ_x	ρ_y	ρ_z
6STFW-L8	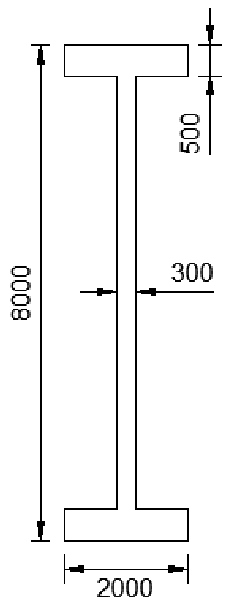	**16.5**	2.75	**6**	10	f'_c=40 MPa	F_y=400 MPa F_u=640 MPa E_s=200 GPa E_{sh}=3 GPa e_{sh}=0.007	0.5%	1.0%	0.5%	0.5%	0.5%	0.5%	0.5%	0.1%	0.5%
12STFW-L8		**33.0**	2.75	**12**	10	VecTor2 default values used for other parameters		0.5%	1.0%	0.5%	0.5%	0.5%	0.5%	0.5%	0.1%	0.5%
18STFW-L8		**49.5**	2.75	**18**	10			0.5%	1.0%	0.5%	0.5%	0.5%	0.5%	0.5%	0.1%	0.5%
24STFW-L8		**66.0**	2.75	**24**	10			0.5%	1.0%	0.5%	0.5%	0.5%	0.5%	0.5%	0.1%	0.5%

Table 2.15 Rectangular walls: analysis results for the effect of wall aspect ratio on the average principle strain angle (Note: values of ‘c’ reported were used to back-calculate the average storey strain angle and do not represent the actual concrete compression depth of the wall at the given global drift).

						1st storey				2nd storey			
Wall ID	**Drift**	ε_t^{max}	l_{pw}^* (mm)	**c (mm)**	**θ°**	$\gamma_{VecTor2}$	Φ_{avg} (rad/km)	$\varepsilon^*_{cen.}$	$\gamma_{Estimate}$	$\gamma_{VecTor2}$	Φ_{avg} (rad/km)	$\varepsilon^*_{cen.}$	$\gamma_{Estimate}$
6STRW-L8	0.48%	0.0177	1500	1839	77.5	0.0013	1.25	0.0027	0.0013	0.0005	0.42	0.0009	0.0004
	0.61%	0.0196	1750	1839	76.6	0.0016	1.47	0.0032	0.0016	0.0005	0.42	0.0009	0.0005
	0.73%	0.0218	2000	1839	75.9	0.0020	1.74	0.0038	0.0020	0.0005	0.43	0.0009	0.0005
	0.85%	0.0233	2250	1839	74.6	0.0026	1.99	0.0043	0.0026	0.0005	0.44	0.0009	0.0006
	0.97%	0.0250	2750	1839	74.2	0.0032	2.44	0.0053	0.0032	0.0005	0.45	0.0010	0.0006
	1.09%	0.0271	3000	1839	73.3	0.0040	2.78	0.0060	0.0040	0.0005	0.49	0.0011	0.0007
	1.21%	0.0315	3000	1839	73.0	0.0046	3.19	0.0069	0.0046	0.0006	0.50	0.0011	0.0007
12STRW-L8	0.36%	0.0027	0	1839	81.1	0.0003	0.48	0.0010	0.0003	0.0003	0.44	0.0009	0.0003
	0.55%	0.0133	500	1839	77.7	0.0007	0.71	0.0015	0.0007	0.0003	0.45	0.0010	0.0004
	0.74%	0.0165	1500	1839	81.6	0.0008	1.19	0.0026	0.0008	0.0003	0.46	0.0010	0.0003
	0.94%	0.0184	2000	1839	80.1	0.0012	1.51	0.0033	0.0012	0.0007	0.47	0.0010	0.0004
	1.12%	0.0201	3000	1839	78.9	0.0019	2.11	0.0046	0.0019	0.0007	0.50	0.0011	0.0004
	1.30%	0.0218	3250	1839	76.8	0.0026	2.37	0.0051	0.0026	0.0008	0.55	0.0012	0.0006
	1.52%	0.0252	3500	1839	76.0	0.0032	2.81	0.0090	0.0048	0.0009	0.63	0.0020	0.0011
18STRW-L8	1.01%	0.0162	2000	1839	84.1	0.0006	1.37	0.0030	0.0006	0.0006	0.48	0.0010	0.0002
	1.33%	0.0181	3750	1839	82.5	0.0012	2.12	0.0046	0.0012	0.0006	0.64	0.0014	0.0004
	1.70%	0.0212	4250	1839	78.9	0.0023	2.57	0.0056	0.0023	0.0008	0.83	0.0018	0.0007
	2.02%	0.0247	5250	1839	78.1	0.0030	3.17	0.0069	0.0030	0.0012	1.34	0.0029	0.0013
	2.34%	0.0275	6000	1839	76.6	0.0040	3.64	0.0079	0.0040	0.0023	1.82	0.0039	0.0020
	2.71%	0.0314	6250	1839	75.8	0.0049	4.18	0.0090	0.0049	0.0033	2.16	0.0047	0.0025
	3.03%	0.0361	6750	1839	74.6	0.0062	4.86	0.0105	0.0062	0.0040	2.68	0.0058	0.0034
24STRW-L8	1.26%	0.0155	2500	1839	85.9	0.0005	1.51	0.0033	0.0005	0.0006	0.49	0.0011	0.0002
	1.42%	0.0162	3500	1839	85.8	0.0006	1.87	0.0040	0.0006	0.0005	0.58	0.0012	0.0002
	1.59%	0.0168	4250	1839	84.7	0.0008	2.07	0.0045	0.0008	0.0005	0.75	0.0016	0.0003
	1.76%	0.0176	5000	1839	82.0	0.0014	2.27	0.0049	0.0014	0.0005	0.98	0.0021	0.0006
	1.92%	0.0189	5750	1839	80.7	0.0018	2.51	0.0054	0.0018	0.0006	1.28	0.0028	0.0009
	2.11%	0.0204	5750	1839	80.2	0.0021	2.70	0.0058	0.0021	0.0008	1.36	0.0029	0.0010
	2.27%	0.0218	5500	1839	79.6	0.0023	2.85	0.0062	0.0023	0.0011	1.33	0.0029	0.0011

Figure 2.35 shows the effect of wall aspect ratio on the average strain angle of flanged walls. Although the effect is less dramatic than the case of the rectangular walls, a similar trend can be observed. Ratio of the shear to flexural deformation of the walls was severely affected by the wall aspect ratio. Walls with smaller aspect ratios had larger first storey shear-to-flexure deformation ratio. This is shown in Figure 2.36 and Figure 2.37 for rectangular and flanged walls respectively. At large maximum tensile strains, the flanged walls with aspect ratios of 2.06 and 4.13 encountered more shear deformation than flexural in the first storey.

Table 2.16 Flanged walls: analysis results for the effect of wall aspect ratio on the average principle strain angle (Note: values of ‘c’ reported were used to back-calculate the average storey strain angle and do not represent the actual concrete compression depth of the wall at the given global drift).

						1st storey				2nd storey			
Wall ID	**Drift**	ε_t^{max}	l_{pw}^* (mm)	**c (mm)**	**θ°**	$\gamma_{VecTor2}$	Φ_{avg} (rad/km)	$\varepsilon^*_{cen.}$	$\gamma_{Estimate}$	$\gamma_{VecTor2}$	Φ_{avg} (rad/km)	$\varepsilon^*_{cen.}$	$\gamma_{Estimate}$
6STFW-L8	0.36%	0.0163	1250	485	81.0	0.0011	0.94	0.0033	0.0011	0.0010	0.41	0.0014	0.0005
	0.55%	0.0206	1750	485	81.2	0.0015	1.31	0.0046	0.0015	0.0011	0.42	0.0015	0.0005
	0.73%	0.0228	2500	485	80.2	0.0022	1.76	0.0062	0.0022	0.0011	0.45	0.0016	0.0006
	0.91%	0.0272	3250	485	80.1	0.0030	2.42	0.0085	0.0030	0.0013	0.53	0.0019	0.0007
	1.09%	0.0297	3750	485	79.2	0.0039	2.80	0.0099	0.0039	0.0014	0.69	0.0024	0.0010
	1.27%	0.0316	4250	485	77.9	0.0049	3.12	0.0110	0.0049	0.0018	0.91	0.0032	0.0014
	1.45%	0.0326	4500	485	76.0	0.0061	3.27	0.0115	0.0061	0.0022	1.04	0.0036	0.0019
12STFW-L8	0.45%	0.0163	1000	485	85.2	0.0005	0.87	0.0031	0.0005	0.0006	0.45	0.0016	0.0003
	0.76%	0.0191	2250	485	83.7	0.0011	1.43	0.0050	0.0011	0.0007	0.47	0.0017	0.0004
	1.06%	0.0222	3750	485	81.4	0.0023	2.14	0.0075	0.0023	0.0009	0.64	0.0023	0.0007
	1.36%	0.0253	4750	485	79.4	0.0036	2.61	0.0092	0.0036	0.0016	0.99	0.0035	0.0014
	1.67%	0.0262	5750	485	76.2	0.0052	2.83	0.0100	0.0052	0.0029	1.41	0.0049	0.0026
	1.97%	0.0298	5750	485	75.7	0.0062	3.22	0.0113	0.0062	0.0040	1.56	0.0055	0.0030
	2.27%	0.0326	6250	485	75.0	0.0072	3.57	0.0125	0.0072	0.0053	1.88	0.0066	0.0038
18STFW-L8	0.51%	0.0070	1500	485	85.1	0.0004	0.63	0.0022	0.0004	0.0005	0.47	0.0017	0.0003
	0.77%	0.0170	1750	485	86.7	0.0005	1.14	0.0040	0.0005	0.0005	0.48	0.0017	0.0002
	1.01%	0.0190	3750	485	84.9	0.0012	1.85	0.0065	0.0012	0.0006	0.62	0.0022	0.0004
	1.25%	0.0207	4250	485	82.2	0.0021	2.09	0.0073	0.0021	0.0009	0.75	0.0026	0.0007
	1.52%	0.0238	5250	485	81.5	0.0027	2.53	0.0089	0.0027	0.0016	1.14	0.0040	0.0012
	1.78%	0.0256	6000	485	79.8	0.0037	2.80	0.0098	0.0037	0.0029	1.47	0.0052	0.0019
	2.02%	0.0267	6250	485	78.0	0.0046	2.94	0.0103	0.0046	0.0036	1.60	0.0056	0.0025
24STFW-L8	0.76%	0.0127	2250	485	88.5	0.0002	1.04	0.0037	0.0002	0.0004	0.49	0.0017	0.0001
	0.94%	0.0161	3500	485	88.0	0.0004	1.56	0.0055	0.0004	0.0004	0.56	0.0020	0.0001
	1.12%	0.0179	4000	485	86.2	0.0008	1.80	0.0063	0.0008	0.0005	0.66	0.0023	0.0003
	1.29%	0.0188	4250	485	84.2	0.0014	1.92	0.0067	0.0014	0.0005	0.72	0.0025	0.0005
	1.47%	0.0207	5750	485	83.6	0.0018	2.26	0.0079	0.0018	0.0010	1.19	0.0042	0.0009
	1.65%	0.0223	6000	485	82.9	0.0022	2.45	0.0086	0.0022	0.0015	1.32	0.0046	0.0012
	1.82%	0.0237	6250	485	82.2	0.0026	2.62	0.0092	0.0026	0.0021	1.45	0.0051	0.0014

Figure 2.38 plots the value of shear deformation in the first storey of the rectangular walls against maximum tensile strain. Despite the difference in wall aspect ratios, the magnitude of the shear deformation is not affected. All the data points fall on a curve close to straight line. A similar observation is made for the flanged walls reported (see Figure 2.39). The explanation to this lies in the combination of the effect of the average storey principle strain angle and the average storey centroidal strain used to calculate average first storey shear strain from Eq 2.7.

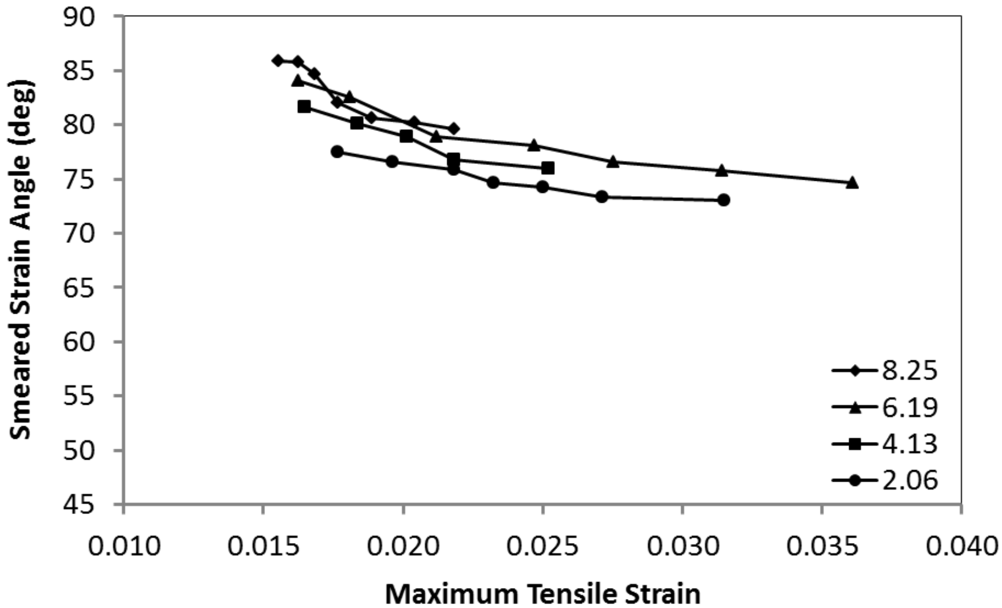

Figure 2.34 Effect of aspect ratio of rectangular walls on the average principle strain angle.

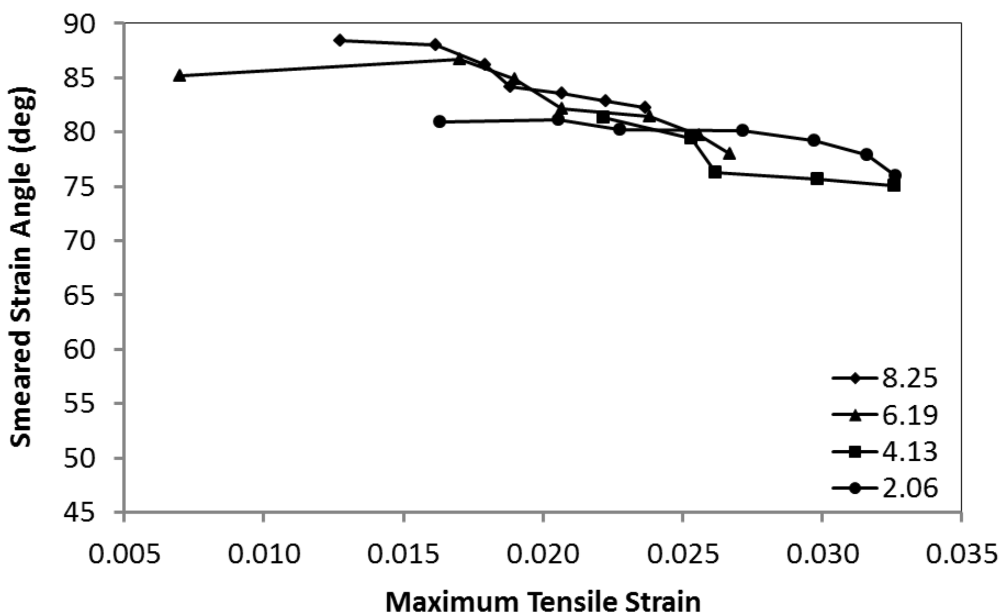

Figure 2.35 Effect of aspect ratio of flanged walls on the average principle strain angle.

Walls with smaller aspect ratios had a larger average shear stress over their cross-section which resulted in a smaller concrete stress angle and hence, smaller principle strain angle in individual elements. This meant that elements in the walls with smaller aspect ratios could have had more shear strain per unit vertical strain.

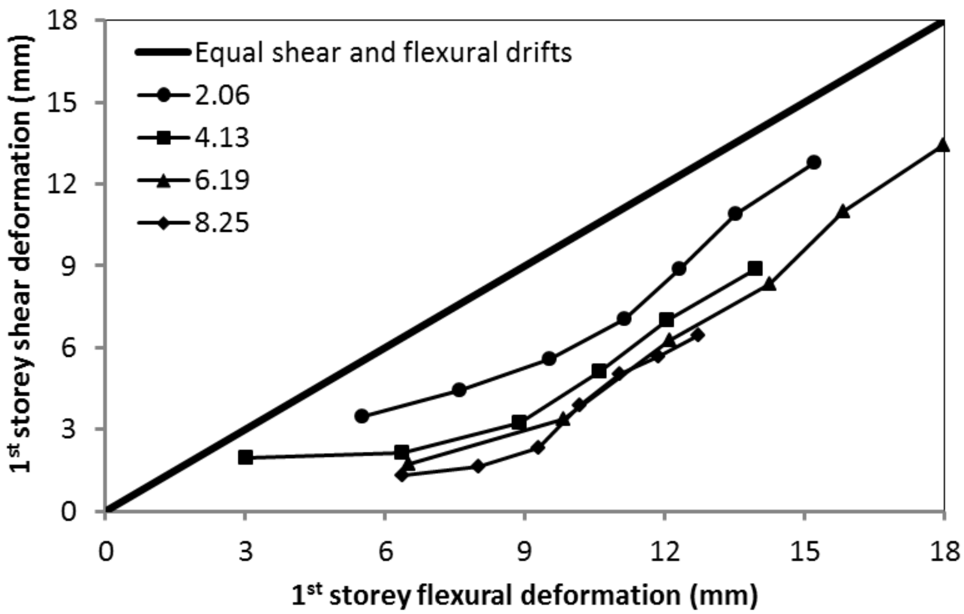

Figure 2.36 Effect of aspect ratio of rectangular walls on 1st storey shear to flexural drift ratio.

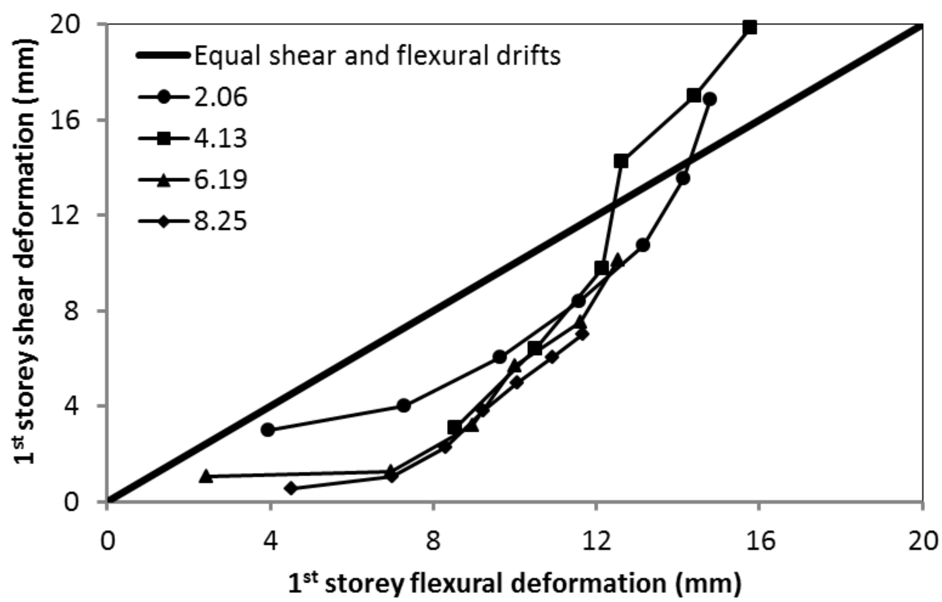

Figure 2.37 Effect of aspect ratio of flanged walls on 1st storey shear to flexural drift ratio.

However, plastic hinge length of the wall was also significantly affected by wall aspect ratio. Walls with larger aspect ratios had longer plastic hinge lengths. At the same maximum tensile strain, the curvatures at the base of the walls were also the same because the cross-sections were identical. With a larger plastic hinge length, average curvature of the first storey was greater for taller walls which resulted in a larger average centroidal strain.

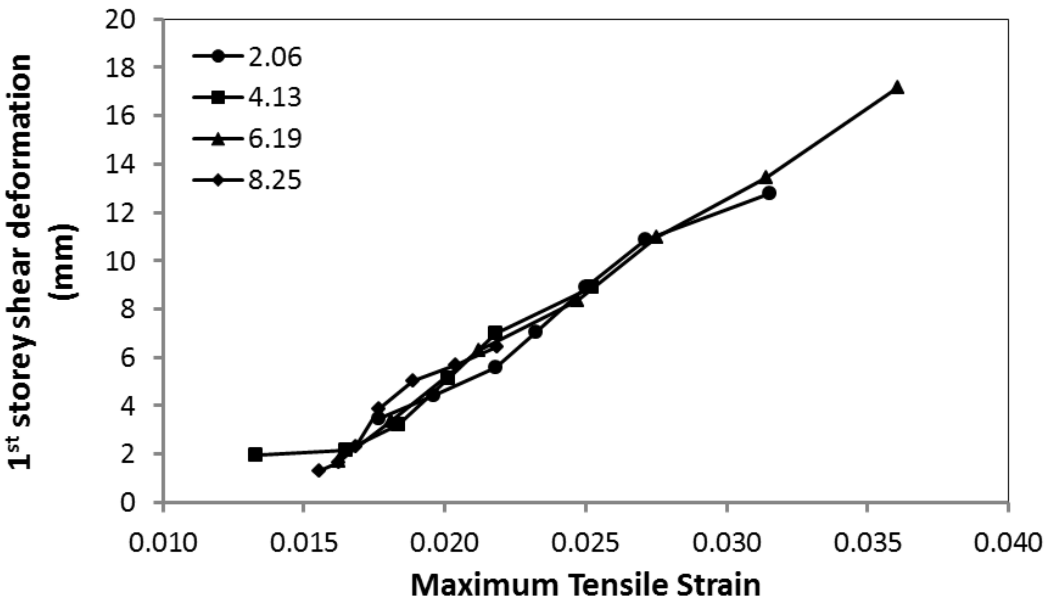

Figure 2.38 Influence of aspect ratio of rectangular walls on 1st storey shear deformation.

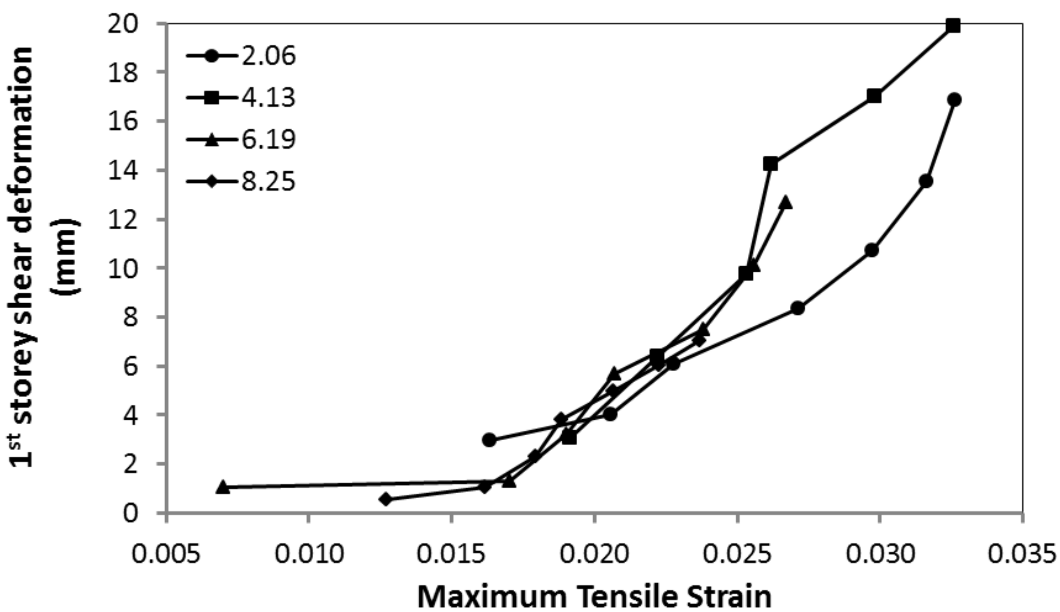

Figure 2.39 Influence of aspect ratio of flanged walls on 1st storey shear deformation.

In summary, although the shorter walls had a smaller average strain angle increasing average shear strain, they had a smaller average centroidal strain reducing average shear strain. The combination of these two factors was such that it made the walls with the very different aspect ratios have nearly the same first storey shear deformation at a given maximum tensile strain.

2.8.5 Effect of number of floor slabs in the wall plastic hinge region

Floor slabs alter the concrete cracking pattern in shear walls. Generally, cracks do not propagate through the slabs because of the large in-pane axial stiffness of the slabs. This forces inclined cracks to stop below the floor slab and start as flexural cracks above the slab. Since crack angle is tied to strain angle in VecTor2, the effect of presence of floor slabs in the wall plastic hinge region needs to be investigated.

For this purpose, a 10 m long rectangular wall with a width of 300 mm was chosen. The wall had 2% vertical and 1% horizontal and out-of-plane distributed reinforcement in its end region that was 1 m long on each face of the wall. 0.5% distributed steel was provided in all three directions in the web region. Width of the floor slab region was 1500 mm with 0.5% distributed horizontal and out-of-plane steel. 0.1% vertical steel was provided in the slab region so that the slab vertical steel did not exceed the vertical steel modeled in the web region. Axial load producing uniform compressive stress of $0.10f'_cA_g$ was applied at the top of the wall while the wall was pushed by point loads at the top. The wall was 60.5 m (22 storeys) high. Length and height of the wall were proportioned to achieve a relatively large plastic hinge length with several slabs at the base of the wall falling in the plastic hinge zone. At 2% global drift, wall plastic hinge was more than 3 storeys high. The wall with uniform floor slab spacing served as the standard case. To study the effect of number of slabs in the plastic hinge region on the average strain angle, the second and third floor slabs were removed one after the other and the same pushover analysis was conducted.

Figure 2.40 shows the cracking pattern of the walls with 3, 2 and 1 slab in the plastic hinge region. The orientation of the lines in each element is parallel to the element concrete stress angle and the width of the line is representative of crack width. Note how inclined cracks stop underneath the floor slabs and start as flexural (horizontal) cracks above with cracks not penetrating through the slab.

Table 2.17 summarizes the analysis results for the three walls considered in this section. Despite the similarities in the results for plastic hinge length and the relation between maximum curvature and global drift, the average principle strain angles slightly differed from wall to wall (see Figure 2.41).

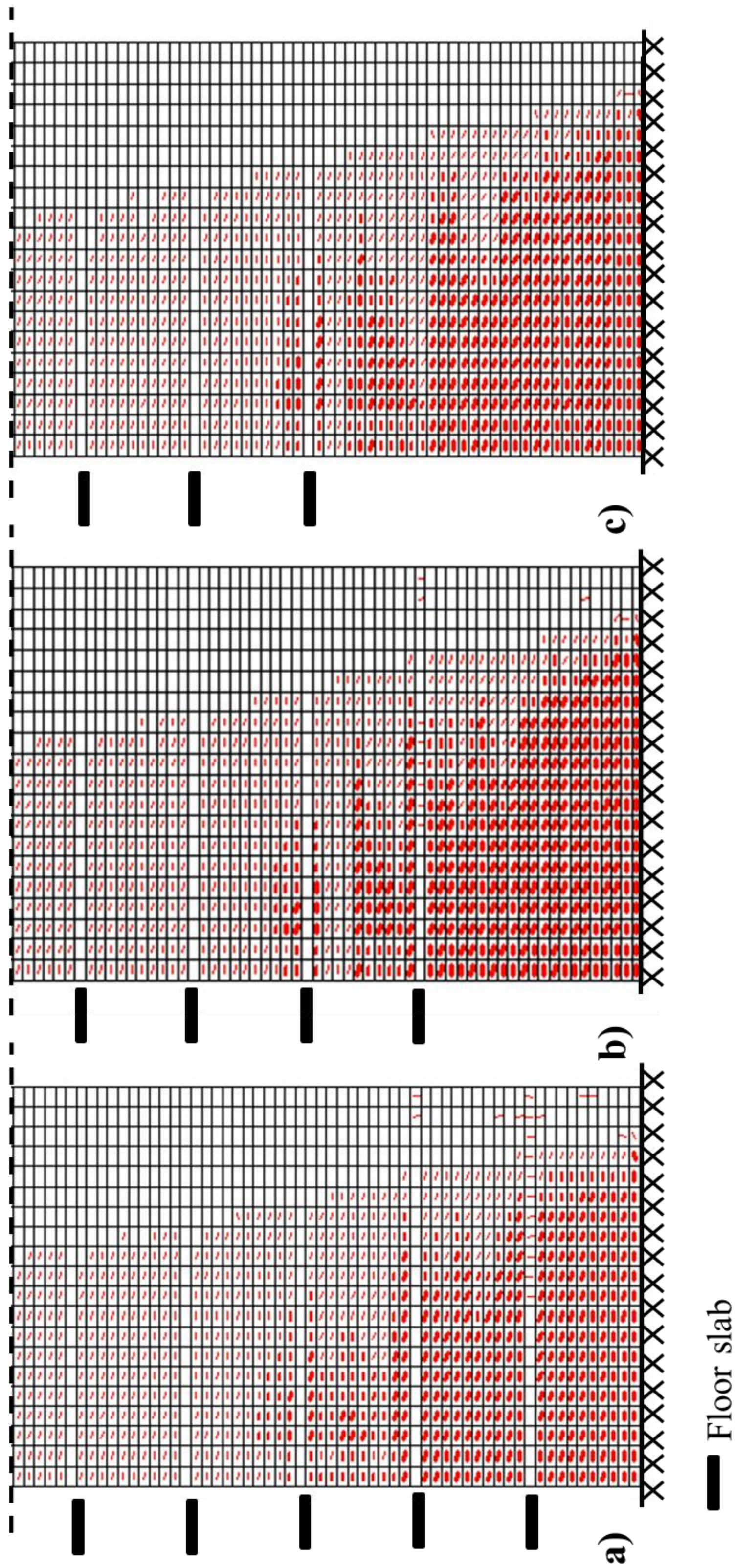

Figure 2.40 Crack pattern of wall 15STRW-L10 with a) three, b) two, and c) one floor slab in the wall plastic hinge region.

Table 2.17 Analysis results for the effect of number of slabs in the plastic hinge region of wall 15STRW-L10 on the average principle strain angle (Note: values of 'c' reported were used to back-calculate the average storey strain angle and do not represent the actual concrete compression depth of the wall at the given global drift).

						1st storey	
	global drift	Φ_{max} (rad/km)	l_{pw}^{*} (mm)	c (mm)	ε^{t}_{max}	γ_{ave}	θ°
3 slabs in wall plastic hinge region	0.52%	1.60	5250	1979	0.0129	0.0003	87.9
	0.88%	2.29	7000	1979	0.0183	0.0011	84.9
	1.24%	2.97	8250	1979	0.0238	0.0018	83.5
	1.60%	3.67	9250	1979	0.0294	0.0027	82.2
	1.96%	4.33	9750	1979	0.0348	0.0037	81.1
2 slabs in wall plastic hinge region	0.52%	1.47	5250	1979	0.0118	0.0004	87.2
	0.88%	2.20	6750	1979	0.0176	0.0011	84.5
	1.24%	2.82	8000	1979	0.0226	0.0019	82.6
	1.61%	3.41	9000	1979	0.0273	0.0028	81.5
	1.98%	4.11	9500	1979	0.0330	0.0043	79.3
1 slab in wall plastic hinge region	0.52%	1.51	4500	1979	0.0121	0.0003	87.5
	0.88%	2.20	6750	1979	0.0177	0.0011	84.7
	1.24%	2.79	7750	1979	0.0224	0.0020	82.5
	1.61%	3.42	8750	1979	0.0275	0.0027	81.6
	1.97%	4.04	9250	1979	0.0324	0.0041	79.5

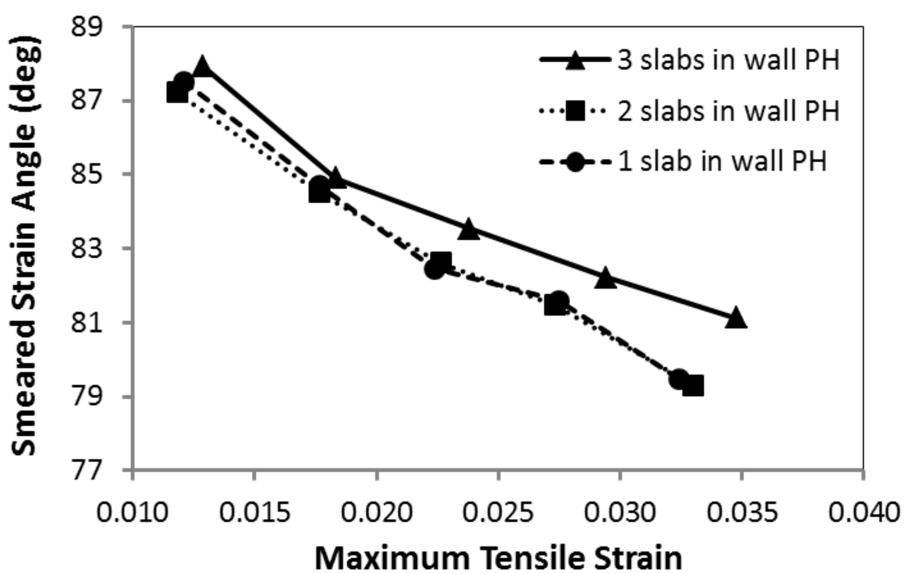

Figure 2.41 Effect of number of slabs in the plastic hinge region of wall 15STRW-L10 on the average principle strain angle.

The average principle strain angle dropped a couple of degrees when the first floor slab was excluded. The reason for this can be explained comparing the cracking pattern of the two walls (see Figure 2.40). Since in VecTor2 concrete stress angle and the total strain angle are forced to be equal, crack pattern is a good indication of element strain angles. The wall with the most number of slabs in the plastic hinge region had a larger (closer to horizontal) average crack angle which resulted in a larger average strain angle. As the floor slabs were removed one by one, the average crack angle became smaller (closer to vertical) causing more shear strain per unit vertical strain in each element resulting in a smaller average principle strain angle.

2.9 Shear Strain Model

The simple method for estimating wall shear strain presented in Section 2.7 proved to yield accurate estimations of shear strain for the case of the 10-storey rectangular wall example when average storey principle strain angles observed during the VecTor2 analysis were used. To be able to estimate the average storey principle strain angle that would result in accurate estimation of shear strains of a given wall, a parametric study was carried out in Section 2.8 with the final conclusion being that the average first-storey principle strain angle was not overly sensitive to or significantly affected by any of the parameters considered. Figure 2.42 summarizes the entire data on average 1st storey principle strain angles of all the walls considered in the parametric study against the recorded maximum tensile strain. Note that the average first-storey principle strain angles were back-calculated to give the exact average first storey shear strain observed in the VecTor2 analysis.

The average principle strain angle decreased with maximum tensile strain which translated to more shear strain per unit vertical strain according to Eq 2.7. Despite this observed trend, a constant average principle strain angle of 75 degrees is chosen as an input parameter to the proposed shear strain model. From Figure 2.42, it is obvious that the proposed constant 75 degree average principle strain angle is a lower bound for the true average principle strain angle at lower maximum tensile strains resulting in over-estimation of shear strain per unit vertical strain. However, because at small maximum tensile strains shear strains are deemed to be small, the errors are thought to be negligible. At higher maximum tensile strains, the proposed constant

75 degree average principle storey strain angle offers nearly an average value for the observed average principle strain angles resulting in a more accurate estimation of average storey shear strains.

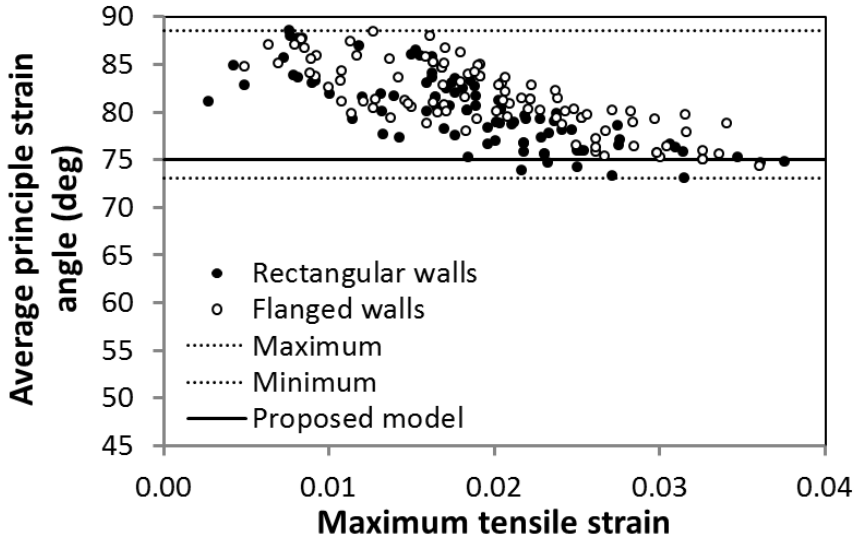

Figure 2.42 Summary of average strain angles from parametric study.

The proposed model for estimating wall shear strain in its final form is presented in Eq 2.9. If a principle strain angle of 75 degrees is substituted in Eq 2.7 and the vertical tensile strain in the same equation is replaced by ε_v from Eq 2.8, then shear strain at any level along the height of the wall can be estimated as

$$\gamma = \varphi\left(\frac{l_w}{2} - c\right)\,|tan(2 \times 75°)| = 0.577\left(\frac{l_w}{2} - c\right)\varphi \qquad \textbf{Eq 2.9}$$

In this equation, l_w is the length of the wall, c is the concrete compression depth, and φ is the curvature of the wall at the point of interest. If the concrete compression depth is considered to be approximately constant over the plastic hinge length, shear strain would then become proportional to curvature as shown below.

$$\gamma = k\varphi \qquad \textbf{Eq 2.10}$$

Where

$$k = 0.577\left(\frac{l_w}{2} - c\right) \quad \textbf{Eq 2.11}$$

This will result in the shapes of the curvature and shear strain profiles to be the same which is consistent with observations made in tests by Beyer et al. (2008), Brueggen (2009), and many others. The accuracy of the proposed model in predicting average storey shear strain is verified in the following sections.

2.9.1 Verification of the proposed shear strain model using walls considered in the parametric study

In this section, the accuracy of the proposed shear strain model for estimating average 1st and 2nd storey shear strains of the walls considered in the parametric study is examined. Ultimate concrete compression depth is calculated from a section analysis using the material stress-strain curves and equivalent concrete rectangular stress block. Average storey curvature is obtained from curvature profiles obtained from the VecTor2 analysis. These two parameters were used alongside the length of the wall to make predictions of the average storey shear strain using Eq 2.10.

Estimates of average storey shear strain are plotted against average storey shear strains obtained from the Vector2 analyses in Figure 2.43. Data points falling below the 45 degree line indicate over-estimation of shear strain by the proposed shear strain model and vice versa. It can be seen that the model provides an upper bound or a safe estimate for the average 1st storey shear strains observed in the VecTor2 analyses while it gives a closer to average estimation of the average 2nd storey shear strain.

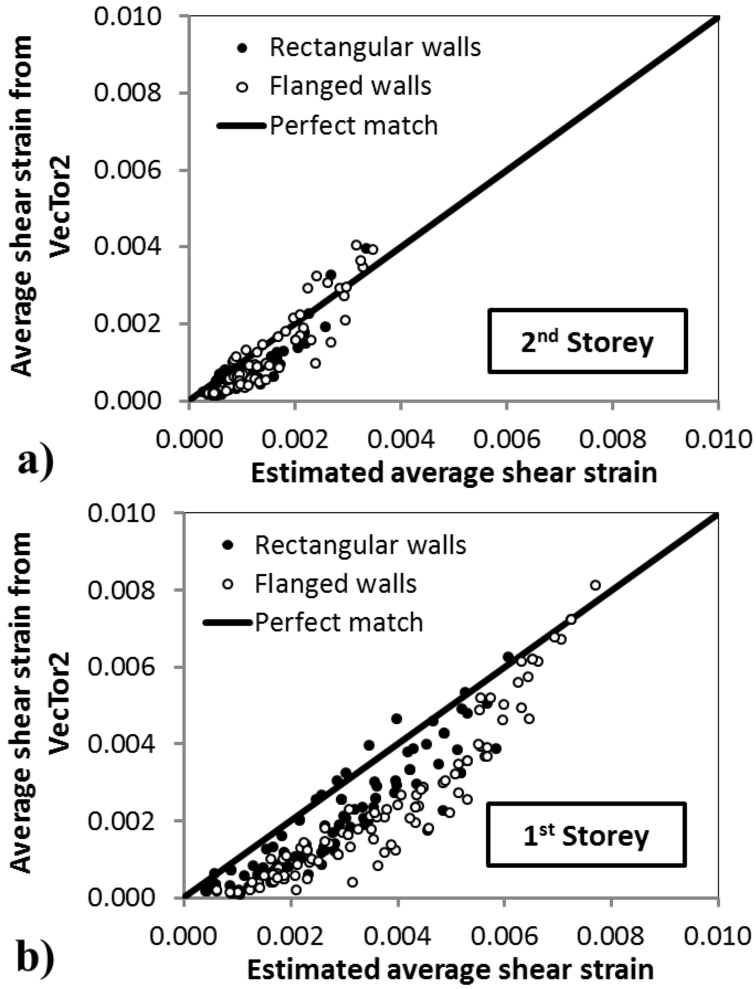

Figure 2.43 Verification of the proposed shear strain model for predicting average shear strain in a) first storey and b) second storey of walls considered in the parametric study.

2.9.2 Verification of the proposed shear strain model using real test data

To further examine the accuracy of the proposed shear strain model, it is used to estimate shear strains observed in experiments by other researchers.

The first set of specimens considered here are two of the specimens tested by Thomsen and Wallace (1995), namely, RW2 and TW2 with both flange in tension and compression all of which had a height to length ratio of 3.0. During the test, average storey shear strain was measured using an X configuration of potentiometers assuming constant curvature distribution over the storey height. This meant that no differential change in lengths of the diagonals was attributed to flexural deformation of the panel. Hence, to compare the reported shear strains to those predicted by the model, reported shear strains from the tests had to be corrected. For this purpose, measurements of total rotation in the first storey (called base rotation in the test report) was used to estimate flexural deformation occurring in the first storey assuming the centre of the rotation being located at two-thirds of the storey height from the top of the storey. The obtained flexural deformation was then subtracted from measured total deformation of the first storey which had already been corrected for strain penetration effects to get the true shear deformation of the first storey. Average shear deformation of the first storey would then be the total shear deformation of the first storey divided by the storey height.

In order to estimate shear strains observed during the tests using the shear strain model, base rotation was divided by the first storey height to get the average first storey curvature. Concrete compression depth was calculated from a section analysis and first storey average shear strain was then calculated using Eq 2.10. The estimated shear strains are plotted against those observed during the test in Figure 2.44a.

Another test data used to verify the accuracy of the proposed shear strain model were results for specimen NTW1, a T-shaped wall with aspect ratio of 3.2 under bi-directional loading, tested by Brueggen (2009) and five rectangular walls with aspect ratios of 2.4, WSH2 to WSH6, tested by Dazio (1999). Since curvature had been measured over smaller intervals over the height of the wall for these specimens, shear deformations reported in the test were considered an accurate representation of the true shear strain. In other words, measurement of the distribution of curvature over the height of the plastic hinge region made determination of the centre of rotation possible. This approach accurately distinguished between contributions of flexure (curvature) and shear strain to the total first storey deformation. With the average curvature known from the curvature profiles given in the test reports and the concrete compression depth calculated from section analysis, Eq 2.10 was then used to estimate average first storey shear strain. Estimated average first storey shear strains for these specimens are also plotted against those observed during the test in Figure 2.44a.

All the data plotted in Figure 2.44a are for walls whose behaviour and mode of failure was dominated by flexure. Adequate shear reinforcement was provided for all of those walls to prevent yielding of the shear reinforcement and ensure that maximum bending strength was reached well before shear failure occurred. According to this figure, the proposed shear strain model very accurately estimated the average first storey shear strains observed during the test. The scatter of the test data on either side of the perfect match line is minor throughout the range of data which suggests that the proposed shear strain model predicted shear strains with consistent accuracy at all levels of global drift.

Another set of test data used to examine the accuracy of the proposed shear strain model was the data from phases I and II of Portland Cement Association (PCA) tests carried out by Oesterle et al. (1976 &1979). The testing program included rectangular, barbell shaped, and flanged walls all with aspect ratio of 2.4 subjected to sustained axial compressive loads between 0.3% and 13.7% of $f'_c A_g$ under reverse cyclic loading. A few specimens were tested under monotonic loading and hence, are excluded from this study. The specimens included here are R1, R2, B1, B3, B2, B5R, F1, B6, B7, and F2. Some specimens were excluded because of lack of accuracy in measurement of deflection components during the test as explained next.

Plastic hinge length of all of the specimens fell within the first 1.83 m (6ft) of the specimen and hence, it is desired to estimate the average shear strain observed within this region. Several mechanisms contributed to the total deformation of the specimen at the top of the plastic hinge length. The first was the sliding of the three construction joints located below the 6ft level, the first one at the base, the second at 3ft level, and the third just below the 6ft level. Measurement of sliding along construction joints was not always accurate for all specimens which resulted in some specimens being excluded from this study. Flexural deformations were calculated using measured rotations at the base, over the bottom 3ft, and over the bottom 6ft of the specimen. In order to calculate flexural deformations from measured rotations, Oesterle et al. assumed the rotation to be concentrated at the mid-height of each measurement panel while in this study, centre of rotation was assumed to be located at 0.6 times of the panel height from the top of the panel to offer a more realistic representation of the actual curvature distribution. Deformations due to sliding of construction joints and flexural deformations were then subtracted from measured total deformations to obtain the true shear deformation of the specimens. Total plastic hinge shear deformation was then divided by the plastic hinge length (1.83 m or 6ft) to obtain average plastic hinge shear strain. Average plastic hinge curvature obtained from measurements of rotation was then used to estimate average plastic hinge shear strain using the proposed shear strain model.

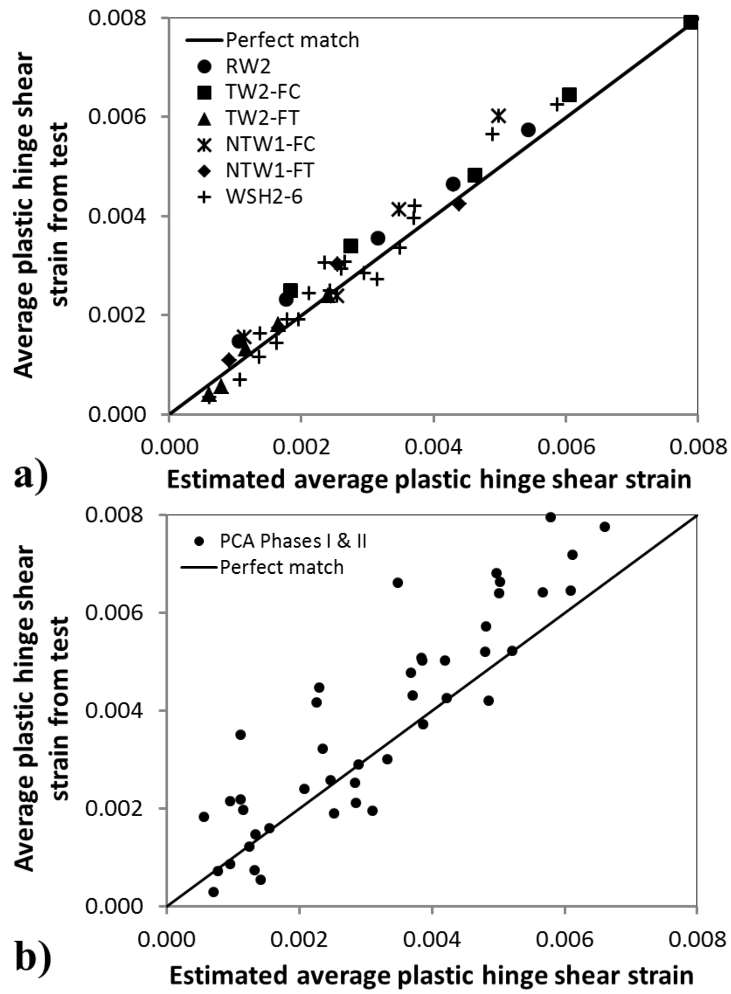

Figure 2.44 Estimates of average plastic hinge shear strain observed in tests by other researchers: a) flexure-dominated walls, and b) walls governed by formation of a shear failure mechanism.

Results of the prediction are plotted in Figure 2.44b. The wide scatter of data points on either side of the perfect match line indicated that the model was much less accurate in predicting shear strains of specimens from the PCA tests. The model generally underestimated the observed shear strain. The explanation is rather simple. The specimens were subjected to high shear stresses because of their small height to length ratio. This resulted in excessive yielding of shear reinforcement and sliding along diagonal cracks. Yielding of (horizontal) shear reinforcement meant that horizontal strains were no longer negligible in comparison to vertical strain hence defying the basic assumption made in the derivation of Eq 2.7. The extra shear strain induced because of yielding of shear reinforcements could not be captured by the proposed shear strain model, neither could the model capture the additional shear strain caused by sliding along diagonal cracks.

It is therefore concluded that the proposed shear strain model can estimate shear strains of flexural walls with great accuracy as long as the aspect ratio is large enough and adequate shear reinforcement is provided to ensure flexure-dominated response where shear strains induced due to slippage along diagonal cracks and yielding of shear reinforcement are negligible in comparison to those resulting from large tensile vertical strains in the web. Since the input parameters required to make estimates of shear strain are readily available to designers, the method proves to be one that can be easily implemented into standard design procedures.

2.10 Conclusions

The following conclusions can be drawn based on the material presented in this chapter:

1. Experiments on flexural shear walls have shown that although shear deformation constitutes a minor portion of the total wall displacement at the top, its contribution to the wall deformation profile within the plastic hinge region is significant compared to that of flexural deformation; a phenomenon that is of great importance when calculating deformation demands on the gravity load system.

2. The direct link between curvature and shear strain of flexural walls observed in tests by other researchers is demonstrated in FE analysis. Wall curvature and shear strain profiles were shown to be similar in shape with shear strains growing rapidly after formation of a flexural hinge in the wall. The interaction between flexural and shear deformations is further explained using fundamental structural mechanics theory.

3. VecTor2 was proven to be a reliable tool for predicting shear strains in flexural reinforced concrete walls. Shear strains observed in VecTor2 analysis were concentrated in areas where flexural yielding occurred which complies with the behaviour observed in tests by other researchers.

4. VecTor2 analyses carried out in this chapter revealed that horizontal strains in the web region of flexural walls were negligible compared to vertical and shear strains. Shear strains were concentrated in area with large vertical tensile strains. Based on this observation, the main source of shear strains in flexural walls was identified as presence of large vertical strains in areas with diagonal cracks.

5. The average principle strain angle in the plastic hinge region of walls considered in the parametric study proved not to be overly sensitive to parameters such as vertical steel ratio, axial compressive load carried by the wall, wall length, wall height-to-length ratio, and presence of floor slabs within the plastic hinge region.

6. A simple model for estimating shear strains in flexural walls was presented. The only input parameter to the model is an average tensile strain which can be easily calculated by the designer from wall curvature profile. The model proved to be reliable and accurate in estimating shear strains observed in tests on flexural shear walls with adequate shear reinforcement. Given the curvature profile of the wall, in addition to average storey shear strains, the model can also give the shear strain profile along the height of the wall plastic hinge region.

CHAPTER 3 Nonlinear Analysis of Shear Walls Accounting for Foundation Rotation

3.1 Introduction

It is a standard structural analysis procedure to model shear walls resting on spread footings with fully-fixed boundary conditions such that no rotation could occur in the support. In reality however, no matter how large and oversized a foundation is, some amount of rotation will occur under eccentric loading. Sizeable foundation rotation may take place under seismic loading as a result of either uplift or compressive displacement of the underlying soil, or in most circumstances, a combination of the two. Magnitude of the rotation incurred is highly dependent on the foundation overturning strength relative to the wall bending strength. Large foundations supporting weak walls are less susceptible to large rotations while weaker foundations supporting stronger walls are more likely to experience large rotations.

Rotation of the shear wall foundation changes the displacement profile of the building which results in additional deformation demands on the gravity-load system. Therefore, quantifying the amount of foundation rotation that can take place in a wall's foundation is essential to ensuring that the gravity-load system is capable of resisting the deformation demands during seismic excitation. In order to understand the behaviour of shear walls accounting for foundation rotation and to be able to make a good estimate of foundation rotation, the full spectrum of relative wall-to-foundation strengths will therefore have to be studied.

The term "rocking" has been extensively used in the literature to refer to the oscillations of a rigid block on a solid surface in which case the block can only rotate by lifting off from the surface simply called liftoff. The rocking problem is a good realistic representation of foundations resting on solid ground such as rock. Despite the fact that foundation flexibility due to compression of the underlying soil is not captured by the rocking problem, the word "rocking" has been repeatedly used to refer to oscillations of foundations on soft grounds such as soils. In this study however, because foundation's flexibility is considered to result from both separation of the foundation from the underlying soil on the tension side (i.e. liftoff) and compressive displacement of the soil on the compression side, the term rocking is only used to refer to the classical rigid block rocking case.

Previous research on rotational behaviour of foundations shows that accounting for the flexibilities in the foundation can be used as an effective way of resisting earthquake effects. Works of Housner (1963) and Priestley et al. (1978) are two examples of such evidence. Despite this, uncertainties still remain regarding controlling negative effects of foundation rotation such as permanent soil displacements and increase in building displacements due to rotation of the foundation. Sections below summarizes the available numerical tools for modelling foundation flexibility and the existing methods for estimating foundation rotation of a given shear wall.

3.1.1 Dynamic response of foundations in the elastic range

Dorby and Gazetas (1986) were the first to provide a solution for the dynamic response of arbitrarily shaped foundations in full contact with an elastic half-space resembling a deep homogeneous soil deposit. Dimensionless charts were provided to assist with calculation of stiffness and damping coefficients of the foundation. Dorby et al. (1986) then verified the analytical formulations of Dorby and Gazetas (1986) against free vibration tests on surface foundation on moist sand. Gazetas (1991) presented algebraic formulas for stiffness and damping coefficients of surface and embedded foundations on/in an elastic half-space. The accuracy of the formulation was verified against experiments by Gazetas and Stokoe (1991).

3.1.2 Existing approaches to numerical modeling of soil-structure interaction

A method for modeling soil-structure interaction that has gained popularity among researchers because of its simple concept is the use of macro-element models. In this method, nonlinear vertical, horizontal, and rotational stiffnesses of a foundation are embedded into an element called a macro-element placed underneath the foundation. Development of such a model requires considerable calibration of numerical parameters against test results to accurately capture the nonlinear material behaviour and the existing coupling of stiffnesses in various directions. Paolucci et al. (2007), Grange et al. (2008), and Figini et al. (2011) were among the researchers who developed a macro-element model for simulating the hysteretic rotational response of foundations. Gajan and Kutter's (2009a) Contact Interface Model (CIM) is also a form of a macro-element.

Despite the analytical elegance of macro-element models and their effectiveness in predicating experimental results, they do not seem to have gained much popularity with design engineers. The need for calibration of the model against test results of the soil under consideration requires financial resources that are usually not available to small and medium size projects.

An alternative numerical solution to the seismic response of structures accounting for foundation rotation has come in the form of modeling the soil as a 3D finite element (FE) mesh with stiffness and strength characteristics of the soil material embedded in the elements. An example of such approach is the work by Anastasopoulos et al. (2011). They developed a simplified constitutive model for analysis of the cyclic response of shallow foundations based on a kinematic hardening constitutive model with Von Mises failure criterion capable of modelling both the low-strain stiffness and ultimate resistance of clays and sands. The constitutive model was proven to be able to predict results of centrifuge tests on clay under cyclic loading and tests on sand with acceptable accuracy. The model is made suitable for implementation in commercial FE codes such as ABAQUS through a user subroutine.

Among the various numerical approaches to modeling soil-structure interaction, the Beam-on-Non-linear-Winkler-Foundation (BNWF) method has been repeatedly used by researchers. In this method, the foundation is modeled as a beam resting on a bed of vertical nonlinear springs with compression characteristics adjusted to represent the behaviour of the soil material. The gap elements between the foundation and the soil springs allow the foundation to separate from the soil simulating uplift while viscous dampers model radiation damping accounting for the energy that radiates away from the foundation and into the soil as a result of impact. The method owes its popularity to its concept being easily understandable to engineers who are not geotechnical experts and the numerical modeling being more visual. Performance indicators such as amount of lift-off and maximum soil compressive displacement can be readily obtained from the model which makes the method more attractive to design engineers.

The use of nonlinear Winkler springs for modeling soil-structure interaction has been recognized in FEMA 356 (see Figure 3.1). Modeling the foundation on a series of vertical springs results in the rotational and the vertical stiffnesses of the foundation to become coupled. In order to account for the correct coupling, the soil underneath the end-regions at the toes of the foundation has to be made stiffer. FEMA 356 defines the length of the end-regions as one-sixth of the foundation width and provides expressions for calculating the stiffness per unit length of foundation in those regions. The remainder of the required vertical stiffness is evenly distributed over the middle region of the foundation.

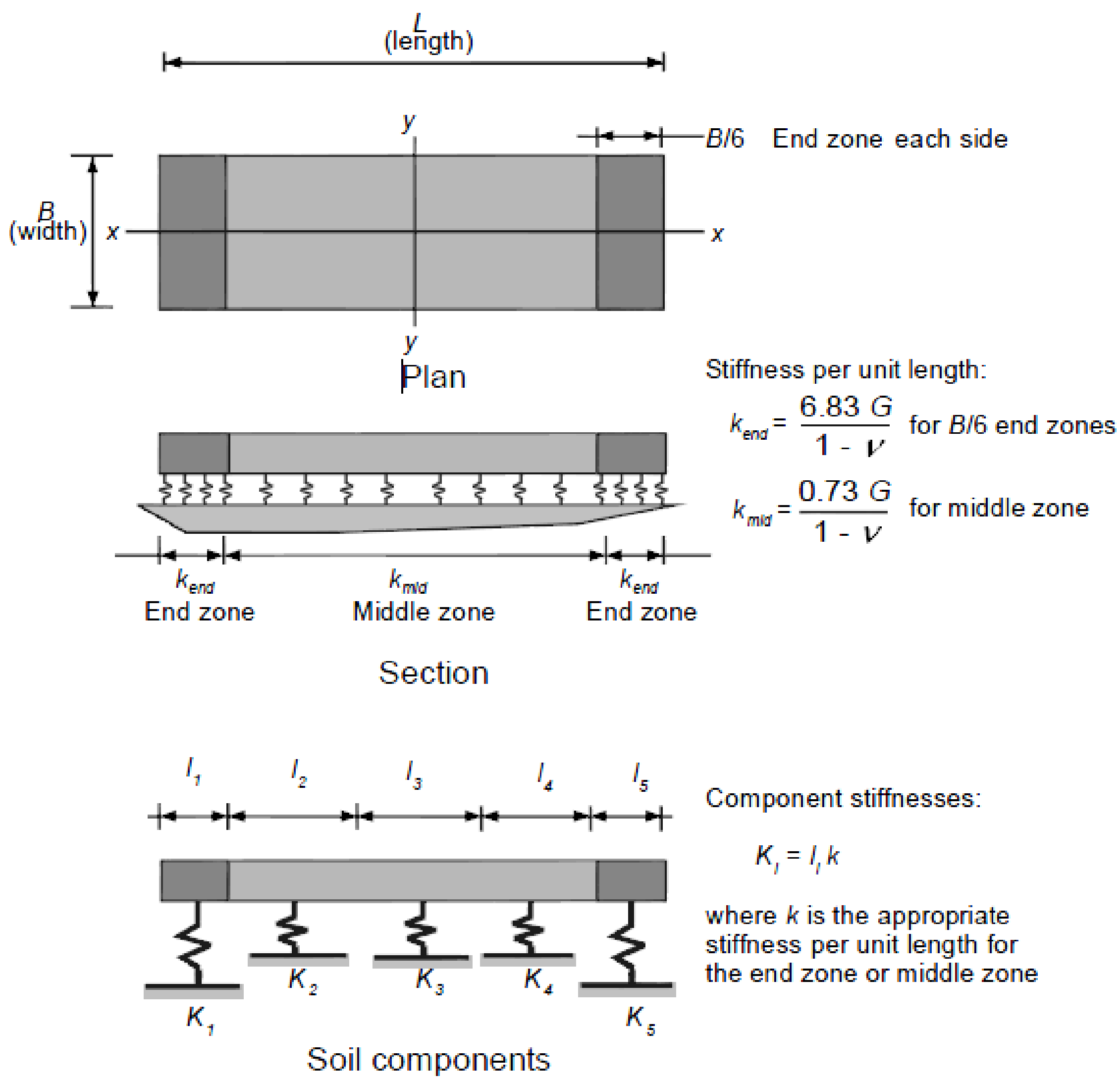

Figure 3.1 Distribution of vertical stiffness underneath the foundation as per guidelines on FEMA 356 – Figure from FEMA 356.

Harden et al. (2005) carried out an in depth study on application of nonlinear Winkler springs to modeling the cyclic response of shallow foundations. Model parameters, including material models and stiffness distribution underneath the foundation were calibrated against a suite of tests considering foundations on both clay and sand type material. In a following publication, Harden et al. (2006) investigated the relationship between strength reduction and increase in displacement of systems with flexible foundations to balance the benefits versus consequences of foundation rotation in a performance based earthquake engineering context. Ugalde et al. (2010) used nonlinear Winkler springs to model the response of bridges on shallow foundations accounting for rotational flexibility of the foundation. Anderson (2003), Filiatrault et al. (1992), and Le Bec (2003) also used nonlinear Winkler springs to model the interaction between the foundation and the underlying soil. The work of these researchers is discussed in more detail later on as the direction of this research has been influenced by them.

Allotey and El Naggar (2003) presented an analytical solution to the foundation moment-rotation response considering all possible states including uplift-only, yield-only, and combined uplift and yield states. Their work also uses the nonlinear Winkler spring concept but with a continuous bed of springs instead of using a discrete number of springs underneath a rigid foundation. The work of Allotey and El Naggar is further discussed in Section 4.1.1.

3.1.3 Existing design procedures for accounting for foundation rotation

The most complete form of existing design procedures for incorporating soil-structure interaction into structural design can be found in the series of publication by the Federal Emergency Management Agency (FEMA). FEMA 273 introduces a simple method for accounting for flexibility of the foundation in structural analysis (see Figure 3.2). In this method, the interaction between the structural component of the foundation and the soil on which it rests is modeled using uncoupled elasto-plastic rotational and translational springs. Guidelines are provided for choosing the stiffness of each of the springs. The stiffnesses are calculated using equations for elastic stiffness of a rigid plate resting on a half-space elastic material such as the ones formulated by Gazetas (1991) but with an effective soil shear modulus (G) used instead of the initial shear modulus (G_0). G_0 can be estimated from the soil mass density and shear wave velocity as follows.

$$G_0 = \rho V_s^2 \quad \textbf{Eq 3.1}$$

FEMA 273 also provides an alternate formula for estimating G_0 using the effective stress and blow count normalized for 1.0 ton per square foot confining pressure and 60% energy efficiency of hammer. The effective shear modulus that must be used to estimate the foundation rotational stiffness would then vary from 50% to 20% of G_0 depending on the effective peak acceleration of the ground motion. In the absence of detailed geotechnical data, FEMA 273 instructs the designer to use half and twice the best estimates of stiffness to account for the variability in soil properties. Guidelines are also provided for choosing the soil ultimate bearing capacity. Ultimate overturning strength of the foundation can then be calculated using the soil ultimate bearing capacity for the vertical load resisted by the foundation.

In FEMA 356 which superseded FEMA 273, it is stated that the soil shear modulus reduction factors recommended by FEMA 273 provisions overestimate the modulus reduction effects for site classes A, B, and C. According to provisions of FEMA 356, for these three site classes, the minimum shear modulus reduction factor is 0.60 and rapidly increases towards unity with decreasing effective peak acceleration. Revisions to the soil shear modulus reduction factors were primarily implemented to avoid overestimating the reductions in design forces due to accounting for the flexibility of the foundation. Having smaller reductions on the soil shear modulus which results in a stiffer foundation would reduce the first mode of vibration period of the system in turn increasing the base shear and design forces. Nevertheless, FEMA 356 also requires upper and lower bounds to be applied to soil properties and analysis to be made with both sets of parameters to bound the problem.

Guidelines of FEMA 273 are applied in FEMA 274 in a demonstrative example where a shear wall building is analyzed. Adding rotational flexibility of the foundation to the model is shown to lengthen the period of the structure which results in reduction in load demands on the shear wall at the expense of larger building displacements. It is recognized that rotation of the foundation relaxes demands on the shear wall and is a suitable mechanism for resisting earthquake forces provided that the gravity-load frame can maintain its load-carrying capacity despite the additional displacements.

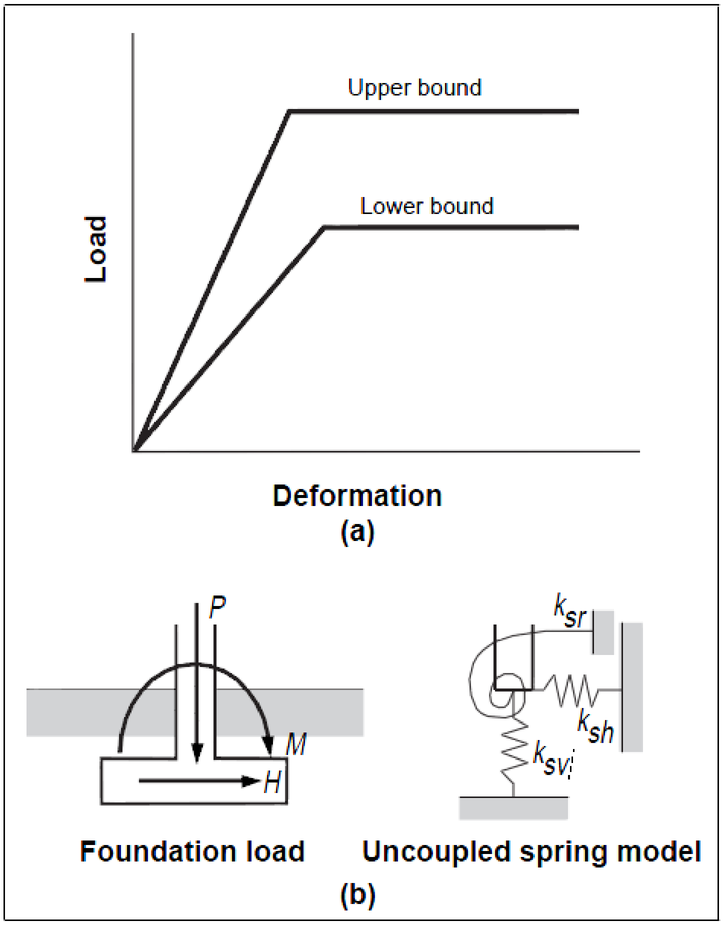

Figure 3.2 (a) Idealized elasto-plastic load-deformation behavior for soils (b) Uncoupled spring model for rigid footings – Figure from FEMA 273.

3.1.4 Selected experiments on rotational response of foundations by other researchers

Numerous tests have been performed on the rotational response of foundations among which, one of the most valuable is a series of tests known as the TRISEE tests presented in Negro et al. (1998) and Negro et al. (2000). Further reference is made to this test in Section 3.2.6. The TRISEE tests have been used as the basis for developing numerical models for rotational response of shallow foundations by many researchers. Macro-element models of Paolucci et al. (2007), Grange et al. (2008), and Figini et al. (2011) were all partly calibrated to match the TRISEE test results. Allotey and El Naggar (2003) validated their solution for the foundation moment rotation response against the TRISEE tests.

Another set of tests on foundation rotations that has been referred to by many researchers is the centrifuge tests carried out by Gajan and Kutter (2008). Gajan and Kutter conducted several centrifuge experiments to study the rotational behavior of shallow footings supported by sand and clay soil stratums, under slow lateral cyclic loading and dynamic shaking. The experiments showed that the ratio of the total foundation area (A) to the minimum bearing area required to resist the vertical load (A_c) can be directly correlated with the foundation's rotational behaviour. Foundations with A/A_c of about 10 did not suffer large permanent settlements as a result of rotation, had sufficient self-centering ability, and dissipated seismic energy corresponding to about 20% damping ratio. Results of the 2008 tests were further discussed in Gajan and Kutter (2009b).

Algie (2011) conducted a series of experiments on foundations embedded in Auckland residual clay. Some of the results and findings from Algie's work are presented in Pender et al. (2013). Forced vibration tests were performed on the foundations using an eccentric mass shaker mounted on top of the frame supported by two foundations. Snap-back tests were also performed by first pulling the frame to a specific displacement and then suddenly releasing it so that the foundations would rock freely. Further reference is made to Algie's work in Section 3.2.6 regarding soil damping.

3.1.5 Anderson (2003)

Anderson investigated the behaviour of 7, 15 and 30 storey shear walls accounting for foundation rotation. In his study, the walls were elastic with masses lumped at floor slab levels. Wall stiffness and mass were adjusted such that the first period of vibration of the fixed-base wall was 0.1N where N was the number of storeys. The percentage of the floor mass' weight supported directly by the shear wall was called Mass Ratio (MR). Three different mass ratios of 0.2, 0.4, and 0.6 were chosen for each wall-foundation combination. 5% viscous damping was assigned to the wall elements to account for energy dissipation due to flexural deformation of the shear wall.

All foundations were square with 21 soil springs equally spaced underneath. An initial study with the footings constructed from linear elastic beam elements revealed that no appreciable flexural deformation occurred in the footing and hence, all footings were modeled to be rigid in bending. The soil springs were elastic-perfectly plastic (EPP) with a gap element that could simulate foundation lift-off. Two types of soil were chosen, rock and clay. The rock had very high stiffness and strength (q_{ult}=10MPa and E=10000 MPa) and hence, most of the foundation rotation on rock came from foundation lift-off. The clay was much softer and weaker (q_{ult}=3.6MPa and E=60 MPa) causing most of the foundation rotation to come from yielding of the soil springs in compression. The foundations were sized for overturning strengths corresponding to R values of 1.0, 1.5, 2.0, and 3.5. R was defined as the ratio of the elastic bending demand obtained from the equivalent static forces given by NBCC 1995 to the foundation overturning strength. The size of the foundation was also checked for service load conditions with the allowable soil bearing pressure being one-third of the ultimate soil bearing capacity but the static or serviceability condition never governed the size of the foundation. Elastic stiffness of the springs was chosen such that the elastic rotational stiffness of the foundation matched that given by Veletsos and Wei (1971). No damping was assigned to the soil spring or the gap elements. In other words, radiation damping of the soil was ignored to enhance rotations of the foundation.

Dynamic analysis was performed using 11 ground motions records modified to match the spectrum given in NBCC 1995. The mean of the envelope responses resulting from each of the 11 ground motion records were used for studying the behaviour of various structures considered in his study.

Figure 3.3 summarizes the results of Anderson's study. As expected, structures with foundations designed for larger R values experienced more rotation and therefore, more increase to their global drift. For all cases, walls with larger mass ratios experienced more foundation rotation. This was again not surprising as foundations with larger mass ratios require a smaller foundation size to achieve a certain R value. As the buildings became taller, the top displacement response of the wall-foundation structure became less sensitive to the mass ratio. It was therefore concluded that shorter buildings are more susceptible to foundation rotation than taller ones. Comparing analysis results for 30 storey structures on rock and clay, a much larger increase in global drift was observed in structures on rock than ones on clay.

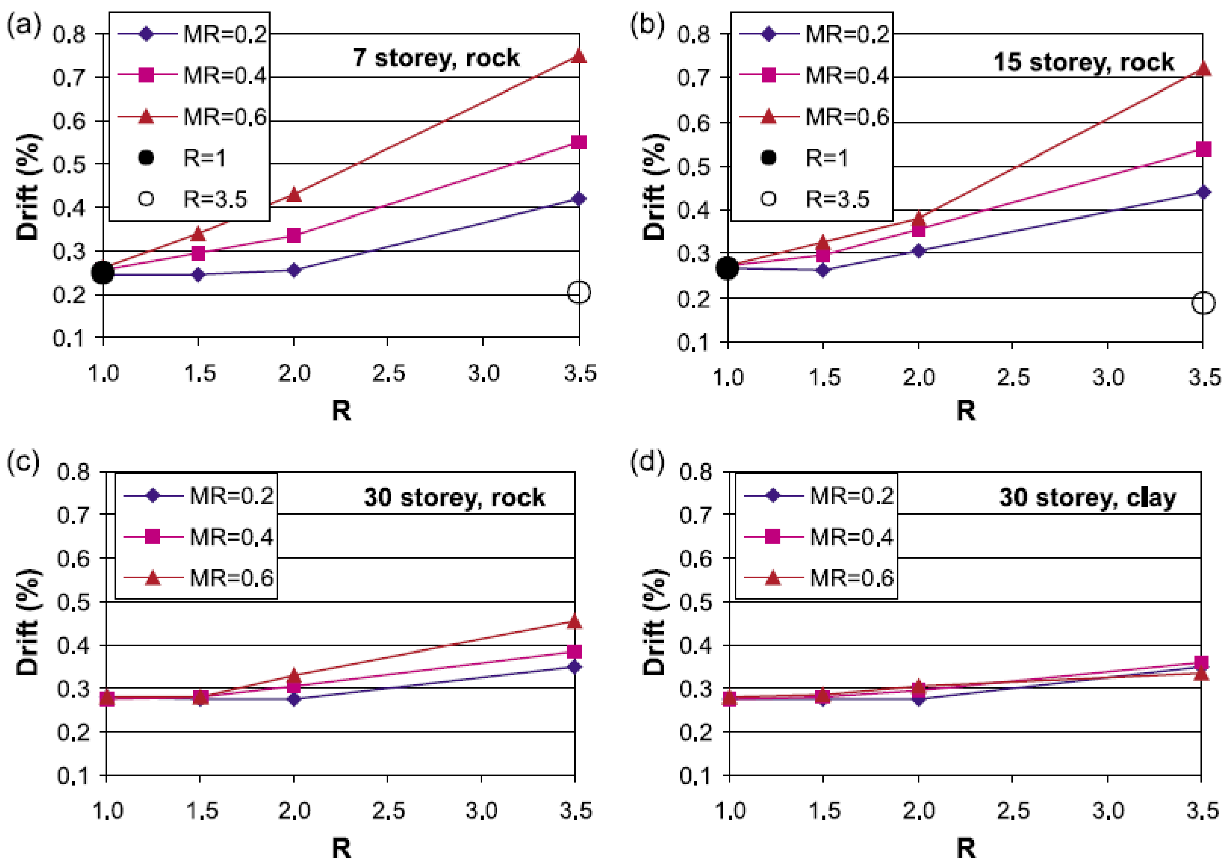

Figure 3.3 Drift ratio versus foundation R value: (a) 7-storey structure on rock foundation, (b) 15-storey structure on rock foundation, (c) 30-storey structure on rock foundation, and (d) 30-storey structure on clay foundation - Figure from Anderson (2003). Note: Values of R in the figure legends represent the ratio of the elastic moment to the wall bending strength.

For the 7 and 15 storey walls on rock, global drift of the elastic wall on an R=3.5 foundation was compared to that of a nonlinear EPP wall with a fixed base. The wall had a value of R also equal to 3.5 with R in this case being the ratio of the elastic moment to the wall bending strength. It was shown that foundation rotation can significantly increase global drifts of the system compared to the global drift of a fixed-base structure. Anderson therefore concluded that in such cases, the foundation overturning strength must be higher than the bending capacity of the wall to reduce foundation rotation and force a flexural hinge to form in the wall.

Anderson's work was crucial in showing what an impact the amount of vertical load supported by the foundation (i.e. mass ratio) has on the behaviour of shear walls with flexible foundations. Also, Anderson proved that shorter buildings are far more susceptible to increased deformations due to foundation rotation than taller buildings. However, in his work, Anderson either considered elastic shear walls on nonlinear inelastic foundations or a nonlinear wall with a fixed-base. The rationale behind focusing on elastic shear walls with flexible foundations was that elastic shear walls could induce much larger moments into the foundation and therefore produced more rotation. Although this correctly represented the worst case scenario, it took away the opportunity to study the interaction between wall bending strength and foundation overturning capacity. In reality, both the shear wall and the foundation are nonlinear and inelastic. Therefore, an obvious follow-up to Anderson's study would be one that accounts for nonlinear behaviours of both the wall and the foundation.

3.1.6 Other Canadian research on shear walls with flexible foundations

Filiatrault et al. (1991) published results of a study on the behaviour of a typical wall-type reinforced concrete structure with a foundation that was unable to develop a plastic hinge in the wall. The structure was a 21 storey core-type reinforced concrete building located in seismic zone 4 as specified in NBCC 1995. The core sat on a 17 x 17 m square footing. Three different models were used to analyze the building's behaviour under the action of horizontal ground motion. Model 1 consisted of the elastic core wall sitting on a rigid or fixed foundation. Model 2 had a footing that was capable of yielding in flexure sitting on soil springs that could simulate soil yielding in compression and foundation uplift in addition to the inelastic core wall capable of producing a flexural hinge. Model 3 incorporated all of the features of Model 2 with the addition of truss and beam elements to include the effect of the parking structure with peripheral retaining walls in the first two storeys of the building.

Nine ground motion records from SMCAT 1989 were chosen that had peak horizontal accelerations and peak horizontal velocities within the range specified by NBCC 1990 for seismic zone 4. From these nine records, two which had an acceleration response spectrum similar to that in NBCC 1980 were chosen to be used in the structural analysis. Because the response spectra of the two chosen records were a bit jagged, fundamental period of the structure was varied by 10% either way and the highest value of the response was reported.

The structural analysis platform chosen was DRAIN-2D. Soil elements were modeled using axial truss elements as hangers. The elements were stressed in tension and possibly yielded in tension to model the soil compressive behaviour. Elastic buckling of the truss elements at very low compressive forces was used to model foundation uplift. The soil was assumed to be hard till with a shear modulus of 200 MPa, a Poisson's ratio of 0.2, and an ultimate bearing capacity of 1.5 MPa. Properties of the individual hangers were adjusted so that the elastic rotational stiffness of the foundation matched that of an equivalent circular foundation given by Das (1983) as follows.

$$K_r = \frac{8GR_0^3}{3(1-\nu)} \qquad \textbf{Eq 3.2}$$

Among the three models, Model 3 had the smallest top displacement and not the fixed-base Model 1 as the forces in the parking structure slabs prevented large bending moments to occur at foundation level. Model 2 had the largest top displacement. Another important observation in this work was that introduction of a flexible foundation reduced the wall base shear much less than it reduced the bending moment demand on the wall. Shear demand in Model 3 was the highest because of the large forces induced in the floor slabs of the parking structure.

Because in none of their original analysis the overall building overturning stability was compromised, Filiatrault et al. repeated some of the analysis with a magnified ground motion record that had a 40% increase compared to the original record. Compared to the original ground motion, the magnified ground motion resulted in 39% increase in base shear demand, 288% increase in maximum top displacement, and an 18% increase in bending moment demand. To consider the worst case scenario, length of the footing was reduced to be equal to the length of the core wall and the magnified earthquake was applied to the structure. Surprisingly, the maximum top displacement increased by only 12% compared to the case with the full foundation size. The uplift of the foundation was even reduced compared to the 17 m square foundation case. Despite the lower foundation overturning resistance, shear forces kept increasing. Even in this extreme case, the stability of the structure was not compromised and the structure did not collapse.

The work published by Filiatrault et al. explained some key points of the fundamental behaviour of walls with flexible foundations especially considering the simple analysis tools used. A continuation of their work could improve on the following aspects. The soil spring backbone curve was elastic perfectly-plastic (EPP) which was a good approach considering the numeric tools available at the time. With the new models available such as the QzSimple1 material in OpenSees, the cyclic response of the soil can be modeled accounting for compression softening of the soil resulting a more sophisticated unloading and loading pattern. EPP flexural elements were used to model the wall whereas modeling the flexural behaviour of the wall using a nonlinear fibre section could yield a more realistic representation of the wall's behaviour. With a fibre section, the nonlinear moment-curvature response of the wall will be accounted for. Also, over strength of the wall due to steel strain hardening which could intensify foundation rotation will be automatically accounted for. Filiatrault et al. investigated the behaviour of a single wall with a certain flexural strength sitting on two foundation sizes. To better understand the interaction between wall flexural strength and foundation overturning resistance, a broader study is required which considers more wall-foundation combinations.

A recent Canadian publication on foundation rotations is the work of Le Bec (2009). In his Master's thesis, Le Bec studied the seismic behaviour of ductile reinforced concrete walls with flexible foundations. Parts of the results were also published in Koboevic et al. (2010). The study focused on a 10-storey rectangular shear wall which was part of a reinforced concrete building with six walls in total (three in each direction). Response Spectrum Analysis was performed on a 3D model of the building following provisions of NBCC 2005. The most heavily loaded wall was then designed and detailed for force levels corresponding to R_dR_o of 5.6. The same wall was then modeled in OpenSees using detailed fibre sections assigned to beam-column elements. Only 13% of the weight of the floor mass was supported directly by the wall and the rest was supported by the gravity-load columns (i.e. a mass ratio of 0.13).

Two sand-type soil profiles were considered which had properties corresponding to the average (550 m/s) and lower-bound (360 m/s) shear wave velocity for site class C as specified in NBCC 2005. The lower bound soil was softer and weaker. The wall's foundation was sized keeping equal overhangs in both directions. Three different foundation sizes were designed for the wall assuming a uniform stress block with the soil's ultimate bearing capacity at the toe of the foundation. The smallest foundation was designed for an overturning strength corresponding to the factored wall bending strength (R_dR_o=5.6). The midsized foundation was designed for the nominal wall bending strength (R_dR_o=4.6). The largest foundation had an overturning capacity equivalent to R_dR_o=2.0.

Nonlinear Winkler springs were used to simulate the interaction between the foundation and underlying soil in OpenSees. The portion of the foundation directly underneath the wall was modeled as a rigid beam because of the wall's high in-plane bending stiffness would prevent the foundation from bending. Foundation overhangs were modeled as elastic beams as no hinging is supposed to occur in a well-designed foundation. The QzSimple1 material for sand was used for the soil springs. Smaller spring spacing was used closer to the foundation toes than that used in the middle strip of the foundation following recommendations of FEMA 356 such that both the elastic vertical and rotational stiffnesses of the group of soil springs matched the elastic stiffness properties of the foundation on the given soil. Soil suction was eliminated to increase foundation rotation but radiation damping was included in the soil springs.

10 earthquake records were selected from the database of simulated ground motions proposed by Atkinson (2009) which had response spectra close to the NBCC 2005 spectrum. Although the individual response spectra were quite jagged, the mean of the 10 followed the NBCC spectrum nicely.

The general conclusion was that accounting for soil-structure interaction decreases the seismic force demands without increasing the top displacement of the wall significantly. As the soil was weakened and softened and the foundations became smaller, force demands kept decreasing and top wall displacements increased but maximum top wall displacement always remained comparable to that of the fixed-base wall. Maximum soil compressive displacement rarely exceeded 45 mm, a fairly small amount considering the size of the foundation. The results showed that "foundation rocking has great potential to reduce the seismic force demand on building structures and can provide an interesting alternative energy dissipation mechanism".

The results from this study describe accounting for flexibility in the foundation as a promising energy dissipation mechanism for the structures considered. It must be noted that the analysis was done on a very ductile wall (R_dR_o=5.6) while it is the stronger walls with much lower values of R_dR_o that are more susceptible to foundation rotation as they are capable of inducing larger bending moments in the foundation. Furthermore, in all of the cases considered, the foundation was either stronger than the wall or as strong as. The more critical cases certainly are ones in which the foundation is weaker than the wall. Also, the wall's mass ratio was 0.13 which is a lower bound of the probable vertical load resisted by a typical wall. The smaller vertical load resulted in a larger foundation needed to achieve a certain foundation overturning strength. Therefore, a larger axial load will result in smaller a foundation and consequently more severe rotation. In addition, the two soil profiles considered in the study were fairly strong and stiff. Permanent soil deformations may become problematic in the case of weaker and softer soils.

3.1.7 Discussion

Analytical tools for studying soil-structure interaction have been developed and used by many researchers. Among the numerical tools, the use of nonlinear Winkler springs seems to have gained more popularity as it is relatively simple to understand and implement. It also is capable of including all types of rotational nonlinearity such as soil yielding and foundation uplift. Nonlinear Winkler springs along with gap elements which can model the separation between the soil and the footing are used in this study to model the nonlinear rotational behaviour of the foundation.

The existing vast literature on foundation rotation has been mostly focused on the behaviour of the soil-foundation interaction. This type of work includes most of the experiments carried out on flexible foundations and the development of numerical models that have followed. The literature on the influence of foundation rotation on the response of the superstructure and particularly shear walls is scarce. The few examples of works of other researchers that have focused on the response of shear walls accounting for foundation rotation presented earlier confirms that a limited range of combinations of wall and foundation strengths have been studied. This study aims at using modern analytical tools to simulate the nonlinear behaviour of both the soil and the wall and study various combinations of wall to foundation relative strengths to better understand the behaviour of shear walls accounting for foundation rotation and to be able to estimate the amount of foundation rotation in a given wall-foundation system.

Most of the previous works have focused on one or two types of soil. It has been shown that for a softer and weaker soil, most of the nonlinearity in the foundation comes from soil compression while on stronger and stiffer mediums such as rock, almost all of the rotation is a result of uplift. It is of interest therefore to study the behaviour of wall-foundation systems on a number of soil types ranging from clay to rock to observe the transition from the compression-dominated behaviour to the uplift-dominated cases.

Simple design-friendly methods such as the one described in FEMA 273 have been developed which account for flexibility of the foundation and incorporate its effects in structural design. The method described in FEMA 273 uses a single elasto-plastic spring to model the rotational response of the foundation. This approach does not realistically capture the mechanisms resulting in that flexibility such as foundation uplift and soil yielding in compression. Moreover, foundation rotational stiffness varies greatly with foundation rotation which makes prediction of the actual hysteretic response using a single elasto-plastic spring impossible. The method is primarily aimed at making conservative estimates of the maximum displacement demands accounting for flexibility of the building's supports.

The objective of CHAPTER 3 is to better understand the interaction between nonlinear behaviours of both the shear wall and the soil through Nonlinear Time-History Analysis (NTHA) of a broad range of shear wall strengths and foundation overturning capacities on various soil types. CHAPTER 4 uses the results of NTHA of CHAPTER 3 to formulate a simple design-oriented method for predicting foundation rotation of a given wall-foundation system. The optimal goal of the research presented in CHAPTER 3 and CHAPTER 4 is to provide step-by-step guidelines for predicting the response of shear walls accounting for foundation rotation based on results of NTHA on a broad range of wall-foundation systems and soil types.

3.2 Numerical Modeling and Analysis Method

In order to accurately capture the behaviour of shear walls accounting for foundation rotation without adding unnecessary complexities into the numerical modeling, certain assumptions had to be made on both the material and system levels. Material characteristics such as stiffness, strength, and cyclic behaviour needed to be chosen such to represent the real response accurately but yet be simple enough to be formulated in finite element (FE) structural analysis. To narrow down the scope of this study, only the 2D response of such wall-foundation systems was studied. OpenSees was chosen as the modeling and analysis platform for the study as it has a diverse library of materials and elements and is well suited to NTHA. Figure 3.4 shows a schematic view of the structural modeling. Assumptions made on material properties and numerical modeling procedures are described in the following sections.

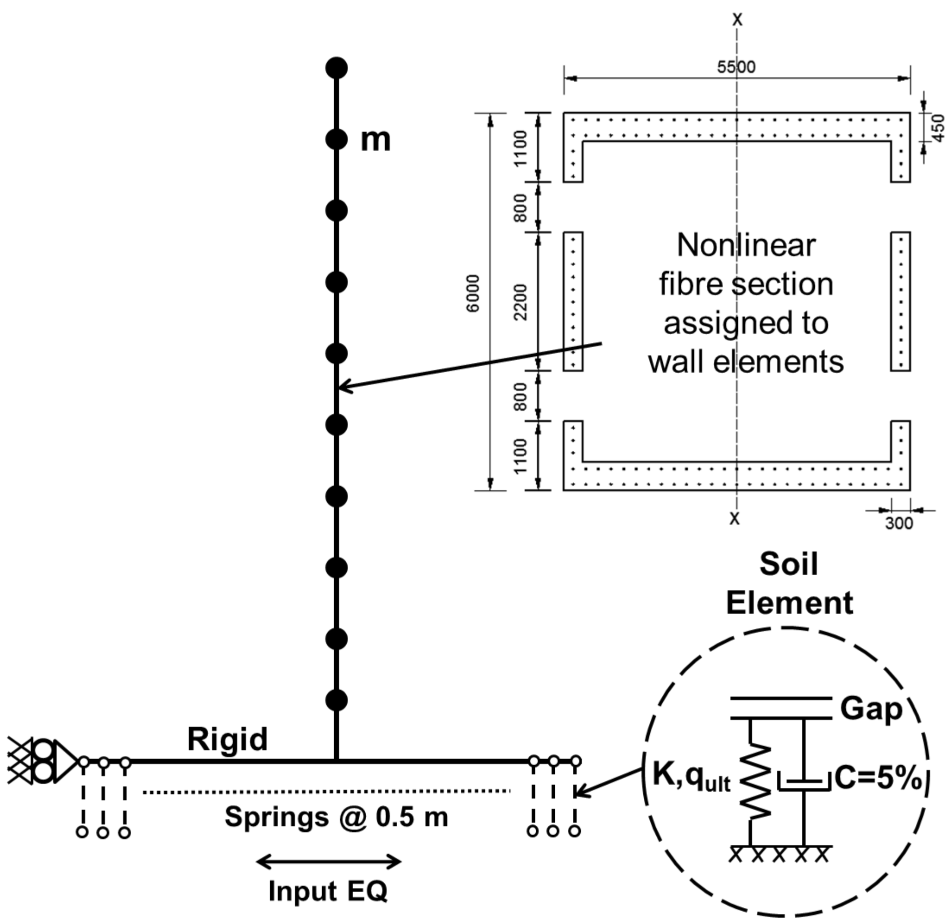

Figure 3.4 Schematic view of 2D modeling of shear walls with a flexible foundation.

3.2.1 Modeling of the shear wall

Walls of three different heights having 5, 10, and 20 storeys were considered in this study with total heights of 15.7, 29.7, and 57.7 m respectively. The walls were modeled as elastic flexural members having a flexural stiffness calculated from uncracked section properties. All walls had their seismic mass and its associated compressive axial load on the wall lumped at floor slab levels and uniformly distributed over the height. These sets of walls were used to conduct a pilot study on wall height to determine which wall height was more severely affected by the negative effects of foundation rotation (see Section 3.5). The behaviour of 10-storey walls was found to be more critically affected by accounting for foundation rotation and therefore, the Core NTHA focused on 10-storey walls.

A group of four nonlinear 10-storey walls of various bending strengths were designed for this study. Figure 3.5 shows the cross-section of the nonlinear 10-storey walls. Other shear wall specifications are given in Table 3.1. The walls were 5.5 m long and 6.0 m wide having a footprint close to being square. First storey height was 4.5 m since most 10-storey buildings have lobbies or mezzanines with high ceilings. The uniform storey height above was 2.8 m. Seismic mass was lumped at floor slab locations and was adjusted such that the elastic fundamental period of the wall with a fixed base was 0.1N with N being the number of storeys (i.e. first mode period of 1.0 sec for 10-storey walls). Axial compressive load on the wall resulting from gravity was expressed as a percentage of the weight of the seismic mass lumped at floor slab levels called the Mass Ratio (MR), and was uniformly distributed over the height of the wall. All four nonlinear 10-storey walls had a MR of 0.4 as standard.

Web steel reinforcement ratio was kept constant at 0.25%. Steel ratio of the flanges was constant in the first 3 storeys where the plastic hinge was expected to form and decreased linearly over the fourth to seventh storeys to a constant value of 0.5% in the top three storeys. The considerable variation among flange vertical steel ratios of the walls within the plastic hinge region was intended to investigate the effect of wall bending strength on the wall-foundation system behaviour. Wall bending strength could have been increased by keeping the flange steel ratio the same while increasing the wall length. This option was considered not to be suitable as wall length affects wall plastic hinge length significantly which would have made comparison of performance parameters of various walls difficult. To avoid introducing wall length as an additional parameter, wall bending strength was increased by increasing the flange steel ratio and keeping the wall cross-section the same. Even though the steel ratio in the flange of wall 10R13 is too high for practical purposes, it is considered acceptable for the purpose of this study.

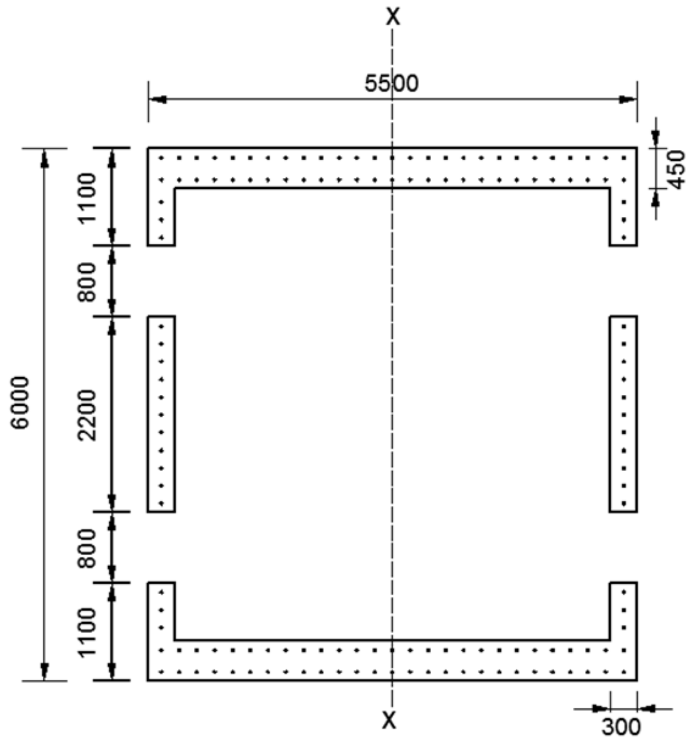

Figure 3.5 Cross-section of nonlinear 10-storey shear walls (dimensions in millimetres) – bending takes place about the X-X axis.

Maximum elastic bending moment demand of the walls was estimated using Response Spectrum Analysis (RSA) of an elastic wall with the same geometry as the nonlinear walls but with flexural stiffness equal to 70% of the uncracked wall stiffness. The spectrum used in the RSA was the 2475 year return period Uniform Hazard Spectrum (UHS) given in Figure 3.13. The wall bending strength at full yield was then expressed as

$$R_w = \frac{M_{RSA}}{M_y} \qquad \textbf{Eq 3.3}$$

Where M_{RSA} is the maximum elastic bending moment demand from RSA and M_y is the probable bending strength of the wall accounting for steel strain hardening. The elastic bending moment demand was found to be 488,275 kN.m. Figure 3.6 shows the envelopes of wall moment-curvature responses for the four walls. Note the difference in the yield moment strength among the walls. R_w was then incorporated into the wall's ID. For example, wall 10R13 is a 10-storey shear wall with an R_w of 1.3. In general, the focus has been on strong walls (i.e. walls with relatively small values of R_w) since stronger walls induce larger moments in the foundation and hence are more prone to additional displacements from rotation of their foundation.

Table 3.1 Specifications of nonlinear 10-storey shear walls.

Floor	Height (m)	Compressive Axial Force Carried by the Shear Wall (kN)	Flange reinforcing steel ratio			
			10R27	10R20	10R17	10R13
Base	0	41550	1.09%	2.63%	3.55%	5.45%
1st	4.5	37395	1.09%	2.63%	3.55%	5.45%
2nd	7.3	33240	1.09%	2.63%	3.55%	5.45%
3rd	10.1	29085	0.97%	2.19%	2.93%	4.46%
4th	12.9	24930	0.85%	1.76%	2.32%	3.47%
5th	15.7	20775	0.73%	1.33%	1.71%	2.48%
6th	18.5	16620	0.61%	0.90%	1.10%	1.48%
7th	21.3	12465	0.49%	0.49%	0.49%	0.49%
8th	24.1	8310	0.49%	0.49%	0.49%	0.49%
9th	26.9	4155	0.49%	0.49%	0.49%	0.49%
10th	29.7	-----	-----	-----	-----	-----

The probable bending strength of the wall was defined as the average of bending moment envelopes at the base of the wall obtained from NTHA of the fixed-base wall subjected to the 10 spectrally-matched ground motions. The effect of steel strain hardening was therefore included in calculation of the probable bending strength of the wall. Since all of the walls considered in this study were flanged walls, the probable bending strength of the wall was very close to the wall nominal strength after the entire vertical steel in the tension flange of the wall had yielded (see Figure 3.6). The probable wall bending strength is therefore denoted as M_y. Table 3.2 summarizes the factored, nominal, and probable bending strengths of the four nonlinear walls considered in this study. Values of R_w calculated based on each of the three definitions for wall bending strength are given in Table 3.3. Note that values of R_w calculated using the probable wall bending strength are used in the remainder of this study wherever reference is made to R_w.

Table 3.2 Factored, nominal, and probable bending strengths of the four nonlinear walls considered in the NTHA (note: wall factored bending strength was calculated using material strength reduction factors of 0.65 and 0.85 for concrete and the reinforcing steel respectively).

Wall ID	Factored Strength (kN.m)	Nominal Strength (kN.m)	Probable Strength (kN.m)
10R13	327700	374900	375000
10R17	249000	281900	302548
10R20	211100	235600	261219
10R27	150500	161100	190796

Table 3.3 Values of R_w calculated using the various definitions of wall bending strength.

Wall ID	R_w based on Factored Strength	R_w based on Nominal Strength	R_w based on Probable Strength
10R13	1.49	1.30	**1.30**
10R17	1.96	1.73	**1.61**
10R20	2.31	2.07	**1.87**
10R27	3.24	3.03	**2.56**

Nonlinear fibre elements were used to construct the cross-section of the shear walls. Concrete04 material based on the work of Popovics (1973) was used to define the stress-strain relationship of the concrete material. Concrete compressive strength was chosen to be 30 MPa with the secant modulus of concrete calculated as $4500\sqrt{f'c}$ (in MPa units). The value used for concrete crushing strain was 0.0035 in compression. Concrete strain at maximum compressive stress was calculated using the concrete secant modulus to be 0.0021. Tensile strength was chosen to be 1.9 MPa. The cyclic response of the stress-strain relationship also accounted for cumulative compressive strains due to crushing (compressive stresses beyond f'_c) as well as concrete tension stiffening. Table 3.4 summarizes the various input parameters for the concrete material model. In the table, f'_c is the concrete compressive strength, e'_c is the concrete strain at f'_c, e_{cu} is the maximum permissible concrete compressive strain, E_c is the secant stiffness of concrete in compression, f_t is the concrete tensile strength, e_t is the concrete strain at f_t, and the residual stress parameter is the loading point value defining the exponential curve parameter to define the residual stress simulating concrete tension stiffening.

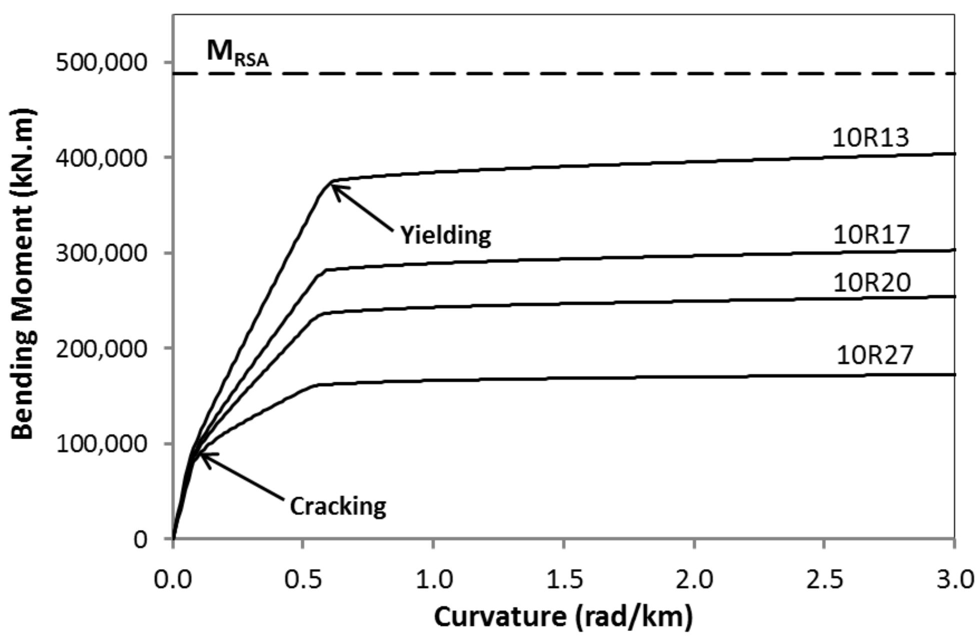

Figure 3.6 Plastic hinge zone bending moment-curvature envelopes of the four nonlinear 10-storey shear walls.

Steel01 material (bilinear stress-strain relationship) was used to model the reinforcing steel in the fiber sections. Yield strength of 400 MPa and elastic modulus of 200 GPa were assumed. The secondary slope of the steel stress-strain relationship defining the strain hardening response was set to 1% of the initial elastic slope. Other parameters were kept at their default values suggested by the program. Unloading of the steel fibers loaded to beyond their yield capacity occurs with a slope parallel to the initial elastic slope of the stress-strain curve. Input parameters for the steel material models are listed in Table 3.5 where F_y is the yield strength, E is the elastic modulus of steel, and parameters a_1 to a_4 are parameters defining the hysteretic behaviour of the steel.

Table 3.4 Input parameters for the concrete material model.

Concrete04 Material in OpenSees	
f'_c (MPa)	30
e'_c	-0.0021
e_{cu}	-0.0035
E_c (MPa)	24647
f_t (MPa)	1.9
e_t	7.7E-05
Residual stress parameter	0.1

The fiber sections were then assigned to force-based beam-column elements with 5 integration points to construct the shear wall model. 3% of critical damping was assigned to the beam-column elements.

Table 3.5 Input parameters for the steel material model.

Steel01 Material in OpenSees	
F_y (MPa)	400
E (MPa)	200,000
Parameter a_1	0
Parameter a_2	1
Parameter a_3	0
Parameter a_4	1

Fiber models are very useful in predicting flexural deformations of structural members but cannot capture shear deformations. However, once the flexural deformation profile of the wall is obtained, inelastic shear deformations in the plastic hinge region of the wall can be estimated using the procedure described in CHAPTER 2 and added to the flexural deformation profile if need be. Wall shear deformation is neglected in this chapter since flexural behaviour of the wall accounting for foundation rotation is of interest.

3.2.2 Modeling of the footing

In this study, footing is referred to the structural element designed to transfer the loads from the shear wall to the underlying soil called the foundation. Flexibility of the foundation therefore refers to the flexibility of the underlying soil material and not the flexural rigidity of the footing on which the wall rests.

In a study on seismic behaviour of reinforced concrete ductile shear walls accounting for foundation rotation, Koboevic et al. (2010) modeled the portion of the footing directly underneath the wall to be rigid and used elastic beam elements for the footing overhangs. This modeling procedure seems realistic as the wall will significantly stiffen the footing out of its plane and hence assuming the footing to be rigid in that region is reasonable. Also, footing depth must be designed to prevent any damage to the footing in the event of an earthquake which justifies the use of elastic beam elements to model footing overhangs. However, such a detailed model for the footing does not contribute a great deal to the accuracy of the overall predicted response of the wall-foundation structure. Footings of core walls are usually 1.5 m to 2.5 m deep and the boundaries of the wall are often not far away from the edges of the footing. Furthermore, the portion of the footing directly underneath the core is stiffened by the core wall and will remain nearly rigid. This suggests that very little deformation will be induced in the footing itself as a result of its rotation. Anderson (2003) did some initial analysis with the walls sitting on elastic footings and discovered that the results were very similar to the cases were the footings were assumed to be perfectly rigid. In another paper on walls with flexible foundations by Filiatrault et al. (1992), the footing was also assumed to be rigid. In this study, footings are assumed to be rigid ignoring their flexural deformations. This would eliminate the need for designing footings of different sizes with various thicknesses. Assuming the footings to be rigid eliminates yet another parameter from the study which makes comparison of results easier and makes for better understanding of the behaviour of wall-foundation systems.

3.2.3 Modeling of the soil-structure interaction

To simulate the nonlinear behaviour of the soil and the interaction between the footing and the underlying soil, nonlinear Winkler springs were used (see Figure 3.4). A series of nonlinear soil elements were spread underneath the footing with the properties of the elements adjusted to best represent the behaviour of the soil in both elastic and nonlinear phases of the response. QzSimple1 material readily available in OpenSees was chosen for this study. Each soil element constructed using this material is composed of a nonlinear spring in parallel with a viscous damper both in series with a gap element which connects to the footing. The nonlinear spring in the QzSimple1 material was formulated to mimic the monotonic backbone curves for the compressive force-displacement response at the tip of drilled shafts in clay and driven piles in sand. Even though the material was formulated based on experimental results for piles and drilled shafts, the local response underneath a spread footing is similar to that at the tip of a caisson or pile. The extensive use of the model by other researchers to model the soil-structure interaction underneath a foundation confirms this statement. Works of Le Bec (2009), Koboevic et al. (2010), Algie (2011), and publications such as PEER report 2005/04 are examples of studies done on foundation rotation with the QzSimple1 material used as Winkler springs.

The footing was fixed against horizontal movement as shown schematically in Figure 3.4 ignoring the interaction of the thickness of the footing with the soil and the frictional interaction of the underlying soil with the underside of the footing. This modeling assumption ignores any damping resulting from soil-structure interaction in the horizontal direction. Also, sliding of the foundation is neglected. Both of these phenomena reduce the rotational excitation of the foundation and were therefore excluded from the numerical model. Horizontal movements of the footing was ignored in numerical simulations of shear walls accounting for foundation rotation carried out by Filiatrault (1991), Anderson (2003), Le Bec (2009), and Koboevic (2010). Neglecting the soil-structure interaction in the horizontal direction in this study will therefore make for better comparison of the results with observations made in previous research.

Figure 3.7 shows the non-dimensional monotonic response backbones of the QzSimple1 material. Z_{50} is the displacement at which 50% of the ultimate bearing capacity is mobilized. The only inputs to the model are Z_{50} defining the initial elastic stiffness and q_{ult} being the ultimate bearing capacity. The sand curve starts with a much stiffer response but quickly softens whereas the clay keeps a nearly constant elastic stiffness up to the point where about 50% of the ultimate bearing capacity is mobilized. However, in reality, sand is usually much stiffer and much stronger than clay.

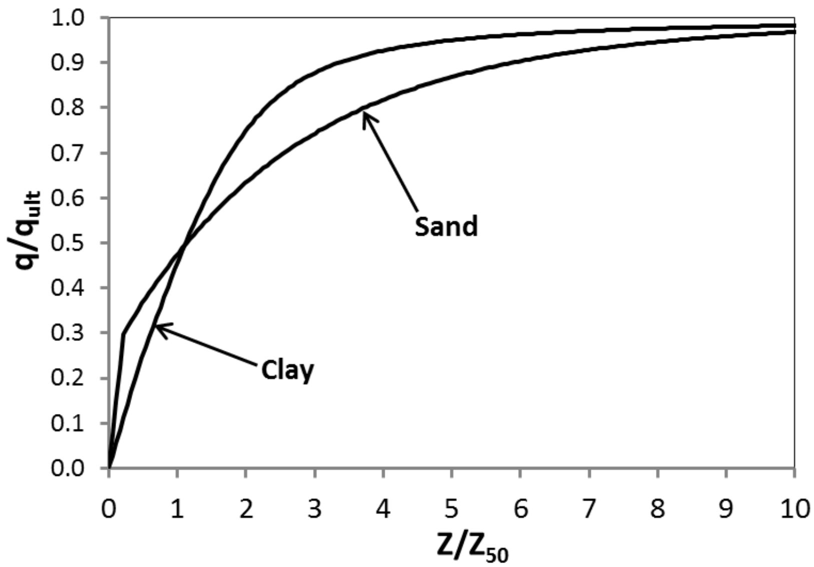

Figure 3.7 Non-dimensional backbone curves defining the QzSimple1 material used for soil springs.

Deformation of the soil spring in monotonic compression is divided into two parts one being the elastic deformation which is recoverable upon unloading and the other being the plastic soil deformation which cannot be recovered after unloading. Therefore, total deformation of the soil spring (Z) can be decomposed into the elastic portion (Z_e) and the plastic portion (Z_p) as follows.

$$Z = Z_e + Z_p$$ **Eq 3.4**

Elastic displacement at any given load (q) would be

$$Z_e = \frac{q}{k_e}$$ **Eq 3.5**

where k_e is the initial elastic stiffness of the soil element. The plastic displacement is given by

$$Z_p = CZ_{50}\left[\left(\left(1 - \frac{q}{q_{ult}}\right)\left(\frac{1}{1 - C_r}\right)\right)^{\frac{-1}{n}} - 1\right]$$ **Eq 3.6**

In this equation, q_{ult} is the ultimate bearing capacity of the soil, Z_{50} is the displacement at which a bearing pressure of $0.50q_{ult}$ is mobilized and C, n and C_r are constants related to the type of the soil whether sand or clay. C_r is the fraction of q_{ult} beyond which the soil will exhibit inelastic deformation. For bearing pressure less than $C_r.q_{ult}$, Z_p will be zero. C and n are numeric constants that define the compression softening of the backbone curve. Values of the constants used for clay and sand type soils are summarized in Table 3.6.

Table 3.6 QzSimple1 material constants for clay and sand type soils.

	Clay	Sand
C_r	0.2	0.3
n	1.2	5.5
C	0.35	12.3

For clay type soils, even though C_r is 0.2, the plastic displacement component of the soil remains small compared to the elastic displacement component up to a bearing pressure of $0.5q_{ult}$. This is because the value of n and C for clay type soils are such that the soil spring starts to soften only at very high bearing pressures. The elastic stiffness however is maintained only up to $0.2q_{ult}$. The value of C_r for sand type soils is 0.3 hence the plastic component will start to develop at bearing pressure of $0.3q_{ult}$. In this case, n and C are such that the soil spring softens and the plastic displacement component grows rapidly beyond pressures of $0.3q_{ult}$. Softening of sand type soils is so quick that it produces a visible kink in the backbone curve (see Figure 3.7).

As for the cyclic response of the QzSimple1 material, as long as the compressive displacement stays below the linear limit (i.e. $0.2q_{ult}$ for clay and $0.3q_{ult}$ for sand), no residual displacement is produced in the soil. When the nonlinear spring is compressed beyond the linear elastic range, unloading will occur on a line parallel to the initial linear part of the backbone curve. At high compressive stresses such as 85% q_{ult}, a very small portion of the displacement is recovered once the load has been reversed (i.e. little rebound of the soil).

Soil suction (or tension) was completely neglected even though in reality some suction can develop. This decision was made so to enhance the cyclic rotational motion of the foundation. Cyclic behaviour of the nonlinear spring in compression and lack of suction allows for significant accumulation of non-recoverable soil compressive displacement. Because the nonlinear part of the soil displacement does not rebound or is not cyclic, little damping needs to be associated with the nonlinear soil springs. This is different than radiation damping which accounts for radiation of energy away from the wall-foundation system upon impact on the soil. Properties of the viscous damper inherent in the QzSimple1 material were adjusted to capture soil radiation damping. The subject of soil radiation damping is discussed in Section 3.2.6.

Gazetas (1991) first introduced equations for computing the uncoupled elastic translational and rotational stiffnesses of a rigid foundation sitting on an elastic half-space medium. Gazetas' formulations for the uncoupled vertical translational stiffness K'_z and the rotational stiffness $K'_{\theta y}$ of a rectangular foundation as summarized in ATC-40 and PEER report 2005/04 are as follows.

$$K'_z = \frac{GL}{1-\nu}\left[0.73 + 1.54\left(\frac{B}{L}\right)^{0.75}\right]$$ **Eq 3.7**

$$K'_{\theta y} = \frac{G}{1-\nu} I_y^{0.75}\left[3(\frac{L}{B})^{0.15}\right]$$ **Eq 3.8**

In the equations above, G is the elastic shear modulus of the soil, ν is the Poisson's ratio, L is the foundation length, B is the foundation width, and I_y is equal to $BL^3/12$. These stiffnesses are surface stiffnesses as if the foundation is placed on the surface of the soil. To consider the effect of embedment on foundation stiffness, Gazetas proposed multipliers to be applied to the surface stiffnesses.

$$e_z = \left[1 + 0.0095\frac{D}{B}\left(1 + 1.3\frac{B}{L}\right)\right]\left[1 + 0.2\left(\frac{2L+2B}{LB}d\right)^{0.67}\right]$$ **Eq 3.9**

$$e_{\theta y} = 1 + 0.92(\frac{2d}{L})^{0.62}\left[1.5 + (\frac{2d}{L})^{1.9}(\frac{d}{D})^{-0.60}\right]$$ **Eq 3.10**

Where d is the thickness of the foundation and D is the depth at which the foundation is placed. The total uncoupled stiffnesses would then be.

$$K_z = e_z K'_z$$ **Eq 3.11**

$$K_{\theta y} = e_{\theta y} K'_{\theta y} \qquad \textbf{Eq 3.12}$$

For a given foundation size, a sufficient number of closely spaced soil elements are necessary to accurately capture the soil response. In a parametric study, Koboevic et al. (2010) discovered that the number of springs modeled did not have a noticeable effect on the results when the spacing between the springs was less than 12% of the length of the foundation. In this study, soil springs were spaced at 0.5 m and uniformly along the entire length of the foundation. Since the wall length is 5.5 m, the smallest realistic foundation length would also be 5.5 m. A constant spring spacing of 0.5 m translates to 9% of the length of the smallest foundation which is less than 12% and therefore acceptable.

With uniform spacing of identical soil springs, either the vertical elastic stiffness or the rotational elastic stiffness can be matched to the values given by equations Eq 3.11 and Eq 3.12 respectively. A detailed methodology presented in PEER 2005/04 suggests modeling stronger soil springs near the ends of the foundation such that both the elastic vertical and elastic rotational stiffnesses of the foundation could be matched to the values given by Gazetas' equations. Even though a complete formulation is given for spacing of the springs, length of the end regions etc., uniformly spaced identical soil springs were used in this study to reduce complexity.

Because the rotational motion of the foundation is the focus of this chapter, stiffness of the soil springs was adjusted such that the uncoupled rotational stiffness given by Gazetas' formula for an effective soil shear modulus of elasticity G_{eff} was achieved. This resulted in an uncoupled vertical elastic stiffness greater than that proposed by Gazetas; however, because the input excitation was horizontal, little or no vertical vibration was expected and hence, this simplification did not reduce from the accuracy and credibility of the analysis results. The major parameter affected by using a higher elastic vertical stiffness was the initial settlement of the foundation due to gravity loads which for a well-sized foundation would be much smaller than vertical deformations induced due to severe rotation of the foundation. See Section 3.2.4 for soil properties used for the QzSimple1 soil elements and further explanation on how the elastic stiffness of individual soil springs were adjusted to match the desired initial foundation rotational stiffness given by Gazetas.

3.2.4 Soil properties used in NTHA

In order to carry out a series of nonlinear time-history analysis (NTHA) to study the effect of foundation rotation on deformation profile of shear walls, an informed decision needed to be made on the types and properties of the soil. This was done by considering soil properties used by previous researchers, personal communication with geotechnical experts, information available in standard soil mechanics literature, and provisions of building codes.

Table 3.7 summarizes soil parameters used by previous researchers to study foundation rotations. It is obvious that even for a similar type of soil, the properties used by various researchers are greatly different.

Table 3.7 Soil properties used by previous researchers to study foundation rotation.

Type of Soil	**Author(s)**	**E (MPa)**	**G_{eff} (MPa)**	**q_{ult} (MPa)**	**v**
Soft Clay	Ghalibafian (2006)	125	**43.0**	**0.04**	**0.45**
Clay	Anderson (2003)	**60**	20.7	**3.60**	0.45
Clay	Gazetas and Apostolu (2004)	**20**	6.90	**2.67**	0.45
Upper bound site class C	Koboevic et al. (2010)	**1780**	**710**	**1.70**	0.25
Lower bound site class C	Koboevic et al. (2010)	**700**	**270**	**1.10**	0.25
Sand 90% relative density	PEER report 2005/04	22.5	**8.65**	**1.10**	0.30
Hard Till	Filiatrault et al. (1992)	480	**200**	**1.50**	0.20
Rock	Anderson (2003)	**10000**	4167	**10.0**	0.20

Note: Bold numbers are given by the authors and those non-bold are calculated.

This is not surprising however because of the massive variation in soil conditions and various methods of evaluating soil stiffness and strength. It seems that in terms of type, the soils used are generally either clay, sand, or till. Therefore, it is worthwhile to focus on identifying the upper and lower bounds of the properties of each type of soil.

It is a common practice in geotechnical engineering to estimate the elastic shear modulus of soils from shear wave velocity (see Eq 3.13). Typical values of soil elastic modulus and Poisson's ratios are given in Table 3.8 and Table 3.9. Also, bearing capacity of foundations can be estimated from bearing capacity equations available in the literature using cohesion c and the internal friction angle φ for the soil. Clays are assumed to have zero or minimal internal angle of friction and resist load only due to cohesion. On the other hand, sands are deemed to have zero or minimal cohesion and be able to provide bearing only through interlocking of grains or their internal friction angle. Typical values of soil internal friction angle given by Das (2001) are presented in Table 3.10.

In a personal communication with Dr. Wijewickreme at the University of British Columbia, a set of lower bound and upper bound properties for each type of soil was obtained. The data is summarized in Table 3.11.

Table 3.8 Typical values for soil elastic modulus – Data from Das (2001).

Type of Soil	E (kPa)
Soft Clay	1,800-3,500
Hard Clay	6,000-14,000
Loose Sand	10,000-28,000
Dense Sand	35,000-70,000

The small strain elastic shear modulus was calculated as follows,

$$G_0 = \rho V_s^2 \qquad \textbf{Eq 3.13}$$

Table 3.9 Typical values of soil Poisson's ratios – Data from Das (2001).

Type of Soil	v
Loose Sand	0.2-0.4
Medium Sand	0.25-0.4
Dense Sand	0.3-0.45
Silty Clay	0.2-0.4
Soft Clay	0.15-0.25
Medium Clay	0.2-0.5

Where V_s is the small-strain shear wave velocity and ρ is the density of the soil. The elastic modulus, E, could then be calculated from the effective shear modulus G and the Poisson's ratio, ν, using

$$E = 2(1+\nu)G \qquad \textbf{Eq 3.14}$$

Table 3.10 Typical values of internal friction angle of soils – Data from Das (2001).

Type of Soil	ϕ (deg)
Sand: rounded grains	
Loose	27-30
Medium	30-35
Dense	35-38
Sand: angular grains	
Loose	30-35
Medium	35-40
Dense	40-45
Sandy Gravel	34-48
Silts	26-35

Table 3.11 Soil properties obtained through personal communication with Dr. Wijewickreme.

Type of Soil	V_s (m/s)	ρ (kg/m^3)	G_0 (MPa)	ν	E_{max} (MPa)	S_u (kPa)	ϕ (deg)	q_{ult} (kPa)
Clay *(NC-OC)*	40-200	1200-1800	1.92-72	0.4-0.5	5.38-216	10-100	-----	89-650
Sand *(loose to very dense)*	100-500	1700-2200	17-550	0.25-0.35	42.5-1485	-----	30-44	1170-15000
Till	600-1000	2000-2200	720-2200	0.2	1728-5280	-----	38-50	4630-57000

S_u shown in Table 3.11 is the undrained cohesion of clay. The undrained cohesion is used because in the event of an earthquake, there is not sufficient time for the excess pore water pressure to dissipate through seepage and hence, loading conditions would be close to the undrained testing condition.

Bearing capacity is generally a property of the foundation and not a property of the soil. Footing shape and depth considerably influence the bearing capacity of a foundation. For the purpose of this study, all of the footings will be square footings and will be placed at the same depth. Hence, using a constant ultimate bearing capacity q_{ult} independent of the foundation size for each type of soil is reasonable. Also, it reduces the number of parameters to be studied and makes for better comparison of results.

There are a number of formulations for estimating the ultimate bearing capacity of foundations. Meyerhof (1953) suggested the use of an effective foundation length to account for eccentricity of the applied load. Meyerhof's formulation is as follows.

$$q_{ult} = cN_c\lambda_{cs}\lambda_{cd} + qN_q\lambda_{qs}\lambda_{qd} + \frac{1}{2}\gamma L' N_\gamma \lambda_{\gamma s}\lambda_{\gamma s} \qquad \textbf{Eq 3.15}$$

In this equation, c is the cohesion of the soil, λ terms are shape and depth factors, γ is the unit weight of the soil, and the N factors can be found knowing the internal friction angle of the soil. L' is the effective foundation length defined as L-2e where 'e' is the eccentricity of the load. The upper and lower bound ultimate bearing capacities shown in Table 3.11 are then calculated using Meyerhof's method for a 12.5 m by 12.5 m located at a depth of 2.0 m assuming an eccentricity of 2.5 m or $L/6$.

A set of realistic soil parameters had to be chosen if the results of the study were to be a good representative of the common professional practice. Therefore, the help of a professional geotechnical consultant was needed. Ernest Naesgaard, an experienced and well-known geotechnical consultant in Vancouver, was asked to assist with the choice of soil parameters for this study. After considering the behaviour of various types of soil in cyclic compression, appropriate stiffness and strength parameters, factor of safety associated with bearing capacity, and the basis for sizing of the foundation given a set of soil properties, five types of soil were chosen for the core study. The soils ranged from medium clay through three types of sand to rock. Table 3.12gives the properties of the 5 soil types. In this table, q_{ult} is the ultimate bearing capacity used to define nonlinear soil springs in OpenSees (see Figure 3.7), q_f is the factored soil bearing capacity of the soil used to calculate the foundation overturning capacity as shown in Figure 3.10, q_a is the allowable soil bearing stress under service load conditions, V_s is the small strain shear wave velocity, G_0 is the small strain shear modulus, and G_{eff} is the effective shear modulus of elasticity used to calibrate the stiffness of the QzSimple1 soil springs in OpenSees.

Table 3.12 Soil properties used in NTHA.

	Clay	Loose Sand	Medium Sand	Dense Sand	Rock
q_{ult} (kPa)	400	400	800	1600	20000
q_f (kPa)	200	200	400	800	10000
q_a (kPa)	133	133	267	533	7000
V_s (m/s)	200	325	360	760	>760
G_0 (MPa)	43.1	57.1	186	825	5555
G_{eff} (MPa)	21.5	21.5	70.0	311	5555

Figure 3.8 compares stiffness and strength parameters chosen for Clay with properties used for clay type soils by other researchers. The scatter in properties used by other researchers is obvious. The stiffness parameter chosen for clay is in the middle of the range of stiffnesses used by others. In terms of strength, the Clay is closer to the lower bound. Properties of clay also fall within the range of clay properties suggested by Dr. Wijewickreme. Note that values on the vertical axis of the figure are G_{eff} and not G_0. Values of G_0 suggested by Dr. Wijewickreme reported in Table 3.11 are divided by 2 to get the corresponding G_{eff}. Stiffness and strength parameters used for the three Sand soils are compared with properties of sand type soils used by other researchers in Figure 3.9. Again, the scatter of soil properties is obvious. However, stiffness and strength properties chosen for the three Sand soils cover the range of soil strength and stiffnesses used by other researchers.

The overturning capacity of the foundation was calculated using a factored bearing strength (q_f) as opposed to the ultimate bearing capacity (see Figure 3.10). This was to reflect the factor of safety that a geotechnical consultant would apply to the ultimate bearing capacity reported to the structural designer. The factor of safety accounts for uncertainties in the soil material and also prevents excessive settlements. In this study, the factor of safety on soil bearing capacity was chosen to be 2.0 resulting in q_f being equal to $0.5q_{ult}$. This reduction will have little effect on the calculated overturning strength of a foundation if the depth of the compression block (L-2e) is small compared to the lever arm (e) which would be the case for a large foundation on a strong soil. For a small foundation on relatively weak soil however, using a smaller bearing capacity will reduce the lever arm and consequently, the foundation overturning capacity to a greater extent. In other words, lightly loaded foundations on stronger soils will have a smaller overstrength and heavily loaded foundations on weaker soils will have a larger overstrength because of using q_f instead of q_{ult} in evaluating the foundation overturning strength.

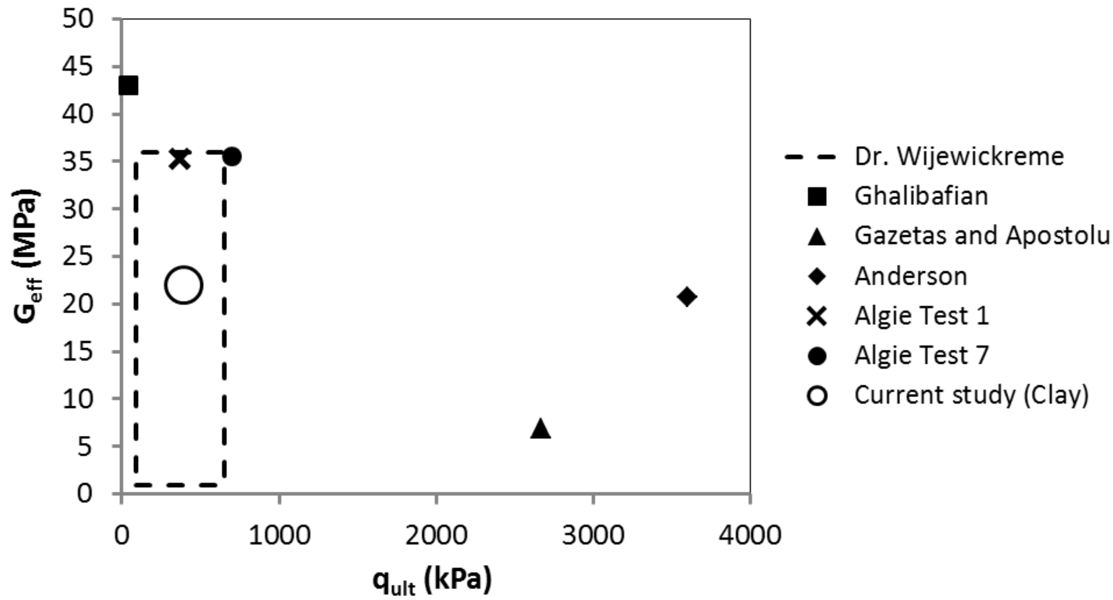

Figure 3.8 Comparison of stiffness and strength properties of Clay used in this study with values used for clay type soils by other researchers.

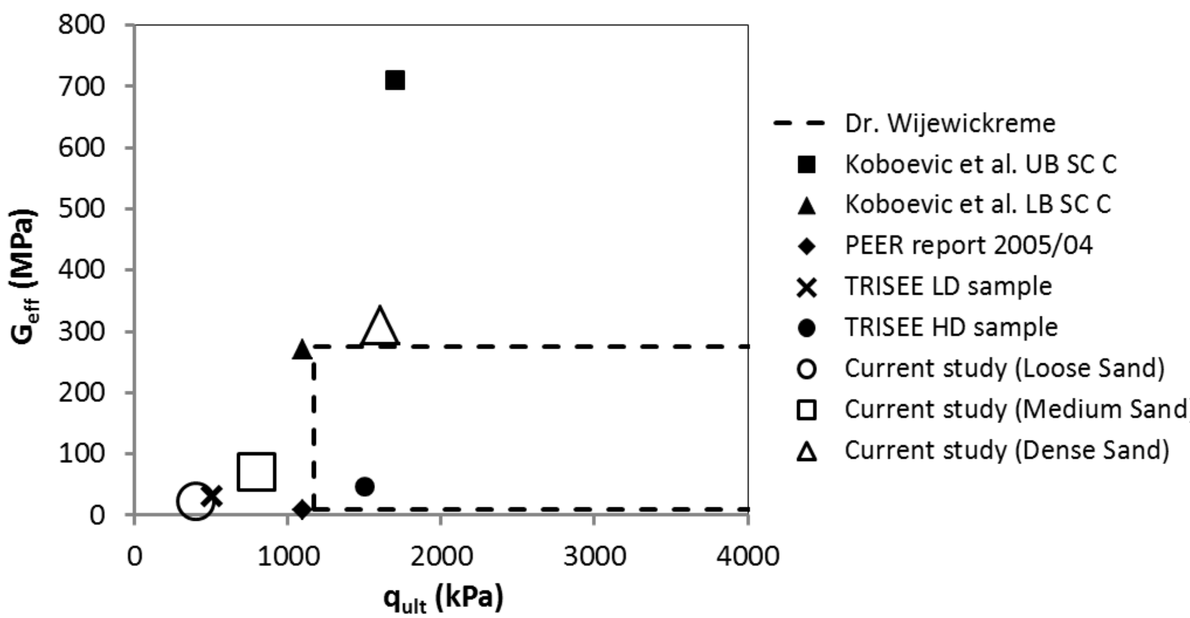

Figure 3.9 Comparison of stiffness and strength properties of the three types of Sand used in this study with values used for sand type soils by other researchers.

The factored overturning capacity of the foundation is expressed as R_f defined as

$$R_f = \frac{M_{RSA}}{M_{oc}} \qquad \textbf{Eq 3.16}$$

Where M_{RSA} is the maximum elastic bending moment demand from Response Spectrum Analysis (RSA) and M_{oc} is the factored foundation overturning capacity as shown in Figure 3.10. In each set of analysis, the foundation was sized for a certain R_f ranging from 1.3 to 3.4 but it was ensured that the allowable bearing stress was not exceeded under service load conditions. The allowable stress check did not govern for the range of foundation sizes considered here.

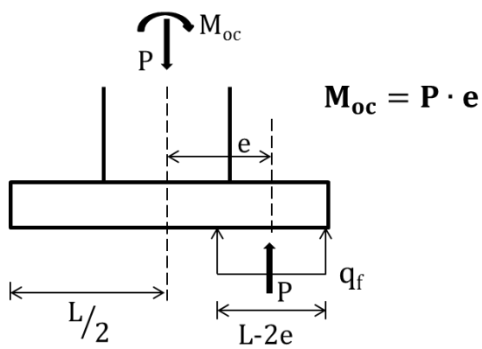

Figure 3.10 Uniform stress block used to calculate foundation overturning capacity.

Note that because the factored bearing capacity q_f is used in calculating M_{oc} instead of q_{ult}, the ultimate overturning capacity of the foundation M_{ult} would be larger than M_{oc}. The ratio of M_{ult}/M_{oc} is a measure of foundation overstrength. Foundation overstrength would be greater for larger foundations on softer soils. In such cases, the percentage increase in the lever arm of the resultant soil reaction force obtained from the uniform stress block of Figure 3.10 would be larger if q_{ult} is substituted for q_f. For foundation sizes and soil properties used in this study, foundation overstrength ranged from 1.0 to 1.8. It is important to note the difference between the definitions of R_f and R_w as R_w was calculated using the probable wall bending strength in Eq 3.3 and therefore, R_w is a closer measure of the maximum bending strength of the wall. Structural engineers can make relatively accurate estimates of the probable bending strength of a shear wall as concrete and steel strengths can be estimated with much greater accuracy compared to the soil ultimate bearing capacity. Structural engineers are usually provided with a factored bearing capacity for the soil and therefore, estimating the ultimate overturning capacity of a foundation is much more difficult for a structural engineer; hence the reason for defining R_w using the wall's probable bending strength and R_f using the foundation's factored overturning capacity.

The clay QzSimple1 model was used to model Clay soil springs while the sand QzSimple1 model was used for Loose, Medium, and Dense Sand. Elastic-Perfectly Plastic (EPP) springs along with gap elements were used to model Rock as the rock was expected to remain fairly elastic under compression up to the point of crushing. To define the backbone curve of the QzSimple1 soil springs in monotonic compression (Figure 3.7), the ultimate bearing capacity (q_{ult}) and the deformation at 50% of q_{ult} Z_{50} were needed. The ultimate bearing capacities used were the values given in Table 3.12. Values of Z_{50} were chosen to match the elastic rotational stiffness of the foundation to that given by Gazetas' formula (Eq 3.12) using the effective shear modulus G_{eff} as explained next.

For Clay where the clay QzSimple1 material was used, the backbone curve of an individual soil spring had a constant slope up to $0.2q_{ult}$. The initial elastic stiffness of the springs was therefore equal to $\frac{0.5q_{ult}}{Z_{50}}$. For a given foundation size, Z_{50} was then adjusted such that the initial elastic rotational stiffness matched the stiffness obtained from Gazetas' equation (Eq 3.12) using G_{eff} as reported in Table 3.12. This is illustrated in Figure 3.11. Note that G_{eff} for Clay is half of G_0.

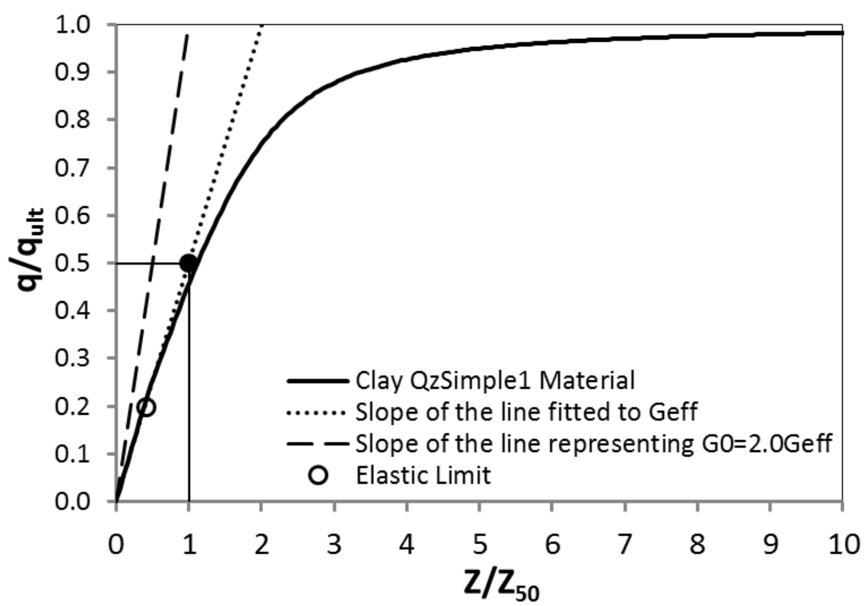

Figure 3.11 Calibrating the stiffness of the Qzsimple1 clay material for Clay.

For the three types of Sand, the sand QzSimple1 model was used. Initial slope of the non-dimensional backbone curve of the sand QzSimple1 material is about 2.65 times that of the clay QzSimple1 material. The sand material maintains this large initial stiffness up to $0.3q_{ult}$ and then softens rapidly (see Figure 3.7). The large initial slope is a good realistic model for the behaviour of sands as they tend to be very stiff initially and then soften quite fast. Z_{50} for the three sands was therefore adjusted such that the initial elastic foundation rotational stiffness would match the value given by Gazetas' equation (Eq 3.12) using G_0 reported in Table 3.12 as the soil shear modulus. Values of G_{eff} for the three types of sand define the slope of the line connecting the origin to the point of $[Z_{50}, 0.5q_{ult}]$ and are therefore equal to $G_0/2.65$. This is further illustrated in Figure 3.12.

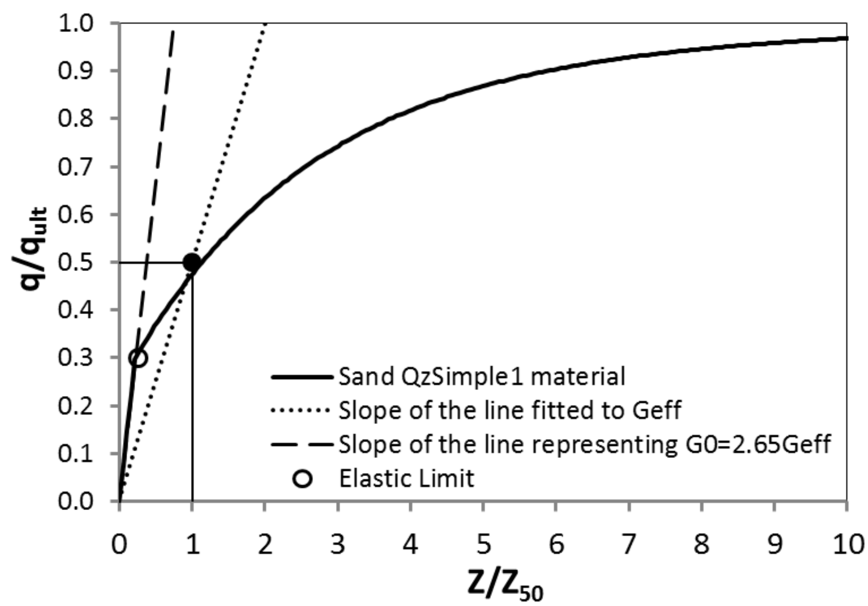

Figure 3.12 Calibrating the stiffness of the Qzsimple1 sand material for the three types of Sand.

Soil shear modulus of elasticity and Poisson's ratios needed to calculate the initial elastic rotational stiffness of the foundations as modeled in the NTHA using Gazetas's equation (Eq 3.8) are given in Table 3.13. Note that values of G are equal to G_{eff} for Clay and Rock and equal to G_0 for the three types of Sand. This is consistent with the definitions presented in Figure 3.11 and Figure 3.12. Foundation sizes for the Core NTHA are summarized in Table 3.16. Foundation sizes for other parts of the study can be found in Appendix A.

Table 3.13 Soil stiffness properties needed to calculate the initial elastic rotational stiffness of the foundations as modeled in the NTHA.

	Clay	Loose Sand	Medium Sand	Dense Sand	Rock
G (MPa)	21.5	57.1	186	825	5555
ν	0.30	0.30	0.30	0.30	0.20

Properties of Clay and Loose Sand were chosen such that for a given foundation size, the only difference in the foundation response would come from the difference in the shape of the two backbone curves. This was done by giving both soils the same ultimate bearing capacity but G_0 of the Loose Sand being 2.65 times the G_{eff} of the Clay. This exercise was intended for studying the effect of the shape of the soil backbone curve on foundation response. In other words, for Clay and Loose Sand where q_{ult} is the same, for the same foundation size, Z_{50} for both the Clay and the Loose Sand would be the same; however, the foundation on Loose Sand would be 2.65 times stiffer in the initial elastic range.

Because EPP springs were used to model Rock, elastic stiffness of the springs were adjusted such that the initial elastic foundation rotational stiffness would match that given by Gazetas' equation (Eq 3.12) using G_0. Note that G_{eff} and G_0 are the same for Rock as little or no softening is expected for Rock up until the point of crushing.

Backbone curves of soil springs used in each set of analysis are given Appendix A.

3.2.5 Input ground accelerations used in nonlinear time-history analysis

Ground motions used to carry out NTHA were taken from Dezhdar (2012). Dezhdar did a comprehensive study on the selection of ground motions for his work. He chose 40 ground motion records from the PEER database based on soil class, distance, magnitude, and best fit to the 2475 year return period uniform hazard spectrum (UHS) for Vancouver. 10 of those ground motions all with a 0.005 sec time-step were chosen for this study. The original acceleration records of the ground motions are given in Appendix A. Refer to Dezhdar (2012) for more details on the basis for selecting input ground motion records.

To reduce the scatter in the NTHA to be able to compare the structure's response from individual earthquake records, the 10 ground motions were modified to closely match the UHS over periods ranging from 0 to 10 sec. This was done by breaking the ground motion down into a number of its fundamental mode shapes in the frequency domain and then scaling the amplitude of each mode shape to match the target UHS at that the corresponding modal period.

Figure 3.13 shows the pseudo acceleration and displacement response spectra from the 10 modified ground motions. Note how close the pseudo acceleration response spectra of the individual ground motions are to the UHS. The individual displacement spectra however show noticeable deviation from that for the UHS. This is not surprising as the ground motions were modified with the UHS spectral accelerations as the matching target. Another contributing factor was that accelerations needed to be integrated twice to be converted to displacements. The average of the displacement spectra however follows that for the UHS quite closely except for periods greater than 8.0 sec where it starts to drop. Overall, the modified ground motions are expected to provoke responses in the structure that are very close to the demands from the UHS over a wide range of periods.

Despite the convenience of using spectrally-matched ground motions, some of the original ground motions' characteristics such as low-frequency content are lost in the process of modifying the ground motion records to match the target UHS (see Appendix A). To justify the use of spectrally-matched ground motions in NTHA, the original ground motions were uniformly scaled to best match the UHS over a period range of 0.5 sec to 2.5 sec. This is deemed to be a reasonable period range for 10-storey shear walls accounting for foundation flexibility. The matching was done such that the area under the pseudo accelerations from various ground motions matched that of the UHS between period of 0.5 sec and 2.5 sec.

Figure 3.14 shows a summary of the accuracy of the scaling process. Despite the significant deviation of the individual earthquake spectra from the UHS, the average of the 10 uniformly-scaled records follows the UHS closely. For scaling accuracy of individual records refer to Appendix A.

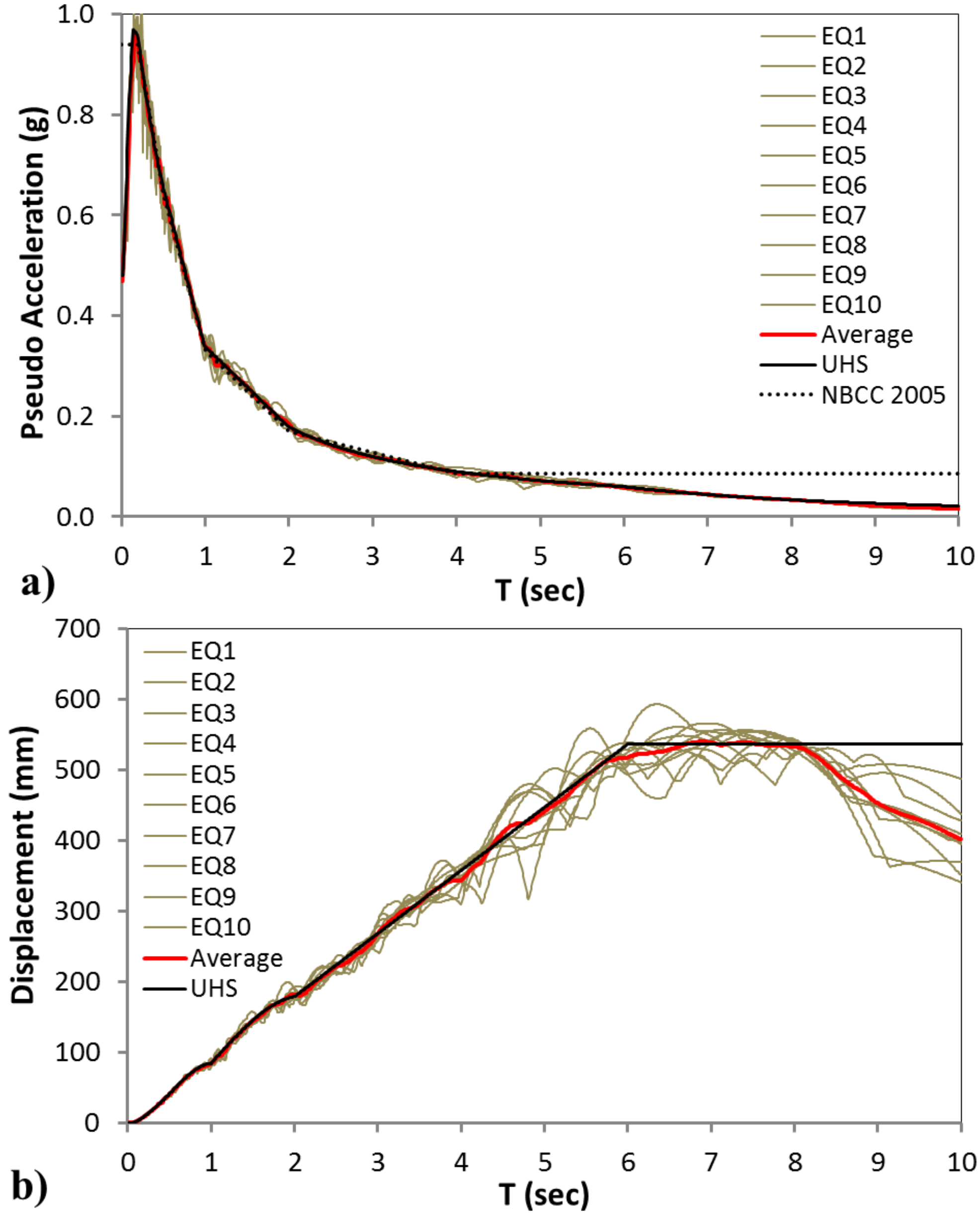

Figure 3.13 a) Pseudo acceleration, and b) displacement response spectra from the 10 modified (spectrally-matched) ground motions with 5% critical damping used in the NTHA.

The ground motions imposed on the foundation of a structure can differ from the free-field motion due to averaging of variable ground motions across the foundation slab, wave scattering, and embedment effects. In FEMA 440, these effects are referred to as kinematic interaction effects, and tend to be important for buildings with relatively short fundamental periods (less than 0.5 sec), large plan dimensions, or basements embedded 3 m or more in soil materials.

FEMA 440 provides guidelines for calculating a ratio of response spectra (RRS) factor which is used to modify the original free-field motion. The RRS is calculated depending on the period of vibration, foundation size and shape, and foundation embedment. For simplicity and to reduce the number of parameters of the study, kinematic effects are neglected in this study and the free-field ground motion is used as an input to the NTHA.

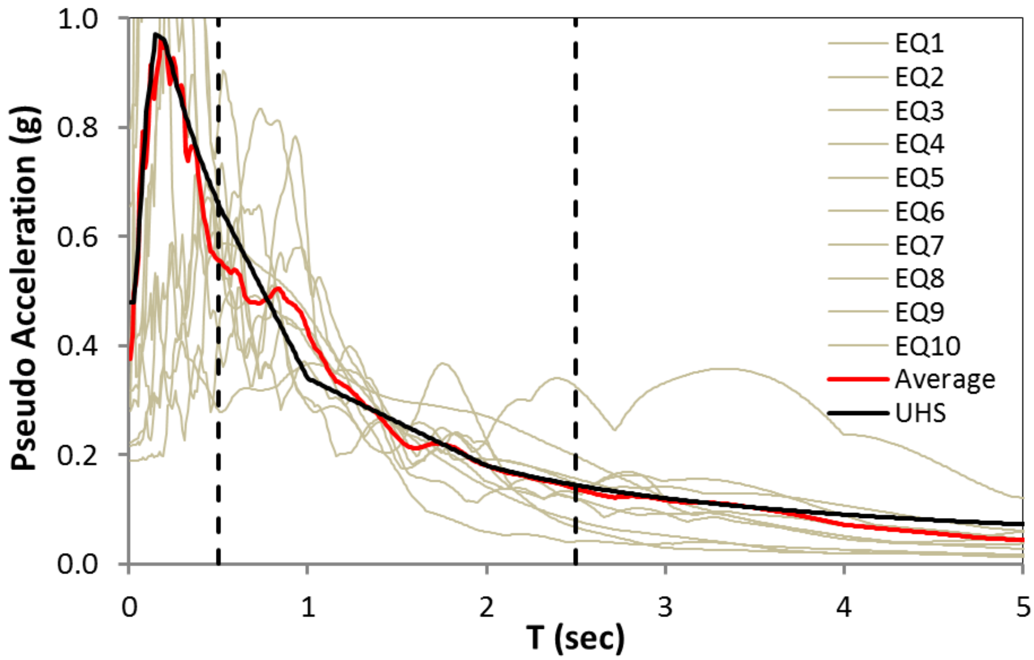

Figure 3.14 Pseudo acceleration response spectra of the 10 uniformly-scaled ground motions with 5% critical damping used to justify the use of spectrally-matched ground motions in NTHA.

3.2.6 Soil damping

The viscous damper embedded in the soil element shown in Figure 3.4 and the QzSimple1 material in OpenSees is intended to capture radiation damping due to dissipation of energy through the soil upon foundation impact. Too little damping could result in unrealistic large foundation rotations while too much damping could underestimate foundation rotation and hence wall maximum displacement. The amount of damping assigned to the soil elements is therefore a crucial parameter and needs attention.

Evidence of radiation damping has been observed by other researchers in experiments. In tests known as the TRISEE test on high density (HD) and low density (LD) Ticino sand, Negro et al. (1998) measured dampings between 1% and 6% of critical damping based on the initial elastic rotational stiffness. Figure 3.15 summarizes damping ratios observed during the TRISEE test against the maximum rotation that the foundation achieved. The effective damping ratio was seen to drop quite quickly with increasing foundation rotation as a smaller length of the foundation was in contact with the underlying soil at larger rotations. Results on LD sand produced more damping as the LD sand was softer and weaker than the HD sand which resulted in larger compressive displacements in the soil and a larger contact area of the foundation.

Figure 3.16 shows equivalent damping calculated based on the secant stiffness to the point of maximum rotation. As the foundation starts to rock and uplift and soil yielding in compression take place, rotational stiffness decays severely (see Figure 3.17). Because the secant stiffness to the point of maximum rotation was much smaller than the initial elastic stiffness, the calculated equivalent damping was much larger than that obtained based on elastic stiffness. Note that in the QzSimple1 elements in OpenSees, the damping ratio is always related to the elastic stiffness of the foundation and therefore, damping values in Figure 3.15 are the focus.

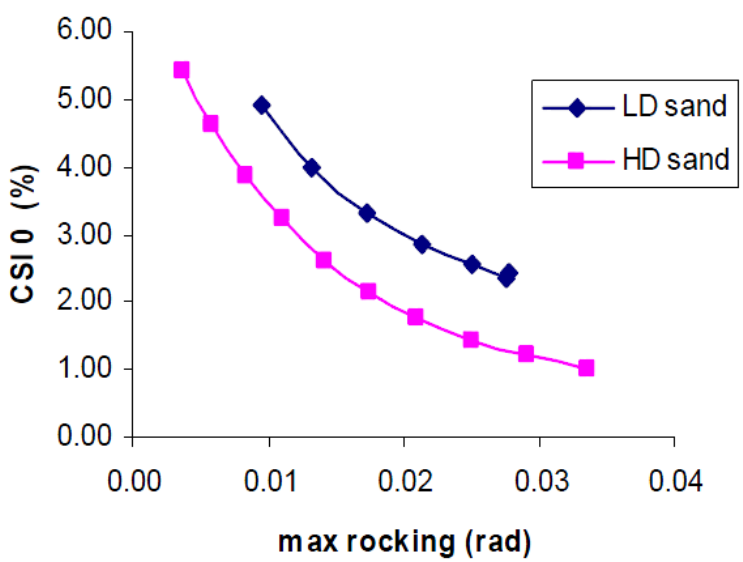

Figure 3.15 Elastic equivalent damping based on the initial elastic stiffness observed in the TRISEE tests – Figure from Negro et al. (1998).

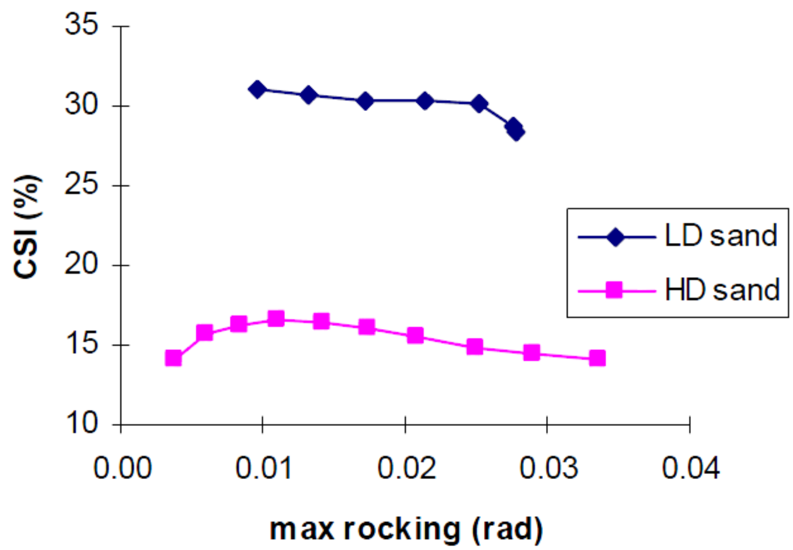

Figure 3.16 Equivalent damping based on the secant stiffness observed in the TRISEE tests – Figure from Negro et al. (1998).

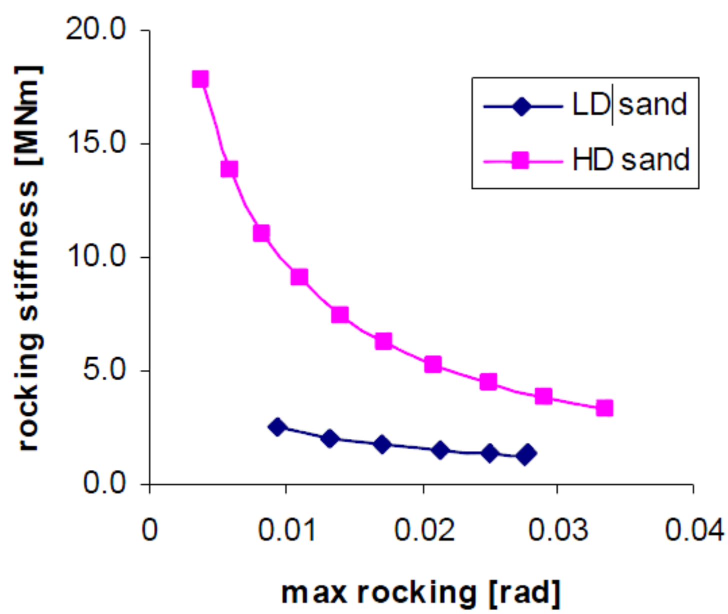

Figure 3.17 Rotational stiffness for the two sand specimens from the TRISEE tests - Figure from Negro et al. (1998).

Gajan and Kutter (2008) present their observations on energy dissipation in centrifuge tests carried out on foundations supported on sand and clay. Normalized energy dissipation was expressed as the damping ratio calculated following the definition by Kramer (1996) as follows:

$$\xi = \frac{1}{4\pi} \frac{Area\ of\ M - \theta\ hysteresis\ loop}{1/2\,(M_{max}^{cycle})(\theta_{max}^{cycle})}$$ **Eq 3.17**

Gajan and Kutter defined A as the total foundation area and A_c as the minimum foundation area required to resist the vertical load applied onto the foundation. With this definition, foundations with A/A_c between 1.5 and 3.0 showed 25% to 30% damping, those with A/A_c in the range of 3 to 8 had 15% to 25% damping, and foundation with A/A_c between 8 and 15 demonstrated a damping ratio ranging from 15% to 20%.

Algie (2011) conducted a series of tests on Auckland residual clay. Algie followed Kramer's definition of damping given in Eq 3.17. Algie reports damping ratios between 8% and 15% observed during the forced-vibration testing phase. In the snap-back testing phase, because no distinct "loop" could be observed in the moment-rotation hysteresis, Kramer's definition could not be applied. Instead, Algie used the logarithmic decrement method given in Chopra (2007) to evaluate the amount of damping. Damping ratios as high as 50% were recorded during the snap-back tests with the average of the damping ratios being around 25% based on the logarithmic decrement method.

Two factors that could have contributed to the damping values observed in Algie's test being so large are explained below. First is the shape of the foundations which were 2.0 m long and 0.4 m wide and 0.4 m deep. This long and narrow shape meant that soil friction against foundation side-walls was much larger compared to that of a foundation with nearly square footprint.

Second, it is important to note that the type of damping associated with QzSimple1 elements in OpenSees is elastic viscous damping which has to be calculated based on the initial elastic stiffness of the foundation. Damping ratios calculated using Kramer's definition or the logarithmic decrement method account for the change in the system's natural frequency with increased foundation rotation which is perfectly suitable for flexible foundations. However, the damping ratio calculated from the latter two formulations is expressed in terms of the average system frequency of vibration over one cycle which is definitely very different than the system's natural frequency calculated using the initial elastic stiffness. This becomes evident comparing damping ratios recorded in the TRISEE tests using the elastic vs. secant stiffnesses (compare Figure 3.15 to Figure 3.16). While damping ratios for LD sand calculated using the elastic stiffness remained below 5%, the ones calculated based on the secant stiffness exceeded 30%. Use of the logarithmic decrement method to find the equivalent damping ratio could have been another reason for the high levels of damping observed in Algie's test.

To further justify the level of damping associated with the soil elements in the NTHA, a pilot study on soil damping was performed. Wall 10R20 was modeled with a 12.5 m square foundation on a soil with ultimate bearing capacity of 1.54 MPa and effective shear modulus G_{eff} of 126 MPa. The level of damping assigned to the soil elements was then varied from 0 to 30% in increments of 5%. For each level of damping in the soil, NTHA was done with the 10 spectrally-matched ground motions. Figure 3.18 shows the average of top wall displacements from the 10 ground motions. Top wall displacement keeps decreasing at a steady rate as soil damping is increased.

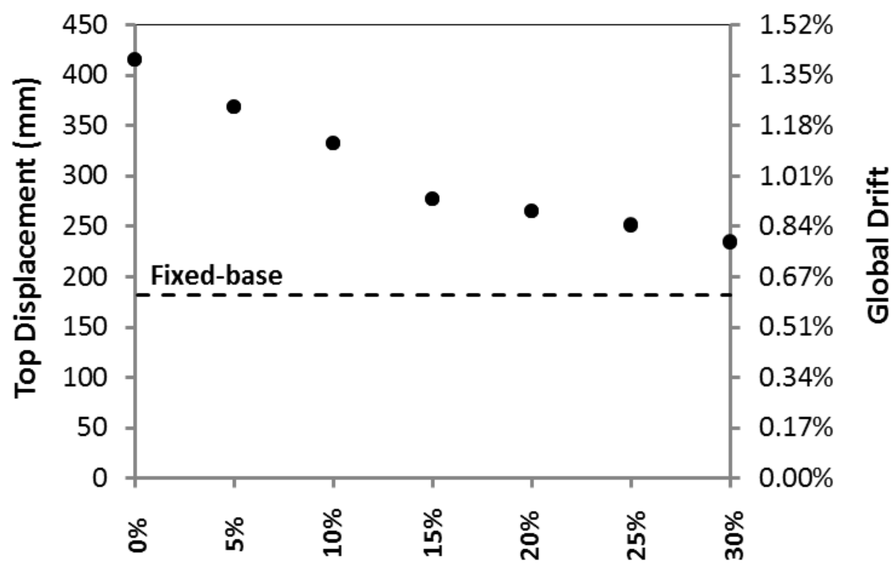

Figure 3.18 Average of top displacement envelopes of wall 10R20 with a 12.5 m square foundation with various soil damping ratios.

Figure 3.19a shows the time-history response of the wall's top displacement from EQ7 for soil damping of 0%, 5%, and 10%. When no damping was included in the soil, the maximum wall top displacement occurred at about 30.47 sec and was 547 mm. This was despite the strong shaking period of the input ground motioned having ended well before 20 sec. The figure suggests that because no soil damping was considered, the structure went into an unrealistically undamped cyclic motion in which the amplitude of the vibration kept increasing. When as little as 5% damping was added to the soil elements, the peak top wall displacement occurred at 19.51 sec (within the strong shaking time period of the input ground motion) and was 460 mm. The amplitude of the oscillation of the structure started decreasing as the input ground motion died down demonstrating a much more realistic behaviour. Increasing the soil damping further to 10% did not affect the time of occurrence of maximum top wall displacement; however, the amplitude of oscillation of top wall displacement decreased noticeably. For EQ3 on the other hand (Figure 3.19b), the time of occurrence of the maximum top wall displacement did not seem to be affected by soil damping. From the 10 spectrally-matched ground motions, lack of radiation damping in the soil did not result in unrealistically undamped oscillation of the wall for 8 of the records. In 1 of the remaining 2 cases, 5% damping was sufficient to eliminate the unrealistically-undamped oscillations while in the other, at least 10% damping was needed (see Appendix A for complete results).

Since viscous damping is incorporated in the QzSimple1 elements and the damping ratio is expressed in terms of the initial elastic stiffness, results of Figure 3.15 are the most relevant to this study. 5% of the critical damping based on the initial elastic stiffness of the foundation was used in the remainder of this study to account for soil damping as this level of damping effectively eliminated unrealistically undamped behaviour in the pilot study and agreed with the TRISEE test results. Using a lower damping in the soil would result in larger foundation rotations and hence would be conservative in estimating additional wall displacements due to rotation of the foundation.

Damping associated with foundation-soil interaction either from hysteretic behaviour of the soil or radiation damping can significantly supplement damping that occurs in a structure due to inelastic action of structural components. According to FEMA 440, these foundation damping effects tend to be important for stiff structural systems such as shear walls particularly when the underlying soil is relatively soft. FEMA 440 provides guidelines for estimating the effective system damping accounting for foundation damping based on a single degree of freedom representation of the system. In this study however, damping of the nonlinear walls and foundation damping are kept constant at 3% and 5% respectively and the input accelerations to the NTHA have been matched to response spectra corresponding to 5% damping.

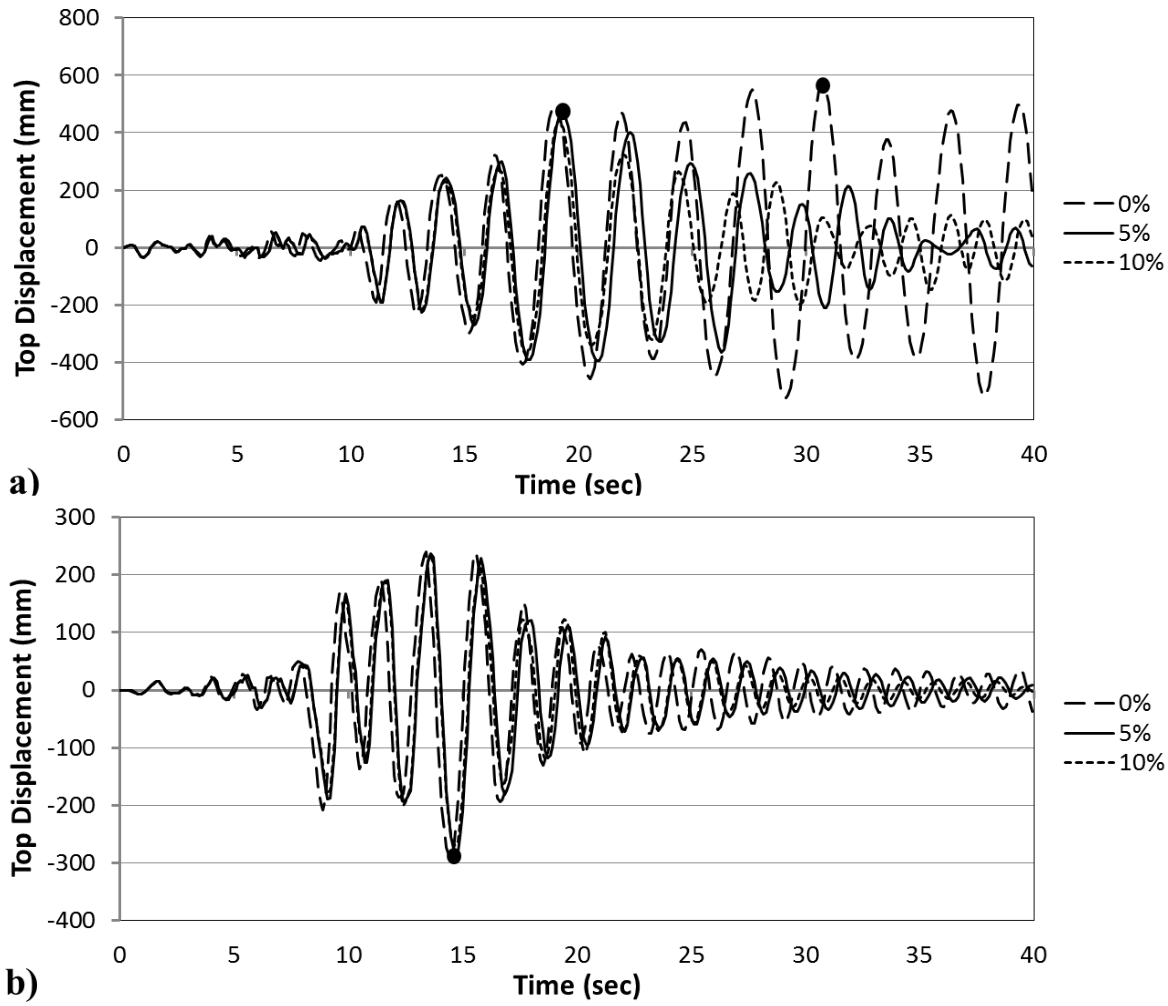

Figure 3.19 Time-history response of wall 10R20 with a 12.5 m square foundation from spectrally-matched a) EQ7, and b) EQ3 for various levels of damping in the soil.

3.2.7 Roadmap to the NTHA

A summary of all of the Nonlinear Time-History Analysis (NTHA) performed in this chapter is presented in Table 3.14. A total of 202 wall-foundation structures were modeled and each ran with 10 ground motion inputs. Sample analysis results are presented in the following sections. Table 3.14 can be used as a guide to the NTHA results presented in Appendix A.

Table 3.14 Summary of nonlinear time-history analysis preformed in this chapter.

Group	Parameter Studied	Input Ground Motion	No. of Storeys	Mass Ratio	Soil Type	R_w	R_f	No. of Cases	No. of NTHA
1	**Soil Type**	SM (10)	10	0.4	CL (15)	2.0	2.0 -> 4.0 (1)	15	150
2	**Scatter of Results**	US (10)	10	0.4	DS, RK (2)	1.3	1.9 -> 3.4 (5)	10	100
3	**Wall Height and Mass Ratio**	SM (10)	5, 10, 20 (3)	0.4, 0.6 (2)	RK	El.	1.3 -> 3.4 (7)	42	420
4	**Core NTHA**	SM (10)	10	0.4	CL, LS, MS, DS, RK (5)	El., 1.3, 1.7, 2.0, 2.7 (5)	1.7 -> 3.3 (5)	125	1250
5		SM (10)	10	0.4	CL, LS, MS, DS, RK (5)	1.3	1.3, 1.6 (2)	10	100
							Total	**202**	**2020**

Notes:

SM = Spectrally Matched
US = Uniformly Scaled
CL = Clay
LS = Loose Sand
MS = Medium Sand
DS = Dense Sand
RK = Rock
El. = Elastic
NTHA = Nonlinear Time-history Analysis

3.3 Sensitivity of Wall-foundation System Response to Soil Properties

A set of soil parameters was chosen to be used in a pilot study to investigate the sensitivity of the response of shear walls with flexible foundations to properties of the soil. Table 3.15 summarizes the chosen soil parameters. Soil properties chosen represent a broad set of soil properties ranging from the upper-bound clays, a variety of sands and lower-bound tills. Wall 10R20 supported on a 12.5 m square foundation was then modeled on each soil type. The ultimate overturning capacity of the foundation for the combined seismic and gravity loads was calculated assuming a uniform bearing pressure of q_{ult} over the effective bearing length equal to L-2e with e being the eccentricity of the load. Foundation size was chosen such that the ratio of the elastic bending moment demand M_{RSA} to the ultimate overturning capacity of the foundation was between 2.0 and 4.0 for the chosen values of q_{ult} to ensure large nonlinear rotation of the foundation.

Table 3.15 Soil properties used in parametric study on soil properties.

	Soil 1	Soil 2	Soil 3	Soil 4	Soil 5
E (MPa)	107	187	327	571	1000
G (MPa)	43	73	126	215	370
ν	0.25	0.28	0.30	0.33	0.35
q_{ult} (kPa)	501	877	1535	2686	4700

3.3.1 Effect of soil type

To investigate the sensitivity of the response of shear walls accounting for foundation rotation to soil properties, wall l0R20 (see Section 3.2.1) with a 12.5 m square foundation was modeled on the 5 types of soil introduced in Table 3.15. Vertical load supported by the foundation was 41550 kN. Figure 3.20 shows the envelope of the response of soil springs in compression for the 5 types of soil. The initial stiffness of the springs was adjusted such that the initial elastic rotational stiffness of the foundation matched the stiffness given by Gazetas. The figure demonstrates how diverse the soils are in terms of stiffness and strength. Foundation bending moment-rotation response of the 12.5 m square foundations is given in Figure 3.21. Moment-rotation curves are less diverse than the backbone response of individual springs in terms of strength. This is due to the different compression depths among various types of soil. With weaker soil springs, a greater number of springs were required to sustain the vertical load on the wall but the reduction in the lever arm of the resultant force was not proportional to the ultimate strength of soil springs. Hence, the difference between the calculated overturning capacities of the foundations on various types of soil was not as big as the difference among the individual soils' ultimate bearing capacity.

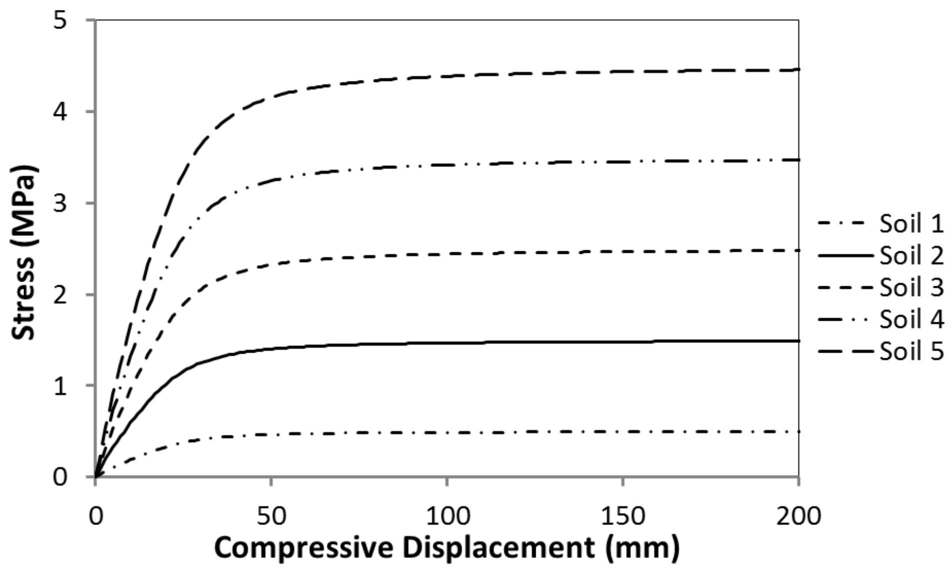

Figure 3.20 Backbone curve of soil springs in monotonic compression for the 5 types of soil introduced in Table 3.15.

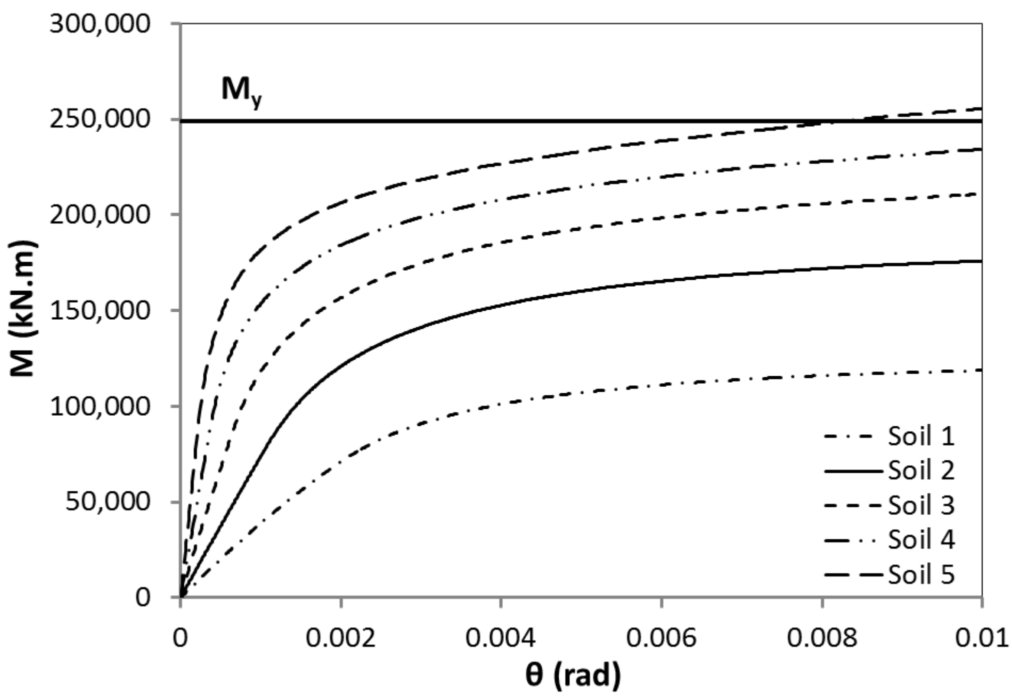

Figure 3.21 Foundation bending moment-rotation response of a 12.5 m square foundation on the 5 types of soil introduced in Table 3.15.

NTHA was carried out using the spectrally matched ground motions. Figure 3.22 shows the average of top displacement and global drift envelopes from the 10 ground motions. As soils get softer and weaker, wall displacements increase initially. However, despite Soil 2 is stronger and stiffer than Soil 1, the wall on Soil 1 experiences smaller maximum deformations. This seemingly counter-intuitive observation can be explained by looking at the average of maximum soil compressive displacements given in Figure 3.23. The slopes of the soil deformation envelopes near the toe of the foundation were found to be proportional to wall global drift envelope. As the soils were initially weakened and softened, the “toe” of the foundation started to “dig in” more and more increasing the top displacement of the wall. However, Soil 1 was so weak and so soft that it required a very large compression depth to support the wall’s vertical load; hence, resulting in a less rounded soil deformation profile and consequently smaller ground slopes at the toe of the foundation.

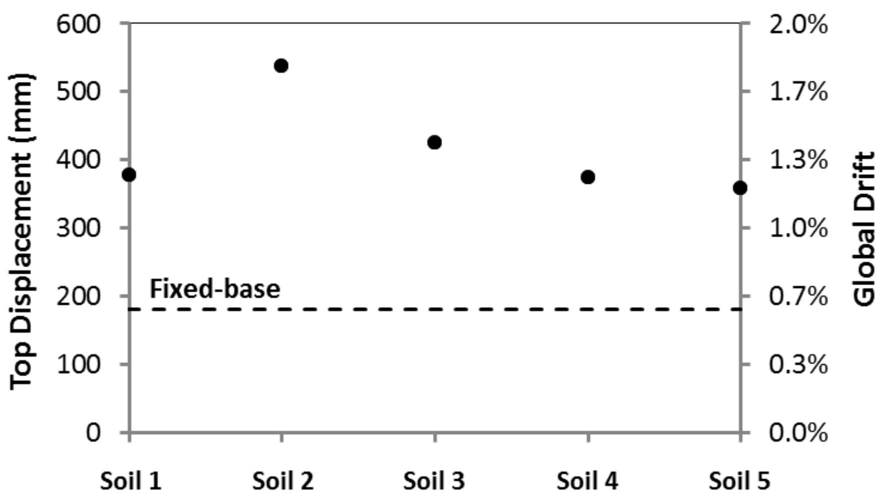

Figure 3.22 Average of top displacement and global drift envelopes of wall 10R20 with a 12.5 m square foundation on various soil types subjected to spectrally-matched ground motions.

Another contributor to Soil 1 resulting in less top wall displacement than Soil 2 is the portion of top displacement resulting from flexural deformation of the wall (see Appendix A). Because Soil 1 was so weak, the foundation could not induce substantial bending moments into the wall which lead to minimal (almost uncracked) flexural deformation of the wall while the wall on soil 2 had greater flexural deformations due to larger moment demands transmitted into the wall because of the stronger soil. This meant that bending of the wall itself did not contribute much to the wall top displacement of the wall on Soil 1.

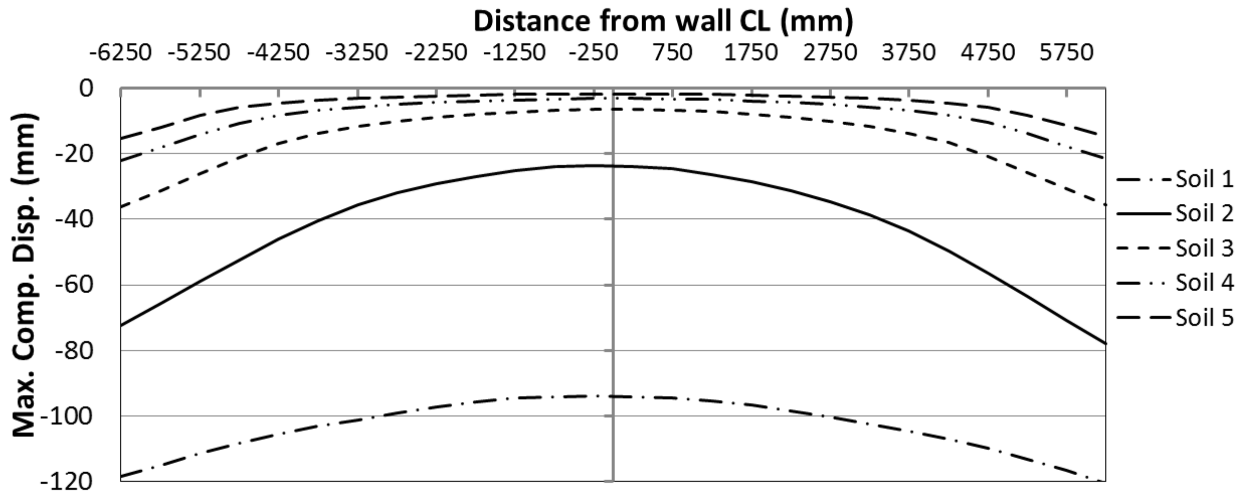

Figure 3.23 Average of maximum soil compressive displacement profiles for a 12.5 m foundation on various soil types subjected to spectrally-matched ground motions.

For all types of soil however, the top displacements of the wall increased considerably compared to the fixed-base case. The increase was more than 200% for the wall on Soil 2. The difference in wall top displacements among the different types of soil however is small bearing in mind the extreme diversity in soil strength and stiffness which suggest that behaviour of shear walls on flexible foundations is not greatly sensitive to the properties of the soil underlying the foundation. The complete set of results is given in Appendix A.

3.3.2 Effect of soil stiffness

To investigate the effect of soil stiffness on the behaviour of shear walls with flexible foundations independent of the soil ultimate bearing capacity, the 5 soil types in Table 3.15 were modified such that they all had the ultimate bearing capacity of Soil 3 (1535 kPa) with all other parameters unchanged. The soils were then identified by their stiffness (G). Figure 3.24 shows the backbone curve for the soil springs in monotonic compression. Note how all the curves have the same strength but different initial stiffnesses. Foundation bending moment-rotation response is plotted in Figure 3.25. Because the ultimate bearing capacity of all 5 soils was the same, all curves will eventually result in the same overturning capacity even though the softer soils will need a larger rotation to develop the full overturning capacity.

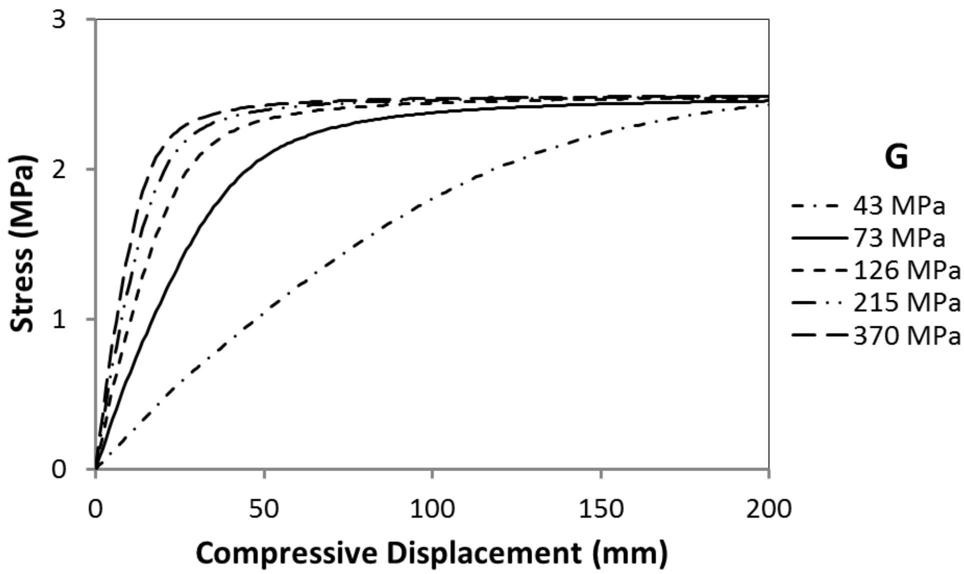

Figure 3.24 Backbone curve of the soil springs in monotonic compression used to investigate the effect of soil stiffness at a constant soil strength.

The five structures were run through NTHA with the 10 spectrally-matched ground motions. Average of wall top displacement and global drift envelopes are given in Figure 3.26. Wall deformation keeps increasing as the soil gets softer. The softest soil results in the largest top wall displacement.

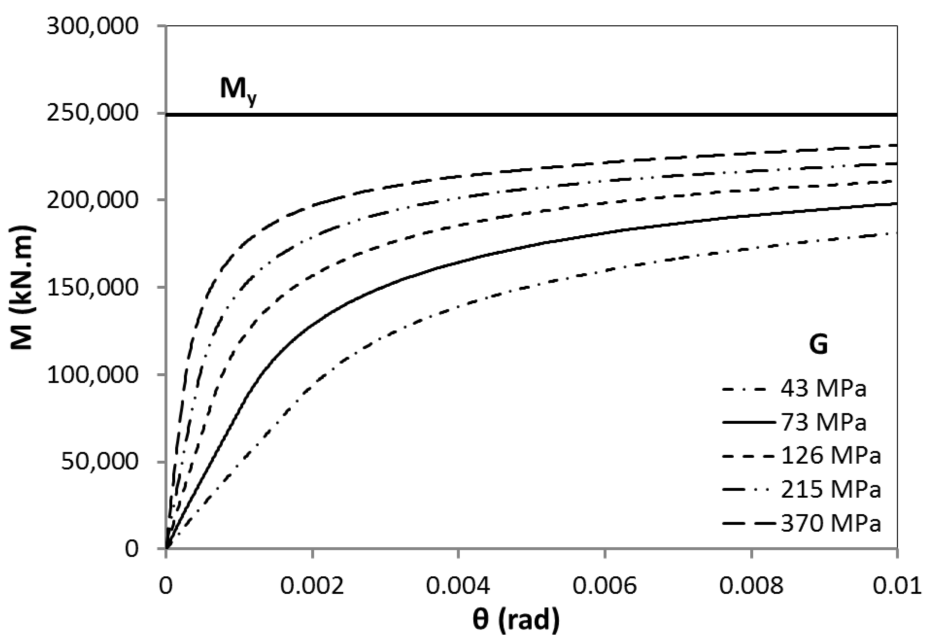

Figure 3.25 Foundation bending moment-rotation response of a 12.5 m square foundation on soils with various stiffnesses but the same strength.

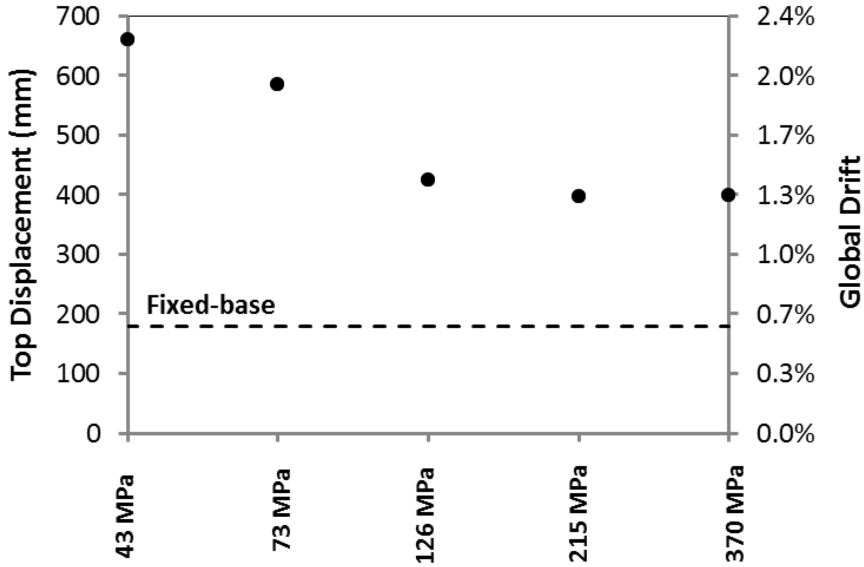

Figure 3.26 Average of top displacement and global drift envelopes of wall 10R20 with a 12.5 m square foundation on soils with various stiffnesses but the same strength subjected to spectrally-matched ground motions.

Soils with the three largest stiffnesses seem to give similar maximum top wall displacements while there was a noticeable jump in top displacement when the soil is further softened. This was mainly because the rate of transition of the soil backbone curve from the elastic into the inelastic range was greatly influenced by the initial stiffness (see Figure 3.24). Even though the stiffness was reduced linearly, the shape of the backbone curve for the two softest soil springs was noticeably different than the other three.

Overall, soil stiffness is found to influence the behaviour of shear walls with flexible foundations; however, even though the stiffness of the soil was reduced by almost 9 times, the top wall displacement on the softest soil was only 60% larger than that on the stiffest. It is therefore concluded that lateral displacement of shear walls with flexible foundations is not critically sensitive to soil stiffness. The complete set of results is given in Appendix A.

3.3.3 Effect of soil ultimate bearing capacity

The final soil parameter studied was the soil ultimate bearing capacity. To investigate the effect of soil ultimate bearing capacity on deformation of shear walls with flexible foundations independently of soil stiffness, 5 different soils were considered. All soils had the stiffness of Soil 3 in Table 3.15 but the ultimate bearing capacity changed from that of Soil 1 to Soil 5. The backbone curve in monotonic compression for the soil springs used to model these 5 soils is given in Figure 3.27. Note how the initial slope of the curves (i.e. stiffness of the spring) is identical for all 5 curves with the only difference being their strengths.

Despite the great difference among the 5 soil spring backbone curves, the difference in the bending moment-rotation responses of the foundation on these 5 different soils is much less (see Figure 3.28). The foundations on the first three strongest soils have a very similar response while there is a gap between the responses of foundations on the two weaker soils. Even though the reduction in the soil ultimate bearing capacity was nearly uniform, foundation moment-rotation responses did not seem to vary in proportion to the soil ultimate bearing capacity. This is attributed to the relative size of the compression zone to the foundation length.

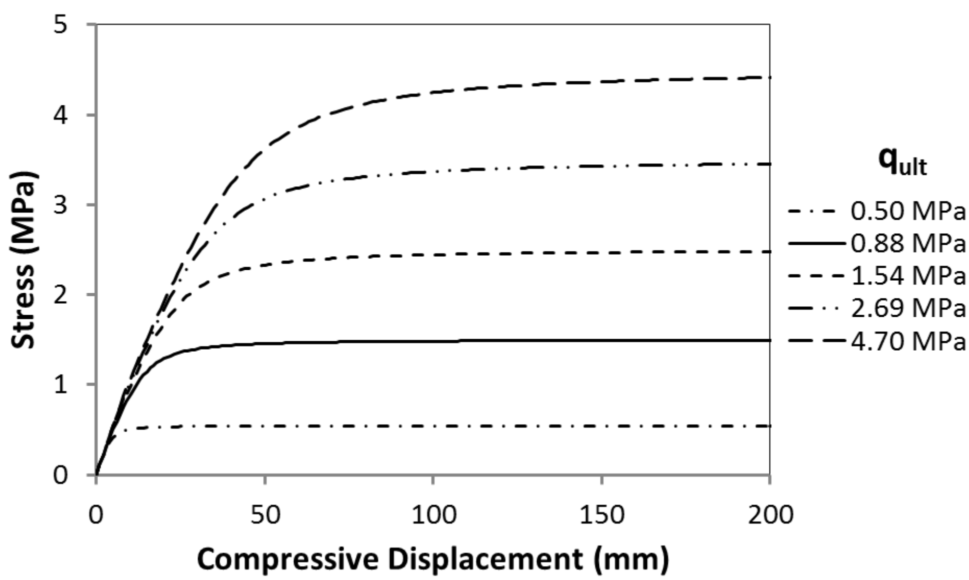

Figure 3.27 Backbone curve of the soil springs in monotonic compression used to investigate the effect of soil ultimate bearing capacity at constant soil stiffness.

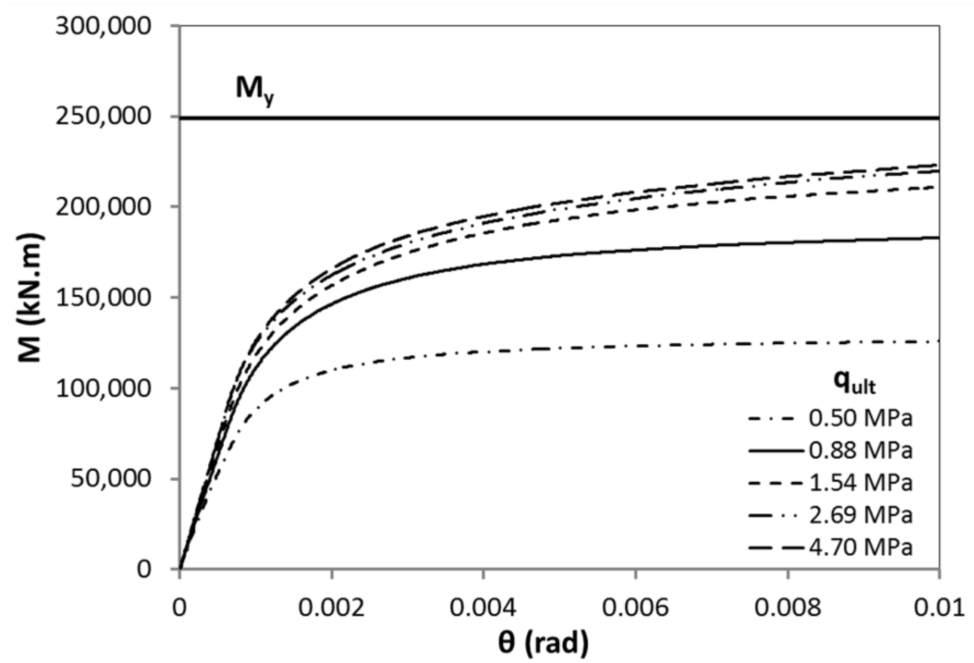

Figure 3.28 Foundation bending moment-rotation response of a 12.5 m square foundation on soils with various ultimate bearing capacities but the same stiffness.

The bending moment sustained by the foundation and its underlying soil is the product of the wall's axial compressive load and the lever arm between the centreline of the wall and the location of the resultant soil reaction. The weaker the soil gets, the larger the compression depth gets and hence, the smaller the lever arm. For the first three strongest soils, the increase in the soil compression depth was small relative to the foundation size and therefor, the overturning capacity did not reduce by much. As the soils got weaker, the compression depth was forced to grow to the point that the resultant soil reaction force was much closer to the centreline of the wall reducing the lever arm and consequently the resisting bending moment significantly. This was confirmed by looking at how the compression depth c (given in Appendix A) changed with soil ultimate bearing capacity.

Figure 3.29 shows the NTHA results for the 12.5 m square foundation on the 5 soils with different ultimate bearing capacities. It is striking how the four strongest soils result in similar top wall displacements while the wall on the weakest soil has the lowest top displacement of them all. This counter-intuitive observation can be explained by looking the maximum soil compressive displacement profile underneath the foundation (Figure 3.30).

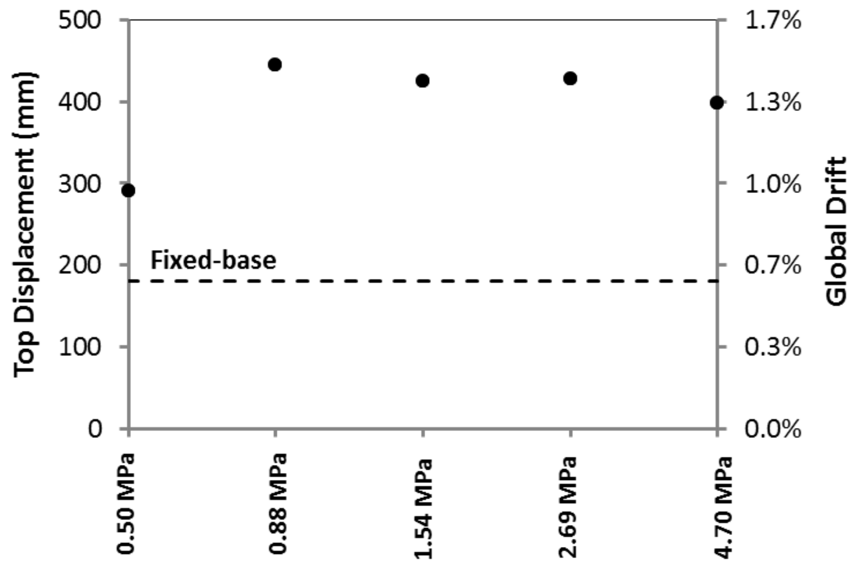

Figure 3.29 Average of top displacement and global drift envelopes of wall 10R20 with a 12.5 m square foundation on soils with various ultimate bearing capacities but the same stiffness subjected to spectrally-matched ground motions.

The maximum soil compressive displacement profile of the 4 stronger soils is quite rounded. This is because the soils were strong enough to support the axial load from the wall over a smaller bearing area. This resulted in the maximum soil compressive displacement profile to be steeper near the toes of the foundation and increase maximum foundation rotation and consequently, wall top displacement. The weakest soil on the other hand was so weak that it required a very large area of soil bearing to withstand the wall's axial load which resulted in large compressive displacements over much larger areas under the foundation. This made the maximum soil compressive displacement profile to be quite flat and reduced maximum foundation rotation. As a result, top wall displacement on the weakest soil was smaller than those on all stronger soils.

It is therefore concluded that decreasing the soil ultimate bearing capacity initially increases wall top displacement but as the soil gets very weak, wall top displacement starts to decrease as the maximum compressive displacement profile of the soil becomes flatter reducing foundation rotation.

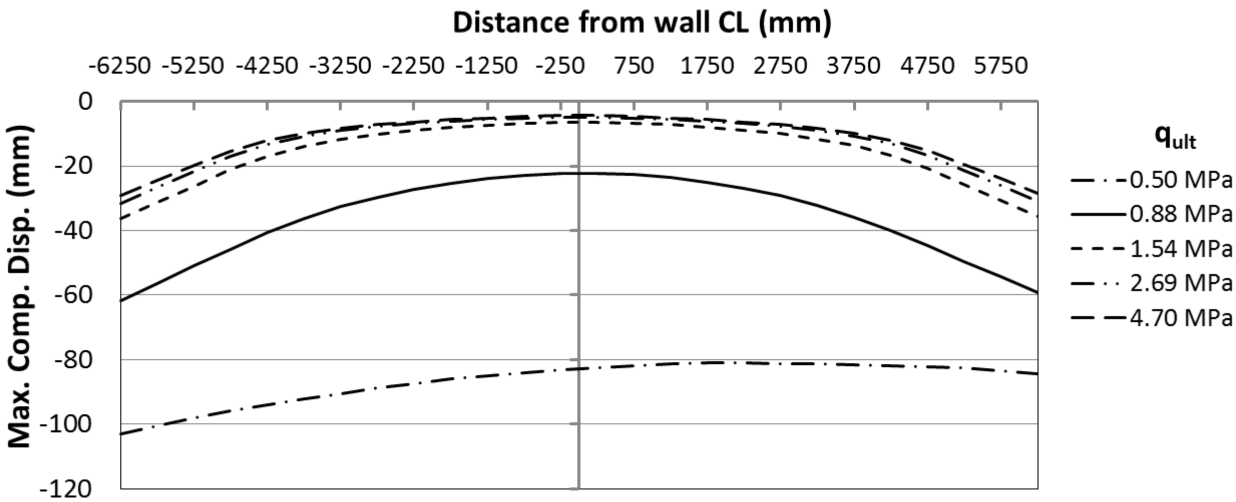

Figure 3.30 Average of maximum soil compressive displacement profiles for various soil ultimate bearing capacities from spectrally-matched ground motions.

Despite the extreme variation in soil strength (almost by a factor of 10), the variation in the envelope of top wall displacement is nowhere as dramatic. Hence, deformation of shear walls with flexible foundation is not overly sensitive to soil strength.

3.4 Scatter in Wall Maximum Response

Section 3.2.5 introduced ground motion records that would be used to carry out the NTHA. 10 ground motion records were chosen and modified to match the UHS over a period range from 0 to 10 sec. Although spectrally-matched records are a very good tool for estimating the mean response of a certain structure, certain natural characteristics of a real ground motion such as low-frequency cycles and repetitive kicks will be lost during the matching process as a result of adding a number of higher frequency waves to the original ground motion record. Gazetas and Apostolou (2004) concluded that “the nature of seismic excitation (specifically its frequency composition and, especially, the presence of a sequence of long duration impulsive cycles) is the controlling factor of the response of a specific system”. It is therefore necessary to quantify the amount of scatter between the response of a wall-foundation structure to the spectrally-matched and the original records uniformly scaled in the relevant period range to roughly match the UHS. To do so, the original ground motion records were uniformly scaled to best match the UHS between periods of 0.5 and 2.5 seconds (see Section 3.2.5) and used to perform NTHA. Only wall 10R13 was considered as it was the strongest nonlinear fibre model wall and hence caused more rotation of the foundation. Among the five soil types, only Rock and Dense Sand were used as they were the two strongest soils and required the smallest foundations to achieve a certain R_f and hence, enhanced rotational action in the foundation.

Figure 3.31 presents a summary of average and maximum top wall displacement and global drifts along with their respective standard deviations among the 10 uniformly-scaled and spectrally-matched ground motions. For both Dense Sand and Rock, the average responses from both spectrally-matched and uniformly-scaled ground motions are quite close. This was promising as the objective of using spectrally-matched ground motions for the Core NTHA was to get a good estimate of the average response. This observation confirms that spectrally-matched ground motions give a reliable estimate of the average wall response.

Standard deviation of the top wall response from uniformly-scaled ground motions is larger than that from spectrally-matched records for both Dense Sand and Rock. This is not surprising as spectrally-matched records' response spectra match the UHS throughout the period range while that of the uniformly-scaled records bounce around and considerably vary from the UHS within the matching period range of 0.5 to 2.5 seconds (compare Figure 3.13 and Figure 3.14). However, the uniformly-scaled records paint a more realistic picture of how much scatter in the top wall displacement might occur depending on the ground motions used. The inevitable scatter in the top wall response must not be ignored when designing a building in real life. The purpose of this study however is to understand the fundamentals of the behaviour of shear walls accounting for foundation rotation and for that, studying the mean or the average of various system response parameters is sufficient. Therefore, only spectrally-matched records are used in the remainder of this chapter.

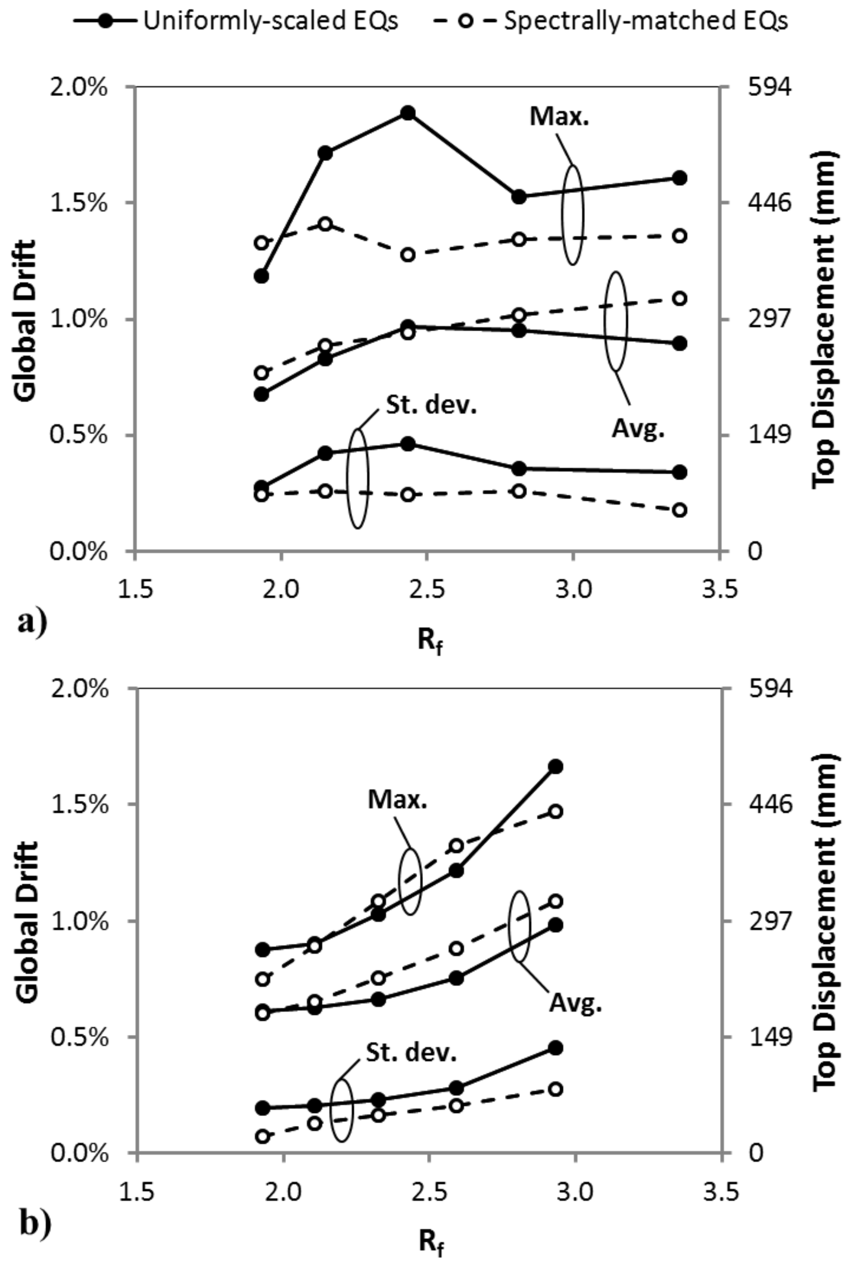

Figure 3.31 Comparison between the scatter in top displacement of wall 10R13 from NTHA using spectrally-matched and uniformly-scaled ground motions on a) Dense Sand, and b) Rock.

A rather different trend is observed when the maximum response of walls on Dense Sand and Rock are compared. The maximum response of walls on Dense Sand from the 10 uniformly-scaled ground motions is consistently larger than that obtained from NTHA using the 10 spectrally-matched records. On the other hand, the two maximum response lines are quite close to each other for analysis carried out on Rock. This observation can be explained by comparing the basic mechanisms of foundation rotation on Dense Sand and on Rock. When the foundation was placed on Dense Sand, two factors contributed to the nonlinearity of the foundation response one being yielding of the soil under compression and the other being foundation liftoff. For Rock however, the soil elements were so stiff and so strong that they very rarely yielded and if yielding occurred, only one or two soil elements at the foundation toe yielded as opposed to foundations on Dense Sand where numerous soil elements yielded in each rotational cycle. This meant that the nonlinearity in the moment-rotation response of foundations on Dense Sand was due to both liftoff and yielding of the soil while the nonlinearity in the response of foundation on Rock was almost entirely due to liftoff. Maximum compressive displacement of the soil elements in the highly nonlinear range is quite sensitive to the individual ground motions' characteristics such as the number of strong kicks (see Section 3.6.5). Therefore, maximum response of walls with foundations on Dense Sand was more sensitive to the type of scaling performed on the original ground motion records than those with foundations on Rock.

3.5 Effects of Wall Height and Mass Ratio (MR)

Anderson (2003) showed that the response of shear walls with a flexible foundation is greatly influenced by wall height and mass ratio (MR), the ratio of the vertical force supported by the wall to the total seismic weight lumped at floor slab location. Shorter walls were shown to experience more increase in their top displacement due to foundation rotation than taller walls. Also, a larger mass ratio was found to increase top wall displacement because of the smaller foundation size needed to achieve a certain overturning strength.

First mode period of the wall-foundation structure can vary significantly with building height. Participation factors of higher modes will also increase as the building gets taller. It is therefore necessary to study the effect of building height on the response of shear wall buildings with flexible foundations before making a decision on what wall height and mass ratio to consider for the Core NTHA of this study.

Flexural deformation of shorter walls is much smaller as shorter walls are stiffer. Therefore, the percentage increase in top displacement of shorter walls due to foundation rotation is likely to be larger. 5-storey shear walls are therefore studied to investigate this phenomenon. Flexural behaviour of shear walls taller than 10 storeys includes a significant contribution from higher modes. Taller walls are more flexible; hence, top displacement of taller walls is likely to be less severely affected by foundation rotation. 20-storey shear walls are also studied to verify this theory.

Mass ratio determines the vertical load supported by the foundation and is a deciding factor in sizing the foundation for overturning capacity. Therefore, mass ratio is also expected to have a noticeable impact on the behaviour of shear walls with flexible foundations. Smaller mass ratios or smaller vertical loads on the foundation require larger foundation sizes to achieve a certain overturning capacity and therefore reduce foundation rotation. Mass ratios greater than 0.6 are unlikely to occur in the real world considering the geometry of shear wall buildings. The tributary floor area of the shear wall as a ratio of the total floor area is usually less than 0.6. Two mass ratios of 0.4 and 0.6 were investigated with 0.4 being the average value and 0.6 representing the upper bound. Foundations with mass ratios of 0.6 support high vertical loads and are therefore smaller in length which increases foundation rotation.

All of the NTHA in this section was done for foundations on Rock since stronger soils require smaller foundations to achieve a certain overturning capacity or R_f and will therefore encounter more foundation rotation. Also, because of the large allowable bearing stress of Rock, it could be ensured that even for mass ratio of 0.6, uniform bearing stress underneath the foundation under service conditions was lower than the allowable and that the service load condition did not govern the sizing of the foundation.

Only elastic walls were considered in this section for two reasons. First is that elastic walls theoretically have infinite strength and can therefore induce much larger bending moments in the foundation compared to the more realistic nonlinear fibre model walls with certain yield strength. Larger bending moment demands on the foundation will result in more severe foundation rotation and will therefore represent the most critical case. Secondly, it would have been difficult to compare the flexural behaviour of nonlinear walls with different heights even if they all had the same R_w because of the complexities introduced by using a nonlinear fibre model for the walls. Walls of various lengths would have been required for each wall height which would have resulted in walls with considerably different plastic hinge lengths.

All of the walls had a seismic mass equivalent to 10387 kN per storey lumped at floor slab levels. Static weight supported directly by the shear wall was adjusted independently of the seismic mass to achieve the desired mass ratio. First storey height of all walls was 4.5 m with the rest of the storeys being 2.8 m tall. Flexural stiffness of the walls was adjusted such that the first mode vibration period was equal to 0.5 sec for the 5-storey, 1.0 sec for the 10-storey, and 2.0 sec for the 20-storey walls (i.e. 0.1 times the number of storeys). Seven different foundation sizes were chosen for each wall height and mass ratio to achieve R_f's ranging from 1.3 to 3.5. R_f was calculated relative to the bending moment demand from RSA of the fixed-base wall. The elastic bending moment demands for the 5, 10 and 20-storey walls were 288, 488, and 962 MN.m respectively.

Figure 3.32 summarizes average maximum top wall displacement and global drift from all NTHA. Despite the absolute values of top wall displacement of the taller walls being larger than those of the shorter walls, the increase in top wall displacement compared to the fixed-base case was smaller. For the 5-storey wall with MR=0.6, for R_f = 2.6, the increase in top wall displacement compared to the fixed base case is more than 350% while for the 20-storey wall with MR=0.6, this increase is about 100% at the same R_f.

Response of the 5-storey walls seemed not to be sensitive to the mass ratio as the results for mass ratios of 0.4 and 0.6 are very similar. This is attributed to the relatively small vertical load supported by the 5-storey walls resulting in a large foundation needed to achieve a certain R_f.

Mass ratio had a much more distinct effect on 10 and 20-storey walls. At lower R_f's, top displacement of 10-storey walls increased with the mass ratio because of the smaller foundation required to achieve a given R_f. As R_f further increased, the walls with MR=0.6 had such small foundations that the foundation isolated the wall at the base preventing the seismic excitation to affect the wall and therefore, at large R_f's, walls with MR=0.6 had smaller top displacements than those with MR=0.4. This isolation of the wall due to very small foundation occurred at much lower R_f's for the 20-storey buildings which is the reason for all 20-storey walls with MR=0.6 having smaller top displacements than those with MR=0.4.

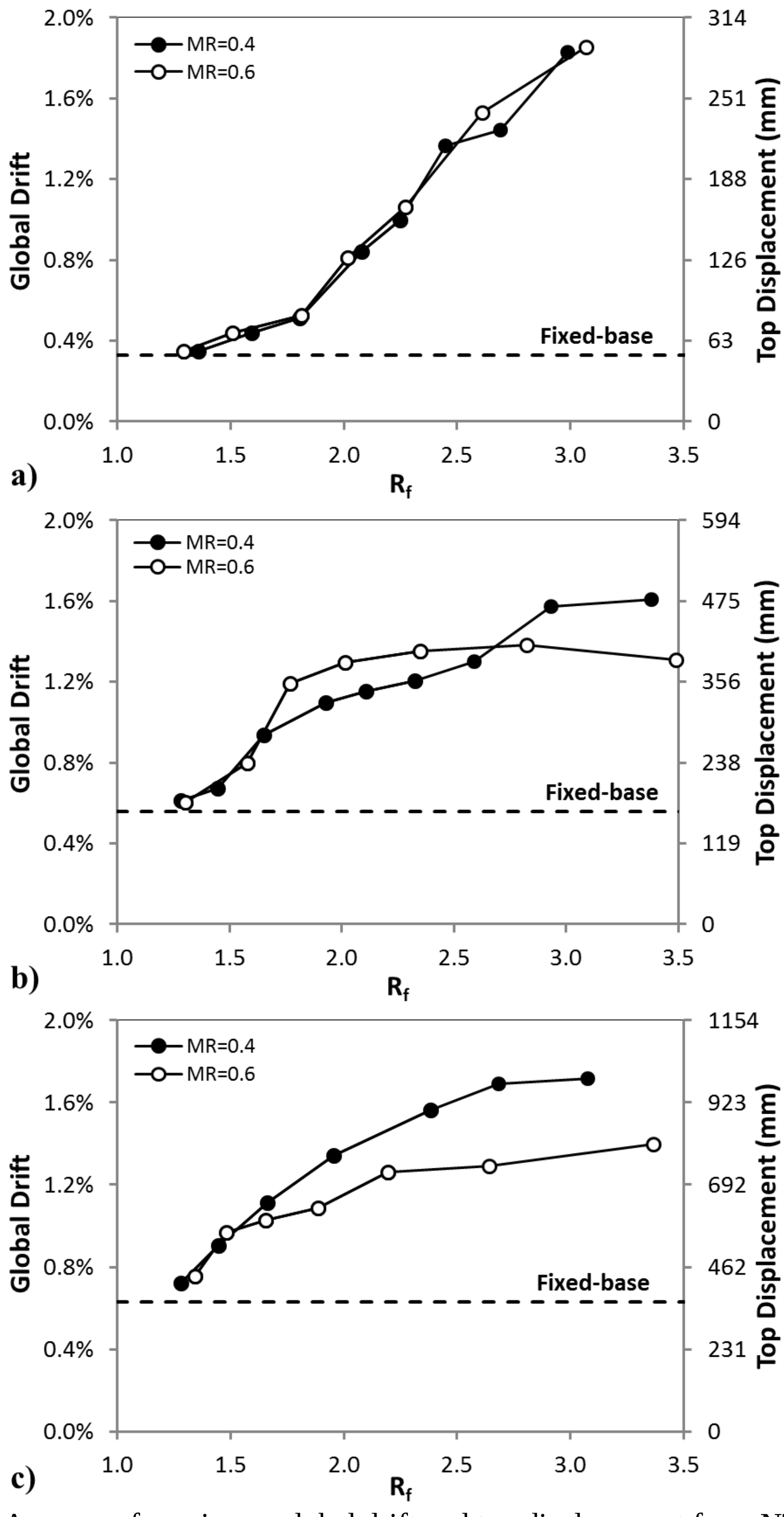

Figure 3.32 Average of maximum global drift and top displacement from NTHA using spectrally-matched ground motions for mass ratios of 0.4 and 0.6 for a) 5-storey, b) 10-storey, and c) 20-storey Elastic walls.

Because all of the foundations were on Rock which had a very high ultimate bearing capacity, the vertical load could be supported by a very small length of the foundation close to the "toe". This meant that compression depth of the foundation was very small and that the foundations could almost stand on their "toe". This fact contributed to the foundations of the taller walls being so small. On a softer and weaker soil, it is more likely that taller walls will require larger foundations as a larger compression depth will be needed to support the gravity load. This confirms that rotation of foundation of taller walls is much more critical on stronger soils, which is why only foundations on Rock are studied in this section. It also shows that on softer and weaker soils, taller buildings are even less prone to increased deformations due to foundation rotation.

The decision was made to focus on 10-storey walls with a mass ratio of 0.4 for the rest of this chapter. Mass ratio of 0.6 was deemed uncommon and rarely encountered in conventional shear walls buildings. Significant contribution of higher modes to the response of 20-storey buildings make for less foundation rotation as foundation rotation which is the focus of this chapter is a first-mode behaviour. Even though the response of the 5-storey walls was the most first-mode dominated, such short buildings did not seem to represent the common height of modern shear wall building construction. Most modern five-storey buildings are built with a concrete structure in the first one or two storeys and the higher floors are typically constructed as a wood frame building. Complete NTHA results are presented in Appendix A.

3.6 Core NTHA

The Core NTHA was done on 10-storey walls using spectrally-matched ground motions. For each wall, five different foundation sizes were chosen to get R_f's ranging from 1.7 to 3.3 for each of the five soil types. Walls 10R13 were also analyzed with two stronger foundations with R_f's close to 1.3 and 1.5 to capture the onset of significant foundation rotations. Table 3.16 summarizes lengths of square footings modeled in the Core NTHA. The following sections summarize the results of the Core NTHA.

Table 3.16 Length of square footings modeled in the Core NTHA

L = B (m)		**Walls modeled on footing**	
	R_f	**10R13 only**	**All 10-storey walls**
Clay and Loose Sand	1.3	*26.5*	-----
	1.5	*24.5*	-----
	1.8	-----	*22.5*
	2.0	-----	*21.5*
	2.3	-----	*20.5*
	2.7	-----	*19.5*
	3.2	-----	*18.5*
Medium Sand	1.3	*22.5*	-----
	1.5	*20.5*	-----
	1.8	-----	*18.5*
	2.0	-----	*17.5*
	2.3	-----	*16.5*
	2.7	-----	*15.5*
	3.2	-----	*14.5*
Dense Sand	1.3	*20.5*	-----
	1.6	*17.5*	-----
	1.9	-----	*15.5*
	2.2	-----	*14.5*
	2.4	-----	*13.5*
	2.8	-----	*12.5*
	3.4	-----	*11.5*
Rock	1.3	*18.5*	-----
	1.7	*14.5*	-----
	1.9	-----	*12.5*
	2.1	-----	*11.5*
	2.3	-----	*10.5*
	2.6	-----	*9.5*
	2.9	-----	*8.5*

3.6.1 General observations

Complete analysis results of the Core NTHA are presented in Appendix A. This section presents results that demonstrate the general trends and conclusions that could be drawn based on the results. Only one type of soil (Medium Sand) is chosen and analysis results for walls 10R13 and 10R27 are presented. Despite this, all of the observations made in this section hold true for other types of soil and other walls.

Figure 3.33 compares the average of displacement envelopes for the two walls. Wall 10R13 experienced larger displacements compared to wall 10R27. This was because wall 10R13 was much stronger than wall 10R27 which resulted in larger bending moments being transferred into the foundation. This in turn caused larger foundation rotations which increased lateral displacement of the wall.

In addition to absolute lateral displacement, the increase in displacement due to foundation rotation relative to the fixed-base wall was much greater for wall 10R13 than wall 10R27. This observation had two reasons. One was that because wall 10R13 was much stronger, it experienced less nonlinear action and smaller hinge rotations in the fixed-base case compared to the weaker wall 10R27 so it had a larger fixed-base top displacement to start with. This could also be explained using the effective elastic flexural stiffness needed to achieve the correct top displacement of the nonlinear walls. For wall 10R13, the effective stiffness was close to $0.90E_cI_g$ while for wall 10R27; this figure was close to $0.60E_cI_g$. The second reason was that because wall 10R27 was much weaker, it transferred smaller moments into the foundation resulting in smaller foundation rotations. This meant that the portion of the wall total displacement due to foundation rotation was much smaller for wall 10R27 than that for wall 10R13.

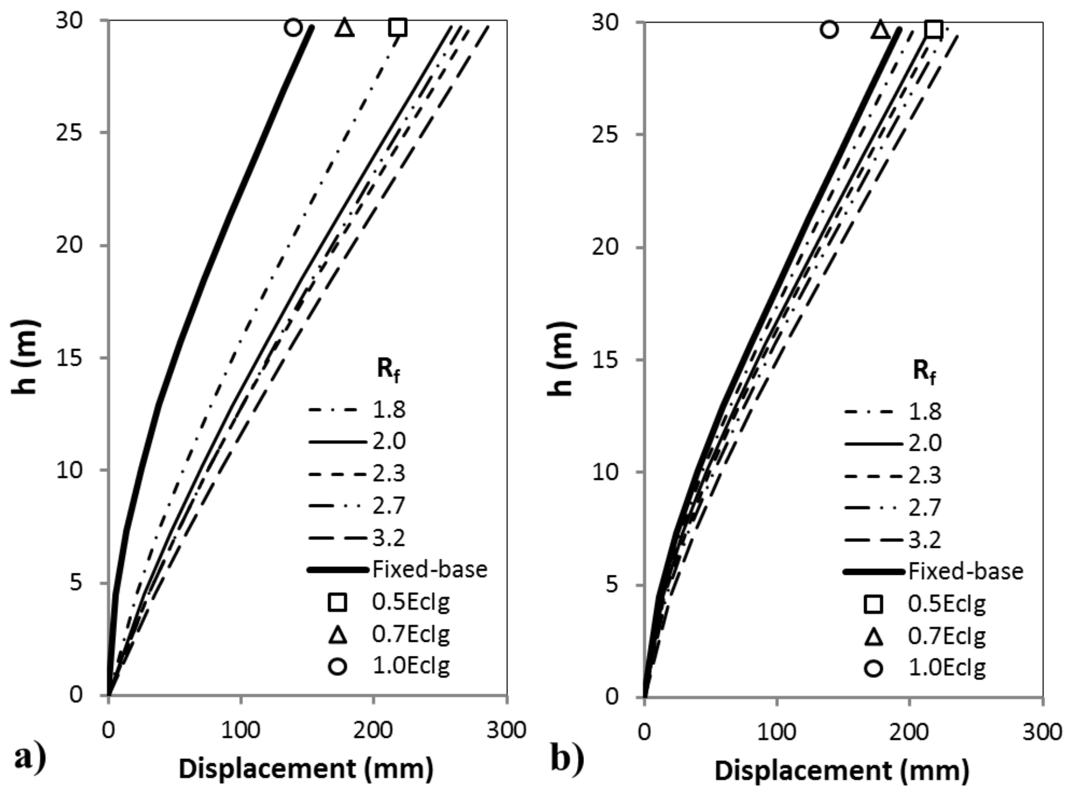

Figure 3.33 Average of displacement envelopes from 10 NTHA using spectrally-matched ground motions for walls a) 10R13, and b) 10R27 on Medium Sand along with top displacements from RSA using various effective stiffnesses.

A similar observation can be made for averages of inter-storey drift envelopes of the two walls (see Figure 3.34). Note that values of average inter-storey drifts are plotted at the top of the storey and average of foundation rotation envelopes are plotted at the base. Larger foundation rotations for wall 10R13 made the drift profile of the wall start at relatively large values at the base. Because the wall was stronger, smaller (mostly elastic) curvatures occurred along the height of the wall resulting in a much smaller part of the wall rotation being due to flexural deformation of the wall. This caused the drift profile to become close to being constant above the second storey. For wall 10R27 on the other hand, foundation rotations were small but because the wall was weak, significant hinging occurred in the wall. This caused the drift profile to keep increasing up until the seventh storey. Even though for both walls maximum drift envelopes were close to 1.0%, the shape of the drift profile was highly dependent on wall strength. A gravity-load frame connected to wall 10R27 would have less rotation demands near the base.

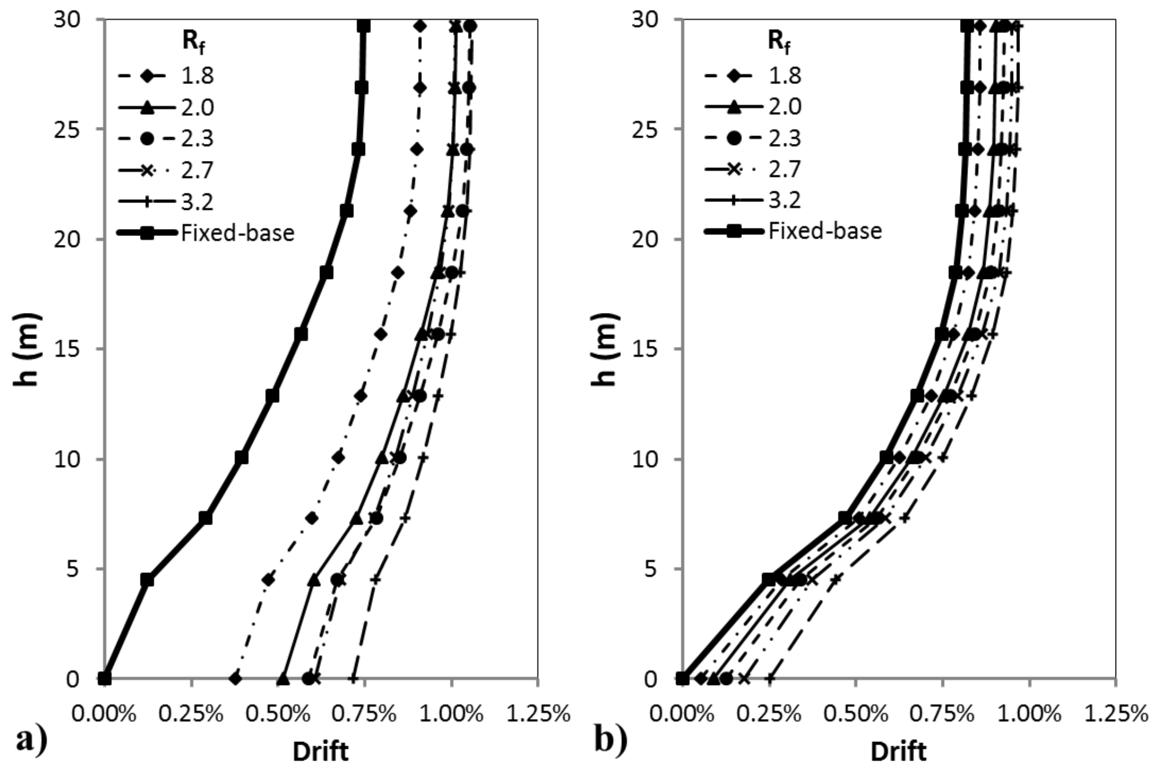

Figure 3.34 Average of inter-storey drift envelopes from 10 NTHA using spectrally-matched ground motions for walls a) 10R13, and b) 10R27 on Medium Sand. (Note: base rotation values are plotted at h=0 and values of average interstory drift are plotted at the top of the storey.)

Figure 3.35 shows average of bending moment envelopes for the two walls. The fixed-base wall 10R13 yielded at its base which means that the maximum bending moment at its base is close to its yield strength but slightly higher due to overstrength from steel strain hardening. 10R13 walls on flexible foundations did not yield because the wall yield strength was higher than the foundation overturning strength. This means that 10R13 walls on flexible foundation remained elastic and that the majority of the wall lateral displacement was due to foundation rotation and not flexural deformation of the wall. Because wall 10R27 was relatively weak, all 10R27 walls on flexible foundations yielded. This was the case even for foundations with R_f larger than 2.7. This was because R_f was calculated using q_f and not q_{ult}. Even for the weakest foundation (R_f=3.2), the actual overturning capacity of the foundation calculated using q_{ult} was still larger than the wall's yield strength. This explains why for the 10R27 walls, a greater part of the total lateral displacement comes from flexural deformation of the walls.

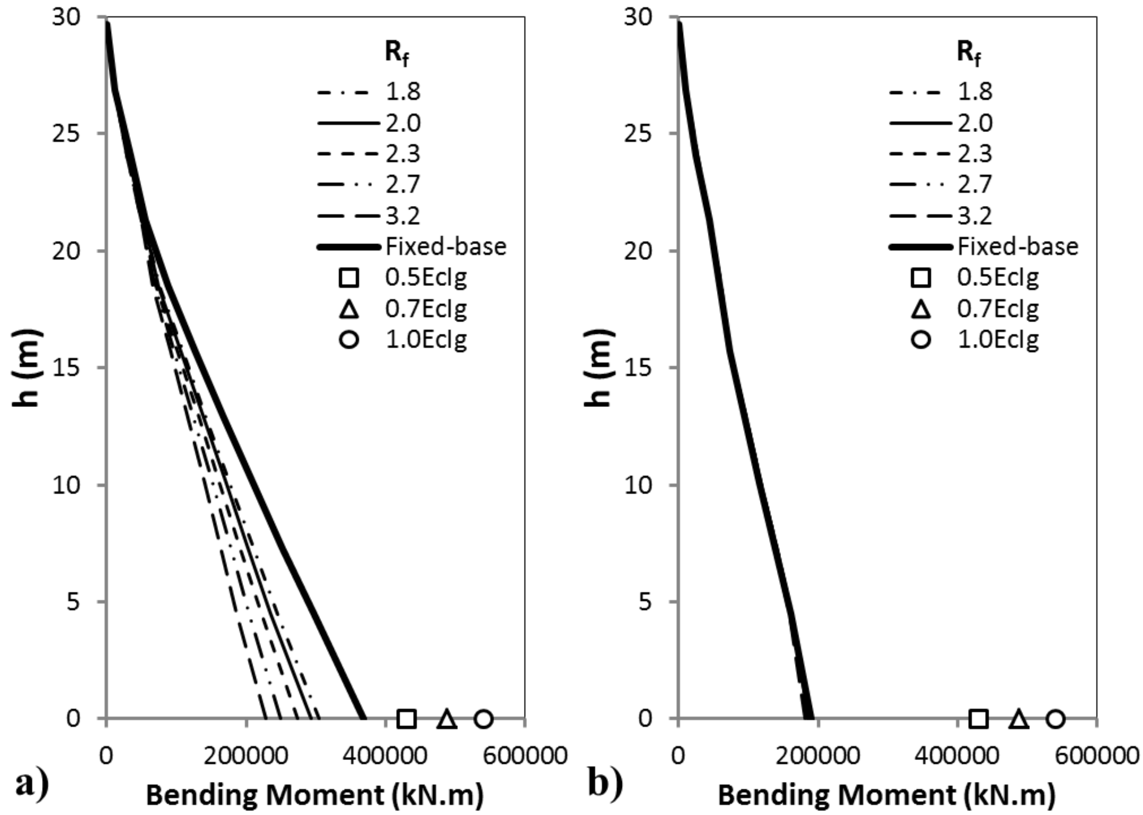

Figure 3.35 Average of bending moment envelopes from 10 NTHA using spectrally-matched ground motions for walls a) 10R13, and b) 10R27 on Medium Sand along with base bending moment estimates from RSA using various effective stiffnesses.

Shear forces were less affected by rotation of the foundation compared to bending moments (Figure 3.36). Average of shear force envelopes of 10R13 walls started to reduce as the foundations got weaker and weaker but the maximum reduction in base shear was only 20% compared to the 40% reduction in average bending moment envelopes. Even less of an effect was observed in shear force envelopes of walls 10R27. Presence of a flexible foundation limited the maximum bending moment in the wall foundation system when the wall was stronger than the foundation. A flexible foundation however did not directly limit the maximum shear force in the wall-foundation system as no shear release was introduced into the system. Presence of a flexible foundation can change the first mode period of vibration significantly. Maximum bending moment at the base of the system is largely driven by the first mode behaviour of the system. A considerable portion of the shear force demand however comes from higher modes which are much less affected by introduction of a flexible foundation.

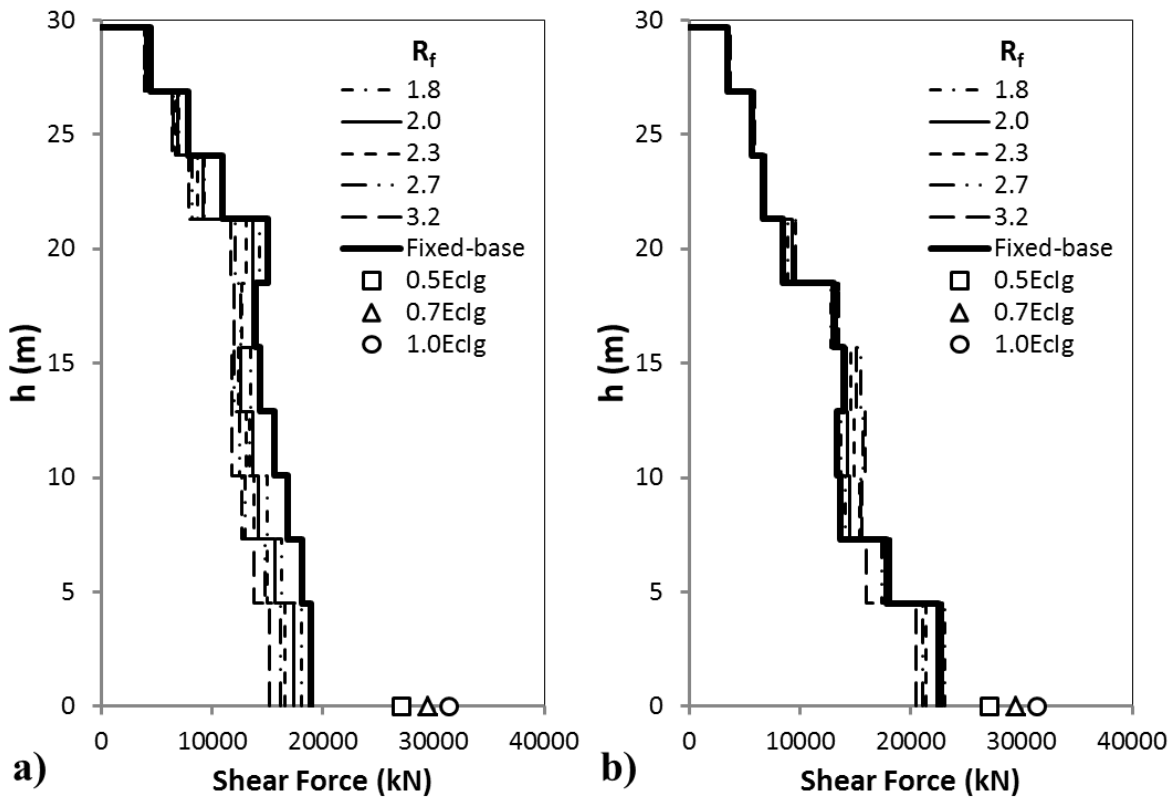

Figure 3.36 Average of shear force envelopes from 10 NTHA using spectrally-matched ground motions for walls a) 10R13, and b) 10R27 on Medium Sand along with base shear force estimates from RSA using various effective stiffnesses.

The behaviour of shear walls with flexible foundations can be further explained by comparing the wall yield strength with the monotonic moment-rotation response of the foundation (see Figure 3.37). Note that the actual hysteretic moment-rotation response of the foundation will differ from the monotonic response as loading and unloading in the soil nonlinear range causes accumulation of residual displacements in the soil. The monotonic response envelopes the actual hysteretic response and is therefore a useful tool for comparing the behaviour of wall-foundation systems with various foundation strengths.

In addition to the wall yield strength and the foundation moment-rotation responses, two sets of dots are shown. The hollow dots show the rotations at which the foundation strengths (calculated using q_f) are mobilized. Bending moments keep increasing beyond the hollow dots. This is because the actual soil springs can be stressed up to q_{ult} and the stresses can move further towards the toe of the foundation increasing the eccentricity of the resultant vertical force.

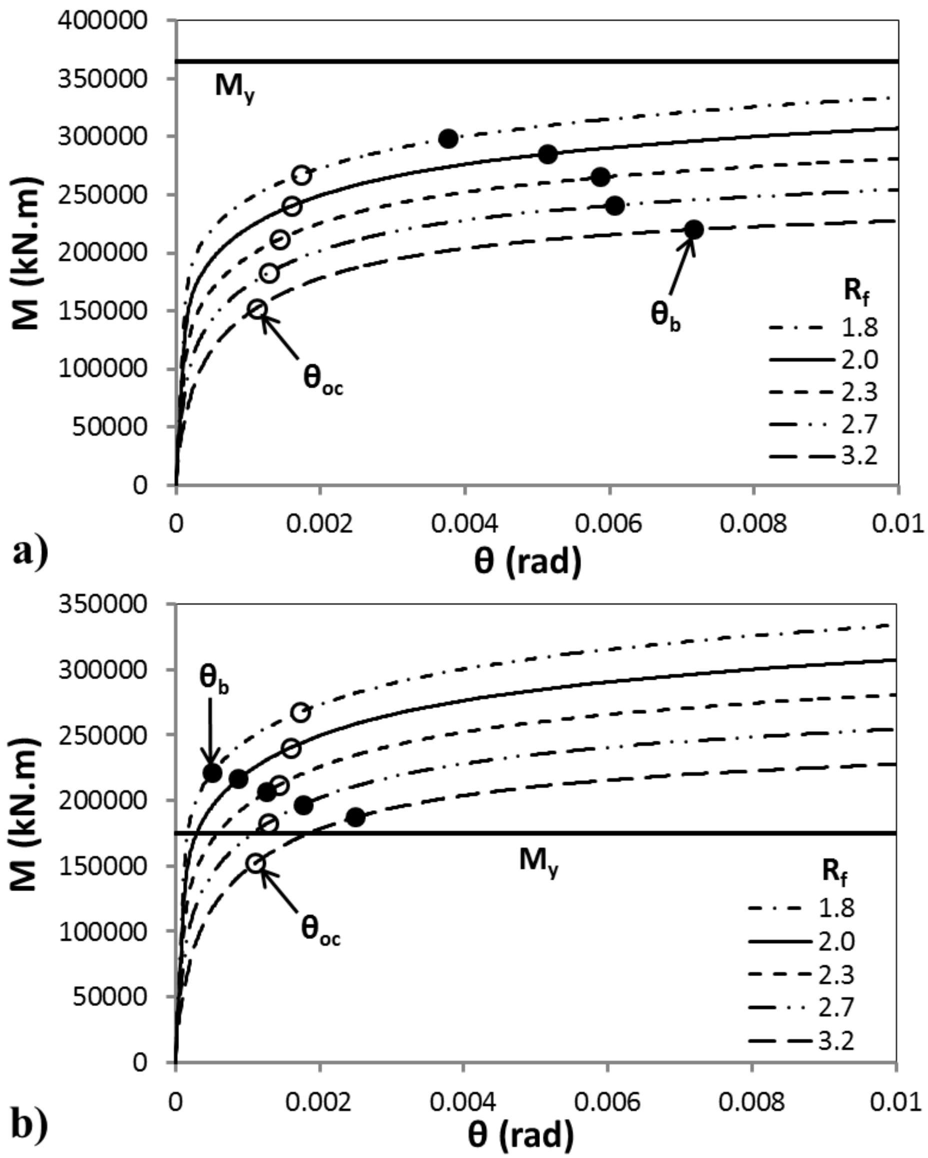

Figure 3.37 Average of maximum foundation rotations (θ_b) from 10 NTHA using spectrally-matched ground motions for walls a) 10R13, and b) 10R27 on Medium Sand plotted on the foundation moment-rotation envelope, along with rotations at which the calculated bending moment capacity of the foundation is mobilized (θ_{oc}).

The solid dots are plotted on the monotonic moment-rotation response at the average of maximum rotation values from each earthquake. Note that in reality, the solid dots must be plotted on the hysteretic response and not the monotonic response. Plotting the solid dots on the monotonic response has caused the bending moment value of the dots to be somewhat higher than the actual bending moment induced in the foundation. This is because the monotonic response is stiffer than the actual hysteretic response.

For wall 10R13, because in all 5 cases the wall was stronger than the foundation, maximum bending moment in the system was governed by the foundation strength and the foundation rotation was dictated by the system displacement demands. This also shows why in none of the cases the 10R13 wall yielded. As for the 10R27 wall, in all 5 cases the foundation ultimate strength was larger than the wall yield strength which is why in all cases, the wall yielded. In this case, the maximum bending moment in the wall-foundation system was governed by the bending strength of the wall (yield strength plus any overstrength due to steel strain hardening). Observe how the solid dots are close to but slightly above the line representing the yield moment of the wall. The difference in the vertical ordinates of the solid dots and the wall yield strength can be attributed to two reasons. One is the wall overstrength from steel strain hardening. The second is the fact that the solid dots must be plotted on the hysteretic moment-response of the foundation and not the monotonic rotation response and hence their vertical ordinate is unrealistic.

The last set of plots discussed in this section is maximum soil compressive displacement plots (Figure 3.38). The curves are the average of maximum soil compressive displacements recorded in each of the 10 ground motions applied to each wall-foundation combination. Even the maximum soil compressive displacement curve for each individual ground motion does not represent the deformed shape of the soil at any point in time. However, the slope of the curves near the toes of the foundation is a good indicator of maximum foundation rotation. Therefore, the slopes of the curves near the toes of the foundation in Figure 3.38 are good approximations of the average of maximum foundation rotation for each wall-foundation combination.

Because wall 10R13 was much stronger than wall 10R27, it transferred much larger moments into the foundations. Larger bending moments to be resisted by the foundation under a constant axial load meant larger eccentricities which in turn resulted in smaller soil compression depths for the same foundation. With a reduced area of contact between the foundation and the soil, the contact pressure increased resulting in larger soil compressive displacements. Hence the curves for wall 10R13 are much more rounded than those for wall 10R27.

In addition to the compressive displacement at the toe, the compressive displacement at the foundation centreline was also much larger for wall 10R13. This was a consequence of rounding of the soil underneath the foundation. When the soil is compressed far into its nonlinear zone, the rebound or the recoverable displacement is very small compared to the total displacement. With the surface of the soil remaining rounded even after the foundation has lifted off in load reversal, the contact area between the foundation and the soil is reduced increasing the contact pressure and consequently, increasing the compressive displacement underneath the centreline of the foundation.

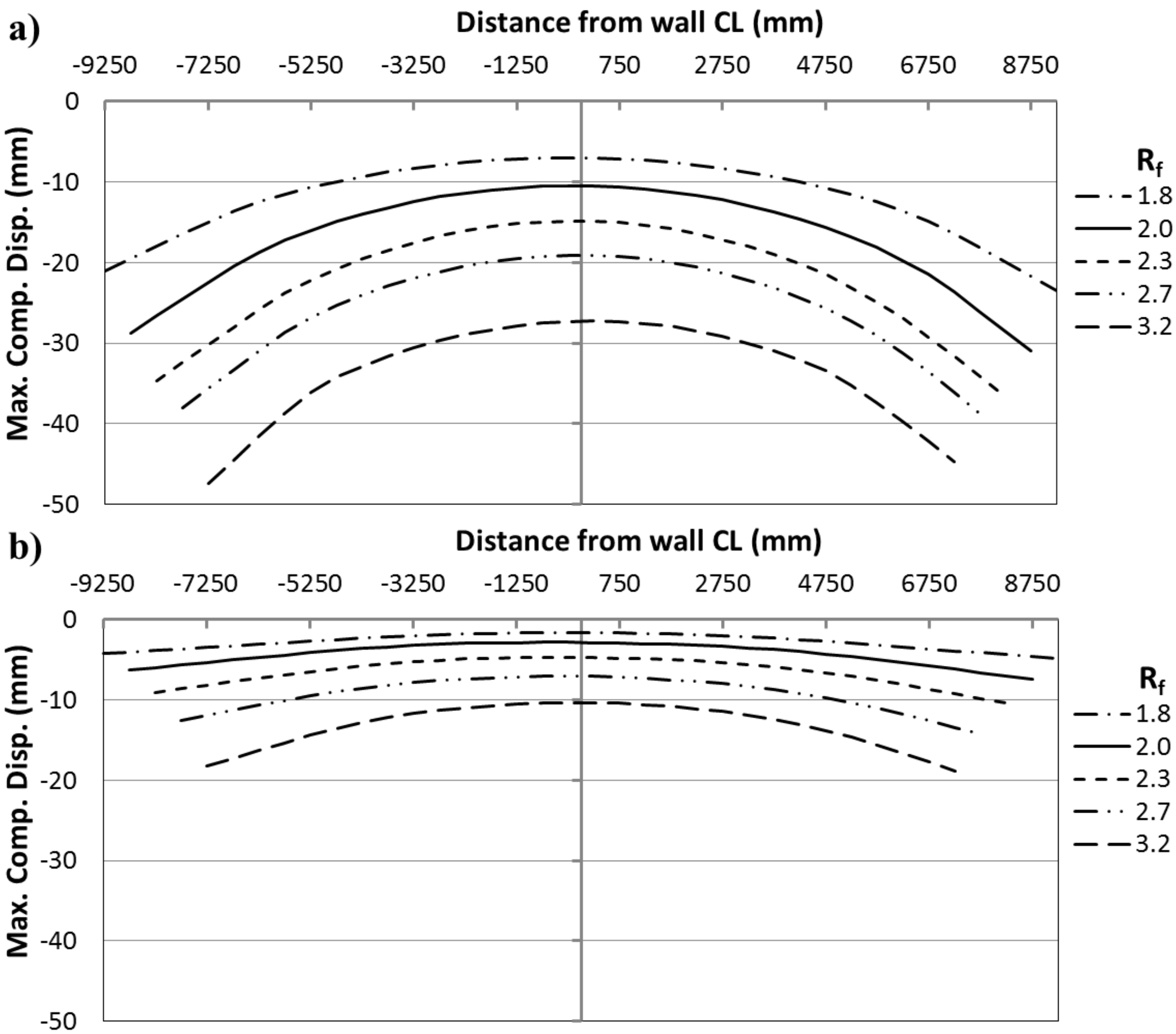

Figure 3.38 Average of maximum soil compressive displacement envelopes from 10 NTHA using spectrally-matched ground motions for walls a) 10R13, and b) 10R27 on Medium Sand.

3.6.2 Global drift and top wall displacement

Increase in top wall displacement is the most convenient parameter that can indicate how much the shear wall's deformation profile is affected by foundation rotation. Top wall displacement is widely used as the performance parameter in performance based seismic design. In addition, many other system demands such as hinge rotation are related to top wall displacement. Therefore, it is important to study the effect that foundation rotation has on top wall displacement.

Average of top wall displacement envelopes from each of the 10 spectrally-matched ground motions are plotted in Figure 3.39 for walls 10R13 and 10R27, the strongest and the weakest nonlinear walls respectively. In general, foundation rotation increases top wall displacement as expected. Top displacement of wall 10R27 experienced a much smaller increase relative to the top displacement of the fixed-base wall. Two factors contributed to this outcome. The first and the more important was that wall 10R27 was not strong enough to impose large bending moments on the foundation and hence, the foundation could not be pushed to large rotations. The second contributing factor is that the displacement of the fixed-base wall 10R27 was larger to begin with because of more severe hinging of the fixed-base wall.

Walls 10R13 however experience a much more severe top displacement increase. This was due to both the top displacement of the fixed-base wall being smaller to begin with and the stronger wall 10R13 being able to impose much larger bending moments on the foundation forcing it to undergo larger nonlinear rotations. Maximum increase in top displacement of wall 10R13 relative to the fixed-base case was about 160% compared to 50% for wall 10R27.

For Clay and the three sands, top displacement starts to grow as R_f becomes larger or the foundation becomes weaker but the curves tend to flatten and reach a plateau. As the foundations became smaller, maximum soil compressive deformations started to grow but the roundedness of the soil surface underneath the foundation did not grow beyond a certain point and in some cases, the surface began to become less rounded. This caused the slopes of the soil surface at the toe of the foundation not to grow beyond a certain point which limited foundation rotation and consequently, top wall displacement.

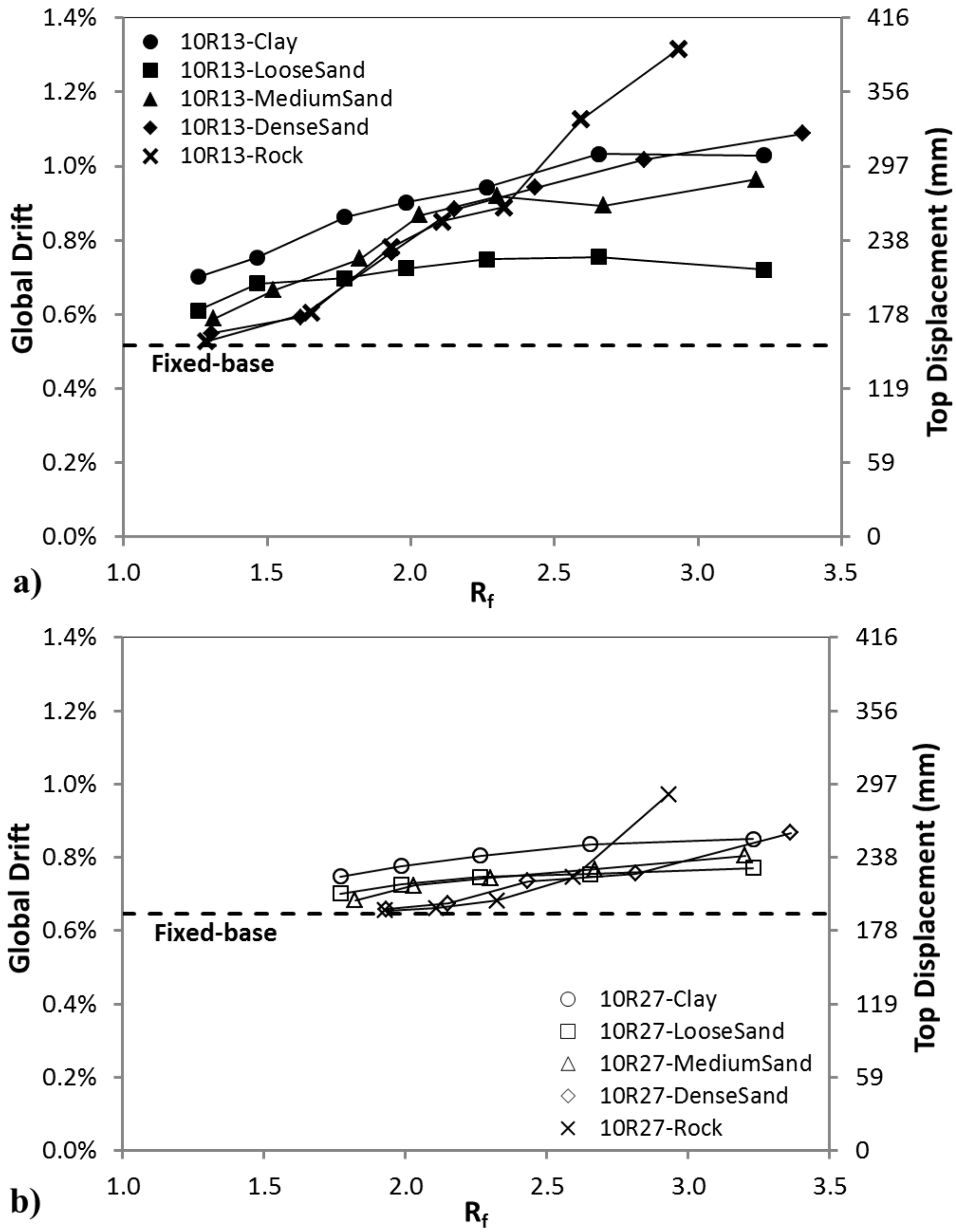

Figure 3.39 Average of maximum global drift and top wall displacement from NTHA using spectrally-matched ground motions for a) wall 10R13, and b) wall 10R27.

For Rock however, top wall displacement kept increasing as the foundation got weaker and not only the curves do not tend to reach a plateau, they appear to take off. Because the Rock was very strong and very stiff causing the soil compression depth to be very small compared to the foundation length, no appreciable foundation overstrength could be gained by using q_{ult} instead of q_f. For the other four types of soil, significant inherent overstrength existed because of considerable change in the lever arm of the resultant vertical force beneath the foundation if R_f was calculated using q_{ult} instead of q_f. This means that once a foundation on Rock lifts off, bending moment at the base of the wall will remain constant while foundation rotation may keep increasing. In addition, no damping was associated with foundations on Rock because compressive deformation of the Rock material was minimal.

Despite the obvious increase in top wall displacement, in no case the wall-foundation became unstable. In other words, rotation of the foundation did not compromise overturning stability of the wall-foundation system. If the increase in top wall displacement due to foundation rotation is to be controlled, the results presented in Figure 3.39 can be used to decide on maximum allowable R_f or the weakest allowable foundation size. Such limits must be imposed considering the strength of the wall and the soil type on which the foundation is being placed.

3.6.3 Base rotation

Foundation rotation causes large drifts at the base of the wall. This concentrated rotation is critical to the demands on the gravity-load system of the building. The additional lateral deformation at the first few floor slab levels due to foundation rotation puts substantial rotation demands at the base of gravity-load columns which can reduce the deformability or ductility of the gravity-load system and consequently, the building as a whole. Therefore, base rotation needs to be studied and quantified.

Average of base rotation envelopes recorded in the Core NTHA for walls 10R13 and 10R27, the strongest and the weakest nonlinear walls respectively, are plotted in Figure 3.40. As expected, wall 10R13 experienced much larger foundation rotations than wall 10R27. The stronger wall could induce larger bending moments into the foundation forcing it to rotate more whereas the weaker wall yielded and hinged before it could push the foundation into severely nonlinear rotations. The stronger the foundation or the smaller the R_f, the smaller was the rotation of the foundation as expected. It is important to note that even with a very strong foundation (i.e. R_f of 1.3), there still was a noticeable amount of foundation rotation. It is therefore necessary to account for foundation rotation no matter how big the foundation might be.

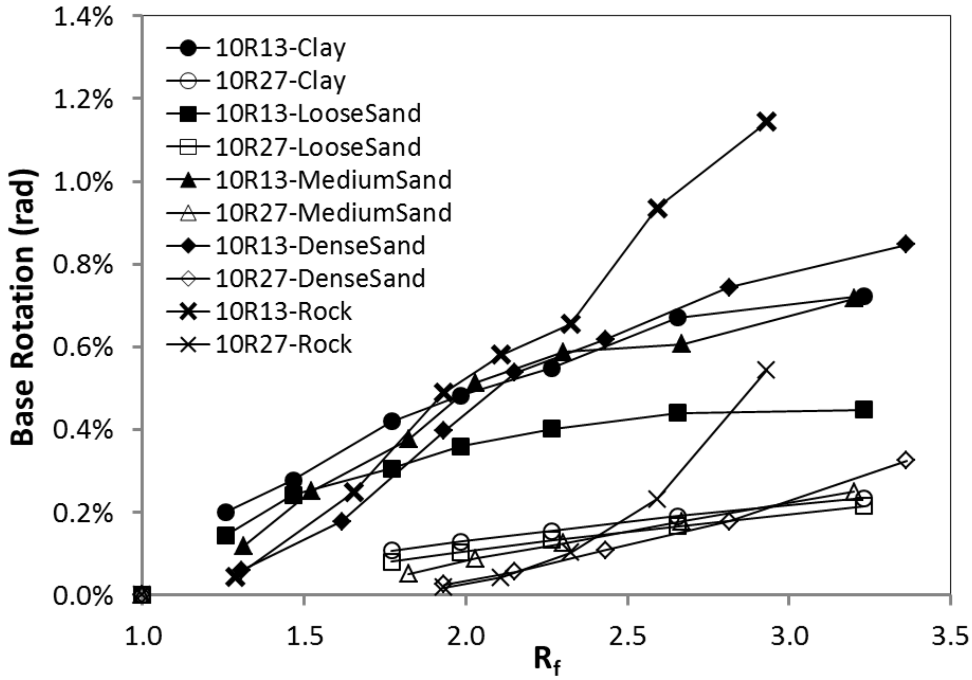

Figure 3.40 Average of maximum base rotations from NTHA using spectrally-matched records for walls 10R13 and 10R27.

Among the 5 soil type, Rock seems to have a distinctive behaviour as foundation rotation keeps increasing with R_f while in other soils, it starts to reach a plateau and level out beyond a certain R_f. As discussed in the previous section, this is because foundations on Rock have no inherent overstrength and that no radiation damping was associated with foundations on Rock. It is obvious that foundations on rock type soils are the most susceptible to rocking.

NBCC 2005 limits R_f to 2.0. While at that R_f the average of foundation rotation envelopes of wall 10R27 are around 0.1%, those of wall 10R13 are in the order of 0.5%. CSA A23.3-04 limits R_f to 2.6. At this R_f, wall 10R13 can have an average of foundation rotation envelopes as high as 0.9% in the case of Rock. Both NBCC 2005 and CSA A23.3-04 state that foundations do not need to be proportioned for forces greater than those associated with an R_f of 2.0 and 2.6 respectively. While these limits seem to be adequate in the case of a weaker wall such as wall 10R27, they are certainly unconservative for a strong wall such as wall 10R13. Not only the limits shall be lowered, but also foundation rotation must be included in the deformation profile of the building and all building components designed to withstand the effect of additional deformations due to foundation rotation.

3.6.4 Interaction between shear wall and foundation strengths

As seen in the previous section, the relative wall to foundation strength is critical to the behaviour of a wall-foundation system. This section further elaborates on the effect that the relative wall to foundation strength has on key wall-foundation system behaviour parameters. Examples demonstrated here are for Clay but the conclusion can well be generalized to other soil types.

Figure 3.41 shows average of maximum first storey and top wall displacements for all walls on Clay. Top displacement is a good indicator of the wall behaviour while the first storey displacement is critical in determining deformation demands that would be critical to the gravity-load system of a shear wall building. As expected, lateral displacement of fixed-base walls increases as the walls get weaker or R_w becomes larger. The weaker the wall is, the sooner the plastic hinging forms and the larger the inelastic rotations. The exact opposite trend is observed for walls with flexible foundations. Lateral displacement of the walls decreases with R_w. The total displacement of the wall can be divided into that due to foundation rotation and that from flexural deformation of the wall. Stronger walls hinge at much greater bending moments and encounter smaller inelastic rotations and therefore have less flexural deformation. However, stronger walls transfer much greater moments into the foundation which results larger foundation rotations and hence, larger portion of their deformation is due to foundation rotation. The balance between lateral deformation from wall flexure and foundation rotation is such that weaker walls will end up having smaller lateral deformations because of experiencing less foundation rotation despite having larger flexural deformations.

Another useful way of looking at the interaction between wall and foundation strengths is by studying the various rotation components (Figure 3.42).

Foundation rotation steadily decreases as the walls become weaker (or R_w becomes larger). Average first storey interstory drift of the walls with flexible foundations also decreases steadily as walls become weaker. Despite the wall plastic hinge forming in the first storey, the majority of the lateral deformation in the first storey is due to foundation rotation since inelastic curvatures in the wall plastic hinge region have to be integrated twice over the height to produce flexural deformation.

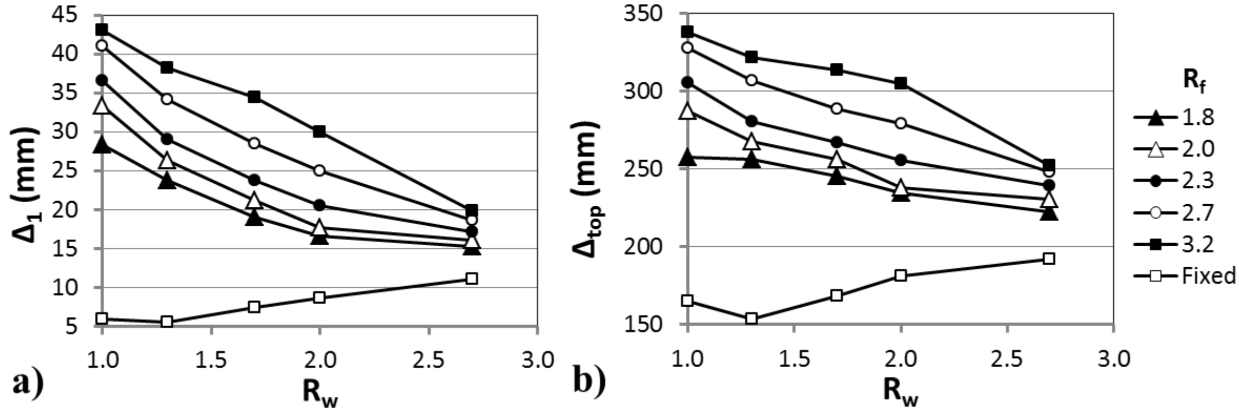

Figure 3.41 Average of maximum a) first storey displacement, and b) top displacement of walls on various foundation sizes on Clay from NTHA using spectrally-matched records. (Note: results for elastic walls are plotted as R_w=1.0)

Average interstory drift of the top storey decreases as the walls get weaker in general but the rate of decrease varies such that for some values of R_f, the drift values either remain constant or increase slightly as the walls become weaker. This is a consequence of transitioning from stronger walls where the majority of the deformation is due to foundation rotation to weaker walls where most of the deformation is flexural. For the same R_f, strong walls will transfer much larger moments into the foundation that results in much larger foundation rotations and hence have larger drifts than weak walls that cannot induce large moments in the foundation. For intermediate walls however, the walls are still strong enough to significantly yield the soil underneath the foundation and cause large foundation rotations but are weak enough to encounter significant hinging and flexural deformation. The combination of the two results in intermediate walls having almost the same or in some cases larger rotations than even the strongest wall.

Figure 3.43 shows average of maximum soil compressive displacements. As expected, stronger walls cause larger compressive displacements in the soil because they are able to transfer larger bending moments into the foundation. Larger moment demands result in smaller compression depth and hence, larger bearing stress which then translate into larger soil compressive displacements. For all fixed-base walls, because the entire wall lateral deformation is flexural, all deformation components keep increasing as the walls get weaker as expected.

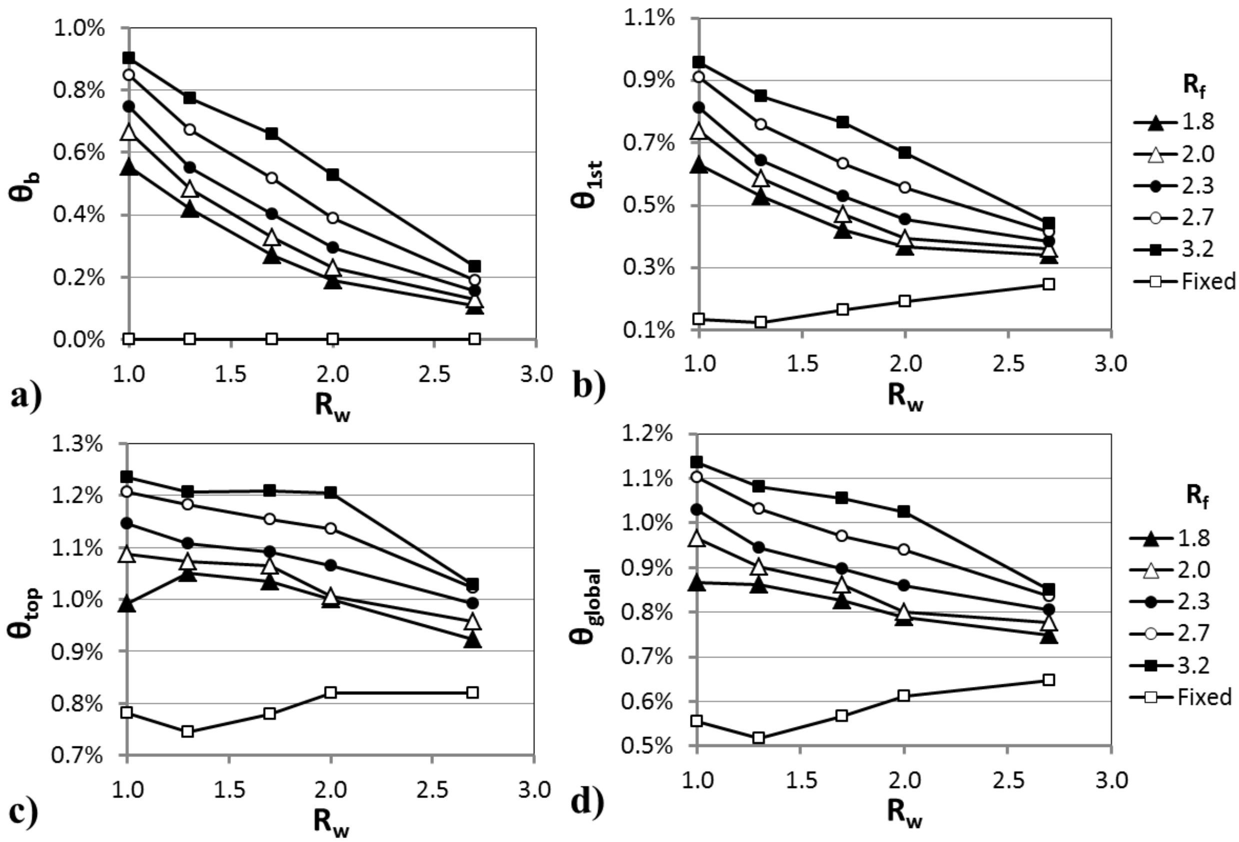

Figure 3.42 Average of maximum a) base rotation, b) first storey interstory drift, c) top storey interstory drift, and d) global drift of walls on various foundation sizes on Clay from NTHA using spectrally-matched records. (Note: results for elastic walls are plotted as R_w=1.0)

There is an important trend that can be observed in all deformation components. As the walls become weaker or R_w increases, the gap between the deformation components of walls with flexible foundations and the fixed-base wall decreases. For example, global drift of wall 10R13 for R_f=3.2 is twice (or 100% larger than) that of the fixed-base wall while global drift of wall 10R27 for the same R_f is only 30% larger than that of the fixed base case. This is partly because global drift of the fixed-base 10R27 wall is greater that the 10R13 wall and partly because the 10R13 wall forces more rotation in the foundation because of its higher strength.

In conclusion, stronger walls are more susceptible to foundation rotation as larger bending moments transferred into the foundation cause larger foundation rotations and that the resulting increase in wall deformation components compared to the fixed-base case are relatively much higher than that for weaker walls.

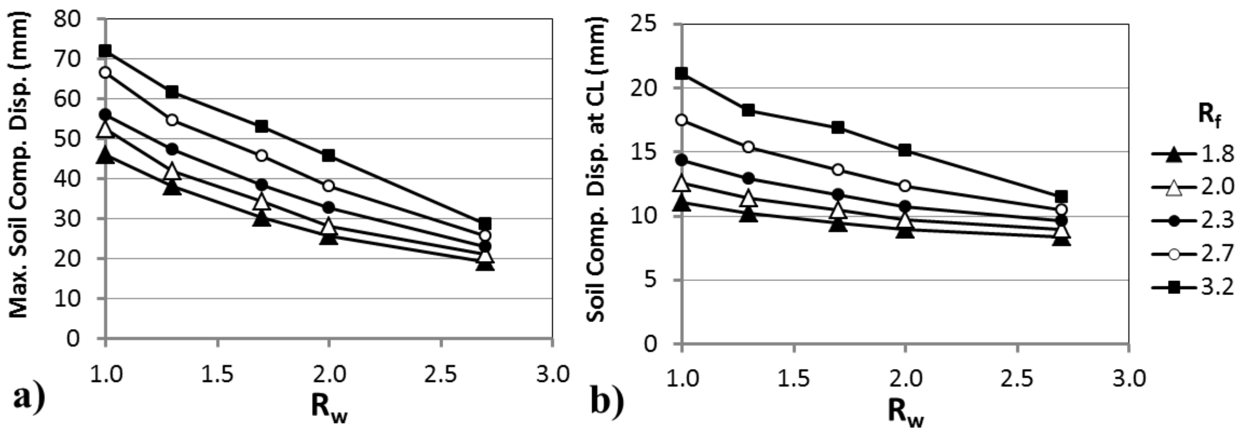

Figure 3.43 Average of maximum soil compressive displacement a) at the toe, and b) underneath the centreline of the foundation for walls on various foundation sizes on Clay from NTHA using spectrally-matched records. (Note: results for elastic walls are plotted as R_w=1.0)

3.6.5 Permanent deformations in the soil

Deformation of the soil underneath the foundation is an important measure of assessing the amount of damage below the foundation due to its rotation. Any yielding of the soil beneath the foundation would be hard to detect or repair and hence, excessive soil damage must be prevented. Permanent soil deformation may cause permanent building tilt and unrecoverable foundation settlement both of which would affect the serviceability of the building.

To study the extent of soil damage observed in the Core NTHA, the case of the 10R13 wall resting on a foundation with R_f=3.2 on Clay (i.e. the strongest nonlinear wall on the softest soil with the highest R_f) was chosen. The Elastic wall would have been more critical but a nonlinear wall was chosen to account for softening of the wall in flexure due to cracking.

Table 3.17 gives a summary of critical components related to permanent deformations in the soil. The first column in the table lists the residual top displacements at the end of the NTHA. Because ground motions may have stronger kicks in one particular direction, resulting permanent deformation of the soil underneath the foundation will not necessarily be symmetrical. This may result in residual foundation rotation and hence, residual building top displacements. The largest residual top displacement observed was 21.9 mm for EQ8 which translates to a global drift of 0.07%. This value is very small and very unlikely to affect building serviceability or cause any concern with the building's structural integrity.

Table 3.17 Residual top wall displacement and maximum soil compressive displacements for wall 10R13 on Clay with R_f=3.2 from NTHA using the 10 spectrally-matched records.

Input GM	$\Delta_{residual}^{top}$ (mm)	Δ_{max}^{CL} (mm)	Δ_{max}^{toe} (mm)
EQ1	8.3	-17.2	-62.5
EQ2	5.0	**-14.1**	**-41.9**
EQ3	1.3	-16.7	-57.4
EQ4	10.7	-22.3	-77.4
EQ5	3.5	-21.6	-70.0
EQ6	**0.3**	**-28.9**	**-97.9**
EQ7	9.6	-18.0	-63.4
EQ8	**21.9**	-19.2	-64.7
EQ9	11.7	-19.6	-73.0
EQ10	2.1	-15.6	-47.4
Min.	**0.3**	**-14.1**	**-41.9**
Max.	**21.9**	**-28.9**	**-97.9**
Avg.	**7.4**	**-19.3**	**-65.6**
St. Dev.	**6.5**	**4.2**	**15.7**

The second and the third columns list residual displacements of the soil underneath the wall centreline and at the foundation toe respectively. Even though all of the ground motions used were scaled to match the same spectrum, there is a great amount of scatter in the residual toe displacement. This matter is explained in the remainder of this section comparing EQ2 and EQ6 which produced the smallest and the largest soil compressive displacements. Note that values reported in the table are maximum soil displacements and not residual soil displacements. Soil elements rebound if the load has been lifted off or reduced. The rebound takes place at the elastic stiffness. Therefore, significance of the soil rebound relative to the maximum soil displacement is dependent on how far into the nonlinear range the soil was pushed. The more the number of nonlinear soil compression cycles, the less significant the rebound will be compared to the maximum compressive displacement.

Figure 3.24 shows maximum soil compressive displacement profiles and the resting position of the foundation at the end of the NTHA for EQ2 and EQ6. Maximum soil deformation profiles along with the resting position of the foundation for each of the 10 input ground motions is provided in Appendix A.

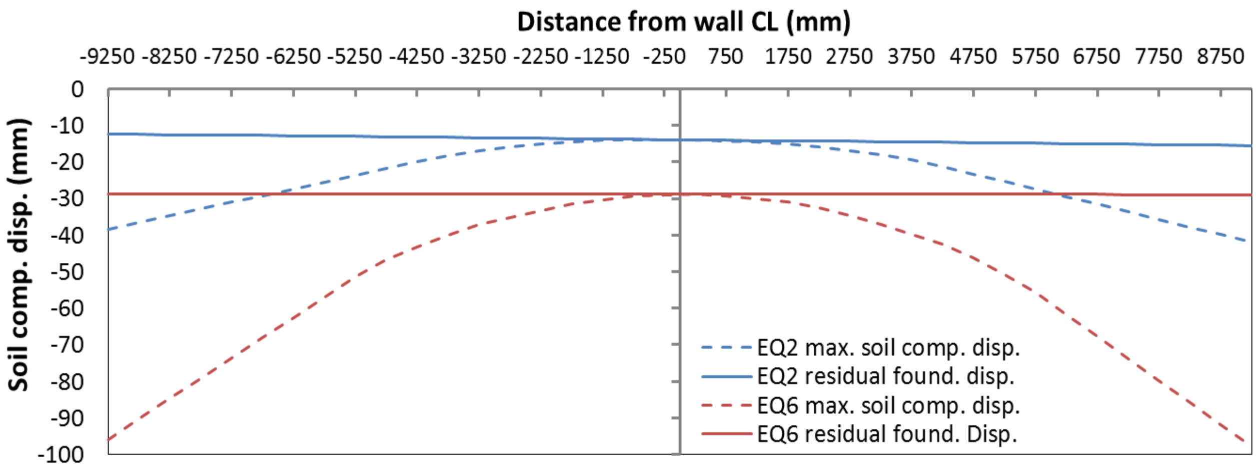

Figure 3.44 Maximum soil compressive displacement and residual foundation displacement of wall 10R13 on Clay with R_f=3.2 from NTHA using spectrally-matched EQ2 and EQ6

Maximum soil compressive displacement profile produced by EQ2 is much flatter than that produced by EQ6. The difference in the degree to which the soil underneath the foundation ratchets down is closely related to characteristics of the input ground motion and explains the scatter in the response of walls with flexible foundations.

To start, take the residual displacement underneath the centreline of the wall. Because the soil underneath the foundation is less rounded from EQ2, the contact area between the foundation and the soil is larger than the case of EQ6. Larger contact area means lower bearing stresses and hence lower residual displacements. This can be confirmed by looking at the soil bearing stress distribution underneath the foundation for the two ground motions shown in Figure 3.45a. The foundation is in contact with the soil along almost its entire length after EQ2 which results in the maximum bearing pressure being just above $0.4q_{ult}$ which is within the elastic response range of the clay elements. Soil bearing pressure at the end of EQ6 is as high as $0.8q_{ult}$ far beyond the elastic response limit and into the nonlinear response range.

A similar explanation can be provided for the difference in maximum soil compressive displacement at the toes of the foundation resulting from the two input ground motions. Because the maximum soil compressive displacement profile resulting from EQ2 is less rounded, compression depth of the foundation under eccentric loading is larger than the case of EQ6. Larger compression depth means smaller bearing stresses and hence, smaller soil compression.

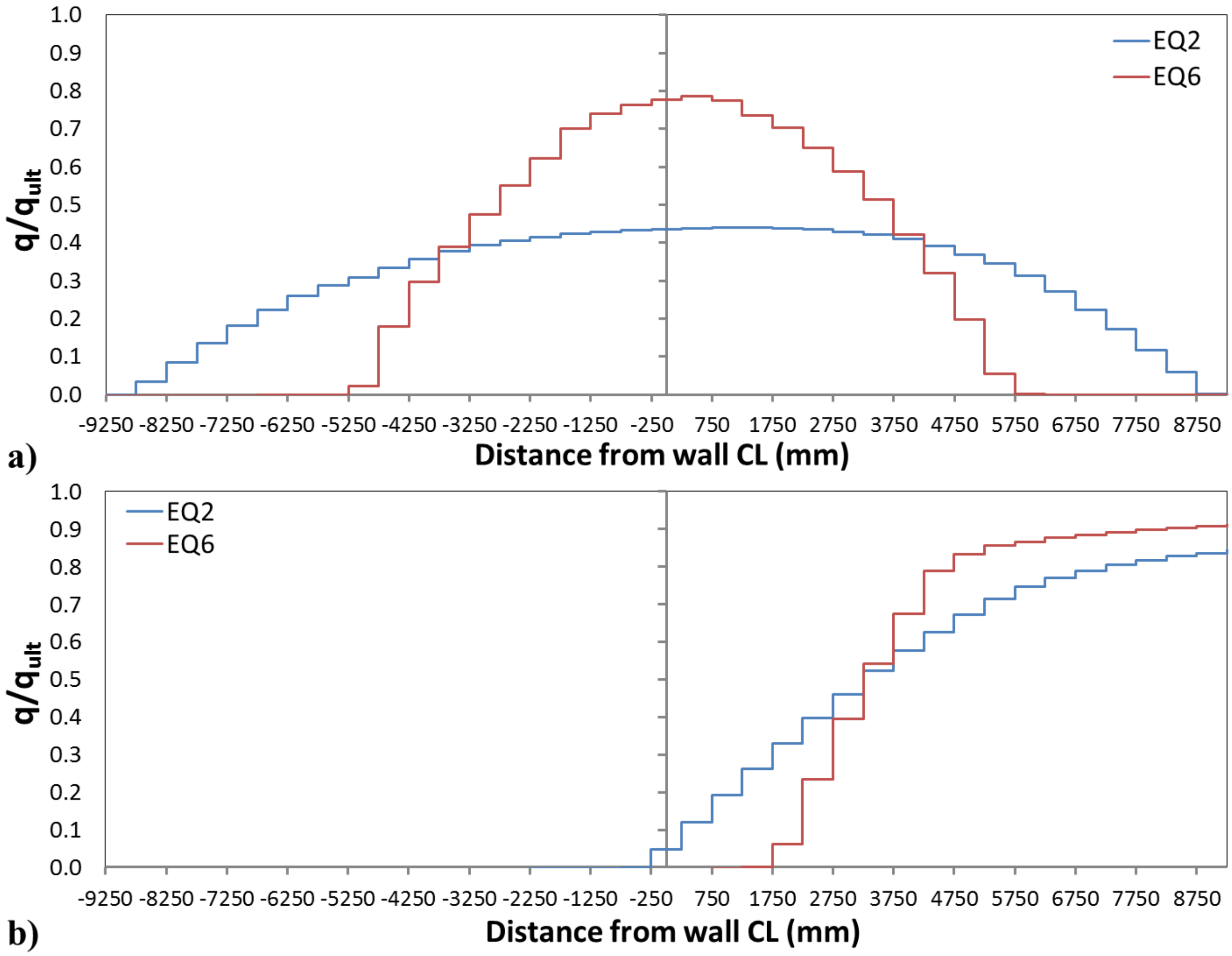

Figure 3.45 Bearing stress distribution underneath wall 10R13 on Clay with R_f=3.2 from NTHA using spectrally-matched EQ2 and EQ6 at a) the end of NTHA, and b) time of occurrence of maximum soil compressive displacement.

Taking a look at the soil bearing stress distribution at the time of occurrence of maximum toe compressive displacement (Figure 3.45b) confirms the hypothesis. The smallest compression depth from EQ2 is more than 9250 mm long while the number reduces to 7500 mm for EQ6. This difference does not look dramatic but the effect that it has on the increase in maximum soil displacements at the toe is quite profound. This decrease in compression depth resulted in increase in the bearing pressure from about $0.8q_{ult}$ for EQ2 to about $0.9q_{ult}$ for EQ6. Considering how flat the backbone curve for the clay elements are beyond $0.85q_{ult}$ (see Figure 3.7), this seemingly small change in bearing pressure causes a huge difference in maximum soil compressive displacement especially when cyclic softening of the soil is added to the equation.

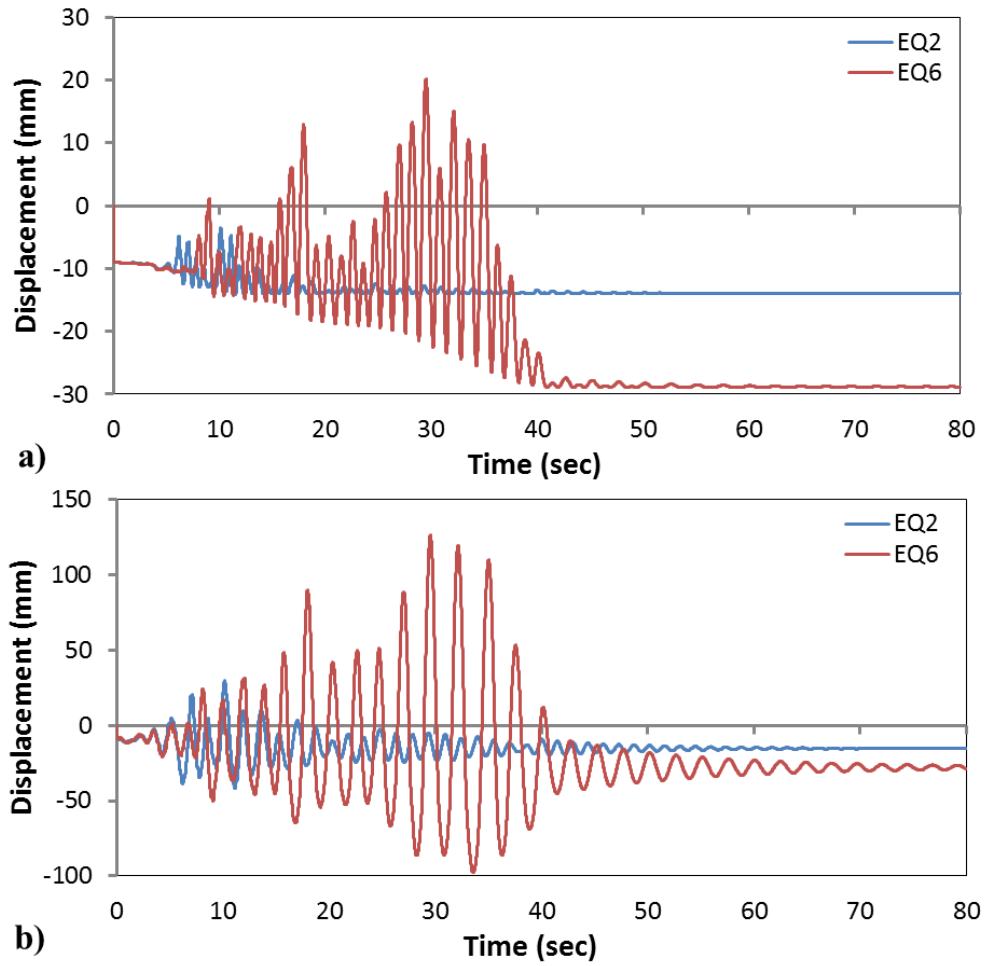

Figure 3.46 Displacement time-histories of the soil element a) underneath wall CL, and b) at foundation toe of wall 10R13 on Clay with R_f=3.2 from NTHA using spectrally-matched EQ2 and EQ6.

Looking at the time-history response of the soil elements can provide further insight into behaviour of flexible foundations and the scatter in residual soil displacements. Figure 3.46a shows the time-history response of the soil element located at the wall centreline during EQ2 and EQ6. For both input ground motions, the response starts at the same static soil settlement of about 9 mm. Maximum compressive displacement experience by the element during EQ2 is about 15 mm. Under EQ6, compressive displacement of the same element keeps getting larger and larger with time as the soil ratchets down and surface of the soil underneath the foundation becomes more and more rounded. A similar explanation can be provided for the response of the soil element at the toe of the foundation (Figure 3.46b). The major difference is that the soil element rebounds significantly after the strong shaking of the input ground motion has passed.

Cyclic ratcheting of the soil and progressive rounding of the soil surface underneath the foundation can be seen in the time-history bearing pressure response of the soil element underneath the wall centreline (Figure 3.47a).

The reason for EQ6 causing much more rounding of the soil, underneath the foundation can be best explained by looking at the time-history response of the bearing stress of the soil element at the toe of the foundation (Figure 3.47b). EQ6 caused the soil element to experience bearing stresses in excess of $0.8q_{ult}$ (the threshold for highly nonlinear soil response) six times while this figure was reduced to only two for EQ2. The instances when this occurred are marked with dots on the plot. Despite both EQ2 and EQ6 being fitted to the same spectrum, EQ6 was such that it forced the element at the toe of the foundation to undergo much more cyclic softening and accumulate more compressive displacement than the EQ2. A similar difference in bearing stress demand was observed in all of the soil elements farther than about a quarter of the foundation's length from the wall centreline. Accumulation of compressive displacements in the soil elements lead to much more rounding of the soil surface due to EQ6.

It is therefore concluded that the response of walls with flexible foundations is largely dependent on the input ground motion and that is because the cyclic compressive displacement of the soil and the degree of rounding of the soil surface are highly sensitive to the input ground motion. This phenomenon also explains the much greater scatter in the response of walls with flexible foundations compared to walls with a fixed base.

The maximum residual building tilt observed in the Core NTHA was 0.07% which is highly unlikely to be problematic. Maximum soil compressive displacement at the foundation toe was less than 100 mm which considering the foundation length of 18500 mm does not seem too worrying. Maximum permanent compressive displacement underneath the centreline of the foundation observed in the Core NTHA was 29 mm (9 mm of which was due to settlement of the soil under service conditions). An extra permanent settlement of 20 mm does not seem to affect serviceability of the building by much and certainly not be a life-safety concern.

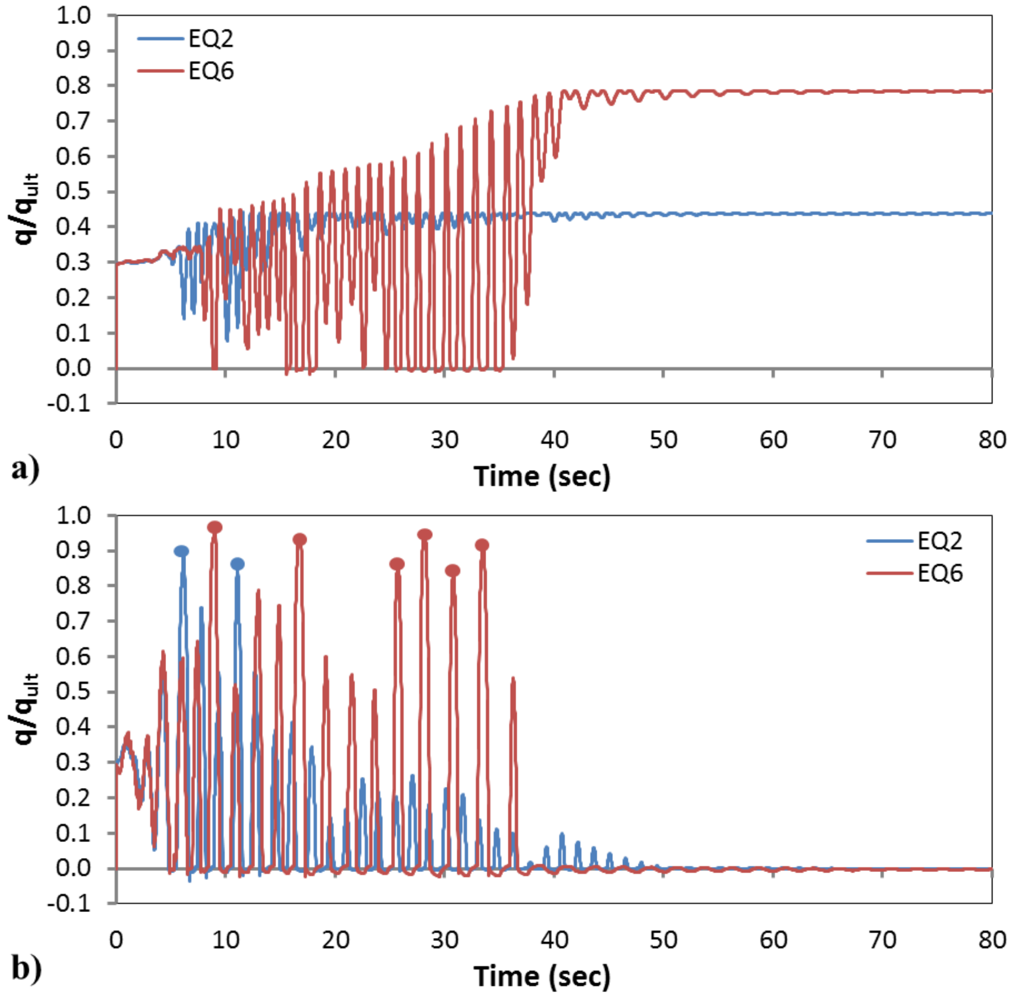

Figure 3.47 Vertical reaction time-histories of the soil element a) underneath wall CL, and b) at foundation toe of wall 10R13 on Clay with R_f=3.2 from NTHA using spectrally-matched EQ2 and EQ6.

Having explained the mechanism of accumulation of soil compressive displacement, Figure 3.48 summarizes maximum soil compressive displacements at the toe and underneath the centreline of the foundation obtained from the Core NTHA. Only results for walls 10R13 and 10R27, the strongest and the weakest nonlinear walls are shown here. As expected, the smaller the foundation got, the average bearing pressure on the soil increased resulting in more soil compressive displacement. Also, softer and weaker soils such as Clay and Loose Sand experienced more compressive displacement than Dense Sand for obvious reasons. Compressive displacements of the Rock are not meaningful as properties of Rock were chosen to have minimal compressive displacement; however, the results are included for completeness.

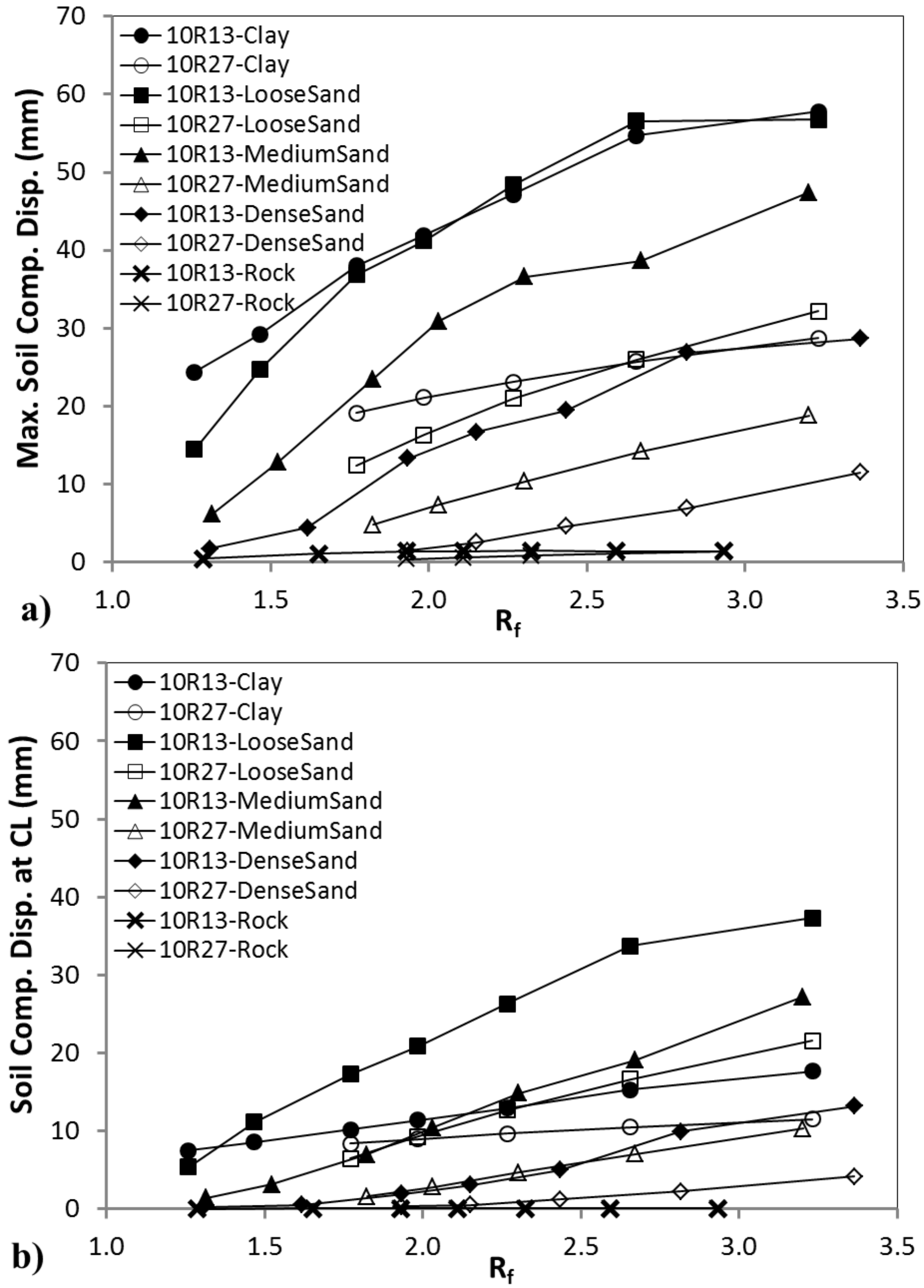

Figure 3.48 Average of maximum soil compressive displacement at a) foundation toe, and b) wall centreline from the Core NTHA for walls 10R13 and 10R27.

Stronger wall 10R13 induced larger moments into the foundation and forced larger compressive displacements of the soil while the weaker wall 10R27 yielded before putting a very high bending demand on the foundation.

The average of maximum soil compressive displacement from the 10 spectrally-matched ground motions recorded in the Core NTHA was less than 60 mm at the toe of the foundation and less than 40 mm underneath the centreline. While neither of those two numbers sound worrying or large enough to hinder serviceability of the building after an earthquake, Figure 3.48 can be used as a guide if maximum probable soil compressive displacements are to be controlled.

3.6.6 Period lengthening due to rotation of the foundation

As the wall begins to rock, the rotational stiffness of the foundation starts to deteriorate because of both soil yielding in compression at the "toe" of the foundation and liftoff. This softening of the wall's support at the base causes the effective fundamental period of vibration of the wall-foundation system to grow; a phenomenon that has been observed in all foundation rotation related research. Therefore, studying the variation of the effective wall-foundation system period may provide a good insight into the behaviour of shear walls with flexible foundations.

Effective periods of wall-foundation systems analysed in the Core NTHA are given in Figure 3.49. Data points shown in the figure were obtained from the average of displacement spectra for the 10 spectrally-matched ground motions (see Figure 3.13). Note that displacement values in the displacement spectra are displacements at first modal heights and not top wall displacements. Modal heights can be found from modal analysis and depend on the distribution of mass and stiffness along the height of the wall. For the four nonlinear walls considered here, the first modal height was found to be 0.76 times the wall height and the elastic lateral displacement at the modal height was 0.667 times the top wall displacement. Average of top wall displacement envelopes from each of the 10 spectrally-matched ground motions were multiplied by 0.667 to get their corresponding displacement values at first modal height. Effective period of the system was then read from the average of displacement spectra for the displacement value at the first modal height.

It is important to note that the displacement at first modal height to top wall displacement ratio of 0.667 applies only to an elastic wall with the same mass and stiffness distribution along its height as the nonlinear walls. In reality, this ratio would be generally higher as foundation rotation and wall hinging causes most of the inelastic rotation to be concentrated near the base with less bending of the wall near the top. The ratio varied from 0.70 to 0.75 for the Core NTHA. However, because the intent is to find the fundamental vibration period of an equivalent elastic structural system that would have the same top displacement as the nonlinear walls of the Core NTHA analysis, the ratio of 0.667 is used in this section. This approach will also be useful in estimating the top displacement of a nonlinear wall with a flexible foundation using an elastic system with the appropriate fundamental period of vibration (see Section 4.2).

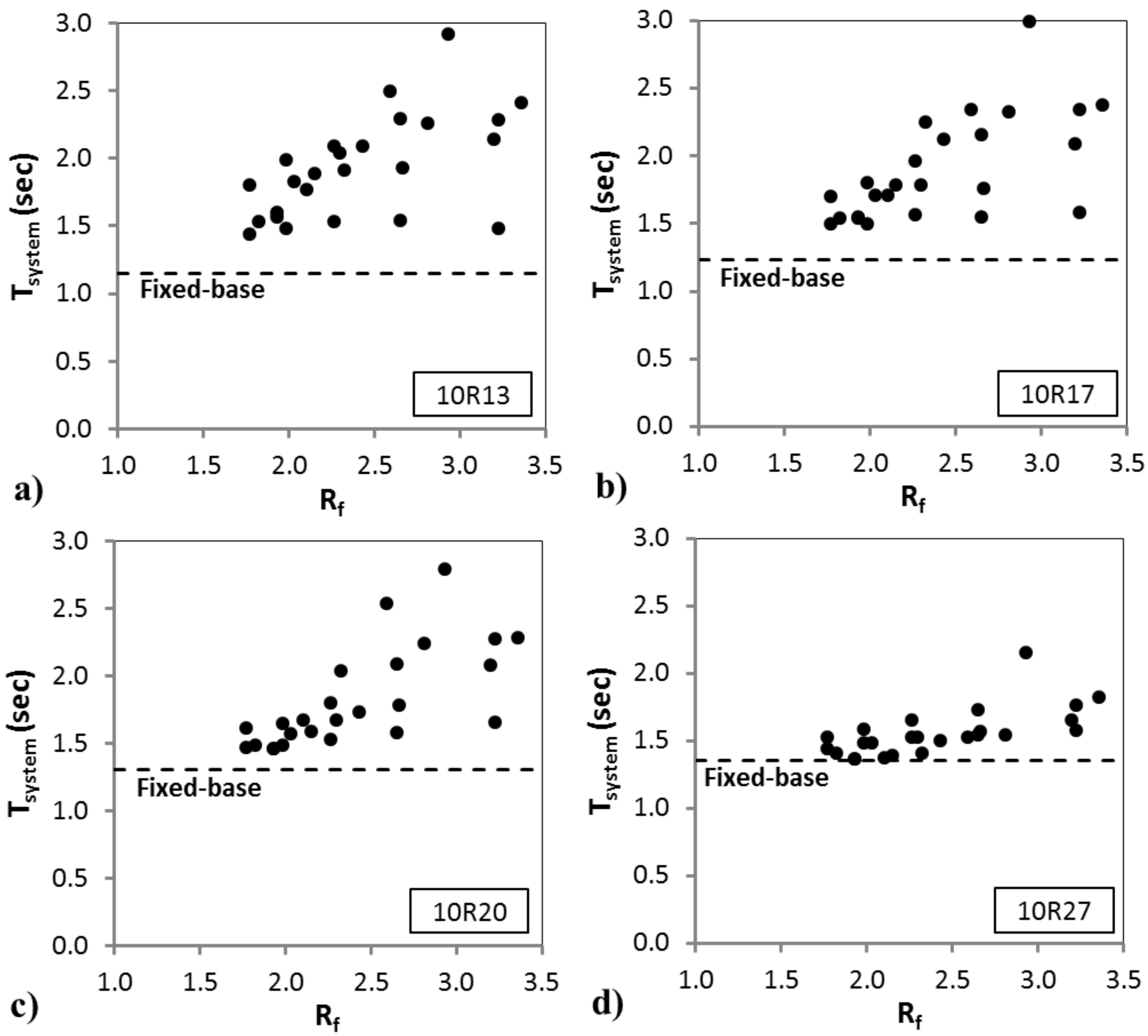

Figure 3.49 Increase in effective period of the wall-foundation system due to foundation rotation for wall a) 10R13, b) 10R17, c) 10R20, and d) 10R27.

Looking at Figure 3.49, it is obvious that the stronger the wall is, the more the period lengthening relative to the period of the fixed-base wall. The stronger walls could induce larger bending moments in the foundation forcing more rotation in the foundation and therefore, more softening of the base. The average of the ratio of effective system period to the fundamental period of the fixed-base wall was 1.68, 1.54, 1.39, and 1.15 for walls 10R13, 10R17, 10R20, and 10R27 respectively.

For all walls however, more period lengthening was observed when the foundations were weaker (or R_f was larger). For the same wall strength, the weaker the foundation got, the more the wall was able to push the foundation into soil yielding and uplift resulting in more period lengthening.

3.6.7 Reduction in maximum bending moment and shear force due to rotation of the foundation

Rotation of the foundation can limit the maximum bending moment at the base of the wall. Shear force demands at the base of the wall could potentially reduce due to foundation rotation. A reduction in design forces on the wall could benefit the design and hence needs careful attention.

Figure 3.50 summarizes the reduction in maximum bending moment demand at the base of walls 10R13 and 10R27 (the strongest and the weakest nonlinear walls) observed in the Core NTHA. A parameter called moment reduction factor (MRF) is defined as the ratio of maximum bending moment demand of the wall with a flexible foundation to that of the fixed-base wall both obtained from NTHA. In other words, the average of base bending moment envelopes from each set of 10 spectrally-matched ground motions would be the average of base bending moment envelopes of the fixed-base wall multiplied by the MRF.

Hardly any reduction in wall bending moment demand can be observed for walls 10R27 regardless of the soil type. This is because the wall was so weak that it always yielded regardless of the foundation strength. Even when wall 10R27 had a foundation with R_f greater than 2.7, the foundation overstrength due to the use of q_f instead of q_{ult} in calculating R_f was still strong enough to develop the yield bending capacity of the wall. The trend observed with walls 10R13 was totally different. When the foundation had an R_f close to 1.3 and was able to develop the yield bending capacity of the wall, MRF was close to 1.0. As the foundation became weaker, it could no longer develop the wall's yield bending capacity and therefor, MRF started to drop. Among the five soil types, the largest reduction in bending moment demand was observed for Rock because foundations on Rock had minimal overstrength beyond their liftoff capacity. Walls on Clay experienced less reduction in bending moment demand as foundations on Clay had a significant overstrength due to R_f being calculated from q_f and not q_{ult}. Therefore, attention should be given to the foundation moment-rotation response and the probable overstrength of the foundation when deciding on reducing bending moment demands on the shear wall.

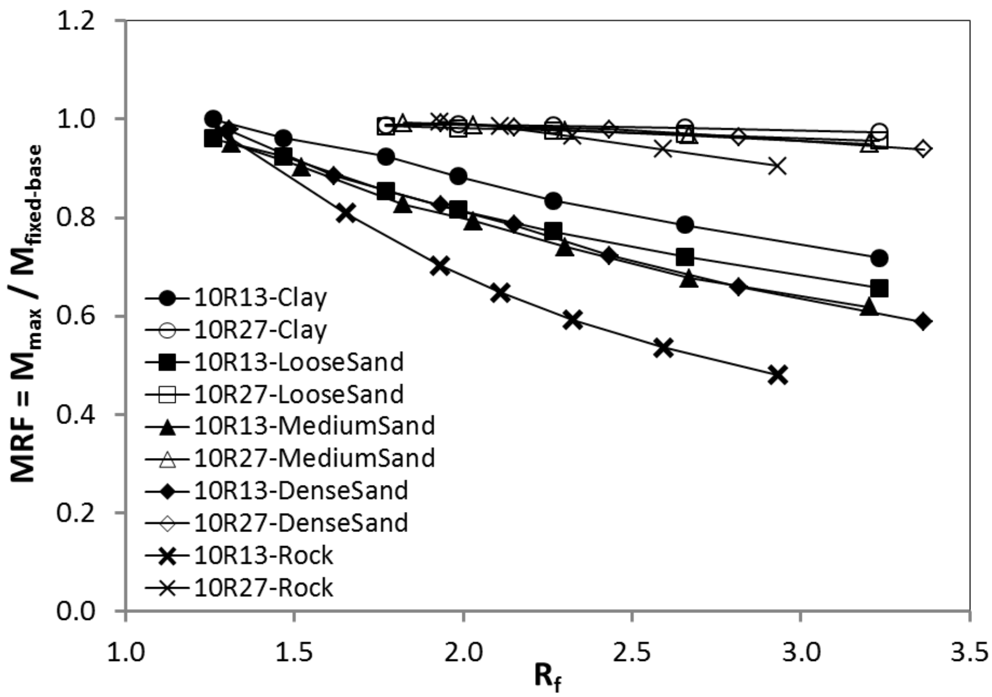

Figure 3.50 Reduction in wall maximum bending moment demand due to foundation rotation observed in the Core NTHA for walls 10R13 and 10R27.

To study the effect of foundation rotation on base shear demand of the wall, a parameter called shear reduction factor (SRF) is defined as the ratio of base shear demand of the wall with a flexible foundation to that of the fixed-base wall both obtained from NTHA. Figure 3.51 shows SRF's for walls 10R13 and 10R27 obtained from the Core NTHA. Not only did wall 10R27 not experience a reduction in base shear demand, but its base shear demand increased slightly due to rotation of the foundation which shows that in some cases, MRF and SRF can be very different.

Some reduction in base shear demand was observed in walls 10R13 but the reduction in base shear demand was much less than that in the maximum bending moment demand. As an example, the lowest MRF was around 0.5 for wall 10R13 on a foundation with R_f of nearly 3.0 on Rock while SRF of the same wall was 0.8. This shows that the effect of foundation rotation on bending moment and shear force demands can be very different.

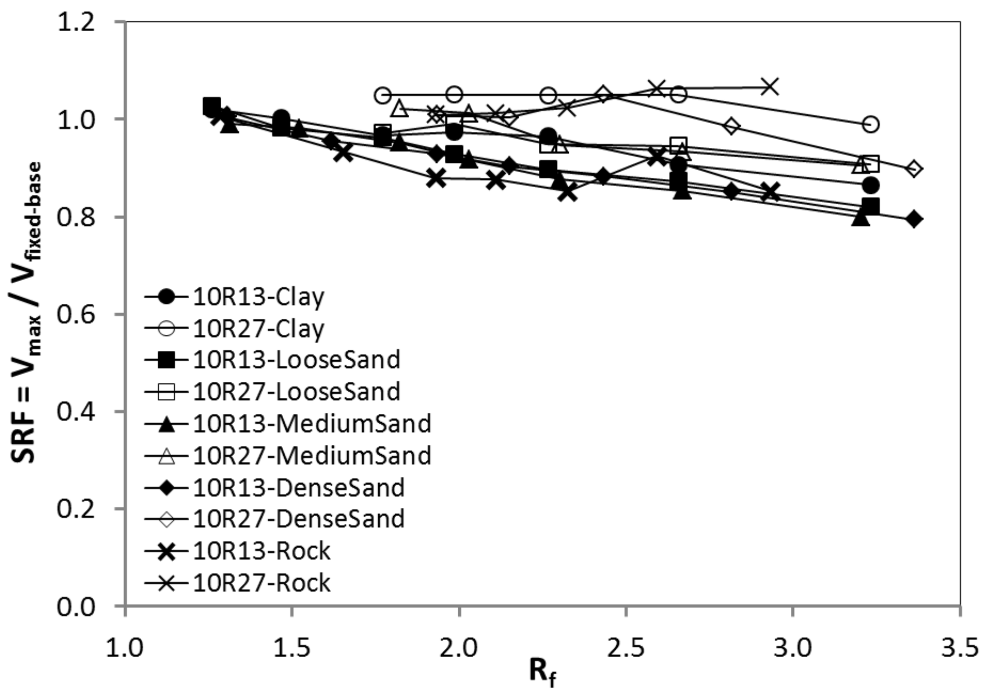

Figure 3.51 Reduction in wall base shear demand due to foundation rotation observed in NTHA

To further illustrate this observation, the ratios of SRF to MRF obtained from the Core NTHA are plotted in Figure 3.52 or walls 10R13 and 10R27. Except for a few data points that are just below 1.0, the ratio is greater than 1.0 which means that less reduction was observed in wall base shear than bending moment demand.

Figure 3.50 and Figure 3.51 can therefore be used as a reference for deciding on what bending moment and shear force reduction factors to use for a given wall-foundation system.

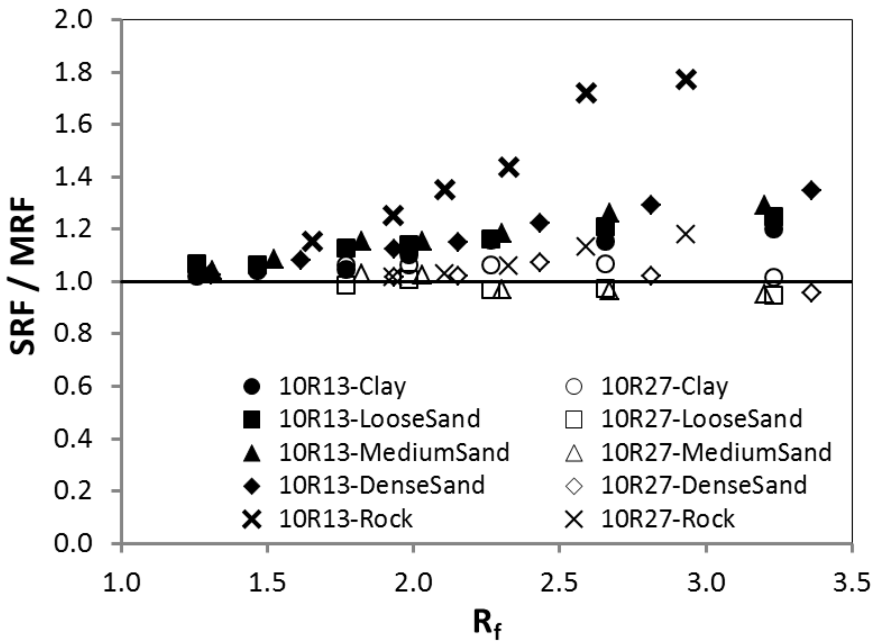

Figure 3.52 Ratio of shear to moment reduction factors for walls 10R13 and 10R27 obtained from the Core NTHA.

3.7 Summary and Conclusions

The main conclusions drawn from this chapter are as follows:

1. Response of shear walls accounting for foundation rotation was shown not to be overly sensitive to input soil properties. A parametric study revealed that for the same foundation size, when the soil properties varied between their extremes within the realistic range of R_f for the given soil strength, the top wall displacement was affected by as little as 20%. Soil response parameters such as permanent deformations in the soil, on the other hand, were more severely affected by the change in the input soil properties.

2. Maximum top wall displacement and foundation rotation proved to be sensitive to soil damping. Soil damping was also shown to affect the hysteretic response of the wall as in undamped or unrealistically underdamped systems, the amplitude of the oscillations kept increasing even after the strong motion phase of the input ground motion record had passed.

3. The mean wall response calculated using spectrally-matched ground motions agreed well with that obtained using uniformly-scaled ground motions; however, scatter of the results among the 10 input ground motions was larger for uniformly-scaled records.

4. Mass ratio was found to have a significant impact on the response of walls when foundation rotation was accounted for. Systems with larger mass ratios needed a smaller foundation to achieve certain foundation strength and therefore experienced larger foundation rotation. Shorter walls were shown to be more susceptible to foundation rotation as the percentage increase in their deformation components compared to the fixed base case was higher than that of taller walls. Similar observations had been made by Anderson (2003) for elastic walls sitting on a bed of elastic-perfectly plastic (EPP) soil springs.

5. Wall-to-foundation strength ratio proved to be a key parameter in predicting the response of shear walls accounting for foundation rotation. In systems where the shear wall strength was smaller than the foundation overturning capacity (i.e. hinging shear walls), maximum bending moment demand of the system was governed by the shear wall strength. Such systems showed smaller foundation rotations because hinging of the shear wall limited the bending moment acting on the foundation. Systems in which the shear wall was stronger than the foundation (i.e. non-hinging shear walls) were much more susceptible to large foundation rotations. Maximum bending moment demand in such systems was governed by the foundation ultimate overturning capacity.

6. Inter-storey drift profile of wall-foundation systems with hinging shear walls was close to that of the fixed-base wall in terms of both magnitude and shape while inter-storey drift of systems with non-hinging shear walls was closer to being uniform over the building height. In systems with hinging shear walls, a much larger portion of the top wall displacement was due to bending of the wall. In systems with non-hinging shear walls, larger rotations induced in the foundation substantially increased the building’s drift profile in the lower storeys causing the inter-storey drift profile to become close to being uniform over the wall height.

7. Allowing the foundation to rotate increased the effective first mode period of vibration compared to the fixed-base wall. The increase in effective first mode period was much more pronounced for systems with stronger shear walls as larger rotations induced in the foundation softened the foundation response more than the case of systems with hinging shear walls.

8. In general, accounting for rotation of shear wall foundations reduces bending moment demands on the shear wall. The reduction in maximum bending moment demand is larger in systems with non-hinging shear walls where the foundation overturning capacity is smaller than the bending strength of the wall. Introducing a flexible foundation resulted in a much smaller reduction in shear force demand on the wall compared to the reduction in bending moment demand. In some cases, even larger shear forces were induced in the shear wall with a flexible foundation compared to the fixed-base wall. The need for different moment and shear reduction factors is therefore obvious.

9. Permanent soil deformations were shown to be sensitive to certain properties of the input ground motion such as the number and direction of large pulses in the ground motion record. Maximum soil permanent deformation was 30 mm at the wall centreline and 100 mm at the "toe" of the foundation. Maximum residual top wall displacement recorded was 22 mm which corresponds to a global drift of 0.07%. In general, systems with non-hinging shear walls experienced larger permanent soil deformations as larger bending moments were induced into the foundation.

10. None of the structures analyzed in this study experienced or even came close to collapse. The increase in wall deformation due to rotation of the foundation was not big enough to threaten the stability of the system. However, the shape of the drift profile of the wall was significantly affected by accounting for foundation rotation. Displacement profile of the wall generally increased due to foundation rotation which may put significant deformation demands on the gravity-load system of the building. In some cases, considerable permanent displacements were observed in the soil which must be considered in evaluating the building's seismic performance.

CHAPTER 4 Simple Methods for Predicting the Response of Shear Walls Accounting for Foundation Rotation

CHAPTER 3 presented the results of Nonlinear Time-History Analysis (NTHA) on a broad range of shear walls with flexible foundations and explained the effect of major system parameters on the response of shear walls with flexible foundations. This chapter is geared towards using the knowledge obtained from studying the data from NTHA presented in CHAPTER 3 to formulate a step-by-step procedure for predicting foundation rotation of a given wall-foundation system.

The chapter begins with predicting the foundation moment-rotation response envelope as it was found in CHAPTER 3 to be a key factor in understanding the behaviour of the wall-foundation system. A simple method for estimating the total top wall displacement is proposed and calibrated to NTHA results of CHAPTER 3. The total top wall displacement is then broken up into its three major components, namely, elastic top displacement, top displacement from wall hinging, and top displacement from foundation rotation. Other sources of displacement such as wall shear strain and wall rocking at its interface with the foundation due to bar slip are ignored. A simple design-oriented procedure is proposed for estimating each of the major top wall displacement components taking into account the relative strengths of the foundation and wall. In the end, the accuracy of the proposed step-by-step procedure for predicting the response of shear walls accounting for foundation rotation is examined by making estimates of foundation rotations recorded in the NTHA of CHAPTER 3.

The concepts behind developing the procedure are validated. The proposed procedure is shown to be of good accuracy for engineering design and suitable for implementation in standard design procedures. Limitations of the work done in this chapter are discussed in Section 8.5.

4.1 Foundation Moment-Rotation Response

As concluded in CHAPTER 3, foundation moment-rotation response is quite useful in explaining and predicting the response of shear walls with flexible foundations. Although the actual hysteretic response is highly dependent on how far into the nonlinear range the soil is pushed and the number of nonlinear cycles in the soil elements, the monotonic foundation response which will envelope the actual hysteretic response is relatively simple to predict. The monotonic foundation response can be directly or indirectly used to estimate key response factors such as maximum bending moment induced in the wall-foundation system, maximum foundation rotation, maximum soil compressive displacement, and a few other useful parameters. It is also useful in determining which is the major energy dissipation mechanism in the system, wall yielding or soil yielding and foundation uplift. Sections below describe a few of the existing methods for developing the foundation moment-rotation response and provide new a method for predicting the monotonic moment-rotation response of a given foundation.

4.1.1 Allotey and El Naggar's method for predicting foundation moment-rotation response

Siddharthan et al. (1992) presented a rigid-plastic model for seismic tilting of rigid retaining walls in which the response of the soil in compression was approximated by an elastic perfectly plastic (EPP) curve. The method proposed solutions for the uplift-only and yield-only cases. The work of Allotey and El Naggar (2003) is based on the same EPP assumption for the soil response; however, it provides a general solution for all cases including circumstances with combined soil yielding and foundation uplift.

Figure 4.1 (originally from FEMA 274) demonstrates the concept behind Allotey and El Naggar's method. Variation of strain along the foundation length is linear (i.e. rigid foundation). As can be seen, states 5 and 6 shown in the figure include both lift-off and soil yielding. The solution was provided for a foundation of length B and a unit width resting on a soil with ultimate bearing capacity of q_u and reaction modulus k_v sustaining a vertical load P. Note that Allotey and El Naggar refer to the foundation length as B while in this study, foundation length is denoted as L and B is the foundation width. B in Allotey and El Naggar's notation is substituted for L to keep the notations of this study consistent.

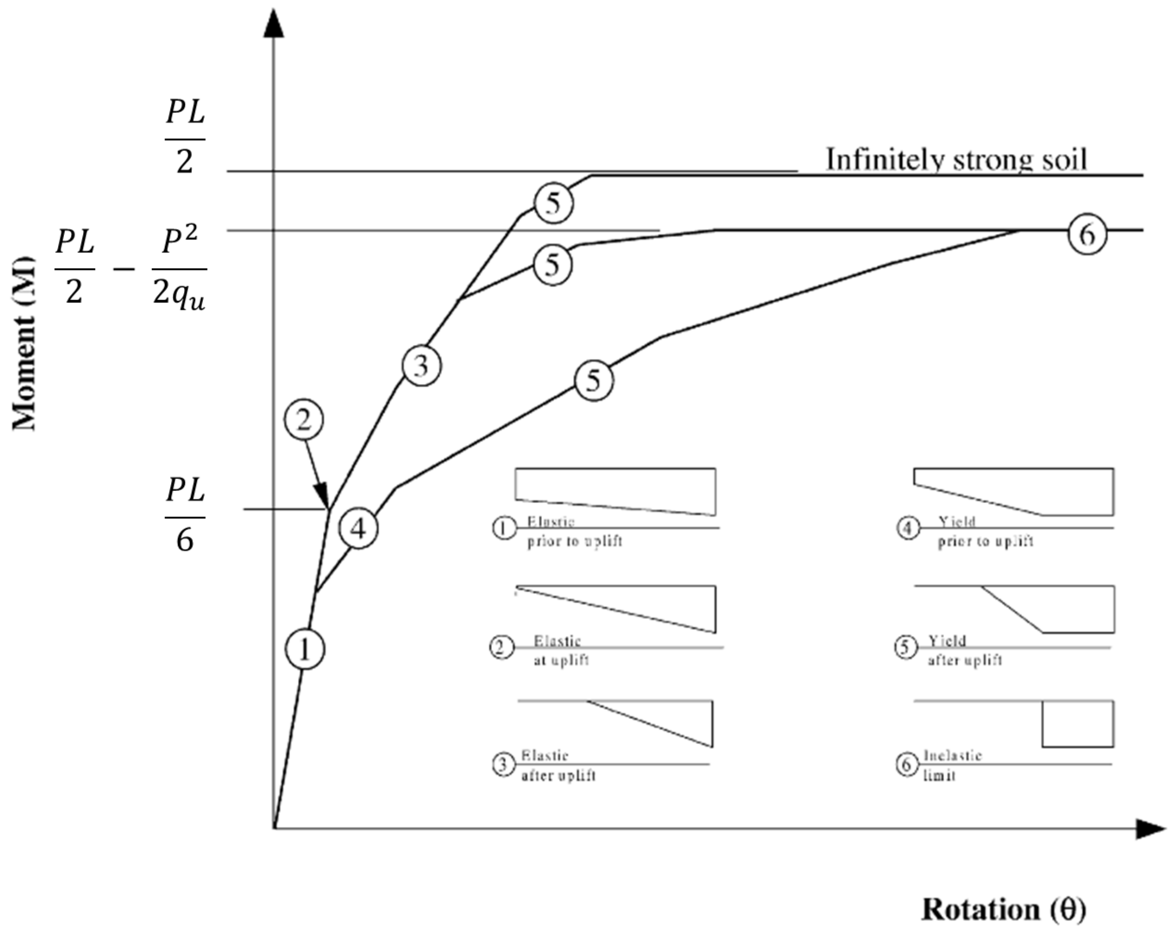

Figure 4.1 Schematics of the different states of foundation moment-rotation response - Figure from Allotey and El Naggar (2003).

The method introduces three non-dimensional parameters as follows:

$$\Psi = \frac{k_v L}{q_u} \quad \textbf{Eq 4.1}$$

$$\chi = \frac{P}{q_u L} \quad \textbf{Eq 4.2}$$

$$M_{qL} = \frac{M}{q_u L^2}$$ **Eq 4.3**

Where Ψ is a measure of the foundation initial elastic rotational stiffness, χ is an indicator of how heavily the foundation is loaded vertically, and M_{qL} is the normalized bending moment relating the actual bending moment M to foundation length and the soil ultimate bearing capacity. With the parameters defined, the complete moment-rotation response is expressed as

$$For\ \chi \leq \frac{1}{2}$$

$$M_{qL} = \begin{Bmatrix} \dfrac{\Psi\theta}{12} & 0 \leq \theta \leq \dfrac{2\chi}{\Psi} \\ \dfrac{\chi}{6}\left(3 - 2\sqrt{\dfrac{2\chi}{\Psi\theta}}\right) & \dfrac{2\chi}{\Psi} \leq \theta \leq \dfrac{1}{2\Psi\chi} \\ \dfrac{1}{2}(\chi - \chi^2) - \dfrac{1}{24\Psi^2\theta^2} & \theta \geq \dfrac{1}{2\Psi\chi} \end{Bmatrix}$$

$$For\ \chi > \frac{1}{2}$$ **Eq 4.4**

$$M_{qL} = \begin{Bmatrix} \dfrac{\Psi\theta}{12} & 0 \leq \theta \leq \dfrac{2(1-\chi)}{\Psi} \\ \dfrac{(1-\chi)}{6}\left(3 - 2\sqrt{\dfrac{2(1-\chi)}{\Psi\theta}}\right) & \dfrac{2(1-\chi)}{\Psi} \leq \theta \leq \dfrac{1}{2\Psi(1-\chi)} \\ \dfrac{1}{2}(\chi - \chi^2) - \dfrac{1}{24\Psi^2\theta^2} & \theta \geq \dfrac{1}{2\Psi(1-\chi)} \end{Bmatrix}$$

Allotey and El Naggar identify χ as being critical to the foundations behaviour. Foundations with χ less than 0.5 experience uplift before soil yielding and their design is not governed by the soil bearing capacity demand. In foundations with χ greater than 0.5, soil yielding occurs prior to uplift and soil bearing capacity is the governing design factor. Another important observation on χ is that the theoretical maximum bending moment capacity of the foundation occurs at χ = 0.5. Any other value of χ would result in a smaller ultimate bending moment capacity.

Allotey and El Naggar's method provides a complete closed-form solution for the foundation moment-rotation response. The major assumptions in the development of the formulas are linear variation of soil strain (i.e. rigid foundation), zero soil suction, and EPP behaviour for the soil under compression both of which are reasonable. EPP behaviour may not provide a good representation of the behaviour of many soils in compression. In addition, a simpler numerical approach is more likely to gain acceptance by the design codes and engineers. Therefore, there is a need for further simplification to the procedure for obtaining the foundation moment-rotation response. Sections 4.1.2 to 4.1.4 introduce the concept behind the proposed method for estimating the foundation moment-rotation response.

4.1.2 Soil spring backbone curves

The cyclic response of the soil is quite complex to predict mainly because of the sensitivity of the amount of nonlinear soil deformation accumulation due to cyclic softening of the soil to the input ground motion. To simplify the process, this section and the subsequent sections in this chapter focus on formulating a simple method for predicting the response of shear walls with flexible foundation taking into account the response of the soil in monotonic compression. QzSimple1 material in OpenSees introduced in Section 3.2.3 is used to simulate the response of the soil. See Figure 3.7 for backbone curves of QzSimple1 material for clay and sand type soils.

4.1.3 Foundation response in elastic range

The rotational stiffness of the foundation in its linear elastic range is given by Gazetas as follows.

$$K_{\theta y} = e_{\theta y} K'_{\theta y} \qquad \textbf{Eq 4.5}$$

$$e_{\theta y} = 1 + 0.92(\frac{2d}{L})^{0.62} \left[1.5 + (\frac{2d}{L})^{1.9}(\frac{d}{D})^{-0.60}\right] \qquad \textbf{Eq 4.6}$$

$$K'_{\theta y} = \frac{G}{1-\nu} I_y^{0.75} \left[3(\frac{L}{B})^{0.15}\right] \qquad \textbf{Eq 4.7}$$

Where

$$I_y = \frac{BL^3}{12}$$ **Eq 4.8**

In these equations, L is the foundation length, B is the foundation width, d is the thickness of the foundation, D is the depth at which the foundation is placed, ν is the Poisson's ratio of the soil, and G is the shear modulus of elasticity of the soil. The soil reaction modulus (compressive displacement per unit pressure) which would result in an elastic stiffness equal to that given by Gazetas would be

$$k_\theta = \frac{K_{\theta y}}{I_y}$$ **Eq 4.9**

If the clay QzSimple1 material is used, G_{eff} must be substituted for G in Eq 4.7 as G_{eff} will result in the correct initial rotational stiffness of foundations on clay type soils (see

Figure 3.11). If the sand QzSimple1 material is used, G_0 must be used as the shear modulus in Eq 4.7 as the initial rotational stiffness of foundations on sand type soils is governed by G_0 (see Figure 3.12). This way, $K_{\theta y}$ will always be equal to true initial rotational stiffness of the foundation and k_θ will represent the initial elastic reaction modulus of the soil. Z_{50} (the displacement required to mobilize $0.5q_{ult}$) could then be calculated from the soil reaction modulus as follows.

$$Z_{50} = \frac{q_{ult}}{2k_\theta} \qquad \textit{for clay}$$ **Eq 4.10**

$$Z_{50} = \frac{q_{ult}}{2k_\theta} \times 2.65 \qquad \textit{for sand}$$ **Eq 4.11**

The 2.65 factor for sand is incorporated to adjust for the ratio of G_0/G_{eff} for sand (compare Figure 3.12 to Figure 3.11). As soon as either the foundation lifts off or the soil at the "toe" of the foundation enters the nonlinear response phase, the response of the foundation begins to soften and Gazetas' elastic stiffness is no longer valid. To find the elastic response limit of the foundation, two scenarios need to be considered. The first is the case where lift-off occurs prior to nonlinear soil response at the "toe" of the foundation (see Figure 4.2a). This is more likely to be the case for foundations bearing a small axial load. In this case, the elastic response limit $\theta_{elastic}$ can be calculated as follows.

$$\theta_{elastic} = \frac{2P}{k_\theta B L^2} \qquad \textbf{Eq 4.12}$$

Provided that

$$q_{max} = \frac{2P}{BL} \leq 0.20 q_{ult}\ for\ clay\ or\ 0.30 q_{ult}\ for\ sand \qquad \textbf{Eq 4.13}$$

The second scenario is when lift-off is preceded by nonlinear soil response at the “toe” of the foundation (Figure 4.2b). This is more likely to be the case for foundations bearing a large axial load in which case, the elastic response limit is calculated as follows.

$$\theta_{elastic} = \frac{2}{L}\left[Z_{max} - \frac{P}{k_\theta BL}\right] \qquad \textbf{Eq 4.14}$$

Provided that

$$q_{max} = \frac{2P}{BL} > 0.20 q_{ult}\ for\ clay\ or\ 0.30 q_{ult}\ for\ sand \qquad \textbf{Eq 4.15}$$

Where Z_{max} is the compressive displacement of the soil at the “toe” of the foundation and can be calculated as

$$Z_{max} = \frac{0.20 q_{ult}}{k_\theta}\ for\ clay\ or\ \frac{0.30 q_{ult}}{k_\theta}\ for\ sand \qquad \textbf{Eq 4.16}$$

The bending moment at the foundation’s elastic limit would then be

$$M_{elastic} = K_{\theta y} \cdot \theta_{elastic} \qquad \textbf{Eq 4.17}$$

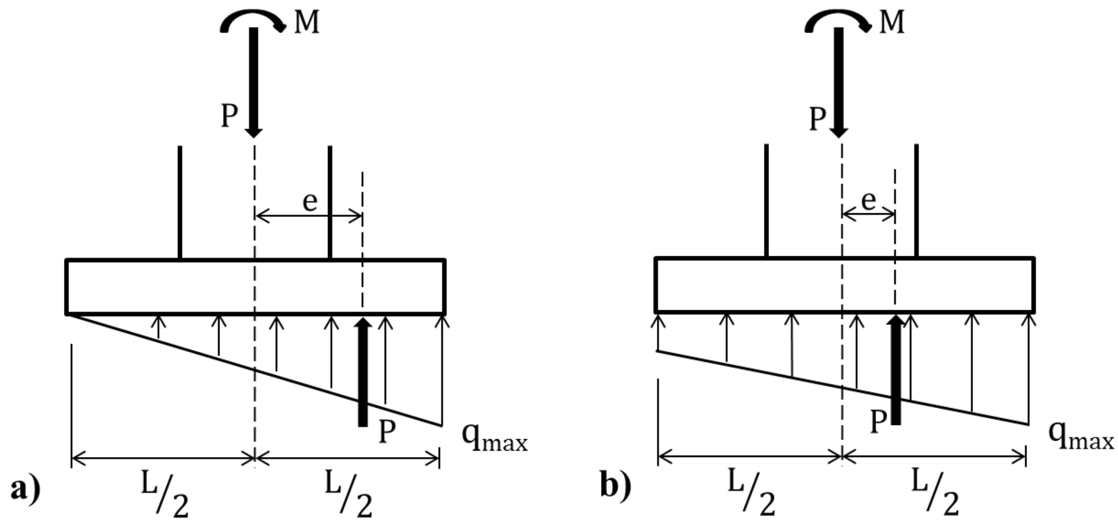

Figure 4.2 Elastic response limit of foundations: a) liftoff occurring prior to nonlinear soil behaviour (low axial load), and b) nonlinear soil behaviour occurring prior to liftoff (high axial load).

4.1.4 Equivalent rectangular stress block (ERSB) concept

Unlike the linear range, predicting the nonlinear response of foundations is much more complex. The actual bearing pressure distribution underneath the foundation will no longer be linear and the location of the resultant force from the soil bearing pressure distribution can no longer be calculated as easily as that in the elastic range. The onset of lift-off is greatly dependent on the magnitude of compressive axial force on the wall and the stiffness of the underlying soil. The compression depth of the foundation, the length of the foundation which is in contact with the soil at a given rotation, is also not easy to determine.

To overcome these complexities, a general method is developed that can predict foundation rotation for a given eccentricity (or bending moment). The method uses a concept similar to the equivalent rectangular stress block used in section analysis of reinforced concrete members. The distinctions are that the soil monotonic compression response is used instead of the concrete stress-strain relationship and that no soil tension (or suction) is considered.

Figure 4.3 demonstrates the equivalent rectangular stress block concept for a foundation of length L and width B sitting on a soil with an ultimate bearing pressure of q_{ult}. A snapshot of the actual bearing pressure distribution underneath the footing at a large rotation is shown in solid line. Because no tension or suction was included, the bearing pressure has dropped to zero where lift-off has occurred. The compression depth of the foundation and the maximum bearing pressure are shown as 'c' and q_{max} (as a ratio of q_{ult}) respectively. The location of the centroid of the area underneath the actual soil bearing pressure is shown as the dotted line. The dashed line is the equivalent rectangular bearing pressure distribution for the given actual bearing pressure. The rectangular block has a maximum bearing pressure of $q_{unif.}$ (as a ratio of q_{ult}) and width of 'a'. The area enclosed by the dashed line is equal to the area underneath the solid line. This ensures that both the actual and the equivalent rectangular bearing pressure distributions produce the same resultant force. In addition to the magnitude of the resultant bearing pressure, the location of the resultant force from the two bearing pressure distributions are also identical as the equivalent rectangular block is placed such that its centroid coincides with that of the actual bearing pressure distribution. In summary, the two bearing pressure distributions in Figure 4.3 have the same resultant axial force and the same resultant bending moment.

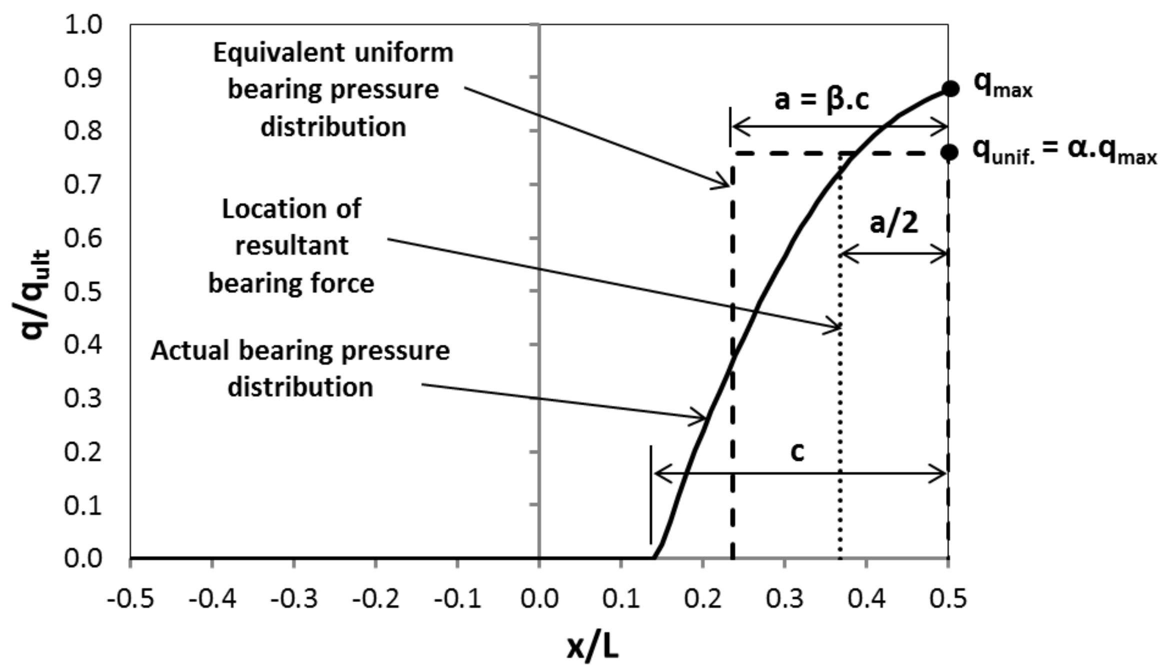

Figure 4.3 Equivalent rectangular stress block concept for soil bearing pressure.

In order to study the relationship between the equivalent rectangular and the actual soil bearing pressure distribution in the nonlinear range, a few parameters need to be defined. α is the ratio of the constant bearing pressure of the equivalent uniform stress distribution to the maximum actual soil bearing pressure at the "toe". β is the ratio of the depth of the equivalent uniform bearing pressure distribution to the actual bearing pressure depth (see Figure 4.3 for visual definitions of α and β). To get the foundation rotation for a given stress distribution, the maximum soil compressive displacement also needs to be known to combine with the actual compression depth. Hence, a third parameter is defined as follows.

$$\gamma = \frac{Z_{max}}{Z_{50}} \qquad \textbf{Eq 4.18}$$

Where Z_{max} is the maximum soil compressive displacement at the toe and Z_{50} is the displacement at which 50% of q_{ult} is mobilized (see Eq 4.10 and Eq 4.11 for definition of Z_{50}).

To formulate a general method that could be applied to any rectangular foundation with any size, aspect ratio, and axial load, all the necessary calculations were performed in a non-dimensional space.

Consider a foundation with length L and width B with 100 equally-sized soil elements placed underneath the foundation and the axial load P applied to it. For any certain amount of rotation θ imposed on the foundation, the compression depth 'c' was found that would result in vertical force equilibrium. Once force equilibrium was established, the magnitude of the axial load multiplied by the distance from the wall centreline to the location of the resultant bearing pressure gave the bending moment required to impose the rotation. θ was then increased gradually to conduct a pushover analysis on the foundation and sweep the entire range of foundation response from elastic to highly nonlinear soil responses. In each sweep, the three parameters α, β, and γ were recorded.

Figure 4.4 shows the behaviour of the three parameters for a foundation sitting on a series of Clay QzSimple1 elements. Three curves are shown in each plot each for a given axial load. Note that the highest axial load considered results in a uniform bearing pressure under service load conditions equal to 0.30qult. This is considered to be the upper limit of allowable soil bearing pressure under service condition for most deformable soils such as clay and sand. All three parameters proved to be independent of the magnitude of the axial load applied to the foundation beyond the foundation lift-off which falls into the elastic response range of the foundation. Note that the elastic response of the foundation was solved in Section 4.1.3. A similar trend was observed for foundations sitting on Sand QzSimple1 elements (see Figure 4.5). Response of the foundation on Sand elements prior to lift-off is not shown in Figure 4.5.

With this observations, the numerical values of the three parameters are tabulated in Table 4.1 for both Clay and Sand type soils at various ratios of $q_{unif.}/q_{ult}$. Below is a step by step procedure for estimating the moment-rotation response of any rectangular foundation on either Clay or Sand type soils.

1. Choose a value of $\frac{q_{unif.}}{q_{ult}}$ and calculate $q_{unif.}$
2. Find ‘a’ from vertical force equilibrium as follows

   $$a = \frac{P}{B \times q_{unif.}} \qquad \textbf{Eq 4.19}$$

3. Calculate the bending moment as

   $$M = P.e \qquad \textbf{Eq 4.20}$$

   where

   $$e = \frac{L-a}{2} \qquad \textbf{Eq 4.21}$$

4. Calculate the rotation as

   $$\theta = \frac{Z_{max}}{c} = \beta\gamma\frac{Z_{50}}{a} \qquad \textbf{Eq 4.22}$$

5. Repeat steps 1 through 4 for other values of $\frac{q_{unif.}}{q_{ult}}$

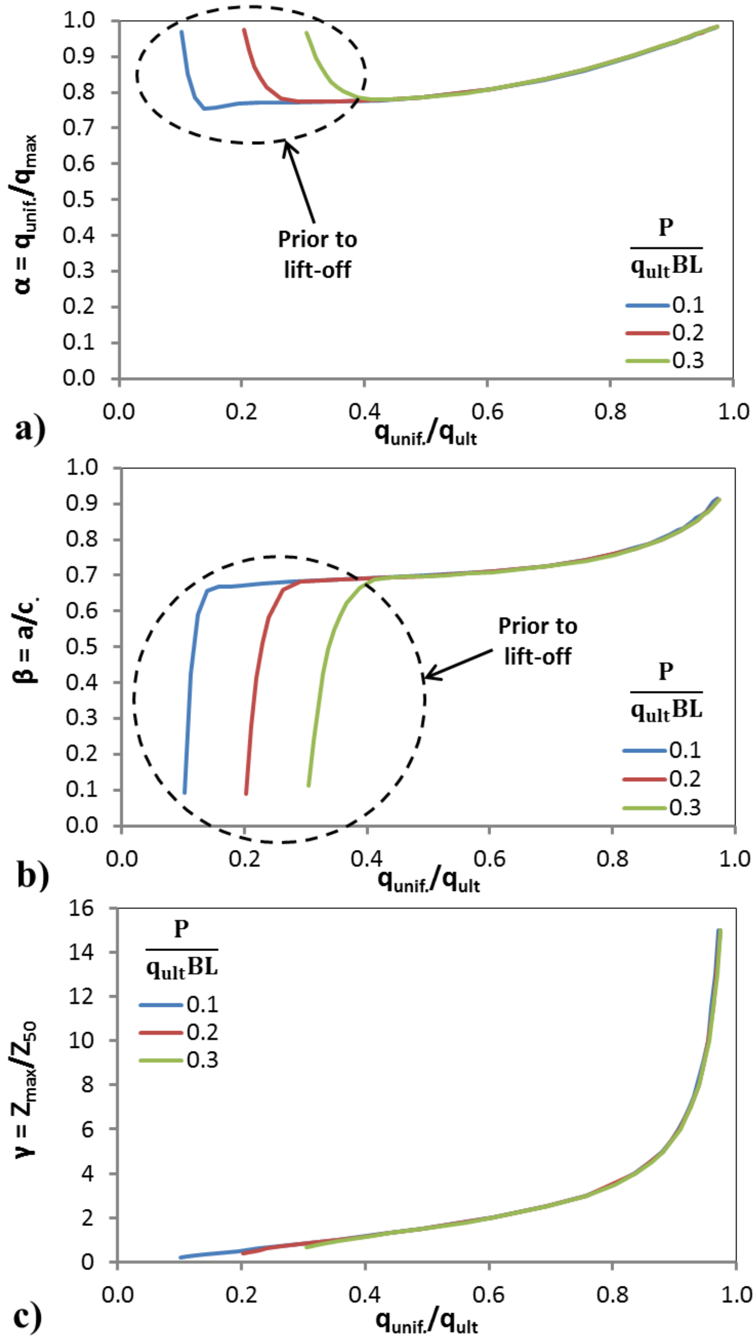

Figure 4.4 Variation of the three key parameters of the equivalent rectangular pressure block concept with vertical compressive load for clay type soils.

The bending moment at $\frac{q_{unif.}}{q_{ult}} = 0.95$ is very close to maximum bending moment that the foundation can resist (without considering any soil suction). Therefore, it is safe to assume that the foundation moment-rotation response is a flat line beyond $\frac{q_{unif.}}{q_{ult}} = 0.95$.

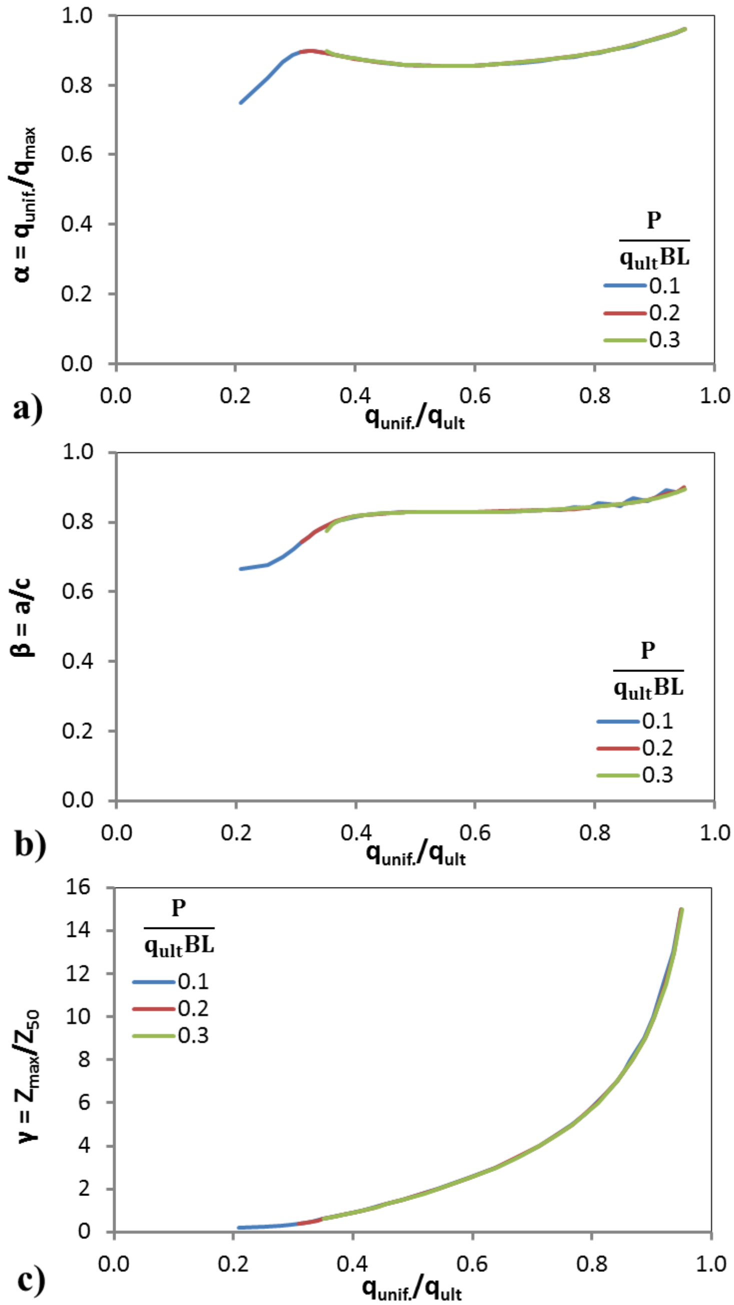

Figure 4.5 Variation of the three key parameters of the equivalent rectangular pressure block concept with vertical compressive load for sand type soils.

Table 4.1 Equivalent rectangular stress block parameters for Clay and Sand type soils.

	Clay			Sand		
$q_{unif.}/q_{ult}$	$\alpha = q_{unif.}/q_{max}$	$\beta = a/c$	$\gamma = Z_{max}/Z_{50}$	$\alpha = q_{unif.}/q_{max}$	$\beta = a/c$	$\gamma = Z_{max}/Z_{50}$
0.40	0.78	0.69	1.2	0.88	0.82	0.9
0.45	0.78	0.70	1.3	0.86	0.83	1.3
0.50	0.79	0.70	1.5	0.86	0.83	1.6
0.55	0.80	0.70	1.8	0.85	0.83	2.1
0.60	0.81	0.71	2.0	0.86	0.83	2.6
0.65	0.82	0.72	2.3	0.86	0.83	3.1
0.70	0.84	0.73	2.6	0.87	0.83	3.8
0.75	0.86	0.74	2.9	0.88	0.84	4.7
0.80	0.88	0.76	3.5	0.89	0.85	5.8
0.85	0.91	0.78	4.3	0.91	0.85	7.3
0.90	0.94	0.82	5.7	0.93	0.87	9.8
0.95	0.97	0.87	9.3	0.96	0.90	14.9

4.1.5 Example predicted foundation moment-rotation curves

The accuracy of foundation moment-rotation response predicted using the simple method described in the previous sections is verified against moment-rotation responses obtained from pushover analysis carried out in OpenSees. Figure 4.6a compares moment-rotation responses of a 19 m square foundation sustaining a vertical compressive force of 41550 kN on Clay in OpenSees with that obtained using the simple procedure outlined in the previous sections. Figure 4.6b repeats the comparison for a 15 m square foundation on Medium Sand.

For both Clay and Medium Sand, the elastic solution and the points in the low and medium nonlinear soil response ranges match the response obtained from OpenSees. In the high nonlinear soil response stages (large rotations) however, the response obtained from OpenSees gives larger bending moments than those predicted using the simple method. This is attributed to the inevitable inclusion of a small amount of soil suction (about $0.005q_{ult}$) in the soil elements in OpenSees to facilitate the numerical procedures required to achieve convergence in each analysis time step. This minimum suction is included in the analysis even if zero soil suction is assigned to the soil elements and cannot be avoided.

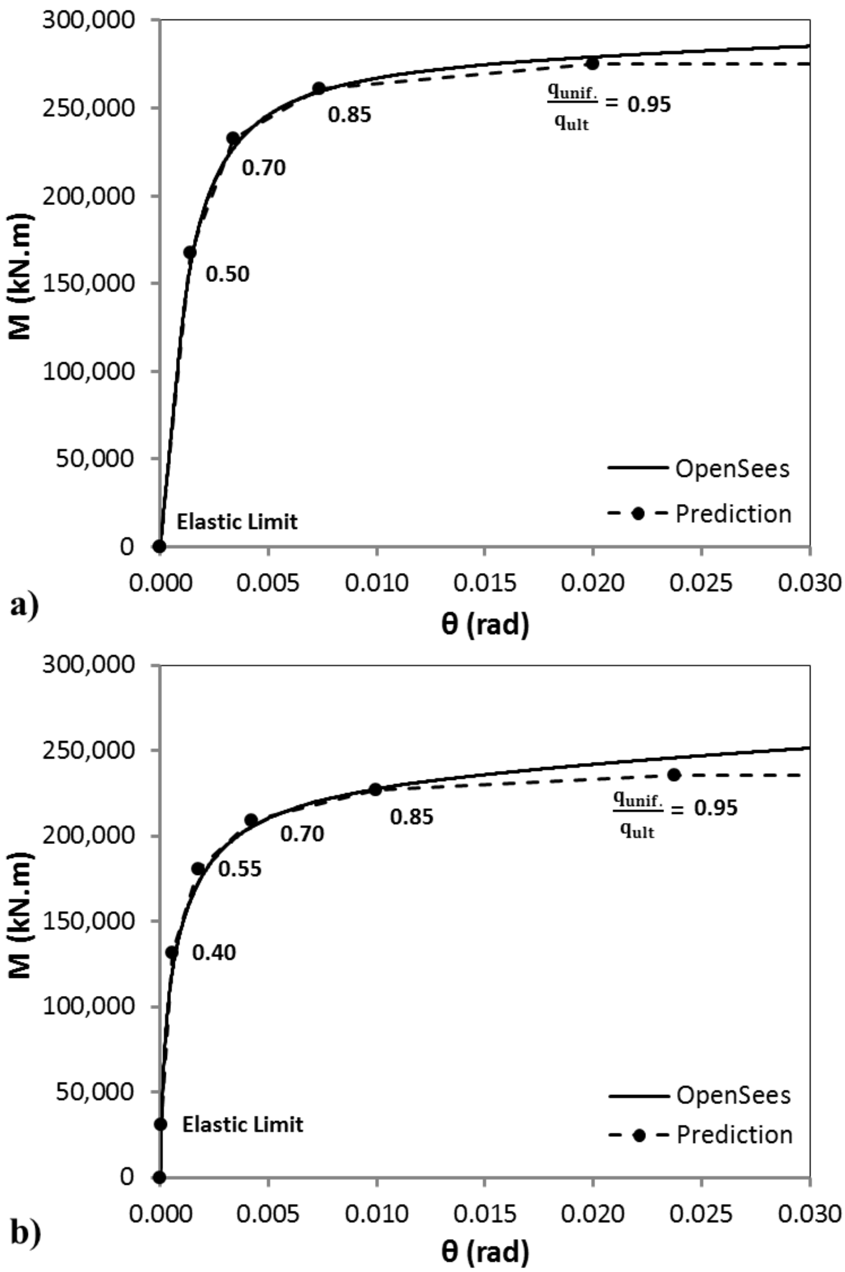

Figure 4.6 Example: verification of the proposed equivalent uniform soil bearing pressure method for estimating moment-rotation response of a) a 19 m square footing on Clay and b) a 15 m square footing on Medium Sand (see Section 3.2.4 for soil specifications).

The amount of suction in each soil element increases as the gap between the soil spring and the foundation increases and consequently, the bending moment resisted by the foundation increases steadily at a slow rate. This artificial foundation over-strength becomes problematic only at foundation rotations greater than 0.02 rad while the maximum foundation rotation recorded in the NTHA in CHAPTER 3 was less than 0.012 rad and well below 0.02. This phenomenon is considered to be a limitation of the QzSimple1 model. Despite this fact, it does not hinder the legitimacy of the Nonlinear Time-History Analysis (NTHA) done with QzSimple1 elements in this study because the recorded foundation rotations did not exceed 0.012.

Note how well the envelope of the foundation moment-rotation response can be estimated using five or six points and with some simple calculations using information that is readily available to the designer. It must not be forgotten that the hysteretic moment-rotation response of a foundation is highly dependent on the number of highly nonlinear soil compression cycles and that the proposed method only predicts the envelope of the hysteretic response. However, as will be shown, the envelope of the foundation moment-rotation response is very useful in estimating foundation rotation of a given wall-foundation system as described earlier in CHAPTER 3. Importance of the foundation moment-rotation response is further illustrated in Section 4.3.

4.2 Estimating Top Wall Displacement

This section presents a simple method for estimating top displacement of a given shear wall accounting for rotation of its foundation. It must be noted that whenever the term top wall displacement is used, it stands for the total wall deformation resulting from rotation of the foundation plus the flexural deformation of the wall. Other possible sources of wall deformation such as shear strain or bar slip are not accounted for.

Figure 4.7 shows the concept behind the simple method for estimating top displacement of walls with flexible foundation presented in this section. On the left hand side, a state of the art modeling technique for simulating the wall-foundation system is shown. The wall is made out of sections with reinforced concrete fibres having nonlinear stress-strain relationships for both steel reinforcement and concrete. The foundation is sitting on QzSimple1 soil elements which can simulate foundation liftoff and the nonlinear behaviour of the soil in cyclic compression and radiation damping. This type of numerical model was subjected to NTHA in CHAPTER 3 with ground motions spectrally-matched to the Uniform Hazard Spectrum (UHS).

On the right hand of the figure, an elastic wall with the same height and the floor mass distribution is shown which has an elastic rotational spring of stiffness K_e at its base. Response Spectrum Analysis (RSA) can be carried out on this simplified structure using the UHS as the input spectrum. Resources needed to carry out such numerical modeling are readily available to any designer. The goal of this section is to provide the appropriate elastic stiffness of the wall and the rotational spring at the base of the simplified structure such that the two structures shown in Figure 4.7 would have the same top displacement.

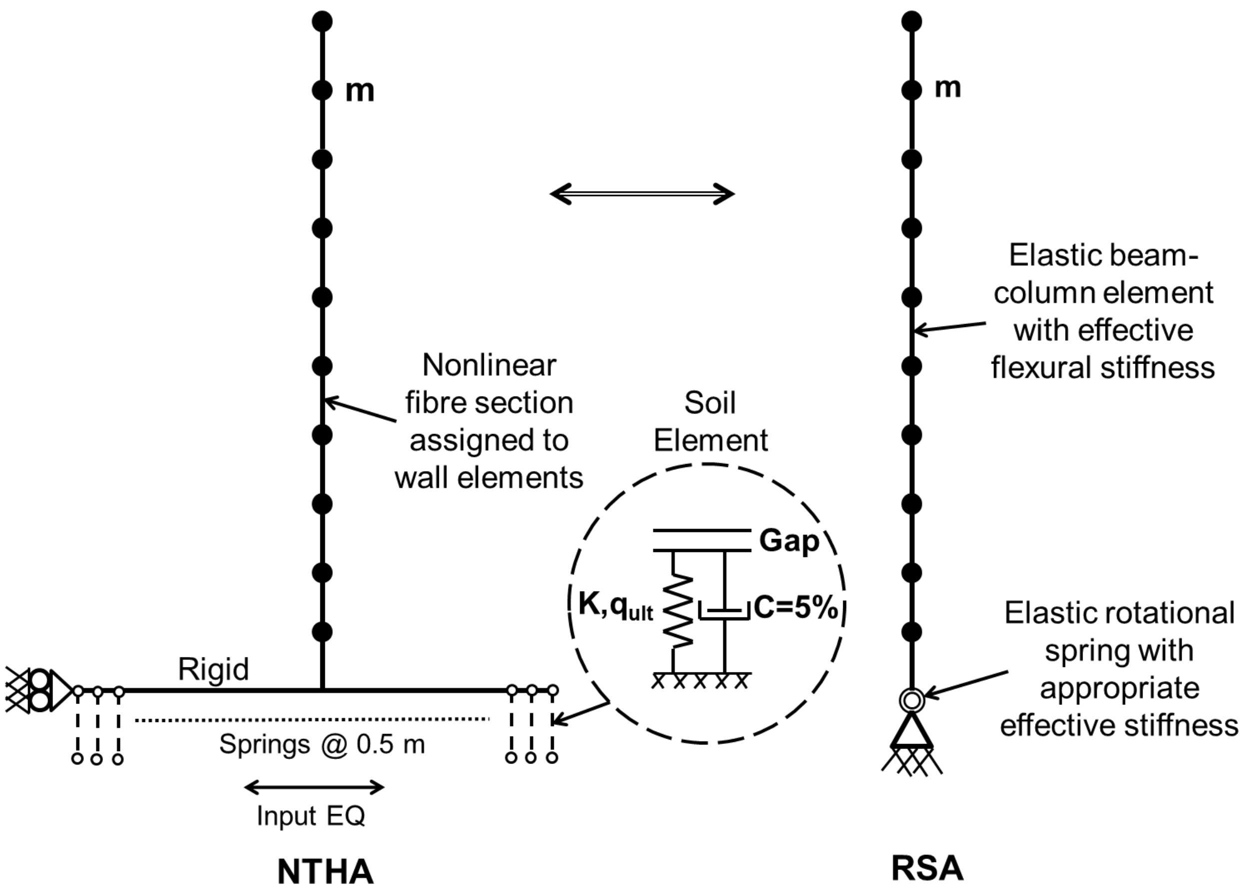

Figure 4.7 Estimating top displacement of nonlinear shear walls with a flexible foundation from RSA of an equivalent elastic wall with a rotational spring at its base.

To start, an effective flexural stiffness must be chosen for the elastic wall in the simplified structure. Results of the Core NTHA presented in Section 3.6 will be used to formulate the method; therefore, flexural stiffness of the wall in the simplified structure needs to be adjusted for each of the four nonlinear walls used in the Core NTHA. Flexural stiffness of the elastic wall in the simplified structure was chosen such that the top displacement of the fixed-base elastic wall from RSA matched the average of top displacement envelopes obtained from NTHA of the nonlinear fixed-base walls subjected to the 10 spectrally-matched ground motions.

Figure 4.8 summarizes the process of choosing the effective flexural stiffness for the elastic wall. RSA was carried out on a 10 storey wall with 6 different elastic stiffnesses for the wall as a ratio of the wall's uncracked gross moment of inertial to get the solid curve in Figure 4.8. Average top displacement envelopes obtained from NTHA for the four nonlinear walls using the 10 spectrally-matched ground-motions were then plotted as dots on the solid curve. The interpolated appropriate effective stiffnesses are shown on the same figure as a ratio of the uncracked gross flexural stiffness. As expected, the weaker the wall, the more the expected nonlinear action and therefore, the more the equivalent elastic wall needed to be softened.

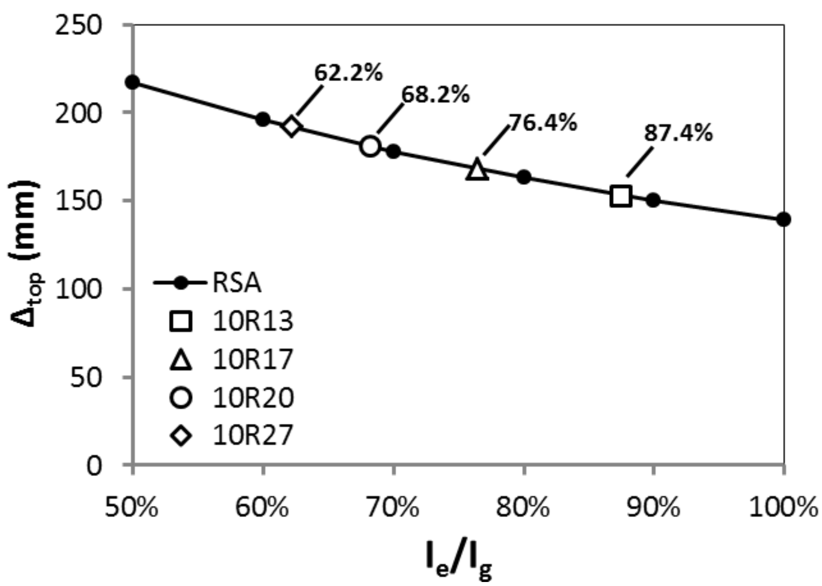

Figure 4.8 Effective flexural stiffness of elastic 10-storey shear walls to match the average maximum top displacement of the fixed-base nonlinear walls from NTHA.

Dezhdar (2012) investigated the parameters influencing the effective stiffness of shear walls and showed that the parameter influencing the effective stiffness the most was the ratio of elastic force demand to strength (i.e. R_w in this study). Dezhdar reports that as R_w increases from 1.0 to 5.0, the effective stiffness of the elastic wall as a ratio of the uncracked gross stiffness reduces from 1.0 to 0.5. This is consistent with the results shown in Figure 4.8 as the effective stiffness ratios ranged from 0.87 to 0.62 while R_w varied from 1.3 to 2.7. The following equation was recommended to be incorporated in CSA A23.3-14 based on the work of Dezhdar. The term $R_d R_0/\gamma_w$ is equivalent to R_w as defined in this study.

$$\frac{I_e}{I_g} = 1 - 0.35\left(\frac{R_d R_0}{\gamma_w} - 1.0\right) \geq 0.5 \qquad \textbf{Eq 4.23}$$

With the effective flexural stiffness of the wall selected from Figure 4.8, elastic walls with appropriate effective flexural stiffness were analyzed using RSA over a wide range of stiffnesses for the elastic rotational spring at their base to generate the four curves shown in Figure 4.9. The figure shows the curves over the entire range of rotational spring stiffnesses used. Note how above a certain elastic rotational stiffness, the maximum top wall displacement remains nearly constant and very close to that of the fixed-base wall.

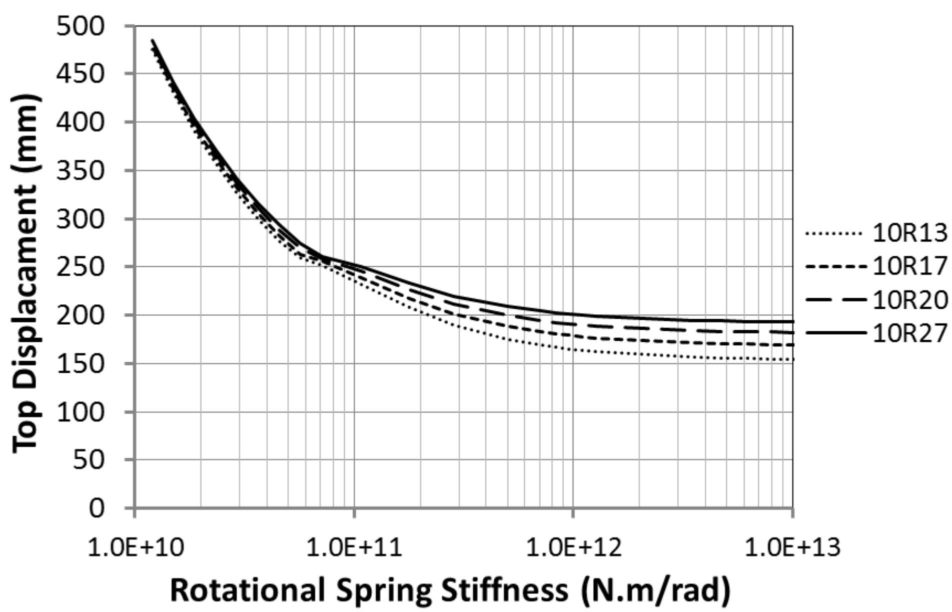

Figure 4.9 Top displacements of elastic 10-storey shear walls with appropriate effective flexural stiffness obtained from RSA with various elastic rotational spring stiffnesses at the base.

In the next step, the appropriate rotational spring stiffness required to match the average of top displacement envelopes from the Core NTHA was interpolated from the curves in Figure 4.9. This was done for each of the four nonlinear walls and for each of the five soil types and for each of the five smallest foundation sizes (i.e. the five largest R_f's) modeled on each type of soil considered in the Core NTHA. This generated 100 data points (see Figure 4.12) which were then used to formulate a simple equation for the effective stiffness of the elastic rotational spring that must be used at the base of the simplified structure in Figure 4.7 to get the correct top wall displacement.

To explain general trends observed in the data, data points for clay are presented next. Figure 4.10 shows the 20 data points for clay. On the top plot, the data points are grouped by foundation strength and plotted against wall strength. On the bottom plot, the same data points are presented but this time the data points for the same wall strength are connected and plotted against foundation strength.

The vertical axis of both plots in Figure 4.10 is K_e/K_{oc}. K_e is the effective elastic rotational spring stiffness required for the simplified structure to have the target top displacement of the complex structure obtained from NTHA. K_{oc} is the secant stiffness of the foundation moment-rotation response to the point of calculated overturning capacity. In other words,

$$K_{oc} = \frac{M_{oc}}{\theta_{oc}} \qquad \textbf{Eq 4.24}$$

Where M_{oc} is the foundation overturning capacity calculated using a uniform soil stress block of q_f=0.5q_{ult} and θ_{oc} is the rotation at the point with ordinate of M_{oc} on the foundation moment-rotation response. From the simple method for estimating the foundation moment-rotation response presented in Section 4.1, K_{oc} could be calculated using the basic soil and foundation properties available to the designer.

Figure 4.10a shows that K_e/K_{oc} is strongly influenced by the wall strength. Stronger walls (smaller R_w's) induced larger base bending moments that increased foundation rotation. Therefore, a softer elastic rotational spring was needed for the simplified structure. Figure 4.10b reveals that K_e/K_{oc} is also dependent on the foundation strength. Values of K_e/K_{oc} are larger for stronger foundations (smaller R_f's). This not surprising as stronger foundations are likely to experience less softening of the soil and therefore, their secant stiffness is less reduced compared to their K_{oc}. Weaker walls resulted in larger secant stiffnesses because wall yielding prevented large bending moments to be transferred to the foundation which made for smaller foundation rotation and therefore, less softening of the foundation response.

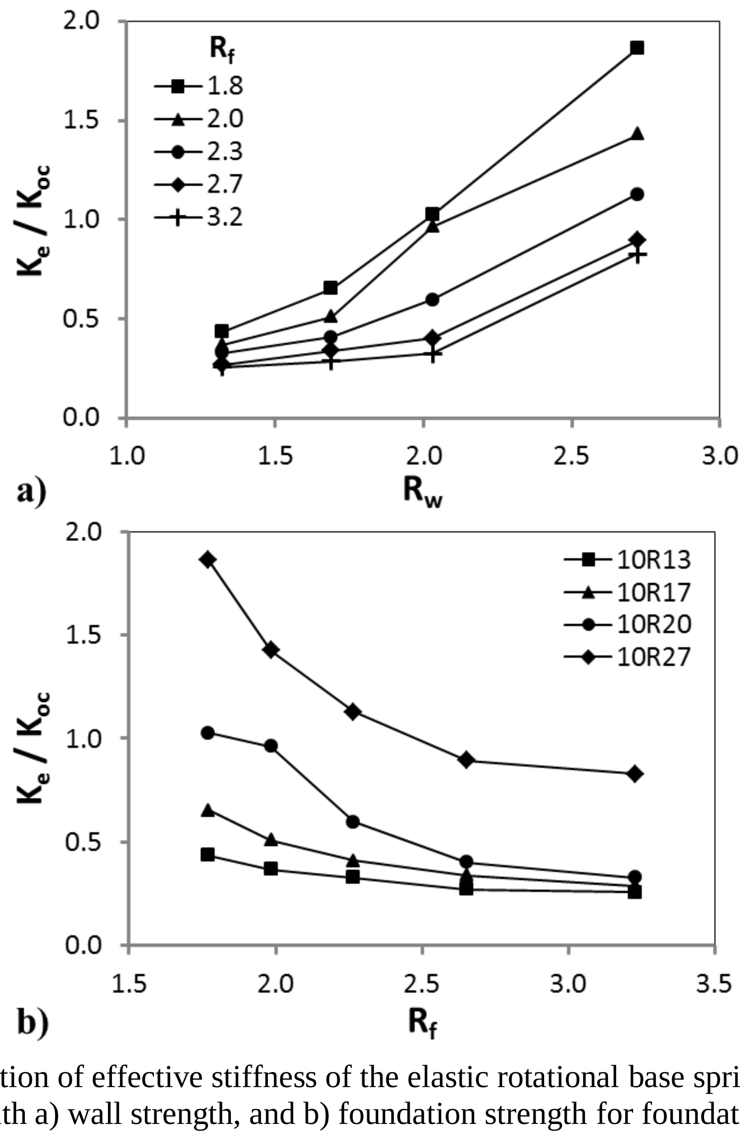

Figure 4.10 Variation of effective stiffness of the elastic rotational base spring of the simplified structure with a) wall strength, and b) foundation strength for foundations on Clay.

K_e/K_{oc} is therefore a function of both wall strength and foundation strength. In Figure 4.11, the same 20 data points of Figure 4.10 are plotted against R_w/R_f. The term R_w/R_f translates to the foundation to wall strength ratio. The data points seem to follow a single curve reasonably well. In this case, an exponential curve gives a good fit with a convergence factor of 0.95 (see Figure 4.11b).

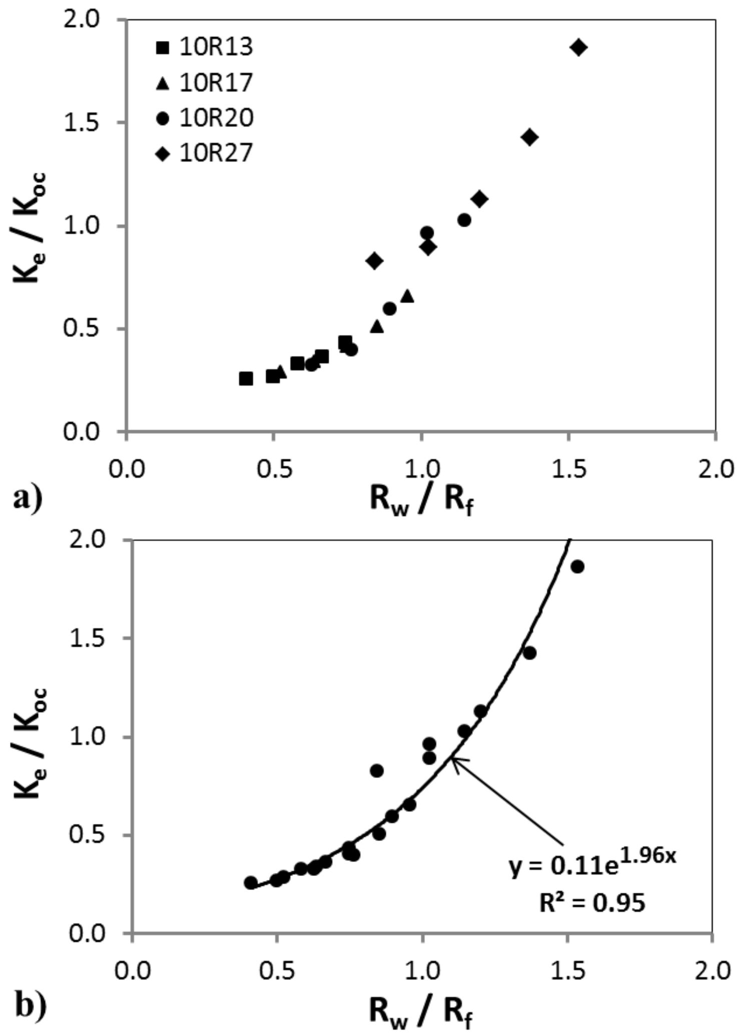

Figure 4.11 Variation of effective stiffness of the elastic rotational base spring of the simplified structure with relative foundation to wall strength for foundations on Clay.

The trend observed above in clay foundations and the conclusions made for clay equally apply to data points from the other 4 types of soil. Figure 4.12 presents all of the 20 data points for the five types of soil totaling 100 data points. From Figure 4.12a, it is obvious that when data points for all five soil types are put together, they do not quite follow the nice trend that was observed by looking at data points for a single soil type. The data points which seem to deviate a lot from the rest are those for Loose Sand while the rest are not far off from an exponential curve (see Figure 4.12b). This can be explained by comparing properties of Clay and Loose Sand.

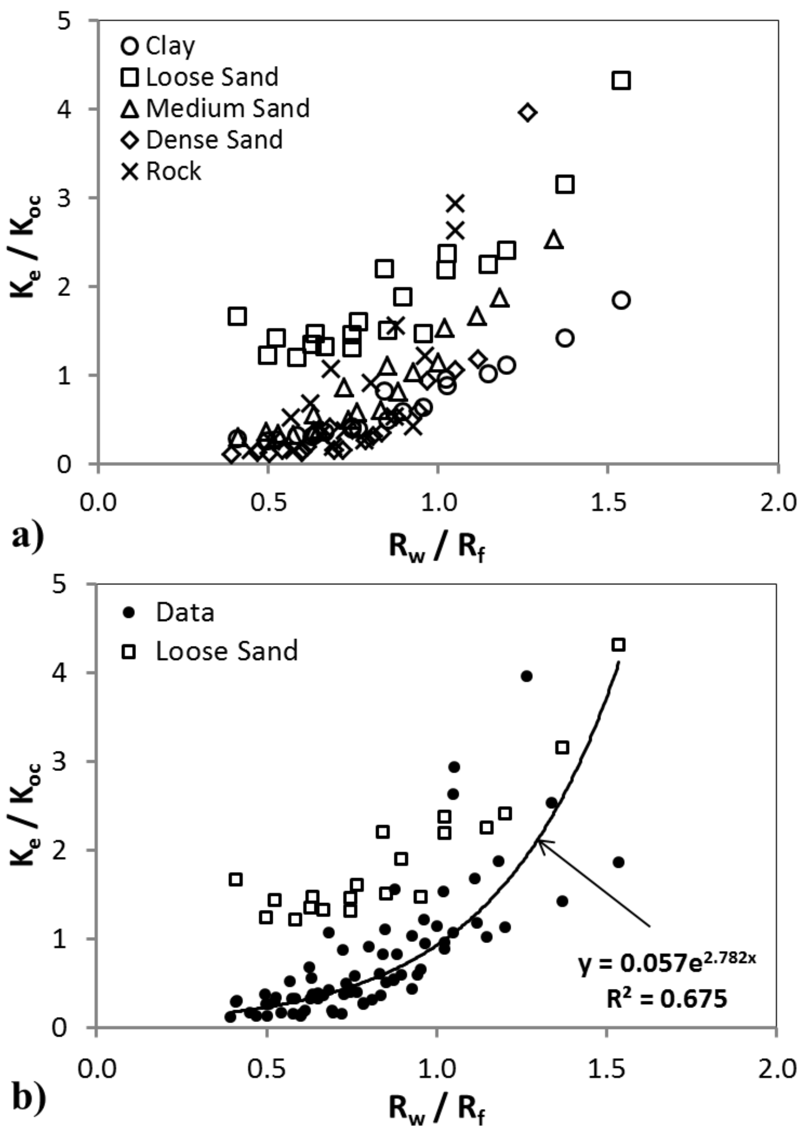

Figure 4.12 Variation of effective stiffness of the elastic rotational base spring of the simplified structure with relative wall to foundation strength for foundations on all five types of soil.

Strength and effective stiffness of Loose Sand were deliberately chosen to be the same as those for Clay to study the effect of the shape of the backbone curve for the soil elements on the response of shear walls with flexible foundations. For each wall, even for the same foundation size, the averages of top wall displacement envelopes were considerably different for Clay and Loose Sand despite the two foundations having the same R_f. This was solely because of the fundamental differences in the hysteretic behaviour of QzSimple1 clay and sand models. Loose Sand elements were much stiffer than clay elements in the elastic range but beyond $0.30q_{ult}$, they softened rapidly which resulted in severe ratcheting down of the soil surface beneath the foundation. Clay elements on the other hand started with a lower elastic stiffness but held on to most of that initial stiffness up to 0.50 q_{ult}. Also because soil rebound always occurred with the initial elastic stiffness, Loose Sand elements experienced a much smaller rebound than Clay elements. These fundamental differences in loading and unloading stiffnesses lead to the soil surface underneath the foundation to be much more rounded for Clay than for Loose Sand with the foundations on Loose Sand having experienced a larger permanent compressive displacement underneath their centreline. The surface of the soil being more rounded for Clay caused larger foundation rotations and consequently larger top wall displacements than the case where the same wall-foundation system was placed on Loose Sand (compare results for Clay and Loose Sand in Appendix A). Having drastically different target displacements in the interpolation process used to get K_e resulted in the data for Loose Sand to stand out from the rest of the pack. Therefore, Loose Sand data was eliminated from the curve fitting process in Figure 4.12b.

Another way of explaining the drastically different behaviour of the Loose Sand data is to compare the foundation moment-rotation response of a foundation on Loose Sand with foundations of the same R_f on other types of soil. Figure 4.13 shows moment-rotation responses of a foundation with R_f of 2.0 on Clay, Loose Sand, and Medium Sand. The rotation at which the factored overturning capacity is reached (θ_{oc}) is marked with a hollow circle. Note that the slope of the line connecting the origin to the hollow dots is K_{oc}.

Average of foundation rotation envelopes from NTHA of each foundation supporting wall 10R13 is marked with the solid dots. The foundations on Clay and Medium Sand experienced larger rotations than the foundation on Loose Sand. The larger the foundation rotation, the softer the elastic rotational spring at the base of the simplified structure needs to be to match the total top wall displacement of the nonlinear wall-foundation system. In other words, K_e is closely related to the slope of the line connecting the origin to the point marked with the solid dot. The foundations on Clay and Medium Sand have almost the same K_{oc} and because the slopes of the lines connecting the origin to the solid dots on the two moment-rotation response are also close, the two foundations will end up having values of K_e/K_{oc} which are very close to one another.

K_{oc} of the foundation on Loose Sand is smaller than the other two foundations. In addition, the foundation experienced a much smaller average rotation from NTHA. This means that K_e of the foundation on Loose Sand would be larger than the other two foundations. Both of these effects contribute to the value of K_e/K_{oc} for the foundation on Loose Sand being much larger than those for the foundations on Clay and Medium Sand.

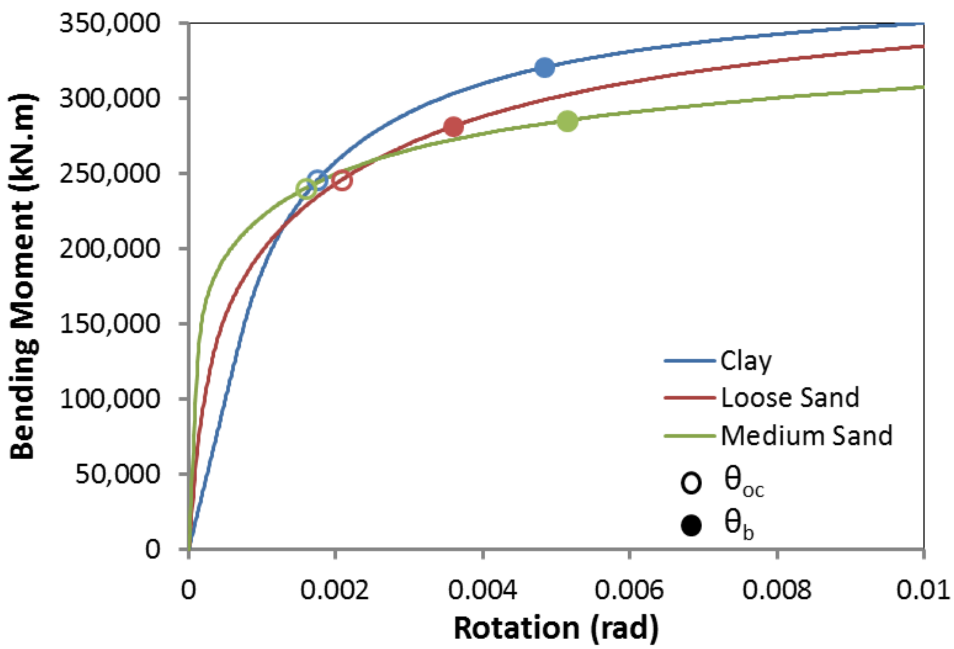

Figure 4.13 Comparison of moment-rotation responses, θ_{oc} and θ_b of foundations with R_f of 2.0 on Clay, Loose Sand, and Medium Sand supporting wall 10R13.

Values of K_e could have been normalized by the initial elastic stiffness of the foundation given by Gazetas' equation (i.e. $K_{\theta y}$) instead of K_{oc} (see Figure 4.14). In this case, the data points for Clay and Loose Sand are spread over the same area. This can be explained by looking at

Figure 4.13 again. The initial stiffness of the foundation on Clay is smaller than that of the foundation on Loose Sand. However, K_e of the foundation on Clay is also smaller than that of the foundation on Loose Sand because the average foundation rotation from NTHA of the foundation on Clay is larger. This results in the values of $K_e/K_{\theta y}$ of the two foundations to be close to one another.

As the soil gets stronger and stiffer, the initial rotational stiffness of the foundations with the same R_f grows so quickly reducing the $K_e/K_{\theta y}$ to extremely low values. The data points in Figure 4.14 are so scattered that makes good curve fitting impossible. Hence, it was decided to normalize K_e by K_{oc} as values of K_{oc} of foundations with the same R_f on different soils were closer to one another than values of $K_{\theta y}$.

It has to be said though that the accuracy of the curve fitted to the data in Figure 4.12 is not as impressive as that for any individual soil such as the one presented in Figure 4.11b for Clay. Nonetheless, the general trend of the data points is captured especially for cases of small R_w/R_f (i.e. stronger walls on weaker foundations) were foundation rotation is critical.

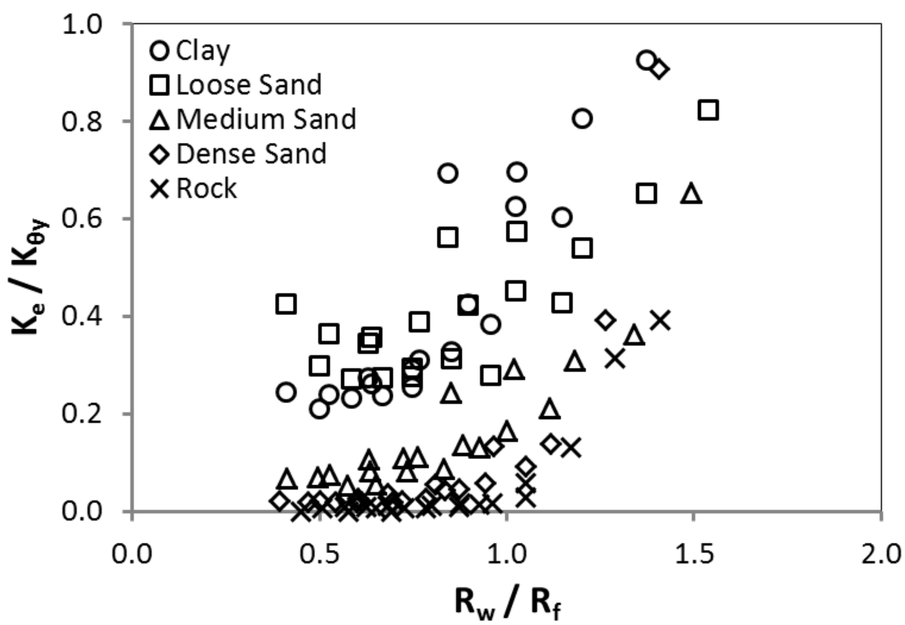

Figure 4.14 Variation of effective stiffness of the elastic rotational spring used in RSA to estimate top wall displacement accounting for foundation rotation with relative wall to foundation strength for foundations all five types of soil.

Figure 4.15 shows estimates of top wall displacement using K_e obtained from the fitted exponential curve of Figure 4.12b. The estimates are compared against target displacements from NTHA. The exponential curve seems to predict the appropriate elastic stiffness of the rotational spring of the simplified structure with very good accuracy. The average of absolute relative errors in predicting top wall displacement was only 7%.

As a concept, the exponential curve fitted to the data works very well. However, as a design procedure that could be easily implemented by engineers, the exponential curve might be labeled too cumbersome. In order to overcome this issue, a second method for estimating K_e is proposed. Instead of using the best fitted curve to estimated K_e/K_{oc}, a bilinear trendline was fitted to the data (see Figure 4.16). The equation for this bilinear trendline curve is

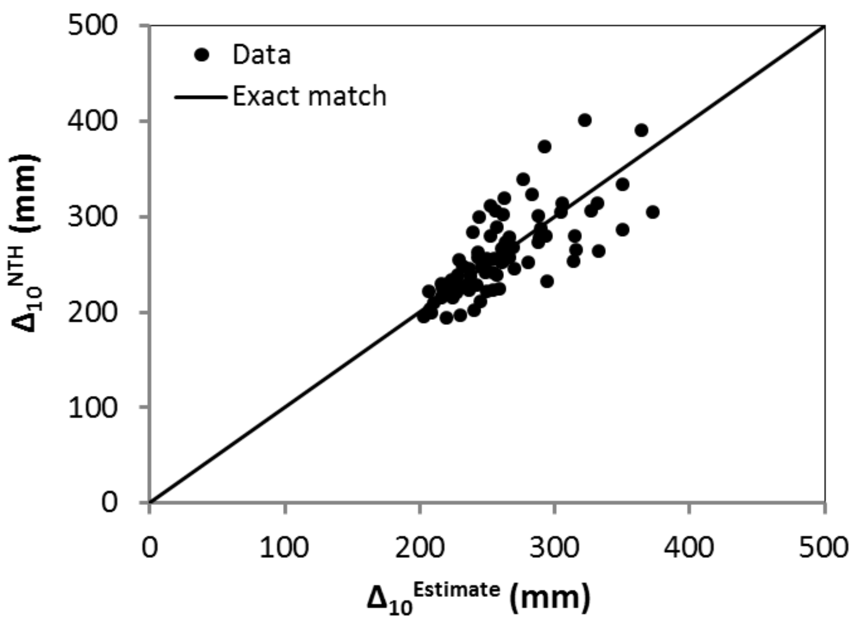

Figure 4.15 Accuracy of estimates of top wall displacement of nonlinear walls with flexible foundations using K_e from the best fit exponential curve.

$$\frac{K_e}{K_{oc}} = 0.30 \quad for \quad \frac{R_w}{R_f} \leq 0.6 \qquad \textbf{Eq 4.25}$$

$$\frac{K_e}{K_{oc}} = 0.3 + 1.9\left(\frac{R_w}{R_f} - 0.6\right) \quad for \quad \frac{R_w}{R_f} > 0.6$$

Figure 4.17 compares estimates of top wall displacement from the simplified structure using K_e obtained from the bilinear trendline with target top wall displacements from NTHA. Despite the simplicity of the bilinear curve equation, the estimated points fall reasonably close to the exact match line. The average of absolute relative error went up from 7% for the exponential curve to 8% for the bilinear trendline. The negligible decrease in accuracy seems to be a small price to pay for the simplicity of the bilinear trendline compared to the exponential curve; hence, the bilinear trendline is shown to be the suitable option for developing design procedures.

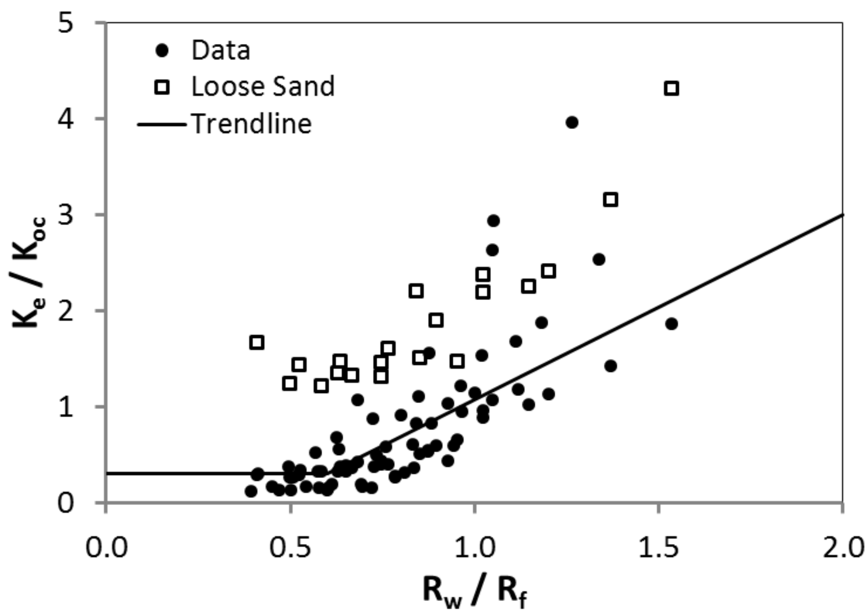

Figure 4.16 Simple bilinear trendline used for estimating equivalent stiffness of the elastic rotational spring at the base of the simplified structure.

So far in this section, estimating the top wall displacement has required performing an RSA of the shear wall with an elastic rotational spring at its base. Having to perform an RSA on a building with more than one core is not as simple as running the same analysis of a single shear wall. Such procedure requires more sophisticated modeling and can be quite time-consuming. Eliminating the need for doing an RSA will therefore make the method more attractive to the design engineer. A simpler method for estimating top wall displacement given the appropriate stiffness of the elastic rotational spring at the base of the wall is proposed next.

A simple seismic analysis method that is well accepted by codes and design engineers is the use of response spectra given the first mode period of the building. The method of course ignores the contribution of higher modes to the response of the building. Higher mode effects are then captured by applying various modification coefficients to different wall response components whether they are deformations or forces. Since top displacement of flexural shear walls is governed mostly by their first mode of vibration, it seems logical to estimate the top wall displacement from a given displacement spectrum using a first mode period that accounts for period lengthening due to foundation rotation.

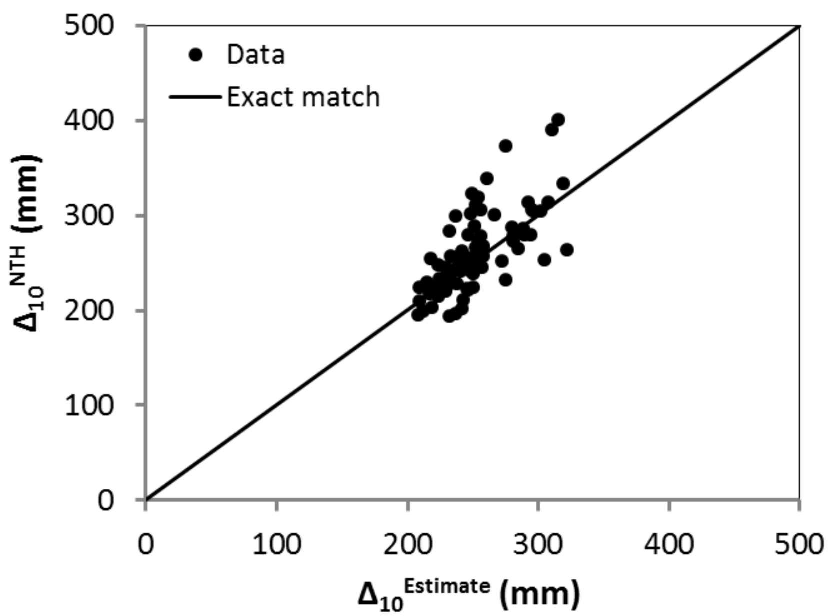

Figure 4.17 Accuracy of estimates of top wall displacement of nonlinear walls with flexible foundations using K_e from the simple bilinear trendline.

Figure 4.18 shows the concept behind estimating the first mode period of the wall-foundation system by combining the first mode period of the wall with a fixed-base and that of the rigid wall with an elastic rotational spring at its base. Calculating the first mode period of the fixed-base structure is simple once an effective elastic flexural stiffness is chosen. Design codes often have guidelines for getting the effective wall flexural stiffness as a portion of the flexural stiffness of the uncracked gross section based on R_w. The first mode period of the rigid wall with an elastic rotational spring at its base is called T_f shown in Figure 4.18. First mode period of the combined wall-foundation system T_s is approximately equal to the square root of sum of squares of the two periods.

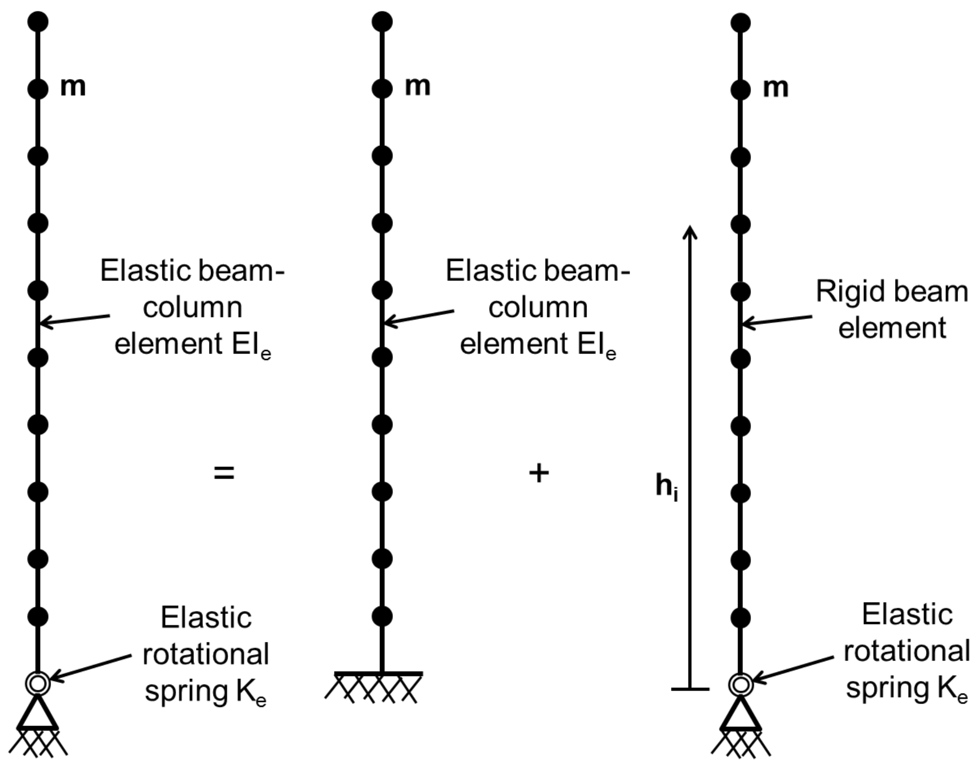

$$\mathbf{T_s \cong \sqrt{T_w^2 + T_f^2}} \qquad \mathbf{T_w = T_1} \qquad \mathbf{T_f = 2\pi\sqrt{\frac{\sum_{i=1}^{10} m h_i^2}{K_e}}}$$

Figure 4.18 Estimating fundamental period of the wall-foundation system from first mode periods of the fixed-base wall and the rigid wall with an elastic rotational spring at its base.

Given the first mode period of the wall-foundation system, one can get the displacement at the first modal height directly from the displacement spectrum (in this case, from Figure 3.13b). Note that the displacements given in the displacement spectrum are displacements at first modal height and not the top wall displacement. The ratio of the displacement at first modal height and top wall displacement is a constant which depends on the distribution of mass and stiffness over the height of the wall. The ratio is commonly referred to as λ_1. The value of λ_1 for the 10-storey walls of this study was 0.76.

Effective rotational spring stiffnesses required to match the top wall displacement from NTHA using RSA of the simplified structure are compared to those back-calculated to result in an effective wall-foundation system period to give the target top wall displacement from the displacement spectrum in Figure 4.19. The two approaches give effective rotational stiffnesses which are remarkably close. The only difference between the two approaches is that the RSA considered the contribution of the first 5 modes of the system while the latter only considered first mode behaviour. The fact that the two effective rotational spring stiffnesses are very similar confirms the theory that the top displacement response of walls with flexible foundations is dominated by their first mode behaviour. This means that the simple bilinear trendline presented earlier can be used to get K_e from R_w/R_f but instead of having to carry out an RSA, top wall displacement can be obtained from the displacement spectrum using the effective first mode period of the wall-foundation system.

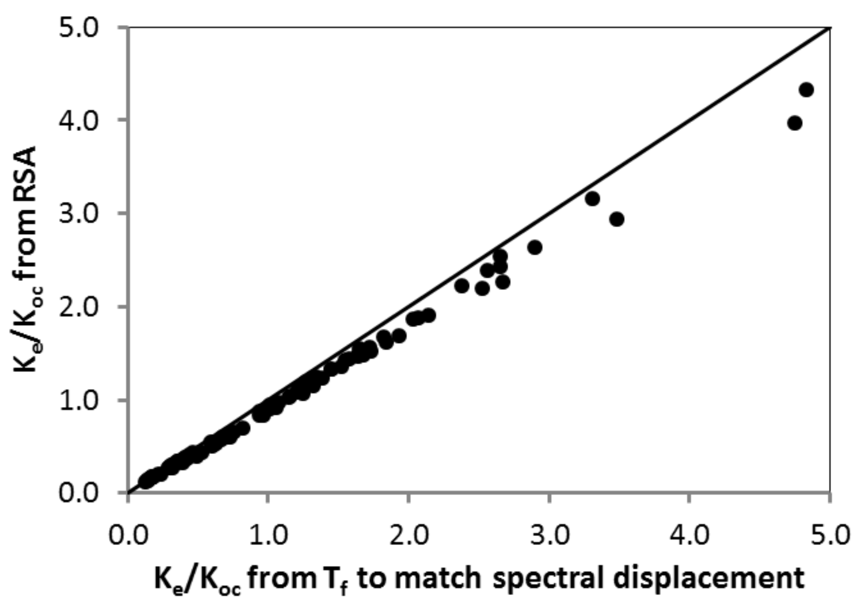

Figure 4.19 Comparison between effective rotational spring stiffnesses required to match the top wall displacement from NTHA using RSA with a linear elastic rotational spring at the base of the wall and using an effective wall-foundation system period required to give the target top wall displacement from the displacement spectrum.

4.3 A Simple Method for Estimating the Displacement Profile of Shear Walls Accounting for Foundation Rotation

This section presents a simple method for estimating the seismic displacement demands on shear walls accounting for foundation rotation. Figure 4.20 shows the major components that contribute to the top displacement of shear walls. Section 4.2 presented a simple method for estimating the total top displacement for a given wall-foundation system. Note that deformations due to shear strains have been ignored since their contribution to top wall displacement is small (see CHAPTER 2). In the subsequent sections, a simple way of estimating the elastic portion of the top wall displacement is presented first. Then a simple logical method is formulated to estimate foundation rotation of a given wall-foundation system.

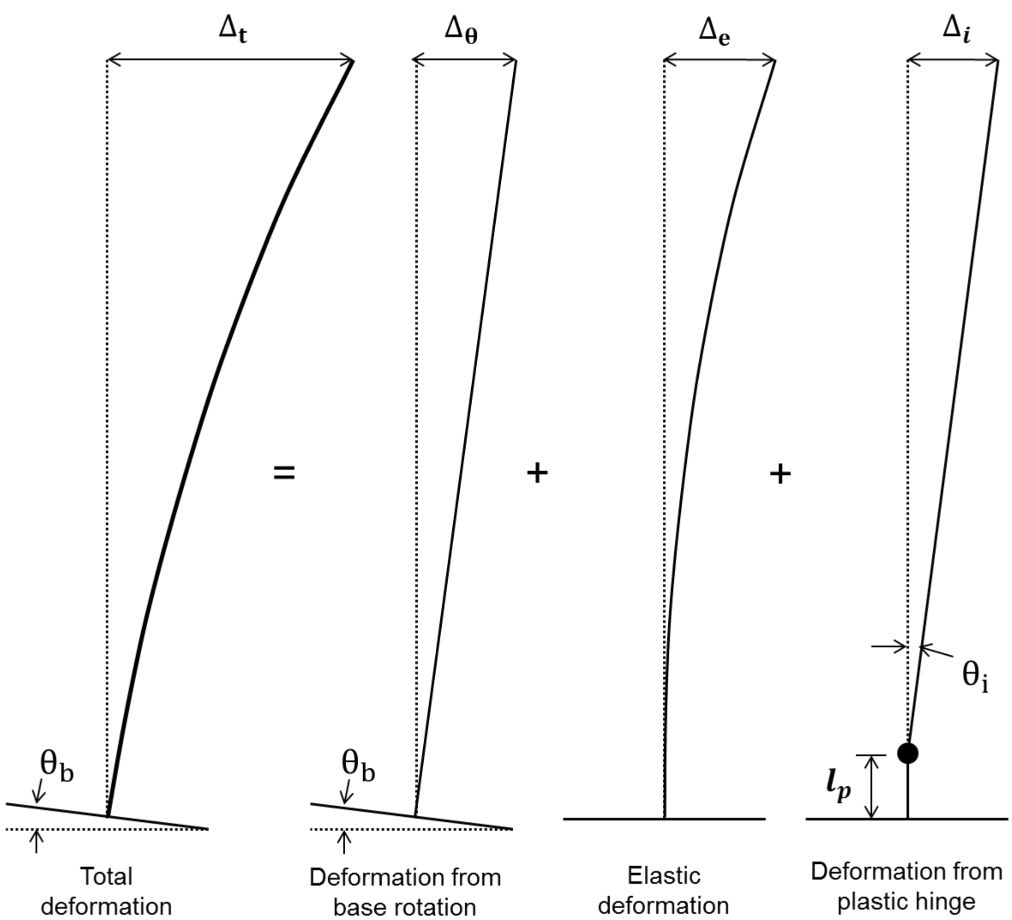

Figure 4.20 Major components of top displacement of shear walls with flexible foundations.

4.3.1 Elastic displacements

Elastic displacements are defined as the portion of the wall's flexural deformation that is not due to plastic hinging of the wall. In other words, elastic displacements of the wall are defined as the total wall flexural deformation minus the deformations from accumulation of inelastic curvatures in the wall's plastic hinge region. Because the four nonlinear walls considered in this study were flanged walls, the point of full yield when the entire vertical reinforcement in the tensile flange has yielded was very pronounced on the section's moment-curvature response (see Figure 3.6). Even though the four walls have very different post-cracking flexural stiffnesses, the point of full yield occurs at almost the same curvature of approximately 0.56 rad/km as can be seen in Figure 3.6. Any curvatures greater than 0.56 rad/km would then be inelastic.

Figure 4.21 shows the average of curvature envelopes from Nonlinear Time-History Analysis (NTHA) for the four nonlinear walls with a fixed base. Inelastic curvatures are shown with the dashed green line for each wall. Note that 5 beam-column elements were modeled in each storey of the wall which is the reason for the curvature profiles being step-wise. In reality, inelastic curvatures have a close to linear distribution over the height of the plastic hinge zone such as that shown by the dashed green line. Inelastic curvatures enclosed by the dashed green lines can then be integrated over the height of the wall to obtain the flexural deformation of the wall due to hinging at the base and the inelastic top wall displacement Δ_i. On the same figure, curvature profiles from Response Spectrum Analysis (RSA) of the wall with the appropriate effective flexural stiffness from Figure 4.8 is given with the dashed blue line. Integrating curvatures from the solid blue line and the dashed blue line will therefore result in the same top wall displacement. Section 3.6 revealed that both the displacement and bending moment profiles of the 10-storey walls were governed by the walls' first mode of vibration. This means that maximum bending moment at the base of the wall and maximum top wall displacement occurred very close in time. The post-yielding bending moment resisted by the nonlinear walls increases with curvature at a very small rate to the point that it can be said it remains almost constant beyond the point of full yield (see Figure 3.6). If the curvature profiles of the nonlinear 10-storey walls are also close in shape to first mode curvature profile of an elastic wall, elastic component of top displacement of the nonlinear walls can be estimated directly from first mode curvatures as follows.

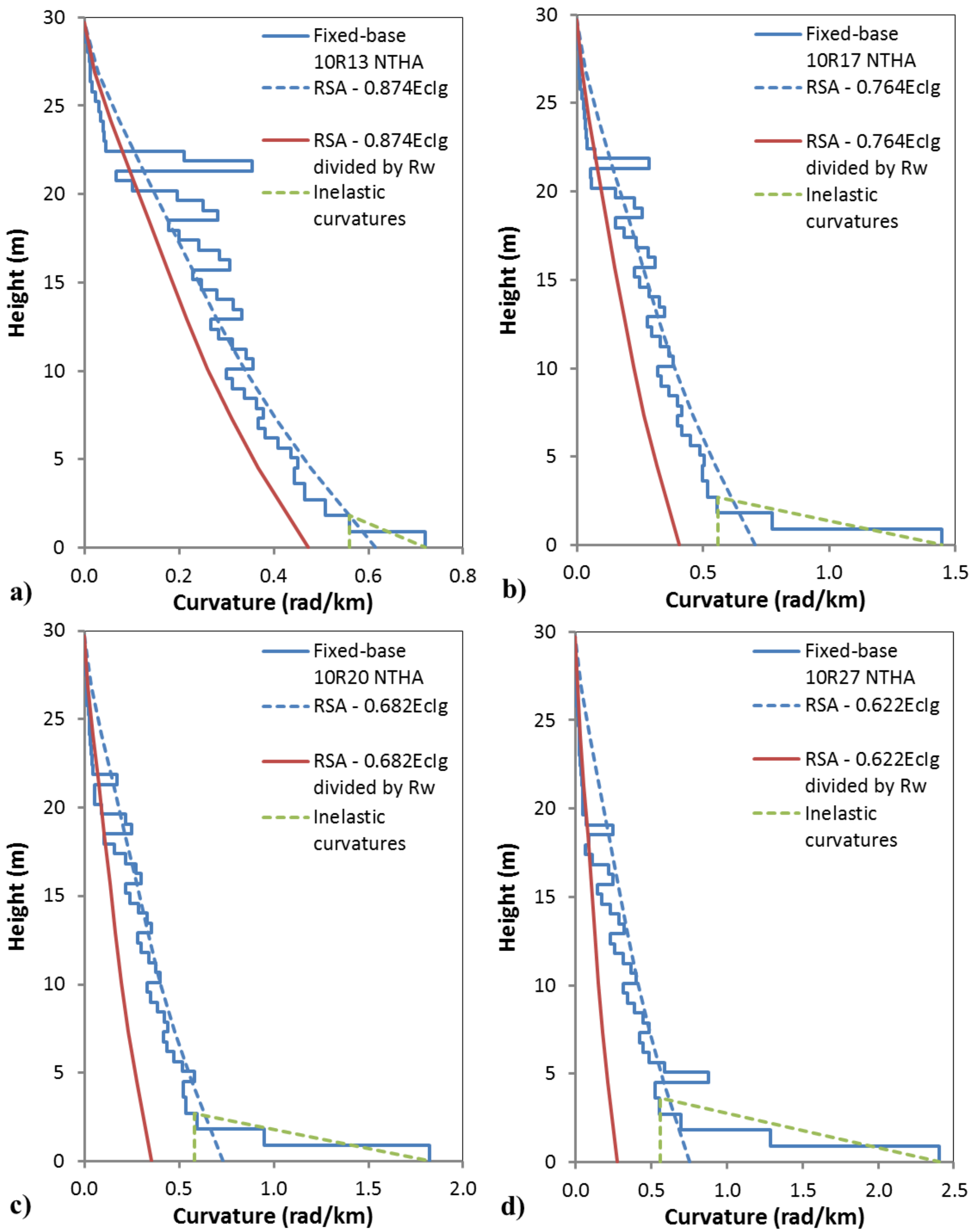

Figure 4.21 Average of curvature envelopes from NTHA, curvature profile from RSA with the effective flexural stiffness to match average of top wall displacement envelopes from NTHA, curvature profile from RSA with appropriate effective stiffness divided by R_w, and inelastic curvatures of the fixed base walls a) 10R13, b) 10R17, c) 10R20, and d) 10R27.

$$\Delta_e = \Delta_t \times \frac{M_y}{M_{RSA}} = \frac{\Delta_t}{R_w} \qquad \textbf{Eq 4.26}$$

In this equation, Δ_t is the total top wall displacement from NTHA which is also the top displacement from RSA with the appropriate wall flexural stiffness, M_{RSA} is the maximum bending moment from RSA and M_y is the wall probable bending strength. The approach linearly scales the total top displacement of the elastic wall to get the elastic portion of the top wall displacement of the nonlinear wall. A similar approach is accepted in CSA A23.3-04 for estimating the elastic top wall displacement due to seismic loads.

Estimates of the elastic component of top displacement of the four fixed-base nonlinear 10-storey walls using Eq 4.26 are given in Figure 4.22. The elastic component of the top wall displacement was calculated by subtracting the top wall displacement due to inelastic curvatures from the total top wall displacement from NTHA. As can be seen, the method underestimates the elastic component of the top wall displacement. The reason becomes evident when comparing the estimated elastic curvature profile of the four fixed-base walls (the solid red lines in Figure 4.21) with the elastic curvatures. The red line consistently underestimates the elastic curvatures.

Had the shape of the walls' elastic curvatures been close to that of the first mode response of an elastic wall with uniform stiffness, the method would have provided near to exact results. Elastic curvatures of the nonlinear walls vary quite a bit above the wall's plastic hinge zone. There is a jump in curvature when moving from the top of a storey to the bottom of the storey above. This can be explained by looking at Figure 4.23 which shows the moment-curvature response of wall 10R13 throughout its height. As can be seen, the variation in the sectional response of the wall throughout its height is very large. This is entirely due to the sectional response of reinforced concrete walls being sensitive to the amount of vertical steel and axial compression resisted by the wall. Vertical steel ratio of the wall's flanges varies quite significantly (see Table 3.1). Axial load on the wall also varies considerably throughout its height. Both of these reasons contribute to the great variation in the wall's sectional response over its height. The nonlinear walls becoming progressively softer and weaker above the plastic hinge zone has resulted in the shape of the wall's curvature profile to be very different than the first mode curvatures of an elastic wall with uniform stiffness over its height. Note that the wall is not yielding over the upper storeys as the curvatures stay well below the yield curvature. The wall is cracked in the upper storeys but the vertical reinforcing steel in the tensile flange has not yielded.

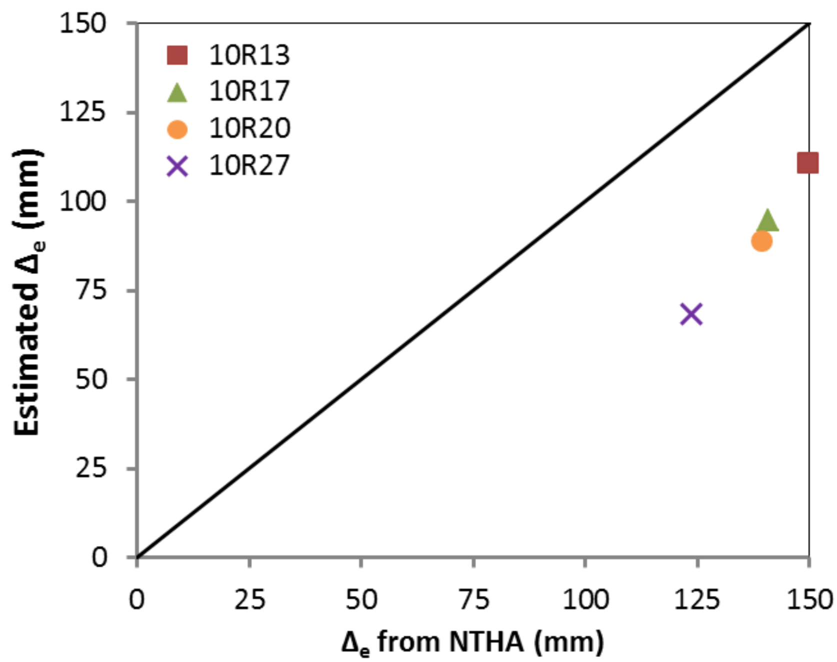

Figure 4.22 Estimates of the elastic component of top displacement of the four nonlinear walls with a fixed-base obtained by dividing the total top wall displacement by R_w.

Underestimating the elastic displacements is conservative from a seismic design view point. A smaller estimated elastic displacement results in a larger inelastic rotation demand on the wall which is conservative for shear wall design. Using a similar method in a design code such as CSA A23.3-04 therefore seems reasonable.

So far only fixed-base nonlinear walls were considered. Next, a similar approach is applied for estimating elastic displacements of walls accounting for foundation rotation.

The method simply scales down the total top wall displacement based on the maximum bending moment at the base of the wall relative to the maximum bending moment from RSA. The method will therefore give exact results when estimating elastic displacements of an elastic wall with uniform flexural stiffness over the height having a plastic hinge at its base.

To apply the method to walls with flexible foundations, total top wall displacement must again be scaled down based on the maximum bending moment demand on the wall. Two scenarios must be considered when determining the maximum bending moment demand in a given wall-foundation system. First, if the wall's bending strength is smaller than the foundation overturning strength (i.e. hinging wall), maximum bending moment of the system will be governed by the wall and will be equal to the wall's probable bending strength M_y (including the effect of steel strain hardening). In this case, the total top wall displacement must be divided by R_w as shown in Eq 4.26. Second, if the wall is stronger than the foundation (i.e. non-hinging wall), maximum bending moment demand of the wall-foundation system will be equal to the foundation overturning strength. In this case, the total top wall displacement must be divided R_f. Note that R_f is calculated using the factored bearing capacity (q_f) of the soil while in reality, the ultimate overturning capacity of the foundation must be calculated using q_{ult}. Using q_f for calculating the foundation overturning strength will therefore result in a smaller maximum bending strength which translates to smaller elastic displacements and a more conservative wall design.

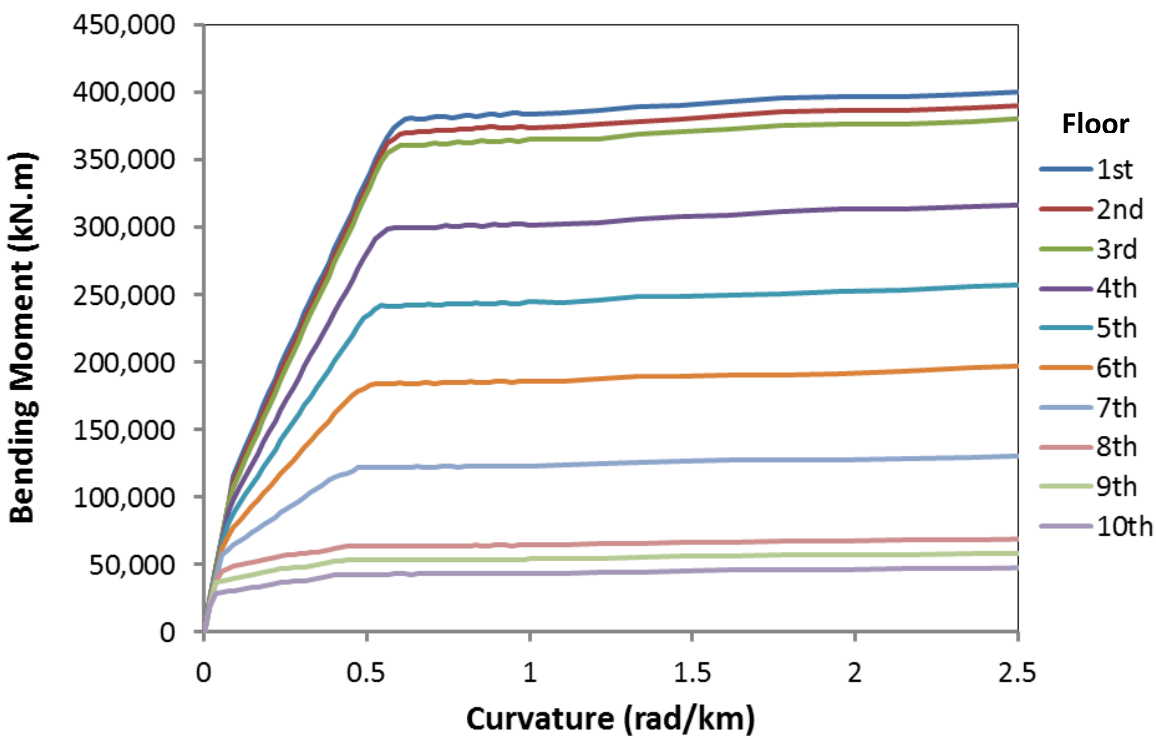

Figure 4.23 Variation of moment-curvature response of wall 10R13 over its height.

In summary, elastic component of top displacement of a walls accounting for rotation of its foundation can be calculated as follows.

$$\Delta_e = \frac{\Delta_t}{\max(R_w, R_f)} \quad \textbf{Eq 4.27}$$

Estimates of the elastic component of top displacement of the four nonlinear walls considered is compared against those observed in the NTHA for all five soil types and all foundation sizes paired with each wall in Figure 4.24. Inelastic component of the top wall displacement due to plastic hinging of the wall was calculated similar to that of the fixed-base walls explained earlier in this section. Contribution of foundation rotation to top wall displacement was calculated by multiplying the average of foundation rotation envelopes by the wall height. Again, since the response of the 10-storey walls was dominated by their first mode of vibration, maximum top wall displacement, maximum bending moment at the base, and maximum foundation rotation occurred very close in time. This confirms that it is valid to combine the maximum values of the three components of the top wall displacement algebraically. Elastic top wall displacement observed in NTHA was then calculated by subtracting the displacements due to average of maximum foundation rotation and average of inelastic curvature envelopes from the average maximum top wall displacement.

The predictions are scattered on either side of the exact match line. The points below the exact match line represent cases where the elastic component of the top wall displacement was underestimated. The shape of the elastic curvature profile of the nonlinear walls being dramatically different from the first mode curvature profile of an elastic wall with uniform flexural stiffness is the major contributor to this underestimation as explained earlier.

In many cases however, the method overestimated elastic displacements which would be unconservative for designing the wall. Elastic displacements of the stronger walls are more overestimated than that of the weaker walls. The explanation is rather simple. If the walls were stronger than the foundation or R_w was smaller than R_f, the total top wall displacement was divided by R_f to get the elastic component of the top wall displacement. This meant that the total top displacement of two walls with different R_w's supported on the same foundation was divided by the same R_f as long as both walls had R_w's smaller than R_f. At the same time, between the two walls, the one with the smaller R_w (stronger wall) had a larger total top displacement because it could induce larger foundation rotations. Therefore, the elastic displacement of the stronger wall was more overestimated than that of the weaker wall.

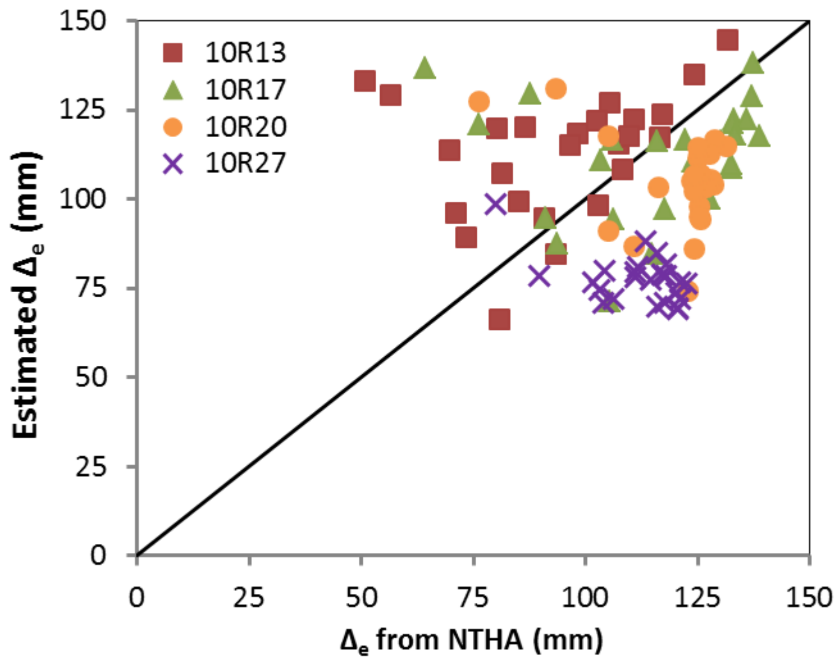

Figure 4.24 Estimates of the elastic component of the top displacement of the four nonlinear walls from the Core NTHA obtained using Eq 4.27.

Eq 4.27 is therefore unable to distinguish between walls of various strengths as long as the wall is stronger than the foundation or in other words, R_w is smaller than R_f. To overcome this deficiency, the term $1/R_w$ is added to R_f in the denominator of Eq 4.27 to get the following equation.

$$\Delta_e = \frac{\Delta_t}{\max(R_w, R_f + \frac{1}{R_w})} \qquad \textbf{Eq 4.28}$$

Note that for large values of R_w, the term $1/R_w$ would be small compared to R_f or R_w and that R_w would still be the greater of the two terms in the denominator of Eq 4.28. This modification will therefore not affect cases with large values of R_w or systems with hinging shear walls.

Estimates of the elastic component of top displacements of the four nonlinear walls considered in the Core NTHA are given in Figure 4.25. Addition of the term $1/R_w$ successfully reduced the estimated elastic component of the top wall displacement for systems with non-hinging shear walls without affecting the estimates for systems with hinging shear walls. Most of the data points are now below the exact match line which translates to reasonably underestimating the elastic displacements and a reasonably conservative wall design. Only a few of the data points are above the line which is considered insignificant. It is therefore concluded that the method presented in Eq 4.28 is suitable for estimating the elastic component of top displacements of shear walls accounting for rotation of their foundation.

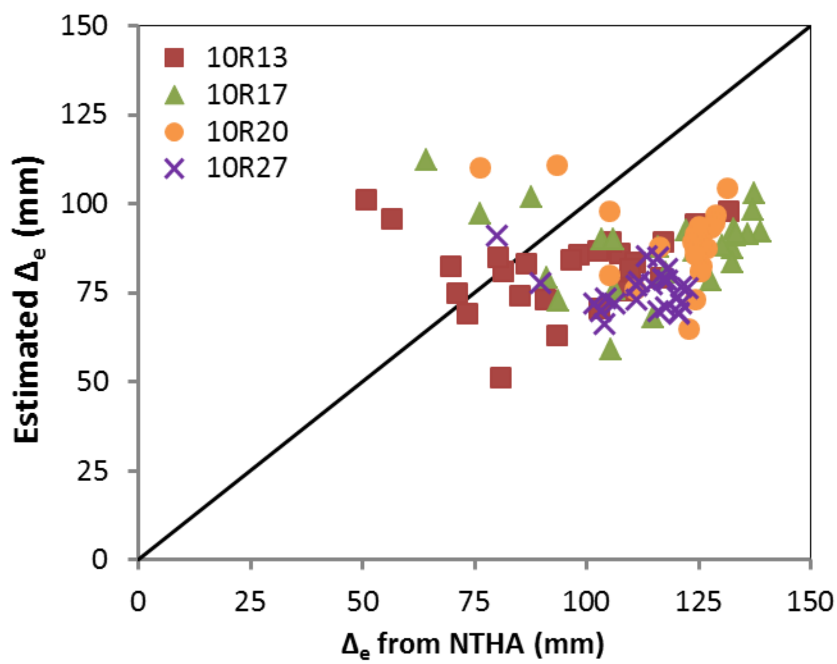

Figure 4.25 Estimates of the elastic component of the top displacement of the four nonlinear walls from the Core NTHA obtained using Eq 4.28.

With the elastic component of the top wall displacement in hand, the remainder of the top displacement demand needs to be divided between top displacement due to foundation rotation and top displacement due to hinging of the wall. Two scenarios may occur one where the foundation is strong enough to yield the wall and one where the wall is stronger than the foundation and does not hinge. The two scenarios are explained in the following two sections.

4.3.2 Hinging shear wall

Whether the shear wall is likely to yield or not can be determined from the foundation moment-rotation response. Figure 4.26 shows an example moment-rotation response of a wall-foundation system where the foundation is stronger than the wall. In such a system, the wall will yield under severe seismic excitation and a considerable portion of the top displacement will come from inelastic rotations of the wall plastic hinge and therefore, the wall hinge rotation needs to be determined.

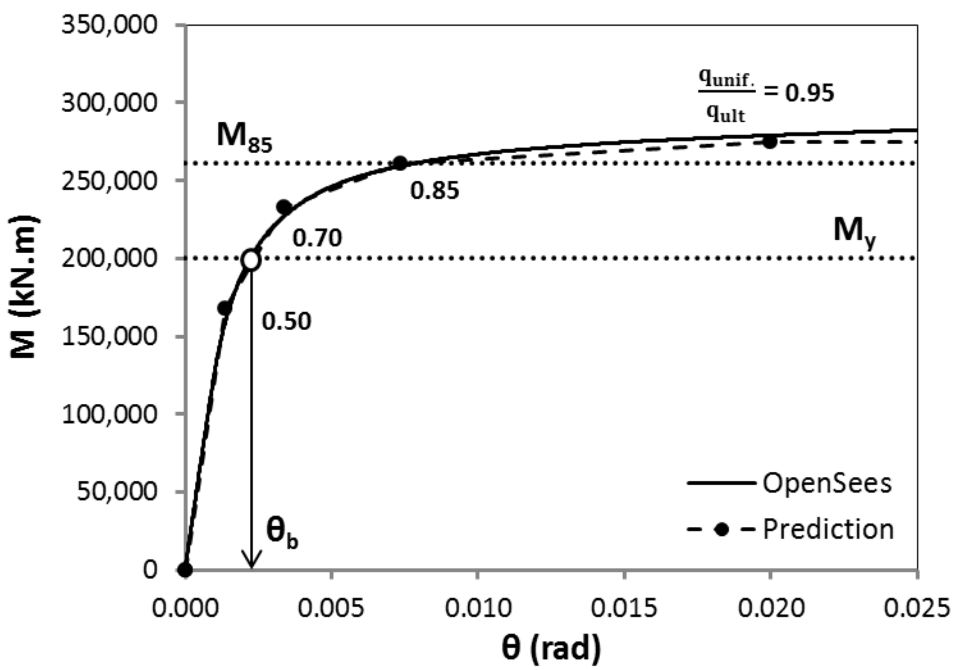

Figure 4.26 Example of a hinging wall with a flexible foundation – estimating the base rotation demand from the foundation moment-rotation response.

The foundation moment-rotation response becomes quite flat beyond the point of $q_{unif.}/q_{ult} = 0.85$. The foundation bending moment at the point of $q_{unif.}/q_{ult} = 0.85$ (called M_{85}) is used as the foundation strength in determining if the wall is likely to yield or not. The reason for choosing M_{85} to distinguish between hinging and non-hinging shear walls is that beyond this point, the increase in the bending moment resisted by the foundation is small. The accuracy of the estimated foundation rotation was found not to be sensitive to this assumption.

If the wall is weaker than the foundation, it will limit the maximum bending moment induced in the system. With the maximum bending moment known, foundation rotation (θ_b) can be estimated directly from the moment-rotation response as shown in Figure 4.26. Since the wall may have some overstrength beyond its yield bending moment, it is probable that the actual bending moment induced in the foundation is larger than the wall yield strength resulting in a larger θ_b. However, the variation in the maximum bending moment induced in the foundation will not make a big difference in the estimated θ_b as the slope of the foundation moment-rotation response at the point of its intersection with the line showing the wall yield strength is relatively steep. This is because the foundation has not yet entered its highly nonlinear behaviour range.

Because the foundation moment-rotation response envelopes the actual hysteretic foundation response, it does not account for softening of the response due to hysteretic compression of the soil. Again, since the wall is not strong enough to force significant nonlinear rotational cycles in the foundation, the actual foundation rotation will be only slightly larger than that estimated from the envelope response. In addition, underestimating the foundation rotation will result in a larger hinge rotation demand for a given total top wall displacement demand and hence, the approach would be conservative.

With foundation rotation estimated, the portion of the top displacement due to foundation rotation will simply be the foundation rotation multiplied by the wall height. The elastic top displacement can be estimated using the method described in Section 4.3.1. In this case, the total top wall displacement can be divided by R_w to estimate the elastic portion of the top wall displacement. With the wall top displacement due to foundation rotation and the elastic top displacement subtracted from the total top wall displacement demand, the inelastic top wall displacement is obtained. The inelastic top wall displacement can in turn be used to calculate the inelastic rotation demand in the wall's plastic hinge zone.

4.3.3 Non-hinging shear wall

In a system where the foundation is not strong enough to yield the wall such as the example shown in Figure 4.27, the wall will remain elastic and hence, the inelastic top wall displacement will be zero. Note that again, foundation strength is considered to be M_{85} (instead of the actual maximum bending moment that the foundation can resist assuming a uniform stress block of q_{ult} at its "toe") and compared to M_y to determine if the wall hinges or not.

In this case, the total top wall displacement can be divided by $R_f + 1/R_w$ to calculate the elastic component of the top wall displacement as described in Section 4.3.1. The elastic top displacement can then be subtracted from the total top wall displacement to get the top wall displacement due to foundation rotation. Foundation rotation demand would then be the non-elastic top displacement divided by the height of the wall.

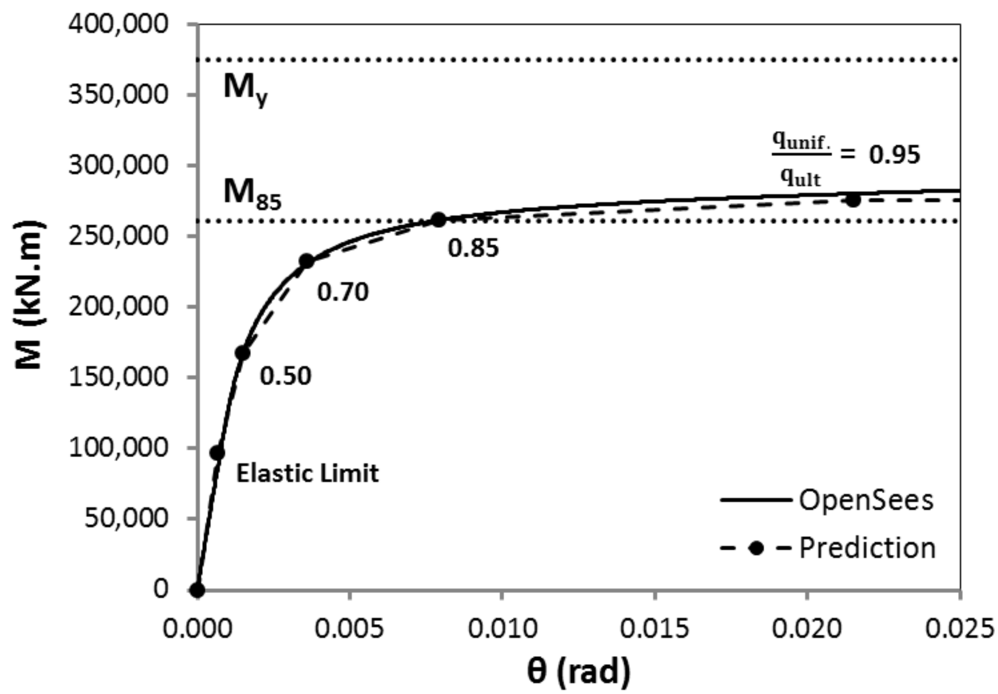

Figure 4.27 Example of a non-hinging shear wall with a flexible foundation – estimating the maximum wall bending moment demand from the foundation moment-rotation response.

As the method presented at the end of Section 4.3.1 mostly underestimates elastic displacements of the wall, the non-elastic portion of the top wall displacement will be overestimated in most cases. This results in overestimating the foundation rotation which is reasonably conservative and desirable for implementation in design procedures and codes.

4.3.4 Prediction of foundation rotation from NTHA results

This section combines all of the previous sections of this chapter and demonstrates the simple step by step method for predicting the response of shear walls accounting for foundation rotation. The ultimate goal of the proposed simple method is to predict the top wall displacement and foundation rotation of a given wall-foundation system with good accuracy. The accuracy of the proposed method is examined by making predictions of the foundation rotations recorded in NTHA on 10-storey walls presented earlier in CHAPTER 3.

Top wall displacement was estimated using the method described in Section 4.2. Foundation moment rotation response was approximated by 5 points obtained using the equivalent rectangular soil stress block concept presented in Section 4.1. Maximum bending moment induced in the system was taken as either M_y or M_{85} depending on whether the wall hinged or not, respectively. Elastic displacements of the wall were estimated using the method described in Section 4.3.1. If the wall did not hinge, the elastic top wall displacement was subtracted from the total top wall displacement to give the top wall displacement due to foundation rotation. This displacement value was then divided by the wall height to get the foundation rotation. If the wall hinged, then foundation rotation was obtained directly from the foundation moment-rotation response for the given wall bending strength. Estimated foundation rotations are then compared to those recorded in NTHA.

Figure 4.28 shows the accuracy of the proposed method. Data points for hinging and non-hinging shear walls have been distinguished from one another. As expected, non-hinging shear walls (i.e. stronger shear walls) induce more rotation in the foundation. Figure 4.28a shows the predictions with the total top wall displacement estimated using the exponential fit (see Figure 4.12b). The method seems to predict foundation rotation with reasonable accuracy. The average of absolute relative error in prediction was 29% with a standard deviation of 26%. Predictions of top wall displacement used to get data points in Figure 4.28b were done using the bilinear trendline (see Figure 4.16 or Eq 4.25). Again, the method proves to be reasonably accurate in predicting foundation rotation. In this case, the average of absolute relative error was 30% with a standard deviation of 27%. Given how simpler the bilinear trendline is compared to the exponential fit, it is the obvious choice for implementation in any design procedure.

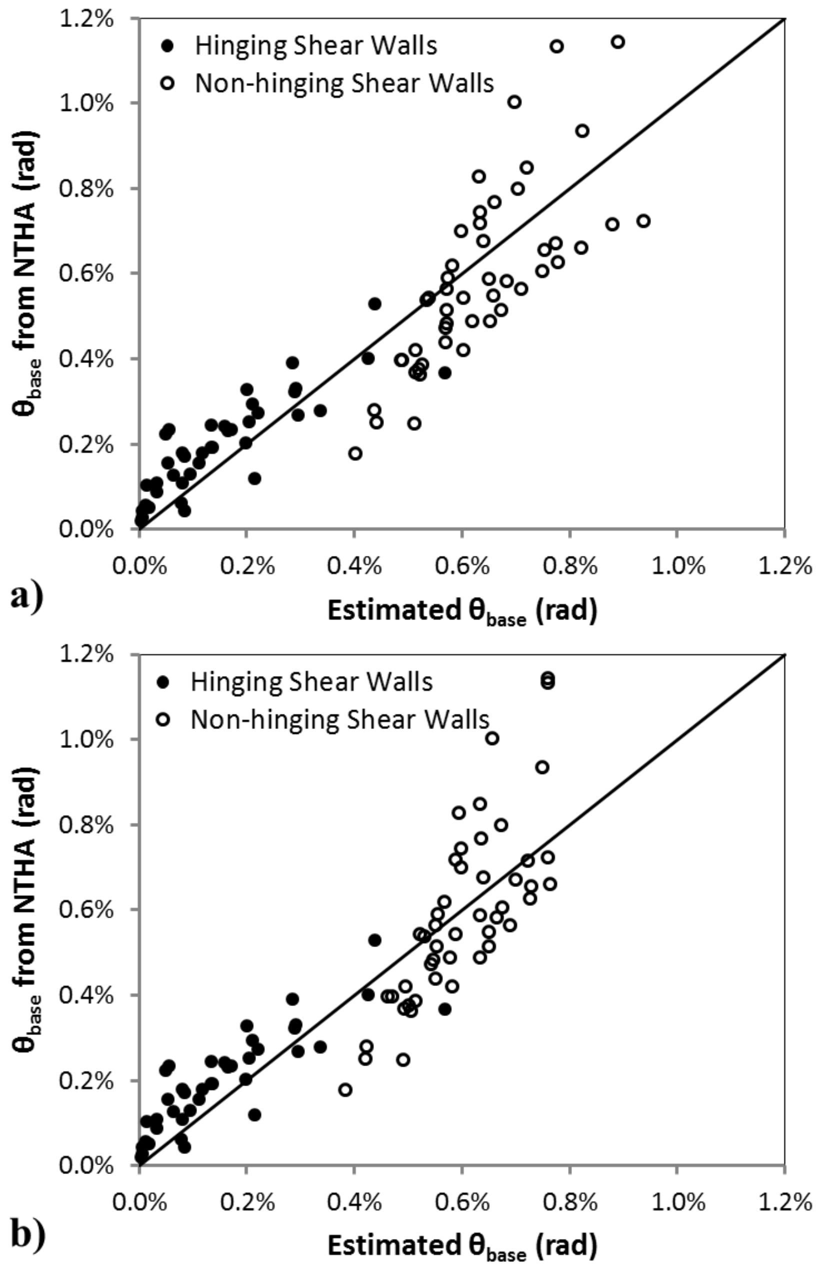

Figure 4.28 Estimating foundation rotation demand with top wall displacement demands obtained using K_e from a) best fit exponential curve, and b) simple bilinear trendline.

The accuracy of the method is remarkable considering the simplicity of all of the steps involved. Bear in mind that all of the information used as an input to the method are readily available to the design engineer.

The method as presented is aimed at making the most accurate predictions with errors on each side of the exact match line. For implementation in codes and standard design procedures, a more conservative approach may be desired. To achieve this, the best fit bilinear trendline in Figure 4.16 can be replaced by a more conservative bilinear envelope curve to consistently overestimate top wall displacement.

4.4 Summary and Conclusions

A summary of the main contributions of this chapter is as follows.

1. A step-by-step method was formulated to obtain the monotonic moment-rotation response of a given foundation using geotechnical information available to the design engineer. It was shown that an excellent approximation of the foundation moment-rotation response can be made by obtaining as few as five points along the curve. The equivalent rectangular stress block concept widely used for nonlinear sectional analysis of reinforced concrete structures was applied to nonlinear soil bearing pressure distribution underneath a foundation. Even though the method was formulated for the QzSimple1 material available in OpenSees, the use of the equivalent rectangular stress block concept for simulating nonlinear bearing pressure distribution underneath a foundation can be generalized to other soil Winkler models with a different backbone curve shape.

2. Total top displacement of walls with flexible foundations was estimated using Response Spectrum Analysis (RSA) of a simplified structure with an elastic wall having an effective flexural stiffness supported by an elastic rotational spring at its base. Effective stiffness of the elastic rotational spring was formulated based on the ratio of the foundation overturning strength to the wall yield strength.

3. The method used in CSA A23.3-04 for estimating the elastic component of the top displacements of nonlinear shear walls with a fixed-base was expanded to account for flexibility in the wall foundation. The modifications made to the concept were proven to

increase the accuracy of the method in accounting for the rotation of shear wall foundations.

4. A complete method was developed for estimating the rotation of shear wall foundations for a given wall-foundation system. The method takes into account the relative wall-to-foundation strengths. In systems with hinging shear walls, foundation rotation is obtained directly from the foundation moment-rotation response. In systems with non-hinging shear walls, the elastic component of the top wall displacement is first estimated using the foundation overturning capacity as the maximum bending moment demand in the system and an effective wall flexural stiffness assuming a first mode behaviour. Total top wall displacement is in turn estimated from RSA of a simplified structure with an elastic wall supported on an elastic rotational spring. The elastic top wall displacement is then subtracted from the total top wall displacement and the result divided by the wall height to get the foundation rotation. The method was proven to have good accuracy for engineering practice.

CHAPTER 5 Moment-Curvature Response of Reinforced Concrete Gravity-load Columns

5.1 Introduction

Due to the large axial compressive load resisted by gravity-load columns, very little shear strains develop in the column. Gravity load columns may have elongated cross-sections with cross-section lengths close to the buildings' typical storey height. Despite this, the large compressive axial force that needs to be resisted by the column prevents large tensile strains and consequently large shear strains from developing as elongated columns need a large concrete compression depth to resist the compressive axial load because of their narrow cross-sectional width. Assuming shear strains are negligible in the column (see Section 6.7), deformation of gravity-load columns will be dominated by flexure. This makes the moment-curvature response of the column the obvious tool for investigating its structural behaviour. Bending moments induced in the column due to forces exerted on it at floor slab levels can be converted to curvatures using the moment-curvature response of the columns. Curvatures in turn could be integrated over the column height to calculate the lateral displacement profile of the column. Also, various damage levels such as concrete cover spalling, yielding of vertical reinforcement, and crushing of concrete can be related to curvature and be depicted from the moment-curvature response.

Because the moment-curvature response of the column is used to estimate deformation demands on columns in CHAPTER 6, this chapter is dedicated to studying the sectional response of gravity-load columns to better understand and simulate the flexural behaviour of gravity-load columns. In this chapter, the uniaxial moment-curvature behaviour of reinforced concrete column sections sustaining a compressive axial force is studied. Various column cross-sections, concrete strengths, reinforcement ratios, and axial loads are considered and the influence of each parameter on column's flexural behaviour is investigated. Long-term effects of sustained axial load and effects of concrete cover spalling and loss of vertical reinforcement due to either buckling or fracturing on moment strength and curvature capacity are also studied.

5.2 Moment-Curvature Behaviour of Reinforced Concrete Columns

As described earlier, assuming shear strains are negligible in gravity-load columns, structural behaviour of the columns will be dominated by flexure. Flexural response of a reinforced concrete section is best represented by the section's moment-curvature response. This section presents results of a parametric study that was undertaken to better understand the moment-curvature response of gravity-load columns. The following sections present the study parameters, assumptions, methods of analysis, and findings of the parametric study.

5.2.1 Probable compressive axial load on gravity-load columns accompanied by seismic forces

Designing the column cross-section for the maximum probable axial load demand from the governing gravity load combination offers a good starting point for sizing a gravity-load column. Estimating the axial load demand is usually done by assuming a tributary slab area for the column based on floor plans. The dead and live loads from the tributary area are then calculated for all floors slabs above and multiplied by appropriate load factors given in the design code being used. The designer then proportions the column dimensions and reinforcements so that the axial load capacity of the column considering material strength reduction factors exceeds the load demand. This simple approach usually provides a good starting point for sizing the columns and in many cases, columns sized using this simple method turn out not to need any further modification to resist demands from other load-cases.

For seismic design however, using the axial load demand just mentioned will be overly conservative; hence, building codes have different load factors for earthquake load combinations. Furthermore, live loads are reduced to account for the probability of maximum occupancy and other uncertainties requiring the column to resist lower axial load levels accompanied by seismic demands. The objective of this section is to investigate the seismic axial load demand on a wide range of columns designed according to common practice. Calculations of this section are based on the provisions of National Building Code of Canada (NBCC 2005) and the American Society for Civil Engineers (ASCE 7-05) manual as representatives of North American design standards.

To consider a variety of building configurations, different values for design parameters had to be chosen based on common practice and rule-of-thumb. Square columns of 400, 750, and 1000 mm sides were used for 10, 30, and 50-storey buildings respectively. Two slab thicknesses of 178 mm (7") and 254 mm (10") were considered. 25 kN/m^3 was used for unit weight of reinforced concrete. The load tributary area of the column was then calculated assuming a span of 30 times the thickness of the slab on either side (i.e. total tributary area of 900 times the square of slab thickness for interior columns). Storey height was fixed at 2.75 m. To account for variation in occupancy and use, both residential and office applications were studied. Weight of partitions and mechanical equipment on the floor slabs was adjusted to suit the type application of the building.

A23.3-04 refers to the maximum factored axial compressive resistance of a column as Pr_{max}. It was assumed that the columns were designed such that the total axial load demand from the gravity load-case was equal to Pr_{max}. Axial load from the seismic load-case P_s was then expressed as a ratio of Pr_{max}. Details of calculations based on NBCC 2005 and ASCE 7-05 are given in Appendix B and Appendix C respectively.

Final results are summarized in Table 5.1. The ratio P_s/Pr_{max} varied by less than 10% when the design was based on either NBCC 2005 or ASCE 7-05 considering the broad range of building configurations. The difference in the seismic load-case DL factor between the two codes (1.0 in NBCC 2005 and 1.2 in ASCE 7-05) caused P_s/Pr_{max} to be higher for ASCE 7-05. P_s/Pr_{max} varied between 70% and 75% for columns designed to NBCC 2005 while it ranged from 80% to 89% when the design was based on ASCE 7-05.

It was assumed that the preliminary section design was such that the column was proportioned to have exactly the same axial capacity as the demand gravity load. However, this is not the case in real practice and columns end up having much higher axial strength than the demand gravity loads due to rounding up of column dimensions and reinforcement sizes. This will cause Pr_{max} to increase and hence, the actual P_s/Pr_{max} to be somewhat less than the values shown in Table 5.1. Therefore, the range of P_s/Pr_{max} used in the rest of this chapter is taken to be from 65% to 85%. It is assumed to vary from 65% to 75% using NBCC 2005 and from 75% to 85% in ASCE 7-05.

Table 5.1 Typical ratios of compressive axial load on gravity-load columns from seismic load-case to that from gravity load-case based on provisions of a) NBCC 2005, and b) ASCE 7-05.

a)

		Residential		Office	
		Slab Thickness (mm)		Slab Thickness (mm)	
	P_S / Pr_{max}	**178**	**254**	**178**	**254**
# of Storeys	**10**	72%	74%	70%	72%
	30	74%	75%	72%	73%
	50	75%	74%	73%	74%

b)

		Residential		Office	
		Slab Thickness (mm)		Slab Thickness (mm)	
	P_S / Pr_{max}	**178**	**254**	**178**	**254**
# of Stories	**10**	85%	88%	80%	84%
	30	87%	89%	82%	85%
	50	89%	89%	84%	85%

Compressive strength of the gross concrete cross-section ($f'_c A_g$) is extensively used by engineers as an indication of the column's axial load-carrying capacity. It is therefore useful to express the seismic axial load demand as a ratio of the gross concrete cross-section's compressive strength. Table 5.2 provided ratios of $P_s/f'_c A_g$ for the same set of building configurations considered earlier. f'_c is assumed to be 60MPa as the mid-range for 28-day compressive strength of concrete used in mid-rise and high-rise buildings. Values of $P_s/f'_c A_g$ vary from about 20% to 55% based on both NBCC 2005 and ASCE 7-05.

Table 5.2 Typical ratios of compressive axial load on gravity-load columns from seismic load-case to compressive strength of the gross concrete cross-section assuming 28-day concrete compressive strength of 60 MPa based on provisions of a) NBCC 2005, and b) ASCE 7-05.

a)

		Residential		Office	
		Slab Thickness (mm)		Slab Thickness (mm)	
	P_S/f'_cA_g	**178**	**254**	**178**	**254**
# of Stories	**10**	18%	47%	21%	53%
	30	18%	42%	20%	47%
	50	19%	42%	21%	46%

b)

		Residential		Office	
		Slab Thickness (mm)		Slab Thickness (mm)	
	P_S/f'_cA_g	**178**	**254**	**178**	**254**
# of Stories	**10**	20%	52%	21%	56%
	30	20%	48%	21%	51%
	50	21%	48%	23%	51%

5.2.2 Column cross-section aspect ratios

Considering the fact that column cross-sectional dimensions significantly affect their flexural stiffness and deformability, columns with cross-sections of several lengths were analyzed. Figure 5.1 shows column dimensions considered to represent the range of aspect ratios encountered in a typical architectural or construction plans.

To account for the effect of steel reinforcement on stiffness and flexural capacity, three different reinforcement ratios of 1, 2, and 3% of the gross cross-section of the column were considered. These numbers represent the range of the amount of reinforcement used in common practice considering practicality and construction efficiency. The total amount of reinforcing steel was distributed evenly along the perimeter of the column cross-section.

Three different concrete strengths of 40, 60, and 80 MPa were used. Parabolic stress-strain relation was assumed for concrete (refer to Section 5.2.3 for further details) and the maximum permissible compressive concrete strain was taken to be 0.0035, 0.0033, and 0.0031 for 40, 60, and 80 MPa concrete respectively (see Ozbakkaloglu, and Saatcioglu (2004) for more details).

A study of the probable axial load on gravity column was carried out in Section 5.2. It was shown that the axial load used along with seismic loads varies from 67% to 89% of Pr_{max}. Three axial load levels of 65%, 75%, and 85% of Pr_{max} were used to study the influence of axial compression on sectional behaviour of gravity columns under seismic deformation demands.

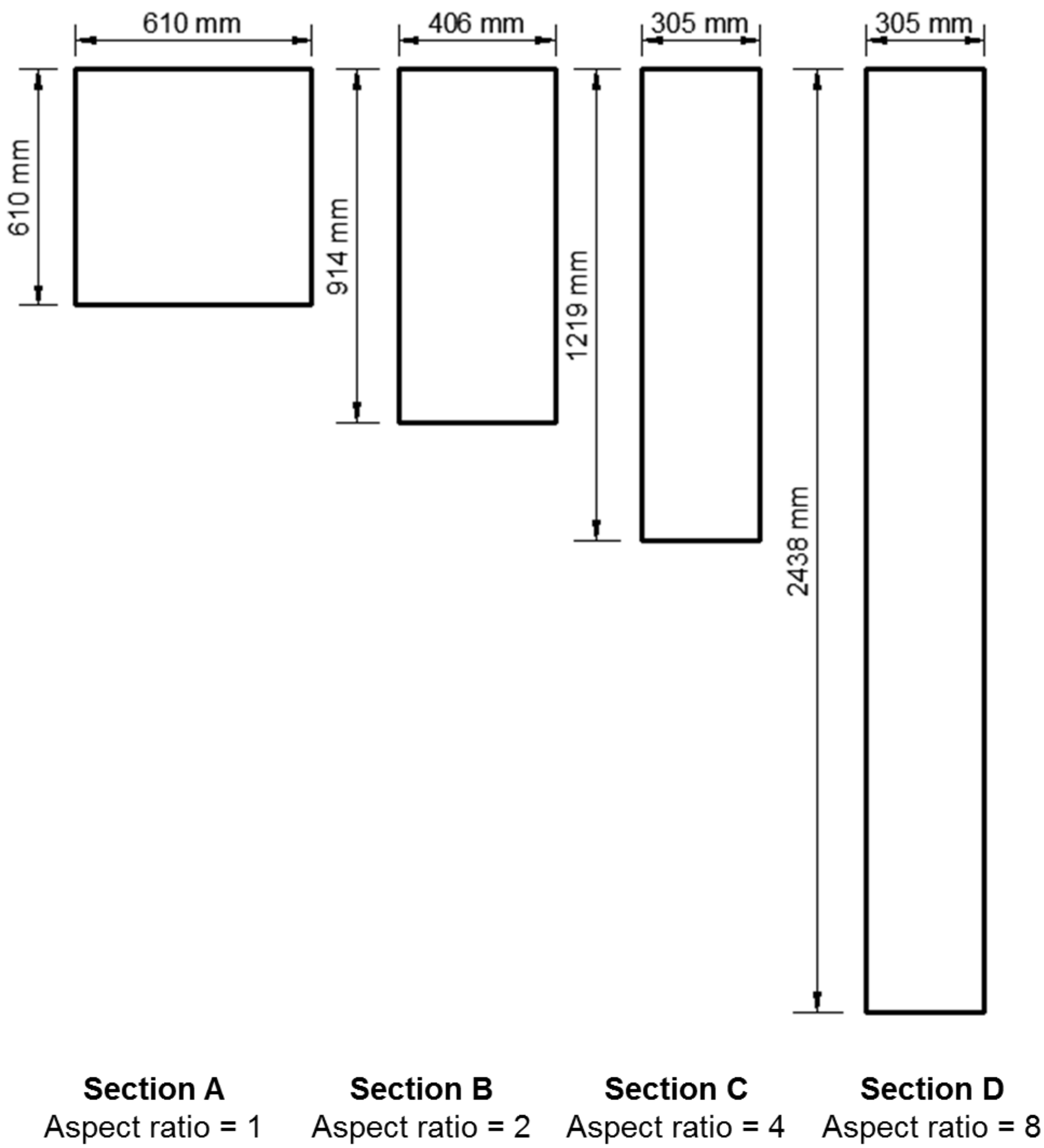

Figure 5.1 Column cross-sections used in the study of moment-curvature behaviour.

5.2.3 Sectional analysis procedure

In order to study the column flexural behaviour under a certain axial load, a typical section analysis program was developed using MATLAB. Plane sections were assumed to remain plane after bending which resulted in linear variation of strain across the height of the column cross-section. Elastic-perfectly plastic (EPP) behaviour was assumed for steel reinforcement assuming that the effect of steel strain hardening is incorporated as a part of seismic load factors in building codes (e.g. R_{sh} in NBCC 2005). Steel yield strength was kept constant at 400 MPa with elastic modulus of 200,000 MPa which gave the steel yield strain of 0.002 for both tension and compression. Steel rupture strain was taken as 0.05.

A more complex stress-strain relationship was used for concrete. Concrete behaviour in tension was assumed to be linear up until the cracking strength. Concrete tension stiffening was modeled for tensile strains beyond the cracking strain. Equations below show the analytical parameters used to model concrete behaviour in tension. Eq 5.4 is the tension stiffening model by Bentz (2000).

$$E_{ct} = 4500\sqrt{f'_c} \qquad (MPa\ units)$$ **Eq 5.1**

$$f_{cr} = 0.33\sqrt{f'_c} \qquad (MPa\ units)$$ **Eq 5.2**

$$\varepsilon_{cr} = \frac{f_{cr}}{E_{ct}}$$ **Eq 5.3**

$$f_c = \frac{f_{cr}}{1+\sqrt{500(\varepsilon_c - \varepsilon_{cr})}}$$ **Eq 5.4**

In the equations above, E_{ct} is the secant stiffness for concrete, f_{cr} is the tensile cracking strength, ε_{cr} is the cracking strain, and f_c is the tensile concrete stress.

For compression, Popovic's formula (Eq 5.5) was used where parameter 'k' defines concrete compression softening behaviour and parameter 'n' accounts for the effect of concrete strength on the shape of the stress-strain curve. See Collins and Mitchell (1991) for more details.

$$f_c = f'_c \left[\frac{n \left(\frac{\varepsilon_c}{\varepsilon'_c} \right)}{n - 1 + \left(\frac{\varepsilon_c}{\varepsilon'_c} \right)^{nk}} \right] \qquad \textbf{Eq 5.5}$$

Where

$$\varepsilon'_c = \frac{\mathrm{n}}{\mathrm{n}-1} . \frac{\mathrm{f}'_c}{\mathrm{E}_{ct}}$$

$$\mathrm{n} = 0.8 + \frac{\mathrm{f}'_c}{17} \quad \text{(MPa units)}$$

$$\mathrm{k} = 1.0 \text{ if } |\varepsilon_c| < |\varepsilon'_c| \text{ else } \mathrm{k} = \max\left(0.67 + \frac{\mathrm{f}'_c}{62}, 1\right) \quad \text{(MPa units)}$$

Analysis stopped when maximum permissible compressive concrete strain was reached. 0.0035, 0.0033, and 0.0031 were used as maximum permissible concrete strains for 40, 60, and 80 MPa concrete respectively (see Ozbakkaloglu, and Saatcioglu (2004) for more details). Due to high axial compression, section failure was governed by crushing of concrete fibres on the outer side of the compression zone. In other words, steel rupture did not occur prior to concrete crushing. No material resistance factors were applied and the results represent nominal column strength.

5.2.4 Moment-curvature analysis results

Figure 5.2 shows analysis results of Section A (see Figure 5.1 for Section A dimensions) for axial load level of 0.75 Pr_{max}. As expected, response of the section with various concrete strengths and reinforcing steel ratios vary considerably in terms of ultimate bending strength and flexural stiffness. To facilitate comparison of different curves and finding trends in the flexural behaviour of the section, analysis results were normalized to reduce the range of variation of numerical values. Bending moment were normalized by the moment strength (M_n) and curvature values were multiplied by EI_g/M_n where EI_g is the slope of the initial elastic segment of the moment-curvature curve which was obtained by dividing the moment value at a curvature of 0.15 rad/km by the corresponding curvature. Normalized moment-curvature responses for Section A with an axial load of 0.75 Pr_{max} are normalized and plotted in Figure 5.3.

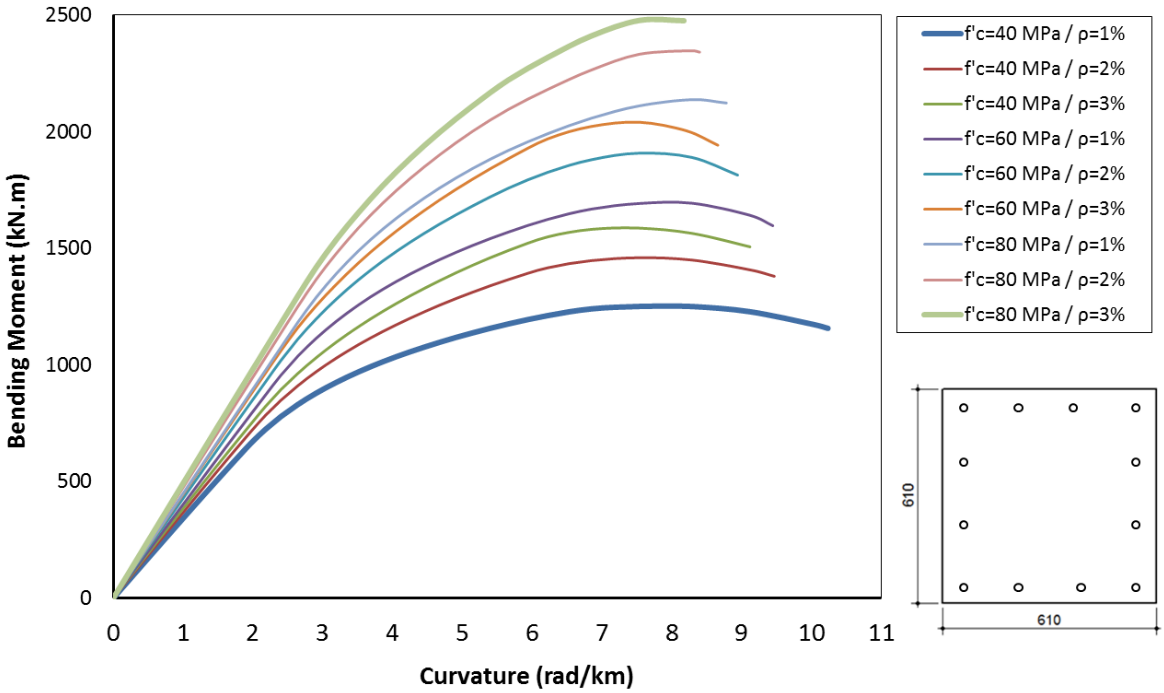

Figure 5.2 Moment-curvature analysis results for Section A for axial load of 0.75 Pr_{max}.

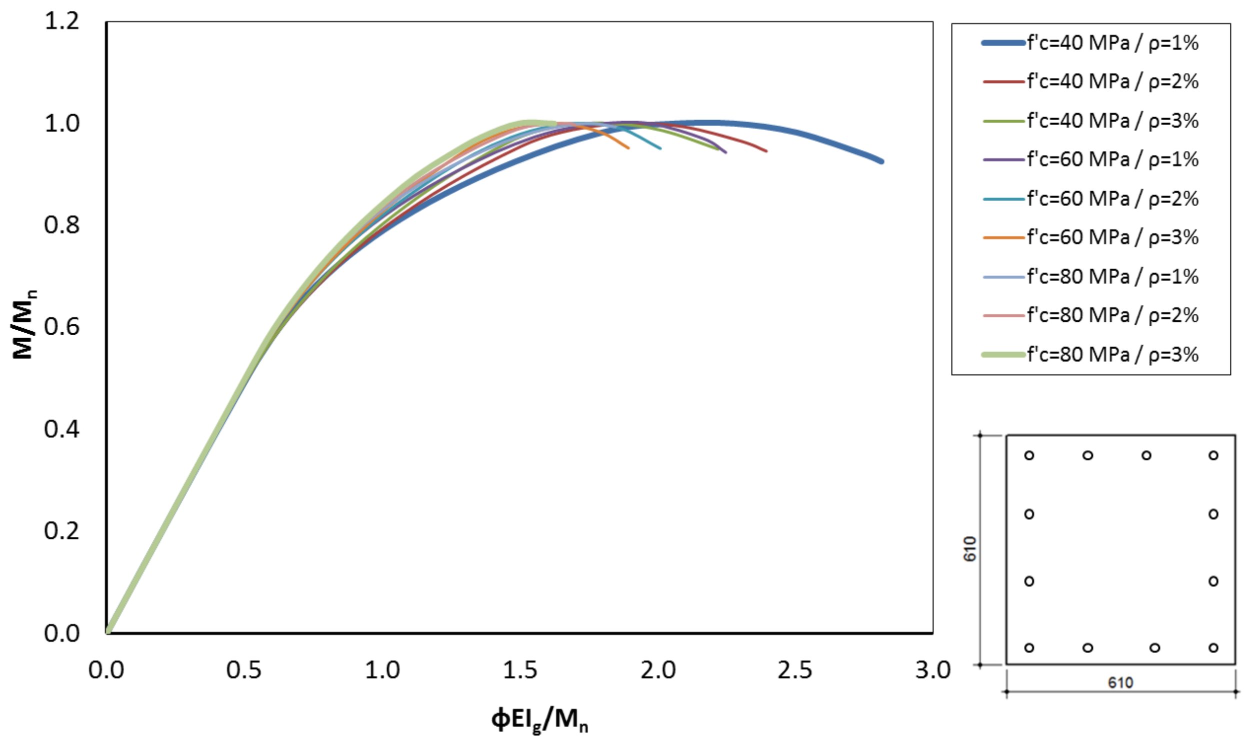

Figure 5.3 Normalized moment-curvature response of Section A for axial load of 0.75 Pr_{max}.

As seen in Figure 5.3, the initial slope of the normalized moment-rotation response of Section A with the various concrete strengths and reinforcement ratios is 1.0 and all the curves have a maximum normalized moment value of 1.0. However, the normalized curvature value at which the ultimate bending strength occurs varies for the different curves.

5.2.5 A simple approximate approach

It was desired to study the trends in flexural behaviour of column sections to find a simple way of approximating the column moment-curvature response to facilitate structural analysis of gravity-load columns connected to shear walls. The manner in which data was normalized in Section 5.2.4 forced the curves to be identical in their linearly elastic portion with all having a primary slope of unity. As nonlinear behaviour was triggered, curves started to deviate from the initial straight line at different points and followed an inconsistent path thereafter. Although the overall scatter in the normalized coordinates was not great, ultimate curvature points which are critical in design varied considerably (see Figure 5.3). However, for the same concrete strength, steel reinforcement ratio, and axial load as a fraction of Pr_{max}, normalized moment-curvature plots appeared to be identical for all cross-sections regardless of the aspect ratio or column dimensions. This phenomenon is demonstrated in Figure 5.4 for an axial load of 0.75 Pr_{max} using concrete strength of 40 MPa and 1% steel reinforcement ratio.

On the same plot, a fifth order polynomial is fitted to the actual curve using the least square of errors method. It is visually proven that a fifth order polynomial is almost an exact representation of the column moment-curvature behaviour. A similar procedure was followed for other load levels and other sectional properties. It was observed that this observation applied to all other columns considered in this study.

To further examine the flexural behaviour of gravity columns, for each case, a fifth order polynomial was fitted to the original normalized moment-curvature plots and the polynomial parameters were recorded. Corrections had to be made to ensure that the fitted curve passed through the origin (a simple axis transformation). Final curve-fitting results are summarized in Table 5.3.

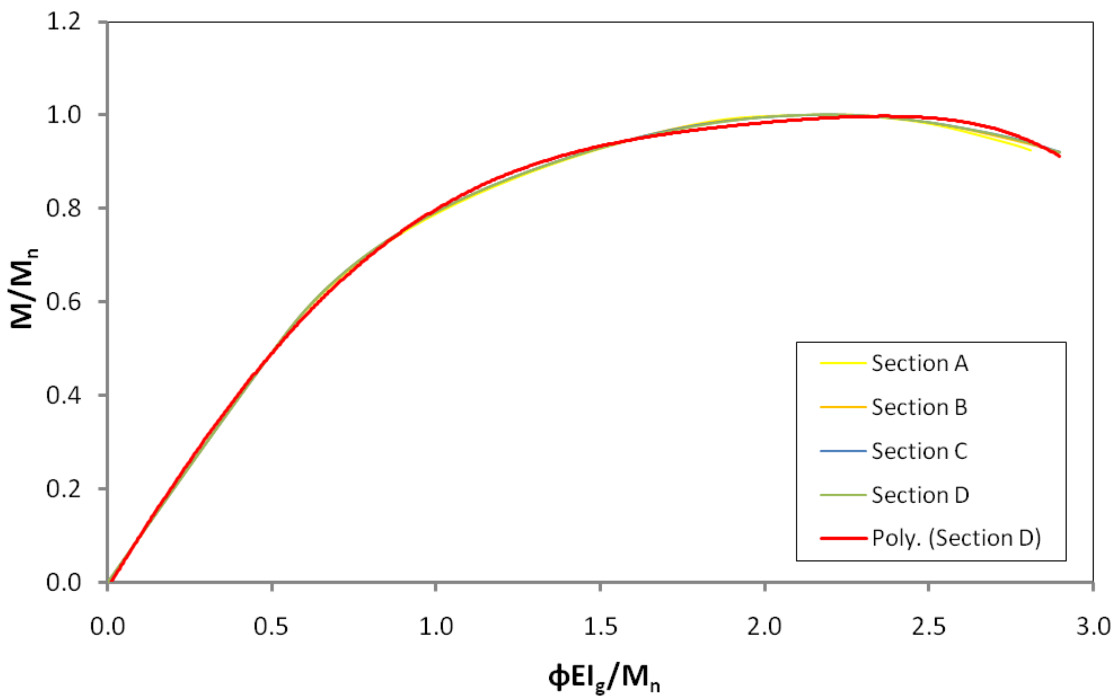

Figure 5.4 Normalized moment-curvature plots for Sections A, B, C, and D for concrete strength of 40 MPa and steel reinforcement ratio of 1% at an axial load of 0.75Prmax (see Figure 5.1 for definition of Sections A through D).

Table 5.3 Summary of curve-fitting results for normalized moment-curvature response

		P = 0.65 Pr_{max}			P = 0.75 Pr_{max}			P = 0.85 Pr_{max}		
	ρ	f'c (MPa)			f'c (MPa)			f'c (MPa)		
		40	60	80	40	60	80	40	60	80
a1	1%	1.14	1.04	0.93	1.06	0.91	0.78	0.96	0.81	0.78
	2%	1.10	1.00	0.89	1.01	0.89	0.78	0.93	0.83	0.81
	3%	1.06	0.96	0.86	0.98	0.87	0.78	0.92	0.86	0.85
a2	1%	-0.542	-0.110	0.524	-0.198	0.610	1.608	0.297	1.278	1.680
	2%	-0.415	0.107	0.821	0.028	0.796	1.717	0.462	1.175	1.451
	3%	-0.277	0.322	1.102	0.174	0.917	1.712	0.527	1.003	1.164
a3	1%	0.129	-0.318	-1.175	-0.184	-1.212	-2.879	-0.711	-2.169	-2.930
	2%	0.016	-0.620	-1.707	-0.439	-1.523	-3.164	-0.913	-2.017	-2.548
	3%	-0.122	-0.942	-2.249	-0.602	-1.733	-3.215	-0.966	-1.717	-2.021
a4	1%	-0.0121	0.1713	0.6206	0.0991	0.6165	1.7051	0.3208	1.1893	1.7898
	2%	0.0327	0.3414	0.9891	0.2172	0.8308	1.9882	0.4235	1.1295	1.5741
	3%	0.0934	0.5430	1.4030	0.2956	0.9913	2.0962	0.4409	0.9495	1.2200
a5	1%	-0.0002	-0.0269	-0.1090	-0.0144	-0.1072	-0.3580	-0.0483	-0.2367	-0.4125
	2%	-0.0070	-0.0604	-0.1956	-0.0344	-0.1594	-0.4499	-0.0685	-0.2371	-0.3784
	3%	-0.0174	-0.1053	-0.3039	-0.0490	-0.2044	-0.4997	-0.0722	-0.2052	-0.2997
$(\Phi EIg/Mn)^{max}$	1%	3.78	2.94	2.34	3.14	2.37	1.79	2.62	1.94	1.57
	2%	3.03	2.50	2.06	2.64	2.12	1.68	2.30	1.84	1.52
	3%	2.66	2.22	1.85	2.35	1.93	1.60	2.13	1.77	1.49

Where

$$\frac{\mathrm{M}}{\mathrm{M}_n} = \mathrm{a}_5\left(\frac{\Phi\mathrm{EI}_g}{\mathrm{M}_n}\right)^5 + \mathrm{a}_4\left(\frac{\Phi\mathrm{EI}_g}{\mathrm{M}_n}\right)^4 + \mathrm{a}_3\left(\frac{\Phi\mathrm{EI}_g}{\mathrm{M}_n}\right)^3 + \mathrm{a}_2\left(\frac{\Phi\mathrm{EI}_g}{\mathrm{M}_n}\right)^2 + \mathrm{a}_1\left(\frac{\Phi\mathrm{EI}_g}{\mathrm{M}_n}\right)$$

The great variation in polynomial parameters means that a separate moment-curvature analysis and curve-fitting must be carried out for each individual column. Expressing the column moment-curvature response as a fifth-order polynomial however is suitable for structural analysis programing. This concept is used in CHAPTER 6 to analyze the demands on gravity-load columns due to deformation of the shear wall.

5.3 Effect of Creep on Column Moment-Curvature Response

Creep is defined as the increase in concrete strain under sustained axial compression. In a reinforced concrete section, sustained axial load causes the concrete to soften with time decreasing the axial load carried by the concrete and transferring more of the axial load to the steel reinforcement. Therefore, reinforcement strain will in turn increase accelerating yielding of the vertical steel when the column is bent under imposed seismic deformations. The rate of creep is rather fast at early stages of loading and decreases exponentially with time such that only one year after loading, 95% of the total creep has already occurred.

Figure 5.5 demonstrates the effect of creep on concrete stress-strain relation. Creep is usually quantified using the creep coefficient (C_t) defined in Eq 5.6. Creep coefficient gives the long-term strain as a multiple of the elastic strain. It can also be used to express the effective long-term stiffness as multiple of the secant modulus as shown in Eq 5.7.

$$C_t = \frac{\varepsilon_{creep}}{\varepsilon_{elastic}} \qquad \textbf{Eq 5.6}$$

$$E_{CS_{eff}} = \frac{E_{cs}}{1 + C_t} \qquad \textbf{Eq 5.7}$$

C_t can be as high as 3 but a creep coefficient of 2 was chosen as a typical value to investigate the effect of creep on long-term concrete moment-curvature response.

A 305x1220 mm column with 1% vertical reinforcement uniformly distributed around the perimeter of the column made of 40 MPa concrete subject to an axial compression equal to $0.5f'_cA_g$ was used to investigate the effect of creep on column flexural behaviour. Low vertical steel accompanied by high axial force was chosen to exaggerate the increase in vertical steel strain as concrete softened. In other words, this combination represents the worst case scenario for the unbeneficial long-term effects on flexural response of a gravity-load column.

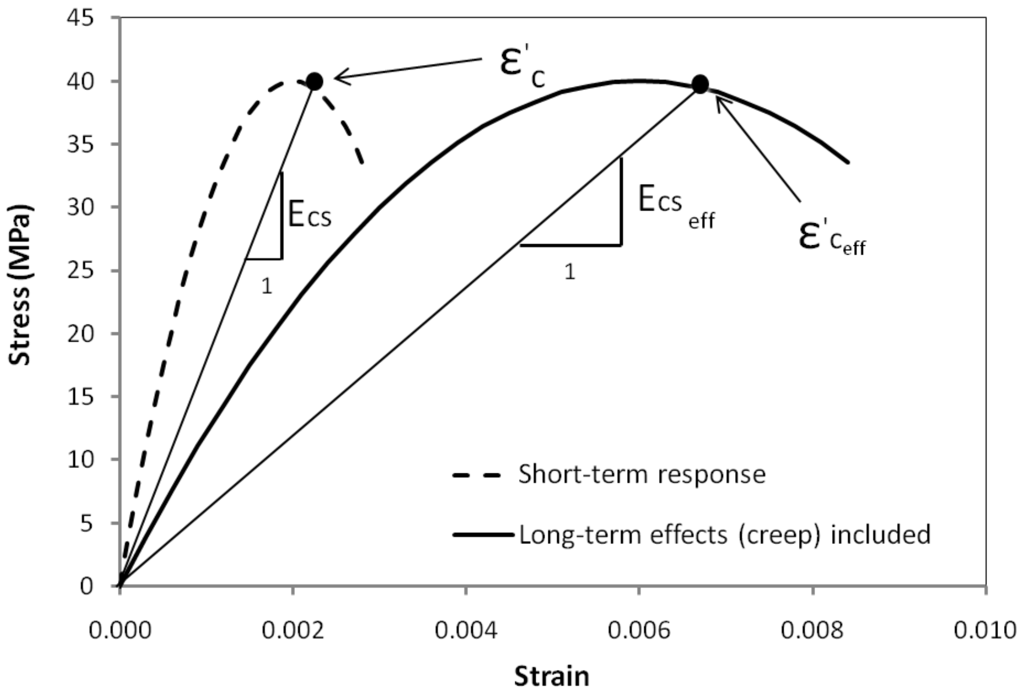

Figure 5.5 Effect of creep on concrete stress-strain relation.

Section analysis was carried out in two steps. In the first, the axial load was applied and long-term concrete stress-strain relation in Figure 5.5 was used alongside elastic-perfectly plastic (EPP) stress-strain relation for the steel to solve for the uniform section strain ε^* that balances the applied axial force. In the second step, section curvature was increased assuming linear variation of strain over the section length (i.e. plane sections were assumed to remain plane after bending). Because during a seismic event short-term concrete response properties apply, additional forces due to bending of the section were calculated using the short-term concrete response shown in Figure 5.5. To do this, the origin of the short-term concrete stress-strain curve was shifted to the point with abscissa $\varepsilon^*/(1 + C_t)$ and the axial load excluded from calculations. The origin of the steel stress-strain relation was transferred to point with abscissa ε^*. At any additional curvature level, section strain profile was found such that no net axial force resulted from adding forces from concrete and steel fibers. Bending moment was then calculated about the centroidal axis of the member where the axial load was applied in the first step. Curvature was increased until concrete was crushed at total compressive strain of 0.0035 or in other words, when concrete strain due to bending the column added to $\varepsilon^*/(1 + C_t)$ exceeded maximum permissible concrete compressive strain. Analysis results are given in Figure 5.6.

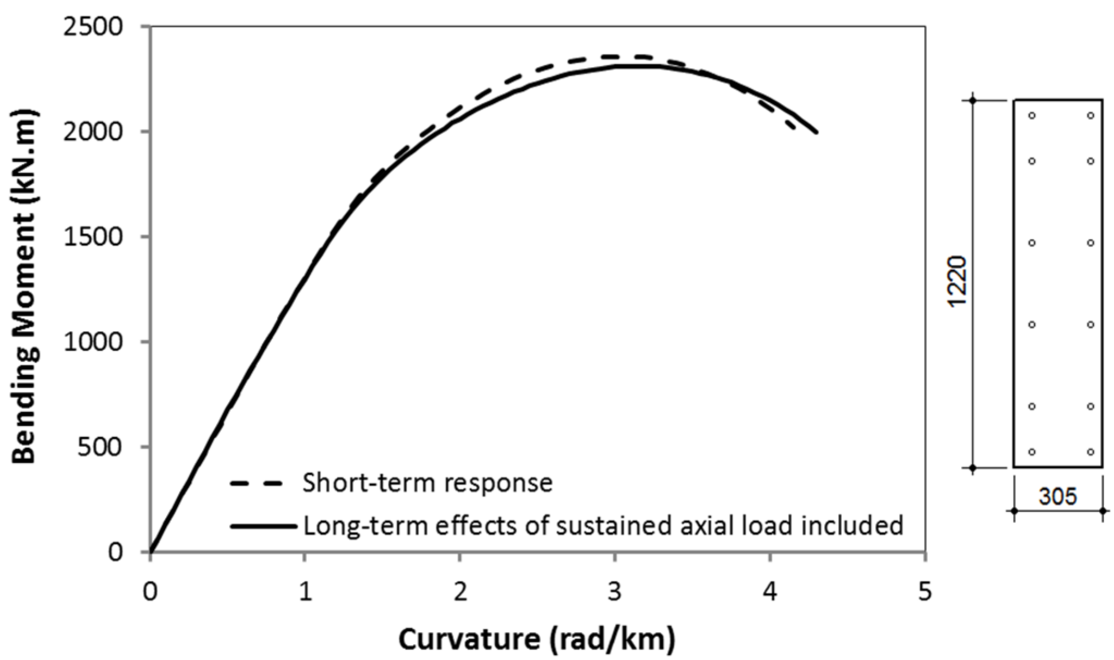

Figure 5.6 Effect of creep on concrete moment-curvature response.

Section uniform compressive strain ε^* was found to be 1.76e-3 accounting for the long-term response of concrete while it was 0.67e-3 when short-term concrete response was used. Even in this worst-case scenario, vertical reinforcement did not yield due to the sustained axial compression but uniform section compressive strain increased dramatically. This resulted in the vertical reinforcement yielding in compression much sooner when the section was bent which in turn dropped the moment strength by 5%. However, column maximum curvature capacity was increased by 3% which was because yielding of vertical steel in the compression zone at lower curvatures decreased the concrete compression depth allowing larger section curvatures before concrete crushing. Influence of concrete creep on column drift capacity is considered negligible since neither the curvature capacity nor moment strength is influenced by much.

5.4 Effect of Damage to the Column on Moment-Curvature Response

During sever seismic excitation in which a shear wall building bends violently back and forth, gravity-load columns are subjected to cyclic deformations imposed on them due to bending of the shear wall. This action causes stress reversal at the two faces of the column one being in compression and the other in tension at a time and the other way around in the next half of the cycle. As the seismic waves propagate through the building site, vibrations become larger in magnitude due to both occurrence of maximum acceleration and softening of the shear wall which when combined with cyclic deformation causes damage to the gravity column. Under compression, the typical forms of damage observed in gravity-load columns are spalling of concrete cover, buckling of vertical reinforcement in the absence of anti-buckling ties, and eventually crushing of concrete. On the tension side, damage will be in the form of cracking of concrete and fracturing of the vertical steel. Vertical reinforcements buckled and then straightened in the next half of the cycle are prone to early tensile fracture.

It is desired to study the effect of various stages of damage on the moment-curvature behaviour of gravity-load columns. Two column cross-sections with dimensions of 610 x 610 mm and 305 x 1830 mm were considered. For the results to be consistent and comparable, axial load was chosen to be $0.4f'_cA_g$ and vertical reinforcement ratio was kept at 2% of the gross cross-section with the reinforcing bars distributed uniformly along the perimeter of the cross-section. 40 MPa concrete was used to model column cross-section with 0.0035 as the maximum compressive concrete strain. The distance from the column face to the centre of the outset layer of reinforcement was kept constant at 60 mm which was then considered as the thickness of the concrete cover.

Two damage stages were considered. In the first damage stage, concrete cover was lost on both compression (top) and tension (bottom) faces of the column and vertical reinforcement had buckled under compression. In the second, concrete cover and outer layer reinforcing bars were lost on both faces of the cross-section to model the damaging effect of cyclic loading deformation. Figure 5.7 shows a schematic view of the 305 x 1830 mm column at various damage levels. Moment strength and curvature capacity of the damaged sections are then compared to that of the undamaged column.

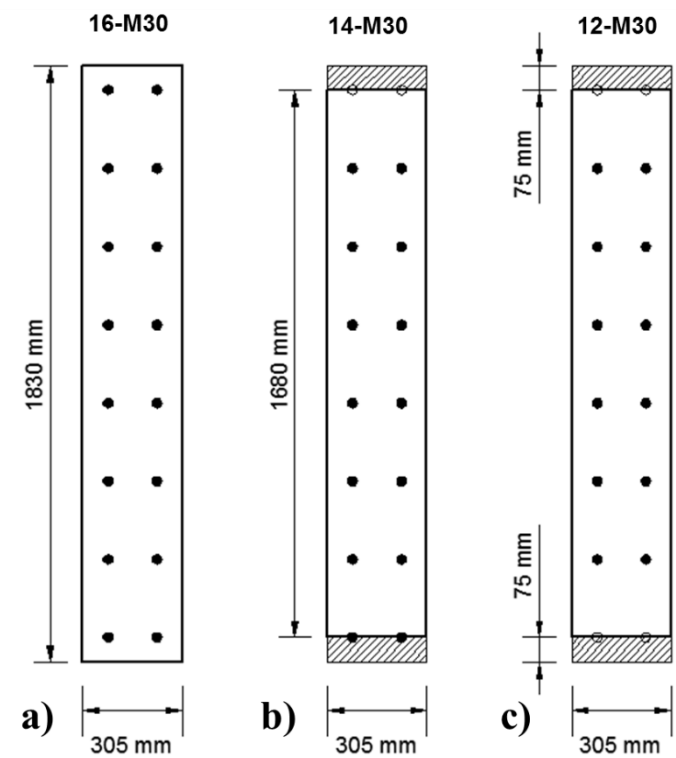

Figure 5.7 Different levels of damage of column cross-section: a) undamaged section, b) concrete cover lost on both column faces and compression steel bars buckled, c) concrete cover and the outer layer of reinforcement lost.

Moment curvature responses of the two cross-sections are plotted in Figure 5.8 and Figure 5.9 respectively. In both cases it is observed that damage to the column both softens and weakens the section response. For the 610 x 610 mm column, strength loss due to damage was 48% while the 305 x 1830 mm column lost only 23% of its strength due to the same level of damage. A rather similar trend is observed when considering loss of section flexural stiffness due to damage. This is because the width of the 610 x 610 mm column is twice as large as that of the

305 x 1830 mm column resulting in more concrete being lost due to cover spalling. In addition, a much larger proportion of the section's total steel is placed along the faces of the 610 x 610 mm column compared to the 305 x 1830 mm column resulting in a larger proportion of reinforcement being lost due to damage. 63% of the vertical reinforcements of the 610 x 610 mm column were placed at the faces of the cross-section and lost due to various levels of damage while only 25% of the 305 x 1830 mm column's vertical reinforcements were placed near the faces of the section. Loss of the outer tensile steel layer did not affect either the strength or the stiffness as much as loss of concrete area due to cover spalling and that was because tensile steel was stressed well below yielding at the column strength point due to presence of high axial load on the column. However, since less tensile reinforcement was present at damage level 2, compression depth of the cross-section became smaller which lead to a higher curvature capacity under fixed ε_c^{max}.

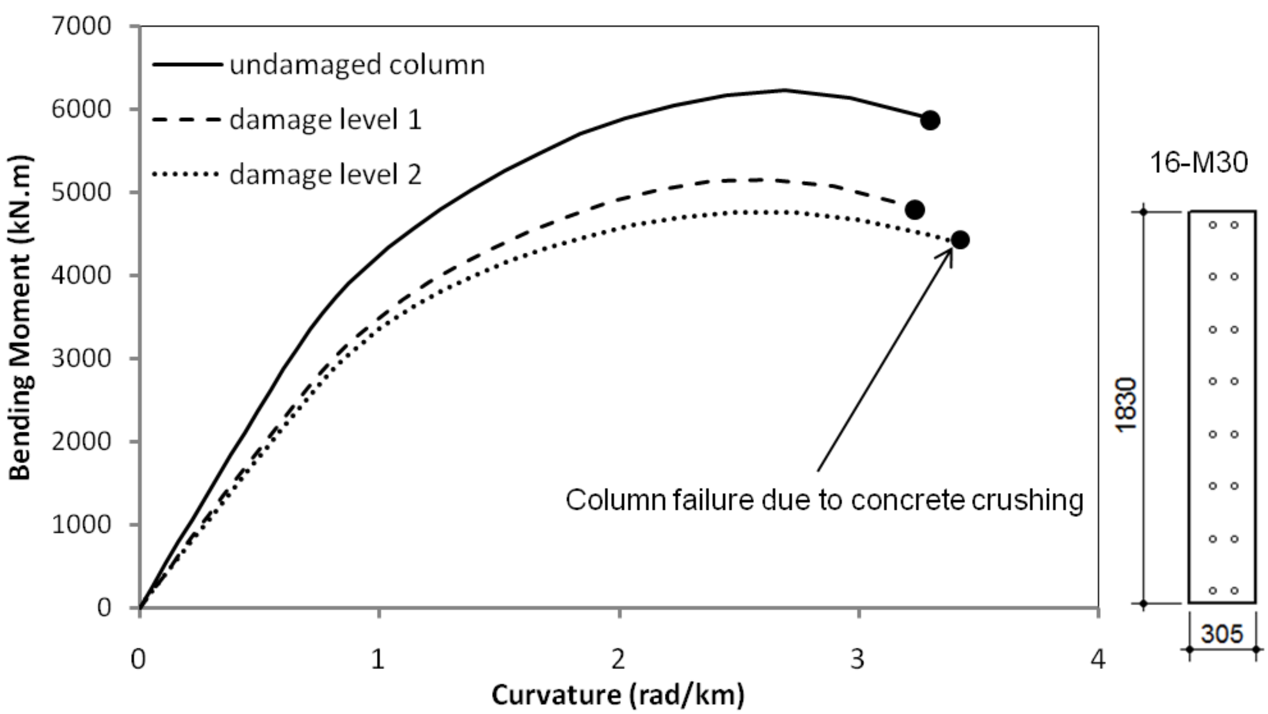

Figure 5.8 Effect of different stages of damage (cover loss and bar buckling/rupture) on moment-curvature response of a 305 x 1830 mm column section.

It is concluded that as columns grow in length (cross-section height), less reduction in strength results due to damage because columns of greater length have lower portion of their vertical reinforcement concentrated at the outer layers close to the two faces of the section and that less portion of the gross cross-section is lost due to cover spalling.

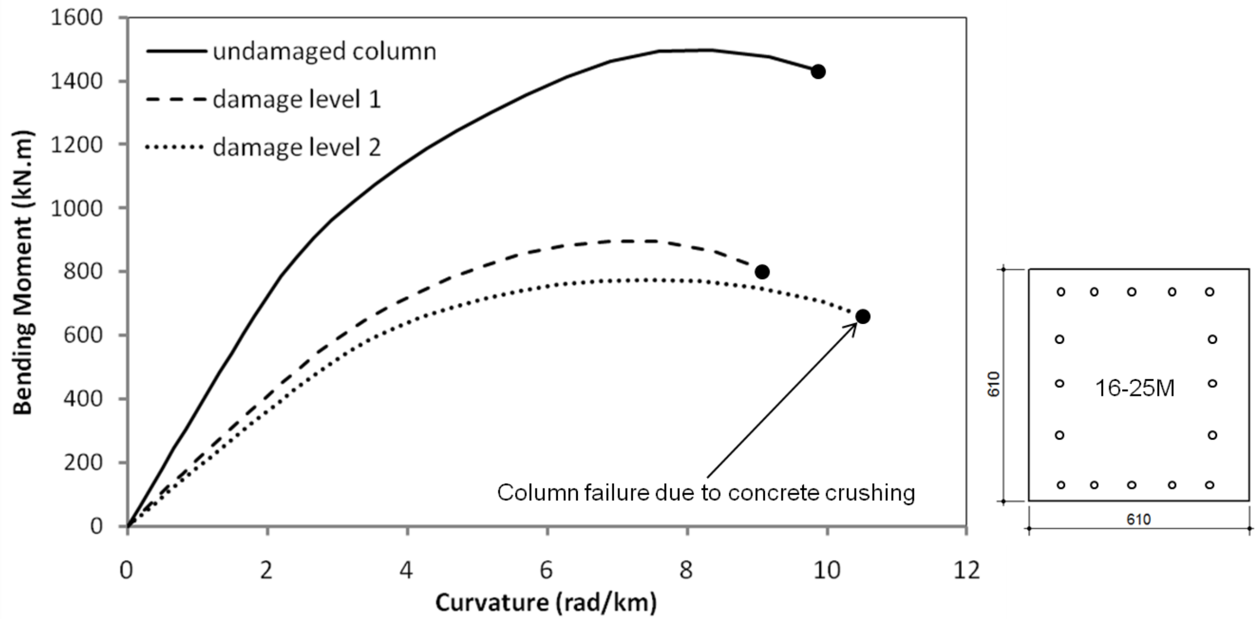

Figure 5.9 Effect of different stages of damage (cover loss and bar buckling/rupture) on moment-curvature response of a 610 x 610 mm column section.

Based on the results presented in Figure 5.8 and Figure 5.9, the effect of damage on column's maximum curvature capacity is not as substantial as its effect on bending strength. As concrete cover was lost the section became shorter and more flexible but because the same axial force had to be sustained by the smaller section, the depth of the concrete compression zone was not noticeably affected. Because curvature capacity was assumed to be governed by maximum concrete compressive strain, minimal change in compression depth at a constant maximum permissible concrete strain resulted in curvature capacities of the damaged section and the undamaged sections to be close.

5.5 Neutral Axis Depth of Gravity-load Columns at Failure

In building codes, failure of a concrete column is usually characterized by exceeding a maximum concrete strain. As an example, in NBCC 2005, the maximum permissible concrete compressive strain in absence of confining reinforcement is 0.0035. When a gravity column is bent to its ultimate capacity according to the code, concrete strain at the extreme compression fiber would be 0.0035 and the axial load would be resisted by the resultant forces from concrete and steel fibres. The curvature at which the column cross-section fails however depends on the depth of the compression zone or in other words the neutral axis depth. Assuming plane sections remain plane after bending, curvature at failure would be the maximum concrete compressive strain ε_c^{max} divided by the section neutral axis depth c. Hence, at a fixed maximum concrete compressive strain, the smaller the neutral axis depth is, the higher column curvature capacity will be resulting in a more flexible section.

Because in this study columns are assumed to fail once a certain curvature is exceeded which can also be expressed as a certain neutral axis depth, this section examines various methods that can be used to calculate the neutral axis depth and hence curvature capacity of gravity columns. Provisions of NBCC 2005 are used whenever the exact results are compared against a simplified approach used in a building code. Section 5.2 revealed that for columns designed to NBCC 2005 provisions, axial load accompanied by seismic demands ranged between 65% and 75% of Pr_{max}. Assuming that columns are designed to have just enough strength to carry P_f (the axial load resulting from gravity load combination), Pr_{max} will be equal to P_f but if the column is over-designed, then Pr_{max} will be greater that P_f. Hence the range of column axial load can practically vary from 60% to 75% of Pr_{max}.

Another measure of the intensity of the axial compression is the load as a fraction of gross concrete strength $f'_c A_g$. It is useful to convert the axial load combined with seismic effects (P_s) expressed as a fraction of Pr_{max} to one that is expressed as a ratio of concrete gross strength which gives a better feel for the magnitude of the axial load. Maximum permissible concrete compressive strain was considered to be 0.0035 regardless of concrete strength which is the way NBCC 2005 treats concrete sections. Figure 5.10 shows the extreme bounds of the results of this conversion for three levels of steel reinforcement as a ratio of the gross cross-section.

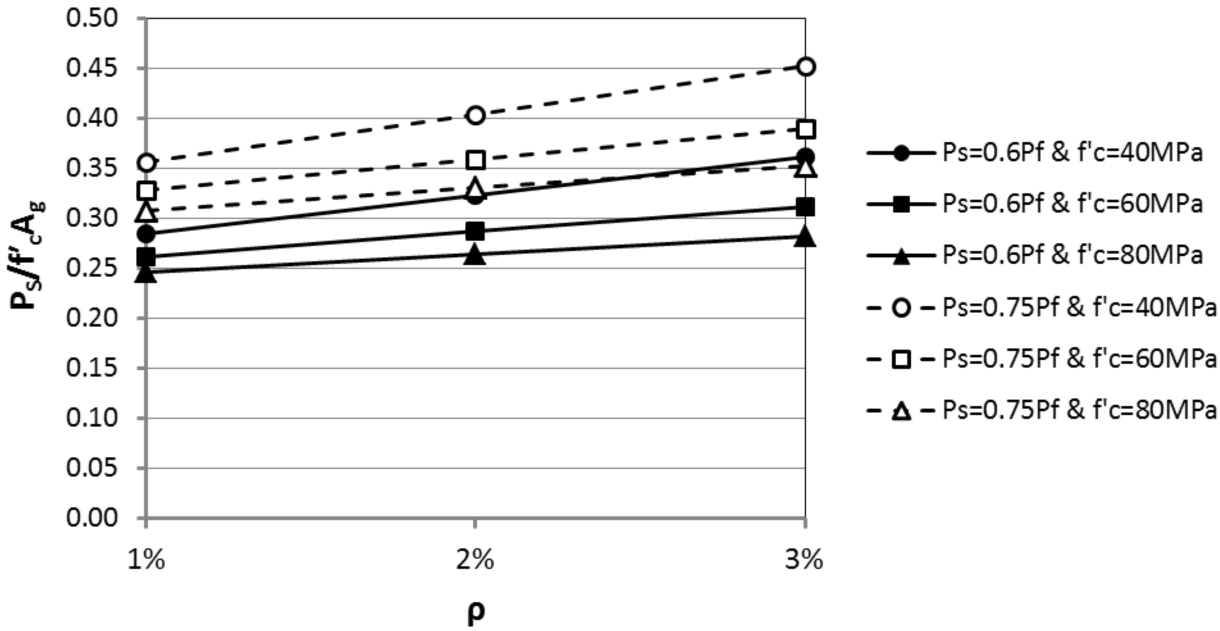

Figure 5.10 Seismic axial load demand as a ratio of gross concrete compressive strength.

As expected, the higher P_s/P_f is, the larger P_s/f'_cA_g will be. As more steel reinforcement is added to the section, Pr_{max} and consequently P_f and P_s become larger while f'_cA_g remains constant resulting in larger P_s/f'_cA_g. At lower concrete strengths effect of addition of steel reinforcement was more pronounced. It is concluded that P_s/f'_cA_g varies from 25% to 45% for the broad range of columns considered in this study.

With the probable axial compressive load on the column determined, one can calculate the strain profile and therefore the neutral axis depth of the column cross-section at failure. Several methods can be used to obtain the compression depth of a column cross-section at failure each based on some simplifying assumptions but all assuming linear strain profile over cross-section length (or depth). Three most commonly used methods are presented here.

The first and the most elaborate method is sectional analysis. In this method, the cross section is divided into a fine mesh of stripes or fibres. Material properties and stress-strain relation for both concrete and steel are then assigned to the corresponding fibres. At a certain section strain profile, strain is calculated for each fibre and then translated into stress using material constitutive relation. Stress is then multiplied by the fibre area and integrated to calculate axial load and bending moment about the centroidal axis. This method is expected to give near exact results for all section strains (curvatures) including the state near to column failure.

The second method is section analysis using the equivalent stress block defined by the two factors α_1 and β_1 which define the intensity of the concrete stress and depth of the stress block respectively. The two factors are calculated such that the resultant force of the stress block is equivalent to that obtained from integrating concrete stress over the compression depth of the section and hence can only be used at the ultimate state. Contribution of steel reinforcement to both axial compression and bending moment can then be added to the resultant of concrete stress to obtain the total reaction of the section. Predicting neutral axis depth using is method is also expected to be of good accuracy.

The third method is rather simple and is the one given in NBCC 2005. This method ignores the effect of steel reinforcement on section neutral axis depth assuming the net steel force is negligible at column failure. Eq 5.8 shows the formula used in NBCC 2005 to calculate neutral axis depth.

$$c = \frac{P_s}{\alpha_1 \beta_1 \Phi_c f'_c b} \qquad \textbf{Eq 5.8}$$

The code equation simply uses a force balance between the applied axial compression and resultant of the concrete stress. This method can give a good approximation of the neutral axis depth of the column at failure as long as the net steel force is negligible. If this turns out not to be the case, then Eq 5.9 must be used.

$$c = \frac{P_s - P_{ns}}{\alpha_1 \beta_1 \Phi_c f'_c \, b} \qquad \textbf{Eq 5.9}$$

where P_{ns} is the net steel force.

Because in this study failure of the column cross-section is detected when a certain curvature threshold is exceeded and at a fixed maximum concrete strain, curvature can be linked to neutral axis depth. Further attention is given to prediction of section compression depth at failure. Results obtained from the code simplified approach are compared against those from more rigorous analysis to ensure that the code provision is safe for the broad range of columns sections considered in this study.

It is common practice to distribute column reinforcement evenly around the perimeter of the section. In the case of elongated column sections with narrow width, this construction method results in uniformly distributed reinforcement along the column length (i.e. equally spaced rows of reinforcing bars each having the same amount of steel). It is therefore reasonable to assume that reinforcement is distributed evenly over the length of elongated columns. Note that, it is the elongated columns that are expected to have a lower curvature capacity due to developing longer compression zone at failure. Variation of net steel force as a ratio of full yield strength and gross concrete strength with neutral axis depth is shown in Figure 5.11 and Figure 5.12 respectively.

Elastic-perfectly plastic behaviour was assumed for steel and maximum compressive concrete strain was fixed at 0.0035. As expected and can be seen on the figures below, the net steel force vanished when neutral axis depth was at section mid-length and the steel forces on either sides of the neutral axis cancelled each other out.

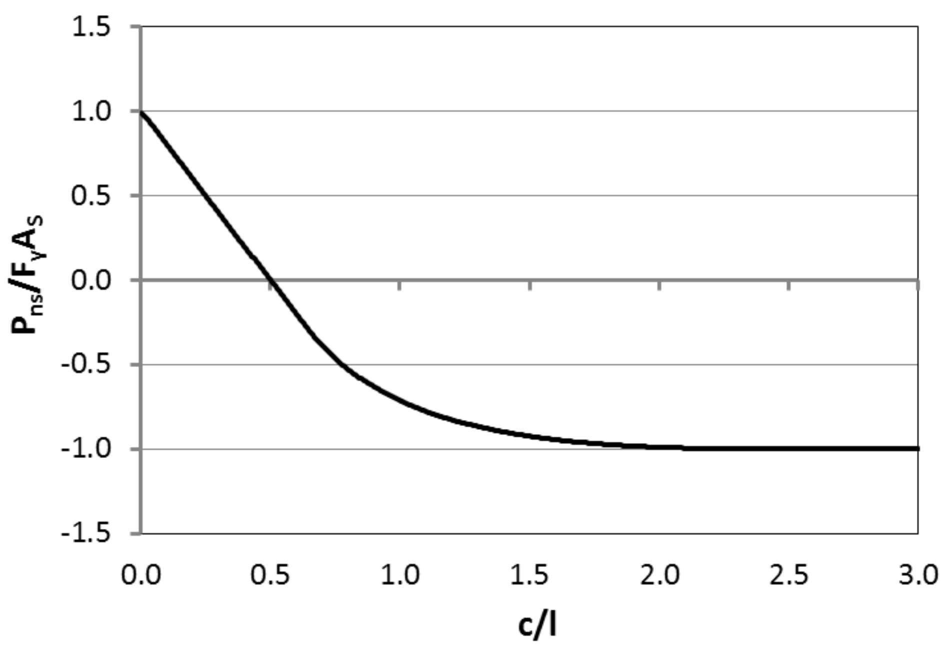

Figure 5.11 Variation of the net steel force as a ratio of section full yield strength with section compression depth.

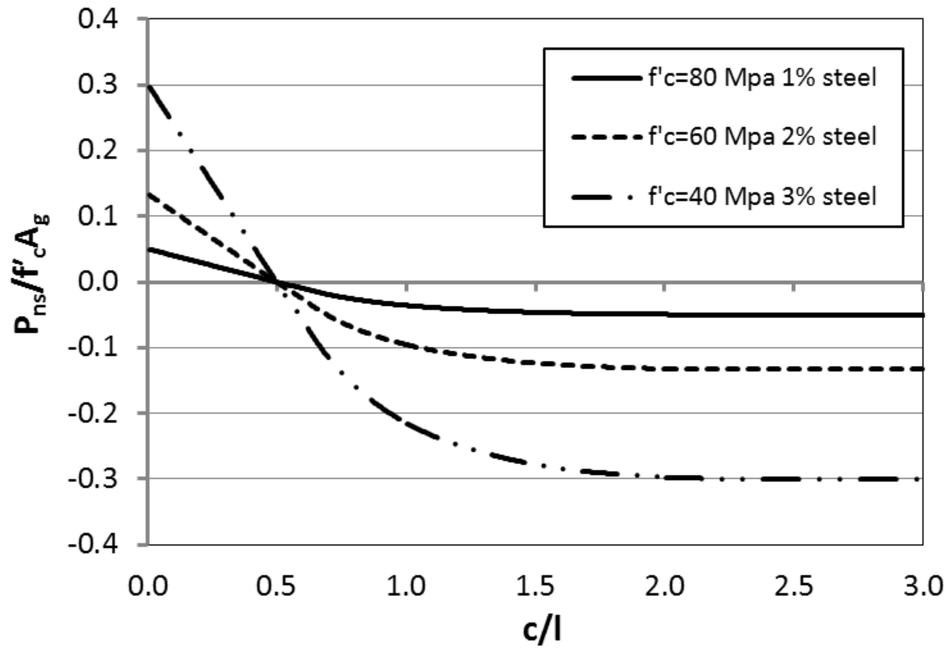

Figure 5.12 Variation of the net steel force as a ratio of gross concrete strength with section compression depth.

To express the net steel force as a ratio of gross concrete strength, various concrete strengths and steel ratios were used. The net steel force as a ratio of gross concrete force was the greatest when concrete strength was the lowest and steel ratio the highest and vice versa; hence, Figure 5.12 shows the extreme bounds of the net steel force at column failure that can be encountered in the broad range of column cross-sections considered in this study. The results suggest that as long as the section neutral axis depth falls between 45% and 60% of the column length, Eq 5.8 is capable of predicting the neutral axis depth at failure with acceptable precision.

To investigate whether the error in Eq 5.8 is on the safe side or not, compression depth of a 1220 mm long column section was calculated using both Eq 5.8 and the exact solution accounting for the net steel force. In order to make general conclusions, three concrete strengths of 40, 60 and 80 MPa combined with three steel ratios of 1, 2 and 3% was used. The results are presented in Figure 5.13.

a) b) c)

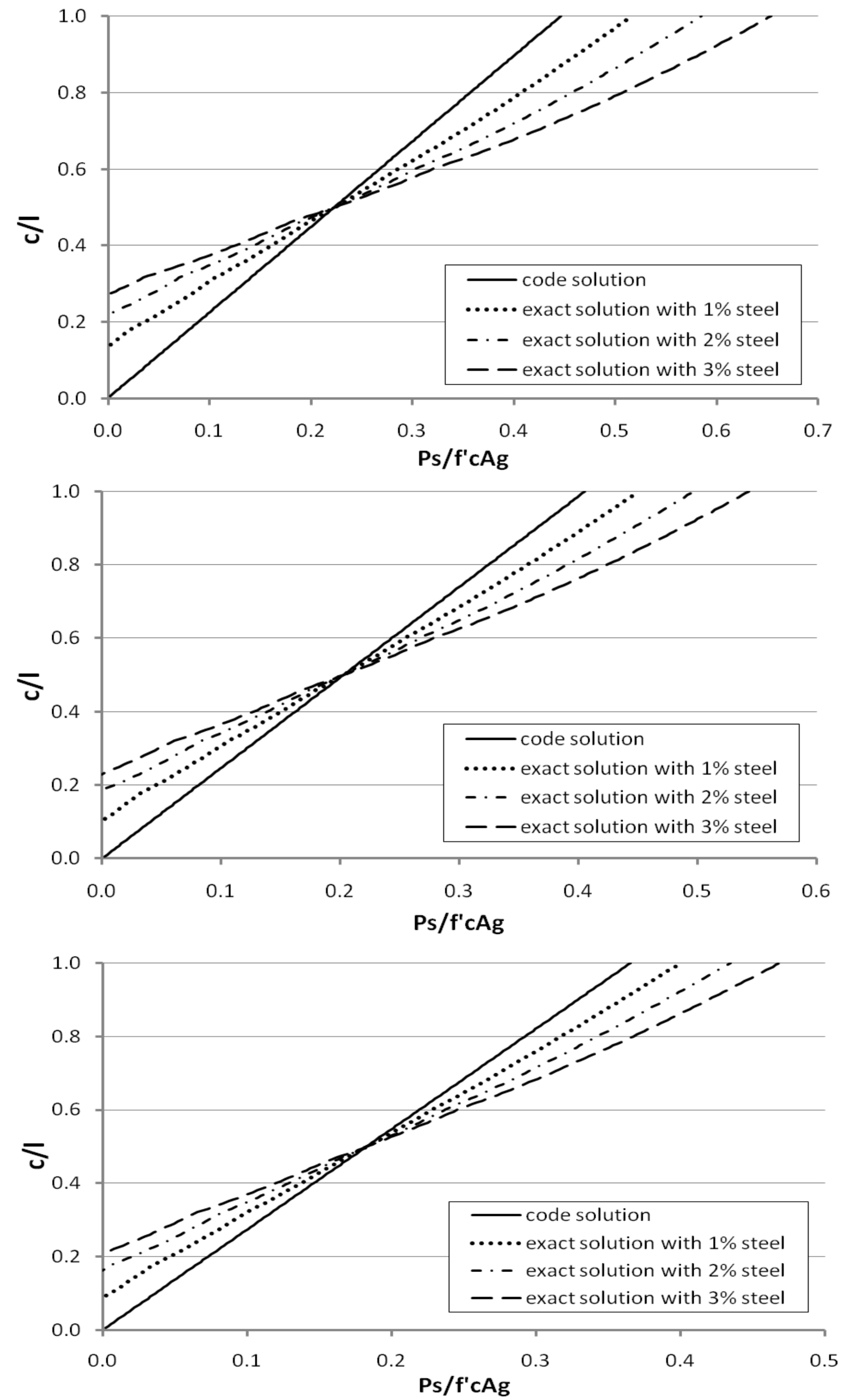

Figure 5.13 Accuracy of calculation of neutral axis depth of a 1220 mm long column section at failure neglecting steel forces for concrete strength of: a) 40 MPa, b) 60 MPa, and c) 80 MPa.

As expected and explained earlier, all of the curves meet when neutral axis depth is equal to half of the section length and the contribution of steel reinforcements on opposite sides of the neutral axis cancel each other out. Also the higher the steel reinforcement ratio is, the greater the error in the code simplified method will be.

It was shown earlier in this section that P_s/f'_cA_g is expected to vary between 25% and 45%. Based on this observation and the results presented in Figure 5.13, it is seen that the simplified code approach always suggests a larger neutral axis depth than the exact value. At a fixed maximum permissible concrete strain, the larger the neutral axis depth is, the lower the curvature capacity will be and hence, the code approach will always underestimate column curvature capacity. In other words, when the column is assumed to fail when a certain curvature capacity is exceeded, it will always be safe if column curvature capacity is calculated using the neutral axis depth suggested by the code. Although always on the safe side, the error in code prediction can be substantial at high axial load and hence column curvature capacity will be greatly underestimated. The more accurate section analysis method is recommended in those circumstances.

5.6 Summary and Conclusions

Listed below are the main findings of this chapter:

1. The seismic axial load demand was shown to vary from 25% to 45% of the compressive strength of the gross concrete cross-section considering a broad range of concrete strengths, steel ratios and building configurations.

2. The shape of the column moment-curvature response under the same average vertical stress was shown to be the same for columns with the same concrete strength and steel ratio regardless of the aspect ratio of the column's cross-section. Furthermore, the shape of the moment-curvature response was shown to be accurately approximated using a 5^{th} order polynomial.

3. Accounting for long-term effects of sustained compressive axial load was shown not to significantly affect either curvature capacity or bending strength of gravity-load columns.

4. Damage of the column cross-section was shown to have much more of an adverse effect on the column’s bending strength than its curvature capacity.

5. Neglecting the net steel force resultant in section analysis of column cross-sections was shown to result in a larger concrete compression depth and consequently a smaller curvature capacity.

CHAPTER 6 Structural Analysis of Gravity-load Columns Connected to Shear Walls with Flat Plate Floor Slabs

6.1 Introduction

As explained in CHAPTER 1, seismic deformations of the shear wall imposed on the gravity-load resisting system of the building induces additional curvature demands in the gravity-load columns. In shear wall building with flat plate floor slabs, flexural stiffness of the thin flat plate floor slabs is usually not large enough to induce significant curvature demands on the columns near the top of the building due to frame action of the floor slabs (see Section 7.11). Therefore, in such systems with the wall developing a plastic hinge at its base, maximum column seismic curvature demand is also expected to occur at the base of the column. As will be proven later in the chapter, curvature demand at the base of the column is governed mostly by the lateral deformation of the wall at the top of the first storey and becomes progressively less influenced by the displacements at higher floors. Shear strains in a flexural wall are the largest in the plastic hinge zone (see CHAPTER 2). In addition, foundation rotation adds a constant drift to the deformation profile of the wall which increases the displacement at the lower levels significantly. All of these effects contribute to the maximum column curvature demand occurring within the wall plastic hinge zone or simply at the base of the column.

To ensure that the gravity-load system can withstand the imposed shear wall deformations, seismic curvature demands need to be estimated and compared to the columns’ curvature capacity. This chapter aims at providing a structural analysis algorithm for evaluating seismic demands on gravity-load columns of shear wall buildings with flat plate floor slabs within the wall plastic hinge region. A nonlinear structural analysis methodology is proposed and verified against a sophisticated finite element analysis program. The method is further optimized for accuracy as well as computational efficiency. The simple analysis procedure is then used to perform a parametric study on seismic demands on gravity-load columns of shear wall buildings with flat plate floor slabs in CHAPTER 7.

6.2 Literature Review on the Behaviour of Gravity-load Column under Combined Axial Compression and Flexural Loading

To better model the nonlinear behaviour of gravity-load columns for the purpose of structural analysis, a number of tests on reinforced concrete columns under combined axial compression and bending are studied. Sections below briefly introduce the tests and provide a summary of the key observations made and conclusions drawn from the experiments.

6.2.1 Ibrahim and MacGregor (1996)

Ibrahim and MacGregor tested 20 high-strength (60 to 90 MPa) and ultra-high-strength (115 to 130 MPa) concrete columns. 14 specimens had rectangular cross-sections and 6 were triangular. 5 of the columns had no reinforcing steel (i.e. plain concrete). The tie reinforcement of rectangular columns satisfied or exceeded the minimum requirements of Section 7.10.5 of ACI 318-M895 and Clause 7.6.5 of the Canadian Code CAN3 A23.3-M46 but it never complied with either code's requirements for columns in seismic regions. In other words, none of the specimens were detailed for seismic ductility. The specimens were then subjected to a combined axial compression and flexure. Specimens were loaded such that the location of the neutral axis was kept fixed at a selected location within the specimens.

Plain concrete rectangular specimens failed suddenly and in an explosive manner. This behaviour was more severe for the case of ultra-high-strength specimens. Spalling of the concrete cover was more gradual for high-strength than ultra-high-strain specimens and occurred at maximum compression strains between 0.0034 and 0.0043.

Bending moment dropped after concrete cover spalling. For well-confined specimens, the moment reached a second peak after cover spalling which depended on lateral confinement and concrete strength. For poorly-confined specimens, the small increase bending in capacity of the confined core could not compensate for the loss of cross section due to cover spalling. Rectangular specimens showed that the effectiveness of lateral confinement after cover spalling was slightly reduced by increasing concrete strength.

In conclusion, failure of high-strength concrete columns with tie spacing equal to the least column dimension was shown to be sudden and brittle while well-confined columns could sustain the applied loads through large deformations.

6.2.2 Lloyd and Rangan (1996)

Lloyd and Rangan conducted an experimental study on the behaviour and strength of high-strength concrete columns under eccentric compression. 36 specimens in total were tested half of which had a 175 mm square section and the other half consisted of 300x100 mm column sections loaded in bending about the weak axis. Two concrete mixes producing concrete strengths of about 60 and 95 MPa were used. 4 mm ties spaced at 60 mm were provided as lateral reinforcement.

The general mode of failure observed was flexural with concrete spalling in the compression zone. Columns with large load eccentricities experienced sheet spalling of concrete while ones with smaller eccentricities and larger concrete strengths suffered shear-like failure across the column depth.

The provided lateral reinforcement was not sufficient to prevent buckling of the longitudinal reinforcement in the case of specimens with smaller eccentricities. These specimens failed in a sudden and brittle manner with little or no post-peak deformation capacity regardless of concrete strength. On the other hand, the provided lateral reinforcement prevented buckling of the longitudinal reinforcement in the case of specimens with higher eccentricities. These columns cracked and deformed significantly prior to failure and exhibited a somewhat ductile behaviour.

Even though the spacing of the lateral reinforcement was less than the column's shortest cross-sectional dimension, the provided lateral reinforcement failed to ensure considerable ductile behaviour beyond the point of concrete cover spalling. It is therefore reasonable to conclude that gravity load columns not detailed for seismic ductility do not demonstrate reliable post-peak ductility.

6.2.3 Legeron and Paultre (2000)

In their experimental program, Legeron and Paultre tested 6 high-strength 305 mm square concrete columns under cyclic flexure and constant axial load. The main parameters in the study were the level of column axial load and the volumetric ratio of confinement steel. Three axial load levels of 15, 25, and 40% of $f'_c A_g$ were selected expecting failure modes to vary from yielding and possibly rupture of the tensile reinforcement at lower axial load levels to crushing of concrete at high axial loads. Tie configuration was kept constant with the tie spacing being either 130 mm or 60 mm. A tie spacing of 60 mm provided 95% of the confinement steel required by the ACI code. The specified concrete strength was 100 MPa.

At failure, the section just above the base of the column was undamaged for about 40 mm. This was due to the confinement provided by the foundation. The length of the damaged region (i.e. plastic hinge zone) at the bottom of the column increased with axial load. The plastic hinge length varied from approximately one column depth to over three column depths as axial load increased from 10% to 40% of $f'_c A_g$.

At lower axial load levels, concrete spalled off just after yielding of the tensile steel while at higher axial loads, concrete cover spalling was observed before yielding was reached.

The specimens with the lowest axial load level exhibited a ductile behaviour and were able to sustain large inelastic cyclic displacements. Energy dissipation capacity and ductility were decreased with increase in axial load. As expected, specimens with larger volumetric ratio of confinement steel had more energy dissipation capacity and ductility.

Bending moment at the base of the columns dropped after cover spalling and even in specimens with lower axial loads, larger top displacements did not result in base moments higher than that recorded at the onset of cover spalling. It is therefore concluded that bending moment at cover spalling must be used as bending moment strength of gravity-load columns.

Note that typical concrete gravity-load columns are not detailed for seismic ductility and usually have much less confinement steel than the specimens tested by Legeron and Paultre (2000). Tie spacing is often equal to the column's smallest dimension. Hence, typical gravity-load columns cannot be expected to have a ductile behaviour and dissipate considerable hysteretic energy.

6.2.4 Bae and Bayrak (2003)

Bae and Bayrak investigated the accuracy of the rectangular stress block parameters specified in ACI 318-02 in predicting axial load and bending moment strengths of high strength concrete columns with 66 MPa $<f'_c<$140 MPa. ACI provisions were proven to give unsafe estimates of the column axial and bending capacities for high strength concrete. This phenomenon was attributed to early cover spalling in high strength concrete columns.

Reviewing test results of 224 specimens available in the literature, Bae and Bayrak reported that the maximum section compressive strain at the onset of cover spalling ranged from 0.0022 to 0.0048. Presence of transverse (confinement) reinforcement was likely to lower the cover spalling strain. Considering all the data reported in the literature and choosing a safer lower-bound approach, Bae and Bayrak adopted a fixed cover spalling strain of 0.0025 in their study.

Based on an analytical study, two strength reduction factors were proposed, namely, $\gamma_1$and $\gamma_2$to account for the effect of cover spalling on axial and flexural strengths respectively. It was found that cover thickness, section size, and the amount and distribution of longitudinal reinforcement did not influence $\gamma_1$and γ_2. $\gamma_1$was shown to be constant up to a concrete strength of 80 MPa and reduced as concrete strength was increased. γ_2 remained constant up to a concrete strength of 60 MPa and decreased beyond that point as concrete strength was further increased. γ_2 decreased more rapidly at higher axial load levels.

Bae and Bayrak then applied both the ACI 318-02 provisions and their own strength reduction factors to the 224 test specimens available in literature and demonstrated that their method gives a safer estimate of axial and flexural strengths of high as well as normal strength concrete columns.

6.2.5 Bae and Bayrak (2008)

Bae and Bayrak conducted an experimental study aimed at understanding the mechanisms of formation of plastic hinges in gravity-load columns. Their literature review had shown somewhat contradictory observations by other researchers on the parameters affecting the formation of plastic hinges in reinforced concrete members. Prior to Bae and Bayrak (2008), axial load was not thought to play a major role in defining the plastic hinge length of gravity-load columns. This was mainly because most of the experimental studies had been done on beams where axial loads are not critical. Therefore, their research was aimed at reconciling the differences encountered in previous research resulting in development of an expression that can be used to estimate plastic hinge length of columns more accurately for various axial load levels.

Plastic hinge length is key to determining the ductility of columns. It defines the region over which inelastic curvatures are distributed. These inelastic curvatures make up the majority of the column's nonlinear flexural rotation. Since columns have little shear deformation, flexural deformations dominate their total displacement profile and hence, need to be estimated with great accuracy if drift capacity of the column is of concern.

In the four specimens that Bae and Bayrak tested, the effect of axial load on plastic hinge length (l_p) was evident. l_p increased with increasing axial load. It was also observed that as concrete compressive strains reached a critical value, concrete cover spalled off. Subsequently, yielding of longidunal steel on the compression side occurred which was followed by crushing of the concrete core. These accumulations of damage lead to formation of the plastic hinge.

Bae and Bayrak then carried out an analytical study to formulate an empirical expression for estimating l_p. They assumed that the plastic hinge length was equal to the length over which the longitudinal steel on the compression side yields minus the undamaged region just above the base of the column due to stub confinement. A sectional analysis with core concrete modeled as confined concrete and cover concrete modeled as unconfined concrete was used. Based on observations by previous researchers, it was assumed that maximum moment capacity is reached prior to formation of a plastic hinge and that the magnitude of concrete compressive strains experienced by the core when maximum moment capacity is reached at the critical section of the column can give a good indication of formation of a plastic hinge.

Bae and Bayrak proposed the following expression for estimating plastic hinge length of concrete columns.

$$\frac{l_p}{h} = \left[0.3\left(\frac{P}{P_0}\right) + 3\left(\frac{A_s}{A_g}\right) - 0.1\right]\left(\frac{L}{h}\right) + 0.25 \geq 0.25 \qquad \textbf{Eq 6.1}$$

In this equation, h is the depth (length) of the column, P is the axial load, P_0 is the axial load capacity of the column, A_s is the total area of longitudinal steel, A_g is the gross concrete area, and L is the distance from the critical section to the point of contra-flexure. 0.25 is added to account for the undamaged region due to stub confinement. The increase in the plastic hinge length with increase in axial load and longitudinal reinforcement ratio is clearly depicted in this expression. The proposed expression was proven to give accurate estimates of l_p for the four columns tested by Bae and Bayrak.

6.2.6 Discussion and Summary

A vast amount of experimental studies on gravity-load reinforced concrete columns are available in the literature a number of which were selected here based on axial load, concrete strengths, and reinforcement details most representative of gravity-load columns and presented earlier. The following are conclusions or evidence that all or most of the tests considered here share in common.

Concrete cover spalling has been shown to considerably reduce the column bending moment capacity. Gravity-load columns were shown not to have appreciable ductility beyond the point of cover spalling. The onset of cover spalling was shown to vary considerably and be highly influenced by the magnitude of the axial load on the column, amount of transverse reinforcement, concrete strength and the axial load eccentricity and therefore very hard to predict. Results from all tests reached the consensus that failure of gravity-load columns is not ductile.

If a plastic hinge model is to be used to model the response of the column beyond its peak bending moment, certain assumptions need to be made on the length and the distribution of inelastic curvatures over the height of the plastic hinge. The tests studied earlier showed that for an undamaged column with no cover spalling, curvatures varied almost linearly over the plastic hinge length. If the column experienced cover spalling, then the curvatures were almost constant over the damaged zone or the plastic hinge zone. Section 6.3 introduces the same concept and elaborates on the assumptions made on curvature distribution over the height of the column's plastic hinge zone. Assumptions on column plastic hinge length are stated as needed throughout the chapter.

It must be noted however that from a performance-based engineering viewpoint, some damage to the shear wall might be acceptable as shear walls are designed for ductility. Gravity-load columns on the other hand are primarily designed to withstand the weight of the building and are not detailed for seismic ductility. Therefore, excessive damage to the gravity-load system directly impacts life-safety of the building and must be avoided. Even though the behaviour of the column beyond the point of peak bending strength or after concrete cover spalling is modeled in this chapter, attention needs to be paid to the damage associated with any curvature demand on the column in the column's plastic response range.

6.3 Inelastic Curvature Concentration in Gravity-Load Columns

When a gravity-load column sustaining substantial axial compression is pushed with a horizontal point load from floor slabs due to deformation of the SFRS, bending moments along the height of the column induce a curvature profile that will result in the displacement profile imposed by the SFRS. At small deformations, the column behaves almost as an elastic beam-column with a constant flexural stiffness. As the deformation increases, maximum bending moment at the base of the column becomes progressively greater causing the bottom part of the column to soften due to both softening of concrete and yielding of steel in compression and yielding of the tensile steel. This makes the fixed end of the column to behave nonlinearly while the parts above remain elastic. This results in a curvature profile that is no longer uniformly varying. More curvature gets concentrated at the base of the column and less in the upper parts. At the ultimate state just before failure, excessive curvatures at the base of the column can cause vertical steel bars to buckle under compression, concrete cover to spall off and tensile steel bars to fracture. Losing the concrete cover and the outer layer of vertical reinforcement over a certain height makes the fixed end of the column even more flexible resulting in highly concentrated curvature in that region. Damage can also be in the form of diagonal cracking due to combination of shear and flexure. This damaged softened zone is known as the column plastic hinge zone.

Inelastic curvature concentration in gravity-load columns can be further explained using a typical moment-curvature response of a column (Figure 6.1). The initial linear part of the curve is the region where both concrete and reinforcing steel are behaving linearly. As curvature is increased, concrete starts to soften causing the moment-curvature response to curve downward. Yielding of steel (either in compression or tension) starts near the peak strength point. Bending moment strength starts to decay past the peak strength point. This strength loss is due to concrete losing strength due to excessive compressive strain. The column is assumed to fail with concrete crushing at concrete maximum compressive strain of 0.0035 if no confinement reinforcement is provided. Flexural stiffness of the gravity-load column or the slope of the moment curvature response is nearly constant over the elastic range. Stiffness starts to decay due to softening and concrete and yielding of steel which results in larger curvatures for the same moment increment compared to the elastic region. This causes significant curvature concentration at the base of a gravity-load column pushed to deformation profile of the SFRS.

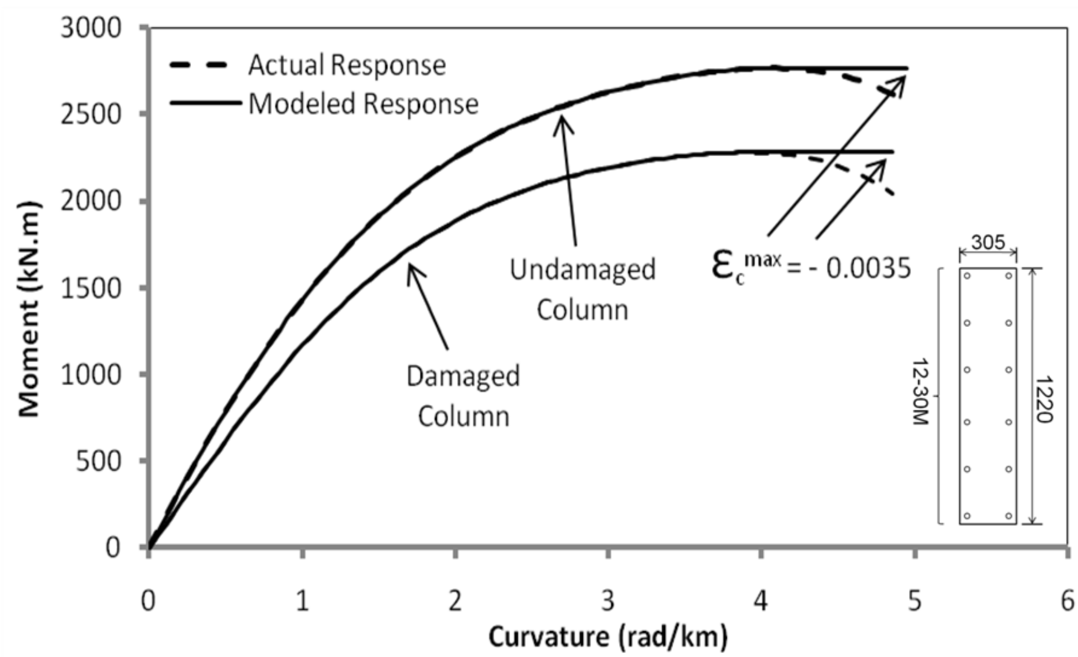

Figure 6.1 Moment-curvature response of a gravity-load column. (Note: damage to column includes spalling of concrete cover and buckling of outer reinforcement on compression face.)

If seismic demands on gravity-load columns are to be studied, a logical analytical model has to be implemented to capture inelastic curvature concentration on the plastic hinge zone. This can be done by assuming a certain curvature distribution along the height of the inelastic behaviour region and associating addition of curvature with certain stiffness.

As for the assumption on curvature distribution, it is best to select a model that is a close representation of how gravity-load columns behave when pushed laterally in tests carried out on gravity columns (see Section 6.2). For this purpose, two scenarios are considered (see Figure 6.2).

When the column cross-section does not experience damage in the inelastic behaviour zone and the section maintains its original dimensions, maximum bending moment occurs at the base of the column and inelastic curvatures are expected to be distributed linearly over the column plastic hinge region. When the column suffers damaged in the inelastic behaviour region (whether the damage is in the form of losing concrete cover, bar buckling under compression or bar fracturing under tension), the damaged section becomes much softer than the rest of the column causing even more curvature concentration in the damaged region. Sections in the damaged region end up having almost the same properties and a uniform crack pattern is observed over the height of the damaged zone. This suggests that it is reasonable to assume a uniform inelastic curvature over the height of the damaged region.

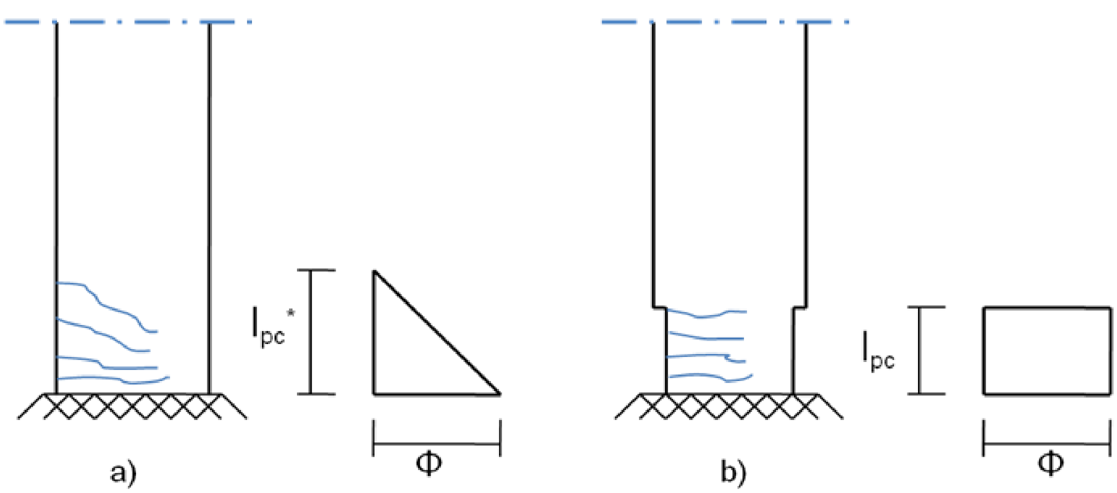

Figure 6.2 Assumptions on inelastic curvature distribution in the column plastic hinge zone: a) undamaged column, b) damaged column.

To simplify the structural modelling and analysis procedure, perfectly plastic post-peak behaviour is assumed as can be seen in Figure 6.1. Plastic curvature zone is used for the term plastic hinge zone interchangeably throughout the rest of this chapter. Since the purpose of this chapter is estimating the curvature demand on gravity-load columns pushed to a certain lateral displacement profile, obtaining the real bending moment profile at column failure is not of interest provided that the curvature profile accurately resembles the real case. This issue is described in detail in Section 6.4 where structural modeling and analysis procedure is presented.

6.4 Nonlinear Structural Analysis Procedure

When the Seismic Force Resisting System (SFRS) of a building deforms in the event of an earthquake, slabs force gravity-load columns to undergo the same amount of lateral deflection at storey levels as that of the wall or “go along for the ride”. This means that columns are pushed to certain displacements at floor levels putting a flexibility or curvature demand on the columns. A nonlinear structural analysis algorithm is developed which given the moment-curvature behaviour of the column and the imposed lateral displacement profile at floor levels can analyze the curvature demand throughout the height of the column.

To analyze the column under a specified lateral displacement profile defined at floor levels, the column can be modelled as a cantilever beam-column neglecting the rotational restraint provided by the slabs. Appropriate boundary conditions at the base and adequate number of floors above the base must be modelled to get a reasonable estimate of the curvature demand within the wall plastic hinge zone. In this section, a 5-storey cantilever column fixed at the base is used to demonstrate the structural analysis procedure.

Figure 6.3 shows a schematic view of the idealized structures. The column is connected to the SFRS (shear wall) at storey levels. If the slabs are thought of as a rigid link due to their high in-plane stiffness, they exert lateral horizontal storey forces (P) on the column causing it to undergo the same deformation as the shear wall at that floor slab levels. The storey forces then produce bending moments (M) along the column height and from the bending moment diagram, the curvature (Φ) profile can be obtained knowing the moment-curvature behaviour of the column. Neglecting shear deformation of the column, curvatures can then be integrated to obtain the displacement profile along the height of the column. The column can be divided into several equally sized elements along the height of each storey to facilitate numerical integration. Curvature is considered to be constant over the height of the element and is computed using the bending moment at elements' mid-height. The problem in hand will then be finding the set of storey forces (P) which produce the target displacements (Δ) at corresponding floor slab levels.

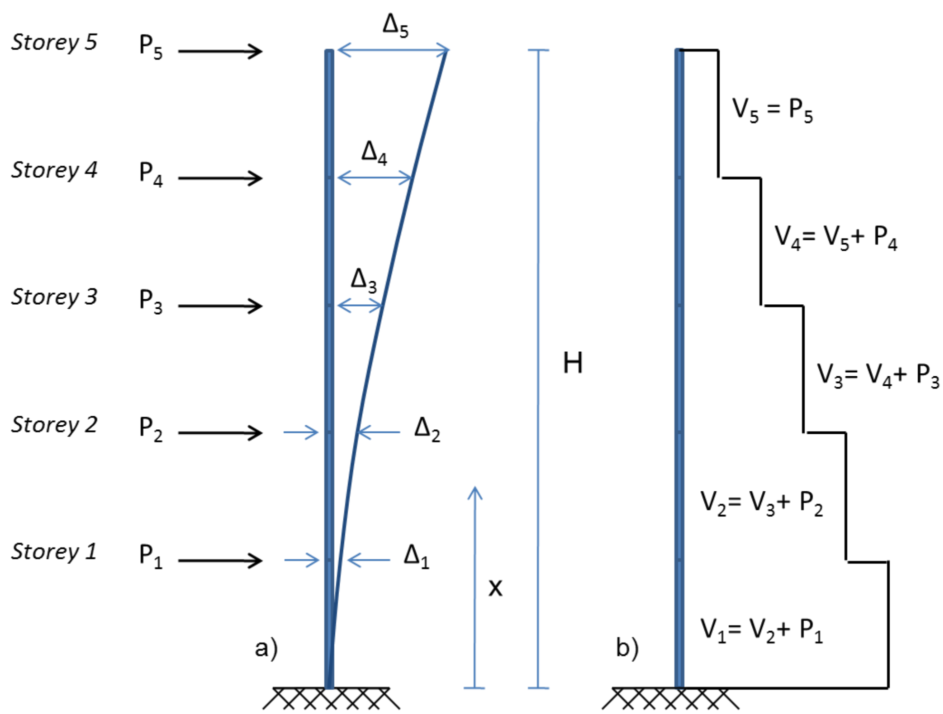

Figure 6.3 Idealized column structure: a) storey forces and displacement profile, b) shear force diagram.

A mathematical presentation of the structural analysis algorithm is given in Appendix D. Floor displacements (Δ) are considered to be a function of storey shears (V). First order Taylor series expansion is applied to the floor displacements (Δ) and multi-variant Newton-Raphson iteration procedure is adapted to solve for the unknown storey shears (V) which will result in the desired displacement profile. The simple fifth order polynomial approximation for column's moment-curvature response presented in Section 5.2.5 is used. A pushover analysis is then performed with the column pushed to deformation profiles of the wall at progressively larger global drifts until column curvature capacity is reached. See Section 6.5 for more on wall displacement profile.

The analysis procedure just mentioned however is valid only for the ascending part of the column moment-curvature response. In other words, for this algorithm to be able to find the storey forces resulting in the target displacements, column stiffness should be positive (i.e. additional bending moments needed for increase in curvature). Since for a column fixed at the base maximum bending moment always occurs at the base of the column, this condition holds true up until the element at the very bottom of the column reaches the column moment strength called the "yield" point. To model the strength decay portion of the column's flexural behaviour, a plastic curvature model is used (see Section 6.3). The state of the column at "yielding" is recorded, that is, both the displacement and curvature profiles are stored. From thereafter, as the column is further pushed, to keep the maximum bending moment at the base constant at the column strength (i.e. perfectly plastic post-peak response), an inflection point is forced at the base of the column. This ensures no addition of moment at the base while the fixed (zero rotation) boundary condition at the base is still satisfied. Based on the state of the column at "yield", moment-curvature relation for each element is modified using a simple axis transformation technique and used to calculate curvatures in excess of the state of the column at "yield". Additional floor displacements beyond the "yield" state are now considered target displacements and additional storey forces and consequently additional curvatures are found to result in the target wall displacement profile.

Although the bending moment diagram of the column at the end of the analysis will differ from the real case (i.e. strength decay resulting in bending moment at the base of the column at failure to be less than the column strength in reality), curvature profile is expected to represent the real case. Since the focus of this chapter is on quantifying curvature demands on gravity-load columns subject to specified lateral displacements, obtaining the real bending moment profile is not of interest. The accuracy of the proposed analysis method is compared to the results from a nonlinear finite element analysis of a 20-storey shear wall building in Section 6.6.

6.5 Wall Displacement Profile used in the Pushover Analysis

When a column is tied to a shear wall at closely-spaced floor slabs, it is forced to follow the wall displacement profile at floor slab levels exhibiting a curvature profile very similar to that of the wall. Consequently, the shape of the wall deformation profile in terms of distribution of curvature and shear strains significantly influences curvature demands on the gravity-load column. To carry out a thorough pushover analysis on the column, wall displacements at floor slab levels must be increased with the correct proportions simulating the actual displacement profile that the column will be subjected to at various levels of global drift. For this purpose, flexural and shear deformation are treated separately. It is shown that bilinear curvature distribution along the height of the wall accurately resembles the post-yield wall deformation profile and can be used to carry out the pushover analysis described in the following sections. Since the shear strain profile of flexural shear walls are similar in shape to the curvature profile (see CHAPTER 2), shear strain profile of the wall is also assumed to be bilinear.

6.5.1 Flexural deformation

Elastic deformation profile of a uniform 20-storey shear wall is shown in Figure 6.4 due to its 1st mode static inertial forces, an inverted triangular (i.e. linearly varying) load, and a tip load. In order to do the modal analysis, the wall was modeled as a cantilever with uniform flexural stiffness of 475 GN.m^2 and uniform floor height of 2.75 m with 45 tons of mass lumped at floor levels. The numbers were chosen such that the fundamental vibration period of the structure was 1 second. Since for the other two cases the load profile was available, curvatures were readily computed from the bending moments and were then integrated to obtain the displacement profile. Curvature profiles are normalized to give a unit top displacement.

Nonlinear deformations of a plastic hinge model with linearly varying curvature over the height of first 3 storeys and zero curvature above was then added to the elastic deformations (i.e. the plastic hinge length was chosen to be 3 floors high). Maximum nonlinear wall curvature was then tuned to get a displacement ductility factor of 2.0 (1/2 of the total top displacement being elastic) and 3.5 (1/3.5 of the total top displacement being elastic) respectively. The results are shown in Figure 6.5 and Figure 6.6 respectively. Note that elastic top displacement is one unit.

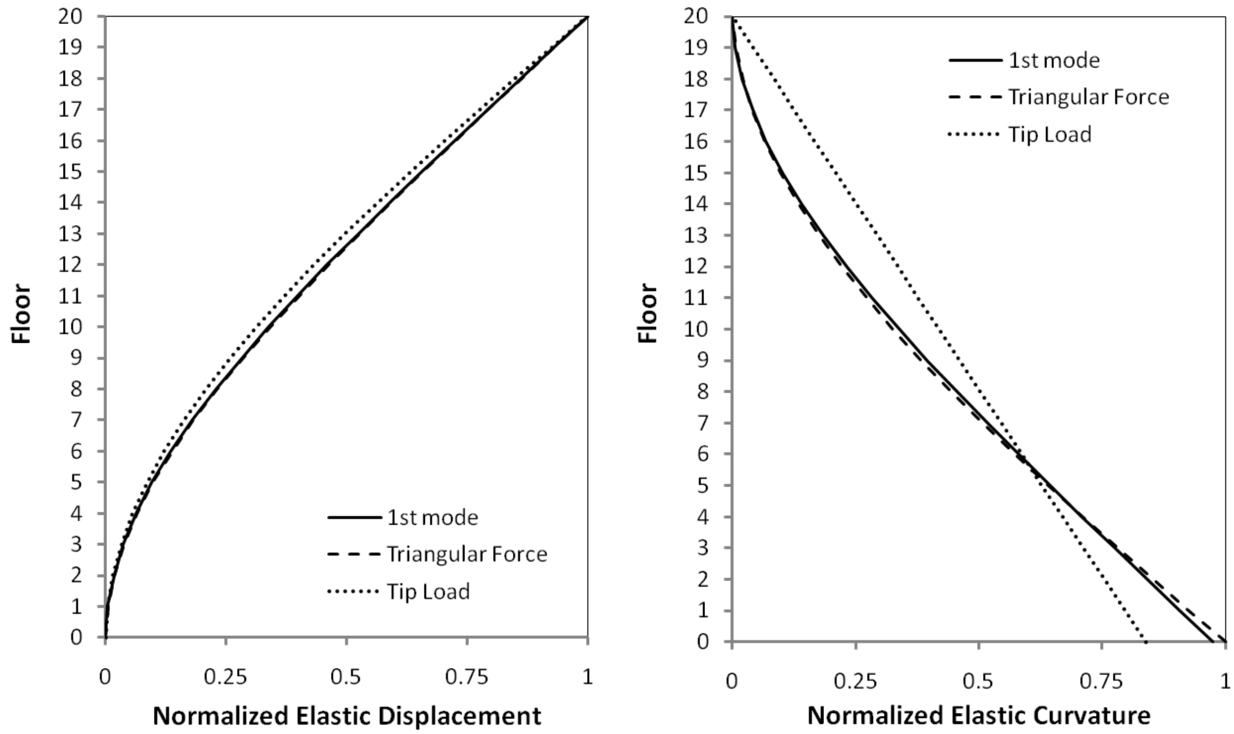

Figure 6.4 Elastic deformation and curvature profiles of a 20-storey shear wall.

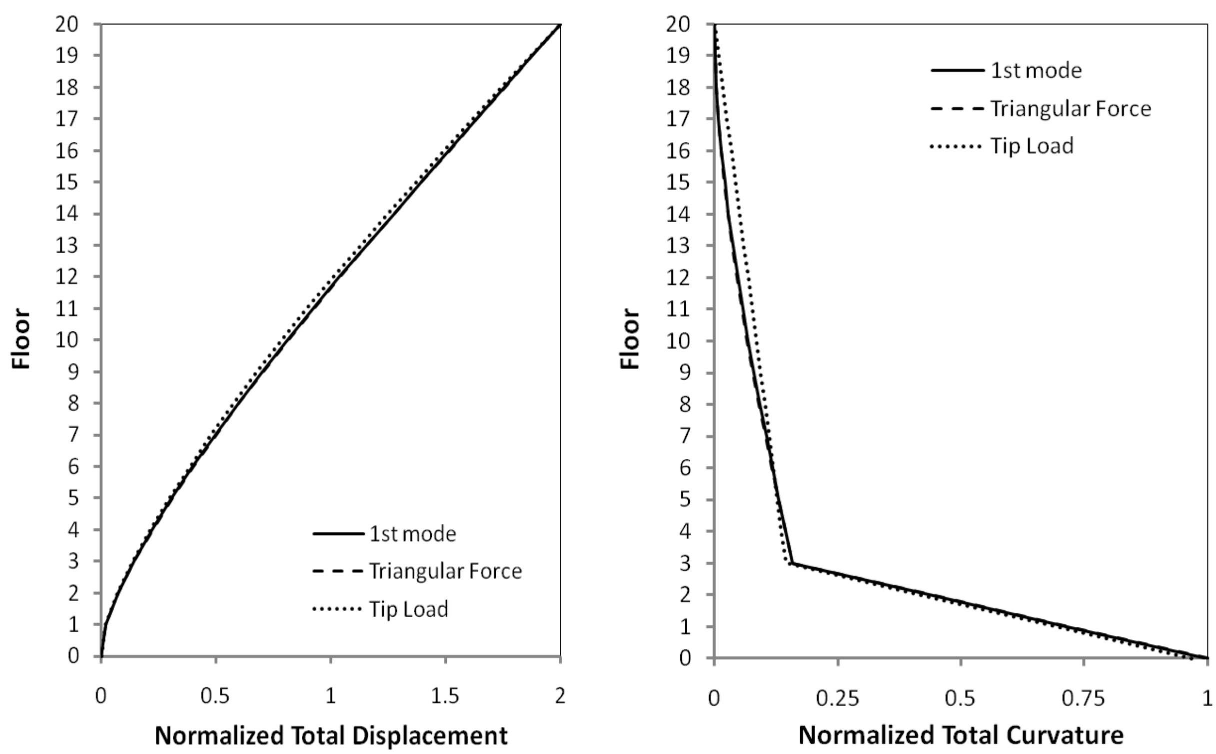

Figure 6.5 Total displacement and curvature profiles of a 20-storey shear wall at displacement ductility of 2.0.

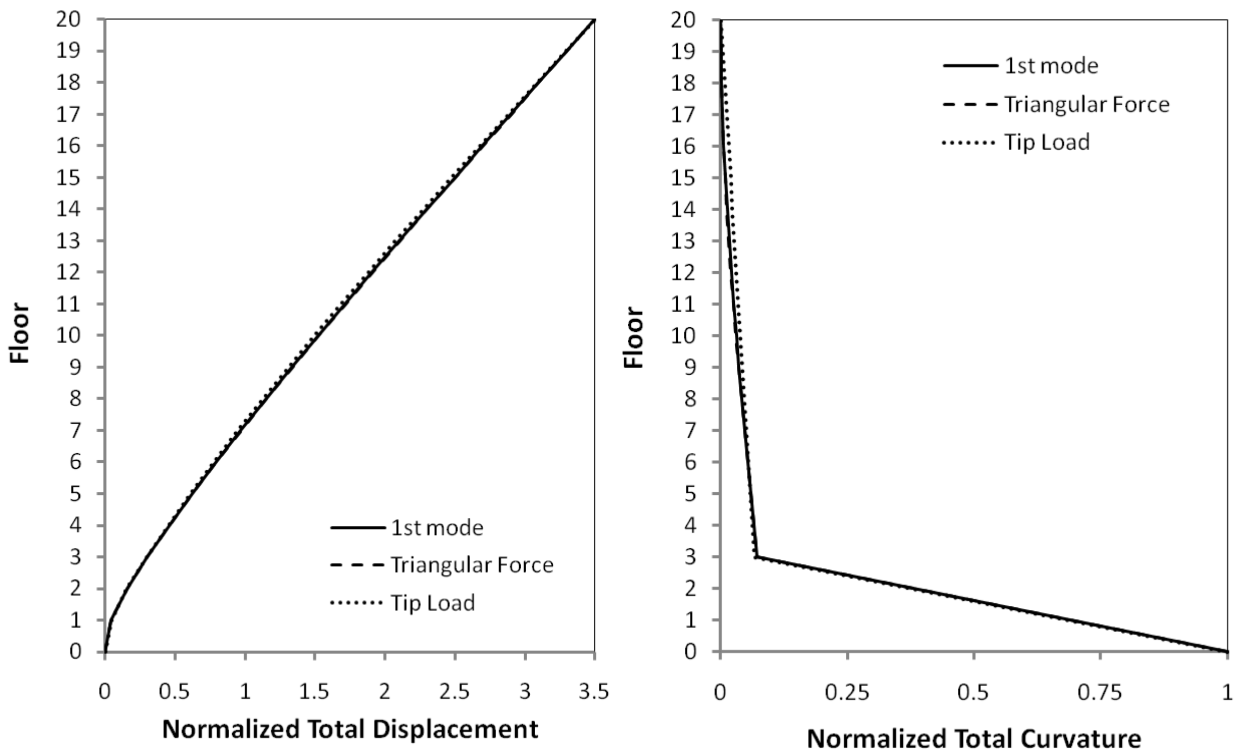

Figure 6.6 Total displacement and curvature profiles of a 20-storey shear wall at displacement ductility of 3.5.

When the response is elastic, while the displacement profiles resulting from the three pushover loads are very similar, curvature profile due to a tip load gives lower maximum curvature at the base of the wall because curvature is more evenly distributed over the height of the wall. Curvature profile resulting from a triangular load however agrees closely with the first mode response. Using a tip load to carry out a pushover analysis will then be un-conservative in terms of estimating maximum wall curvature in the elastic response stage. When nonlinear curvatures from a plastic hinge model were added to the elastic response, the deformation profiles became almost identical for all load types and the maximum curvature resulting from pushing the wall to the same top displacement using either of the load patterns became almost the same. Since shear walls are designed for high ductility and are expected to develop large inelastic curvatures, critical flexibility demands are accompanied by a highly nonlinear response. This suggests that as long as columns connected to the wall fail when the wall is demonstrating a high ductility, it does not matter what loading profile is used since maximum elastic curvatures are out-ruled by concentrated nonlinear curvatures at the base of the wall.

In order to develop a simple wall deformation model that can be used to carry out pushover analysis on the column, since the shape of the elastic deformation was proved to be insignificant; the point load push scenario discussed above is used. A point-load at the top of the wall will result in linear moment and curvature profiles. Adding linearly varying inelastic curvatures from a plastic hinge model to the elastic curvatures will then result in a bilinear curvature profile along the height of the wall. As the point-load at the top of the wall increases, maximum curvature at the base of the wall increases until it reaches the wall yield curvature. When the load is further increased, curvatures in the plastic hinge zone of the wall keep increasing while the elastic curvatures above remain almost the same. In a pushover analysis, maximum curvature at the base of the wall is increased until the column curvature capacity governed the by maximum permissible concrete strain is reached.

6.5.2 Shear deformation (strain)

Wall shear strain (deformation) is defined as the portion of the wall lateral displacement in addition to that resulting from integrating curvatures over the wall height (flexural deformation). Shear strain in the wall and consequently shear deformation is considerable when vertical reinforcements of the wall yield in zones with inclined flexural-shear cracks. Shear deformation become particularly important in the wall plastic hinge region or first few stories at the bottom of the wall where flexural displacements are rather small relative to the shear deformation. Because shear strain is a consequence of yielding of vertical reinforcement in flexure, it is expected to follow the pattern of the wall curvature profile. See CHAPTER 2 for more on distribution of shear strain along the height of the wall.

In conclusion, bilinear curvature profile resulting from a tip load can accurately predict maximum wall curvature at ductility factors of 2 and greater and therefore will be used in the following sections whenever a column pushover analysis is required. Shear strain is also assumed to have a bilinear profile along the height of the wall with the same plastic hinge length as the curvature profile. As shear deformations in flexural shear walls are a result of large vertical tensile strains in the presence of inclined cracks, the amount of shear strain would be proportional to curvature at any point in the wall’s plastic hinge region.

6.6 A Demonstrative Example

In this section, the accuracy of the nonlinear analysis method presented in Section 6.4 using the approximate wall deformation profile discussed in Section 6.5 is compared to that of a nonlinear finite element (FE) analysis program for a 20-storey shear-wall building. The FE analysis was done as a part of a Master's Thesis by Alfredo Bohl (2006). Complete modeling details and analysis results can be found in the reference and hence are exempted from this document. Only general modelling assumptions and structural properties are reported here. It is shown that the proposed nonlinear analysis method is capable of predicting the curvature demand on gravity-load columns with great accuracy and low computation cost using information available to a design engineer. It is also demonstrated that the approximate bilinear curvature and shear strain simplification used to model the wall deformation profile accurately represents the real deformation profile of a nonlinear shear wall.

6.6.1 Finite element (FE) analysis procedure

Bohl (2006) modelled a 20-storey reinforced concrete shear-wall using VecTor2. The cantilever wall had a cross-section of 7620x508 mm and carried an axial compressive force of 15484 kN. A gravity-load column 953 by 508 mm with 20-M25 as vertical reinforcement carrying an axial load of 7742 kN and fixed at the base was connected to the wall at floor slab levels using rigid links. Concrete strength for both the wall and the column was 40 MPa. The complete mesh consisted of 345 nodes, 20 rigid links, 242 rectangular elements, and 8 triangular ones. Denser mesh was used throughout the first 10 storeys of the structure while the mesh became successively courser above the 10^{th} floor. At the base, 24 elements along the wall length and 7 along the height of each storey were used while these figures were reduced to 5 and 2 at the top respectively. As for the column, 3 elements along the column length and 7 along the storey height were used at the base with the numbers reducing to 1 and 2 at the top respectively. However, to account for additional flexural stiffness provided by the slab at floor levels, elements with 5 times the width of the column were modelled at floor slab levels. This procedure was followed only in the first 10 storeys of the structure with one element being as high as the slab thickness and the rest of the storey height being covered by 6 equally sized elements. 40 MPa concrete and steel with yield strength of 400 MPa was used.

The system was subjected to a monotonically increasing lateral point load exerted at the top of the wall and a displacement-controlled pushover analysis was carried out with steps of 1 mm in wall top displacement.

4 levels of global (top) drift of 0.5, 1.0, 1.5, and 2.0% are considered here to compare to the proposed structural analysis approach. There were 4 nodes (3 elements) along the length of the column. To obtain a value for lateral column displacement at each floor slab level, horizontal displacements of the corresponding 4 nodes were averaged. Even at 2.0% global drift, the vertical displacements of the 4 nodes just above the base of the column (location of maximum curvature concentration and nonlinearity) suggested that shear deformation was insignificant in the column (see Figure 6.7). This suggested that plane sections remained plane and that average curvatures could be obtained from the vertical displacements of the 2 nodes at the opposite faces of the column assuming constant curvature along the gage length equal to the height of the element below. This observation also confirms that no shear deformation was induced in the column.

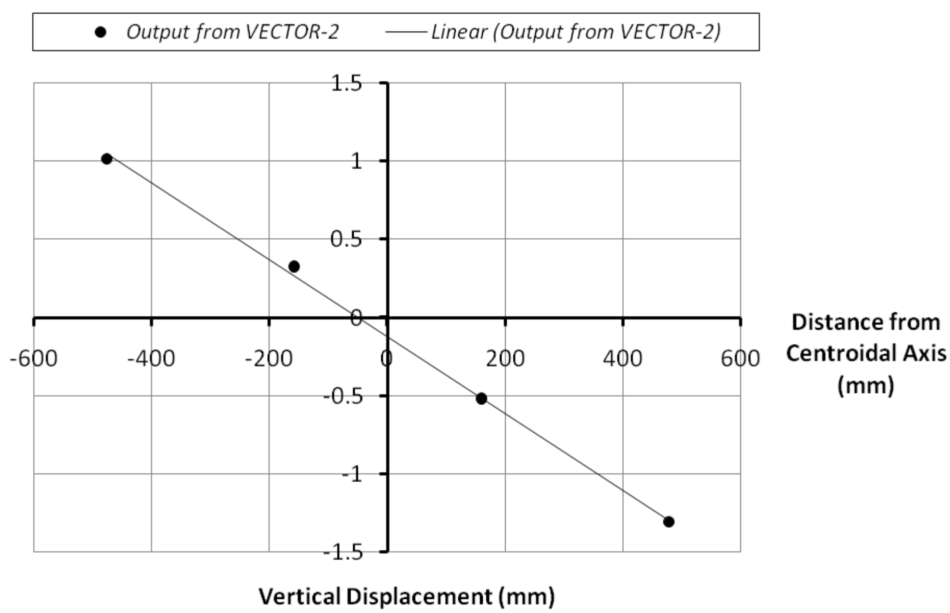

Figure 6.7 Vertical deformation profile at the base of the column at 2% global drift.

6.6.2 Bilinear wall model vs. deformation profile from FE analysis

To carry out a pushover analysis using the proposed nonlinear structural analysis method described in Section 6.4, deformation profile of the shear wall needed to be generated at each push step and be used as an input to the structural analysis algorithm. Flexural and shear deformations were calculated separately and then combined to give the wall total lateral deformation profile. Bilinear profile was assumed for both curvature and shear strain. The resulting total deformation is then compared to that obtained from the FE example introduced in Section 6.6.1.

Figures below summarize the results at 3 different global drift levels of 1%, 1.5%, and 2.0%. Curvatures were extracted from FE results using nodal displacements along the length of the wall with the assumption that the slope of the straight line connecting the nodes at the two ends of the wall length is the average section rotation. Average rotation values were then used to calculate average element curvatures which are plotted in Figure 6.8, Figure 6.9 and Figure 6.10. Note that the drops in wall curvatures from FE results at floor slab levels is because stiffer elements were used at floor slab levels to simulate the stiffening effect of the floor slab. Wall deformation value at each horizontal level was taken as the average of horizontal deformation of the nodes at that level.

FE results suggested that wall plastic hinge length was 3 storeys high with a yield curvature at the top of the plastic hinge zone equal to 0.32 rad/km. Hence, for the approximate bilinear model, the same properties were used and the maximum wall curvature at the base was chosen to be equal to that obtained from FE results at each drift level. Maximum wall curvature at the base was treated as the push variable and increased linearly throughout the push until the column reached its curvature capacity. Since shear strain was a consequence of yielding of wall vertical reinforcement in flexure, just like the curvature profile, bilinear distribution was used for shear strain as well. Again, properties of the bilinear shear strain distribution were chosen based on the FE results in such a way that they account all of the wall horizontal deformation that could not be depicted by integrating wall curvatures over the height. Maximum shear strain at the base of the wall was then tied to wall maximum curvature and was increased monotonically with maximum wall curvature.

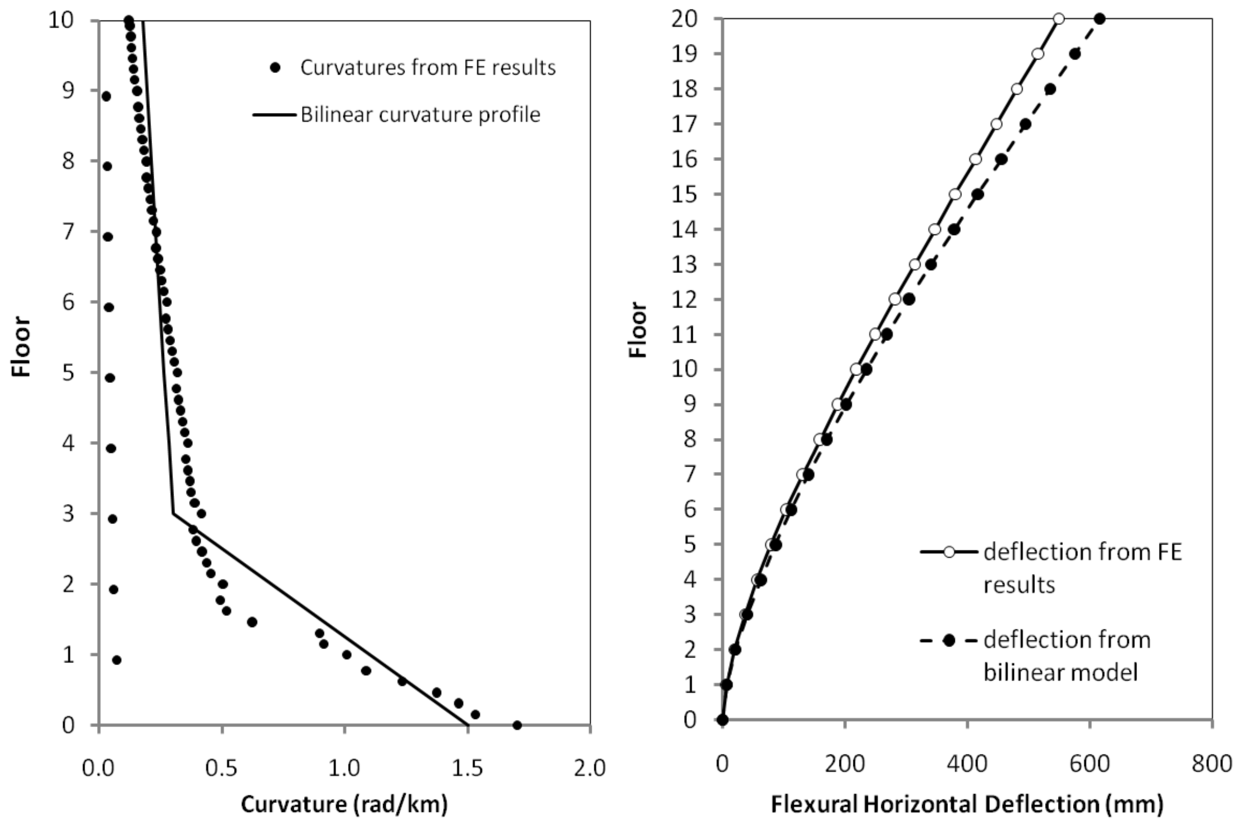

Figure 6.8 Flexural response from bilinear model vs. FE results at 1% global drift.

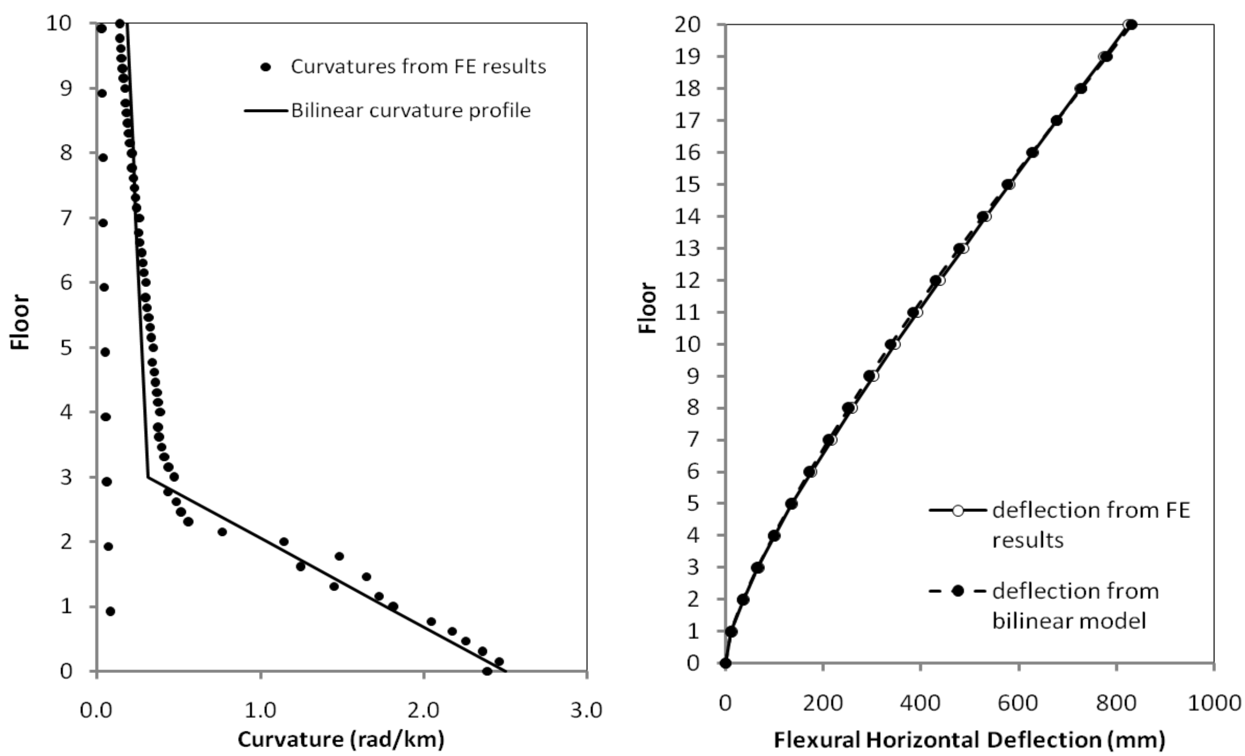

Figure 6.9 Flexural from bilinear model vs. FE results at 1.5% global drift.

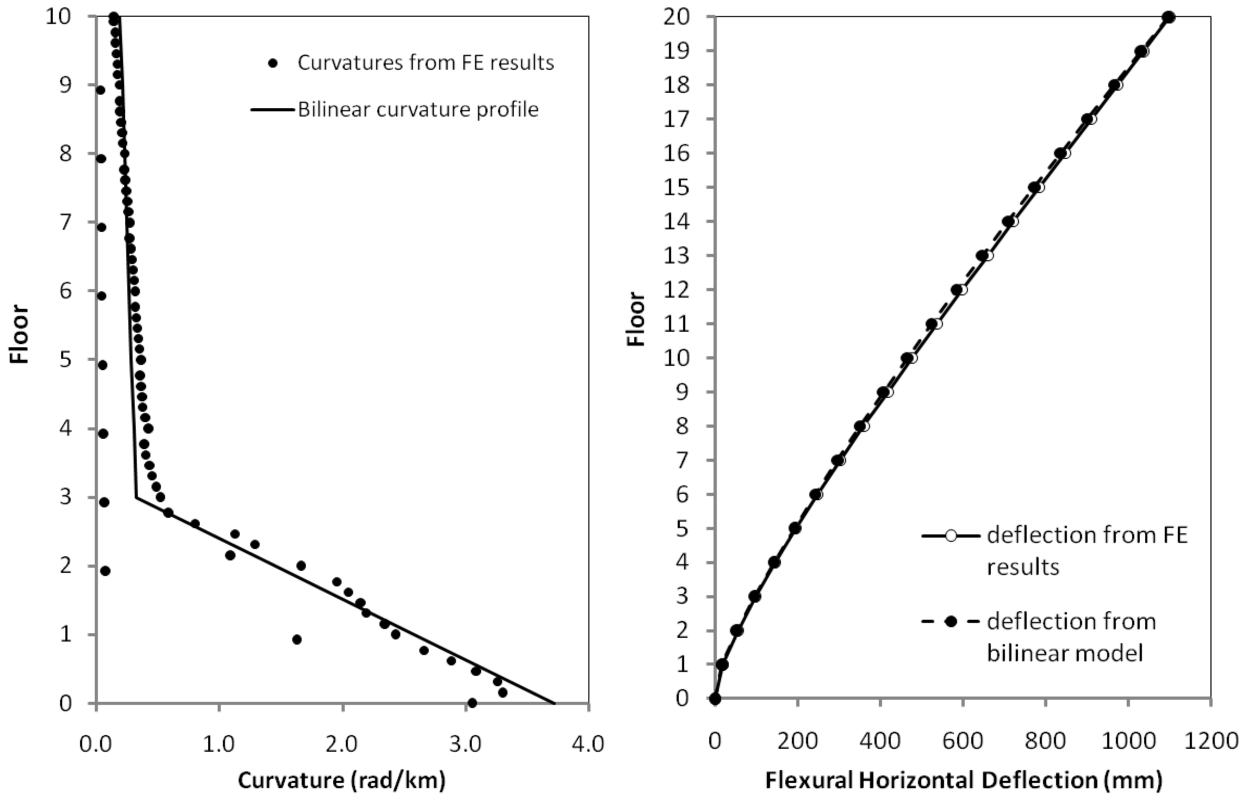

Figure 6.10 Flexural response from bilinear model vs. FE results at 2% global drift.

Figures above suggest that the bilinear model closely followed the trend of the deformation profile of the FE shear wall. The accuracy of the model increased with the drift level. This was due to the wall encountering more nonlinear behaviour at higher drift levels increasing concentration of curvature in the plastic hinge zone.

The displacement profile from the bilinear shear strain model is compared to that from FE wall in Figure 6.11. FE shear deformations were calculated by subtracting flexural deformations obtained from integrating curvatures over the height of the wall from the total lateral deflection profile. Shear strain at the top of the wall plastic hinge was chosen to be 0.0001 and was decreased linearly to zero at the top of the wall. Shear strain in the plastic hinge region of the wall was also varied linearly with maximum shear strain at the base of the wall being equal to 0.00012 at wall yielding and 0.00215 when wall maximum curvature was 10 times the yield curvature. This resulted in shear strains to be proportional to curvature.

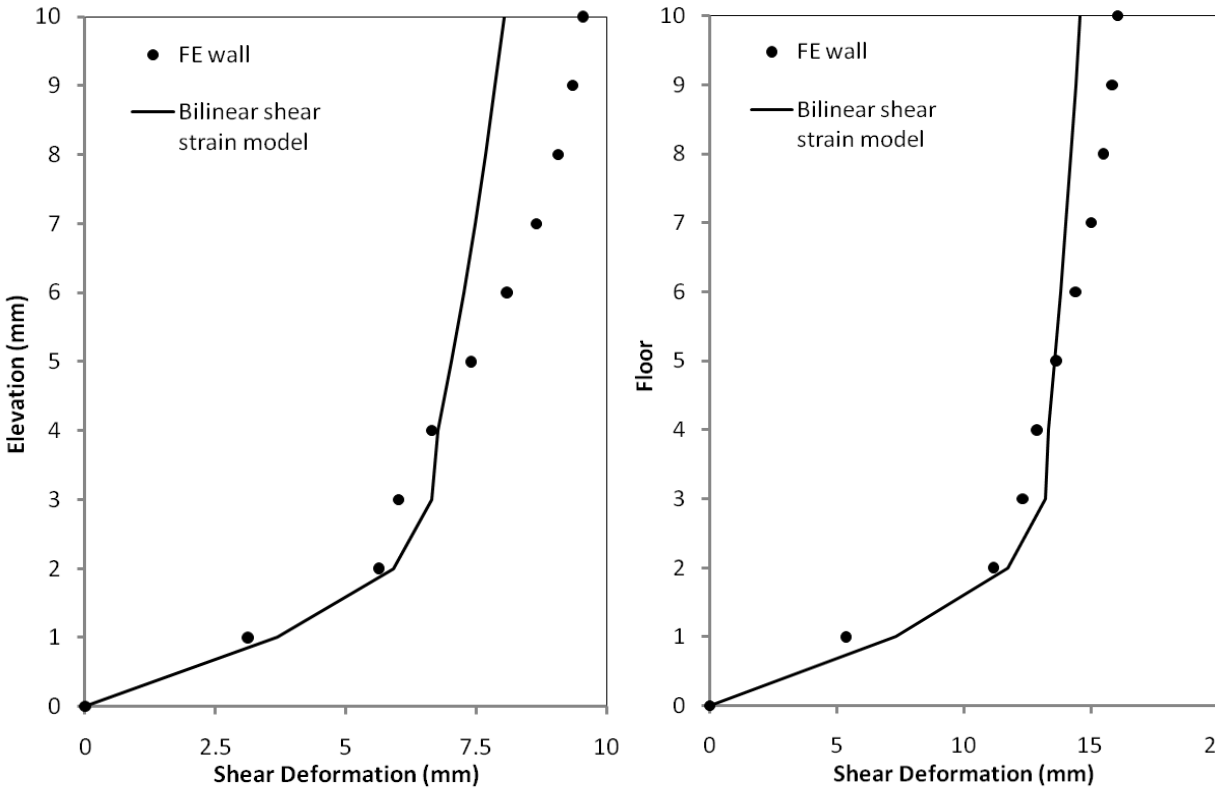

a) b)

Figure 6.11 Shear deformations from bilinear shear strain profile vs. FE results at: a) 1.5%, and b) 2.0% global drifts.

As shown in Figure 6.11, the proposed bilinear shear strain model accurately simulates the wall shear deformation profile in the first 5 storeys; however, the simple model underestimated shear deformation in the storeys above. It is proven in Section 6.9 that while maximum curvature demand on gravity-load columns is highly sensitive to wall deformation values at the first few floors levels, it is not affected by deflection values at higher levels. Therefore, the accuracy of the bilinear shear strain model was acceptable. This approximate model is used in the remainder of this study alongside the bilinear curvature distribution model whenever a pushover analysis is carried out.

6.6.3 Solution using the proposed nonlinear structural analysis method

The moment-curvature response of the column section is plotted in Figure 6.12. On the same figure, the fitted 5th order polynomial approximation and the response used for modeling column behaviour are also plotted. Note that the modeled response has zero stiffness beyond the peak strength of the column where a perfectly-plastic response was modeled with linear curvature variation over the column plastic hinge length.

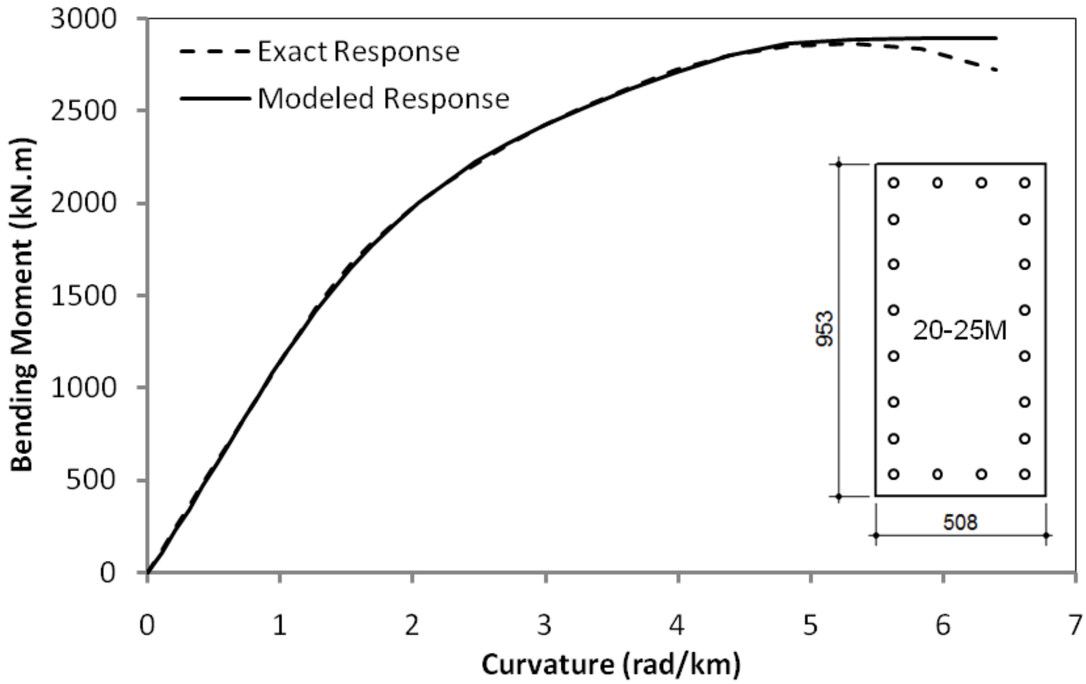

Figure 6.12 Column moment-curvature response.

General analysis procedure is described in Section 6.3. The column was fixed at the base. 20-storeys above the base were considered in the structural analysis and each storey was divided into 7 constant-curvature elements of identical size. Since the displacement profile of the wall was readily available, the steps corresponding to the selected global drift levels of 0.5%, 1.0%, 1.5%, and 2.0% were directly inputted to the analysis program to obtain curvature profiles along the column height. Because at 2.0% global drift level the column had already “yielded” or passed the peak moment strength point, the load-step at which the column first “yielded” had to be found to obtain the state of the column at “yield”. It was found that the column “yielded” soon after the 1.5% global drift level at 1.54 % top drift. Looking at the FE analysis results at 2.0% global drift suggested that the column plastic hinge length was close to the storey height; hence a value of 2.7 m was used as column plastic hinge length.

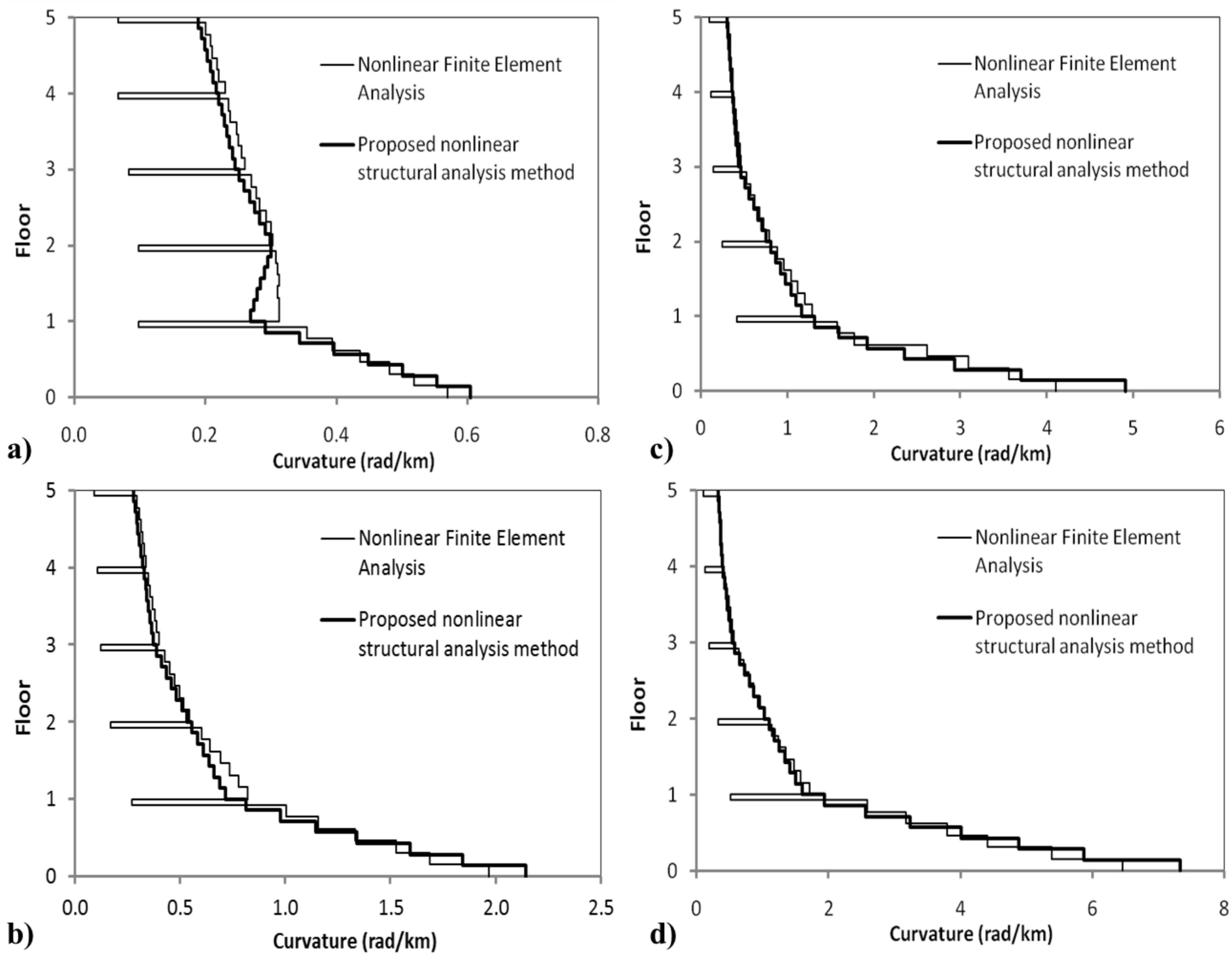

Figure 6.13 Curvature demand prediction at global drifts of: a) 0.5%, b) 1%, c) 1.5% and d) 2%.

Analysis results are plotted and compared against those obtained from the original FE analysis in Figure 6.13. The sudden drops in curvature values at floor slab levels seen in the original FE results are due to modelling stiffer elements to account for the rotational rigidity provided by the slab.

It is observed that the curvature profiles obtained from the proposed nonlinear structural analysis procedure closely follow the trend of those from the FE analysis. The maximum error in prediction of maximum curvature at the base of the column is 15% at 1.5% global drift. The predicted maximum curvatures however were always greater than those obtained from FE analysis which means the proposed analysis methodology gives a reasonably safe estimate of the maximum column curvature demand.

6.7 Shear Strains in Gravity-Load Columns

So far, it has been assumed that deformation of the column is solely due to flexure and any shear strain in the column has been neglected. This section examines this fundamental assumption. Figure 6.14 shows shear strain profiles of the wall and the column modeled by Bohl (2006) and introduced in Section 6.6.1 in the first 10 storeys at 2% global drift. It is clear that shear strains in the column are easily negligible compared to wall shear strains.

The column experiencing much smaller shear strains is entirely attributed to the larger axial stress on the column. The wall in this example carried an axial load equivalent to $0.10f'_cA_g$ while the column carried an axial load equal to $0.40f'_cA_g$. As explained in CHAPTER 2, shear strains in flexural reinforced concrete members are generated in areas with large average tensile strains. Large compressive axial stresses on the column therefore considerably increase the concrete compression depth reducing the section average tensile strain which in turn decreases the formation of shear strains in the column. This is further confirmed in Figure 6.15 where the section strains at centroid of two columns with extremely different cross-section aspect ratios are compared. Both columns carried an axial load equal to $0.40f'_cA_g$. In this case, the axial load proves to be so large that the section average strain remains negative (compressive) up to the maximum concrete compressive strain of 0.0035. This proves that shear strains are negligible even in columns with elongated cross-sections.

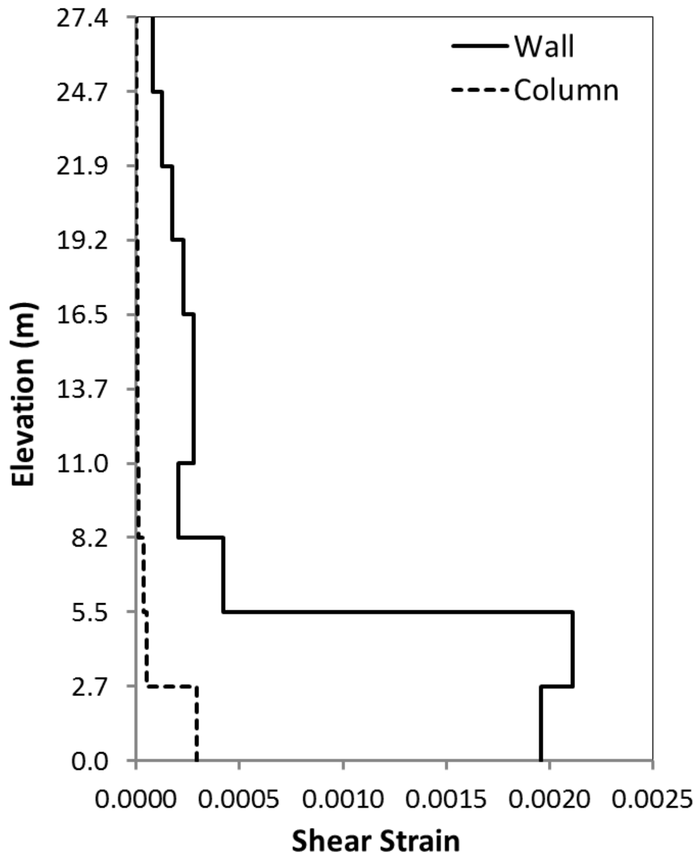

Figure 6.14 Shear strain profiles of the shear wall and the column introduced in Section 6.6.1 modeled by Bohl (2006) at 2% global drift obtained from Vector2.

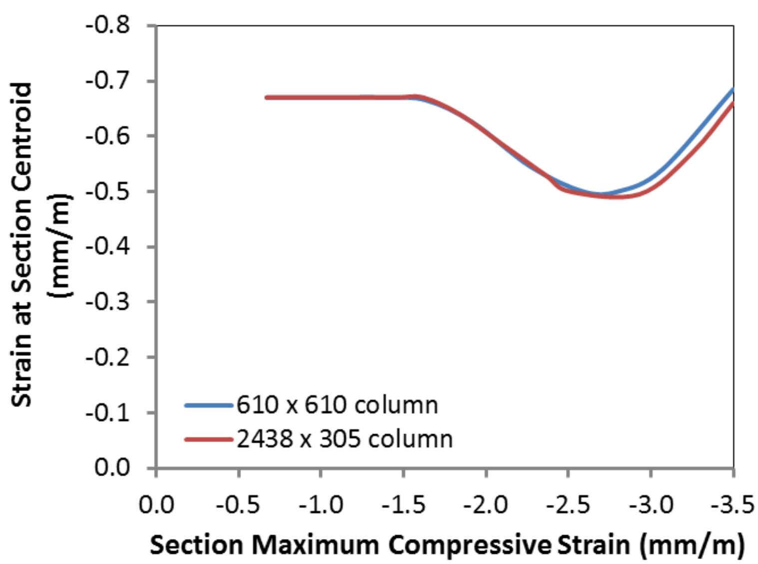

Figure 6.15 Comparison of average section strain of a 610x610 mm and a 2438x305 mm column cross-section both with 2% vertical steel ratio and concrete strength of 60 MPa carrying an axial load equivalent to $0.4f'_cA_g$ at various section maximum compressive strains.

6.8 Number of Constant Curvature Elements Required for an Accurate Estimate of Column Curvature Demand

In the preceding section, the column was modeled with 7 constant curvature elements in each storey to make the analysis procedure similar to that carried out in the FE program. Bending moments due to storey forces were computed at elements' mid height and then converted to curvature values using the column moment-curvature response. These curvature values were considered to be constant over the element height (constant curvature elements) and were then integrated to get the column displacement profile.

When the storey shear force (moment gradient) is high, changes in bending moment values over the height of a single element can be significant. This effect becomes even more important in the column plastic hinge zone where large inelastic curvatures are concentrated. Elements in that region are very soft due to yielding of the column vertical steel in compression and softening of the concrete and hence, a small change in the moment value causes a great increase in element curvature. In that case, elements must be short enough or sufficient number of constant curvature elements must be used in a single storey to capture the correct column curvature demand.

To investigate the effect of number of constant curvature elements required for an accurate estimate of column curvature demand, a column fixed at the base with 20 storeys modelled above the base was considered with the same structural configuration as the problem presented in Section 6.5. Figure 6.12 shows the approximate moment-curvature response of the column. To encounter significant curvature concentration at the base of the column, total floor displacements including wall shear deformation were imposed on the column.

Because concentration of curvature occurred in the first storey in the case of a column fixed at the base, only the number of elements in the first storey was varied while 7 elements were used in the storeys above. The results may then be applied to other columns provided that sufficiently large number of constant curvature elements is used over the height of the storey in which column curvature concentration occurs. Figure 6.16 shows the global drifts at which the columns reached its curvature capacity versus the number of constant curvature elements used in the first storey.

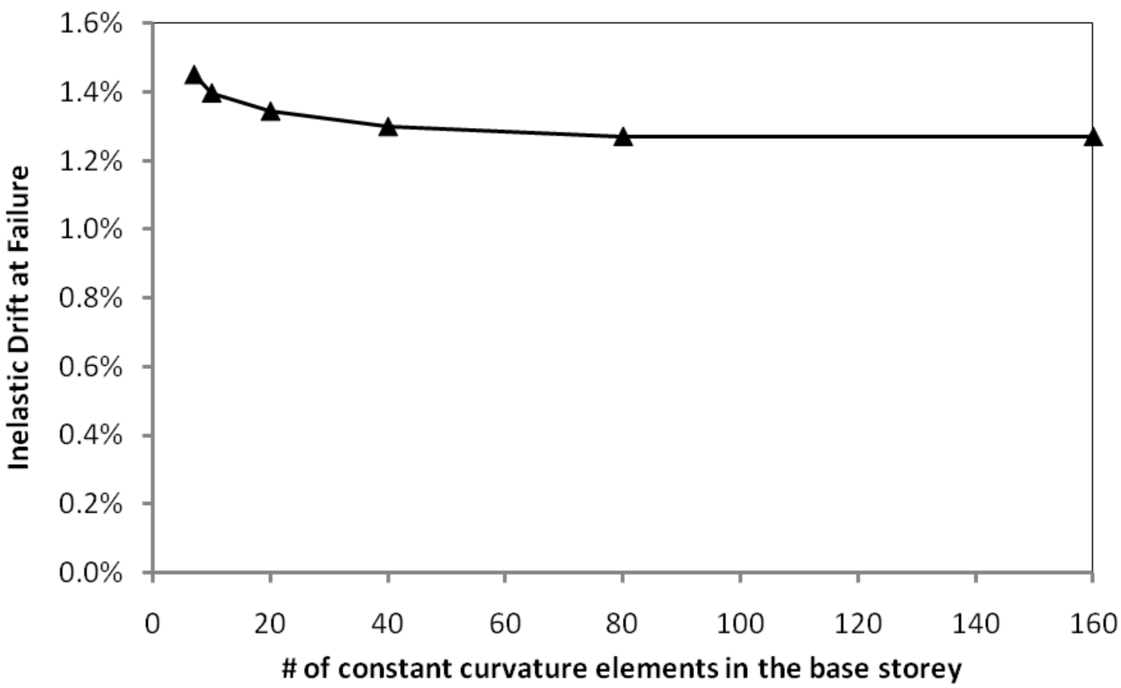

Figure 6.16 Effect of number of constant curvature elements in the base storey on column drift capacity. (Note: The column was assumed to reach its drift capacity once the column curvature capacity governed by maximum permissible compressive concrete strain of 0.0035 was reached.)

As the number of elements in the base storey was increased, maximum column curvature at the base was captured more accurately by the element at the base reducing the calculated column drift capacity defined as exceeding the column curvature capacity limited by concrete crushing strain. Based on the analysis results, column drift capacity did not have a pronounced decrease when the number of elements in the base storey increases beyond 80. Hence, using 80 constant curvature elements over the height of the storey in which column plastic curvatures occur gives an accurate estimate of column curvature demand. This guideline is followed in the remainder of this chapter. Although only 7 elements were used to model the storeys above the first floor, because in those regions column curvatures were in the linear elastic range of the moment-curvature response, adding more elements did not increase the accuracy of column drift capacity estimation.

6.9 Number of Floors Required for an Accurate Estimate of Column Curvature Demand

In this section, the effect of number of floors considered in modelling a non-linear column on the accuracy of the predicted curvature demand is investigated. To carry out the analysis, the column described in Section 6.6 was used; a 20-storey 953x508 mm column reinforced with 20 25-M reinforcing bars distributed along the perimeter and carrying an axial load of 7742 kN. Column plastic hinge height was taken to be equal to the column length (953 mm), wall plastic hinge length was 8.25 m (i.e. close to 3 floors high). Bilinear approximation was used to simulate the deformation profile of the wall in both flexure and shear. Two cases one with wall shear deformation included and the other excluding wall shear deformation were imposed on the column. Pushover analysis started with 3 floors modeled above the base. Number of floors modeled was increased until no further change in column curvature demand could be observed from modelling additional floors. A summary of the results is presented in Figure 6.17.

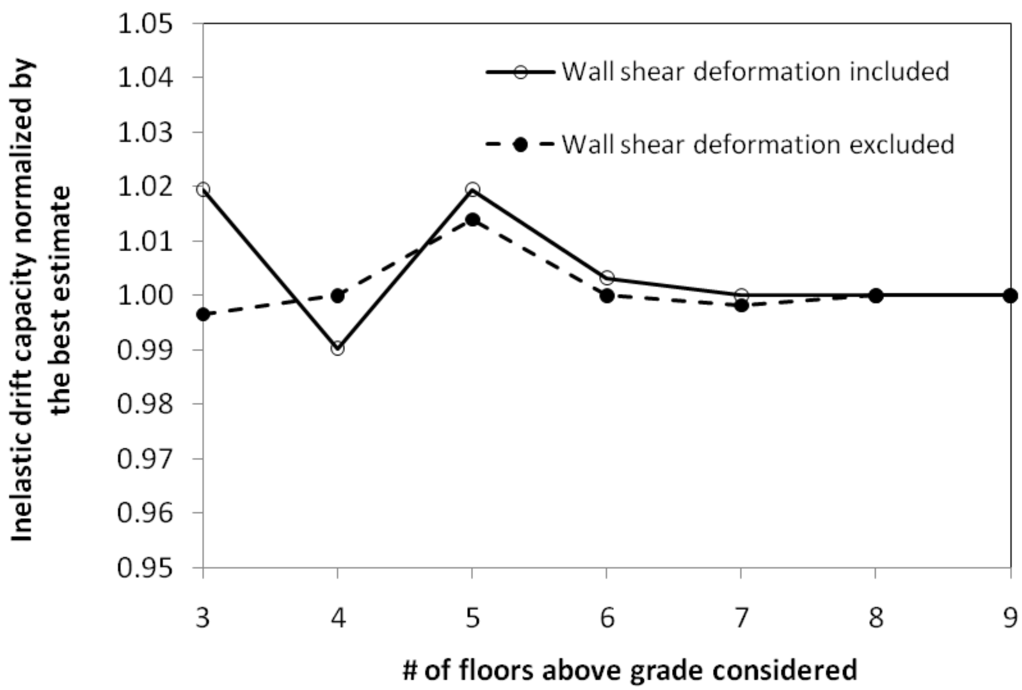

Figure 6.17 Number of floors required for an accurate estimate of column inelastic drift capacity. (Note: The column was assumed to reach its drift capacity once the column curvature capacity governed by maximum permissible compressive concrete strain of 0.0035 was reached.)

Figure 6.17 shows that a minimum of 8 floors should be considered in the structural model used to predict curvature demands on the 20-storey column examined here. As additional storeys were modelled beyond the 8th floor, no significant change in column curvature demand could be observed. Note that even with 5 storeys modeled, the error in estimating inelastic drift capacity was less than 2%. While drift capacity was highly sensitive to displacement values at the first 3 floor, it was not noticeably affected by amount of displacement at higher floors.

Because wall plastic hinge length was close to 3 storeys high, an unexpected fluctuation in inelastic drift capacity was observed when the number of floors modelled increased from 3 to 4 but as the number of floors considered in the analysis increased beyond 5 floors, addition of a floor to the analysis model decreased the drift capacity. It should be noted that the scale of the drift capacity fluctuation is not great at all and that including only 5 floors in the analysis would have provided an accurate estimate for design purposes. It is concluded that at least 5 floors must be modeled to get the best estimate of the inelastic drift capacity of a multi-storey shear-wall building. The number of floors modelled must be a few more than the wall plastic hinge height.

6.10 Summary and Conclusion

Below is a summary of key contributions of this chapter.

1. Reviewing the findings of a number of experiments on reinforced concrete columns under combined axial compression and bending revealed that gravity-load columns have very little ductility beyond the point of cover spalling. Inelastic curvatures were found to vary linearly over the column’s plastic hinge region prior to concrete cover spalling. After cover spalling, inelastic curvatures were found to be uniformly distributed over the height of the damaged region.

2. A nonlinear structural analysis algorithm for estimating curvature demands in gravity-load columns of shear wall buildings with flat plate floor slabs was formulated. The accuracy of the structural analysis procedure was verified against state of the art finite element analysis routine for reinforced concrete structures.

3. The bilinear model for wall curvature and shear strain profiles was shown to closely approximate flexural and shear deformation profiles of the wall obtained using the state of the art finite element analysis software for reinforced concrete structures.

4. Shear strains in gravity-load columns were proven to be negligible and the deformation of the column was shown to be almost entirely due to flexure. The large axial compressive stresses on the column reduced the section average tensile strain which resulted in shear strains being close to zero even in the case of wall-like columns with elongated cross-sections.

5. Column curvature demand was found to be very sensitive to the displacement of the lower floor slabs of the buildings and become less affected by displacement of the higher floor slabs. Including as few as five storeys in the structural analysis procedure provided accurate estimates of the column curvature demand.

CHAPTER 7 Parametric Study on Seismic Demands on Gravity-load Columns in Shear Wall Buildings with Flat Plate Floor Slabs

7.1 Introduction

In this chapter, a parametric study is conducted to examine and understand the effect of various column or wall parameters or building configurations on the seismic curvature demand on gravity-load columns. The structural analysis algorithm developed in CHAPTER 6 is used to estimate curvature demand on gravity-load columns within the plastic hinge region of shear wall building with flat plate floor slabs. A set of standard parameters is defined and in each section, variation of column curvature demand with respect to a single variable is studied keeping the rest constant at their standard value.

Parameters studied include wall shear strain, height of column's plastic hinge zone, column and wall lengths, effect of damage of the column, fixity of the column at grade level, and presence of a taller first storey. The most dominant parameters controlling curvature demand on gravity-load columns are identified which enables the designer to focus on quantifying these parameters with more accuracy to ensure that the gravity-load system can withstand the deformation demands dictated by the shear wall. Behaviour of gravity-load columns subjected to the imposed displacement profile of a shear wall is examined analytically in great detail. Wherever possible, simple expressions are developed for estimating the seismic curvature demand from wall maximum curvature given basic information available to the designer.

7.2 Standard Parameters

In each of the following sections, the effect of a single parameter on column curvature demand is studied while keeping the rest of the variables at their standard value. For this purpose, a set of standard parameters is defined and in each subsection, variation of column curvature demand with respect to one of the parameters under consideration is studied. Table 7.1 summarizes standard parameters used throughout this chapter. Note that wall deformation profile imposed on the column was that of the FE example described in Section 6.6.2 except for when the parameter under consideration was a property of the shear wall.

Table 7.1 Standard parameters for: a) gravity-load column, b) shear wall.

a)

Column Parameters		
Parameter	**Value**	**Description**
b	305 mm	cross-section width (1 ft)
l	1830 mm	cross-section length (6 ft)
f'_c	40 MPa	concrete strength in compression
ε_c^{max}	0.0035	concrete compressive strain capacity
F_y	400 MPa	steel yield strength
ρ	2.0%	vertical reinfrocement ratio
l_{pc}*	610 mm	height of linearly distributed plastic curvatures for undamaged column
l_{pc}	305 mm	height of uniformly distributed plastic curvatures for damaged column
P	9000 kN	column axial compressive load ($0.4f'_cA_g$)

b)

Wall Parameters		
Parameter	**Value**	**Description**
h_w	54.86 m	wall height (20 storeys)
h_f	2.743 m	floor height
b_w	508 mm	wall width
l_w	7800 mm	wall length
l_{pw}*	8.23 m	wall plastic hinge length
P	15484 kN	wall axial load ($0.1f'_cA_g$)

Figure 7.1 shows the real moment-curvature response of the standard column section used in the parametric study. Perfectly plastic behaviour was used to model moment-curvature response of the column beyond the peak bending strength. Damage was modeled as concrete cover spalling on both faces of the column and bar buckling on the compression face of the column (damage level 1 in Figure 5.8). The undamaged column "yielded" or reached its peak strength at curvature of 2.70 rad/km and failed due to concrete crushing at curvature of 3.25 rad/km. These figures were 2.60 rad/km and 3.20 rad/km for the damaged column respectively.

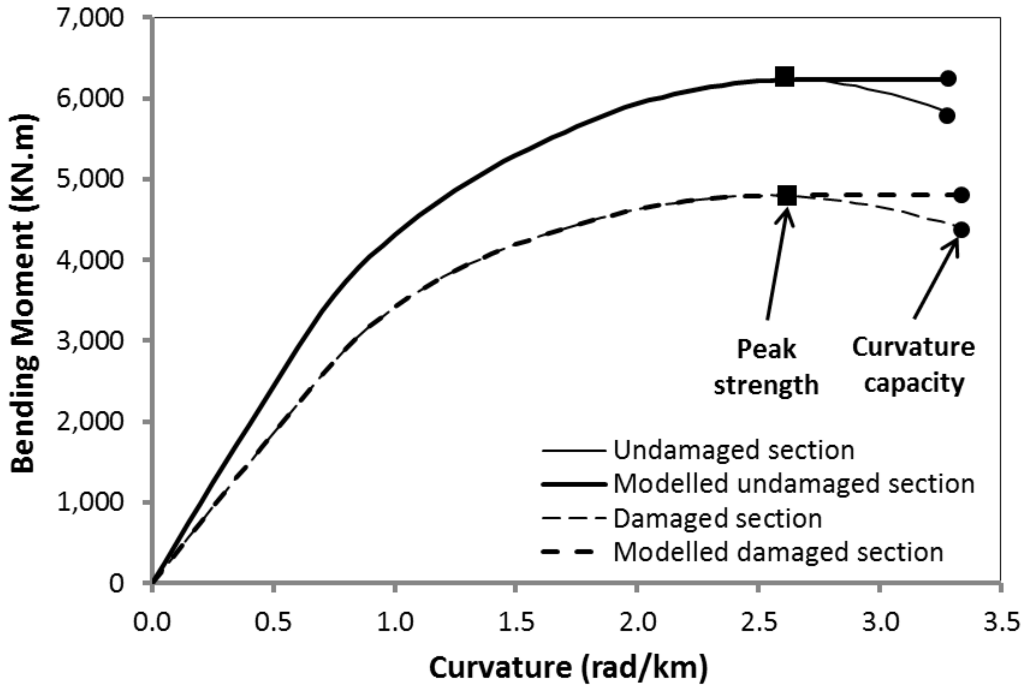

Figure 7.1 Actual and modelled moment-curvature responses of the undamaged and damaged sections of the standard column.

7.3 Wall Shear Strain (γ_{wall})

To study the influence of wall shear strain on column curvature demand, shear deformation of the wall example introduced in Section 6.6 was separated from flexural deformations. Two sets of pushover analysis were carried out, one with the column being pushed only with the wall's flexural deformation profile and the second with both flexural and shear deformation profiles. All other wall and column parameters were kept at their standard values.

Figure 7.2 shows column pushover analysis results when no damage was modeled in the column. The column went into the plastic behaviour zone at curvature of 2.70 rad/km and failed due to concrete crushing when maximum curvature of 3.25 rad/km was reached. When wall shear deformations were excluded, column curvature demand remained fairly close to wall maximum curvature. When wall shear strain was included, maximum column curvature grew more rapidly than wall maximum curvature reducing drift capacity of the gravity-load column.

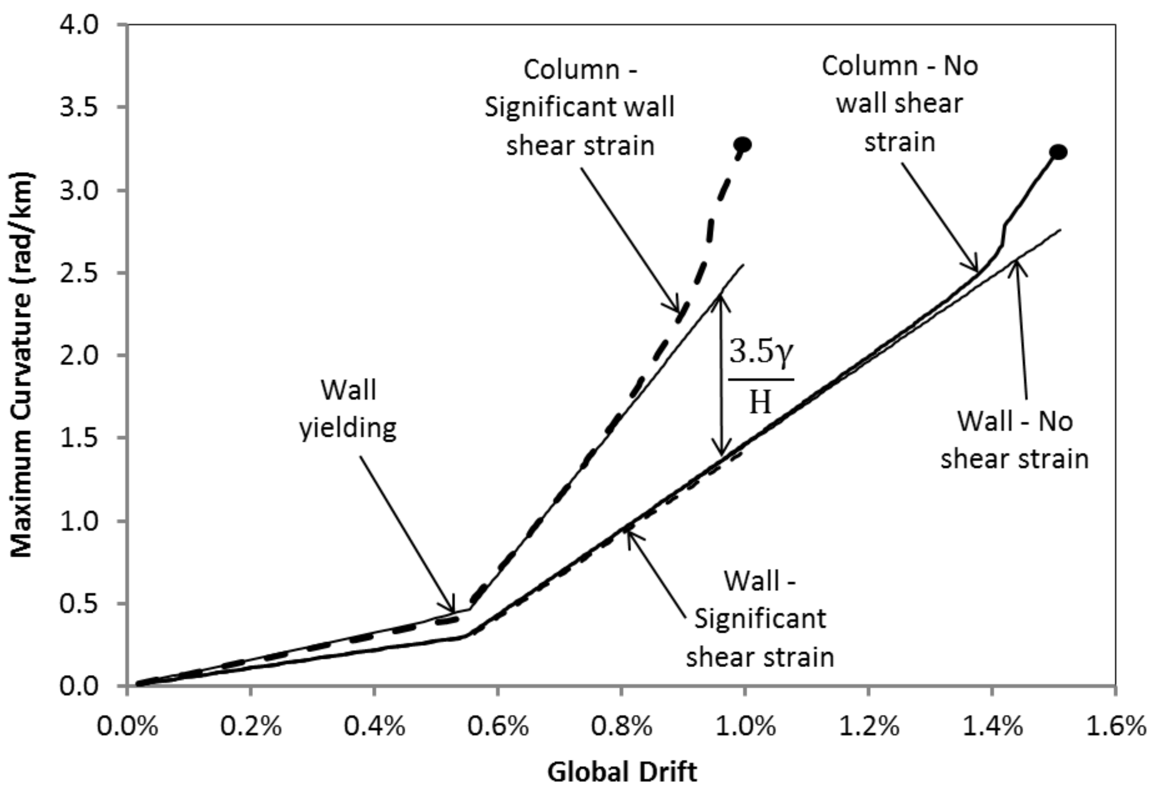

Figure 7.2 Increase in column curvature demand due to wall shear strain.

Including wall shear strain reduced global drift capacity by 34% compared to the case where no wall shear deformation existed. This observation can be further explained using curvature profiles at column failure (Figure 7.3). When no shear deformation was included in the analysis, both wall and column exhibited purely flexural behaviours and since the column was tied to the wall at closely spaced floor slabs, wall and column curvature profiles remained nearly identical up to the commencing of column plastic behaviour (Figure 7.3a). As the column was pushed further, considerable curvature was added at the base of the column causing the column maximum curvature to deviate from that of the wall until the point of concrete crushing.

When wall shear deformation was added to flexural deformations, since column behaviour was still dominated by flexure, it was forced to compensate for the extra imposed rotation by developing highly concentrated curvatures at its base. This caused the column maximum curvature to deviate from maximum wall curvature from the very beginning of the pushover analysis up to the point of column failure (Figure 7.3b). In other words, since wall shear deformation at the first few stories was substantial in comparison to flexural deformations at those levels, maximum column curvature being highly sensitive to the total lateral displacement at the first floor level caused an exponential increase in column curvature demand. Maximum column curvature being considerably greater than that of the wall resulted in the column going plastic at its base much earlier and reaching its curvature capacity at a much lower global drift compared to the case where no wall shear strain was included.

Figure 7.4a shows the deformation profiles of both the shear wall and the column at failure when no wall shear strain was included. In this figure it is almost impossible to tell the two deformation profiles apart. Figure 7.4b shows the deformation profiles of both the shear wall and the column at failure when wall shear strain was included. It is obvious that including wall shear strain increased lateral deformation at the first floor level by almost 40% putting additional rotation demand on the column that was attached to the wall. This extra rotation demand required the column to exhibit higher curvature concentration at its base at lower global drift levels compared to the case where no wall shear strain was included which caused a huge reduction in column drift capacity.

In conclusion, it was shown that accounting for the correct wall shear strain (deformation) is critical to estimating column curvature demand and hence attention should be paid to evaluating wall shear strain when estimating column curvature demands. It is therefore desirable to derive simple formulas that can estimate the additional column curvature demand due to wall shear strain.

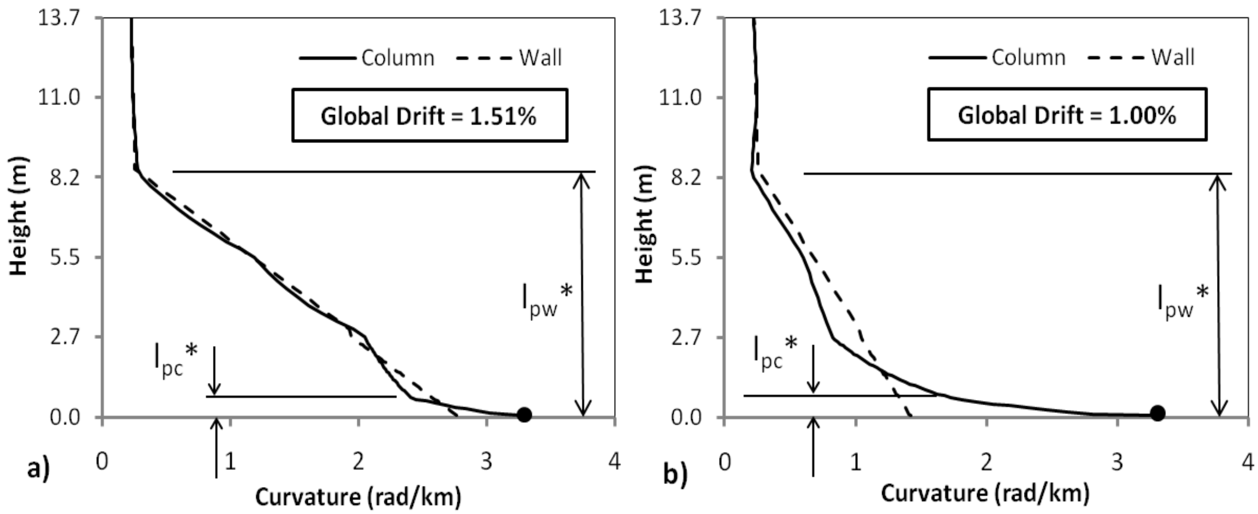

Figure 7.3 Curvature profiles of the undamaged column when curvature capacity has been reached: a) no wall shear strain, b) 100% of standard wall shear strain included.

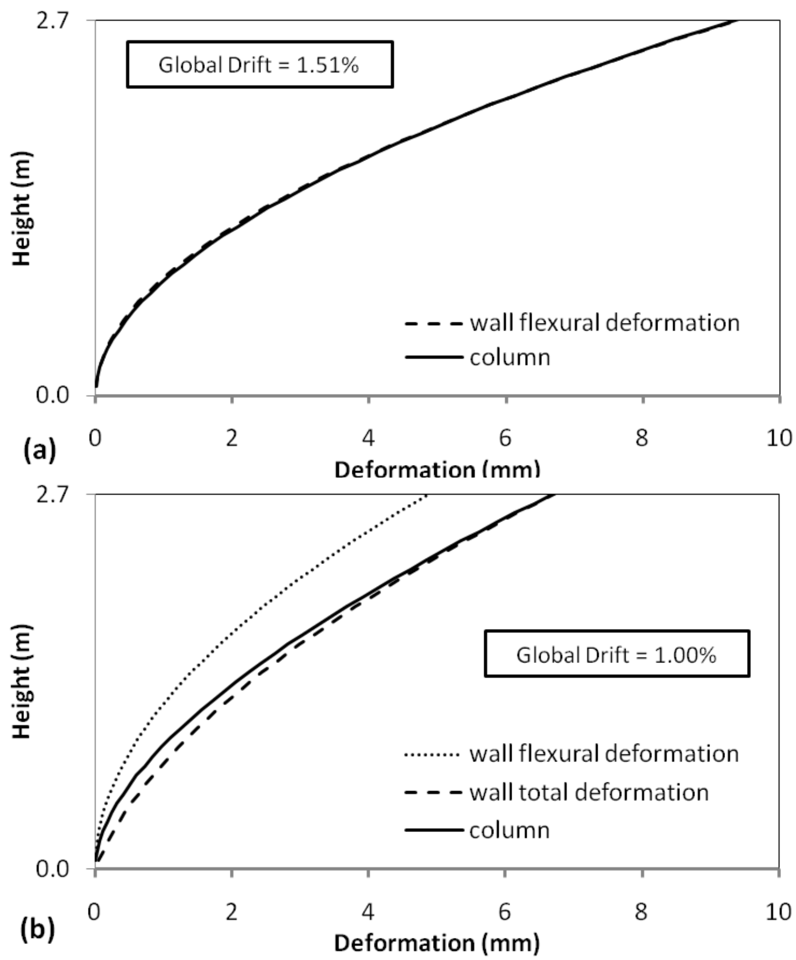

Figure 7.4 Deformation profiles at the point of column curvature capacity: a) no wall shear strain, b) 100% of wall shear strain applied (no column damage modeled).

7.3.1 Simple methods for estimating column curvature demand due to imposed wall deformation in the presence of wall shear strain

As shown in Figure 7.5, the effect of a constant (uniform) wall shear strain can be treated as concentrated rotation of the column support. If wall shear strain is constant, then the wall shear deformation profile will be a straight line with a slope equal to the constant shear strain. The effect of such imposed deformation profile on the column is identical to the case where the floor slabs are fixed in place (i.e. modeled as pinned supports) and the base of the column rotated by an angle equal to the wall shear strain.

Even though in reality, wall shear strain will not be constant over the height of the plastic hinge, if the plastic hinge is several storeys high, the variation of wall shear strain over the first storey can be ignored and an average wall shear strain over the first storey can be used. As long as the column remains fairly elastic or its flexural behaviour can be modeled using an effective elastic stiffness, the bending moment M_b required to rotate the base of the column by an amount equal to the wall shear strain γ is

$$M_b = \frac{4EI}{H} \cdot \gamma \qquad \textbf{Eq 7.1}$$

Using the standard moment distribution structural analysis procedure to analyze the elastic column structure, the final residual moment at the base of the column will be

$$M_b\left(1 - \frac{1}{8}\right) = \frac{7}{8}M_b = \frac{3.5EI}{H} \cdot \gamma \qquad \textbf{Eq 7.2}$$

The resulting additional curvature demand at the base of the column due to wall shear strain will then be

$$\varphi_s = \frac{M_b}{EI} = \frac{3.5}{H} \cdot \gamma \qquad \textbf{Eq 7.3}$$

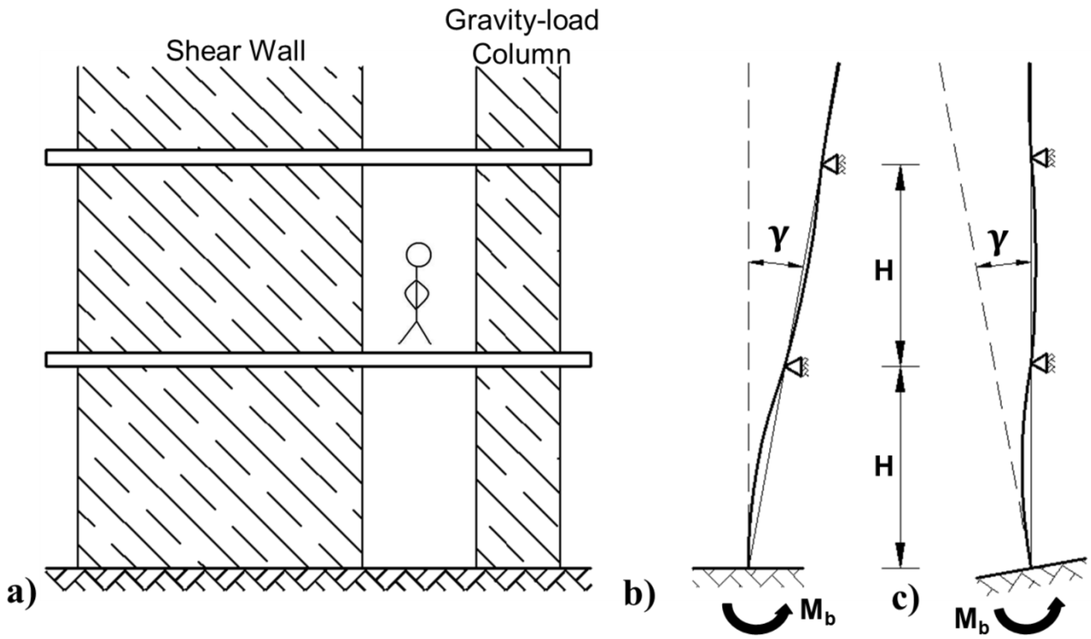

Figure 7.5 Effect of wall shear strain on gravity-load columns treated as support rotation at the base of the column: a) scheme of the wall-column system, b) lateral deformation of floor slabs due to uniform wall shear strain, and c) bending of the gravity-load due to support rotation.

In Figure 7.2, the estimated additional column curvature demand due to wall shear strain using Eq 7.3 is shown. The same line is shown in Figure 7.6 as Approx. 1. Note that the actual wall maximum shear strain at the base was substituted for γ in Eq 7.3. Eq 7.3 accurately predicted the additional column curvature due to shear deformation of the wall as long as the column remained in the elastic range. As the column experiences inelastic bending, more curvature was concentrated at its base and because Eq 7.3 was formulated for an elastic column, it underestimates column curvature demand.

An alternative way of using Eq 7.3 is to estimate γ from the shear strain model formulated in Section 2.9 and presented in Eq 2.10 and Eq 2.11. Substituting for γ in Eq 7.3 from the shear strain model presented in Section 2.9 gives the total column curvature demand as

$$\varphi_d = \varphi_{max} + \varphi_s = \varphi_{max} + \frac{3.5}{\mathrm{H}} \times 0.577\left(\frac{l_w}{2} - c\right) \cdot \varphi_{max} \qquad \textbf{Eq 7.4}$$

Where φ_{max} is the wall maximum curvature, φ_s is the additional column curvature demand due to wall shear strain, l_w is the wall length and c is the wall ultimate concrete compression depth. Rearranging the equation above gives

$$\varphi_d = \varphi_{max}\left[1 + \frac{2.0}{H}\left(\frac{l_w}{2} - c\right)\right] = \varphi_{max}\left[1 + \frac{l_w - 2c}{H}\right] \qquad \textbf{Eq 7.5}$$

Note that all of the parameters needed to estimated φ_d are either readily available to the designer or can be easily calculated. The line labeled Approx. 2 in Figure 7.6 shows estimates of φ_d for the column using the ultimate concrete compression depth for c. This line constantly overestimates column curvature demand up until the point of column failure where it meets the curvature demand obtained from the pushover analysis. Two phenomena contribute to this overestimation of column curvature demand. First is the fact that the shear strain model formulated in Section 2.7 somewhat overestimates wall shear strain. The second contributor is the use of ultimate wall concrete compression depth for c throughout the pushover analysis. Use of a smaller c will result in larger estimates of wall shear strain and subsequently, larger estimates of column curvature demand.

If the correct value of c is calculated from sectional analysis and used in estimating φ_d , column curvature demand at lower drift levels will be less overestimated. This is shown by the line labeled Approx. 3 in Figure 7.6. As expected, lower curvature demand is estimated at lower building drifts compared to that predicted by Approx. 2. Note that Approx. 2 and Approx. 3 are close to each other once the column experiences high nonlinear bending as the concrete compression depth approaches its ultimate value.

Another approach to formulating a simple method for estimation of additional column curvature demand due to wall shear strain is to consider the curvature profile of the column when pushed to the displacement profile of the shear wall having considerable shear strain. In Figure 7.7, the wall curvature and shear strain profiles are shown. Note that the wall total deformation will be the sum of the flexural and shear deformation components obtained from integrating curvatures and shear strains over the height.

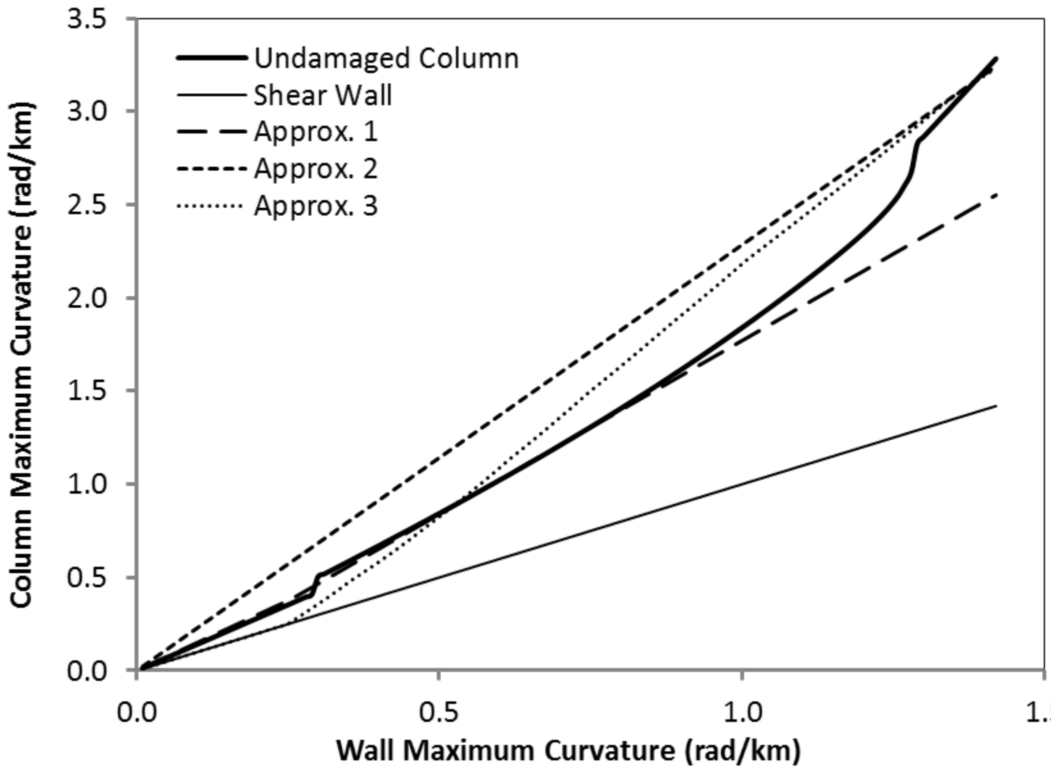

Figure 7.6 Estimating column curvature demand due to imposed wall deformation from wall maximum curvature in the presence of wall shear strain.

Figure 7.7c shows the approximate column curvature profile. Because the column does not develop significant shear strain, it can only deform in flexure. For the wall and column to have the same deformation profile at floor slab levels, displacement from the hatched area on the column curvature profile must compensate for the wall shear deformation. Because the imposed deformation of the second floor slab is the most critical to column curvature demand at the base, attention will be focused on the wall-column system deformation compatibility at the second floor slab. Wall shear deformation at the second floor slab is given by

$$\Delta_{s1} = \gamma_{avg} \cdot H \qquad \textbf{Eq 7.6}$$

Where γ_{avg} is the average wall shear strain in the first storey and H is the first storey height. If the wall plastic hinge length is several storeys high, γ_{avg} can be conservatively replaced with the maximum wall shear strain at the base γ_{max}. Hence

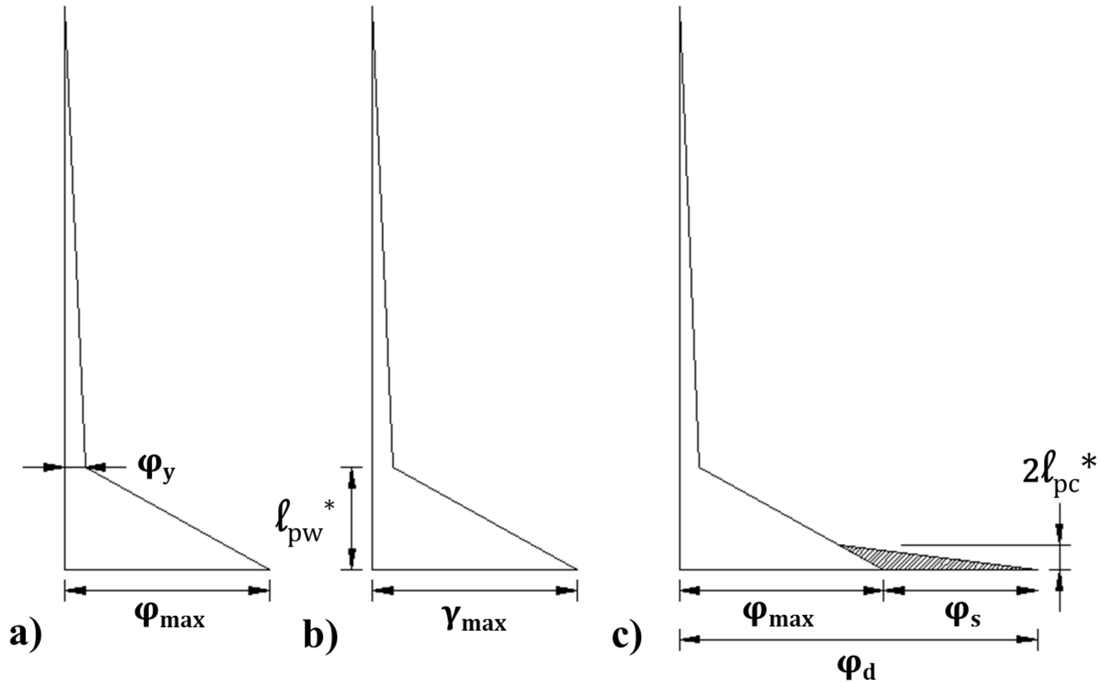

Figure 7.7 Schematics of a) curvature profile of the shear wall, b) shear strain profile of the shear wall, and c) curvature profile of the gravity-load column.

$$\Delta_{s1} = \gamma_{max} \cdot H \quad \textbf{Eq 7.7}$$

To satisfy deformation compatibility of the wall-column system at the second floor slab level, Δ_{s1} must be equal to the flexural deformation from the hatched area on the column curvature profile.

$$\Delta_{s1} = \gamma_{max} \cdot H = \frac{2\varphi_s l_{pc}^*}{2}\left(H - \frac{2l_{pc}^*}{3}\right) \quad \textbf{Eq 7.8}$$

Rearranging gives

$$\varphi_s = \frac{\gamma_{max} H}{l_{pc}^*\left(H - \frac{2l_{pc}^*}{3}\right)} \cong \frac{\gamma_{max}}{l_{pc}^*} \quad \textbf{Eq 7.9}$$

Note that a simplification was made assuming that the column plastic hinge length is considerably shorter than the first storey height. Estimations of column curvature demand using Eq 7.9 is shown in Figure 7.8 as the line labeled Approx. 4. The actual wall maximum shear strain was used to predict wall curvature demand in this case. It is clear that Eq 7.9 can accurately estimate column curvature if the actual wall maximum shear strain is used.

To further simplify the use of this approximate method, wall maximum shear strain is predicted from the simple shear strain model presented in Section 2.9 as follows.

$$\varphi_s \cong \frac{\gamma_{max}}{l_{pc}^*} = \frac{1}{l_{pc}^*} \cdot 0.577 \left(\frac{l_w}{2} - c \right) \varphi_{max} \cong \frac{0.3(l_w - 2c)}{l_{pc}^*} \varphi_{max} \qquad \textbf{Eq 7.10}$$

Where l_w is the wall length and c is the ultimate wall concrete compression depth. The total column curvature demand would then be

$$\varphi_d = \varphi_{max} + \varphi_s = \varphi_{max} \left[1 + 0.3 \frac{(l_w - 2c)}{l_{pc}^*} \right] \qquad \textbf{Eq 7.11}$$

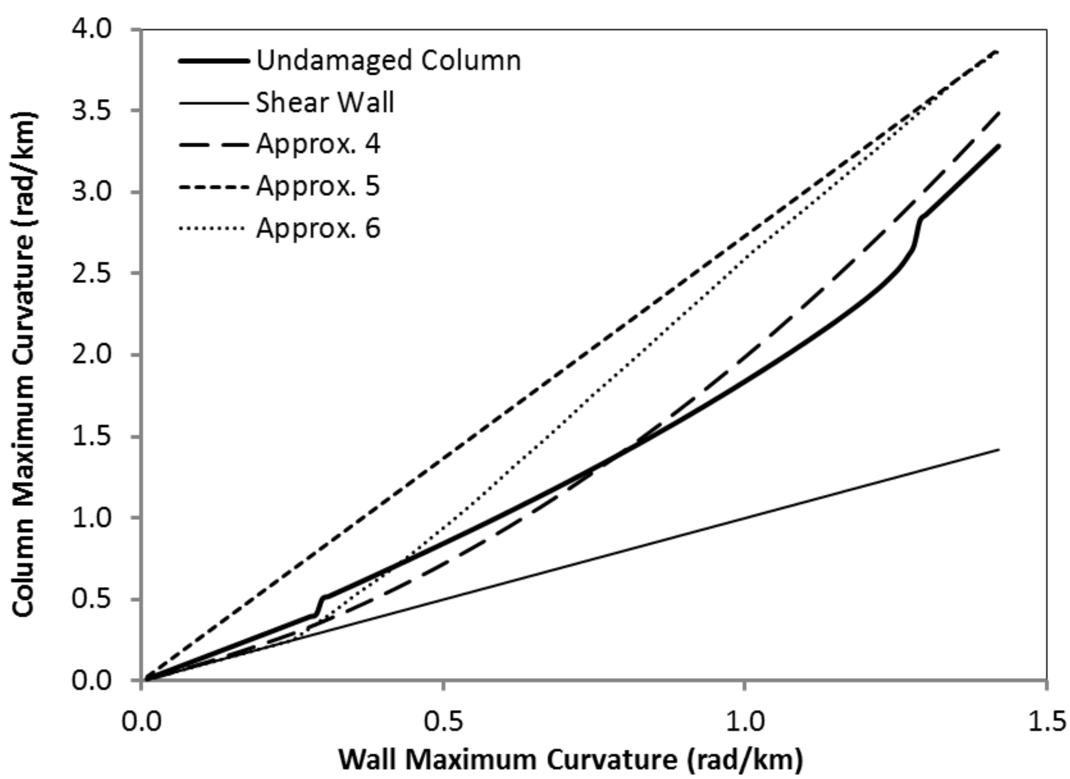

Figure 7.8 Estimating column curvature demand due to imposed wall deformation from wall maximum curvature in the presence of wall shear strain.

Column curvature demand estimated using Eq 7.11 is shown in Figure 7.8 as Approx. 5. Eq 7.11 constantly overestimates column curvature demand partly because the shear strain model somewhat overestimates wall shear strain and partly because the ultimate wall concrete compression depth is used throughout the pushover analysis. Approx. 6 on the same figure is made with the wall concrete compression depth calculated from section analysis at each wall maximum curvature. As expected, Approx. 6 is less conservative and converges to Approx. 5 at high wall maximum curvatures.

In summary, the simple equations provided make reasonably conservative estimates of the column curvature demand using simple wall and column parameters readily available to the designer. The effect of wall shear strain on curvature demand of columns fixed at their base can therefore be taken into account to ensure the gravity frame system has adequate deformation capacity to tolerate the lateral displacements imposed on it by the shear wall.

7.4 Column Length

As the length to width ratio of a gravity-load column cross-section increases, maximum curvature that the cross-section can withstand decreases. This is because a certain concrete area is needed to resist the axial load on the column while it is being bent. The smaller the width of the column, the larger will be the compression depth which in turn accelerates concrete crushing at the compression face of the column. In other words, at a certain curvature, the column with the smaller compression depth will have smaller maximum compressive strain.

It is intended to study the effect of column length on column curvature demand by subjecting five columns with various lengths to the deformations imposed by the shear-wall introduced in Section 6.6.2. Column cross-sections chosen are the same as those in Figure 7.9. Concrete strength of 40 MPa was chosen. To make comparison possible, columns sections were given 2% vertical reinforcement uniformly distributed around their perimeter all having to carry an axial load of $0.40f'_cA_g$. Analysis was stopped when maximum concrete strain reached 0.0035. For simplicity, wall shear strain (deformation) was excluded from the analysis in this section.

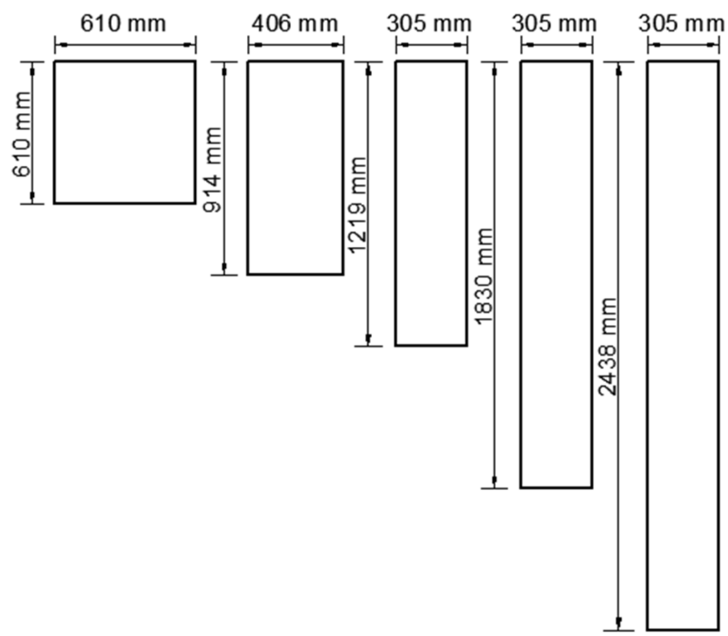

Figure 7.9 Column cross-sections used to study the effect of column length on column curvature demand.

Figure 7.10 shows pushover analysis results for the five columns studied. In the absence of wall shear strain, all column curvature profiles closely followed that of the wall up until softening and yielding of the elements at the base of the columns when maximum column curvature started to deviate from that of the wall. This was because the column could exhibit flexural deformations only and when it was subjected to wall deformations which had no shear component, the column being tied to the wall at closely spaced floor slabs was forced to demonstrate a curvature profile very similar to that of the wall. However the longer the column was, the sooner it reached its peak strength and the lower was the curvature capacity; hence global drift capacity was dramatically affected by column length. Figure 7.11a compares curvature profiles of the 1.8 m long column section to those of the wall at various global drift levels. The minor discrepancy between shear wall and column curvature profiles did not result in noticeable difference in deformation profiles of the two (see Figure 7.11b).

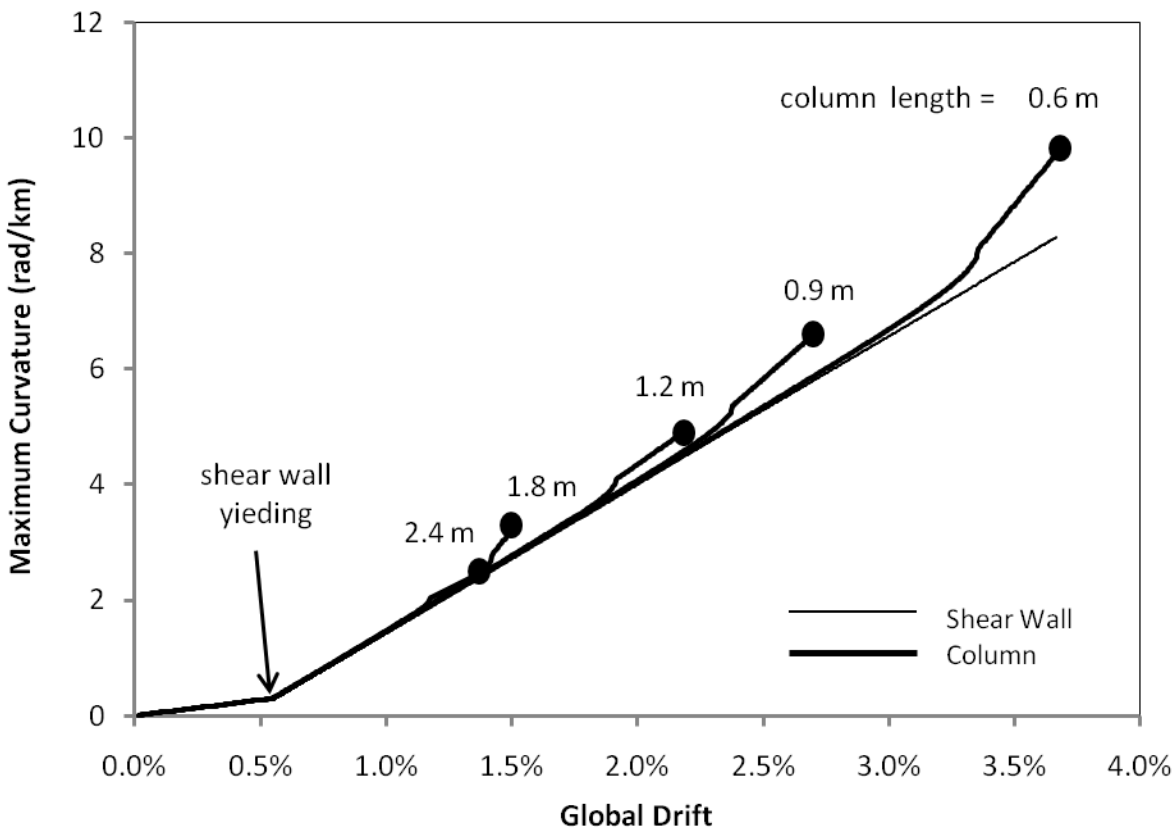

Figure 7.10 Reduction in column global drift capacity with increase in column length (no wall shear strain, no column damage).

Table 7.2 gives a numerical summary of the pushover analysis results for the five columns at failure. Note that maximum curvature amplification factors at are close to unity which indicates that maximum column curvature demand is close to the wall maximum curvature.

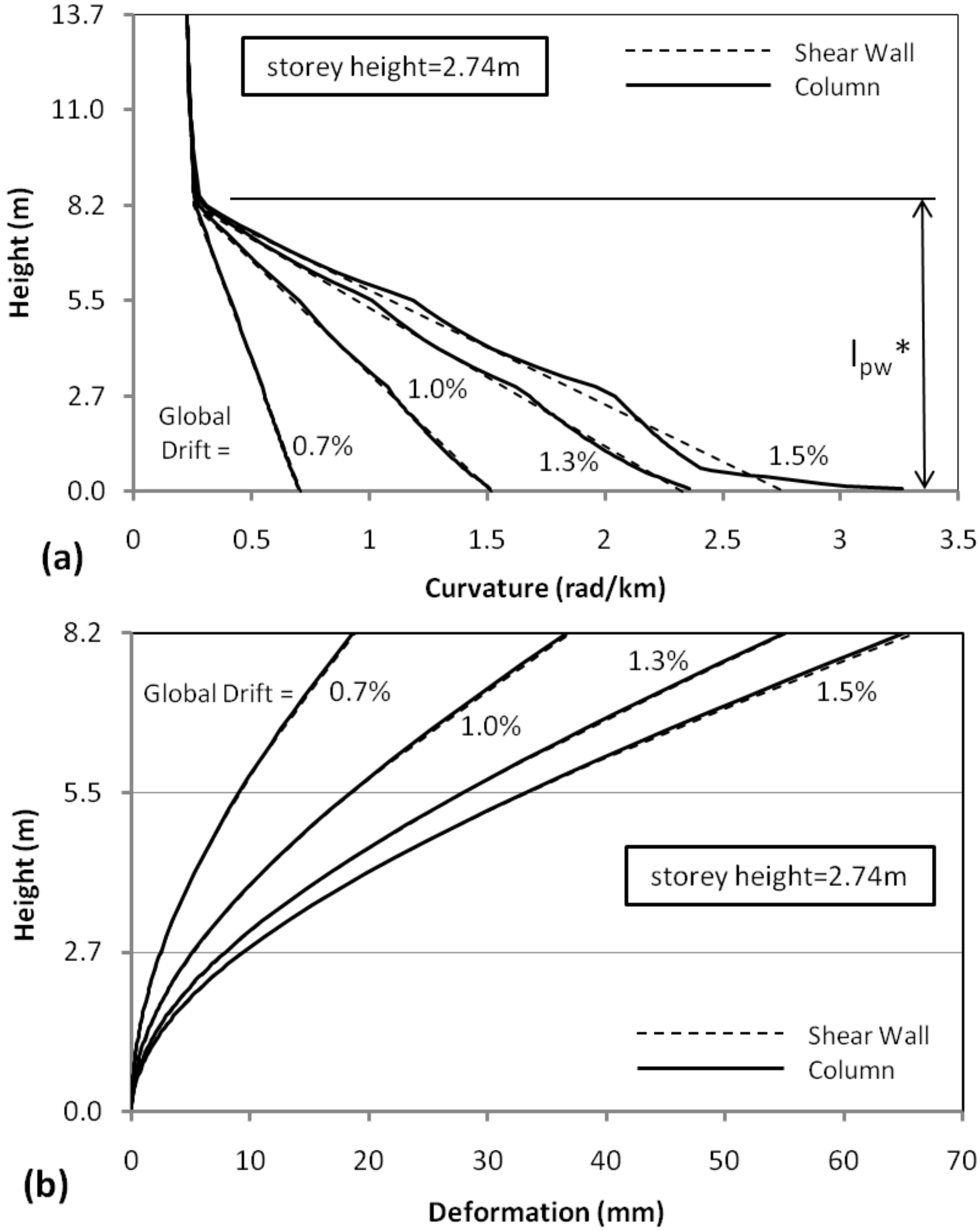

Figure 7.11 Comparison of responses of the shear wall and the 1.8 m column section in the wall plastic hinge zone: a) curvature profiles, b) deformation profiles. (Note: No wall shear strain and no column damage were modeled.)

To gain further insight into the flexural behaviour of columns of various cross-sectional lengths tied to a shear wall, pushover curves and moment-curvature responses of the 2.4 m and the 0.6 m column sections are compared in Figure 7.12 and Figure 7.13 respectively.

Table 7.2 Numerical summary of pushover analysis results for columns of various cross-sectional lengths at the point of column failure (no wall shear strain, no column damage).

Column Length (m)	Wall Maximum Curvature (rad/km)	Column Maximum Curvature (rad/km)	Global Drift	Normalized Global Drift	Column Maximum Curvature Amplification Factor
0.6	8.28	9.71	3.66%	1.000	1.17
0.9	5.79	6.56	2.69%	0.734	1.13
1.2	4.49	4.91	2.18%	0.596	1.09
1.8	2.76	3.26	1.51%	0.412	1.18
2.4	2.39	2.45	1.11%	0.304	1.03

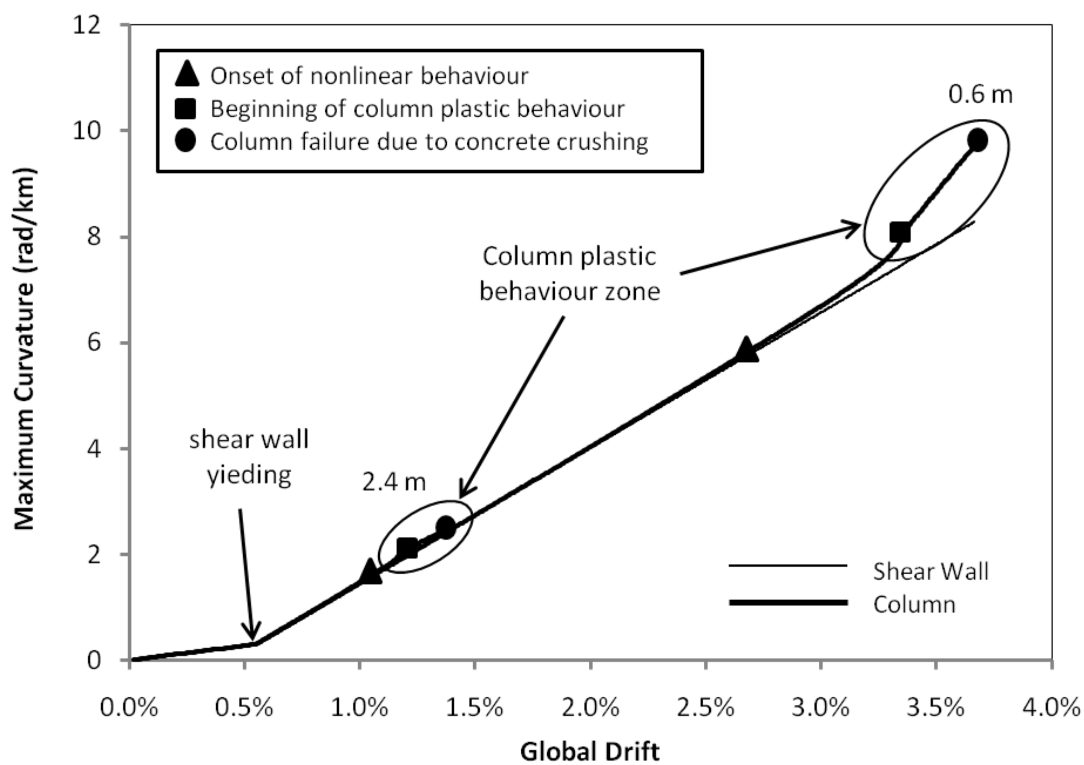

Figure 7.12 Pushover analysis results for the 2.4 m and 0.6 m long column cross-sections (no wall shear strain, no column damage).

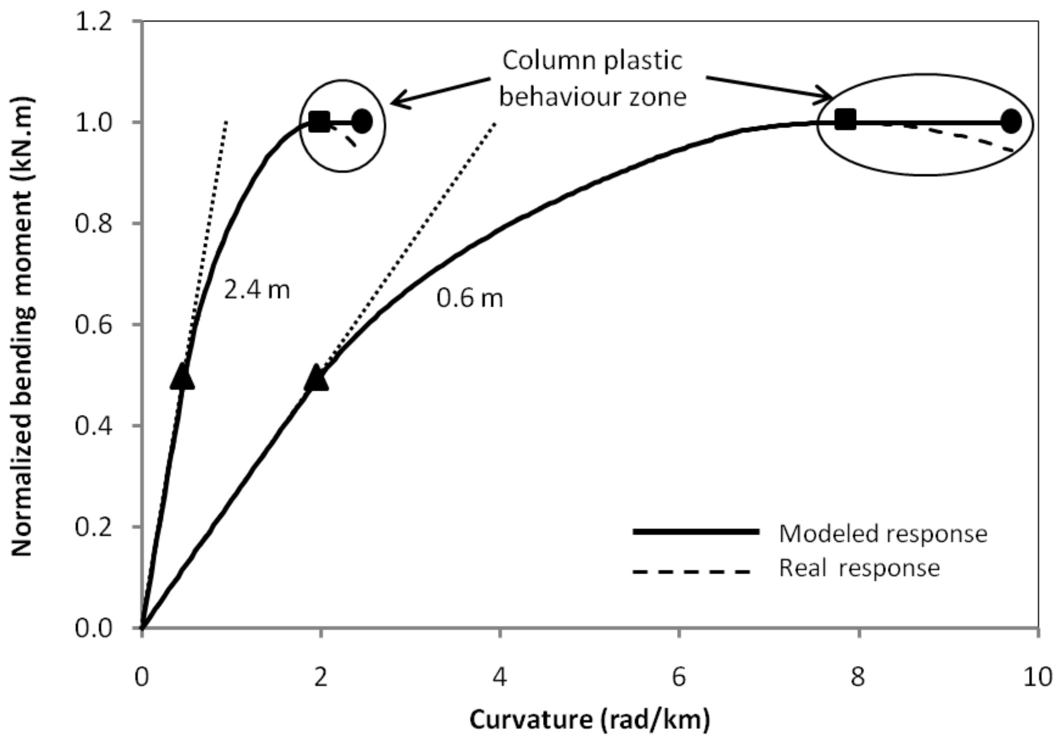

Figure 7.13 Moment-curvature response of the 2.4 m and 0.6 m long columns.

According to Figure 7.12 both columns have the same maximum curvature as that of the wall up until the onset of column nonlinear behaviour at the element at the base of the column. Column stiffness at the base keeps decreasing as the column is pushed to the point when maximum bending moment at the base of the column reaches column's moment strength and plastic behaviour is triggered. From thereafter, a plastic curvature model with linear curvature distribution over a height equal to the column length was added to elastic curvatures of the column structure with a forced inflection point at the base. Curvature profile and bending moments of this modified structure were then added to those of the column at the beginning of plastic behaviour. This ensured no addition of moment at the base of the column beyond the section strength while the zero rotation boundary condition at the base was maintained.

However, maximum curvature demand of the 0.6 m column deviated more noticeably from wall maximum curvature compared to that of the 2.4 m wall. Also, the plastic behaviour zone of the 0.6 column was larger than that of the 2.4 m column section. This can be explained by looking at Figure 7.13. Bending moments are normalized by the moment strength to make comparison of the two curves easier. Loss of sectional flexural stiffness after the onset of nonlinear behaviour was more rapid in the case of the 0.6 m column section resulting in noticeable concentration of inelastic curvatures at the base of the column. Length of the column's plastic behaviour zone was directly related to the curvature range from the peak point of the moment-curvature response to the point of concrete crushing. Because the 0.6 m long cross-section was more flexible, it had a longer plastic behaviour zone which resulted in a considerable additional drift capacity of the column coming from the plastic behaviour zone.

In conclusion, all columns of various lengths tend to demonstrate the same pushover response in early stages of the push in the absence of wall shear strain. The longer the column length, the sooner its maximum curvature deviates from that of the wall which when combined with reduction in column curvature capacity with length, results in lower drift capacity.

7.5 Wall Length (l_{pw}*)

The next parameter studied is the wall length which determines the length of the wall plastic hinge zone. Wall plastic hinge zone is the section at the base of the wall which undergoes significant yielding producing inelastic rotation. Inelastic curvatures concentrate in the plastic hinge region with the maximum at the base and are assumed to vary linearly over the wall plastic hinge length. With a fixed wall curvature capacity, the taller the plastic hinge is, the higher the building drift capacity will be. Wall plastic hinge length is usually expressed as multiples of wall length and varies between 1.0 to 1.6 times the wall length.

To examine the effect of wall plastic hinge length on column global drift limit, four wall lengths of 7.8, 9.4, 10.9 and 12.5 m were chosen with wall plastic hinge length being equal to the wall length keeping the rest of the parameters at their standard value (see Table 7.1 for standard parameters). Pushover analysis was conducted using the analysis methodology described in Section 6.4 with no wall shear strain and no column damage considered.

Figure 7.14 shows column pushover analysis for various wall lengths. It was observed that column global drift capacity increased as wall length became larger. This observation can be explained in a rather simple way. Because no wall shear strain was considered, column curvature profiles followed that of the wall very closely throughout the pushover analysis. However, when wall length was larger, higher global drifts came at lower wall maximum curvatures. In other words, the slope of the wall curvature plots was inversely proportional to wall length making the longest wall the most flexible. This resulted in inelastic curvatures being distributed over a larger height and away from the base of the wall. This in turn reduced curvature concentration at the base of the column which demonstrated a curvature profile similar to that of the wall.

Another observation is that column plastic behaviour starts at the same wall maximum curvature at which the column fails. In other words, if the point of column failure on the column pushover curve is projected onto that of the wall, it crosses the wall pushover curve at the point with the same curvature as that of the point of beginning of column plastic behaviour (see Figure 7.14). This suggests that one could calculate wall global drift at wall maximum curvature of Φ_{plc} defined in Figure 7.15 and get an accurate estimate of the column global drift capacity.

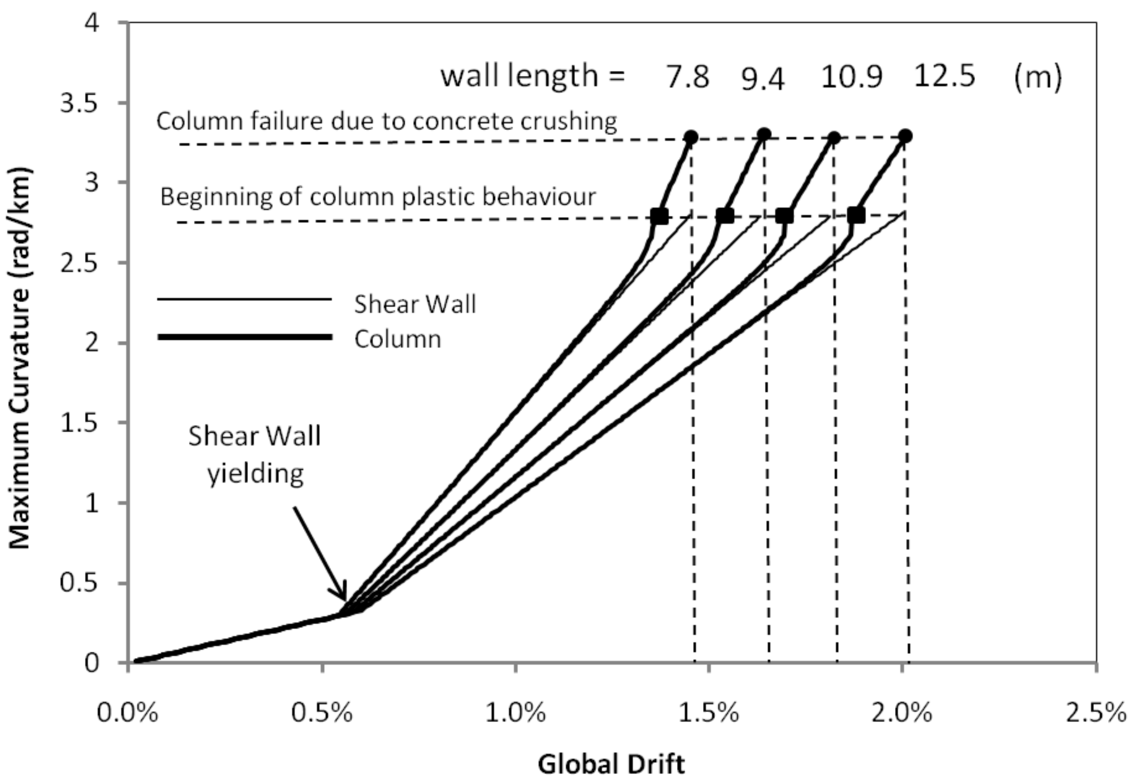

Figure 7.14 Increase in column drift capacity with wall length (no wall shear strain, no column damage).

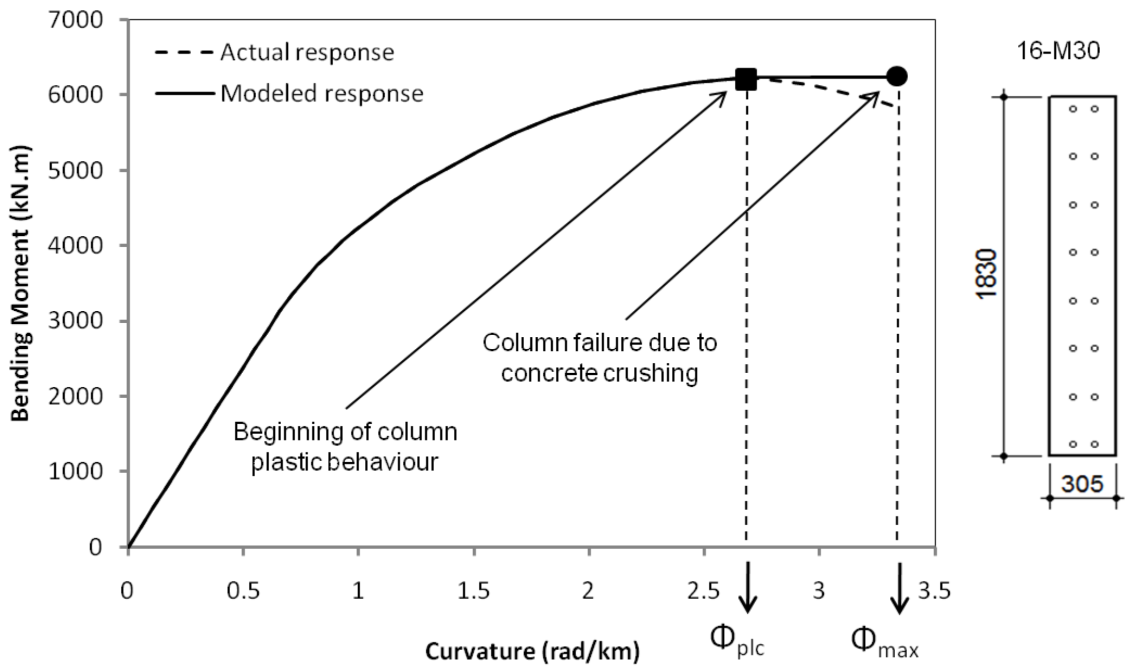

Figure 7.15 Moment-curvature response of the 1.8 m long column section.

Shown in Table 7.3 is a numerical summary of pushover analysis results at the point of column failure. Note that column maximum curvature amplification factor is the same for all wall lengths considered. Wall length clearly affects column global drift capacity and hence, accounting for the correct wall plastic hinge length in calculating lateral deformation profile of the building is critical when column drift capacities are to be checked.

Table 7.3 Numerical summary of column pushover analysis results at the point of column failure for the standard column connected to walls of various lengths (no wall shear strain, no column damage).

l_{pw}* (m)	Wall Maximum Curvature (rad/km)	Column Maximum Curvature (rad/km)	Global Drift	Normalized Global Drift	Column Maximum Curvature Amplification Factor
7.8	2.80	3.27	1.45%	0.725	1.17
9.4	2.79	3.26	1.63%	0.816	1.17
10.9	2.79	3.26	1.81%	0.906	1.17
12.5	2.81	3.26	2.00%	1.000	1.16

7.6 Height of Column Plastic Hinge Zone (l_{pc}*)

Column plastic hinge region is the length of the column over which inelastic curvatures are generated due to yielding of vertical reinforcement in compression and concrete softening. Concrete cover is expected to spall over the height of column plastic hinge zone further reducing both the strength and stiffness of the column. Curvatures in the plastic behaviour region vary approximately linearly from the maximum at the base to the top. Height of the column plastic hinge region is usually estimated using expressions fitted to extensive experimental work and is believed to increase with axial load.

In order to study the effect of height of column plastic hinge region on column curvature demand, 3 values of l_{pc}* of 305, 610, and 1220 mm were used. Note that l_{pc}* equal to 610 mm is the standards height of column plastic behaviour zone. Wall shear strain and damage to the column were excluded from the analysis. Other analysis parameters were kept at their standard values described in Table 7.1.

Pushover analysis results are shown in Figure 7.16. As expected, column flexibility increases with height of the column plastic behaviour zone. The explanation is rather simple. Since column curvature capacity is limited by concrete crushing and hence is constant regardless of l_{pc}*, at maximum column curvature, the column with the larger l_{pc}* will have greater inelastic rotation. This is demonstrated in Figure 7.17 where column curvature profiles for l_{pc}* of 305 mm and 1220 mm at the point of column failure are compared. In both cases, column failure occurred when column maximum curvature reached 3.27 rad/km when concrete reached its maximum compressive strain. At that point, the column with the larger l_{pc}* could concentrate more plastic curvature in the first floor which resulted in additional inelastic rotation and consequently additional global drift capacity. Although column curvatures vaguely followed the wall curvature pattern, there was a considerable deviation between the two. Column curvatures fluctuated around the bilinear wall curvature pattern with noticeable concentration at the base of the column. In Figure 7.18 the deformation profiles of the column and the wall are compared for the two cases of l_{pc}* equal to 305 mm and 1220 mm. The difference in the curvature profiles does not translate to any noticeable difference in the deformation profiles. Note that both the wall and the column had the same deformation values at floor slab levels.

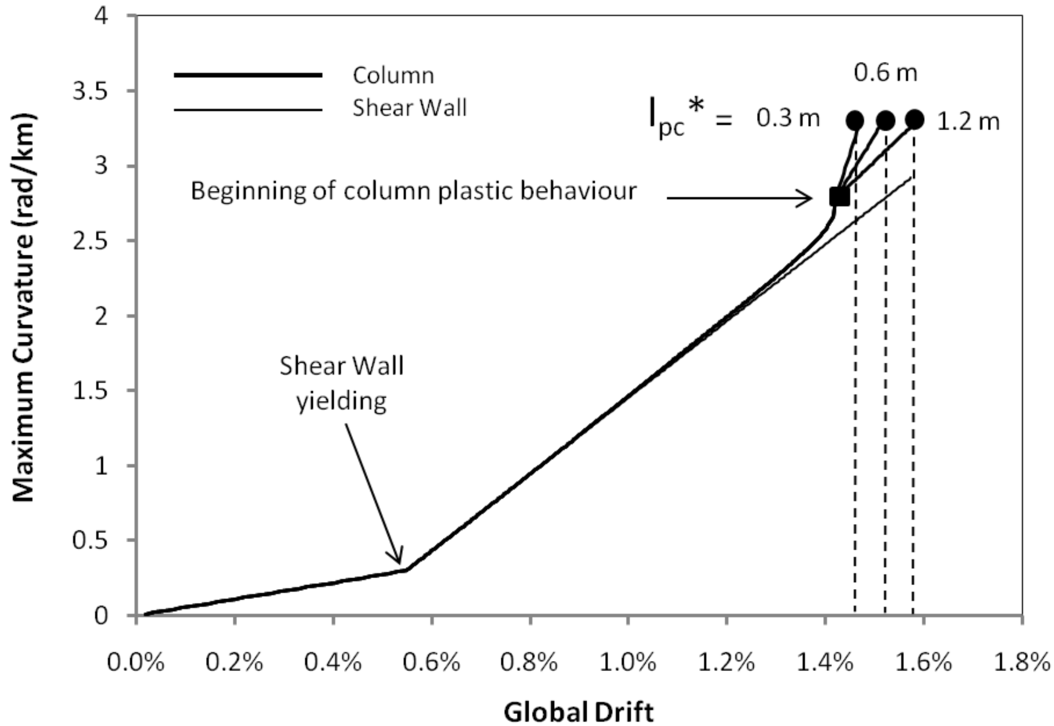

Figure 7.16 Effect of height of column plastic curvature zone on drift capacity (no wall shear strain, no column damage).

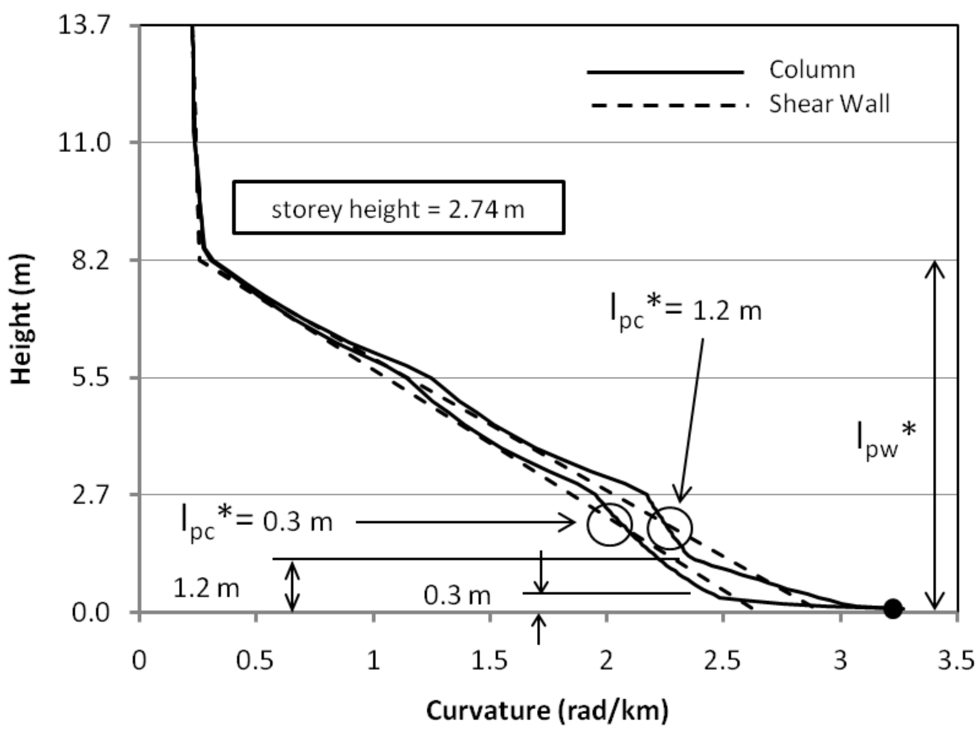

Figure 7.17 Column curvature profiles at failure for different column plastic hinge heights (no wall shear strain, no column damage).

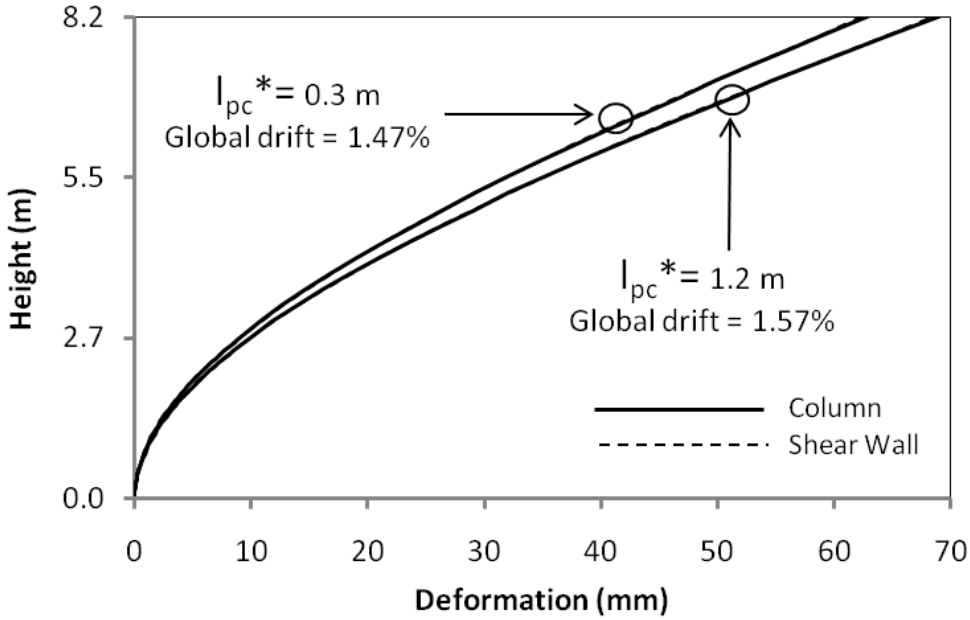

Figure 7.18 Comparison of deformation profiles of the shear wall and the 1.8 m column section in the wall plastic hinge region for column plastic hinge heights of 0.3 m and 1.2 m (no wall shear strain, no column damage).

Although the effect of l_{pc}* is not that great in this example (i.e. less than 5% change in column drift capacity), column flexibility can be seriously affected by l_{pc}* if the peak bending strength point and failure point on the column moment-curvature response are further apart. Hence, it is concluded that an accurate estimate of l_{pc}* should be made if column drift capacity is to be calculated when the gap between the curvature at column peak bending strength and curvature capacity of the column is large.

Table 7.4 Numerical summary of pushover analysis results at column failure for various values of l_{pc}* (no wall shear strain, no column damage).

l_{pc}* (mm)	Wall Maximum Curvature (rad/km)	Column Maximum Curvature (rad/km)	Global Drift	Normalized Global Drift
305	2.65	3.27	1.47%	0.972
610	2.76	3.26	1.51%	1.000
1220	2.92	3.26	1.57%	1.041

7.7 Effect of Damage to the Column on its Curvature Demand

When the column is bent excessively in the event of an earthquake, various levels of damage occur at the base of the column where large curvatures are concentrated. Damage can be in the form cracking, losing the concrete cover, buckling of reinforcement under compression, and fracture of vertical reinforcement in tension. Having a weaker section at the base of the column which still needs to sustain the total axial load of the column can decrease column flexibility and its drift capacity.

To study the effect of damage to the column on its drift capacity, two levels of damage are considered. The two levels of damage are shown in Figure 5.7 for the standard column. Damage level 1 entails loss of the concrete cover on both faces and buckling of vertical reinforcement on the compression face. In damage level 2, vertical reinforcement on the tension face of the section is ruptured in addition to the damage caused in level 1. Figure 5.8 shows moment-curvature responses of column cross-sections at various damage levels. Note that maximum curvature capacities are 3.25, 3.20 and 3.30 rad/km for the undamaged, damage level 1 and damage level 2 sections respectively.

Damage was assumed to occur at the base of the column over a length equal to the smallest column section dimension which in practice is nearly equal to the tie spacing. Pushover analysis was done on the column at each of the described damaged levels and the results were compared to those of the undamaged column. Moment-curvature response of the damaged section was assigned to elements at the base of the column over the height of l_{pc}. Refer to Section 5.4 for a discussion on how damage to the section affected moment-curvature response of the column. Two sets of analysis were done one with no shear strain of the wall included and the other with shear deformation included in wall displacement profile. All other parameters were kept at their standard value (see Table 7.1).

Figure 7.19 shows pushover analysis results of the column at various damage levels when no wall shear strain was included in the analysis. Maximum curvature demand of the undamaged column closely followed the wall maximum curvature up until softening of the column. Maximum curvature demands of the damaged columns however deviated from wall maximum curvature from the very beginning of the pushover curve.

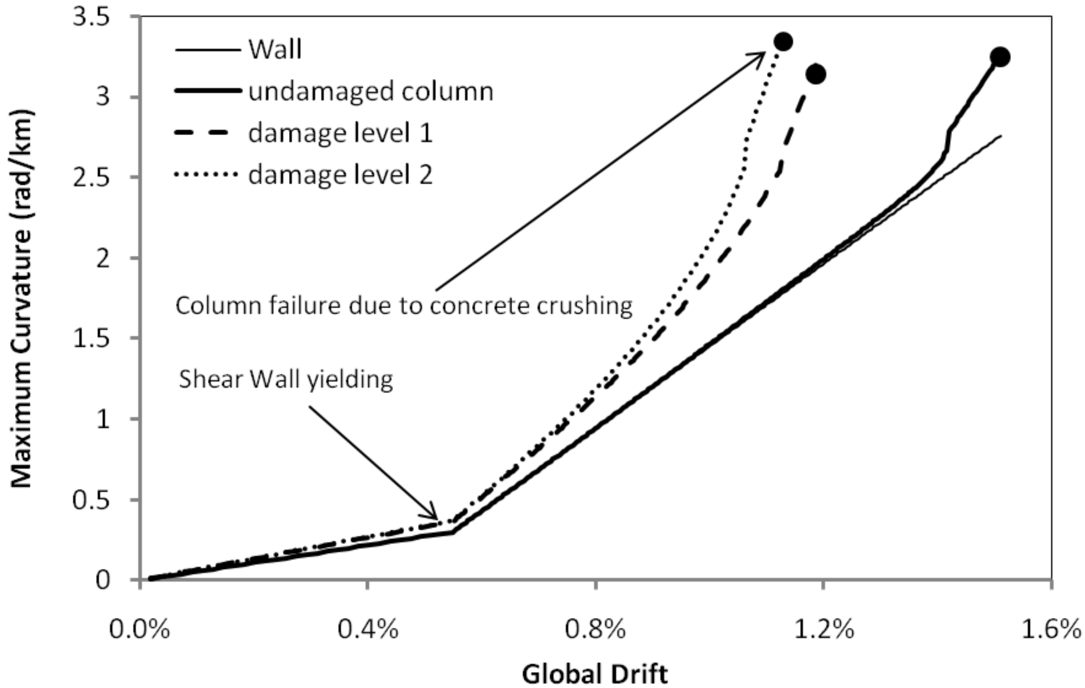

Figure 7.19 Pushover analysis results of the standard column for various damage levels (no wall shear strain).

This observation can be explained looking at curvature profiles of the three columns at the point of column failure. Figure 7.20a shows curvature profile of the undamaged column at failure. It is seen that column curvatures follow the trend of wall curvatures except for in the column plastic hinge zone where column curvatures are concentrated. Shown in Figure 7.20b and Figure 7.20c are curvature profiles at failure for the column at damage levels 1 and 2 respectively. In both of these cases column maximum curvature occurred at the top of the column damaged zone which required the inflection point to be placed at that point during the analysis to ensure no addition of maximum bending moment when modeling column post-peak behaviour. This was because column shear force was negative in the first storey which was in turn because the damaged column section was much softer than the undamaged section. Hence, curvatures reduced from top to the bottom of the first storey. The sudden jump in column curvature occurred at the point of transition from undamaged to damaged section. Since bending moments where continuous over the height of the column, for the same bending moment value, the softer damaged column section produced much larger curvatures than the undamaged section. Note that all three curvature profiles occurred at different global drift levels.

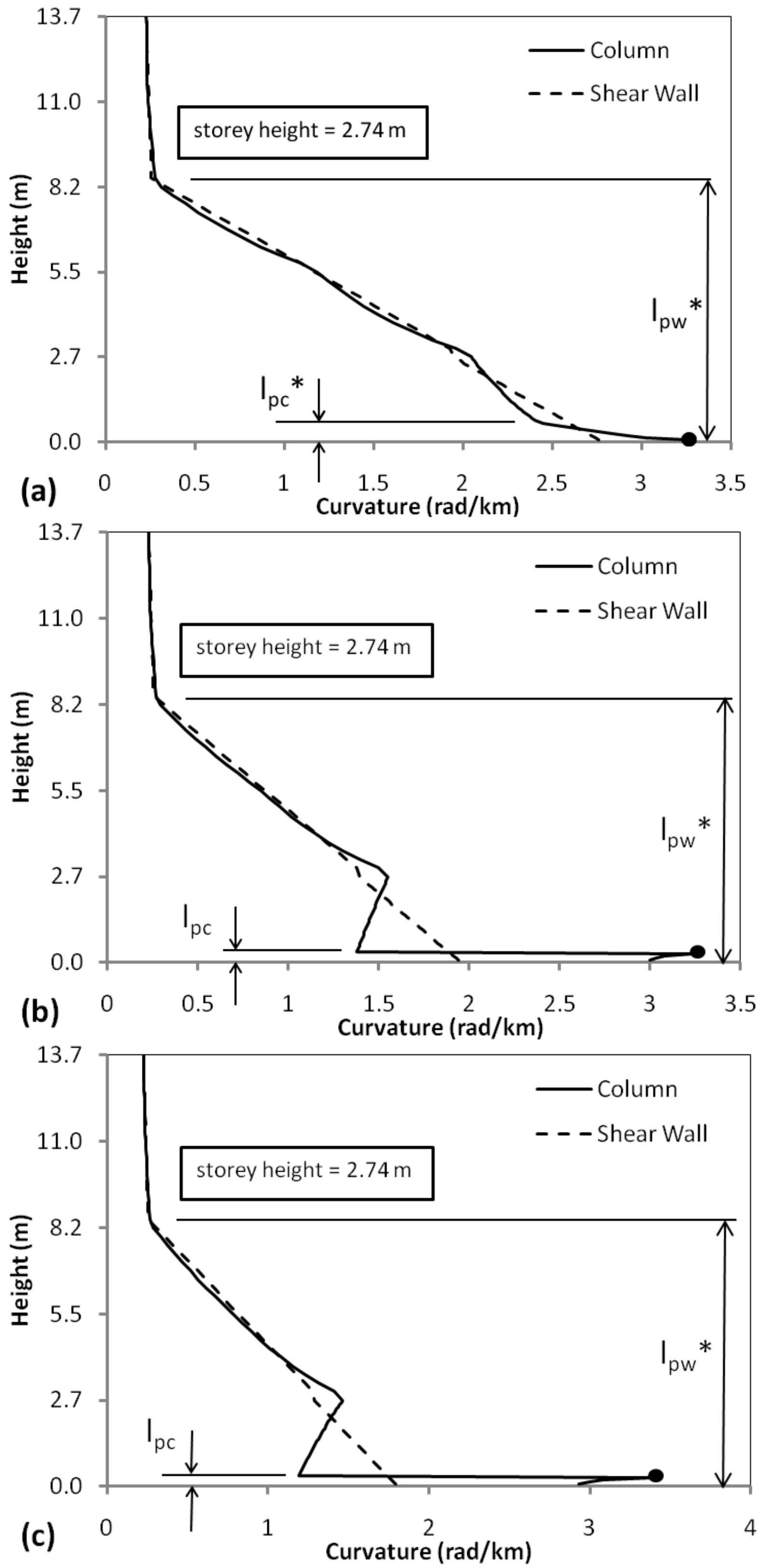

Figure 7.20 Comparison of wall and standard column curvature profiles at column failure: a) undamaged column, b) damage level 1, c) damage level 2 (no wall shear strain).

Figure 7.21 shows pushover analysis results for the standard column at various damage levels in the presence of wall shear strain. Column maximum curvature demand deviated from wall maximum curvature from the very beginning of the pushover curve which was the result of wall shear strain (see Section 7.3). As column damage progressed, column global drift capacity was reduced.

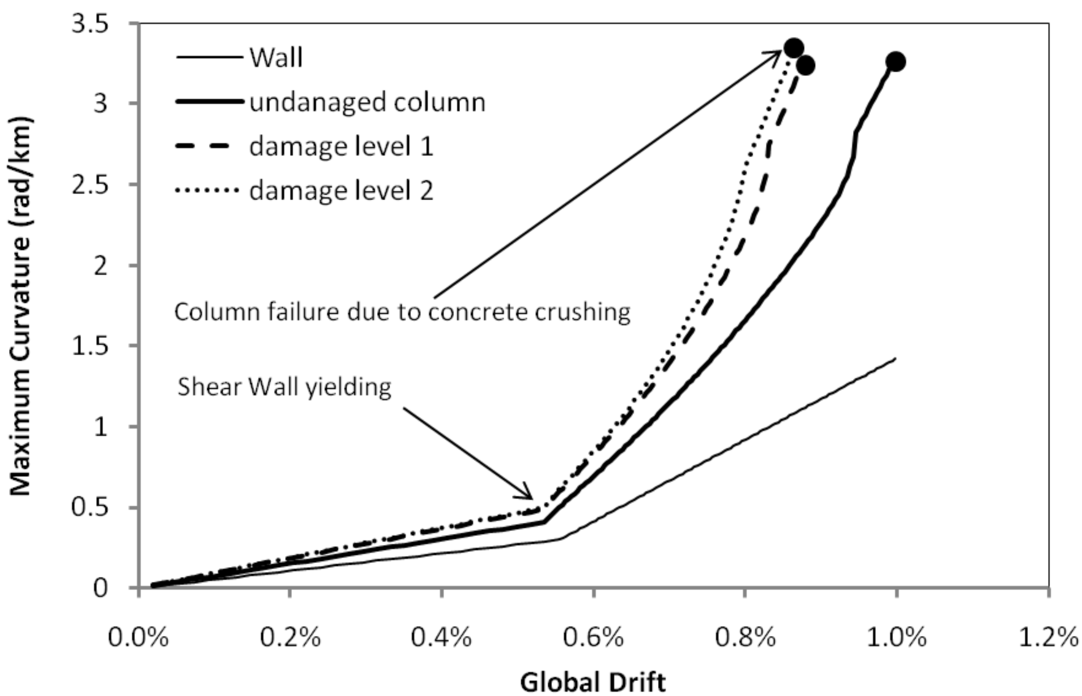

Figure 7.21 Pushover analysis results of the standard column for various damage levels (wall shear strain included).

Figure 7.22 compares wall and column curvature profiles at column failure for various column damage levels. Addition of wall shear strain put a large rotation demand at the base of the column. Despite the bottom part of the column being softer due to damage, shear force in the first storey was always positive which caused column maximum curvature to occur at the base. Curvature profile of the undamaged column was smooth despite the highly concentrated curvatures in the column plastic hinge zone while curvature profiles of the damaged columns experienced a sudden jump at the top of the damaged zone. Again, note that the figures represent the state of the column at different global drift levels (different wall maximum curvatures).

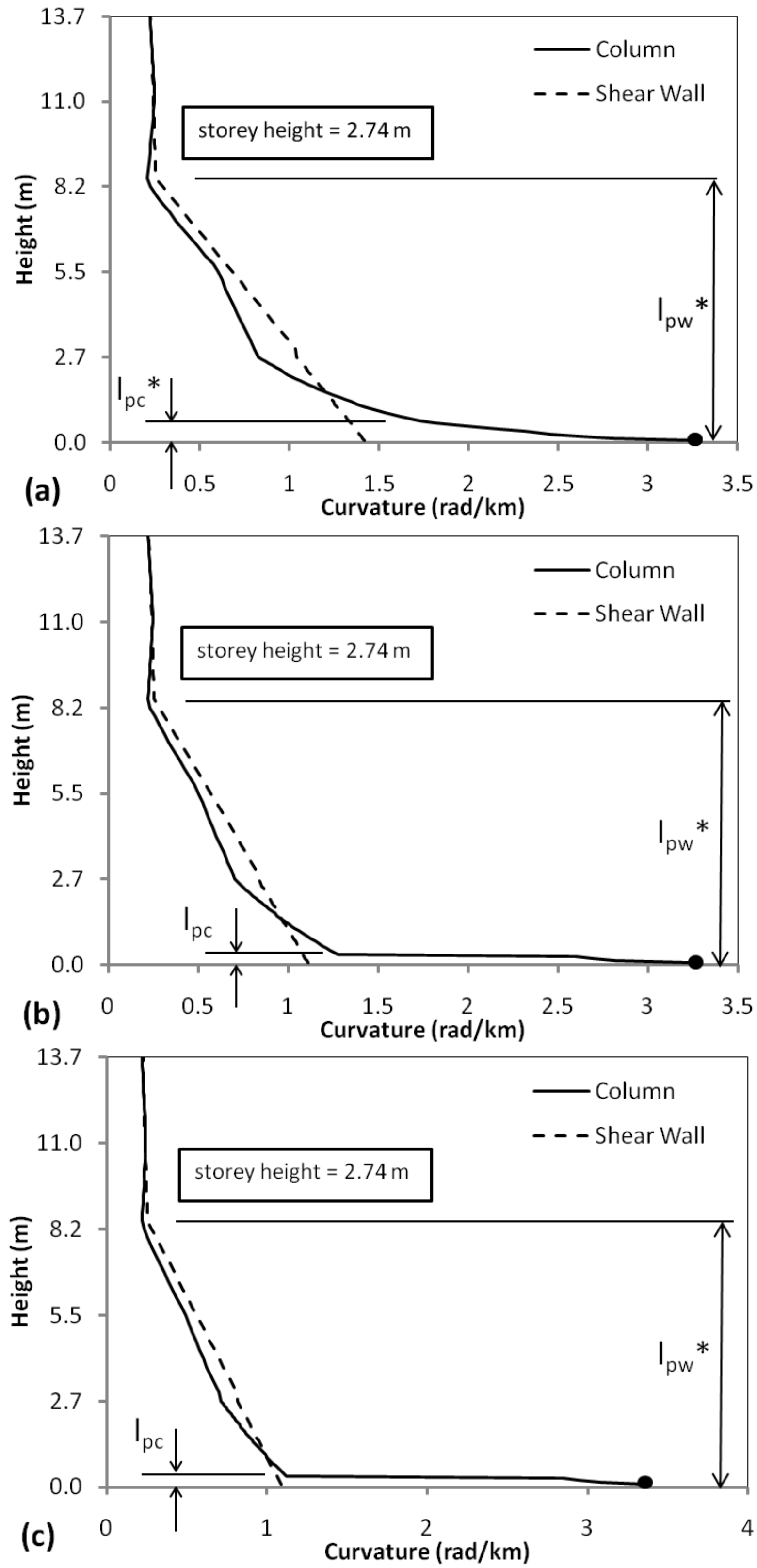

Figure 7.22 Comparison of wall and standard column curvature profiles at column failure: a) undamaged, b) damage level 1, c) damage level 2 (wall shear strain included).

Deformation profiles of the column and the wall in the first storey can give further insight into the effect of damage on column behaviour. Figure 7.4 shows deformation profiles of the undamaged column at failure with and without wall shear strain. Discussion of those results is presented in Section 7.3.

Figure 7.23 compares wall and column deformation profiles at the point of column failure for damage level 1. Results are presented for both cases of no wall shear strain and with wall shear strain included. The global drift at which the column failed is also shown on the charts.

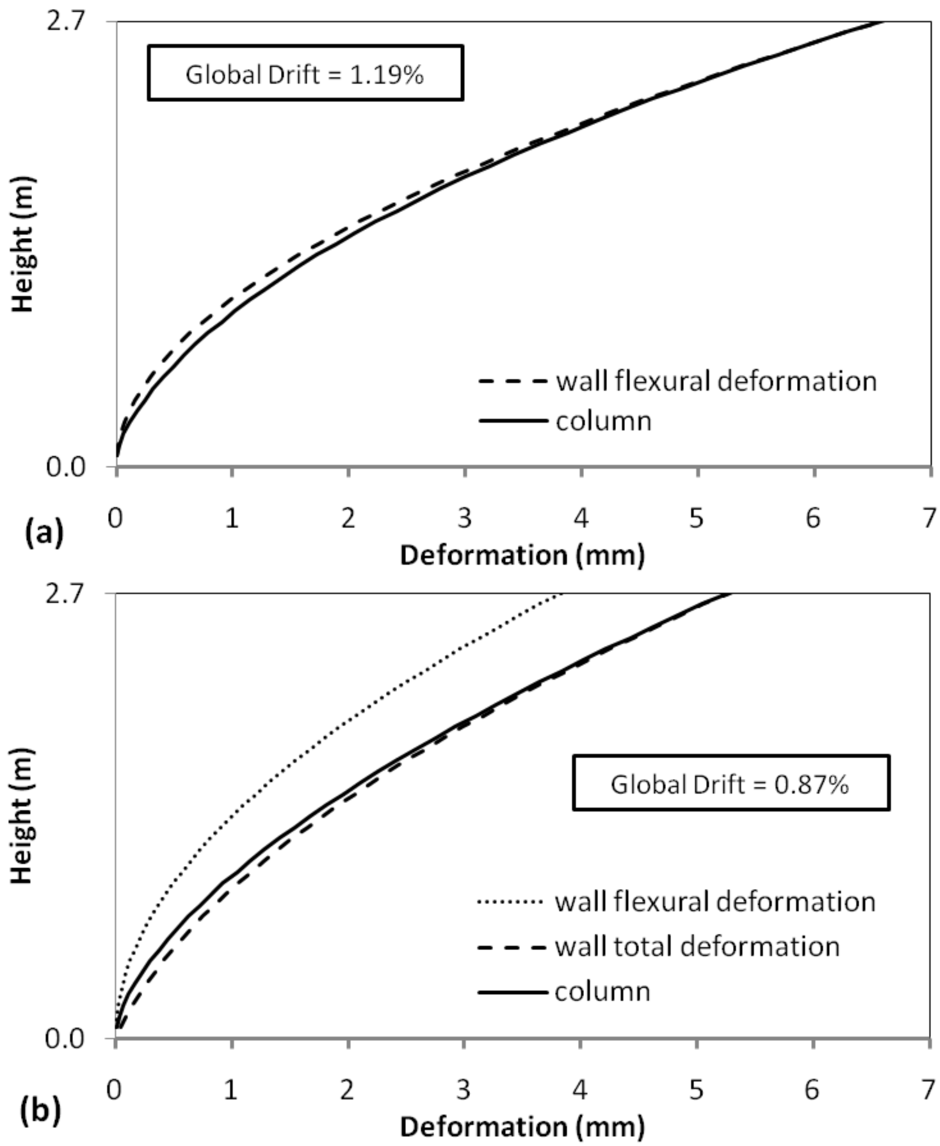

Figure 7.23 Comparison of wall and column deformation profiles at the point of column failure for damage level 1: a) no wall shear strain, b) wall shear strain included.

Comparing Figure 7.4a to Figure 7.23a reveals that damage of the column caused significant concentration of curvature at the base of column which translated into concentrated rotation at the base of the column. This caused deformation profiles of the wall and the column in the first storey to be distinct whereas the two were almost the same in the case of the undamaged column Figure 7.4a.

As mentioned in Section 7.3, wall shear strain demanded extra rotation at the base of the column. Since the column could only deform in flexure, it had to distribute curvature along its height to accommodate the extra rotation demand. In this case, having a softer section at the base of the column helped concentrate curvatures and rotation at the base of the column but since less curvature existed in the undamaged parts of the column in the first storey, column global drift capacity was still less than the case of the undamaged column (compare Figure 7.4b to Figure 7.23b). Analysis results at the point of column failure are summarized in Table 7.5.

Table 7.5 Summary of pushover analysis results demonstrating the effect of damage on column drift capacity: a) no wall shear strain, b) wall shear strain included.

a)

Damage level	Wall Maximum Curvature (rad/km)	Column Maximum Curvature (rad/km)	Global Drift	Normalized Global Drift	Column Maximum Curvature Amplification Factor
no damage	2.76	3.26	1.51%	1.000	1.18
level 1	1.94	3.23	1.19%	0.787	1.66
level 2	1.79	3.38	1.13%	0.749	1.89

b)

Damage level	Wall Maximum Curvature (rad/km)	Column Maximum Curvature (rad/km)	Global Drift	Normalized Global Drift	Column Maximum Curvature Amplification Factor
no damage	1.42	3.28	1.00%	1.000	2.31
level 1	1.11	3.24	0.87%	0.877	2.92
level 2	1.09	3.37	0.87%	0.869	3.09

Since damage of the column section has significant effect on column drift capacity, variation of column drift capacity with height of the damaged zone l_{pc} is studied next. Three values of l_{pc} equal to 0.3, 0.6, and 0.9 m were chosen. The 0.3 m value is the standard value used in previous analysis. Because bar buckling occurs in between two consecutive ties, it was deemed unrealistic to lose the bars at the compression face of the column over a height greater than tie spacing which was assumed to be equal to column section width of 0.3 m. Hence damage was only modeled in the form of loss of concrete cover to the centre of reinforcement over the length l_{pc}.

Figure 7.24 shows the pushover analysis results for the columns with various l_{pc}'s. Note that wall shear strain was included in the analysis. At l_{pc} equal to 0.3 m, drift capacity of the damaged column was less than that of the undamaged column. When l_{pc} was further increased, because the column was able to distribute plastic curvatures over a greater height, more inelastic rotation could be resisted which caused the drift capacity of the damaged column to increase even beyond that of the undamaged column.

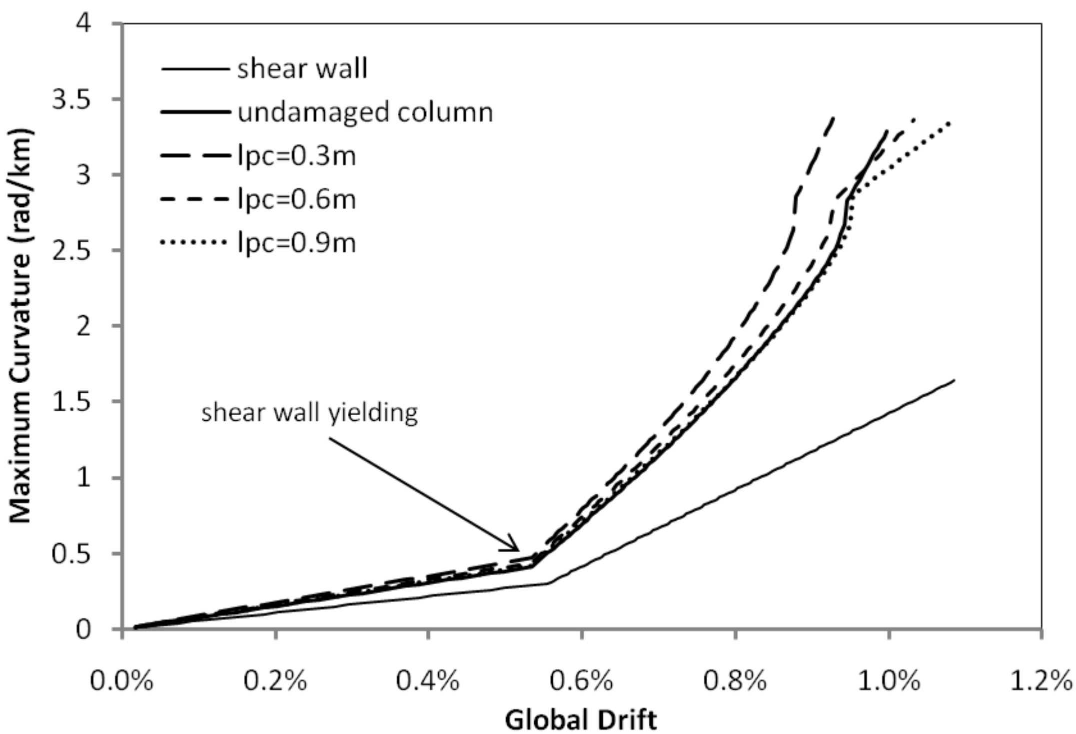

Figure 7.24 Increase in column global drift capacity with l_{pc} in the presence of wall shear strain (damage to the column was modeled as loss of concrete cover to the centre of reinforcement on both faces of the column).

Since the column has to withstand a certain axial load, concrete compression depth of the damaged section will be larger than that of the undamaged section reducing section curvature capacity. However, more inelastic curvature can be concentrated in the damaged zone of the column compared to the undamaged case which will increase column drift capacity.

In conclusion, at small values of l_{pc}, damage to the column always reduced column drift capacity. However, if l_{pc} was large enough, additional inelastic rotation coming from concentration of plastic curvatures in column's damaged zone could even increase column drift capacity especially in the presence of wall shear strain.

7.7.1 Simple methods for estimating curvature demand of damaged columns due to imposed wall deformation in the presence of wall shear strain

It is desirable to derive a simple method for estimating curvature demand of columns accounting for the effect of damage at the base of the column, particularly when significant wall shear strain exists. This can be done by comparing the curvature profiles of the wall and the column (see Figure 7.25).

In a damaged column, inelastic curvatures will be concentrated in the damaged zone close to the base of the column. To satisfy deformation compatibility of the wall-column system, the column's flexural deformation from the inelastic curvature concentrated in the damaged zone must be equal to the wall first storey shear deformation.

$$\Delta_{s1} = \gamma_{avg} \cdot H \cong \gamma_{max} \cdot H = \varphi_s l_{pc} (H - \frac{l_{pc}}{2}) \qquad \textbf{Eq 7.12}$$

Where γ_{avg} is the average wall shear strain in the first storey. Note that if the wall plastic hinge length is several storeys high, γ_{avg} can be conservatively approximated by γ_{max}. Rearranging gives

$$\varphi_s = \frac{\gamma_{max} \cdot H}{l_{pc}(H - \frac{l_{pc}}{2})} \cong \frac{\gamma_{max}}{l_{pc}} \qquad \textbf{Eq 7.13}$$

If actual wall maximum curvature is added to φ_s from Eq 7.13, column curvature demand will be estimated as shown by Apporx. 1 in Figure 7.26. The accuracy of the prediction confirms that the concept behind derivation of Eq 7.13 is correct.

Eq 7.13 is very similar to Eq 7.9 with l_{pc}^* replaced by l_{pc}. Hence, if wall maximum shear strain is to be estimated from the shear strain model presented in Section 2.9, the total column curvature demand can be obtained similar to Eq 7.11 but with replacing l_{pc}^* with l_{pc} as follows.

$$\varphi_d = \varphi_{max} + \varphi_s = \varphi_{max}\left[1 + 0.3\frac{(l_w - 2c)}{l_{pc}}\right] \quad \textbf{Eq 7.14}$$

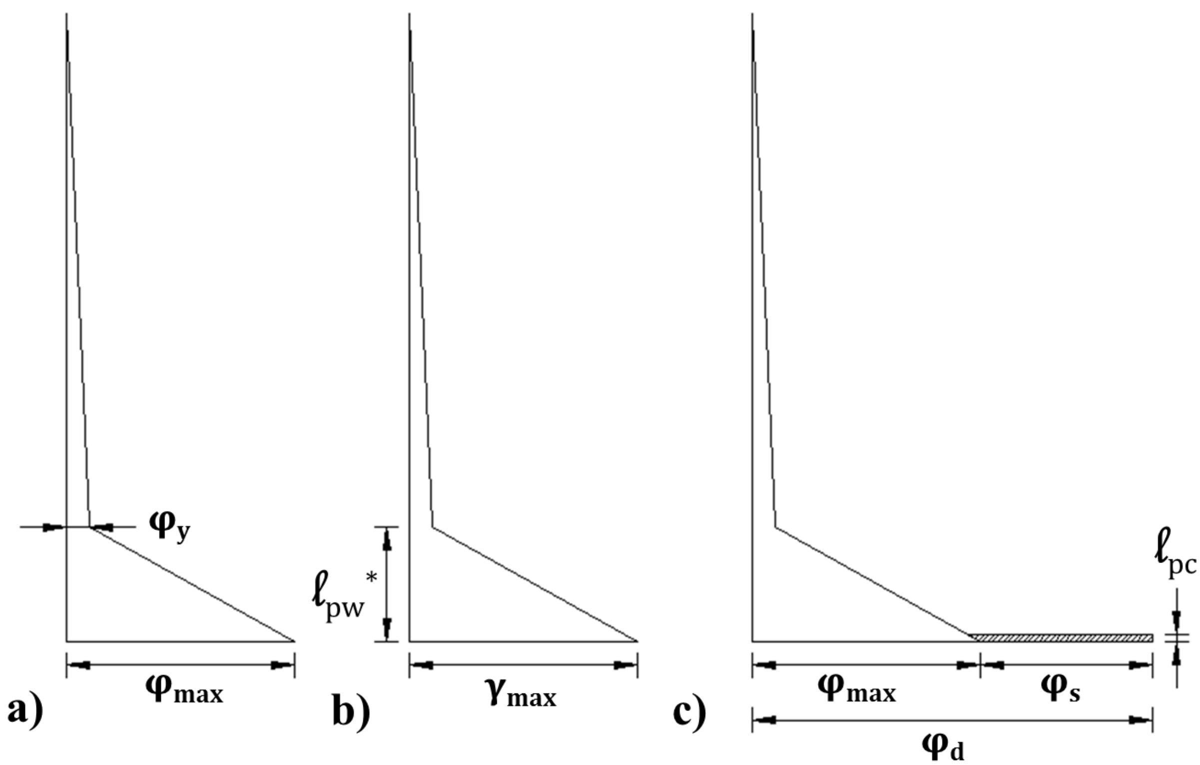

Figure 7.25 Schematics of a) curvature profile of the shear wall, b) shear strain profile of the shear wall, and c) curvature profile of the damaged gravity-load column

The line labelled Approx. 2 in Figure 7.26 is obtained using the ultimate wall concrete compression depth in Eq 7.14 which results in overestimating of wall maximum shear strain and consequently overestimation of column curvature demand. If wall concrete compression depth is calculated from section analysis at every wall maximum curvature, Approx. 3 will result which is less conservative as expected.

Either of approximations 2 and 3 seems to grossly overestimate curvature demand of a damaged column. This deficiency is because the wall maximum shear strain was used instead of the wall average shear strain in the first storey. The accuracy of the prediction can be improved if the wall average curvature over the first storey height is used to estimate wall shear strain from the model presented in Section 2.9 instead of the wall maximum curvature used here.

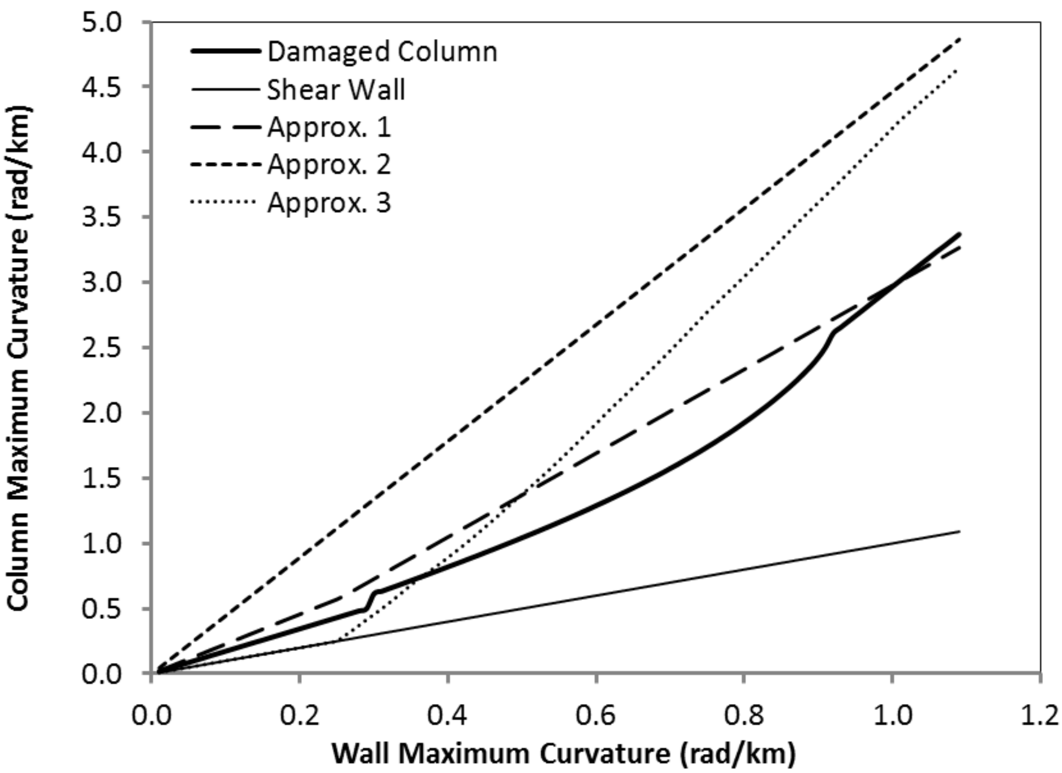

Figure 7.26 Estimating curvature demand of the damaged column from wall maximum curvature in the presence of wall shear strain.

7.8 Taller First Storey

It is common to design high-rise concrete buildings that have a taller first or first few storeys. The taller storey(s) at the base usually functions as a shopping mall, mezzanine, lobby, or a ballroom and hence requires a higher ceiling than typical floors. In this type of construction, the first floor can be as high as 5 times a typical storey height. The column not being tied closely to the wall at the base by floor slabs can relax the constraints on column deformation profile; hence, a different flexural deformation profile can be expected of the column.

To investigate the consequences of eliminating the first few floor slabs connecting the column to the wall, the standard wall and column section were considered with the first floor height being 1, 2, 3, 4, and 5 times the typical. This meant that the first storey height was 2.7, 5.5, 8.2, 11.0, and 13.7 m respectively. Height of column plastic curvature zone was kept constant for all cases. To investigate the effect of damage of the column in addition to the influence of having a taller first storey, analysis were also carried out for damage level 1. Refer to Section 5.4 for definition of various levels of damage and a discussion on how damage to the section affected moment-curvature response of the column. Analysis was done both including and excluding wall shear deformation since wall shear strain was proved to have significant effect on column maximum curvature demand.

Figure 7.27 shows pushover curves for the undamaged column with various first storey heights for the case where no wall shear strain was included. As the first storey height increased from 2.7 to 8.2 m, global drift capacity decreased. Since the wall deformation profile was purely flexural, connecting the column to the wall at closely spaced floor slabs enabled the wall to bend the column more gradually such that the column could distribute curvature over the bottom 8.2 m of its height. When the first floor height was 8.2 m or in other words the second and third floor slabs were eliminated, bending moment diagram of the column had to be linear in the bottom 8.2 m forcing significant curvature concentration at the base of the column which reduced column global drift capacity.

The complete opposite trend was observed when column first storey height was increased beyond 8.2 m where column global drift capacity increased with first storey height. This can be explained bearing in mind that wall plastic hinge length was 8.2 m. In general, column maximum curvature demand is highly sensitive to the target deformation value at first floor level which puts a certain rotation demand on the column. When column first storey height increased beyond wall plastic hinge length, because wall curvatures were elastic above the plastic hinge length, little rotation demand was added to the column while the taller first storey height of the column enabled it to distribute curvature more evenly throughout its height. This resulted in less concentration of curvature at the base of the column and hence higher global drift capacity.

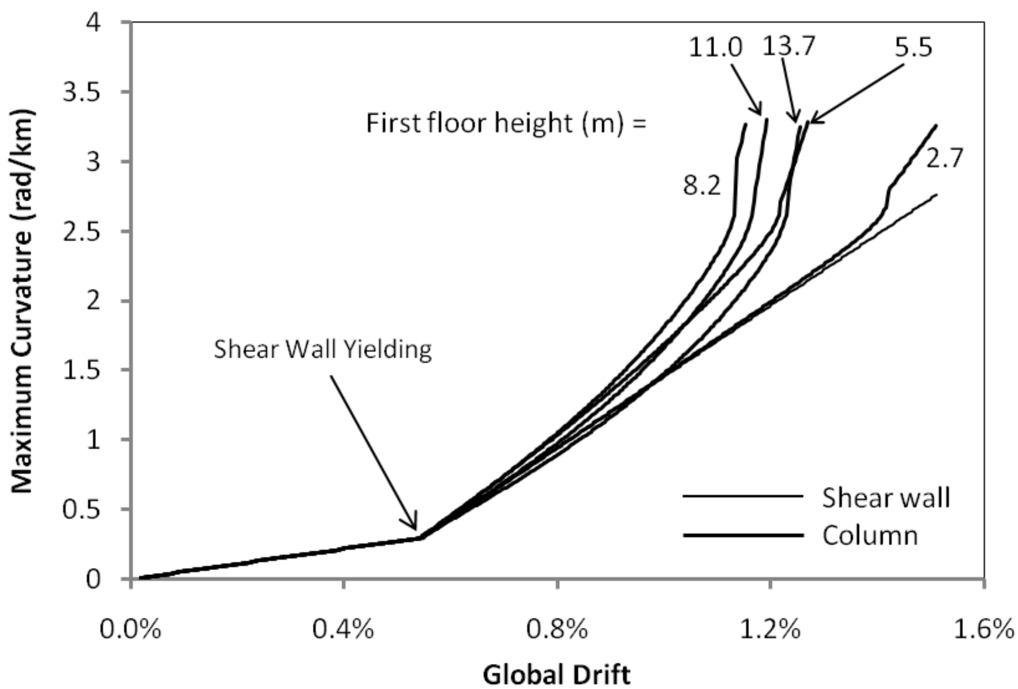

Figure 7.27 Pushover analysis results for columns with various first storey heights (no wall shear strain, no damage of the column).

Figure 7.28 compares the wall curvature profile to that of the columns with various first storey heights at the point of column failure. Note how the difference in maximum curvatures of the wall and the column is related to global drift capacity. Pushover analysis results can be further explained by looking at the shape of column deformation profiles at failure. All column deformation profiles were normalized to give a unit deformation at 13.7 m above the base (see Figure 7.29a). From Figure 7.29c it is clear how column drift capacity is tied to the rotation demand at the base of the column. Higher rotation at the base resulted in decreases drift capacity.

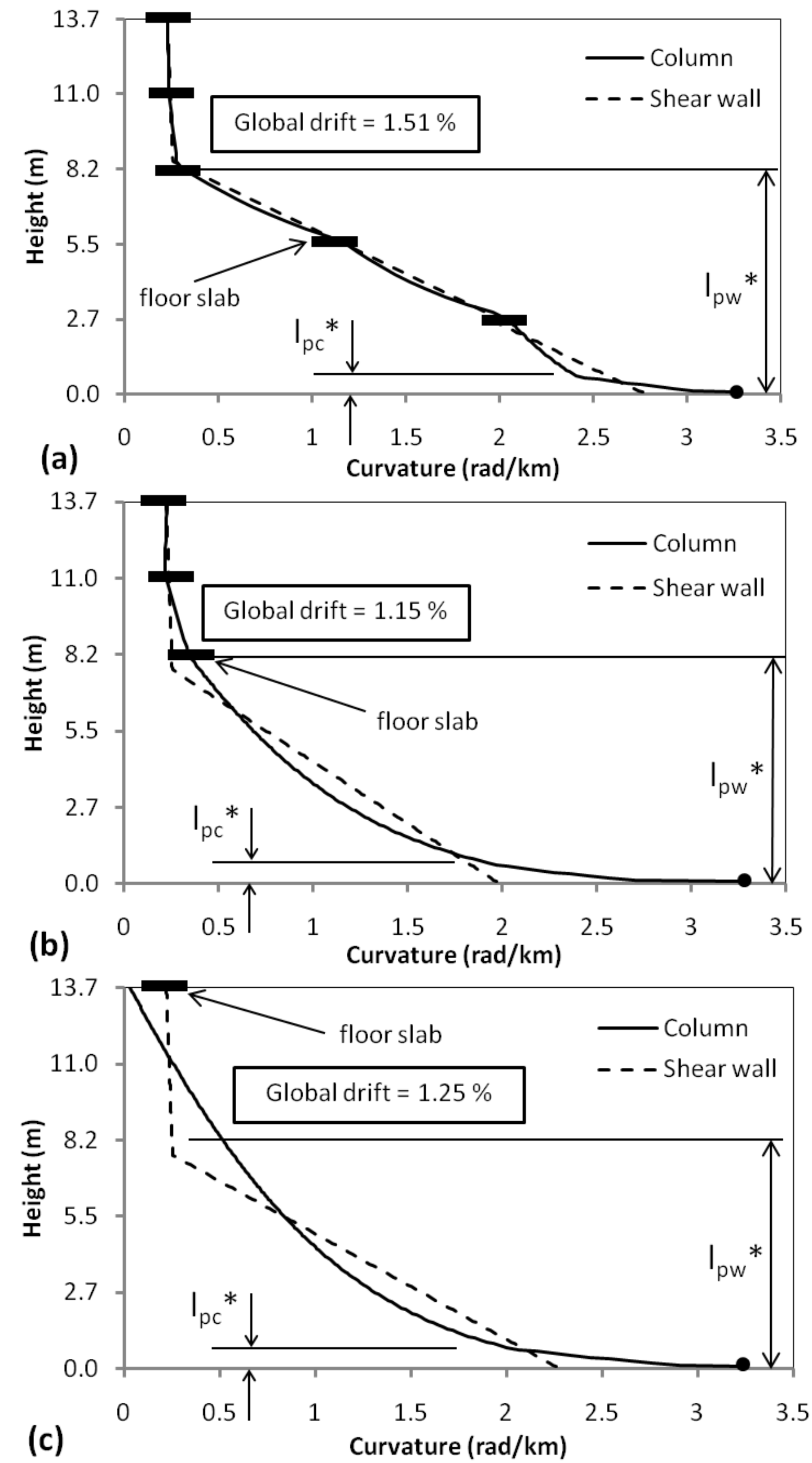

Figure 7.28 Comparison of wall and column curvatures at failure for various column first storey heights of: a) 2.7 m, b) 8.2 m, c) 13.7 m (no wall shear strain, no damage of the column).

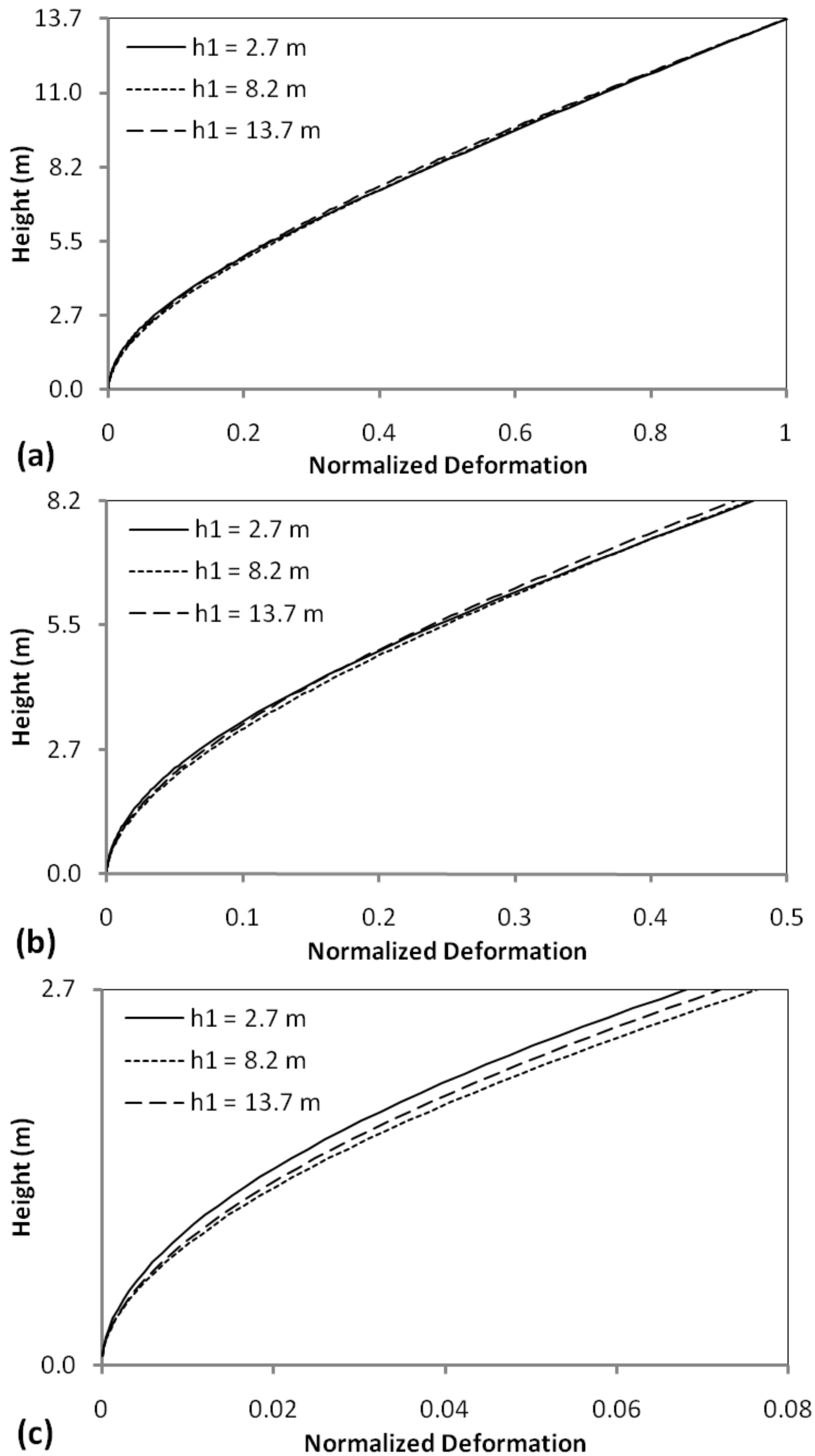

Figure 7.29 Comparison of shape of column deformation profiles at failure for various first storey heights of: a) 2.7 m, b) 8.2 m, c) 13.7 m (no wall shear strain, no damage of the column).

A similar trend was observed when column damage was modeled. However, the variation in column drift capacity with first storey height was relatively smaller. This was because having a softer section at the base of the column enabled the column to better resist curvature concentration at the base.

Table 7.6 shows a summary of pushover analysis results at column failure for both cases of undamaged and damaged column. Although damage of the column generally reduced column drift capacity, the drops in drift capacity relative to the standard case of uniform storey height of 2.7 m was less when column damaged was modeled.

Table 7.6 Summary of pushover analysis results for columns with various first storey heights at failure for: a) undamaged column, b) damaged column (no wall shear strain).

a)

First Storey Height (m)	Wall Maximum Curvature (rad/km)	Column Maximum Curvature (rad/km)	Global Drift	Normalized Global Drift
2.7	2.76	3.26	1.51%	1.000
5.5	2.30	3.29	1.27%	0.841
8.3	1.97	3.27	1.15%	0.763
11.0	2.09	3.31	1.19%	0.790
13.7	2.26	3.25	1.25%	0.831

b)

First Storey Height (m)	Wall Maximum Curvature (rad/km)	Column Maximum Curvature (rad/km)	Global Drift	Normalized Global Drift
2.7	1.94	3.23	1.19%	1.000
5.5	1.61	3.24	1.02%	0.858
8.3	1.47	3.23	0.97%	0.814
11.0	1.53	3.24	0.99%	0.833
13.7	1.63	3.27	1.03%	0.863

A rather different behaviour was seen when wall shear strain was included in the wall deformation profile. In the presence of wall shear strain, global drift capacity of the column kept increasing with first storey height as shown in Figure 7.30.

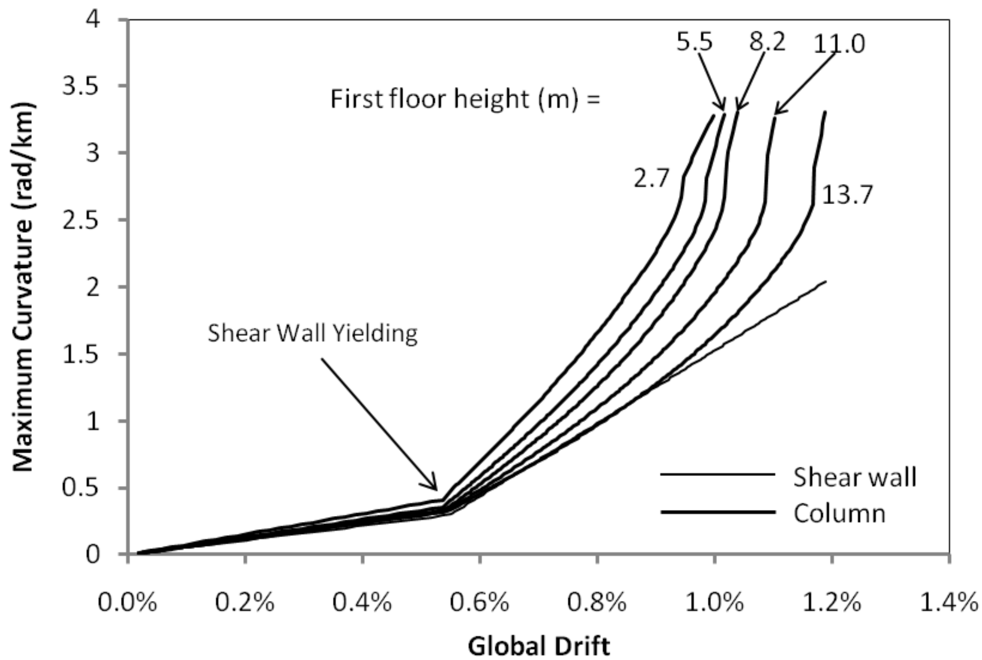

Figure 7.30 Pushover analysis results for columns with various first storey heights (wall shear strain included, no damage of the column).

In the presence of wall shear strain, the column could still only deform in flexure and had to meet target displacement values at floor levels by distributing curvature over its height. Addition of wall shear strain put an extra rotation demand at the base of the column as discussed in detail in Section 7.3. As column first storey height became larger or in other words as floor slabs were eliminated, the column had the freedom to distribute curvature more evenly throughout a taller height which resulted in less curvature concentration at the base and consequently higher drift capacity.

Figure 7.31 compares wall and column curvature profiles at the point of column failure. It is clearly seen how eliminating the lower floor slabs that connect the wall to the column relaxed the constraints on column deformation profile and allowed for a better curvature distribution over the height of the column.

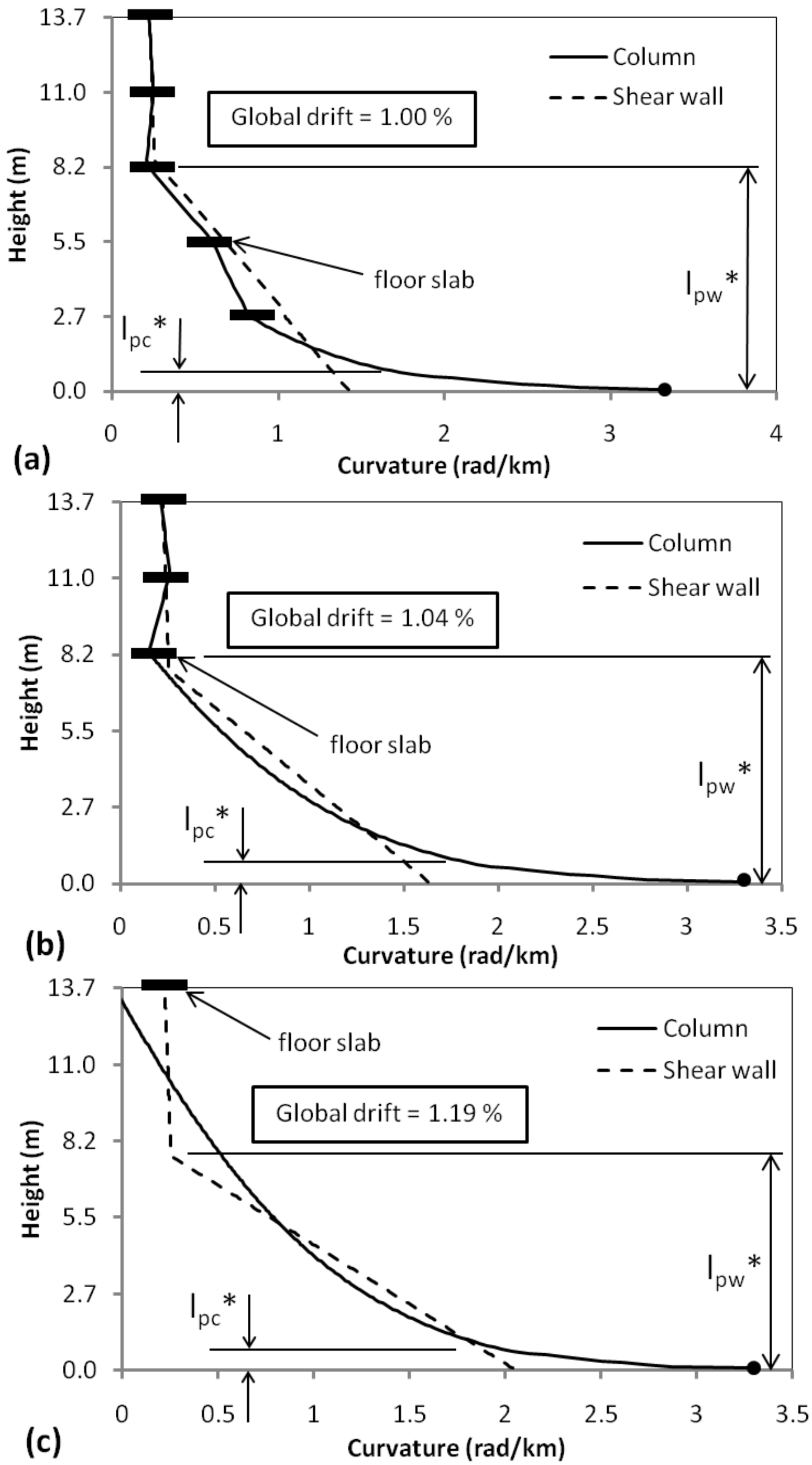

Figure 7.31 Comparison of wall and undamaged column curvature profiles at failure for various column first storey heights of: a) 2.7 m, b) 8.2 m, c) 13.7 m (no wall shear strain).

Again, a similar trend was observed when column damage was modeled. Similar to the case with no wall shear strain, the variation in column drift capacity with first storey height was relatively smaller than that for the undamaged column.

Table 7.7 shows a summary of pushover analysis results at column failure for both cases of undamaged and damaged column when wall shear strain was included. Although damage of the column generally reduced column drift capacity, the increase in drift capacity relative to the standard case of uniform storey height of 2.7 m was less when column damaged was modeled.

Table 7.7 Summary of pushover analysis results for columns with various first storey heights at failure for: a) undamaged column, b) damaged column (wall shear strain included).

a)

First Storey Height (m)	Wall Maximum Curvature (rad/km)	Column Maximum Curvature (rad/km)	Global Drift	Normalized Global Drift
2.7	1.42	3.28	1.00%	1.000
5.5	1.57	3.29	1.02%	1.018
8.3	1.63	3.31	1.04%	1.040
11.0	1.80	3.27	1.10%	1.104
13.7	2.04	3.30	1.19%	1.191

b)

First Storey Height (m)	Wall Maximum Curvature (rad/km)	Column Maximum Curvature (rad/km)	Global Drift	Normalized Global Drift
2.7	1.11	3.24	0.87%	1.000
5.5	1.18	3.22	0.87%	0.997
8.3	1.21	3.22	0.88%	1.011
11.0	1.34	3.21	0.93%	1.064
13.7	1.46	3.23	0.98%	1.115

7.9 Fixity of the Column at the Base

In the analysis results presented so far in this chapter, the column was assumed to be fully fixed against rotation at the base. Although this is an ideal assumption and the zero rotation condition at the base of the column does not exist in the real world, the model is a good representation of the case when the gravity-load column rests on very long basement walls (Figure 7.32).

On the other hand, not all columns rest on shear walls. In buildings with basement levels, gravity-load columns usually continue below grade all the way to the foundation level. Basement storeys are surrounded by perimeter earth retaining walls. These walls make the entire basement storeys act like a solid box due to their high in-plane stiffness allowing basement floor slabs to have very little lateral deformation. If no beams run in between the columns and the floors are flat concrete slabs, they do not offer considerable resistance against column rotation; hence, out-of-plane rotational rigidity of the slabs can be neglected. In such a building, having the column pinned at floor levels below the grade with no lateral deformation at the pin levels would be a good analytical model for column boundary conditions below grade (Figure 7.33).

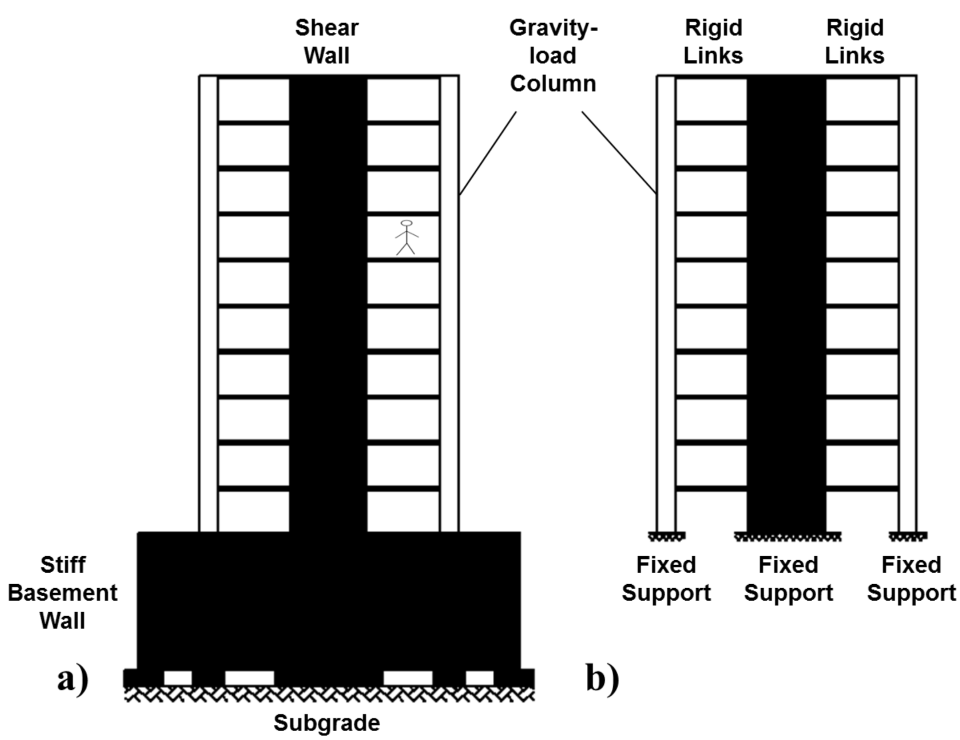

Figure 7.32 Column resting on a stiff basement walls: a) real structure, b) idealization.

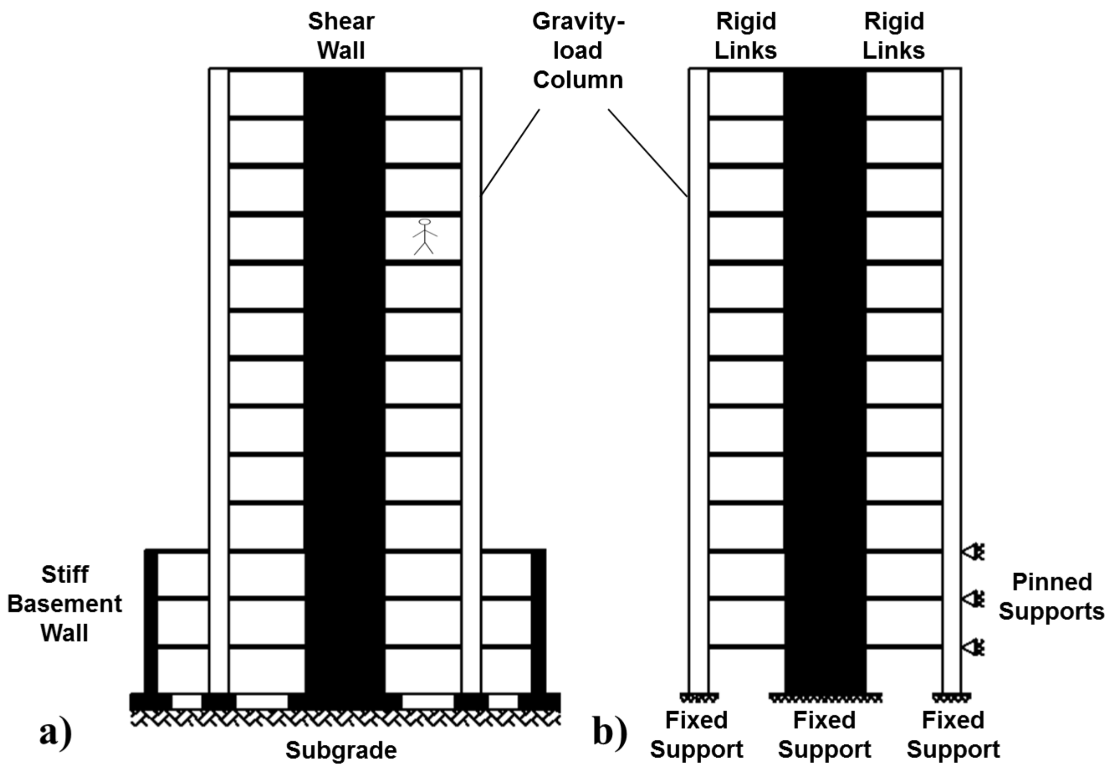

Figure 7.33 Column continuing below grade: a) real structure, b) idealization.

The two cases presented in the figures above are the extremes in terms of column boundary condition below grade level. In the presence of floor beams or slab bands, rotational rigidity of the members framing into the column at floor levels should be taken into account (see Section 7.11). However, comparing column behaviour in these two extreme cases will result in a better understanding of the importance of modelling the correct column boundary conditions.

The same nonlinear structural analysis procedure used for columns fixed at the base can still be applied to columns with basement levels. The desired number of floors is added with the corresponding target displacement values set at zero at basement floor slabs.

The first step is to determine how column global drift capacity is affected by the number of floors below the grade considered similar to the analysis carried out in Section 6.9. The standard column described in Section 7.2 was modeled with 0, 1, 2, 3, 4, and 5 levels below grade and pushed to failure. Summary of results is shown in Figure 7.34.

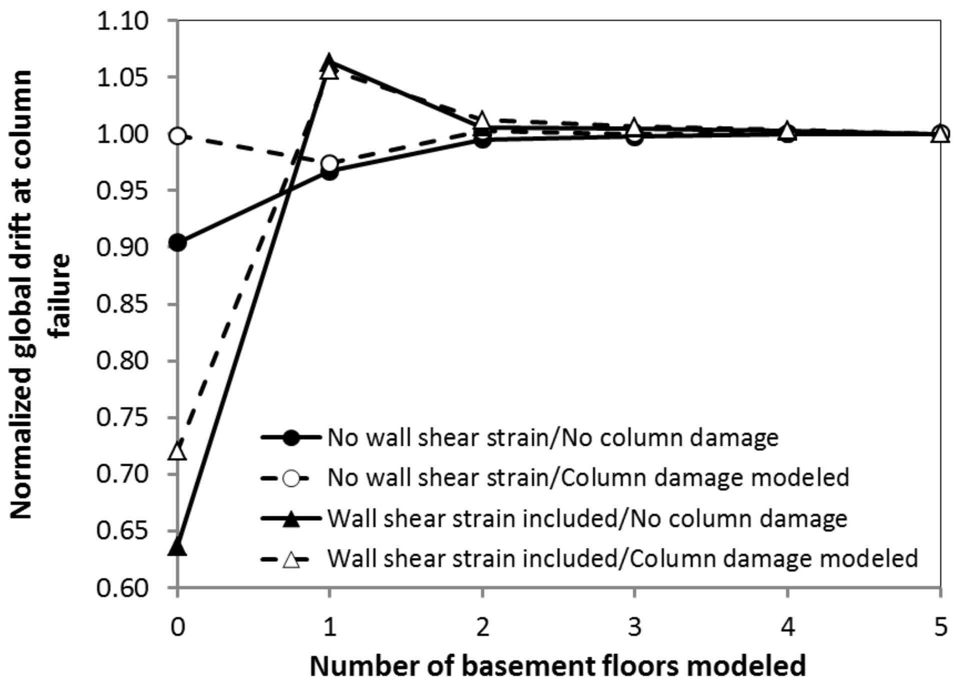

Figure 7.34 Effect of number of basement floors on column drift capacity.

Four cases were studied. Two settings for wall shear strain (with and without including shear strain in wall deformation profile) were used and the analysis was done with and without modeling damage of the column. According to Figure 7.34, when the number of modeled basement floors increased beyond three, the change in column drift capacity was insignificant. It is then concluded that even if the building has more than three basement levels, modeling three floors below grade will give an accurate estimate of the column global drift capacity.

When no shear strain was included in the wall deformation profile, modeling basement floors increased column drift capacity by less than 10% while when shear strain was added to wall flexural deformations, an additional 50% drift capacity was achieved. As mentioned earlier in this chapter, wall shear strain creates an additional rotation demand at the base of a column fixed at the grade level. When the column continued below grade, a significant part of the additional rotation demand due to wall shear strain was cancelled out by rotation of the column at grade level in the same direction. This enabled the column to exhibit the target displacement profile without needing to bend excessively at the grade level which resulted in additional drift capacity.

Figure 7.35 shows slope and deformation profiles of the standard column at failure when five floors below grade level were modeled. The column merely bends below the third basement level but has a rotation of more than 0.001 rad at the grade level. The deformation profiles shows how the column was sleeved against displacement at floor levels below grade due to presence of basement walls but was free to rotate.

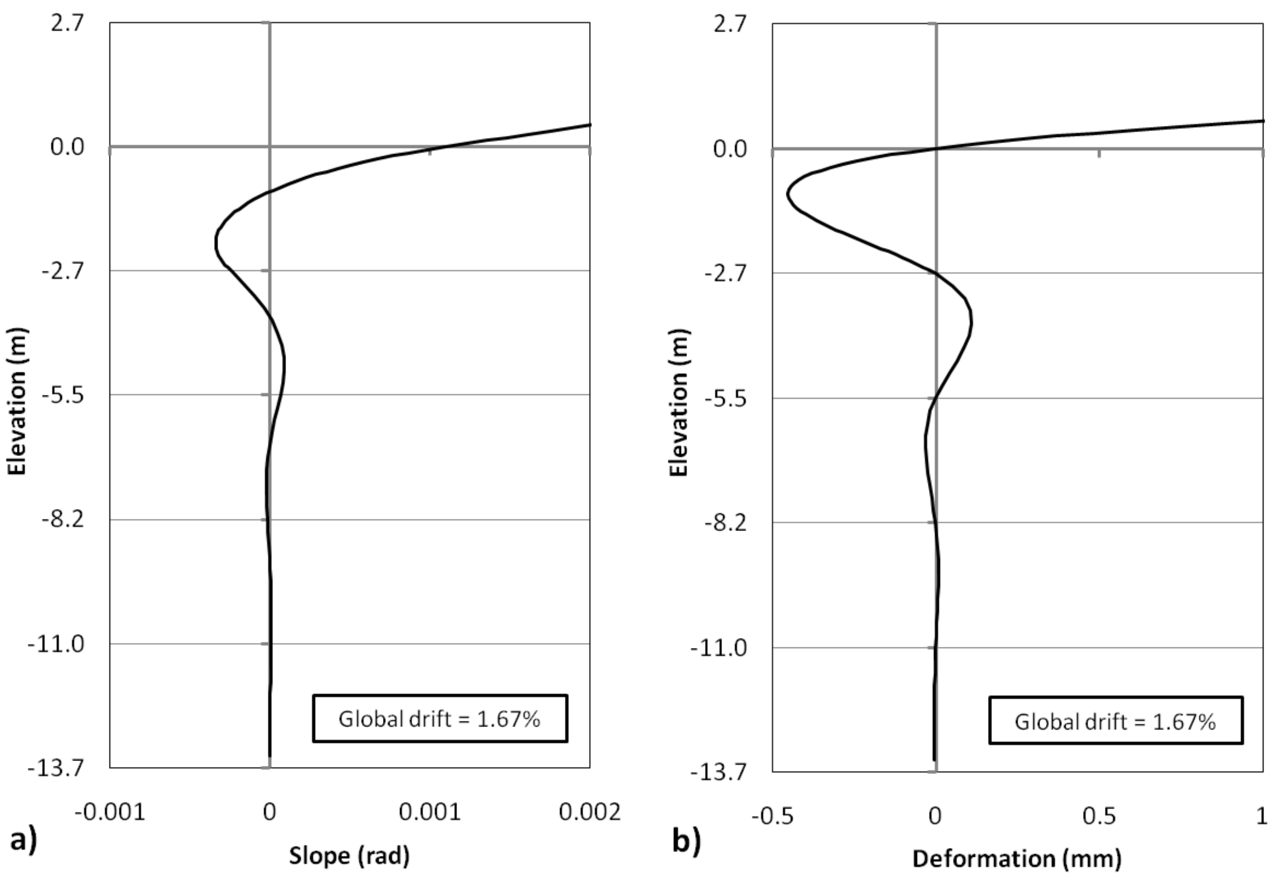

Figure 7.35 a) slope, and b) deformation profiles of the undamaged column with five basement floors at failure (no wall shear strain).

To study the effect of column fixity at grade level, the four cases with the column continuing three floors below the grade were examined in more detail. Pushover analysis results for the undamaged and damaged columns when no wall shear strain was included are shown in Figure 7.36. It was shown in the previous sections of this chapter that for a column fixed at the base, maximum curvatures of the undamaged column and that of the wall were identical along a great part of the pushover curve. Column maximum curvature demand was higher than wall maximum curvature at the point of column failure. When three basement levels were added, column maximum curvature demand dropped to be even less than wall maximum curvature for the majority of the curve and nearly equal to wall maximum curvature at column failure. In comparison to the fixed-base column, adding three basement levels increased column drift capacity from 1.51% to 1.67%. Drift capacity of the damaged column however did not increase after adding three basement levels which can be best explained by looking at curvature profiles of the column and the wall at the point of column failure (Figure 7.37).

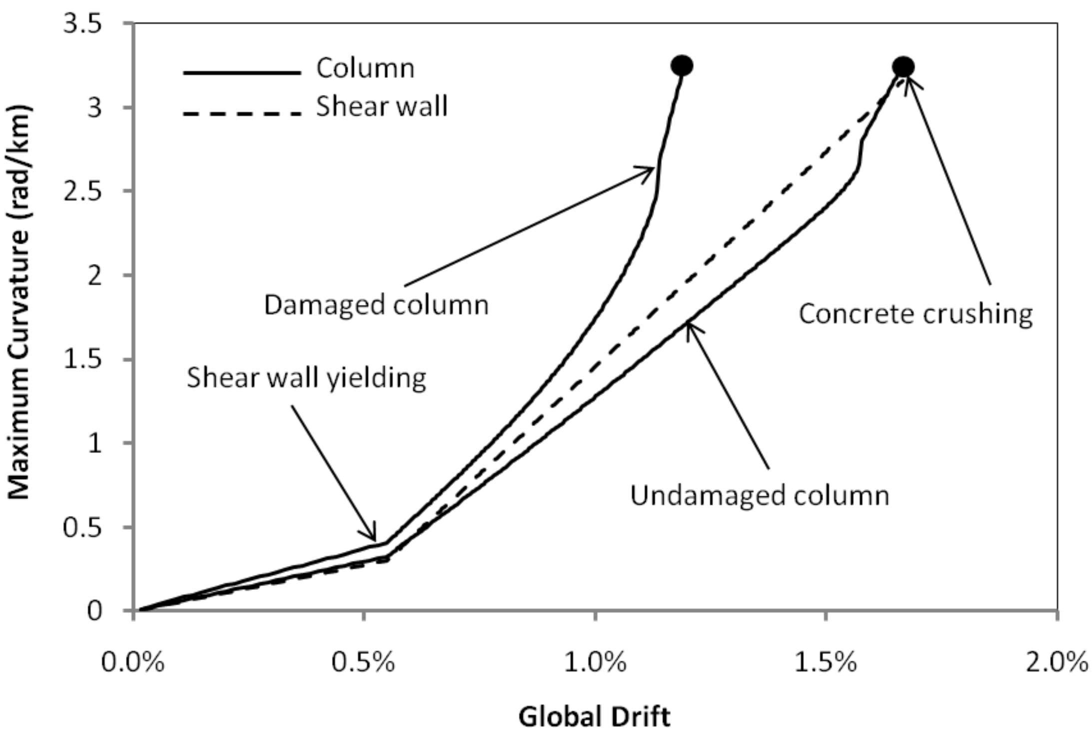

Figure 7.36 Pushover analysis results for the standard column continuing 3 levels below grade (no wall shear strain).

It is striking to see that column maximum curvature occurs at the top of the first storey and not at the grade level. Since wall shear strain was excluded from the analysis, deformation profile of the wall was purely flexural. Flexural deformations result from integrating curvatures along the height of the wall and need more height to develop significant drifts than shear deformation. This causes the deformation at the first floor level to be much less than that of the second floor and the levels above. With the column being free to rotate at the grade level, the column could accommodate the target displacement at first floor level without bending severely. But since the target deformation at the second floor level was considerably larger, the column was forced to concentrate inelastic curvatures on either side of the second floor slab to meet the target deformation profile of the wall. Because of this, the column plastic curvature model presented in Section 6.3 needed to be applied on both sides of the maximum column curvature location with the same assumptions on column plastic curvature distribution.

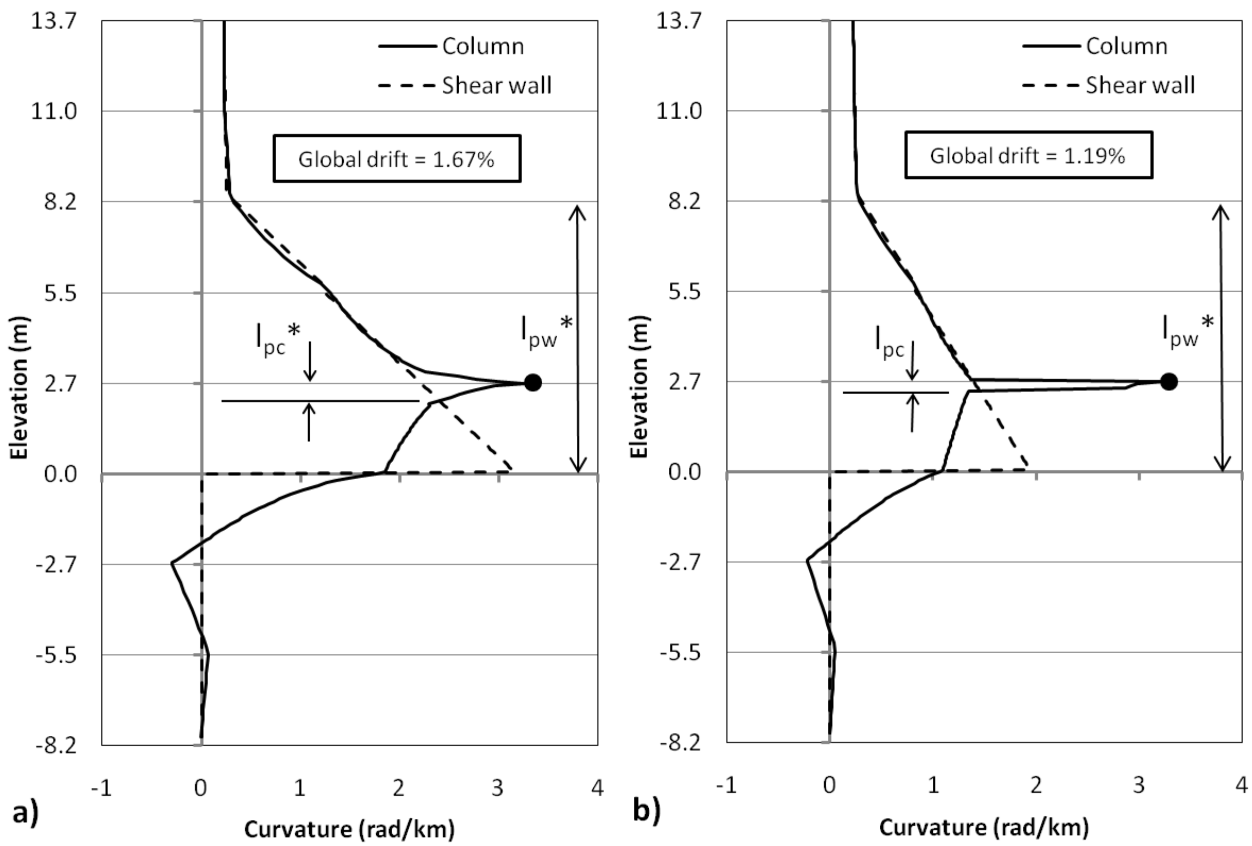

Figure 7.37 Curvature profiles of the standard column with 3 basement levels at failure: a) undamaged column, b) damaged column (no wall shear strain).

Having the maximum column curvature at the top of the first storey as opposed to the column plastic hinge being at the grade level in the case of the fixed-base column resulted in less contribution from column plastic curvatures to global drift capacity. This negative effect was balanced by the additional drift capacity gained from column being able to rotate at grade level.

Figure 7.38 shows pushover analysis results for the column with three basement levels when wall shear strain was included in the wall deformation profile. In the case of the undamaged column, maximum curvature demand was less than wall maximum curvature over a large part of the curve and increased to be greater than wall maximum curvature only when the column experienced highly nonlinear behaviour. In comparison to the case with the same column fixed at the base where column maximum curvature demand was always greater than wall maximum curvature, addition of three basement floors increased column drift capacity from 1.00% to 1.51%. Wall shear strain increased the deformation at first floor level by a significant percentage which put a high rotation demand at the base of the column fixed at grade level. With the addition of basement, the column was allowed to rotate at grade level allowing the column to tolerate the rotation demand from wall shear strain without the need to bend excessively.

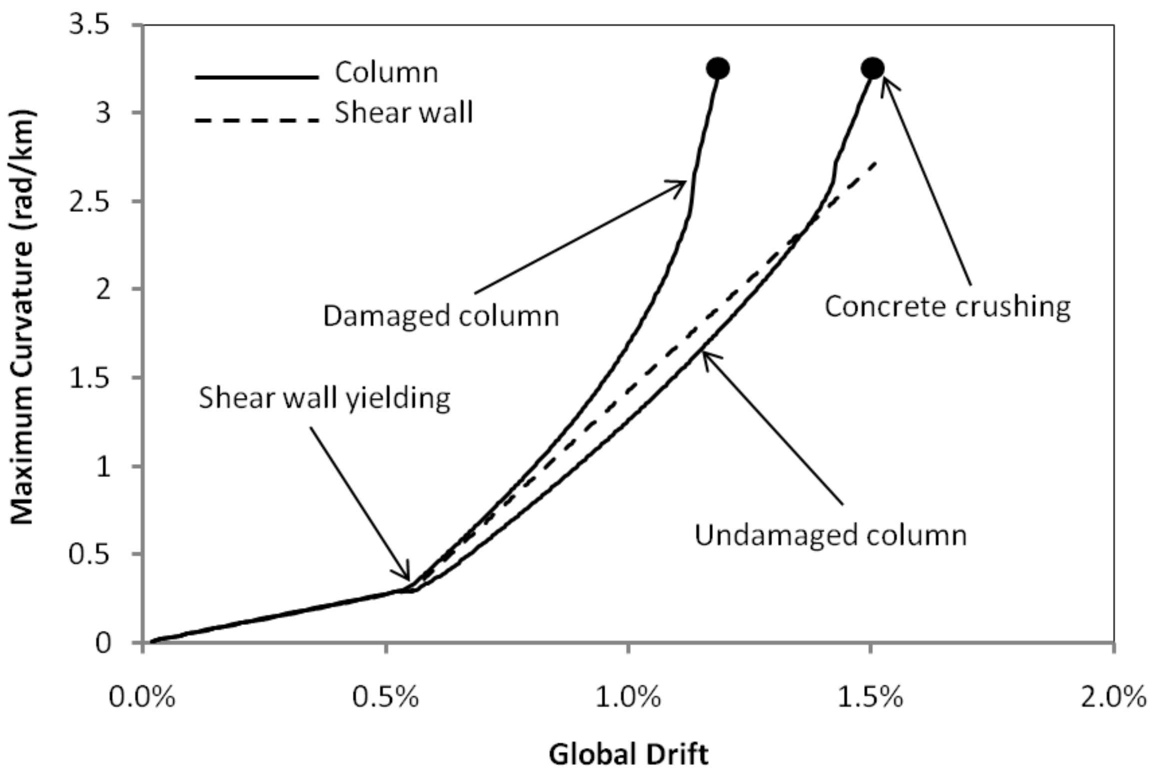

Figure 7.38 Pushover analysis results for the standard column continuing 3 levels below grade (wall shear strain included).

As for the damaged column, maximum curvature demand was consistently greater than wall maximum curvature but the difference between the two was much less than the case of the fixed-base column. Drift capacity of the damaged column increased from 0.87% to 1.19% when three basement floors were added. The observed behaviour can be explained by comparing column and wall curvature profiles at the point of column failure (Figure 7.39).

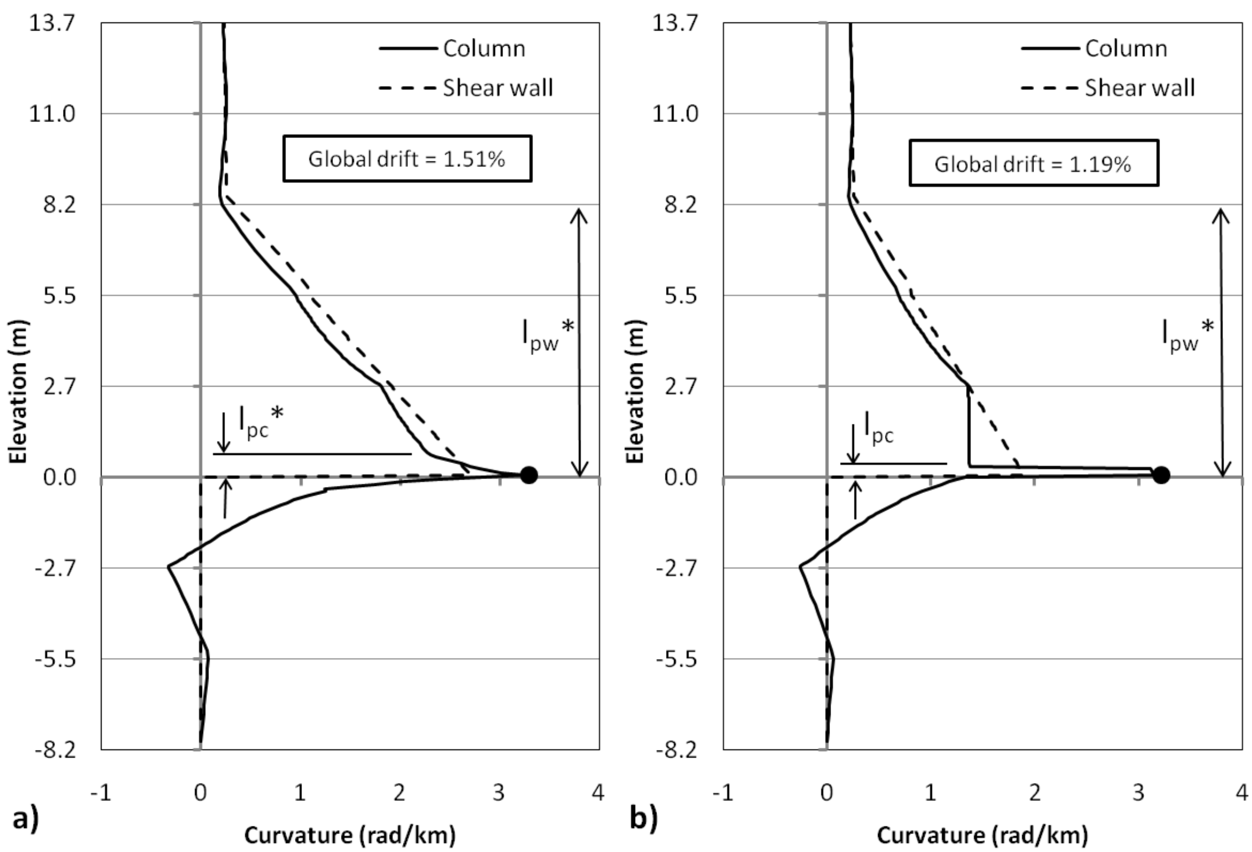

Figure 7.39 Curvature profiles of the standard column with 3 basement levels at failure: a) undamaged column, b) damaged column (wall shear strain included).

Unlike the cases where no wall shear strain was included in the wall deformation profile, in the presence of wall shear strain, column maximum curvature occurred at the grade level similar to all cases with a fixed-base column. This means the global drift resulting from column plastic curvatures were similar to the cases of the columns with and without basement floors while having the column free to rotate at the grade level increased column drift capacity.

Table 7.8 summarizes column drift capacities for the entire parametric study carried out on the fixed-base standard column. Note that highlighted cells represent the standard case.

Table 7.8 Summary of global drift capacity of the fixed-base standard column.

Parameter		No shear strain		With shear strain	
		Undamaged	Damaged	Undamaged	Damaged
Column Length (m)	0.6	3.66%	2.57%	2.15%	1.83%
	0.9	2.69%	1.86%	1.61%	1.38%
	1.2	2.18%	1.47%	1.34%	1.06%
	1.8	1.51%	1.19%	1.00%	0.87%
	2.4	1.11%	0.79%	0.72%	0.57%
lpw* (m)	7.8	1.45%	1.14%	0.95%	0.85%
	8.2	1.51%	1.19%	1.00%	0.87%
	9.4	1.63%	1.25%	1.07%	0.93%
	10.9	1.81%	1.37%	1.15%	1.00%
	12.5	2.00%	1.48%	1.29%	1.08%
lpc* (mm)	305	1.47%	1.09%	0.97%	0.82%
	610	1.51%	1.19%	1.00%	0.87%
	1220	1.57%	1.28%	1.03%	1.02%
% of wall shear strain applied	0	1.51%	1.19%	-----	-----
	25	-----	-----	1.32%	1.09%
	50	-----	-----	1.18%	1.00%
	75	-----	-----	1.06%	0.94%
	100	-----	-----	1.00%	0.87%
Damage level	0	1.51%	-----	1.00%	-----
	1	-----	1.19%	-----	0.87%
	2	-----	1.13%	-----	0.87%
First Floor Height (m)	2.7	1.51%	1.19%	1.00%	0.87%
	5.5	1.27%	1.02%	1.02%	0.87%
	8.3	1.15%	0.97%	1.04%	0.88%
	11.0	1.19%	0.99%	1.10%	0.93%
	13.7	1.25%	1.03%	1.19%	0.98%

The entire parametric study that was done on the fixed-base standard column was repeated for the case where the column had 3 basement floors. Drift capacities of the standard column with three basement levels are summarized in Table 7.9. Again, the highlighted cells represent the standard case and hence have the same numeric value.

Table 7.9 Summary of global drift capacity of the standard column with three basements

Parameter		No shear strain		With shear strain	
		Undamaged	Damaged	Undamaged	Damaged
Column Length (m)	0.6	4.23%	2.00%	3.68%	2.02%
	0.9	2.96%	1.72%	2.58%	1.69%
	1.2	2.32%	1.48%	2.05%	1.41%
	1.8	1.67%	1.19%	1.51%	1.19%
	2.4	1.34%	1.02%	1.23%	1.02%
lpw* (m)	7.8	1.60%	1.15%	1.43%	1.13%
	8.2	1.67%	1.19%	1.51%	1.19%
	9.4	1.76%	1.24%	1.62%	1.24%
	10.9	1.89%	1.30%	1.81%	1.38%
	12.5	2.03%	1.40%	2.02%	1.49%
lpc* (mm)	305	1.62%	1.13%	1.47%	1.12%
	610	1.67%	1.19%	1.51%	1.19%
	1220	1.74%	1.35%	1.57%	1.30%
% of wall shear strain applied	0	1.67%	1.19%	-----	-----
	25	-----	-----	1.84%	1.25%
	50	-----	-----	1.83%	1.32%
	75	-----	-----	1.64%	1.25%
	100	-----	-----	1.51%	1.19%
Damage level	0	1.67%	-----	1.51%	-----
	1	-----	1.19%	-----	1.19%
	2	-----	1.10%	-----	1.06%
First Floor Height (m)	2.7	1.67%	1.19%	1.51%	1.19%
	5.5	1.82%	1.32%	1.41%	1.11%
	8.3	1.50%	1.17%	1.30%	1.06%
	11.0	1.43%	1.15%	1.32%	1.07%
	13.7	1.47%	1.17%	1.39%	1.11%

Comparing Table 7.9 to Table 7.8 one could tell the similarities and differences in column behaviour with and without basement levels. The trend in change of column global drift capacity with column length, wall plastic hinge length, height of column plastic hinge zone, and column damage level is the same for both the fix-based column and the one with three basements. Hence, the same logic used in previous sections to describe the behaviour of the fix-based column apply to the case were the column has three basement levels.

However, while stepwise addition of wall shear strain to wall deformation profile progressively decreased the drift capacity of the fixed-base column, drift capacity of the column with three basements fluctuated as percentage of applied wall shear strain increased. This unexpected behaviour can be explained by looking at curvature profiles at column failure for different levels of wall shear strain (Figure 7.40).

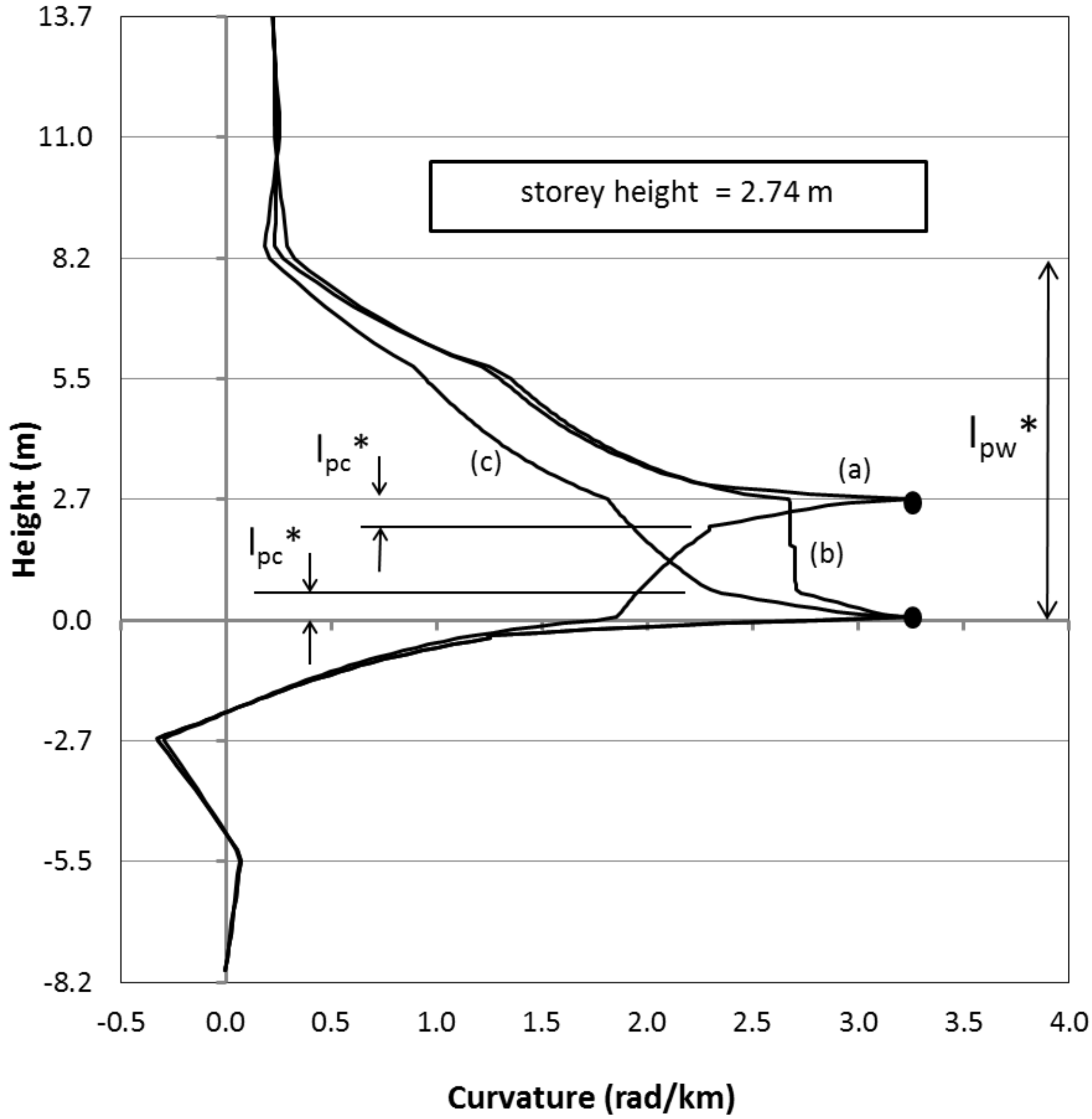

Figure 7.40 Curvature profiles of the undamaged standard column with three basement levels at failure: a) no wall shear strain applied (global drift = 1.67%), b) 50% of wall shear strain applied (global drift = 1.83%), c) 100% of wall shear strain applied (global drift = 1.51%).

When no wall shear strain was applied (Figure 7.40a), column maximum curvature was located at the top of the first storey as expected. At 50% applied wall shear strain (Figure 7.40b) the additional rotation demand at first floor level made the column maximum curvature occur at the base. Since at column failure shear force in the first storey was nearly zero, a lot of inelastic curvature was concentrated over the entire height of the first storey which increased column drift capacity significantly. This made the column to demonstrate its highest drift capacity when 50% of wall shear strain was applied. As the percentage of applied wall shear strain was further increased (Figure 7.40c) less inelastic curvature was accumulated in the first floor reducing wall global drift capacity.

The trend in change of column drift capacity with height of the first storey is also different for the two cases of the fixed-base column and the one with three basements. The difference can be explained by looking at how wall deformation profile (column target displacements at floor levels) can be accommodated by column boundary conditions and first floor height. A similar approach used to describe the unexpected behaviour of the column with three basements at various levels of applied wall shear strain can be used to explain the trend in change of column flexibility with first storey height. The figures and discussion is therefore excluded from the text for brevity.

A few summary figures are presented next to facilitate comparison between column behaviour with a fixed based and with three basements. The trend in variation of column global drift capacity with respect to height of column plastic curvature zone, wall plastic hinge length, and column damage level was so simple and so similar for both cases of column boundary conditions at grade level that is excluded from the summary figures below. Effect of column length, percentage of wall shear strain applied, and column first storey height is compared for the two cases of fixed-base column and the column with three basements in the figures below. As expected, columns continuing below grade reach their curvature capacity at a higher building global drift compared to the fixed-base columns. This is attributed to the added flexibility at the base of the column due to presence of basement floors.

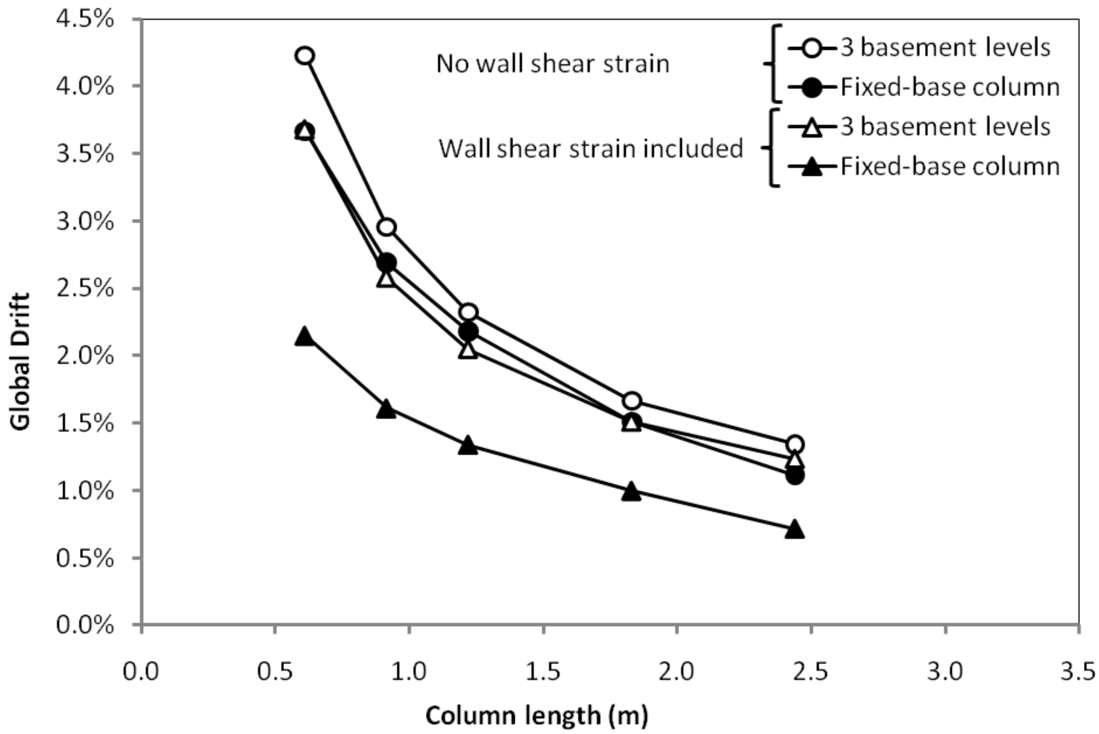

Figure 7.41 Effect of column length on global drift capacity of the undamaged standard column.

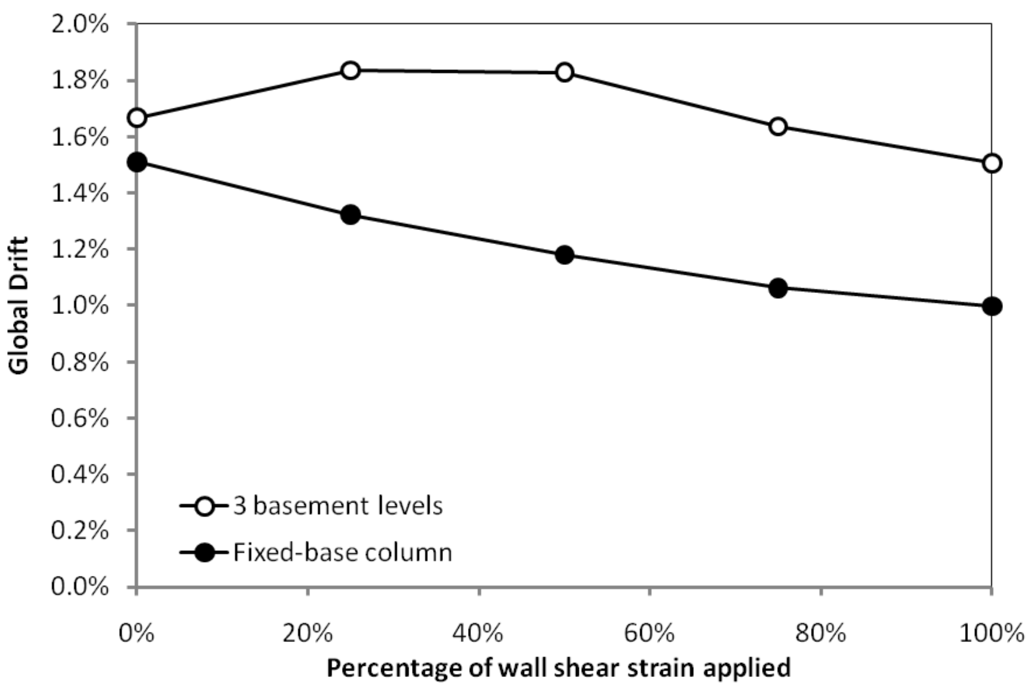

Figure 7.42 Effect of percentage of applied wall shear strain on global drift capacity of the undamaged standard column.

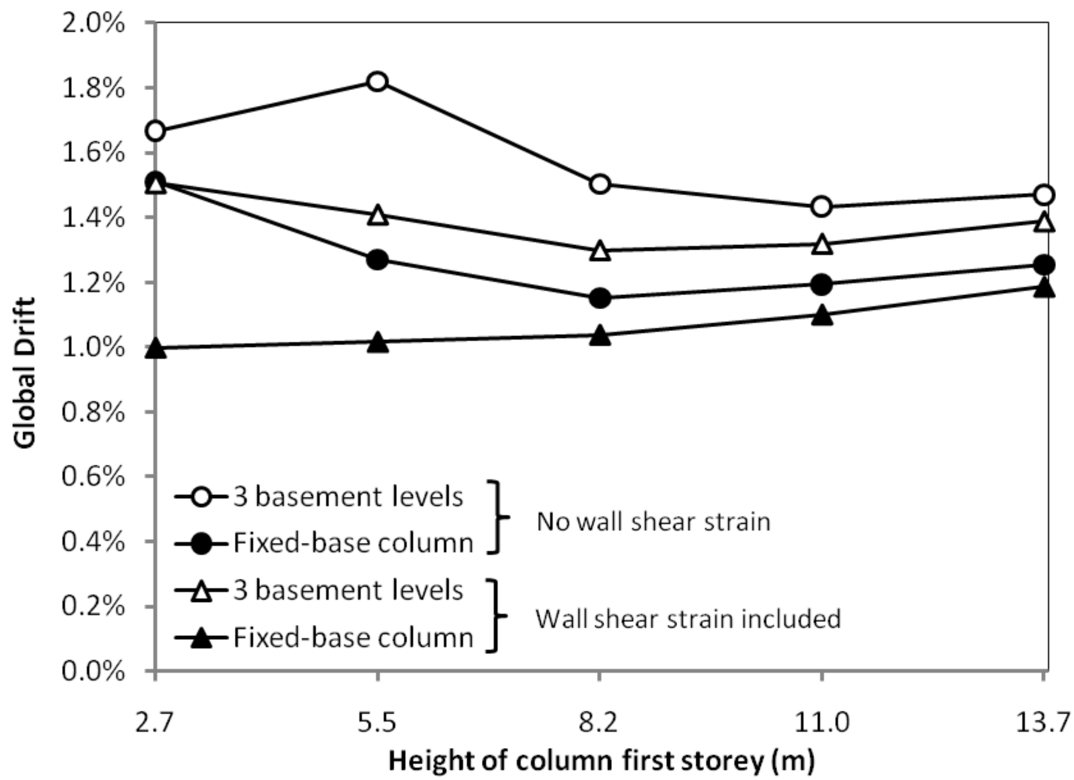

Figure 7.43 Effect of taller first storey on global drift capacity of the undamaged standard column.

7.9.1 Simple methods for estimating column curvature demand due to imposed wall deformation with column continuing below grade level

The column continuing below grade through basement levels allows for rotation of the column at grade level and reduces column curvature demand. It is therefore beneficial to take advantage of this relaxation of column curvature demand in design.

Figure 7.44 shows curvature profile of the column below grade. Note that the column was considered to be fixed against lateral displacement at basement floor slab levels due to presence of stiff basement walls. The curvature profile shown in the figure was obtained using moment distribution structural analysis procedure assuming that the column continues for several floor below grades and remains elastic in that region. The total rotation of the column at grade level could then be found by integrating column curvatures below grade or would simply be equal to the net area enclosed by the column curvature profile below grade.

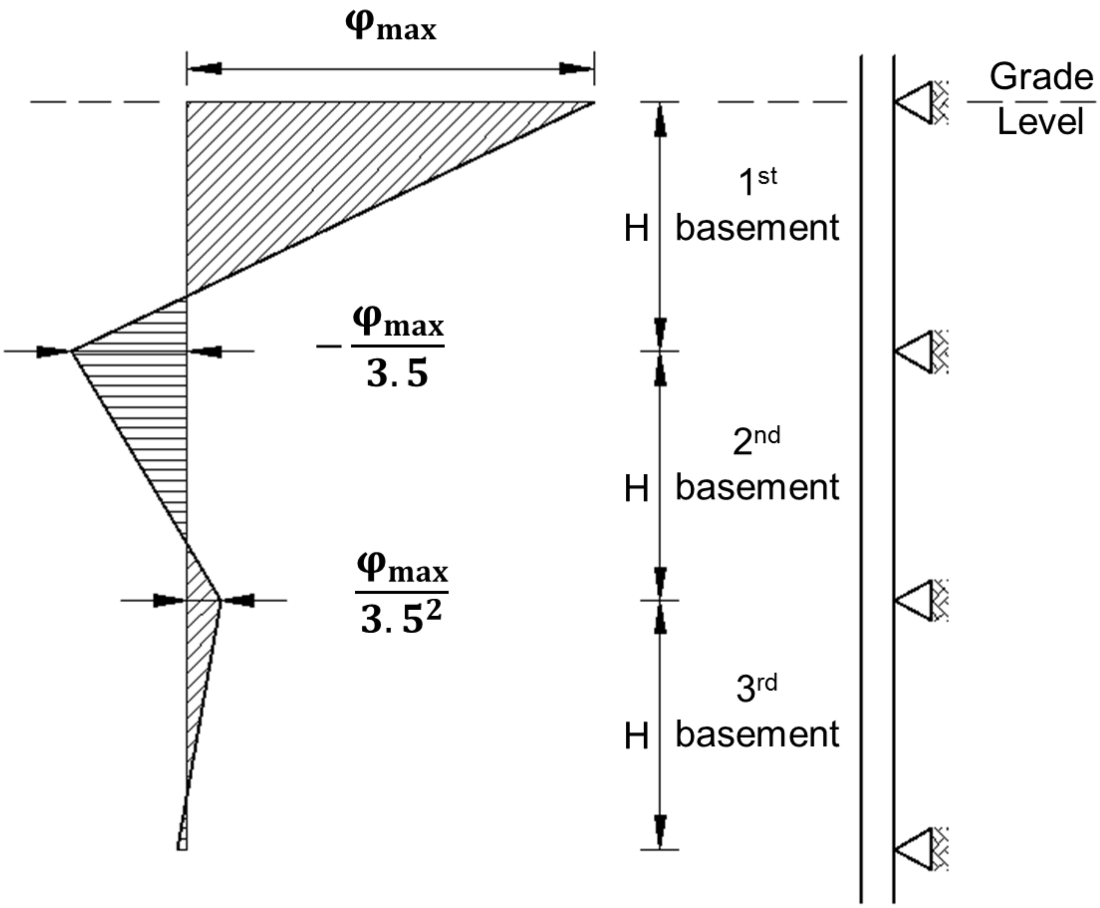

Figure 7.44 Schematic curvature profile of a column continuing below grade level in a building with rigid basement walls.

The net rotation occurring in the first basement storey would then be

$$\theta_1 = \varphi_{max} \cdot H \left(\frac{0.778}{2} - \frac{0.222}{2}\right) = 0.357\varphi_{max} \cdot H \qquad \textbf{Eq 7.15}$$

The net rotation occurring in the second basement storey would be that occurring in the first divided by 3.5 and in the opposite direction to θ_1.

$$\theta_2 = \frac{-0.357}{3.5}\varphi_{max} \cdot H = -0.102\varphi_{max} \cdot H \qquad \textbf{Eq 7.16}$$

Considering that the column curvature profile decreases in magnitude rapidly down the basement floors, it is accurate enough to consider only the first two basement storeys in calculating column rotation at the base.

$$\theta = \theta_1 + \theta_2 \cong \frac{\varphi_{max} \cdot H}{4} \qquad \textbf{Eq 7.17}$$

If wall shear strain is treated as rotation of the column support (see Figure 7.5) then the rotation of the column at its base can simply be subtracted from average wall shear strain. If the storey heights above and below the grade are equal, a procedure similar to that used to derive Eq 7.3 can be used to obtain the additional column curvature demand from wall shear strain.

$$\varphi_s = \frac{3.5(\gamma_{max} - \theta)}{H} \qquad \textbf{Eq 7.18}$$

Wall maximum shear strain is used instead of wall average shear strain over the first storey assuming that wall plastic hinge length is several storeys high.

Approx. 1 shown in Figure 7.45 gives estimates of column curvature demand using Eq 7.18. The prediction is quite accurate up until when the column experiences severe inelastic behaviour where column curvature demands are underestimated.

This concept can be further simplified for design purpose if the wall shear strain model presented in Section 2.7 is used to get wall maximum shear strain.

$$\varphi_s = \frac{3.5(\gamma_{max} - \theta)}{H} = \frac{3.5}{H}\left[0.577\varphi_{max}\left(\frac{l_w}{2} - c\right) - \frac{\varphi_{max} \cdot H}{4}\right]$$

$$= \varphi_{max}\left[\frac{l_w - 2c}{H} - \frac{3.5}{4}\right] \qquad \textbf{Eq 7.19}$$

Hence, the total column curvature demand would be

$$\varphi_d = \varphi_{max} + \varphi_s = \varphi_{max}\left[1 + \frac{l_w - 2c}{H} - \frac{3.5}{4}\right] = \varphi_{max}\left[0.125 + \frac{l_w - 2c}{H}\right] \qquad \textbf{Eq 7.20}$$

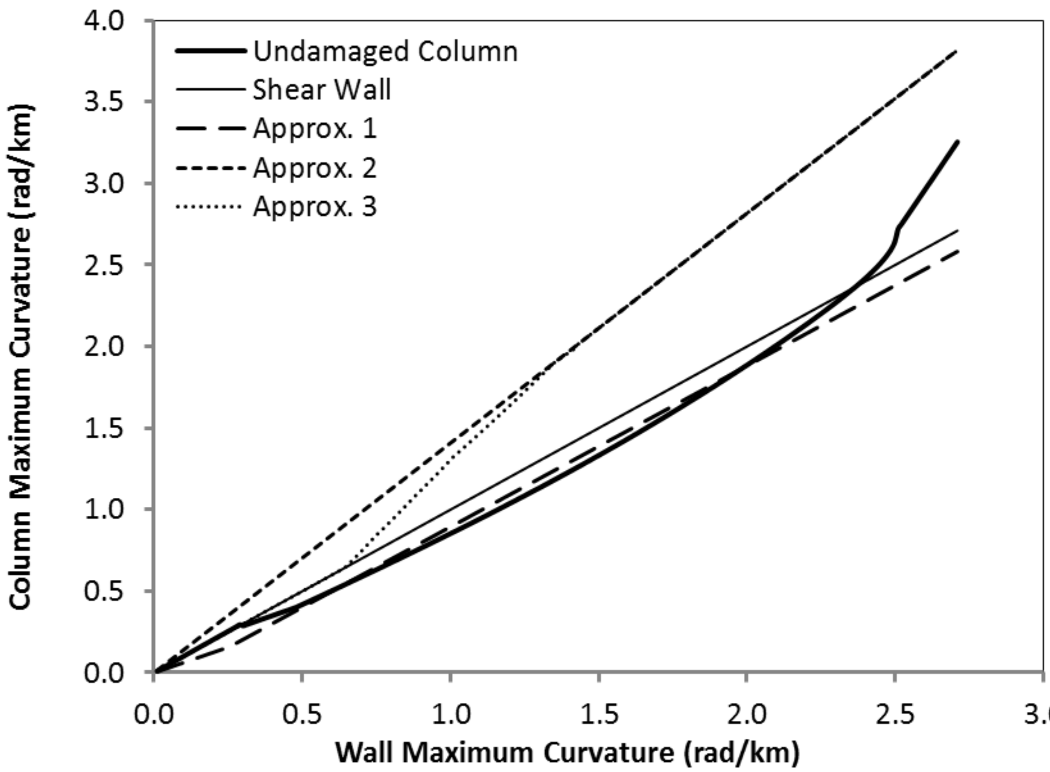

Figure 7.45 Estimation of column curvature demand due to imposed wall deformation with column continuing below grade for several basement levels (wall shear strain included).

If wall ultimate concrete compression depth is used, the line labelled Approx. 2 in Figure 7.45 will result which consistently over estimates column curvature demand. If wall concrete compression depth is calculated from section analysis at each given wall maximum curvature, the line labelled Approx. 3 in Figure 7.45 will be obtained. Approx. 3 is less conservative than Approx. 2 at smaller wall maximum curvatures but converges to Approx. 2 at higher wall maximum curvatures as expected.

Another approach would be to use the deformation compatibility of the wall-column system at the second floor level similar to that done to obtain Eq 7.9. Rotation of the base of the column θ due to column curvatures below grade can be directly deducted from wall shear strain as follows.

$$\varphi_s = \frac{\gamma_{max} - \theta}{l_{pc}^*}$$ **Eq 7.21**

The line called Approx. 4 in Figure 7.46 gives estimations of the column curvature demand using the actual wall maximum shear strain in Eq 7.21. As can be seen, the method does a good job of predicting column curvature demand except for when the column becomes highly nonlinear.

To simplify the method even further, the shear strain model introduced in Section 2.7 is used for maximum wall shear strain.

$$\varphi_s = \frac{\gamma_{max} - \theta}{l_{pc}^*} = \frac{\varphi_{max}}{l_{pc}^*}\left[0.577\left(\frac{l_w}{2} - c\right) - \frac{H}{4}\right] = \frac{\varphi_{max}}{l_{pc}^*}\left[\frac{l_w}{3.46} - \frac{c}{1.73} - \frac{H}{4}\right] \qquad \textbf{Eq 7.22}$$

With some approximation, the equation above becomes

$$\varphi_s = \frac{\varphi_{max}}{l_{pc}^*}\left[\frac{l_w}{4} - \frac{c}{2} - \frac{H}{4}\right] = \frac{\varphi_{max}}{l_{pc}^*}\left[\frac{l_w - 2c - H}{4}\right] \qquad \textbf{Eq 7.23}$$

The total column curvature demand will then be

$$\varphi_d = \varphi_{max}\left[1 + \frac{l_w - 2c - H}{4l_{pc}^*}\right] \qquad \textbf{Eq 7.24}$$

If the wall ultimate concrete compression depth is used throughout, the line labeled Approx. 5 in Figure 7.46 will result which consistently overestimates column curvature demand. If the wall concrete compression depth is calculated from section analysis at each given wall maximum curvature, the line called Approx. 6 in Figure 7.46 will be obtained. Approx. 6 is less conservative than Approx. 5 at smaller wall maximum curvatures but converges to Approx. 5 at higher wall maximum curvatures as expected. Overestimation of column curvature demand in Approx. 5 and 6 is mainly because the shear strain model presented in Section 2.7 overestimates wall maximum shear strain.

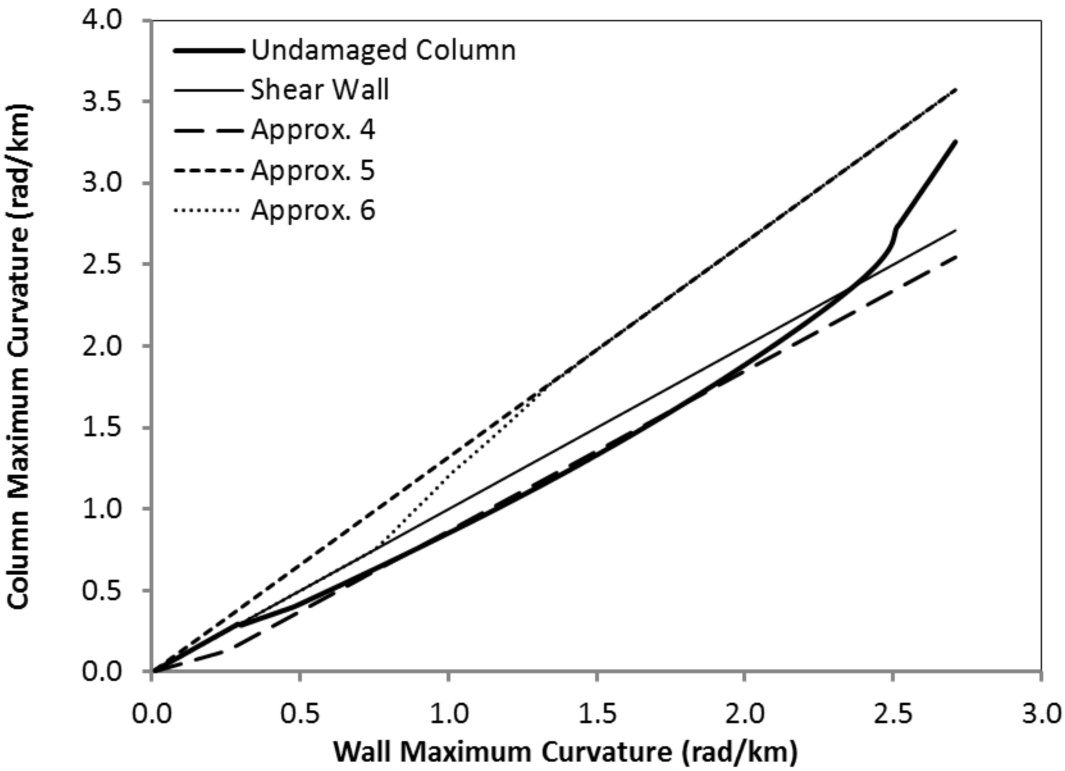

Figure 7.46 Estimating column curvature demand due to imposed wall deformation with column continuing below grade for several basement levels (wall shear strain included).

If the column is damaged, a similar strategy can be used to estimate column curvature demand by simply replacing l_{pc}^{*} with l_{pc}.

$$\varphi_s = \frac{\gamma_{max} - \theta}{l_{pc}} \qquad \textbf{Eq 7.25}$$

If the actual wall maximum shear strain is used in Eq 7.25, column curvature demand will be predicted as Approx. 1 in Figure 7.47. The method predicts column curvature demand reasonably accurately up until when the column demonstrates highly nonlinear behaviour.

With the use of the shear strain model presented in Section 2.9, Eq 7.25 can be expanded as follows similar to the manner by which Eq 7.24 was obtained.

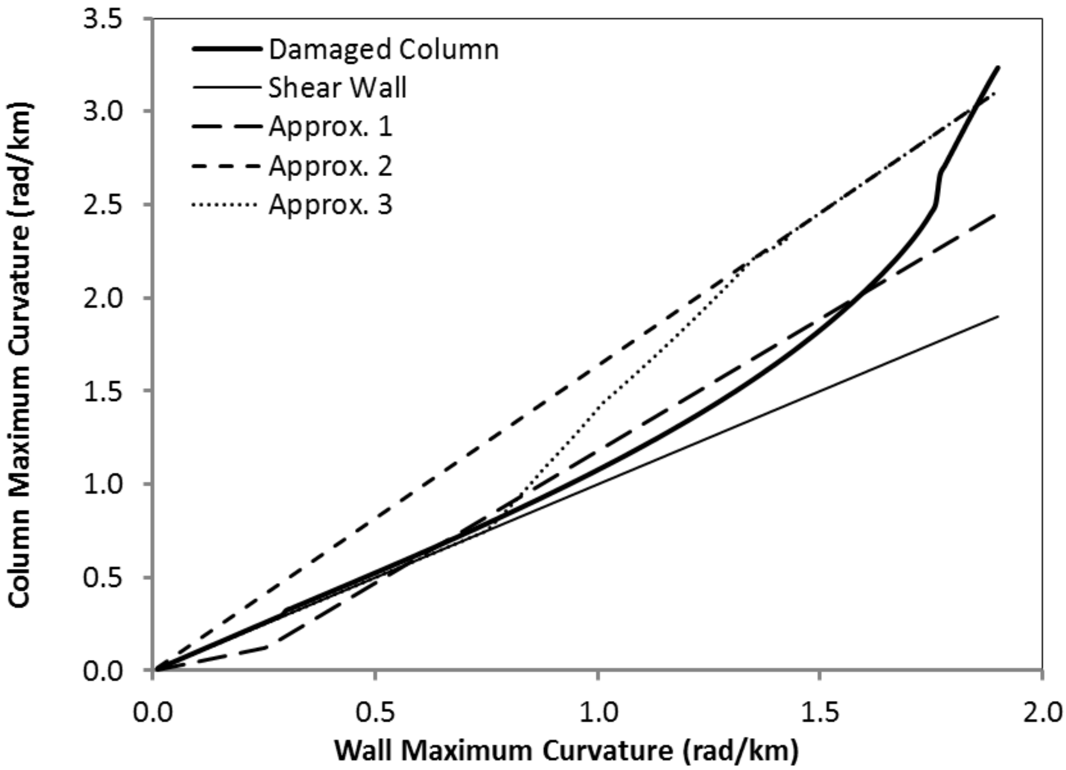

Figure 7.47 Estimation of column curvature demand due to combined effects of the imposed wall deformation with column continuing for several basement levels and column damage

$$\varphi_d = \varphi_{max}\left[1 + \frac{l_w - 2c - H}{4l_{pc}}\right] \qquad \textbf{Eq 7.26}$$

Again, if the wall ultimate concrete compression depth is used throughout, the line labeled Approx. 2 in Figure 7.47 will result which consistently over estimates column curvature demand. If the wall concrete compression depth is calculated from section analysis at each given wall maximum curvature, the line called Approx. 3 in Figure 7.47 will be obtained. Approx. 3 is less conservative than Approx. 2 at smaller wall maximum curvatures but converges to Approx. 2 at higher wall maximum curvatures as expected.

In summary, the simple methods formulated in this section can reasonably accurately predict column curvature demand when the column is able to rotate at grade level due to presence of basement floors. Although the formulas were derived for the special case of uniform storey heights, the same concept can be used to obtain formulas for other cases.

7.10 Inter-storey Drift

Inter-storey drift capacity is a useful parameter often used as a measure of column flexibility. In the analysis carried out in this chapter, because wall plastic hinge was modeled at the base, at the point of column failure, maximum inter-storey drift always occurred in the first storey. Therefore, in this study, maximum inter-storey drift is equivalent to the first storey drift.

Table 7.10 and Table 7.11 give a summary of first storey drifts at column failure for the fixed-base standard column and for the one with three basement level respectively. Comparing first storey drifts at column failure to the corresponding global drift capacities one can find similar trends in how the column flexibility varies with respect to various analysis parameters. Looking at the section in the tables where the effect of applied wall shear strain is studied or comparing the numbers for the case with no wall shear strain to those with wall shear strain shows what a tremendous effect wall shear strain on column inter-storey drift capacity. As before, numbers corresponding to the standard case are highlighted.

In Figure 7.48 all data points from the analysis carried out in this chapter are plotted. Clearly, it is impossible to find a distinct relationship between maximum inter-story drift and global drift from this plot. However, it was found that while global drift ranged from 0.8% to 2.0%, inter-storey drift varied from 0.2% to 1.0%.

Because the columns were forced to have the same lateral deformation at floor slab levels as those of the wall, the relationship between maximum inter-storey drift and global drift at the point of column failure becomes independent of column parameters. In other words, this relationship only depends on the shape of the wall deformation profile and is not influenced by column parameters such as column length, column damage level, fixity of the column at the base, and height of column plastic hinge zone. This phenomenon is demonstrated in Figure 7.49. A straight line can be fitted to the data points which suggests that first-storey drift and global drift are proportional for the same wall; a consequence of assuming bilinear curvature distribution along the height of the wall. Shear strain changes the slope of the fitted straight line because wall shear strain changes the shape of the wall lateral deformation profile and hence the relationship between inter-storey and global drifts.

Table 7.10 Summary of first storey drift capacity of the fixed-base standard column.

Parameter		No shear strain		With shear strain	
		Undamaged	Damaged	Undamaged	Damaged
Column Length (m)	0.6	1.01%	0.67%	0.73%	0.60%
	0.9	0.71%	0.45%	0.50%	0.40%
	1.2	0.55%	0.33%	0.39%	0.27%
	1.8	0.34%	0.24%	0.24%	0.19%
	2.4	0.29%	0.19%	0.22%	0.15%
lpw* (m)	7.8	0.34%	0.24%	0.24%	0.19%
	8.2	0.34%	0.24%	0.24%	0.19%
	9.4	0.35%	0.25%	0.24%	0.20%
	10.9	0.35%	0.25%	0.24%	0.20%
	12.5	0.36%	0.27%	0.24%	0.20%
lpc* (mm)	305	0.33%	0.23%	0.21%	0.17%
	610	0.34%	0.24%	0.24%	0.19%
	1220	0.36%	0.26%	0.27%	0.25%
% of wall shear strain applied	0	0.34%	0.24%	-----	-----
	25	-----	-----	0.31%	0.23%
	50	-----	-----	0.28%	0.21%
	75	-----	-----	0.25%	0.20%
	100	-----	-----	0.24%	0.19%
Damage level	0	0.34%	-----	0.24%	-----
	1	-----	0.24%	-----	0.19%
	2	-----	0.22%	-----	0.19%
First Floor Height (m)	2.7	0.34%	0.24%	0.24%	0.19%
	5.5	0.50%	0.35%	0.40%	0.31%
	8.3	0.56%	0.42%	0.51%	0.39%
	11.0	0.68%	0.51%	0.63%	0.49%
	13.7	0.80%	0.60%	0.77%	0.58%

Effect of wall plastic hinge length on the relationship between inter-storey and global drift is demonstrated in Figure 7.50. Again, walls with and without shear strain are distinguished because of the change in wall deformation profile due to various levels of wall shear strain included.

Table 7.11 Summary of first storey drift capacity of the standard column with three basements.

		No shear strain		With shear strain	
Parameter		Undamaged	Damaged	Undamaged	Damaged
Column Length (m)	0.6	1.19%	0.49%	1.38%	0.68%
	0.9	0.79%	0.41%	0.91%	0.54%
	1.2	0.59%	0.33%	0.69%	0.42%
	1.8	0.39%	0.24%	0.46%	0.32%
	2.4	0.29%	0.19%	0.34%	0.25%
lpw* (m)	7.8	0.39%	0.24%	0.45%	0.32%
	8.2	0.39%	0.24%	0.46%	0.32%
	9.4	0.38%	0.24%	0.46%	0.32%
	10.9	0.37%	0.22%	0.47%	0.33%
	12.5	0.37%	0.22%	0.49%	0.33%
lpc* (mm)	305	0.37%	0.22%	0.44%	0.30%
	610	0.39%	0.24%	0.46%	0.32%
	1220	0.41%	0.29%	0.49%	0.37%
% of wall shear strain applied	0	0.39%	0.24%	-----	-----
	25	-----	-----	0.48%	0.28%
	50	-----	-----	0.52%	0.33%
	75	-----	-----	0.48%	0.33%
	100	-----	-----	0.46%	0.32%
Damage level	0	0.39%	-----	0.46%	-----
	1	-----	0.24%	-----	0.32%
	2	-----	0.23%	-----	0.29%
First Floor Height (m)	2.7	0.39%	0.24%	0.46%	0.32%
	5.5	0.77%	0.50%	0.63%	0.44%
	8.3	0.79%	0.56%	0.70%	0.52%
	11.0	0.85%	0.63%	0.80%	0.60%
	13.7	0.97%	0.71%	0.93%	0.68%

When the column had a taller first storey, maximum inter-storey drift still occurred in the first storey and was calculated by dividing the lateral deformation at the top of that storey by the corresponding storey height. This change in definition of maximum inter-storey height also changed the relationship between maximum inter-storey and global drifts (see Figure 7.51).

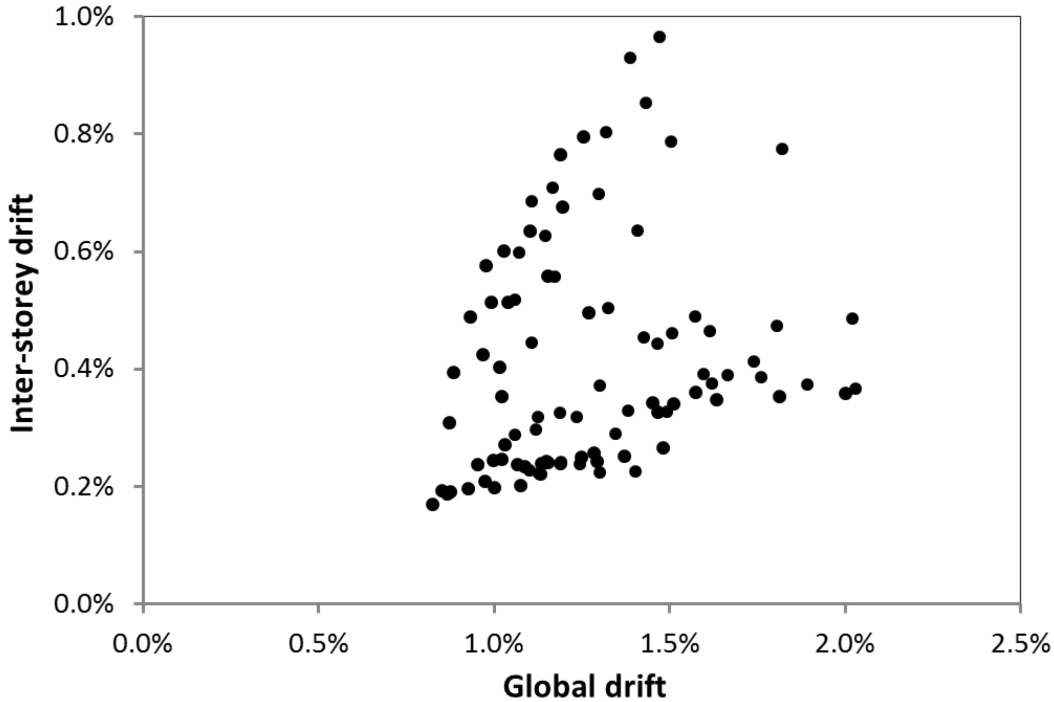

Figure 7.48 Relationship between inter-storey drift and global drift at column failure: all data points plotted.

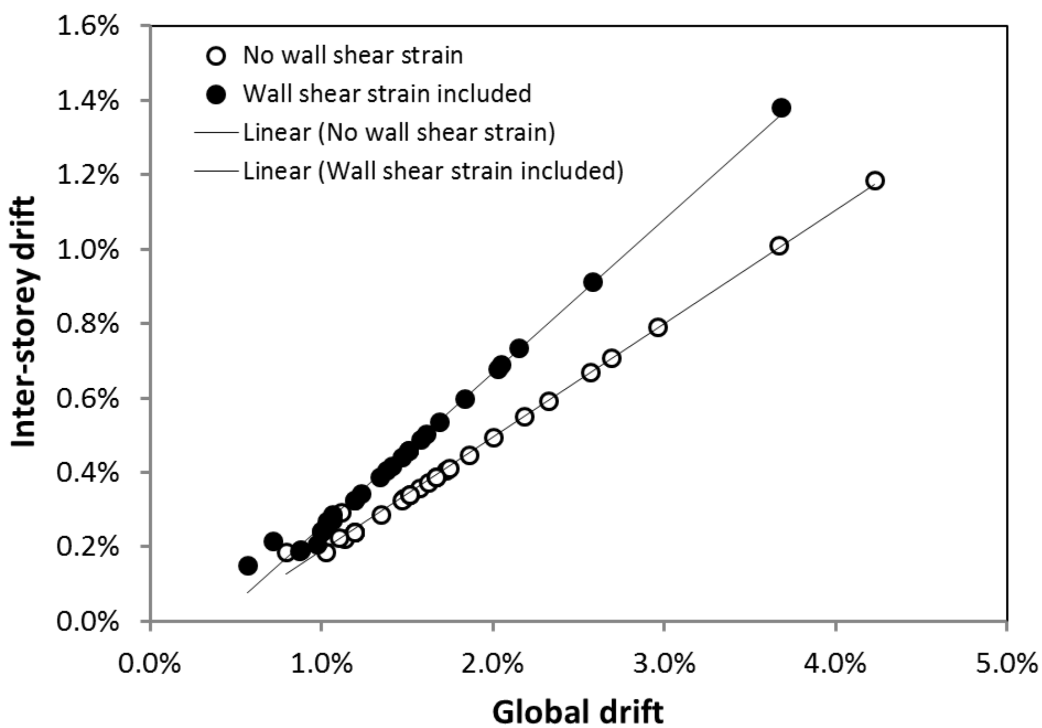

Figure 7.49 Relationship between inter-storey drift and global drift at column failure for all data points with l_{pw}*=8.2m and first floor height of 2.74m.

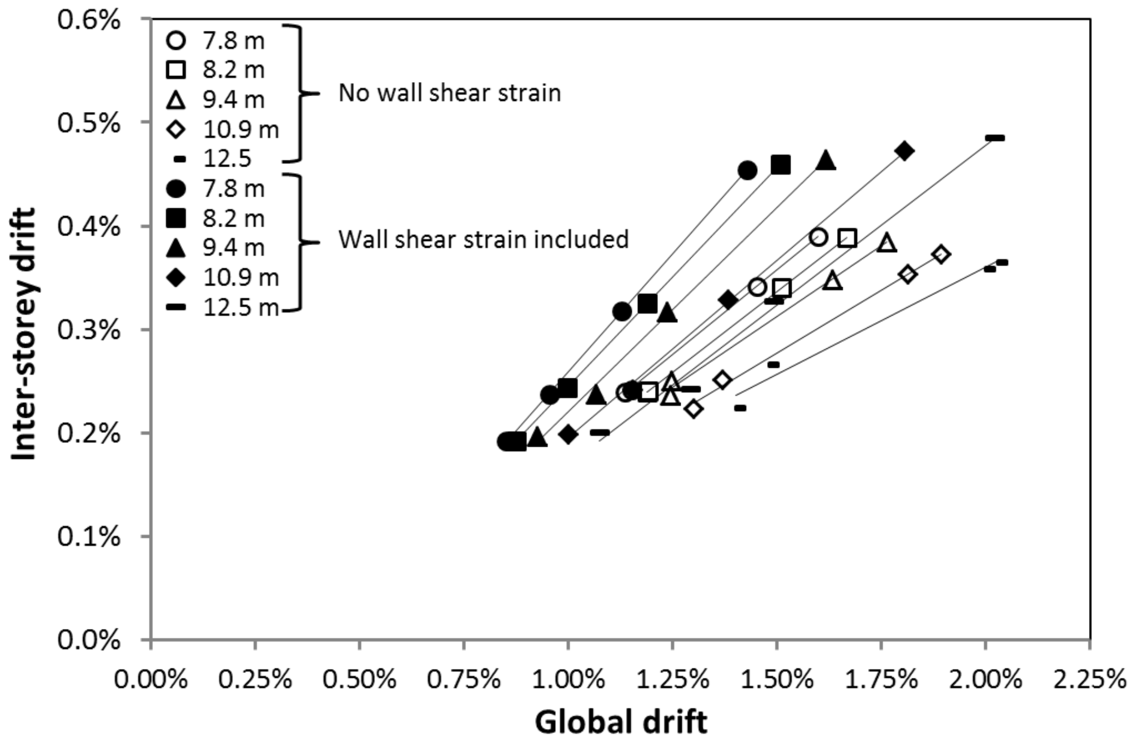

Figure 7.50 Relationship between inter-storey drift and global drift for various wall plastic hinge lengths (first floor height=2.74m).

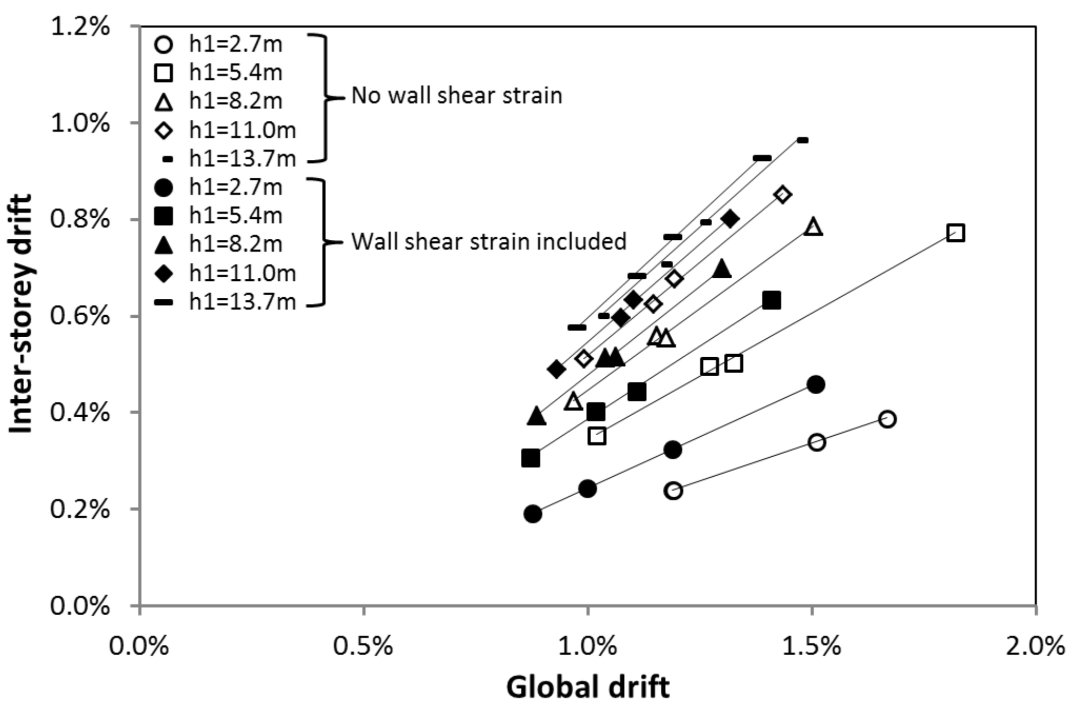

Figure 7.51 Relationship between inter-storey drift and global drift for various first storey heights (wall plastic hinge length=8.2m).

7.11 Effect of Members Framing into the Column on its Curvature Demand

So far in this chapter, the flexural stiffness of members framing into the column such as floor slabs or beams has been ignored as the framing members were modeled as pin-ended rigid links forcing the column to have the same horizontal deformation as that of the wall at storey levels. While this is a good approximation when the framing members are thin flat plate slabs, it underestimates column curvature demand in a building with relatively stiff beams running between columns. Assuming the building has uniformly-spaced identical floor slabs or framing members throughout its height, additional column curvature demand due to flexural stiffness of the framing members would be the largest in areas where the building drift is the largest. In a shear wall building with the wall hinging at the base, maximum building drifts occur near the top of the building. In that region, wall curvatures are elastic and almost negligible. The wall is not bent and undergoes rigid body movement. Storey height is often constant near the top of the building and floor slabs, beams, and columns do not change in cross-section.

Figure 7.52 shows a scheme of the region near the top of a building with relatively thin framing members and relatively stiff columns. In this case, the framing members will bend in double curvature. If the flexural stiffness of the framing member is totally ignored, the column will not bend at all and will have a deformation profile identical to the wall. In this case, no curvature will be induced in the column. Accounting for flexural stiffness of these members forces the beam-column joints to rotate less than the wall drift θ_w and puts the column in double curvature; hence, column curvature demand will no longer be zero.

Figure 7.53 shows a similar scheme but for a building with very stiff beams framing into relatively flexible columns. If the beams are stiff enough, they will bend in single curvature and the beam-column joints will rotate in the opposite direction of the building drift. The columns will again bend in double curvature; however, the column curvature demand will be much greater than the case presented in Figure 7.52.

This section provides a simple method for estimating additional column curvature demand due to flexural stiffness of members framing into the column near the top of a shear wall building. The objective of the section is to assist with the decision making on whether or not framing action causes significant additional curvature demands on the column.

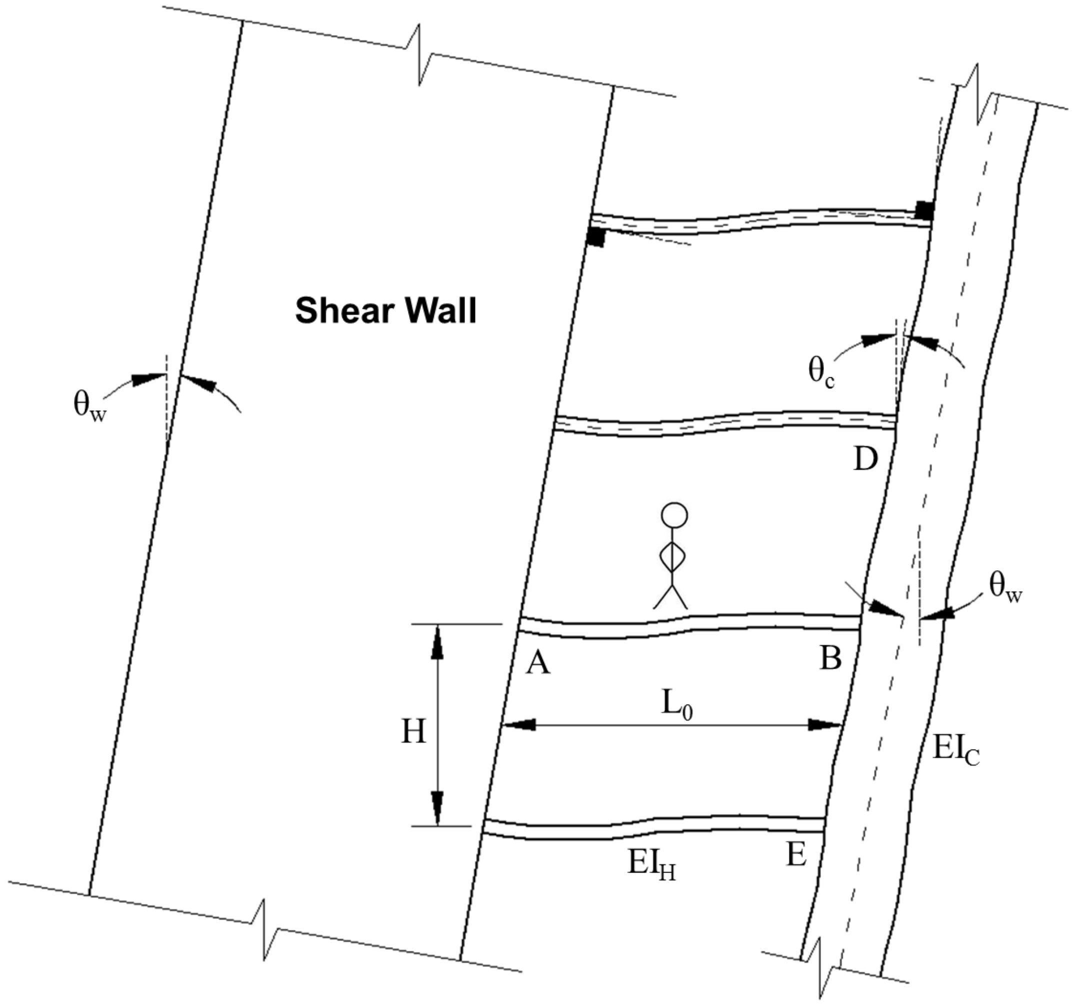

Figure 7.52 Thin slabs framing into a relatively stiff gravity-load column.

Because the building drift is uniform near the top of the building and the wall is not bent, little nonlinear behaviour is expected from other structural members in that region. No severe cracking is likely to occur in the columns, beams, floor slabs, or beam-column joints. Hence, the flexural behaviour of the members in that region can be accurately modeled using an effective elastic flexural stiffness. Elastic analysis can then be used to calculate additional column curvature demand resulting from the flexural stiffness of members framing into the column. This is a fundamental assumption on which the derivations in this section are based.

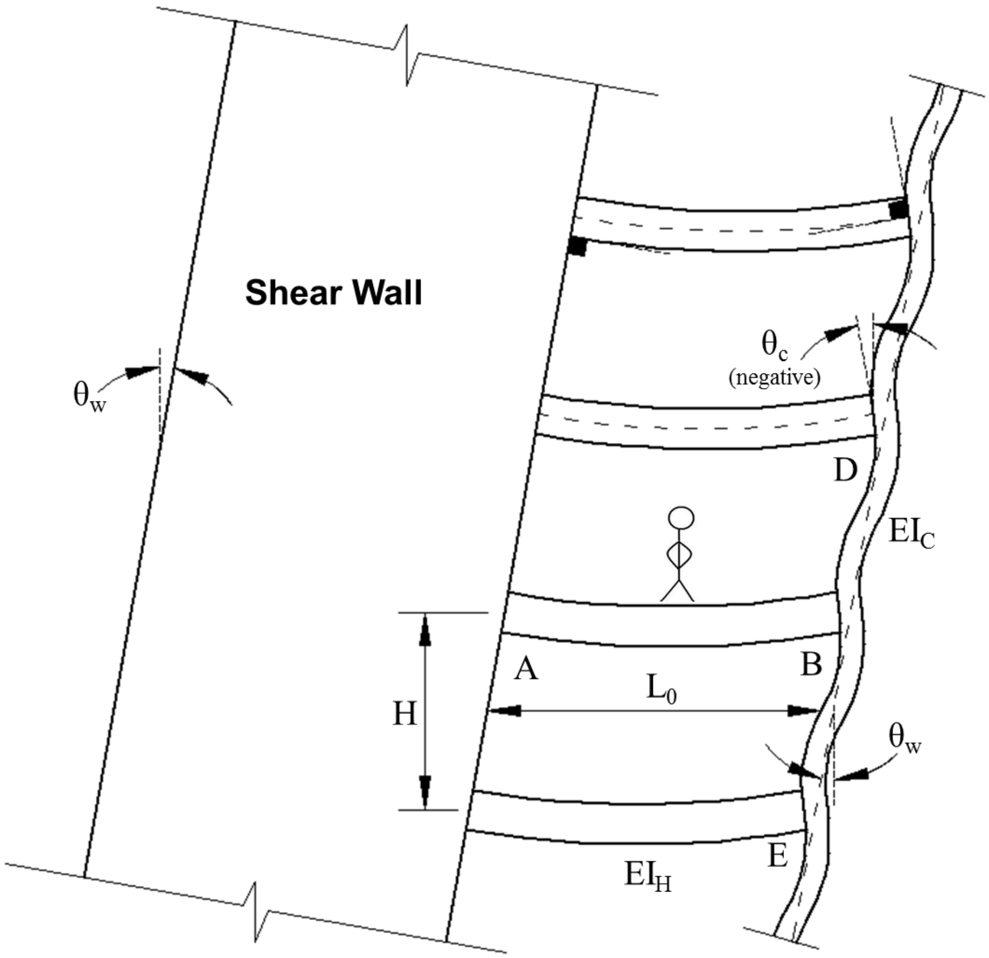

Figure 7.53 Stiff beams framing into a relatively flexible gravity-load column.

Considering the frame ABDE and using slope-deflection formulation, the internal moments in the framing member AB and the columns BD and BE can be written in terms of the joint rotations (θ) and member chord rotation (Ψ) as follows.

$$M_{BA} = \frac{2EI_H}{L_0}[2\theta_B + \theta_A - 3\Psi_{AB}]$$ **Eq 7.27**

$$M_{BD} = \frac{2EI_C}{H}[2\theta_B + \theta_D - 3\Psi_{BD}]$$ **Eq 7.28**

$$M_{BE} = \frac{2EI_C}{H}[2\theta_B + \theta_E - 3\Psi_{BE}]$$ **Eq 7.29**

In the upper portion of a shear wall where wall curvatures are very small and storey drift is uniform, rotation of joint A is equal to the wall drift θ_W. If storey heights are uniform and the column and the framing members do not change in cross-section, the clockwise rotation of the beam-column joints will be identical and equal to θ_C. If axial deformation of the column and the framing members are ignored, the chord rotation of the column will be equal to θ_W and the framing members will have zero chord rotation (i.e. $\Psi_{AB} = 0$).

Rotational equilibrium at joint B requires that

$$M_{BA} + M_{BD} + M_{BE} = 0 \qquad \textbf{Eq 7.30}$$

Hence

$$\frac{2EI_H}{L_0}(2\theta_C + \theta_W) = \frac{12EI_c}{H}(\theta_W - \theta_C) \qquad \textbf{Eq 7.31}$$

Rearranging gives

$$\theta_C\left[\frac{4EI_H}{L_0} + \frac{12EI_C}{H}\right] = \theta_W\left[\frac{12EI_C}{H} - \frac{2EI_H}{L_0}\right] \qquad \textbf{Eq 7.32}$$

Let α be the ratio of the effective flexural stiffness of the column to that of the framing members.

$$\alpha = \frac{EI_C/H}{EI_H/L_0} \qquad \textbf{Eq 7.33}$$

Then

$$\theta_C = \frac{6\alpha - 1}{6\alpha + 2}\theta_W \qquad \textbf{Eq 7.34}$$

Eq 7.34 gives the beam-column clockwise rotation as a function of α and the wall drift. If α is equal to 1/6, then θ_C will be zero. For values of α greater than 1/6 (i.e. stiffer columns), θ_C will be positive resulting in a system deformation profile such as the one shown in Figure 7.52. If α is smaller than 1/6 (i.e. flexible columns), then θ_C will be negative and the system will deform similar to Figure 7.53.

Substituting Eq 7.34 into Eq 7.28 gives the column bending moment demand as

$$M_{BD} = \frac{6EI_C}{H}(\theta_C - \theta_W) = \frac{6EI_C}{H}\theta_W\left(\frac{6\alpha - 1}{6\alpha + 2} - 1\right) = \frac{6EI_C}{H}\theta_W(\frac{-3}{6\alpha + 2}) \qquad \textbf{Eq 7.35}$$

Column curvature demand will then be the bending moment demand on the column divided by its effective flexural rigidity.

$$\varphi_c = \left|\frac{M_{BD}}{EI_C}\right| = \frac{18}{6\alpha + 2} \times \frac{\theta_W}{H} = (\frac{9}{3\alpha + 1})(\frac{\theta_W}{H}) \qquad \textbf{Eq 7.36}$$

To check the accuracy of the previous derivation, an elastic model of the frame ABDE was built in SAP2000 with fixed values for H and L_0. The flexural stiffness of the framing members and the column was then changed to get various values of α.

Figure 7.54 compares results from SAP2000 with estimates of column curvature demand obtained from Eq 7.36. As can be seen, the equation predicts column curvature demand very accurately for values of α greater than 3.0. Column curvature demand starts to increase rapidly for values of α smaller than 5.0 which is the case for buildings with relatively flexible columns and relatively stiff beams. As long as α remains greater than 20, additional column curvature demands due to framing action will be insignificant. Note that flexible columns have a large curvature capacity and hence can tolerate higher curvature demand. It is therefore concluded that Eq 7.36 provides an exact estimate of the additional column curvature demand due to flexural stiffness of framing members given the building drift and basic elastic properties of the structural members.

Another effect that framing members may have on the column is exerting additional axial load on the column due to shear forces created in the framing members. For example, in Figure 7.52, because member AB is bent in double curvature, the shear force induced in member AB at point B will act as an additional axial compressive force on the column BE. This additional axial compression can reduce the column curvature capacity and hence, needs to be taken into account. Note that if a framing member similar to AB in terms of structural properties existed on the right side of the column, the shear force from that member would have acted as an upward axial force on the column reducing the additional column compression force from member AB. However, if framing members are present on one side of the column only such as in corner columns or if the framing members on either side of the column are not structurally identical, there will be a resultant differential axial load on the column.

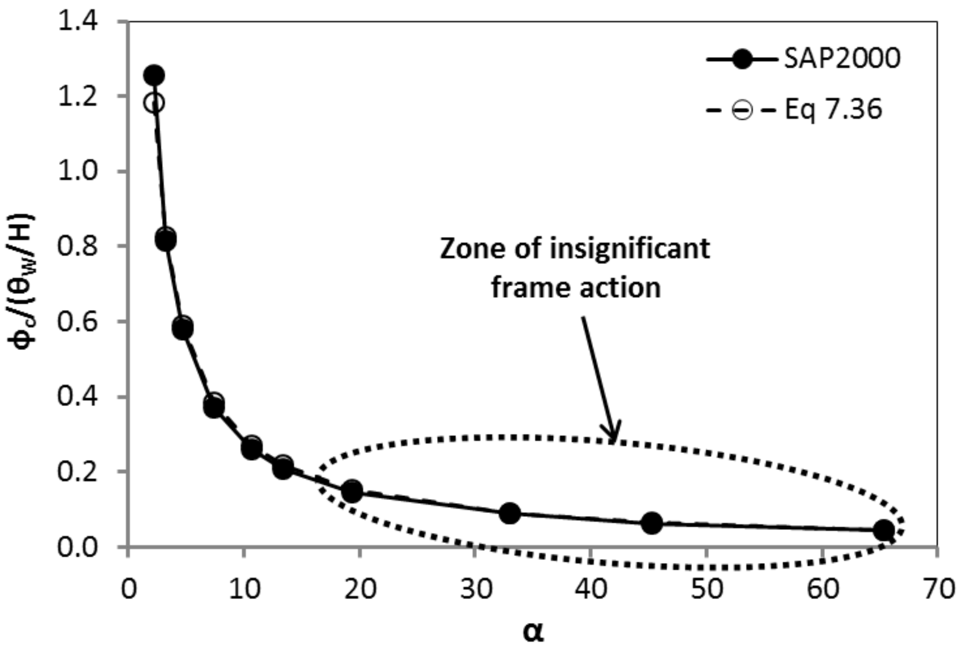

Figure 7.54 Validation of the proposed method for estimating additional column curvature accounting for the effect of framing members.

The additional axial load on the column can be derived using a similar approach to what was used earlier to find additional column curvature demand. In Figure 7.52, the additional axial compressive load on the column at point B will be equal to the shear force in member AB acting at end B. Again, this force can be obtained using slope deflection formulation as follows.

For member AB,

$$M_{AB} = \frac{2EI_H}{L_0}[2\theta_A + \theta_B - 3\Psi_{AB}] = \frac{2EI_H}{L_0}[2\theta_W + \theta_C] \quad \textbf{Eq 7.37}$$

$$M_{BA} = \frac{2EI_H}{L_0}[2\theta_B + \theta_A - 3\Psi_{AB}] = \frac{2EI_H}{L_0}[2\theta_C + \theta_W] \quad \textbf{Eq 7.38}$$

Rotational equilibrium of member AB requires that V_{BA}, the shear force in member AB at end B acting upward on member AB and downward on the column, be equal to

$$V_{BA} = \frac{M_{AB} + M_{BA}}{L_0} = \frac{6EI_H}{L_0^2}(\theta_C + \theta_W) \quad \textbf{Eq 7.39}$$

Incorporating Eq 7.32 into Eq 7.39 gives

$$V_{BA} = \frac{6EI_H}{L_0^2} \cdot \left(1 + \frac{6\alpha - 1}{6\alpha + 2}\right)\theta_W \quad \textbf{Eq 7.40}$$

or

$$V_{BA} = \frac{6EI_H}{L_0^2} \cdot \frac{12\alpha + 1}{6\alpha + 2}\theta_W = \frac{6EI_C}{L_0 H} \cdot \frac{12\alpha + 1}{\alpha(6\alpha + 2)}\theta_W \quad \textbf{Eq 7.41}$$

Similar to column curvature demand, the additional axial load on the column from the framing member estimated by Eq 7.41 is compared against elastic analysis in SAP2000. As shown in Figure 7.55, Eq 7.41 accurately estimates the additional axial force demand on the column. Also, for values of α greater than 10, the additional axial load on the column due to framing action is negligible.

In conclusion, this section provides simple equations for estimating additional curvature demand and axial load on columns resulting from framing action. It was assumed that the building has a uniform storey height with identical horizontal members framing into the column throughout the building height. It is only in this case that the effects of framing action on the column are most critical near the top of the building where the building drift is the highest. Other cases such as presence of a taller first storey or stiff framing members such as transfer girders in the lower floors of the building may prove to cause more severe framing action. Studying such circumstances has not been the subject of this section as the section is aimed at providing a simple decision making tool on the significance of framing action in estimating seismic demands on gravity-load columns in a typical shear wall building.

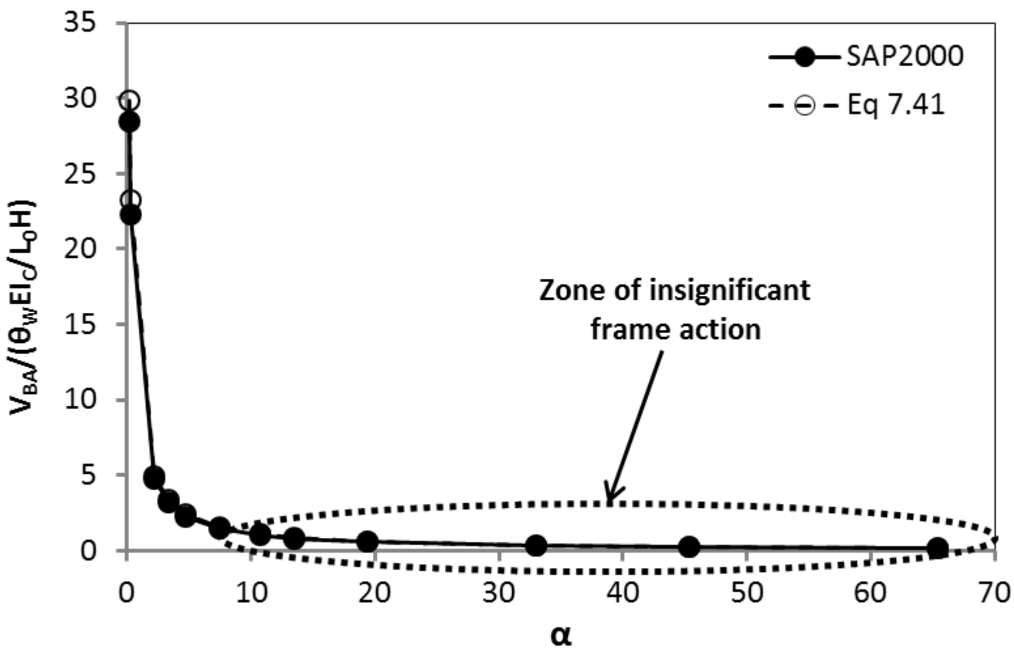

Figure 7.55 Validation of the proposed method for estimating additional column axial load demand from shear forces induced in the members framing into the column.

7.12 Effect of Foundation Rotation

Rotation of the shear wall foundation can significantly increase the wall lateral deformation at the top of the first storey or the displacement demand at the second floor slab which results in additional curvature demands on the column. In Section 7.3.1, it was shown that the effect of wall shear strain can be treated as rotation of the base of the wall by an amount equal to the first storey average shear strain (see Figure 7.5). A similar approach can then be used to estimate additional column curvature demand due to foundation rotation. This is done by substituting the average first storey shear strain γ in Eq 7.3 by the foundation rotation θ_b to get the following equation.

$$\varphi_s = \frac{M_b}{EI} = \frac{3.5}{H} \cdot \theta_b \qquad \textbf{Eq 7.42}$$

H is the height of the first storey. Note that the additional column curvature demand has to be added to the wall maximum curvature and column curvature demand due to wall shear strain to obtain the total column curvature demand.

7.13 Summary and Conclusions

1. In the absence of wall shear strain, as long as the column is tied to the shear wall with uniformly-spaced flat plate floor slabs, column curvature demand remains almost equal to the wall maximum curvature up until the point of formation of a plastic hinge at the base of the column. After plastic hinging of the column, column curvature demand would be larger than but close to the wall maximum curvature.

2. Shear strains constitute a significant part of the wall's deformation profile within the wall plastic hinge zone. Wall shear strain results in significant additional lateral displacement at the top of the first storey forcing large rotational demands on the columns. The additional rotation demand results in further curvature concentration at the base of the column increasing column curvature demand. Simple equations were developed to estimate additional column curvature demand due to wall shear strain.

3. For a given average compressive axial stress on the column, the greater the length of the column cross-section, the smaller the column curvature capacity would be. Columns with elongated cross-sections require a larger concrete compression depth to withstand the axial load and hence, have a much smaller curvature capacity. Elongated columns will therefore reach their curvature capacity at lower building drifts.

4. Shear walls with longer plastic hinge lengths distribute inelastic curvatures over a greater height. When connected to gravity-load columns with closely spaced floor slabs, walls with longer plastic hinge lengths bend the column more gradually over the height of the building reducing concentration of curvature at the base of the column.

5. In general, columns with larger plastic hinge lengths reach their curvature capacity at higher building drifts. Gravity-load columns do not demonstrate a ductile behaviour beyond the point of peak bending strength. Therefore, the reduction in column curvature demand due to a larger column plastic hinge region does not result in a significant increase in building drift capacity. Height of the column plastic hinge region is therefore considered not to be a critical parameter in estimating column curvature demand or building drift capacity.

6. Column damage causes further concentration of inelastic curvatures at the base of the column and increases column curvature demand for given wall maximum curvature reducing the building drift at which the column curvature capacity is consumed. Simple expressions were developed for estimating column curvature demand taking into account the concentration of curvature at the base of the column due to damage of the column.

7. In buildings with columns extending several floors up from grade level before framing into a floor slab, global drift capacity of the building governed by the columns reaching their curvature capacity can either increase or decrease due to presence of a taller first storey depending on level of wall shear strain and column boundary conditions at the grade level.

8. Relaxing the fixity of the column at grade level due to the column continuing below grade reduces column curvature demand for a given wall maximum curvature. Column plastic hinge may form either at grade level or at the top of the first storey depending on the level of wall shear strain. Simple design-oriented expressions were formulated for estimating column curvature demand accounting for flexible boundary conditions of the column at grade level.

9. Flexural stiffness of members framing into the column results in additional curvature and axial load demand on the column. Simple equations were formulated to estimate the additional curvature and axial load demand on columns near the top of shear wall buildings with uniform storey height and identical horizontal framing members throughout their height. The equations are intended for use as a decision-making tool on the significance of framing action in a given shear wall building.

10. Rotation of the shear wall foundation can be treated similar to wall shear strain as both effects cause additional rotation of the column by increasing the lateral deformation of the shear wall at the second floor slab. A simple equation is provided for estimating additional column curvature demand due to rotation of the shear wall foundation.

CHAPTER 8 Summary of Contributions and Recommendations for Future Work

8.1 Overview of Contributions

The subject of this thesis is determining the seismic deformation demands on gravity-load columns over the height of the plastic hinge region of shear wall buildings and ensuring that the demands are less than the deformation capacity of the columns. As previous work had defined the flexural deformation of shear walls, this study focused on the two other very important deformation components of shear walls, namely shear deformation in the plastic hinge region of walls, and rigid body movement of walls due to foundation rotation. Both of these building deformation components are critical for estimating the deformation demands on gravity-load columns.

Once the complete deformation profile of the shear walls has been defined, including the influence of flexural deformations, shear deformations and foundation rotation, an analysis must be done to determine the deformation demands on the gravity-load columns. A simple analysis procedure was developed to determine the deformation demands on gravity-load columns when the floor systems consist of flat plate slabs or the out-of-plane bending stiffness of the floor systems can be ignored for simplicity. The sections below elaborate on each of the three main contributions of this study.

8.2 Shear Strains in Plastic Hinge Region of Flexural Shear Walls

Experiments on flexural shear walls by other researchers have shown that although shear deformations constitute only a small portion of the top wall displacement, their contribution to the wall deformation profile within the plastic hinge zone is significant compared to flexural deformations. Therefore, shear deformations are critical to determining curvature demands on gravity-load columns in shear wall buildings as they substantially increase the building deformation profile in the wall plastic hinge region.

Despite the previous work on verification of the Modified Compression Field Theory (MCFT) and finite element program VecTor2, which uses the MCFT, for the prediction of wall stiffness, strength, hysteretic behaviour, and mode of failure, the accuracy of VecTor2 in predicting shear strains in the plastic hinge region of flexural walls had not previously been verified. Thus it was done as part of the current study by comparing predictions of VecTor2 with the results of large-scale tests.

The mechanisms leading to large shear strains in flexural walls were examined using VecTor2. Shear strain was found to be concentrated in areas with large vertical tensile strains in the presence of flexural-shear cracks. This was consistent with experimental evidence in the literature and further verified by VecTor2. The plane sections remain plane assumption was found to be valid in the wall plastic hinge zone resulting in vertical strains varying linearly over the wall length. Horizontal strains were found to be near zero and therefore negligible. Shear stresses were zero on the portion of the wall cross-section under tension where shear strains were the largest. Shear stresses were at their maximum on the compression side where shear strains were virtually zero. This observation confirmed that shear strains in flexural shear walls are not a consequence of shear stresses.

Based on these observations, a simple model was developed to estimate shear strain profile within the plastic hinge regions of flexural shear walls using an average vertical strain and an average strain angle. Average vertical strain is estimated from concrete compression depth and wall curvature assuming linear variation of vertical strains across the wall length. A parametric study was conducted to examine the effect of parameters such as wall compressive axial load, vertical steel ratio, wall length, wall aspect ratio, and the number of slabs crossing the plastic hinge zone on the strain angle. None of the parameters were found to critically influence the strain angle and hence, an empirically derived strain angle of 75° was proposed. The proposed model was then used to predict shear strains observed in experiments on flexural shear walls by other researchers and found to be very accurate despite its simplicity and using only basic information available to structural designers.

8.3 Rotation of Shear Wall Foundations

Rotation of shear wall foundations results in an increase in the wall lateral deformation profile which affects the curvature demands on the gravity-load columns. Behaviour of shear walls accounting for foundation rotation was studied through a total of about 2000 Nonlinear Time-History Analysis (NTHA).

Soil properties such as type, stiffness, and ultimate bearing capacity were shown to influence foundation rotation and permanent deformations of the wall; however, the top wall displacement was found to be much less sensitive to the input soil properties than the soil compressive displacement. As the soil became weaker and softer, foundation rotation stopped increasing while permanent soil compressive deformations kept increasing. The percentage increase in top wall displacement due to foundation rotation was shown to be larger for shorter height walls. Foundations bearing a smaller vertical load were shown to be less susceptible to foundation rotation as a larger foundation size was needed to achieve a certain overturning capacity than more heavily loaded foundations.

A comprehensive study was conducted on five different 10-story shear wall buildings, where each building had five different size foundations designed on each one of five different soil types. Each combination of building (shear walls) – soil type – foundation size was subjected to 10 ground motions and the results are reported systematically in Appendix A. This valuable data was used here to develop important conclusions that are needed to determine the demands on gravity-load columns, and was also used to develop significant changes to the foundation requirements of the 2015 Canadian building code (Adebar et al. 2014).

Analysis of the results from the comprehensive study revealed that the wall bending strength relative to the foundation overturning strength can be used to explain the fundamentals of the wall-foundation system behaviour. In wall-foundation systems where the foundation is stronger than the wall (hinging shear walls), the maximum bending moment induced in the system is equal to the wall bending strength. In systems with a strong wall and a relatively weak foundation (non-hinging shear walls), the maximum system bending moment is governed by the foundation overturning capacity. Inter-storey drift profile of hinging shear walls was closer to that of a fixed-base wall while for non-hinging walls, large foundation rotation and relatively small wall flexural deformation caused the inter-storey profile to be generally larger and closer to being constant over the building height. Softening of the soil in compression and separation between the footing and the underlying soil caused the effective system period of vibration to increase. The shift in the effective system period was larger for non-hinging shear walls as larger foundation rotation resulted in more softening of the foundation response. In general, accounting for foundation rotation was shown to reduce force demands on the shear wall. However, bending moment demands were reduced more than shear force demands and in some cases, the shear force demand was higher than that of the fixed-base wall. Hinging shear walls experienced smaller soil compressive displacements underneath their foundation as hinging of the wall limited the amount of bending moment resisted by the foundation. The shape of the maximum soil displacement profile underneath the foundation was found to have a significant effect on the amount of foundation rotation and was found to be sensitive to the shape of the backbone curve of the soil springs in compression.

Since the nonlinear behaviour of the foundation could best be represented by its moment-rotation response, a simple step-by-step method for obtaining the monotonic foundation moment-rotation response was developed. The method applied the well-known equivalent rectangular stress block concept used in section analysis of reinforced concrete members to represent the soil bearing pressure distribution underneath the foundation. The method uses only basic information available to the designer and is simple enough for implementation in a design office.

Results from the extensive NTHA carried out on shear walls considering foundation rotation were then used to formulate a procedure for estimating foundation rotation in a given wall-foundation system. Effective stiffness of an elastic rotational spring was calibrated to give a good estimate of the top wall displacement through Response Spectrum Analysis (RSA) when placed at the base of an elastic model of the wall. With the top displacement known, a method for estimating the elastic portion of the top displacement was then formulated taking into account the relative strengths of the wall and the foundation. Using the foundation moment-rotation response obtained earlier and comparing the wall bending strength to the foundation overturning strength, a comprehensive rational method for estimating maximum foundation rotation was developed which is simple enough to be used by structural engineers.

8.4 Deformation Demands on Gravity-load Columns

An investigation confirmed that shear strains are usually very small in gravity-load columns; therefore, the horizontal displacement demands on gravity-load columns will cause primarily flexural deformations of the columns. Moment-curvature relationships for the columns and an assumed plastic hinge model were used to model the flexural behaviour of the columns.

To better understand the flexural behaviour of columns, moment-curvature response of a broad range of column cross-sections with various section aspect ratios, concrete strengths, vertical steel ratios and axial loads were studied. It was found that for a given concrete strength, steel ratio, and axial load as a ratio of the section's factored axial capacity, the shape of the normalized non-dimensional moment-curvature response was independent of the cross-section size. In addition, a fifth-order polynomial was found to fit the shape with excellent accuracy which was then used in the developed nonlinear structural analysis algorithm.

Damage of the column cross section in the form of concrete cover spalling and loss of vertical steel due to buckling and fracture was shown to reduce the section's ultimate bending strength without severely affecting the curvature capacity. Accounting for long-term effects of the sustained axial load was shown not to have a significant effect on the moment-curvature response of the column as seismic load demands on the column are not sustained loads. Ignoring the vertical steel in estimating the ultimate concrete compression depth of columns was shown to give upper-bound estimates of the actual compression depth which is conservative when curvature capacity of the section is concerned given a fixed maximum permissible concrete compressive strain.

A structural analysis algorithm was developed specifically for assessing curvature demands on gravity-load columns of shear wall buildings where the out-of-plane bending stiffness of the floor systems is ignored. Both flexural and shear deformations were considered to obtain the wall deformation profile used as an input to the structural analysis algorithm. Wall inelastic curvatures were assumed to vary linearly over the wall plastic hinge length. Shear strain profile of the wall was assumed to have a shape similar to the wall curvature profile. Plastic hinging of the column was incorporated into the structural analysis by assuming certain curvature distribution patterns over the column plastic hinge zone consistent with observations made in tests by other researchers. It was shown that an accurate estimate of the column curvature demand in the plastic hinge region of shear wall buildings could be obtained by imposing the displacements of as few as three floor slabs on the column. The accuracy of the structural analysis algorithm was verified using state-of-the-art numerical modeling tools for reinforced concrete structures.

A parametric study was conducted to evaluate the influence of various wall and column parameters on curvature demand on columns in the plastic hinge region of shear wall buildings with flat plate floor slabs. It was shown that in the absence of wall shear strain, curvature profiles of the wall and the column remained similar and that curvature demand of the column was always close to maximum wall curvature. Column curvature demand exceeded maximum wall curvature when plastic hinging occurred in the column. Based on tests by other researchers on gravity-load columns under combined compression and bending, columns fail shortly after the formation of a plastic hinge at the base of the column. This was further confirmed analytically as the column curvature demand reached the column curvature capacity soon after the plastic hinge occurred at the base of the column.

Wall shear strain significantly added to the displacement at the second floor slab level. This additional displacement imposed an extra rotation demand on the column which caused column curvature demand to increase and be significantly larger than the wall maximum curvature. Simple design-oriented methods were proposed for estimating curvature demand in columns under imposed wall deformations with significant wall shear strain. The effect of wall foundation rotation on column curvature demand is very similar to that of wall shear strain as rotation of the wall foundation also imposes additional rotation demand on the column causing curvature concentration at the column base. Simple expressions were also developed for estimating column curvature demand due to rotation of the shear wall foundation.

At a given average compressive axial stress on the column, columns with smaller cross-sectional lengths were shown to have larger curvature capacities. Column curvature demand at a given building drift was shown to decrease with an increase in the height of the wall plastic hinge as walls with larger plastic hinge lengths distribute inelastic curvatures over a larger height bending the column more gradually within the wall plastic hinge zone. Height of the column plastic hinge hand did not seem to have a significant effect on the building drift at which column curvature capacity was reached. Gravity-load columns are heavily loaded in compression and the difference between curvature at peak bending strength (i.e. point of formation of a plastic hinge in the column) and curvature capacity governed by concrete crushing is small. This resulted in the column to have very little ductility beyond the point of formation of a plastic hinge.

Damage of the column in the form of loss of concrete cover and buckling or fracturing of the vertical reinforcing steel was found to cause further concentration of curvature in the column's damaged region increasing column curvature demand. Simple design-oriented equations were formulated to estimate column curvature demand considering curvature concentration due to damage of the column cross-section.

Presence of a taller first storey was found to either increase or decrease curvature demand of the column depending on the level of shear strain in the wall. At lower wall shear strains, presence of a taller storey increased column curvature demand at a given global drift and vice versa. Fixity of the column at grade level against rotation was found to have a significant effect on column curvature profile. Maximum column curvature occurred at the second floor slab when the wall had minimal shear strain, while for all other cases, maximum column curvature always occurred at grade level.

Members framing into the column were shown to potentially increase column curvature demands near the top of the building where inter-storey drifts are the highest. Simple formulas were developed for estimating curvature demand and additional compressive axial load on the column due to framing action of members framing into the column. The expressions developed serve as a useful decision-making tool on the significance of framing action in a given shear wall building.

8.5 Recommendations for Future Work

The first of the three parts of this thesis, on shear strains in the plastic hinge regions of flexural walls, was completed to the point that there is no obvious additional work needed. On the other hand, the second part of this thesis, on rotation of foundations, is such a large topic that all possible questions could not have been answered if that had been the only topic of this thesis. In order to complete the other two parts of this thesis, the study on foundation rotation had to have a very limited scope.

The majority of the nonlinear analyses were done on 10-storey shear walls because they were found to be more susceptible to foundation rotation than taller walls. Studying foundation rotation of shear walls of different heights is a natural extension to this research. Additional work is also needed on buildings with different mass ratios and using different soil characteristics and different nonlinear soil models.

The effective stiffness of the elastic rotational spring used at the base of an elastic model of the wall to estimate top wall displacement accounting for foundation rotation presented in Section 4.2 was fitted to data gathered from 10-storey buildings only. Thus a similar study on other height walls would be a good continuation of this work and will further expand the rational method proposed for estimating foundation rotation.

All nonlinear analyses were done in a 2D space so extending the work to 3D is another obvious follow-up to this research. Rotation of a shear wall's foundation could be studied in a 3D space with the ground motion applied in two orthogonal horizontal directions to study the simultaneous rotational behaviour of the foundation about two orthogonal axes.

Finally, the third part of this study was limited in scope to estimating curvature demands on columns in the plastic hinge region of shear walls with flat plate floor slabs. In such systems, faming action of the horizontal members framing into the column is negligible due to the low flexural stiffness of the flat plate floor slabs. Additional column curvature demands due to presence of stiff framing members such as beams or transfer girders are something that deserves additional study.

Bibliography

ABAQUS [Computer software], ABAQUS Inc., Providence, RI.

Adebar, P., Bazargani, P., and Chin, H. (2012). “Seismic Deformation Demands on Gravity-Load Columns in Shear Wall Buildings”, 15th World Conference on Earthquake Engineering, Lisbon, Portugal, 4615.

Adebar, P., Bazargani, P., Mutrie, J., and Mitchell, D. (2010). “Safety of Gravity-load Columns in Shear Wall Buildings Designed to Canadian Standard CSA A23.3”, Canadian Journal of Civil Engineering, 37(11): 1451-1461.

Adebar, P., DeVall, R., Bazargani, P., and D.L. Anderson (2014). “SEISMIC DESIGN OF FOUNDATIONS: THE 2015 CANADIAN BUILDING CODE”, Tenth U.S. National Conference on Earthquake Engineering, Anchorage, Alaska, USA.

Adebar, P., Mutrie, J., and DeVall, R. (2005). “Ductility of Concrete Walls: the Canadian Seismic Design Provisions 1984 to 2004”, Canadian Journal of Civil Engineering, 32(6): 1124-1137.

Algie, T. B. (2011). “Nonlinear Rotational Behaviour of Shallow Foundations on Cohesive Soil”, Doctoral Thesis, The University of Auckland, Department of Civil and Environmental Engineering, New Zealand.

Allotey, N., and El Naggar, M. H. (2003). “Analytical moment–rotation curves for rigid foundations based on a Winkler model”, Soil Dynamics and Earthquake Engineering, 23: 367–381.

Anastasopoulos, I., Gelagoti, F., Kourkoulis, R., and Gazetas, G. (2011). “Simplified Constitutive Model for Simulation of Cyclic Response of Shallow Foundations: Validation against Laboratory Tests”, J. Geotech. Geoenviron. Eng., 137:1154-1168.

Anderson, D. L. (2003). “Effect of Foundation Rocking on the Seismic Response of Shear Walls”, Canadian Journal of Civil Engineering, 30(2): 360-365.

Atkinson, G. M. (2009). “Earthquake time histories compatible with the 2005 National building code of Canada uniform hazard spectrum”, Canadian Journal of Civil Engineering, 36(6): 991-1000.

Bae, S., and Bayrak, O. (2008). “Plastic Hinge Length of Reinforced Concrete Columns”, ACI Structural Journal, 105(3):290-300.

Bae, S., and Bayrak, O. (2003). “Early Cover Spalling in High-Strength Concrete Column”, Journal of Structural Engineering, 129(3): 314–323.

Bazargani, P., and Adebar, P. (2010). “Estimating Seismic Demands on Gravity-Load Columns in Concrete Shear Wall Buildings.” Proceedings of the 9th U.S. National and 10th Canadian Conference on Earthquake Engineering, Toronto, ON, 1011.

Bazargani, P., and Adebar, P. (2014), “Interstory drifts from shear strains at base of high-rise concrete shear walls”, submitted to ASCE Journal of Structural Engineering, February 2014.

Bentz, E.C. (2000). “Sectional Analysis of Reinforced Concrete”, PhD Thesis, Department of Civil Engineering, University of Toronto.

Beyer, K., Dazio, A., and Priestley, M. J. N. (2011). “Shear Deformations of Slender Reinforced Concrete Walls under Seismic Loading”, ACI Structural Journal, V. 108(2): 167-177.

Beyer, K., Dazio, A., and Priestley, M. J. N. (2008). “Quasi-Static Cyclic Tests of Two U Shaped Reinforced Concrete Walls”, Journal of Earthquake Engineering, 12:1023–1053.

Bohl, A. (2006). “PLASTIC HINGE LENGTH IN HIGH-RISE CONCRETE SHEAR WALLS”, Master’s Thesis, The University of British Columbia, Vancouver, Canada.

Bohl, A. and Adebar, P. (2011). “Plastic Hinge Lengths in High-Rise Concrete Shear Walls”, ACI Structural Journal, 108(2): 148-157.

Brueggen, B. L. (2009). “Performance of T-shaped Reinforced Concrete Structural Walls under Multi-Directional Loading”, Doctoral dissertation, The University of Minesota.

Chopra, A. K. (2007). “Dynamics of Structures - Theory and Applications to Earthquake Engineering”, 3rd edition, Upper Saddle River, NJ, USA, ISBN 0-13-156174-X.

Collins, M.P. and Mitchell, D. (1991). “Prestressed Concrete Structures”, Prentice-Hall 1991, pp 760.

Collins, M. P., and Mitchell, D. (1977). “Prestressed Concrete Structures”, Response Publications, Toronto, ON, Canada, 1997, 766.

CSA Committee A23.3 “Design of Concrete Structures: Structures (Design) – A National Standard of Canada” Canadian Standards Association 2004, Rexdale, Canada.

Das, B. M. (2002). “Principles of Geotechnical Engineering”, fifth edition, Brooks/Cole, Pacific Grove, CA, USA, ISBN 0-534-38742-X, pp 262-312.

Das, B. M. (1999). “Shallow Foundations – Bearing Capacity and Settlement”, CRC Press, Boca Raton, Florida, USA, ISBN 0-8493-1135-7, pp 104.

Das, B.M. (1983). “Fundamentals of soil dynamics”. Elsevier, New York, N.Y.

Dazio, A., Wenk, T., and Bachmann, H. (1999). “Tests on RC Structural Walls under Cyclic-Static Action”, IBK Report No. 239, ETH, Zurich.

Dezhdar, E. (2012). “SEISMIC RESPONSE OF CANTILEVER SHEAR WALL BUILDINGS”, Doctoral Thesis, The University of British Columbia, Vancouver, BC, Canada.

Dobry, R., and Gazetas, G. (1986). "Dynamic response of arbitrarily shaped foundations", J. Geotech. Engrg., ASCE, 112(2):109-135.

Dobry, R., Gazetas, G., and Stokoe, K. H. (1986). "Dynamic response of arbitrarily shaped foundations: Experimental verification", J. Geotech. Engrg., ASCE, 112(2):136-149.

FEMA 273, “NEHRP Guidelines for the Seismic Rehabilitation of Buildings”, prepared for Building Seismic Safety Council by the Applied Technology Council (ATC-33 project), Washington, D.C., USA.

FEMA 274, “NEHRP Commentary on Guidelines for the Seismic Rehabilitation of Buildings”, prepared for Building Seismic Safety Council by the Applied Technology Council (ATC-33 project), Washington, D.C., USA.

FEMA 356, “Prestandard and Commentary for the Seismic Rehabilitation of Buildings. Applied Technology Council”. prepared for Federal Emergency Management Agency by American Society of Civil Engineers, Washington, D.C., USA.

FEMA 440, “Improvement of Nonlinear Static Seismic Analysis Procedures”, prepared for the Department of Homeland Security Federal Emergency Management Agency by applied Technology Council (ATC-55 project), Washington, D.C., USA.

Figini, R., Paolucci, R., and Chatzigogos, C. T. (2011). “A macro-element model for non-linear soil–shallow foundation–structure interaction under seismic loads: theoretical development and experimental validation on large scale tests”, Earthquake Engng Struct. Dyn. 41:475–493.

Filiatrault, A., Anderson, D.L., and DeVall, R.H. (1992). “Effect of a weak foundation on the seismic response of core wall type buildings”, Canadian Journal of Civil Engineering, 19: 530-539.

Gajan, S., and Kutter, B. L. (2009a). “Contact interface model for shallow foundations subjected to combined cyclic loading”, Journal of Geotechnical and Geoenvironmental Engineering, 135(3): 407-419.

Gajan, S., and Kutter, B. L. (2009b). “Effects of Moment-to-Shear Ratio on Combined Cyclic Load-Displacement Behavior of Shallow Foundations from Centrifuge Experiments”, Journal of Geotechnical and Geoenvironmental Engineering, 135(8): 1044-1055.

Gajan, S., and Kutter, B. L. (2008). “Capacity, settlement, and energy dissipation of shallow footings subjected to rocking.” J. Geotech. Geoenviron. Eng., 134(8): 1129–1141.

Gazetas, G., and Stokoe, K. H. (1991). "Vibration of embedded foundations theory versus experiment", J. Geotech. Engrg., ASCE, 117(9): 1382-1401.

Gazetas, G. (1991). “FORMULAS AND CHARTS FOR IMPEDANCES OF SURFACE AND EMBEDDED FOUNDATIONS”, Journal of Geotechnical Engineering, 117(9): 1363-81.

Ghalibafian, H. (2006). “Evaluation of the effects of nonlinear soil-structure interaction on the inelastic seismic response of pile-supported bridge piers”, Doctoral Thesis, The University of British Columbia, Vancouver, BC, Canada.

Grange, S., Kotronis, P., and Mazars, J. (2008). “A macro-element for a circular foundation to simulate 3D soil-structure interaction”, International Journal for Numerical and Analytical Methods in Geomechanics 32:1205–1227.

Harden, C., Hutchinson, T., and Moore, M. (2006). “Investigation into the Effects of Foundation Uplift on Simplified Seismic Design Procedures”, Earthquake Spectra 22(3): 663–692.

Harden, C., Hutchinson, T., Martin, G. R., and Kutter, B. L. (2005). “Numerical modeling of the nonlinear cyclic response of shallow foundations”, PEER Report 2005/04, U.C., Berkeley.

Hines, E. M. (2002). “Seismic Performance of Hollow Rectangular Reinforced Concrete Bridge Piers with Confined Corner Elements”, Doctoral dissertation, University of California, San Diego, USA.

Housner, G. W. (1963). “The behaviour of inverted pendulum structures during earthquakes”, Bulletin of the Seismological Society of America, 53(2): 403-417.

Ibrahim, H. H. H., and MacGregor, J. G. (1996). “Tests of Eccentrically Loaded High-Strength Concrete Columns”, ACI Structural Journal, 93(5):1-10.

Koboevic, S., Le Bec, A., and Tremblay, R. (2010). “Seismic Behaviour of Reinforced Concrete Ductile Shear Walls on Rocking Foundations”, 14th ECEE conference, Ohrid, Macedonia.

Kramer, S. (1996). “Geotechnical Earthquake Engineering”, Prentice Hall, Upper Saddle River, N.J.

Le Bec, A. (2009). “Effects of rocking of shallow foundation on seismic response of reinforced concrete shear walls”, M.Sc. Thesis, CGM Dept., Ecole Polytechnique de Montréal, Montréal, QC (In French).

Légeron, F., and Paultre, P. (2000). “Behavior of High-Strength Concrete Columns under Cyclic Flexure and Constant Axial Load”, ACI Structural Journal, 97(4):591-601.

Lloyd, N. A., and Rangan, V. (1996). “Studies on High Strength Concrete Columns under Eccentric Compression”, ACI Structural Journal, 93(6): 631-638.

MATLAB & SIMULINK [Computer software], The MathWorks.

Meyerhof, G. G. (1953). “The bearing capacity of foundation under eccentric and inclined load”, proceedings of the third international conference on soil mechanics and foundation engineering, Zurich, Switzerland, 440.

National Research Council Canada. (2005). National Building Code of Canada. Canadian Commission on Building and Fire Codes, Institute for Research in Construction, Ottawa, Ontario.

Negro, P., Paolucci, R., Pedretti, S., and Faccioli, E. (2000). “Large-scale soil-structure interaction experiments on sand under cyclic loading”, Proceedings of the 12th World Conference on Earthquake Engineering, Auckland, New Zealand, paper # 1191.

Negro, P., Verzeletti, G., Molina, J., Pedretti, S., Lo Presti, D., and Pedroni, S. (1998). “Large-scale geotechnical experiments on soil–foundation interaction”, Special publication No. I.98.73, Ispra, Italy: Joint Research Center, European Commission.

Oesterle, R.G., Aristizabal-Ochoa, Shiu, K. N., and Corley, W.G. (1984). “Web crushing of reinforced concrete structural walls”, ACI Journal, May-June 1984, 231-241.

Oesterle, R.G., Aristizabal-Ochoa, J.D., Fiorato, A.E., Russell, H.G., and Corley, W.G. (1979). “Earthquake Resistant Structural Walls – Tests of Isolated Walls – Phase II”, Report to National Science Foundation, Portland Cement Association.

Oesterle, R.G., Fiorato, A.E., Johal, L. S., Carpenter, J. E., Russell, H.G., and Corley, W.G. (1976). “Earthquake Resistant Structural Walls – Tests of Isolated Walls”, Report to National Science Foundation, Portland Cement Association.

OpenSees [Computer software], Open System for Earthquake Engineering Simulation (OpenSees), Computer Program and Supporting Documentation, Pacific Engineering Research Centre, University of California, Berkeley [14 May 2008].

Ozbakkaloglu, T., and Saatcioglu, M. (2004). “Rectangular Stress Block for High Strength Concrete”, ACI Structural Journal, 110(4):475-483.

Palermo, D., and Vecchio, F. J. (2004). “Compression Field Modeling of Reinforced Concrete Subjected to Reversed Loading: Verification”, ACI Structural Journal, 101(2): 155-164.

Palermo, D., and Vecchio, F. J. (2004). “Simulation of Cyclically Loaded Concrete Structures Based on the Finite-Element Method”, Journal of Structural Engineering, 133(5):728-738.

Paolucci, R., di Prisco, C., Vecchiotti, M., Shirato, M., and Yilmaz, M.T. (2007). “SEISMIC BEHAVIOUR OF SHALLOW FOUNDATIONS: LARGE SCALE EXPERIMENTS VS. NUMERICAL MODELLING AND IMPLICATIONS FOR PERFORMANCE BASED

DESIGN", 1st US-Italy Seismic Bridge Workshop, European Center for Training and Research in Earthquake Engineering (EUCENTRE) in Pavia, Italy.

Park, R., and Paulay, T. (1975). "Reinforced Concrete Structures", John Wiley and Sons, New York.

Pender, M. J., Algie, T. B., Storie, L. B., and Salimath R. (2013). "Rocking controlled design of shallow foundations", NSEE 2013 Annual Conference, Florida, USA.

Popovics, S. (1973). "A numerical approach to the complete stress strain curve for concrete", Cement and concrete research, 3(5): 583-599.

Priestley, M. J. N., Evison, R. J., and Carr, A. J. (1978). "Seismic response of structures free to rock on their foundations", Bulleting of the New Zeland national society for earthquake engineering, 11(3): 141-150.

SAP2000 [Computer software], Computers and Structures Inc.

Shiu, K. N., Daniel, J. I., Aristizabal-Ochoa, J.D., Fiorato, A.E., and Corley, W.G. (1981). "Earthquake resistant structural walls – tests of walls with and without openings", Report to The National Science Foundation, Washington, D.C., USA.

Siddharthan, R. V., Ara, S., Norris, G.M. (1992). "Simple rigid plastic model for seismic tilting of rigid walls", J Struct Eng., ASCE, 118(2): 469–87.

Standards New Zealand (1976). "NZS 4203: Code of Practice for General Structural Design and Design Loadings for Buildings", Wellington, New Zealand.

Thomsen, J.H., and Wallace, J. W. (2004). "Displacement-Based Design of Slender Reinforced Concrete Structural Walls – Experimental Verification" Journal of Structural Engineering, 130(4): 618-630.

Thomsen, J. H., and Wallace, J. W. (1995). "Displacement-Based Design of RC Structural Walls: Experimental Studies of Walls with Rectangular and T-shaped Cross Sections", Report No.CU/CEE-95/96, Department of Civil and Environmental Engineering, Clarkson University, Potsdam, New York.

Ugalde, J. A., Kutter, B. L., and Jeremic, B. (2010). "Rocking Response of Bridges on Shallow Foundations", PEER Report 2010/101, U.C., Davis.

Vallenas, J. M., Bertero, V. V., and Popov, E. P. (1979). "Hysteretic behavior of reinforced concrete structural walls", Report No. UCB/EERC-79/20, University of California, Berkley, California, USA.

Vecchio, F. J., Lai, D., Shim, W., and Ng, J. (2001). “DISTURBED STRESS FIELD MODEL FOR REINFORCED CONCRETE: VALIDATION”, Journal of Structural Engineering, 127(4): 350-358.

Vecchio, F. J. (2000). “DISTURBED STRESS FIELD MODEL FOR REINFORCED CONCRETE: FORMULATION”, Journal of Structural Engineering, 126(9): 1070-1077.

Vecchio, F. J., and Collins, M. P. (1986). ‘‘The modified compression field theory for reinforced concrete elements subjected to shear.’’ ACI J., 83(2): 219–231.

VecTor2, VecTor Analysis Group, Department of Civil Engineering, University of Toronto, Toronto, ON, Canada. http://www.civ.utoronto.ca/vector/

Veletsos, A.S., and Wei, Y.T. (1971). “Lateral and rocking vibration of footings”, ASCE Journal of the Soil Mechanics and Foundations Division, 97(9): 1227–1248.

Wang, T. Y., Bertero, V. V., and Popov, E. P. (1975). “Hysteretic behavior of reinforced concrete framed walls”, Report No. EERC 75-23, University of California, Berkley, California, USA.

Wijewickreme, D. (2012), Personal communication, February.

Wong, P. S. and Vecchio, F. J. (2002). “VECTOR2 & FORMWORKS USER’S MANUAL”. http://www.civ.utoronto.ca/vector/

Appendix A Rotation of Shear Wall Foundations

A.1 Input Ground Accelerations

Original (un-scaled), spectrally-matched, and uniformly-scaled ground motion records used in the NTHA are given below.

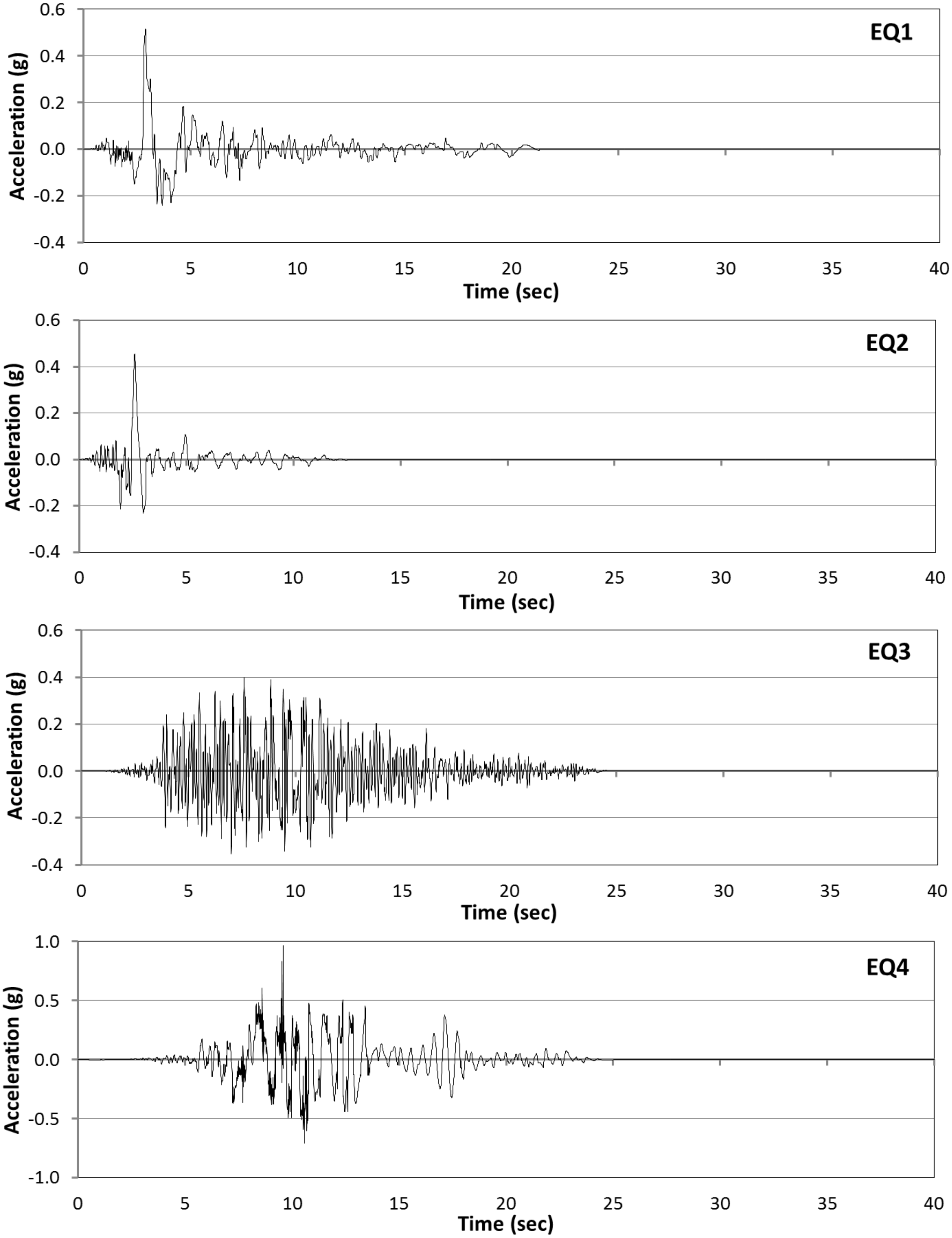

Figure A.1 Original (un-scaled) input ground accelerations

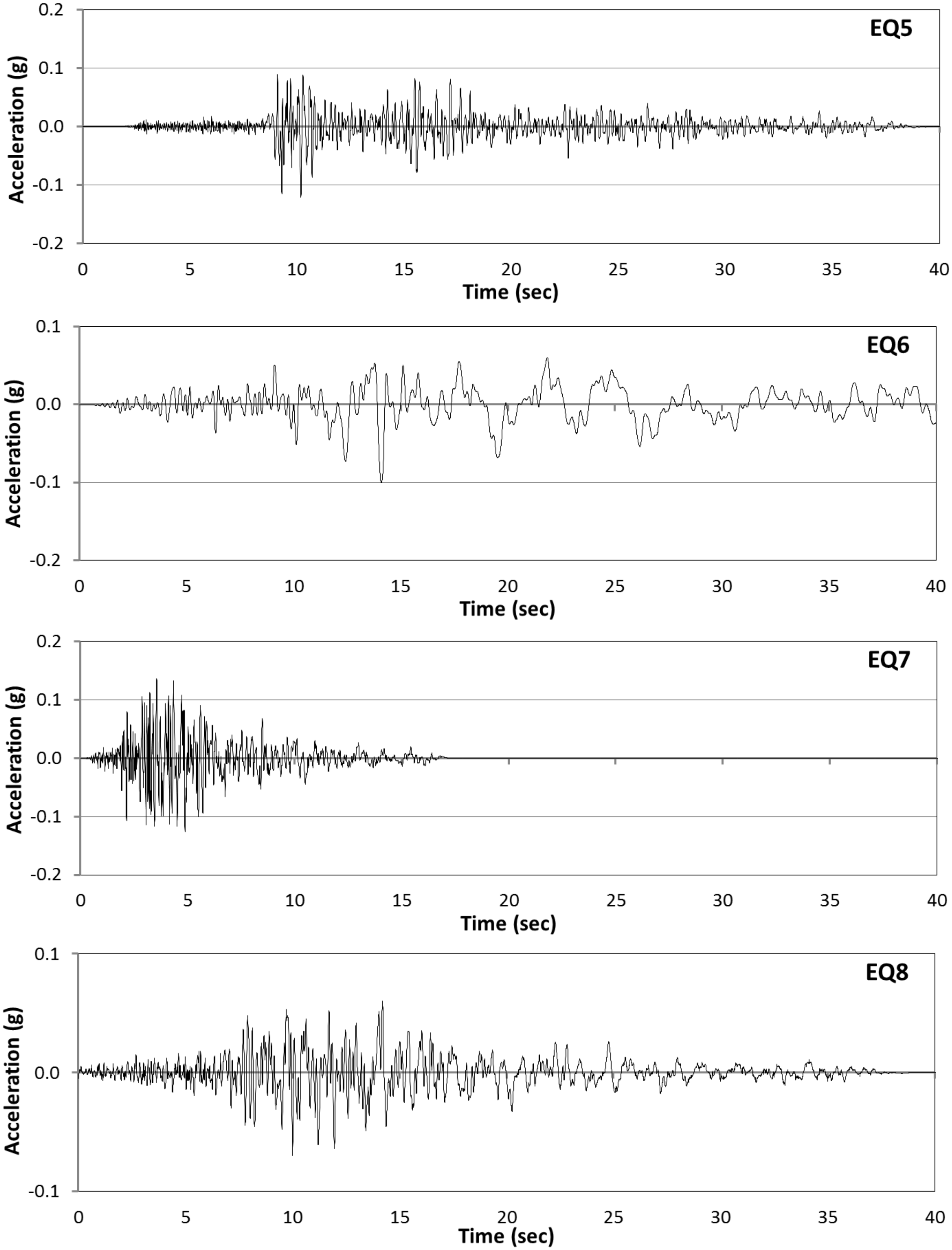

Figure A.1 (continued)

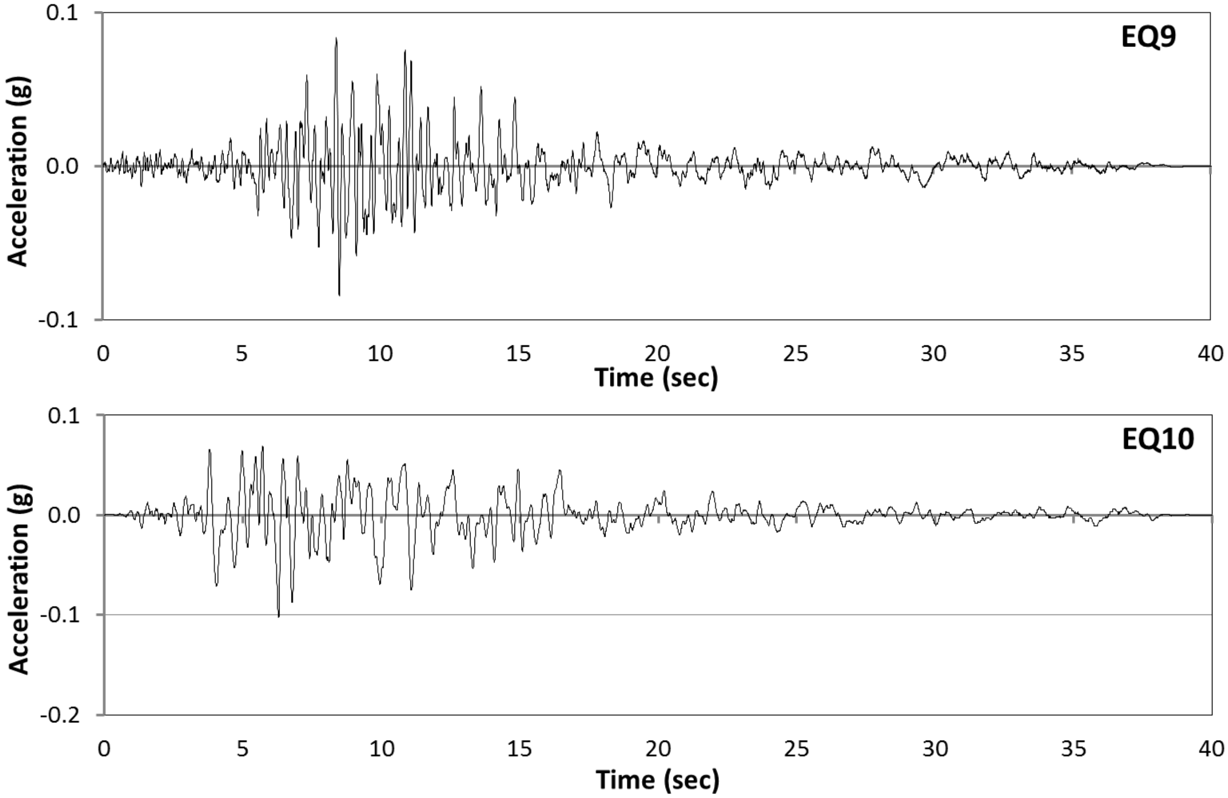

Figure A.1 (continued)

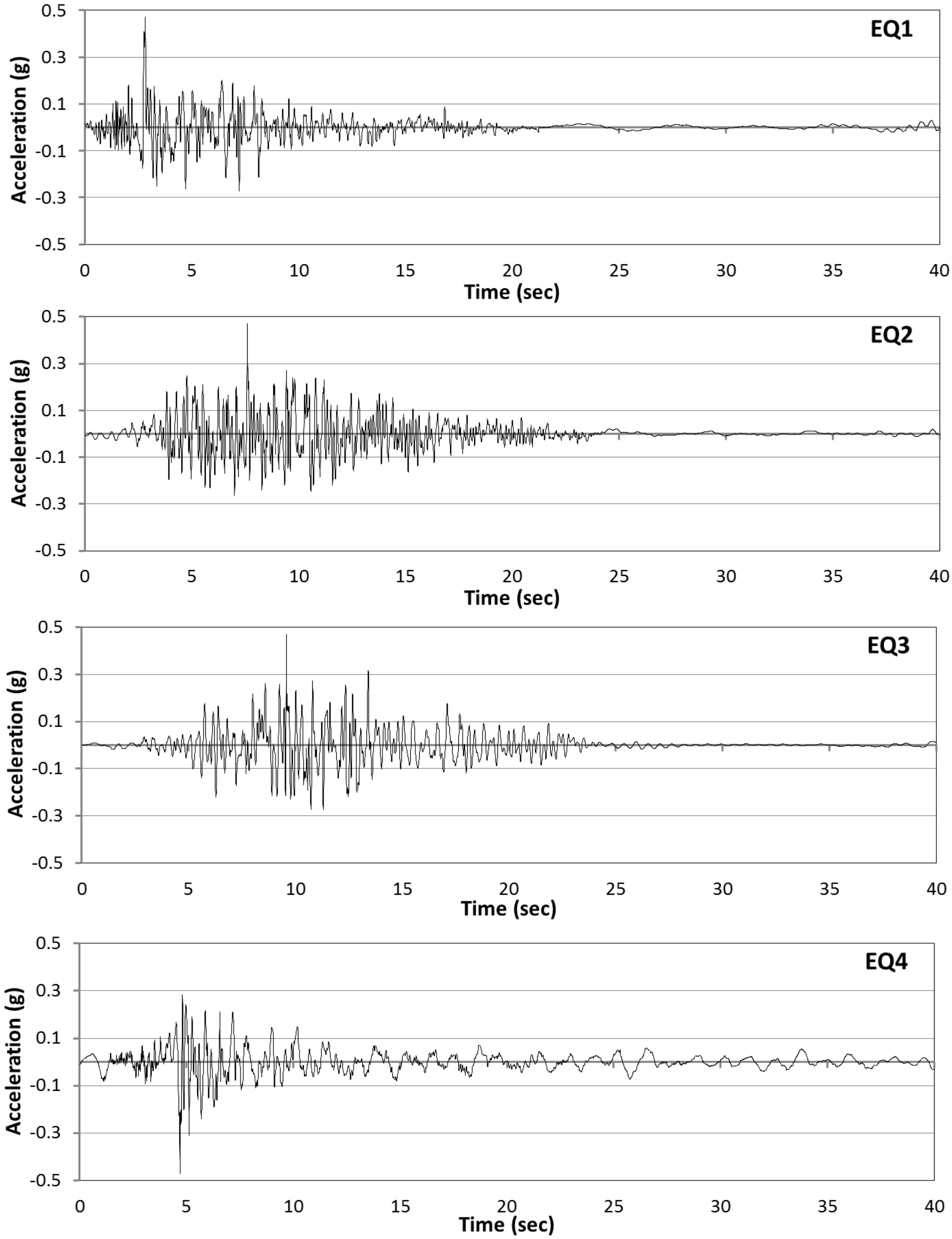

Figure A.2 Input ground accelerations modified to match the target response spectrum throughout the entire range of vibration periods

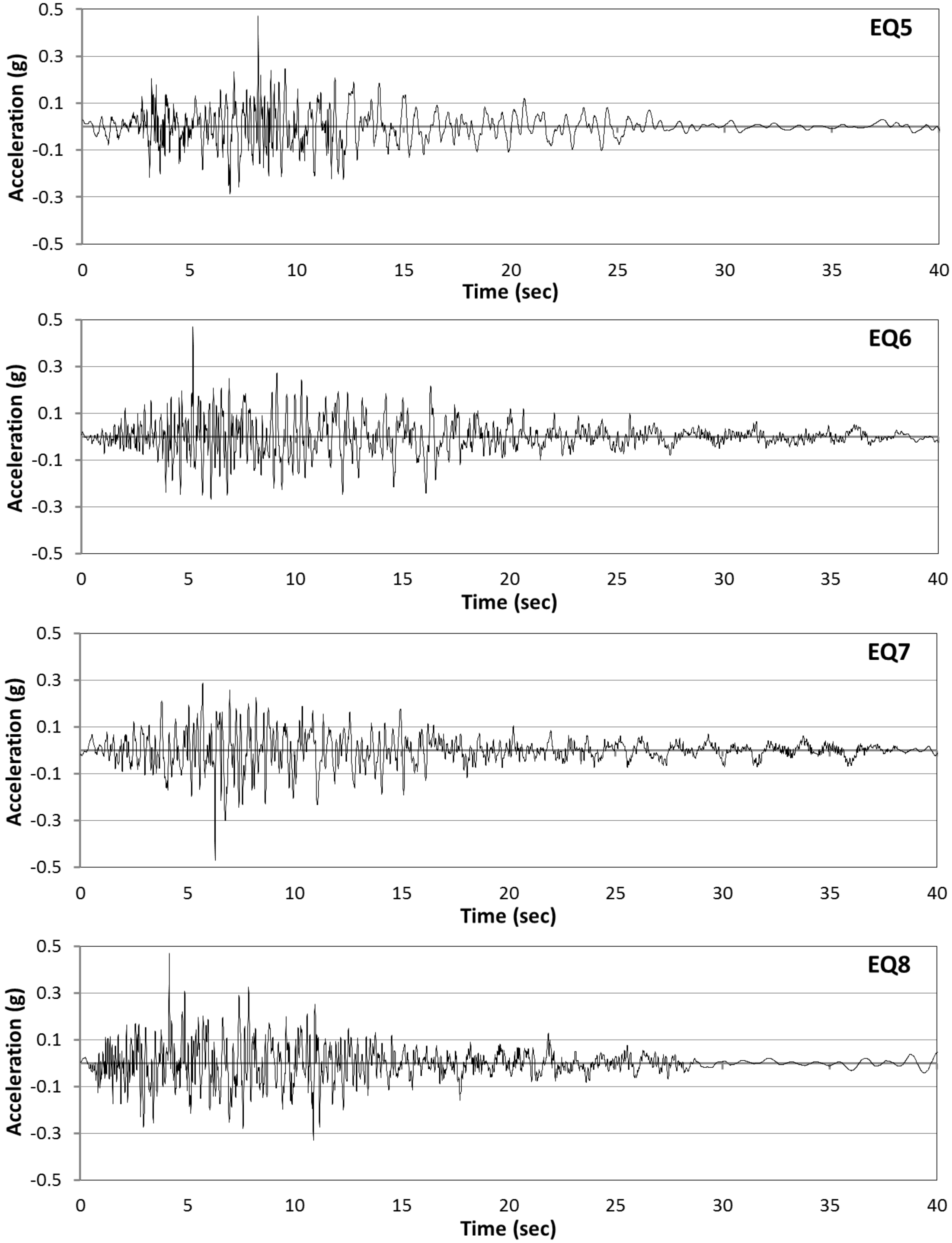

Figure A.2 (continued)

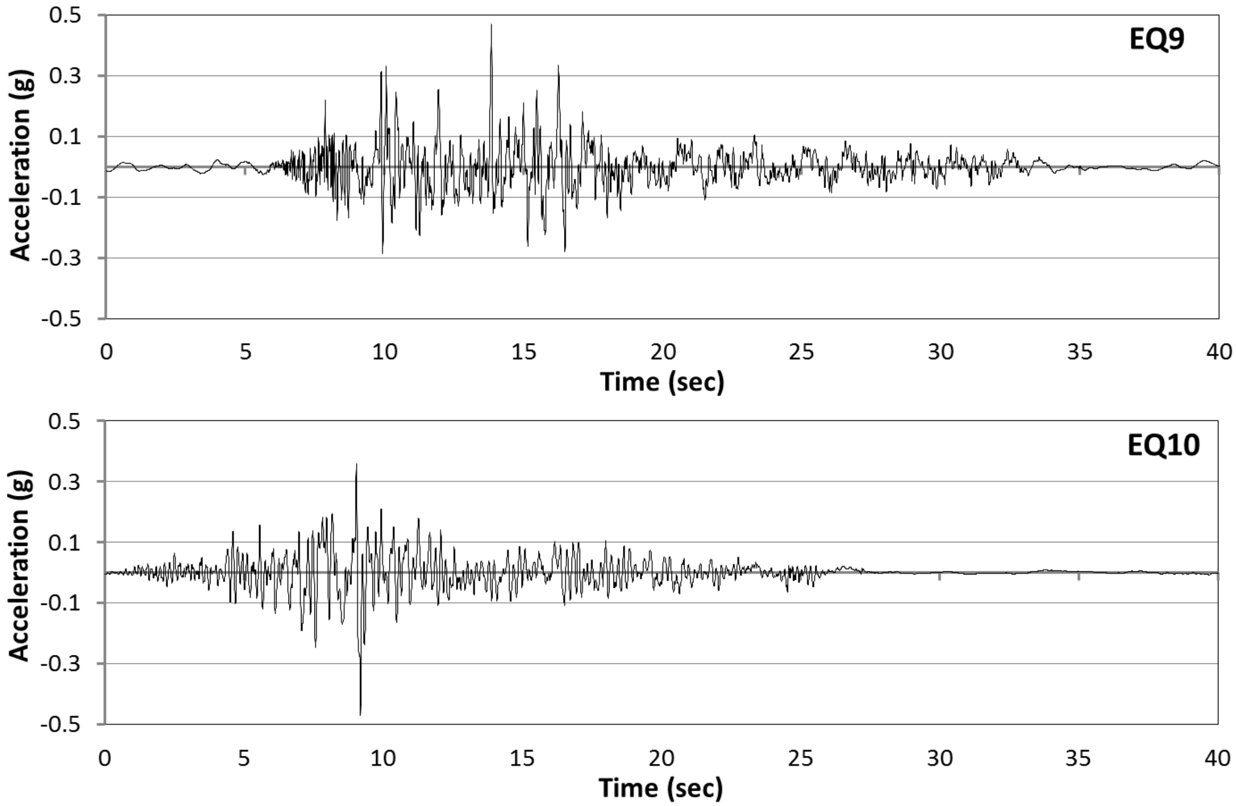

Figure A.2 (continued)

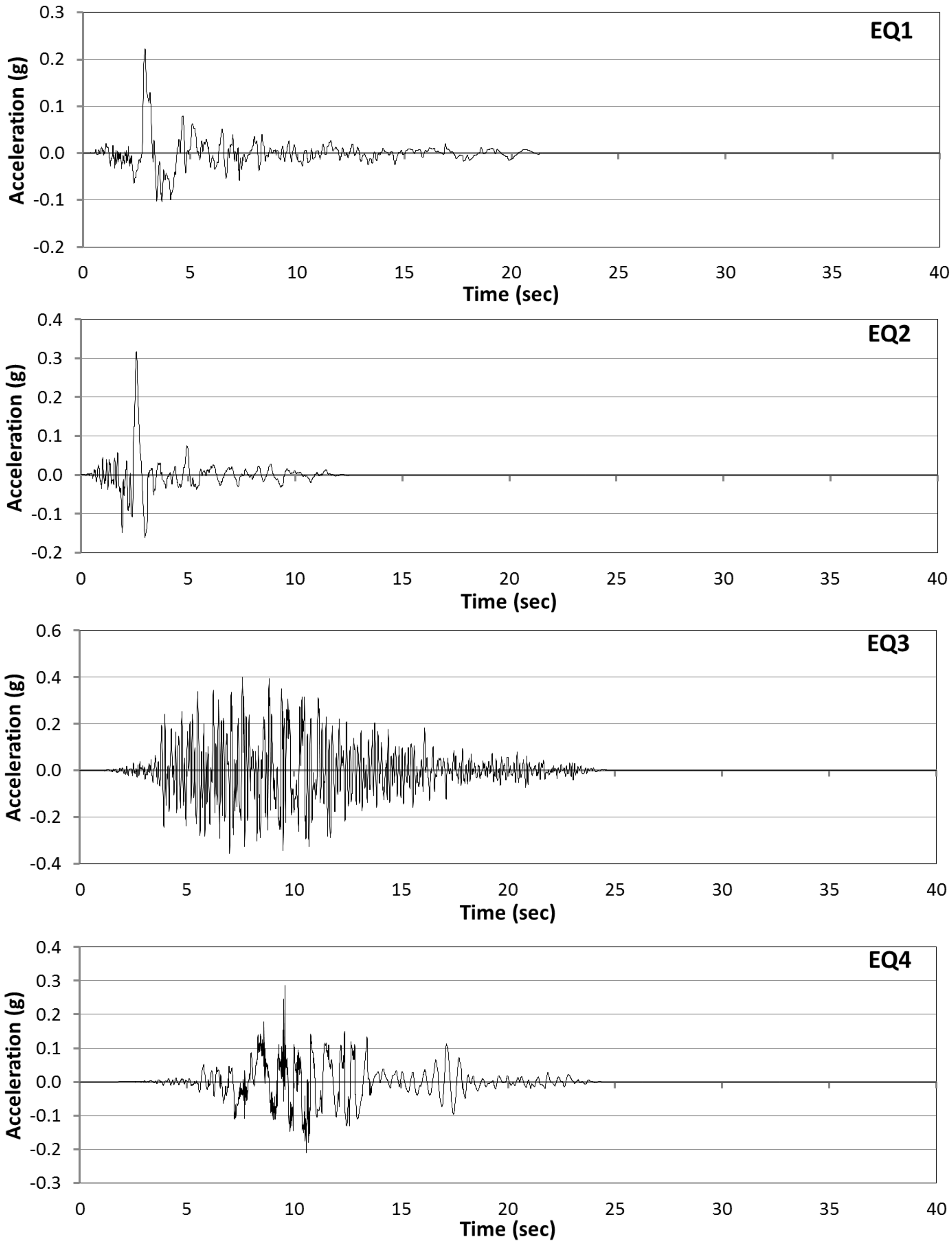

Figure A.3 Input ground motions uniformly-scaled to achieve best match to the target response spectrum between vibration periods of 0.5 sec and 2.5 sec

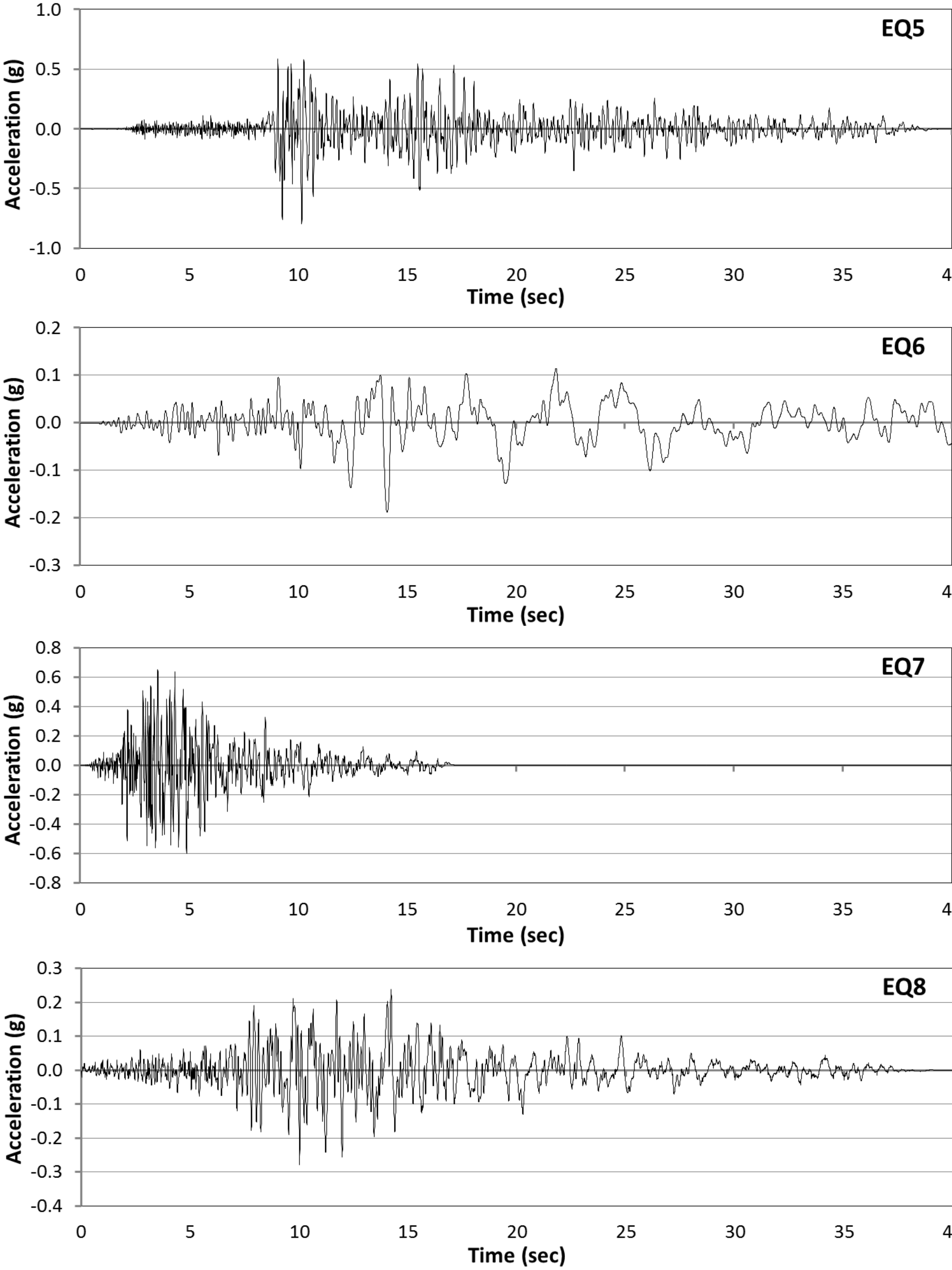

Figure A.3 (continued)

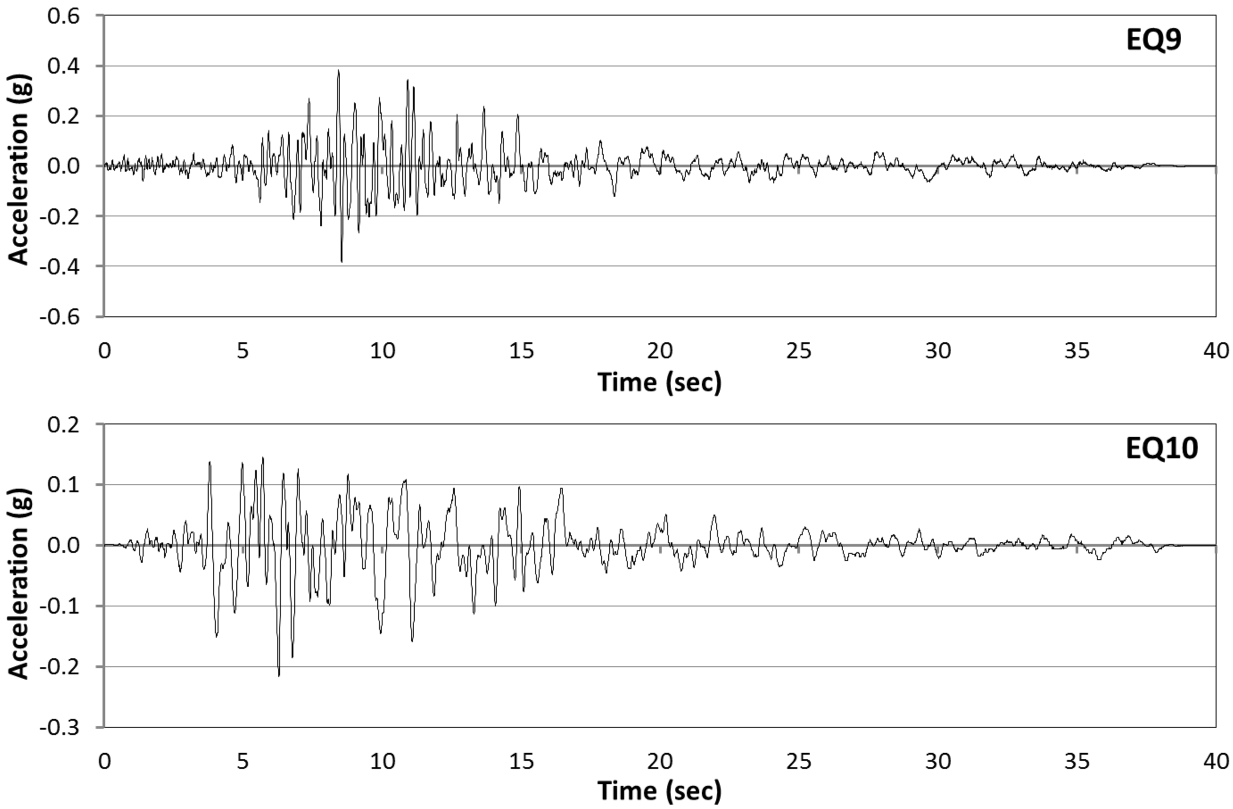

Figure A.3 (continued)

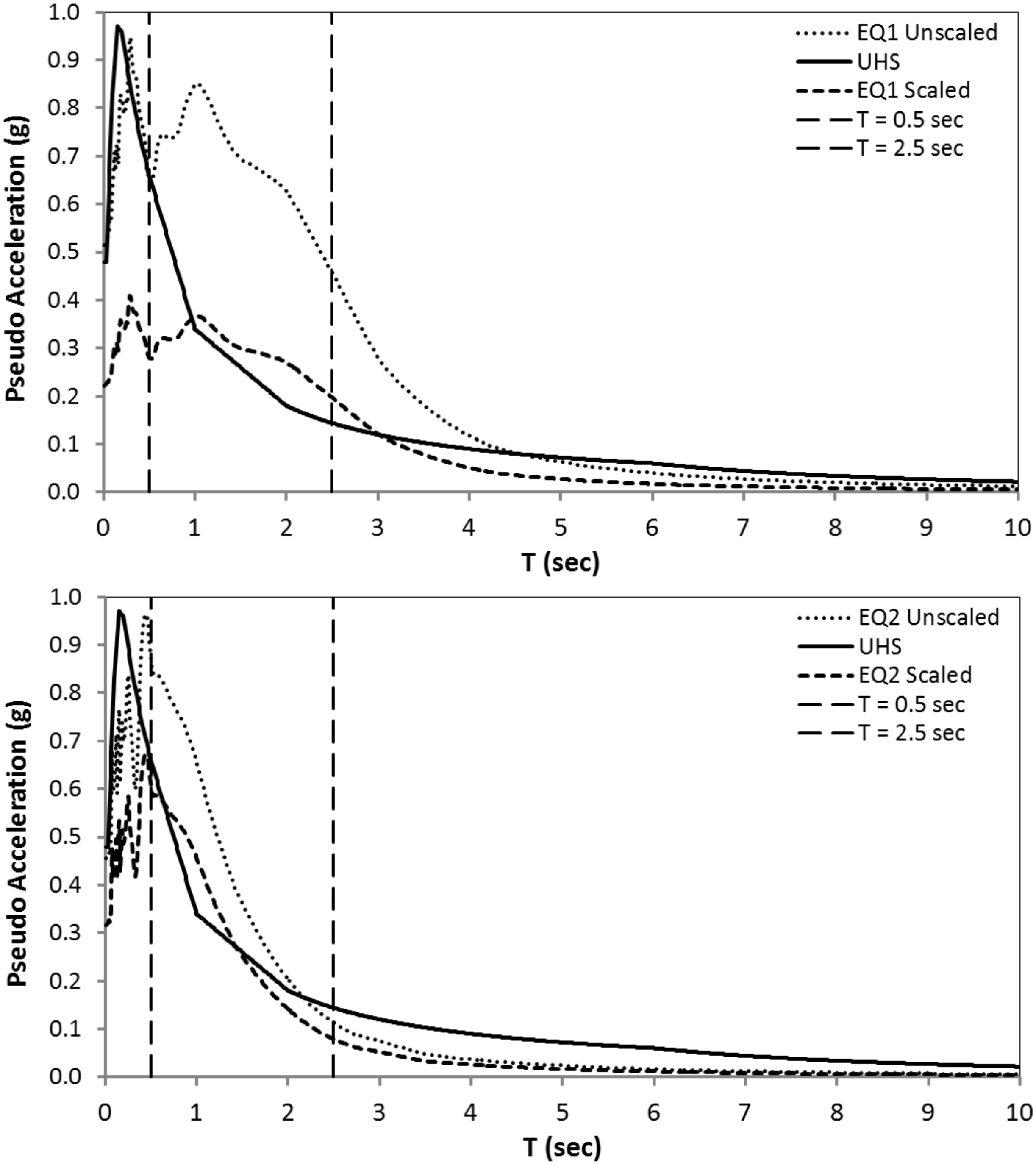

Figure A.4 Response spectra of original (un-scaled) input ground motions and accuracy of uniformly-scaled input ground motions

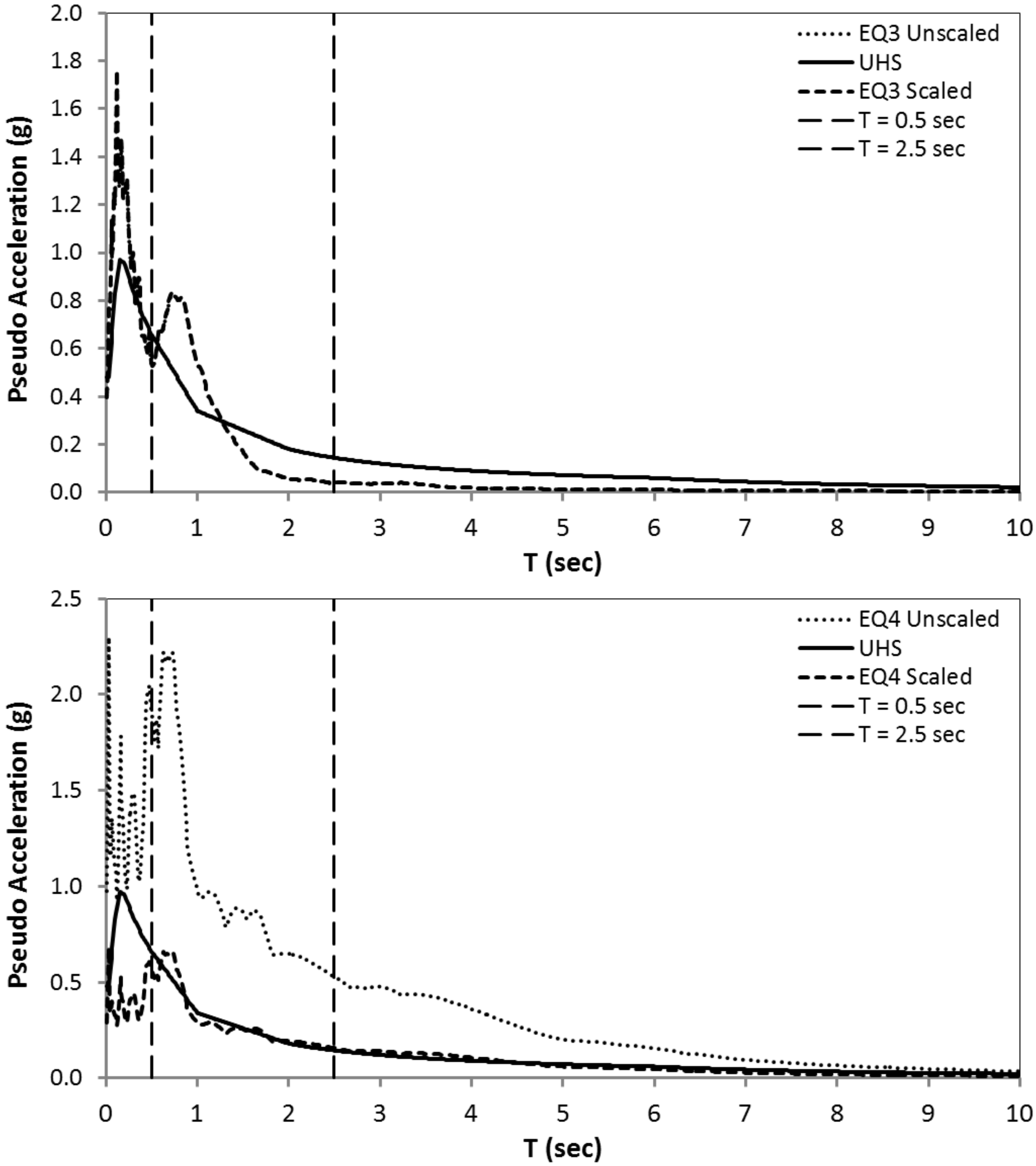

Figure A.4 (continued)

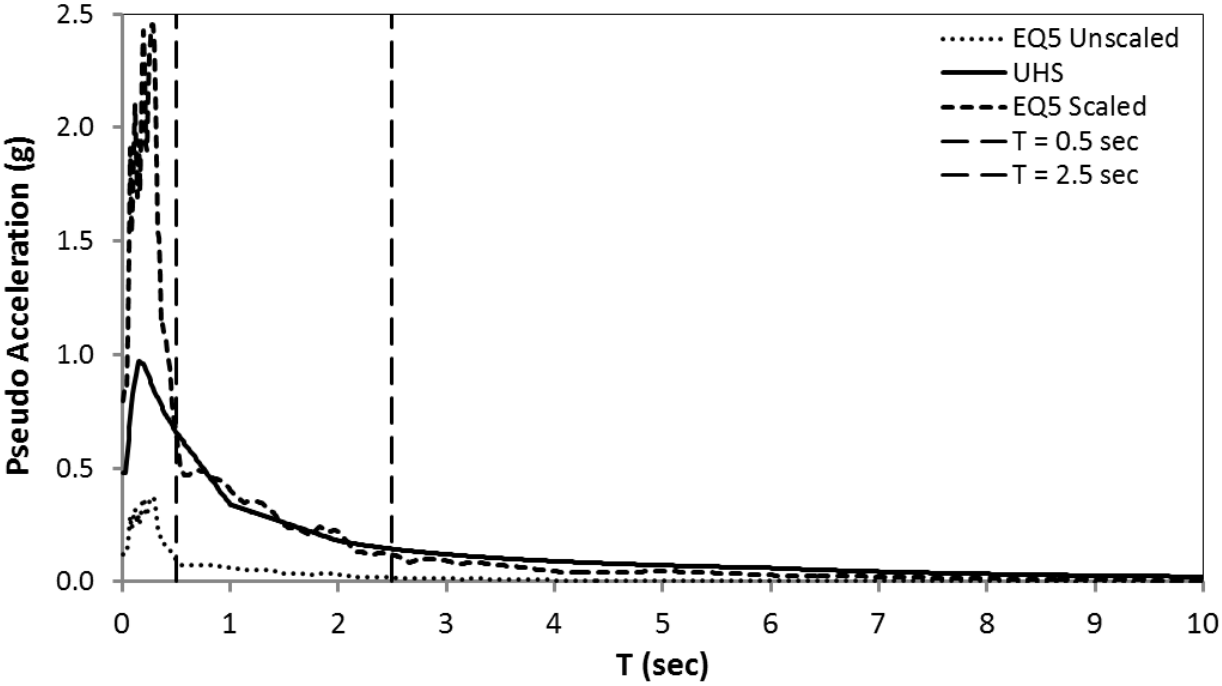

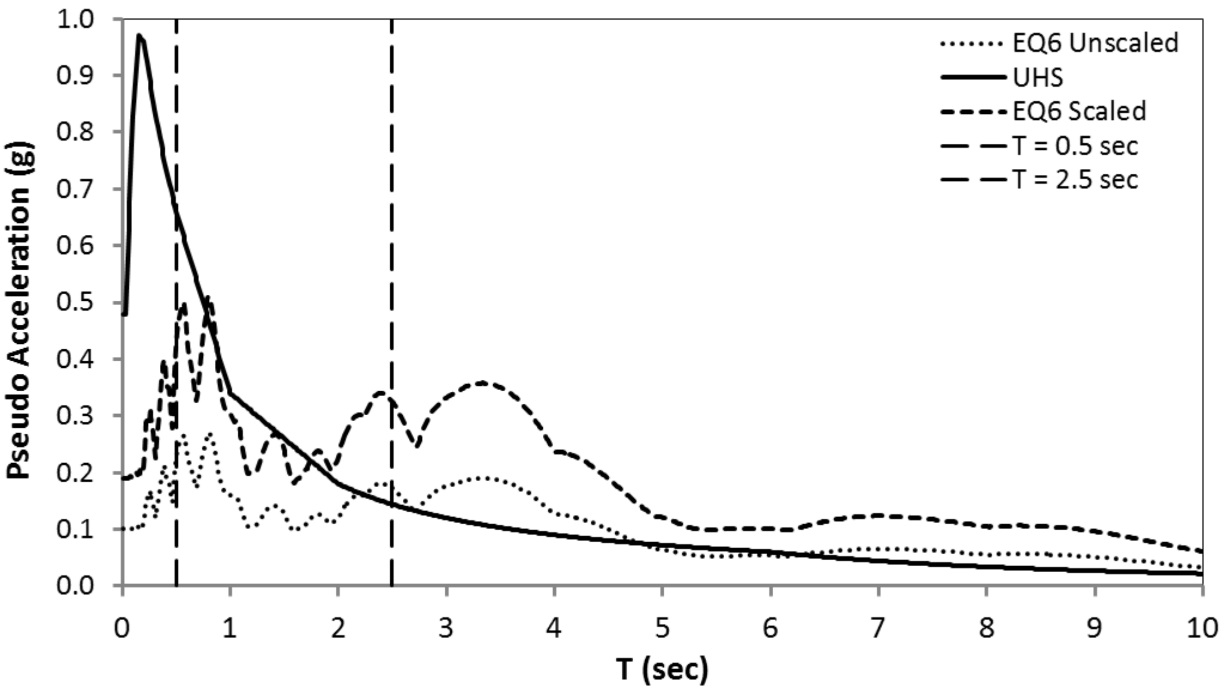

Figure A.4 (continued)

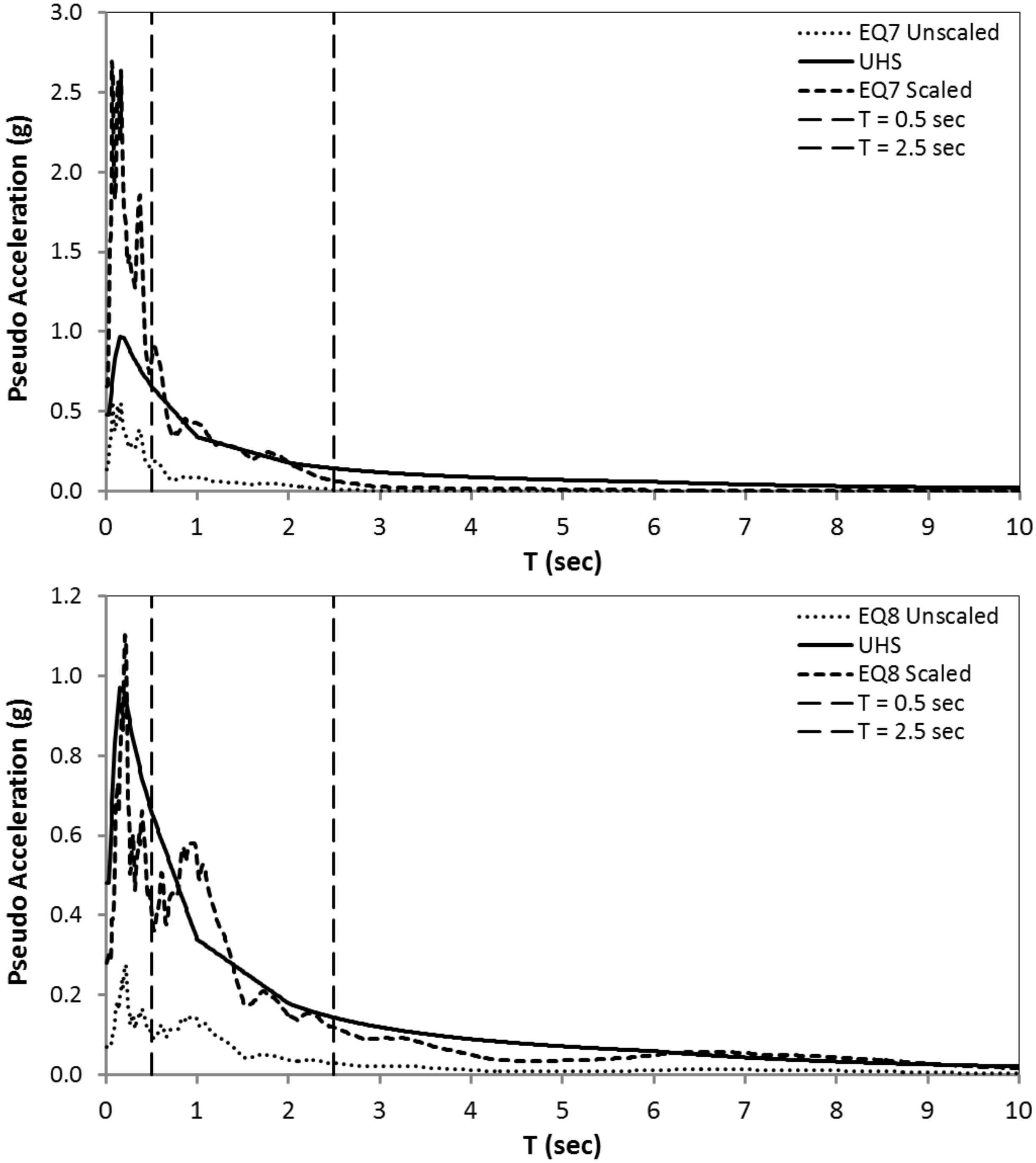

Figure A.4 (continued)

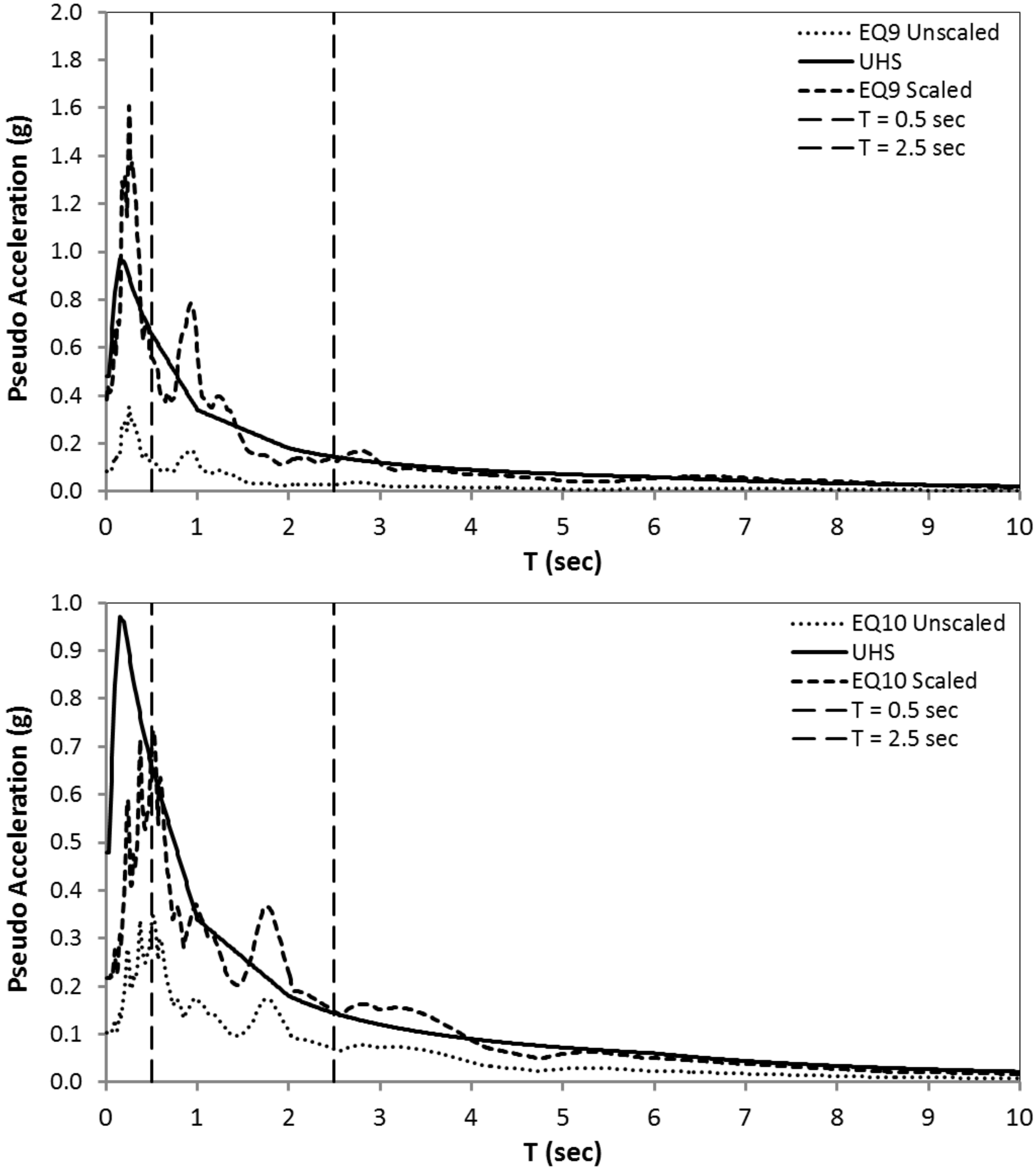

Figure A.4 (continued)

A.2 Effect of Soil Properties on Rotation of Shear Walls Foundations

Extended summary of results from NTHA on the effect of soil type, soil stiffness and soil ultimate bearing capacity are presented in the section below.

A.2.1 Soil type

Table A.1 Shear wall specifications

N	10
L_w (mm)	5500
P (kN)	41550
M_{RSA} (kN.m)	488000
M_y (kN.m)	249000
R_w	1.96

Table A.2 Summary of nonlinear dynamic analysis

Soil Type	Soil 1	Soil 2	Soil 3	Soil 4	Soil 5
E (MPa)	107	187	327	571	1000
G_{eff} (MPa)	42.8	73	126	215	370
v	0.25	0.28	0.3	0.33	0.35
q_{ult} (kPa)	501	877	1535	2686	4700
L (mm)	12500	12500	12500	12500	12500
B (mm)	12500	12500	12500	12500	12500
a (mm)	6635	3790	2165	1238	707
s (mm)	11.69	7.02	4.14	2.48	1.46
M_{oc} (kN.m)	121851	180946	214700	233978	244995
θ_{oc} (rad)	0.0139	0.0143	0.0120	0.0099	0.0074
$T_{Estimate}$ (sec)	2.00	1.67	1.43	1.28	1.17
T_{model} (sec)	2.30	1.77	1.42	1.27	1.16
Δ_1 (mm)	52.9	73.0	52.9	43.7	39.3
Δ_{10} (mm)	378	537	425	374	358
Avg. Max. θ_b (rad)	0.0114	0.0155	0.0108	0.0086	0.0075
Avg. Max. Uplift (mm)	40.8	114.8	97.5	84.8	77.8
Avg. Max. Comp. Disp. (mm)	-126.4	-80.3	-37.7	-23.1	-15.8
Avg. Max. q_{max}/q_{ult}	99%	96%	90%	71%	53%

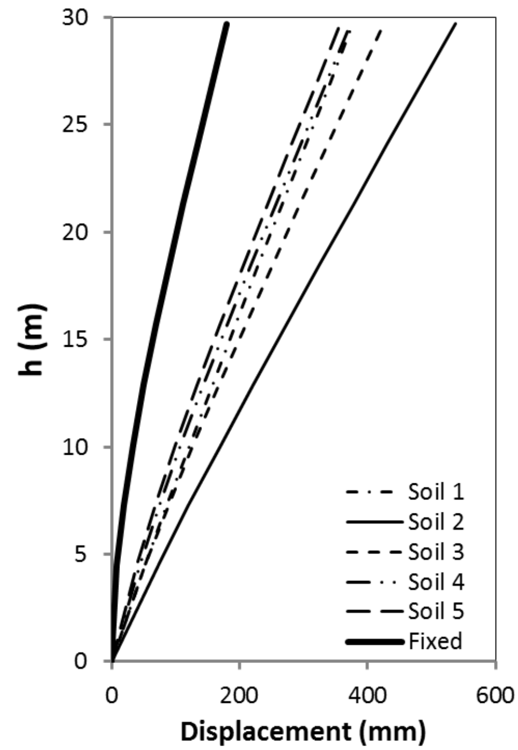

Figure A.5 Average displacement envelopes of wall 10R20 with a 12.5 m square foundation on various soil types

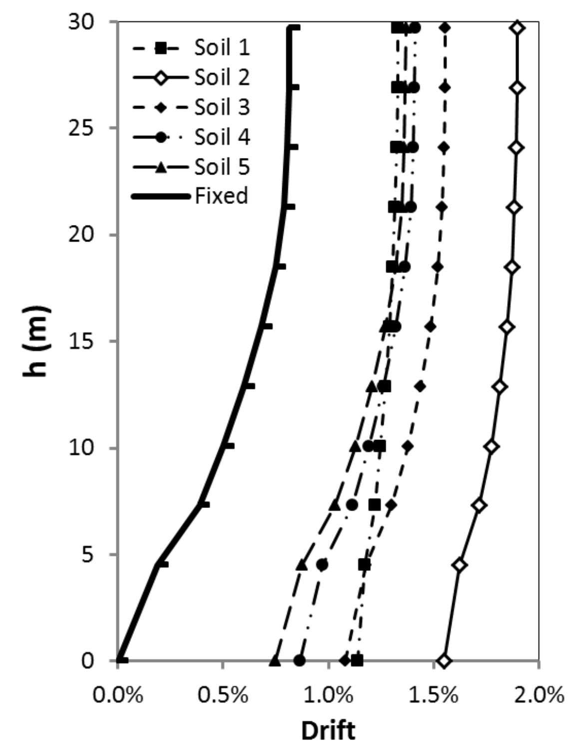

Figure A.6 Average drift envelopes of wall 10R20 with a 12.5 m square foundation on various soil types (Note: base rotation values are plotted at h=0 and values of average interstory drift are plotted at the top of the storey.)

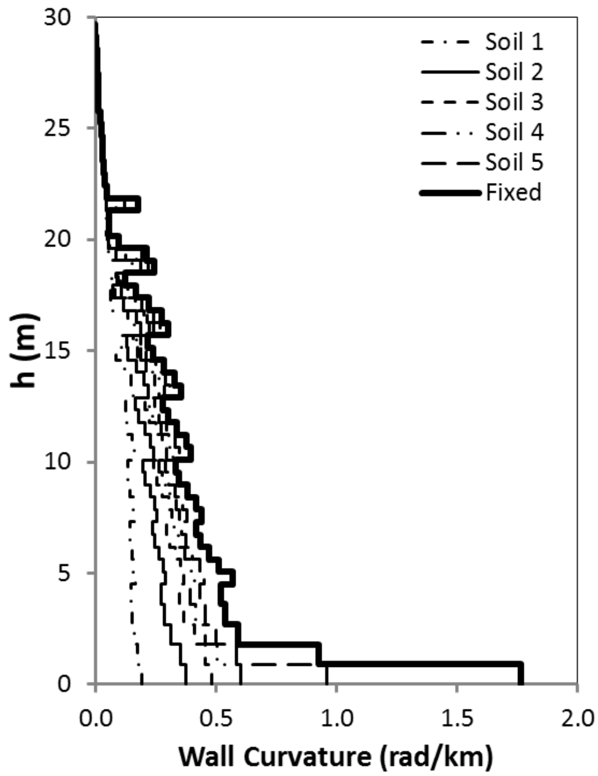

Figure A.7 Average curvature envelopes of wall 10R20 with a 12.5 m square foundation on various soil types

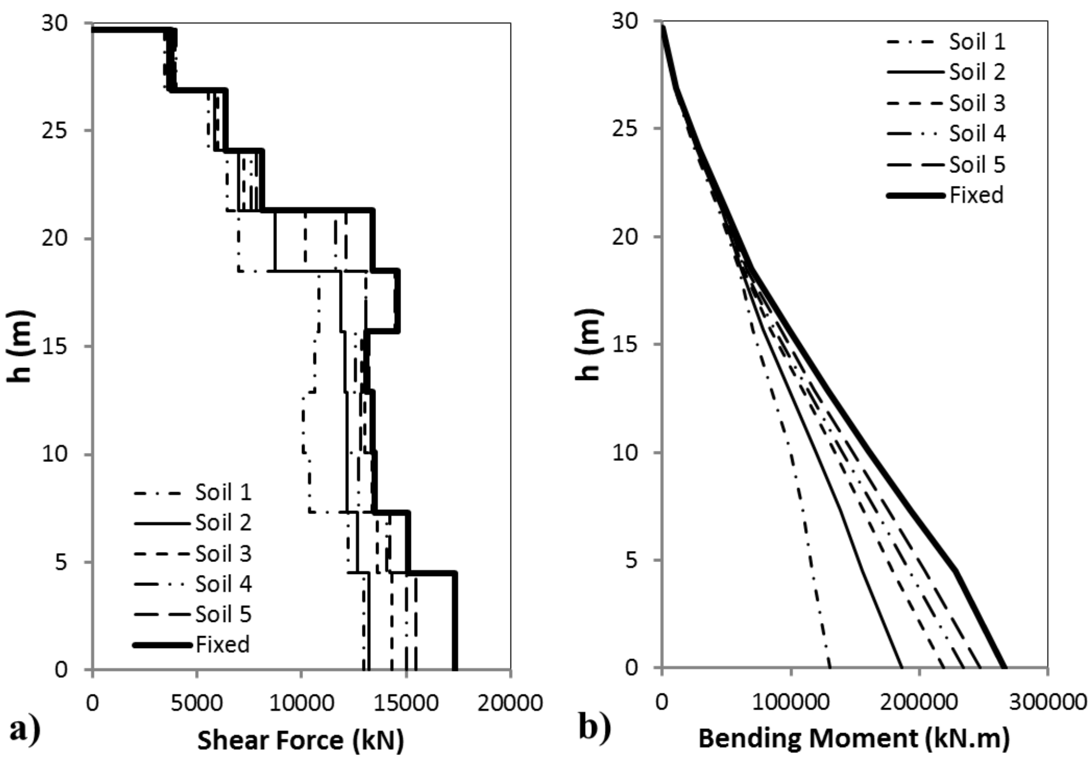

Figure A.8 Average wall a) shear force envelopes, and b) bending moment envelopes of wall 10R20 with a 12.5 m square foundation on various soil types

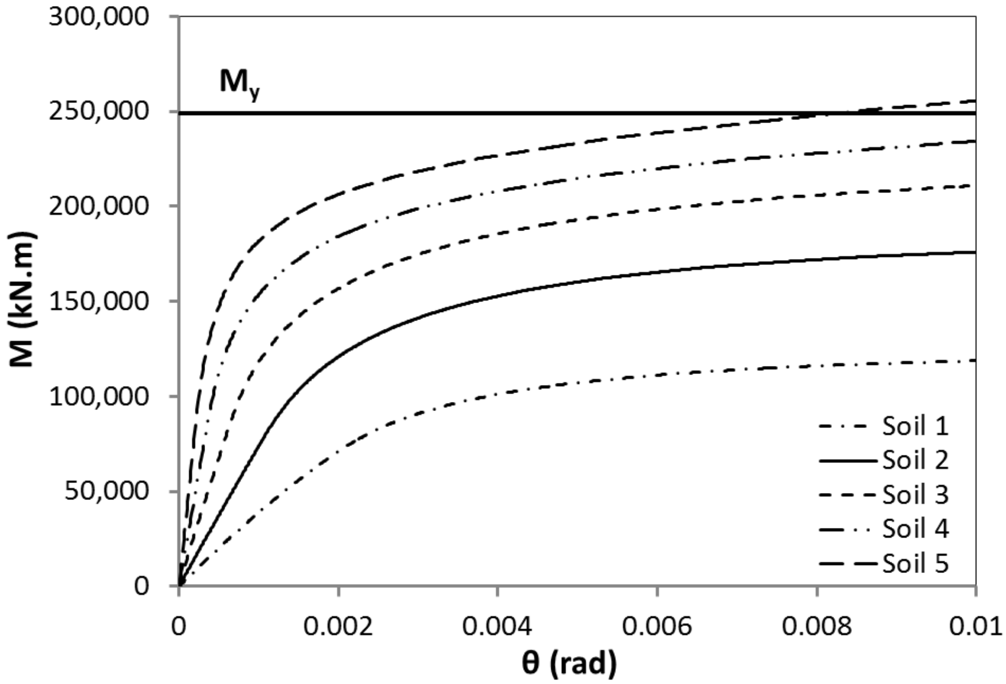

Figure A.9 Bending moment versus base rotation of the 12.5m square foundation on various soil types

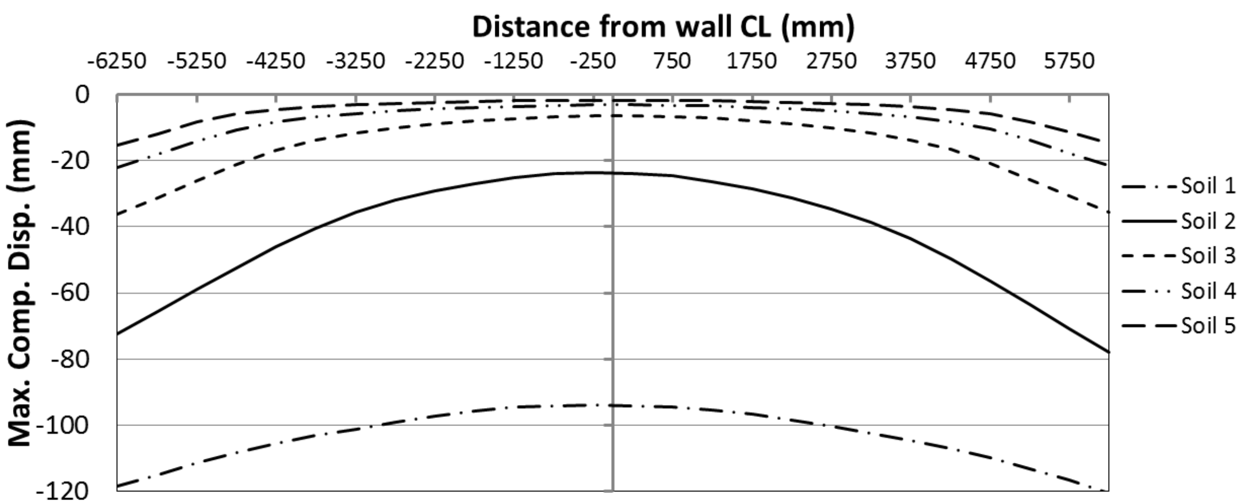

Figure A.10 Average of maximum soil compressive displacement profiles for various soil types

A.2.2 Soil stiffness

Table A.3 Shear wall specifications

N	10
L_w (mm)	5500
P (kN)	41550
M_{RSA} (kN.m)	488000
M_y (kN.m)	249000
R_w	1.96

Table A.4 Summary of nonlinear dynamic analysis

Soil Shear Modulus of Elasticity	**43 MPa**	**73 MPa**	**126 MPa**	**215 MPa**	**370 MPa**
E (MPa)	107	187	327	571	1000
G_{eff} (MPa)	42.8	73	126	215	370
ν	0.25	0.28	0.3	0.33	0.35
q_{ult} (kPa)	1535	1535	1535	1535	1535
L (mm)	12500	12500	12500	12500	12500
B (mm)	12500	12500	12500	12500	12500
a (mm)	2165	2165	2165	2165	2165
s (mm)	11.69	7.01	4.14	2.48	1.46
M_{oc} (kN.m)	214700	214700	214700	214700	214700
θ_{oc} (rad)	0.0340	0.0204	0.0120	0.0072	0.0042
$T_{Estimate}$ (sec)	2.00	1.67	1.43	1.28	1.17
T_{model} (sec)	1.97	1.65	1.42	1.27	1.16
Δ_1 (mm)	89.6	77.9	52.9	47.8	46.7
Δ_{10} (mm)	660	586	425	397	399
Avg. Max. θ_b (rad)	0.0190	0.0164	0.0108	0.0096	0.0093
Avg. Max. Uplift (mm)	159.3	145.8	97.5	90.2	89.4
Avg. Max. Comp. Disp. (mm)	-78.5	-59.1	-37.7	-30.0	-26.8
Avg. Max. q_{max}/q_{ult}	81%	84%	90%	93%	97%

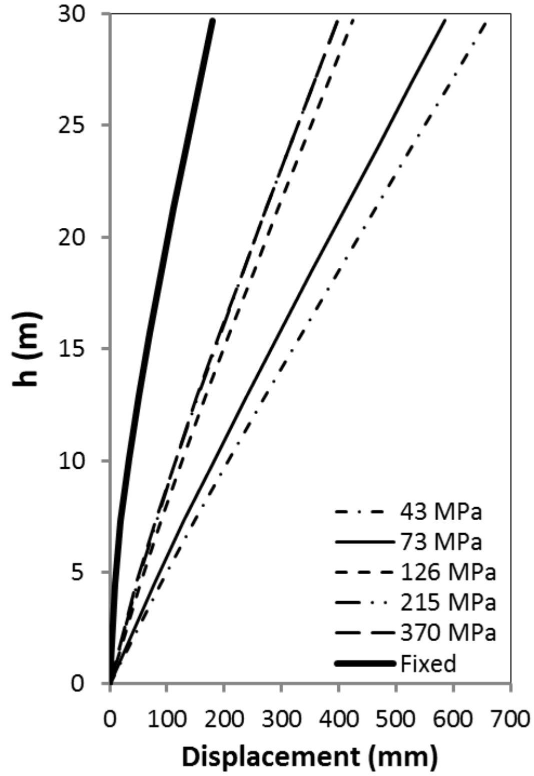

Figure A.11 Average displacement envelopes of wall 10R20 with a 12.5 m square foundation on various soil stiffnesses

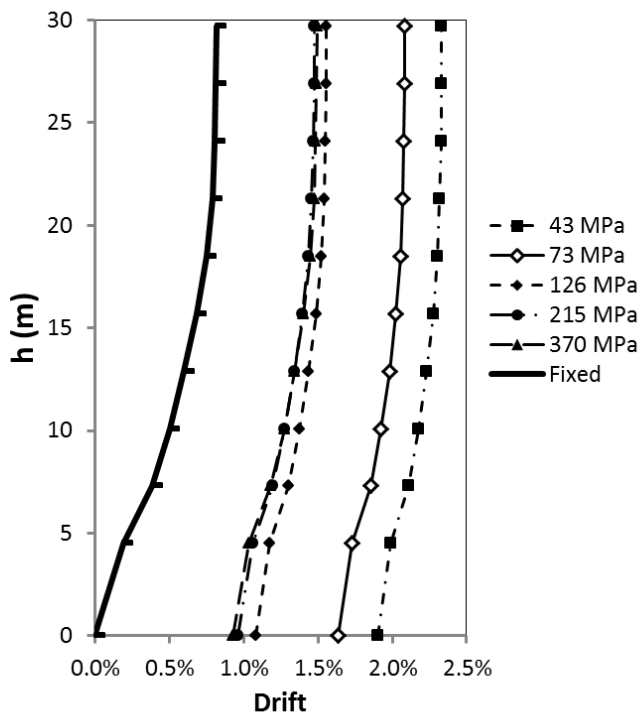

Figure A.12 Average drift envelopes of wall 10R20 with a 12.5 m square foundation on various soil stiffnesses (Note: base rotation values are plotted at h=0 and values of average interstory drift are plotted at the top of the storey.)

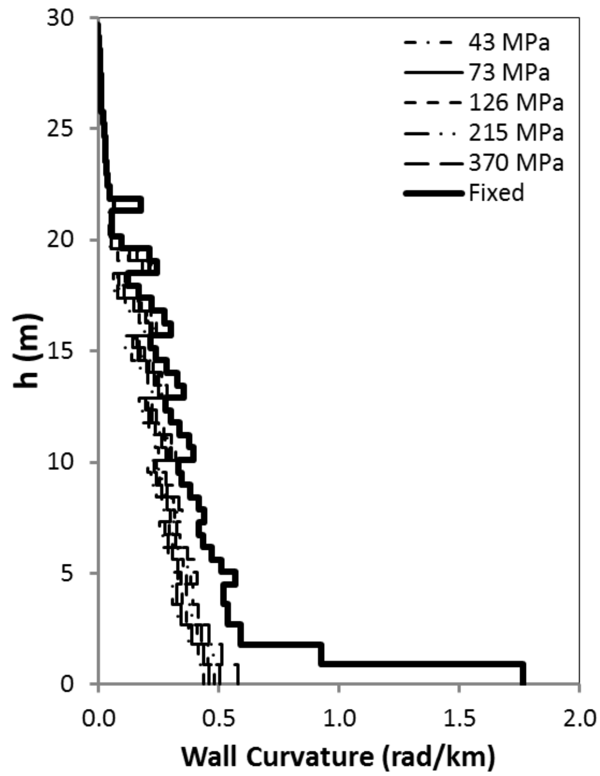

Figure A.13 Average curvature envelopes of wall 10R20 with a 12.5 m square foundation on various soil stiffnesses

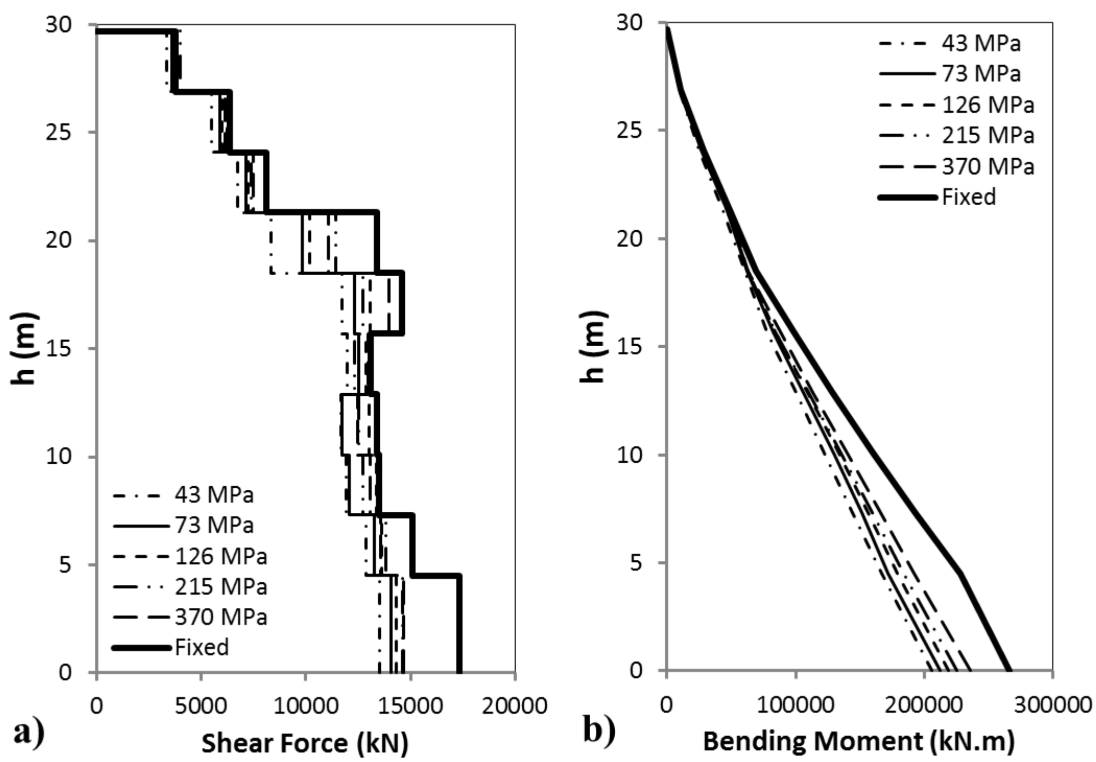

Figure A.14 Average wall a) shear force envelopes, and b) bending moment envelopes of wall 10R20 with a 12.5 m square foundation on various soil stiffnesses

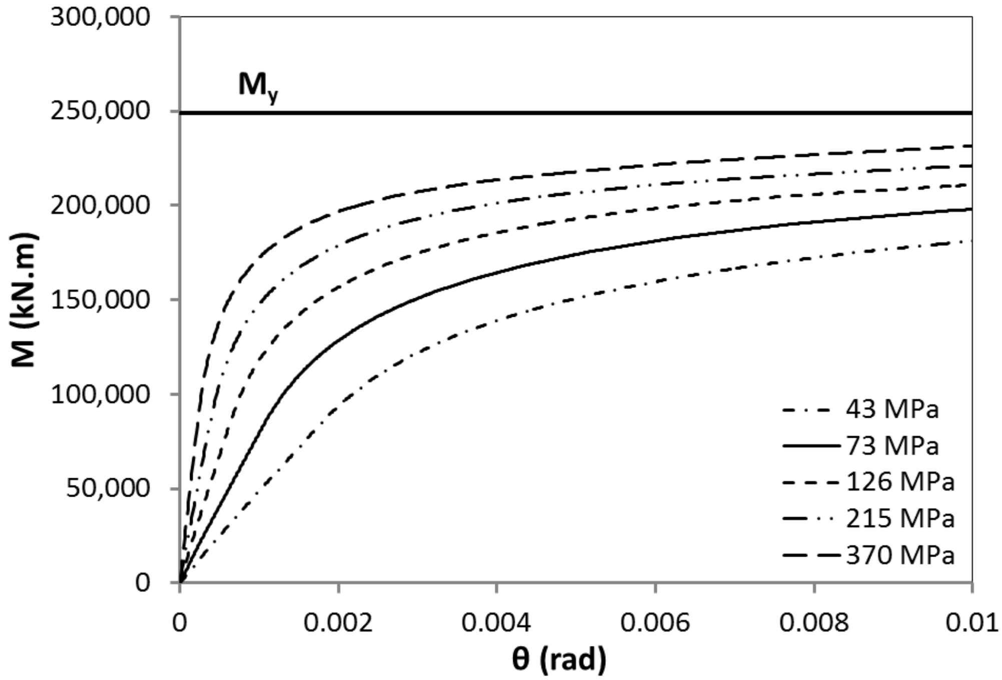

Figure A.15 Bending moment versus base rotation of the 12.5m square foundation on various soil stiffnesses

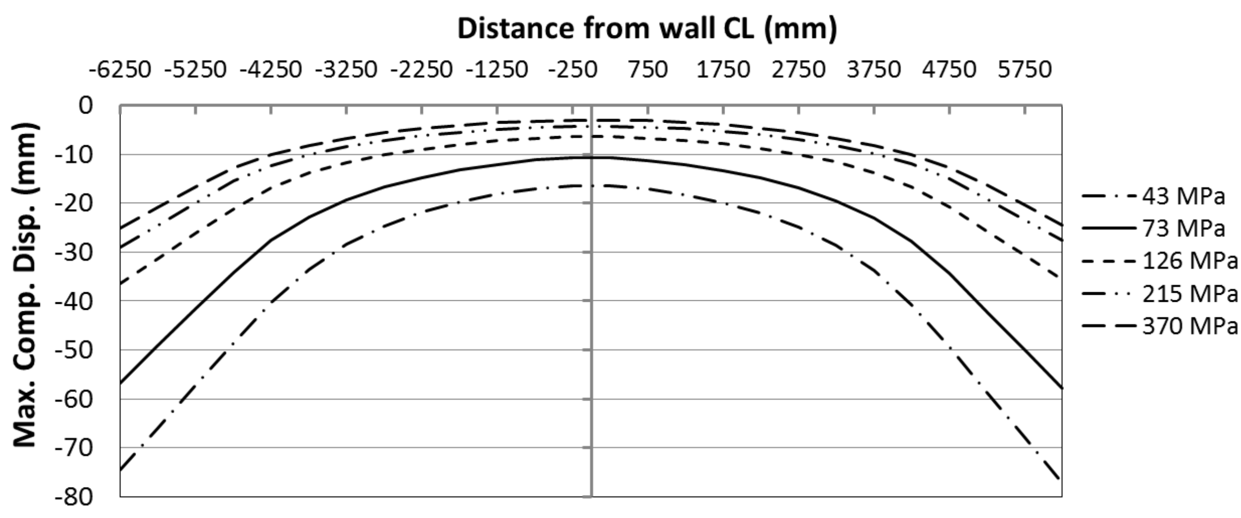

Figure A.16 Average of maximum soil compressive displacement profiles for various soil stiffnesses

A.2.3 Soil ultimate bearing capacity

Table A.5 Shear wall specifications

N	10
L_w (mm)	5500
P (kN)	41550
M_{RSA} (kN.m)	488000
M_y (kN.m)	249000
R_w	1.96

Table A.6 Summary of nonlinear dynamic analysis

Ultimate Bearing Capacity	0.50 MPa	0.88 MPa	1.54 MPa	2.69 MPa	4.70 MPa
E (MPa)	327	327	327	327	327
G_{eff} (MPa)	126	126	126	126	126
v	0.3	0.3	0.3	0.3	0.3
q_{ult} (kPa)	501	877	1535	2686	4700
L (mm)	12500	12500	12500	12500	12500
B (mm)	12500	12500	12500	12500	12500
a (mm)	6635	3790	2165	1238	707
s (mm)	4.14	4.14	4.14	4.14	4.14
M_{oc} (kN.m)	121851	180946	214700	233978	244995
θ_{oc} (rad)	0.0049	0.0084	0.0120	0.0165	0.0209
$T_{Estimate}$ (sec)	1.43	1.43	1.43	1.43	1.43
T_{model} (sec)	1.58	1.50	1.42	1.42	1.42
Δ_1 (mm)	39.9	58.4	52.9	52.3	48.1
Δ_{10} (mm)	291	444	425	427	398
Avg. Max. θ_b (rad)	0.0085	0.0122	0.0108	0.0106	0.0097
Avg. Max. Uplift (mm)	35.0	93.5	97.5	99.8	91.0
Avg. Max. Comp. Disp. (mm)	-110.2	-63.8	-37.7	-32.8	-29.9
Avg. Max. q_{max}/q_{ult}	100%	98%	90%	64%	37%

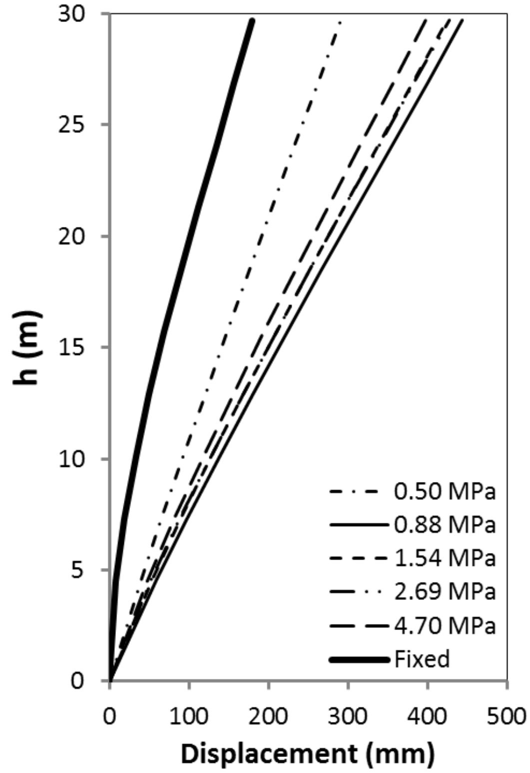

Figure A.17 Average displacement envelopes of wall 10R20 with a 12.5 m square foundation on various soil ultimate bearing capacities

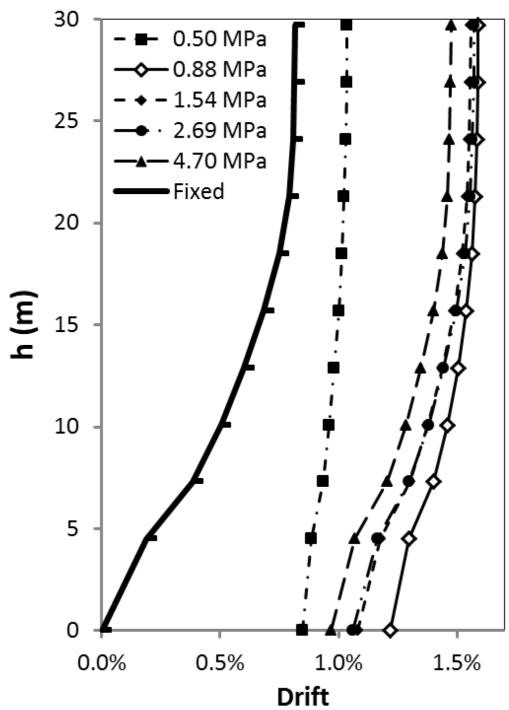

Figure A.18 Average drift envelopes of wall 10R20 with a 12.5 m square foundation on various soil ultimate bearing capacities (Note: base rotation values are plotted at h=0 and values of average interstory drift are plotted at the top of the storey.)

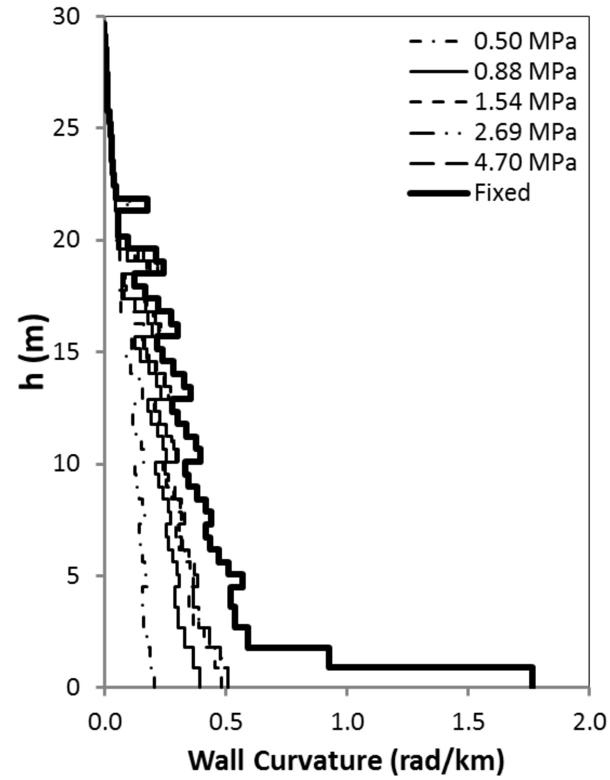

Figure A.19 Average curvature envelopes of wall 10R20 with a 12.5 m square foundation on various soil ultimate bearing capacities

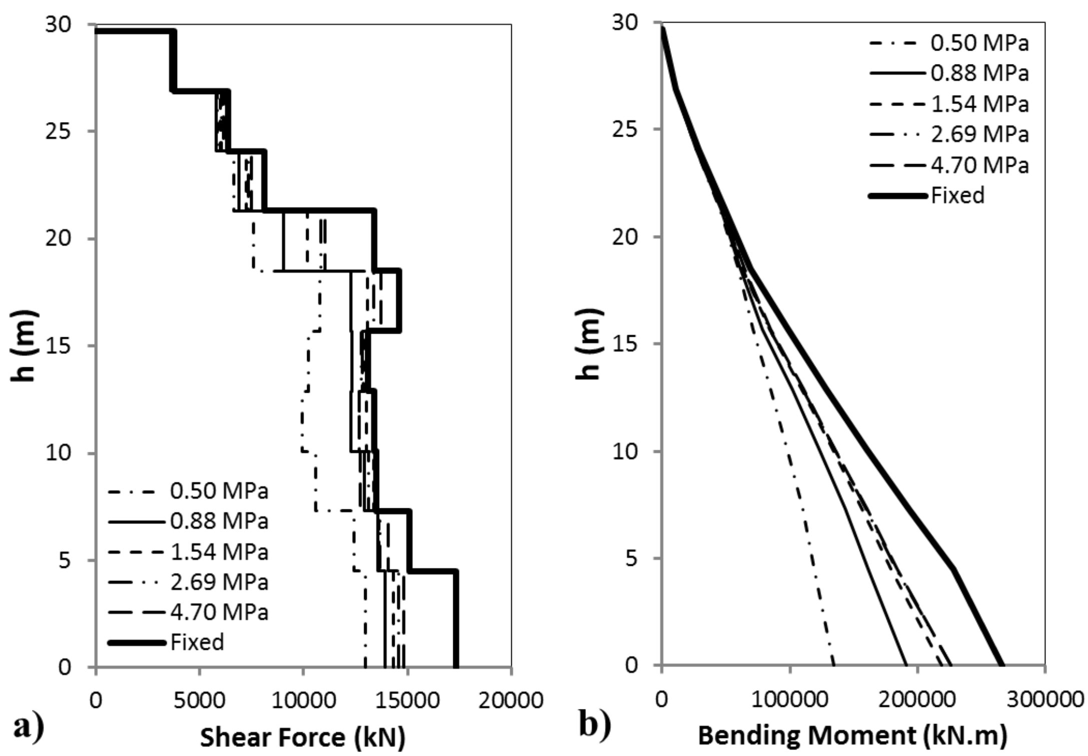

Figure A.20 Average wall a) shear force envelopes, and b) bending moment envelopes of wall 10R20 with a 12.5 m square foundation on various soil ultimate bearing capacities

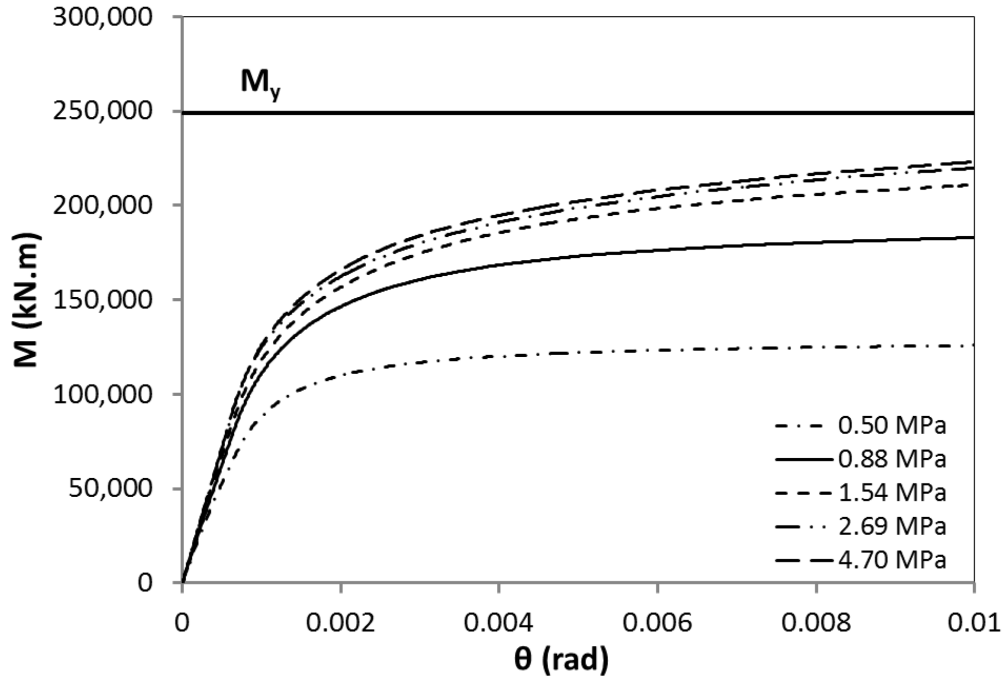

Figure A.21 Bending moment versus base rotation of the 12.5m square foundation on various soil bearing capacities

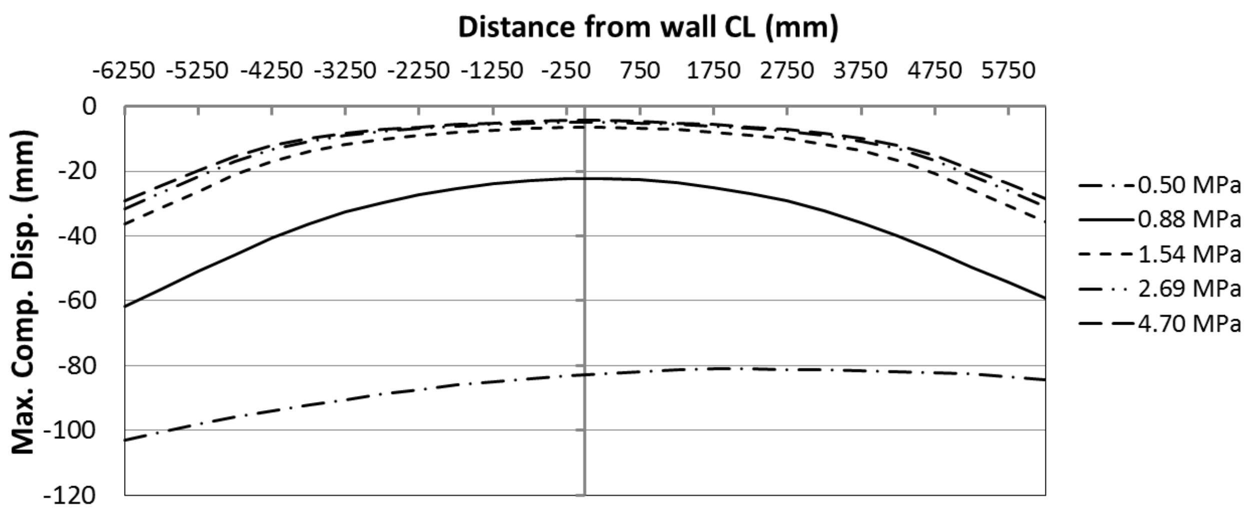

Figure A.22 Average of maximum soil compressive displacement profiles for various soil bearing capacities

A.3 Parametric Study on Soil Damping

Extended summary of NTHA results on the effect of soil damping on rotation of shear wall foundations is presented in this section.

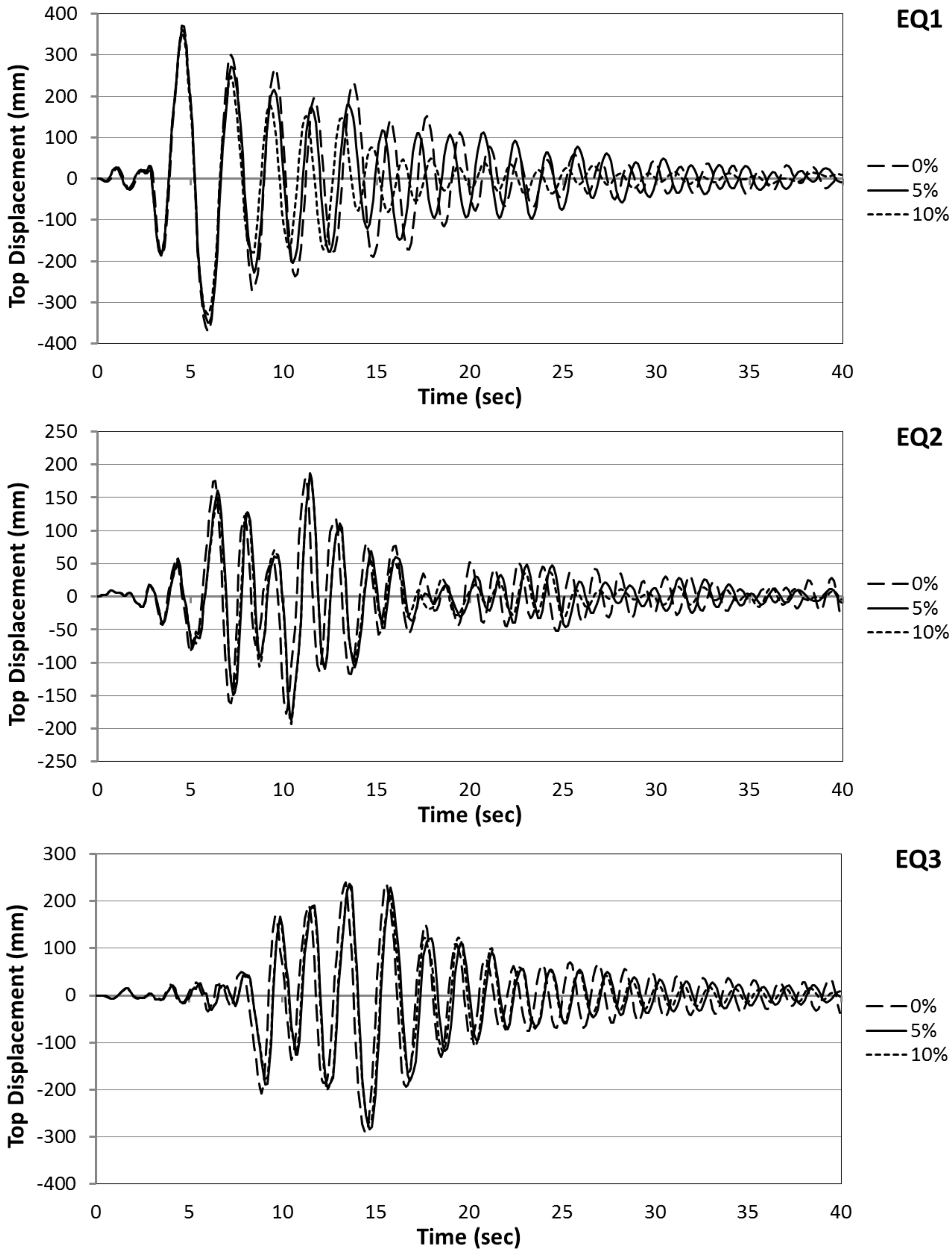

Figure A.23 Top displacement time-histories for various levels of soil damping

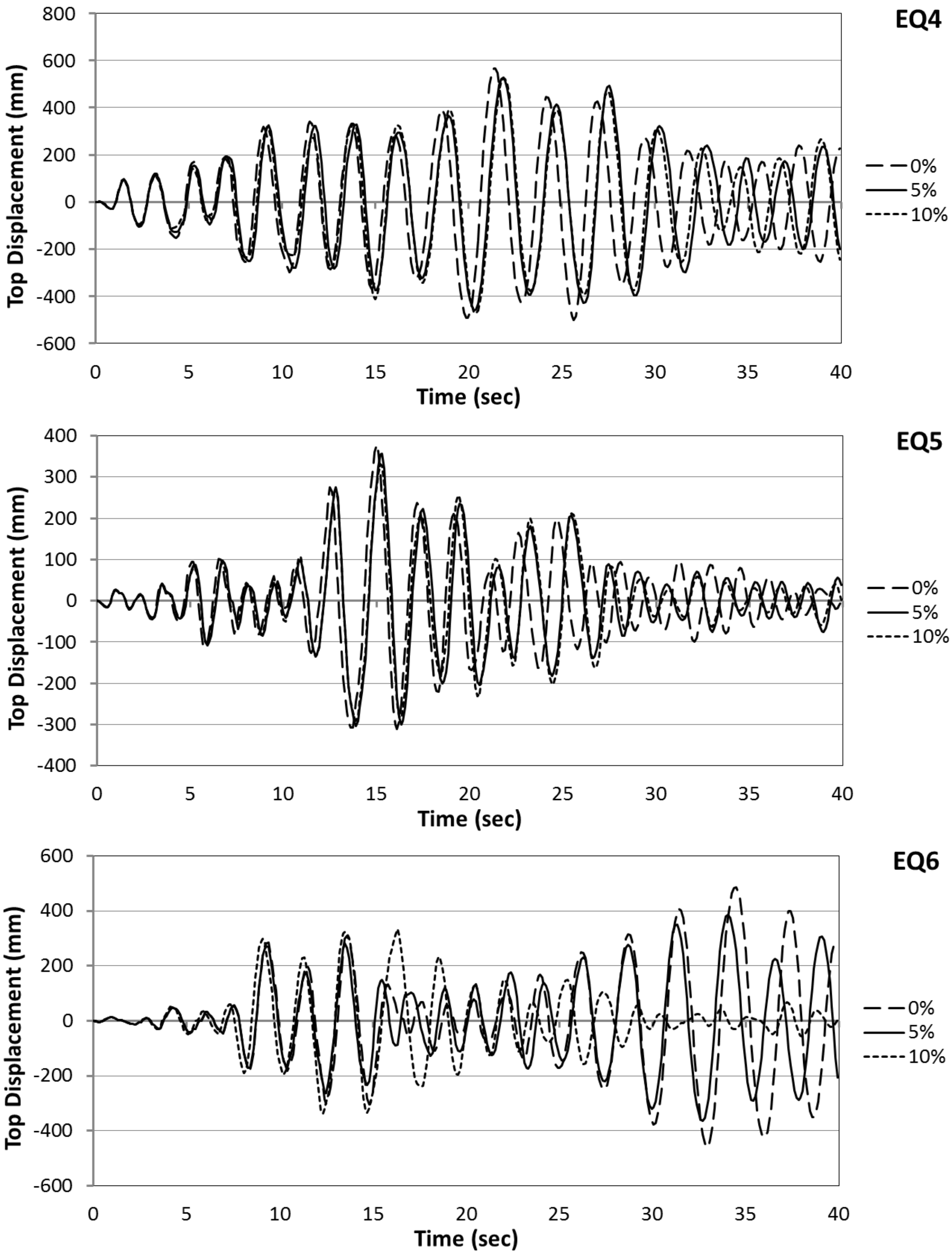

Figure A.23 (continued)

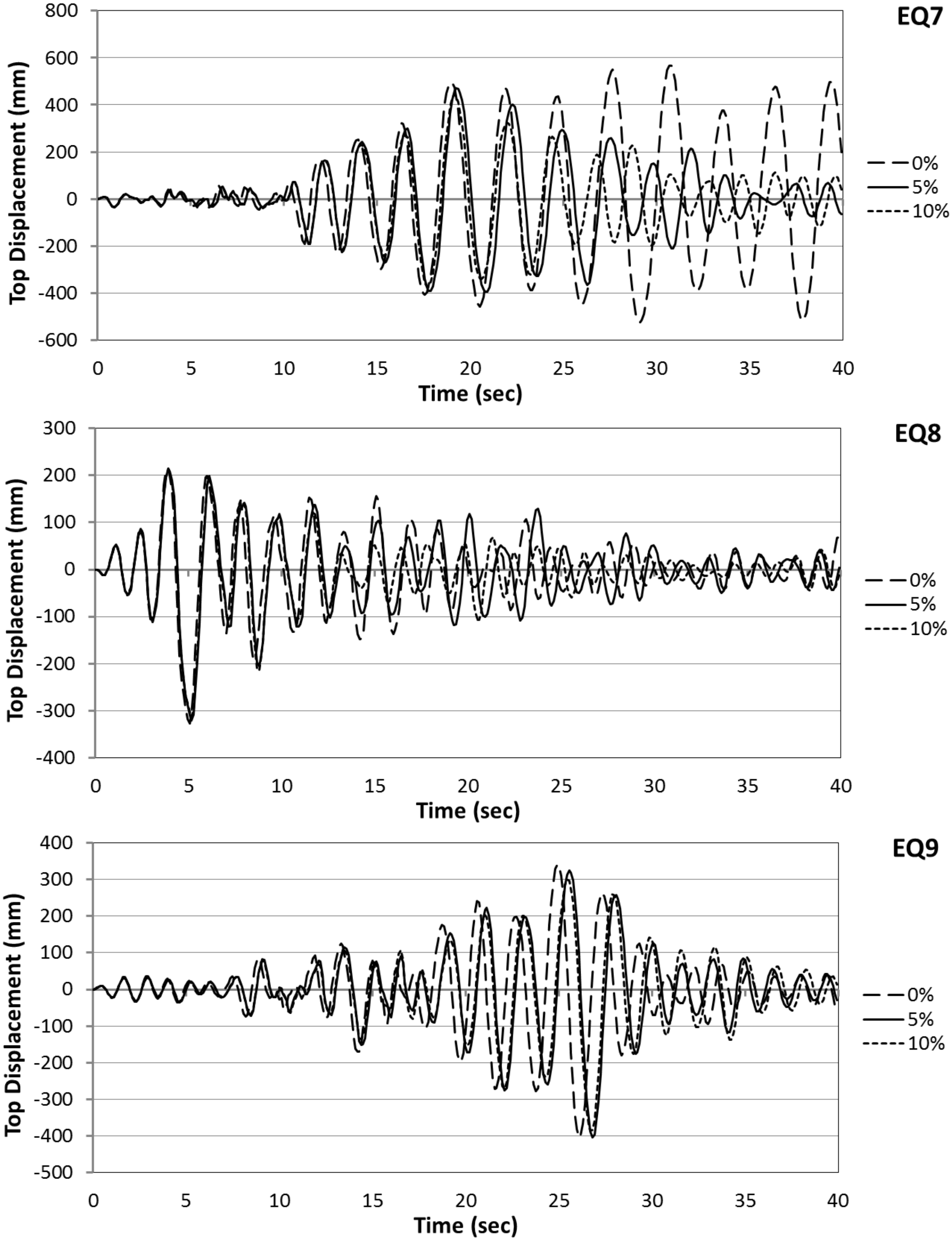

Figure A.23 (continued)

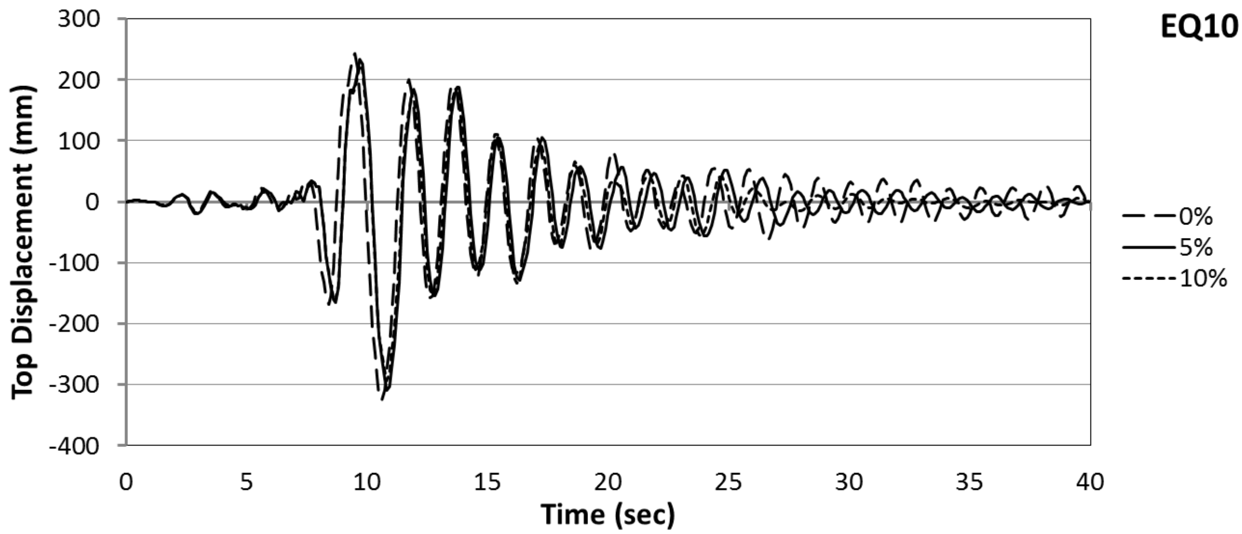

Figure A.23 (continued)

Table A.7 Properties for wall 10R20

N	10
L_w (mm)	5500
P (kN)	41550
M_{RSA} (kN.m)	488000
M_y (kN.m)	249000
R_w	1.96

Table A.8 Summary of parametric study on soil damping

Soil Damping	**0%**	**5%**	**10%**	**15%**	**20%**	**25%**	**30%**
E (MPa)	550	550	550	550	550	550	550
G_{eff} (MPa)	212	212	212	212	212	212	212
v	0.3	0.3	0.3	0.3	0.3	0.3	0.3
q_{ult} (kPa)	2500	2500	2500	2500	2500	2500	2500
R_f	2.10	2.10	2.10	2.10	2.10	2.10	2.10
L (mm)	12500	12500	12500	12500	12500	12500	12500
B (mm)	12500	12500	12500	12500	12500	12500	12500
a (mm)	1330	1330	1330	1330	1330	1330	1330
s (mm)	2.46	2.46	2.46	2.46	2.46	2.46	2.46
M_{oc} (kN.m)	232065	232065	232065	232065	232065	232065	232065
θ_{oc} (rad)	0.0095	0.0095	0.0095	0.0089	0.0089	0.0089	0.0089
$T_{Estimate}$ (sec)	1.28	1.28	1.28	1.28	1.28	1.28	1.28
T_{model} (sec)	1.26	1.26	1.26	1.26	1.26	1.26	1.26
Δ_1 (mm)	49.7	42.9	37.8	30.2	28.4	26.4	24.2
Δ_{10} (mm)	415	368	332	277	265	251	234
Avg. Max. θ_b (rad)	0.0099	0.0084	0.0072	0.0056	0.0051	0.0049	0.0044
Avg. Max. Uplift (mm)	99.0	81.9	68.5	51.9	46.1	44.0	39.0
Avg. Max. Comp. Disp. (mm)	-25.2	-22.8	-21.0	-18.6	-17.7	-17.3	-16.4
Avg. Max. q_{max}/q_{ult}	95%	93%	87%	82%	79%	77%	75%

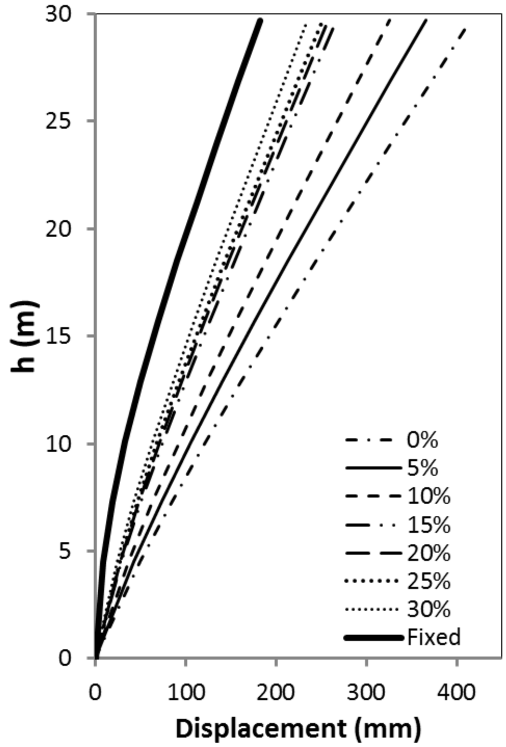

Figure A.24 Average of displacement envelopes of wall 10R20 for various levels of soil damping

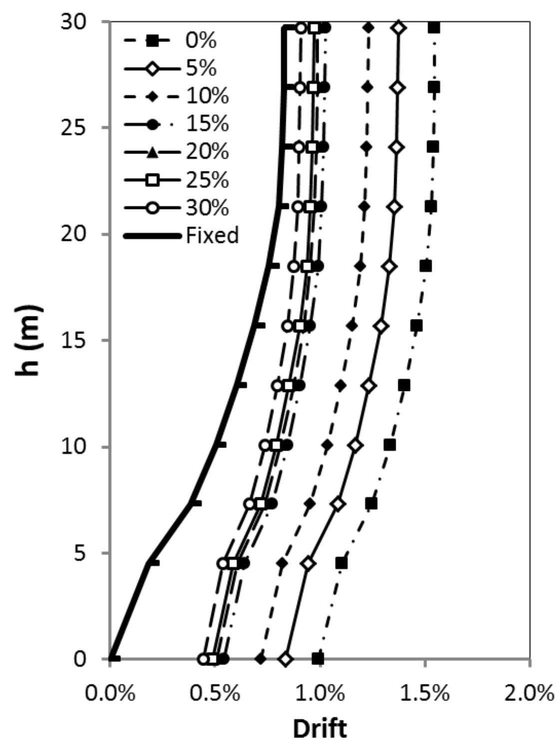

Figure A.25 Average of drift envelopes of wall 10R20 for various levels of soil damping (Note: base rotation values are plotted at h=0 and values of average interstory drift are plotted at the top of the storey.)

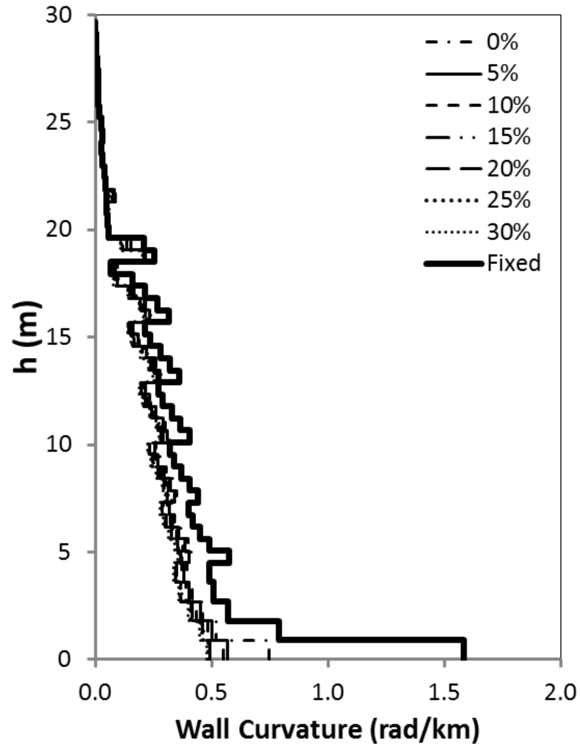

Figure A.26 Average of curvature envelopes of wall 10R20 for various levels of soil damping

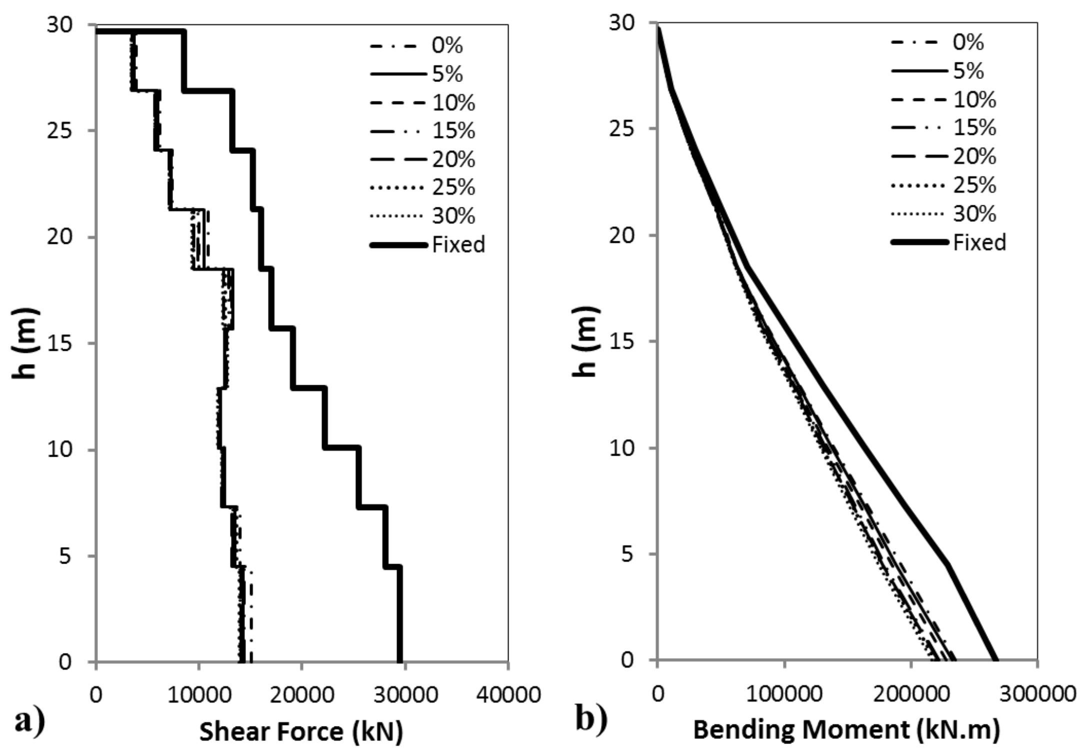

Figure A.27 Average of a) shear force, and b) bending moment envelopes of wall 10R20 for various levels of soil damping

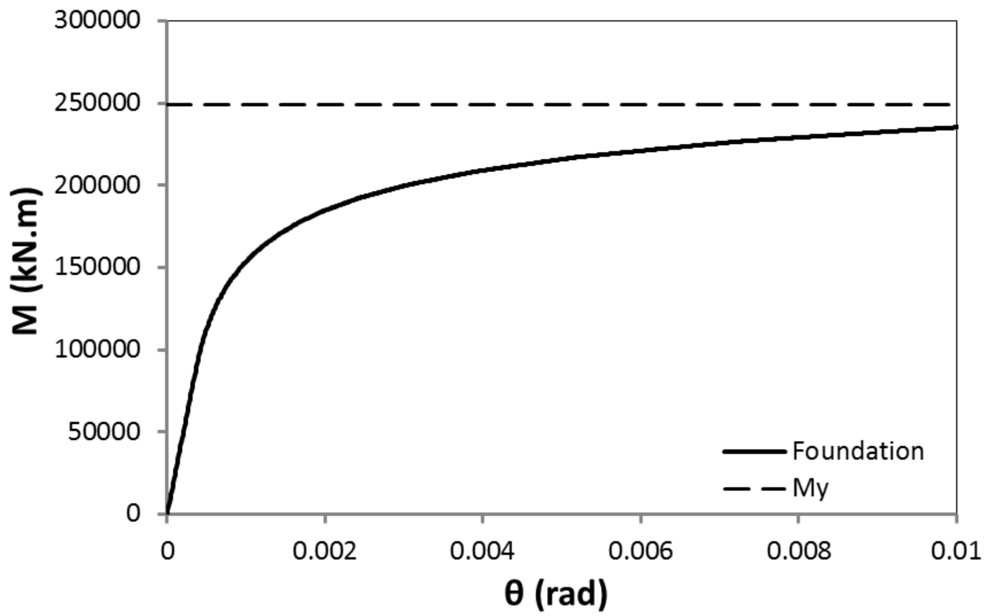

Figure A.28 Bending moment-rotation response of the foundation of wall 10R20

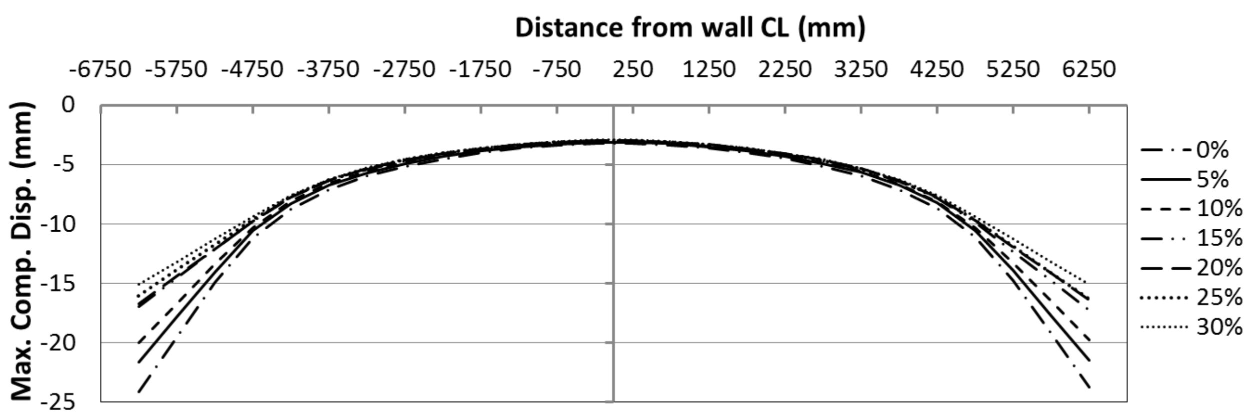

Figure A.29 Average of maximum soil compressive displacements underneath the footing for wall 10R20 for various levels of soil damping

A.4 Scatter in the Response of Shear Walls Accounting for Foundation Rotation

This section presents an extended summary of results from NTHA using uniformly-scaled ground motions for shear walls on Dense Sand and Rock.

A.4.1 Dense Sand

Table A.9 Shear wall properties for wall 10R13

N	10
L_w (mm)	5500
P (kN)	41550
M_{RSA} (kN.m)	488000
M_y (kN.m)	369000
R_w	1.32

Table A.10 Summary of nonlinear dynamic analyses for wall 10R13 on Dense Sand

R_f	1.9	2.2	2.4	2.8	3.4
E (MPa)	809	809	809	809	809
G_{eff} (MPa)	311	311	311	311	311
v	0.3	0.3	0.3	0.3	0.3
q_a (kPa)	533	533	533	533	533
q (kPa)	173	198	228	266	314
q_f (kPa)	800	800	800	800	800
q_{ult} (kPa)	1600	1600	1600	1600	1600
L (m)	15.5	14.5	13.5	12.5	11.5
B (m)	15.5	14.5	13.5	12.5	11.5
a (mm)	3351	3582	3847	4155	4516
s (mm)	0.26	0.28	0.29	0.31	0.33
M_{oc} (kN.m)	252399	226824	200536	173367	145086
θ_{oc} (rad)	0.0009	0.0008	0.0007	0.0007	0.0006
θ_y (rad)	0.0130	0.0207	0.0338	0.0585	-----
$T_{Estimate}$ (sec)	1.00	1.01	1.03	1.04	1.07
T_{model} (sec)	0.96	0.96	0.97	0.98	0.99
Δ_1 (mm)	18.8	26.2	33.2	34.4	32.7
Δ_{10} (mm)	201	246	287	283	266
Avg. Max. θ_b (rad)	0.0033	0.0050	0.0066	0.0070	0.0067
Avg. Max. Uplift (mm)	40.9	56.5	166.8	64.0	54.1
Avg. Max. Comp. Disp. (mm)	-10.2	-15.9	-61.7	-24.0	-27.4
Avg. Max. q_{max}/q_{ult}	70%	77%	86%	89%	93%

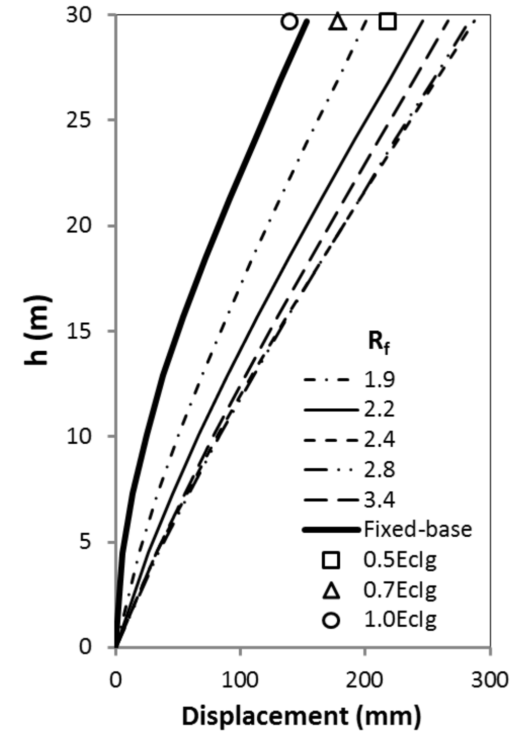

Figure A.30 Average of displacement envelopes for wall 10R13 on Dense Sand along with estimated top displacements of the fixed-base wall from RSA using various effective stiffnesses

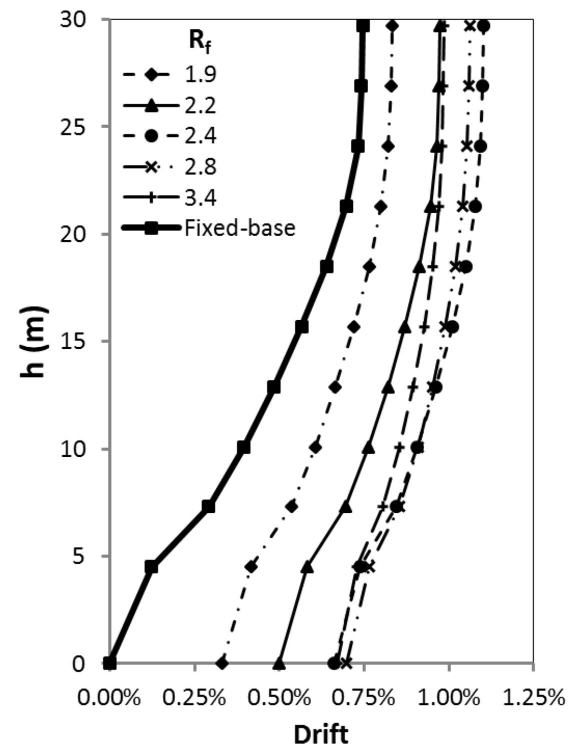

Figure A.31 Average of drift envelopes for wall 10R13 on Dense Sand (Note: base rotation values are plotted at h=0 and values of average interstory drift are plotted at the top of the storey.)

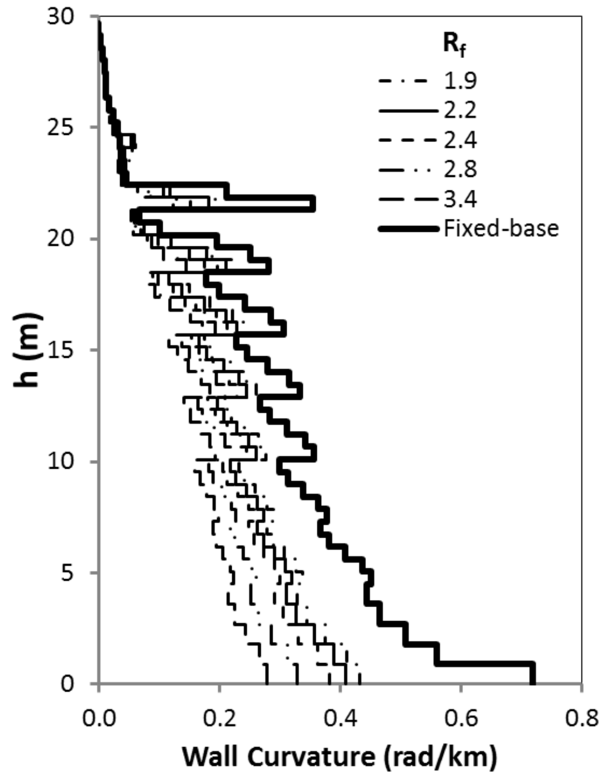

Figure A.32 Average of curvature envelopes for wall 10R13 on Dense Sand

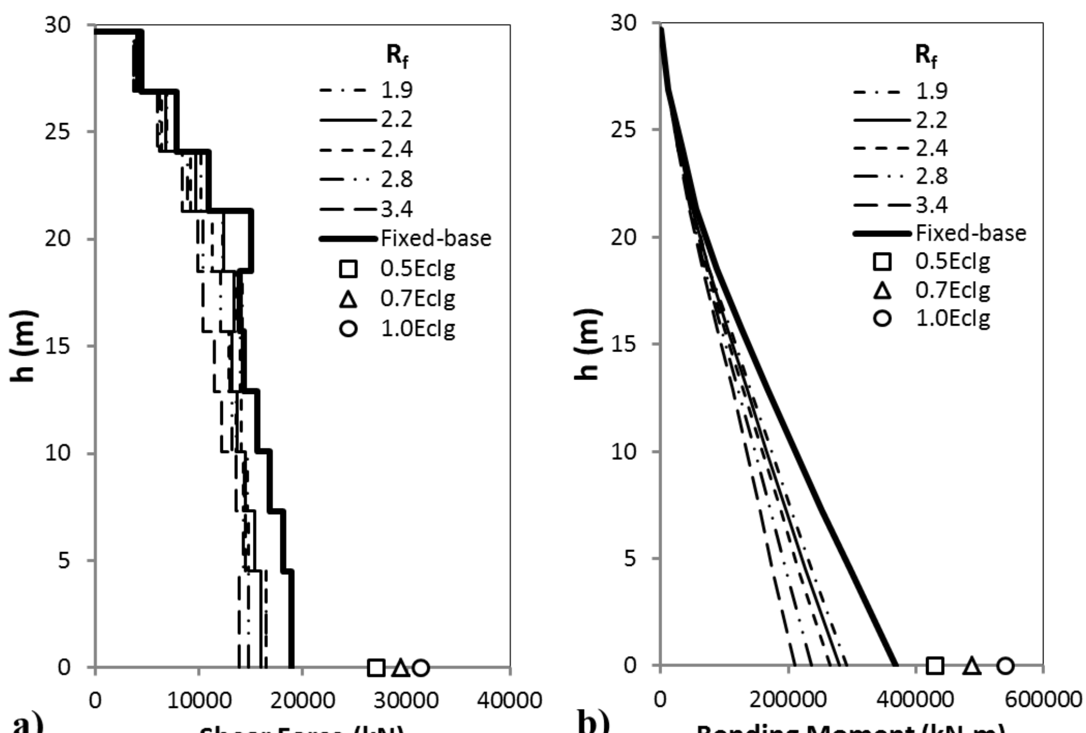

Figure A.33 Average of a) shear force, and b) bending moment envelopes for wall 10R13 on Dense Sand along with estimated maximum quantities for the fixed-base wall from RSA using various effective stiffnesses

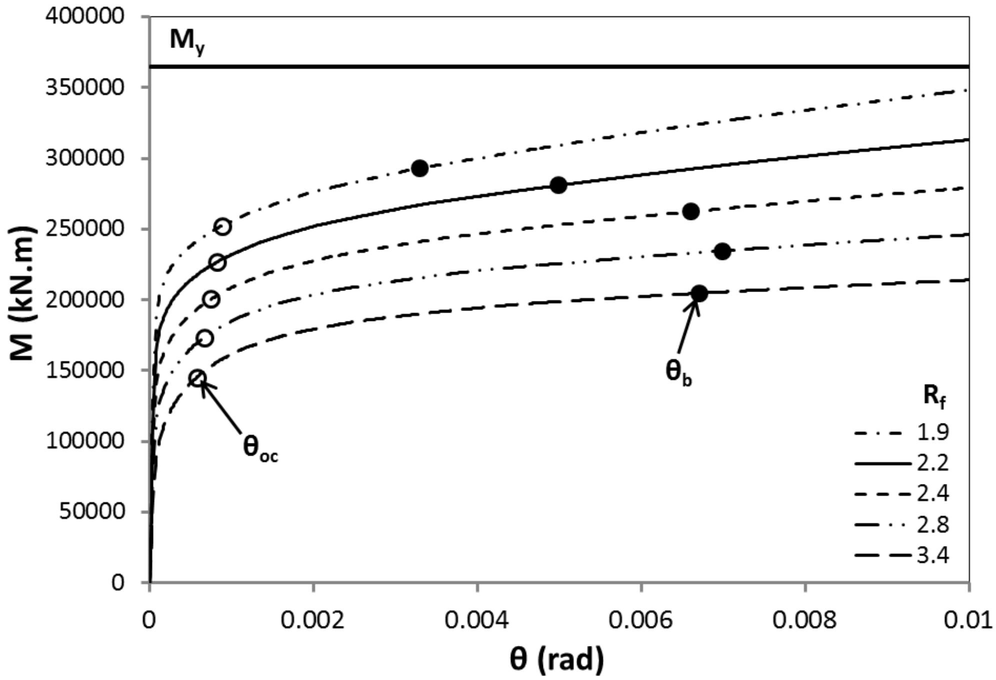

Figure A.34 Bending moment-rotation response of the foundation of wall 10R13 on Dense Sand

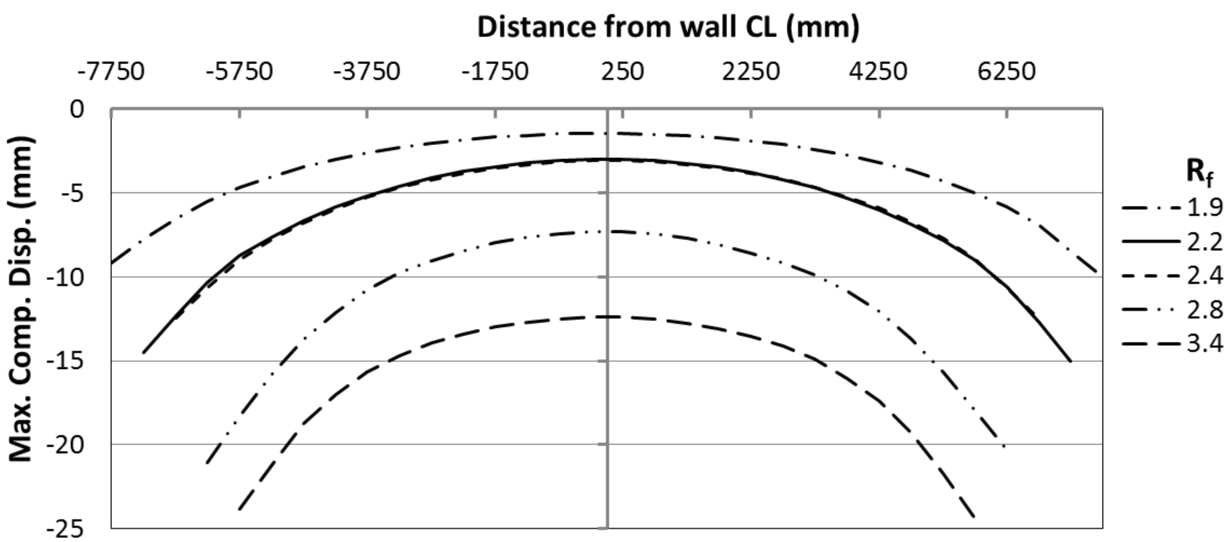

Figure A.35 Average of maximum soil compressive displacements underneath the footing for wall 10R13 on Dense Sand

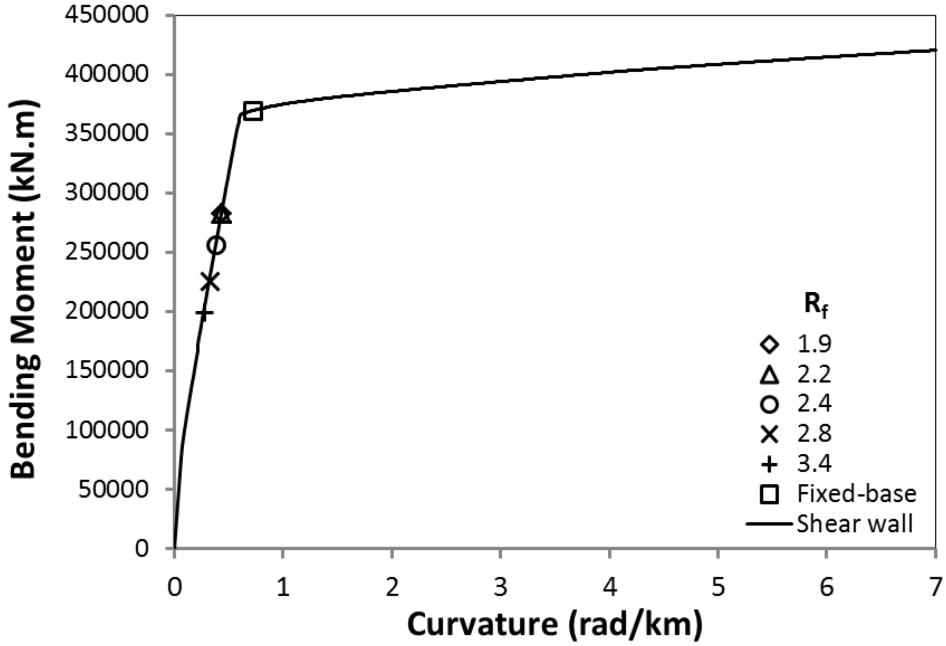

Figure A.36 Moment-curvature response of wall 10R13 along with average of maximum recorded curvatures at the base on Dense Sand

A.4.2 Rock

Table A.11 Shear wall properties for wall 10R13

N	10
L_w (mm)	5500
P (kN)	41550
M_{RSA} (kN.m)	488000
M_y (kN.m)	369000
R_w	1.32

Table A.12 Summary of nonlinear dynamic analyses for wall 10R13 on Rock

R_f	1.9	2.1	2.3	2.6	2.9
E (MPa)	20000	20000	20000	20000	20000
G_{eff} (MPa)	8333	8333	8333	8333	8333
v	0.2	0.2	0.2	0.2	0.2
q_a (kPa)	3000	3000	3000	3000	3000
q (kPa)	266	314	377	460	575
q_f (kPa)	10000	10000	10000	10000	10000
q_{ult} (kPa)	20000	20000	20000	20000	20000
L (m)	12.5	11.5	10.5	9.5	8.5
B (m)	12.5	11.5	10.5	9.5	8.5
a (mm)	332	361	396	437	489
s (mm)	0.06	0.06	0.07	0.07	0.08
M_{oc} (kN.m)	252782	231406	209917	188276	166432
θ_{oc} (rad)	0.0025	0.0023	0.0021	0.0018	0.0015
θ_y (rad)	0.1000	0.1000	0.1000	0.1000	0.1000
$T_{Estimate}$ (sec)	0.94	0.95	0.95	0.95	0.96
T_{model} (sec)	0.94	0.95	0.95	0.95	0.96
Δ_1 (mm)	24.8	24.9	33.4	39.6	46.3
Δ_{10} (mm)	228	220	272	307	344
Avg. Max. θ_b (rad)	0.0048	0.0049	0.0068	0.0083	0.0099
Avg. Max. Uplift (mm)	58.3	54.8	70.4	77.4	82.4
Avg. Max. Comp. Disp. (mm)	-1.3	-1.3	-1.4	-1.4	-1.4
Avg. Max. q_{max}/q_{ult}	29%	33%	37%	42%	47%

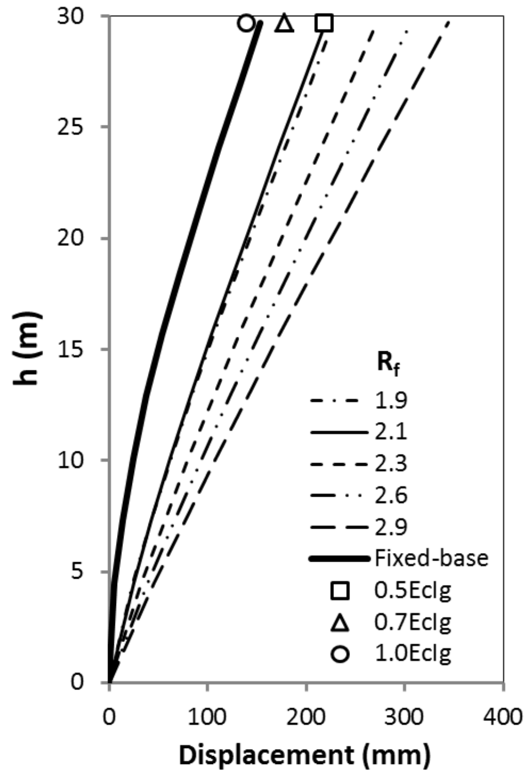

Figure A.37 Average of displacement envelopes for wall 10R13 on Rock along with estimated top displacements of the fixed-base wall from RSA using various effective stiffnesses

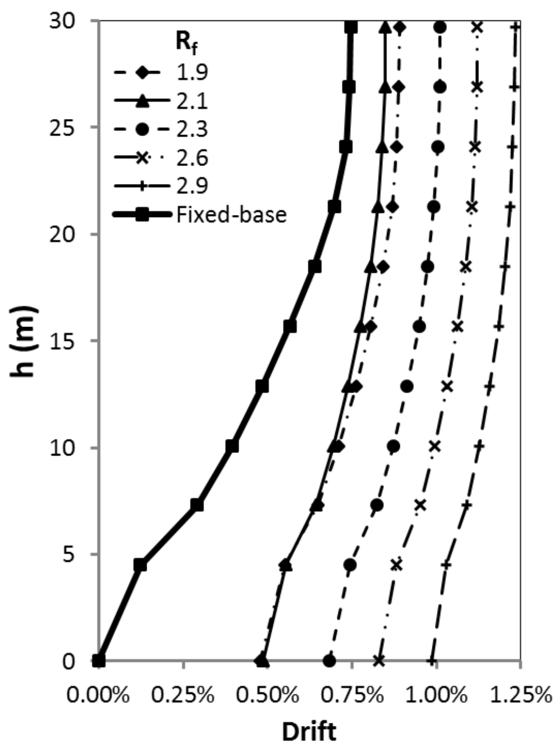

Figure A.38 Average of drift envelopes for wall 10R13 on Rock (Note: base rotation values are plotted at h=0 and values of average interstory drift are plotted at the top of the storey.)

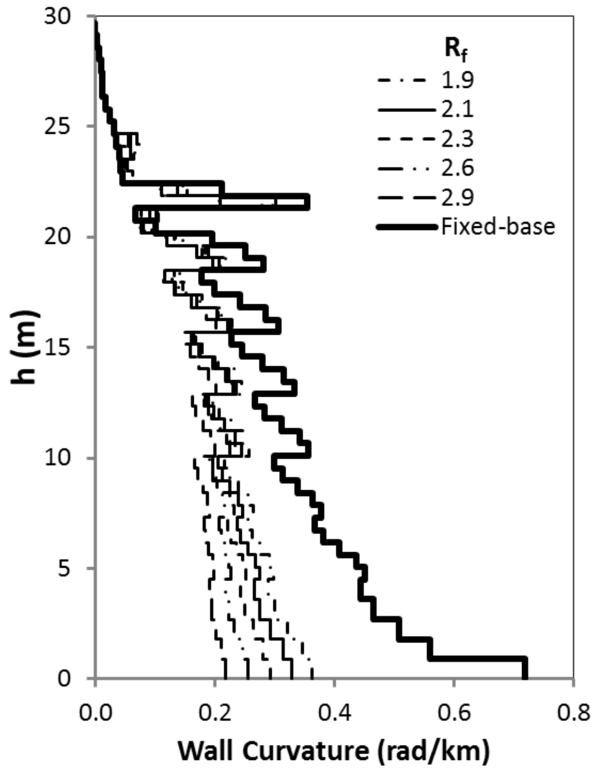

Figure A.39 Average of curvature envelopes for wall 10R13 on Rock

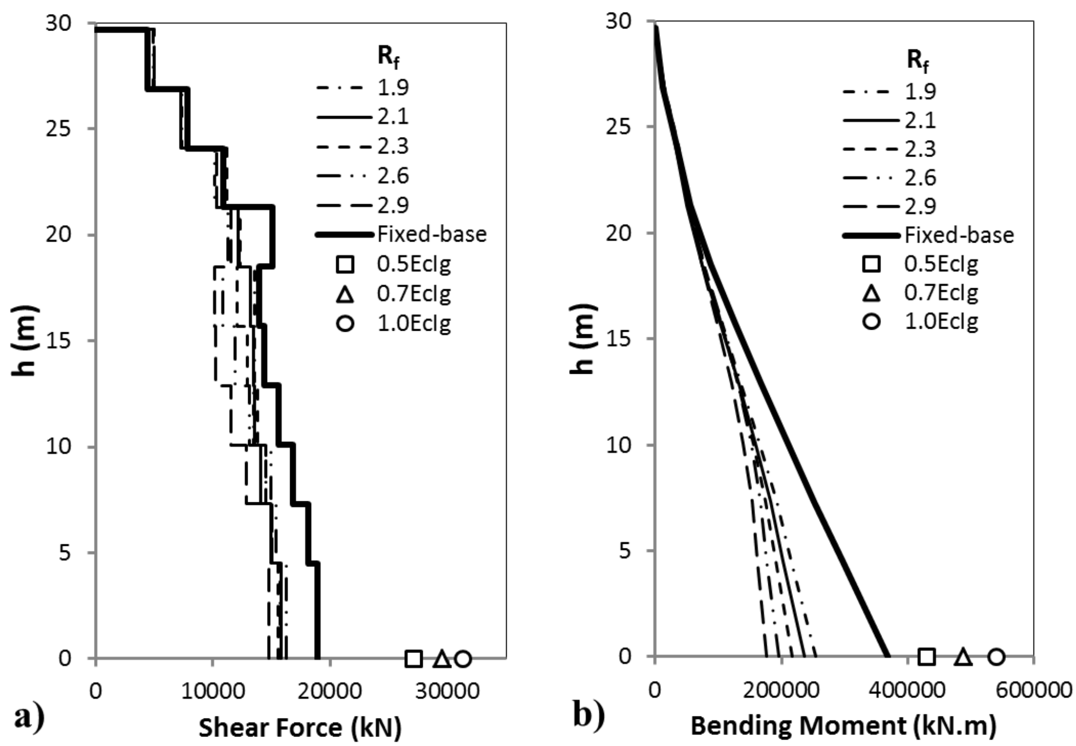

Figure A.40 Average of a) shear force, and b) bending moment envelopes for wall 10R13 on Rock along with estimated maximum quantities for the fixed-base wall from RSA using various effective stiffnesses

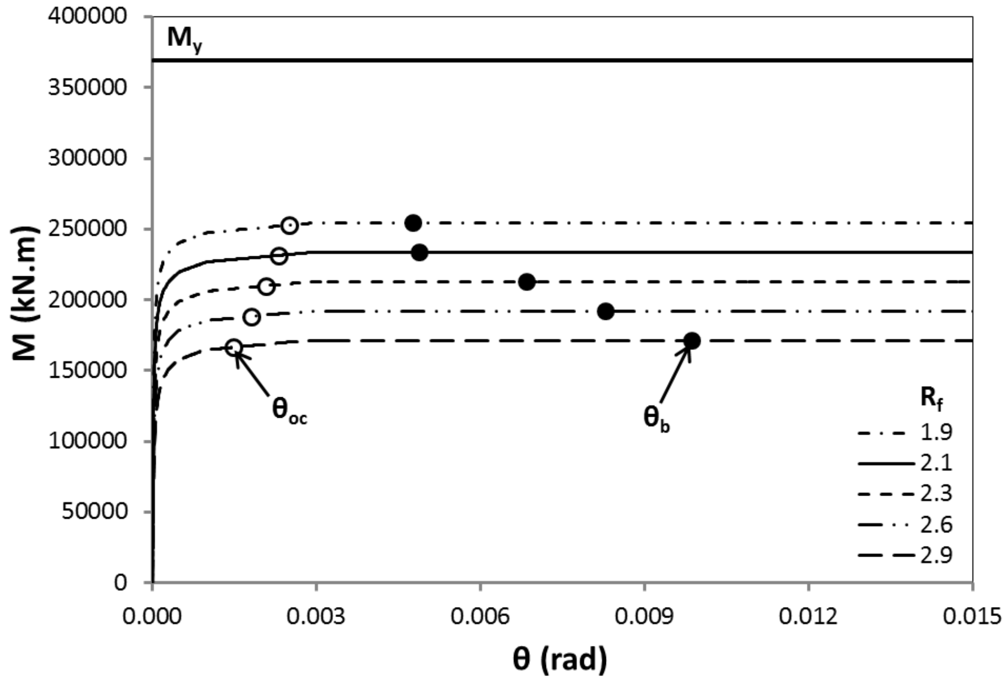

Figure A.41 Bending moment-rotation response of the foundation of wall 10R13 on Rock

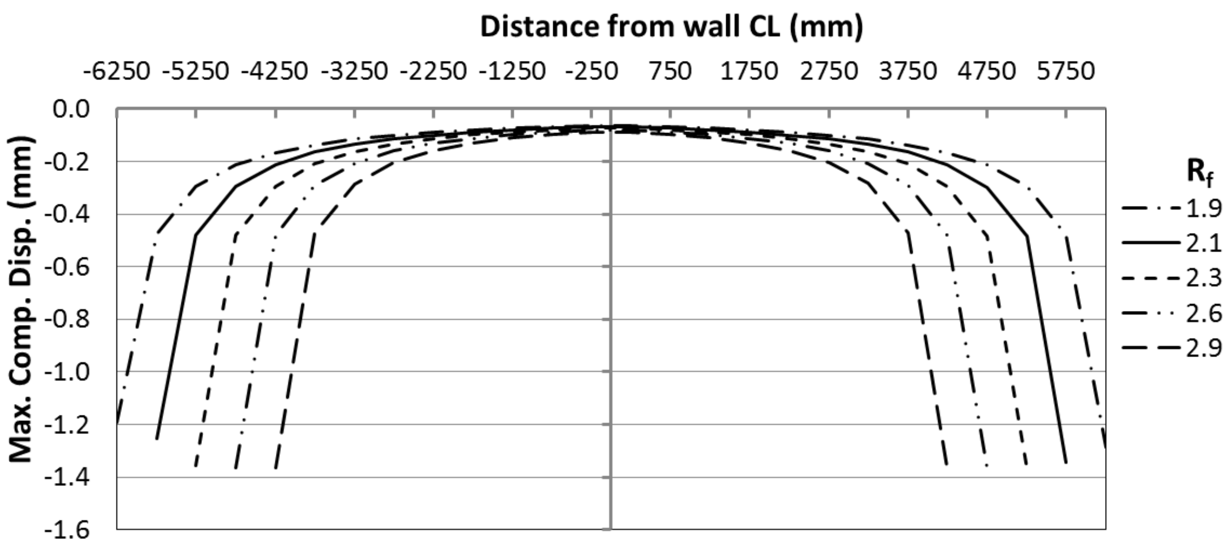

Figure A.42 Average of maximum soil compressive displacements underneath the footing for wall 10R13 on Rock

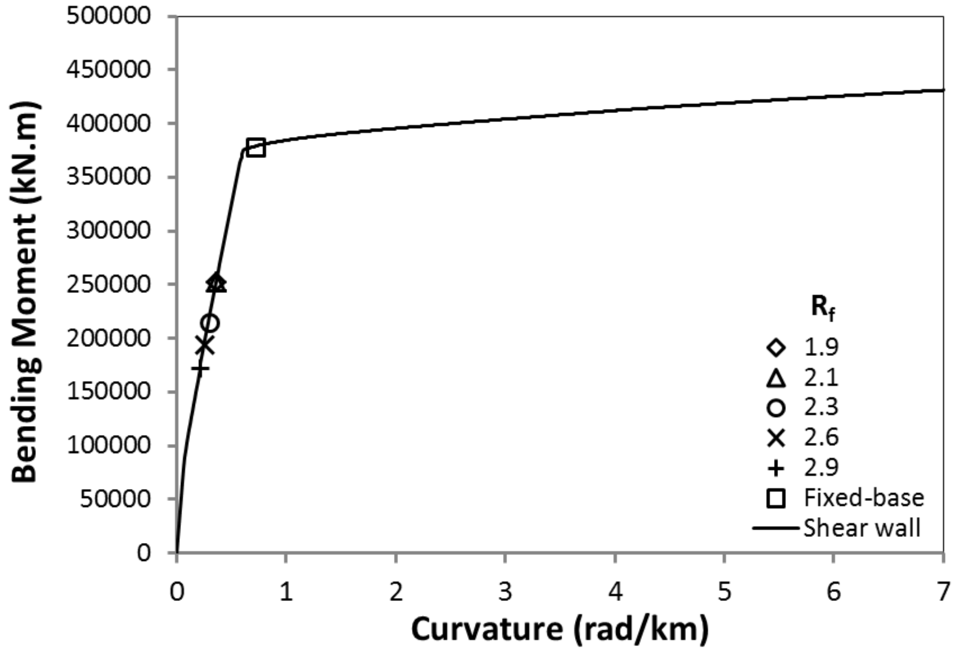

Figure A.43 Moment-curvature response of wall 10R13 along with average of maximum recorded curvatures at the base on Rock

A.5 Effect of Wall Height and Mass Ratio (MR)

This section presents an extended summary of NTHA results on the effect of wall height and mass ratio on the response of shear walls accounting for foundation rotation.

A.5.1 5-Storey walls

Table A.13 Shear wall properties for wall 5ElasticMR40

Shear Wall Properties	
N	5
L_w (mm)	5500
P (kN)	20775
M_{RSA} (kN.m)	288000
M_y (kN.m)	-----
R_w	1.00

Table A.14 Summary of nonlinear dynamic analyses for wall 5ElasticMR40 on Rock

R_f	1.4	1.6	1.8	2.1	2.2	2.4	2.7
E (MPa)	20000	20000	20000	20000	20000	20000	20000
G_{eff} (MPa)	8333	8333	8333	8333	8333	8333	8333
v	0.2	0.2	0.2	0.2	0.2	0.2	0.2
q_a (kPa)	7000	7000	7000	7000	7000	7000	7000
q (kPa)	49	68	86	114	133	157	188
q_f (kPa)	10000	10000	10000	10000	10000	10000	10000
q_{ult} (kPa)	20000	20000	20000	20000	20000	20000	20000
L (m)	20.5	17.5	15.5	13.5	12.5	11.5	10.5
B (m)	20.5	17.5	15.5	13.5	12.5	11.5	10.5
a (mm)	101	119	134	154	166	181	198
s (mm)	0.007	0.008	0.008	0.009	0.010	0.011	0.011
M_{oc} (kN.m)	211891	180548	159614	138633	128117	117580	107014
θ_{oc} (rad)	0.00133	0.00134	0.00132	0.00129	0.00126	0.00123	0.00119
$T_{Estimate}$ (sec)	0.5006	0.5009	0.5012	0.5018	0.5022	0.5028	0.5035
T_{model} (sec)	0.5012	0.5015	0.5019	0.5024	0.5028	0.5033	0.5040
Δ_1 (mm)	9.8	14.4	18.4	33.7	41.0	57.9	61.7
Δ_5 (mm)	55	69	81	132	156	214	226
Avg. Max. θ_b (rad)	0.0012	0.0023	0.0033	0.0068	0.0085	0.0123	0.0132
Avg. Max. Uplift (mm)	23.5	40.0	50.7	91.3	105.4	140.7	137.9
Avg. Max. Comp. Disp. (mm)	-0.67	-0.73	-0.72	-0.70	-0.69	-0.68	-0.67
Avg. Max. q_{max}/q_{ult}	9%	12%	13%	15%	17%	18%	20%

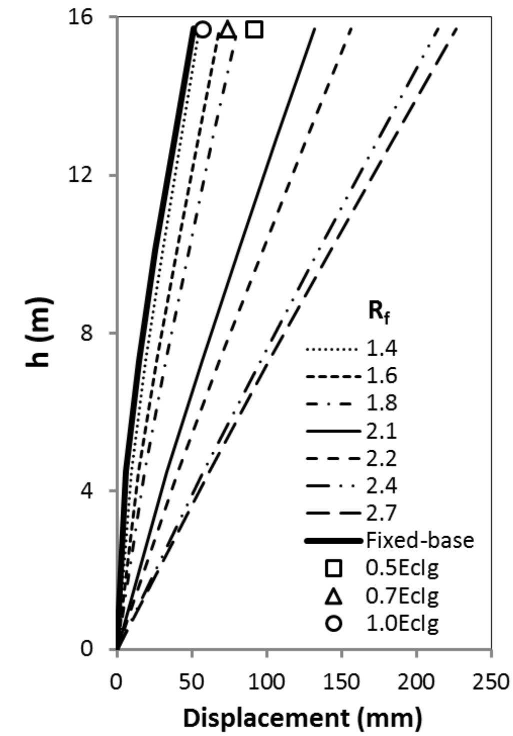

Figure A.44 Average of displacement envelopes for wall 5ElasticMR40 on Rock along with estimated top displacements of the fixed-base wall from RSA using various effective stiffnesses

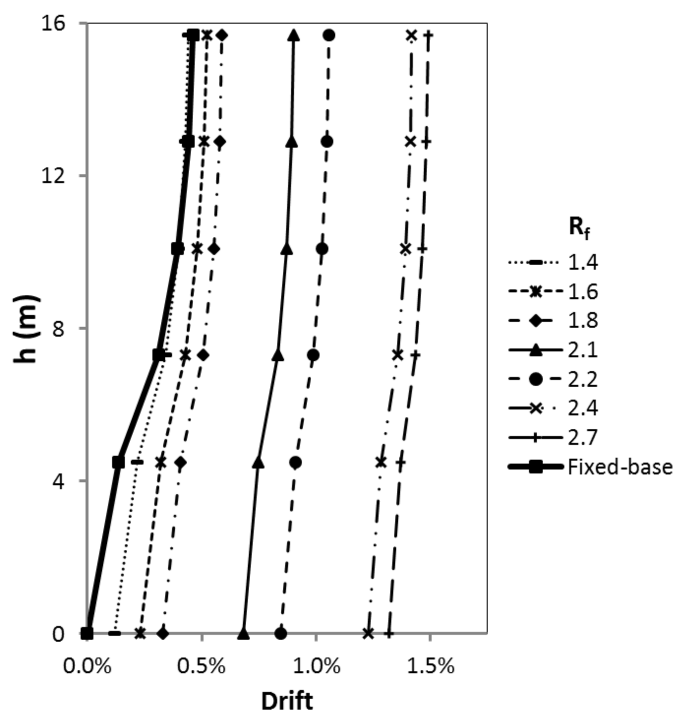

Figure A.45 Average of drift envelopes for wall 5ElasticMR40 on Rock (Note: base rotation values are plotted at h=0 and values of average interstory drift are plotted at the top of the storey.)

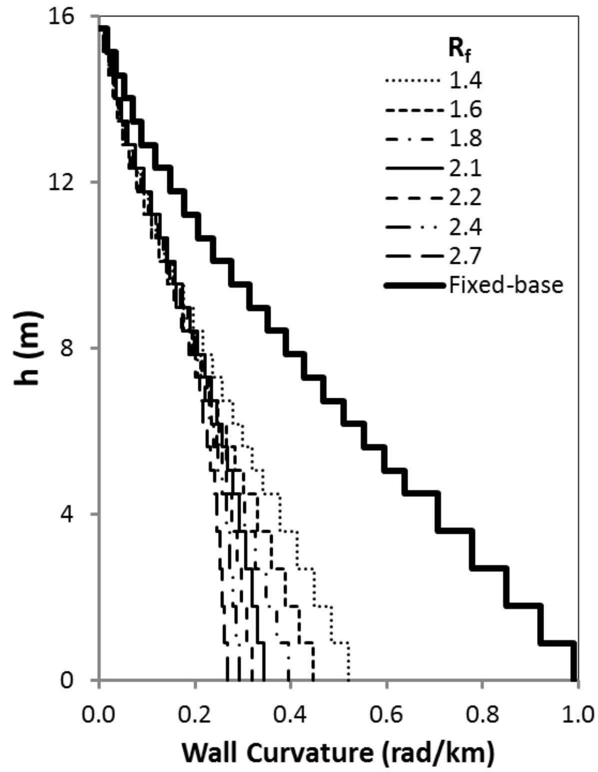

Figure A.46 Average of curvature envelopes for wall 5ElasticMR40 on Rock

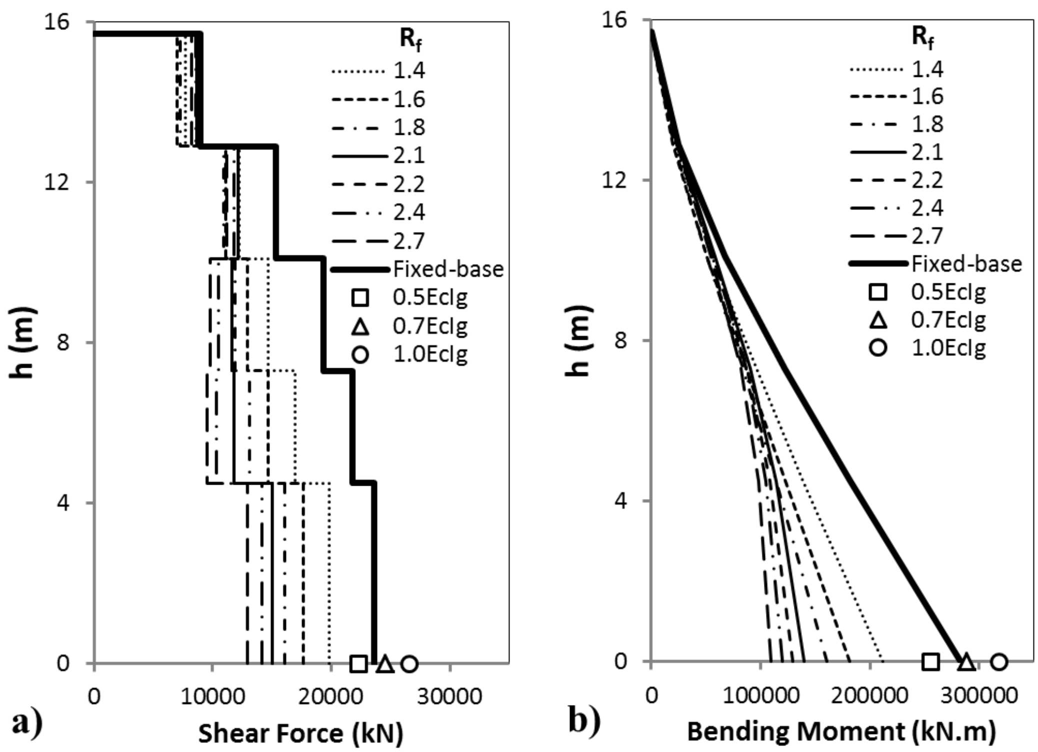

Figure A.47 Average of a) shear force, and b) bending moment envelopes for wall 5ElasticMR40 on Rock along with estimated maximum quantities for the fixed-base wall from RSA using various effective stiffnesses

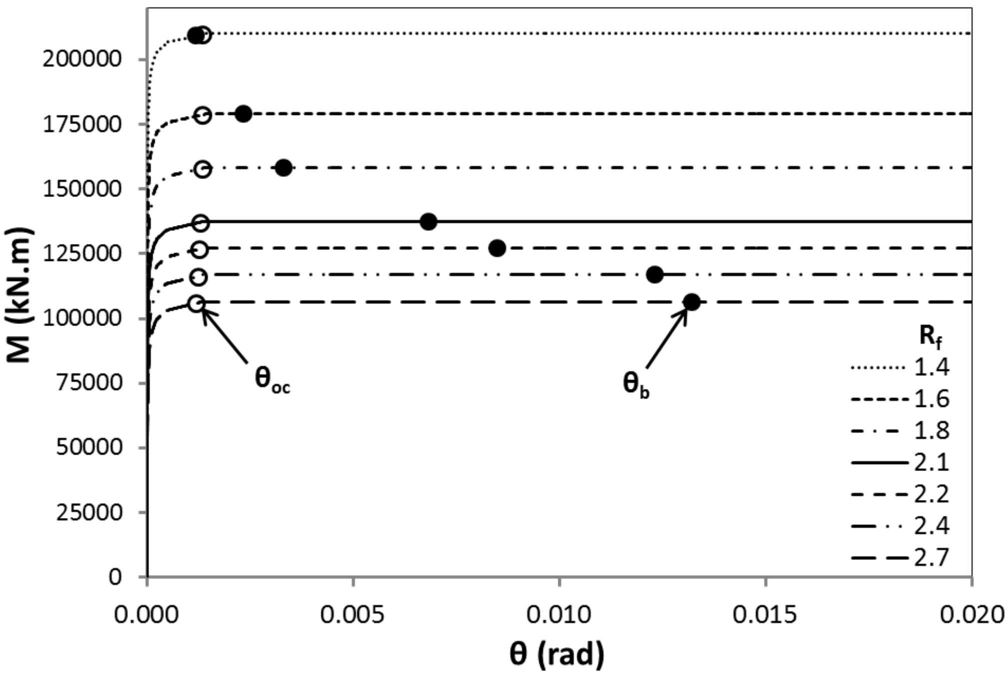

Figure A.48 Bending moment-rotation response of the foundation of wall 5ElasticMR40 on Rock

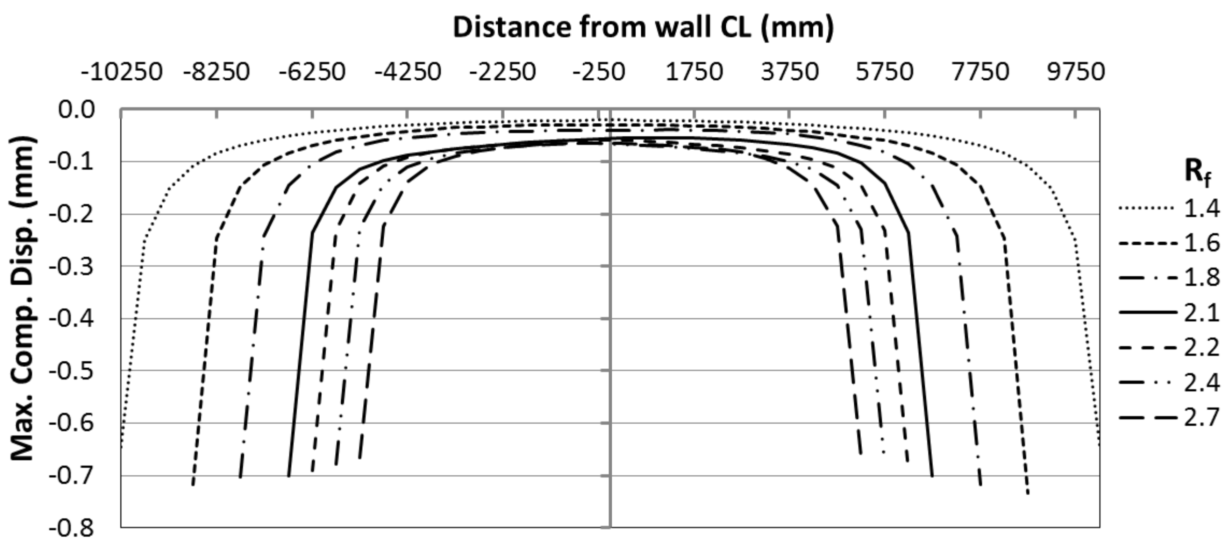

Figure A.49 Average of maximum soil compressive displacements underneath the footing for wall 5ElasticMR40 on Rock

Table A.15 Shear wall properties for wall 5ElasticMR60

Shear Wall Properties	
N	5
L_w (mm)	5500
P (kN)	31163
M_{RSA} (kN.m)	288000
M_y (kN.m)	-----
R_w	1.00

Table A.16 Summary of nonlinear dynamic analyses for wall 5ElasticMR60 on Rock

R_f	1.3	1.5	1.8	2.0	2.3	2.6	3.1
E (MPa)	20000	20000	20000	20000	20000	20000	20000
G_{eff} (MPa)	8333	8333	8333	8333	8333	8333	8333
v	0.2	0.2	0.2	0.2	0.2	0.2	0.2
q_a (kPa)	7000	7000	7000	7000	7000	7000	7000
q (kPa)	148	199	283	345	431	554	738
q_f (kPa)	10000	10000	10000	10000	10000	10000	10000
q_{ult} (kPa)	20000	20000	20000	20000	20000	20000	20000
L (m)	14.5	12.5	10.5	9.5	8.5	7.5	6.5
B (m)	14.5	12.5	10.5	9.5	8.5	7.5	6.5
a (mm)	215	249	297	328	367	416	479
s (mm)	0.013	0.015	0.017	0.018	0.020	0.021	0.023
M_{oc} (kN.m)	222583	190884	158979	142911	126728	110385	93808
θ_{oc} (rad)	0.00166	0.00156	0.00179	0.00163	0.00144	0.00121	0.00093
$T_{Estimate}$ (sec)	0.5015	0.5022	0.5035	0.5046	0.5061	0.5084	0.5119
T_{model} (sec)	0.5024	0.5032	0.5043	0.5053	0.5067	0.5089	0.5122
Δ_1 (mm)	9.5	14.0	18.9	32.2	44.0	65.5	80.4
Δ_5 (mm)	55	69	83	127	167	240	291
Avg. Max. θ_b (rad)	0.0011	0.0022	0.0034	0.0064	0.0091	0.0140	0.0174
Avg. Max. Uplift (mm)	14.5	26.3	34.7	60.2	76.7	104.0	112.1
Avg. Max. Comp. Disp. (mm)	-0.80	-0.98	-1.00	-0.97	-0.95	-0.91	-0.87
Avg. Max. q_{max}/q_{ult}	16%	24%	30%	33%	37%	42%	48%

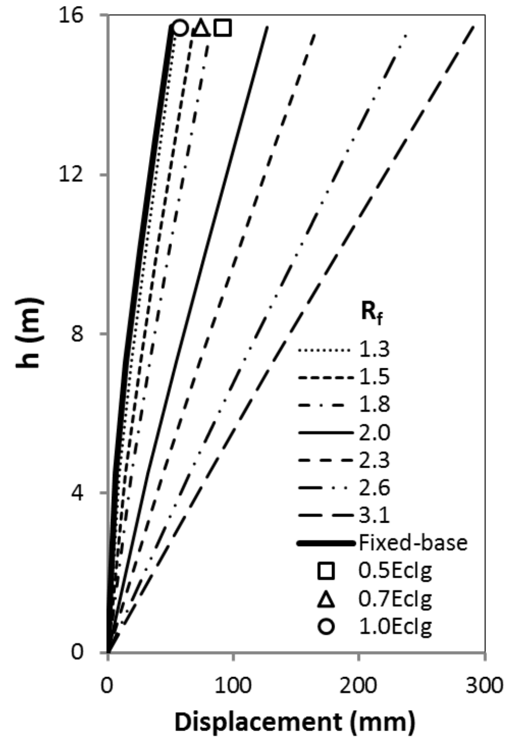

Figure A.50 Average of displacement envelopes for wall 5ElasticMR60 on Rock along with estimated top displacements of the fixed-base wall from RSA using various effective stiffnesses

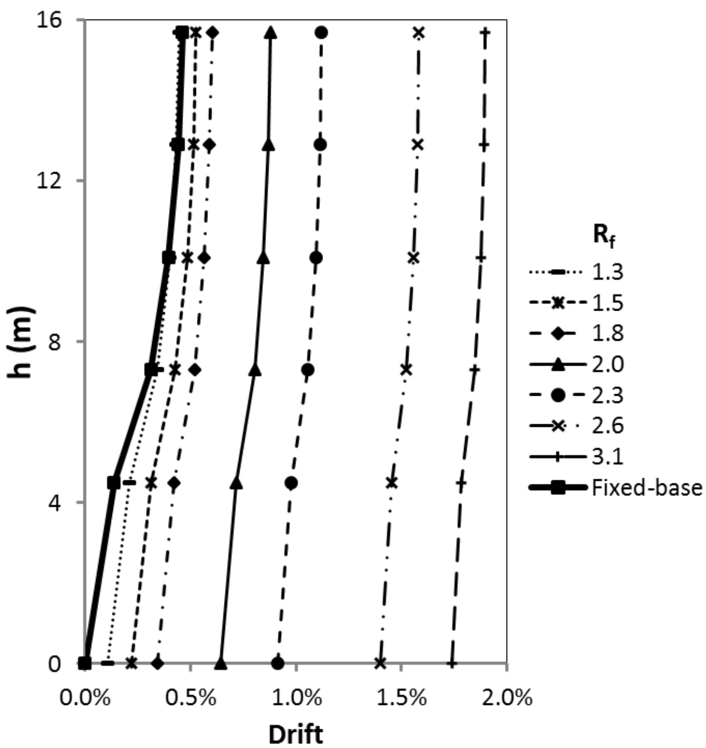

Figure A.51 Average of drift envelopes for wall 5ElasticMR60 on Rock (Note: base rotation values are plotted at h=0 and values of average interstory drift are plotted at the top of the storey.)

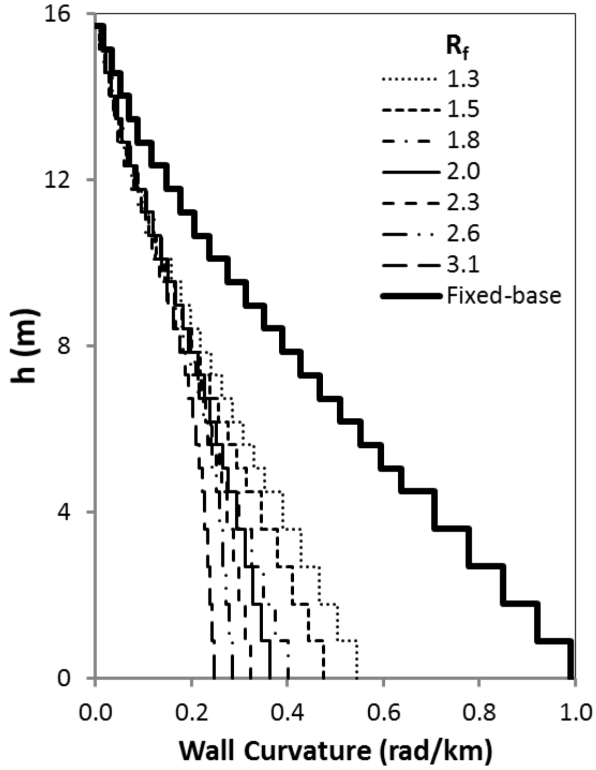

Figure A.52 Average of curvature envelopes for wall 5ElasticMR60 on Rock

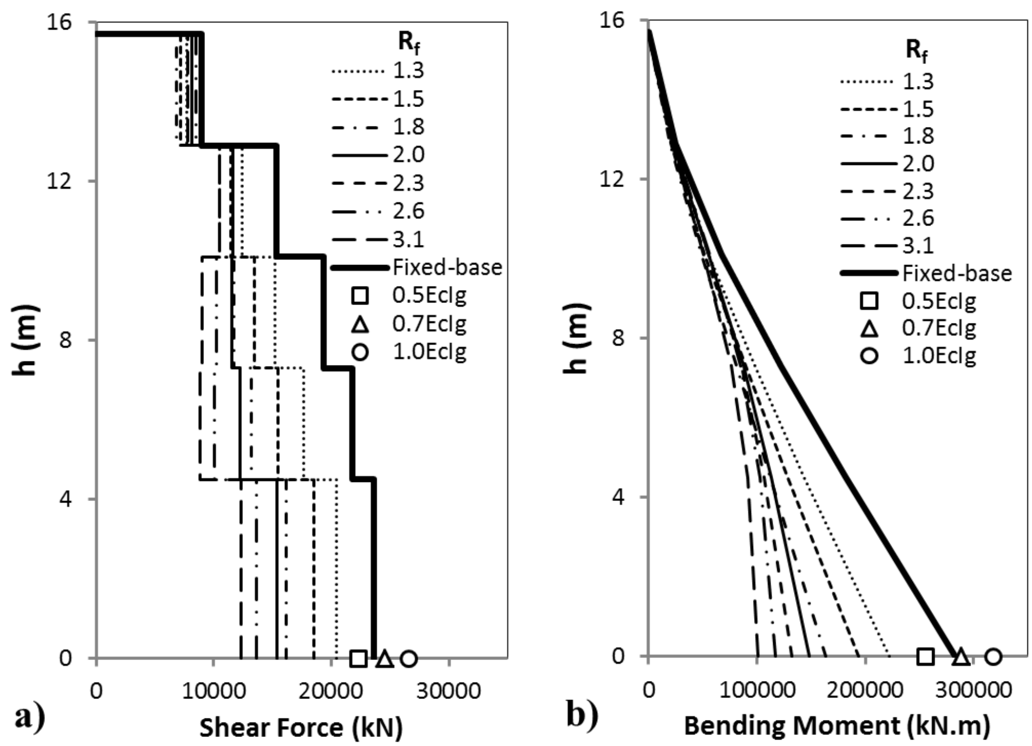

Figure A.53 Average of a) shear force, and b) bending moment envelopes for wall 5ElasticMR60 on Rock along with estimated maximum quantities for the fixed-base wall from RSA using various effective stiffnesses

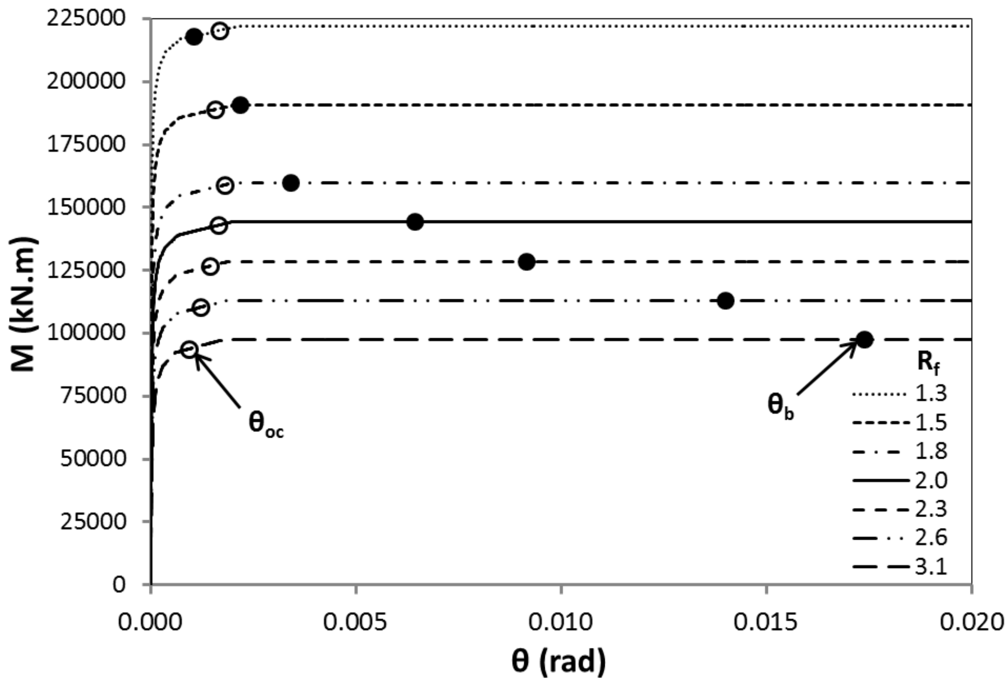

Figure A.54 Bending moment-rotation response of the foundation of wall 5ElasticMR60 on Rock

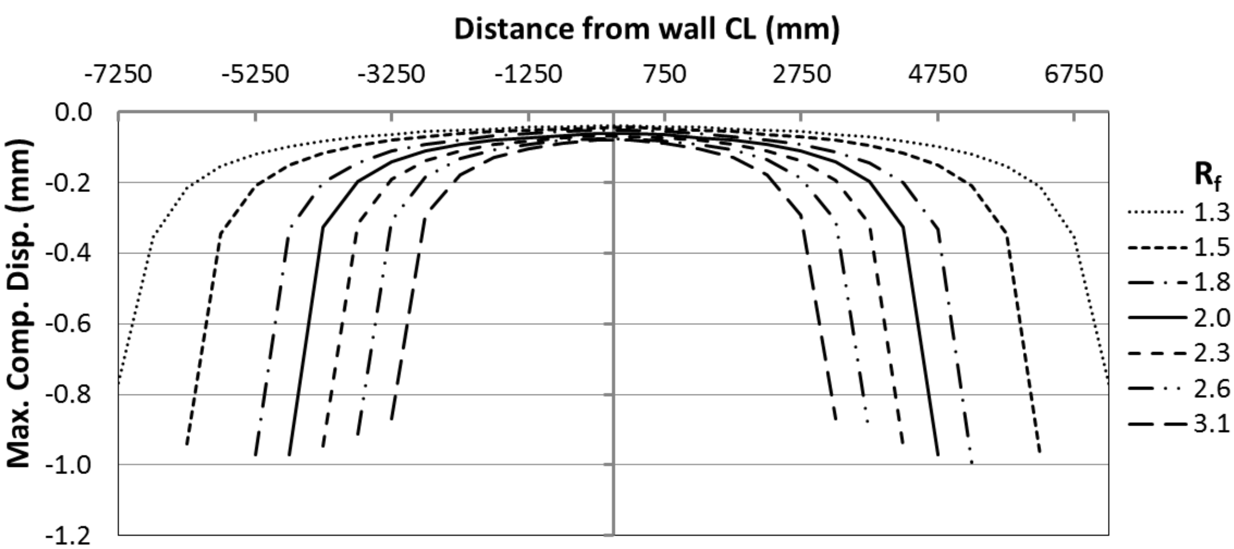

Figure A.55 Average of maximum soil compressive displacements underneath the footing for wall 5ElasticMR60 on Rock

A.5.2 10-Storey walls

Table A.17 Shear wall properties for wall 10ElasticMR40

N	10
L_w (mm)	5500
P (kN)	41550
M_{RSA} (kN.m)	488000
M_y (kN.m)	-----
R_w	1.00

Table A.18 Summary of nonlinear dynamic analyses for wall 10ElasticMR40 on Rock

R_f	1.3	1.4	1.7	1.9	2.1	2.3	2.6
E (MPa)	20000	20000	20000	20000	20000	20000	20000
G_{eff} (MPa)	8333	8333	8333	8333	8333	8333	8333
ν	0.2	0.2	0.2	0.2	0.2	0.2	0.2
q_a (kPa)	267	267	267	7000	7000	7000	7000
q (kPa)	121	153	198	266	314	377	460
q_f (kPa)	10000	10000	10000	10000	10000	10000	10000
q_{ult} (kPa)	20000	20000	20000	20000	20000	20000	20000
L (m)	18.5	16.5	14.5	12.5	11.5	10.5	9.5
B (m)	18.5	16.5	14.5	12.5	11.5	10.5	9.5
a (mm)	225	252	287	332	361	396	437
s (mm)	0.01	0.02	0.02	0.06	0.06	0.07	0.07
M_{oc} (kN.m)	379672	337556	295284	252782	231406	209917	188276
θ_{oc} (rad)	0.0029	0.0028	0.0026	0.0025	0.0023	0.0021	0.0018
θ_y (rad)	-----	-----	-----	-----	-----	-----	-----
$T_{Estimate}$ (sec)	1.06	1.06	1.06	1.07	1.07	1.07	1.08
T_{model} (sec)	1.08	1.08	1.08	1.08	1.08	1.08	1.09
Δ_1 (mm)	16.3	19.9	33.3	42.0	45.6	48.2	52.7
Δ_{10} (mm)	182	199	278	326	343	358	386
Avg. Max. θ_b (rad)	0.0028	0.0037	0.0068	0.0088	0.0096	0.0102	0.0113
Avg. Max. Uplift (mm)	50.4	59.3	96.5	108.2	109.4	106.1	105.8
Avg. Max. Comp. Disp. (mm)	-1.4	-1.4	-1.4	-1.5	-1.5	-1.5	-1.4
Avg. Max. q_{max}/q_{ult}	21%	25%	29%	33%	36%	40%	44%

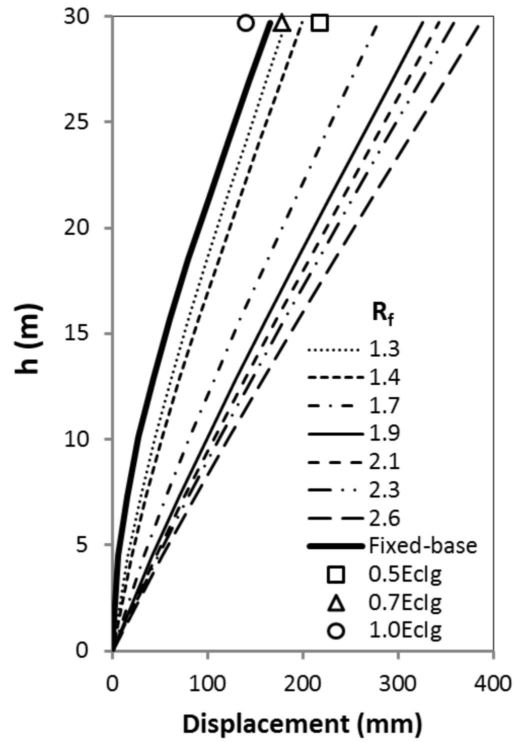

Figure A.56 Average of displacement envelopes for wall 10ElasticMR40 on Rock along with estimated top displacements of the fixed-base wall from RSA using various effective stiffnesses

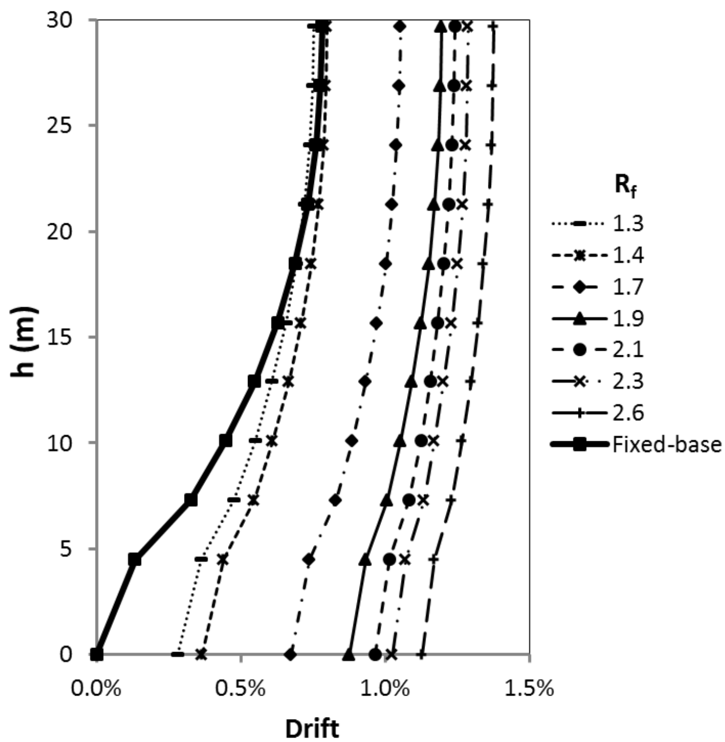

Figure A.57 Average of drift envelopes for wall 10ElasticMR40 on Rock (Note: base rotation values are plotted at h=0 and values of average interstory drift are plotted at the top of the storey.)

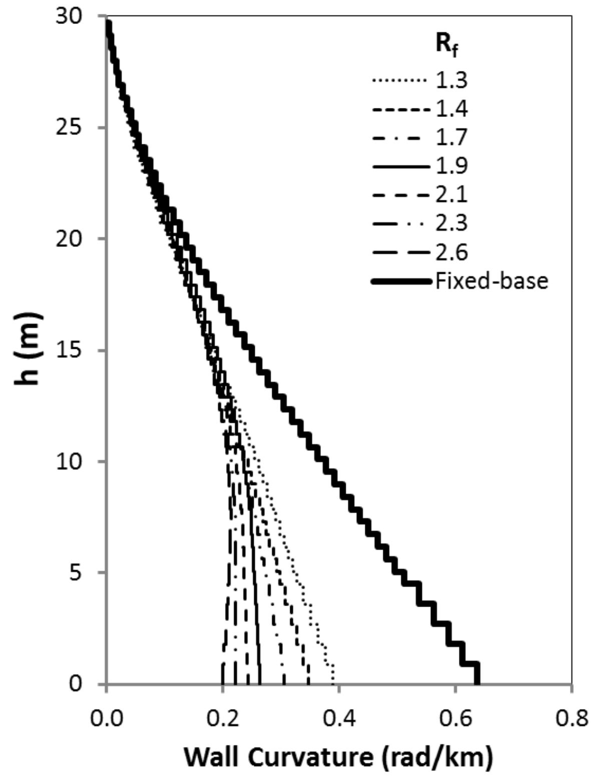

Figure A.58 Average of curvature envelopes for wall 10ElasticMR40 on Rock

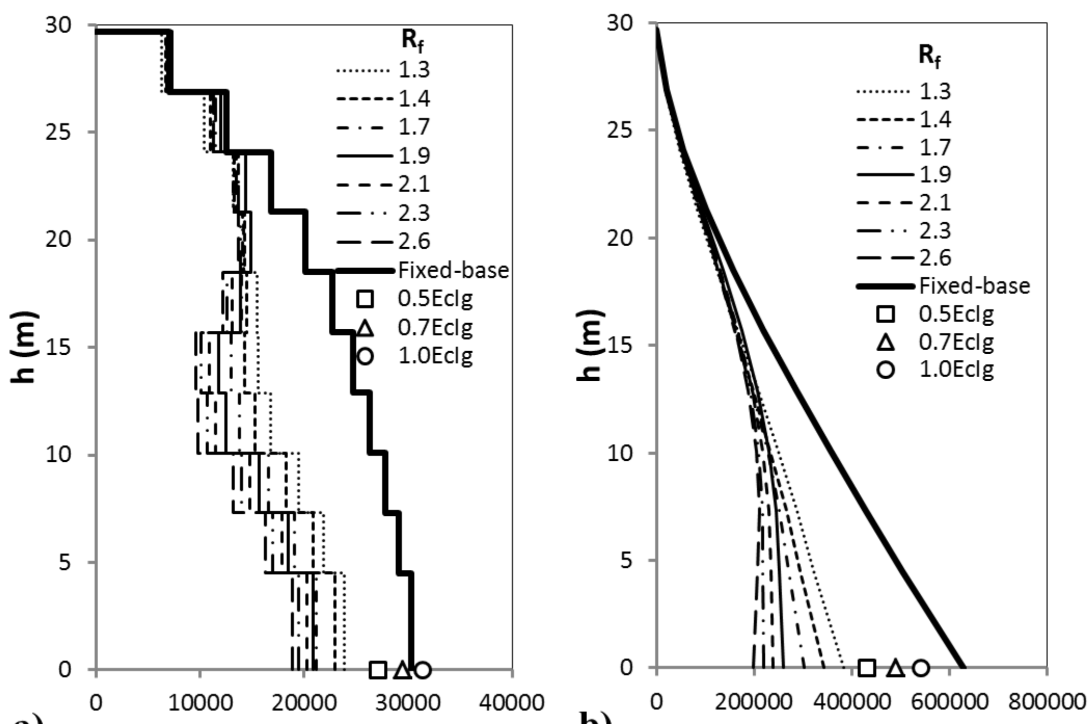

Figure A.59 Average of a) shear force, and b) bending moment envelopes for wall 10ElasticMR40 on Rock along with estimated maximum quantities for the fixed-base wall from RSA using various effective stiffnesses

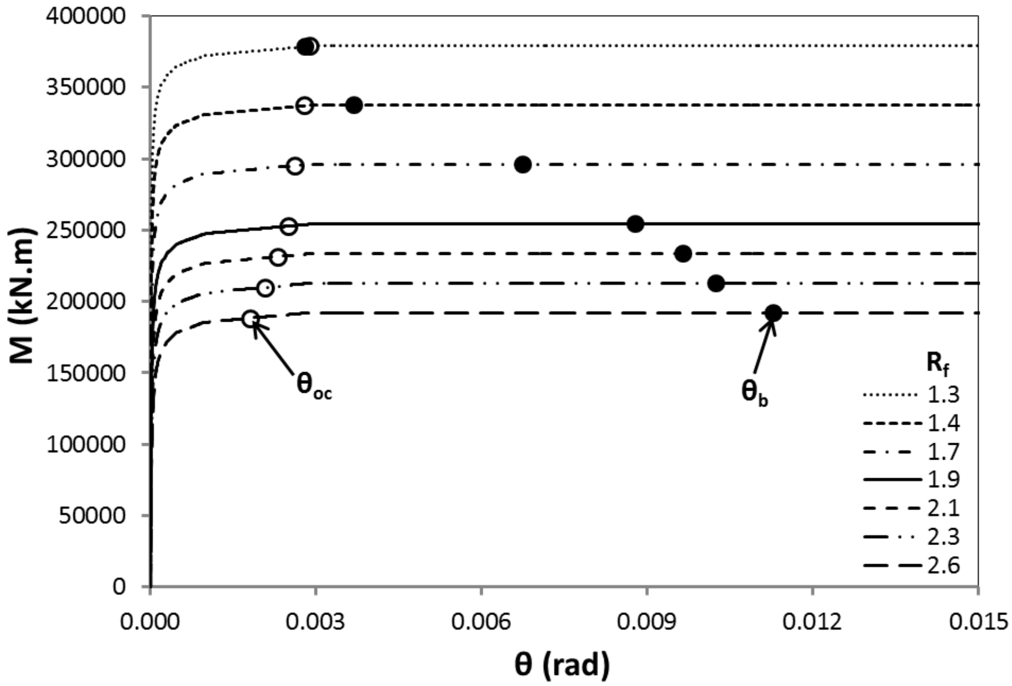

Figure A.60 Bending moment-rotation response of the foundation of wall 10ElasticMR40 on Rock

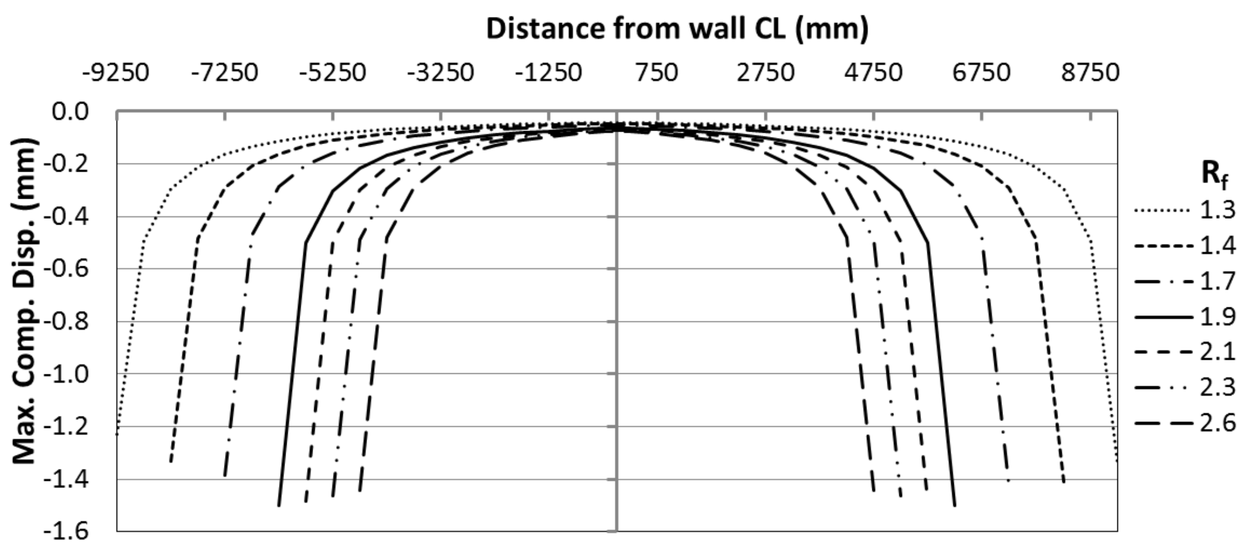

Figure A.61 Average of maximum soil compressive displacements underneath the footing for wall 10ElasticMR40 on Rock

Table A.19 Shear wall properties for wall 10ElasticMR60

Shear Wall Properties	
N	10
L_w (mm)	5500
P (kN)	62325
M_{RSA} (kN.m)	488000
M_y (kN.m)	-----
R_w	1.00

Table A.20 Summary of nonlinear dynamic analyses for wall 10ElasticMR60 on Rock

R_f	1.3	1.6	1.8	2.0	2.3	2.8	3.5
E (MPa)	20000	20000	20000	20000	20000	20000	20000
G_{eff} (MPa)	8333	8333	8333	8333	8333	8333	8333
ν	0.2	0.2	0.2	0.2	0.2	0.2	0.2
q_a (kPa)	7000	7000	7000	7000	7000	7000	7000
q (kPa)	399	565	691	863	1108	1475	1889
q_f (kPa)	10000	10000	10000	10000	10000	10000	10000
q_{ult} (kPa)	20000	20000	20000	20000	20000	20000	20000
L (m)	12.5	10.5	9.5	8.5	7.5	6.5	5.5
B (m)	12.5	10.5	9.5	8.5	7.5	6.5	6.0
a (mm)	499	594	656	733	831	959	1039
s (mm)	0.09	0.10	0.11	0.12	0.13	0.14	0.15
M_{oc} (kN.m)	373994	308709	275600	242032	207823	172676	139024
θ_{oc} (rad)	0.0023	0.0014	0.0013	0.0011	0.0009	0.0006	0.0005
θ_y (rad)	-----	-----	-----	-----	-----	-----	-----
$T_{Estimate}$ (sec)	1.07	1.07	1.08	1.08	1.09	1.10	1.12
T_{model} (sec)	1.08	1.09	1.09	1.09	1.10	1.11	1.13
Δ_1 (mm)	16.1	26.2	44.9	50.7	54.2	56.5	53.9
Δ_{10} (mm)	179	238	354	385	402	411	389
Avg. Max. θ_b (rad)	0.0028	0.0051	0.0094	0.0107	0.0115	0.0121	0.0116
Avg. Max. Uplift (mm)	32.7	51.8	86.7	88.9	84.5	76.8	58.1
Avg. Max. Comp. Disp. (mm)	-1.8	-2.1	-2.2	-2.1	-2.1	-2.0	-5.9
Avg. Max. q_{max}/q_{ult}	40%	57%	66%	73%	83%	96%	100%

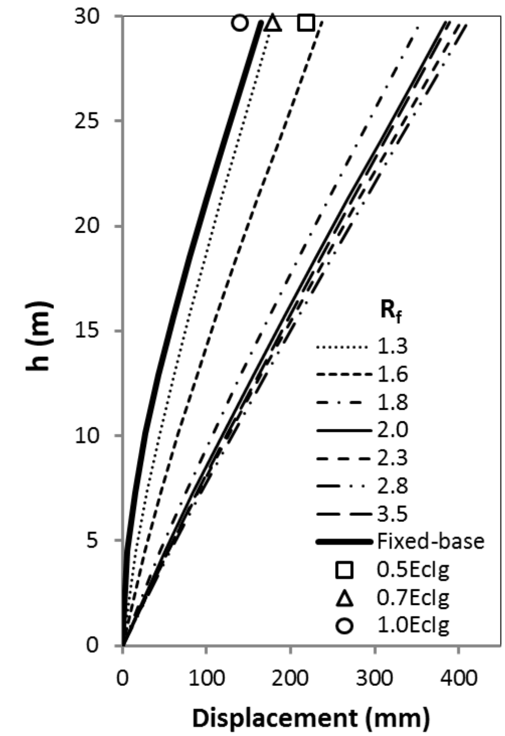

Figure A.62 Average of displacement envelopes for wall 10ElasticMR60 on Rock along with estimated top displacements of the fixed-base wall from RSA using various effective stiffnesses

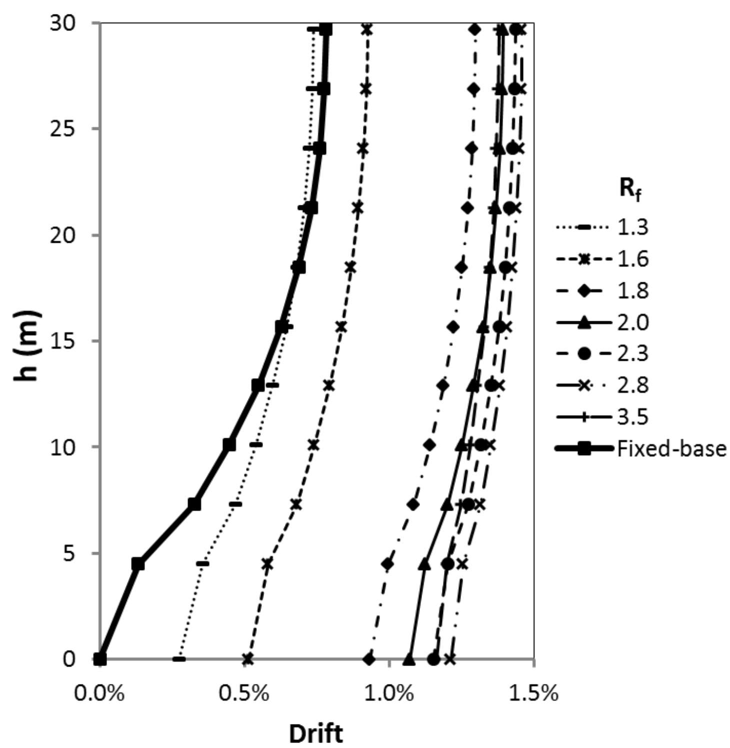

Figure A.63 Average of drift envelopes for wall 10ElasticMR60 on Rock (Note: base rotation values are plotted at h=0 and values of average interstory drift are plotted at the top of the storey.)

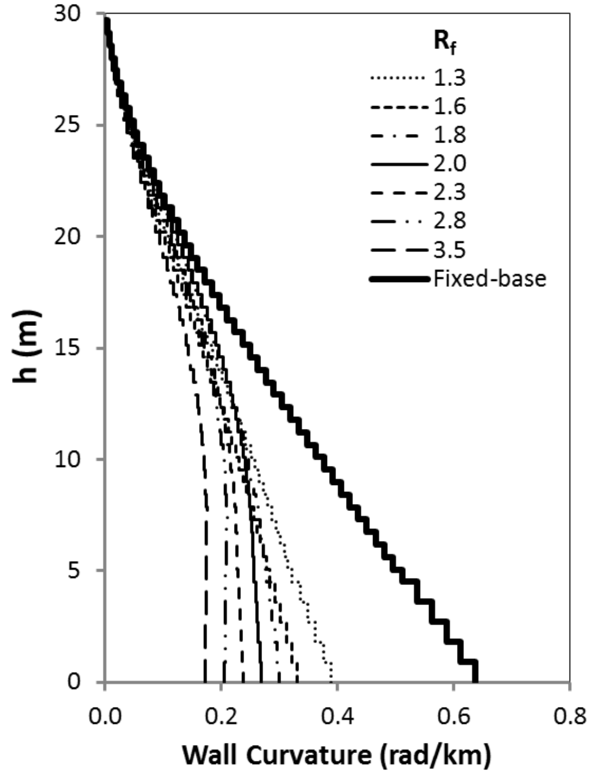

Figure A.64 Average of curvature envelopes for wall 10ElasticMR60 on Rock

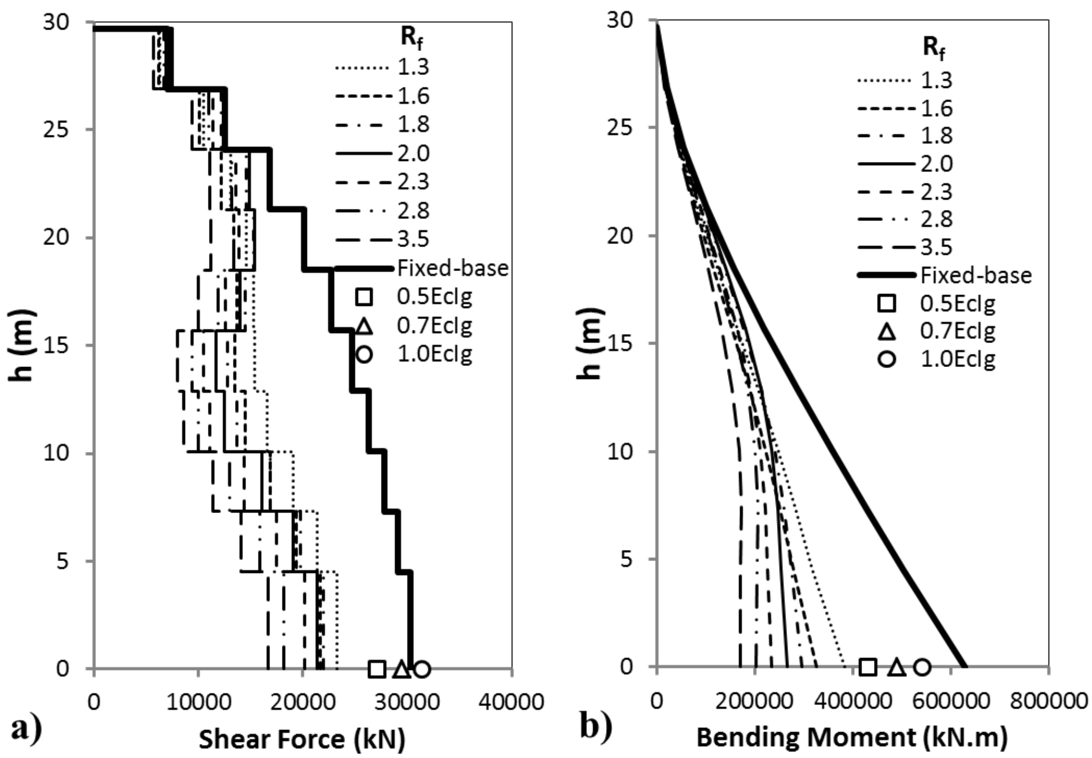

Figure A.65 Average of a) shear force, and b) bending moment envelopes for wall 10ElasticMR60 on Rock along with estimated maximum quantities for the fixed-base wall from RSA using various effective stiffnesses

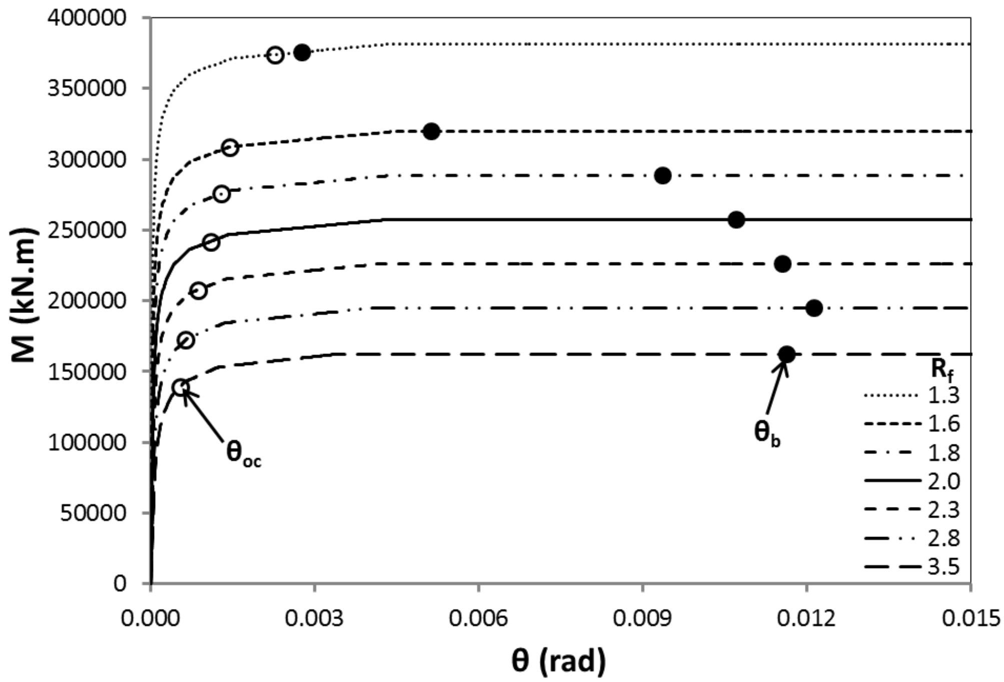

Figure A.66 Bending moment-rotation response of the foundation of wall 10ElasticMR60 on Rock

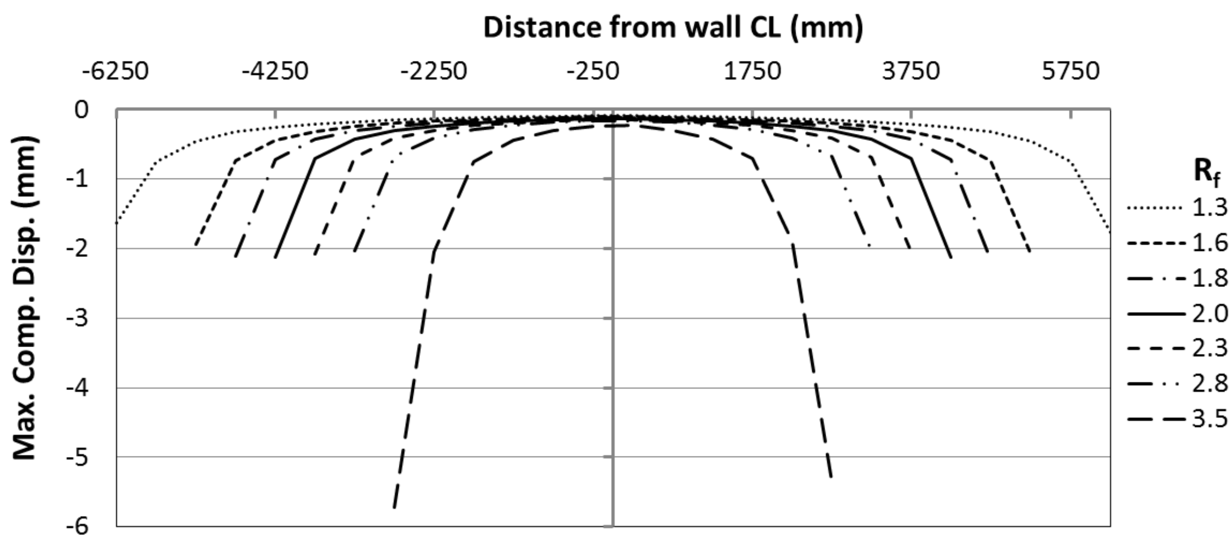

Figure A.67 Average of maximum soil compressive displacements underneath the footing for wall 10ElasticMR60 on Rock

A.5.3 20-Storey walls

Table A.21 Shear wall properties for wall 20ElasticMR40

Shear Wall Properties	
N	20
L_w (mm)	5500
P (kN)	83100
M_{RSA} (kN.m)	961600
M_y (kN.m)	-----
R_w	1.00

Table A.22 Summary of nonlinear dynamic analyses for wall 20ElasticMR40 on Rock

R_f	1.3	1.4	1.7	2.0	2.4	2.7	3.1
E (MPa)	20000	20000	20000	20000	20000	20000	20000
G_{eff} (MPa)	8333	8333	8333	8333	8333	8333	8333
v	0.2	0.2	0.2	0.2	0.2	0.2	0.2
q_a (kPa)	7000	7000	7000	7000	7000	7000	7000
q (kPa)	243	305	395	532	754	921	1150
q_f (kPa)	10000	10000	10000	10000	10000	10000	10000
q_{ult} (kPa)	20000	20000	20000	20000	20000	20000	20000
L (m)	18.5	16.5	14.5	12.5	10.5	9.5	8.5
B (m)	18.5	16.5	14.5	12.5	10.5	9.5	8.5
a (mm)	449	504	573	665	791	875	978
s (mm)	0.08	0.09	0.10	0.12	0.13	0.14	0.16
M_{oc} (kN.m)	750011	664649	578663	491753	403391	358380	312554
θ_{oc} (rad)	0.0038	0.0031	0.0022	0.0018	0.0013	0.0011	0.0009
θ_y (rad)	-----	-----	-----	-----	-----	-----	-----
$T_{Estimate}$ (sec)	2.01	2.01	2.02	2.03	2.04	2.05	2.07
T_{model} (sec)	2.01	2.01	2.02	2.03	2.04	2.05	2.07
Δ_1 (mm)	20.2	30.5	40.5	53.2	63.8	70.5	72.0
Δ_{10} (mm)	184	244	303	380	446	485	494
Avg. Max. θ_b (rad)	0.0040	0.0064	0.0087	0.0115	0.0139	0.0154	0.0158
Avg. Max. Uplift (mm)	72.3	102.6	122.5	141.0	143.4	143.8	131.4
Avg. Max. Comp. Disp. (mm)	-2.5	-2.8	-2.9	-3.0	-2.9	-2.9	-2.8
Avg. Max. q_{max}/q_{ult}	36%	45%	55%	67%	79%	88%	98%

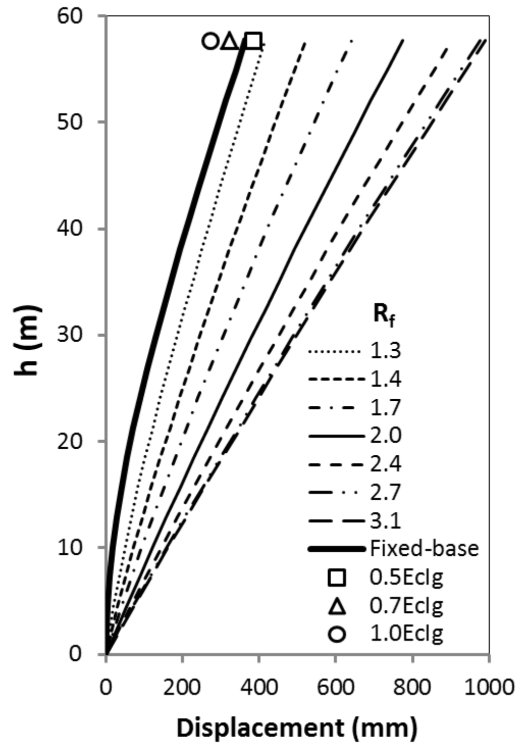

Figure A.68 Average of displacement envelopes for wall 20ElasticMR40 on Rock along with estimated top displacements of the fixed-base wall from RSA using various effective stiffnesses

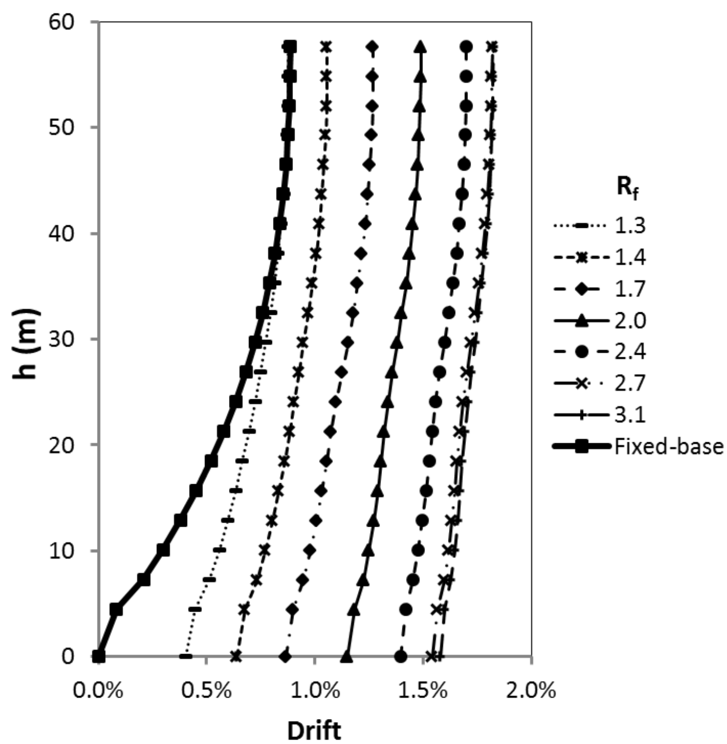

Figure A.69 Average of drift envelopes for wall 20ElasticMR40 on Rock (Note: base rotation values are plotted at h=0 and values of average interstory drift are plotted at the top of the storey.)

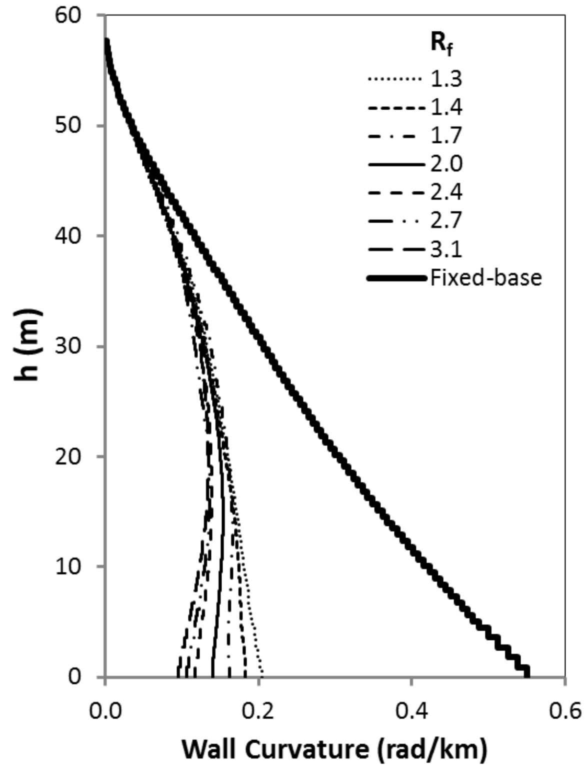

Figure A.70 Average of curvature envelopes for wall 20ElasticMR40 on Rock

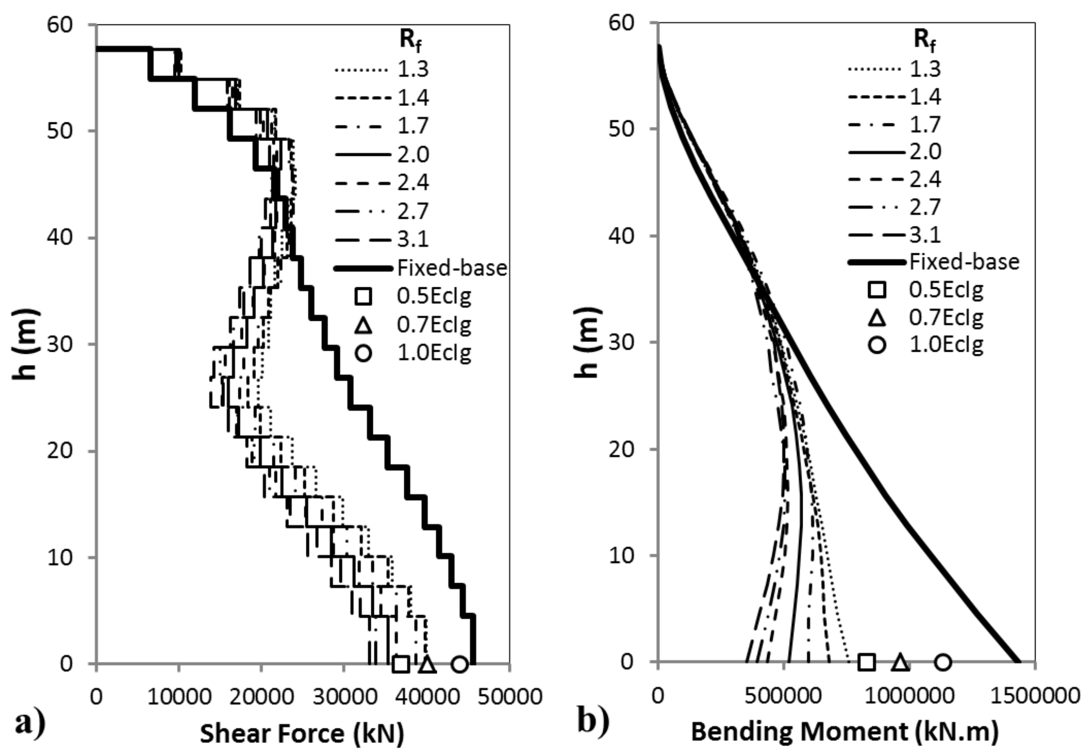

Figure A.71 Average of a) shear force, and b) bending moment envelopes for wall 20ElasticMR40 on Rock along with estimated maximum quantities for the fixed-base wall from RSA using various effective stiffnesses

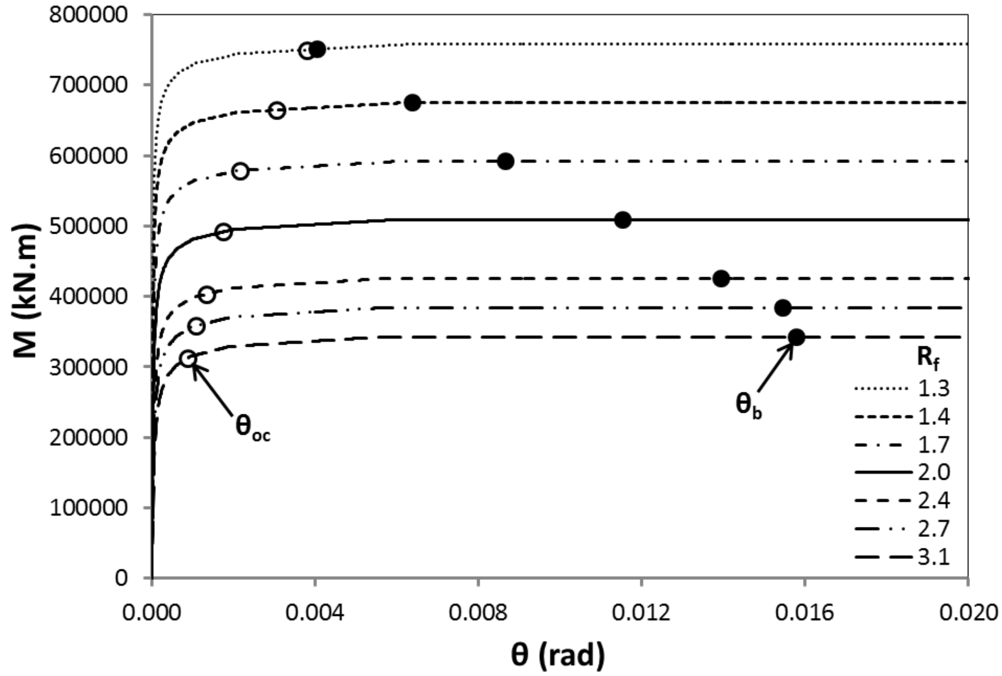

Figure A.72 Bending moment-rotation response of the foundation of wall 20ElasticMR40 on Rock

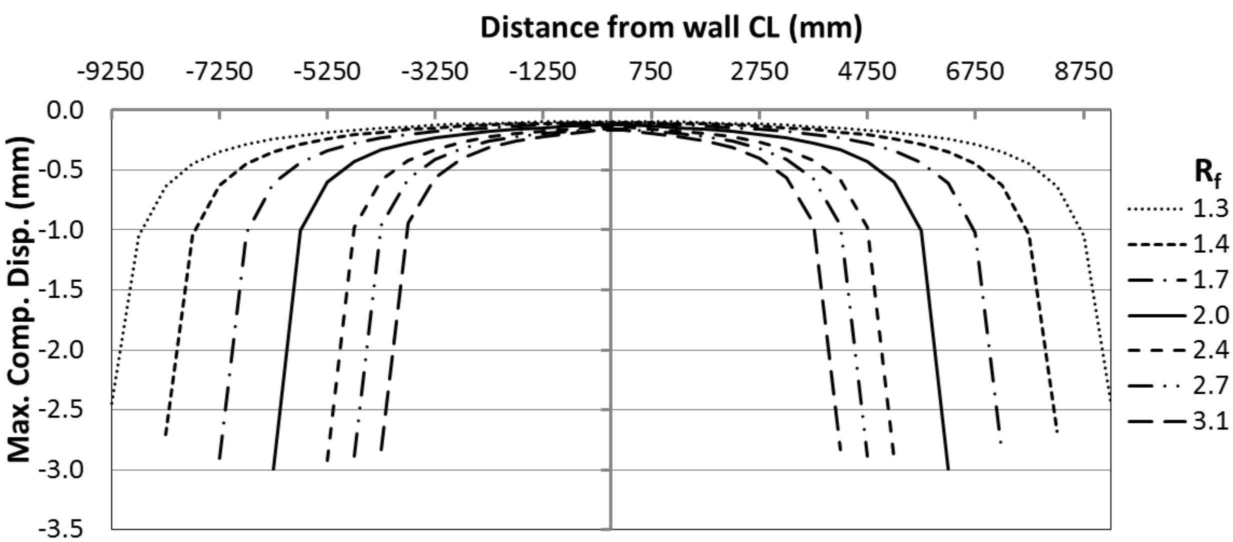

Figure A.73 Average of maximum soil compressive displacements underneath the footing for wall 20ElasticMR40 on Rock

Table A.23 Shear wall properties for wall 20ElasticMR60

Shear Wall Properties	
N	20
L_w (mm)	5500
P (kN)	124650
M_{RSA} (kN.m)	961600
M_y (kN.m)	-----
R_w	1.00

Table A.24 Summary of nonlinear dynamic analyses for wall 20ElasticMR60 on Rock

R_f	1.3	1.5	1.7	1.9	2.2	2.6	3.4
E (MPa)	20000	20000	20000	20000	20000	20000	20000
G_{eff} (MPa)	8333	8333	8333	8333	8333	8333	8333
ν	0.2	0.2	0.2	0.2	0.2	0.2	0.2
q_a (kPa)	7000	7000	7000	7000	7000	7000	7000
q (kPa)	798	943	1131	1381	1725	2216	2950
q_f (kPa)	10000	10000	10000	10000	10000	10000	10000
q_{ult} (kPa)	20000	20000	20000	20000	20000	20000	20000
L (m)	12.5	11.5	10.5	9.5	8.5	7.5	6.5
B (m)	12.5	11.5	10.5	9.5	8.5	7.5	6.5
a (mm)	997	1084	1187	1312	1466	1662	1918
s (mm)	0.17	0.19	0.20	0.22	0.24	0.26	0.29
M_{oc} (kN.m)	716912	649183	580424	510311	438365	363853	285592
θ_{oc} (rad)	0.0014	0.0012	0.0010	0.0008	0.0007	0.0005	0.0004
θ_y (rad)	-----	-----	-----	-----	-----	-----	-----
$T_{Estimate}$ (sec)	2.03	2.03	2.04	2.05	2.07	2.10	2.14
T_{model} (sec)	2.03	2.04	2.05	2.06	2.07	2.10	2.14
Δ_1 (mm)	21.5	32.7	36.3	40.5	48.6	51.3	57.3
Δ_{10} (mm)	194	263	281	300	351	363	399
Avg. Max. θ_b (rad)	0.0043	0.0069	0.0077	0.0087	0.0105	0.0111	0.0125
Avg. Max. Uplift (mm)	50.8	74.6	76.2	76.9	82.7	76.3	73.2
Avg. Max. Comp. Disp. (mm)	-3.3	-4.2	-4.7	-5.4	-6.6	-7.2	-8.3
Avg. Max. q_{max}/q_{ult}	73%	90%	97%	100%	100%	100%	100%

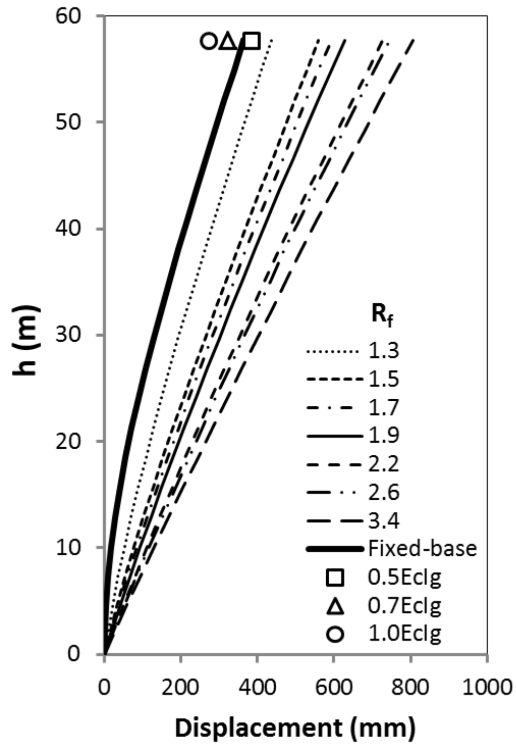

Figure A.74 Average of displacement envelopes for wall 20ElasticMR60 on Rock along with estimated top displacements of the fixed-base wall from RSA using various effective stiffnesses

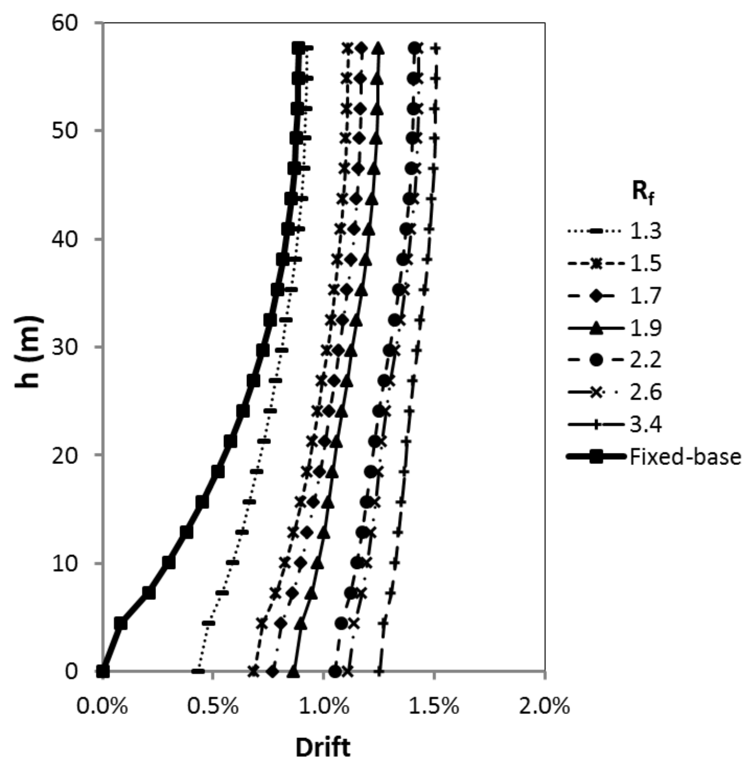

Figure A.75 Average of drift envelopes for wall 20ElasticMR60 on Rock (Note: base rotation values are plotted at h=0 and values of average interstory drift are plotted at the top of the storey.)

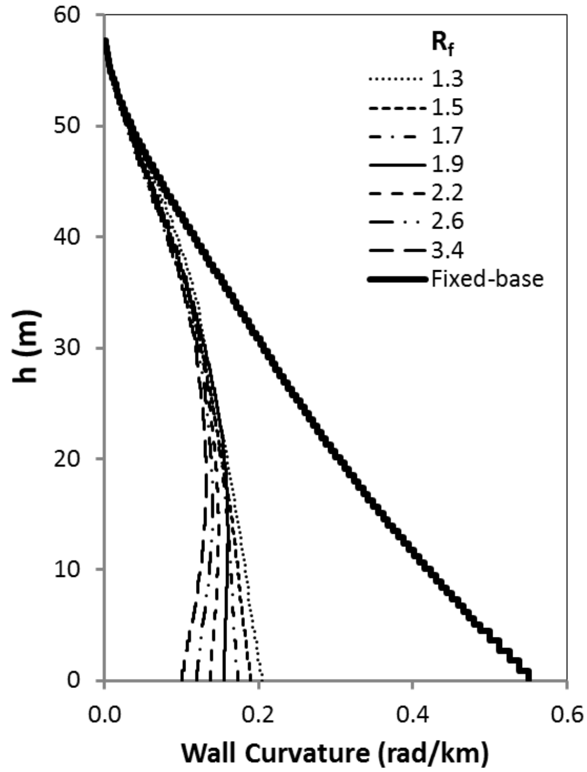

Figure A.76 Average of curvature envelopes for wall 20ElasticMR60 on Rock

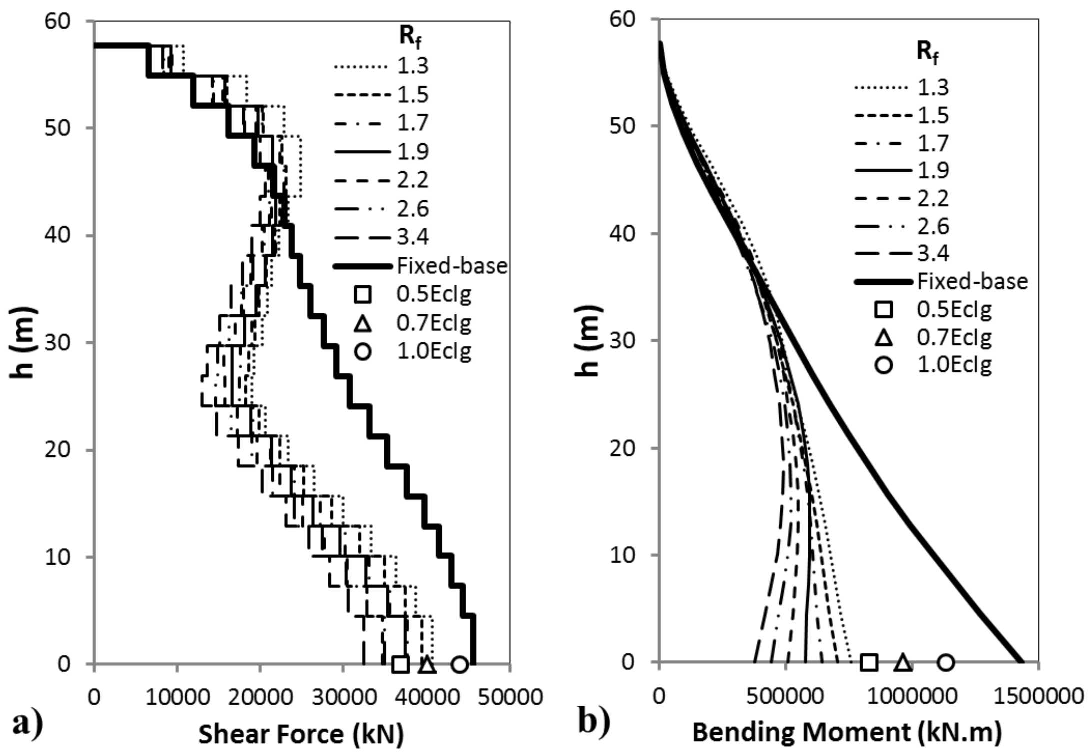

Figure A.77 Average of a) shear force, and b) bending moment envelopes for wall 20ElasticMR60 on Rock along with estimated maximum quantities for the fixed-base wall from RSA using various effective stiffnesses

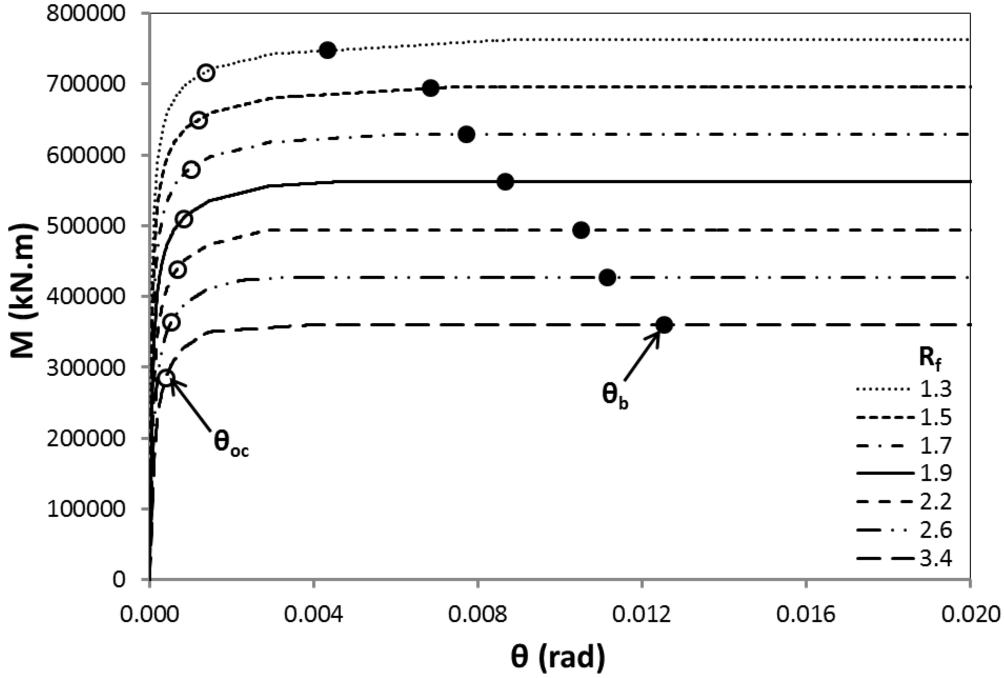

Figure A.78 Bending moment-rotation response of the foundation of wall 20ElasticMR60 on Rock

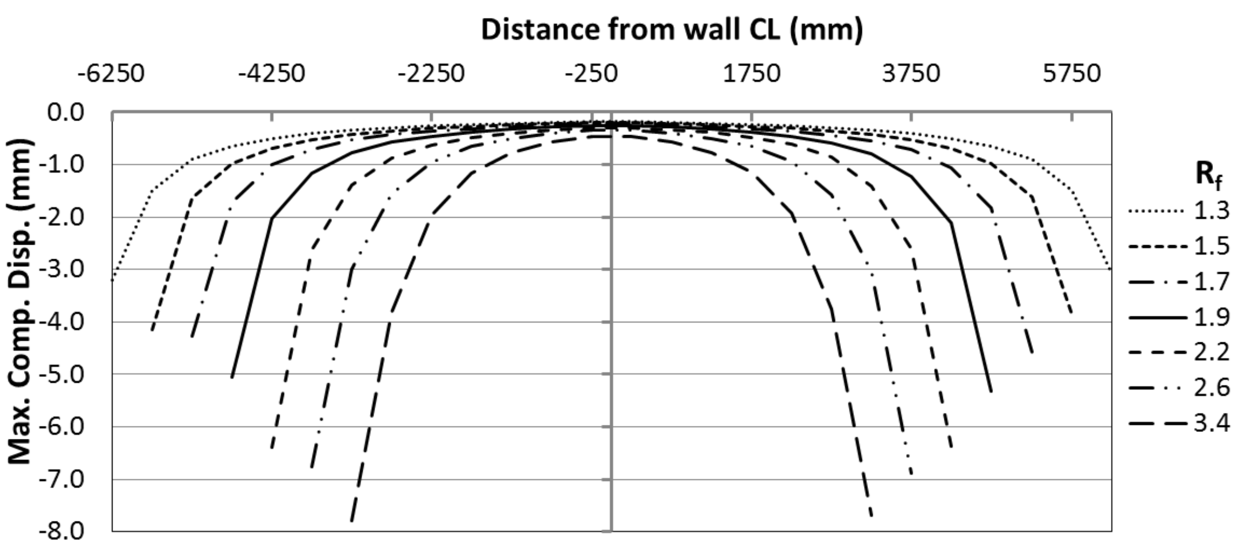

Figure A.79 Average of maximum soil compressive displacements underneath the footing for wall 20ElasticMR60 on Rock

A.6 Core NTHA – Summary of Results

Sections below present an extended summary of the core NTHA for the five types of soil considered in this study.

A.6.1 Clay

Table A.25 Properties of Clay

G_0 (MPa)	43
G_{eff} (MPa)	22
v	0.3
E (MPa)	57
q_{ult} (kPa)	400
q_f (kPa)	200
q_a (kPa)	133
V_s (m/s)	200

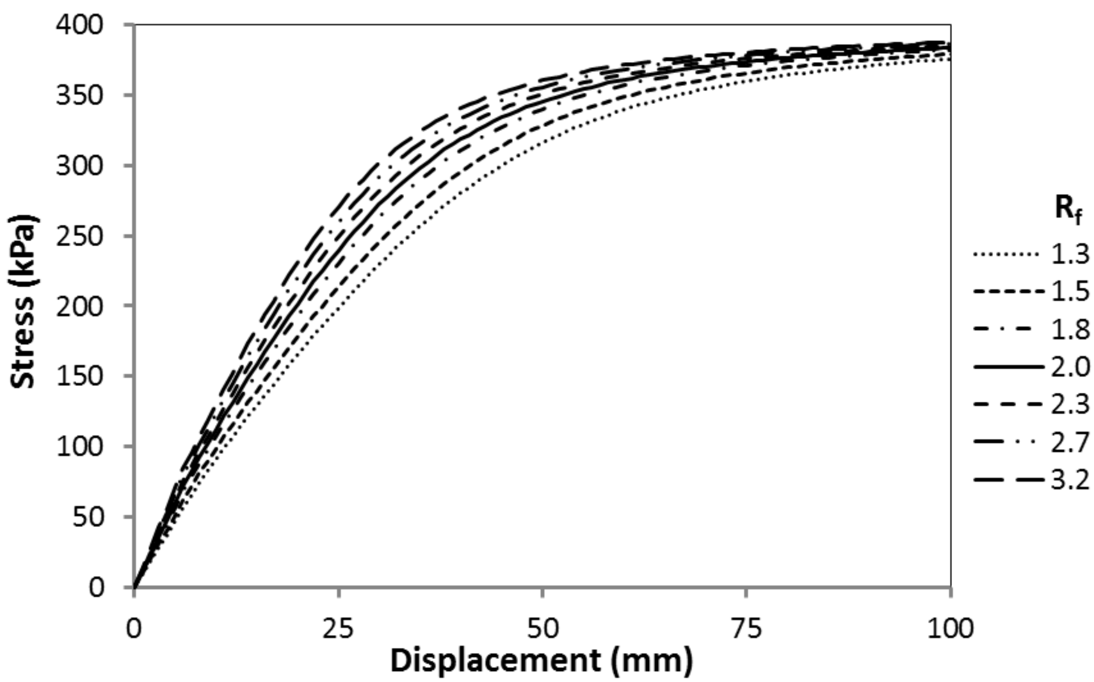

Figure A.80 Soil spring responses in monotonic compression for Clay

Table A.26 Shear wall properties for wall 10R27

N	10
L_w (mm)	5500
P (kN)	41550
M_{RSA} (kN.m)	488000
M_y (kN.m)	179000
R_w	2.73

Table A.27 Summary of nonlinear dynamic analyses for wall 10R27 on Clay

R_f	1.8	2.0	2.3	2.7	3.2
E (MPa)	57	57	57	57	57
G_{eff} (MPa)	22	22	22	22	22
v	0.3	0.3	0.3	0.3	0.3
q_a (kPa)	133	133	133	133	133
q (kPa)	82	90	99	109	121
q_f (kPa)	200	200	200	200	200
q_{ult} (kPa)	400	400	400	400	400
L (m)	22.5	21.5	20.5	19.5	18.5
B (m)	22.5	21.5	20.5	19.5	18.5
a (mm)	9233	9663	10134	10654	11230
s (mm)	7.47	7.76	8.07	8.41	8.78
M_{oc} (kN.m)	275615	245918	215351	183779	151040
θ_{oc} (rad)	0.0019	0.0018	0.0016	0.0014	0.0013
θ_y (rad)	0.0008	0.0009	0.0011	0.0014	0.0017
$T_{Estimate}$ (sec)	1.32	1.35	1.39	1.38	1.48
T_{model} (sec)	1.33	1.37	1.42	1.44	1.53
Δ_1 (mm)	15.3	16.2	17.2	18.7	19.9
Δ_{10} (mm)	222	230	239	248	252
Avg. Max. θ_b (rad)	0.0011	0.0013	0.0016	0.0019	0.0023
Avg. Max. Uplift (mm)	4.8	6.3	8.2	10.8	13.7
Avg. Max. Comp. Disp. (mm)	-19.5	-21.5	-23.7	-26.4	-29.6
Avg. Max. q_{max}/q_{ult}	48%	55%	62%	70%	79%

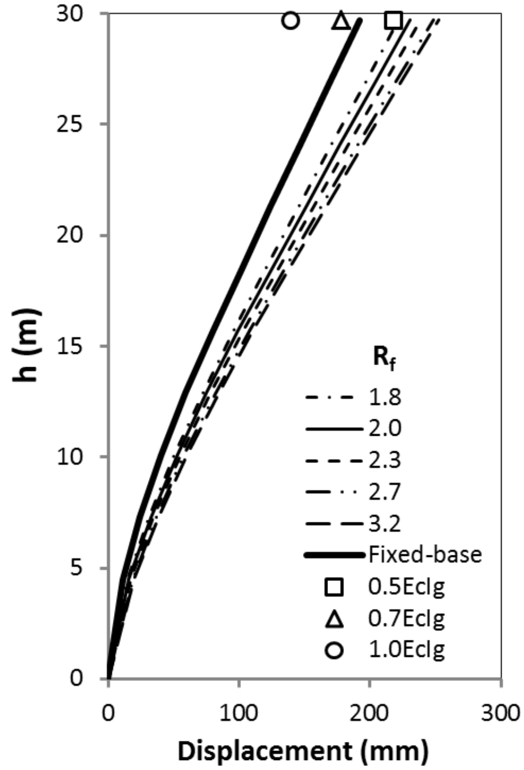

Figure A.81 Average of displacement envelopes for wall 10R27 on Clay along with estimated top displacements of the fixed-base wall from RSA using various effective stiffnesses

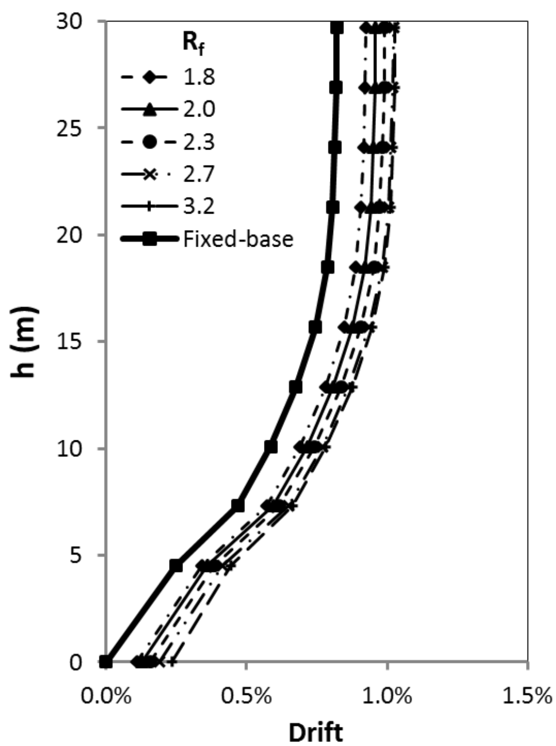

Figure A.82 Average of drift envelopes for wall 10R27 on Clay (Note: base rotation values are plotted at h=0 and values of average interstory drift are plotted at the top of the storey.)

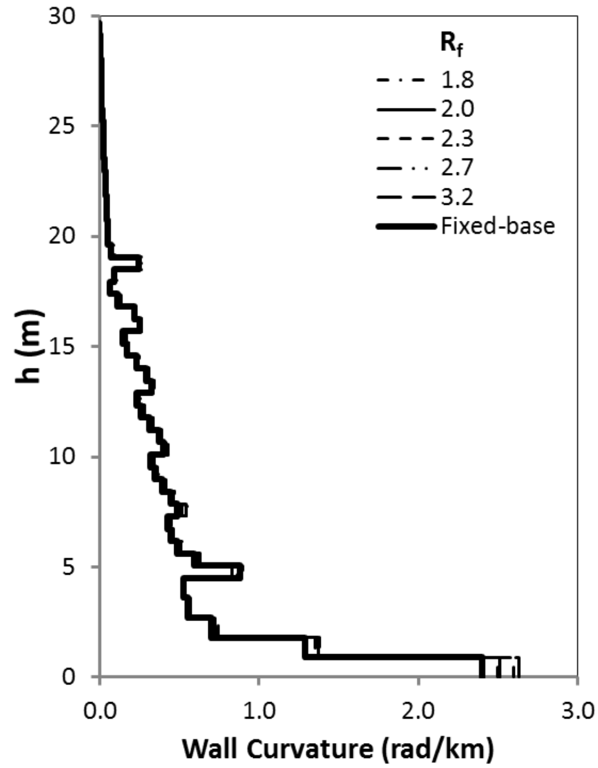

Figure A.83 Average of curvature envelopes for wall 10R27 on Clay

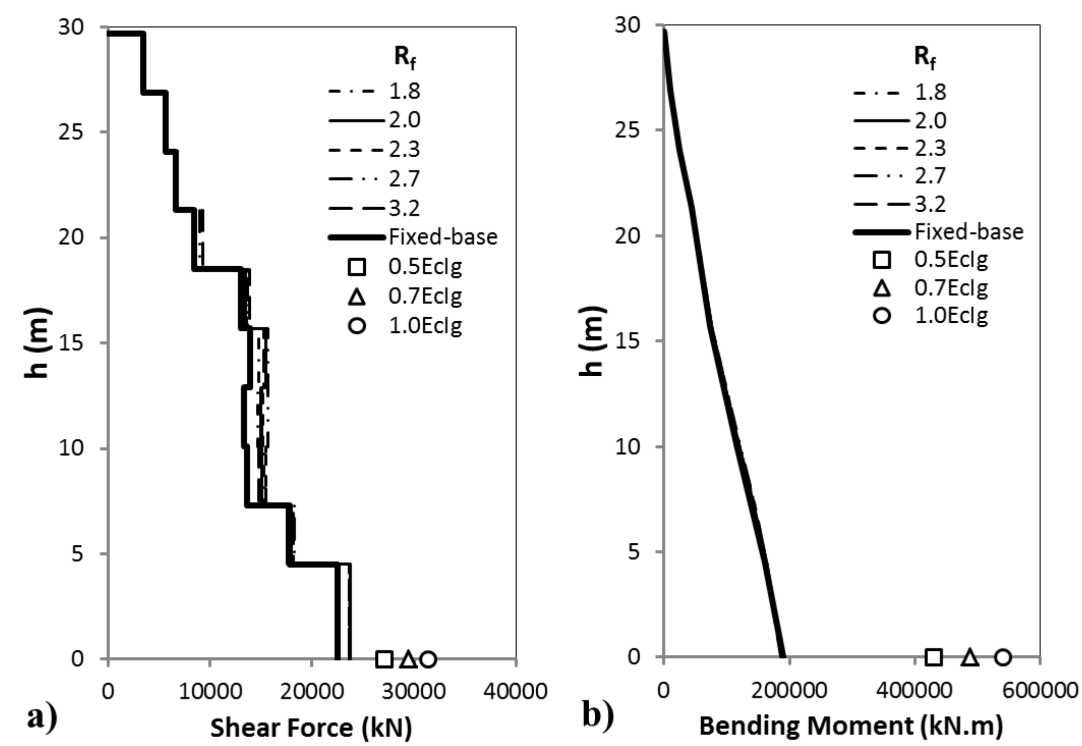

Figure A.84 Average of a) shear force, and b) bending moment envelopes for wall 10R27 on Clay along with estimated maximum quantities for the fixed-base wall from RSA using various effective stiffnesses

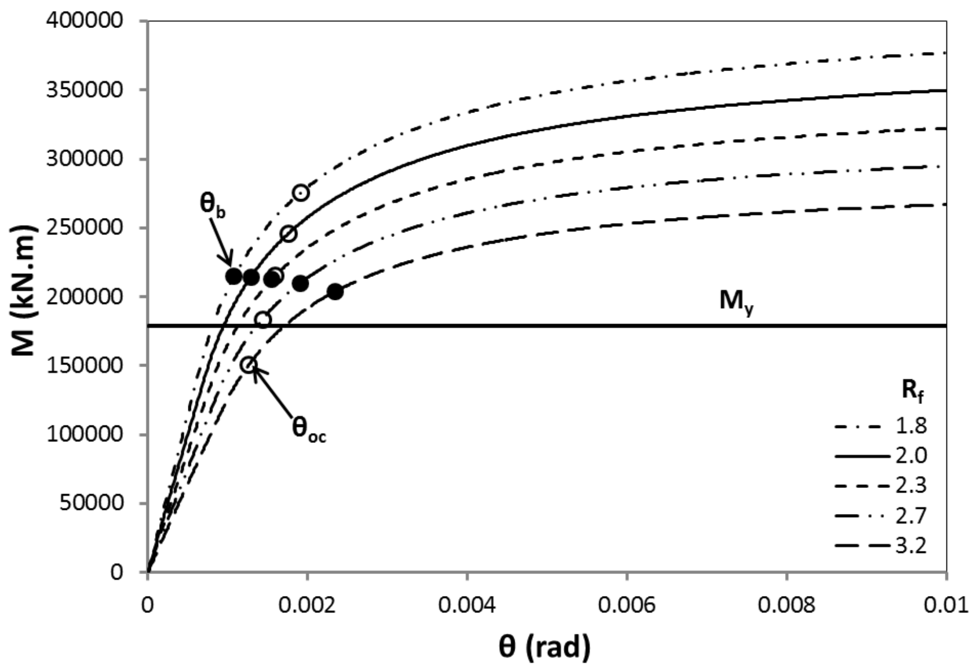

Figure A.85 Bending moment-rotation response of the foundation of wall 10R27 on Clay

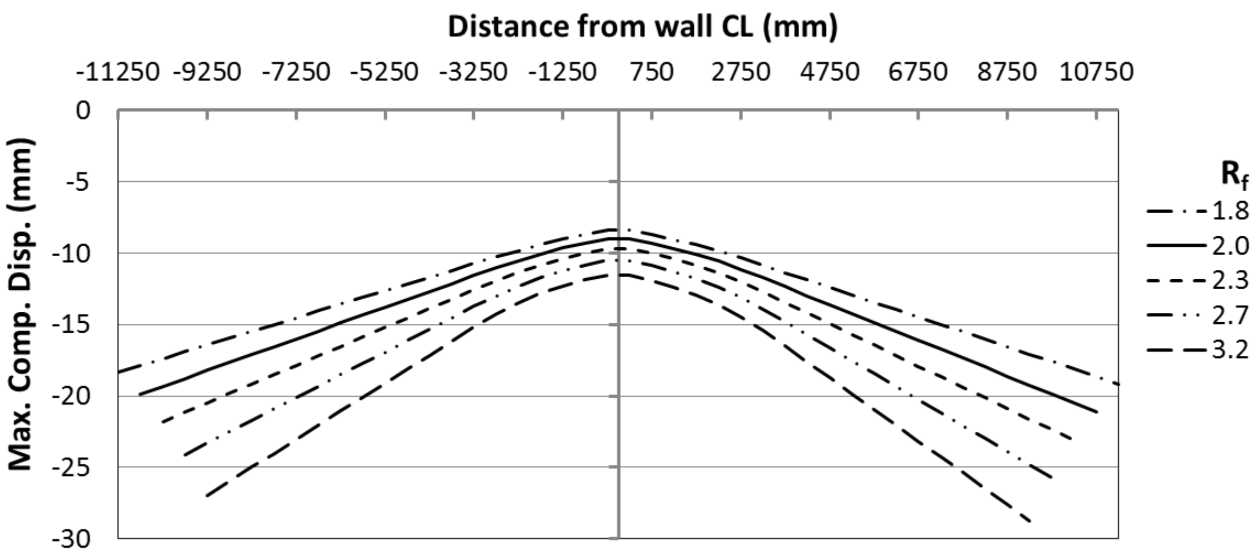

Figure A.86 Average of maximum soil compressive displacements underneath the footing for wall 10R27 on Clay

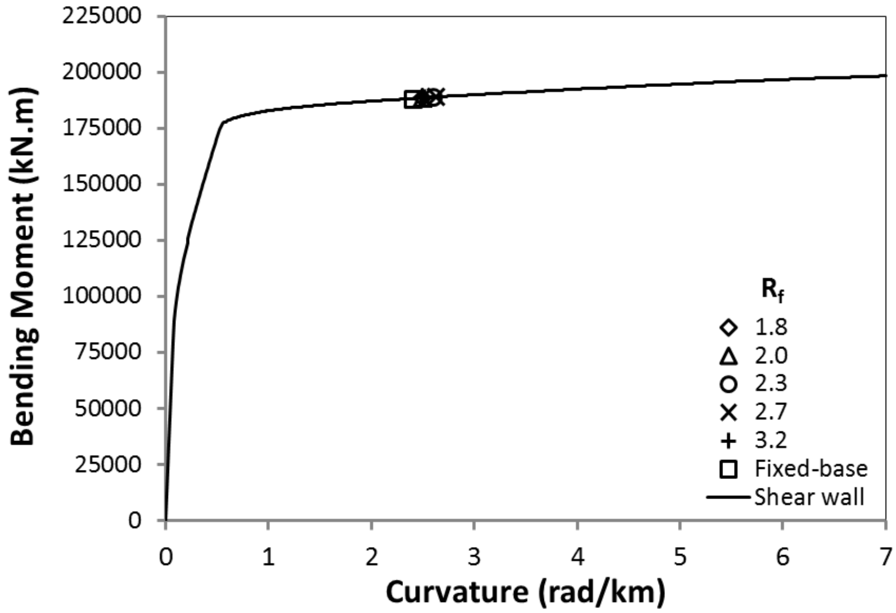

Figure A.87 Moment-curvature response of wall 10R27 along with average of maximum recorded curvatures at the base on Clay

Table A.28 Shear wall properties for wall 10R20

N	10
L_w (mm)	5500
P (kN)	41550
M_{RSA} (kN.m)	488000
M_y (kN.m)	249000
R_w	1.96

Table A.29 Summary of nonlinear dynamic analyses for wall 10R20 on Clay

R_f	1.8	2.0	2.3	2.7	3.2
E (MPa)	57	57	57	57	57
G_{eff} (MPa)	22	22	22	22	22
v	0.3	0.3	0.3	0.3	0.3
q_a (kPa)	133	133	133	133	133
q (kPa)	82	90	99	109	121
q_f (kPa)	200	200	200	200	200
q_{ult} (kPa)	400	400	400	400	400
L (m)	22.5	21.5	20.5	19.5	18.5
B (m)	22.5	21.5	20.5	19.5	18.5
a (mm)	9233	9663	10134	10654	11230
s (mm)	7.47	7.76	8.07	8.41	8.78
M_{oc} (kN.m)	275615	245918	215351	183779	151040
θ_{oc} (rad)	0.0019	0.0018	0.0016	0.0014	0.0013
θ_y (rad)	0.0015	0.0018	0.0023	0.0033	0.0054
$T_{Estimate}$ (sec)	1.27	1.30	1.34	1.43	1.43
T_{model} (sec)	1.30	1.34	1.38	1.47	1.50
Δ_1 (mm)	16.6	17.8	20.5	25.0	30.0
Δ_{10} (mm)	234	238	255	279	305
Avg. Max. θ_b (rad)	0.0019	0.0023	0.0029	0.0039	0.0053
Avg. Max. Uplift (mm)	16.8	20.5	26.8	36.5	49.2
Avg. Max. Comp. Disp. (mm)	-26.3	-29.1	-33.2	-39.4	-48.4
Avg. Max. q_{max}/q_{ult}	62%	69%	78%	86%	92%

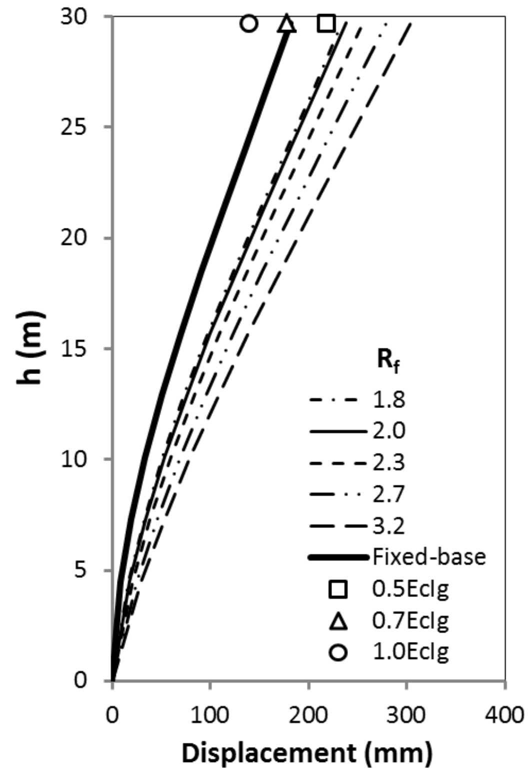

Figure A.88 Average of displacement envelopes for wall 10R20 on Clay along with estimated top displacements of the fixed-base wall from RSA using various effective stiffnesses

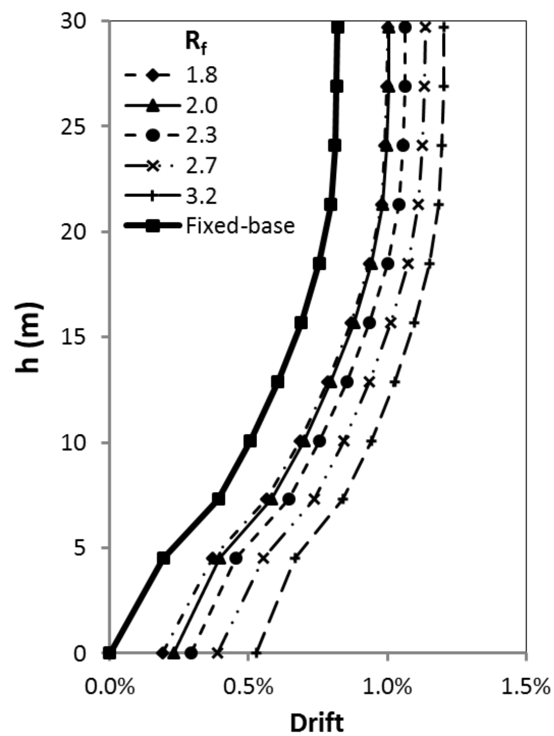

Figure A.89 Average of drift envelopes for wall 10R20 on Clay (Note: base rotation values are plotted at h=0 and values of average interstory drift are plotted at the top of the storey.)

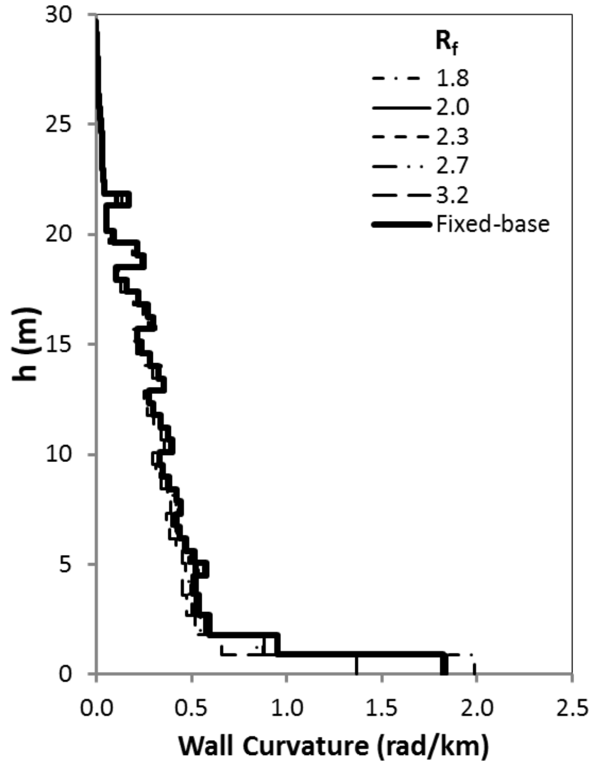

Figure A.90 Average of curvature envelopes for wall 10R20 on Clay

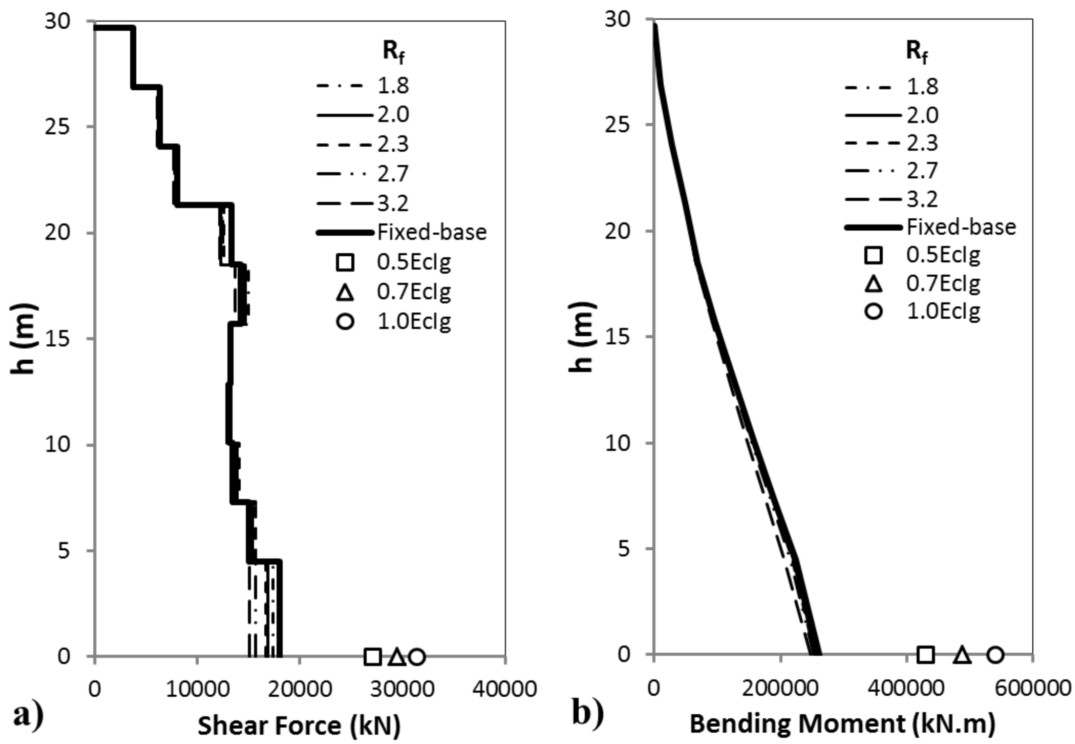

Figure A.91 Average of a) shear force, and b) bending moment envelopes for wall 10R20 on Clay along with estimated maximum quantities for the fixed-base wall from RSA using various effective stiffnesses

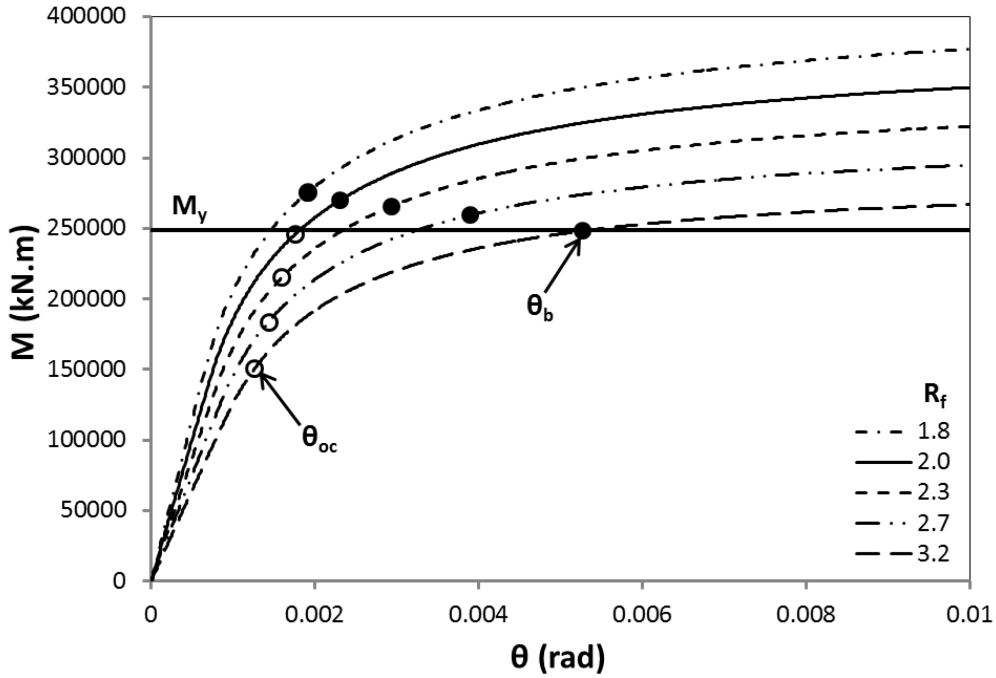

Figure A.92 Bending moment-rotation response of the foundation of wall 10R20 on Clay

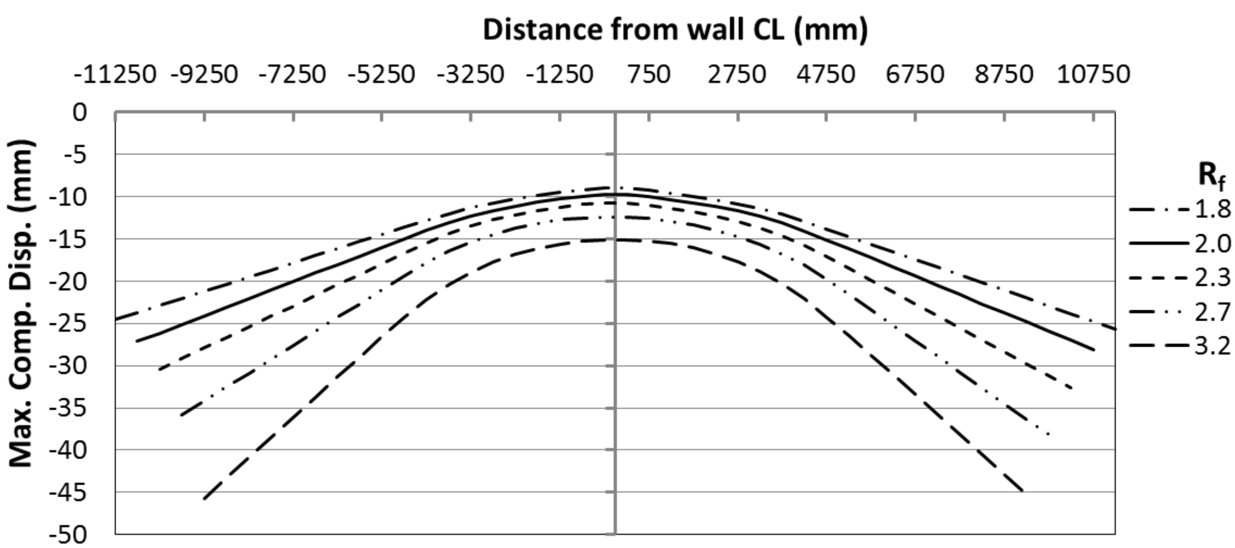

Figure A.93 Average of maximum soil compressive displacements underneath the footing for wall 10R20 on Clay

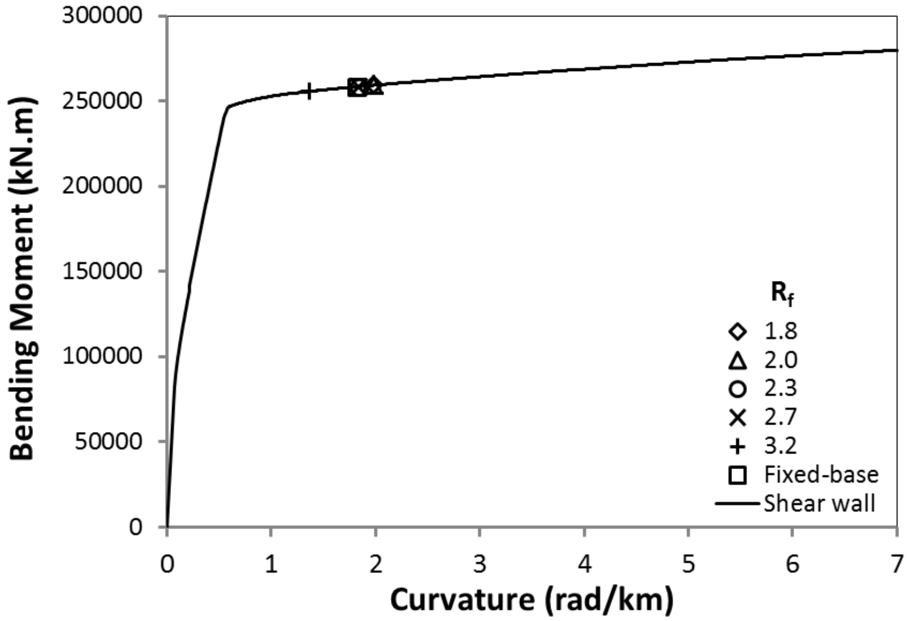

Figure A.94 Moment-curvature response of wall 10R20 along with average of maximum recorded curvatures at the base on Clay

Table A.30 Shear wall properties for wall 10R17

N	10
L_w (mm)	5500
P (kN)	41550
M_{RSA} (kN.m)	488000
M_y (kN.m)	289000
R_w	1.69

Table A.31 Summary of nonlinear dynamic analyses for wall 10R17 on Clay

R_f	**1.8**	**2.0**	**2.3**	**2.7**	**3.2**
E (MPa)	57	57	57	57	57
G_{eff} (MPa)	22	22	22	22	22
v	0.3	0.3	0.3	0.3	0.3
q_a (kPa)	133	133	133	133	133
q (kPa)	82	90	99	109	121
q_f (kPa)	200	200	200	200	200
q_{ult} (kPa)	400	400	400	400	400
L (m)	22.5	21.5	20.5	19.5	18.5
B (m)	22.5	21.5	20.5	19.5	18.5
a (mm)	9233	9663	10134	10654	11230
s (mm)	7.47	7.76	8.07	8.41	8.78
M_{oc} (kN.m)	275615	245918	215351	183779	151040
θ_{oc} (rad)	0.0019	0.0018	0.0016	0.0014	0.0013
θ_y (rad)	0.0022	0.0029	0.0043	0.0080	0.0383
$T_{Estimate}$ (sec)	1.25	1.29	1.32	1.37	1.42
T_{model} (sec)	1.28	1.32	1.37	1.42	1.48
Δ_1 (mm)	19.0	21.2	23.8	28.5	34.4
Δ_{10} (mm)	245	256	267	288	314
Avg. Max. θ_b (rad)	0.0027	0.0033	0.0040	0.0052	0.0066
Avg. Max. Uplift (mm)	29.3	35.3	42.4	53.6	65.4
Avg. Max. Comp. Disp. (mm)	-31.7	-35.4	-39.8	-47.0	-56.8
Avg. Max. q_{max}/q_{ult}	70%	78%	85%	90%	93%

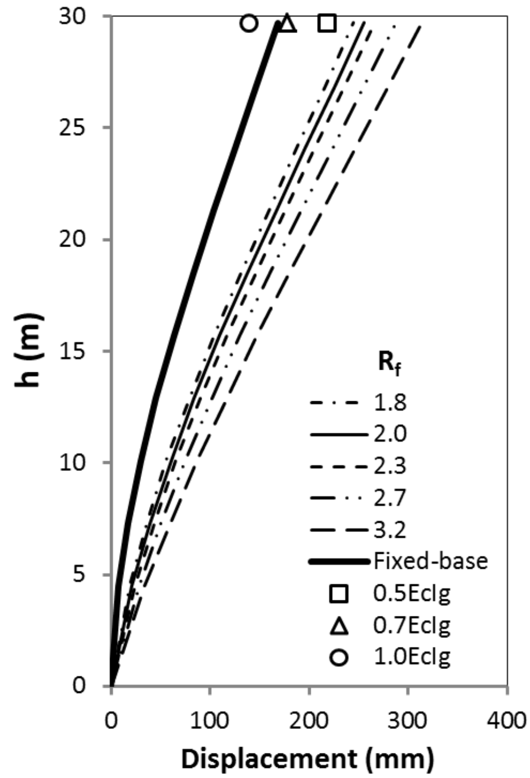

Figure A.95 Average of displacement envelopes for wall 10R17 on Clay along with estimated top displacements of the fixed-base wall from RSA using various effective stiffnesses

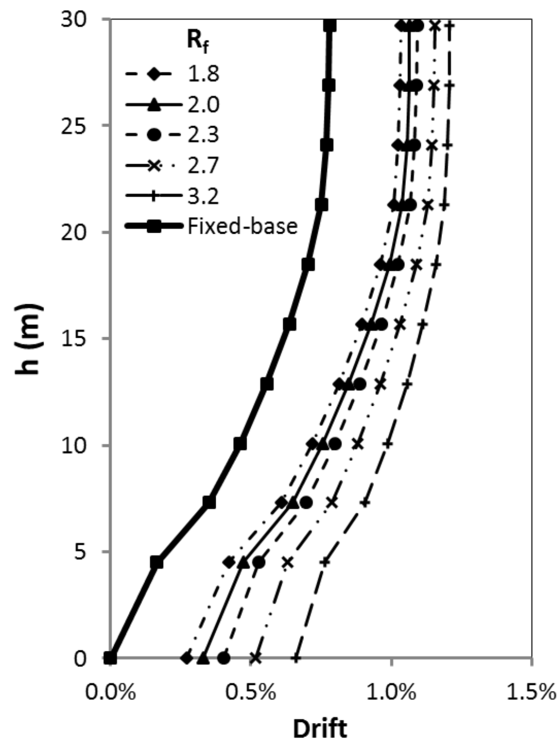

Figure A.96 Average of drift envelopes for wall 10R17 on Clay (Note: base rotation values are plotted at h=0 and values of average interstory drift are plotted at the top of the storey.)

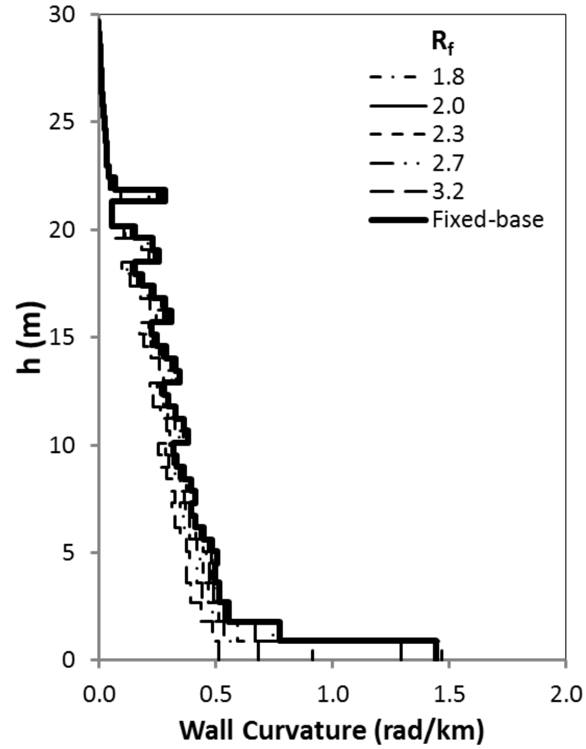

Figure A.97 Average of curvature envelopes for wall 10R17 on Clay

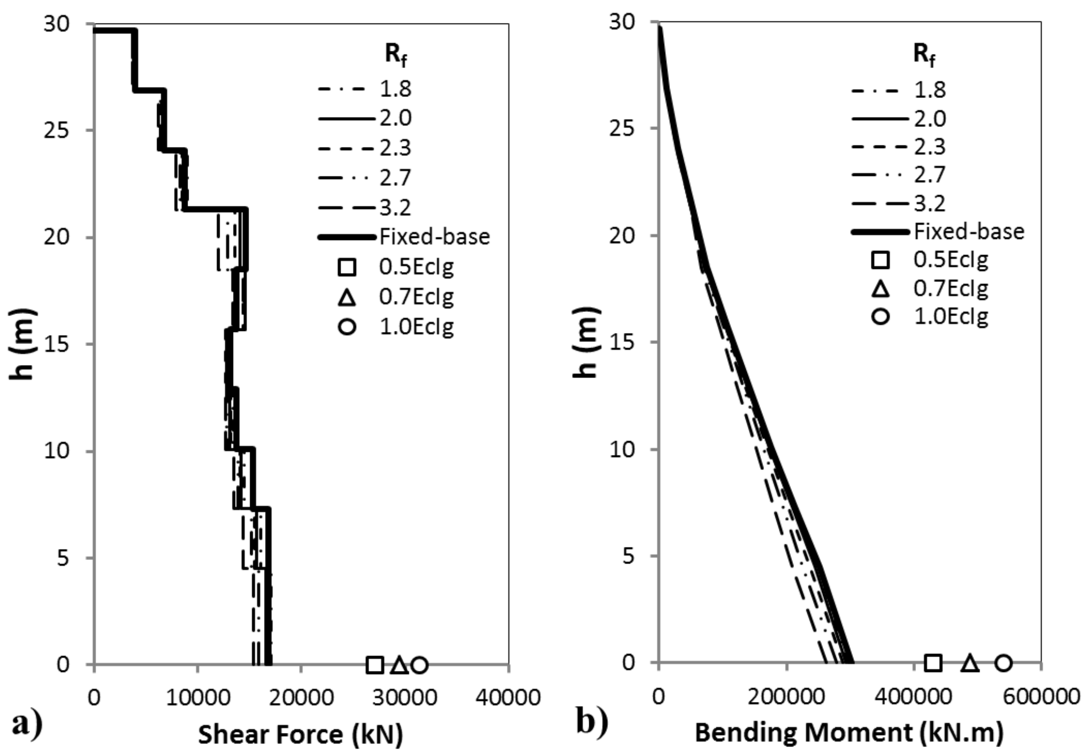

Figure A.98 Average of a) shear force, and b) bending moment envelopes for wall 10R17 on Clay along with estimated maximum quantities for the fixed-base wall from RSA using various effective stiffnesses

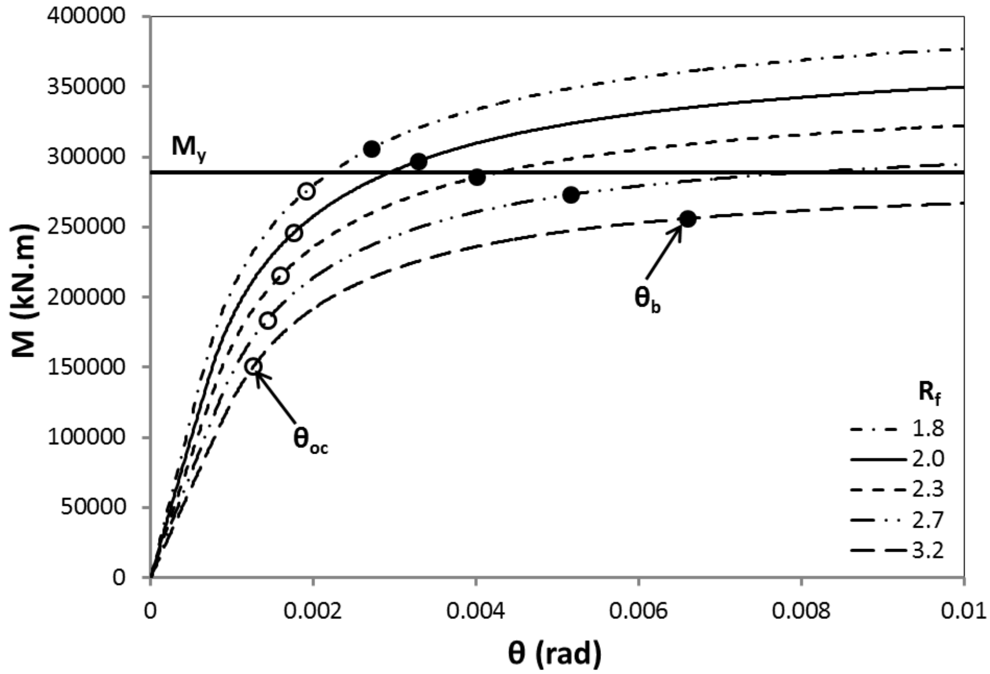

Figure A.99 Bending moment-rotation response of the foundation of wall 10R17 on Clay

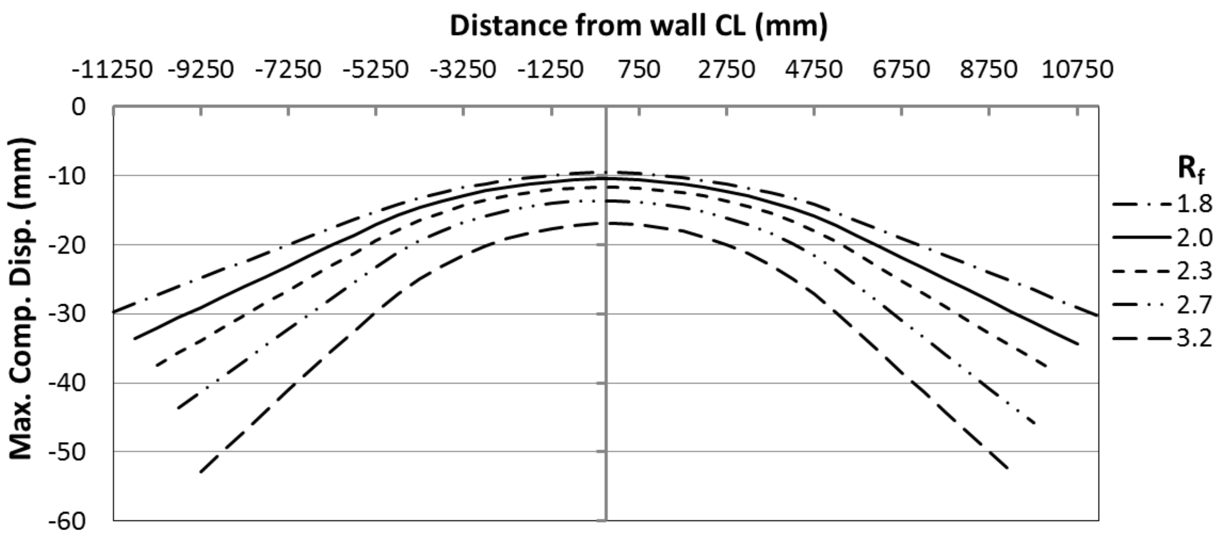

Figure A.100 Average of maximum soil compressive displacements underneath the footing for wall 10R17 on Clay

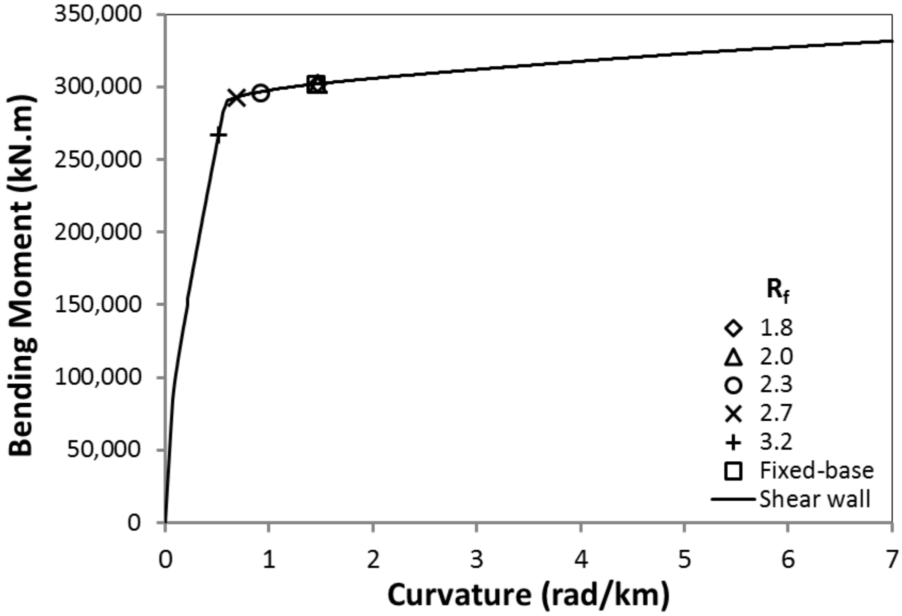

Figure A.101 Moment-curvature response of wall 10R17 along with average of maximum recorded curvatures at the base on Clay

Table A.32 Shear wall properties for wall 10R13

N	10
L_w (mm)	5500
P (kN)	41550
M_{RSA} (kN.m)	488000
M_y (kN.m)	369000
R_w	1.32

Table A.33 Summary of nonlinear dynamic analyses for wall 10R13 on Clay

R_f	1.3	1.5	1.8	2.0	2.3	2.7	3.2
E (MPa)	57	57	57	57	57	57	57
G_{eff} (MPa)	22	22	22	22	22	22	22
ν	0.3	0.3	0.3	0.3	0.3	0.3	0.3
q_a (kPa)	133	133	133	133	133	133	133
q (kPa)	59	69	82	90	99	109	121
q_f (kPa)	200	200	200	200	200	200	200
q_{ult} (kPa)	400	400	400	400	400	400	400
L (m)	26.5	24.5	22.5	21.5	20.5	19.5	18.5
B (m)	26.5	24.5	22.5	21.5	20.5	19.5	18.5
a (mm)	7840	8480	9233	9663	10134	10654	11230
s (mm)	6.52	6.97	7.47	7.76	8.07	8.41	8.77
M_{oc} (kN.m)	387669	332824	275615	245918	215351	183779	151040
θ_{oc} (rad)	0.0024	0.0022	0.0019	0.0018	0.0016	0.0014	0.0013
θ_y (rad)	0.0020	0.0033	0.0080	0.0205	0.0626	-----	-----
$T_{Estimate}$ (sec)	1.13	1.17	1.22	1.25	1.29	1.34	1.39
T_{model} (sec)	1.11	1.15	1.25	1.29	1.34	1.39	1.46
Δ_1 (mm)	14.6	17.7	23.7	26.3	29.0	34.2	36.0
Δ_{10} (mm)	208	224	256	268	280	307	306
Avg. Max. θ_b (rad)	0.0020	0.0028	0.0042	0.0048	0.0055	0.0067	0.0072
Avg. Max. Uplift (mm)	26.4	36.2	54.1	59.6	64.1	74.6	73.1
Avg. Max. Comp. Disp. (mm)	-26.9	-31.9	-40.3	-44.3	-48.6	-56.3	-61.0
Avg. Max. q_{max}/q_{ult}	54%	66%	80%	86%	89%	92%	94%

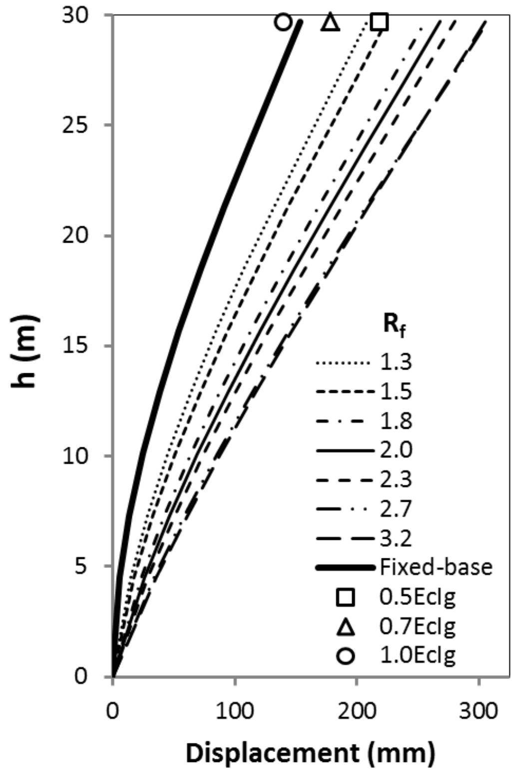

Figure A.102 Average of displacement envelopes for wall 10R13 on Clay along with estimated top displacements of the fixed-base wall from RSA using various effective stiffnesses

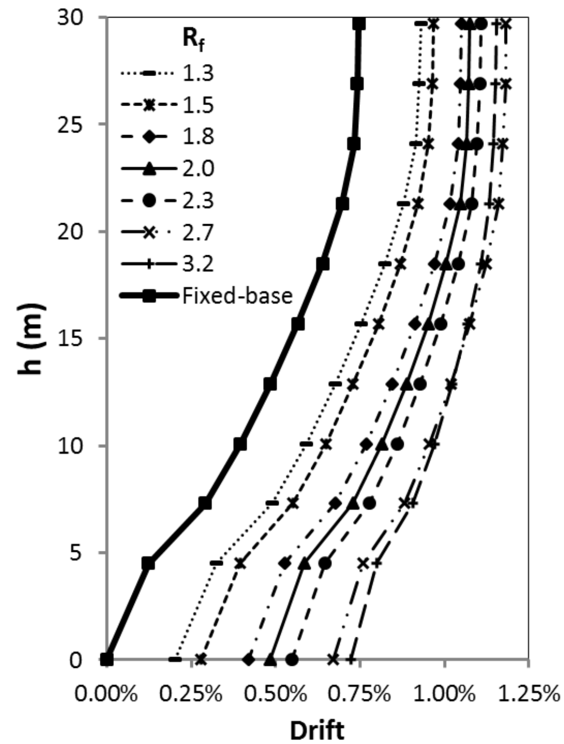

Figure A.103 Average of drift envelopes for wall 10R13 on Clay (Note: base rotation values are plotted at h=0 and values of average interstory drift are plotted at the top of the storey.)

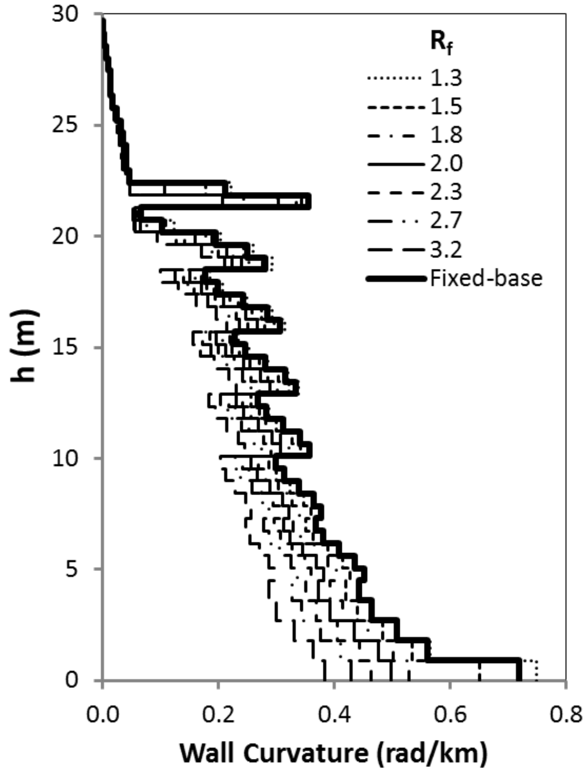

Figure A.104 Average of curvature envelopes for wall 10R13 on Clay

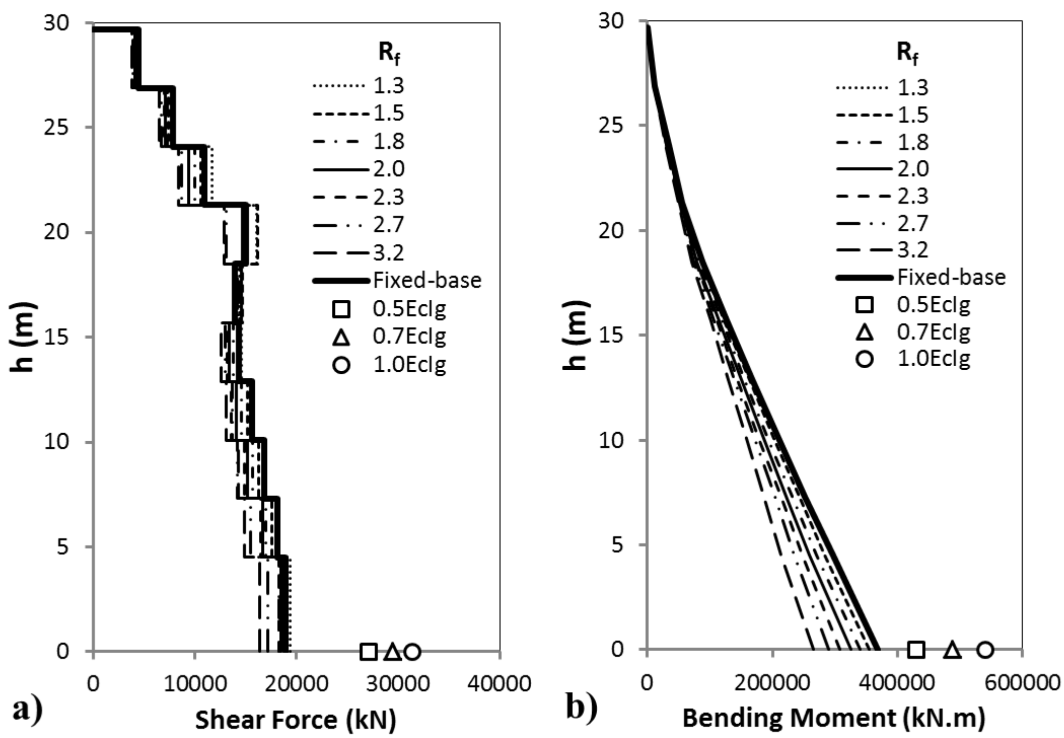

Figure A.105 Average of a) shear force, and b) bending moment envelopes for wall 10R13 on Clay along with estimated maximum quantities for the fixed-base wall from RSA using various effective stiffnesses

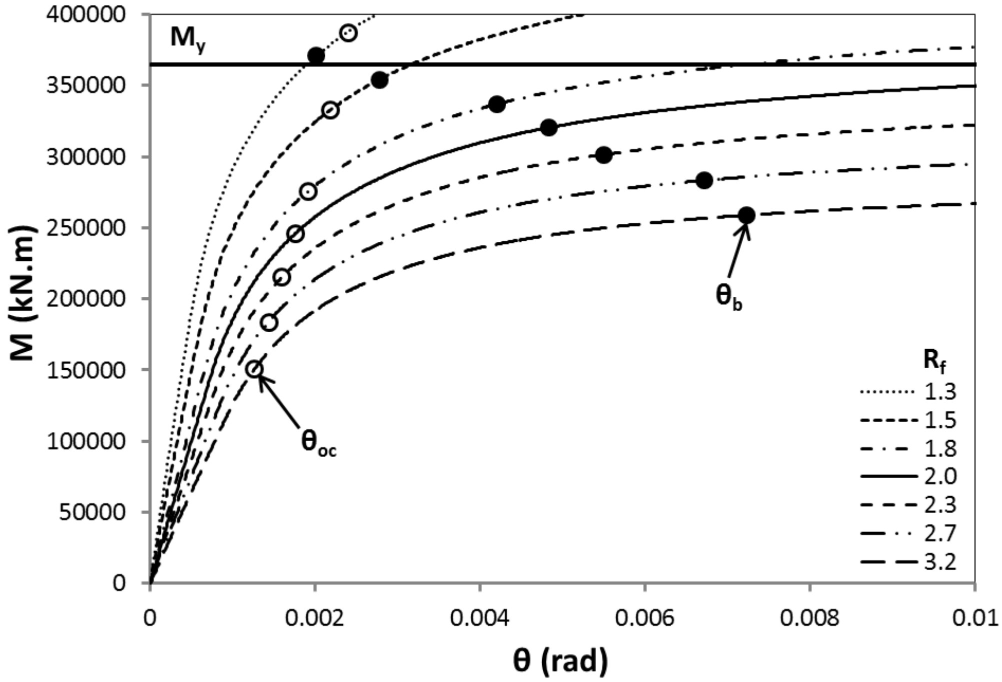

Figure A.106 Bending moment-rotation response of the foundation of wall 10R13 on Clay

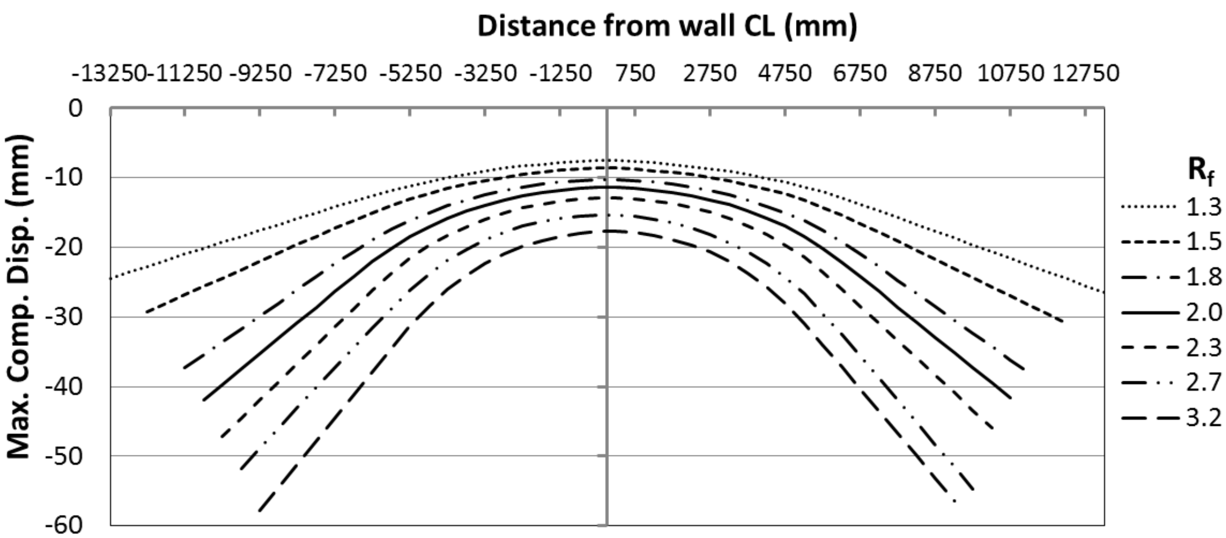

Figure A.107 Average of maximum soil compressive displacements underneath the footing for wall 10R13 on Clay

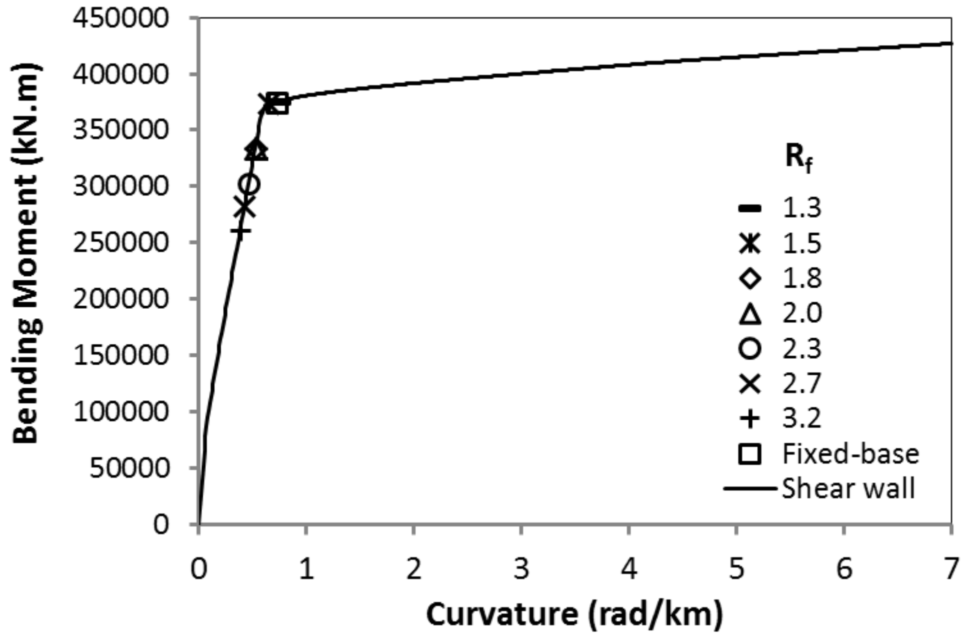

Figure A.108 Moment-curvature response of wall 10R13 along with average of maximum recorded curvatures at the base on Clay

Table A.34 Shear wall properties for wall 10Elastic

N	10
L_w (mm)	5500
P (kN)	41550
M_{RSA} (kN.m)	488000
M_y (kN.m)	-----
R_w	1.00

Table A.35 Summary of nonlinear dynamic analyses for wall 10Elastic on Clay

R_f	**1.8**	**2.0**	**2.3**	**2.7**	**3.2**
E (MPa)	57	57	57	57	57
G_{eff} (MPa)	22	22	22	22	22
v	0.3	0.3	0.3	0.3	0.3
q_a (kPa)	133	133	133	133	133
q (kPa)	82	90	99	109	121
q_f (kPa)	200	200	200	200	200
q_{ult} (kPa)	400	400	400	400	400
L (m)	22.5	21.5	20.5	19.5	18.5
B (m)	22.5	21.5	20.5	19.5	18.5
a (mm)	9233	9663	10134	10654	11230
s (mm)	7.47	7.76	8.07	8.41	8.78
M_{oc} (kN.m)	275615	245918	215351	183779	151040
θ_{oc} (rad)	0.0019	0.0018	0.0016	0.0014	0.0013
θ_y (rad)	-----	-----	-----	-----	-----
$T_{Estimate}$ (sec)	1.32	1.35	1.38	1.42	1.47
T_{model} (sec)	1.36	1.40	1.44	1.49	1.55
Δ_1 (mm)	28.4	33.3	36.6	41.0	43.1
Δ_{10} (mm)	257	287	306	328	338
Avg. Max. θ_b (rad)	0.0055	0.0067	0.0074	0.0085	0.0090
Avg. Max. Uplift (mm)	76.7	88.9	93.0	97.8	92.8
Avg. Max. Comp. Disp. (mm)	-47.9	-54.4	-59.7	-67.5	-73.7
Avg. Max. q_{max}/q_{ult}	87%	90%	93%	94%	95%

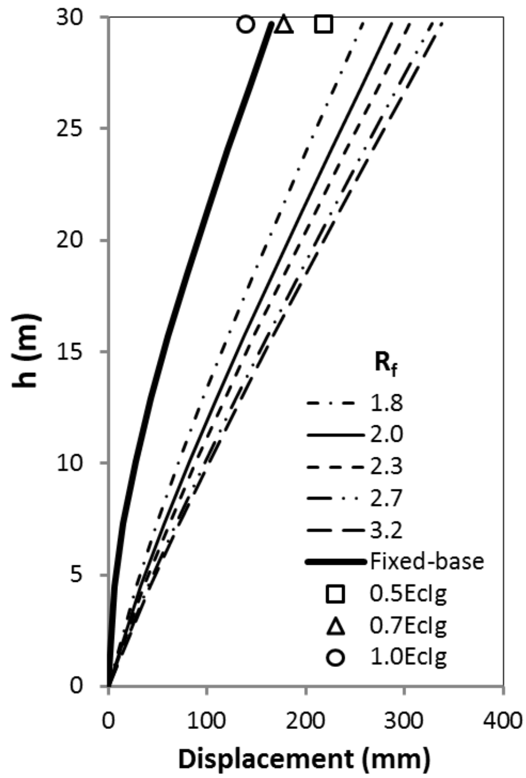

Figure A.109 Average of displacement envelopes for wall 10Elastic on Clay along with estimated top displacements of the fixed-base wall from RSA using various effective stiffnesses

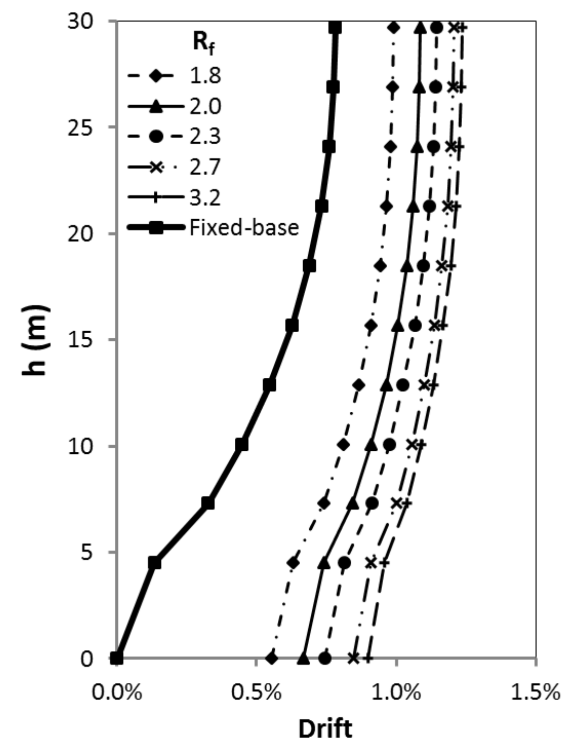

Figure A.110 Average of drift envelopes for wall 10Elastic on Clay (Note: base rotation values are plotted at h=0 and values of average interstory drift are plotted at the top of the storey.)

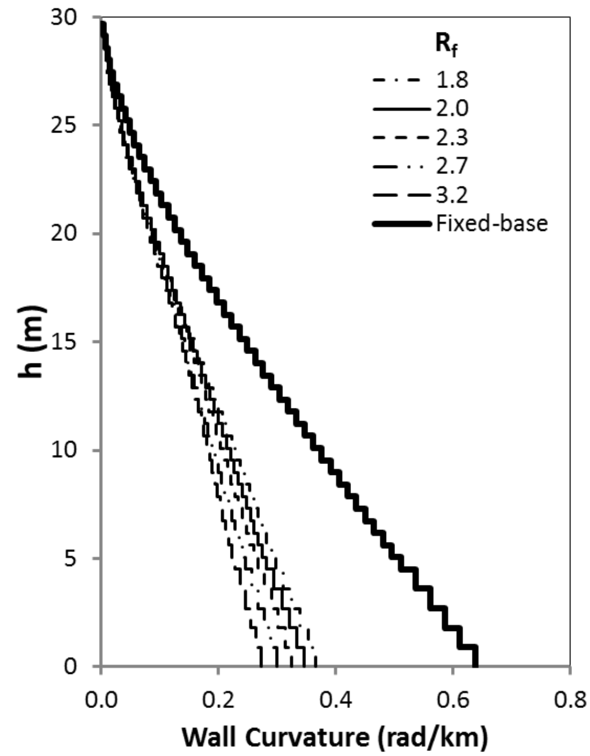

Figure A.111 Average of curvature envelopes for wall 10Elastic on Clay

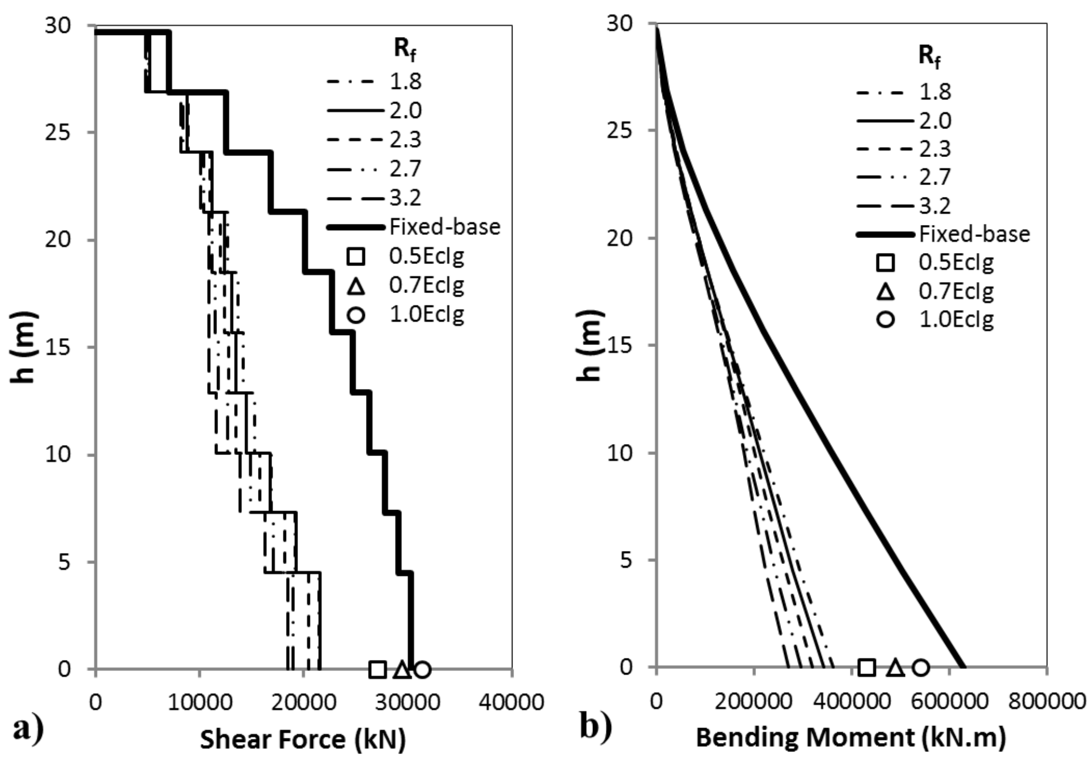

Figure A.112 Average of a) shear force, and b) bending moment envelopes for wall 10Elastic on Clay along with estimated maximum quantities for the fixed-base wall from RSA using various effective stiffnesses

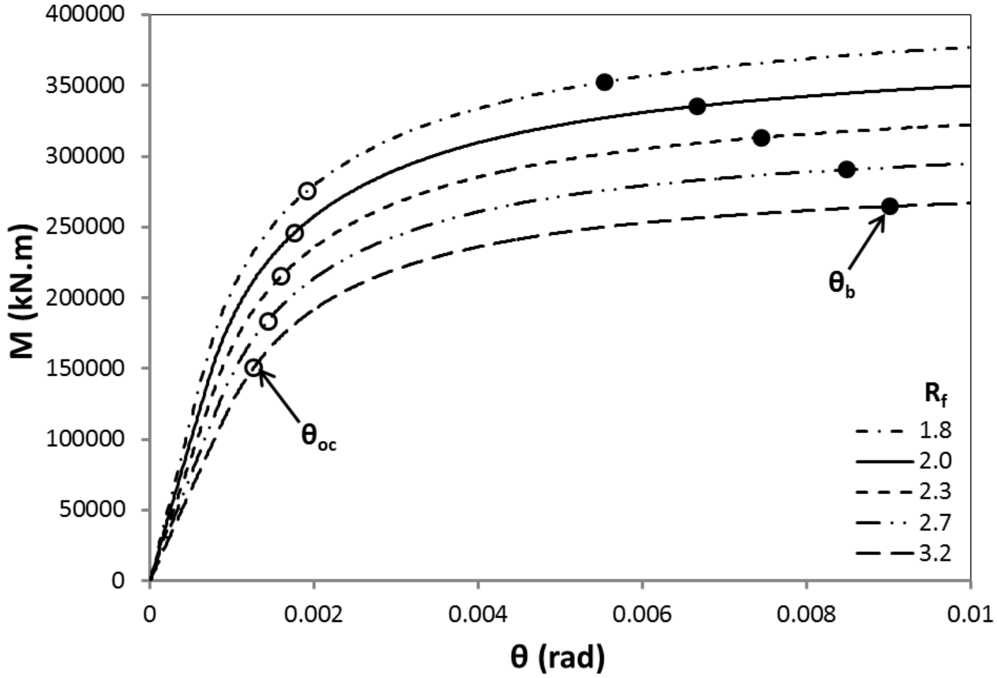

Figure A.113 Bending moment-rotation response of the foundation of wall 10Elastic on Clay

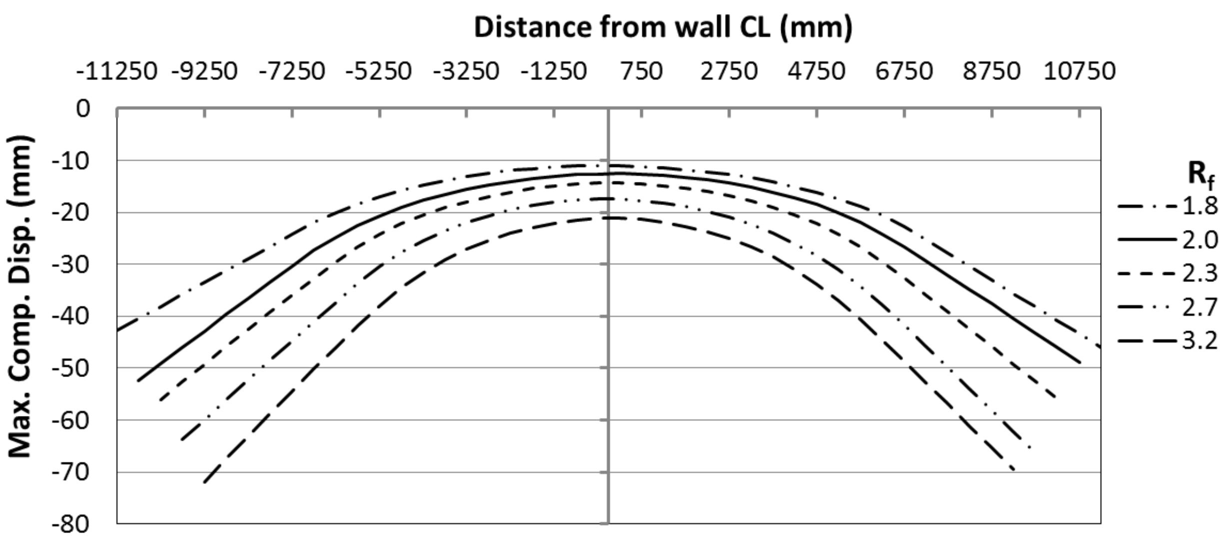

Figure A.114 Average of maximum soil compressive displacements underneath the footing for wall 10Elastic on Clay

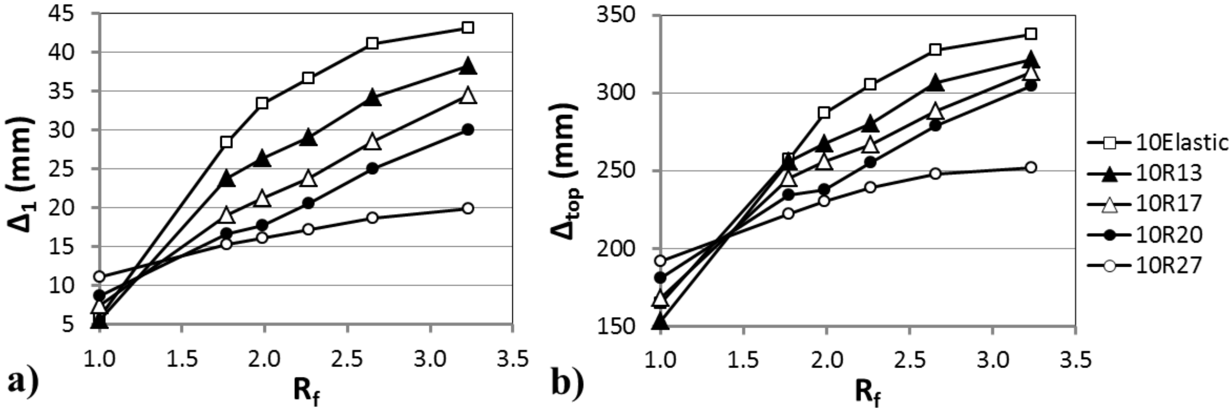

Figure A.115 Summary of average maximum a) first storey displacements, and b) top displacements for 10 storey walls on Clay sorted by wall strength

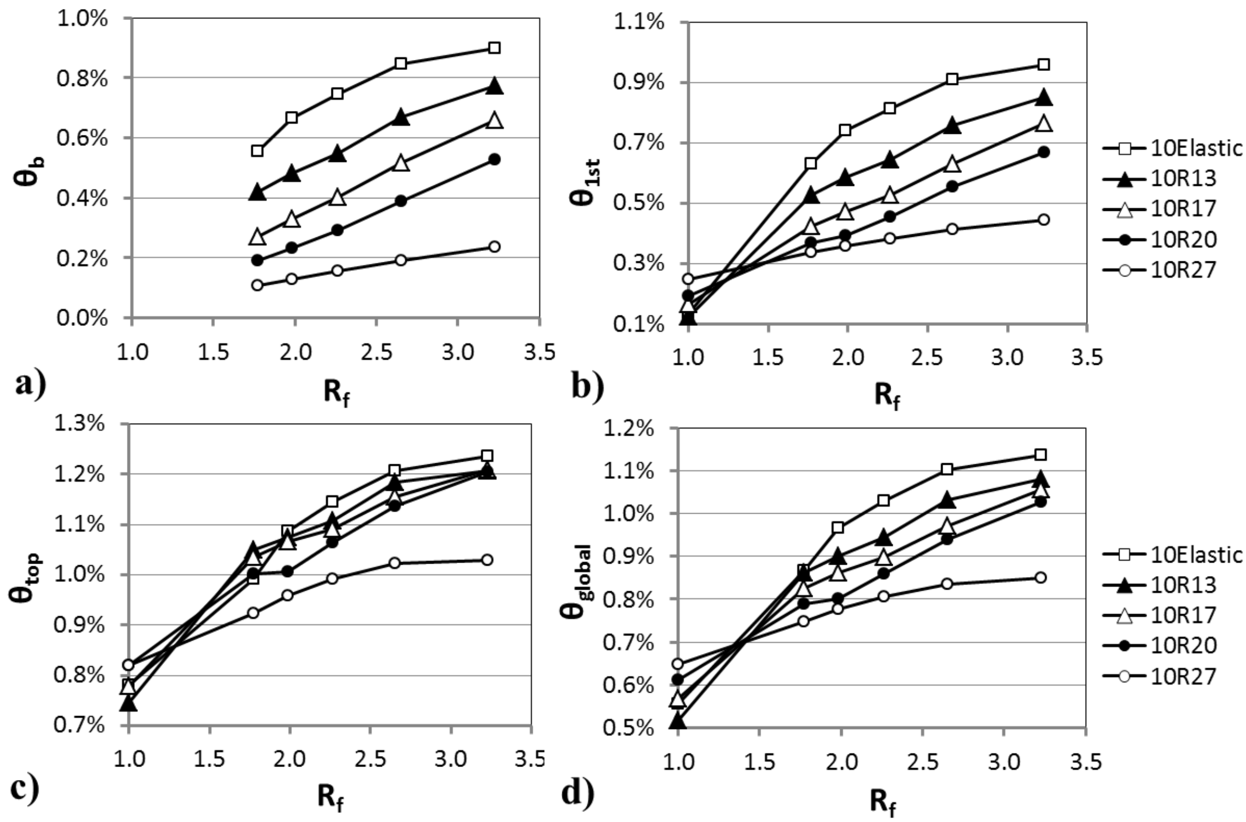

Figure A.116 Summary of average maximum a) base rotations, b) 1st storey inter-storey drifts, c) top storey inter-storey drifts, and d) global drifts of 10 storey walls on Clay sorted by wall strength

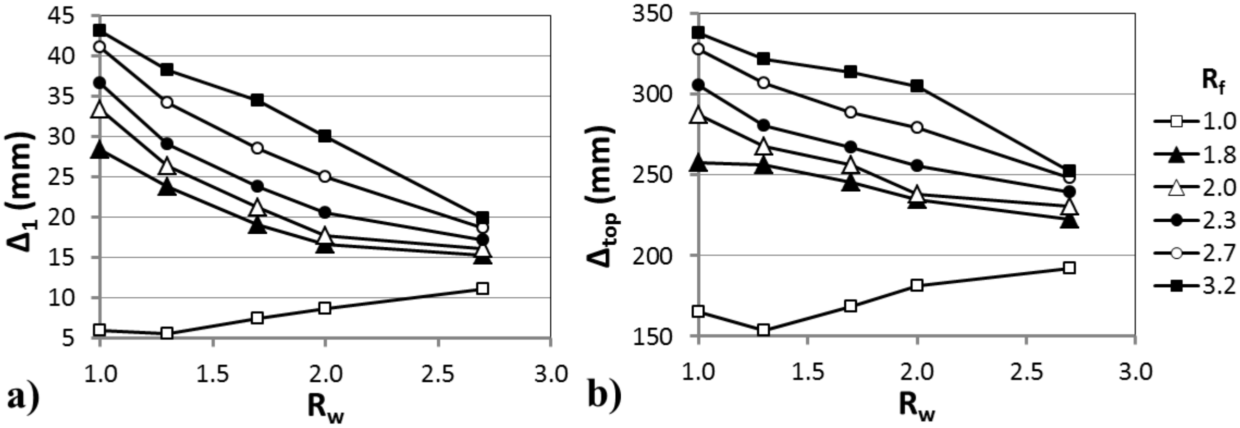

Figure A.117 Summary of average maximum a) first storey displacements, and b) top displacements for 10 storey walls on Clay sorted by foundation size

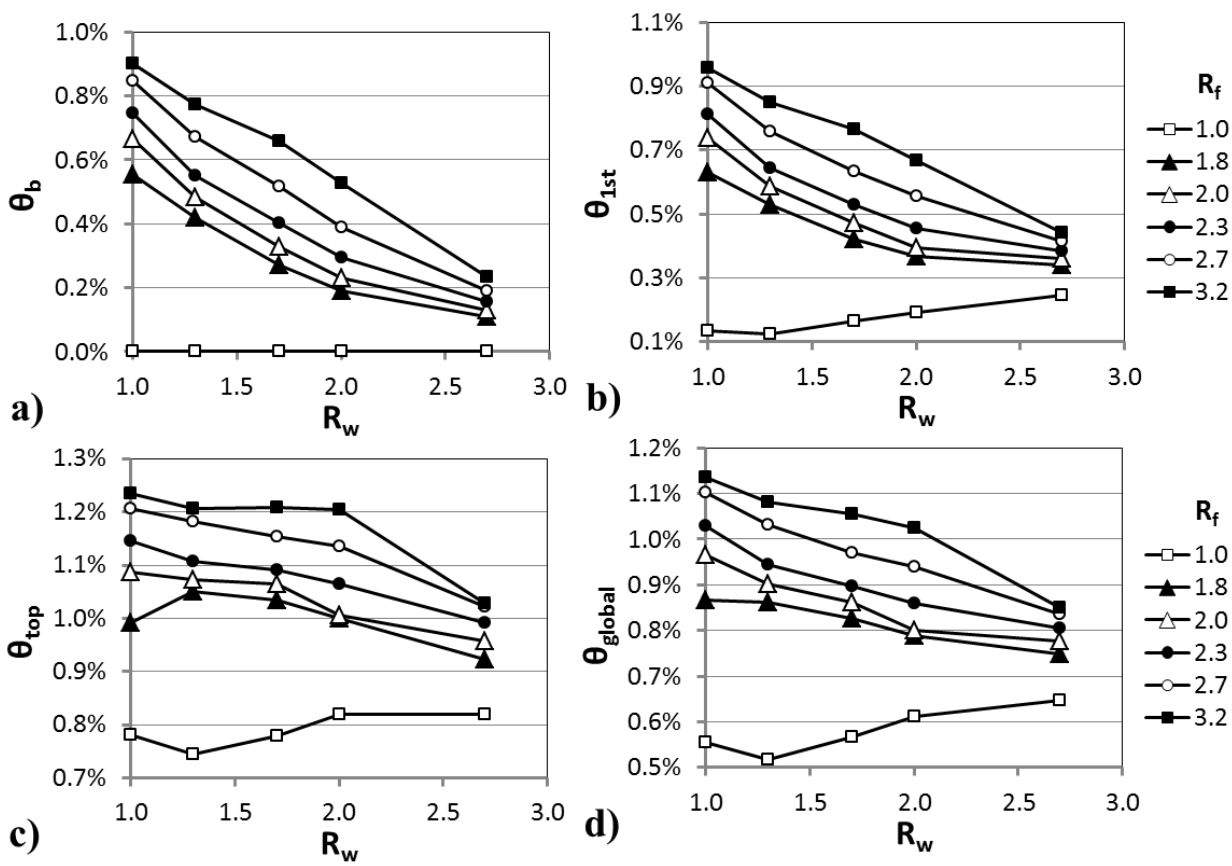

Figure A.118 Summary of average maximum a) base rotations, b) 1st storey inter-storey drifts, c) top storey inter-storey drifts, and d) global drifts of 10 storey walls on Clay sorted by foundation size

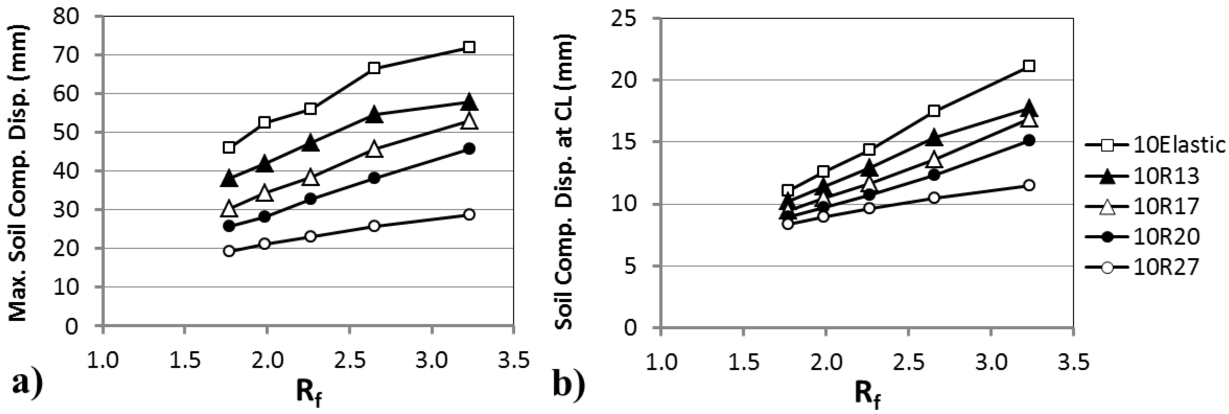

Figure A.119 Summary of average maximum soil compressive displacement at a) foundation toe, and b) foundation centreline for 10 storey walls on Clay sorted by wall strength

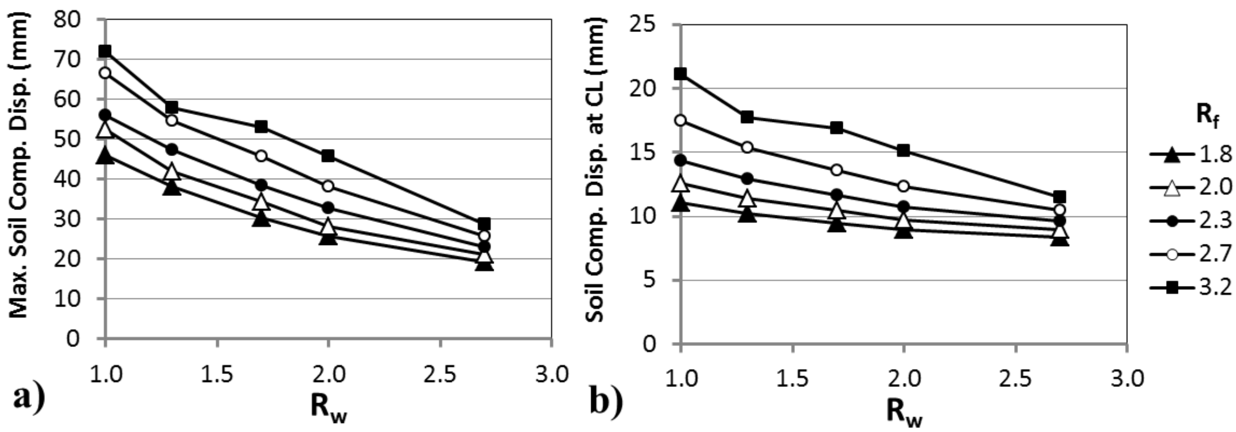

Figure A.120 Summary of average maximum soil compressive displacement at a) foundation toe, and b) foundation centreline for 10 storey walls on Clay sorted by foundation size

A.6.2 Loose Sand

Table A.36 Properties of Loose Sand

G_0 (MPa)	57
G_{eff} (MPa)	22
ν	0.3
E (MPa)	57
q_{ult} (kPa)	400
q_f (kPa)	200
q_a (kPa)	133
V_s (m/s)	325

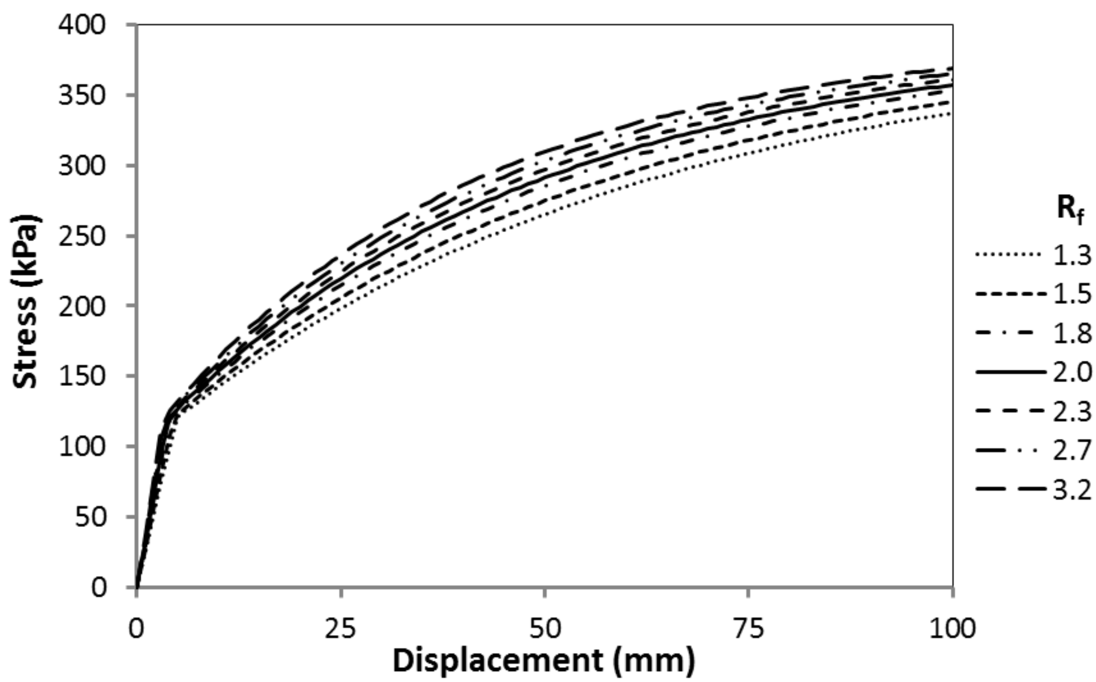

Figure A.121 Soil spring responses in monotonic compression for Loose Sand

Table A.37 Shear wall properties for wall 10R27

N	10
L_w (mm)	5500
P (kN)	41550
M_{RSA} (kN.m)	488000
M_y (kN.m)	179000
R_w	2.73

Table A.38 Summary of nonlinear dynamic analyses for wall 10R27 on Loose Sand

R_f	1.8	2.0	2.3	2.7	3.2
E (MPa)	57	57	57	57	57
G_{eff} (MPa)	22	22	22	22	22
v	0.3	0.3	0.3	0.3	0.3
q_a (kPa)	133	133	133	133	133
q (kPa)	82	90	99	109	121
q_f (kPa)	200	200	200	200	200
q_{ult} (kPa)	400	400	400	400	400
L (m)	22.5	21.5	20.5	19.5	18.5
B (m)	22.5	21.5	20.5	19.5	18.5
a (mm)	9233	9663	10134	10654	11230
s (mm)	2.82	2.93	3.05	3.17	3.31
M_{oc} (kN.m)	275615	245918	215351	183779	151040
θ_{oc} (rad)	0.0022	0.0021	0.0019	0.0017	0.0016
θ_y (rad)	0.0005	0.0007	0.0011	0.0016	0.0023
$T_{Estimate}$ (sec)	1.32	1.35	1.39	1.38	1.48
T_{model} (sec)	1.14	1.16	1.17	1.19	1.21
Δ_1 (mm)	13.5	14.1	15.2	16.4	18.3
Δ_{10} (mm)	208	215	222	224	229
Avg. Max. θ_b (rad)	0.0008	0.0010	0.0013	0.0017	0.0021
Avg. Max. Uplift (mm)	5.2	5.7	6.1	6.5	7.2
Avg. Max. Comp. Disp. (mm)	-13.1	-17.1	-21.7	-26.9	-33.8
Avg. Max. q_{max}/q_{ult}	41%	47%	53%	60%	68%

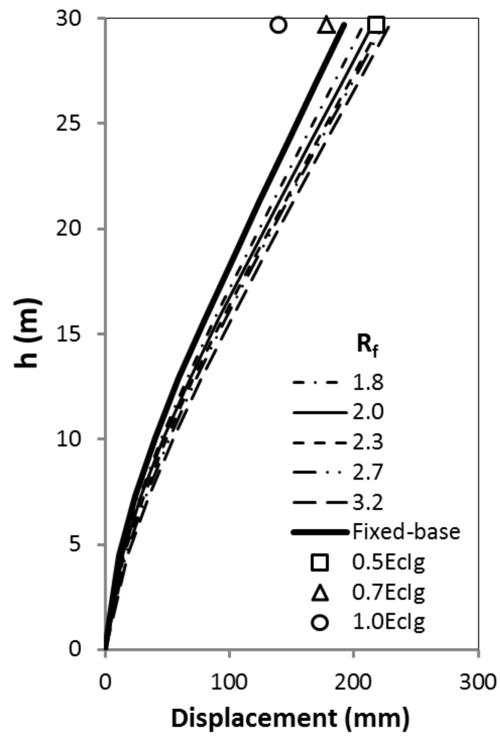

Figure A.122 Average of displacement envelopes for wall 10R27 on Loose Sand along with estimated top displacements of the fixed-base wall from RSA using various effective stiffnesses

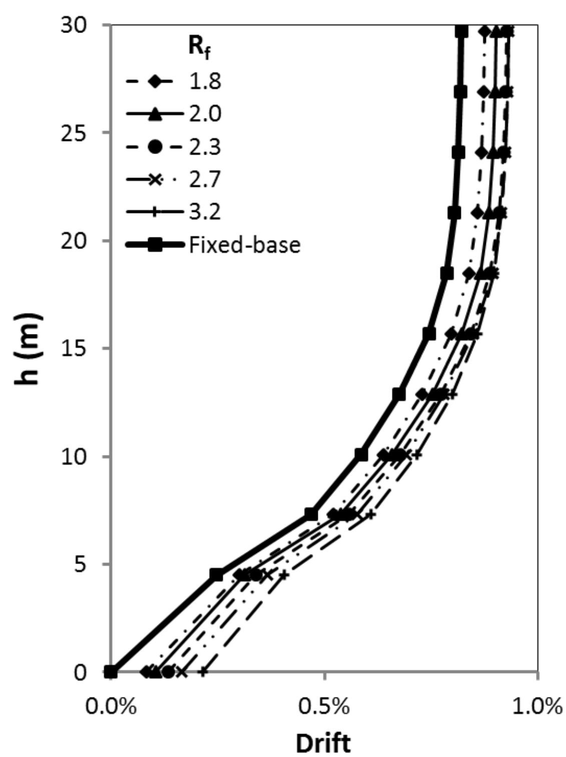

Figure A.123 Average of drift envelopes for wall 10R27 on Loose Sand (Note: base rotation values are plotted at h=0 and values of average interstory drift are plotted at the top of the storey.)

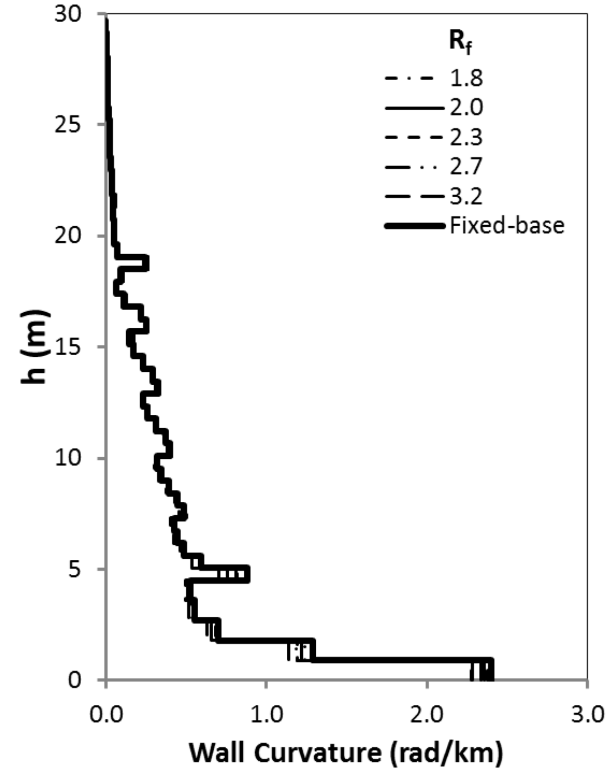

Figure A.124 Average of curvature envelopes for wall 10R27 on Loose Sand

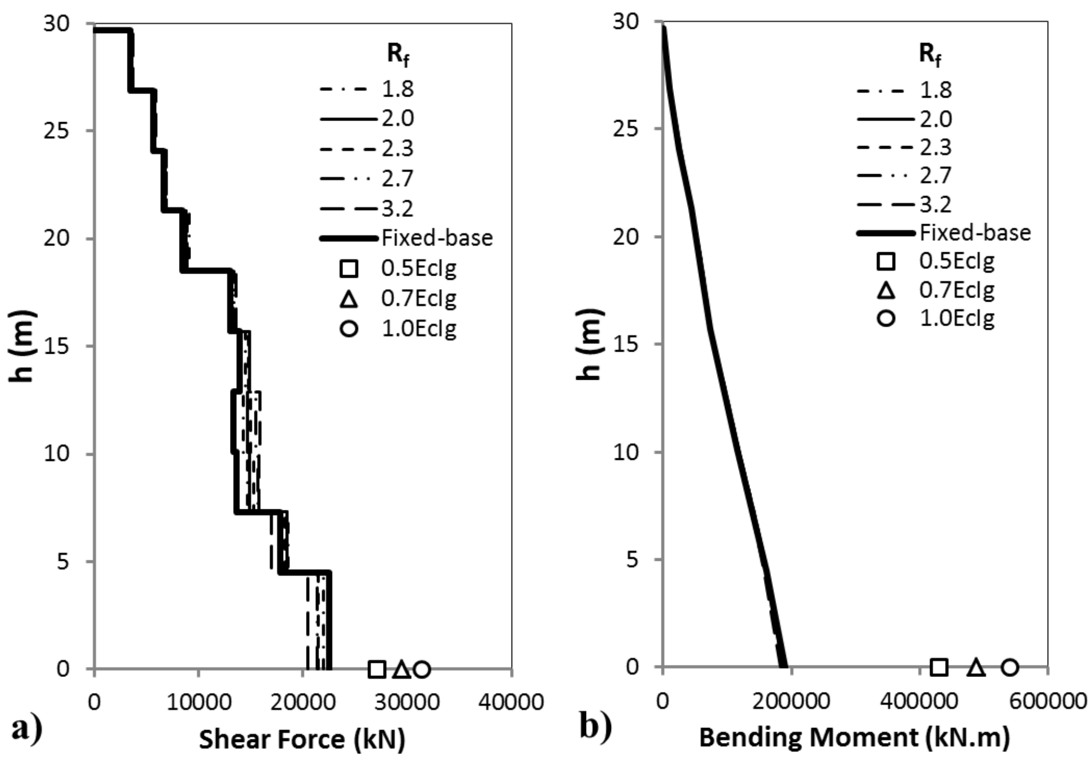

Figure A.125 Average of a) shear force, and b) bending moment envelopes for wall 10R27 on Loose Sand along with estimated maximum quantities for the fixed-base wall from RSA using various effective stiffnesses

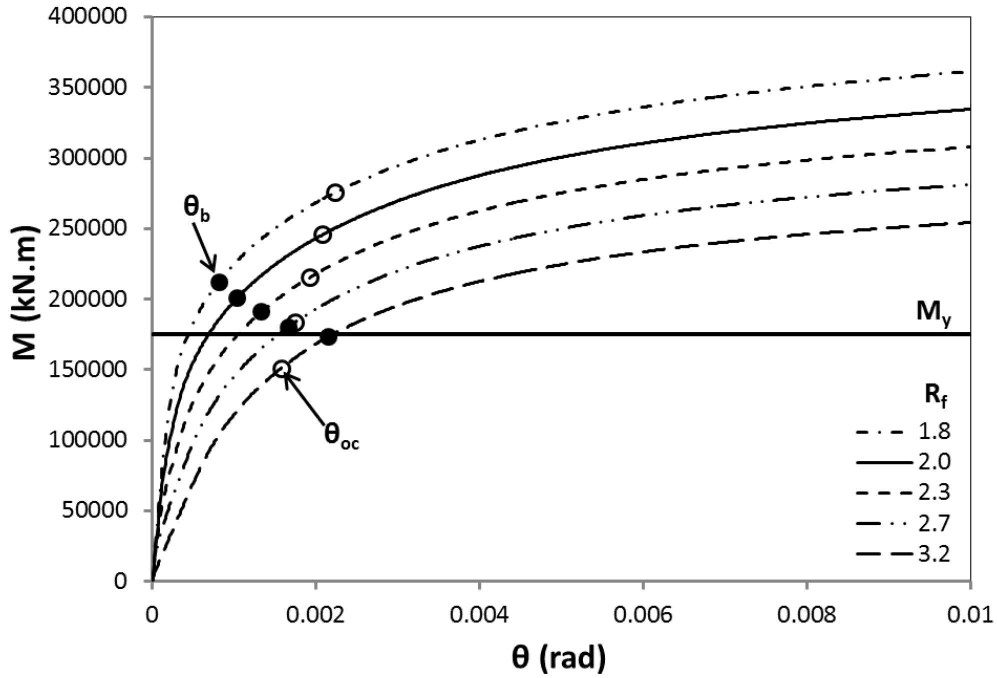

Figure A.126 Bending moment-rotation response of the foundation of wall 10R27 on Loose Sand

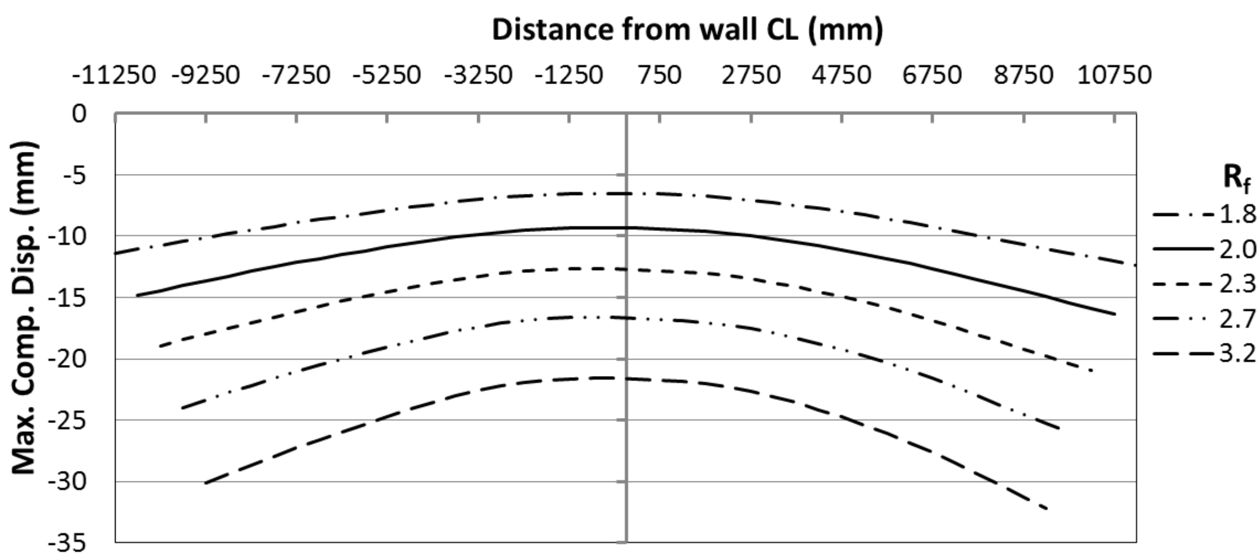

Figure A.127 Average of maximum soil compressive displacements underneath the footing for wall 10R27 on Loose Sand

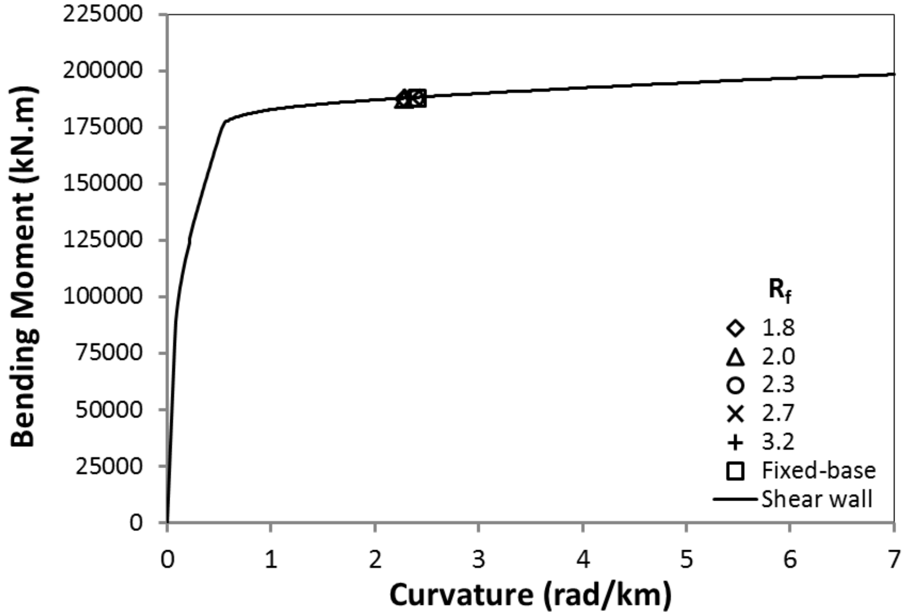

Figure A.128 Moment-curvature response of wall 10R27 along with average of maximum recorded curvatures at the base on Loose Sand

Table A.39 Shear wall properties for wall 10R20

N	10
L_w (mm)	5500
P (kN)	41550
M_{RSA} (kN.m)	488000
M_y (kN.m)	249000
R_w	1.96

Table A.40 Summary of nonlinear dynamic analyses for wall 10R20 on Loose Sand

R_f	1.8	2.0	2.3	2.7	3.2
E (MPa)	57	57	57	57	57
G_{eff} (MPa)	22	22	22	22	22
v	0.3	0.3	0.3	0.3	0.3
q_a (kPa)	133	133	133	133	133
q (kPa)	82	90	99	109	121
q_f (kPa)	200	200	200	200	200
q_{ult} (kPa)	400	400	400	400	400
L (m)	22.5	21.5	20.5	19.5	18.5
B (m)	22.5	21.5	20.5	19.5	18.5
a (mm)	9233	9663	10134	10654	11230
s (mm)	2.82	2.93	3.05	3.17	3.31
M_{oc} (kN.m)	275615	245918	215351	183779	151040
θ_{oc} (rad)	0.0022	0.0021	0.0019	0.0017	0.0016
θ_y (rad)	0.0015	0.0022	0.0032	0.0049	0.0087
$T_{Estimate}$ (sec)	1.27	1.30	1.34	1.43	1.43
T_{model} (sec)	1.11	1.12	1.13	1.15	1.17
Δ_1 (mm)	14.6	16.0	17.6	19.5	22.4
Δ_{10} (mm)	213	215	222	229	239
Avg. Max. θ_b (rad)	0.0017	0.0021	0.0025	0.0031	0.0039
Avg. Max. Uplift (mm)	15.0	16.9	18.2	20.0	20.7
Avg. Max. Comp. Disp. (mm)	-23.1	-28.6	-34.8	-42.8	-55.1
Avg. Max. q_{max}/q_{ult}	52%	58%	65%	72%	77%

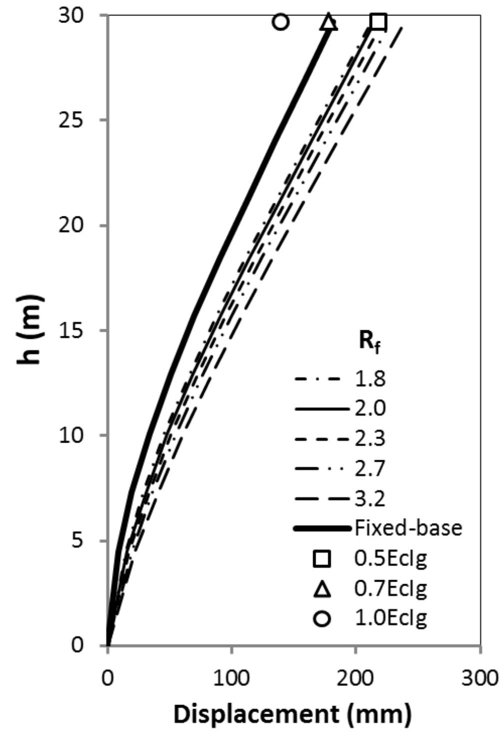

Figure A.129 Average of displacement envelopes for wall 10R20 on Loose Sand along with estimated top displacements of the fixed-base wall from RSA using various effective stiffnesses

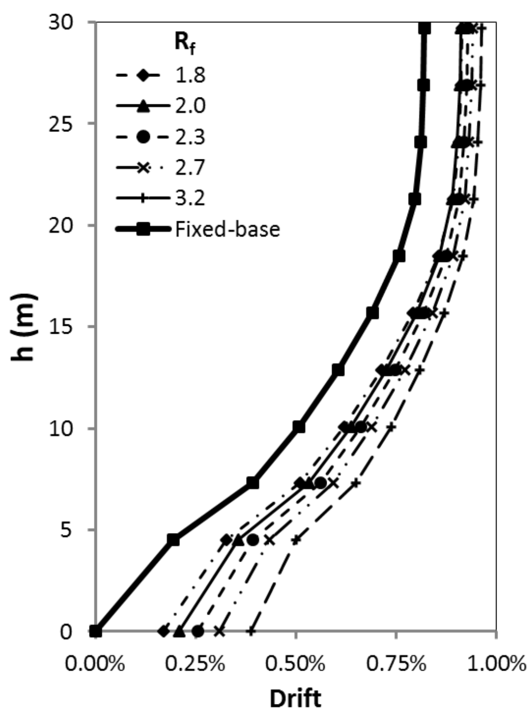

Figure A.130 Average of drift envelopes for wall 10R20 on Loose Sand (Note: base rotation values are plotted at h=0 and values of average interstory drift are plotted at the top of the storey.)

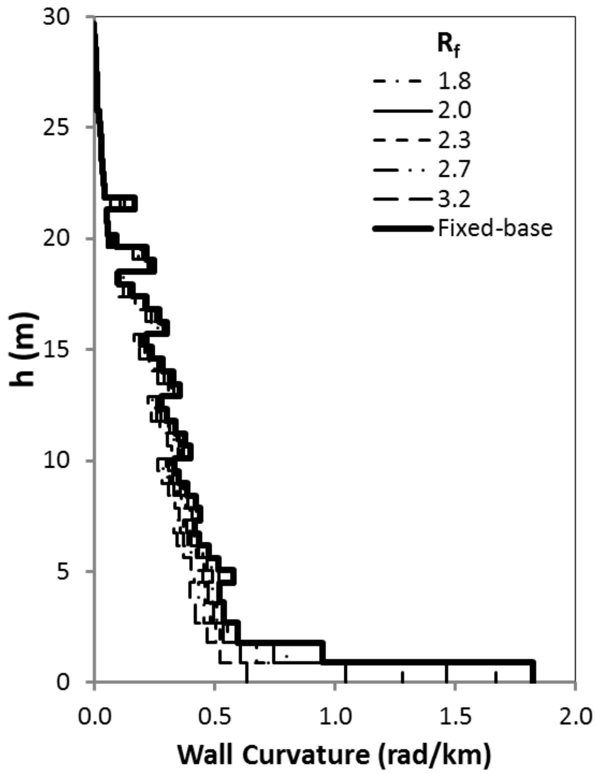

Figure A.131 Average of curvature envelopes for wall 10R20 on Loose Sand

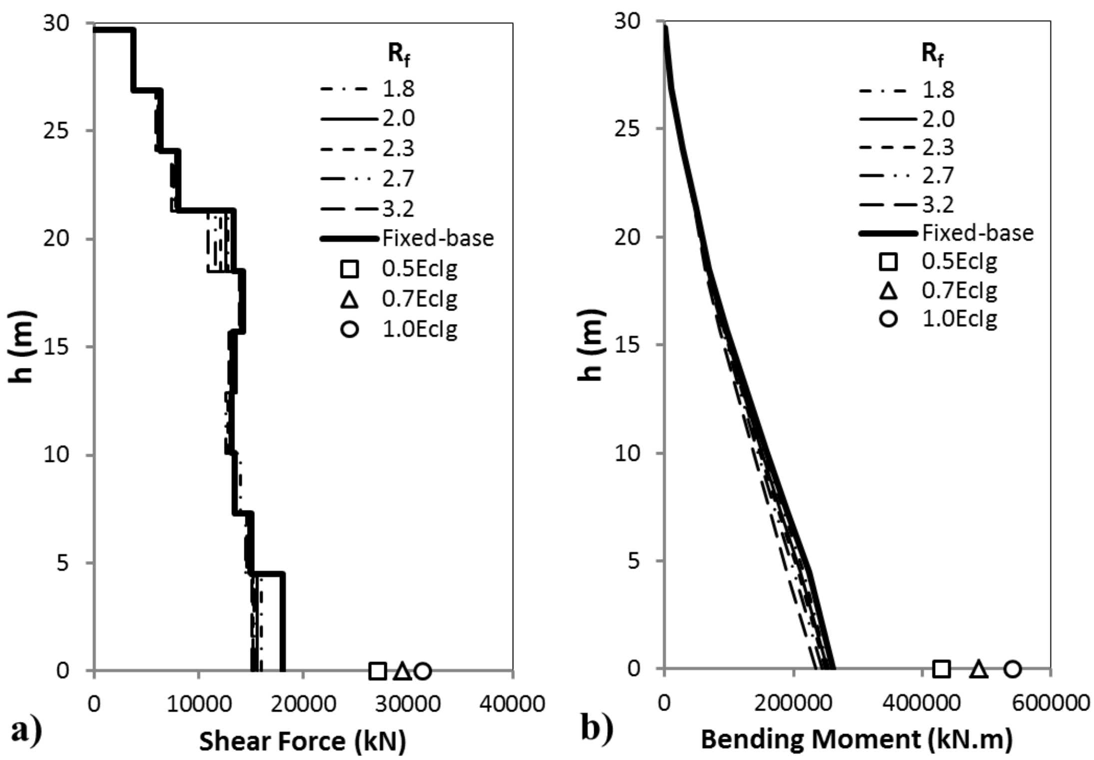

Figure A.132 Average of a) shear force, and b) bending moment envelopes for wall 10R20 on Loose Sand along with estimated maximum quantities for the fixed-base wall from RSA using various effective stiffnesses

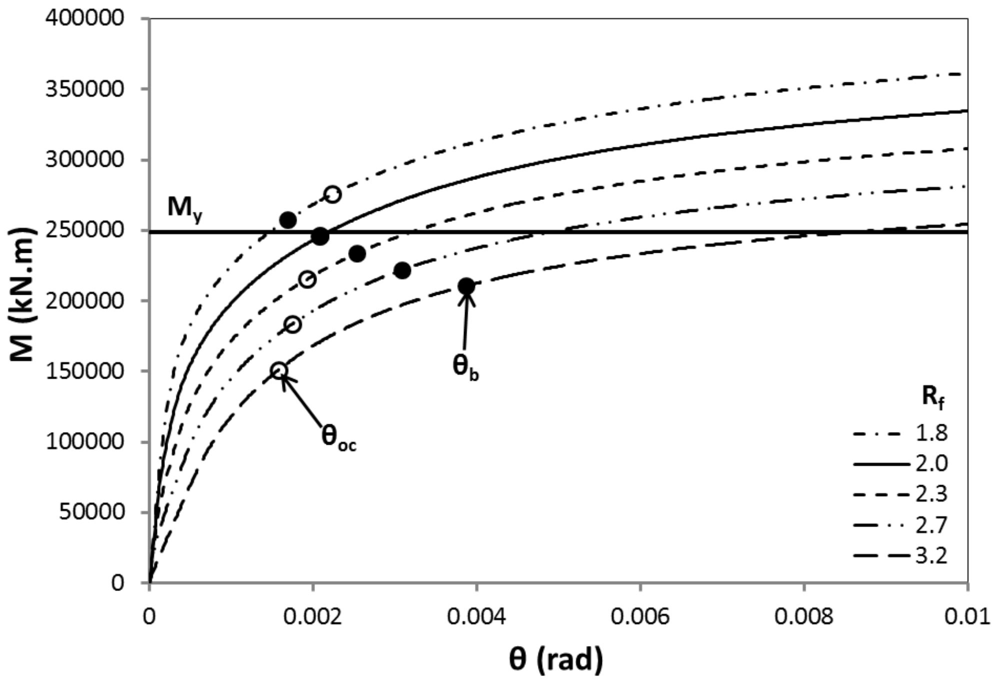

Figure A.133 Bending moment-rotation response of the foundation of wall 10R20 on Loose Sand

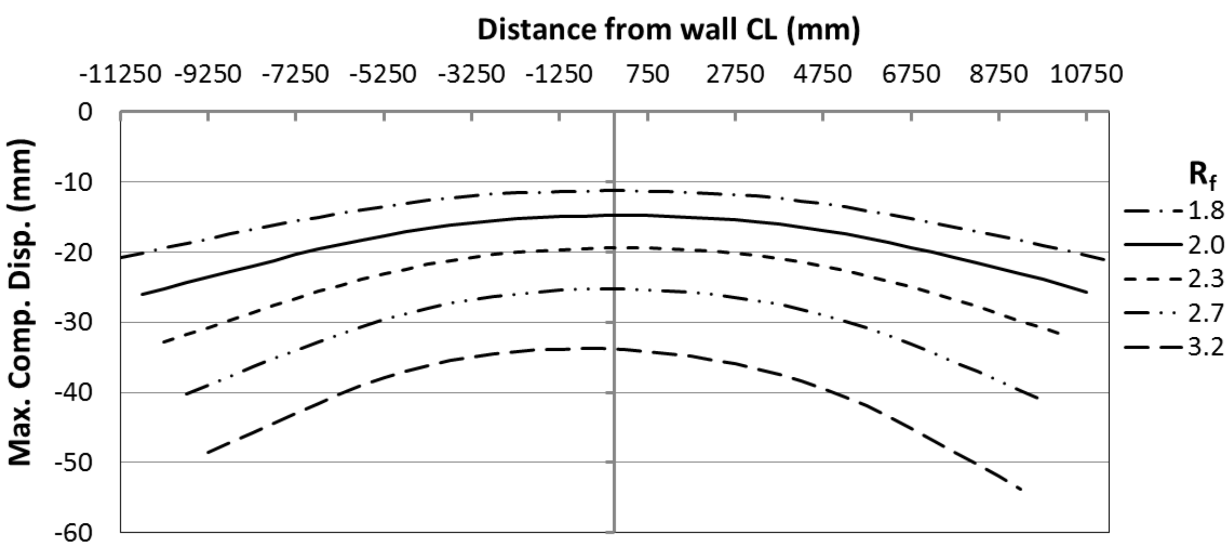

Figure A.134 Average of maximum soil compressive displacements underneath the footing for wall 10R20 on Loose Sand

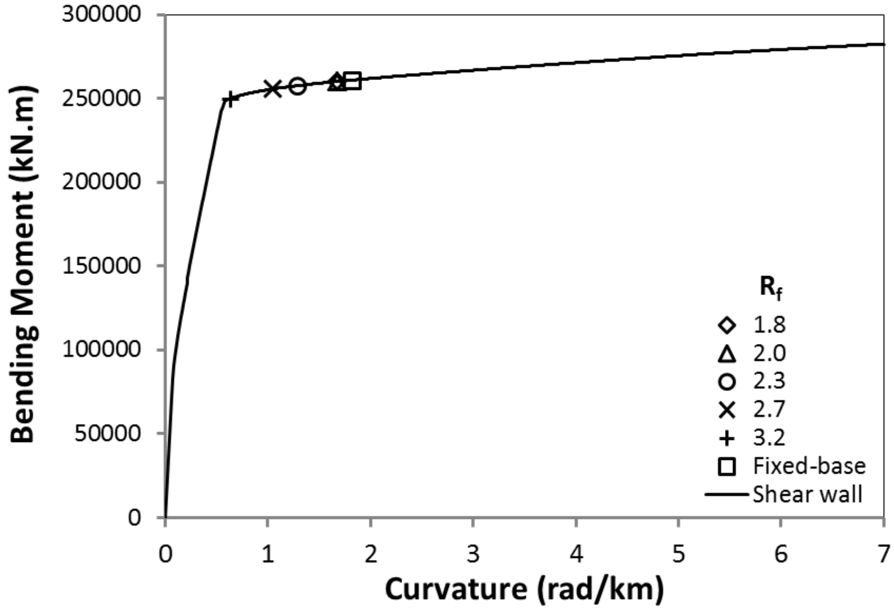

Figure A.135 Moment-curvature response of wall 10R20 along with average of maximum recorded curvatures at the base on Loose Sand

Table A.41 Shear wall properties for wall 10R17

N	10
L_w (mm)	5500
P (kN)	41550
M_{RSA} (kN.m)	488000
M_y (kN.m)	289000
R_w	1.69

Table A.42 Summary of nonlinear dynamic analyses for wall 10R17 on Loose Sand

R_f	1.8	2.0	2.3	2.7	3.2
E (MPa)	57	57	57	57	57
G_{eff} (MPa)	22	22	22	22	22
v	0.3	0.3	0.3	0.3	0.3
q_a (kPa)	133	133	133	133	133
q (kPa)	82	90	99	109	121
q_f (kPa)	200	200	200	200	200
q_{ult} (kPa)	400	400	400	400	400
L (m)	22.5	21.5	20.5	19.5	18.5
B (m)	22.5	21.5	20.5	19.5	18.5
a (mm)	9233	9663	10134	10654	11230
s (mm)	2.82	2.93	3.05	3.17	3.31
M_{oc} (kN.m)	275615	245918	215351	183779	151040
θ_{oc} (rad)	0.0022	0.0021	0.0019	0.0017	0.0016
θ_y (rad)	0.0027	0.0041	0.0065	0.0125	0.0417
$T_{Estimate}$ (sec)	1.25	1.29	1.32	1.37	1.42
T_{model} (sec)	1.08	1.10	1.11	1.13	1.15
Δ_1 (mm)	16.6	17.5	19.8	21.1	23.0
Δ_{10} (mm)	217	218	227	224	230
Avg. Max. θ_b (rad)	0.0024	0.0027	0.0033	0.0037	0.0042
Avg. Max. Uplift (mm)	23.4	23.6	26.2	25.4	23.7
Avg. Max. Comp. Disp. (mm)	-30.7	-35.2	-42.3	-49.5	-59.4
Avg. Max. q_{max}/q_{ult}	59%	64%	70%	74%	79%

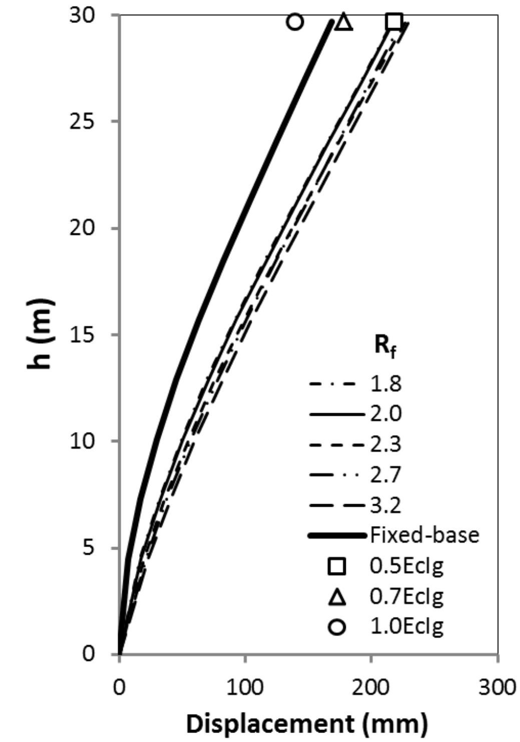

Figure A.136 Average of displacement envelopes for wall 10R17 on Loose Sand along with estimated top displacements of the fixed-base wall from RSA using various effective stiffnesses

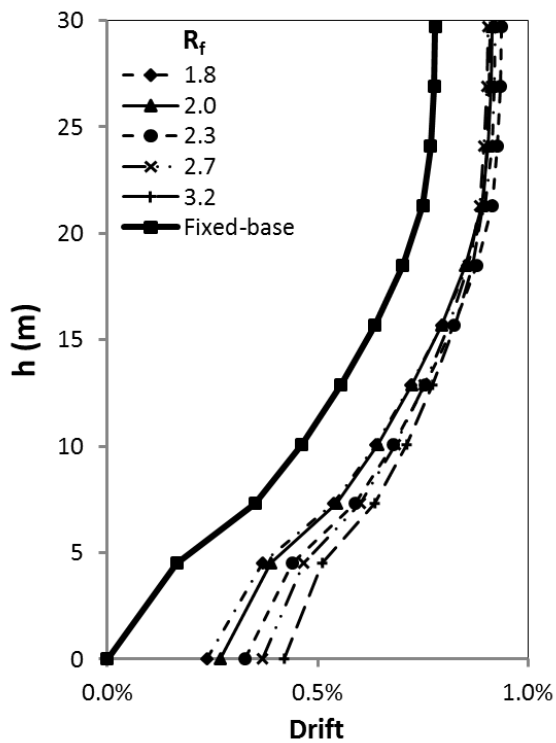

Figure A.137 Average of drift envelopes for wall 10R17 on Loose Sand (Note: base rotation values are plotted at h=0 and values of average interstory drift are plotted at the top of the storey.)

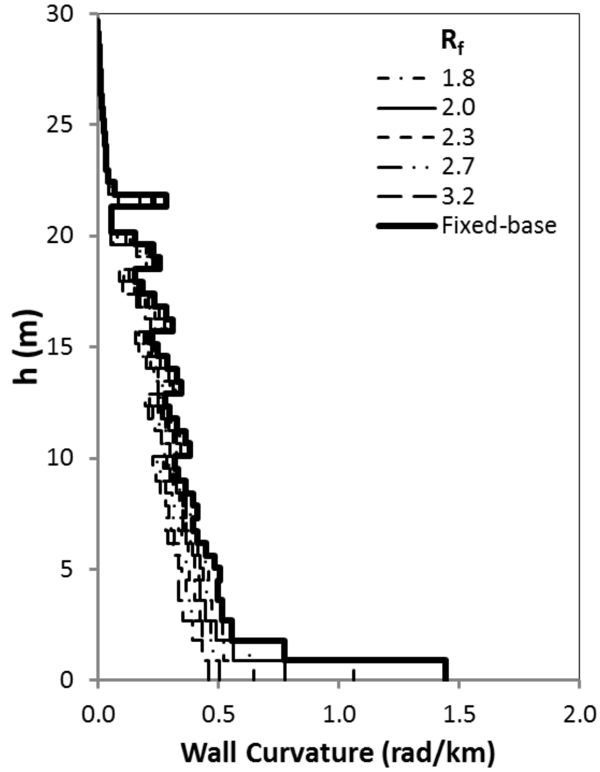

Figure A.138 Average of curvature envelopes for wall 10R17 on Loose Sand

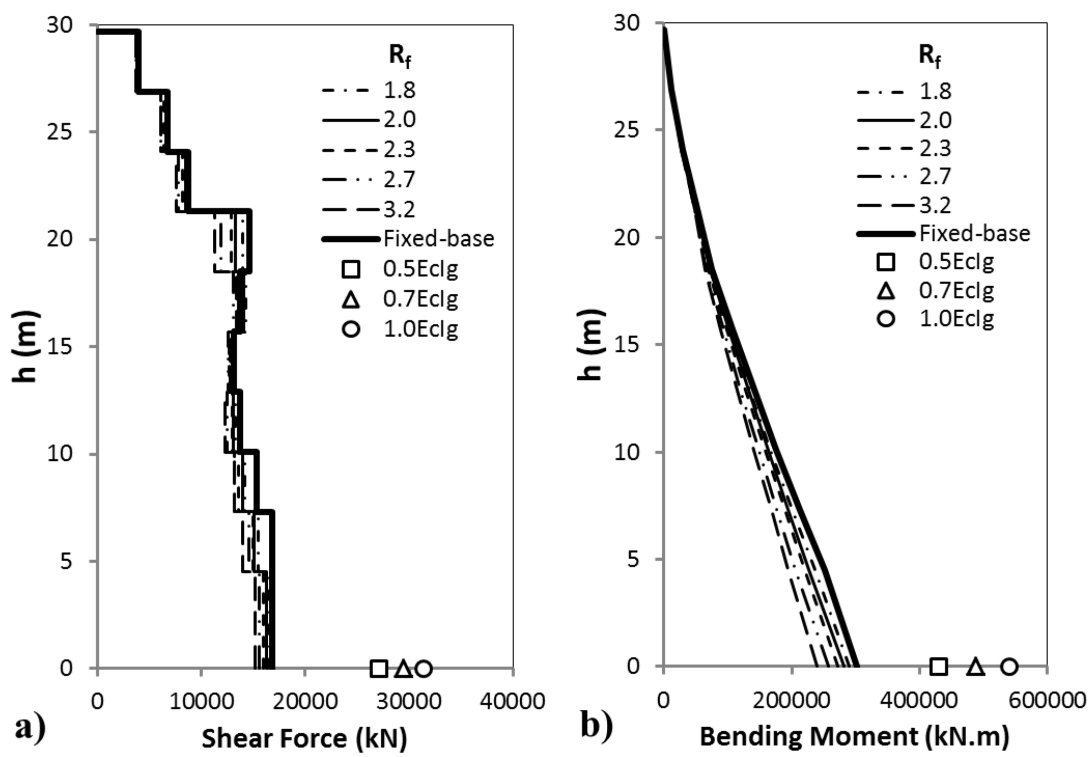

Figure A.139 Average of a) shear force, and b) bending moment envelopes for wall 10R17 on Loose Sand along with estimated maximum quantities for the fixed-base wall from RSA using various effective stiffnesses

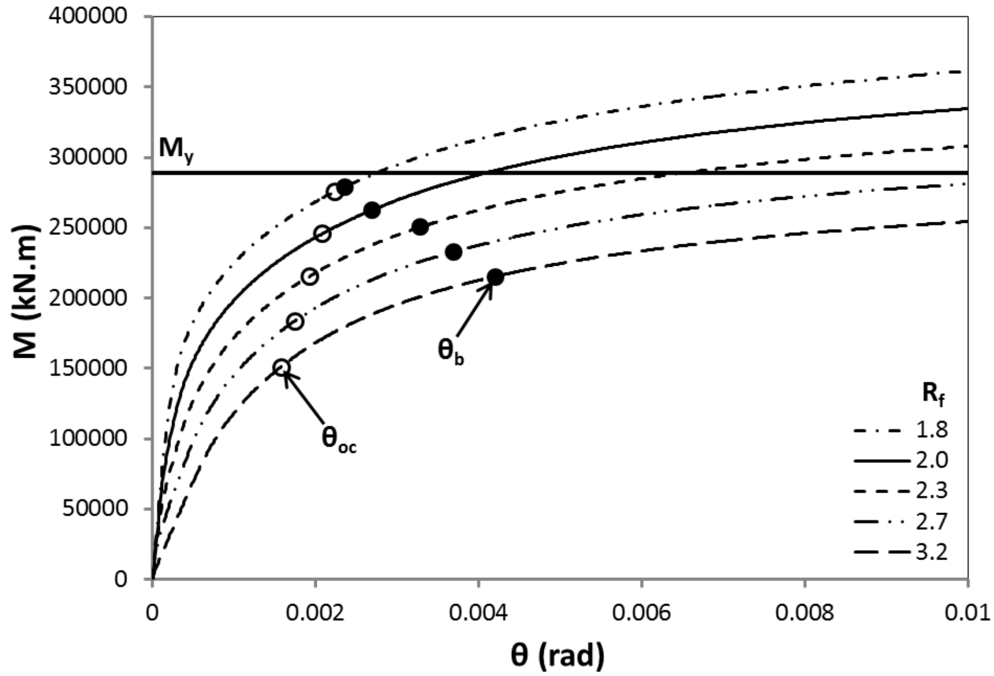

Figure A.140 Bending moment-rotation response of the foundation of wall 10R17 on Loose Sand

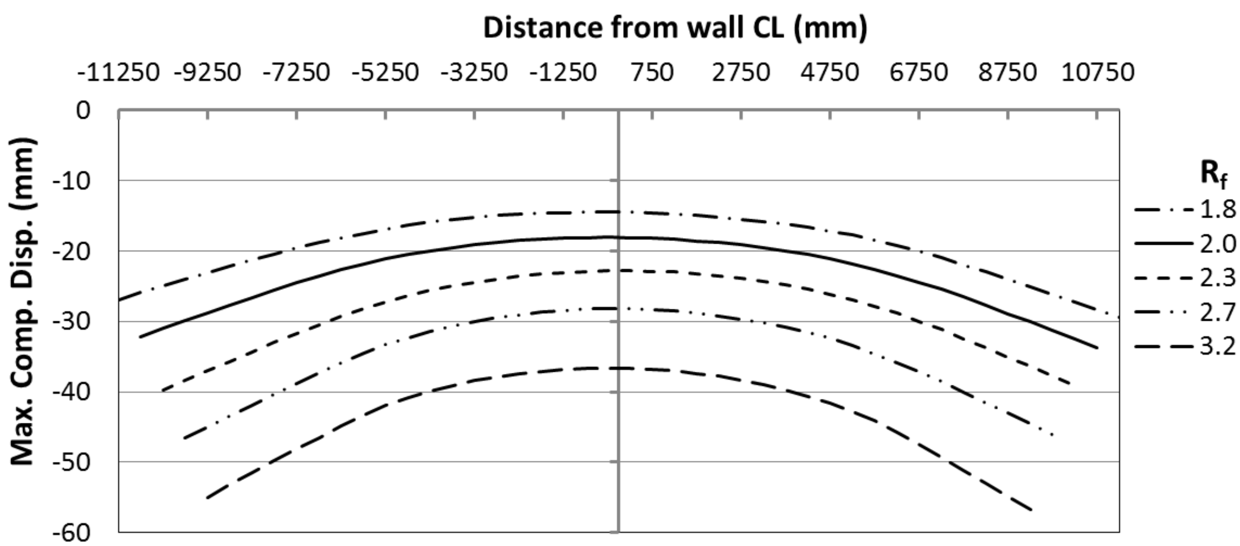

Figure A.141 Average of maximum soil compressive displacements underneath the footing for wall 10R17 on Loose Sand

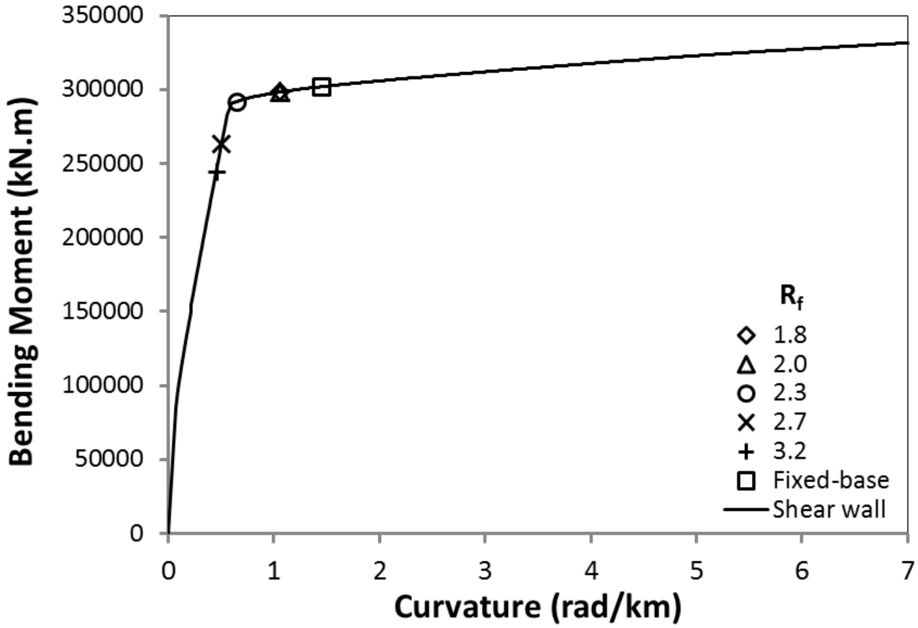

Figure A.142 Moment-curvature response of wall 10R17 along with average of maximum recorded curvatures at the base on Loose Sand

Table A.43 Shear wall properties for wall 10R13

N	10
L_w (mm)	5500
P (kN)	41550
M_{RSA} (kN.m)	488000
M_y (kN.m)	369000
R_w	1.32

Table A.44 Summary of nonlinear dynamic analyses for wall 10R13 on Loose Sand

R_f	1.3	1.5	1.8	2.0	2.3	2.7	3.2
E (MPa)	57	57	57	57	57	57	57
G_{eff} (MPa)	22	22	22	22	22	22	22
ν	0.3	0.3	0.3	0.3	0.3	0.3	0.3
q_a (kPa)	133	133	133	133	133	133	133
q (kPa)	59	69	82	90	99	109	121
q_f (kPa)	200	200	200	200	200	200	200
q_{ult} (kPa)	400	400	400	400	400	400	400
L (m)	26.5	24.5	22.5	21.5	20.5	19.5	18.5
B (m)	26.5	24.5	22.5	21.5	20.5	19.5	18.5
a (mm)	7840	8480	9233	9663	10134	10654	11230
s (mm)	6.52	6.97	2.82	2.93	3.05	3.17	3.31
M_{oc} (kN.m)	387669	332824	275615	245918	215351	183779	151040
θ_{oc} (rad)	0.0026	0.0025	0.0022	0.0021	0.0019	0.0017	0.0016
θ_y (rad)	0.0019	0.0044	0.0119	0.0256	0.0646	-----	-----
$T_{Estimate}$ (sec)	1.13	1.17	1.22	1.25	1.29	1.34	1.39
T_{model} (sec)	1.01	1.02	1.05	1.06	1.08	1.09	1.11
Δ_1 (mm)	11.7	15.7	18.1	20.3	21.9	23.3	23.2
Δ_{10} (mm)	181	203	207	215	222	224	214
Avg. Max. θ_b (rad)	0.0015	0.0024	0.0031	0.0036	0.0040	0.0044	0.0045
Avg. Max. Uplift (mm)	20.5	30.9	32.1	34.4	32.7	29.9	28.2
Avg. Max. Comp. Disp. (mm)	-18.2	-28.6	-37.3	-43.2	-50.2	-57.6	-60.9
Avg. Max. q_{max}/q_{ult}	44%	54%	64%	69%	73%	77%	81%

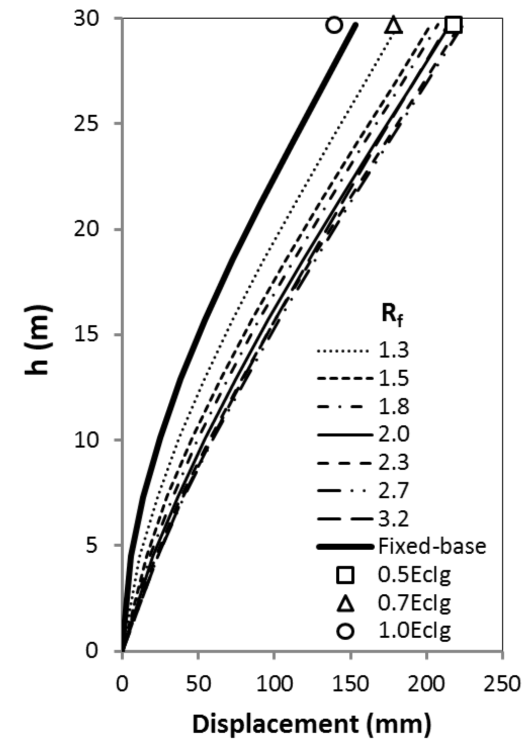

Figure A.143 Average of displacement envelopes for wall 10R13 on Loose Sand along with estimated top displacements of the fixed-base wall from RSA using various effective stiffnesses

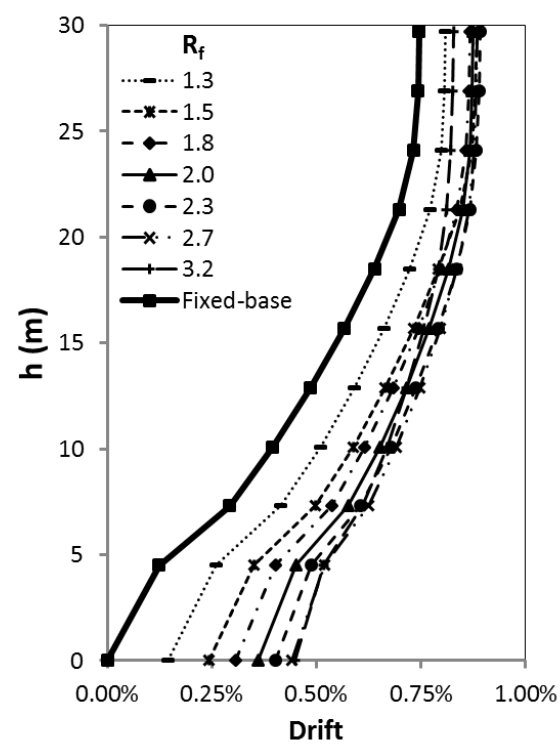

Figure A.144 Average of drift envelopes for wall 10R13 on Loose Sand (Note: base rotation values are plotted at h=0 and values of average interstory drift are plotted at the top of the storey.)

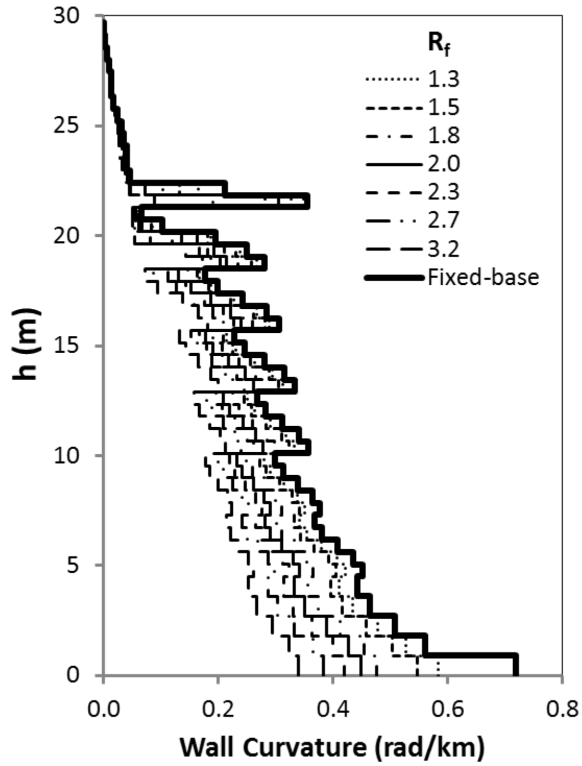

Figure A.145 Average of curvature envelopes for wall 10R13 on Loose Sand

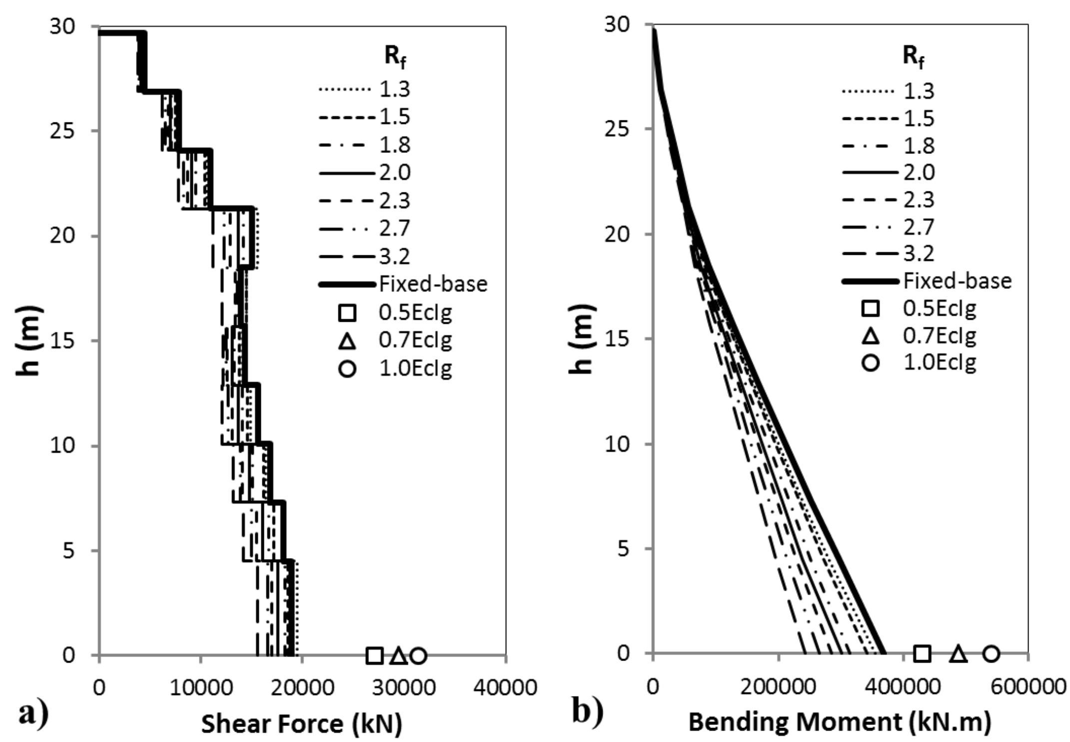

Figure A.146 Average of a) shear force, and b) bending moment envelopes for wall 10R13 on Loose Sand along with estimated maximum quantities for the fixed-base wall from RSA using various effective stiffnesses

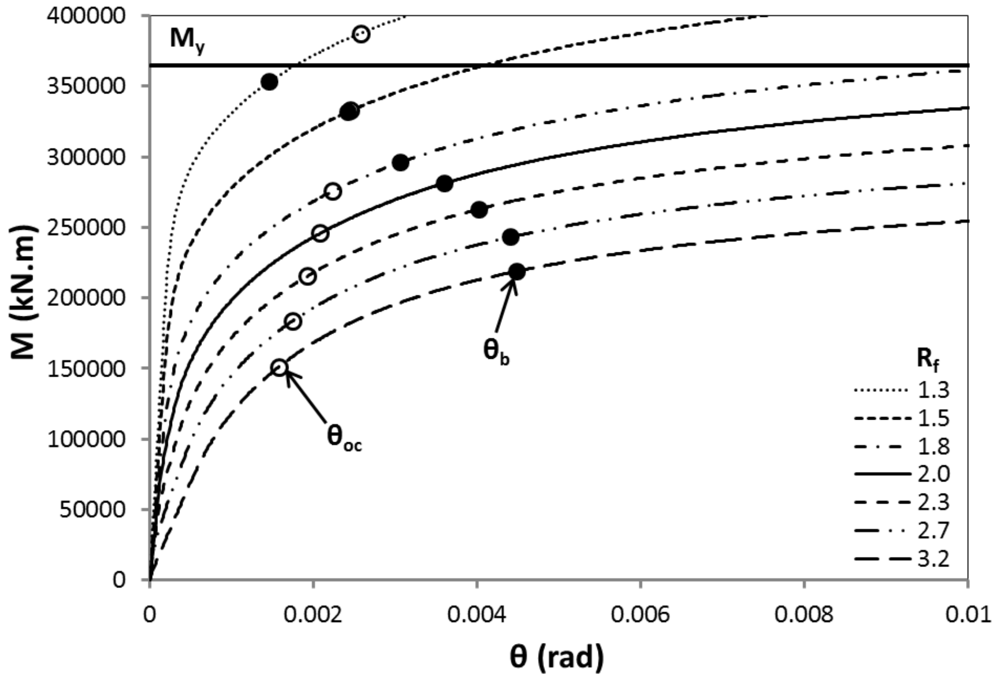

Figure A.147 Bending moment-rotation response of the foundation of wall 10R13 on Loose Sand

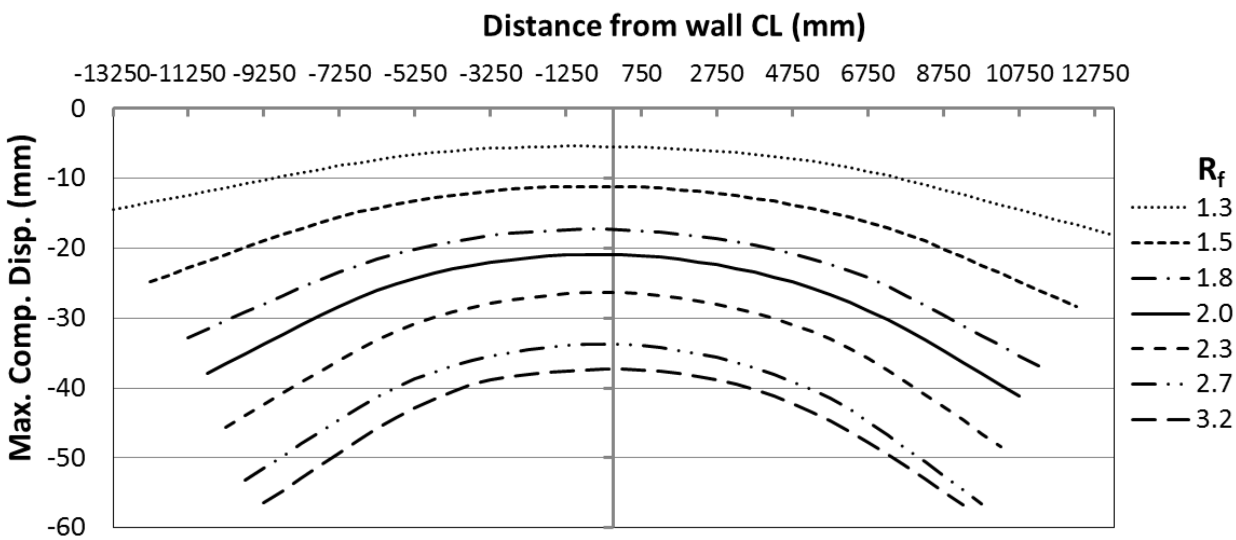

Figure A.148 Average of maximum soil compressive displacements underneath the footing for wall 10R13 on Loose Sand

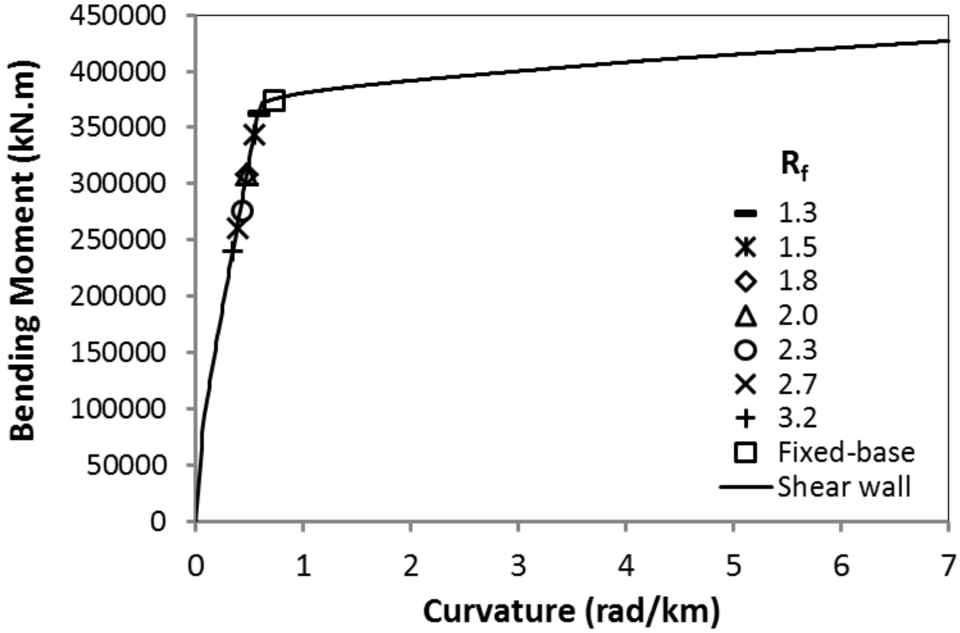

Figure A.149 Moment-curvature response of wall 10R13 along with average of maximum recorded curvatures at the base on Loose Sand

Table A.45 Shear wall properties for wall 10Elastic

N	10
L_w (mm)	5500
P (kN)	41550
M_{RSA} (kN.m)	488000
M_y (kN.m)	-----
R_w	1.00

Table A.46 Summary of nonlinear dynamic analyses for wall 10Elastic on Loose Sand

R_f	1.8	2.0	2.3	2.7	3.2
E (MPa)	57	57	57	57	57
G_{eff} (MPa)	22	22	22	22	22
v	0.3	0.3	0.3	0.3	0.3
q_a (kPa)	133	133	133	133	133
q (kPa)	82	90	99	109	121
q_f (kPa)	200	200	200	200	200
q_{ult} (kPa)	400	400	400	400	400
L (m)	22.5	21.5	20.5	19.5	18.5
B (m)	22.5	21.5	20.5	19.5	18.5
a (mm)	9233	9663	10134	10654	11230
s (mm)	2.82	2.93	3.05	3.17	3.31
M_{oc} (kN.m)	275615	245918	215351	183779	151040
θ_{oc} (rad)	0.0022	0.0021	0.0019	0.0017	0.0016
θ_y (rad)	-----	-----	-----	-----	-----
$T_{Estimate}$ (sec)	1.32	1.35	1.38	1.42	1.47
T_{model} (sec)	1.18	1.19	1.20	1.22	1.24
Δ_1 (mm)	23.2	25.7	26.5	27.0	26.2
Δ_{10} (mm)	217	233	234	232	221
Avg. Max. θ_b (rad)	0.0044	0.0050	0.0052	0.0054	0.0053
Avg. Max. Uplift (mm)	51.2	51.9	46.9	39.8	33.0
Avg. Max. Comp. Disp. (mm)	-49.9	-56.8	-62.0	-69.2	-72.3
Avg. Max. q_{max}/q_{ult}	70%	74%	77%	80%	82%

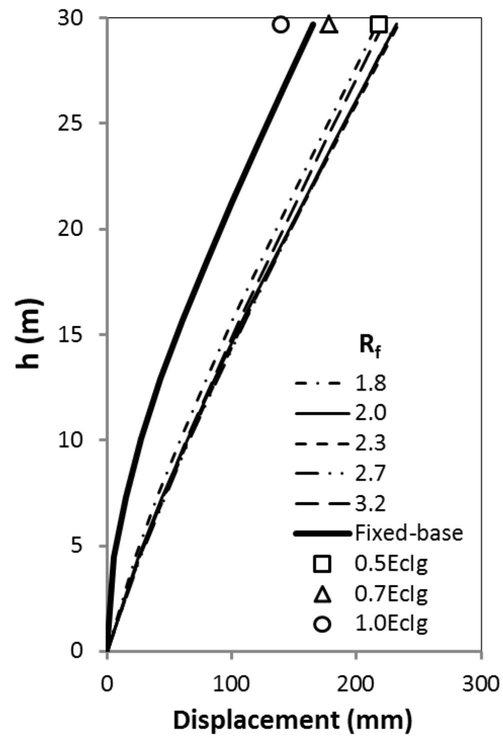

Figure A.150 Average of displacement envelopes for wall 10Elastic on Loose Sand along with estimated top displacements of the fixed-base wall from RSA using various effective stiffnesses

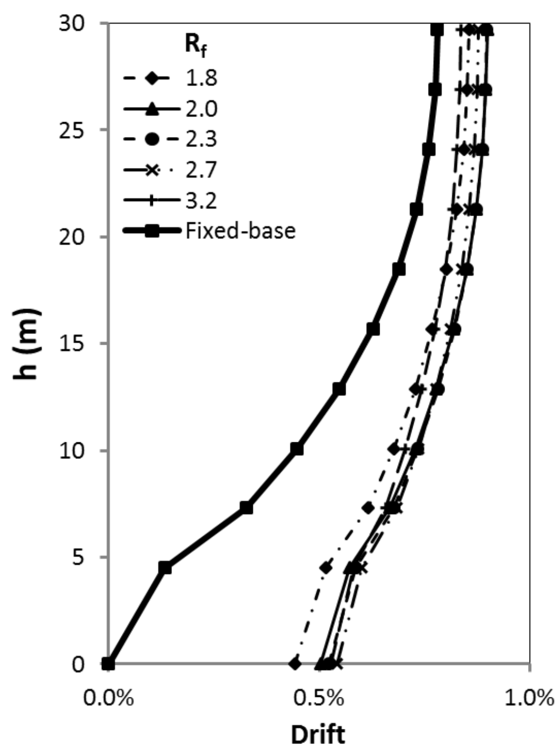

Figure A.151 Average of drift envelopes for wall 10Elastic on Loose Sand (Note: base rotation values are plotted at h=0 and values of average interstory drift are plotted at the top of the storey.)

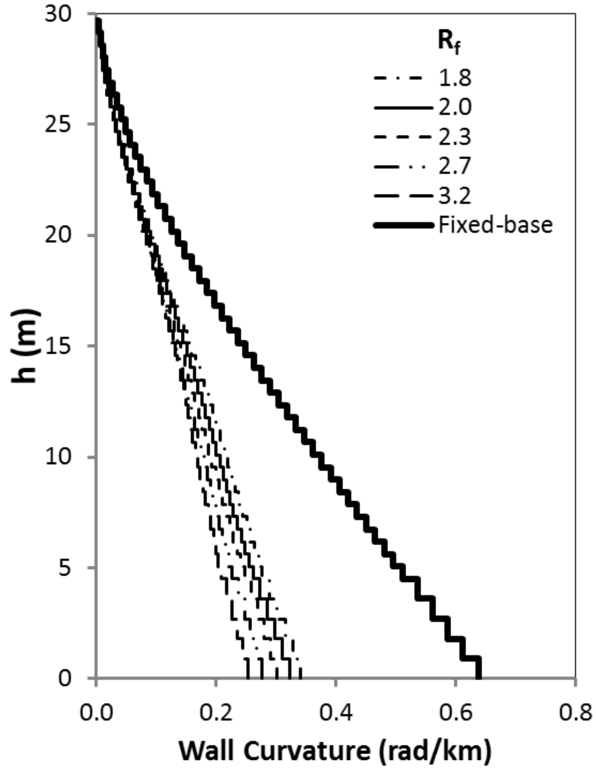

Figure A.152 Average of curvature envelopes for wall 10Elastic on Loose Sand

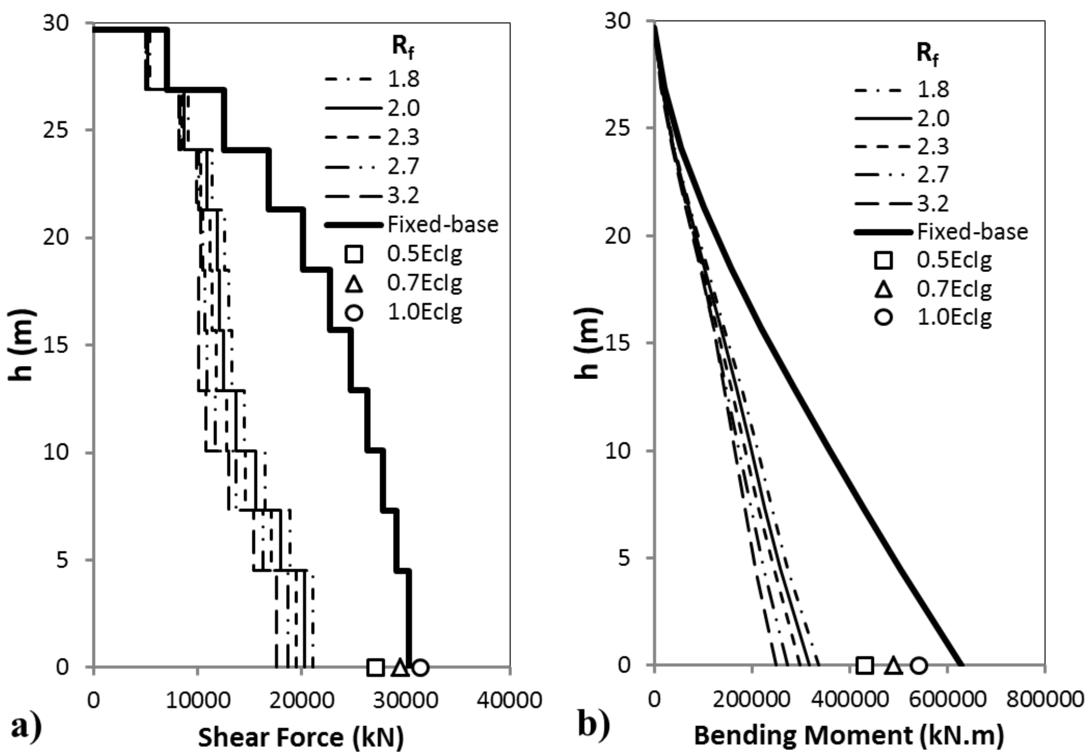

Figure A.153 Average of a) shear force, and b) bending moment envelopes for wall 10Elastic on Loose Sand along with estimated maximum quantities for the fixed-base wall from RSA using various effective stiffnesses

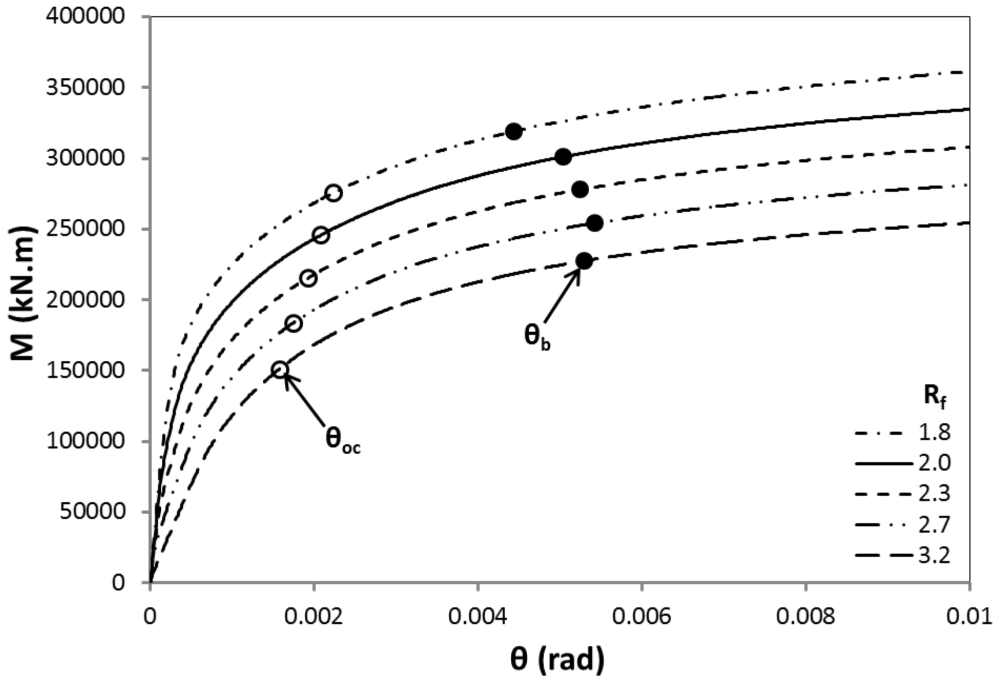

Figure A.154 Bending moment-rotation response of the foundation of wall 10Elastic on Loose Sand

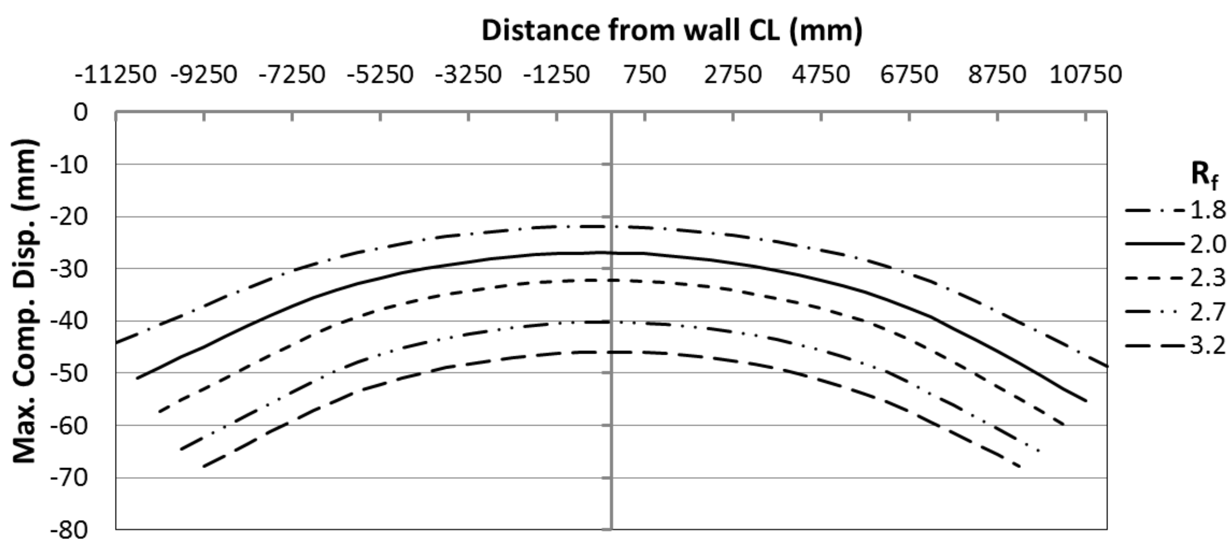

Figure A.155 Average of maximum soil compressive displacements underneath the footing for wall 10Elastic on Loose Sand

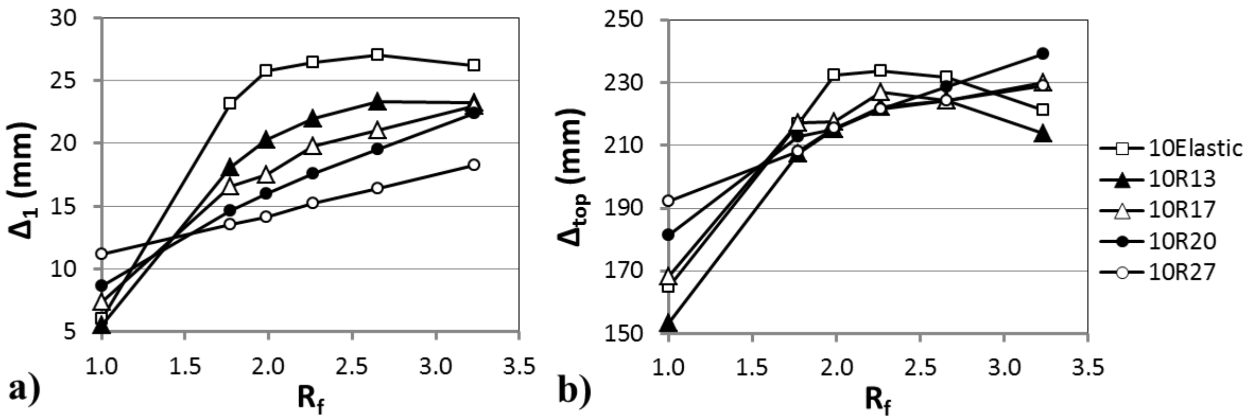

Figure A.156 Summary of average maximum a) first storey displacements, and b) top displacements for 10 storey walls on Loose Sand sorted by wall strength

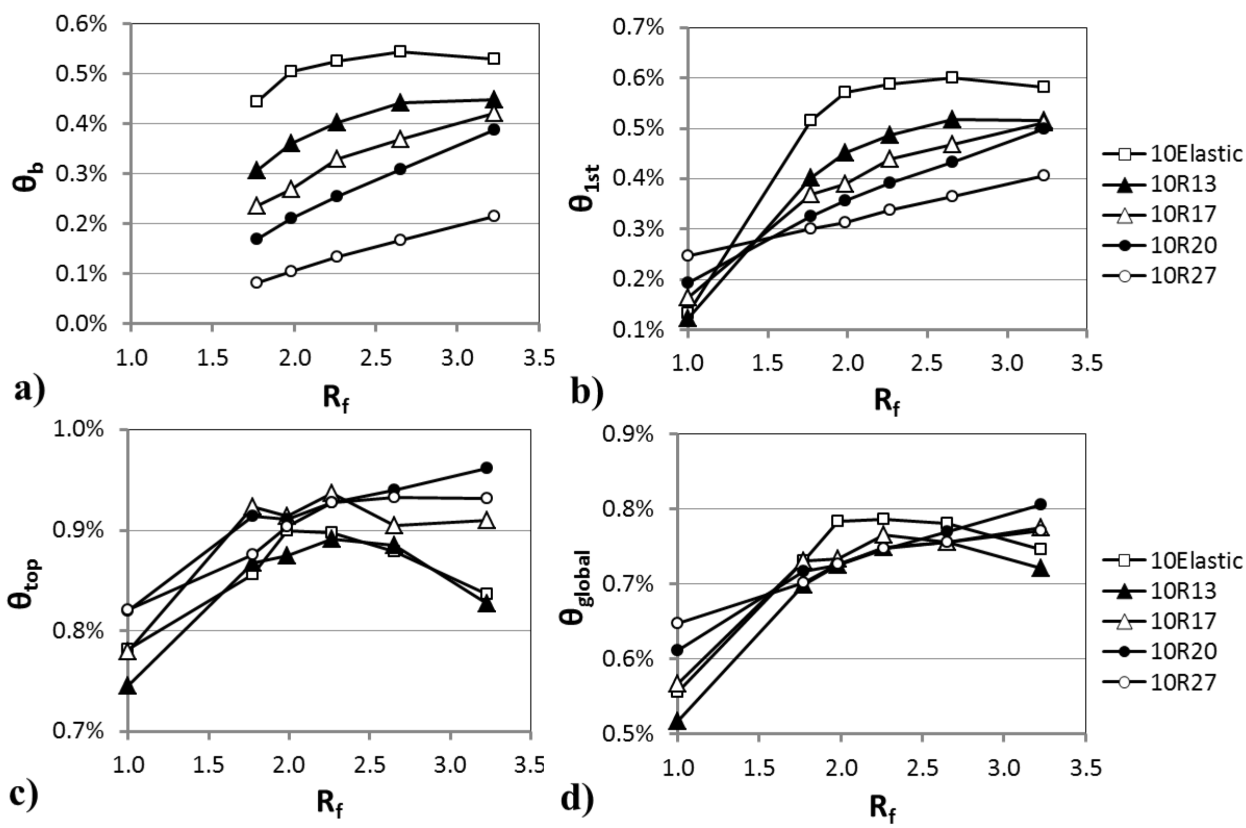

Figure A.157 Summary of average maximum a) base rotations, b) 1st storey inter-storey drifts, c) top storey inter-storey drifts, and d) global drifts of 10 storey walls on Loose Sand sorted by wall strength

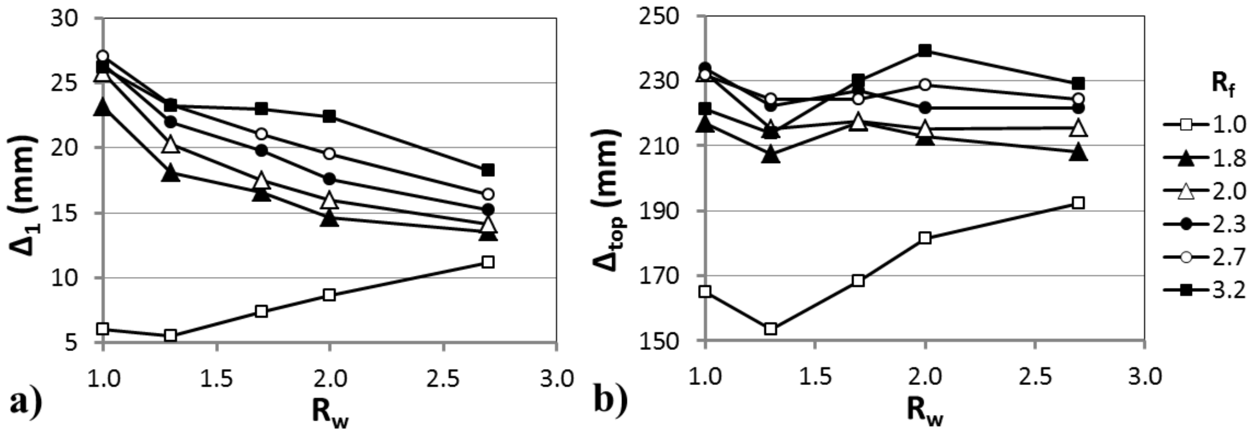

Figure A.158 Summary of average maximum a) first storey displacements, and b) top displacements for 10 storey walls on Loose Sand sorted by foundation size

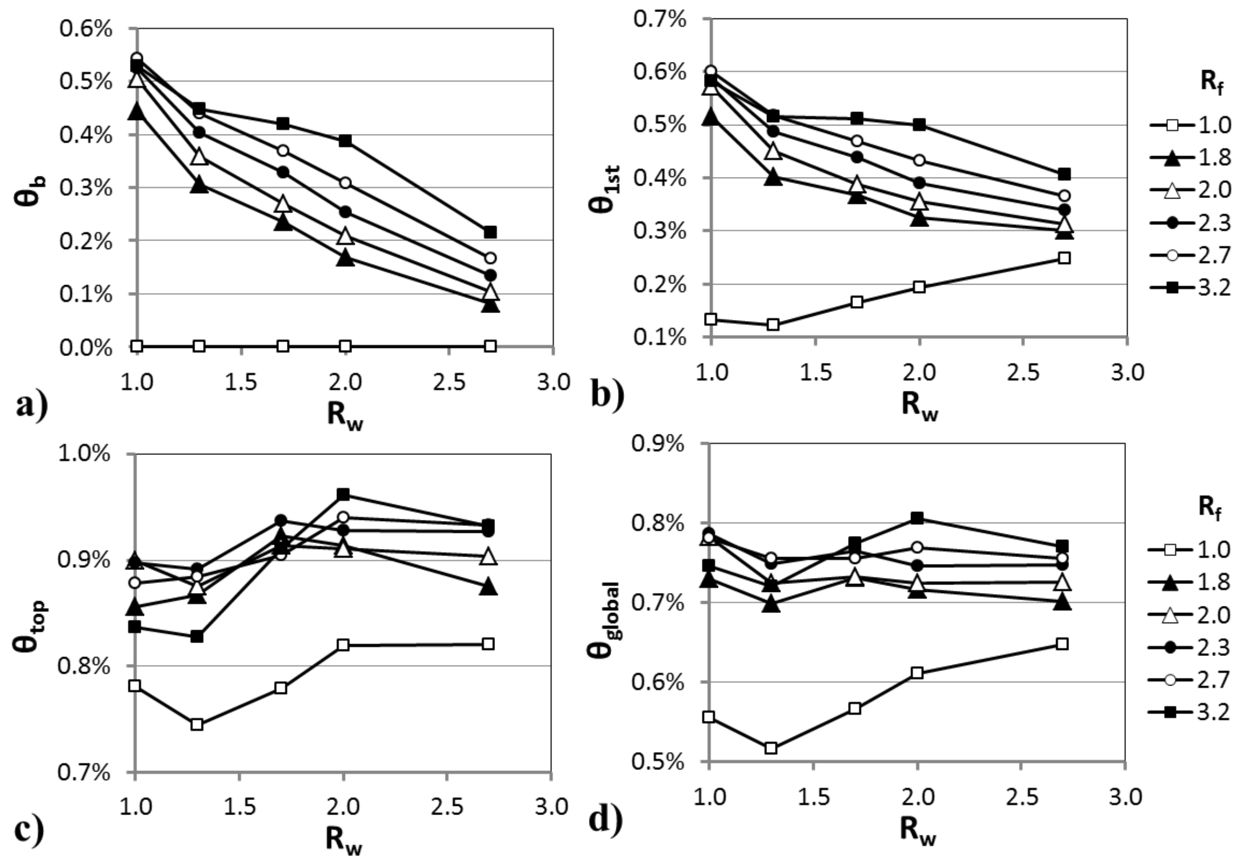

Figure A.159 Summary of average maximum a) base rotations, b) 1st storey inter-storey drifts, c) top storey inter-storey drifts, and d) global drifts of 10 storey walls on Loose Sand sorted by foundation size

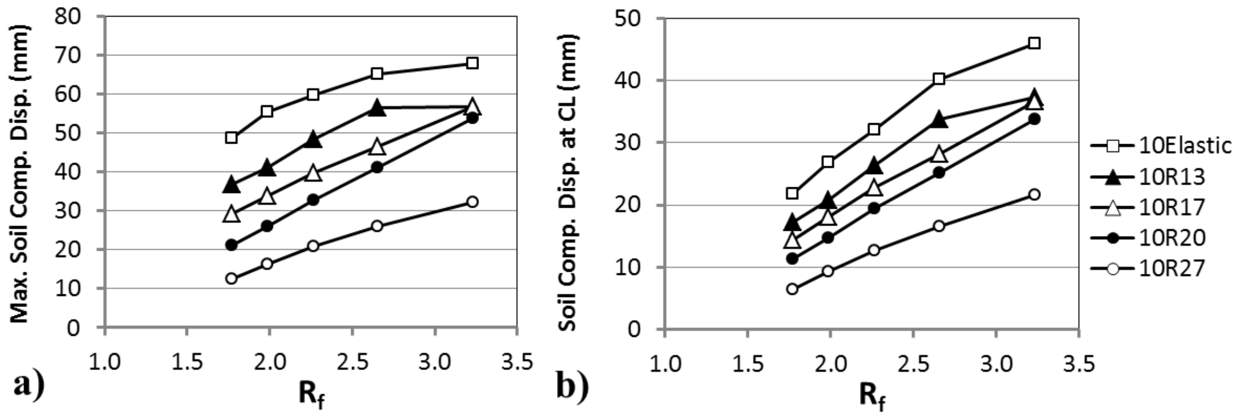

Figure A.160 Summary of average maximum soil compressive displacement at a) foundation toe, and b) foundation centreline for 10 storey walls on Loose Sand sorted by wall strength

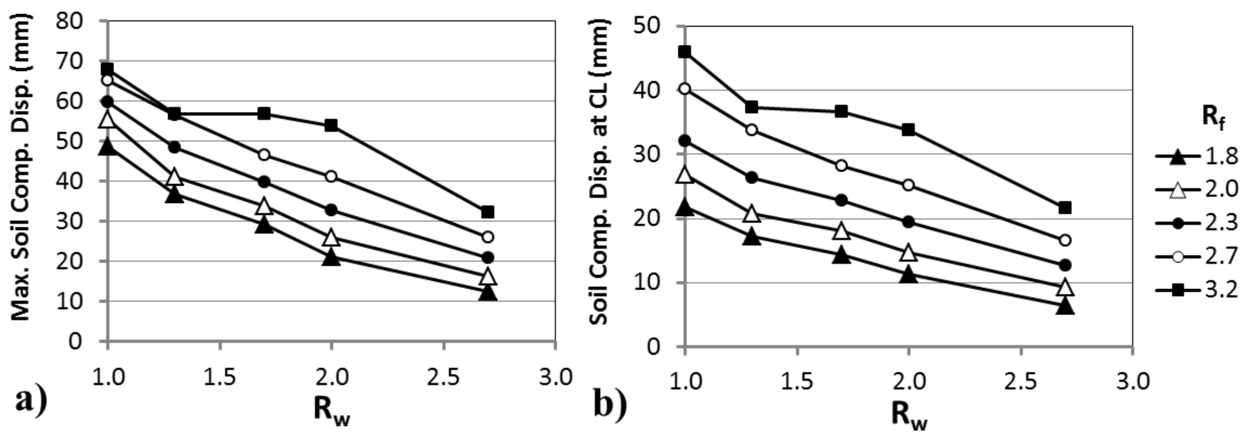

Figure A.161 Summary of average maximum soil compressive displacement at a) foundation toe, and b) foundation centreline for 10 storey walls on Loose Sand sorted by foundation size

A.6.3 Medium Sand

Table A.47 Properties of Medium Sand

G_0 (MPa)	186
G_{eff} (MPa)	70
ν	0.3
E (MPa)	182
q_{ult} (kPa)	800
q_f (kPa)	400
q_a (kPa)	267
V_s (m/s)	360

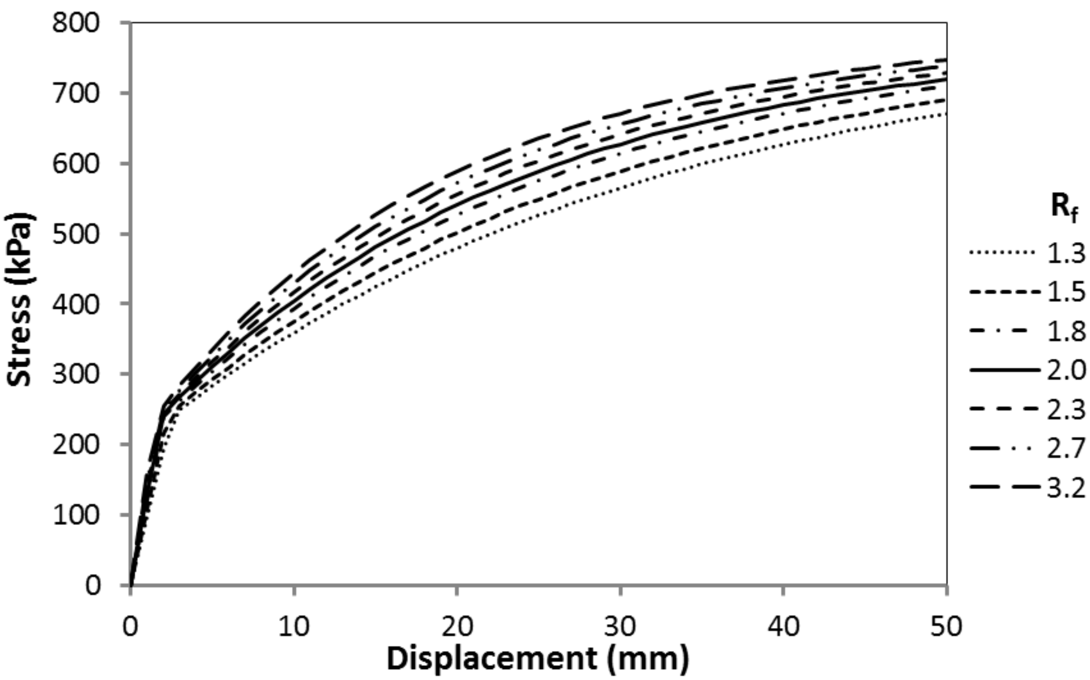

Figure A.162 Soil spring responses in monotonic compression for Medium Sand

Table A.48 Shear wall properties for wall 10R27

N	10
L_w (mm)	5500
P (kN)	41550
M_{RSA} (kN.m)	488000
M_y (kN.m)	179000
R_w	2.73

Table A.49 Summary of nonlinear dynamic analyses for wall 10R27 on Medium Sand

R_f	**1.8**	**2.0**	**2.3**	**2.7**	**3.2**
E (MPa)	182	182	182	182	182
G_{eff} (MPa)	70	70	70	70	70
v	0.3	0.3	0.3	0.3	0.3
q_a (kPa)	267	267	267	267	267
q (kPa)	121	136	153	173	198
q_f (kPa)	400	400	400	400	400
q_{ult} (kPa)	800	800	800	800	800
L (m)	18.5	17.5	16.5	15.5	14.5
B (m)	18.5	17.5	16.5	15.5	14.5
a (mm)	5615	5936	6295	6702	7164
s (mm)	1.02	1.07	1.12	1.17	1.24
M_{oc} (kN.m)	267689	240248	211999	182786	152410
θ_{oc} (rad)	0.0017	0.0016	0.0014	0.0013	0.0011
θ_y (rad)	0.0002	0.0003	0.0006	0.0012	0.0020
$T_{Estimate}$ (sec)	1.21	1.23	1.26	1.29	1.33
T_{model} (sec)	1.10	1.11	1.12	1.13	1.15
Δ_1 (mm)	12.8	14.0	15.2	16.8	19.8
Δ_{10} (mm)	203	215	221	228	239
Avg. Max. θ_b (rad)	0.0005	0.0009	0.0013	0.0018	0.0025
Avg. Max. Uplift (mm)	4.3	7.7	10.1	13.1	16.7
Avg. Max. Comp. Disp. (mm)	-5.1	-7.8	-10.9	-14.8	-20.3
Avg. Max. q_{max}/q_{ult}	38%	46%	54%	64%	75%

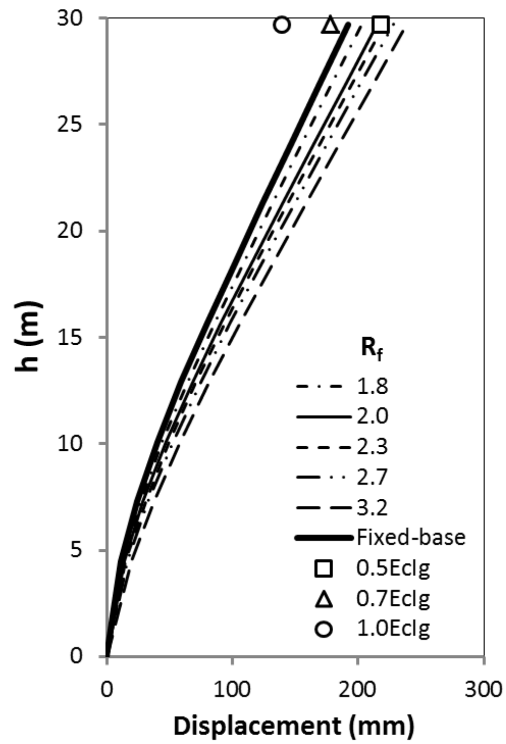

Figure A.163 Average of displacement envelopes for wall 10R27 on Medium Sand along with estimated top displacements of the fixed-base wall from RSA using various effective stiffnesses

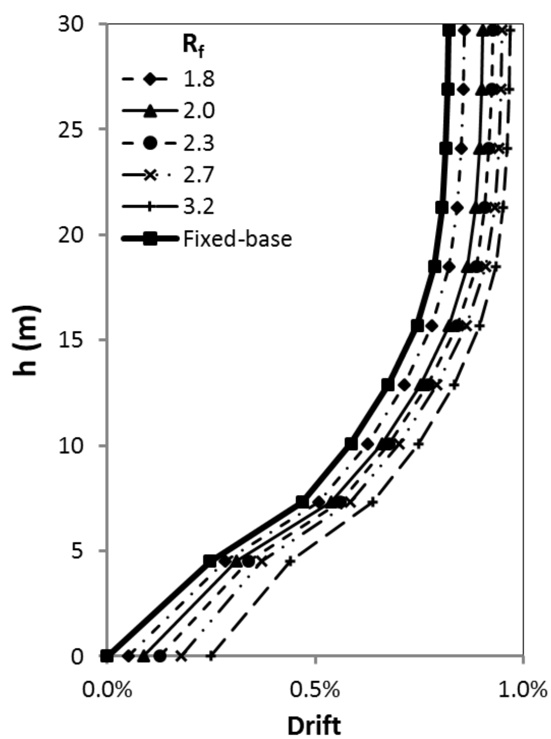

Figure A.164 Average of drift envelopes for wall 10R27 on Medium Sand (Note: base rotation values are plotted at h=0 and values of average interstory drift are plotted at the top of the storey.)

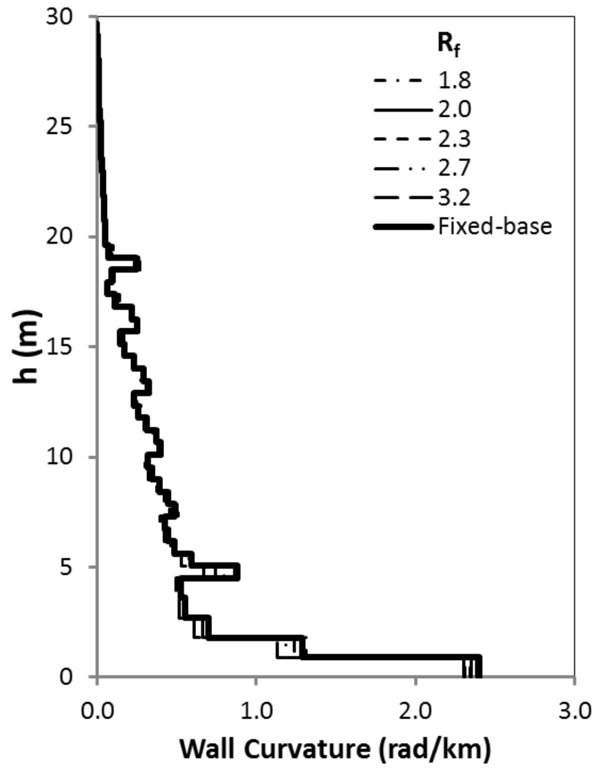

Figure A.165 Average of curvature envelopes for wall 10R27 on Medium Sand

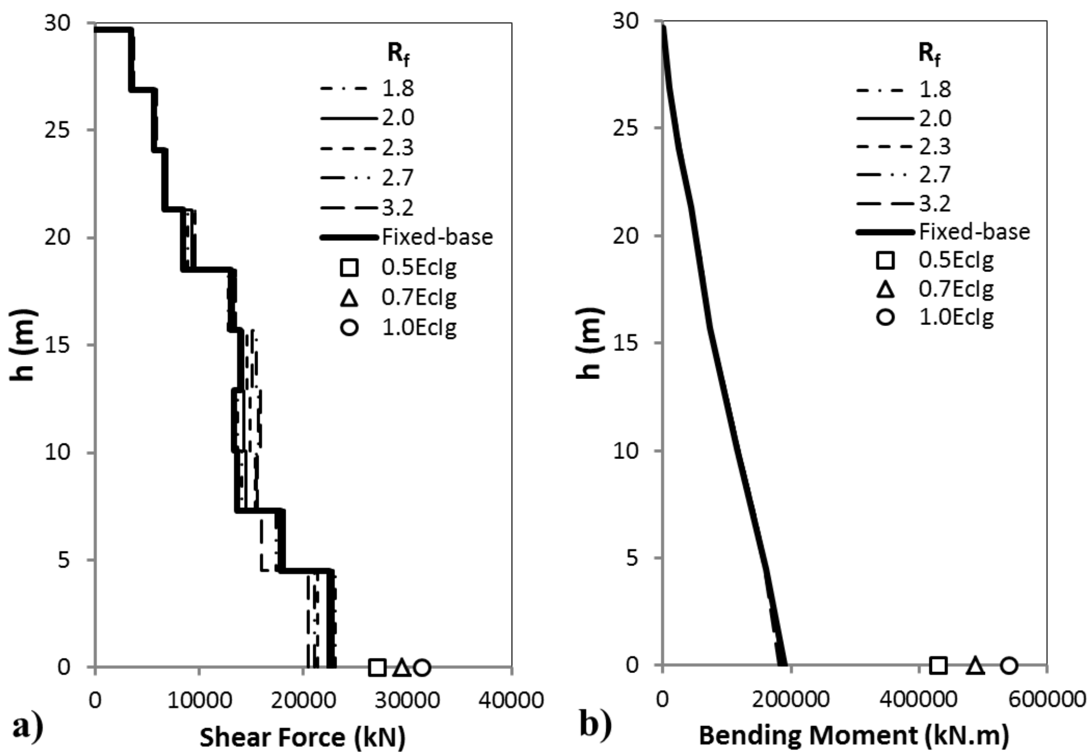

Figure A.166 Average of a) shear force, and b) bending moment envelopes for wall 10R27 on Medium Sand along with estimated maximum quantities for the fixed-base wall from RSA using various effective stiffnesses

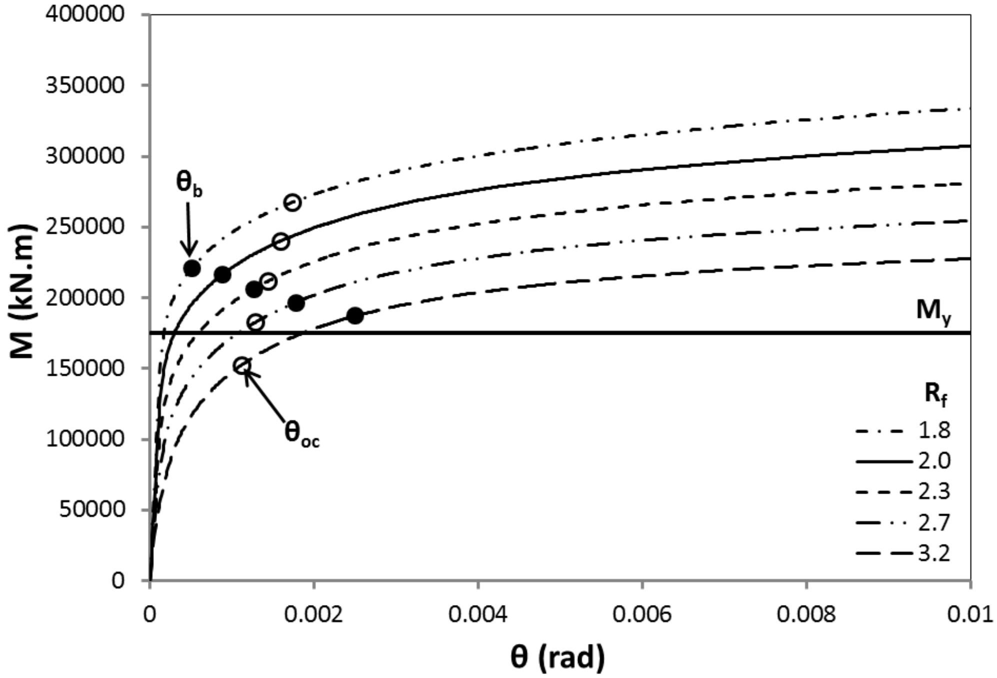

Figure A.167 Bending moment-rotation response of the foundation of wall 10R27 on Medium Sand

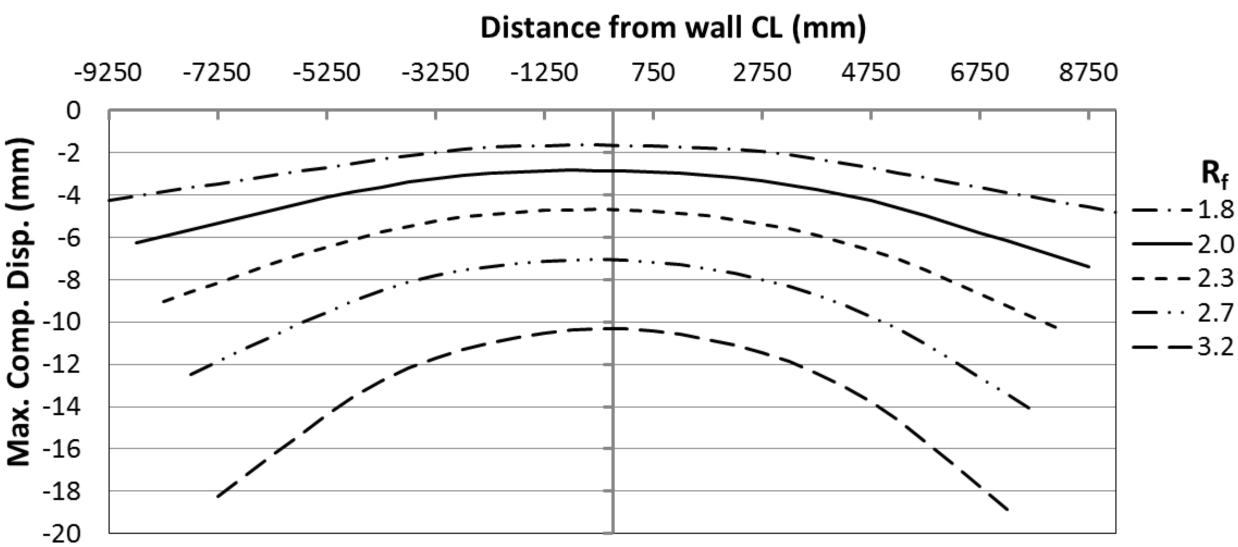

Figure A.168 Average of maximum soil compressive displacements underneath the footing for wall 10R27 on Medium Sand

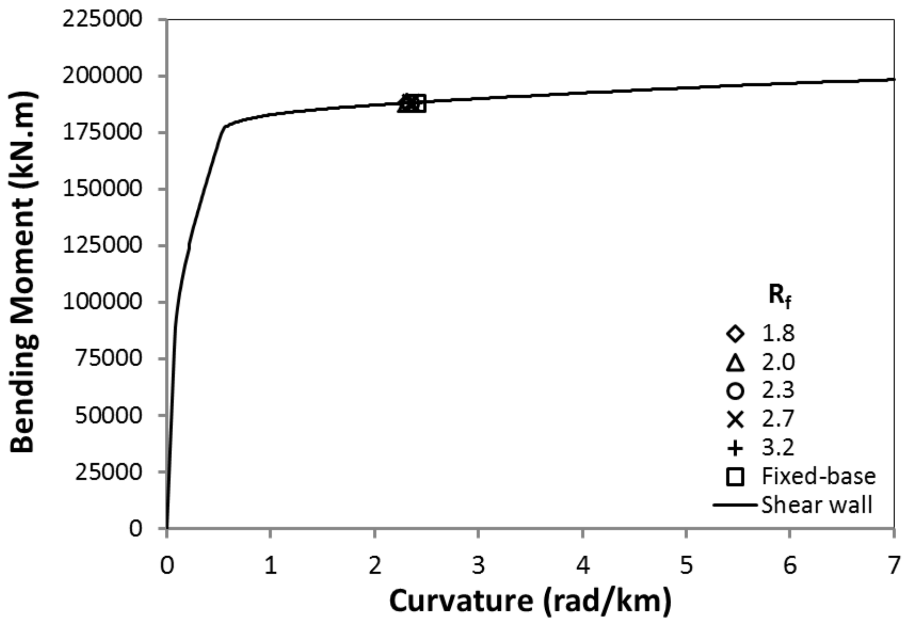

Figure A.169 Moment-curvature response of wall 10R27 along with average of maximum recorded curvatures at the base on Medium Sand

Table A.50 Shear wall properties for wall 10R20

N	10
L_w (mm)	5500
P (kN)	41550
M_{RSA} (kN.m)	488000
M_y (kN.m)	249000
R_w	1.96

Table A.51 Summary of nonlinear dynamic analyses for wall 10R20 on Medium Sand

R_f	1.8	2.0	2.3	2.7	3.2
E (MPa)	182	182	182	182	182
G_{eff} (MPa)	70	70	70	70	70
v	0.3	0.3	0.3	0.3	0.3
q_a (kPa)	267	267	267	267	267
q (kPa)	121	136	153	173	198
q_f (kPa)	400	400	400	400	400
q_{ult} (kPa)	800	800	800	800	800
L (m)	18.5	17.5	16.5	15.5	14.5
B (m)	18.5	17.5	16.5	15.5	14.5
a (mm)	5615	5936	6295	6702	7164
s (mm)	1.02	1.07	1.12	1.17	1.24
M_{oc} (kN.m)	267689	240248	211999	182786	152410
θ_{oc} (rad)	0.0017	0.0016	0.0014	0.0013	0.0011
θ_y (rad)	0.0011	0.0020	0.0037	0.0082	0.0271
$T_{Estimate}$ (sec)	1.15	1.17	1.26	1.23	1.28
T_{model} (sec)	1.06	1.07	1.08	1.09	1.11
Δ_1 (mm)	14.9	17.6	20.6	24.2	30.0
Δ_{10} (mm)	215	228	241	254	278
Avg. Max. θ_b (rad)	0.0017	0.0024	0.0032	0.0042	0.0056
Avg. Max. Uplift (mm)	19.0	25.3	31.9	37.3	44.9
Avg. Max. Comp. Disp. (mm)	-12.5	-16.8	-22.4	-28.6	-39.5
Avg. Max. q_{max}/q_{ult}	54%	63%	73%	80%	86%

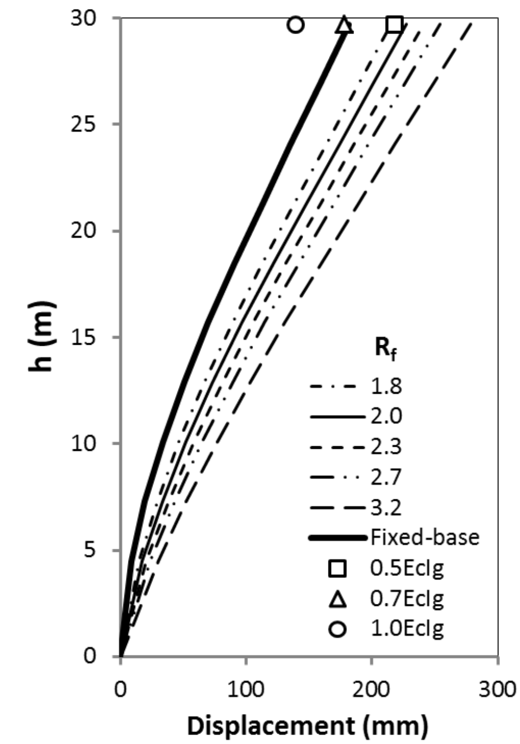

Figure A.170 Average of displacement envelopes for wall 10R20 on Medium Sand along with estimated top displacements of the fixed-base wall from RSA using various effective stiffnesses

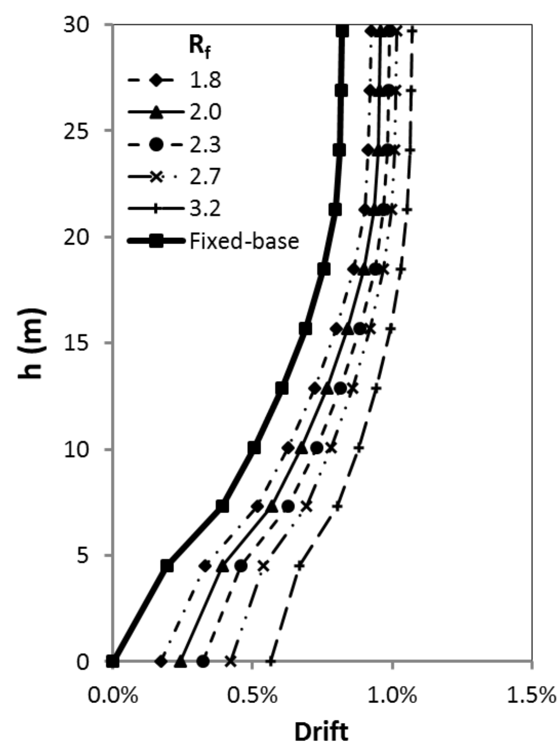

Figure A.171 Average of drift envelopes for wall 10R20 on Medium Sand (Note: base rotation values are plotted at h=0 and values of average interstory drift are plotted at the top of the storey.)

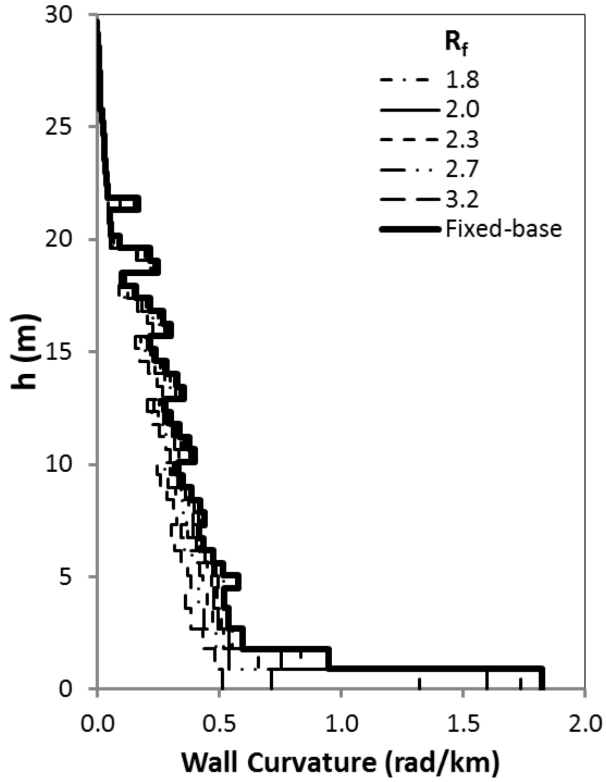

Figure A.172 Average of curvature envelopes for wall 10R20 on Medium Sand

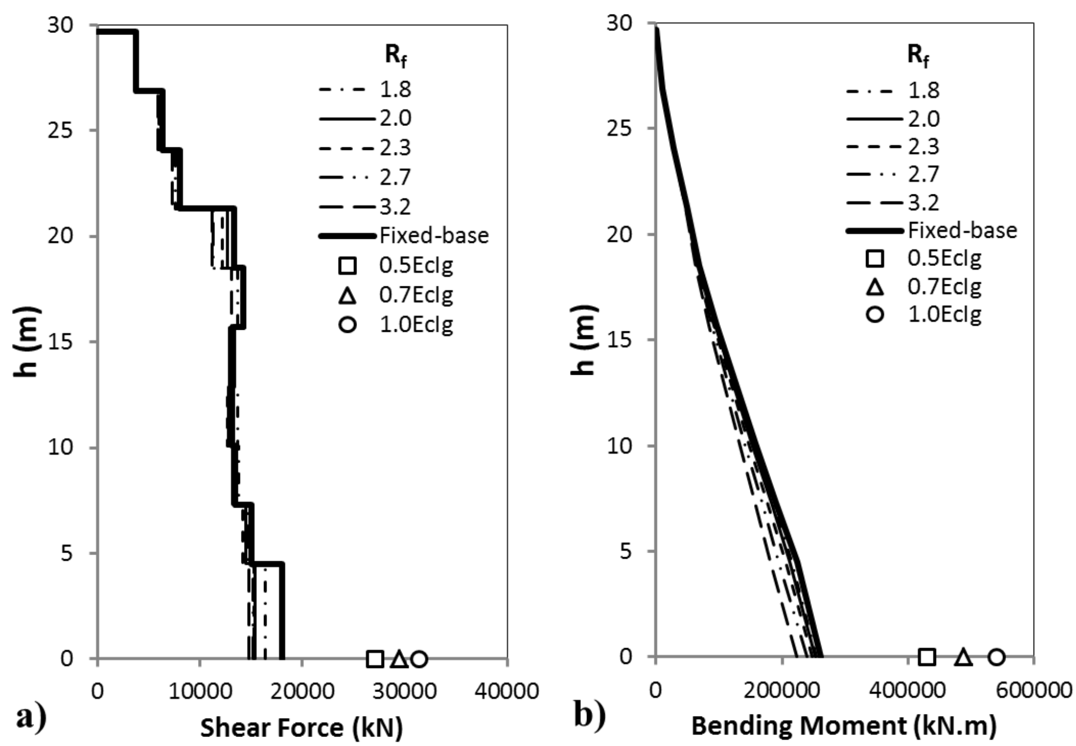

Figure A.173 Average of a) shear force, and b) bending moment envelopes for wall 10R20 on Medium Sand along with estimated maximum quantities for the fixed-base wall from RSA using various effective stiffnesses

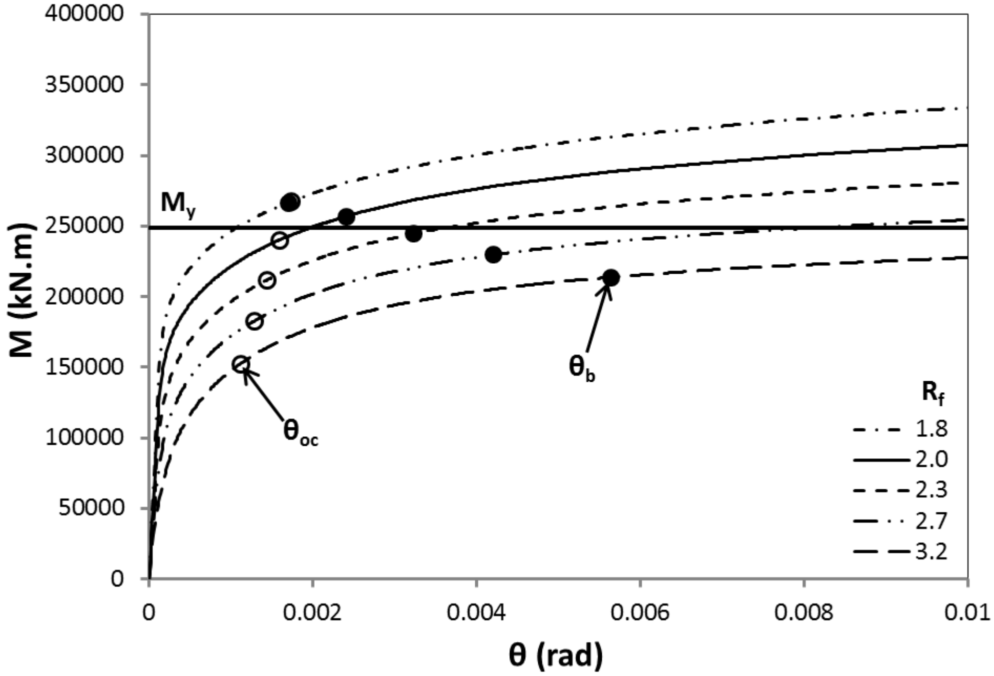

Figure A.174 Bending moment-rotation response of the foundation of wall 10R20 on Medium Sand

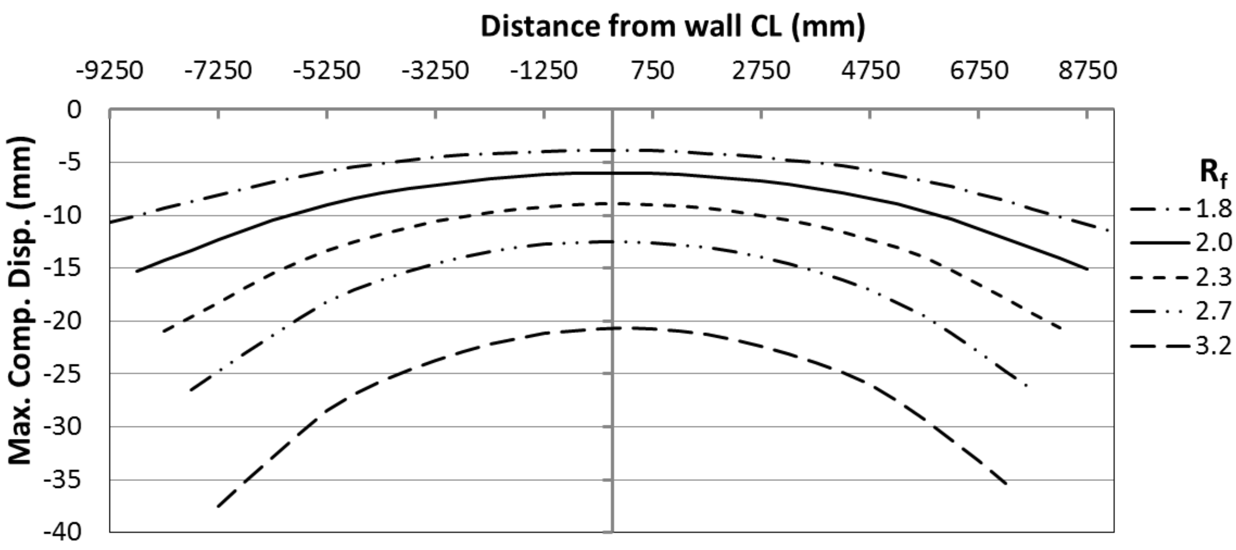

Figure A.175 Average of maximum soil compressive displacements underneath the footing for wall 10R20 on Medium Sand

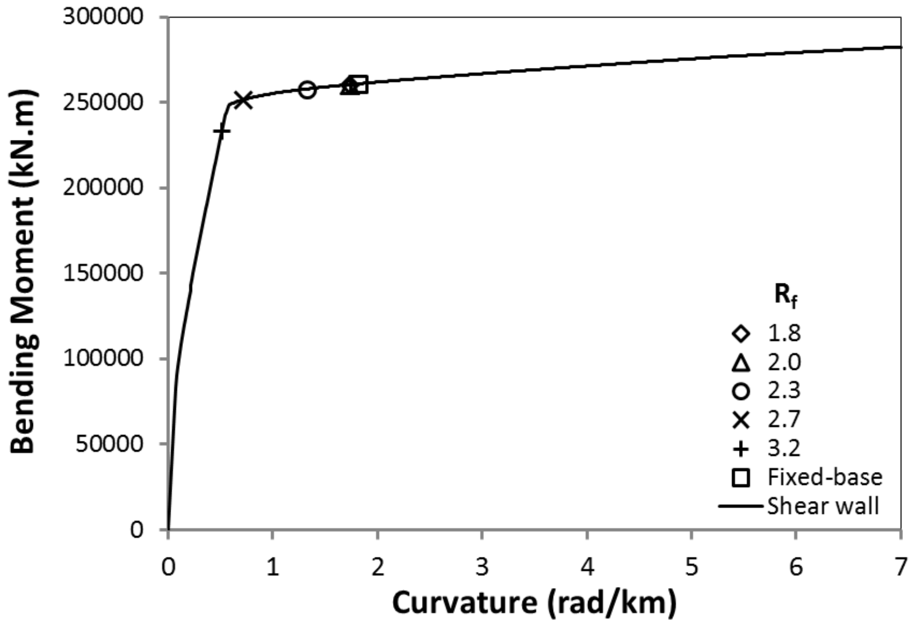

Figure A.176 Moment-curvature response of wall 10R20 along with average of maximum recorded curvatures at the base on Medium Sand

Table A.52 Shear wall properties for wall 10R17

N	10
L_w (mm)	5500
P (kN)	41550
M_{RSA} (kN.m)	488000
M_y (kN.m)	289000
R_w	1.69

Table A.53 Summary of nonlinear dynamic analyses for wall 10R17 on Medium Sand

R_f	1.8	2.0	2.3	2.7	3.2
E (MPa)	182	182	182	182	182
G_{eff} (MPa)	70	70	70	70	70
v	0.3	0.3	0.3	0.3	0.3
q_a (kPa)	267	267	267	267	267
q (kPa)	121	136	153	173	198
q_f (kPa)	400	400	400	400	400
q_{ult} (kPa)	800	800	800	800	800
L (m)	18.5	17.5	16.5	15.5	14.5
B (m)	18.5	17.5	16.5	15.5	14.5
a (mm)	5615	5936	6295	6702	7164
s (mm)	1.02	1.07	1.12	1.17	1.24
M_{oc} (kN.m)	267689	240248	211999	182786	152410
θ_{oc} (rad)	0.0017	0.0016	0.0014	0.0013	0.0011
θ_y (rad)	0.0030	0.0057	0.0132	0.0342	0.0821
$T_{Estimate}$ (sec)	1.13	1.16	1.18	1.22	1.26
T_{model} (sec)	1.04	1.05	1.06	1.07	1.09
Δ_1 (mm)	17.7	21.8	24.5	26.3	32.0
Δ_{10} (mm)	223	246	255	252	280
Avg. Max. θ_b (rad)	0.0027	0.0037	0.0044	0.0049	0.0063
Avg. Max. Uplift (mm)	31.9	40.2	44.2	44.5	50.6
Avg. Max. Comp. Disp. (mm)	-17.5	-24.1	-29.1	-32.4	-43.5
Avg. Max. q_{max}/q_{ult}	62%	71%	77%	82%	87%

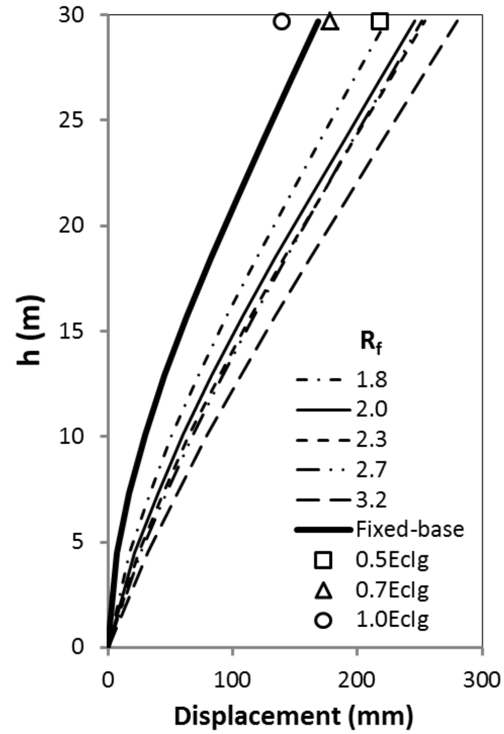

Figure A.177 Average of displacement envelopes for wall 10R17 on Medium Sand along with estimated top displacements of the fixed-base wall from RSA using various effective stiffnesses

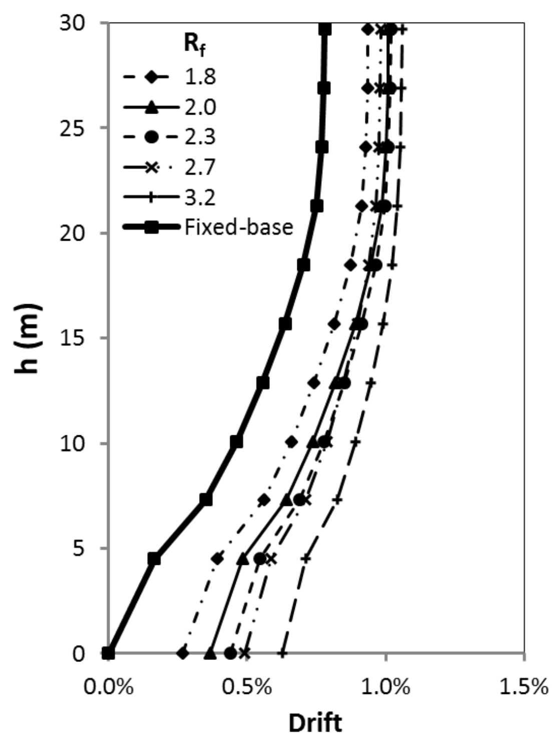

Figure A.178 Average of drift envelopes for wall 10R17 on Medium Sand (Note: base rotation values are plotted at h=0 and values of average interstory drift are plotted at the top of the storey.)

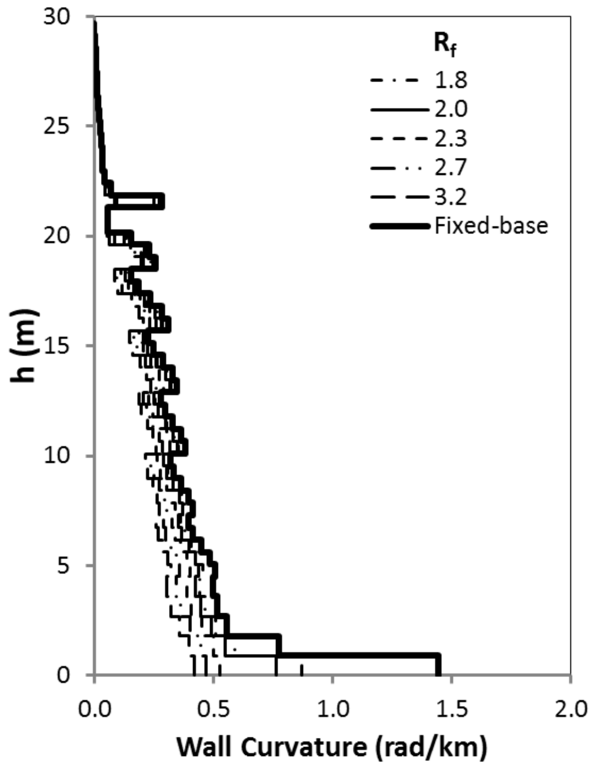

Figure A.179 Average of curvature envelopes for wall 10R17 on Medium Sand

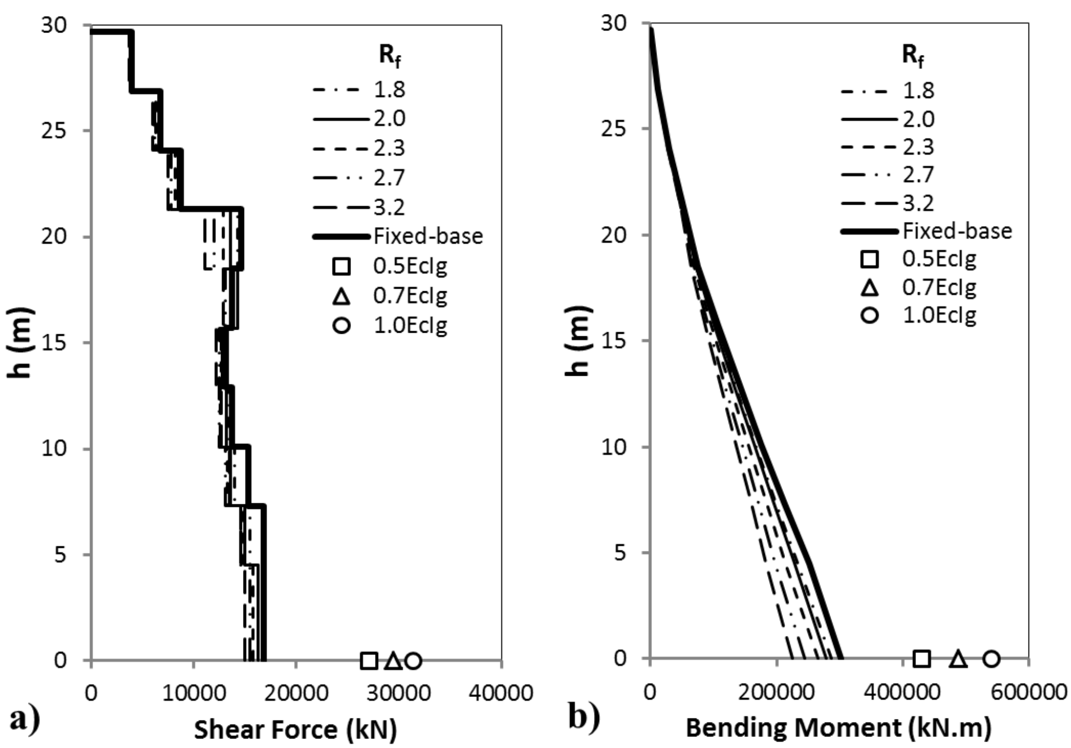

Figure A.180 Average of a) shear force, and b) bending moment envelopes for wall 10R17 on Medium Sand along with estimated maximum quantities for the fixed-base wall from RSA using various effective stiffnesses

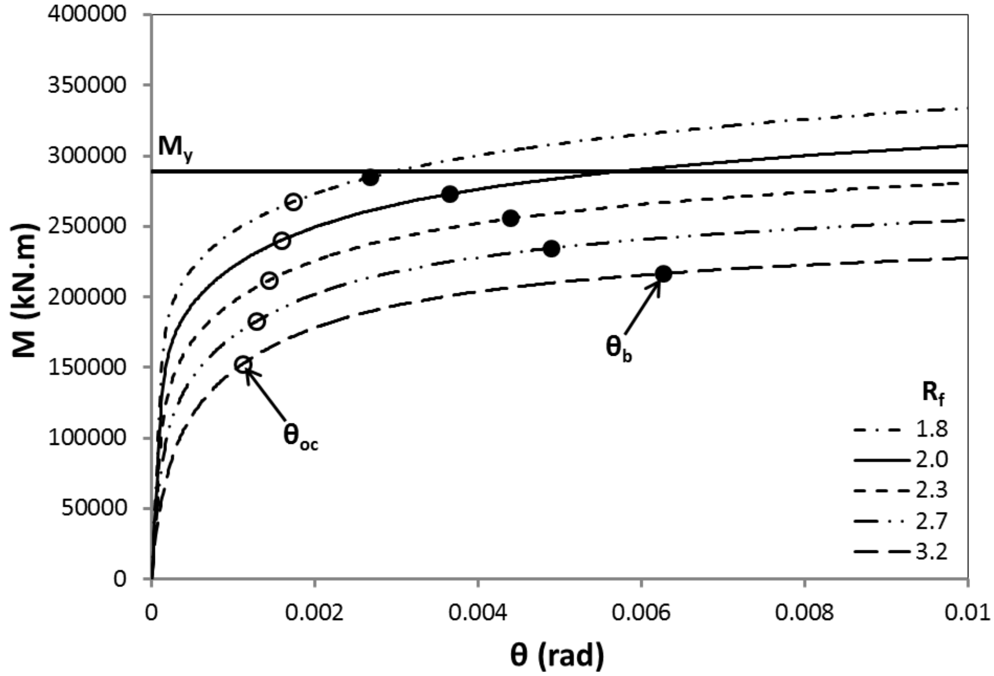

Figure A.181 Bending moment-rotation response of the foundation of wall 10R17 on Medium Sand

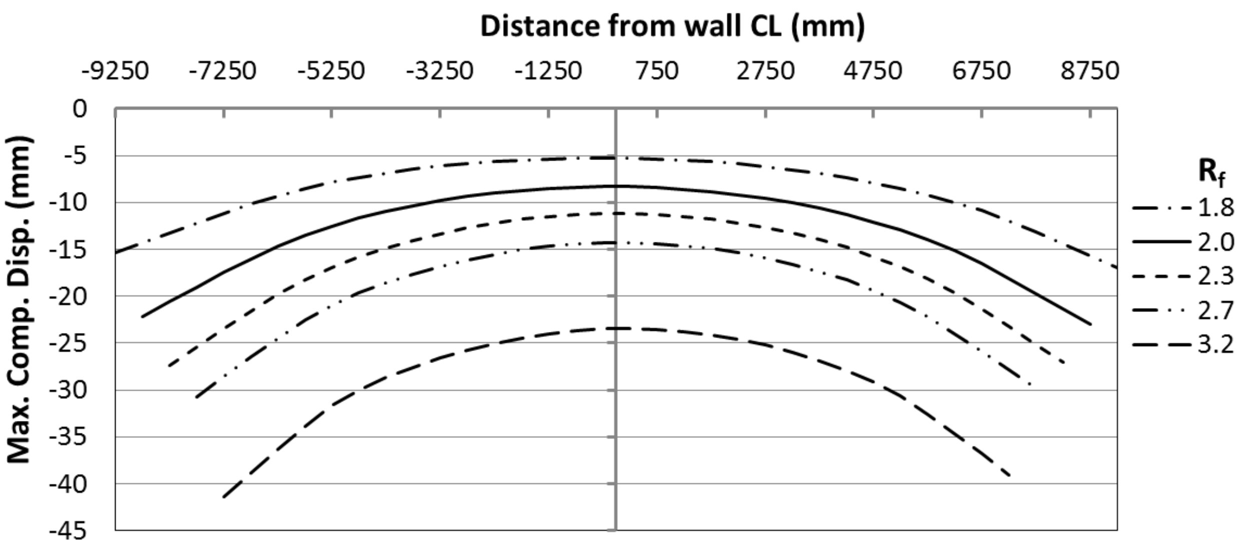

Figure A.182 Average of maximum soil compressive displacements underneath the footing for wall 10R17 on Medium Sand

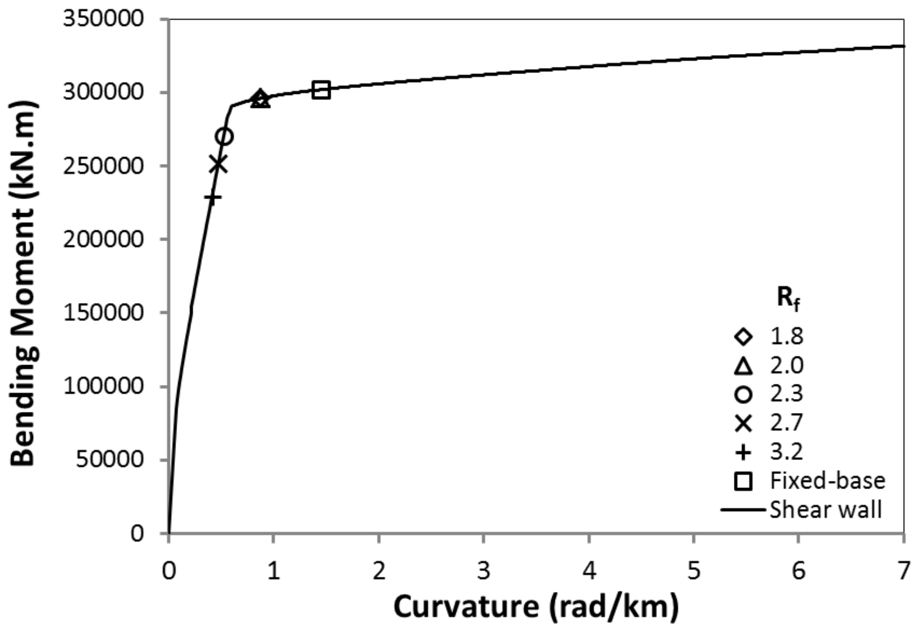

Figure A.183 Moment-curvature response of wall 10R17 along with average of maximum recorded curvatures at the base on Medium Sand

Table A.54 Shear wall properties for wall 10R13

N	10
L_w (mm)	5500
P (kN)	41550
M_{RSA} (kN.m)	488000
M_y (kN.m)	369000
R_w	1.32

Table A.55 Summary of nonlinear dynamic analyses for wall 10R13 on Medium Sand

R_f	**1.3**	**1.5**	**1.8**	**2.0**	**2.3**	**2.7**	**3.2**
E (MPa)	182	182	182	182	182	182	182
G_{eff} (MPa)	70	70	70	70	70	70	70
ν	0.3	0.3	0.3	0.3	0.3	0.3	0.3
q_a (kPa)	233	233	267	267	267	267	267
q (kPa)	82	99	121	136	153	173	198
q_f (kPa)	400	400	400	400	400	400	400
q_{ult} (kPa)	800	800	800	800	800	800	800
L (m)	22.5	20.5	18.5	17.5	16.5	15.5	14.5
B (m)	22.5	20.5	18.5	17.5	16.5	15.5	14.5
a (mm)	4617	5067	5615	5936	6295	6702	7164
s (mm)	0.87	0.94	1.02	1.07	1.12	1.17	1.24
M_{oc} (kN.m)	371526	320619	267689	240248	211999	182786	152410
θ_{oc} (rad)	0.0023	0.0020	0.0017	0.0016	0.0014	0.0013	0.0011
θ_y (rad)	0.0021	0.0068	0.0220	0.0398	0.0709	-----	-----
$T_{Estimate}$ (sec)	1.03	1.06	1.10	1.12	1.15	1.18	1.23
T_{model} (sec)	0.97	0.98	1.00	1.00	1.02	1.03	1.05
Δ_1 (mm)	10.4	16.0	21.2	27.1	30.1	30.6	35.1
Δ_{10} (mm)	175	198	223	258	273	265	286
Avg. Max. θ_b (rad)	0.0012	0.0025	0.0038	0.0051	0.0059	0.0061	0.0072
Avg. Max. Uplift (mm)	18.3	35.7	46.2	58.8	60.8	55.3	57.3
Avg. Max. Comp. Disp. (mm)	-8.6	-15.9	-23.7	-31.8	-37.5	-41.1	-50.0
Avg. Max. q_{max}/q_{ult}	42%	56%	68%	76%	81%	85%	88%

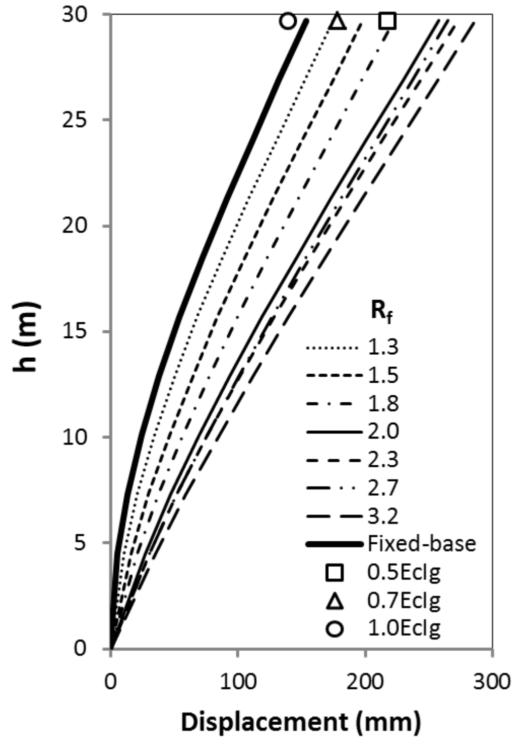

Figure A.184 Average of displacement envelopes for wall 10R13 on Medium Sand along with estimated top displacements of the fixed-base wall from RSA using various effective stiffnesses

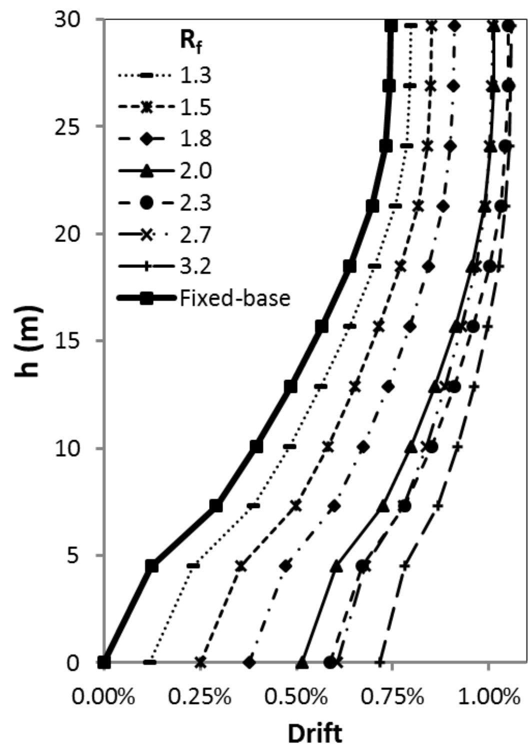

Figure A.185 Average of drift envelopes for wall 10R13 on Medium Sand (Note: base rotation values are plotted at h=0 and values of average interstory drift are plotted at the top of the storey.)

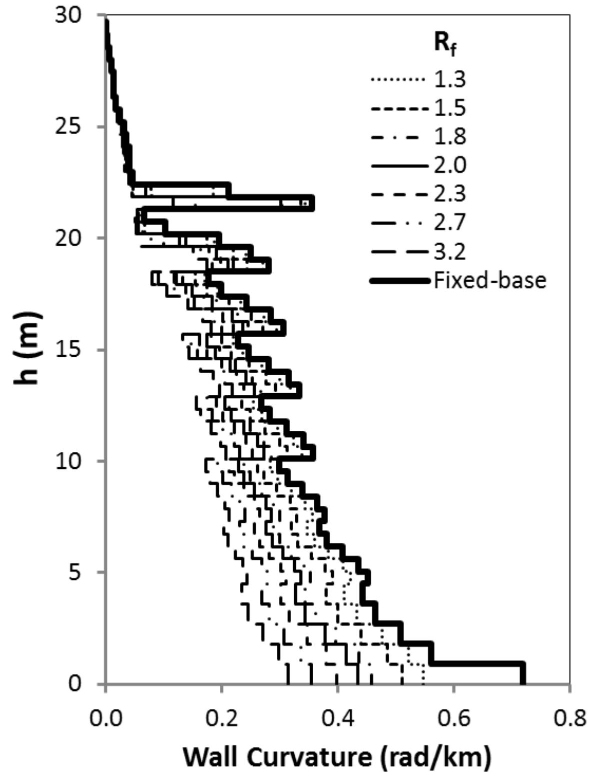

Figure A.186 Average of curvature envelopes for wall 10R13 on Medium Sand

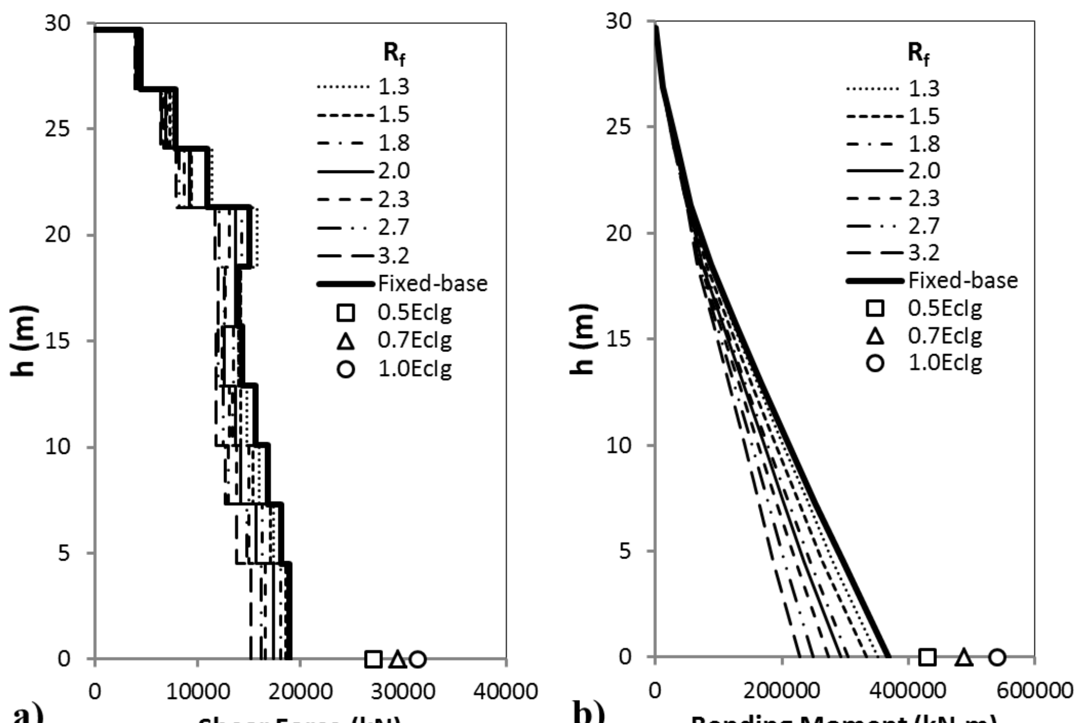

Figure A.187 Average of a) shear force, and b) bending moment envelopes for wall 10R13 on Medium Sand along with estimated maximum quantities for the fixed-base wall from RSA using various effective stiffnesses

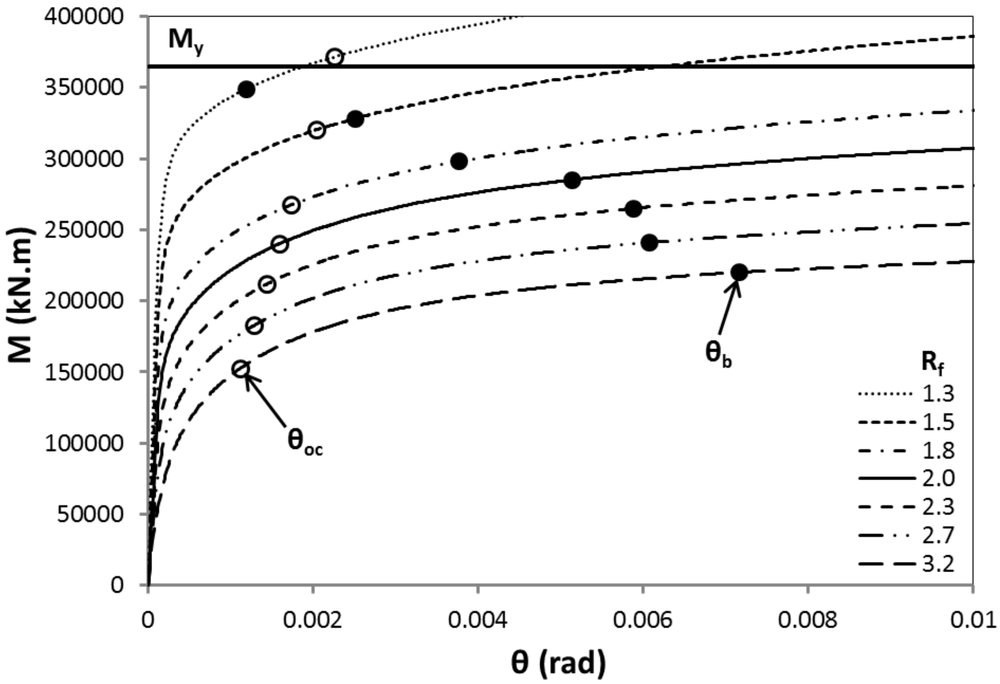

Figure A.188 Bending moment-rotation response of the foundation of wall 10R13 on Medium Sand

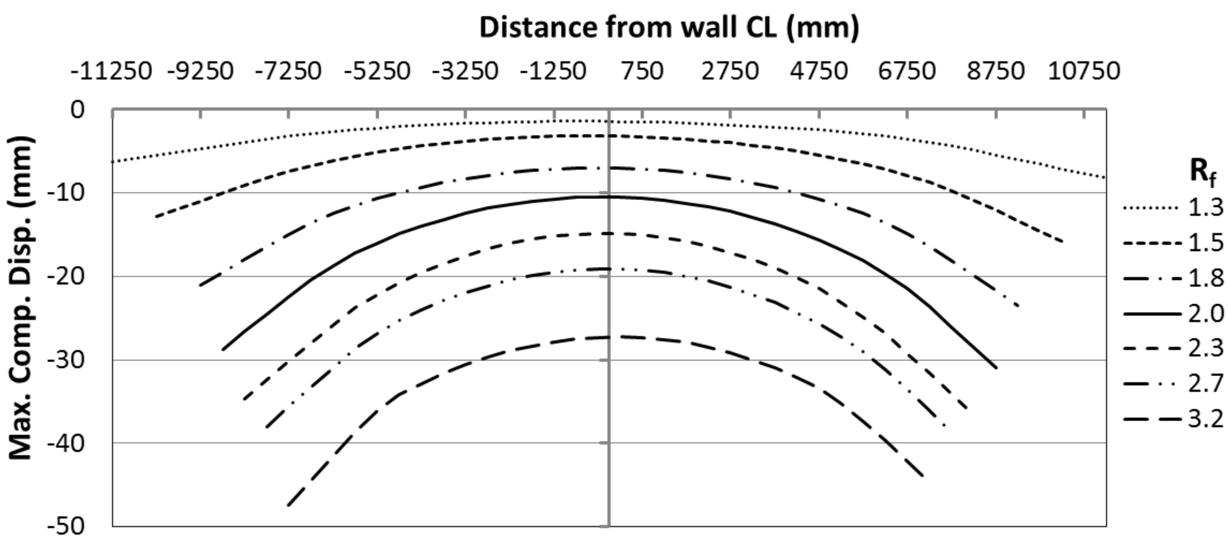

Figure A.189 Average of maximum soil compressive displacements underneath the footing for wall 10R13 on Medium Sand

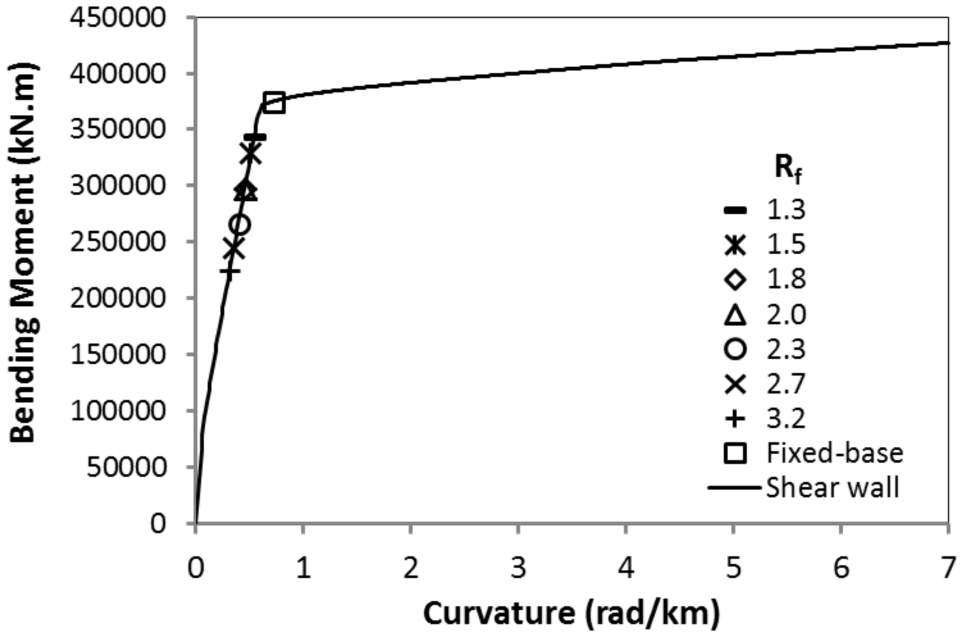

Figure A.190 Moment-curvature response of wall 10R13 along with average of maximum recorded curvatures at the base on Medium Sand

Table A.56 Shear wall properties for wall 10Elastic

N	10
L_w (mm)	5500
P (kN)	41550
M_{RSA} (kN.m)	488000
M_y (kN.m)	-----
R_w	1.00

Table A.57 Summary of nonlinear dynamic analyses for wall 10Elastic on Medium Sand

R_f	1.8	2.0	2.3	2.7	3.2
E (MPa)	182	182	182	182	182
G_{eff} (MPa)	70	70	70	70	70
v	0.3	0.3	0.3	0.3	0.3
q_a (kPa)	267	267	267	267	267
q (kPa)	121	136	153	173	198
q_f (kPa)	400	400	400	400	400
q_{ult} (kPa)	800	800	800	800	800
L (m)	18.5	17.5	16.5	15.5	14.5
B (m)	18.5	17.5	16.5	15.5	14.5
a (mm)	5615	5936	6295	6702	7164
s (mm)	1.02	1.07	1.12	1.17	1.24
M_{oc} (kN.m)	267689	240248	211999	182786	152410
θ_{oc} (rad)	0.0017	0.0016	0.0014	0.0013	0.0011
θ_y (rad)	-----	-----	-----	-----	-----
$T_{Estimate}$ (sec)	1.20	1.22	1.25	1.28	1.32
T_{model} (sec)	1.13	1.14	1.15	1.16	1.18
Δ_1 (mm)	33.5	34.8	34.5	34.3	34.6
Δ_{10} (mm)	284	289	283	275	272
Avg. Max. θ_b (rad)	0.0067	0.0071	0.0071	0.0071	0.0072
Avg. Max. Uplift (mm)	86.9	82.5	74.2	66.6	59.3
Avg. Max. Comp. Disp. (mm)	-38.9	-42.1	-44.4	-46.2	-50.8
Avg. Max. q_{max}/q_{ult}	77%	79%	83%	86%	89%

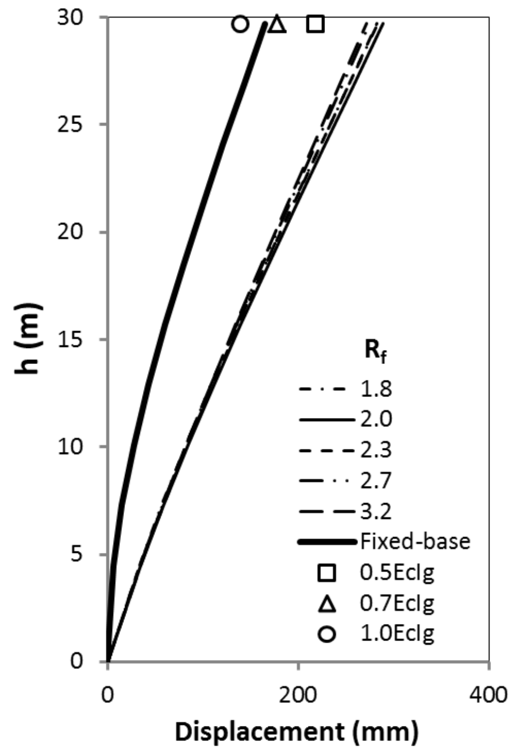

Figure A.191 Average of displacement envelopes for wall 10Elastic on Medium Sand along with estimated top displacements of the fixed-base wall from RSA using various effective stiffnesses

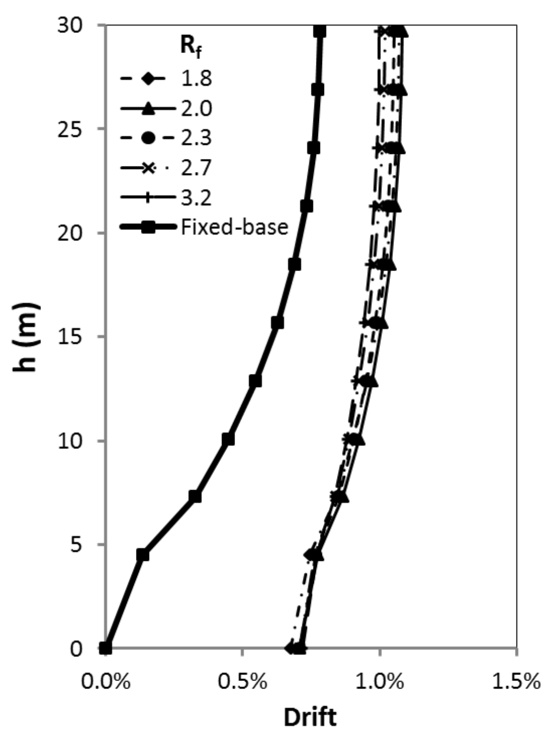

Figure A.192 Average of drift envelopes for wall 10Elastic on Medium Sand (Note: base rotation values are plotted at h=0 and values of average interstory drift are plotted at the top of the storey.)

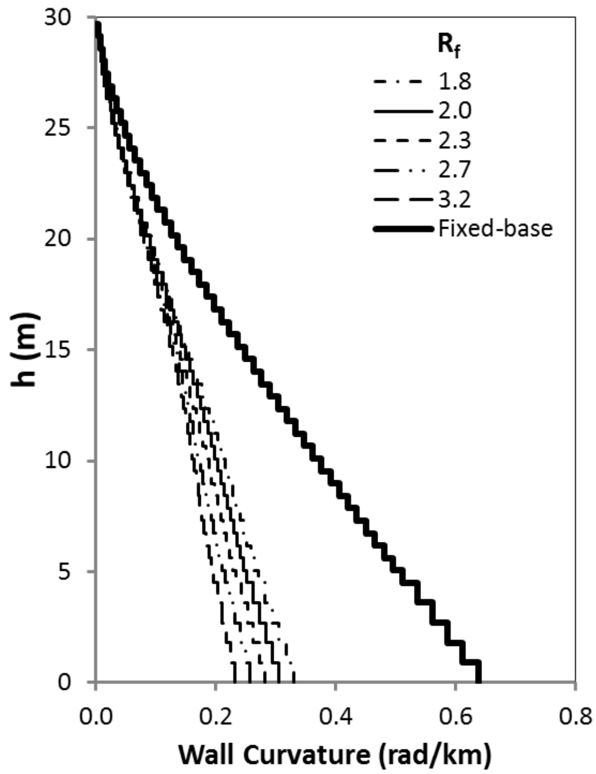

Figure A.193 Average of curvature envelopes for wall 10Elastic on Medium Sand

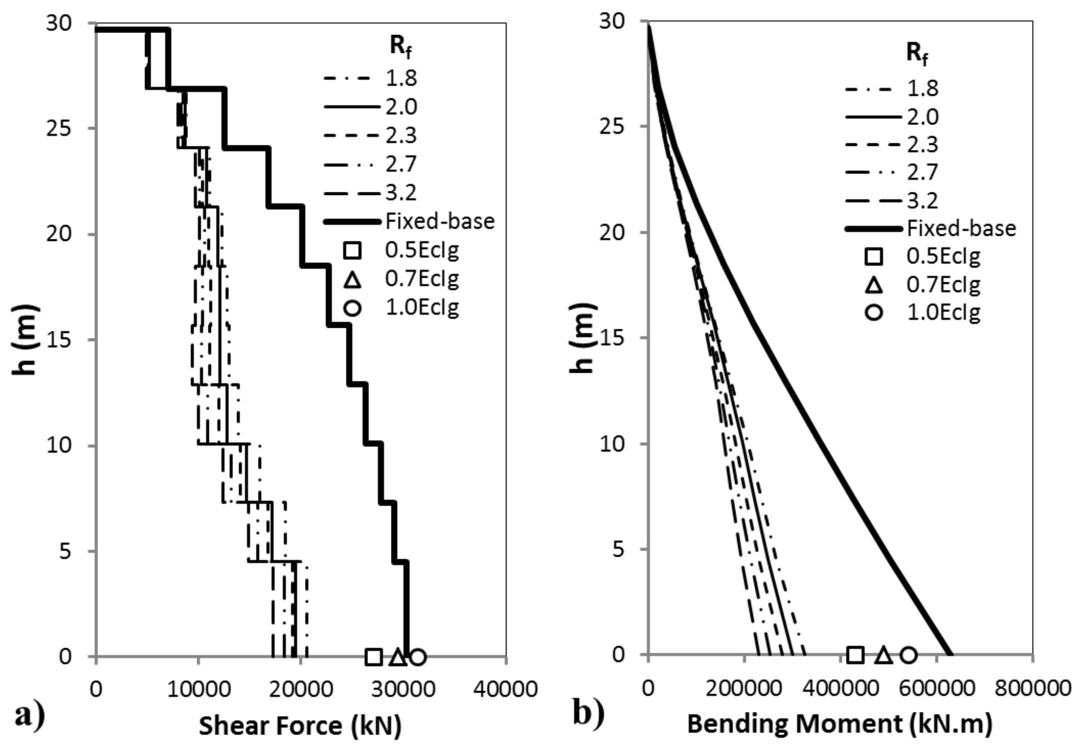

Figure A.194 Average of a) shear force, and b) bending moment envelopes for wall 10Elastic on Medium Sand along with estimated maximum quantities for the fixed-base wall from RSA using various effective stiffnesses

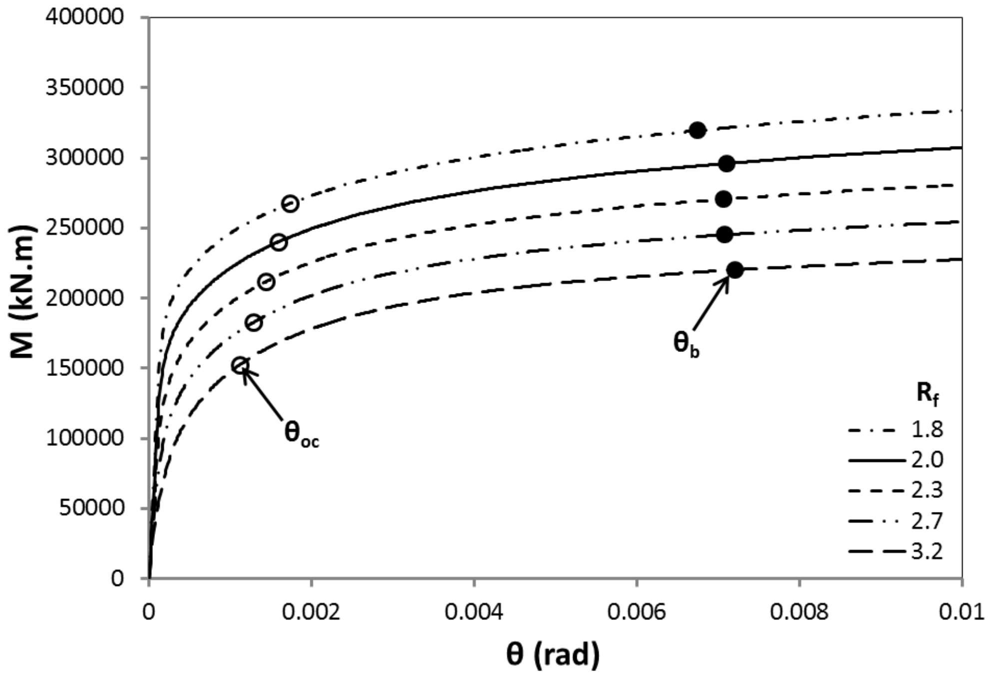

Figure A.195 Bending moment-rotation response of the foundation of wall 10Elastic on Medium Sand

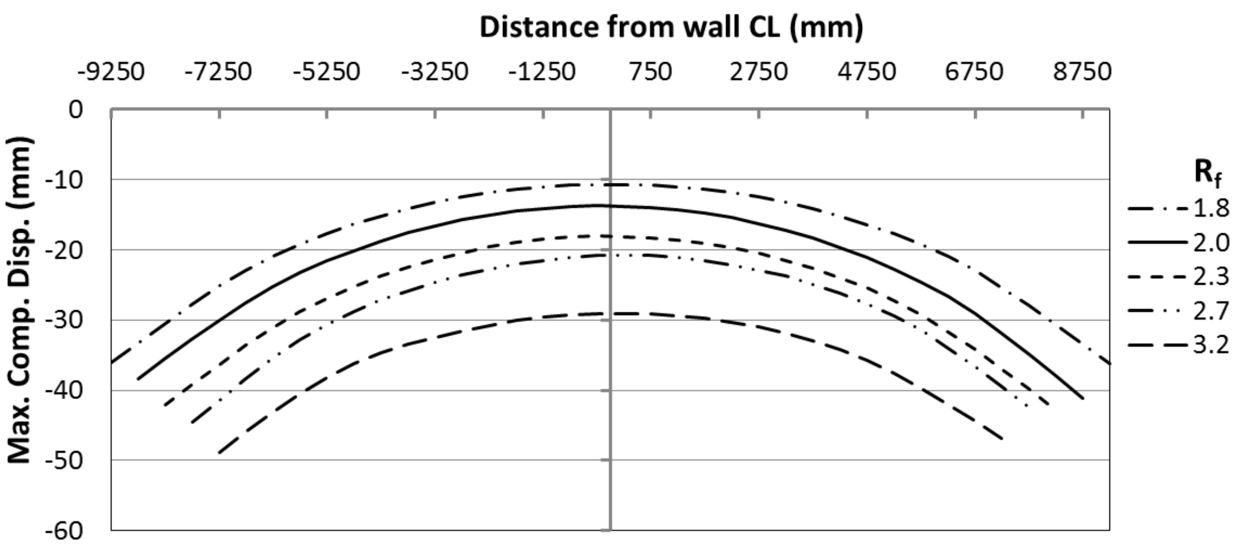

Figure A.196 Average of maximum soil compressive displacements underneath the footing for wall 10Elastic on Medium Sand

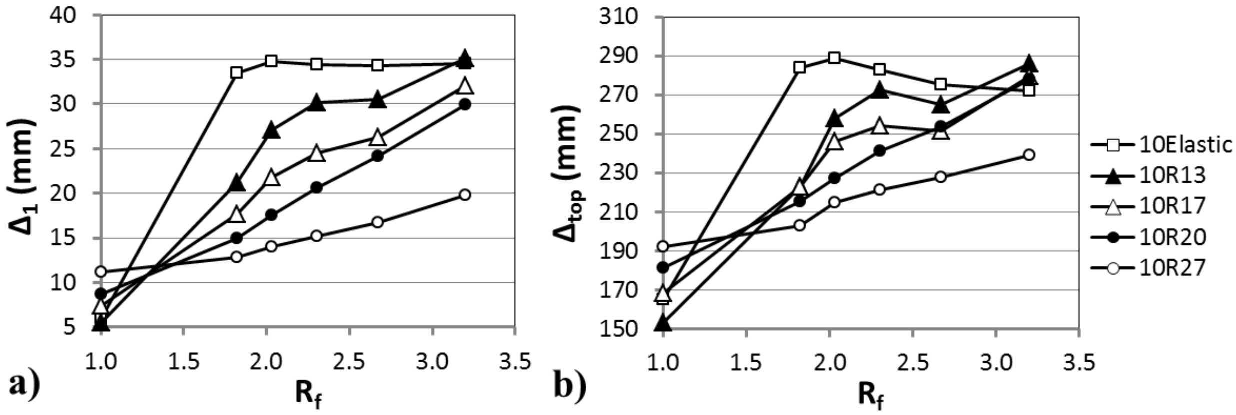

Figure A.197 Summary of average maximum a) first storey displacements, and b) top displacements for 10 storey walls on Medium Sand sorted by wall strength

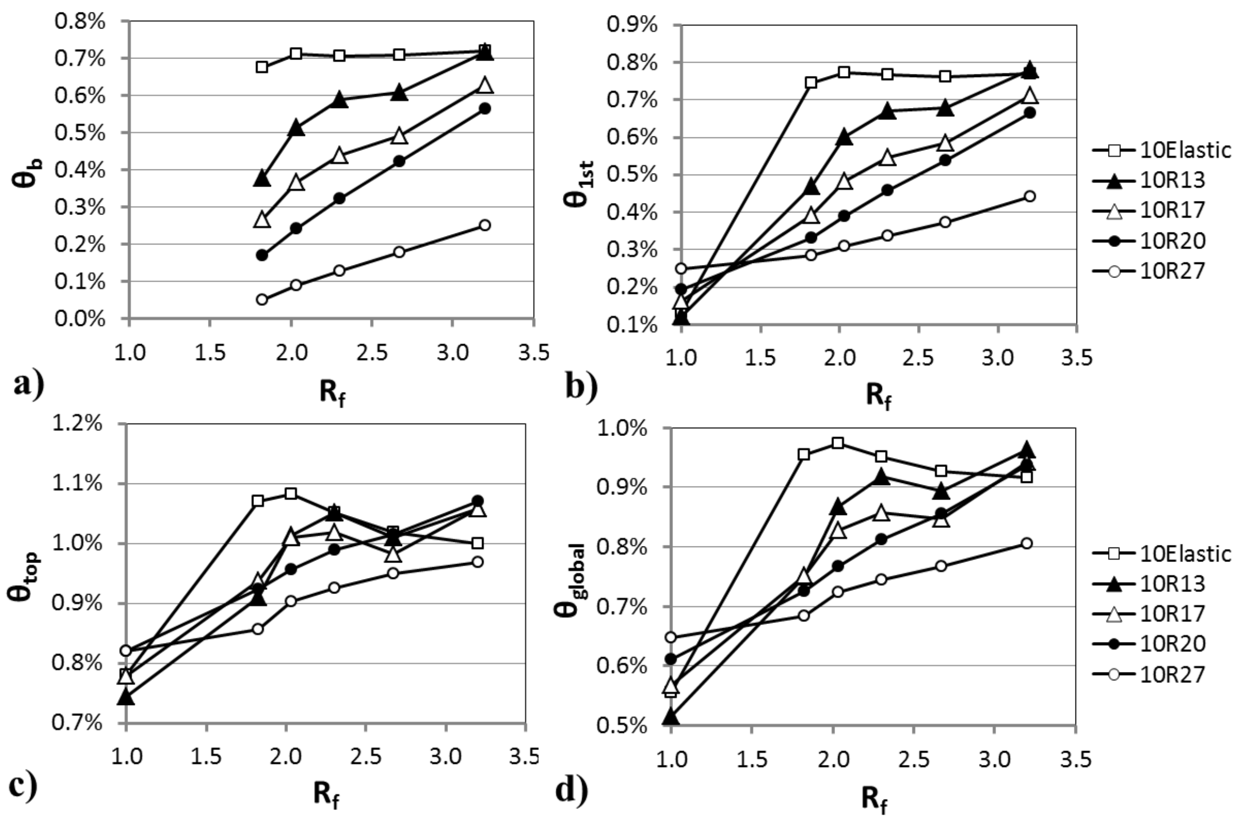

Figure A.198 Summary of average maximum a) base rotations, b) 1st storey inter-storey drifts, c) top storey inter-storey drifts, and d) global drifts of 10 storey walls on Medium Sand sorted by wall strength

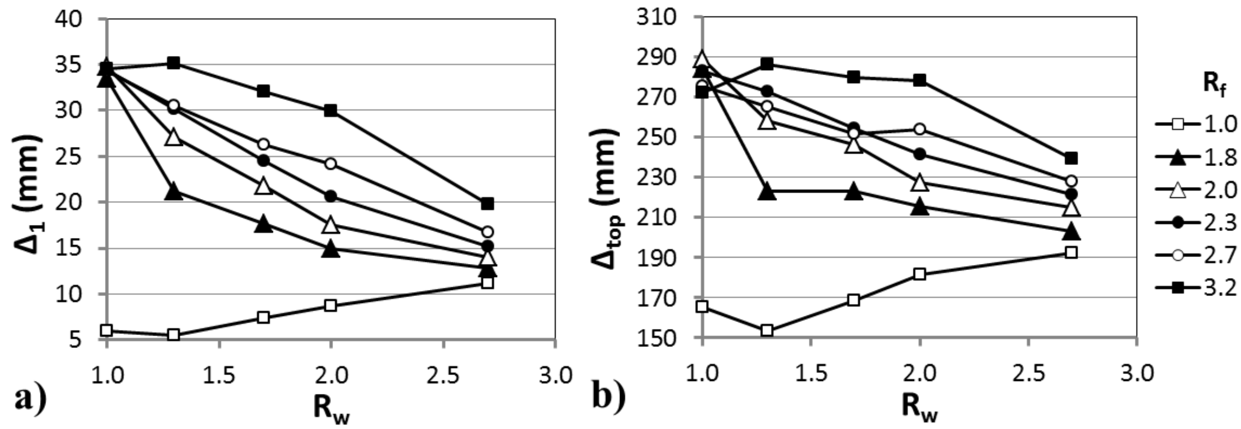

Figure A.199 Summary of average maximum a) first storey displacements, and b) top displacements for 10 storey walls on Medium Sand sorted by foundation size

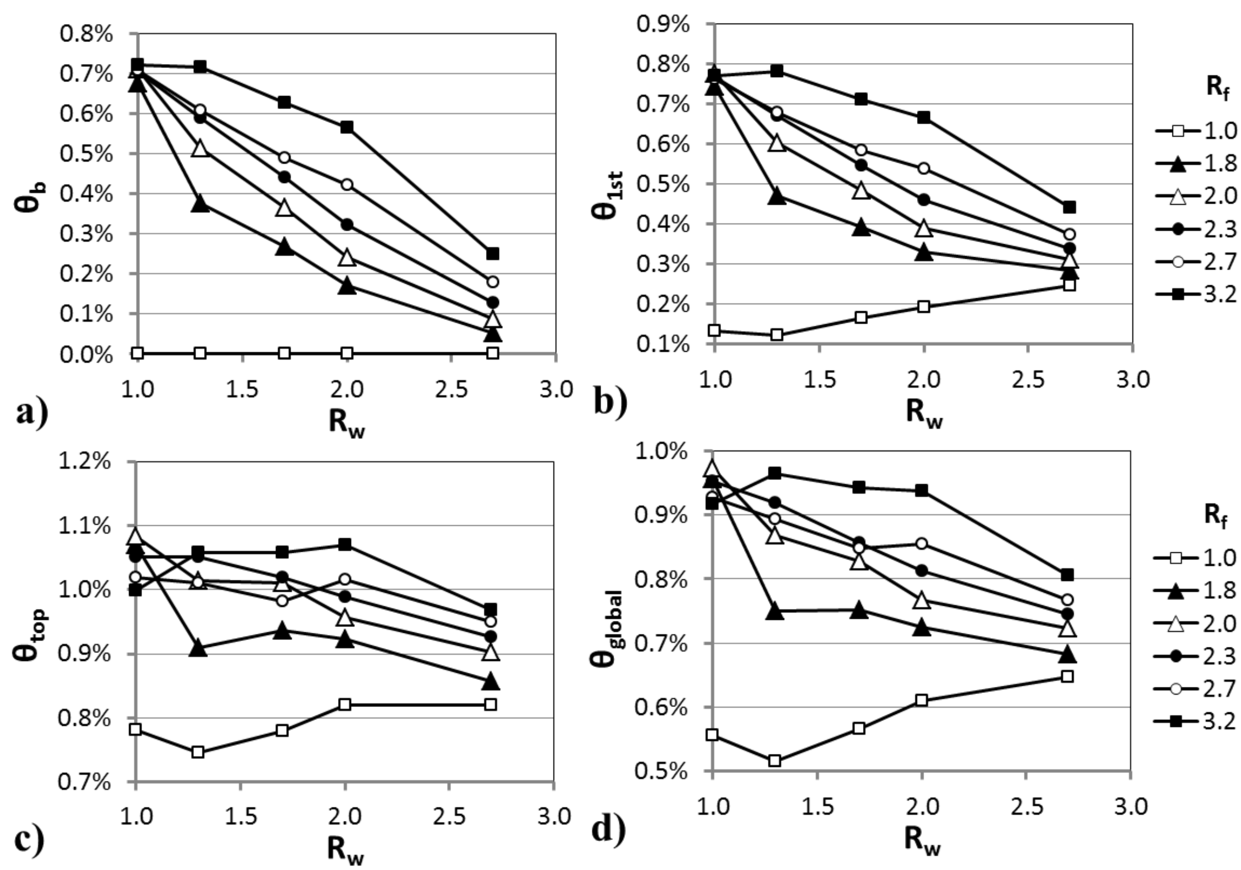

Figure A.200 Summary of average maximum a) base rotations, b) 1st storey inter-storey drifts, c) top storey inter-storey drifts, and d) global drifts of 10 storey walls on Medium Sand sorted by foundation size

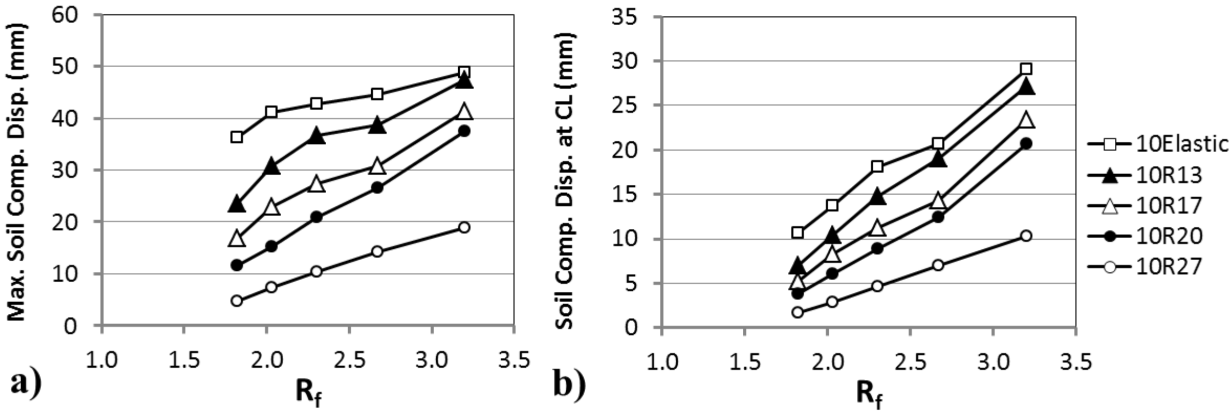

Figure A.201 Summary of average maximum soil compressive displacement at a) foundation toe, and b) foundation centreline for 10 storey walls on Medium Sand sorted by wall strength

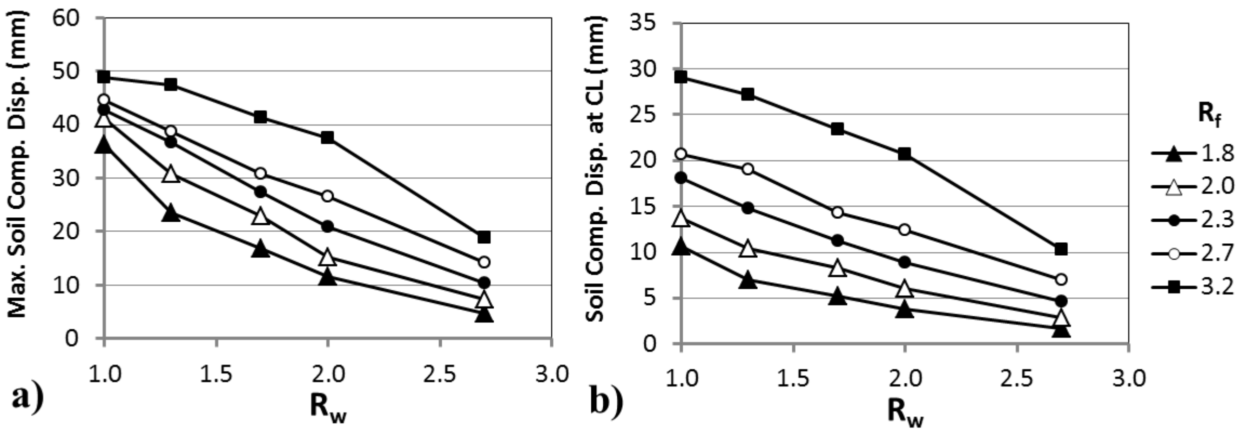

Figure A.202 Summary of average maximum soil compressive displacement at a) foundation toe, and b) foundation centreline for 10 storey walls on Medium Sand sorted by foundation size

A.6.4 Dense Sand

Table A.58 Properties of Dense Sand

G_0 (MPa)	825
G_{eff} (MPa)	311
v	0.3
E (MPa)	809
q_{ult} (kPa)	1600
q_f (kPa)	800
q_a (kPa)	533
V_s (m/s)	760

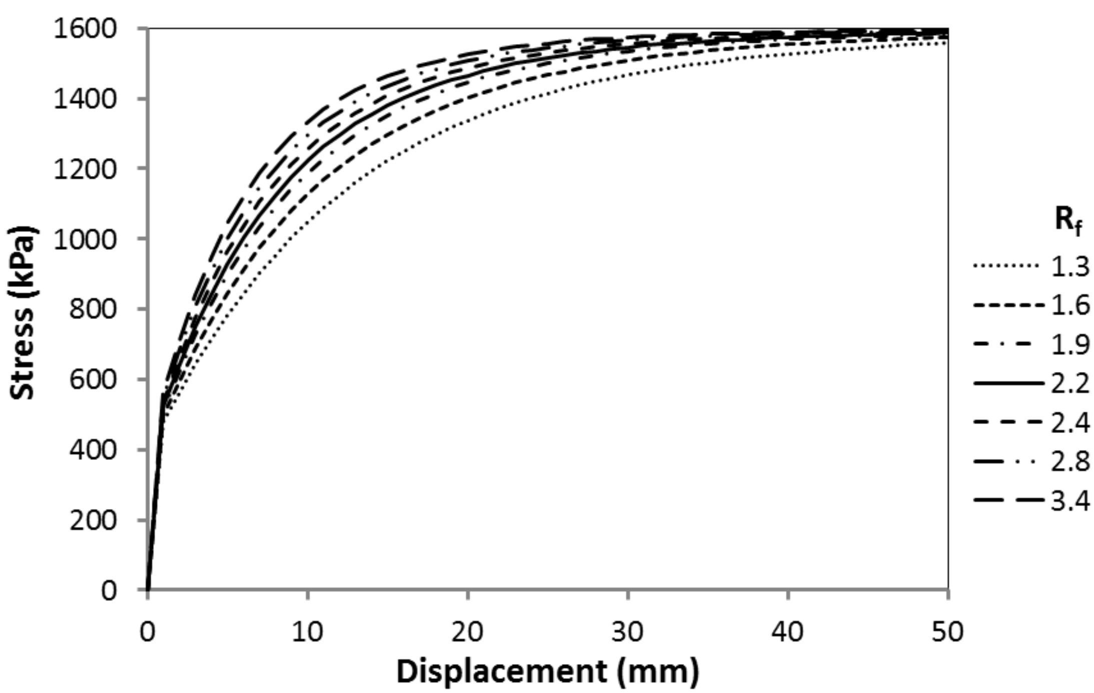

Figure A.203 Soil spring responses in monotonic compression for Dense Sand

Table A.59 Shear wall properties for wall 10R27

N	10
L_w (mm)	5500
P (kN)	41550
M_{RSA} (kN.m)	488000
M_y (kN.m)	179000
R_w	2.73

Table A.60 Summary of nonlinear dynamic analyses for wall 10R27 on Dense Sand

R_f	**1.9**	**2.2**	**2.4**	**2.8**	**3.4**
E (MPa)	809	809	809	809	809
G_{eff} (MPa)	311	311	311	311	311
v	0.3	0.3	0.3	0.3	0.3
q_a (kPa)	533	533	533	533	533
q (kPa)	173	198	228	266	314
q_f (kPa)	800	800	800	800	800
q_{ult} (kPa)	1600	1600	1600	1600	1600
L (m)	15.5	14.5	13.5	12.5	11.5
B (m)	15.5	14.5	13.5	12.5	11.5
a (mm)	3351	3582	3847	4155	4516
s (mm)	0.26	0.28	0.29	0.31	0.33
M_{oc} (kN.m)	252399	226824	200536	173367	145086
θ_{oc} (rad)	0.0009	0.0008	0.0007	0.0007	0.0006
θ_y (rad)	0.0001	0.0001	0.0003	0.0008	0.0020
$T_{Estimate}$ (sec)	1.12	1.13	1.15	1.16	1.19
T_{model} (sec)	1.07	1.07	1.07	1.08	1.09
Δ_1 (mm)	11.8	12.6	14.9	16.9	22.9
Δ_{10} (mm)	196	200	218	225	257
Avg. Max. θ_b (rad)	0.0003	0.0006	0.0011	0.0018	0.0033
Avg. Max. Uplift (mm)	2.4	5.3	9.8	15.2	25.1
Avg. Max. Comp. Disp. (mm)	-1.6	-2.9	-4.9	-7.2	-12.5
Avg. Max. q_{max}/q_{ult}	36%	46%	60%	72%	87%

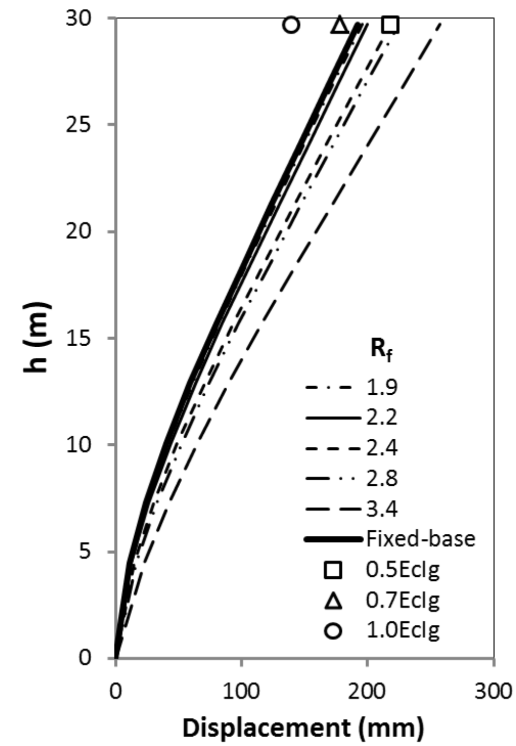

Figure A.204 Average of displacement envelopes for wall 10R27 on Dense Sand along with estimated top displacements of the fixed-base wall from RSA using various effective stiffnesses

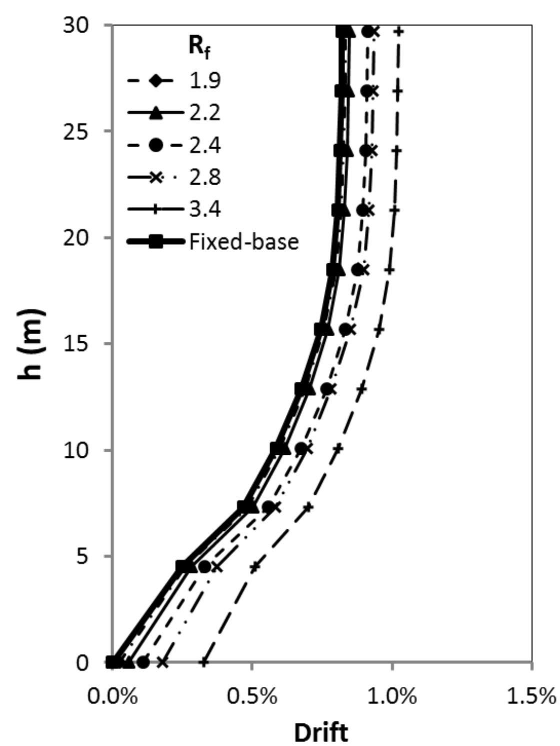

Figure A.205 Average of drift envelopes for wall 10R27 on Dense Sand (Note: base rotation values are plotted at h=0 and values of average interstory drift are plotted at the top of the storey.)

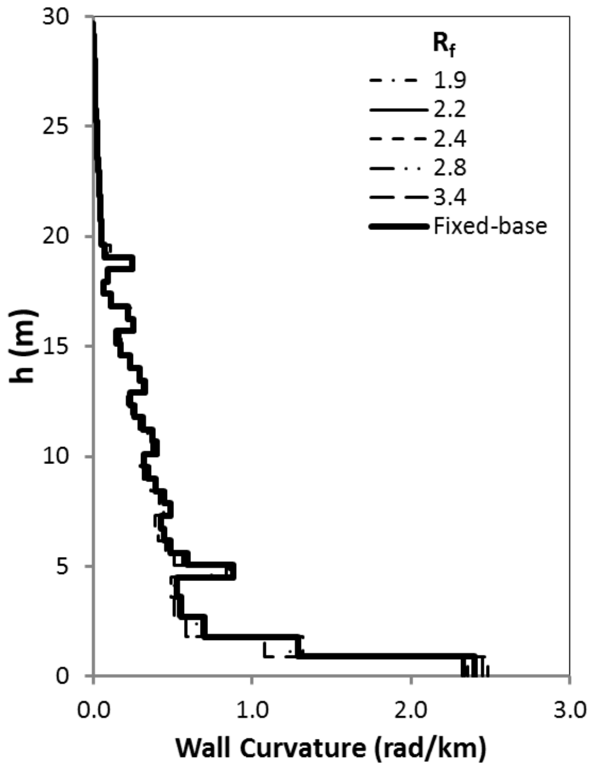

Figure A.206 Average of curvature envelopes for wall 10R27 on Dense Sand

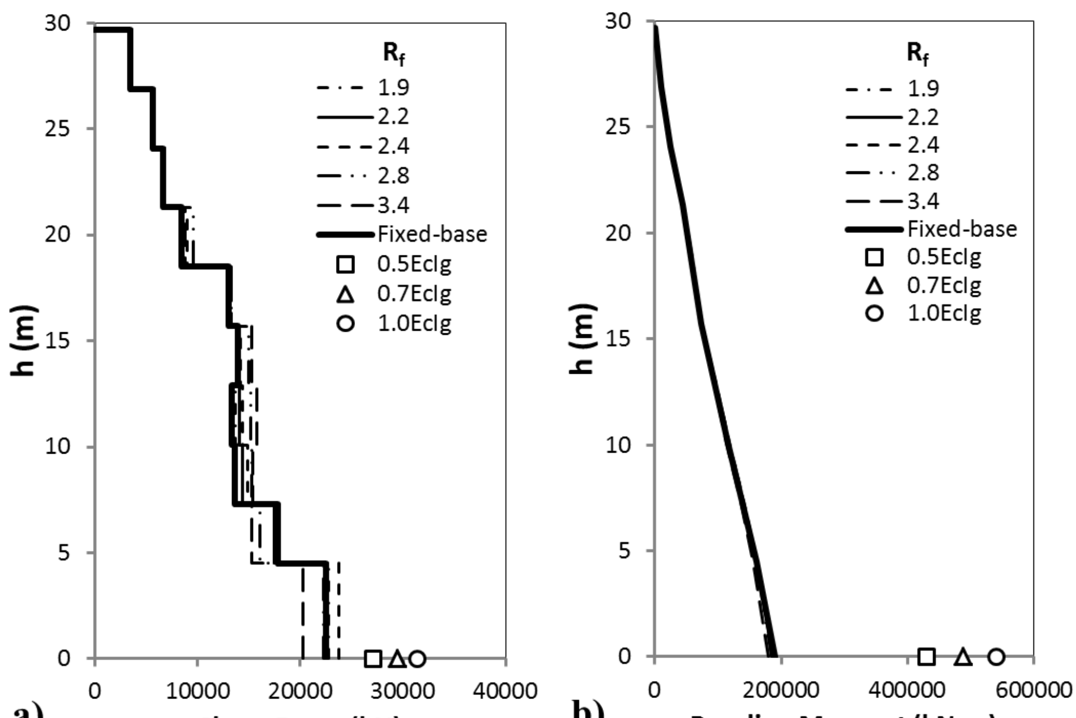

Figure A.207 Average of a) shear force, and b) bending moment envelopes for wall 10R27 on Dense Sand along with estimated maximum quantities for the fixed-base wall from RSA using various effective stiffnesses

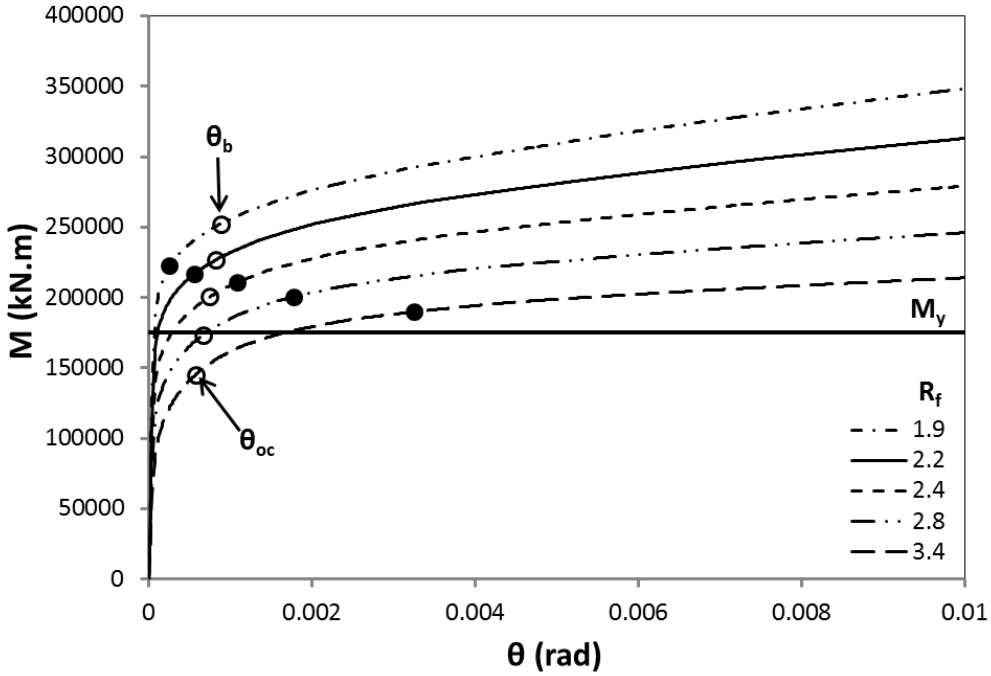

Figure A.208 Bending moment-rotation response of the foundation of wall 10R27 on Dense Sand

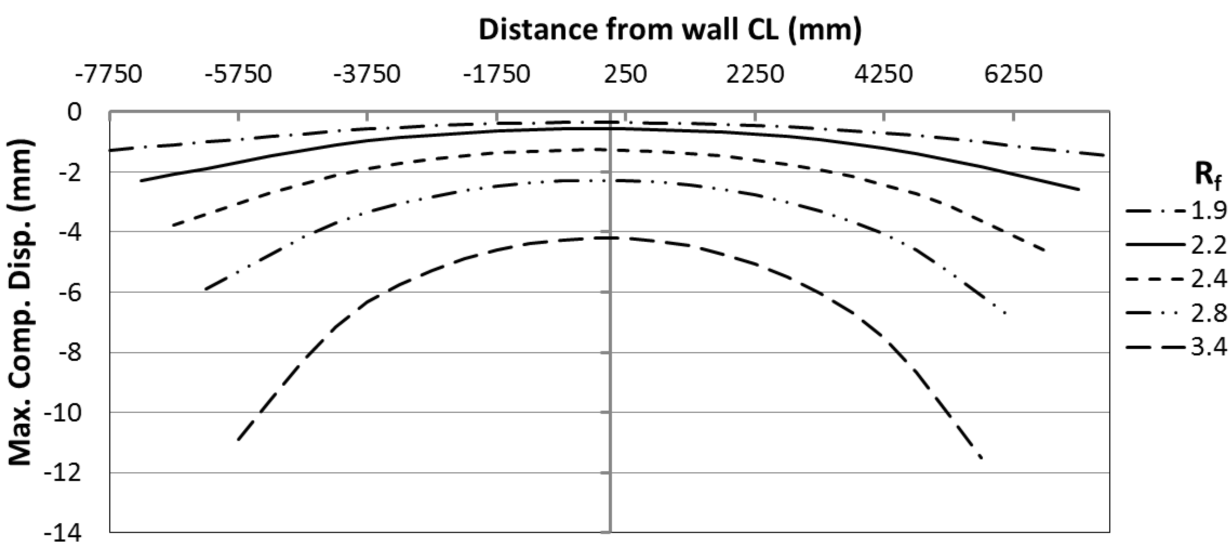

Figure A.209 Average of maximum soil compressive displacements underneath the footing for wall 10R27 on Dense Sand

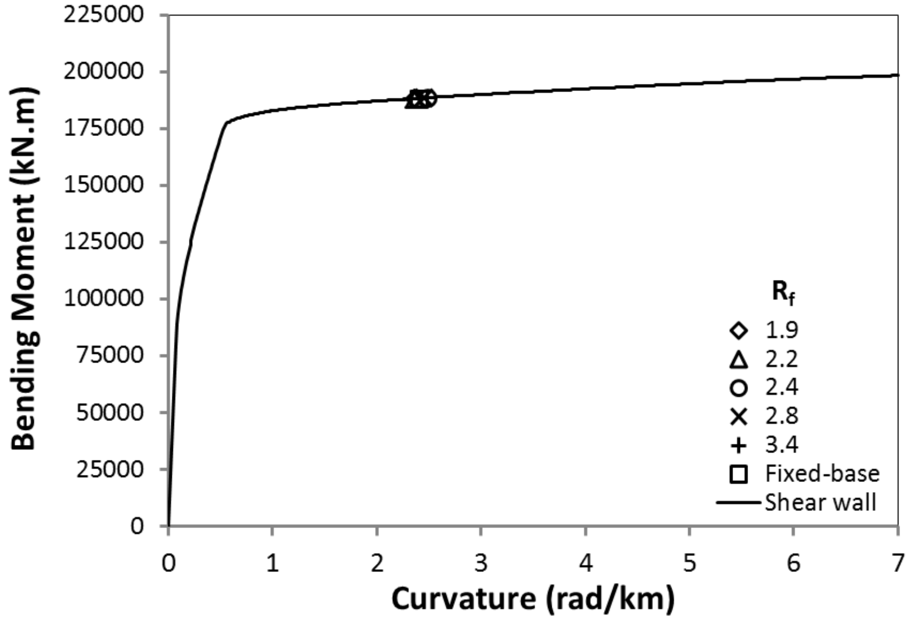

Figure 8 Moment-curvature response of wall 10R27 along with average of maximum recorded curvatures at the base on Dense Sand

Table A.61 Shear wall properties for wall 10R20

N	10
L_w (mm)	5500
P (kN)	41550
M_{RSA} (kN.m)	488000
M_y (kN.m)	249000
R_w	1.96

Table A.62 Summary of nonlinear dynamic analyses for wall 10R20 on Dense Sand

R_f	**1.9**	**2.2**	**2.4**	**2.8**	**3.4**
E (MPa)	809	809	809	809	809
G_{eff} (MPa)	311	311	311	311	311
v	0.3	0.3	0.3	0.3	0.3
q_a (kPa)	533	533	533	533	533
q (kPa)	173	198	228	266	314
q_f (kPa)	800	800	800	800	800
q_{ult} (kPa)	1600	1600	1600	1600	1600
L (m)	15.5	14.5	13.5	12.5	11.5
B (m)	15.5	14.5	13.5	12.5	11.5
a (mm)	3351	3582	3847	4155	4516
s (mm)	0.26	0.28	0.29	0.31	0.33
M_{oc} (kN.m)	252399	226824	200536	173367	145086
θ_{oc} (rad)	0.0009	0.0008	0.0007	0.0007	0.0006
θ_y (rad)	0.0008	0.0018	0.0044	0.0108	0.0259
$T_{Estimate}$ (sec)	1.06	1.07	1.08	1.10	1.12
T_{model} (sec)	1.02	1.03	1.03	1.04	1.05
Δ_1 (mm)	14.2	17.9	22.5	31.6	34.7
Δ_{10} (mm)	211	230	249	300	306
Avg. Max. θ_b (rad)	0.0015	0.0024	0.0037	0.0059	0.0068
Avg. Max. Uplift (mm)	18.0	26.7	37.5	53.0	54.9
Avg. Max. Comp. Disp. (mm)	-5.9	-8.9	-12.9	-21.6	-23.8
Avg. Max. q_{max}/q_{ult}	60%	73%	84%	91%	94%

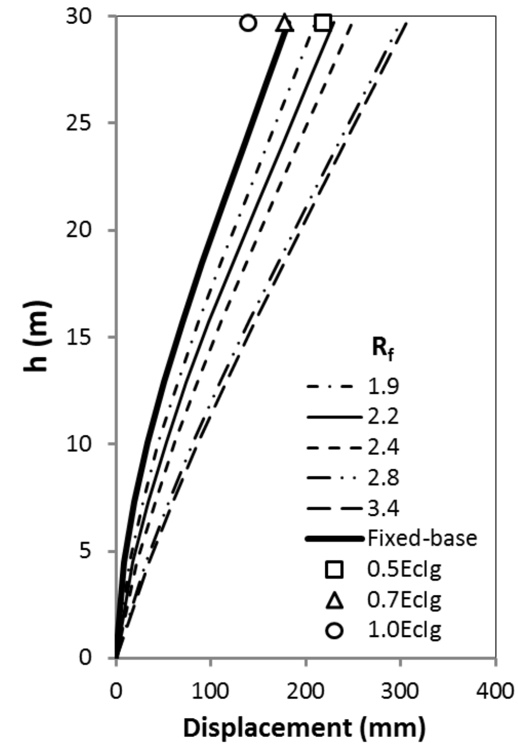

Figure A.210 Average of displacement envelopes for wall 10R20 on Dense Sand along with estimated top displacements of the fixed-base wall from RSA using various effective stiffnesses

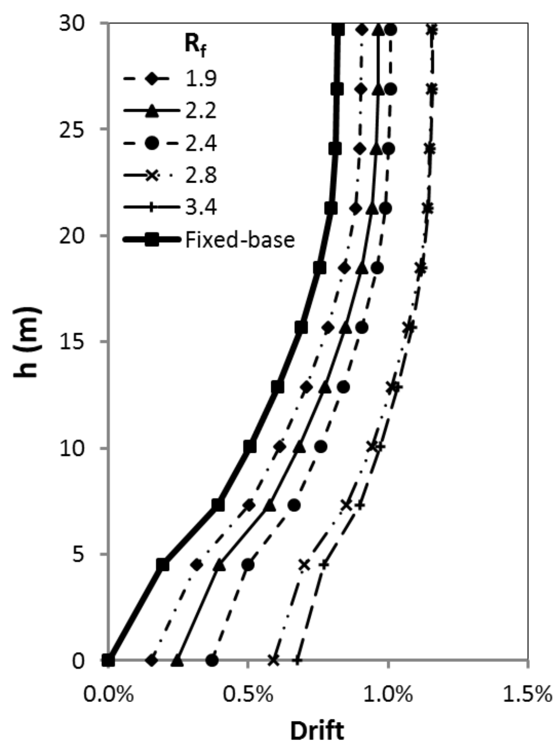

Figure A.211 Average of drift envelopes for wall 10R20 on Dense Sand (Note: base rotation values are plotted at h=0 and values of average interstory drift are plotted at the top of the storey.)

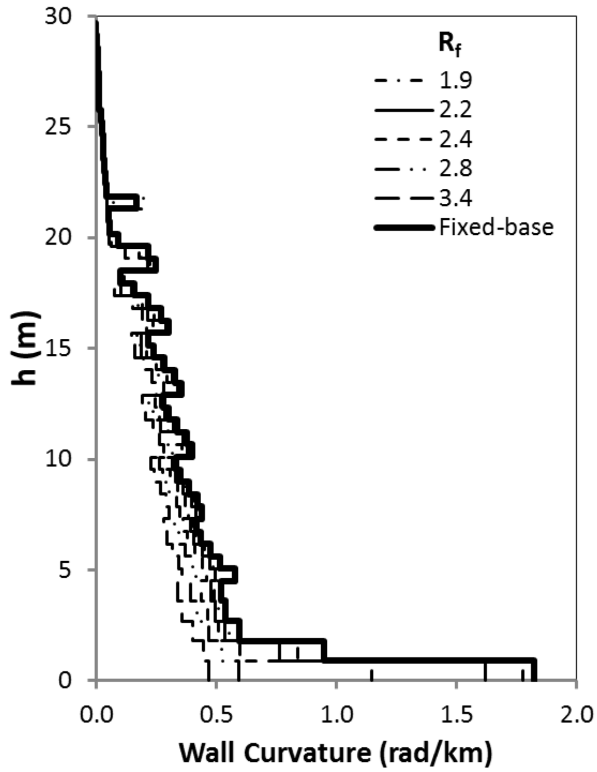

Figure A.212 Average of curvature envelopes for wall 10R20 on Dense Sand

a)

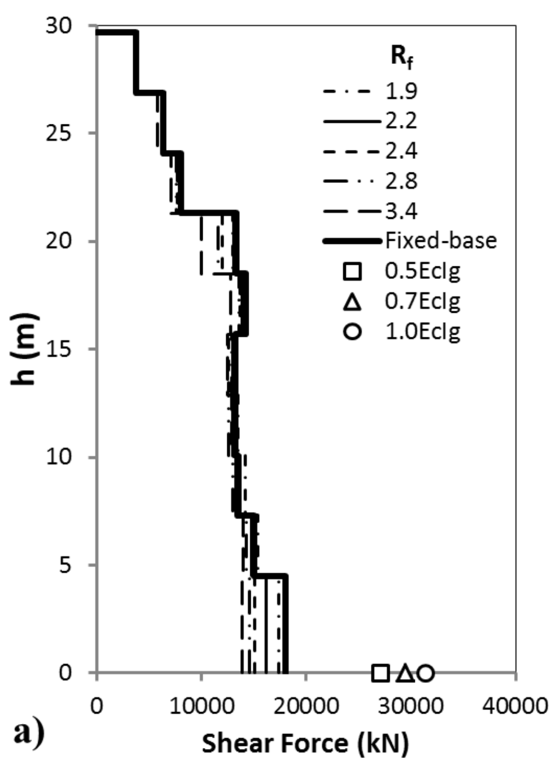

b)

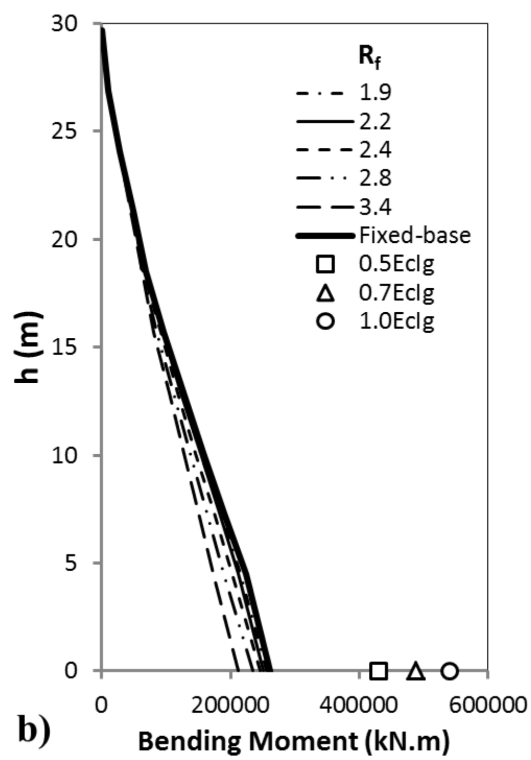

Figure A.213 Average of a) shear force, and b) bending moment envelopes for wall 10R20 on Dense Sand along with estimated maximum quantities for the fixed-base wall from RSA using various effective stiffnesses

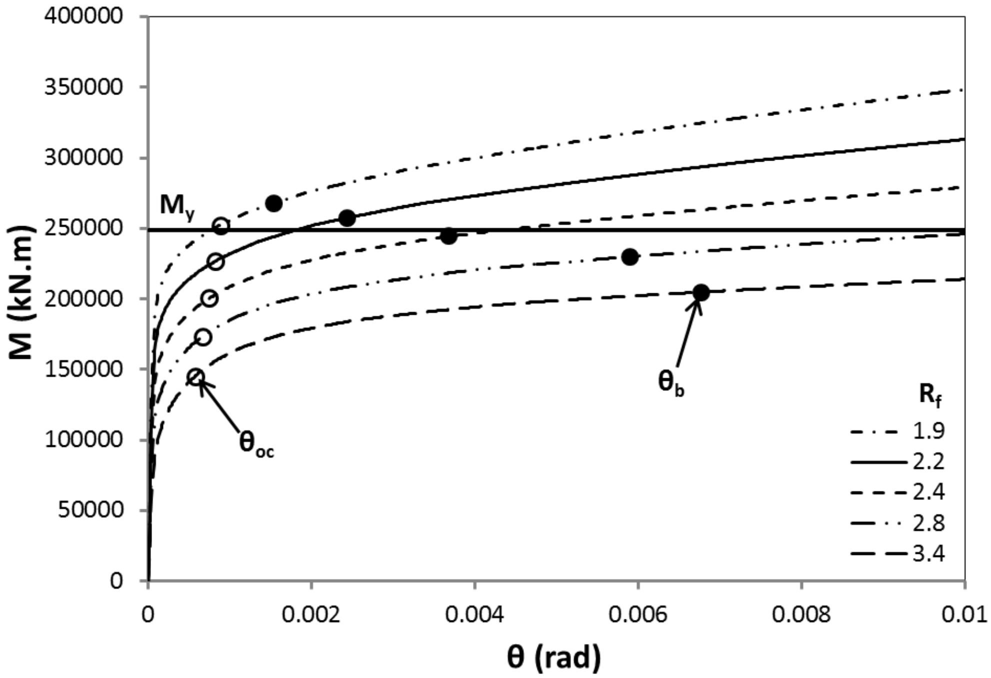

Figure A.214 Bending moment-rotation response of the foundation of wall 10R20 on Dense Sand

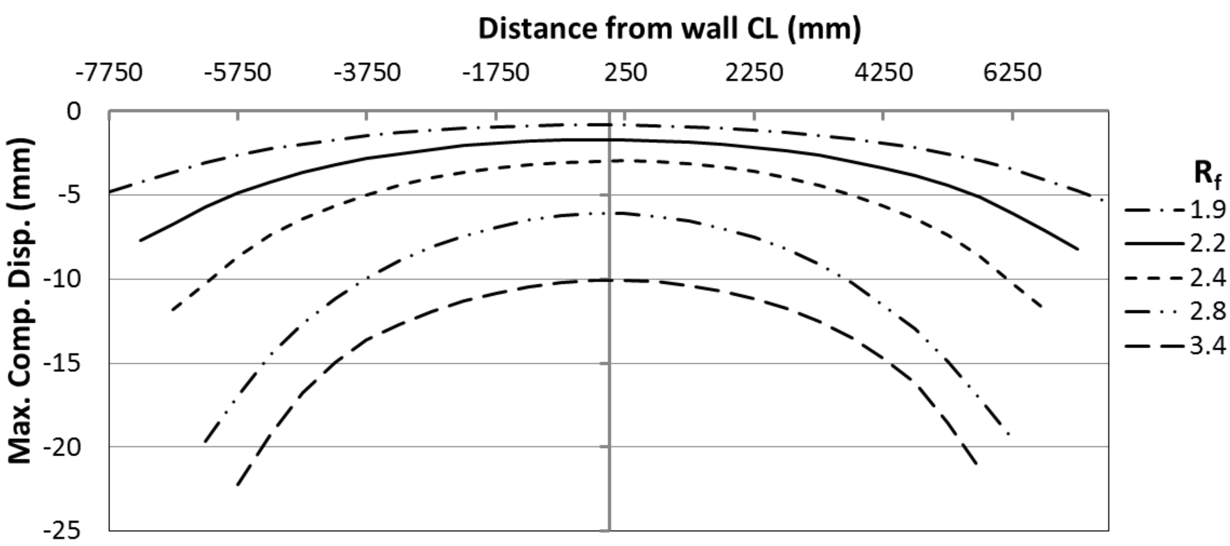

Figure A.215 Average of maximum soil compressive displacements underneath the footing for wall 10R20 on Dense Sand

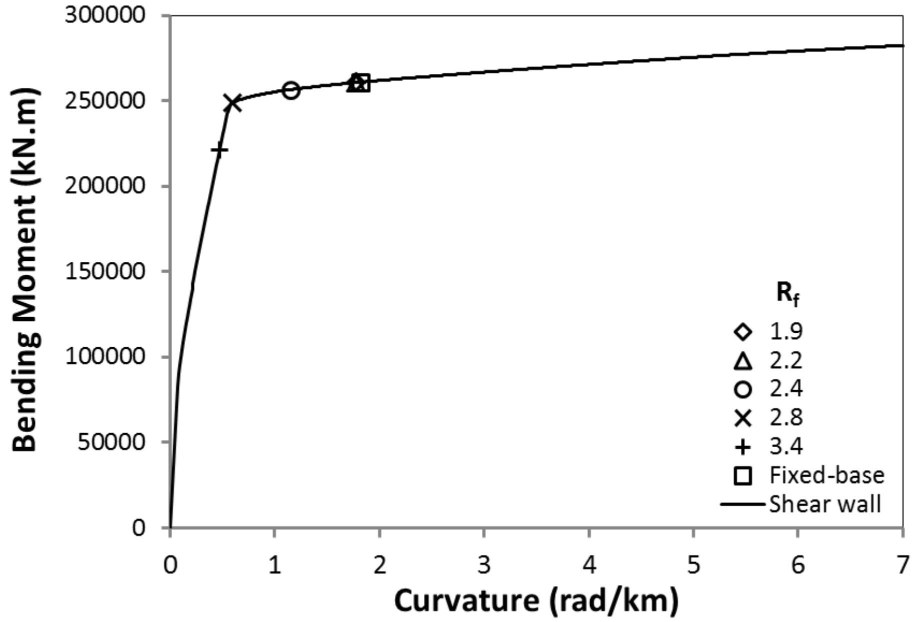

Figure A.216 Moment-curvature response of wall 10R20 along with average of maximum recorded curvatures at the base on Dense Sand

Table A.63 Shear wall properties for wall 10R17

N	10
L_w (mm)	5500
P (kN)	41550
M_{RSA} (kN.m)	488000
M_y (kN.m)	289000
R_w	1.69

Table A.64 Summary of nonlinear dynamic analyses for wall 10R17 on Dense Sand

R_f	1.9	2.2	2.4	2.8	3.4
E (MPa)	809	809	809	809	809
G_{eff} (MPa)	311	311	311	311	311
v	0.3	0.3	0.3	0.3	0.3
q_a (kPa)	533	533	533	533	533
q (kPa)	173	198	228	266	314
q_f (kPa)	800	800	800	800	800
q_{ult} (kPa)	1600	1600	1600	1600	1600
L (m)	15.5	14.5	13.5	12.5	11.5
B (m)	15.5	14.5	13.5	12.5	11.5
a (mm)	3351	3582	3847	4155	4516
s (mm)	0.26	0.28	0.29	0.31	0.33
M_{oc} (kN.m)	252399	226824	200536	173367	145086
θ_{oc} (rad)	0.0009	0.0008	0.0007	0.0007	0.0006
θ_y (rad)	0.0030	0.0061	0.0123	0.0244	0.0497
$T_{Estimate}$ (sec)	1.04	1.05	1.06	1.08	1.11
T_{model} (sec)	1.00	1.00	1.01	1.02	1.03
Δ_1 (mm)	18.4	23.2	29.2	35.7	38.1
Δ_{10} (mm)	225	254	284	312	319
Avg. Max. θ_b (rad)	0.0028	0.0040	0.0054	0.0070	0.0077
Avg. Max. Uplift (mm)	34.0	44.4	55.1	81.1	60.3
Avg. Max. Comp. Disp. (mm)	-9.5	-13.6	-19.4	-24.8	-29.3
Avg. Max. q_{max}/q_{ult}	71%	80%	87%	92%	95%

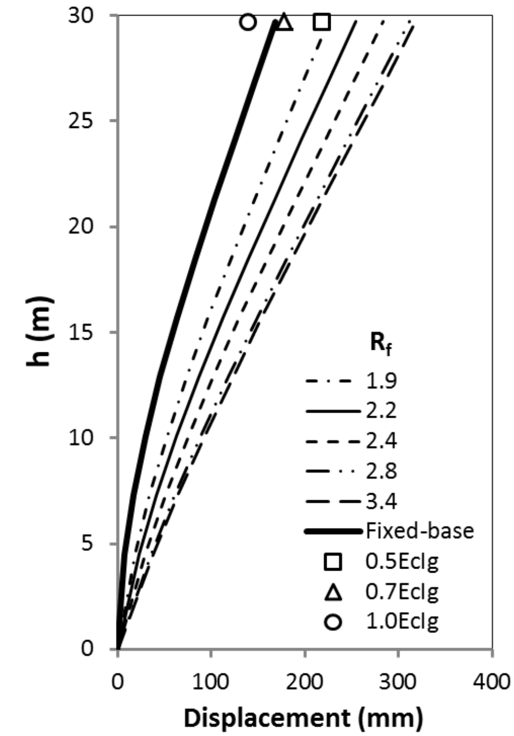

Figure A.217 Average of displacement envelopes for wall 10R17 on Dense Sand along with estimated top displacements of the fixed-base wall from RSA using various effective stiffnesses

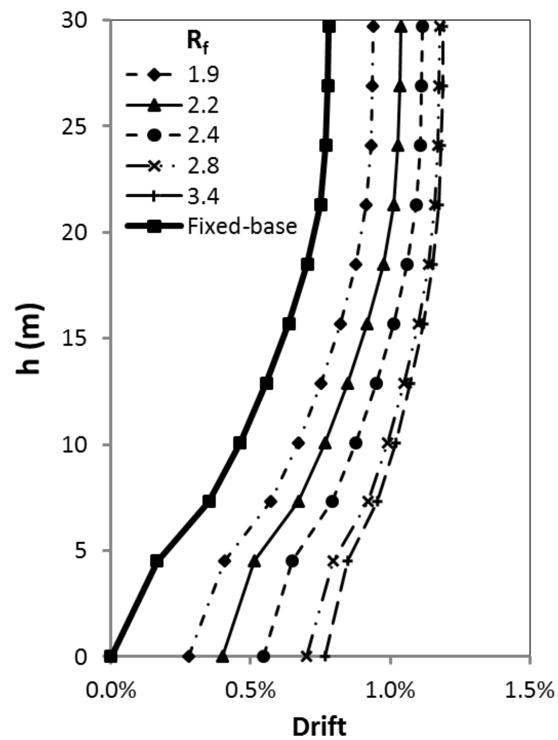

Figure A.218 Average of drift envelopes for wall 10R17 on Dense Sand (Note: base rotation values are plotted at h=0 and values of average interstory drift are plotted at the top of the storey.)

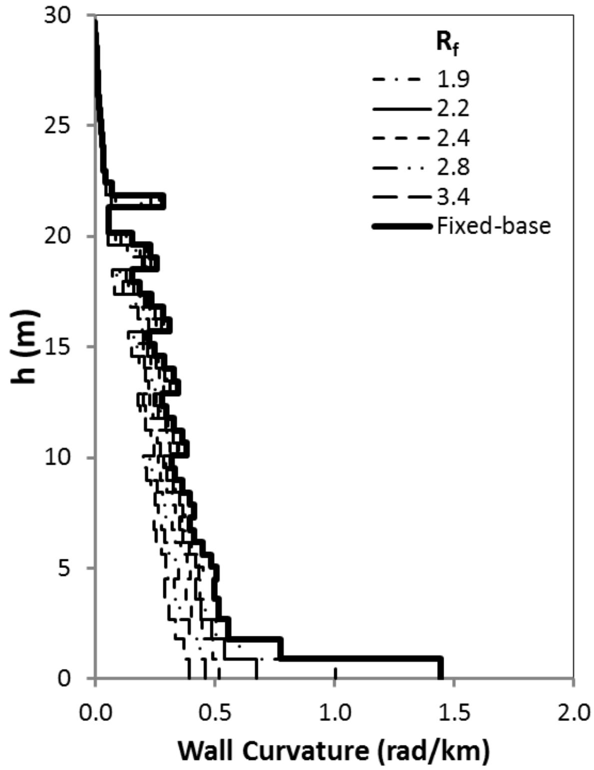

Figure A.219 Average of curvature envelopes for wall 10R17 on Dense Sand

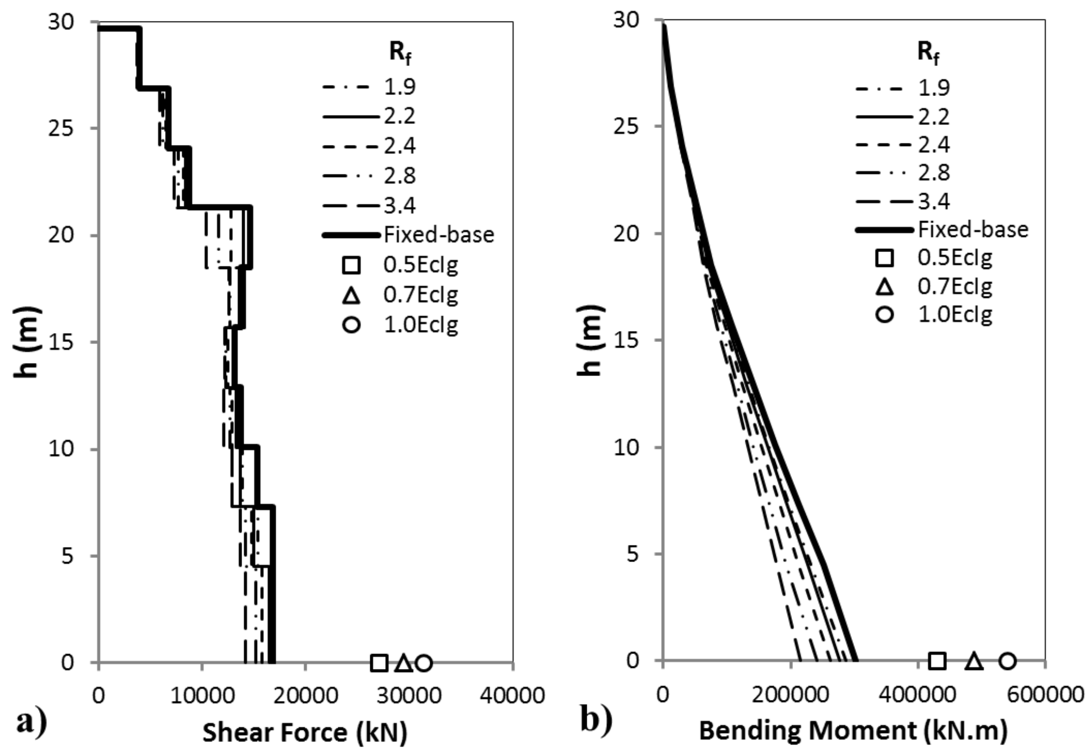

Figure A.220 Average of a) shear force, and b) bending moment envelopes for wall 10R17 on Dense Sand along with estimated maximum quantities for the fixed-base wall from RSA using various effective stiffnesses

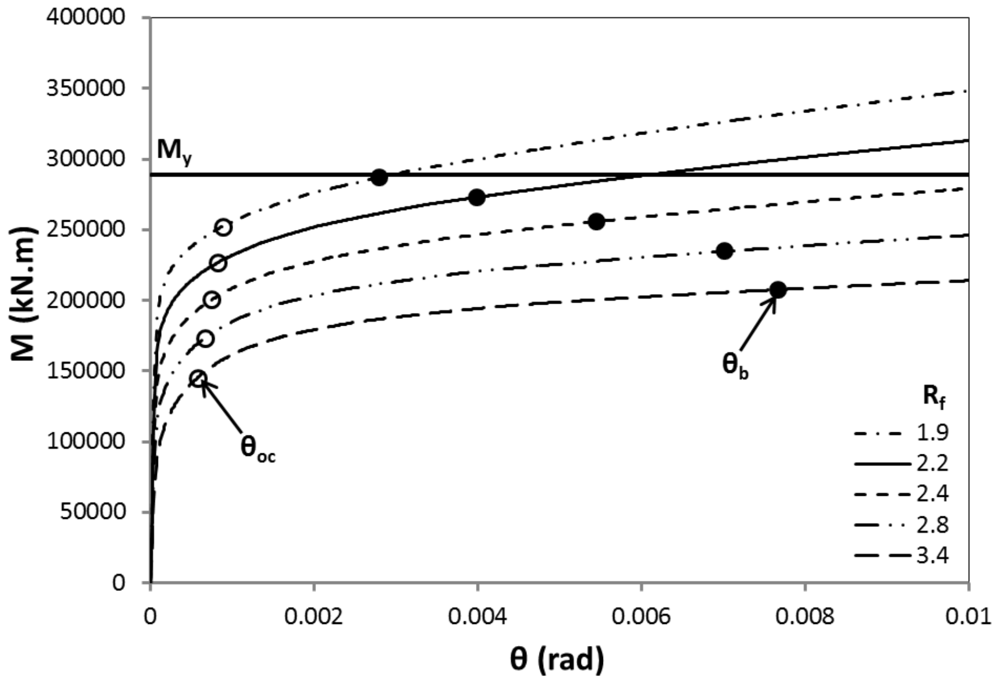

Figure A.221 Bending moment-rotation response of the foundation of wall 10R17 on Dense Sand

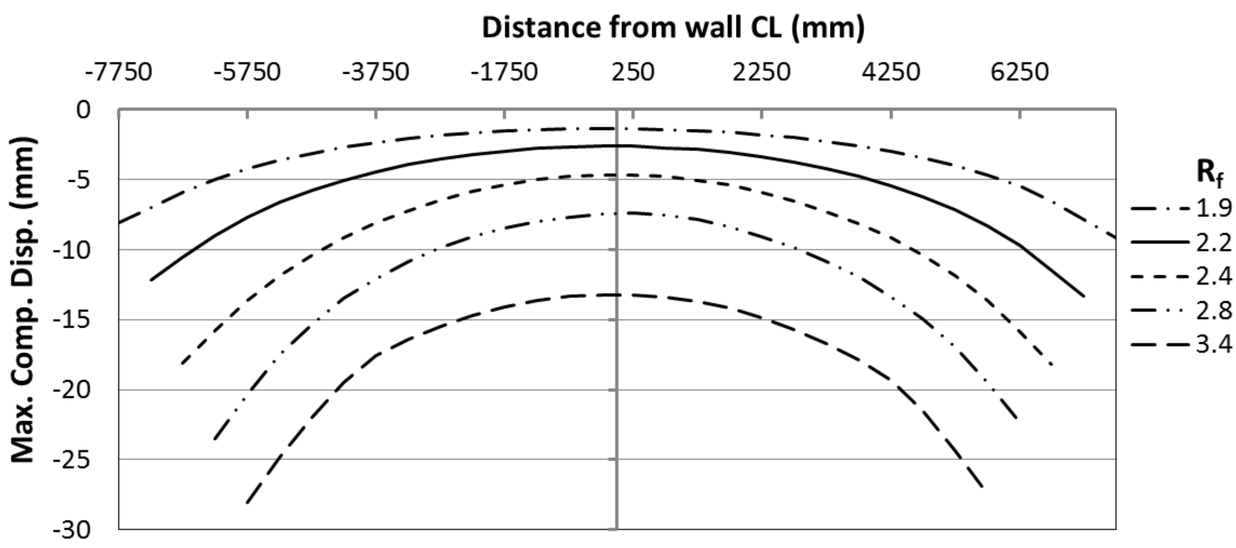

Figure A.222 Average of maximum soil compressive displacements underneath the footing for wall 10R17 on Dense Sand

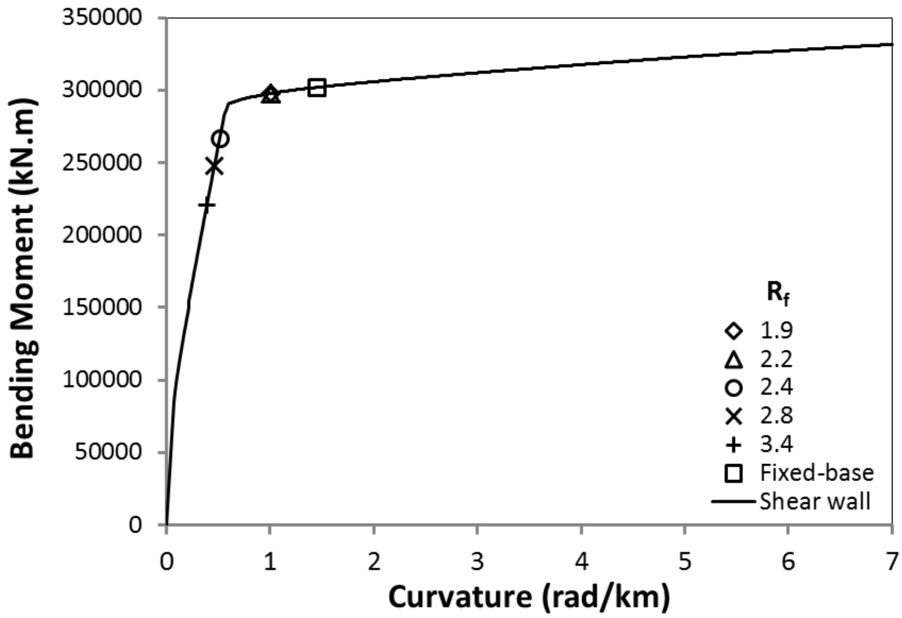

Figure A.223 Moment-curvature response of wall 10R17 along with average of maximum recorded curvatures at the base on Dense Sand

Table A.65 Shear wall properties for wall 10R13

N	10
L_w (mm)	5500
P (kN)	41550
M_{RSA} (kN.m)	488000
M_y (kN.m)	369000
R_w	1.32

Table A.66 Summary of nonlinear dynamic analyses for wall 10R13 on Dense Sand

R_f	1.3	1.6	1.9	2.2	2.4	2.8	3.4
E (MPa)	809	809	809	809	809	809	809
G_{eff} (MPa)	311	311	311	311	311	311	311
ν	0.3	0.3	0.3	0.3	0.3	0.3	0.3
q_a (kPa)	500	500	533	533	533	533	533
q (kPa)	99	136	173	198	228	266	314
q_f (kPa)	800	800	800	800	800	800	800
q_{ult} (kPa)	1600	1600	1600	1600	1600	1600	1600
L (m)	20.5	17.5	15.5	14.5	13.5	12.5	11.5
B (m)	20.5	17.5	15.5	14.5	13.5	12.5	11.5
a (mm)	2534	2968	3351	3582	3847	4155	4516
s (mm)	0.21	0.24	0.26	0.28	0.29	0.31	0.33
M_{oc} (kN.m)	373253	301905	252399	226824	200536	173367	145086
θ_{oc} (rad)	0.0009	0.0009	0.0009	0.0008	0.0007	0.0007	0.0006
θ_y (rad)	0.0008	0.0050	0.0130	0.0207	0.0338	-----	-----
$T_{Estimate}$ (sec)	0.97	0.98	1.00	1.01	1.03	1.04	1.07
T_{model} (sec)	0.95	0.95	0.96	0.96	0.97	0.98	0.99
Δ_1 (mm)	8.0	12.6	22.1	28.1	31.4	36.6	40.8
Δ_{10} (mm)	163	176	228	262	280	302	323
Avg. Max. θ_b (rad)	0.0006	0.0018	0.0040	0.0054	0.0062	0.0074	0.0085
Avg. Max. Uplift (mm)	9.8	25.0	48.3	61.3	63.8	67.4	66.8
Avg. Max. Comp. Disp. (mm)	-2.6	-6.2	-13.6	-17.5	-20.5	-27.6	-30.9
Avg. Max. q_{max}/q_{ult}	38%	58%	77%	84%	89%	94%	96%

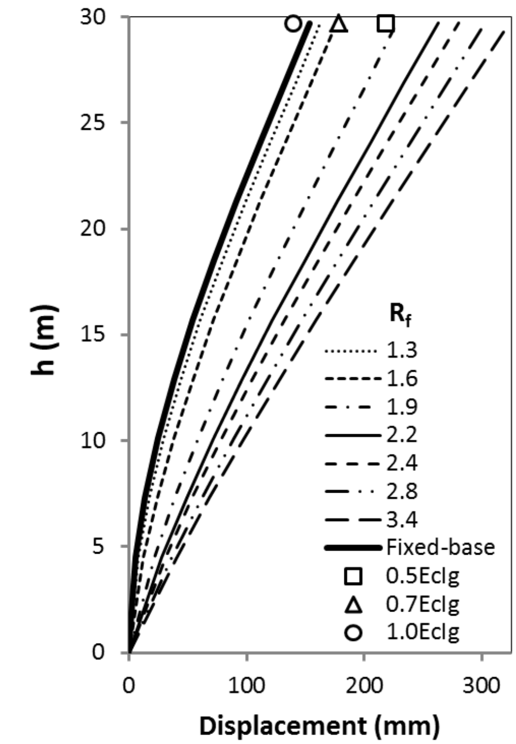

Figure A.224 Average of displacement envelopes for wall 10R13 on Dense Sand along with estimated top displacements of the fixed-base wall from RSA using various effective stiffnesses

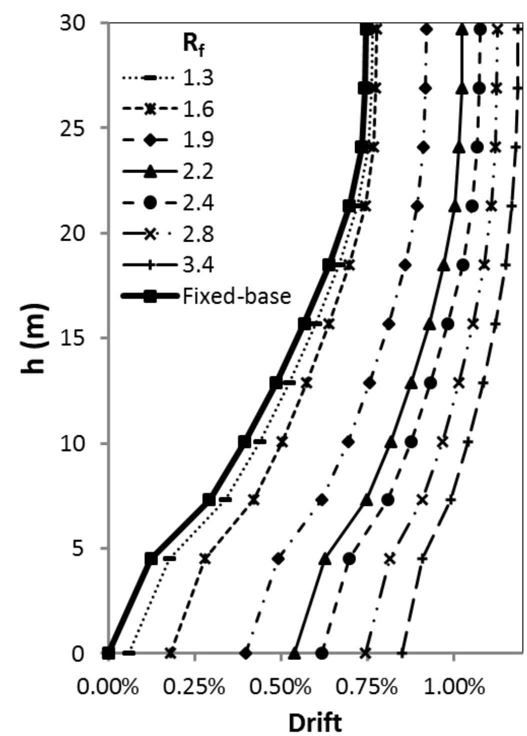

Figure A.225 Average of drift envelopes for wall 10R13 on Dense Sand (Note: base rotation values are plotted at h=0 and values of average interstory drift are plotted at the top of the storey.)

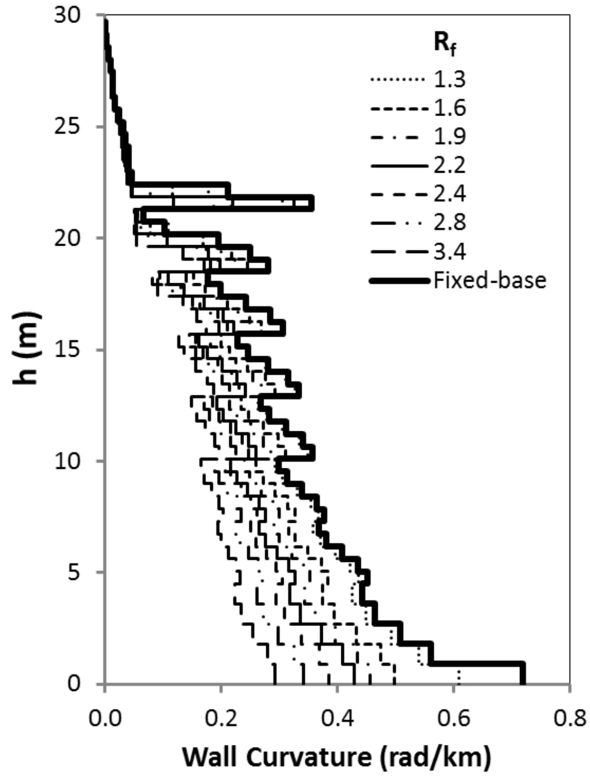

Figure A.226 Average of curvature envelopes for wall 10R13 on Dense Sand

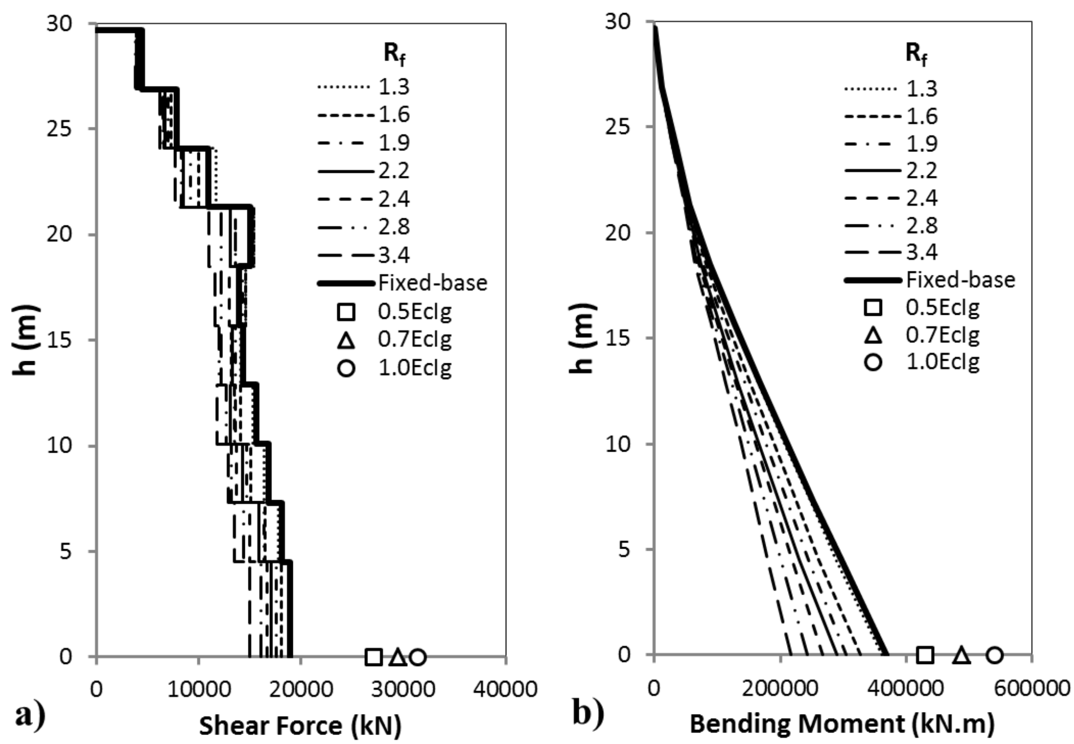

Figure A.227 Average of a) shear force, and b) bending moment envelopes for wall 10R13 on Dense Sand along with estimated maximum quantities for the fixed-base wall from RSA using various effective stiffnesses

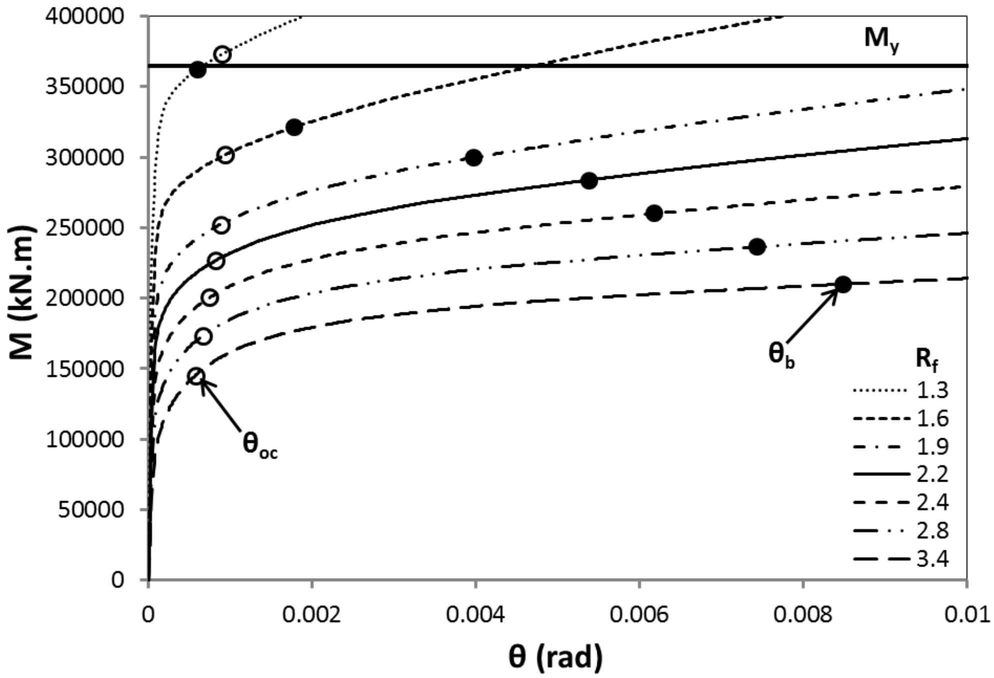

Figure A.228 Bending moment-rotation response of the foundation of wall 10R13 on Dense Sand

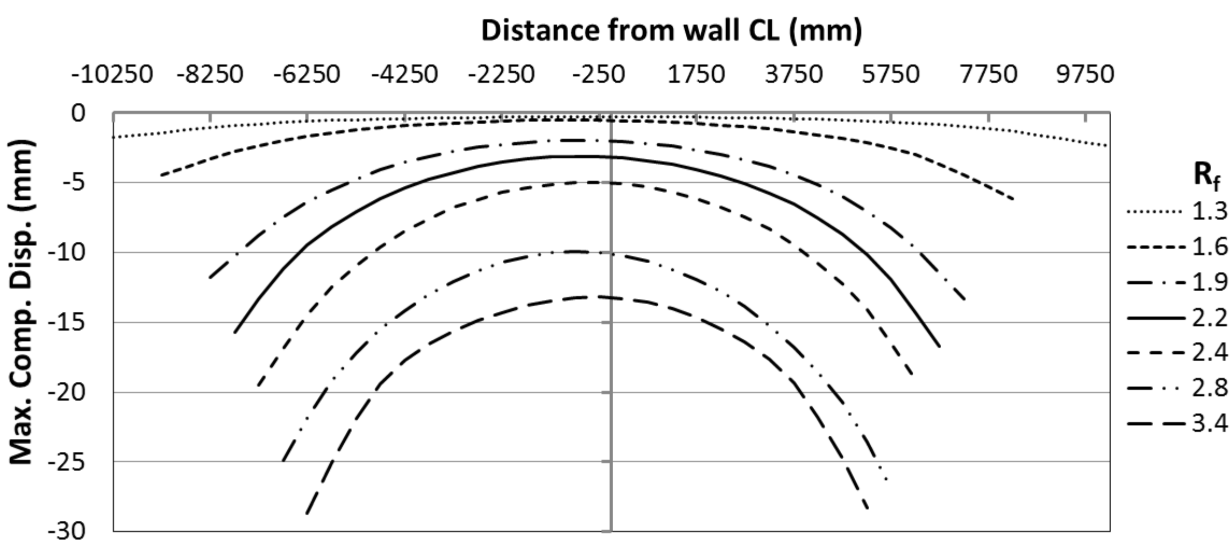

Figure A.229 Average of maximum soil compressive displacements underneath the footing for wall 10R13 on Dense Sand

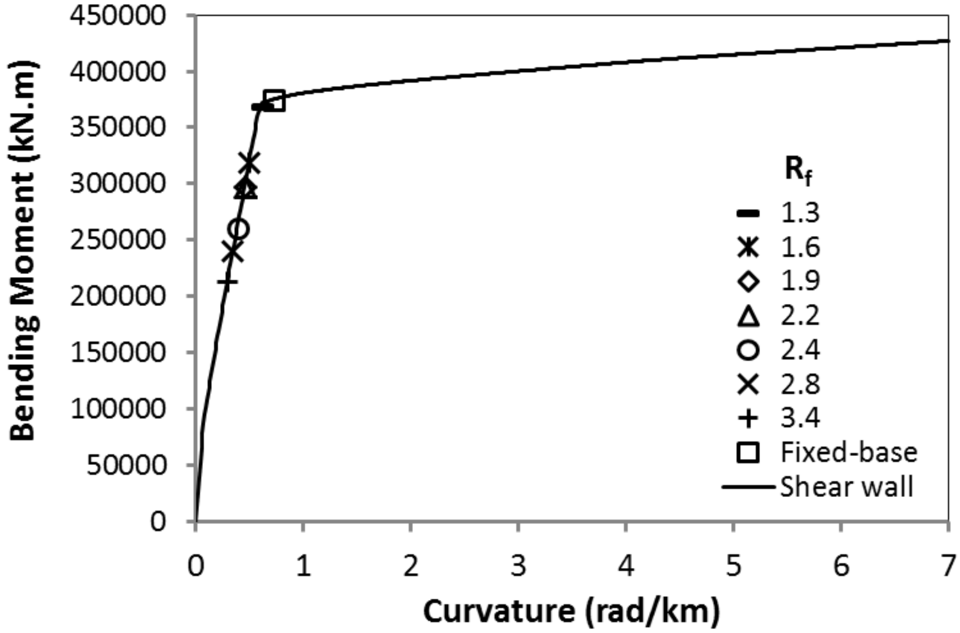

Figure A.230 Moment-curvature response of wall 10R13 along with average of maximum recorded curvatures at the base on Dense Sand

Table A.67 Shear wall properties for wall 10Elastic

N	10
L_w (mm)	5500
P (kN)	41550
M_{RSA} (kN.m)	488000
M_y (kN.m)	-----
R_w	1.00

Table A.68 Summary of nonlinear dynamic analyses for wall 10Elastic on Dense Sand

R_f	1.9	2.2	2.4	2.8	3.4
E (MPa)	809	809	809	809	809
G_{eff} (MPa)	311	311	311	311	311
v	0.3	0.3	0.3	0.3	0.3
q_a (kPa)	533	533	533	533	533
q (kPa)	173	198	228	266	314
q_f (kPa)	800	800	800	800	800
q_{ult} (kPa)	1600	1600	1600	1600	1600
L (m)	15.5	14.5	13.5	12.5	11.5
B (m)	15.5	14.5	13.5	12.5	11.5
a (mm)	3351	3582	3847	4155	4516
s (mm)	0.26	0.28	0.29	0.31	0.33
M_{oc} (kN.m)	252399	226824	200536	173367	145086
θ_{oc} (rad)	0.0009	0.0008	0.0007	0.0007	0.0006
θ_y (rad)	-----	-----	-----	-----	-----
$T_{Estimate}$ (sec)	1.12	1.13	1.15	1.16	1.19
T_{model} (sec)	1.07	1.07	1.11	1.11	1.12
Δ_1 (mm)	31.6	35.5	33.4	38.4	40.7
Δ_{10} (mm)	273	293	273	300	312
Avg. Max. θ_b (rad)	0.0063	0.0073	0.0068	0.0080	0.0086
Avg. Max. Uplift (mm)	78.4	82.5	70.1	73.4	70.5
Avg. Max. Comp. Disp. (mm)	-21.0	-24.7	-24.0	-26.7	-29.7
Avg. Max. q_{max}/q_{ult}	84%	87%	91%	94%	97%

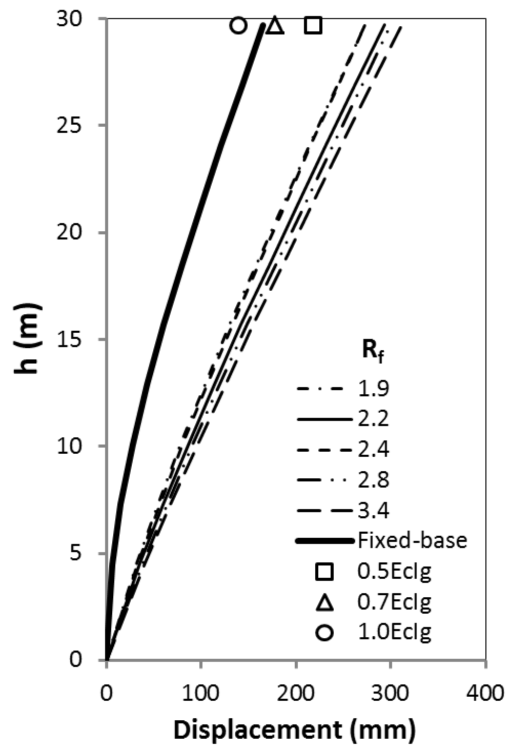

Figure A.231 Average of displacement envelopes for wall 10Elastic on Dense Sand along with estimated top displacements of the fixed-base wall from RSA using various effective stiffnesses

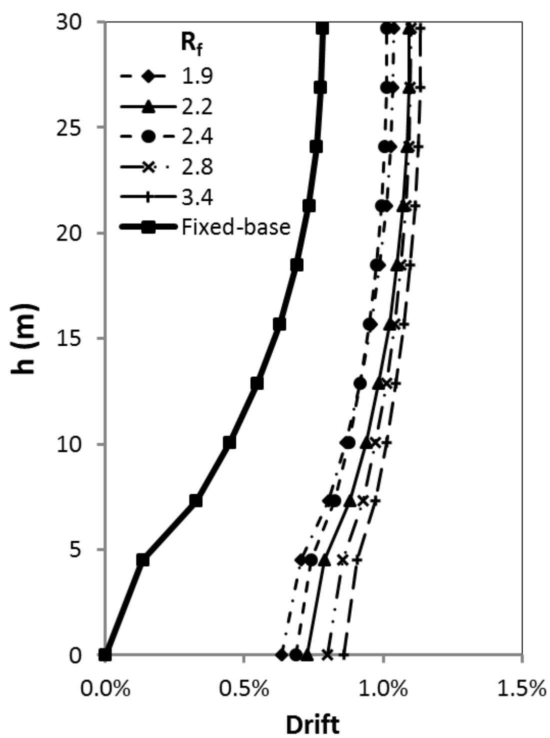

Figure A.232 Average of drift envelopes for wall 10Elastic on Dense Sand (Note: base rotation values are plotted at h=0 and values of average interstory drift are plotted at the top of the storey.)

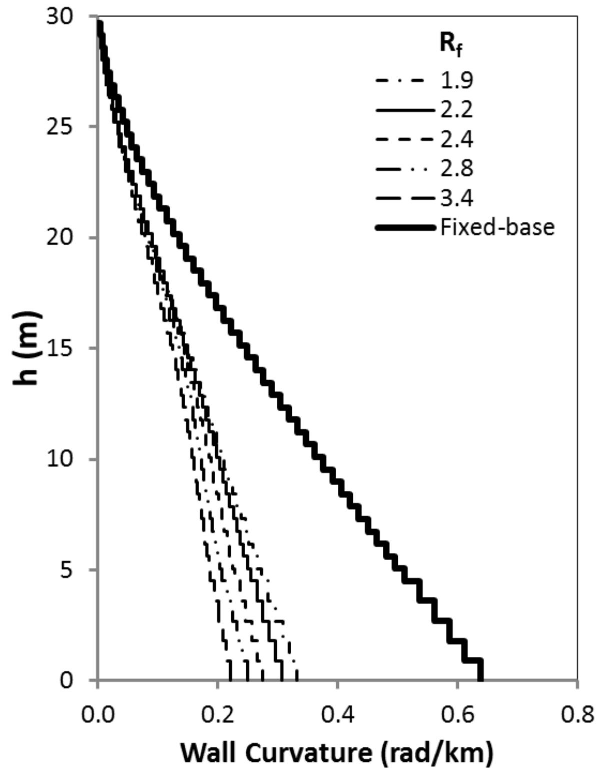

Figure A.233 Average of curvature envelopes for wall 10Elastic on Dense Sand

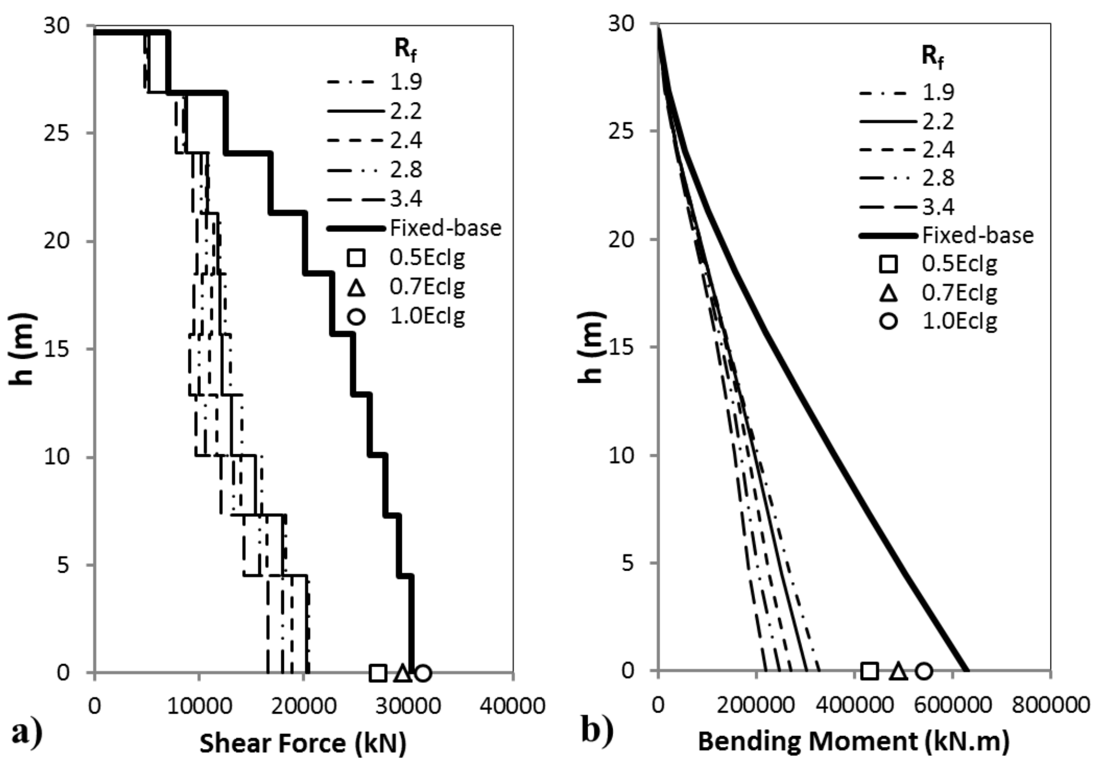

Figure A.234 Average of a) shear force, and b) bending moment envelopes for wall 10Elastic on Dense Sand along with estimated maximum quantities for the fixed-base wall from RSA using various effective stiffnesses

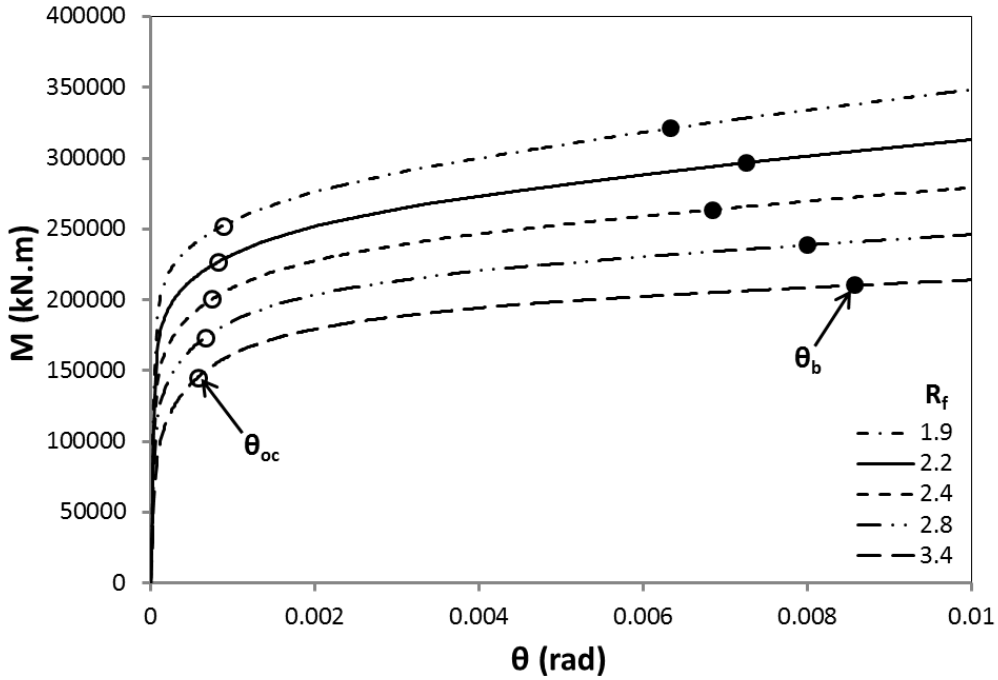

Figure A.235 Bending moment-rotation response of the foundation of wall 10Elastic on Dense Sand

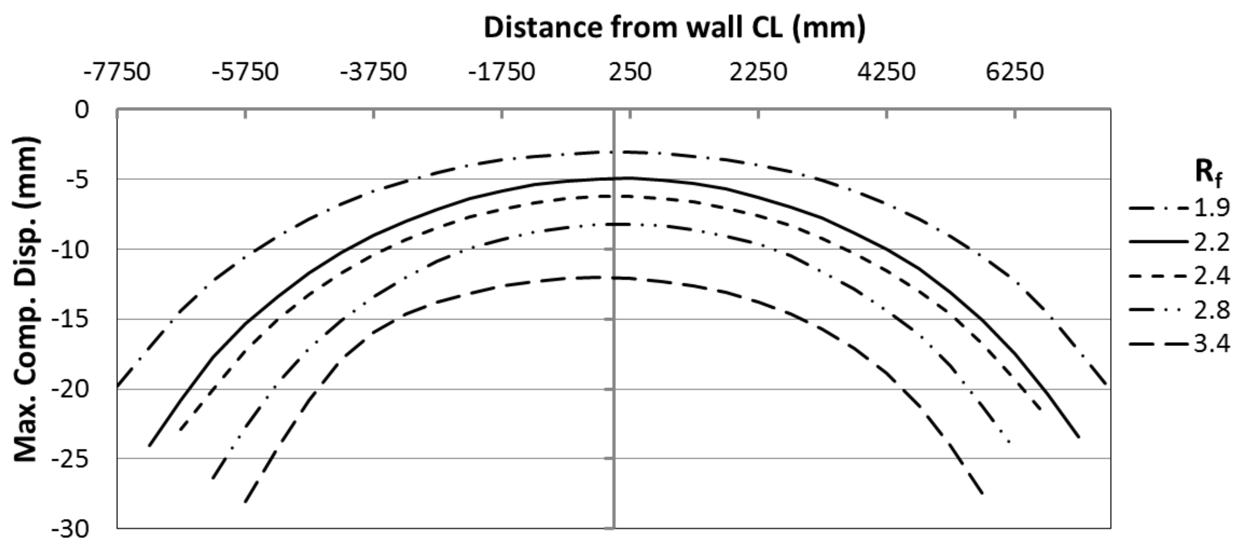

Figure A.236 Average of maximum soil compressive displacements underneath the footing for wall 10Elastic on Dense Sand

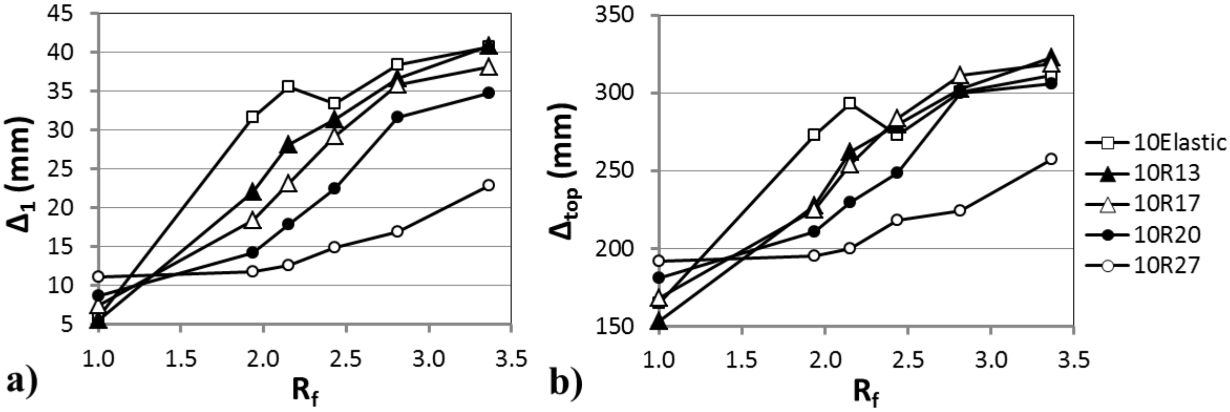

Figure A.237 Summary of average maximum a) first storey displacements, and b) top displacements for 10 storey walls on Dense Sand sorted by wall strength

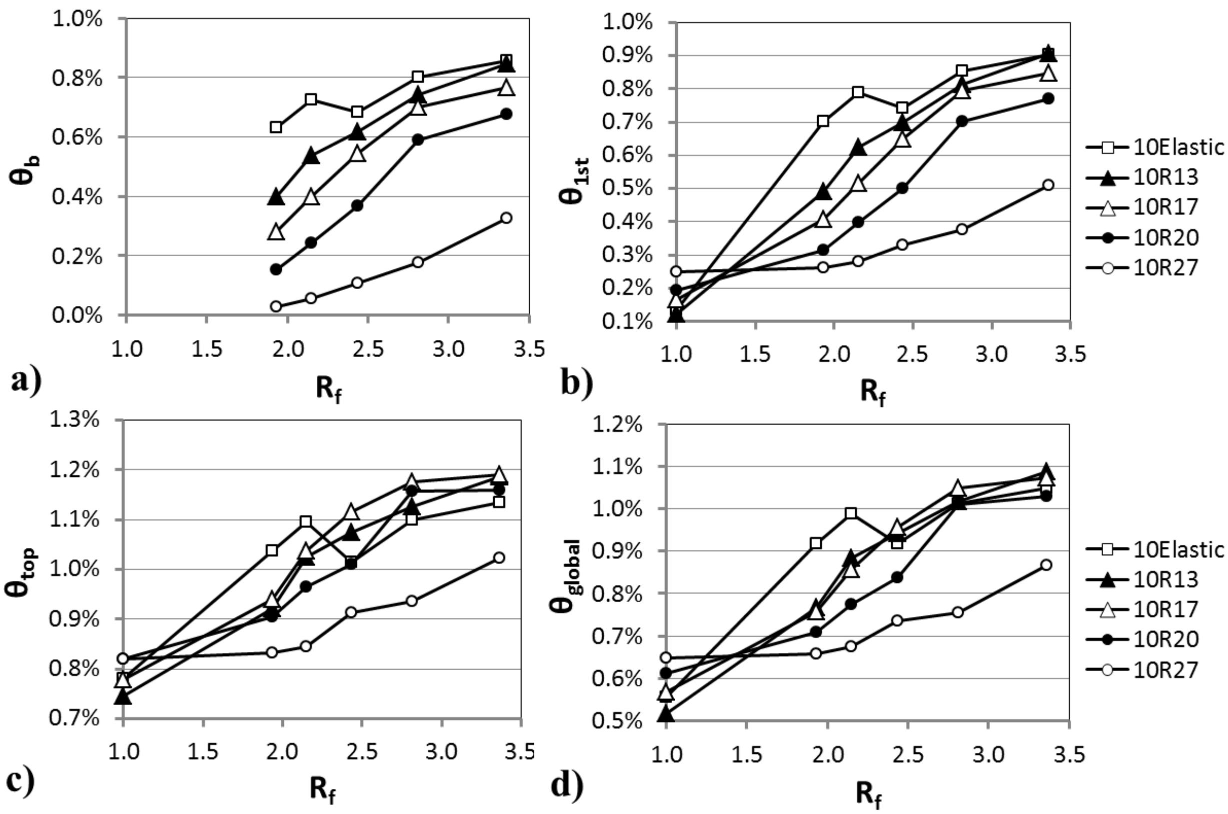

Figure A.238 Summary of average maximum a) base rotations, b) 1st storey inter-storey drifts, c) top storey inter-storey drifts, and d) global drifts of 10 storey walls on Dense Sand sorted by wall strength

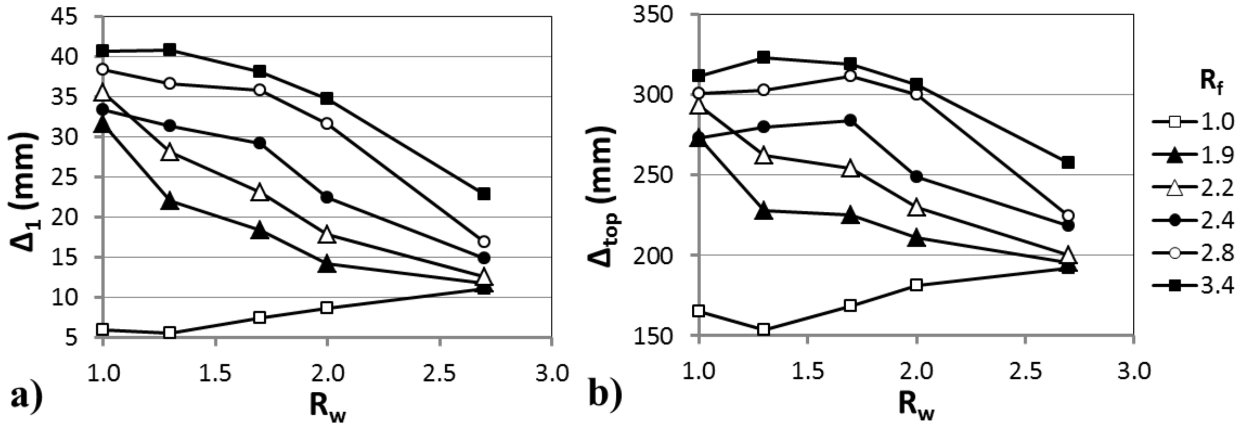

Figure A.239 Summary of average maximum a) first storey displacements, and b) top displacements for 10 storey walls on Dense Sand sorted by foundation size

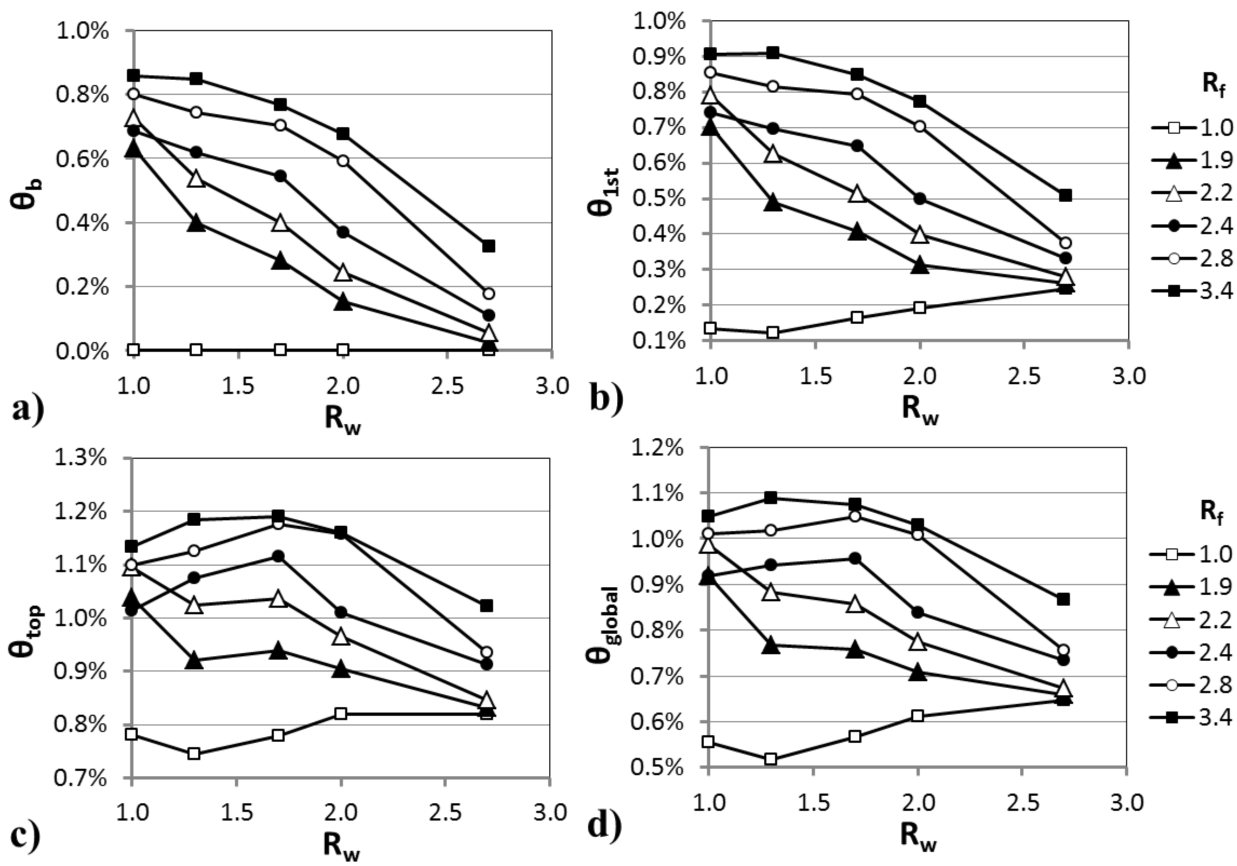

Figure A.240 Summary of average maximum a) base rotations, b) 1st storey inter-storey drifts, c) top storey inter-storey drifts, and d) global drifts of 10 storey walls on Dense Sand sorted by foundation size

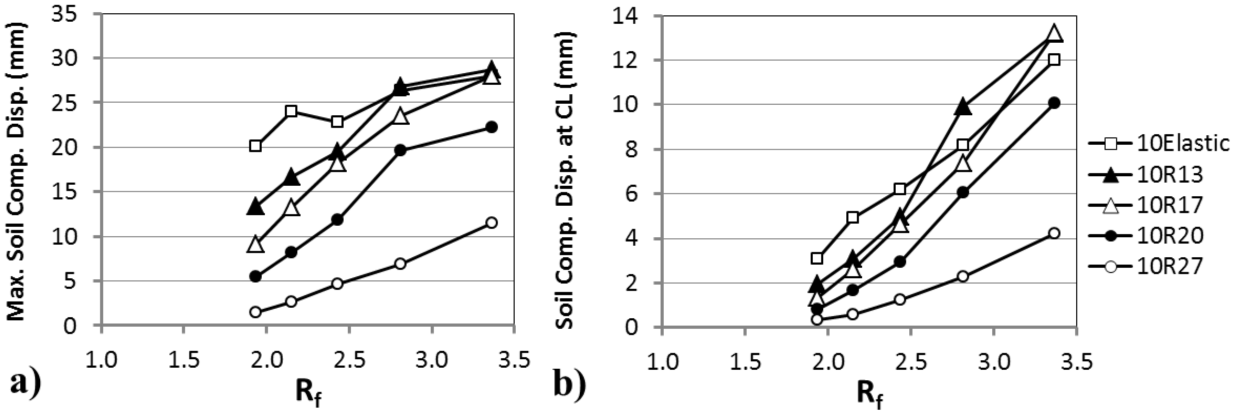

Figure A.241 Summary of average maximum soil compressive displacement at a) foundation toe, and b) foundation centreline for 10 storey walls on Dense Sand sorted by wall strength

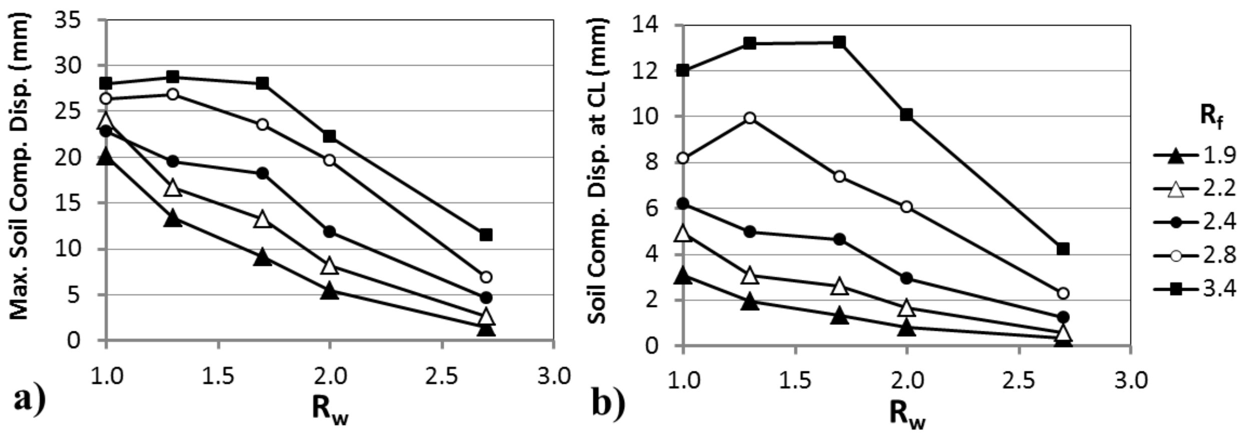

Figure A.242 Summary of average maximum soil compressive displacement at a) foundation toe, and b) foundation centreline for 10 storey walls on Dense Sand sorted by foundation size

A.6.5 Rock

Table A.69 Properties of Rock

G_0 (MPa)	8333
G_{eff} (MPa)	8333
ν	0.2
E (MPa)	20000
q_{ult} (kPa)	20000
q_f (kPa)	10000
q_a (kPa)	7000
V_s (m/s)	>760

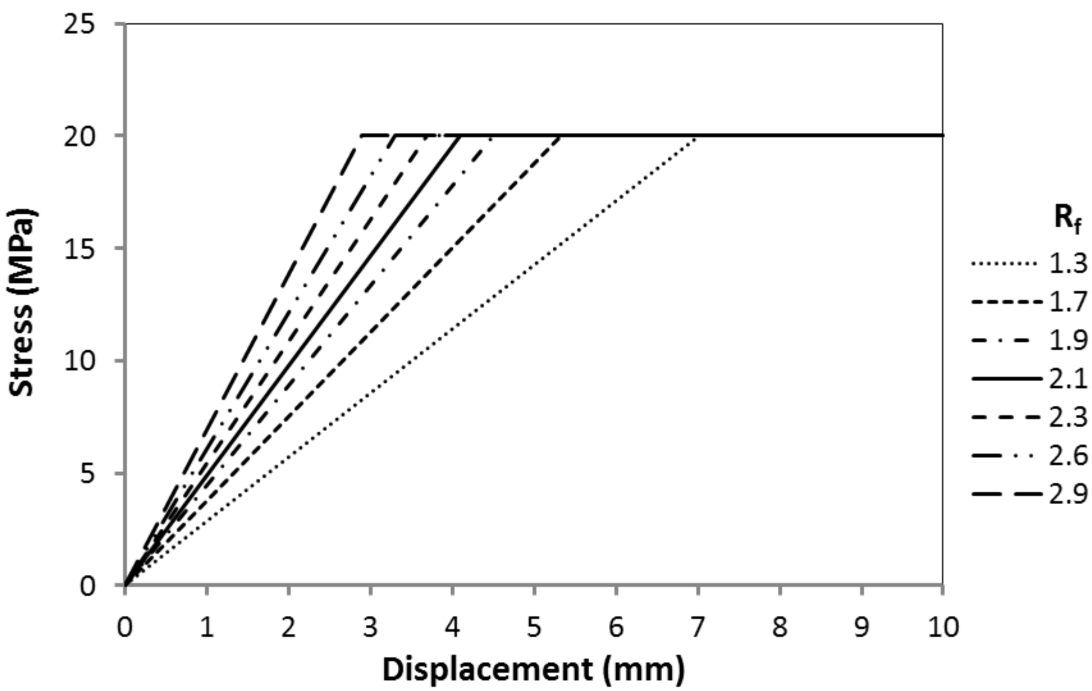

Figure A.243 Soil spring responses in monotonic compression for Rock

Table A.70 Shear wall properties for wall 10R27

N	10
L_w (mm)	5500
P (kN)	41550
M_{RSA} (kN.m)	488000
M_y (kN.m)	179000
R_w	2.73

Table A.71 Summary of nonlinear dynamic analyses for wall 10R27 on Rock

R_f	1.9	2.1	2.3	2.6	2.9
E (MPa)	20000	20000	20000	20000	20000
G_{eff} (MPa)	8333	8333	8333	8333	8333
v	0.2	0.2	0.2	0.2	0.2
q_a (kPa)	7000	3000	3000	3000	3000
q (kPa)	266	314	377	460	575
q_f (kPa)	10000	10000	10000	10000	10000
q_{ult} (kPa)	20000	20000	20000	20000	20000
L (m)	12.5	11.5	10.5	9.5	8.5
B (m)	12.5	11.5	10.5	9.5	8.5
a (mm)	332	361	396	437	489
s (mm)	0.06	0.06	0.07	0.07	0.08
M_{oc} (kN.m)	252782	231406	209917	188276	166432
θ_{oc} (rad)	0.0025	0.0023	0.0021	0.0018	0.0015
θ_y (rad)	0.0000	0.0001	0.0001	0.0005	0.1000
$T_{Estimate}$ (sec)	1.01	1.01	1.01	1.02	1.02
T_{model} (sec)	1.05	1.05	1.06	1.06	1.06
Δ_1 (mm)	11.4	11.7	13.6	18.5	31.1
Δ_{10} (mm)	194	197	203	221	289
Avg. Max. θ_b (rad)	0.0002	0.0004	0.0010	0.0023	0.0054
Avg. Max. Uplift (mm)	1.9	4.2	9.9	20.8	44.9
Avg. Max. Comp. Disp. (mm)	-0.5	-0.7	-0.9	-1.2	-1.4
Avg. Max. q_{max}/q_{ult}	10%	16%	26%	38%	48%

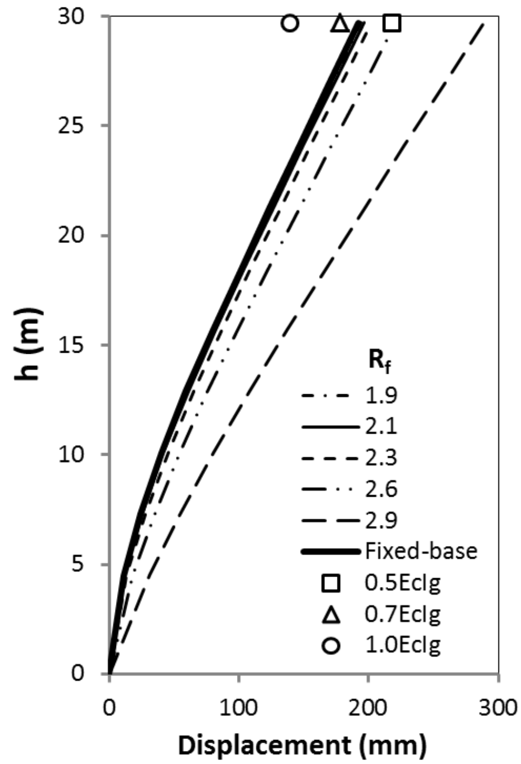

Figure A.244 Average of displacement envelopes for wall 10R27 on Rock along with estimated top displacements of the fixed-base wall from RSA using various effective stiffnesses

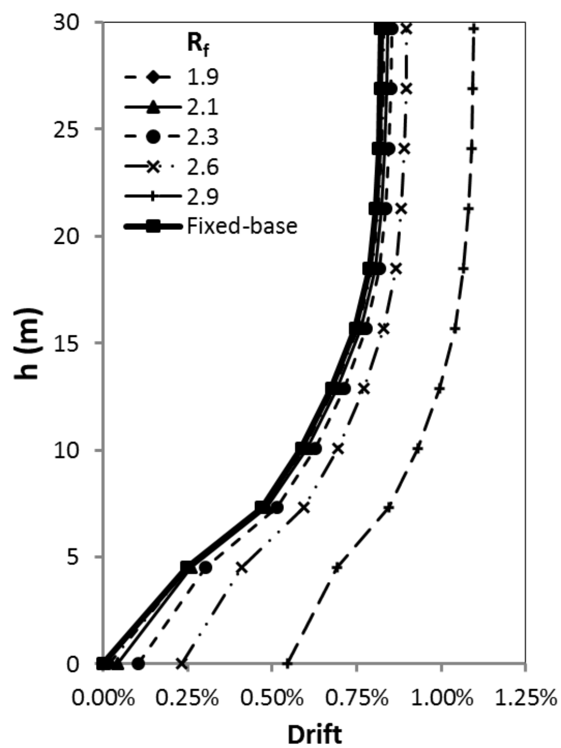

Figure A.245 Average of drift envelopes for wall 10R27 on Rock (Note: base rotation values are plotted at h=0 and values of average interstory drift are plotted at the top of the storey.)

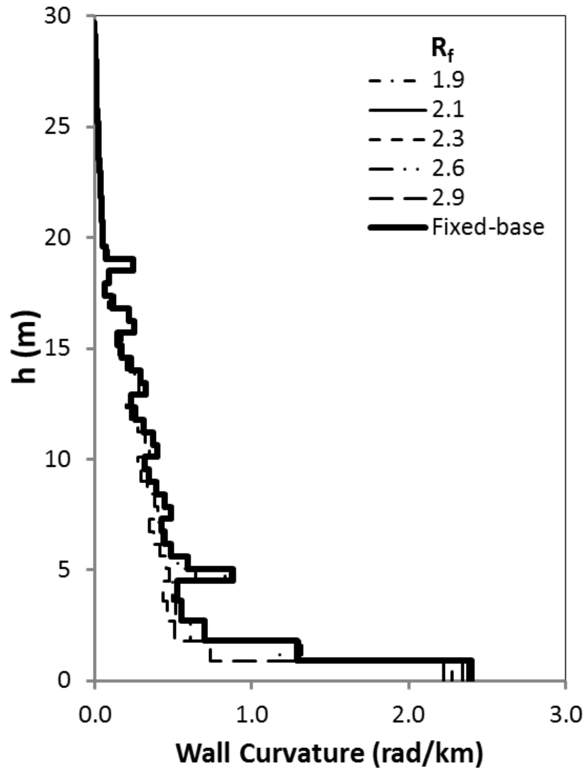

Figure A.246 Average of curvature envelopes for wall 10R27 on Rock

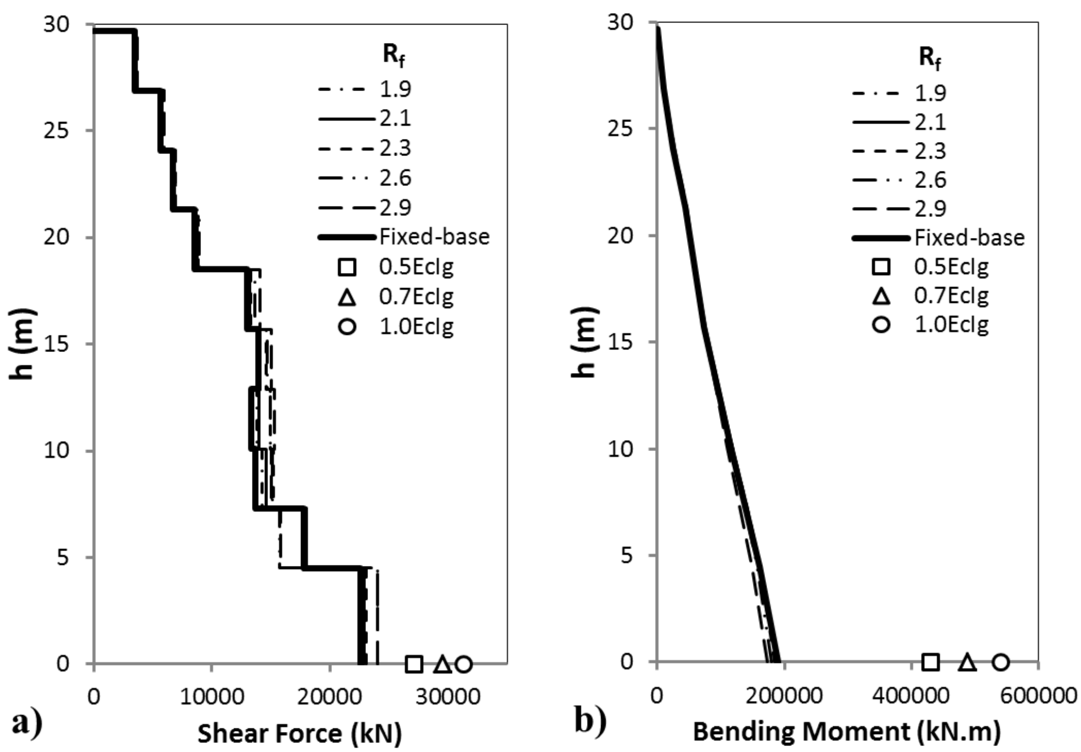

Figure A.247 Average of a) shear force, and b) bending moment envelopes for wall 10R27 on Rock along with estimated maximum quantities for the fixed-base wall from RSA using various effective stiffnesses

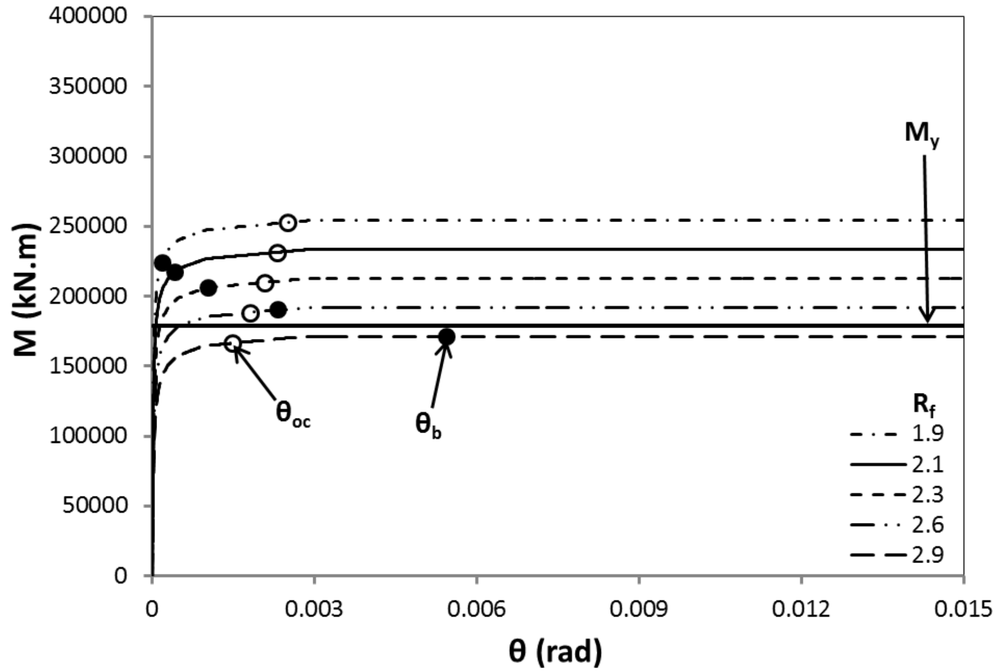

Figure A.248 Bending moment-rotation response of the foundation of wall 10R27 on Rock

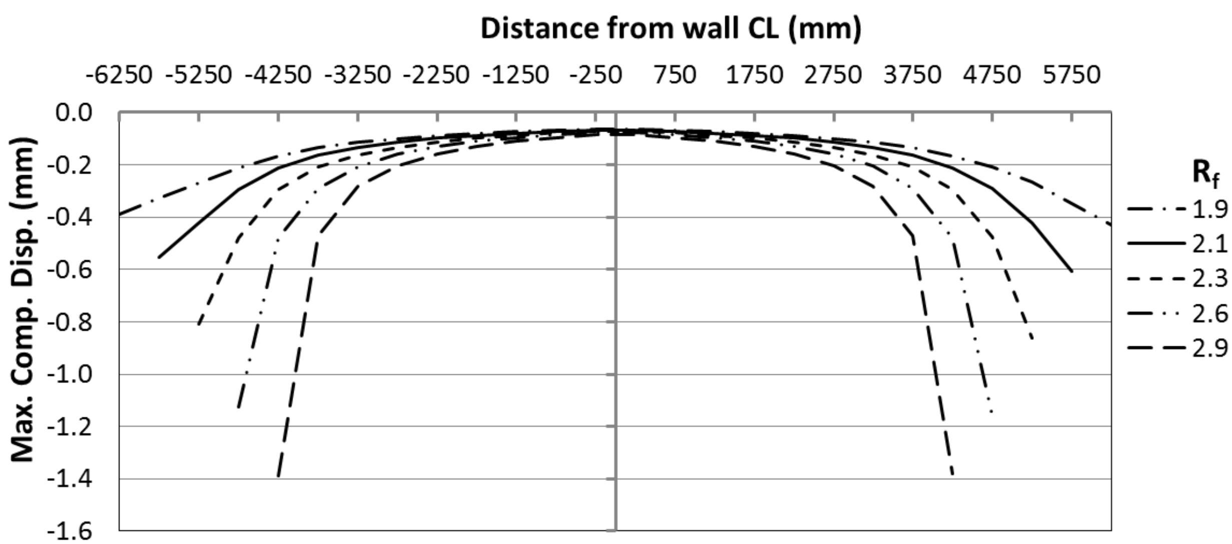

Figure A.249 Average of maximum soil compressive displacements underneath the footing for wall 10R27 on Rock

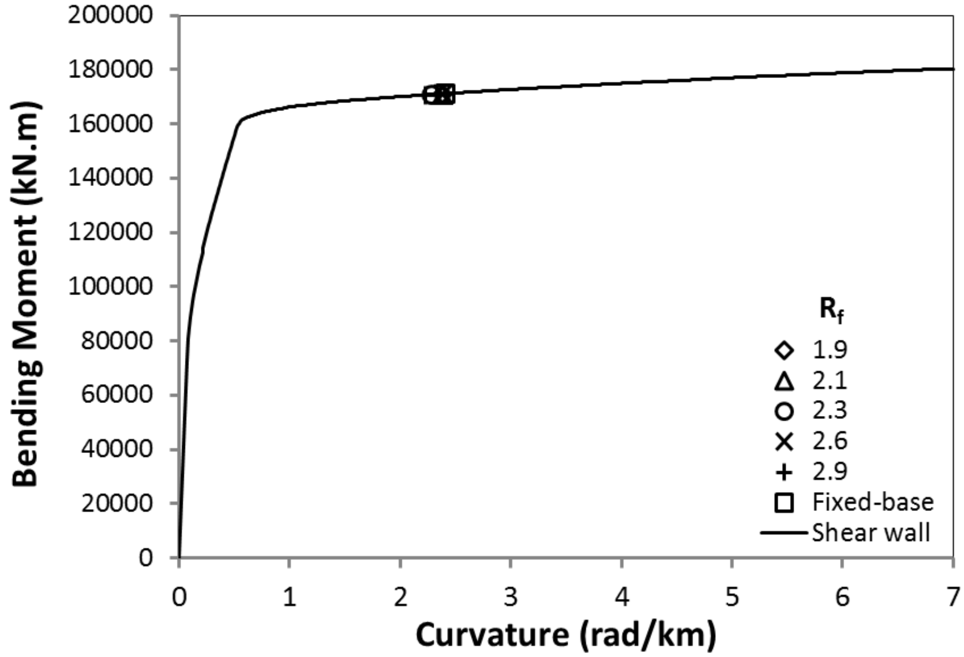

Figure A.250 Moment-curvature response of wall 10R27 along with average of maximum recorded curvatures at the base on Rock

Table A.72 Shear wall properties for wall 10R20

N	10
L_w (mm)	5500
P (kN)	41550
M_{RSA} (kN.m)	488000
M_y (kN.m)	249000
R_w	1.96

Table A.73 Summary of nonlinear dynamic analyses for wall 10R20 on Rock

R_f	1.9	2.1	2.3	2.6	2.9
E (MPa)	20000	20000	20000	20000	20000
G_{eff} (MPa)	8333	8333	8333	8333	8333
v	0.2	0.2	0.2	0.2	0.2
q_a (kPa)	3000	3000	3000	3000	3000
q (kPa)	266	314	377	460	575
q_f (kPa)	10000	10000	10000	10000	10000
q_{ult} (kPa)	20000	20000	20000	20000	20000
L (m)	12.5	11.5	10.5	9.5	8.5
B (m)	12.5	11.5	10.5	9.5	8.5
a (mm)	332	361	396	437	489
s (mm)	0.06	0.06	0.07	0.07	0.08
M_{oc} (kN.m)	252782	231406	209917	188276	166432
θ_{oc} (rad)	0.0025	0.0023	0.0021	0.0018	0.0015
θ_y (rad)	0.0014	0.1000	0.1000	0.1000	0.1000
$T_{Estimate}$ (sec)	1.01	1.01	1.01	1.02	1.02
T_{model} (sec)	1.01	1.01	1.01	1.02	1.02
Δ_1 (mm)	16.3	22.5	29.9	41.1	48.3
Δ_{10} (mm)	211	241	273	339	374
Avg. Max. θ_b (rad)	0.0022	0.0039	0.0057	0.0083	0.0100
Avg. Max. Uplift (mm)	26.6	43.0	58.0	77.3	83.8
Avg. Max. Comp. Disp. (mm)	-1.3	-1.4	-1.4	-1.4	-1.4
Avg. Max. q_{max}/q_{ult}	28%	35%	39%	44%	49%

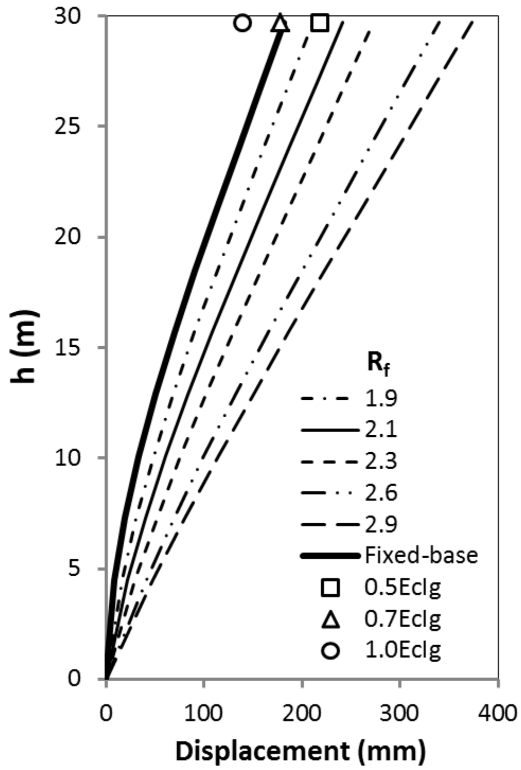

Figure A.251 Average of displacement envelopes for wall 10R20 on Rock along with estimated top displacements of the fixed-base wall from RSA using various effective stiffnesses

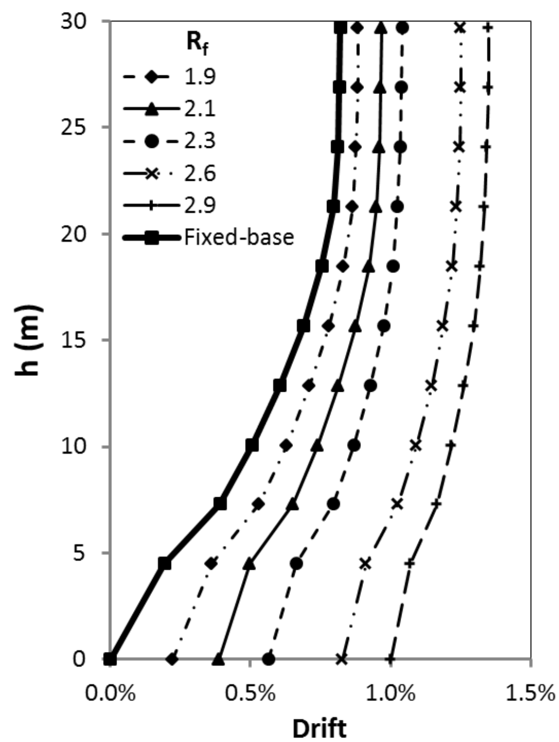

Figure A.252 Average of drift envelopes for wall 10R20 on Rock (Note: base rotation values are plotted at h=0 and values of average interstory drift are plotted at the top of the storey.)

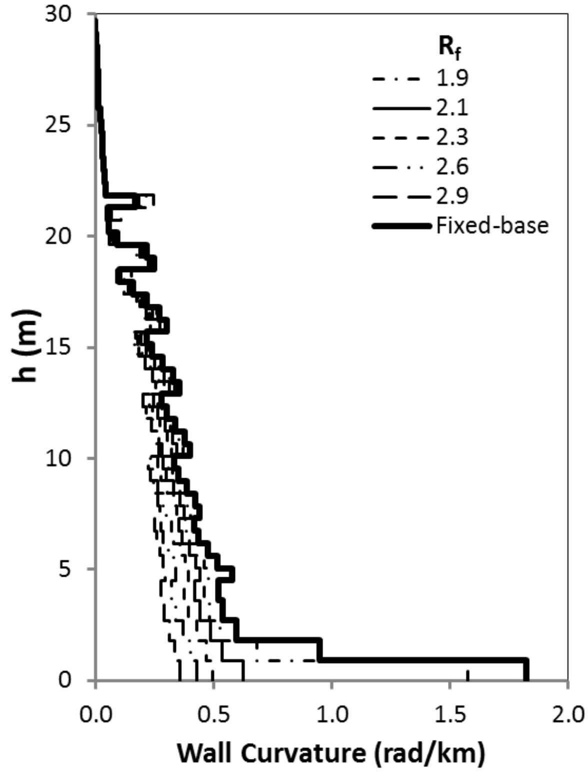

Figure A.253 Average of curvature envelopes for wall 10R20 on Rock

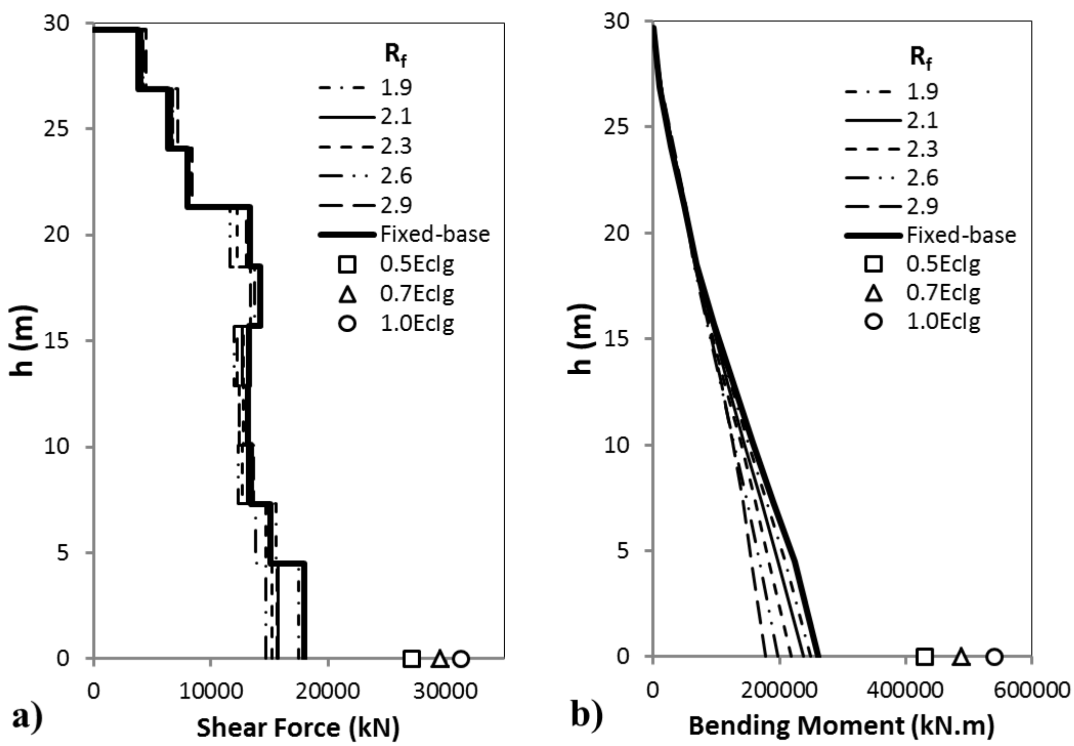

Figure A.254 Average of a) shear force, and b) bending moment envelopes for wall 10R20 on Rock along with estimated maximum quantities for the fixed-base wall from RSA using various effective stiffnesses

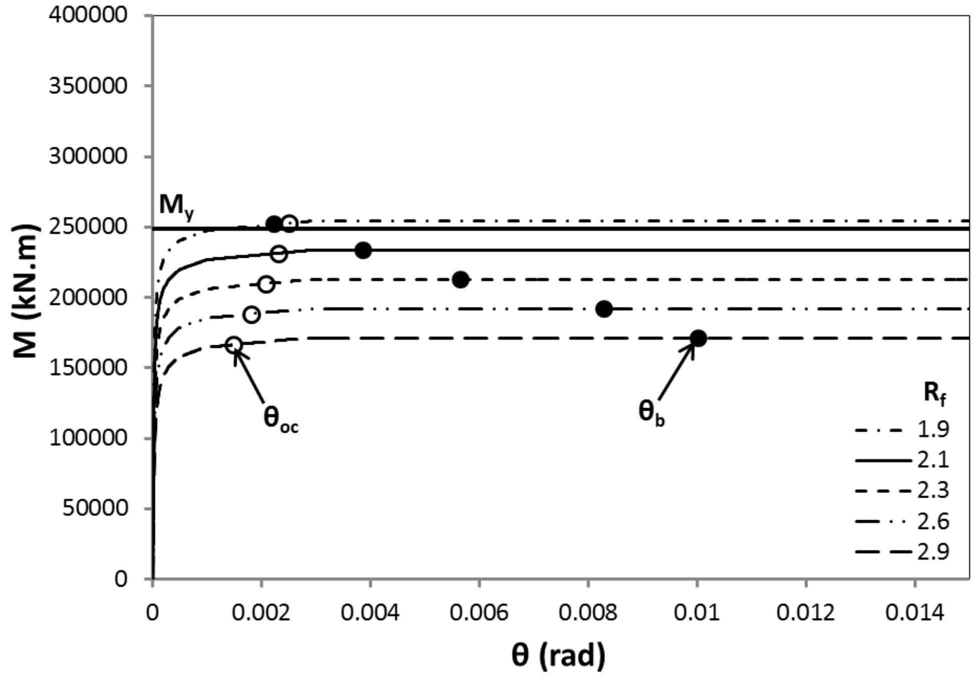

Figure A.255 Bending moment-rotation response of the foundation of wall 10R20 on Rock

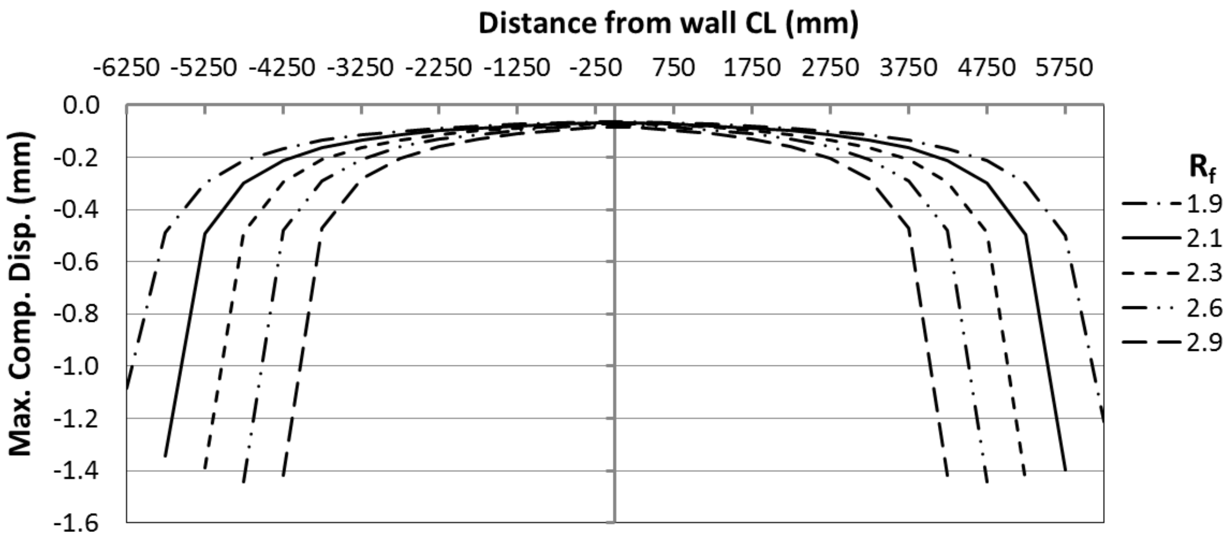

Figure A.256 Average of maximum soil compressive displacements underneath the footing for wall 10R20 on Rock

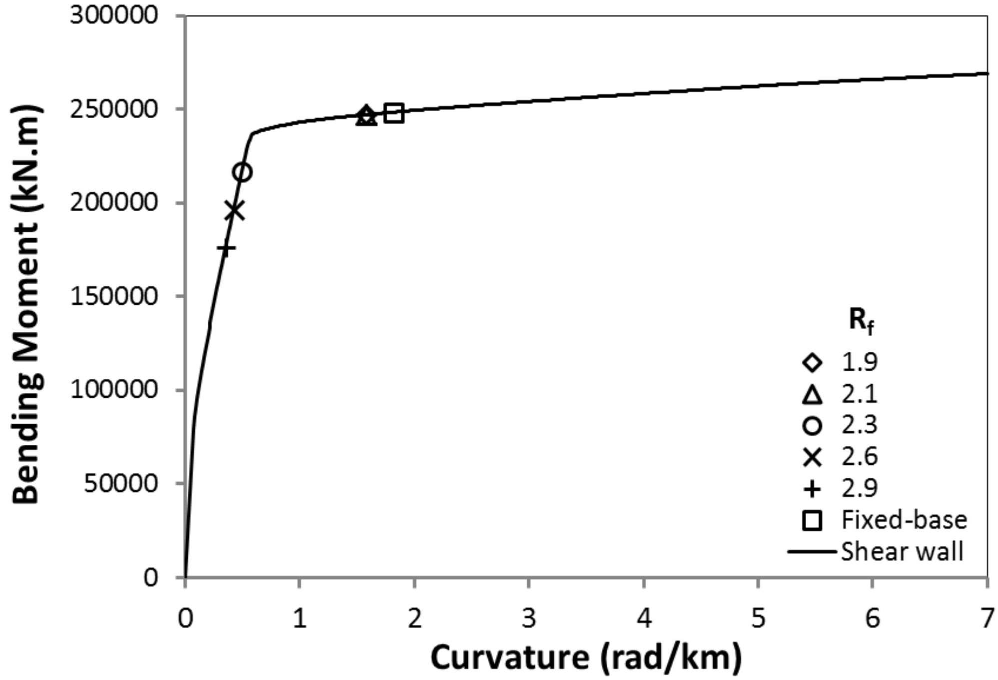

Figure A.257 Moment-curvature response of wall 10R20 along with average of maximum recorded curvatures at the base on Rock

Table A.74 Shear wall properties for wall 10R17

N	10
L_w (mm)	5500
P (kN)	41550
M_{RSA} (kN.m)	488000
M_y (kN.m)	289000
R_w	1.69

Table A.75 Summary of nonlinear dynamic analyses for wall 10R17 on Rock

R_f	1.9	2.1	2.3	2.6	2.9
E (MPa)	20000	20000	20000	20000	20000
G_{eff} (MPa)	8333	8333	8333	8333	8333
v	0.2	0.2	0.2	0.2	0.2
q_a (kPa)	3000	3000	3000	3000	3000
q (kPa)	266	314	377	460	575
q_f (kPa)	10000	10000	10000	10000	10000
q_{ult} (kPa)	20000	20000	20000	20000	20000
L (m)	12.5	11.5	10.5	9.5	8.5
B (m)	12.5	11.5	10.5	9.5	8.5
a (mm)	332	361	396	437	489
s (mm)	0.06	0.06	0.07	0.07	0.08
M_{oc} (kN.m)	252782	231406	209917	188276	166432
θ_{oc} (rad)	0.0025	0.0023	0.0021	0.0018	0.0015
θ_y (rad)	0.1000	0.1000	0.1000	0.1000	0.1000
$T_{Estimate}$ (sec)	0.99	0.99	0.99	0.99	1.00
T_{model} (sec)	0.99	0.99	0.99	0.99	1.00
Δ_1 (mm)	21.0	25.4	35.9	39.0	53.6
Δ_{10} (mm)	224	246	301	314	401
Avg. Max. θ_b (rad)	0.0036	0.0047	0.0072	0.0080	0.0113
Avg. Max. Uplift (mm)	44.2	52.9	73.9	74.5	94.9
Avg. Max. Comp. Disp. (mm)	-1.4	-1.4	-1.5	-1.4	-1.4
Avg. Max. q_{max}/q_{ult}	31%	34%	39%	44%	49%

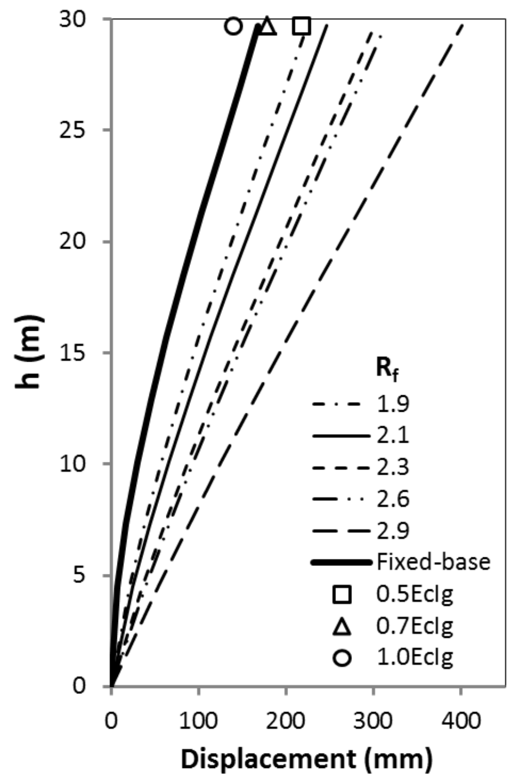

Figure A.258 Average of displacement envelopes for wall 10R17 on Rock along with estimated top displacements of the fixed-base wall from RSA using various effective stiffnesses

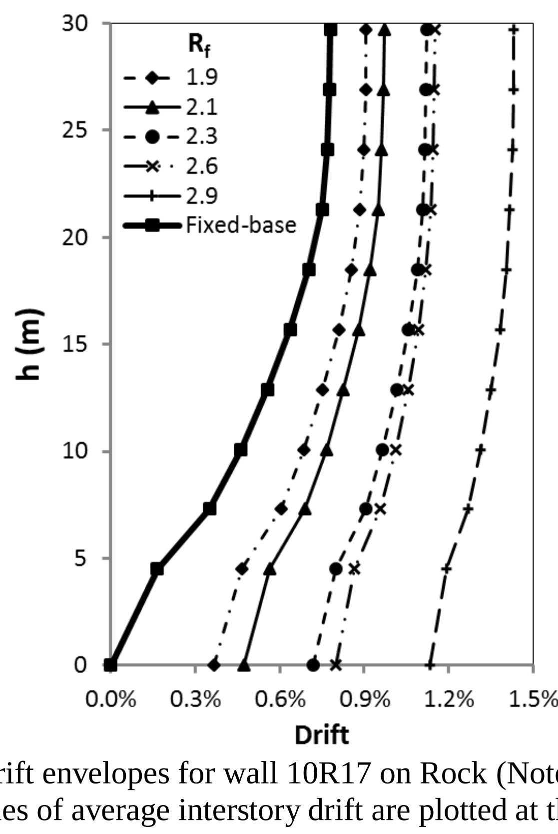

Figure A.259 Average of drift envelopes for wall 10R17 on Rock (Note: base rotation values are plotted at h=0 and values of average interstory drift are plotted at the top of the storey.)

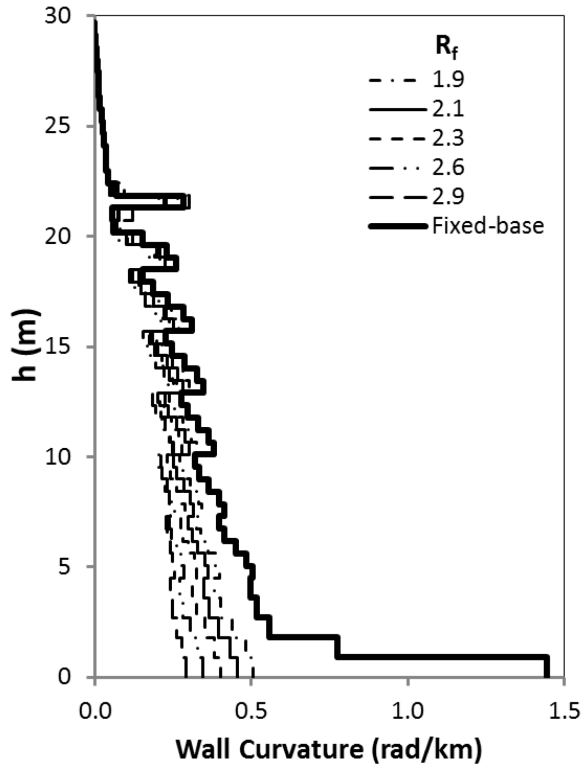

Figure A.260 Average of curvature envelopes for wall 10R17 on Rock

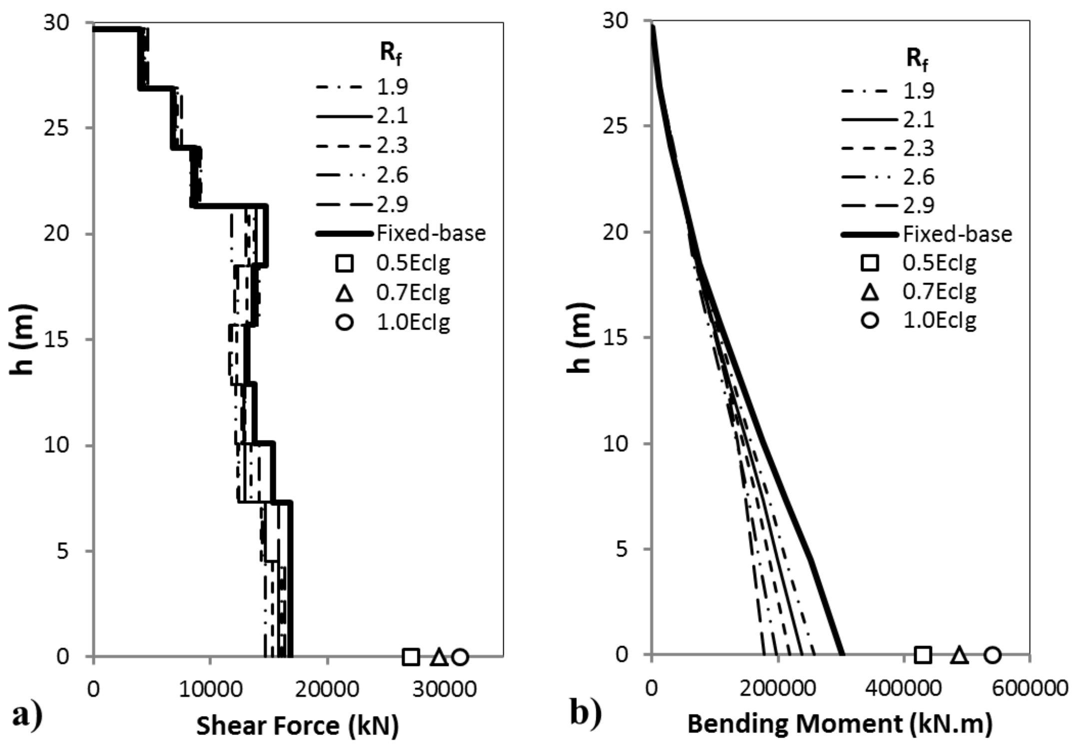

Figure A.261 Average of a) shear force, and b) bending moment envelopes for wall 10R17 on Rock along with estimated maximum quantities for the fixed-base wall from RSA using various effective stiffnesses

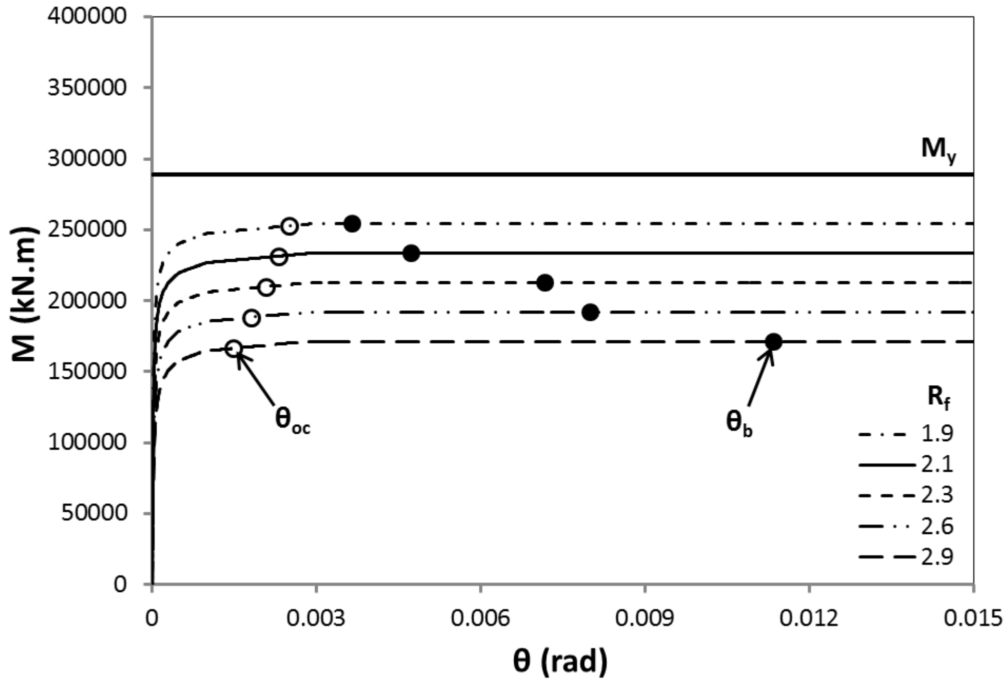

Figure A.262 Bending moment-rotation response of the foundation of wall 10R17 on Rock

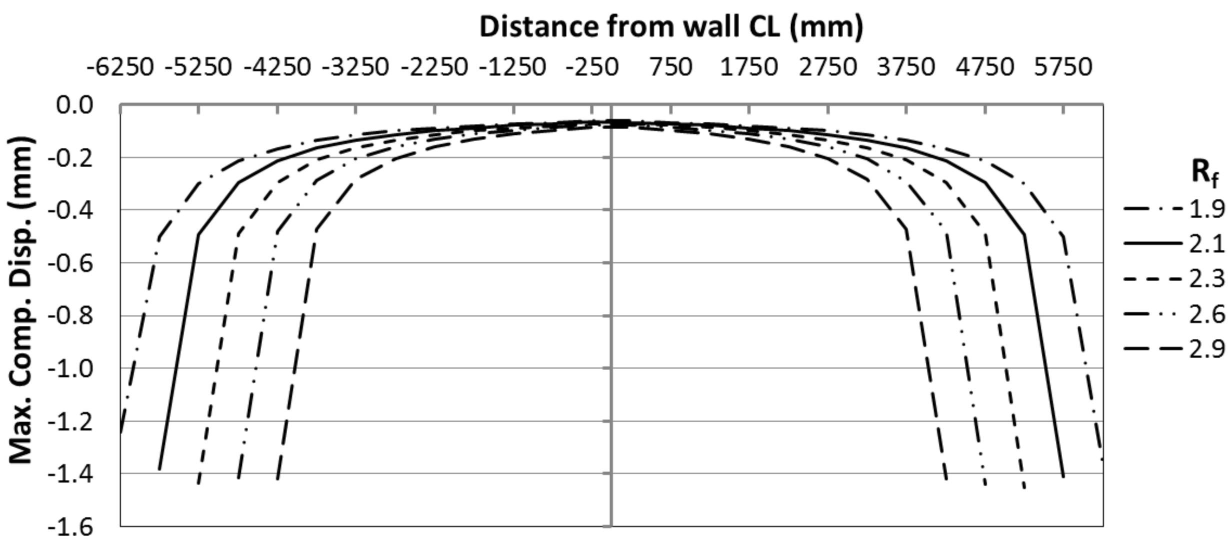

Figure A.263 Average of maximum soil compressive displacements underneath the footing for wall 10R17 on Rock

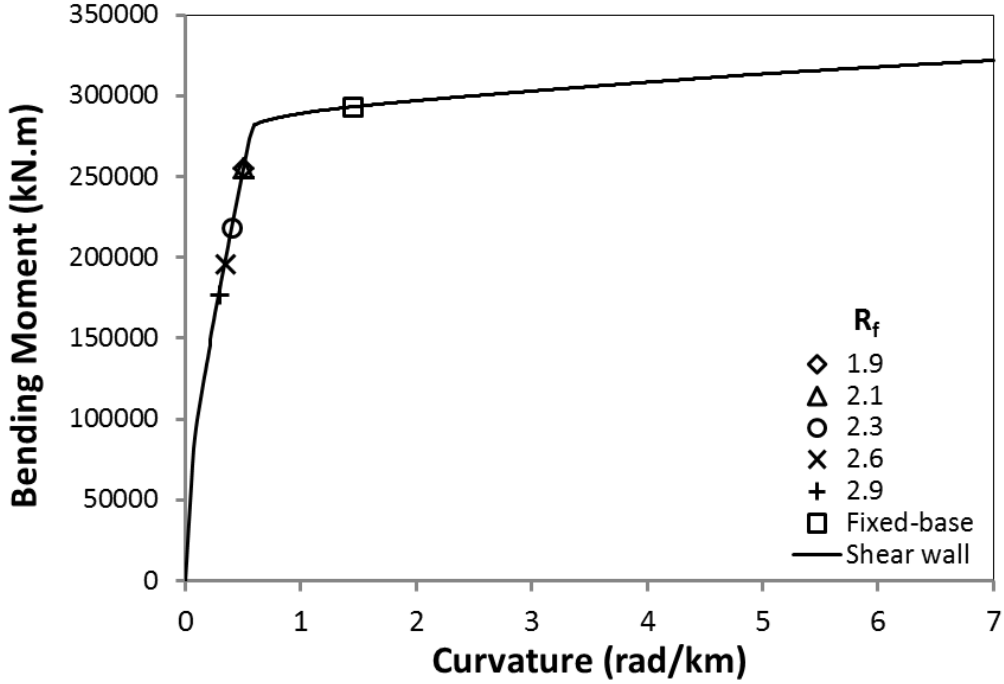

Figure A.264 Moment-curvature response of wall 10R17 along with average of maximum recorded curvatures at the base on Rock

Table A.76 Shear wall properties for wall 10R13

N	10
L_w (mm)	5500
P (kN)	41550
M_{RSA} (kN.m)	488000
M_y (kN.m)	369000
R_w	1.32

Table A.77 Summary of nonlinear dynamic analyses for wall 10R13 on Rock

R_f	1.3	1.7	1.9	2.1	2.3	2.6	2.9
E (MPa)	20000	20000	20000	20000	20000	20000	20000
G_{eff} (MPa)	8333	8333	8333	8333	8333	8333	8333
ν	0.2	0.2	0.2	0.2	0.2	0.2	0.2
q_a (kPa)	7000	7000	3000	3000	3000	3000	3000
q (kPa)	121	198	266	314	377	460	575
q_f (kPa)	10000	10000	10000	10000	10000	10000	10000
q_{ult} (kPa)	20000	20000	20000	20000	20000	20000	20000
L (m)	18.5	14.5	12.5	11.5	10.5	9.5	8.5
B (m)	18.5	14.5	12.5	11.5	10.5	9.5	8.5
a (mm)	225	287	332	361	396	437	489
s (mm)	0.02	0.02	0.06	0.06	0.07	0.07	0.08
M_{oc} (kN.m)	379672	295284	252782	231406	209917	188276	166432
θ_{oc} (rad)	0.0031	0.0028	0.0025	0.0023	0.0021	0.0018	0.0015
θ_y (rad)	0.0008	0.1000	0.1000	0.1000	0.1000	-----	-----
$T_{Estimate}$ (sec)	0.94	0.94	0.94	0.95	0.95	0.95	0.96
T_{model} (sec)	0.94	0.94	0.94	0.95	0.95	0.95	0.96
Δ_1 (mm)	7.1	15.2	25.4	29.2	32.2	44.4	53.5
Δ_{10} (mm)	157	180	232	253	264	334	391
Avg. Max. θ_b (rad)	0.0004	0.0025	0.0049	0.0058	0.0066	0.0094	0.0114
Avg. Max. Uplift (mm)	7.4	34.7	59.7	65.4	67.3	87.5	95.8
Avg. Max. Comp. Disp. (mm)	-0.7	-1.3	-1.5	-1.5	-1.5	-1.4	-1.4
Avg. Max. q_{max}/q_{ult}	9%	25%	33%	36%	40%	44%	49%

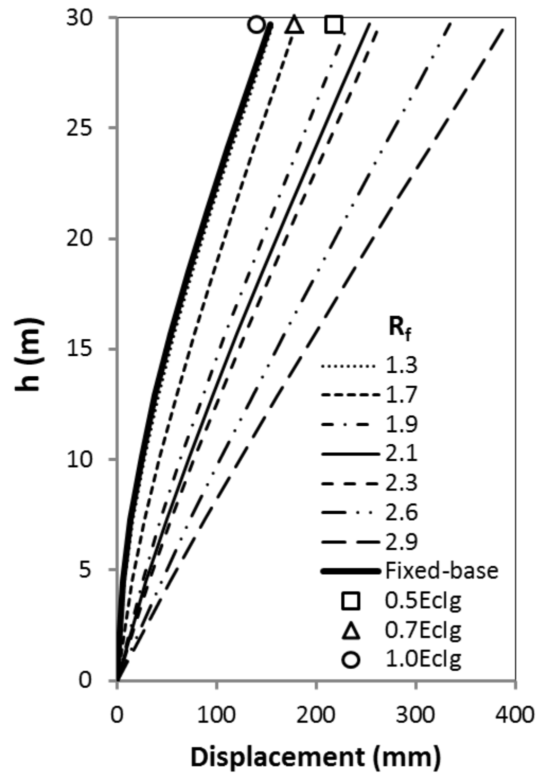

Figure A.265 Average of displacement envelopes for wall 10R13 on Rock along with estimated top displacements of the fixed-base wall from RSA using various effective stiffnesses

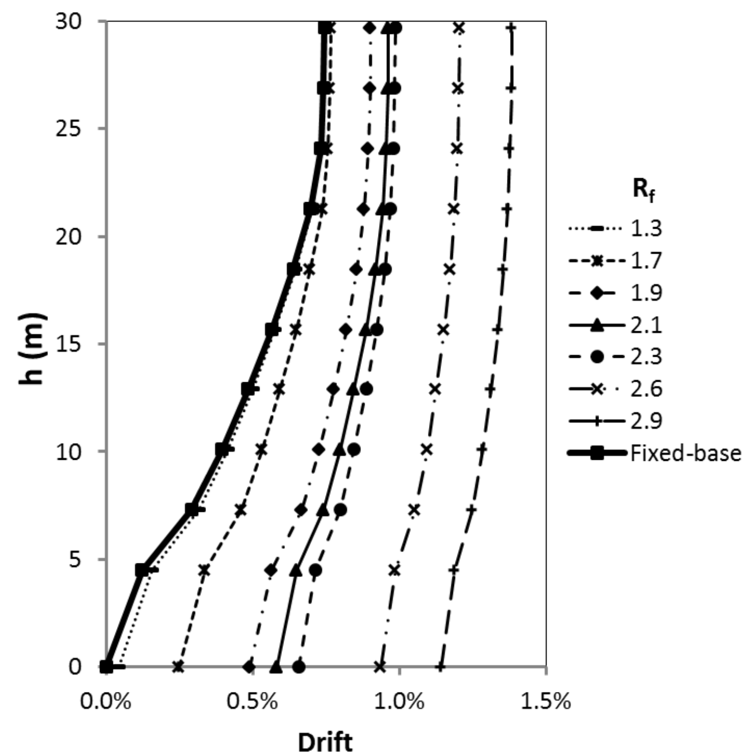

Figure A.266 Average of drift envelopes for wall 10R13 on Rock (Note: base rotation values are plotted at h=0 and values of average interstory drift are plotted at the top of the storey.)

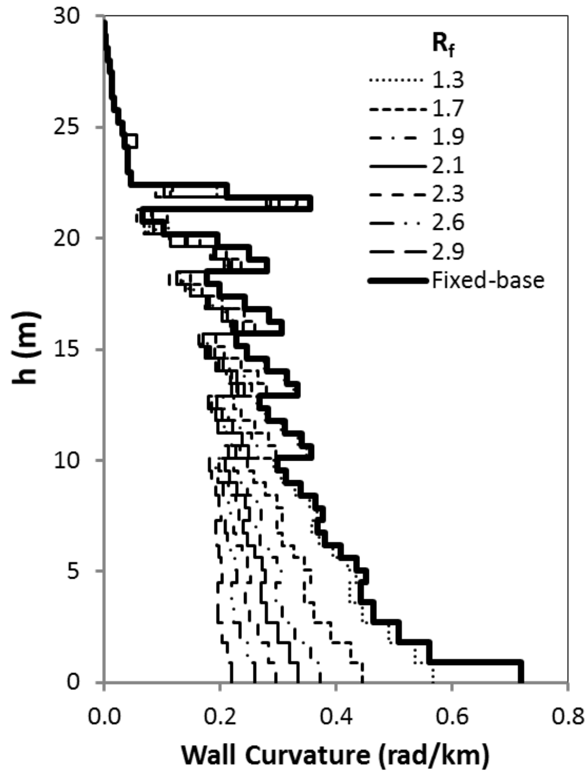

Figure A.267 Average of curvature envelopes for wall 10R13 on Rock

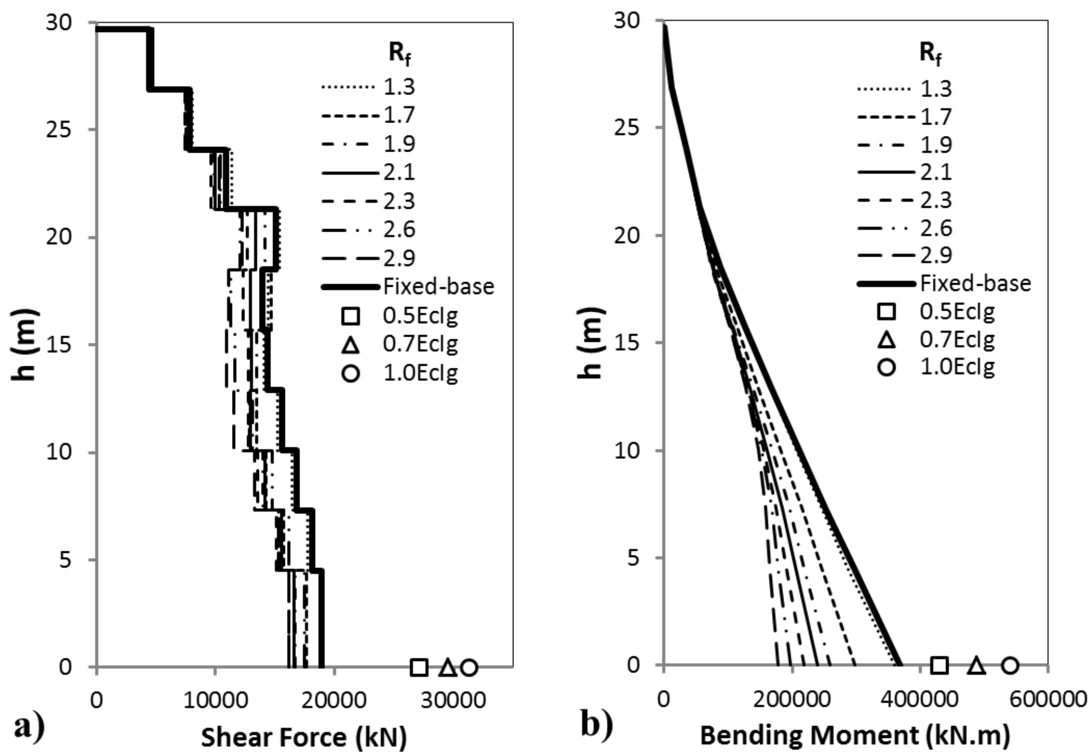

Figure A.268 Average of a) shear force, and b) bending moment envelopes for wall 10R13 on Rock along with estimated maximum quantities for the fixed-base wall from RSA using various effective stiffnesses

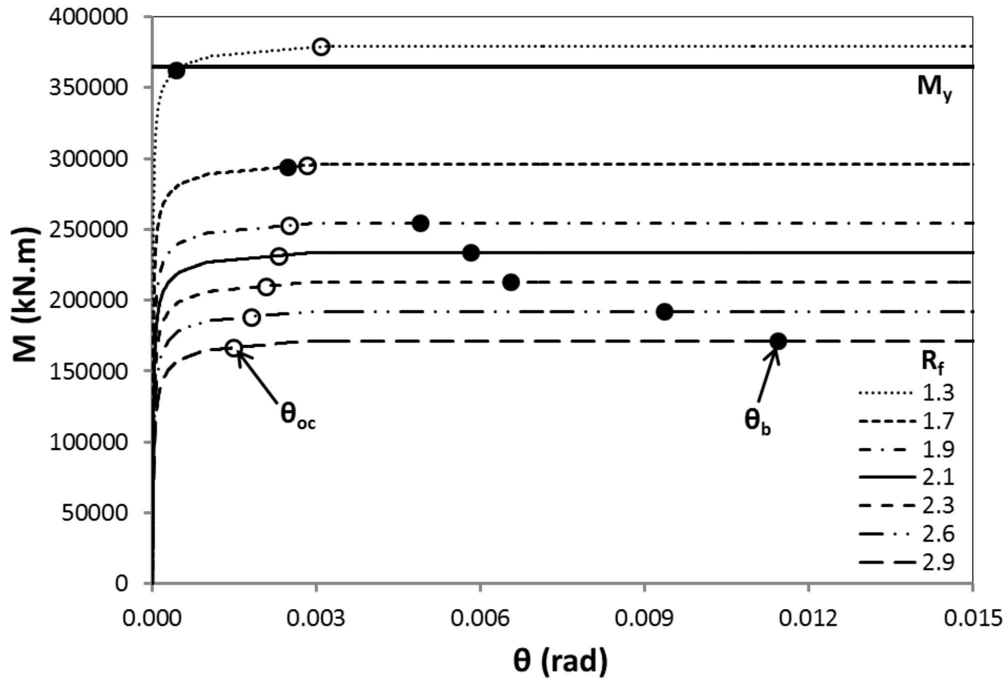

Figure A.269 Bending moment-rotation response of the foundation of wall 10R13 on Rock

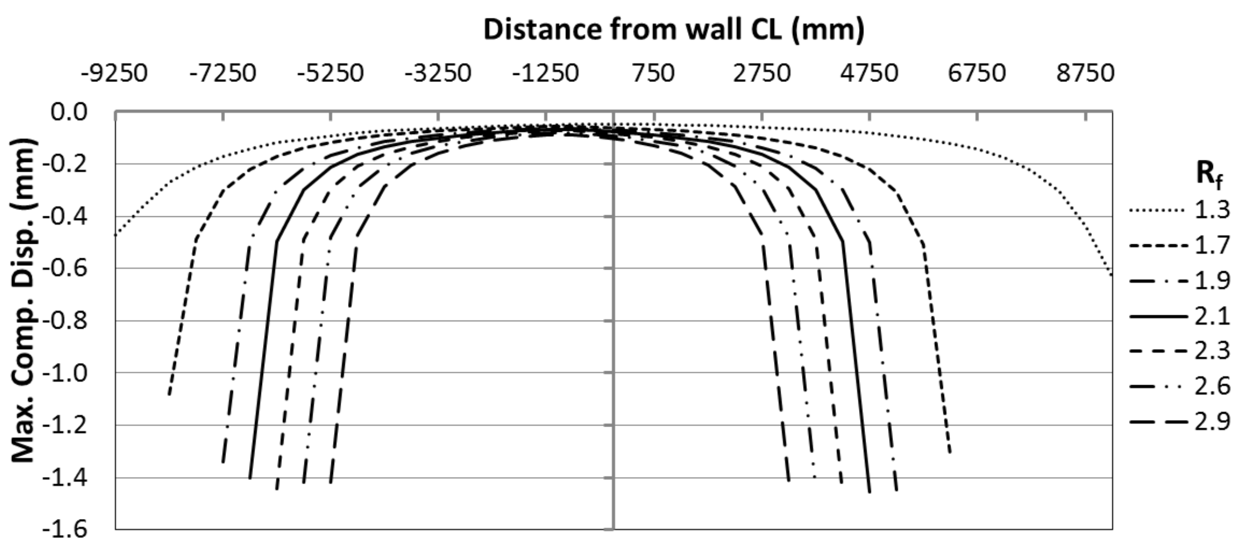

Figure A.270 Average of maximum soil compressive displacements underneath the footing for wall 10R13 on Rock

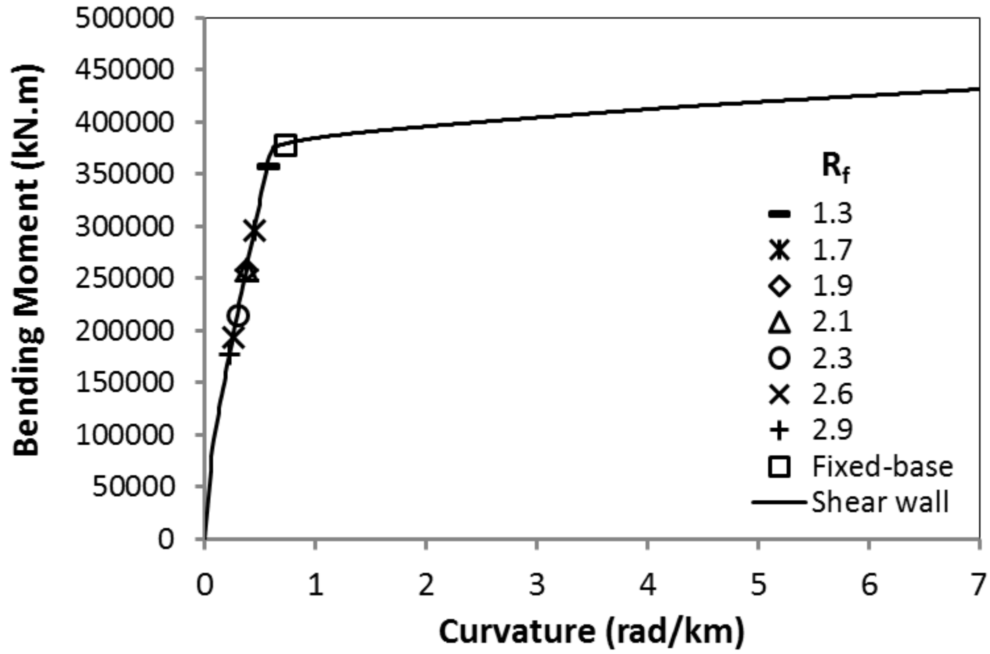

Figure A.271 Moment-curvature response of wall 10R13 along with average of maximum recorded curvatures at the base on Rock

Table A.78 Shear wall properties for wall 10Elastic

N	10
L_w (mm)	5500
P (kN)	41550
M_{RSA} (kN.m)	488000
M_y (kN.m)	-----
R_w	1.00

Table A.79 Summary of nonlinear dynamic analyses for wall 10Elastic on Rock

R_f	1.3	1.4	1.7	1.9	2.1	2.3	2.6
E (MPa)	20000	20000	20000	20000	20000	20000	20000
G_{eff} (MPa)	8333	8333	8333	8333	8333	8333	8333
ν	0.2	0.2	0.2	0.2	0.2	0.2	0.2
q_a (kPa)	267	267	267	7000	7000	7000	7000
q (kPa)	121	153	198	266	314	377	460
q_f (kPa)	10000	10000	10000	10000	10000	10000	10000
q_{ult} (kPa)	20000	20000	20000	20000	20000	20000	20000
L (m)	18.5	16.5	14.5	12.5	11.5	10.5	9.5
B (m)	18.5	16.5	14.5	12.5	11.5	10.5	9.5
a (mm)	225	252	287	332	361	396	437
s (mm)	0.01	0.02	0.02	0.06	0.06	0.07	0.07
M_{oc} (kN.m)	379672	337556	295284	252782	231406	209917	188276
θ_{oc} (rad)	0.0029	0.0028	0.0026	0.0025	0.0023	0.0021	0.0018
θ_y (rad)	-----	-----	-----	-----	-----	-----	-----
$T_{Estimate}$ (sec)	1.06	1.06	1.06	1.07	1.07	1.07	1.08
T_{model} (sec)	1.08	1.08	1.08	1.08	1.08	1.08	1.09
Δ_1 (mm)	16.3	19.9	33.3	42.0	45.6	48.2	52.7
Δ_{10} (mm)	182	199	278	326	343	358	386
Avg. Max. θ_b (rad)	0.0028	0.0037	0.0068	0.0088	0.0096	0.0102	0.0113
Avg. Max. Uplift (mm)	50.4	59.3	96.5	108.2	109.4	106.1	105.8
Avg. Max. Comp. Disp. (mm)	-1.4	-1.4	-1.4	-1.5	-1.5	-1.5	-1.4
Avg. Max. q_{max}/q_{ult}	21%	25%	29%	33%	36%	40%	44%

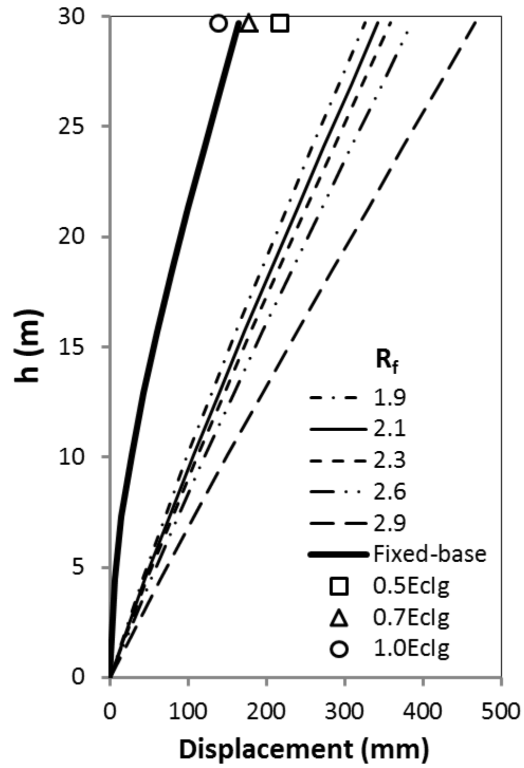

Figure A.272 Average of displacement envelopes for wall 10Elastic on Rock along with estimated top displacements of the fixed-base wall from RSA using various effective stiffnesses

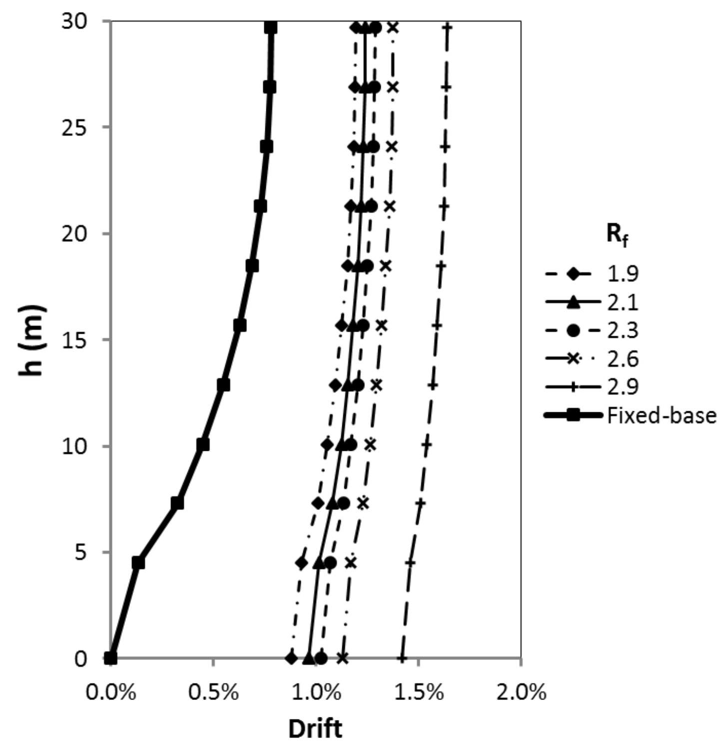

Figure A.273 Average of drift envelopes for wall 10Elastic on Rock (Note: base rotation values are plotted at h=0 and values of average interstory drift are plotted at the top of the storey.)

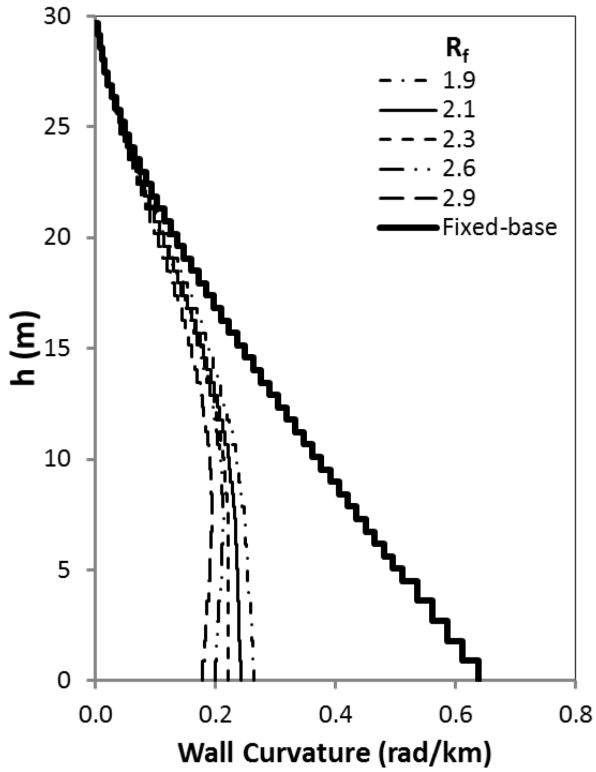

Figure A.274 Average of curvature envelopes for wall 10Elastic on Rock

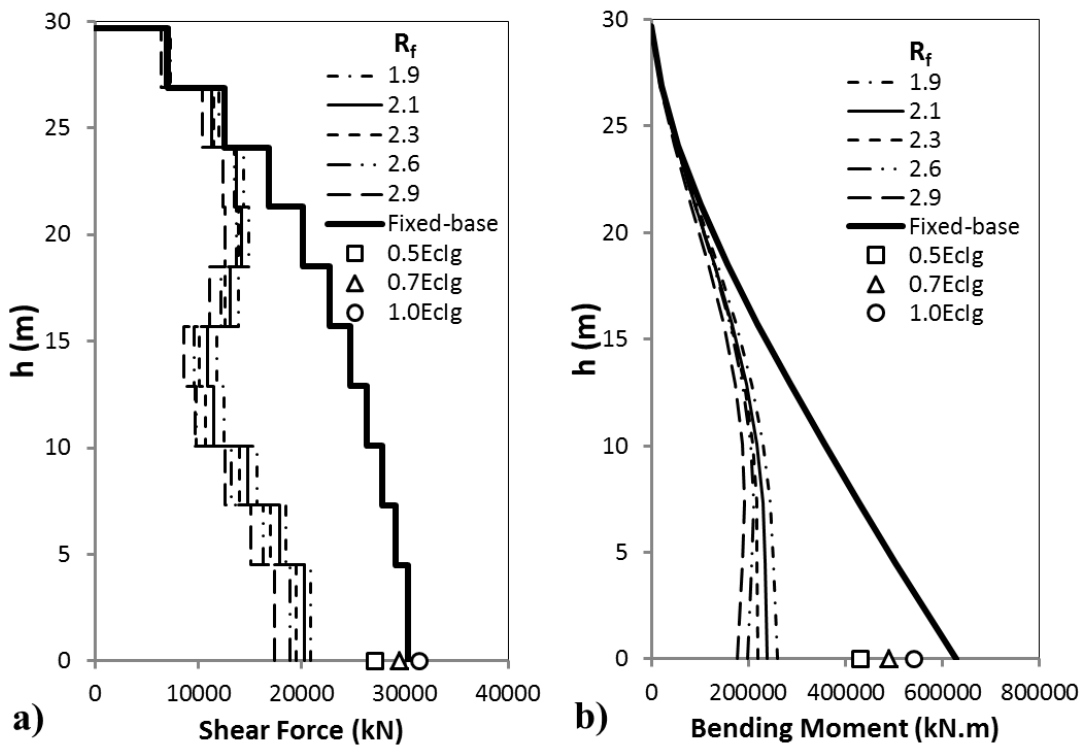

Figure A.275 Average of a) shear force, and b) bending moment envelopes for wall 10Elastic on Rock along with estimated maximum quantities for the fixed-base wall from RSA using various effective stiffnesses

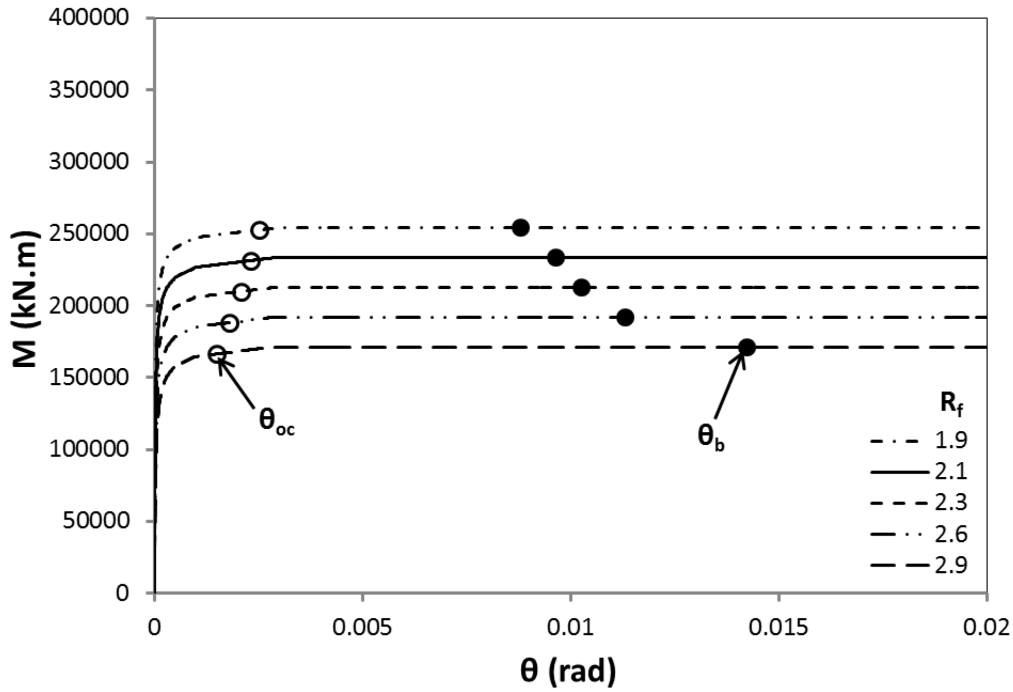

Figure A.276 Bending moment-rotation response of the foundation of wall 10Elastic on Rock

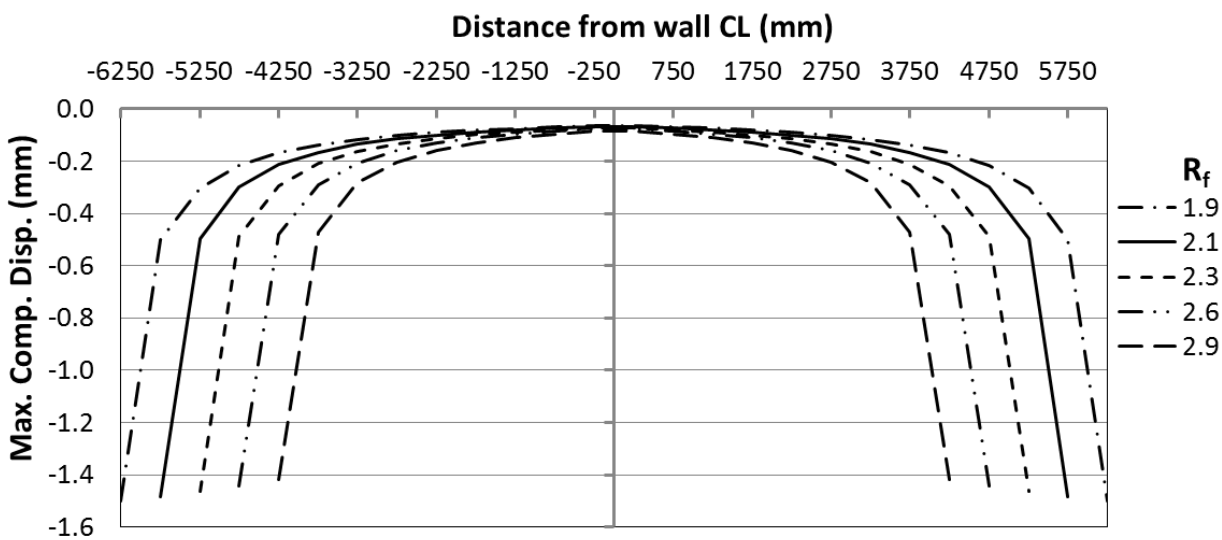

Figure A.277 Average of maximum soil compressive displacements underneath the footing for wall 10Elastic on Rock

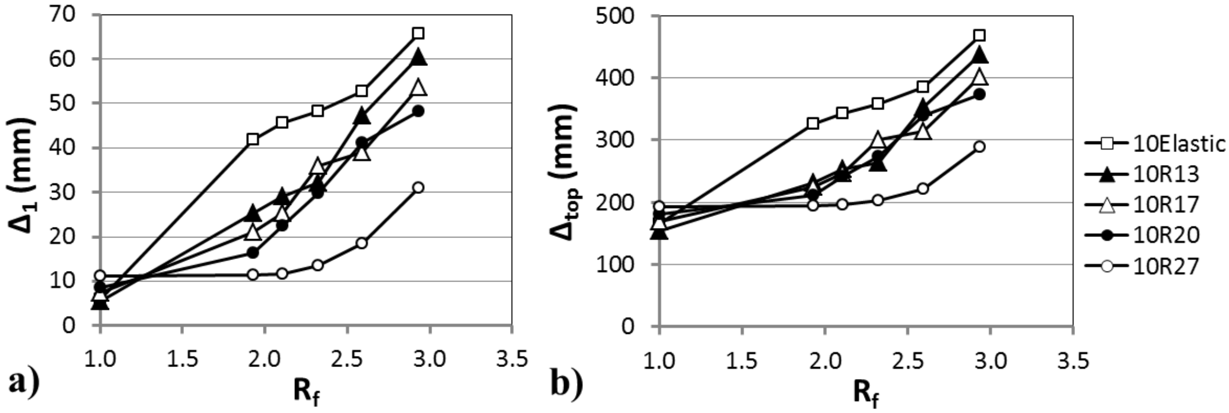

Figure A.278 Summary of average maximum a) first storey displacements, and b) top displacements for 10 storey walls on Rock sorted by wall strength

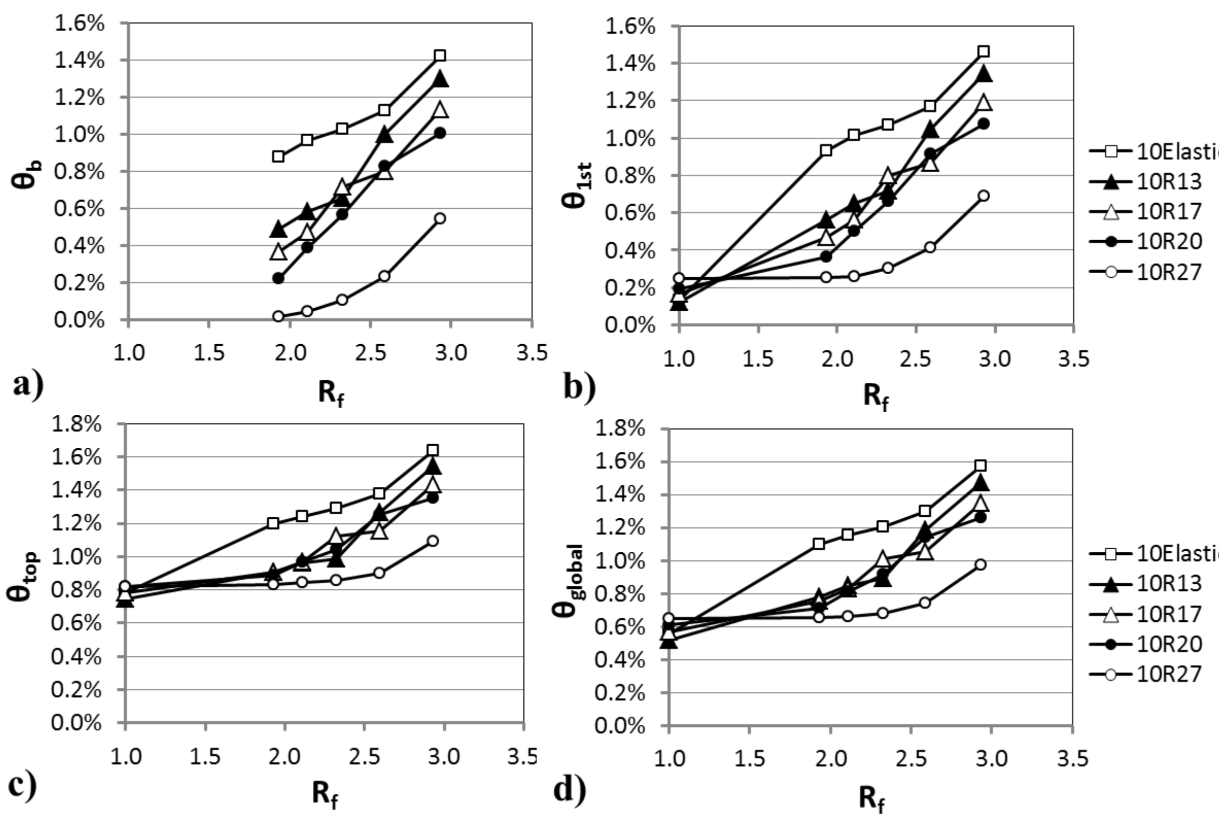

Figure A.279 Summary of average maximum a) base rotations, b) 1st storey inter-storey drifts, c) top storey inter-storey drifts, and d) global drifts of 10 storey walls on Rock sorted by wall strength

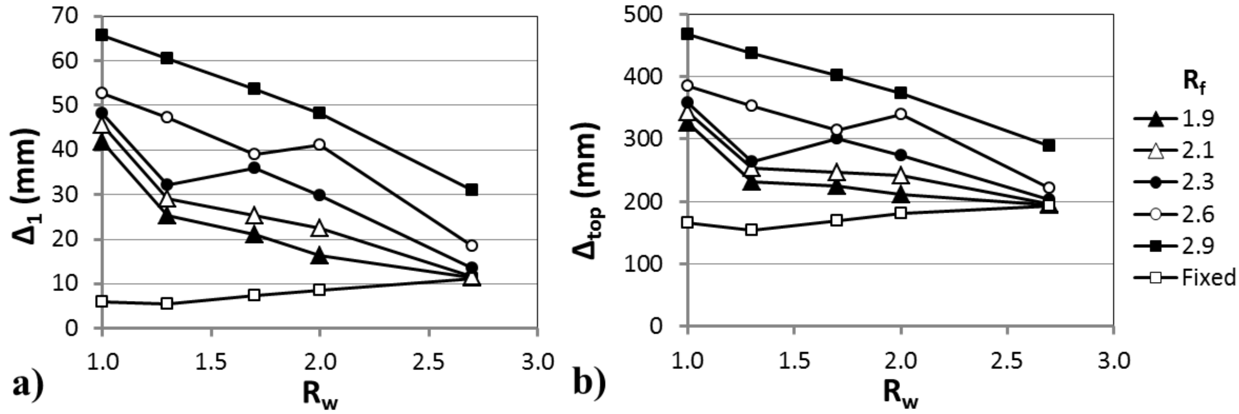

Figure A.280 Summary of average maximum a) first storey displacements, and b) top displacements for 10 storey walls on Rock sorted by foundation size

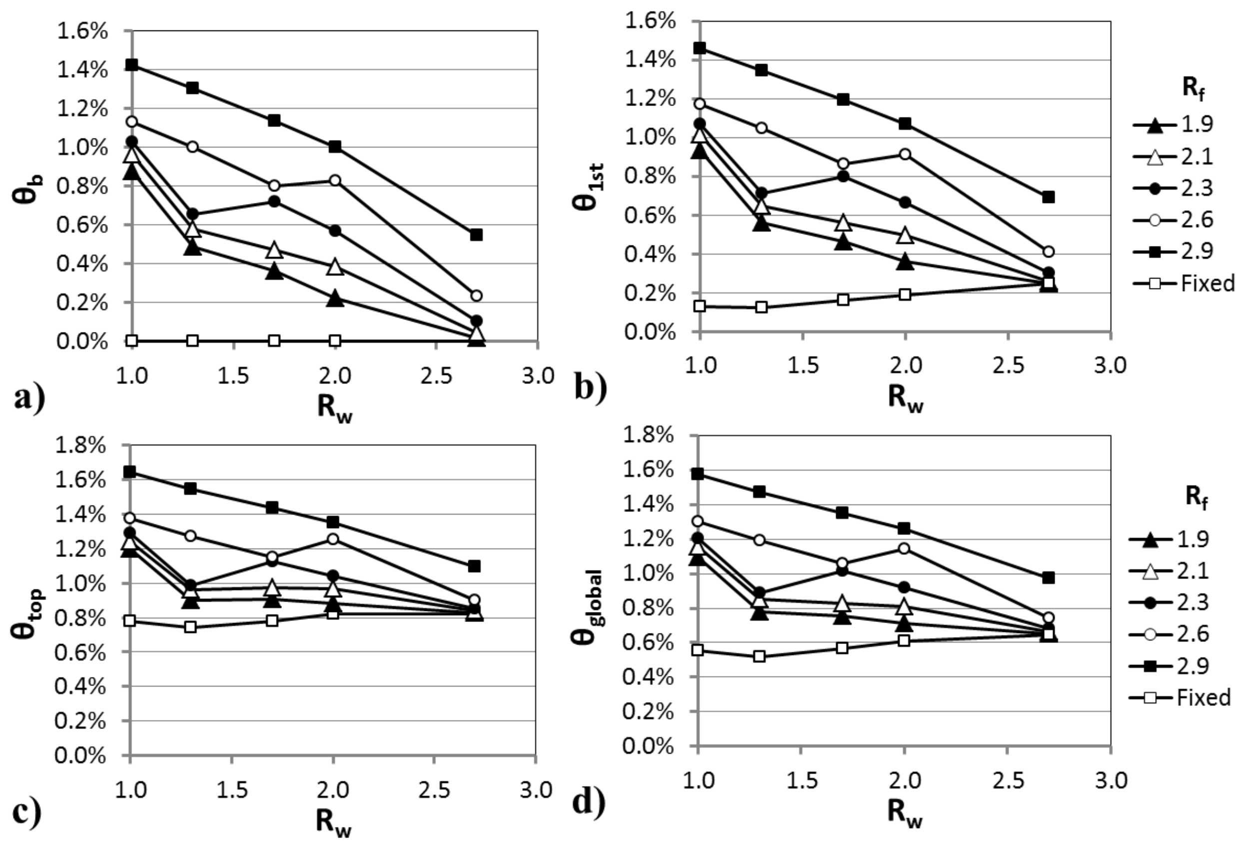

Figure A.281 Summary of average maximum a) base rotations, b) 1st storey inter-storey drifts, c) top storey inter-storey drifts, and d) global drifts of 10 storey walls on Rock sorted by foundation size

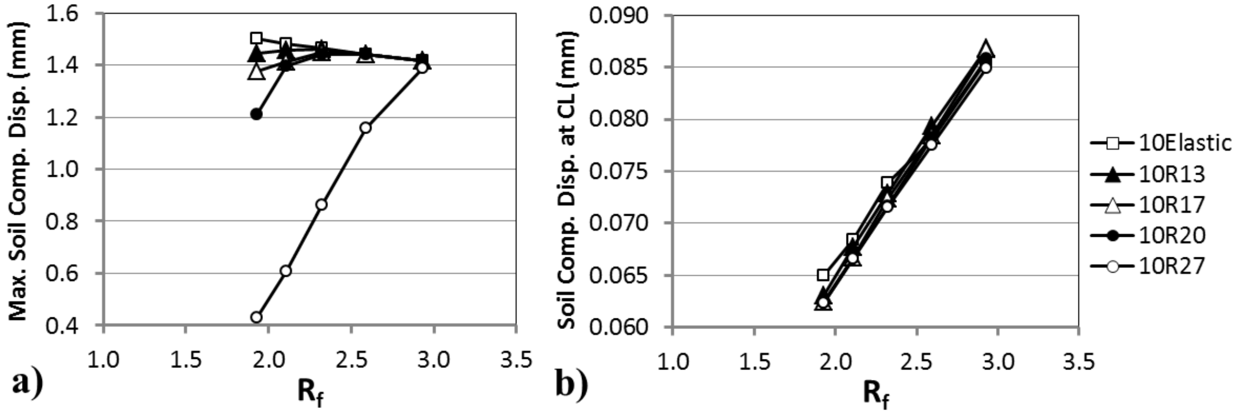

Figure A.282 Summary of average maximum soil compressive displacement at a) foundation toe, and b) foundation centreline for 10 storey walls on Rock sorted by wall strength

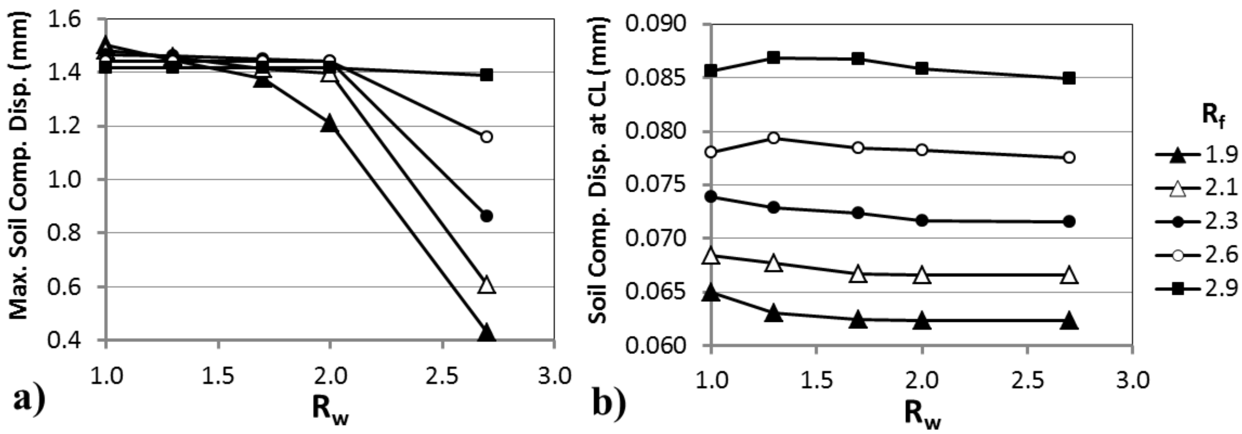

Figure A.283 Summary of average maximum soil compressive displacement at a) foundation toe, and b) foundation centreline for 10 storey walls on Rock sorted by foundation size

A.7 Example Estimated Foundation Moment-rotation Response

A.7.1 19.0 m square foundation on clay

Step-by-step calculations required for estimating the envelope of the moment-rotation response of a 19.0 m square foundation on Clay supporting an axial load of 41550 kN are demonstrated in this section.

The elastic rotational stiffness of the foundation is first calculated using Gazetas' formulation shown below. Table A.80 gives a summary of parameters used to evaluate the elastic rotational stiffness.

$$\mathrm{K}_{\theta y} = \mathrm{e}_{\theta y}\mathrm{K'}_{\theta y}$$

$$\mathrm{e}_{\theta y} = 1 + 0.92\left(\frac{2\mathrm{d}}{\mathrm{L}}\right)^{0.62}\left[1.5 + \left(\frac{2\mathrm{d}}{\mathrm{L}}\right)^{1.9}\left(\frac{\mathrm{d}}{\mathrm{D}}\right)^{-0.60}\right]$$

$$\mathrm{K'}_{\theta y} = \frac{G_{eff}}{1-\nu}\mathrm{I}_{\mathrm{y}}^{0.75}\left[3\left(\frac{\mathrm{L}}{\mathrm{B}}\right)^{0.15}\right]$$

Where

$$\mathrm{I}_{\mathrm{y}} = \frac{\mathrm{BL}^3}{12}$$

The soil reaction modulus and Z_{50} can then be calculated as follows.

$$\mathrm{k}_{\theta} = \frac{\mathrm{K}_{\theta y}}{\mathrm{I}_{\mathrm{y}}} = 14111\ \frac{\mathrm{kN/m^2}}{\mathrm{m}}$$

$$\mathrm{Z}_{50} = \frac{\mathrm{q}_{\mathrm{ult}}}{2\mathrm{k}_{\theta}} = \frac{400\ \mathrm{kPa}}{2\mathrm{k}_{\theta}} = 14.17\ \mathrm{mm}$$

The next step is to determine the elastic response limit.

$$\mathrm{q}_{\max} = \frac{2\mathrm{P}}{\mathrm{BL}} = \frac{2\times 41550\ \mathrm{kN}}{19\times 19\ \mathrm{m^2}} = 230\ \mathrm{kPa}$$

Table A.80 Summary of parameters needed to evaluate the elastic rotational stiffness of the foundation using Gazetas' formulation

G_0 (MPa)	43
G_{eff} (MPa)	22
v	0.3
L (m)	19.0
B (m)	19.0
D (m)	2.0
d (m)	2.0
I_y (m^4)	10860
$k'_{\theta y}$ (kN.m/rad)	9.820E+07
$e_{\theta y}$	1.56
$K_{\theta y}$ (kN.m/rad)	1.532E+08

Since q_{max} is greater than $0.2q_{ult}$=80 kPa, soil nonlinear behaviour will occur before foundation lift-off. Therefore, the elastic response limit would be

$$\theta_{elastic} = \frac{2}{L}\left[\frac{0.20q_{ult}}{k_\theta} - \frac{P}{k_\theta BL}\right] = -0.00026 \text{ rad}$$

The elastic response limit has been calculated as a negative number. This is because the uniform bearing pressure underneath the foundation under the action of the vertical load alone is 115 kPa which is larger than the elastic limit of the Clay QzSimple1 material. Therefore, in this case, the elastic response range is non-existent. In other words, nonlinear soil response is encountered as soon as the vertical load is applied on the foundation.

The equivalent rectangular stress block concept is used, to obtain a few points on the moment-rotation response in the nonlinear range. An arbitrary value of $\frac{q_{unif.}}{q_{ult}}$ is chosen and the uniform stress block depth is calculated from vertical force equilibrium as follows.

$$a = \frac{P}{B \times q_{unif.}}$$

The eccentricity of the resultant soil bearing pressure will be

$$e = \frac{L - a}{2}$$

Multiplying the resultant force by the eccentricity will then give the bending moment for the chosen $\frac{q_{unif.}}{q_{ult}}$. The foundation rotation for the chosen $\frac{q_{unif.}}{q_{ult}}$ is obtained as follows.

$$\theta = \frac{Z_{max}}{c} = \beta\gamma\frac{Z_{50}}{a}$$

β and γ are equivalent uniform stress block parameters defined and given in the body of the thesis. A number of $\frac{q_{unif.}}{q_{ult}}$ have to be chosen and the few steps above repeated to accurately trace the moment-rotation envelope. Bending moment can be considered to be constant after $\frac{q_{unif.}}{q_{ult}} = 0.95$. Table A.81 summarizes the parameters used to predict the moment-rotation response of the foundation in the nonlinear range. The data points along with the elastic response range are plotted in Figure A.248 and compared with the response obtained from OpenSees.

Table A.81 Summary of predicting foundation moment-rotation response in the nonlinear range

$q_{unif.}/q_{ult}$	α	β	γ	a (m)	e (m)	θ (rad)	M (kN.m)
0.50	0.79	0.70	1.54	10.93	4.03	0.00139	167567
0.70	0.84	0.73	2.55	7.81	5.59	0.00337	232469
0.85	0.91	0.78	4.28	6.43	6.28	0.00737	261103
0.95	0.97	0.87	9.33	5.75	6.62	0.02001	275168

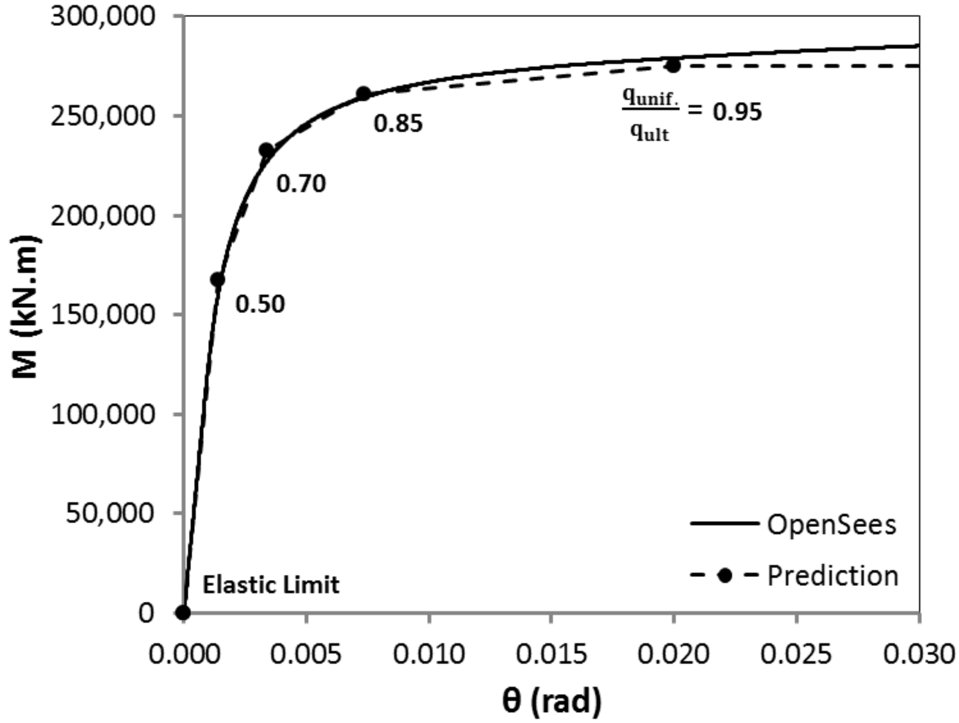

Figure A.284 Estimated moment-rotation envelope response of a 19.0 m square footing on Clay carrying an axial load of 41550 kN

A.7.2 15.0 m square footing on Medium Sand

Step-by-step calculations required for estimating the envelope of the moment-rotation response of a 15.0 m square foundation on Medium Sand supporting an axial load of 41550 kN are demonstrated in this section. Because the procedure is similar to that for the clay foundation in the previous section, some details are eliminated for brevity.

Table A.82 summarizes the parameters used to solve for the moment-rotation response of the foundation in the elastic range. Note that for Sand, G_0, the initial (or small strain) soil shear modulus of elasticity is 2.65 times G_{eff}. This is reflective of the realistic behaviour of sand type soils. The soil reaction modulus and Z_{50} can then be calculated as follows.

$$k_\theta = \frac{K_{\theta y}}{I_y} = 61725 \ \frac{kN/m^2}{m}$$

$$Z_{50} = \frac{q_{ult}}{2k_\theta} = \frac{800\ \text{kPa}}{2k_\theta} = 6.48\ \text{mm}$$

Table A.82 Summary of parameters needed to evaluate the elastic rotational stiffness of the foundation using Gazetas' formulation

G_0 (MPa)	186
G_{eff} (MPa)	70
v	0.3
L (m)	15.0
B (m)	15.0
D (m)	2.0
d (m)	2.0
I_y (m^4)	4219
$k'_{\theta y}$ (kN.m/rad)	1.570E+08
$e_{\theta y}$	1.66
$K_{\theta y}$ (kN.m/rad)	2.604E+08

The next step is to determine the elastic response limit.

$$q_{max} = \frac{2P}{BL} = \frac{41550\ \text{kN}}{15 \times 15\ \text{m}^2} = 369\ \text{kPa}$$

Since q_{max} is greater than $0.3q_{ult}$=240 kPa, soil nonlinear behaviour will precede foundation lift-off. Therefore, the elastic response limit would be

$$\theta_{elastic} = \frac{2}{L}\left[\frac{0.30q_{ult}}{k_\theta} - \frac{P}{k_\theta BL}\right] = 0.000045\ \text{rad}$$

The bending moment at the elastic response limit would then be

$$M_{elastic} = 2.65K_{\theta y} \cdot \theta_{elastic} = 31125\ \text{kN.m}$$

The data points used to estimate the moment-rotation response in the inelastic range are summarized in Table A.83. Figure A.285 compares the predicted moment-rotation response with that obtained from OpenSees.

Table A.83 Summary of predicting foundation moment-rotation response in the nonlinear range

$q_{unif.}/q_{ult}$	α	β	γ	a (m)	e (m)	θ (rad)	M (kN.m)
0.40	0.88	0.82	0.91	8.66	3.17	0.000557	131791
0.55	0.85	0.83	2.08	6.30	4.35	0.001773	180837
0.70	0.87	0.83	3.83	4.95	5.03	0.004185	208863
0.85	0.91	0.85	7.31	4.07	5.46	0.009937	226997
0.95	0.96	0.90	14.91	3.64	5.68	0.023752	235906

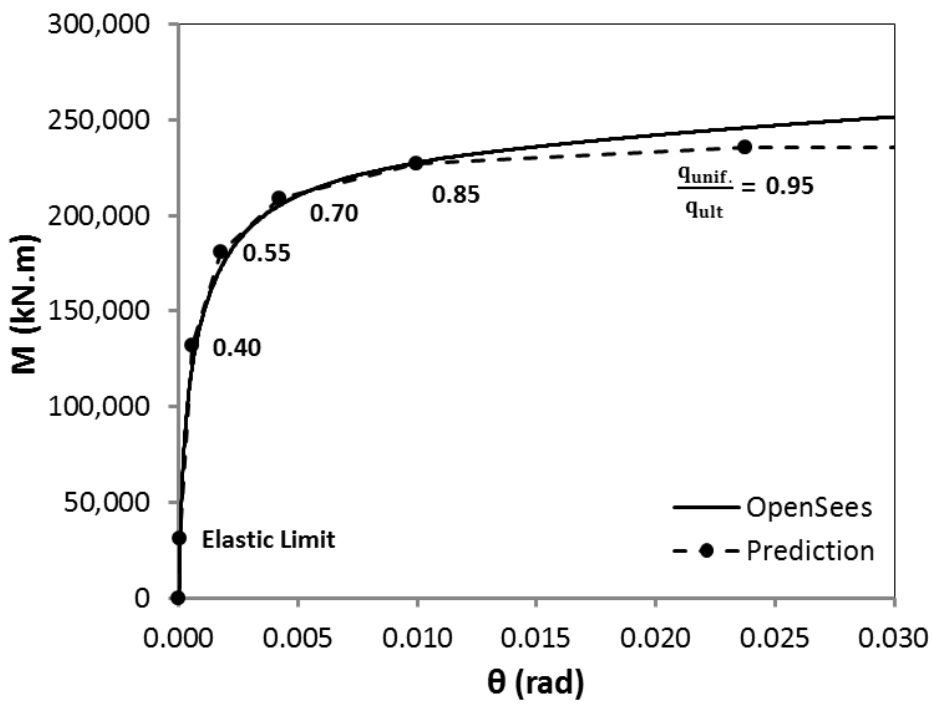

Figure A.285 Estimated moment-rotation envelope response of a 15.0 m square footing on Medium Sand carrying an axial load of 41550 kN

Appendix B Calculations for Probable Seismic Compressive Axial Force on Gravity-load Columns based on Provisions of NBCC 2005

Source of Load	Residential	Office
Mechanical Equipment (KPa)	0.25	0.5
Live Load (LL) (KPa)	1.9	3.1
Partitions (KPa)	0.5	1.0
Partial Dead Load (DL)[1] (KPa)	**0.75**	**1.5**
Total LL per Storey[2] (KPa)	**1.9**	**3.1**

1. = mechanical equipment + partitions

2. = Live Load (LL)

# of Storeys	Column Dimension (cm)	Column Self Weight per Storey[1] (KN)
10	40	**11.00**
30	75	**38.67**
50	100	**68.75**

1. = (column dimension cm / 100)^2 x 2.75 m x 25 KN/m^3

Slab Thickness (in)	**7**	**10**
Probable Span[1] (m)	5.33	7.62
Column Tributary Area[2] (m^2)	28.45	58.06
Slab Dead Load[3] (KPa)	**4.45**	**6.35**

1. = slab thickness (in) x 2.54/100 (m/in) x 30
2. = probable span (m) x probable span (m)
3. = slab thickness x 2.54/100 (m) x 25 (KN/m^3)

		Residential		**Office**	
		Slab Thickness (in)		Slab Thickness (in)	
	Total LL[1] (KN)	**7**	**10**	**7**	**10**
# of Storeys	**10**	541	1103	882	1800
	30	1622	3310	2646	5400
	50	2703	5516	4410	9000

1. = total LL per storey (KPa) x # of storeys x column tributary area (m^2)

	Total DL[1] (KN)	Residential Slab Thickness (in) 7	Residential Slab Thickness (in) 10	Office Slab Thickness (in) 7	Office Slab Thickness (in) 10
# of Storeys	10	1588	4233	1801	4668
	30	5594	13528	6234	14834
	50	10828	24050	11895	26228

1. = ((partial DL +slab DL) x column tributary area + column self weight) x # of storeys

	Gravity Load Combination[1,2] (KN)	Residential Slab Thickness (in) 7	Residential Slab Thickness (in) 10	Office Slab Thickness (in) 7	Office Slab Thickness (in) 10
# of Storeys	10	2379	6002	2894	6996
	30	7983	18939	9409	21580
	50	15159	33671	17402	37619

1. NBCC 2005 Table 4.1.3.2.
2. = max{ 1.4DL , 1.25DL + 1.5LL}

	LL Reduction Factor[1]	Residential Slab Thickness (in) 7	Residential Slab Thickness (in) 10	Office Slab Thickness (in) 7	Office Slab Thickness (in) 10
# of Storeys	10	0.49	0.43	0.49	0.43
	30	0.41	0.38	0.41	0.38
	50	0.38	0.36	0.38	0.36

1 = $0.3 + (9.8 / (\# \text{ of storeys} \times \text{column tributary area } (m^2)))^{1/2}$

	Seismic Load Combination[1,2] (KN)	Residential Slab Thickness (in) 7	Residential Slab Thickness (in) 10	Office Slab Thickness (in) 7	Office Slab Thickness (in) 10
# of Storeys	10	1719	4470	2016	5055
	30	5924	14148	6773	15847
	50	11345	25038	12739	27839

1. NBCC 2005 Table 4.1.3.2.
2. = 1.0DL + 0.5LL x LL reduction factor

	P_S[1] / Pr_{max}[2,3]	Residential Slab Thickness (in) 7	Residential Slab Thickness (in) 10	Office Slab Thickness (in) 7	Office Slab Thickness (in) 10
# of Storeys	10	72%	74%	70%	72%
	30	74%	75%	72%	73%
	50	75%	74%	73%	74%

1. = seismic load combination (KN)
2. CSA Standard A23.3-04 Equations (10-8), (10-9), and (10-10)
3. = specified maximum axial load resistance = gravity load combination (KN)

Appendix C Calculations for Probable Seismic Compressive Axial Force on Gravity-load Columns based on Provisions of ASCE 7-05

Source of Load	Residential	Office
Mechanical Equipment (KPa)	0.25	0.5
Live Load (LL) (KPa)	1.92	3.1
Partitions (KPa)	0.72	1.0
Partial Dead Load (DL)[1] (KPa)	**0.25**	**0.5**
Total LL per Storey[2] (KPa)	**2.64**	**4.1**

1. = mechanical equipment
2. = Live Load (LL) + Partitions

# of Storeys	Column Dimension (cm)	**Column Self Weight per Storey[1] (KN)**
10	40	**11.00**
30	75	**38.67**
50	100	**68.75**

1. = (column dimension cm / 100)^2 x 2.75 m x 25 KN/m^3

Slab Thickness (in)	**7**	**10**
Probable Span[1] (m)	5.33	7.62
Column Tributary Area[2] (m^2)	28.45	58.06
Slab Dead Load[3] (KPa)	**4.45**	**6.35**

1. = slab thickness (in) x 2.54/100 (m/in) x 30
2. = probable span (m) x probable span (m)
3. = slab thickness x 2.54/100 (m) x 25 (KN/m^3)

		Residential		**Office**	
		Slab Thickness (in)		Slab Thickness (in)	
	Total LL[1] (KN)	**7**	**10**	**7**	**10**
# of Stories	**10**	751	1533	1167	2381
	30	2253	4599	3500	7142
	50	3756	7665	5833	11903

1. = total LL per storey (KPa) x # of storeys x column tributary area (m^2)

	Total DL[1] (KN)	Residential Slab Thickness (in) 7	Residential Slab Thickness (in) 10	Office Slab Thickness (in) 7	Office Slab Thickness (in) 10
# of Stories	10	1446	3942	1517	4087
	30	5168	12657	5381	13092
	50	10117	22599	10472	23325

1. = ((partial DL +slab DL) x column tributary area + column self weight) x # of storeys

	Gravity Load Combination[1,2] (KN)	Residential Slab Thickness (in) 7	Residential Slab Thickness (in) 10	Office Slab Thickness (in) 7	Office Slab Thickness (in) 10
# of Stories	10	2216	5712	2567	6429
	30	7643	18131	8697	20282
	50	14543	32024	16299	35608

1. ASCE 7-05 2.3.2.
2. = max{ 1.4DL , 1.2DL + 1.6LL}

	LL Reduction Factor[1,2]	Residential Slab Thickness (in) 7	Residential Slab Thickness (in) 10	Office Slab Thickness (in) 7	Office Slab Thickness (in) 10
# of Stories	10	0.40	0.40	0.40	0.40
	30	0.40	0.40	0.40	0.40
	50	0.40	0.40	0.40	0.40

1. ASCE 7-05 4.8.1.
2. = max{0.25 + 4.57/(4 x column tributary area (m2) x # of storeys) , 0.40}

	Seismic Load Combination[1,2] (KN)	Residential Slab Thickness (in) 7	Residential Slab Thickness (in) 10	Office Slab Thickness (in) 7	Office Slab Thickness (in) 10
# of Stories	10	1885	5037	2054	5381
	30	6652	16108	7157	17139
	50	12891	28651	13733	30370

1. ASCE 7-05 2.3.2.
2. = 1.2DL + 0.5LL

	$P_S{}^{1} / Pr_{max}{}^{2,3}$	Residential Slab Thickness (in) 7	Residential Slab Thickness (in) 10	Office Slab Thickness (in) 7	Office Slab Thickness (in) 10
# of Stories	10	85%	88%	80%	84%
	30	87%	89%	82%	85%
	50	89%	89%	84%	85%

1. = seismic load combination (KN)
2. CSA Standard A23.3-04 Equations (10-8), (10-9), and (10-10)
3. = specified maximum axial load resistance = gravity load combination (KN)

Appendix D Mathematical Presentation of the Nonlinear Structural Analysis Algorithm used to Analyze Gravity-load Columns under Imposed Lateral Deformations

The column is connected to the shear wall at storey levels. If the slab is thought of as a rigid link, it exerts a lateral horizontal storey force (P_i) on the column causing it to undergo the same deformation as that of the shear wall at that floor slab levels. The storey forces then produce bending moments (M) along the column height and from the bending moment diagram, the curvature (Φ) profile can be obtained knowing the moment-curvature behaviour of the column. Neglecting shear deformation of the column, curvatures can then be integrated to obtain the displacement profile along the height of the column as follows.

$$\Delta(x) = \int_0^x \Phi(x).(H - x)\ dx$$

The column can be divided into several equally sized elements along the height of each storey to facilitate numerical integration. Curvature is considered to be constant over the height of the element and is computed using the bending moment at elements' mid-height. The problem in hand will then be finding the set of storey forces (P_i) which produce the target displacements at corresponding floor slab levels.

Floor displacements (Δ_i) are considered to be a function of storey shears (V_i) as follows.

$$\Delta_i = F_i(V_1,V_2,V_3,V_4,V_5)$$

A first order Taylor series expansion is applied to the floor displacements (Δ_i) and multi-variant Newton-Raphson iteration procedure is adapted to solve for the unknown storey shears (V_i) which will result in the desired target displacement profile. The following set of equations explains the iteration procedure for a 5-storey building. Note that i and j can assume any integer from 1 to 5.

$$\Delta_i^{t+1} = \Delta_i^t + \sum_{j=1}^{5} \frac{\partial Fi}{\partial Vj}|V_j^t \, (V_j^{t+1} - V_j^t)$$

Rearranging the equation above gives,

$$\sum_{j=1}^{5} \frac{\partial Fi}{\partial Vj}|V_j^t \, V_j^{t+1} = \Delta_i^{t+1} - \Delta_i^t + \sum_{j=1}^{5} \frac{\partial Fi}{\partial Vj}|V_j^t \, V_j^t$$

In a matrix format, the equation above can be written as

$$[K_{ij}][V_j]=[C_j]$$

Where

$[K_{ij}]$ is a 5x5 matrix containing the derivatives of the storey displacements with respect to storey shear forces at step “t”

$[V_j]$ is the 5x1 vector of storey shear forces

$[C_j]$ is the 5x1 vector of constants from $\Delta_i^{t+1} - \Delta_i^t + \sum_{j=1}^{5} \frac{\partial Fi}{\partial Vj}|V_j^t \, V_j^t$

To solve for the revised storey forces, the equation above can be rearranged as

$$[V_j]= [K_{ij}]^{-1} [C_j]$$

Analysis is triggered at an arbitrary storey shear values V_i^t (e.g. linearly varying storey shear forces along the height of the structure). At each step, the derivatives of the storey displacements with respect to each floor shear force ($\frac{\partial Fi}{\partial Vj}$) are found numerically, that is, a unit (e.g. 1 kN) shift is applied to each storey shear in turn and the variation in each floor displacement value is calculated respectively (the fundamental definition of the derivative). Revised storey shears V_i^{t+1} are then used to calculate the displacements and iteration process is carried on until acceptable convergence accuracy is achieved. The algorithm is designed to take an approximate fifth-order polynomial as the input moment-curvature response of a column and run a pushover analysis by increasing storey displacements simulating the lateral deformation profile of a shear-wall pushed with a point-load at the top. A point-load at the top of the wall will result in a linear moment profile and since the moment-curvature relationship for shear-walls can be approximated by a bilinear curve especially at low axial loads, a bilinear curvature profile along the height of the wall. As the point-load at the top of the wall increases, maximum curvature at the base of the wall increases until it reaches the “yield” curvature. When the load is further increased, curvatures in the plastic hinge zone of the wall keep increasing while the elastic curvatures above remain nearly unchanged. Maximum curvature at the base of the wall is increased until the column fails by concrete crushing.

In order to keep the maximum bending moment constant at the base of the column, the storey force at the first floor level is evaluated in terms of the rest of the storey forces ensuring no addition of moment beyond state of the column at “yield”. The maximum additional curvature of the column plastic curvature model is then treated as an independent variable. At the end of each pushover analysis step, bending moments and curvatures are added up to obtain the total profiles along the height of the column.